5ᵗʰ European & African Conference on Wind Engineering

Under the auspices of IAWE

International Association
for Wind Engineering

FLORENCE ITALY 2009
JULY 19ᵗʰ-23ʳᵈ

Conference Proceedings

Edited by

Claudio Borri (Conference Chairman)
Giuliano Augusti
Gianni Bartoli
Luca Facchini

5th European & African Conference on Wind Engineering

Chairmen:

Claudio Borri (*Chairman*)
Piero D'Asdia (*Co-Chairman*)
Paolo Spinelli (*Co-Chairman*)

International Scientific Committee:

Giuliano Augusti (*Chairman*)
Gianni Bartoli (*Scientific Secretary*)
Chris J. Baker
Jasna Bogunovic-Jakobsen
Andrzej Flaga
Chris Geurts
Adam Goliger
Gerard Grillaud
Vittorio Gusella
Ruediger Höffer
John D. Holmes
Nick P. Jones
Ahsan Kareem

Kenny C. S. Kwok
Guy Larose
Chris W. Letchford
Jiri Náprstek
Hans J. Niemann
Udo Peil
Nikolai A.Popov
Emil Simiu
Giovanni Solari
Ted Stathopoulos
Yukio Tamura
Jacob A. Wisse
Alberto Zasso

Invited Referees:

Terje Leenhart Andersen
Bert Blocken
Arno Brand
Luca Bruno
Melissa D. Burton
Luigi Carassale
Xinzhong Chen
Cyril Fischer
Ondrej Fischer
Jörg Franke
Kurtis R. Gurley
Fred Haan
Peter A. Hitchcock
Erik Hjorth-Hansen
Norbert Hoelscher
Bert Holtslag
Michael Hortmanns

Tracy Kijewski-Correa
Jaromir Kral
K. M. Lam
Massimiliano Lazzari
Massimo Majowiecki
Claudio Mannini
Forrest Masters
Giuseppe Piccardo
Miros Pirner
Stanislav Pospíšil
Maria Pia Repetto
Jörg Sahlmen
Marie Studnickova
Jeroen van Beeck
Gerard van Bussel
Eddy Willemsen

Organising Committee:

Marcello Ciampoli
Luca Facchini (*Coordinator*)
Giorgio Federici
Massimiliano Gioffrè
Saverio Giordano
Vittorio Gusella
A. Luigi Materazzi
Salvatore Noè
Lorenzo Procino
Francesco Ricciardelli
Anna Saetta
Vincenzo Sepe

Conference Secretariat:

Gabriella Montagnani (*Coordinator*)
Nada Bek-Uzarov

Franco Crescioli
Università degli Studi di Firenze
Polo Biomedico e Tecnologico
Viale Morgagni, 85, 50134 Firenze (Italy)
e-mail: secretariat@eacwe5.org

The fifth European & African Conference on Wind Engineering follows the successful series started in Guernsey in 1993 and then continued by the conferences held in Genoa in 1997, Eindhoven in 2001 and Prague in 2005.
The Conference represents an opportunity to exchange researches and experiences among scientists, engineers and teachers in the field of wind engineering.

Università degli Studi di Firenze

Hosted by

CRIACIV

CENTRO DI RICERCA INTERUNIVERSITARIO
DI AERODINAMICA DELLE COSTRUZIONI E
INGEGNERIA DEL VENTO

Under the auspices and with the support of

International Association
for Wind Engineering

FOREWORD

Dear Reader, Dear 5th EACWE Attendee,

The International scientific community of Wind Engineers has found its way back to the Renaissance roots of science and technology and very likely to the original cradle of studies of Wind Engineering.

The 5th European-African Conference of Wind Engineering is hosted in Florence, Tuscany, the city and the region where, in the early 15th century, pioneers moved the first steps, laying down the foundation stones of Mechanics and Applied Sciences (including fluid mechanics). These origins are well reflected by the astonishing visionary and revolutionary studies of Leonardo Da Vinci, whose kaleidoscopic genius intended the human being to become able to fly even 500 years ago… This is why the Organising Committee has decided to pay tribute to such a Genius by choosing Leonardo's "flying sphere" as the brand of 5th EACWE.

After the previous conferences in Guernsey, Genova, Eindhoven, and Prague, wind engineers from Europe, Africa and overseas do not show to have become tired and less passionate about this fascinating topic: more than 120 contributions from all over the world (more than 30 countries) were accepted and accommodated within the 5 plenary and 4 parallel sessions in the 3 days of the technical programme of the conference. Recognising the very hard times and economic restrictions in research funding, this appears a quite lively and passionate response.

Participation from Africa has been given the highest priority, with the main goal of bridging over the Mediterranean sea the European and African research and education communities. Thanks to the help of IAWE, and with a specific action taken by the Organising Committee, the African Association for Engineering Education has been identified as partner in selecting some representatives of the disciplines related to Wind Engineering in Africa. I would like to take this occasion to forward a special and warm welcome to all African colleagues and friends, who might have been able to join us in Florence.

In addition to all "classical" branches and topics of studies in Wind Engineering, an ad hoc session on Wind Energy has been scheduled and successfully addressed by many qualified contributions. This might confirm how the scientific community of Wind Engineers considers the Wind Energy issue more and more relevant to its mission and social commitment. Wind Engineers definitely commit themselves for a cleaner and more environmental friendly technological development.

I wish a fruitful and interesting conference to all attendees and a very pleasant reading of this book of proceedings; last but not least, I shall warmly acknowledge here the work of all colleagues and friends involved in the Conference preparation.

Welcome to Florence!

Claudio Borri,
Chairman of 5th EACWE

TABLE OF CONTENTS

WIND CLIMATE AND ATMOSPHERIC BOUNDARY LAYER

MONITORING OF STRUCTURES AND VIBRATION CONTROL

HUMAN COMFORT, STANDARDS AND CODES

COMPUTATIONAL FLUID DYNAMICS (CFD) AND COMPUTATIONAL WIND ENGINEERING (CWE)

ROOFING SYSTEMS AND CLADDING

STATIC AND DYNAMIC WIND LOADS AND COMBINED EFFECTS

BARC (BENCHMARK ON THE AERODYNAMICS OF A RECTANGULAR 5:1 CYLINDER)

CABLE DYNAMICS

WIND EFFECTS ON SHIELDS AND VEHICLES

KEYNOTE LECTURES

Wind and tall buildings

Y. Tamura

*Director, Wind Engineering Research Center, Tokyo Polytechnic University –
yukio@arch.t-kougei.ac.jp l – 1583 Iiyama Atsugi, Kanagawa, Japan 243-0297*

Keywords: Tall Building, Equivalent Static Wind Load, Habitability, Damping Ratio, Vibration Control

ABSTRACT

This paper presents various topics related to "wind and tall buildings". Starting from some historical matters, it discusses wind related issues relevant to tall building constructions, wind-induced vibration of tall buildings and its monitoring, equivalent static wind load for structural design, design load problems for cladding design and frame design, habitability to building vibrations, damping in tall buildings, vibration control, elasto-plastic behavior of tall buildings, wind-induced vibrations of base-isolated tall buildings, and interference effects. Finally, it introduces future trends.

1. INTRODUCTION

Figure 1(a) shows an article that appeared in an Italian newspaper. It says "*The Mole Antonelliana collapses. An extraordinary wind storm occurred in Turin on May 23, 1953, breaking off the spire of the famous monument, and causing the collapse of a 45-meter length. The Mole Antonelliana was the*

 Contact person: Y. Tamura, Director, Wind Engineering Research Center, Tokyo Polytechnic University, 1583, Iiyama, Atsugi, Kanagawa, Japan 243-0297, TEL & FAX +81 46 242 9547.   E-mail yukio@arch.t-kougei.ac.jp

tallest masonry building in Europe (167.5 meters)" (Freda, 2009). The first tall buildings to appear in Japan might be the traditional wooden pagodas, first built more than 1,300 years ago, and which are still seen in old temples in historic Japanese cities such as Nara and Kyoto. It is often said that there are several reasons for the survival of these relatively tall slender wooden buildings, which have experienced many extremely strong earthquakes and typhoons over a long period. One is that the central pillar (so called "shinbashira") acts as a damping column that absorbs vibration energy. The central pillar contributes to the pagoda's stabilization by repeated contact and separation from the tower structure with increase in damping (Ishida, 1996). Shimada et al. (2003) conducted wind tunnel tests to investigate the aerodynamic characteristics of a five-story pagoda model and pointed out that the mean along-wind overturning moment coefficient is slightly less than that of a square prism with the same height and the same projected area. Furthermore, the crosswind fluctuating force coefficient is much smaller and its power spectrum does not have a clear Strouhal peak. The reason for the latter might be the effect of the five layered roofs preventing generation of coherent Karman vortices with a vertical axis. Even so, very strong typhoons could cause damage to pagodas. Figure 1(b) is a photo showing the 47.8m-high 5-story Shiten'noji Pagoda, which collapsed due to Tyhpoon Muroto on September 21, 1934. The maximum peak gust was estimated to be more than 60m/s. Thus, the history of the development of design and construction methods for tall buildings was a record of fights with strong winds. There are many wind-related problems in construction of tall buildings, but the main problem for engineers is their capability of resistance to wind forces, because higher altitudes mean higher wind speeds, and consequently higher wind forces. Gustave Alexandre Eiffel (1832-1923), famous for the "Eiffel-type wind tunnel" was also very eager to know the actual wind-induced behaviors of structures due to winds to validate his design assumptions concerning wind loads. He tried to conduct full-scale measurements of the response of the tower and of meteorological data including winds at the top of the completed 300m-high Eiffel Tower, then the world's tallest (Davenport, 1975).

(a) Mole Antonelliana (Turin, Italy, 1953)   (b) Shiten'noji Pagoda (Osaka, Japan, 1934)

Figure 1: A newspaper article reporting wind-induced damage to the Mole Antonelliana, which was the tallest masonry building in Europe (167.5m), on May 23, 1953, and collapse of the 5-story Shiten-noji Pagoda (47.8m), a wooden structure, on September 21, 1937.

Buildings and structures including tall buildings naturally have to resist not only wind forces, but also

different kinds of extreme design forces. Especially for tall buildings, the wind force and seismic force are the dominant external design forces, except in some special cases.

The peak horizontal ground acceleration for a strong earthquake can exceed the gravity acceleration of $9.8m/s^2$. For example, the Niigata Chuetsu Earthquake on October 23, 2004, in Japan recorded $13.08m/s^2$ for horizontal ground acceleration and the resultant acceleration of three components was $25.15m/s^2$. With this $13.08m/s^2$ horizontal acceleration, a standing person experienced a pushing force of more than 1.3 times his weight. For example, if his weight were 650N, he would be suddenly hit by a force of 850N force.

A strong typhoon, Maemi, struck Japan on September 11, 2003, and several anemometers at an experimental site for power transmission cables on the Miyakojima Island recorded peak gusts higher than 90m/s as the eye of the typhoon passed the island, as reported by Cao et al. (2009). Incidentally, the official highest peak gust recorded in Japan during a typhoon was 85.3m/s, and this was also recorded on the same Miyakojima Island, in 1966. Although it is obviously impossible, if a person were standing in such an extremely high wind condition, he would be pushed by a tremendously large wind force of more than 3,000N, which is 3 or 4 times the horizontal force caused by the largest level of earthquakes.

In some special regions such as eastern Asia, tall buildings need to resist extremely strong winds and extremely strong earthquakes. It is well known that light, flexible buildings are favorable for resisting seismic forces, while heavy, stiff buildings are favorable for resisting wind forces. Thus, tall buildings in such regions have to satisfy these two completely opposite design criteria, and this can be one of the most difficult design issues. In addition, there are many important issues to be resolved in the design stage, the construction stage, and even in the maintenance stage after completion of a tall building. Without integrated and comprehensive care during these three stages, satisfactory performance of a tall building cannot be expected. Many engineers have devoted themselves to finding good solutions to these problems, and to exploring new methods and technologies. This paper spotlights their efforts and discusses the current status and future trends.

2. WIND RELATED ISSUES WITH TO TALL BUILDING CONSTRUCTION

One of the main purposes of tall building construction is to efficiently utilize the limited land space in urban areas. For a given land space and a required building volume or total floor area, and only from the economical building construction view point, it is obviously better to make a building low-rise with the largest floor area as possible. Comparison of a single-story building and a tall building with the same floor areas shows that the construction cost of the tall building can be significantly larger than that of the low-rise building. However, it is true that potential tenants do not necessarily select low cost, low-rise building. If a building is to be used for economic activities, high cost becomes less important than high quality and high return potential. Business in a monumental or symbolic building such as at Burj Dubai can be more beneficial in some cases. Additionally, the ground floor area of a low-rise building may be 50 times that of a tall building, and the tall building is able to provide a much wider free public space.

Incidentally, if the surrounding area is affected by strong winds due to the construction of the tall building, it provides serious daily life difficulties for building occupants and others in the surrounding area, which may significantly harm the building plan.

2.1 Pedestrian level winds

Wind-induced environmental problems accompanied by tall building construction was first reported by Melbourne & Joubert (1971) and Lawson & Penwarden (1973), and many studies on these phenomena and assessment methods followed, e.g. Isyumov & Davenport (1975), Penwarden and Wise (1975), Gandemer (1975, 1978), Hunt et al. (1976), Cohen et al. (1977), Jackson(1978), Lawson (1978), and Murakami et al. (1979a, 1979b).

As reported by Goliger et al. (2004), a trend is evident in which the re-emergence of space between

buildings becomes a focus for city developments, leading to increased public spending on large-scale retail and leisure amenities. This is accompanied by a growing awareness of the public of their right to safe and comfortable public environments. This trend has led professionals in these environments to recognize the need to invest more time and money in the investigation of the pedestrian level wind environment, amongst other aspects that impact on people living and walking about in public spaces. Furthermore, with densification of urban areas, the importance and need for a proactive and comprehensive approach to environmental controls has become evident. The first Japanese case of negative social impact of wind affected by built environment was reported and publicly debated in 1968. This followed the construction of the 147m-high Mitsui Kasumigaseki Building in Tokyo, which was the first building over 100m high in Japan. This situation triggered research and development of methods and studies for evaluating the environmental wind impact of tall and large buildings in urban areas. The Environmental Effects Assessment Municipal Bylaw (EEAMB) has been enforced by the Metropolis of Tokyo since October 1981. The EEAMB requires wind environmental assessment based on an appropriately conducted wind tunnel study or CFD analysis for buildings more than 100m high and having a total floor area of over $10^5 m^2$. The EEAMB also recommends two assessment methods for wind environmental evaluations, i.e. Murakami et al. (1983) and WEI (1989). More interestingly, full-scale measurements of pedestrian level winds should be conducted one year before and after construction in order to validate the assessment made in the design stage.

It should also be noted that the Prevention and Mediation of Disputes Related to Medium- and High-rise Building Construction Municipal Bylaw (PMDMB) has been enforced by Tokyo Metropolis since October 1978 in order to resolve problems between inhabitants of areas surrounding construction sites and building developers. When the City Office receives a mediation request, a special committee guides both parties to seek resolution following the PMDMB, and in many cases, they can find a compromise and reach building agreement. However, in some cases, the talks escalate to a lawsuit.

A comparative analysis of various types of disputes and complaints were handled in terms of the PMDMB between 1994 and 2002 (Fujii, 2004, Goliger et al., 2004). The importance of various environmental issues in terms of the percentage of the total number of complaints indicates that most referred to shade and to privacy invasion. The wind-induced negative environmental impact due to tall building construction typically refers to around 12% of the cases. Trees including artificial trees, canopies, wind fences, wind shielding panels, and handrails for pedestrians are examples of various countermeasures to strong winds caused by tall building construction seen in Tokyo (Nakamura, 2009).

It had been very difficult for inhabitants to win wind environmental arguments, but the Osaka District Court first acknowledged and judged strong-wind effects due to construction of a 20-story, 56.9m-high condominium in Osaka on October 10, 2002 (Gologer et al., 2004). Although the fact of the strengthening of the wind speed due to a building construction has been well known by engineers for almost 40 years, it is very difficult for society to admit the degree of its social or human impacts. The Right to Wind Environment has been recognized by the public only recently.

2.2   *Wind-induced noise in tall buildings*

Wind-induced acoustic noises generated from corners of tall buildings, louvers, blinds, crosspieces, balustrades, ventilating openings, sashes and so on, annoy occupants, especially in the case of residential apartment buildings, hospitals and hotels. The generated acoustic noise strongly depends on the circumstances, conditions supporting sound sources, and aerodynamic and dynamic characteristics of sound sources, and a prediction method is not easy to generalize. In many cases, a study is made after the problem appears, and it is often accompanied by vibration problems and failure due to fatigue. Curle (1955) made a pioneer work in this field, and Berhault (1977) discussed wind noise in buildings. Suda & Yoshioka (1992, 1994) conducted full-scale measurements of wind-induced acoustic noises in medium-rise and tall buildings for residential use and discussed their

effects on amenity and occupants' discomfort.

   Bies et al. (1997), Nakato et al. (2000), Kitagawa et al. (2001), Haramoto et al. (2002), Suzuki et al. (2002), Casalino & Jacob (2003), Gloerfelt et al. (2005), Ohima et al. (2005), and Seo & Moon (2007) followed, and many recent studies are based on CFD analyses.

   The effects seem to be more serious for tall buildings, and further studies are necessary not only to solve acoustic noise problems but also to test and assess methods.

3. MONITORING OF WIND-INDUCED RESPONSES OF TALL BUILDINGS

Figure 2 shows the full-scale displacement in the along-wind direction of an actual tower 108m high, measured by GPS during strong wind. In Fig.2, the static, quasi-static and resonant components are also clearly identified.
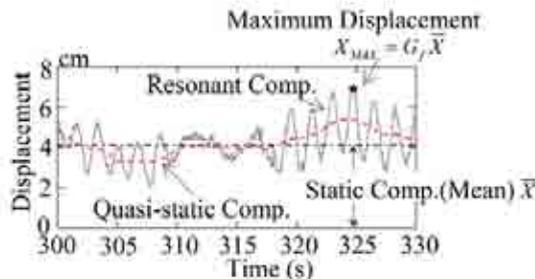
Figure 2: Wind-induced response of a 108m-high tower by GPS (Tamura et al., 2002a)

   As mentioned before, Eiffel (Davenport, 1975) conducted a pioneer work on response monitoring at the 300m-high Eiffel Tower (1889). The importance of response monitoring of tall buildings has been widely recognized and is becoming more significant. Many full-scale data of wind-induced responses of tall buildings have been reported, e.g. Campbell et al. (2005), Li et al. (2003, 2004), and Kijewski-Correa & David (2007). There are several objectives of response monitoring, such as to accurately identify dynamic properties of buildings, to validate methods of wind-induced response prediction, to directly provide necessary information for vibration control systems, to validate efficiency of vibration control devices, to update the FEM model, to check the integrity of structural frames of buildings (health monitoring, damage detection), and so on. A recent trend is the application of the GPS proposed by Çelebi (1998) to monitoring of tall building responses, e.g. Tamura et al. (2002a), Ogaja et al. (2003), Li et al. (2006), Kijewski-Correa et al. (2006a, 2006b), Hristopulos et al. (2007), Rizos et al. (2008), and Park et al. (2008), or its combined use with other transducers such as accelerometers and inclination sensors.

   Hybrid use of response monitoring systems and the FEM model can provide a real-time system for monitoring internal forces in structural members (Tamura et al., 2002), and there is a proposal to create virtual cities consisting of FEM models of tall buildings inside computers, to be installed in a comprehensive urban disaster prevention system (Tamura, 2003).

4. EQUIVALENT STATIC WIND LOAD

The equivalent static wind load (ESWL) reproducing the maximum response of a structure was first introduced by Davenport (1967) as the Gust Loading Factor (GLF) method. Structural design of a building is generally based on maximum "load effects", such as internal forces and stresses in structural members, and in some cases on the maximum story deformation or displacement of a

particular part of the building. The GLF by Davenport (1967) is calculated to reproduce the maximum tip displacement by taking into account only the first vibration mode, and the resultant ESWL is shown to be proportional to the mean wind force distribution. Accurate evaluation of the maximum load effect is very important in the structural design of a building, and many studies on the ESWL followed Davenport (1967), e.g. Simiu (1976), Solari (1982), Kasperski (1992), Davenport (1995), Tamura et al. (1996), Piccardo & Solari (2000, 2002), Zhou & Kareem (2001), Chen & Kareem (2001, 2004), Holmes (2002), Zhou et al. (2003), Repetto & Solari (2004), and Kwon & Kareem (2007).

4.1   Why is ESWL required?

Time domain dynamic response analyses using fluctuating pressure data obtained by a simultaneous multi-channel pressure measuring system (SMPMS) are conducted in the practical design of particular structures such as long-span roof structures, structures with non-linear dynamic characteristics, and buildings adopting non-linear damping devices (Tamura, 2003). Even for tall buildings with complicated sectional shapes changing along the vertical axis, as for many recent tall buildings, eccentricity causes complicated coupled motions of translational and torsional vibration components, and three-dimensional time-domain dynamic response analysis using those resultant fluctuating wind force components or by directly applying pressures obtained by the SMPMS is required to appropriately estimate the combined effects of the various wind force components and the resultant three-dimensional motions. Except for those examples, a simpler but sufficiently accurate method is required for wind resistant design. ESWLs reproducing maximum load effects have been examined for this purpose.

4.2   Is it necessary for ESWL to be a realistic distribution?

The next question is what is required for ESWL? Is it necessary for it to be a realistic distribution? Kasperski (1992) proposed the Load Response Correlation (LRC) approach based on a very sophisticated idea with an insight into the physical mechanism of the wind force and response relation, and Holmes extended it to incorporate proper orthogonal decomposition (POD). LRC can reproduce the most probable wind load distribution causing a particular maximum (minimum) wind load effect, as Tamura et al. (2002b) reported by comparing the LRC results and ensemble averaged actual pressure distributions causing maximum load effects, except for some special cases.

However, if the purpose of ESWL is to reproduce a specific target maximum load effect, any wind load distribution should be acceptable. Even a single concentrated force acting on any point of the structure will be fine, if the purpose is simply to reproduce a specific target load effect.

The GLF by Davenport (1967) assumed the following conditions for estimating the ESWL for a structure.
1 Mean displacement caused by mean wind load is almost proportional to the 1st vibration mode.
2 The contribution of the 1st vibration mode is predominant in the dynamic response and the contribution of other higher modes is negligible.
Under the above conditions, the distribution of the maximum displacement along the vertical axis of a tall building can be proportional to that of the mean displacement caused by the mean wind load. Therefore, even if the target load effect of the GLF is only the maximum tip displacement, the ESWL can also reproduce the maximum displacement at any other story. The temporary and spatially fluctuating pressure field acting on a building never shows the temporary averaged (mean) pressure distribution at any instance. Thus, the mean wind force distribution is a completely 'unrealistic' distribution, and in this regard, there is no difference from a single concentrated load.

Thus, the original ESWL proposed by Davenport (1967) was intended to reproduce not only the target maximum load effect, i.e. the maximum tip displacement, but also the other maximum load effects simultaneously, i.e. the maximum displacements of all other stories. By the way, the reason why Zhou & Kareem (2001) adopted the maximum base-bending moment rather than the maximum

tip displacement was to reproduce the maximum 'internal forces', which are more important than the maximum displacement in the general design of tall buildings.
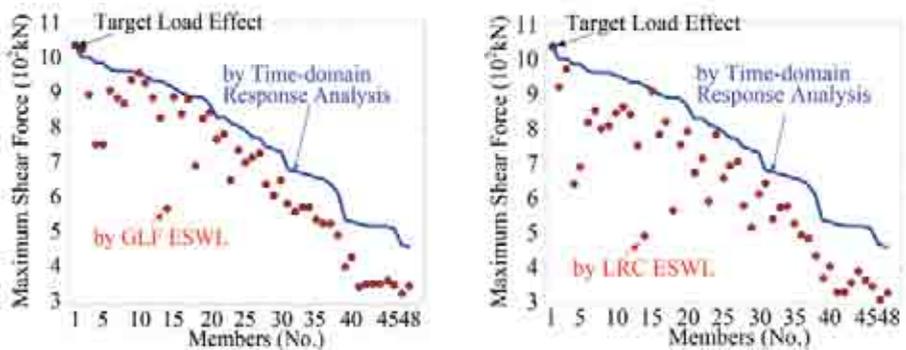
(a) Shear forces reproduced by GLF ESWL   (b) Shear forces reproduced by LRC ESWL

Figure 3: Comparisons of maximum shear forces reproduced by ESWL, GLF and LRC, and actual maximum shear forces obtained by dynamic time domain response analysis (Katsumura et al., 2007a)
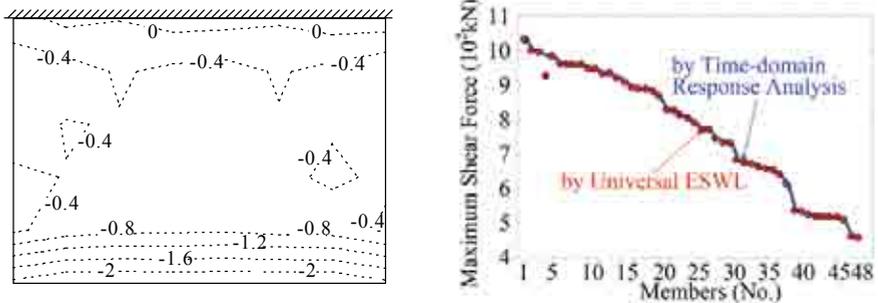
(a) Universal ESWL distribution   (b) Shear forces reproduced by LRC ESWL

Figure 4: Universal ESWL distribution and comparison of reproduced maximum shear forces and actual maximum shear forces obtained by dynamic time domain response analysis (Katsumura et al., 2007a)

As shown in Fig.2, the 1st mode contribution is predominant for the resonant component, but the dynamic response consists not only of the resonant component but also of the background component. The latter is not necessarily proportional to the first vibration mode, and the 2nd condition is not acceptable in some cases. Especially in the case of long-span roof structures, the higher mode contributions are very significant for the maximum internal forces in the structural members, and they never appear simultaneously. Thus, in general, the maximum internal forces appear at different instances, and the ESWL based on the LRC approach by Kasperski (1992) does not guarantee the maximum internal forces in members other than the target one. Figures 3(a) and 3(b) compare the reproduced maximum internal forces in all members of a simple cantilever roof structure obtained by the GLF method and the LRC method (Katsumura et al., 2007a).

The maximum shear force in Member No.1 obtained by time-domain dynamic response analysis showed the largest value of those in all other members, and it was selected as the target maximum load effect in the calculations of ESWL for both the GLF and LRC methods. Therefore, the maximum shear forces in Member No.1 reproduced by GLF ESWL and LRC ESWL completely agree with the actual shear force obtained by the time-domain dynamic response analysis as indicated in the figure.

However, the reproduced maximum shear forces in the other members are basically underestimated by both GLF ESWL and LRC ESWL. It is interesting that GLF ESWL, proportional to the 'unrealistic' mean wind force distribution, gives better estimation than LRC ESWL, based on the 'realistic' instantaneous wind force distribution. This is understandable because the internal forces in the other members do not necessarily reach their maximum values at the same time that the maximum internal force in the targeted Member No.1 appears. As mentioned before, the LRC approach is very sophisticated, and gives the most probable and realistic wind force distribution causing the maximum internal force in a target member (Tamura et al., 2002b). Thus, the LRC approach can catch the typical load distribution condition causing the maximum internal force (or the maximum load effect) in a target member (or at a target position). This strongly suggests that LRC ESWL is too typical for the target load effect, and not for other load effects.

It should be noted that a 'realistic' ESWL distribution is not necessarily better than an 'unrealistic' ESWL distribution in terms of reproduction of the maximum load effects for non-targeted members. Of course, a realistic ESWL-like LRC approach is useful for some particular purpose and has other advantages.

Anyway, it is obvious that the main purpose of ESWL is to reproduce the targeted maximum load effect, and it is also expected to reproduce other non-targeted maximum load effects. These two are very important requirements for ESWLs in practical applications, and it is also true that a 'realistic' wind force distribution essentially does not satisfy the latter requirement except in some special cases and only 'unrealistic' wind force distributions are possible.

Then, if these two requirements are the most important, the next question arises: "Why don't they directly seek an 'unrealistic' wind force distribution reproducing the maximum internal forces simultaneously in all structural members?" In answer to this question, Katsumura et al. (2004, 2005, 2007a, 2007b) proposed to use Universal ESWL to reproduce the maximum load effects in all structural members.

The Universal ESWL distributions are derived by an inverse analysis based on the actual maximum load effects in all members, which are obtained by the dynamic time domain response analysis applying a fluctuating pressure field obtained by SMPMS. Figure 4(a) shows an example of the Universal ESWL distributions, and Fig.4(b) compares the actual maximum shear forces reproduced by the Universal ESWL shown in Fig.4(a) and the actual maximum shear forces obtained by the dynamic time domain response analysis in all members. By applying the simple Universal ESWL distribution shown in Fig.4(a), almost all maximum load effects were almost perfectly reproduced.

It is well known that many novel ideas on ESWL have been proposed and recent improvement of the GLF method is significant. The Gust Front Factor has been proposed by Kwon & Kareem (2007) to envelope the GLF method and to reflect the effects of an unsteady flow field. More studies on ESWL including Universal ESWL are desirable.

5. CLADDING DESIGN AND FRAME DESIGN

There are two problems in the current codes and standards that need to be clarified. One is the different natures of the dynamic characteristics of a building in the elastic region and the plastic region, as shown later. The other is the recurrence periods of the design wind load for structural frames and for cladding/components.

Basically, in some current codes, the same GLF or Gust Response Factor (GRF) based on the dynamic behavior of a building in the elastic region is also used for the ultimate state design. It is necessary to clarify the availability of the "elastic GLF" or "elastic GRF" in the ultimate design stage, in which the building behaves in a plastic manner. Incidentally, in Japan, the ultimate design criteria for main structural frames allow member stresses to be within 1.1 times the allowable stress, i.e. only 10% larger than the elastic limit, so the building should behave in an "almost elastic manner". Thus, fully plastic behavior is not permitted and is not checked in design. Further studies are expected in

this regard.

   The other problem is the design wind load levels for structural frames and for cladding and components. They tend to design cladding and components based on a lower level wind load than the main structural frames, i.e. a shorter recurrence wind load is used for cladding design than for frame design. For example, according to the Building Standard Law of Japan (BSLJ), 50-year-recurrence wind loads are applied for structural frame design with allowable-stress design criteria, and the same recurrence wind loads are estimated for cladding and component design. However, 500-year-recurrence wind loads are applied for the ultimate state structural frame design, but only 100 or 200-year-recurrence loads are applied for cladding and components.

   Structural designers are interested in main frame design, but not in cladding design. However, wind-induced damage is generally triggered by small damage to cladding and components. This can be developed to a larger scale and more severe damage including that to main frames. This "coherent phenomenon" in damage progress is a special feature of wind-induced building damage. The fractured parts of cladding and components can easily become wind-borne debris, and strike downstream buildings. Debris impacts also initiate cladding and component damage to downstream buildings. This "chain of damage" is another special feature of wind-induced damage to buildings in urban areas.

   If the window panes and claddings of a tall building were damaged, property inside the building would be seriously damaged and lose its value, and this property loss could be very significant, especially if only the main structural frames remain. The miserable situation of a building with damaged window panes is often reported after extreme wind attacks in urban areas, e.g. Brewick et al., 2009. Furthermore, in general, the structural design of the main frames assumes the aerodynamic coefficient for the original shape of the building without cladding damage, so that the cladding and components are implicitly assumed to keep their original shape. Therefore, theoretically, there is no reason to accept a lower level of wind load for cladding, except for cases considering the possibility of change of aerodynamic coefficient or reaching a consensus with building owners and occupants or guaranteeing preventive measures of damage coherence or damage chain. It is said that claddings and components are replaced more frequently than main structural frames, so the existing return periods for them are shorter than that of main frames. It is also said that the design recurrence period for cladding and components can be less than that of main frames, but this discussion is not appropriate. A specific cladding element with a proper noun may become expired in a shorter period, but another cladding element with a different proper noun may replace it, and the cladding itself with a common noun always exists as long as the building exists. The replacement is only maintenance action to keep the element's quality up to the level assumed in the design stage. Thus, the existing shorter period of a specific cladding element has no meaning in wind load estimation. As cladding and component damage directly relates to the safety of building and property, the structural designer should play an important role in guaranteeing their performance during strong winds.

   A similar problem should be considered for the design wind loads of scaffolds for building construction, for those of buildings in the construction stage, and for those of so-called "temporary" structures such as site offices. For example, in Japan, the design wind load for scaffolds is defined as 1-year-recurrence wind load, because its average settling period at one construction site is around 6 months (Kasetsu Kogyo Kai, 1999). However, this design wind load estimation concept is completely wrong. Although the average period of the existence of a specific scaffold at an individual site is short, it moves to other places and it exists in the same city or area for a very long time. Even a specific scaffold with a proper noun cannot be used for a long period, many scaffolds with a common noun always exist in an urban area. Then, the acceptable probability of damage to those scaffolds should be discussed. Of course, it is not easy to determine an acceptable level of damage, because it depends on the importance of the target, social, economical and physical impacts of the damage, the economic situation of the society/nation, the historical aspect, and so on. However, it is clear that there is no relation between the design wind load level and its existing period at an individual site. Even if the average period of an individual rent of a rental car were one and a half days, the car cannot be designed based on the length of each individual use. By the way, they say that nets or sheets

covering scaffolding would be removed under strong wind conditions, so a lower level of wind loads can be applied for scaffolding design. This is also obviously doubtful. Removal of nets and sheets is an action of cure providing change of physical parameters such as wind force coefficient and projected area, and it cannot be a reason for reduction of the design wind speed level. Here, the design wind load should be determined based on the acceptable collapse rate or damage rate of the "so-called" temporary structures in the human society. This kind of study is also desired.

Even for the design wind load for main structural frames, the design load level may not be able to be determined based on a lifetime of an individual building. We are living in an individual building, but this building is an important element composing a city and a nation. The function of an individual building is of course important and should be considered in the design load estimation, but the function of the city and the nation is also very important. For the function of the city or nation, the proper nouns of its elements are not important: only the collapse or damage rate of the elements is important. As is well known, there is a concept for determining the optimal design load level based on the probabilistic consideration of the minimum life cycle cost (LCC) of a building including initial construction cost and estimated repairing cost for its estimated lifetime. However, although each building generally belongs to an individual as private property, it is one of the cells or elements composing a city or nation, and they are strongly related to each other as an economic function as well. The Business Continuity Planning (BCP) is an important issue not only for the private sector but also for a city or a nation, and securing BCP can be a key to the security of the city or nation. In particular, tall buildings have an aspect of social property, and damage to them has significant economic and social impacts on a community. Therefore, although the LCC concept is applied in design load estimation, the optimal design load level should be decided considering the city total or nation total LCC as a group of buildings, rather than optimization of the LCC of an individual building. In that case, the cost conversion of social security or national security should be included.

6. HABITABILITY TO BUILDING VIBRATIONS

There have been many studies on human comfort and habitability under building vibrations. Reed (1971), Jeary et al. (1988), Fujimoto and Ohkuma (1988), Tamura et al. (1988), Nakata et al. (1993), and Denoon (2000) studied human responses under full-scale conditions. Chen and Robertson (1973), Kanda et al. (1988, 1990), Shioya et al. (1992), Shioya & Kanda (1993), Nakata et al. (1993), Denoon (2000), Inoue et al. (2003), and Burton et al. (2003, 2006, 2007) conducted experimental studies under laboratory conditions using an artificial room mounted on an exciting facility. Melbourne & Cheung (1988) and Melbourne & Palmer (1992) proposed maximum peak acceleration criteria for any return period, and this was reflected in the AS1170.2-1989 Commentary (1989). There are several other guidelines relevant to the evaluation of habitability under horizontal vibrations of tall buildings: ISO6897 (1984), BS6841 (1987), ECCS (1987), NBCC (1990), ISO2631-1 (1997), AIJ-Guidelines (2004), and ISO10137 (2007). AIJ-Guidelines (2004) and ISO10137 (2007) adopt 1-year recurrence peak acceleration as an index, although ISO6897 refers to the root mean square (rms) value for evaluation of habitability under vibration. The main reason for this is that the peak or maximum value is more easily understood by designers, owners and occupants than the rms value. As both values can be converted by using a peak factor, there is no substantial difference between them. The reason for adoption of 1-year-recurrence peak acceleration is that this value relates more to daily comfort than extreme events.

Tamura (1998) summarized the probabilistic human perception thresholds by connecting the results for the low-frequency region from 0.125Hz to 0.33Hz by Shioya et al. (1992) and the high frequency region from 1.0Hz to 6.0Hz by Nakata et al. (1993), as shown in Fig.5(a). These experiments were made basically for uni-axial sinusoidal motions, but tests were also conducted for random motions and for bi-lateral elliptic motions simulating wind-induced building motions (Tamura, 2003). Randomness did not seem to affect the perception threshold. The perception threshold for random motions was almost the same as that for sinusoidal motions, as shown in Kanda

et al. (1990). Thus, the motion perception for wind-induced vibration of a building might be simply based on the acceleration amplitude and its predominant natural frequency. In Fig.5(a), probabilistic perception thresholds obtained for an actual 10-story building by Jeary et al. (1988) and the average perception thresholds obtained at two air-traffic-control towers and one port-operation tower by Denoon (2000) are also shown in Fig.5(a). They almost coincide with the laboratory data.

Figure 5(b) shows the AIJ-Guidelines (2004), which only give five curves: H-10, H-30, H-50, H-70 and H-90 instead of some recommended lines. The number of each curve indicates the perception probability as a percentage. Figure 5(c) compares other major codes. Incidentally, the ISO6897 minimum and average perception thresholds coincide with the lowest probabilistic perception threshold shown in Fig.5(a). ISO10137(2007) gives two guidelines, for "Office" and "Residence", and the given curve for "Residence" is close to the 90% level of the probabilistic perception threshold given in Figs. 5(a) and 5(b).

As did Kawana and Hisada (2002), Kawana et al. (2008a) conducted vibration monitoring of a tall building and questionnaire studies on occupants comfort, and reported that many occupants first perceive vibration by visual cues inside office rooms rather than by body sensation or outside visual cues. Kijewski et al. (2007) also pointed out the importance of visual cues in motion perception in tall buildings, in which standing occupants perceived vibration from outside views. Kawana et al. (2008b) studied the probability of seeing various visual cues in office and residential rooms, and Kawana et al. (2008c) discussed the motion perception probability only from visual cues inside rooms considering the probability of seeing visual cues. The probabilistic perception thresholds from "only visual cues" (OVC) are also indicated as Vis-1% - Vis-23% in Fig. 5(b) (Kawana et al., 2008c). In the low frequency region less than 2Hz, the OVC probabilistic perception threshold can be lower than the probabilistic perception threshold by only body sensation, thus suggesting that occupants in tall buildings perceive vibrations from visual cues rather than from body sensations.
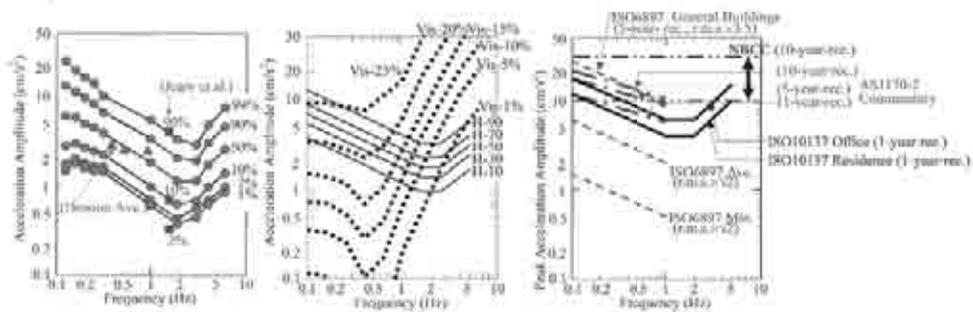
(a) Perception threshold by only body sensation

(b) Perception threshold by only visual cues and AIJ-Guidelines (2004) (H-10 - H-90)

(c) Habitability criteria/guidelines

Figure 5: Probabilistic perception thresholds for horizontal motions by only body sensation (Tamura, 2003), by only visual cues (residential buildings) (Kawana et al., 2008c), AIJ-Guideline (2004) and other habitability criteria and guidelines

Tamura et al. (2006) introduced two habitability evaluation methods: a deterministic method and a probabilistic method. The deterministic method based on probabilistic perception thresholds, i.e. H-10 - H-90 curves given in AIJ-Guidelines (2004), is used to decide a target criterion based on the database of the peak acceleration responses of existing non-complaint buildings with various different usages (Tamura et al, 2006). The probabilistic method is used to design the building to satisfy the criteria based on perception probability in terms of the target Perception Index, which is similar to the Reliability Index in the LRFD method (Kanda et al., 1993, Tamura et al., 2006).

Bashor & Kareem (2007) also proposed a probabilistic evaluation method based on FORM. These studies as well as accumulation of full-scale information are desired.

There are many problems to be solved: effects of visual cues, effects of acoustic cues, effects of postures, effects of mental and physical conditions, wide dispersions in individual differences in human comfort, effects of social and economic situations, only very few field data on the compliance rate, and so on. The problem is still far from being solved.

7. DAMPING IN BUILDINGS

Improvement and development of vibration measurement techniques and damping evaluation methods have enabled damping data to be made more reliable, e.g. Jeary (1986, 1992), Tamura and Suganuma (1996), Tamura et al. (2000, 2002c).

Figure 6 shows evidence of amplitude dependency of dynamic characteristics of buildings, and of the contribution of secondary members. It clearly shows that the damping ratio increases with amplitude, while the natural frequency decreases (Tamura and Suganuma, 1996). These results are attributed to the same physical reason, i.e. the contribution of secondary members and their stick-slip phenomena. In the small amplitude regime, connections, joints or contact surfaces of various building components stick to each other. However, if the amplitude increases, they begin to slip, thus providing friction damping but losing their stiffness. This is the main reason for the increasing damping and decreasing natural frequency with increase in vibration amplitude shown in Fig.6. However, if the amplitude reaches a certain level at which all connections slip, the number of slipping connections does not increase any more with increase in amplitude, and the damping ratio shows its peak. Tamura (2006) suggests the existence of a "critical tip drift ratio $(x_H/H)_{cr}$" at around 10^{-5} - 10^{-4}, where the damping ratio decreases with amplitude from the critical tip drift ratio.
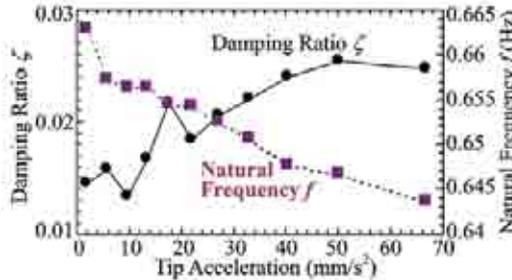
Figure 6: Variation of dynamic characteristics of a 99m-high steel-framed building (Tamura and Suganuma, 1996)

Tamura et al. (2000) recommended the following formula for the fundamental natural frequency f_1 (Hz) as a function of building height H(m), based on the Japanese Damping Database (JDD) compiled from reliable information on dynamic properties of 285 buildings, including necessary information on building dimensions, soil and foundation types, building usage, cladding types, amplitude level, measurement and evaluation methods, and so on.

$$f_1 = \begin{cases} \dfrac{1}{0.015H} = \dfrac{67}{H} \text{ (Low-amplitude)}, \dfrac{1}{0.018H} = \dfrac{56}{H} \text{ (High-amplitude): RC and SRC buildings} & (1a) \\ \dfrac{1}{0.020H} = \dfrac{50}{H} \text{ (Low-amplitude)}, \dfrac{1}{0.024H} = \dfrac{42}{H} \text{ (High-amplitude): S buildings} & (1b) \end{cases}$$

Ellis (1980) proposed a simple approximation for the fundamental natural frequency $f_1 = 46/H$ for buildings of all structural types, and this is widely used in some codes or standards. Japanese results for both RC/SRC and S buildings give a higher natural frequency than Ellis' proposal in the low amplitude regime, and those for RC/SRC-buildings also give higher values even in the high amplitude regime. Incidentally, higher mode natural periods are proportional to the fundamental natural period (Tamura et al., 2000).

Based on JDD and considering the amplitude dependency shown in Fig.6, formulae for predicting the fundamental damping ratios for RC-buildings and S-buildings are given as:

$$\zeta_1 = \begin{cases} 0.014 f_1 + 470 \dfrac{x_H}{H} - 0.0018 = \dfrac{0.93}{H} + 470 \dfrac{x_H}{H} - 0.0018 : \text{RC buildings} & (2a) \\[2ex] 0.013 f_1 + 400 \dfrac{x_H}{H} + 0.0029 = \dfrac{0.65}{H} + 400 \dfrac{x_H}{H} + 0.0029 : \quad \text{S buildings} & (2b) \end{cases}$$

These formulae consist of a frequency dependent term, an amplitude dependent term, and a constant. It is important that the frequency dependent terms, $0.014 f_1$ and $0.013 f_1$ in Eqs.(2a) and (2b), cannot be attributed to the frequency effect. It is likely to be due to the soil-structure interaction (SSI). The natural frequency of buildings is expressed with satisfactory accuracy by a simple function of height H, as shown in Eqs. (1a) and (1b). A building with a higher natural frequency is basically a lower-height building, where the SSI effects become more significant, resulting in a higher damping ratio. This is reflected in the frequency dependent term, and it may be more reasonably expressed by a function of building height H rather than natural frequency f_1, as shown in the above formulae. Incidentally, Eq.(5a) coincides closely with all the known full-scale amplitude data of RC-buildings in the database, and the correlation coefficient was estimated at 88% (Tamura et al., 2000). However, it should be noted that the formulae are essentially applicable within the range $x_H/H \le 2 \times 10^{-5}$. Based on the above results, recommendations for design damping ratios were made for "Habitability" level and "Safety" level (Tamura et al., 2000).

8. VIBRATION CONTROL

The accuracy of the structural damping in a building is very low, and there is a significant uncertainty in the predicted wind-induced responses; thus the reliability of structural design is also very low. However, a certain amount of damping is guaranteed by using damping devices, and the reliability of structural damping can thus be improved significantly.

The method of reducing the response by increasing the stiffness has been commonly applied in wind resistant design. Wind-induced displacement contains static and quasi-static components, which clearly decrease with increasing stiffness. If the stiffness K_S is doubled, the displacement is halved, because it is proportional to $1/K_S$. In addition, the sectional area is accordingly increased, which has a great effect in reducing member stress. However, the acceleration amplitude, which is usually a representative parameter in checking the habitability of a building to vibration, is the product of the displacement amplitude of the resonant component and the square of the circular natural frequency $(2\pi f_S)^2$. Because $(2\pi f_S)^2$ increases in proportion to stiffness K_S, its contribution cancels out the decrease in displacement due to the increase in stiffness. Thus, the acceleration does not decrease significantly. That is to say, the increase in stiffness does not lead to any improvement in building habitability to vibration (Tamura 2003).

Because the resonant velocity $U_{cr} = f_S D/S_t$ becomes higher when the stiffness is increased, the probability of vortex-induced vibration decreases. This is effective in reducing fatigue damage. However, since the aerodynamic force increases for higher wind speed, the vibration amplitude remains almost unchanged regardless of stiffness once vortex-resonance happens.

One feature in suppressing wind-induced vibration is the applicability of aerodynamic means. That is to say, it is possible to decrease the wind force input by changing the shape of the structure. Tall

buildings vulnerable to winds are slender and flexible structures, so it is important to develop a method for suppressing responses in the crosswind direction due to Karman vortices. There are many aerodynamic methods for suppressing vortex resonance of cylindrical structures: helical strakes, perforated shrouds, and slats. Other methods are chamfered corners, corner cutting, vented fins, opening holes (Dutton & Isyumov, 1990) for tall buildings and other prism-like structures. Chamfered corners and corner cutting are widely used for actual tall buildings. There are some proposals for using active aerodynamic devices such as rotors placed at the corners (Modi et al., 1995), jet flow control and so on. Opening holes in the top of the building can inhibit the formation of the Karman vortex, but it should be noted that there is a possibility of increasing response at low wind speeds, thus adversely affecting residential habitability.

Vibration can be controlled by disturbing coherent vortex shedding along the vertical axis by changing the sectional shape with building height. When the sectional shape is changed along the vertical axis, the vortex shedding frequency that corresponds to the sectional shape varies with building height. Thus, axially synchronized vortex shedding cannot be formed (Shimada & Hibi, 1995).

The wind-induced response of a structure is comparatively stationary compared with the seismic response, thus making it easier to apply a vibration control system. Vibration control systems for suppressing wind responses of tall buildings include Passive Tuned Mass Dampers (TMD), Hybrid Mass Dampers (HMD), Active Mass Dampers (AMD), sloshing-type Tuned Liquid Dampers (TLD), Visco-elastic Dampers (VED), Viscous Fluid Dampers (VFD), Oil Damper (OD), Semi-active Oil Dampers (SAOD), Steel Dampers (SD) and so on (Tamura 1990; 1998; Kareem et al., 1999). SD is not appropriate for wind-induced vibration considering the fatigue effect, but almost all are efficient under wind-induced motions. Their efficiency under seismic actions is limited, especially for extremely strong earthquakes. The urgency to install AMDs or HMDs in the early '90s seems to have waned, but considering their cost and maintenance as well as their efficiency, SD may currently be the most commonly used for strong earthquakes. VFDs and VEDs are also widely used for both earthquakes and winds (Tamura, 2003).

As introduced in Tamura (2003), another new trend in Japan is the use of more than two different types of damping devices for different design targets. Four different types of damping devices were installed in the Nippon TV Office (193m, completed in 2003): two TMDs for habitability under wind-induced vibrations, 32 ODs for wind-induced vibrations and weak/medium-class earthquakes, and 64 unbonded bracing dampers (SDs) and 312 link beam dampers (SDs) for extremely strong earthquakes. AMDs for habitability to wind-induced vibrations and SAODs for wind-induced vibrations and extremely strong earthquakes were installed in the Kajima Tower (172m, completed in 2003).

9. EALSTO-PLASTIC OSCILLATIONS OF TALL BUILDINGS

Present wind resistant design criteria generally require mostly elastic behavior for buildings in Japan, because it has not been clarified how they would behave in the non-elastic region under extremely strong wind conditions. Research has been carried out into elasto-plastic response behavior during wind excitation and a forecasting technique (Tsujita et al. 1997). Ohkuma et al. (1997) discussed the relation between power spectrum density of wind force and elasto-plastic energy, and proposed a response estimation method based on the application of energy balance to wind resistant design of buildings. However, these studies were based on the lumped mass system with a single mass or several masses under the bi-linear hysteresis assumption for each story or for the overall structure. Therefore, they do not clarify non-elastic behavior of members and the relationship between story and member deformations, making it impossible to pursue the fracture process of the building in the ultimate state.

In order to achieve performance based design, a building's performance around its ultimate limit state should also be examined. Tamura et al. (2001) described an analytical method that took into

account the non-linearity of individual members, and showed the relationship between member non-elastic behaviors and excitation duration in a time history response analysis. Then, the relationship between member fracture and overall structural behavior were discussed, and the following points were clarified. The level crossing number varies with member plasticity, the P-Δ effect causes a decrement of story shear force at yield point. The cumulative ductility factor is proportional to the excitation duration. Member fractures lower the natural frequency of the structure. Column bending moments increase drastically with beam end fracture, and just before a column fracture, the frame has already shown mostly unstable behavior due to long-columnization. Then, a column fracture immediately induces a structural collapse mechanism (Tamura et al., 2001).
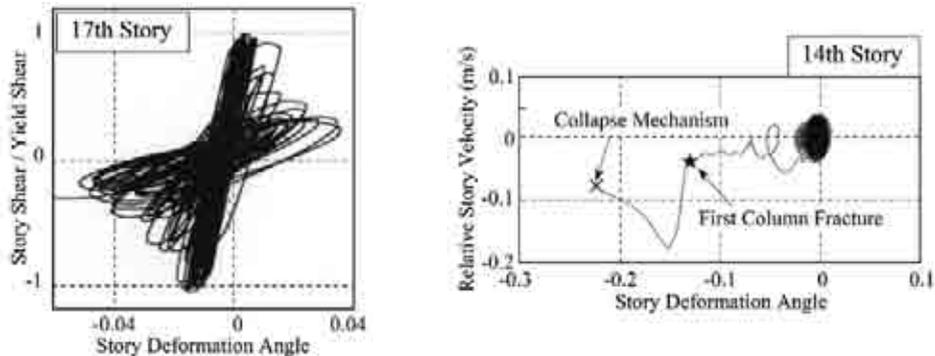
(a) Story shear force and story deformation   (b) Relative story velocity and story deformation
Figure 7 Story shear force and relative story velocity against story deformation angle
(50-story Model, 2000-year recurrence, 0min - 87.3min) (Tamura et al. 2001)

Figure 7(a) shows the relation between the story deformation angle and story shear force of a 50-story frame model (Tamura et al., 2001). The slope of the hysteresis inclines with the member fractures, thus showing decreasing stiffness. Therefore, the natural frequency of the model decreases. Figure 7(b) shows the relation between the story deformation angle and the relative story velocity response, where the orbit departed from the elliptic trace with a significant increase in the story deformation angle just before the beginning of a column fracture. This is induced by long-columnization. Immediately after the first column fracture, the relative story velocity response magnitude increased and reached the building's collapse mechanism. This suggests that the occurrence of plasticity in a column immediately results in a column fracture and collapse mechanism. Therefore, column plasticity or fracture should be avoided.

More studies of this kind may be necessary for wind-induced ultimate limit state design.

10. WIND-INDUCED OSCILLATIONS OF BASE-ISOLATED TALL BUILDINGS

Another recent special feature of tall building design in seismic regions is the adoption of the base-installation system. It is of course possible to design tall buildings to resist extremely strong earthquakes, even for the ground acceleration level exceeding gravity acceleration of $9.8 m/s^2$. One important problem that has recently arisen is excitation by long-period ground motions, which have not been taken into account in past earthquake-resistant design of tall buildings. The dominant period of the ground motion can be more than 5s, which can cause resonant vibrations of tall buildings (Irikura, 2005). However, even if the building structure is safe, the floor acceleration can exceed 1G or more in some cases, and occupants, furniture, and facilities on the floor face a very dangerous situation. Thus, tall buildings for residential use, hospitals, and so forth tend to use base-isolation systems. The base-isolation system aims to minimize the input seismic energy from the ground to the

upper building portion by using special supporting devices with damping systems. The natural frequency of a base-isolated building is longer than that of an ordinary building, because of the soft supporting system for the horizontal motion. Thus, wind-induced displacement of the upper building becomes larger than that of an ordinary tall building, and accurate estimation of the wind-induced displacement of the base-isolated tall building is important for checking the necessary clearance with surroundings. It is of course necessary to consider the combined effects of the along-wind, crosswind and torsional components, but more importantly, the dynamic characteristics of base-isolation devices are complicated.

(a) Lead Rubber Bearings (LRB)   (b) Wind-induced response of a model
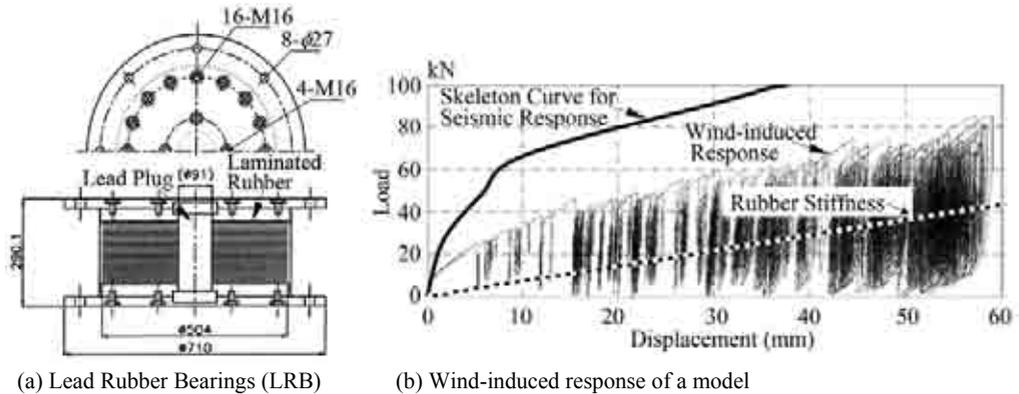
Figure 8: Base-isolation device (LRB) and experimental result of wind-induced response of a building model with LRB base-isolation system (Takenaka et al., 2004)

Takenaka et al. (2004) investigated the behavior of a tall building with a base-isolation system. The base-isolation device was the widely used LRB (Lead Rubber Bearing), which consists of a laminated rubber bearing with a lead plug at the center, as shown in Fig.8(a). Figure 8(b) shows an example of experimental results of wind-induced responses of a tall building model using a 1/2 model of the LRB device. The skeleton curve representing the load-displacement relation empirically obtained as the sum of the laminated rubber bearing stiffness and the lead plug stiffness is shown in the figure by the bold solid curve indicated as "Skeleton Curve for Seismic Design". The most important fact is that the wind-induced response of a tall building does not follow the skeleton curve, and sudden slip-like phenomena and the resonant vibrations are repeatedly observed. In general, the lead plug cannot work as stiffness for the static component and even for the quasi-static component of the wind-induced building response and the temporal variation of the mean-like displacement approximately follows the line representing the rubber stiffness. Thus, if the wind load is estimated at 60kN, the displacement cannot be 7mm as obtained by the skeleton curve, but reaches 40mm or more. This fact is not necessarily well considered in practical design.

11. INTERFERENCE EFFECTS

Wind loads on tall buildings in a group in real environments can be quite different from those on an isolated building. Such surrounding buildings or downstream buildings can significantly increase or decrease wind loads on buildings. Interference effect studies were carried out in the early seventies. This sudden interest could perhaps be traced back to the collapse of three of the eight natural draft cooling towers at Ferrybridge, England in 1965, which was attributed to interference effects (Armit, 1980). Interference effects have been studied by many researchers over the past several decades, e.g. Saunders & Melbourne (1979), Surry & Mallais (1983), Bailey & Kwok (1985),

Taniike (1992), Khanduri et al. (1998), Khanduri (2000), Thepmongkorn et al. (2002), Tang & Kwok (2004), Xie & Gu (2004), Gu & Huang (2005), and Zhao & Lam (2008).

Surry and Mallais (1983) reported on high suction near the ground and at the top of a building for spacing between two buildings and a building of unusual geometry, such as a sharp-cornered tower, but most past studies have focused on wind loads and induced responses of the target building for structural design. These studies have been carried out to try to codify wind loads caused by interference effects, and a comprehensive database is desired for codification and preliminary design, but this requires a huge number of wind tunnel experiments. However, studies to provide general recommendations have not been successful due to the complex nature of the problem and the large variation of building geometries, relative locations of adjacent buildings, wind directions, upstream terrain conditions and so on.

In practical design of tall buildings, interference effects on structural design loads and cladding loads have been examined by using wind tunnel tests with surrounding building models for individual cases. Then, a problem always arises: how to take into account future changes of the surrounding conditions.

12. FUTURE TRENDS

12.1 From compulsory to free style

Tall buildings have been traditionally designed to be symmetric rectangular, triangular or circular in plan, in order to avoid excessive seismic-induced torsional vibrations due to eccentricity, especially in seismic prone regions like Japan. However, recent tall building design has been released from the spell of compulsory symmetric shape design to free-style design.
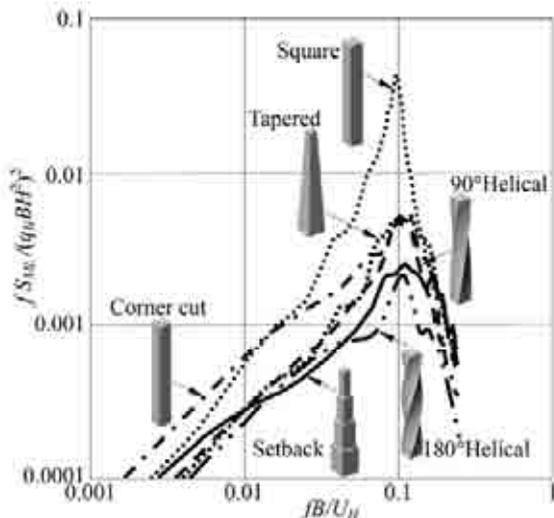
Figure 9: Crosswind overturning moment spectra for tall building models with various configurations (Tanaka et al., 2009)

This is mainly due to architects' and structural designers' challenging demands for novel and unconventional expressions. Development of computer aided analytical techniques and of vibration control techniques using auxiliary devices have also contributed to this trend. Another important

aspect is that rather complicated sectional shapes are basically good with regard to aerodynamic properties for crosswind responses, which is a key issue in tall building wind-resistant design. Figure 9 shows an example of wind-induced responses of tall building models with various configurations: square plan, with corner cut, tapered, with setbacks, 90deg helical, and 180deg helical (Tanaka et al., 2009). Comprehensive studies on the aerodynamic characteristics of various tall building configurations, and studies on corresponding optimal structural systems are necessary.

12.2 Strong needs of e-database based design

Not only for long-span roof structures, but also for tall buildings with complicated configurations, 3D time domain dynamic response analyses based on SMPMS may be necessary for precise studies on wind-induced behaviors in practical design. The current wind load codes and standards contain crosswind and torsional load estimation methods only for tall buildings with simple rectangular and circular sectional shapes, e.g. AIJ-RLB (2004). Therefore, wind tunnel tests using SMPMS are required. However, preliminary studies on wind-induced responses and loading effects should be made based on easier and expedient ways in the early stage of building design.

One way of meeting this requirement is to use e-database-based design (Whalen et al., 1998, Sadek & Simiu, 2002, Zhou et al., 2003, Wang et al., 2003, Tamura, 2003). The aerodynamic database was developed by several groups: NIST Aerodynamic Database (http://fris2. nist.gov/winddata/) at National Institute of Standards and Technology collaborated with The University of Western Ontario; NatHaz Aerodynamic Loads Database (http://www.nd.edu/~nathaz/ database/index.html) at The University of Notre Dame (Zhou et al., 2003, Kwon et al., 2008); *e-wind* (http://www.ce.tku.edu.tw/~ wind/English/english.htm) at Tamkang University (Cheng et al., 2008); and TPU Aerodynamic Database (http://www.wind.arch.t-kougei.ac.jp/system/eng/contents/code/w_it) at Tokyo Polytechnic University (Quan et al., 2007). This trend should be accelerated, and efforts should be made to accumulate and develop electronic aerodynamic databases.

In relation to this, it would be useful to accumulate and develop databases for Universal ESWLs and LRC ESWLs for various structural cases.

12.3 CFD studies for structural design and environmental problems

Recent development of CFD techniques for wind engineering applications is very significant both for the structural design field and the environmental assessment field. Two guides on numerical prediction were recently published by AIJ: AIJ-Guide-NPWLB (2005); and AIJ-Guidebook-CFDWE (2007). The former is for numerical prediction of wind loads on buildings and the latter is for numerical prediction of the pedestrian level wind environment in urban areas. Tamura et al. (2008) summarized the AIJ-Guide-NPWLB (2005) and emphasized that consistency of inflow turbulence characteristics for various numerical models is very significant for appropriate wind load estimation and an accurate time-dependent analysis such as LES is definitely required for wind load estimation.

Yoshie et al. (2007), Tominaga et al. (2008), and Mochida & Lun (2009) introduced and gave commentaries on the AIJ-Guidebook-CFDWE (2007). AIJ-Guidebook-CFDWE (2007) emphasizes a shift from the k-ε model to LES (Large Eddy Simulation) and DES (Detached Eddy Simulation), simulation of microclimates in urban areas (Yoshida et a., 2000a, 2000b), development of a software platform for integrated analysis of urban climate combining micro-scale and meso-scale analyses (Mochida et al., 2000, Murakami, 2004), and development of databases for the pedestrian level wind environment over a wide area based on 3D CFD analyses (CASBEE-HI, 2006) as a recent trend. Trials of hybrid analysis of a meso-scale meteorological model and LES to predict fluctuating wind fields in urban areas (Kishida et al., 2009), and development of virtual anemometers for forecasting wind speed and directions at any point to predict wind-induced damage to buildings by using a meso-scale meteorological model WRF (The Weather Research and Forecasting: http://wrf-model.org/index. php) (Maruyama, 2009) are especially noteworthy.

However, although the CFD technique is still incomplete and under development, careful but positive applications and development of its scope of applications are very necessary, because improvement and maturity of a technology cannot be made without its usage.

12.4 Make the most of cyberinfrastructure: Engineering Virtual Organization

Another recent novel project is an Engineering Virtual Organization named VORTEX-Winds (Virtual Organization for Reducing Toll of EXtreme Winds on society) (Kareem & Kijewski-Correa, 2008). VORTEX-Winds is a cyber-based collaboratory utilizing cyber infrastructure to share intellectual and physical infrastructures among participating member countries and organizations through its collaboration with the University of Notre Dame (ND). Development of VORTEX-Winds in collaboration with ND is one of the important features of the Global COE Program of Tokyo Polytechnic University (Tamura et al., 2008). VORTEX-Winds will house design and analysis modules and knowledge bases involving, for example, aerodynamic databases, wind resistant design databases, and wind hazard databases pooled together from different participants and development of *windwiki* for advancing research, knowledge and education in cyberspace. Successful examples of similar collaborations exist in various fields of science, meteorology and earthquake engineering (Kareem & Kijewski-Correa, 2008). The proposed VORTEX-Winds consists of two parts: E-analysis & Design Modules and Knowledge Base. The former is composed of six modules: Full-scale/Field Site Data Repository, Database-Assisted Design, Uncertainty Modeling, Tele-Experimentation Services, Statistical/ Stochastic Toolboxes, and Computational Platforms. The latter is composed of five bases: Wind-Wiki, Damage Database, Help Desk, Bulletin Boards, and Curriculum Tools. It can offer not only automated and integrated advanced design tools but also an advanced real-time global e-learning platform. Currently, fourteen research and educational organizations around the world are collaborating to develop VORTEX-Winds to share and complement individually owned intellectual and physical resources. Thus, VORTEX-Winds entails pooling of the resources of partners and collaborators from around the world to address problems at the frontiers of wind engineering utilizing cyber infrastructure. In this context, VORTEX-Winds can efficiently integrate CFD, database-based design, and other resources, and can dexterously cope with the future diversity of tall building design (Kareem & Kijewski-Correa, 2009).

Accurate response monitoring techniques and appropriate techniques for evaluating the dynamic properties of buildings enable updating of FEM structural models. Accurate FEM structural models enable prediction of wind-induced responses of buildings with the aid of the aerodynamic database or CFD techniques using the meso-scale meteorological model. A group of accurate FEM structural models of tall buildings compose a virtual city having structural reality in a computer. This virtual city made up in a computer can always be updated based on monitoring outputs, and would be expanded to a comprehensive urban disaster prevention system, and would also change the picture of structural design systems.

13. CONCLUDING REMARKS

This paper has discussed several topics on wind and tall buildings, especially the current status of wind resistant design of tall buildings and relevant state-of-the-art issues. However, some of them simply involve bringing up of questions and presenting problems to be solved, or doubts the author always has. Therefore, it is difficult to derive concluding remarks, but the author wishes that young researchers will try to meet these challenges to find solutions and directions to be taken in the future.

Finally, the author would like to emphasize the importance of development of EVO proposed by Kareem in our wind engineering community.

ACKNOWLEDGEMENTS

REFERENCES

AIJ-Guide-NPWLB (2005). "Guide for numerical prediction of wind loads on buildings, Architectural Institute of Japan, Maruzen, pp.249. (in Japanese)

AIJ-Guidebook-CFDWE (2007). "Guidebook for CFD application to wind environment in urban area", Architectural Institute of Japan, Maruzen, pp.207. (in Japanese)

AIJ-Guidelines (2004). "Guidelines for the evaluation of habitability to building vibration", Architectural Institute of Japan, Maruzen, pp.132. in Japanese

AIJ-RLB (2004). "Recommendations on Loads for Buildings", Architectural Institute of Japan, Maruzen, pp.651 (English version: 2006).

Amanuma S. (1937). "Record in Pictures of Japanese Architectures: Momoyama & Edo eras", Hoshino-shoten

Armitt, J. "Wind loading on cooling towers", *Journal of the Structural Division*., ASCE 1980, 106 (ST3), 623-641

AS 1170.2 (1989). "Australian Standard", SAA Loading Code, Part 2: Wind load.

AS1170.2-1989 Commentary (1989). "A Commentary on the Australian Standard for Wind Load (by Holmes, J.D., Melbourne, W.H. and Walker, G.R.)", pp.72.

Bailey, P.A. and Kwok, K.C.S. (1985). "Interference excitation of twin tall buildings", *Journal of wind Engineering and Industrial Aerodynamics*, 21, 323-338

Basher R., Kareem A. (2007). "Probabilistic performance evaluation of buildings: An occupant comfort perspective", Proceedings of the 12th International Conference on Wind Engineering, Cairns, Australia, July, 2007, 2, 1335-1342.

Berhault J.P.A. (1977). "Wind noise in buildings", Wind Engineering, 1(1), 67-82

Bies, D.A., Pickles, J.M., Leclercq, D.J.J. (1997). "Aerodynamic noise generation by a stationary body in turbulent air stream", Journal of Sound and Vibration, 204 (4), 631-643.

Brewick P., Divel L., Butler K., Bashor R., Kareem A. (2009). "Consequences of urban aerodynamics and debris impact in extreme wind events", Proceedings of the 11th Americas Conference on Wind Engineering, June 22-29, 2009, San Juan, Puerto Rico (to be published)

BS6841 (1987). "Measurement and evaluation of human exposure to whole-body mechanical vibration and repeated shock", British Standards Institute.

Burton, M.D., Denoon R.O., Roberts R.D., Kwok K.C.S., Hitchcock P.A. (2003). "A motion simulator to investigate wind-induced building motion", Proceedings of the 11th International Conference of Wind Engineering, Texas, USA, 1341-1348.

Burton, M.D., Kwok K.C.S., Hitchcock P.A., Denoon R.O. (2006). "Frequency dependence of human response to wind-induced building motion", Journal of Structural Engineering, ASCE, 132, 2, 296-303.

Burton, M.D., Kwok K.C.S., Hitchcock P.A. (2007). "Occupant comfort criteria for wind-excited buildings: Based on motion duration", Proceedings of the 12th International Conference on Wind Engineering, Cairns, Australia, July, 2007, 1, 1207-1214.

Campbell S., Kwok K.C.S., Hitchcock P.A. (2005). "Dynamic characteristics and wind-induced response of two high-rise residential buildings during typhoons", Journal of Wind Engineering and Industrial Aerodynamics, 93, 6, 2005, 461-482.

Cao S.Y., Tamura Y., Kikuchi N., Saito M., Nakayama I., Matsuzaki Y. (2009). "Wind characteristics of a strong typhoon", Journal of Wind Engineering and Industrial Aerodynamics, 97, 11-21.

Casalino, D., Jacob, M. (2003). "Prediction of aerodynamic sound from circular rods via spanwise statistical modelling", Journal of Sound and Vibration, 262 (4), 815-844

CASBEE-HI (2006). "Comprehensive Assessment System for Building Environment Efficiency on Heat Island Relaxation", Institute for Building Environment and Energy Conservation.

Çelebi, M. (1998). "GPS and/or strong and weak motion structural response measurements - Case studies", Structural Engineering World Congress '98, San Francisco, Conference Proceedings on CD-ROM, T193-1.

Chen, P.W. and Robertson, K.E. (1973). "Human perception thresholds to horizontal motion", Journal of Structural Division, ASCE, Vol.98, No.ST8, pp.1681-1695.

Chen, X. and Kareem, A. (2001). "Equivalent static wind loads for buffeting response of bridges." Journal of

Structural Engineering, ASCE, 127(12), 1467-1475.

Chen, X. and Kareem, A. (2004). "Equivalent static wind loads on buildings: New model." Journal of Structural Engineering, ASCE, 130(10), 1425-1435.

Cheng C.M., Wang J.M., Chang C.H. (2008). "e-wind: an integrated engineering solution package for wind sensitive buildings and structures", The 3rd International Symposium on Wind Effects on Buildings and Urban Environment (ISWE3), The 21st Century COE Program, WERC, Tokyo Polytechnic University, Tokyo, Japan, March 4-5, 2008, 127-136.

Cohen H., MacLaren T.I., Moss S.M., Petyk R., Zube E.H. (1977). "Pedestrians and wind in the urban environment", UMSS/IME/R-77/13, University of Massachusetts.

Curle N. (1955). "The influence of solid boundaries upon aerodynamic sound", Proceedings of the Royal Society, A, 231, 505-514.

Davenport, A.G., (1967). "Gust loading factors", Journal of Structural Division, ASCE, 93, pp.11-34.

Davenport, A. G. (1975). "Perspectives on the full-scale measurement of wind effects", Journal of Industrial Aerodynamics, 1, 23-54.

Davenport, A.G. (1995), "How can we simplify and generalize wind loads", Journal of Wind Engineering and Industrial Aerodynamics, 54-55, 657-669.

Denoon, R.O. (2000). "Designing for serviceability accelerations in buildings", PhD Thesis, The University of Queensland, Australia.

Dutton, R. and Isyumov, N. (1990). "Reduction of tall building motion by aerodynamic treatments",Journal of Wind Engineering and Industrial Aerodynamics, 36, pp.739-747

ECCS (1987). "Recommendations for the calculation of wind effects on constructions", TC12, No.52, European Convention for Constructional Steel Work.

Ellis, B.R. (1980). "An assessment of the accuracy of predicting the fundamental natural frequencies of buildings and implications concerning the dynamic analysis of structures", Proceedings of the Institution of Civil Engineers, Part 2, Vol.69, pp.763-776.

Freda A. (2009). University of Genova, *Personal Communication*.

Fujii K. (2004), Environmental Wind Research Inc., *Personal Communication*.

Fujimoto, M., Ohkuma, T. and Tamura, T. (1988). "Human response to wind-induced vibration of tall buildings", Proceedings Vol.I, Symposium/Workshop on Serviceability of Buildings (Movements, Deformations, Vibrations), Ottawa, pp.270-290.

Gandemer J. (1975). "Wind environment around buildings; Aerodynamics concepts", 4th International Conference on Wind Effects on Building and Structures, London, 423-432

Gandemer J. (1978). "Aerodynamic studies of built-up areas made by C.S.T.B. at Nantes, France", Journal of Wind Engineering and Industrial Aerodynamics, 3, 227-240.

Gloerfelt, X., Perot, F., Bailly, C., Juve, D. (2005). "Flow-induced cylinder noise formulated as a diffraction problem for low Mach numbers", Journal of Sound and Vibration, 287 (1), 129-151

Goliger A., Fujii K., Tamura Y. (2004). "Investigating and improving pedestrian wind comfort in windy cities: Case studies from Japan and South Africa", IV Symposium Environmental Effects on Buildings and people - Actions, influences, interactions, discomfort, Susiec, Poland, 16-18 June 2004

Gu, M., Xie, Z.N. and Huang, P. (2005). "Along-wind dynamic interference effects of tall buildings", *Advance in Structural Engineering*, 8(6), 623-635

Haramoto Y., Matsuzaki K., Munekata M., Ohba H. (2002). "An experimental and numerical study of aerodynamic sound generated from an inclined circular cylinder", The Journal of the Acoustical Society of Japan, 282-288. (in Japanese)

Holmes, J.D. (2002), "Effective static load distributions in wind engineering", Journal of Wind Engineering and Industrial Aerodynamics, 90, 91-109.

Hristopulos D., Mertikas S., Arhontakis I.; Brownjohn J. (2007). "Using GPS for monitoring tall-building response to wind loading: filtering of abrupt changes and low-frequency noise, variography and spectral analysis of displacements, GPS Solutions, 11, 2, 85-95

Hunt J.C.R., Poulton E.C., Mumford J.C. (1976). "The effects of wind on people; New criteria based on wind tunnel experiments", Building and Environment, 11, 1-28.

Inoue, K., Ishikawa, T. and Noda, C. (2003). "Evaluation curve and material to explain habitability of horizontal vibration -- Part 1 Evaluation curve based on perception by physical and visual feeling --", Summaries of Technical Papers of Annual Meeting, Architectural Institute of Japan, pp. 299-300 (in Japanese).

Irikura K. (2005) "Long period ground motion caused by strong earthquake and its countermeasure", Symposium on Development of Urgent Earthquake Warning Transmission System and Mitigation of Earthquake Disaster, National Research Institute for Earth Science and Disaster Prevention and REIC, Tokyo, October 14, 2005

Ishida S. (1996). "Scientific study on central pillar (Shinbashira), Why five-storied pagodas do not fall down", Edited by Ueda A., Shinchosha, 175-200 (in Japanese)

ISO2631-1 (1997). "Mechanical vibration and shock - Evaluation of human exposure to whole-body vibration- Part 1: General requirement, International Organization for Standardization.

ISO6897 (1984). "Guidelines for the evaluation of the response of occupants of fixed structures, especially buildings and off-shore structures, to low-frequency horizontal motion (0.063 to 1Hz)", International Organization for

Standardization.

ISO10137 (2007). "Bases for design of structures - Serviceability of buildings and walkways against vibration", International Organization for Standardization.

Isyumov N., Davenport A.G. (1975). "The ground level wind environment in built-up areas", 4th International Conference on Wind Effects on Buildings and Structures, London, Cambridge University Press, 403-422.

Jackson P.S. (1978). "The evaluation of windy environment", 13, 251-260.

Jeary, A.P. (1986). "Damping in tall buildings. A mechanism and a predictor", Journal of Earthquake Engineering and Structural Dynamics, Vol.14, pp.733-750.

Jeary, A.P. (1992). "Establishing non-linear damping characteristics of structures from non-stationary response time-histories", The Structural Engineer, Vol.70, No.4, pp.61-66.

Jeary, A.P., Morris, R.G. and Tomlinson, R.W. (1988). "Perception of vibration - Tests in a tall building", Journal of Wind Engineering and Industrial Aerodynamics, Vol.28, pp.361-370.

Kanda, J., Tamura, Y. and Fujii, K. (1988). "Probabilistic criteria for human perception of low-frequency horizontal motions", Proceedings, Symposium/Workshop on Serviceability of Buildings (Movements, Deformations, Vibrations), Vol.I , Ottawa, pp.260-269.

Kanda, J., Tamura, Y. and Fujii, K. (1990). "Probabilistic perception limits of low-frequency horizontal motions", Proceedings of the Conference with International Participation, Serviceability of Steel and Composite Structures, Pardubice, Czechoslovakia, pp.61-72.

Kanda, J., Tamura, Y., Nakamura, O., and Uesu, K., (1993). "Probabilistic criteria for serviceability limit of wind response", International Colloquium, Structural Serviceability of Buildings, Göteborg, Sweden, IABSE Reports, Vol.69, pp.59-66.

Kareem A., Kijewski, T. and Tamura. Y., (1999). "Mitigation of motions of tall buildings with specific examples of recent applications", Wind & Structures, An International Journal, 2-3, pp.201-251.

Kareem A., Kijewski-Correa T. (2008). "Next frontiers of innovation, discovery and learning in wind engineering: a cyberinfrastructure perspective", The 3rd International Symposium on Wind Effects on Buildings and Urban Environment (ISWE3), The 21st Century COE Program, WERC, Tokyo Polytechnic University, Tokyo, Japan, March 4-5, 2008, 1-17.

Kasetsu Kogyo Kai (1999). "Technical Recommendation for Safety of Scaffolding to Winds", 85

Kasperski M. (1992). "Extreme wind load distributions for linear and nonlinear design", Engineering Structures, 14 (1), 27-34

Katsumura A., Tamura Y. Nakamura O. (2004). "Universal equivalent wind load distribution reproducing maximum load effects on structural members", Proceedings, The 5th International Colloquium on Bluff Body Aerodynamics and Applications (BBAA V), Ottawa, Canada, 11 - 15 July, 2004, 351-354.

Katsumura A., Tamura Y., Nakamura O., (2005). "Maximum wind load effects on a large-span cantilevered roof", Structural Engineering International, IABSE, 15, 4, pp.248-251.

Katsumura A., Tamura Y., Nakamura O., (2007a). "Universal wind load distribution simultaneously reproducing largest load effects in all subject members on large-span cantilevered roof", Journal of Wind Engineering and Industrial Aerodynamics, 95, 1145-1165.

Katsumura A., Tamura Y., Nakamura O., (2007b). "Universal equivalent static wind load distribution on a large-span cantilevered truss roof", Proceedings, The 12th International Colloquium on Wind Engineering (ICWE12), Cairns, Australia, 1 - 6 July, pp.399-406.

Kawana S., Hisada Y. (2002). "Study on habitability of tall buildings to wind-induced motions", Summaries of Master's Thesis, Kogakuin University, 193-196 (in Japanese)

Kawana S., Tamura Y., Matsui M. (2008a). "Study on visual vibration perception -Full-scale measurement of vibration perception and time to see visual cues-", Proceedings of The 4th International Conference on Advances in Wind and Structures, Cheju-do Korea, May 2008, 1415-1425.

Kawana S., Tamura Y., Matsui M. (2008b). "Study of visual perception - Measurement and statistical analysis of the lengths of seeing time", Advances in Structural Engineering, 11, 4, 411-423.

Kawana S., Tamura Y., Matsui M. (2008c). "Study on visual motion perception - Estimation of probability of visual motion perception in consideration of length of setting eyes", Journal of Wind Engineering, JAWE, 33, 3 (116), 75-87. (in Japanese)

Khanduri, A.C. (2000). "Generalization of wind-induced interference effects for two buildings", Wind and Structures, 3(4), 255-266

Khanduri, A.C., Stathopoulos, T. and Bedard, C. (1998). "Wind-induced interference effect on building-a review state-of-the-art", Engineering Structures, 20(7), 617-630

Kijewski-Correa T., David P.J. (2007). "Dynamic behavior of tall buildings under wind: Insights from full-scale monitoring", The Structural Design of Tall and Special Buildings, 471-486.

Kijewski-Correa T., Kareem A., Kochly M. (2006a). "Experimental verification and full-scale deployment of Global Positioning Systems to monitor the dynamic response of tall buildings, Journal of Structural Engineering, ASCE, 132, 1242-1253

Kijewski-Correa T., Kilpatrick J., Kareem A., Kwon D.K., Bashor R., Kochly M., Young B.S., Abdelrazaq A.,

Galsworthy J., Isyumov N., Morrish D., Sinn R.C., Baker W.F. (2006b). "Validating wind-induced response of tall building: synopsis of the Chicago full-scale monitoring program", Journal of Structural Engineering, ASCE, 132, 1509-1523.

Kijewski-Correa T., Pirnia J., Bashor R., Kareem A., Kilpatrick J., Young B., Galworthy J., Isyumov N., Morrish D., Baker W. (2007). "Full-scale performance evaluation of tall buildings under winds", Proceedings of 12th International Conference on Wind Engineering, Cairns, Australia, July, 2007, 1, 351-358.

Kishida T., Tamura T., Okuda Y., Nakamura O., Miyashita K. (2009). "Hybrid analysis of meteorological model and LES for strong wind in urban area - Issue of numerical analysis on non-stationary natural wind-", Wind Engineering, JAWE, 34, 2, (119), 127-128.

Kitagawa M., Ogawa T., Masuda K., Nakayama M. (2001). "Occurrence mechanism of wind noise on balustrade in high-rise apartments", Summaries of Technical Papers, Annual Meeting, Architectural Institute of Japan, 119-120 (in Japanese)

Kwon D.K., Kareem A. (2007). "Gust-front factor: A new framework for the analysis of wind load effects in gust-fronts, Proceedings of the 12th International Conference on Wind Engineering, Cairns, Australia, July 1-6, 2007

Kwon D.K., Kijewski-Correa T., Kareem A. (2008). "E-analysis of high-rise buildings subjected to wind loads", Journal of Structural Engineering, ASCE, 134 (7), 1139-1153

Lawson T.V., Penwarden A.D. (1973). "Acceptable wind speeds in towns", Building Science, 8, 3, 259-267.

Lawson T.V. (1978), "The wind content of the built environment", Journal of Wind Engineering and Industrial Aerodynamics, 3, 93-105.

Li Q.S., Yang K., Wong C.K., Jeary A.P. (2003). "The effect of amplitude-dependent damping on wind-induced vibrations of a super tall building", Journal of Wind Engineering and Industrial Aerodynamics, 91, 9, 1175-1198.

Li Q.S., Xiao Y.Q., Wong C.K., Jeary A.P. (2004). "Field measurements of typhoon effects on a super tall building", Engineering Structures, 26, 2, 233-244.

Li X.J.; Ge L.L., Ambikairajah E., Rizos C.; Tamura Y.; Yoshida Y. (2006). "Full-scale structural monitoring using an integrated GPS and accelerometer system", GPS Solutions, 10, 4, 233-247

Maruyama T. (2009). "development of virtual anemometer forecasting damage to buildings and houses from strong winds", Wind Engineering, JAWE, 34, 2, (119), 147-148.

Melbourne W.H., Joubert P.N. (1971). "Problem of wind flow at base of the tall buildings", 2nd International Conference on Wind Effects on Buildings and Structures, Tokyo, 105-114.

Melbourne, W.H. and Cheung, J.C.K. (1988). "Designing for serviceable accelerations in tall buildings", Proceedings of the Fourth International Conference, Vol.1, Hong Kong & Shanghai, pp.148-155.

Melbourne, W.H. and Palmer, T.R. (1992). "Accelerations and comfort criteria for buildings undergoing complex motions", Journal of Wind Engineering and Industrial Aerodynamics, Nos.41-44, pp.105-116.

Mochida A., Murakami S., Kim S., Kondo H., Shimada A., Genchi Y., Yoshida S. (2000). "Development of software platform for total analysis of urban heat island, Proceedings of 16th National Symposium on Wind Engineeirng, November 29 - December 1, 2000, Tokyo, 137-148.

Mochida A., Lun I.Y.F. (2008). "Prediction of wind environment and thermal comfort at pedestrian level in urban area. Journal of Wind Engineering and Industrial Aerodynamic, 96, 1498-1527

Modi, V. J., Welt, F. and Seto M. L. (1995). "Control of wind-induced instabilities through application of nutation dampers: a brief overview", Engineering Structures, 17-9, pp.626-638

Murakami S., Uehara K., Komine H. (1979a). "Amplification of wind speed at ground level due to construction of high-rise building in urban area", Journal of Industrial Aerodynamics, 4, 343-370.

Murakami S., Uehara K., Deguchi K. (1979b), "New criteria for wind effects on pedestrians--- New criteria based on outdoor observations", International Conference on Wind Engineering, Colorado, 1-12.

Murakami S., Iwasa Y., Morikawa Y. (1983), "Investigation of statistical characteristics of wind at ground level and criteria for assessing wind-induced discomfort", Transactions of the Architectural Institute of Japan, 325, 74-84.

Murakami S. (2004). Indoor /outdoor climate design by CFD based on the software platform, International Journal of Heat and Fluid Flow, 25, 849-863

Nakamura O. (2009). Wind Engineering Institute, *Personal Communication*

Nakata, S., Tamura, Y. and Otsuki, T. (1993). "Study on habitability to horizontal vibration of low rise buildings", International Colloquium on Structural Serviceability of Buildings, Göteborg, Sweden, IABSE Reports, Vol.69, pp.39-44.

Nakato S., Kimura K., Fujino Y., Ogawa T. (2000). "Characteristics of aerodynamic sound from rectangular cylinder with various side ratios", Proceedings of the 16th National Symposium on Wind Engineering, 167-172. (in Japanese)

NBCC (1990). "National Building Code of Canada", Part 4 Structural Design, Chapter 4 Commentaries on Part 4 of the National Building Code.

Ogaja C., Wang J.L., Rizos C. (2003). "Detection of wind-induced response by Wavelet transformed GPS solutions", Journal of Surveying Engineering, ASCE, 129, 99

Ohima T., Terao M., Sekine H. (2005). "Estimation technique for aerodynamic sound radiation from a cylindrical body utilizing partial-span CFD results: its construction and validation through experimental analysis", Journal of Environmental Engineering, 15-22. (in Japanese)

Ohkuma, T., Kurita T., Ninomiya M. (1997). "Response estimation based on energy balance for elasto-plastic vibration of

tall building in across-wind direction", Structural Safety and Reliability, Proceedings of ICOSSAR'97, 1379-1386

Park H.S., Sohn H.G., Kim I.S., Park J.H. (2008). "Application of GPS to monitoring of wind-induced responses of high-rise buildings", The Structural Design of Tall and Special Buildings, 17, 1, 117-132.

Penwarden A.D., Wise A.F.E. (1975). "Wind environment around buildings", Building Research Establish Report, HMSO, pp52.

Piccardo, G. and Solari, G. (2000), "3-D wind-excited response of slender structures: Closed form solution, Journal of Structural Engineering", ASCE, 126,936-943.

Piccardo, G. and Solari, G. (2002). "3-D gust effect factor for slender vertical structures", Probabilistic Engineering Mechanics", 17, 143-155.

Quan Y., Tamura Y., Matsui M., Cao S.Y., Yoshida A. (2007). "TPU aerodynamic database for low-rise buildings", Proceedings of the 12th International Conference on Wind Engineering, Cairns, Australia, July 2-6, 2007, 1615-1622.

Reed, J.W. (1971). "Wind induced motion and human comfort", Research Report 71-42, Massachusetts Institute of Technology.

Repetto, M.P. and Solari, G. (2004). "Equivalent static wind actions on vertical structures", Journal of Wind Engineering and Industrial Aerodynamics, 92, 335-357.

Rizos C., Li X.J., Ge L.L., Tamura Y., Yoshida A. (2008). "How far could GPS go in monitoring structural response to wind events", Proceedings of the 13th Symposium on Deformation Measurement and Analysis, 4th IAG Symposium on Geodesy for Geotechnical and Structural Engineering.

Sadek F., Simiu E. (2002). "Peak non-Gaussian wind effects for database-assisted low-rise building design", Journal of Engineering Mechanics, ASCE, 128, 5, 530-539.

Saunders, J.W. and Melbourne, W.H. (1979). "Buffeting effects of upstream buildings", *Proceedings of the Fifth International Conference on Wind Engineering*, Fort Collins, Colorada, Pergamon Press, Oxford , 593-608

Seo, J.H., Moon, Y.J. (2007). "Aerodynamic noise prediction for long-span bodies", Journal of Sound and Vibration, 306 (3), 564-579.

Shimada, K. and Hibi, K. (1995). "Estimation of wind loads for a super-tall building (SSH)", The Structural Design of tall Buildings, Wiley, New York, 4, 47-60.

Shimada K., Matsui M., Yoshida A., Tamura Y. (2003). "Wind damage to five-story pagodas", Journal of Wind Engineering, 96, 7-20

Shioya, K. and Kanda, J. (1993). "Human perception thresholds of horizontal motion", International Colloquium on Structural Serviceability of Buildings, Göteborg, Sweden, IABSE Reports, Vol.65, pp.45-52.

Shioya, K., Kanda, J., Tamura, Y. and Fujii, K. (1992). "Human perception thresholds of two dimensional horizontal motion", Structures Congress '92, Compact Papers, ASCE, San Antonio, USA, pp.480-483.

Simiu, E. (1976), "Equivalent static wind loads for tall buildings design", Journal of the Structural Division, ASCE, 102, 719-737.

Solari, G. (1982), "Alongwind response estimation: closed form solution", Journal of the Structural Division, ASCE, 108, 225-244.

Suda K., Yoshioka K. (1992). "Full-scale measurements on generation of wind noise in high-rise apartments", The 12th National Symposium on Wind Engineering, Tokyo, Japan, November 30 - December 2, 1994, 61-66.

Suda K., Yoshioka K. (1994). "Full-scale measurements on wind-induced noise at tall apartments", The 13th National Symposium on Wind Engineering, Tokyo, Japan, November 30 - December 2, 1994, 95-100.

Surry, D. and Mallais, W. (1983). "Adverse local wind loads induced by adjacent building", *Journal of Structural Engineering*, ASCE, 109(3), 816-820

Suzuki M., Tamura T., Asahina T., Takaku K. (2002). "A study on aerodynamic sound generated from 2D rectangular cylinder: examination of separation and reattachment flow pattern", Proceedings of the 17th National Symposium on Wind Engineering, 95-100 (in Japanese)

Takenaka Y., Suzuki M., Yoshikawa K., Nakamura T., Kouchiyama O., Ikenaga M. (2004). "Simplified prediction method of wind-induced response of base-isolated tall building using LRB", The 18th National Symposium on Wind Engineering, Tokyo, 365-370

Tamura T., Nozawa K., Kondo K. (2008). "AIJ guide for numerical prediction of wind loads on buildings", Journal of Wind Engineering and Industrial Aerodynamics, 96, 1974-1984

Tamura, Y. (1990). "Suppression of wind induced horizontal vibration", Journal of Wind Engineering, JAWE, 44, pp.71-84.

Tamura, Y. (1998). "Application of damping devices to suppress wind-induced responses of buildings", Journal of Wind Engineering and Industrial Aerodynamics, Vols.74-76, pp.49-72.

Tamura, Y. (2003). "Design issues for tall buildings from accelerations to damping -- Tribute to Hatsuo Ishizaki and Vinod Modi --", Conference Preprints, The 11th International Conference on Wind Engineering, Vol.1, Lubbock, Texas, USA, 81-114.

Tamura Y. (2006). "Amplitude dependency of damping in buildings and estimation techniques", Proceedings of the 12th AWES Wind Engineering Workshop, Keynote Lecture, February 2 - 3, 2006, Queenstown, New Zealand, 17.

Tamura, Y. and Suganuma, S. (1996). "Evaluation of amplitude-dependent damping and natural frequency of buildings during strong winds", Journal of Wind Engineering and Industrial Aerodynamics, Vol.59, pp115-130.

Tamura, Y., Fujii, K. Sato, T., Wakahara, T. and Kosugi, M. (1988). "Wind-induced vibration of tall towers and practical

applications of tuned sloshing damper", Proceedings Vol.I, Symposium/Workshop on Serviceability of Buildings (Movements, Deformations, Vibrations), Ottawa, pp.228-241.

Tamura, Y., Kawai, H., Uematsu, Y., Marukawa, H., Fujii, K., Taniike, Y. (1996), "Wind loads and wind-induced response estimations in the Recommendations for loads on buildings", AIJ 1993, Engineering Structures, 18, 399-411.

Tamura, Y., Suda, K. and Sasaki, A. (2000). "Damping in buildings for wind resistant design", International Symposium on Wind and Structures for the 21st Century, Cheju, Korea, pp.115-130.

Tamura Y., Yasui H., Marukawa H., (2001). "Non-elastic responses of tall steel buildings subjected to across-wind forces", Wind and Structures, An International Journal, 4, 2, 147-162

Tamura Y., Yoshida A., Ishibashi R., Matsui M., Pagnini L.C. (2002a). "Measurement of wind-induced response of buildings using RTK-GPS and integrity monitoring", The Second International Symposium on Advances in Wind and Structures (AWAS'02), 599-606

Tamura, Y., Kikuchi H., Hibi K. (2002b). "Actual extreme pressure distributions and LRC formula", Journal of Wind Engineering and Industrial Aerodynamics, 90, 1959-1971

Tamura, Y., Zhang, L., Yoshida, A., Nakata, S. and Itoh, T. (2002c). "Ambient vibration tests and modal identification of structures by FDD and 2DOF-RD technique", Proceedings of the Structural Engineers World Congress, Yokohama, Japan, T1-1-a-1, pp.8.

Tamura Y., Kawana S., Nakamura O., Kanda J., Nakata S. (2006). "Evaluation perception of wind-induced vibration in buildings", Proceedings of Institution of Civil Engineers, Structures & Buildings, 159(SB5), 283-293.

Tamura Y., Ohkuma T., Ohno T., Ohba M., Yoshie R., Matsui M., Yoshida A., Cao S.Y., Kobayashi N., Ito K. (2008). "Toward new global frontiers in wind engineering - Summary of COE Program", The 3rd International Symposium on Wind Effects on Buildings and Urban Environment (ISWE3), The 21st Century COE Program, WERC, Tokyo Polytechnic University, Tokyo, Japan, March 4-5, 2008, 285-305.

Tanaka H., Tamura Y., Ohtake K., Nakai M., Hayano Y., Koshika N. (2009). "Study on wind force characteristics for super high-rise building with new shape, (Part 1) Comparison of wind force characteristics of various building shapes", Summaries of Technical Papers, Annual Meeting, Architectural Institute of Japan, B-1, Structures I, (to be published) (in Japanese)

Tang, U.F. and Kwok, K.C.S. (2004). "Interference excitation mechanisms on a 3DOF aeroelastic CAARC building model", Journal of wind Engineering and Industrial Aerodynamics, 92, 1299-1314

Taniike, Y. (1992). "Interference mechanism for enhanced wind forces on neighboring tall buildings", Journal of wind Engineering and Industrial Aerodynamics, 41-44, 1073-1083

Thepmongkorn, S., Wood, G.S. and Kwok, K.C.S. (2002). "Interference effects on wind-induced coupled motion of a tall building, Journal of wind Engineering and Industrial Aerodynamics, 90, 1807-1815

Tominaga Y., Mochida A., Yoshie R., Kataoka H., Nozu T., Yoshikawa M., Shirasawa T. (2008). "AIJ guidelines for practical applications of CFD to pedestrian wind environment around buildings", Journal of Wind Engineering and Industrial Aerodynamics, 96, 1749-1761

Tsujita, O., Hayabe, Y., Ohkuma T. (1997). "A study on wind-induced response for inelastic structure", Structural Safety and Reliability, Proceedings of ICOSSAR'97, 1359-1366

Wang J., Cheng C.M., Tens P.T. (2003). "Design wind loads on tall buildings: A wind tunnel data based expert system approach", Proceedings of the 11th International Conference on Wind Engineering, 1, Lubbock, Texas, USA, 511-518

WEI. (1989). New Guide to Wind Environment, revision of 1984ver., Edited by Wind Engineering Institute, Kajima-Shuppan. (in Japanese)

Whalen T., Simiu E., Harris G., Lin Y., Surry D. (1998). "The use of aerodynamic databases for effective estimation of wind effects in main wind-force resisting systems: application to low buildings", Journal of Wind Engineering and Industrial Aerodynamics, 77-78, 685-693.

Xie, Z.N. and Gu, M. (2004). "Mean interference effect among tall buildings", Engineering Structures, 26, 1173-1183

Yoshida S., Murakami S., Mochida A., Ooka R., Tominaga Y., Kim S. (2000a). "Influence of green area ratio on outdoor thermal environment with coupled simulation of convection, radiation and moisture transport", Journal of Architectural Planning and Environmental Engineering, Architectural Institute of Japan, 529, 77-84. (in Japanese)

Yoshida S., Ooka R., Mochida A., Tominaga Y., Murakami S. (2000b). "Study on effect of greening on outdoor thermal environment using three dimensional plant canopy model", Journal of Architectural Planning and Environmental Engineering, Architectural Institute of Japan, 536, 87-94. (in Japanese)

Yoshie R., Mochida A., Tominaga Y., Kataoka H., Harimoto K., Nozu T., Shirasawa T. (2007). "Cooperative project for CFD prediction of pedestrian wind environment in the Architectural Institute of Japan", Journal of Wind Engineering and Industrial Aerodynamic, 95, 1551-1578

Zhao, J.G. and Lam, K.M. (2008). "Interference effects in a group of tall buildings closely arranged in an L- or T-shaped pattern", Wind and Structures, 11(1), 1-18

Zhou, Y. and Kareem, A. (2001), "Gust loading factor: new model", Journal of Structural Engineering, ASCE, 127(2), 168-175.

Zhou, Y., Kijewski, T. and Kareem, A. (2003), "Aerodynamic loads on tall buildings: an interactive database", Journal of Structural Engineering, ASCE, 129 (3), 394-404.

Wind and risk

E. Simiu

National Institute of Standards and Technology – emil.simiu@nist.gov – Gaithersburg MD 20899-8611 -- USA

Keywords: Building technology, risk, performance criteria, structural reliability, wind engineering.

ABSTRACT

This paper surveys risk-related issues pertaining to the performance of structures in wind and the estimation of wind-induced losses. We consider risk within the framework of performance criteria, and provide illustrative examples of wind-related performance criteria developed for safe and serviceable designs. We note the role of uncertainties in specifying measures of risk and developing risk estimates, and the fact that this role is not adequately considered in ASCE 7 Standard design criteria applicable to tall buildings. We also discuss the role of wind speed and directionality effects in risk analysis. We review in some detail performance criteria on wind-induced incipient collapse, as well as methods for estimating mean recurrence intervals of incipient collapse for rigid structures. We point out that similar methods need to be developed for flexible structures. We define and compare nominal and effective risk-consistency, and review recent work on risks in multi-hazard situations. We then consider wind-induced losses, and note that large differences among estimates of such losses by various analysts are due to significant uncertainties in the estimation of extreme wind speeds, aerodynamic effects, and ultimate capacities of structural and architectural engineering components, connections, and assemblies. Finally, we discuss the design of structures with acceptably low risks and low consumption of materials/embodied energy.

Contact: E. Simiu, National Institute of Standards and Technology, 100 Bureau Drive, Gaithersburg, MD 20899-8611, telephone 1 301 975 6076, fax 1 301 869 6275.

1. INTRODUCTION

Risk in structural and architectural engineering can be defined as a measure of the probability that a structure or component thereof will fail to function as intended. In this definition allowance should be made – although it is not always made -- for uncertainties in the estimation of the failure probability. A limit state is characterized by a specified value of an appropriate measurable attribute of the structure's behavior. Exceedance of this value means that failure has occurred.   .

We are primarily interested in failures whose occurrence induced by wind causes a loss of function that is significant from the point of view of a user or an insurer. Examples are structural collapse, or roofing damage allowing water penetration. According to this perspective the exceedance of allowable stresses or the attainment of yield stresses are not failures. We make this distinction because we wish to focus on explicit measures of risks; exceedance of, e.g., the allowable stress can only serve as an implicit measure of risk, and is in and of itself of no significant concern to users. In view of this focus, we will consider risk within the context of performance criteria, in which measures of risk are stated explicitly. This context is useful for loss estimation purposes as well. However, we will also discuss criteria in which measures of risk are implicit.

Risk estimation is needed for the development of criteria governing the design of structures intended to remain functional when subjected to wind loads, under the constraint that costs -- including insurance premiums -- and the consumption of materials and energy are reasonably low, if not optimal. Improved estimates of risk are desirable because they help to achieve designs that are risk-consistent throughout a community and can thus help to enhance community resilience. In addition, risk estimation is needed for the prediction of wind-induced losses, and for the estimation of commensurate insurance costs, including costs covered by the insurer of last resort, the taxpayer.

It has been argued that probabilities of failure inherent in designs based on criteria consecrated by past experience can be assumed to be acceptably low, even though those probabilities are not known. This view has merit. However, past experience is not always directly applicable to novel technologies or practices. Invoking past experience can therefore be imprudent. The New Orleans levees are a case in point.

The estimation of risk is typically difficult, and is an art as much as a science. In structural engineering risks are typically associated with considerable knowledge uncertainties. This is the case, in particular, for estimates of the large mean recurrence intervals (MRIs) specified in safety performance criteria for typical structures, and even more so for MRIs of the order of 10^7 years specified in the U.S. for nuclear power plant designs. (The estimated point estimate of the MRI of an event, in years, is the inverse of the point estimate of the probability of exceedance of that event in any one year; point estimates are estimates that do not account for the existence of knowledge uncertainties.) Not accounting for uncertainties can result in seriously flawed risk estimates. Point estimates of a failure probability should be accompanied by estimates of the distribution of that probability, of which the point estimate is the mean. A percentage point of that distribution should be added to the point estimate to ensure, with adequate confidence, that the performance requirement is satisfied. (We will see that in some important cases this is not done.) The distribution itself depends upon the uncertainties in the individual factors involved in the estimation of risk. In wind engineering these factors include, among others, relevant micrometeorological parameters, aerodynamic coefficients, directional wind speeds, and parameters of the dynamic response.

The definition of acceptable measures of probabilities of failure and their specification are in principle not a structural engineering issue, but rather one involving economic and societal considerations. Nevertheless, structural engineering has much to contribute in this regard, through point estimates of failure probabilities inherent in existing structures, and estimates of corresponding uncertainties, which can provide some guidance to decision makers. Performing estimates of uncertainties is not a simple exercise. First, uncertainties can be so large that inferences on risks

inherent in existing structures may not be helpful in practice. Second, even if this problem did not exist, it is likely that the structures for which estimates would be made would not be mutually risk-consistent, meaning that the inferences made from their analysis would depend upon the type of structure being analyzed.

The purpose of this paper is to survey risk-related issues pertaining to the performance of structures in wind and to the estimation of wind-induced losses. The paper is organized as follows. Section 2 discusses the main elements of typical performance criteria, specification of risk being one of those elements. Section 3 considers attributes, limit states, and acceptable risks defining a number of performance criteria for structures under wind loads. Section 4 discusses wind speed estimation and directionality effects, and points out the distinction between MRIs of wind speeds specified in standards and codes and MRIs of the response to wind. Section 5 considers performance criteria on wind-induced incipient collapse, reviews methods allowing the estimation of mean recurrence interval of incipient collapse for rigid structures, comments on the usefulness of these models for assessing risks inherent in various structures designed by Strength Design criteria, notes the need for similar methods for flexible structures, and discusses nominal vs. effective risk-consistency in design. Section 6 discusses the distinction between nominal risks– risks of exceeding limit states defined by allowable stresses or the attainment of yield stresses, – and effective risks – risks of attaining limit states that are undesirable from a safety point of view (e.g., incipient collapse). Section 7 reviews recent work on risks in multi-hazard situations. Section 8 is devoted to wind-induced losses, and notes that large differences among estimates of such losses by various analysts are due to significant uncertainties in the estimation of extreme wind speeds, aerodynamic effects, and the ultimate capacities of structural and architectural engineering components, connections, and assemblies. Section 9 summarizes conclusions of this work.

2. CONSTITUTIVE ELEMENTS OF TYPICAL PERFORMANCE CRITERIA

A performance criterion pertaining to a specific function of a building or structure must contain the following elements:

1 The definition of a physical, measurable attribute of the behavior of the structure or its site.
2 A functionally meaningful, quantitative specification of that attribute, that is, *a limit state*.
3 Estimates of the risk induced in the structure by the hazard(s) to which the structure is exposed, that is, of the MRI of any specified state associated with the attribute of concern. To be useful, risk estimates must be accompanied by estimates of uncertainties associated with them.
4 A specification of the MRI of the limit state that is acceptable from the point of view of the structure's functionality.

The following is an example of performance requirement: Peak accelerations at the top floors of a building should not exceed 15 mg (0.15 m/s^2) (g denotes the acceleration of gravity) more than, on average, once in 10 years. In this example the measurable attribute is the acceleration, and the limit state is an acceleration of 15 mg. The limit state is functionally meaningful in the sense that occupants subjected to the effects of states more severe than the limit state would be susceptible to debilitating discomfort, and has been established by ergonomic research performed in the 1970s on the relation between building motion and occupant discomfort. Estimates of risks of exceeding those thresholds can be obtained by performing analyses based on aerodynamic tests, directional wind climatological data, models of directional dynamic response and its interfacing with directional wind speeds, and statistical models of stochastic response to wind. Research into levels of tolerance of limit states by building occupants has tentatively established that 10 years is an acceptable MRIs of the 0.15 mg limit state. Building owners have a strong interest in performance requirements with respect to acceleration being satisfied, lest buildings become unattractive to potential buyers or renters.

3. PERFORMANCE CRITERIA: EXAMPLES OF ATTRIBUTES, LIMIT STATES, AND ACCEPTABLE RISKS UNDER WIND LOADS

Criteria designed to assure acceptable functionality are developed and enforced so that costs associated with unserviceable and/or unsafe structures be reduced or eliminated. In this section we briefly describe elements of some performance criteria relevant to safety and serviceability, and in particular the respective acceptable risks.

Serviceability is defined by the non-occurrence of, among others,

1. Pedestrian discomfort due to winds at the ground level near or within the building (e.g., in passageways). The relevant attributes are wind speeds in pedestrian areas, as amplified by the surrounding built environment. Tentative performance criteria are listed, e.g., in (Penwarden and Wise, 1975), in which it is suggested that complaints about wind conditions are not likely to arise if, in pedestrian areas, winds with mean speeds $V > 5$ m/s are estimated to occur less than 10 % of the time. Complaints might arise if such speeds are estimated to occur between 10 % and 20 % of the time. Estimated frequencies higher than 20 % correspond broadly to situations where in existing shopping centers remedial action of various types had to be taken to reduce wind speeds. Methods for estimating the frequency of exceedance of various wind speeds at a site are reviewed in (Penwarden and Wise, 1975; Simiu and Scanlan, 1996). Failure to satisfy such performance criteria has entailed business losses and even serious accidents.

2. Occupant discomfort due to wind-induced tall building motions. The relevant attribute is a measure of the building acceleration at the top floors (e.g., peaks, or r.m.s.). See the example in Section 2 and Simiu and Scanlan (1996). An additional attribute may pertain to relative motions with respect to surrounding buildings, which can be particularly disturbing when torsion is significant.

3. Loss of integrity of cladding and partitions in tall buildings experiencing drift. A relevant attribute is the peak inter-story drift. Tentative criteria require that it not exceed, say, 1/300 to 1/600 of the story height or an absolute limit of, say, 10 mm, whichever is smaller, on average more than once in 20 years. In general the criteria depend upon type of construction, and are controlled by architectural engineering considerations on the one hand, and cost considerations – including cost of insurance -- on the other. Note that the 20-yr MRI requirement implies high probabilities of exceedance of the maximum acceptable drift, that is, about 2/3 in a 20-yr period, and 9/10 in a 50-yr period.

4. Loss of integrity of openings, roofing, and secondary members (Fig. 1) due to high local wind

Figure 1. Damage to community center building, Gulfport, Mississippi, following Hurricane Katrina (2005). Photograph by L. T. Phan.

pressures. The relevant attributes are the strength of glass, doors and roofing, the use or otherwise of protective devices (shutters) for openings, the ability of roofing systems to prevent water penetration, and the strength of secondary members and their connections. Damage to openings can be prevented through the use of specially designed temporary protective panels installed prior to the passage of a hurricane.

5. Loss of integrity of cladding/openings exposed to wind-borne missiles. Relevant attributes are position with respect to sources of wind-borne missiles, and whether protective devices are provided on openings prior to a storm.

Safety is defined by the non-occurrence of:

6. Structural collapse. Decades of vigorous research into nonlinear behavior under seismic loads have led to the development of criteria requiring that structures be designed so that the maximum considered earthquake (MCE) induces a state short of structural collapse (American Society of Civil Engineers, 2006). This assures that collapse due to the MCE, with the consequent loss of life, does not occur. The nominal MRI of that state is 2,500 years (or, equivalently, its probability of exceedance is 2 % in 50 years). No comparable research has been performed to date for structures under wind loads. For this reason safety margins with respect to a state short of structural collapse under wind loads are typically those implicit in either Allowable Stress Design (ASD) or Strength Design (SD).

7. Excessive deformations. It is conceivable that under the action of powerful winds the structure could experience nonlinear deformations so large as to necessitate extensive structural repairs. What those deformations and their probabilities of exceedance should be might be determined in the future with a view to developing appropriate performance criteria.

8. Loss of integrity of roof-to-wall and wall-to-foundation connections in low-rise buildings such as, e.g., single-family homes. The relevant attributes are the ultimate strength of the connections and their deformations under wind loads. Nominal MRIs typically exceed those of wind speeds associated with SD.

9. Loss of integrity of openings, roofing, and secondary members. Items 4 and 5 above are also of concern from a safety viewpoint insofar as such loss of integrity can result in large increases in internal pressures that can lead to roof collapse and other significant structural damage. Nominal MRIs are typically the same as for item 8 above.

10. Loss of integrity of structural components, connections, and assemblies in nuclear power plants exposed to hurricane or tornado winds and wind-borne missiles. The relevant attributes are the strength of the elements in relation to wind-induced pressures and to specified types of missiles and their speeds, and the location of the targets with respect to sources of wind-borne missiles. In the U.S. risks being considered in design are typically of the order of 10^{-6}/yr or 10^{-7}/year.

4. WIND SPEED AND DIRECTIONAL EFFECTS ESTIMATION. MRIs OF WIND SPEEDS VS. MRIs OF WIND-INDUCED RESPONSE

4.1. Estimation of Extreme Wind Speeds

Wind speed estimation is an art that has not yet been fully mastered. Debates concerning the estimation of extremes continue to revolve around the following questions:

1. Is it legitimate to assume that inferences on wind speeds of interest in studies of collapse can be made from 20- to 100-yr data sets? This question pertains not only to, e.g., synoptic or thunderstorm winds, for which the data consist of strong wind speeds, but also to hurricane wind speeds, for which the data consist of climatological features of hurricanes (pressure defect, radius of maximum wind speeds, and so forth). One answer to this question is provided by estimates of the sampling errors in the estimation of extreme wind speeds (see Simiu and Miyata, p. 37), for the Gumbel distribution; similar expressions are available or can be derived for reverse Weibull distributions). Measures of the

uncertainty in the estimation of the wind speeds must be included in the uncertainty estimate for the wind effect being considered, see, e.g. (Minciarelli, 2001; Simiu et al., 2008).

2. How strong is strong, i.e., how low are the wind speeds that may be included in meaningful data sets used to make inferences on extremes? This question concerns two main applications. The first application is the use of peak-over-threshold methods (Scanlan and Miyata, p. 29; Harris, 2006; Simiu, 2007). If the threshold is too low, that is, if among the wind speeds included in the sample are speeds that are meteorologically unrepresentative of extreme wind speeds, the estimates will be biased. If only very high wind speeds are included in the sample, then the estimates will be imprecise. The correct estimates are selected literally by eye from a set of estimates performed for various values of the threshold. The second application is the use of low wind speeds in epochal sets or in the out-crossing approach to the estimation of wind directionality effects (Simiu and Miyata, pp. 29 and 142). In general the estimates, based as they are on winds unrepresentative of extremes, may be expected to be biased unconservatively, especially for long MRIs of the wind effects; see also (Isyumov et al., 2003).

3. Is it legitimate to assume that extreme wind speeds can be inferred from extreme value distributions other than the Gumbel distribution? This question is dealt with in some detail in (Harris, 2006). One argument against the use of reverse Weibull distributions is that they are valid only in an asymptotic sense, and would need to be based on very large sets of data to be appropriate; hence the Gumbel distribution should be used instead. In fact, exactly the same argument concerning asymptotic validity would be applicable to Gumbel distributions; there is no reason to single out other extreme value distributions from the point of view of asymptotic behavior. Reverse Weibull distributions are used in the Australia/New Zealand Standard (2002).

4. How should – and how should not – data from distinct stations be combined into "superstations?" The extreme wind estimates for non-hurricane regions adopted by the ASCE 7 Standard based on "superstations." In our opinion, those "superstations" lack any defensible meterological, climatological, and statistical rationale [11], and their adoption is an example of inadequate oversight on the part of standards committees. Spatial statistics is a mature field, and its results and methods could in the future be applied to the development of improved wind maps [12].

5. How should extreme wind speeds be estimated in regions in which the wind hazard is associated with more than one type of wind, e.g., synoptic winds and thunderstorm winds, or hurricane and non-hurricane winds? The equation governing the estimation of extreme wind speeds, V_1 and V_2, associated with two types of storm, is

$$\text{Prob}(V_1 < v \text{ and } V_2 < v) = \text{Prob}(V_1 < v)\,\text{Prob}(V_2 < v) \tag{1}$$

For a recent application of this approach to a region with both thunderstorm and non-thunderstorm strong winds see Lombardo et al. (2009). The same equation can be applied to hurricane-prone regions for the purpose of estimating wind speeds of interest in design for serviceability.

4.2 Wind directionality effects

To clarify the role of wind directionality we consider directional wind speeds in three successive wind storms for which we assume that winds blow from just two directions. Let the wind speed time series v_{ij} (in m/s) consist of three storm events ($i=1, 2, 3$) with two wind directions ($j=1, 2$):

      Event 1: 54 (dir. 1), 47 (dir. 2),
      Event 2: 41 (dir. 1), 46 (dir. 2),
      Event 3: 47 (dir. 1), 39 (dir. 2).

This set of data describes the wind speeds themselves as well as their dependence on direction. The description of the wind speeds in the three storm events that considers only the maximum wind speed in each event is the following:

      Event 1: 54
      Event 2: 46

Event 3: 47.

Clearly, this description contains less information. This loss of information comes at a price. To see why, consider the case where the aerodynamic coefficients $C_{p,j}$ for the two directions are

0.8 (dir. 1), 1.0 (dir. 2)

The corresponding nominal wind effects are assumed to be, to within a constant dimensional factor, equal to the quantities $C_{p,j}v_{ij}^2$. For the three events, the quantities $[C_{p,j}v_{ij}^2]^{1/2}$ are equal to the squares of the quantities $[C_{p,j}v_{ij}^2]^{1/2}$. For the three events, these quantities are

Event 1: 48 (dir. 1), 47 (dir. 2),
Event 2: 37 (dir. 1), 46 (dir. 2),
Event 3: 42 (dir. 1), 39 (dir. 2),
(e.g., for event 1, dir. 1, $[0.8 \times 54^2]^{1/2}=48$).

Since for each storm event it is the *largest* nominal wind effect that matters, for design purposes we extract from those quantities the following time series (in m/s):

Event 1: 48
Event 2: 46
Event 3: 42

Assuming further that the rate of occurrence of the storm events is 1/yr, it follows from the above calculations that the largest and second largest of these quantities are, respectively, 48 and 46 m/s. The wind effects are proportional to the squares of these quantities, that is, to

2304 and 2116 $(m/s)^2$

respectively. If the calculations were performed without accounting for the directionality of the wind speeds, and the largest pressure coefficient (i.e., $C_p=1$) were used for all directions, then the largest and the second largest of the quantities $[\max_j(C_{p,j})\max_j(v_{ij}^2)]$ would be 54^2 and 47^2, that is,

2916 and 2209 $(m/s)^2$.

A 0.85 directionality reduction factor has been adopted in ASCE 7 to account summarily for directionality effects on rigid buildings. However, estimates of extreme wind effects based on that blanket factor, rather than accounting explicitly for wind directionality, can be in error either on the conservative or unconservative side. Multiplication of the 2916 $(m/s)^2$ and 2209 $(m/s)^2$ wind effects by 0.85 would yield largest and second largest wind effects of

2480 and 1878 $(m/s)^2$,

rather than 2304 and 2116 $(m/s)^2$, as obtained by using a physically realistic model. Note that the largest of the wind effects estimated by disregarding wind directionality and using the blanket directionality reduction factor (i.e., 2480 $(m/s)^2$) is conservative with respect to the largest physics-based estimate of the wind effect (i.e., 2304 $(m/s)^2$). However, if the second largest wind effect were of interest, the difference between the result based on the use of the directionality factor (1878 $(m/s)^2$) and the physics-based result (2116 $(m/s)^2$) would be -11 %, that is, in this instance the directionality factor approach used in ASCE 7 yields an unconservative estimate).

It is commonly assumed that the MRI of the wind effect associated in ASCE 7 with non-directional wind speeds is the same as the nominal MRI of those speeds. This assumption is in general not correct. For example, in our illustration it would be assumed that the ranking of the wind effect induced by the 47 m/s non-directional speed associated with storm event 3 is two. In fact, if directional effects are taken into account, the ranking of the wind effect induced by storm event 3 is three.

The approach just described is applicable to any wind effects, including pressures, dynamic response, and sums of demand-to-capacity ratios used in axial force-bending moments interaction equations. The approach amounts to converting a multi-dimensional time series consisting of the effects of *m* storms in *p* directions into a one-dimensional time series consisting of the largest effects induced by the *m* storms, regardless of their direction. To use terminology introduced in structural reliability, we do not operate in the space of wind speed variables, but rather in the space of wind

effect variables. This approach to the point estimate of the MRI of the wind effects of interest is non-parametric. Figure 2 represents a wind speed and direction dependent response surface for the demand-to-capacity index of a member of tall building analyzed in [14]. Once such a response surface is developed, a one-dimensional time series of that index can be constructed from the matrix of directional wind speeds simulated for a large number of storm events. The value of that index for any MRI can be obtained immediately from that time series and the mean rate of occurrence of the storm events.
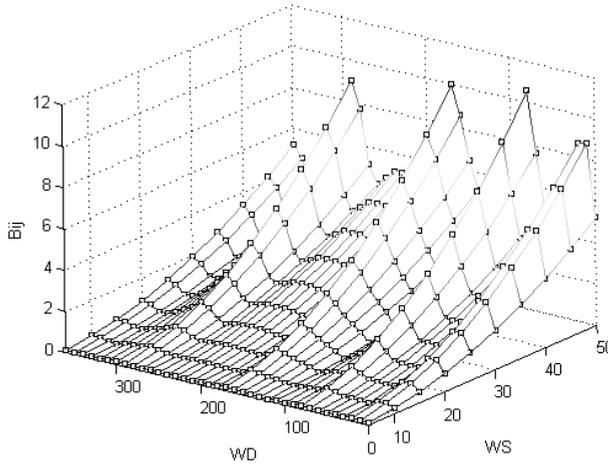
Figure 2. Response surface representing a member's demand-to-capacity index b_{ij} as a function of wind speed WS and direction WD (Spence, 2009).

5. INCIPIENT COLLAPSE

In attempting to define a limit state associated with structural collapse we propose to follow the philosophy inherent in the ASCE 7 Standard provisions for seismic design, as indicated in item 6 of Section 3. We therefore suggest that a relevant limit state is one that is relatively close to but not entailing collapse properly so called, that is, a state of *incipient collapse*. Incipient collapse is associated with the onset of non-convergence due to large deformations calculated by nonlinear finite element analyses with implicit solution schemes. (When a structure is near collapse, the computation of its state of stresses, strains, displacements and rotations is highly nonlinear and prone to divergence in implicit schemes. The usual ways of making progress in the computation at that stage involve reducing the time step (or load increment), removing elements that are no longer able to carry additional loads due to buckling, yielding or other reasons, and using so-called arc length (or Rik's) iterative scheme. These methods are computationally intensive and require frequent user interventions, but they typically do not produce much gain in terms of adding to the time required for full collapse to occur. For these reasons, the concept of incipient collapse was introduced to allow an end to the analysis. In this case, the numerical scheme fails to converge, the analyst has made reasonable efforts to move forward, and engineering judgment indicates that hinges and collapse mechanisms have begun to form, or removal of "hot members" leads to rapid propagation of high levels of distortion to other members.)

We further suggest that the acceptable MRI of the wind-induced incipient collapse event is 2,500 years. Longer MRIs might be appropriate for hospitals, buildings containing expensive equipment, and so forth. Whether our suggestion is acceptable or not should be determined by professional consensus. It can be argued that life safety considerations may not be applicable to wind events, for

which -- unlike for earthquakes -- there may be sufficient lead time for evacuation. However, even if this were true for all storms, it would be desirable that structures have residual integrity if hit by what, to adapt a term used in seismic design practice, we will call the maximum considered windstorm, that is, the windstorm that induces the limit state with a 2,500-yr MRI we just defined.

Is the 2,500-yr MRI criterion satisfied by structures designed in accordance with SD provisions? The answer depends on type of structure. For some structures the post-linear strength reserves may be small; i.e., winds with 1,000-yr point estimates of the MRI, say, may be able to produce incipient collapse (a point estimate is an estimate that assumes knowledge uncertainties are negligible). Such structures would be regarded as unsafe even though they satisfy the ASD or SD criteria. For structures specially designed so that their post-linear strength reserves are large the estimated MRI of incipient collapse can be as high as 100,000 years (Duthinh et al., 2008). In other words, nominal risk-consistency consisting of conformity of member design with SD criteria -- the conceptual linchpin of the ASCE 7 Standard, -- does not achieve effective risk-consistency, that is, consistency in terms of failure probabilities as defined in this paper. Effective risk-consistency can be achieved by implementing our proposed criterion, or alternative criteria accepted by professional consensus, either through ad-hoc nonlinear analyses or through simplified procedures, which remain to be developed, based on extensive nonlinear studies similar to those performed in recent decades for the development of seismic design criteria. Such procedures could help designers consider the possibility of saving materials for structures whose MRIs of incipient collapse are more than one order of magnitude larger than 2,500 years.

5.1 Incipient collapse of rigid structures

We now briefly review recent results obtained by using finite element analyses on rigid structures designed by ASD (Jang et al., 2001; Duthinh et Al. 2008). If wind directionality is explicitly taken into account [14], the point estimate of the MRI of incipient collapse is obtained by performing analyses, similar to pushover analyses, based on directional wind pressure coefficients available in aerodynamic databases. The methodology developed for this purpose is as follows.

1. For each wind direction j, obtain the critical wind speed V_j that, given the pressure coefficients for that direction, will cause the frame to experience incipient collapse. For the m directions for which wind speeds are available in the wind speed database, m wind speeds V_j ($j=1, 2,..., m$) – one for each wind direction -- will cause incipient failure. This set of m wind speeds is a property of the structure.

2. Consider the m directional wind speeds v_{ij} ($i=1, 2, …, n; j=1, 2,…, m$) in each of a large number of storms n for the location of interest (see, e.g., www.nist.gov/wind, Section I, Data Sets, Item 5). Replace each directional wind speed v_{ij} by a "0" if that wind speed is smaller than critical wind speed V_j and by a "1" if it is equal to or greater than V_j. Create a one-dimensional time series consisting, for each storm i, of a "0" if in that storm $v_{ij} < V_j$ for all j ($j=1, 2, …, m$), and of a "1" if $v_{ij} > V_j$ for at least one direction j. To fix the ideas assume $n=9$, and that the one-dimensional time series is

$$(0, 0, 1, 0, 0, 1, 0, 0, 0).$$

Further, assume that the mean arrival rates of the storms is $u=0.5$/yr. The MRI of the incipient failure event is

$$\text{MRI}=1/\{1 – \exp[-u(q/(n+1))]\}=1/\{1-\exp[-0.5(2/(9+1))]\}=9.5 \text{ years},$$

where $q=2$ is the number of storms, out of the total of 9 storms, that produce incipient failure (Simiu and Myata, pp. 34-35). A simpler, more approximate expression, which does not account for the possibility that more than one strong storm can occur in any one year, is

$$\text{MRI}=[(n+1)/q]/0.5=10 \text{ years}.$$

This methodology requires the availability of directional wind speed data for a large number of storms. Typically, data are available for only a relatively small number of storms. To obtain data for the larger number of storms that are required for estimates of the MRI of incipient collapse it is necessary to augment the available wind speeds database. A procedure for doing so, and the attendant software, were developed by Grigoriu (2009) and are available on www.nist.gov/wind.

The estimate of the MRI of incipient collapse just discussed is a point estimate, i.e., it does not account for the effect of the uncertainties in the various component factors of the wind loading and response. In particular, the material properties are assumed to be deterministic. This is convenient, because redundant systems are analogous to parallel systems (as opposed to systems in series), and can involve multiple failure paths, depending upon correlations of members and connection strengths, which are typically unknown. Should only uncertainties associated with the loading be involved, the design load would correspond to a percentage point (e.g., to the 90th percentile) of the probability distribution of the wind effect of interest. Determining such a distribution would require a large number of nonlinear analyses, which we believe would be impractical in the present state of the art. We will discuss subsequently how the distribution of the wind effect can be determined in the simpler case where only linear analyses are required.

The analysis of a typical industrial building portal frame reported in (Duthinh et al., 2008) resulted in a very long MRI of incipient collapse (about 100,000 years) for a structure that had two unusual features: a triangular stiffener at each column support, and a diagonal member abutting on a horizontal and a vertical stiffener at the haunches (Fig. 3). In the absence of these features the MRI of incipient collapse was one to two orders of magnitude lower, even though the ASD criteria were equally satisfied in both cases. Nonlinear analyses can provide a measure of the actual safety benefit of the additional expense entailed by the provision of features like those of Fig. 3. We do not advocate performing nonlinear analyses routinely, at least not in the present state of the art, in which such analyses remain onerous. However, fundamental studies comparable to studies performed for seismic designs would improve the code writers' ability to produce more differentiated and effective design criteria.

(a)   (b)
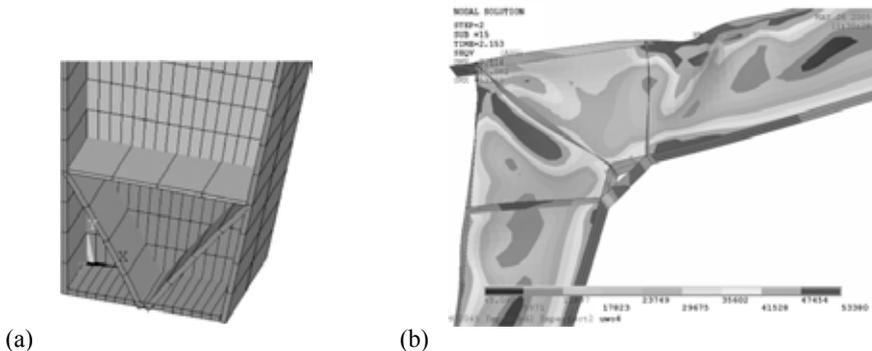
Figure 3: (a) Triangular stiffener at column support; (b) left haunch, von Mises stresses in psi (1 psi= 0.006895 MPa) (Duthinh et al., 2008).

5.2. Incipient collapse of flexible structures

No nonlinear analyses have to our knowledge been performed for dynamically sensitive structures under wind loads. We believe that such analyses, aimed at estimating MRIs of incipient collapse or of specified nonlinear deformations, should be conducted by using methods similar to those applied for

nonlinear seismic analyses, in which stiffness matrices are updated as calculations march in time. These methods would yield only approximate results because, among other reasons, the dependence of damping on deflections is not well understood. The experience of earthquake engineering researchers could be useful in this respect.

The design of flexible structures is commonly governed by inter-story drift criteria. When this is the case, member sizes are larger than required to satisfy SD criteria, hence the MRI of incipient collapse would be larger than would be the case in the absence of serviceability constraints. The extent to which this is the case can be reduced through the provision of tuned mass dampers or other means of controlling deformations due to fluctuating wind loads.

5.3. Aeroelastic effects due to wind speeds with very long MRIs

It is necessary for safety reasons to consider aeroelastic effects on tall, slender buildings under winds with MRIs longer than, say, 750 years (the MRI associated with SD criteria). Vortex-induced oscillations typically occur at relatively low speeds and do not increase monotonically with wind speed. However, winds with long MRIs can produce destructive aeroelastic response, in particular galloping, that increases monotonically with wind speed (Kawai, 1992; see also Dowell, 2004).

6. NOMINAL VS. EFFECTIVE RISK-CONSISTENCY. "MAGIC NUMBERS" AND TALL BUILDING DESIGN

It was noted earlier that the amount of research performed so far on MRIs of nonlinear states is very limited. The goal of such research is not to develop tools for use in everyday design, but rather to create a body of knowledge allowing code writers to develop rational guidelines and specifications tailored to various structural types, on the model of what has been achieved by earthquake engineering research. For the time being, except for special cases, the designer must use whatever approaches are at his disposal to achieve structures that (a) achieve nominal risk consistency and (b) entail reduced risks. Here we refer to nominal risk consistency as consistency with respect to the probability of individual members just attaining first yield, and differentiate it from effective risk consistency, that is, risk consistency in terms of relevant nonlinear limit states as defined earlier.

Risk analysis and engineering judgment -- provided that they are sound -- can be used to good effect to compare the quality of various designs from the point of view of risk even where nominal risk consistency is involved. Such relative assessment of various designs is in fact still a tenet of practical structural reliability.

Figure 3, which we considered earlier, shows details of a portal frame for which column supports and frame hunches are reinforced through judicious detailing. This structure will perform better from a safety point of view than its unreinforced counterpart, even though from an ASD or SD point of view both structures can be designed structures to satisfy current standard requirements.

We now consider the issue of tall, flexible building design. ASD requires that allowable stresses not be exceeded in structural members for wind effects with a typically 50-yr MRI. SD requires, basically, that linear stresses not be exceeded in structural members for wind effects with a 50-yr MRI, amplified via multiplication by a wind load factor that accounts for uncertainties in the wind loading. Analyses by Ellingwood et al. (1979) have established that, for rigid buildings in regions with no hurricanes, a wind load factor of approximately 1.5 should be applied to the 50-yr wind effect to calculate the SD wind load under which stresses in structural members remain linear. Fundamental to that analysis is the dependence of the wind load factor on uncertainties in the various factors that determine the wind effect: wind speed, aerodynamic coefficients, peak value of the response, terrain roughness. According to simplified analyses included in the Commentary to the ASCE Standard, for rigid structures in regions with no hurricanes, multiplication of the 50-yr wind effect by 1.5 yields a wind effect with a 500-yr MRI. However, for reasons that are not clear ASCE 7 eventually adopted a

wind load factor of 1.6, and from those simplified analyses it follows that multiplication of the 50-year effect by 1.6 yields a wind effect with a 720-yr MRI.

Although ASCE 7 specifications do not apply to buildings that can experience vortex shedding effects, the criteria adopted in ASCE 7 for rigid buildings have been adopted, in our opinion uncritically, for tall, flexible building design as well. Indeed, some wind engineering laboratories assume that SD should be based on wind effects with a 720-yr MRI.

In fact, the 720-yr MRI has no universal validity. It is merely a reflection of a set of uncertainties estimated for rigid buildings in non-hurricane regions. If those uncertainties change, the wind loading factor must also change, and so must the MRI of the wind effect producing the SD stresses. The reasons why the overall uncertainty of the wind effect is larger for flexible than for rigid buildings are that, for flexible buildings, (a) dynamic parameter uncertainties, which are irrelevant for rigid buildings, can be significant, and (b) uncertainties in the velocities are more significant than for rigid structures because wind effects for flexible buildings are proportional to wind speeds raised to powers larger than two. Assume the deliberately overdone example of a set of uncertainties so large that the corresponding wind load factor is 10. Clearly, using a 1.6 wind load factor or a 720-yr MRI of the wind effect will not be sufficient to ensure the safety of a structure for which the wind effects are so much more uncertain than they are for a typical rigid structure. It is clear that designing tall, flexible structures so that the SD criteria are satisfied for 720-yr wind effects can render those structures less safe than common one-story rigid buildings. To conclude, effective risk consistency would be improved, if not fully achieved, if wind effects considered in conjunction with SD criteria for the design of flexible buildings were commensurate with the uncertainties appropriate for flexible buildings, rather than being based on "magic numbers" (e.g., 720-yr MRIs) assumed to have universal validity when in fact they do not [6]. This example illustrates the need for sound risk analysis even if only linear effects – and nominal risk consistency – are considered.

7. MULTI-HAZARD DESIGN: RISKS IN REGIONS WITH STRONG WIND AND SEISMIC LOADS

In accordance with the ASCE Standard 7-05, in regions subjected to wind and earthquakes, structures are designed for loads induced by wind and, separately, by earthquakes, and the final design is based on the more demanding of these two loading conditions. Implicit in this approach is the belief that the Standard assures risks of exceedance of the specified limit states that are essentially identical to the risks inherent in the provisions for regions where only wind or earthquakes occur. We draw the attention of designers, code writers, and insurers to the fact that this belief is, in general, unwarranted, and that ASCE 7 provisions are not risk-consistent, i.e., for regions with significant wind and seismic hazards, risks of exceedance of limit states can be up to twice as high as those for regions where one hazard dominates. This conclusion is valid even if the limit states due to wind and earthquake are defined differently, as is the case in ASCE 7. We propose an approach to modifying ASCE 7 provisions which guarantees that risks implicit in its minimum requirements for regions where one hazard dominates are not exceeded for structures in regions with strong wind and seismic hazards.

We now show that implicit in ASCE 7 provisions are risks of exceedance of limit states due to two distinct hazards that can be greater by a factor of up to two than risks for structures exposed to only one hazard. An intuitive illustration of this statement follows. Assume that a motorcycle racer applies for insurance against personal injuries. The insurance company will calculate an insurance premium commensurate with the risk that the racer will be hurt in a motorcycle accident. Assume now that the motorcycle racer is also a high-wire artist. In this case the insurance rate would increase as the risk of injury, within a specified period of time, in either a motorcycle or a high-wire accident will be larger than the risk due to only one of those two types of accident. This is true even though the nature of the injuries sustained in a motorcycle accident and in a high-wire accident may differ. Formally,

$$P(s_1 \cup s_2) = P(s_1) + P(s_2) \qquad\qquad\qquad (2)$$

where $P(s_1)$ is the annual probability of event s_1 (injury in motorcycle accident), $P(s_2)$ the annual probability of event s_2 (injury in high-wire accident), and $P(s_1 \cup s_2)$ is the annual probability of injury due to a motorcycle or high-wire accident. (Note: s_1 and s_2 are mutually exclusive events.)

   Equation 2 similarly holds for a structure for which $P(s_1)$ is the probability of the event s_1 that the wind loads are larger than those required to attain a limit state associated with design for wind, and $P(s_2)$ is the probability of the event s_2 that the earthquake loads are larger than those required to attain the same limit state associated with design for earthquakes. (Note that, as in the earlier example, it is assumed that s_1 and s_2 cannot occur at the same time.) $P(s_1 \cup s_2)$ is the probability of the event that, in any one year, s_1 or s_2 occurs. It follows from Eq. 2 that $P(s_1 \cup s_2) > P(s_1)$, and $P(s_1 \cup s_2) > P(s_2)$, i.e., the risk that a limit state will be exceeded is increased in a multi-hazard situation with respect to the case of only one significant hazard. If $P(s_1) = P(s_2)$ the increase is twofold [62]. Note that s_1 and s_2 *can differ*, as they typically do under ASCE 7 design provisions. In spite of such differences, it is the case that, both for earthquakes and wind, inelastic behavior is allowed to occur during the structure's lifetime. For seismic loading, only the MRI of the maximum considered earthquake is specified; the MRI of the onset of post-elastic behavior is unknown. For wind loading, the MRI of the onset of nonlinear behavior is specified; however, nonlinear behavior is also possible and allowed to occur during the structure's life. A useful way to make "apples and apples" comparisons is to estimate the MRI of the event W that incipient collapse will occur under wind loads and the MRI of the event E that it will occur under seismic loads. For example, if those MRIs are comparable, the MRI of the event that either W or E will occur will be approximately half the MRI of the event W, and approximately half the MRI of event E. Therefore, risks of failure inherent in the load combinations specified in ASCE 7 can be up to twice as for some structures in regions exposed to both strong winds and strong earthquakes than for their counterparts where only one of these hazards is strong. That is, for the former, the minimum requirements with respect to the requisite safety level are violated by current ASCE 7 provisions. One example of a structure that, depending on geographical location, may belong to this category is the supporting structure of a water tower depicted in Figure 4. Tall buildings supported by columns at the lower floors are another example.

Figure 4: Schematic of water tower.

8. WIND-INDUCED LOSS ESTIMATION

In earlier sections we noted that the estimation of wind-induced risk is in practice difficult primarily because it involves estimates of the nonlinear behavior of the structure and its components. For almost two centuries structural and architectural engineers have been avoiding this difficulty by considering predominantly behavior within the linear range. That this strategy has, by and large, been successful explains why design practice for structures subjected to wind loads is dominated by linear methods to this day and why, in spite of significant advantages that would accrue from knowledge of wind-induced nonlinear behavior, modern research into such behavior is still in its infancy.

Wind-induced damage – the cause of huge losses, especially in hurricane-prone regions, -- is associated with nonlinear behavior, and the estimation of such damage cannot be performed by considering behavior in the linear domain. While structural designers have, at least in principle, a choice between linear and nonlinear methods for performing their task, loss estimators don't. This – in addition to uncertainties concerning wind climatology, micrometeorological wind flow features, construction features, exposure (types and numbers of structures with the potential of being harmed), and accuracy and completeness of claim data, -- is one reason why the estimation of wind-induced losses is still far from being an exact science. Estimates by various loss models can differ from each other significantly, perhaps by factors as high as three or four, although the exact extent to which this is the case is not known owing to the proprietary nature of those models.

The analytic development of vulnerability curves (plots of percentage losses versus wind speeds) or of fragility curves (plots of conditional probabilities of exceeding a limit state versus wind speeds) remains a difficult challenge. Recently developed facilities for testing full-scale buildings of small size or large-scale models of larger buildings (Huang et al., 2009), used in conjunction with conventional structural testing laboratories, offer the prospect of allowing such curves to be developed for a variety of components, including components whose damage allows rain penetration, a large source of losses in strong winds. However, so far an appreciable amount of guesswork or use of improvised models is still needed to make up for physical information that is not available.

The Florida Public Hurricane Loss Projection Model (FPHLPM, 2005) was developed to help establish reasonable insurance rates consistent with the best possible loss estimates. To our knowledge it is the only publicly documented loss model in existence. FPHLPM and [21] contain numerous references and materials providing a useful perspective of the current state of the art.

9. CONCLUSIONS

The perspectives on risk offered in this paper are in large part related to the need to achieve, by both analytical and experimental means, long overdue advances in the state of the art on non-linear behavior under wind loads. Such advances would allow the development of performance specifications and improvements in design technologies resulting in higher safety levels than those inherent in ASCE 7 Standard or comparable criteria. This goal would be attained by identifying structures which, although meeting such criteria, are found by analysis or experiment to have low post-elastic strength reserves. By helping to achieve effective risk-consistency with respect to limit states of interest in the context of performance specifications, design methods based, like their earthquake engineering counterparts, on research into nonlinear behavior can contribute to designing structures that are not only safer but, through intervention where the structures exhibit weaknesses or are overdesigned, possibly more economical as well as consuming less embodied energy. Finally, analytical and experimental research into behavior up to failure is indispensable for advancing the state of the art in wind-induced loss prediction and prevention.

A second fundamental theme in this paper is the imperative to develop design criteria by carefully accounting for uncertainties. From our discussion of current tall building design practice we concluded that disregarding this imperative can lead to risks that are higher for tall, dynamically

active structures than for ordinary rigid buildings. We also showed that, according to simple multi-hazard engineering considerations, risks can be higher for some structures in regions subjected to strong wind and seismic hazards than the risks implicit in ASCE design criteria.

Risks in structural engineering, involving as they do potential loss of life and the economic well-being of entire regions or countries, concern not only individuals but also society at large. Structural engineers, and especially standard writers, should collaborate with economists and social scientists in developing appropriate risk criteria for structures subjected to wind loads. Safety issues in wind and seismic engineering differ in many respects, and strict parallels between criteria on risks for these two disciplines should be avoided. Nevertheless, wind engineering has much to learn from developments on risk in seismic engineering, in which, for reasons unrelated to volume of economic losses, structural research efforts have been far more vigorous. We have much work ahead of us.

REFERENCES

ASCE Standard ASCE/SEI 7-05, Minimum Design Loads for Buildings and Other Structures, American Society of Civil Engineers, 2006.

Australian/New Zealand Standard, Structural design actions, Part 2: Wind Actions. Standards Australia/Standards New Zealand, AS/NZS 1170.2:2002.

Duthinh, D., Main, J.A., Wright, A.P., and Simiu, E. (2008). "Low-Rise Steel Structures under Directional Winds: Mean Recurrence Interval of Failure." J. Struct. Engrg. (134), 1383-1387.

Dowell, E.H., et al. (2004). A Modern Course in Aeroelasticity. Kluwer Academic Publishers, Dordrecht.

Ellingwood, E., Galambos, T.V., MacGregor, J.G., Cornell, A.C. (1980). *Development of a Probability Based Load Criterion for American National Standard A 58*, National Bureau of Standards, Washington, D.C.

Florida Public Hurricane Loss Projection Model (2005). Engineering Team Final Report, vols. 1, 2 and 3. Florida International University, Miami, Florida. http://www.cis.fiu.edu/hurricaneloss/documents/Engineering/Engineering_Volume_I.pdf; for vols. II and III replace I by II or III.

Grigoriu, M. (2009). *Algorithms for Generating Large Sets of Synthetic Directional Wind Speed Data for Hurricane, Thunderstorm, and Synoptic Winds*. NIST Technical Note 1636, National Institute of Standards and Technology, Gaithersburg, MD.

Harris, R.I. (2006). "Errors in GEV analysis of wind epoch maxima from Weibull parents." Wind and Structures, 9 (3), 179-191.

Huang, P., Gan Chowdhury, A., Bitsuamlak, A., Liu, R. (2009). "Development of devices and methods for simulation of hurricane winds in a full-scale testing facility." Wind and Structures 12 (in press).

Isyumov, N., Mikitiuk, M.J., Cas, P.C., Lythe, G.R., and Welburn, A. (2003). "Predictions of wind loads and responses from simulated tropical storm passages." Proceedings of the 11th International Conference on Wind Engineering. D.A Smith and C.W. Letchford, eds., Lubbock, Texas.

Jang, S., Lu, L.-W., Sadek, F., Simiu, E. (2002). Database-Assisted Design Wind Load Capacity Estimates for Low-rise Steel Frames, J. Struct. Eng. (128), 1594-1603.

Kawai, H. (1992). "Vortex Induced Vibrations of Prismatic Buildings." Journal of Wind Eng. Ind. Aerodyn. (41-44), 117-128.

Lombardo, F.T., Main,J.A., Simiu, E. (2009), Automated extraction and classification of thunderstorm and non-thunderstorm wind data for extreme-value analysis. J. Wind Eng. Ind. Aerodyn. (in press) *http://dx.doi.org/10.1016/j.jweia.2009.03.001*.

Minciarelli, F., Gioffrè, M., Grigoriu, M., and Simiu, E. (2001). "Estimates of extreme wind effects and wind load factors: influence of knowledge uncertainties. Probabilistic Engineering Mechanics (16), 331-340.

Penwarden, A.D., and Wise, A.F.E. (1975). *Wind Environment Around Buildings.* Building Research Establishment.

Ripley, B.D. (2004). *Spatial Statistics.* John Wiley and Sons, Hoboken.

Simiu, E. (2007). Discussion to "Errors in GEV analysis of wind epoch maxima from Weibull parents." Wind and Structures, 10 (4) 399-400.

Simiu, E., Gabbai, R.D., Fritz, W.P. (2008)."Wind-induced tall building response: a time-domain approach." Wind and Structures (11), 427-440.

Simiu, E., and Miyata, T. (2006). *Design of Buildings and Bridges for Wind: A Practical Guide for ASCE 7 Standard Users and Designers of Special Structures*, Wiley, Hoboken.

Simiu E., Scanlan R. (1996). *Wind effects on Structures*. John Wiley & Sons, New York.

Simiu, E., Wilcox, R., Sadek, F., Filliben, J.J. (2003). "Wind speeds in ASCE 7 Standard Peak-Gust Map: Assessment." J. Struct. Eng. (129), 427-439.

Spence, S.M.J. (2009). *High-Rise Database-Assisted Design 1.1 (HR_DAD_1.1): Concepts, Software, and Examples*. NIST Building Science Series 181, National Inst. Standards and Technol., Gaithersburg, Maryland.

Wind and Music[1]

U. Peil

Technische Universität Carolo-Wilhelmina zu Braunschweig

Institute of Steel Structures, Beethovenstraße 51, 38106 Braunschweig, Germany

u.peil@tu-bs.de

Keywords: Wind instrument, music, pipe, flute, clarinet, waves, vibration, flutter, vortex.

ABSTRACT

The parallels between wind excited structures and wind excited musical instruments are the basic idea of this paper. Vibrations of structures are caused by the same self-excited or motion-induced mechanisms as the vibration in musical instruments. Vibrating engineering structures just produce music at inaudible frequencies.

The paper deals with both parts: on the one hand with waves or high frequency vibrations, i.e. sound and music, and on the other hand with low-frequency vibrations of civil structures like towers, masts, bridges etc. Because many of the sound generating mechanisms show a feedback with the instrument itself, some basics of wave propagation and dynamics of musical instruments are discussed first. Concerning the wind engineering topic, latest research results of the wind engineering group at the Institute for Steel Structures at the Technische Universität Braunschweig, Germany are briefly presented.

---

1   To Carola Bethge, Wolfenbüttel who has aroused my interest for this fascinating topic.

Contact person: Udo Peil, Technische Universität Braunschweig, Beethovenstr. 51 , Fon: +49 531 391 3379, Fax: +49 531 391 4592, Email: u.peil@tu-bs.de

1. INTRODUCTION

Wind effects are often responsible for severe vibration of structures but on the other hand they also may cause music. Resounding thin wires in the natural wind are well known examples. Aeolian harps (see Fig. 1) have been used for thousands of years. In such a harp one or more prestressed wires are excited due to vortex excitation by the streaming air, the sound is amplified by a resonance body.

Figure 1: Aeolian harp

The equation of the vortex frequency is well known to wind engineers:

$$f = 0.2 \frac{v}{d} \quad [Hz] \tag{1}$$

with v as wind speed in [m/s] and d as diameter of the string in [m]. A wind speed of 5m/s causes a tone of 1000Hz with a 1-mm thick string. If the string is tuned to this frequency, a mysterious, melancholic and vague sound is produced.

Two types of sound generation mechanisms occur: first the direct vortex-induced sound and in addition the higher harmonics, the so called overtones of the string itself. Depending on the wind speed, the pitch often changes. This basic excitation effect is also well known in wind engineering: It generates music or structural vibrations, which could be interpreted as music at inaudible frequencies.

In this paper the tone or sound generating mechanisms of wind instruments are discussed and compared with wind excitation processes in wind engineering. Because many of the sound generating mechanisms show a feedback with the instrument itself (just as structural wind excitations often do) some basics of wave propagation and dynamics of musical instruments are discussed first. Concerning the wind engineering field, latest research results of my wind engineering group at the at the Institute for Steel Structures at the Technische Universität Braunschweig, Germany are briefly presented.

2. WAVES AND VIBRATIONS

A wave is a disturbance that propagates through space and time, usually combined with a transfer of energy, which is not associated with a motion of the medium. It oscillates somewhat around its medium position. Mechanical waves may take the form of an elastic deformation or of a variation of pressure.

If two waves with the same amplitude, frequency, and wavelength, but varying phase difference travel in the same direction, the resulting displacement is given in equation 2. The resulting wave is a

travelling wave whose amplitude depends on the phase φ. When the two waves are in phase (φ=0°) they add up, i.e. they interfere constructively and the result has twice the amplitude of the individual waves. When the two waves have opposite phase (φ=180°), they interfere destructively and cancel out each other:

$$y(x,t) = y_A \cdot \sin(kx - \omega t) + y_m \cdot \sin(kx - \omega t + \phi)$$
$$= 2 \cdot y_A \cdot \cos\left(\frac{\phi}{2}\right) \cdot \sin\left(kx - \omega t + \frac{\phi}{2}\right) \tag{2}$$

If two waves with the same amplitude, frequency, and wavelength travel in opposite direction, they cause a so called standing wave. Using the principle of superposition, the resulting string displacement can be written as:

$$y(x,t) = y_A \cdot \sin(kx - \omega t) + y_m \cdot \sin(kx + \omega t)$$
$$= 2 \cdot y_A \cdot \sin kx \cdot \cos \omega t \tag{3}$$

At any change of the mechanical properties of the wave guiding medium or at the boundary conditions, the wave is fully or partly reflected. The reflection is dependent on the type of the boundary condition. A rope or a string, which is fixed at its ends, reflects a wave by changing its sign. A wave in a tube (as a simple model for a pipe or another wind instrument) is reflected at the end of the tube, may it be open or closed. If the end of the tube is open, then the last element at the opening which is pushed by the penultimate element does not have a neighbor element to which the impact can be transferred, the mass inertia is missing. Therefore it moves out, but it is kept by the low pressure which pulls it back into the tube. The pressure sign changes, oncoming pressure is reflected as low pressure and vice versa, cf. Fig. 2. If the pipe is closed, the last element can't move, thus it gets the maximum pressure and gives it back to the penultimate element without changing its sign: oncoming pressure remains pressure and low pressure remains low pressure after reflection at a closed end, see Fig. 3. The reflected wave then travels back through the tube and interferes with the oncoming wave.
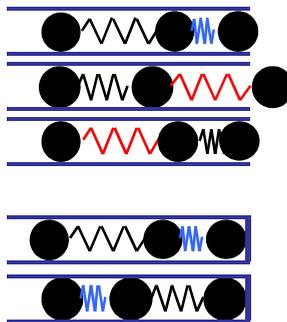
Figure 2: Reflections

If a pipe is harmonically excited at one end, both above mentioned principles interfere. If the frequency of the excitation is such that the generated half wave length fits into the pipe's length, then the reflected wave is perfectly pushed in phase, a large standing wave is generated due to the constructive interference, the excitation is a resonant one. If the frequency of excitation is slightly changed, then the excited wave does not exactly fit the phase of the reflected one, destructive interference occurs, the resulting standing waves show reduced amplitudes, it is a non-resonant excitation. If the excitation frequency is further changed then suddenly a new standing wave occurs with one more half wave length. When the frequency is increased further, a new standing wave with an additional half wave and an accompanying resonant peak occurs, see Fig. 3.

The standing wave generated by the travelling and reflected waves may be interpreted as a usual vibration. The behavior of a vibrating system (string, pipe, bridge) can be explained by wave superposition or by vibration theory. It is the same from two different points of view.
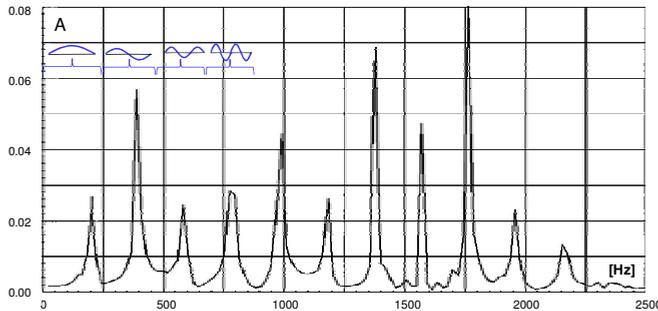
Figure 3: Measured amplitude spectrum

3. NATURAL FREQUENCIES OF STRINGS AND PIPES

Since a simple vibrating string is much easier to imagine than a non-visible longitudinal air vibration in a flute, a clarinet, an oboe or trumpet, some basics are explained first, using the string. Fortunately a transversely vibrating string and the longitudinally vibrating air in a flute or another wind instrument are differ only concerning the direction of vibration, see Fig.4.

transversal vibration

longitudinal vibration
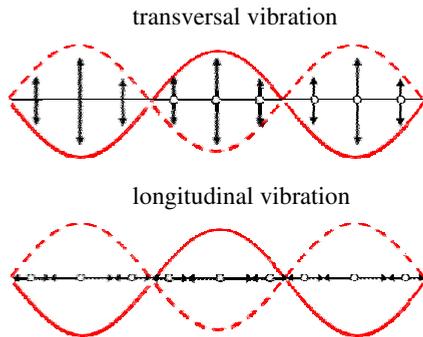
Figure 4: Transverse and longitudinal vibration

The natural frequency of a vibrating string is known to be

$$f = \frac{1}{l} \cdot \frac{1}{2} \sqrt{\frac{S}{m}} \quad [Hz] \tag{4}$$

l is the length, S the pretension force and m the mass of the string. To tune the pitch of the string, the pretension force of the string is adjusted by the peg of the violin. The frequency is then directly dependent on the length of the string: half the length means twice the frequency and so on. The accompanying natural modes are sine waves. The wave length of the n-harmonic has a length of l/n, see Fig. 5. Thus the 2nd mode has a natural frequency which is twice the basic one (octave), the 3rd natural frequency has three times the basic frequency etc. The accompanying notes are shown in Fig. 5.
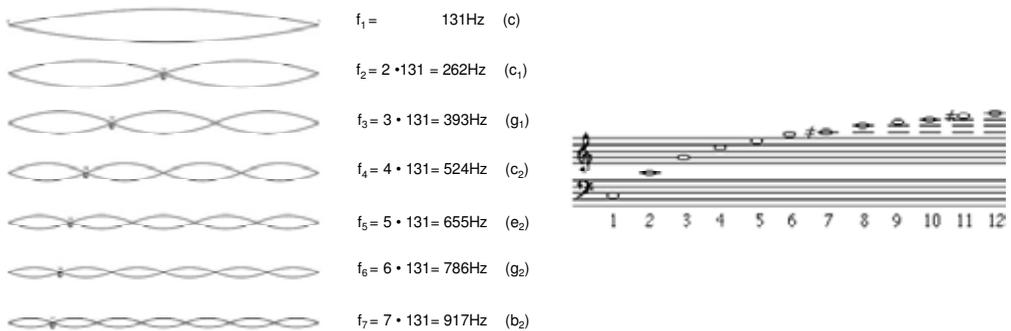
Figure 5: Natural modes of a string or a pipe

If a string is plucked and a finger deliberately touches the middle of the string without pressing it onto the fingerboard, one can hear the octave with the double frequency, because the basic natural mode shape is suppressed. The 2nd mode has not been plucked, but it sounds, since it is included in the original sound. The same happens if the string is touched at one third of the length: the fifth is audible and so on. The original sound includes all higher modes! The frequencies of the modes follow simple relations or fractions of numbers: f2:f1=2:1 (octave), f3:f2=3:2 (fifth), f4:f3=4:3 (fourth) and so on. In the field of acoustics, the 2nd mode is often named the 1st overtone, because it is the 1st mode over the basic tone, the tonic, the 3rd mode is the 2nd overtone and so on.

As already mentioned, all natural modes are included, if a string is plucked or bowed. The mixture of the amplitudes of the modes determines the timbre of the sound: the higher the contributing modes numbers, the brighter (or sharper) the timbre.

Exactly the same occurs if longitudinal vibrations in wind instruments are considered, because only the direction of the vibrations is different. As already mentioned, the natural frequencies of the tube are following exactly the same rational number relations.

As mentioned above, the boundary conditions determine the sign of the reflected wave. At the open end, the pressure difference against the atmosphere equals zero. Thus a recorder or a flute causes a longitudinal vibration with zero pressure at the open end and at the open embouchure hole. All possible overtones must follow these boundary conditions. Thus a complete series of sine functions represents the tonic and the overtones in a flute, Fig. 6 and eq. 5.

$$p(x) = \overline{p} \cdot \sin(n \cdot \frac{\pi \cdot x}{L}); \quad with \; n = 1, 2, 3, 4, ... \tag{5}$$
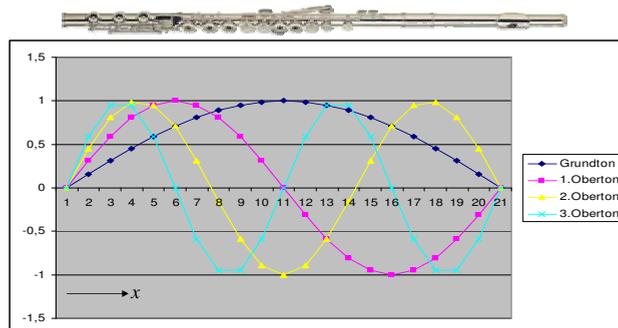
Figure 6: Harmonics of a flute

All other wind instruments have a mouthpiece, which seals the internal pressure against the outside atmosphere. The mouthpiece closes the pipe, thus the wave is reflected without changing its sign. Therefore the pressure reaches its maximum at the mouthpiece. The pressure distribution along a cylindrical pipe can be represented by half sine functions, with a maximum at the mouthpiece and zero pressure at the open end, see Fig. 7. Thus a series of sine functions consisting only of the odd numbers occurs:

$$p(x) = \overline{p} \cdot \sin(n \cdot \frac{\pi \cdot x}{2 \cdot L}); \quad with \ n = 1, 3, 5, 7, ... \tag{6}$$

This is typical of a clarinet. Especially the missing 1st overtone leads to the dark and a little bit hollow sound.
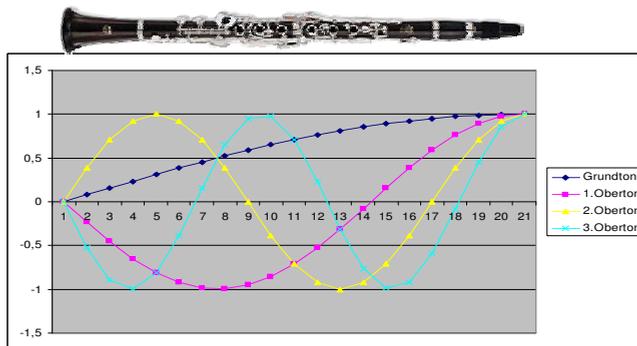
Figure 7: Harmonics of a closed cylindrical pipe (clarinet for instance)

The wavelength of the sine functions of a cylindrical pipe with a mouthpiece is twice the wave length of the flute. Therefore the pitch of the tone is one octave below a flute. This effect is often used for organ pipes. If the open end of a pipe is closed, the pipe sounds one octave lower. This method is much cheaper than to build pipes with twice the length.

If pressure and air speed is increased, the instrument overblows, the pipe jumps into the second mode and the 1st overtone sounds. A flute therefore plays an octave higher. A clarinet overblows in its 1st overtone as well, but it is one fifth higher than the flute, it is the twelfth (octave + fifth) because the even mode is missing. The overblowing effect can be supported by opening a matching finger hole. If for instance a flute opens the c-key, which is exactly in the middle between the mouthhole (embouchure hole) and the open end, than the basic sine wave is suppressed, because the open hole forces the pressure at its maximum to zero, the 2nd harmonic or the 1st overtone becomes now the tonic.

Just a surprising effect shall be discussed at the end of this section. As has been mentioned above, all reed instruments have the boundary condition of a closed tube at the mouthpiece because the lips seal the internal pressure against the free atmospheric pressure. Therefore all reed instruments should overblow into the twelfth as explained above. But only the clarinet performs as expected. What is the reason for this deviating behavior from all other reed instruments?

The reason is the shape of the bore. Only the clarinet has a cylindrical bore, which is what was assumed above in all explanations. All other reed instruments like oboe, bassoon and saxophone have a conical bore. Fig. 8 shows a longitudinal section of clarinet and an oboe. The cylindrical and conical shape is clearly visible. The conical bore considerably changes the acoustic behavior.

The sound in a conical tube changes its intensity and pressure as a function of the distance from the sound generator, the mouthpiece. If we measure the pressure at the open end and then step by step towards the mouthpiece we find that the pressure increases linearly depending on the decreasing distance from the mouthpiece. The approximately constant sound pressure must pass the tapering bore, with a continuously decreasing area, if we look from the open end to the mouthpiece, Fig. 9.

Figure 8: Bore of a clarinet and an oboe

Figure 9: Sound pressure reduction with increasing distance from the mouth piece

This linearly increasing pressure can be taken into account by an amplitude factor 1/r of the sine wave:

$$p(x) \approx \bar{p} \cdot \frac{1}{r} \cdot \sin(n \cdot \frac{\pi \cdot x}{2 \cdot L}); \quad with \; n = 1, 3, 5, 7, ... \tag{7}$$

The known odd numbers of the sine waves fulfill the boundary conditions at the closed end: the pressure has a maximum, Fig. 12 left. An even sine wave however does not fulfill this boundary condition (Fig. 10 right). But due to the additional factor 1/r, the pressure p(r) increases near the bore, so the pressure boundary condition can be met, Fig. 12 right. The wave length of the amplitude modified sine wave is the wave length of the original sine wave, with the even wave number. Thus all harmonics, i.e. all overtones, are sounding and the conical bored instruments overblow into the 1st overtone, i.e. into the octave.
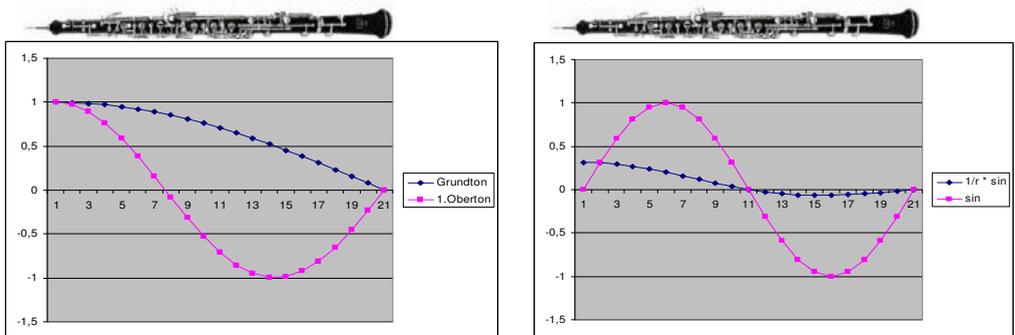
Figure 10: Influence of a conical bore on the action of even harmonics

Due to the standing waves, the pressure at the embouchure hole changes harmonically from over-pressure to low pressure. This harmonically alternating pressure drives the excitation mechanism of all wind instruments fro m flutes to reed and to brass instruments.

4.   NATURAL MODES AND OUR MUSIC SCALE

If a system is excited with two close frequencies, it responds with a so called beat phenomenon. The beat frequency corresponds to the difference in both frequencies, thus e.g. 440 Hz and 440 Hz together produce a beat frequency of 10 Hz. This beat phenomenon is well known in music. It is used e.g. for tuning two strings: if no beat can be heard, both strings have exactly the same frequency, so we can hear just one tone. If both strings are more and more out of tune, the beating frequency increases, so we hear one tone with a pulsating, a beating amplitude. From a certain frequency distance, one cannot hear any beating but an unpleasant roughness of the tone. If the distance of both frequencies is further increased, we hear two tones, see. Fig. 11 and Pierce (1998).
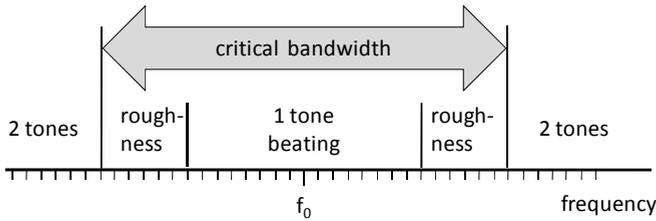
Figure 11: Critical bandwidth, Pierce (1998)

The critical bandwidth depends on the absolute pitch of the frequency f0. The bandwidth is wide if the frequency is low. From about 1000 Hz it increases linearly with the frequency. That is why two bass tones of a piano with a distance of a third (normally a consonant interval) do not produce a pleasant sound, Pierce (1998). Therefore in all piano music there is larger distance between the notes for the left hand, which plays bass notes, than for the right hand.
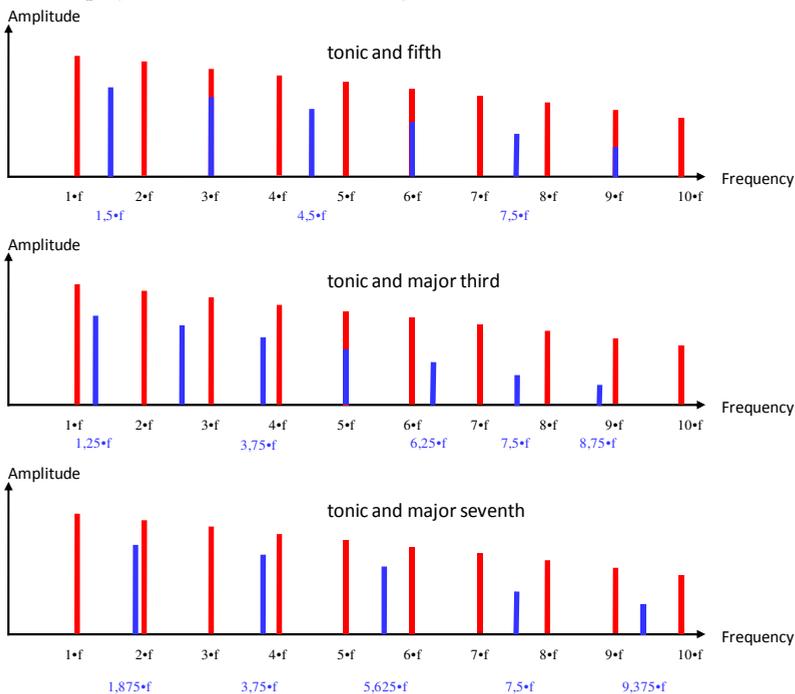
Figure 12: Overton relations for different intervals, Spitzer (2008)

By the way: The simple number relations between the basic tone (tonic) and the overtones are responsible for our usual diatonic scale system. If this scale is used for polyphonic music then many overtones are identical. The sound is harmonic or consonant, only few overtones are inharmonious. This is shown in Fig. 12. The tonic and the fifth have many identical overtones. Some overtones are in between, but the distance is large, no beat phenomena occur. The tonic and the major third are a little bit rougher, in earlier times this interval was considered to be dissonant. The tonic and the major seventh have no identical overtones. The overtones are very close and therefore produce beating phenomena, the sound is dissonant, it "whimpers", Spitzer (2008).

Only strings and wind instruments with a tube as resonator show the above mentioned simple number relations of overtones which can be expressed by fractions. A bell for instance has a 1st overtone of about 2.3•f, the 2nd is about 3.5•f and the 3rd is 4.8•f. This overtone spectrum does not fit for different basic tones (tonics). Thus polyphonic bell music is not very pleasing to the ears, too many overtone dissonances occur.

As already mentioned, our usual music scale is based on the natural modes of a string. All intervals result from the relations over the overtones. As mentioned above, a fifth has always a frequency relation to the tone it is related to of 3/2=1.5, an octave has the relation 2/1=2, a major third 5/4 and so on. This leads to serious problems with the music scale. If we staple 12 fifth, starting for instance with a c_1 with a frequency of 131Hz, the fifth is 1.5•131Hz (g_1). The next fifth to this note is 1.5•1.5•131Hz and so on. The 12th fifth is the $h\#_7$, it has a frequency of 16996 Hz, see Fig. 13. The note $h\#_7$ corresponds to the c_8 key of the piano, see Fig. 13. This tone can also be reached by 7 octaves. The next octave to c_1 is 131 •2 Hz (c_2). Stapling 12 octaves in this way we reach c_8 with 16768Hz, which differs by 1.36% from the same note generated by the fifths, see Fig. 13

$$h\#_7 = 131 Hz \cdot \left(\frac{3}{2}\right)^{12} = 16996\,Hz \qquad c_8 = h\#_7 = 131 Hz \cdot \left(\frac{2}{1}\right)^{7} = 16768\,Hz$$
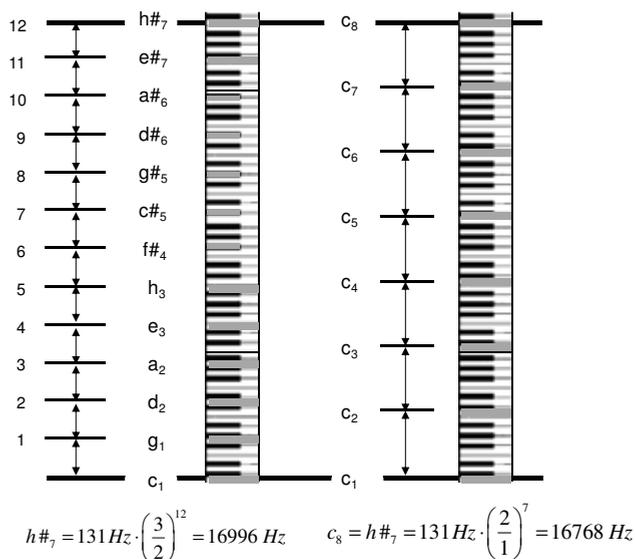
Figure 13: Discrepancy of intervals

This is a serious problem which occupied many people in the past, starting with Pythagoras who found this problem about 550 BC. Many different tuning systems have been developed to overcome this problem: well tempered, mean tone, equal temperament, Werckmeister temperament etc.

5.   EXCITATION MECHANISMS

5.1   Sound excitation

The simplest sound producing excitation mechanism is whistling. How is the sound generated? When air is forced through a small opening or slit e.g. the narrow opening formed by the lips, the fast air-stream moves through slower air. The boundaries of the airstream get resistance from that slower air and tend to peel back and form vortices. These vortices interact with the stream, causing it to move in an undulating path, Fig. 14.
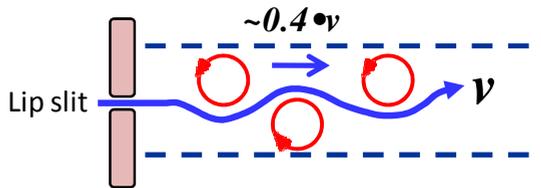
Figure 14: Basic mechanism of whistling

This undulation can actually produce a substantial amount of sound. The undulations in the stream move along the stream at something less than one half the speed of the air in the stream, Hall (1991). The faster the airstream speed, the faster the oscillations of the stream. In addition, the oscillating stream causes a feedback to the lips and the oral cavity (acting as a Helmholtz resonator) thus the pitch can be influenced by both.

An even greater amount of sound can be produced by coupling the slit to an edge. The airstream is separated by a sharp edge and a type of repetitive eddying called vortex shedding takes place on alternate sides of the air jet, like a vibrating air tongue or air reed, see Fig. 15, Hall (1991). Vortex phenomena have only a secondary influence on flute-type sound production; moreover, at usual musical blowing pressures the edge-tone frequencies are so high as to be nearly inaudible. They are only used to initiate the vibration.
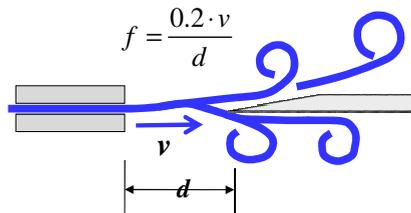
Figure 15: Edge tone excitation

The impulse produced by the edge tone causes a travelling wave in the bore of the flute. This wave is reflected at the open end and then forms a standing wave with alternating harmonic pressure variation at the nearly open mouthpiece with the edge or labium. The alternating pressure now takes control over the movement of the air reed. The alternating pressure of the standing wave causes self-excited vibration of the air reed of the flute, see Fig. 16. If the alternating pressure of the standing wave at the labium is lower than the atmospheric pressure, then the air reed is sucked into the pipe; if the pressure is higher than it is pushed out. Thus the vibrating system is excited exactly in resonance of the pipe.

Fig. 17 is a snapshot of the fluctuating pressure in the bore of the flute. It is calculated by means of the CFD-method using the Lattice-Bolzmann procedure, Tölke et al. (2008). The calculation was performed by the group of Prof. Manfred Krafczyk at the Technische Universität Braunschweig. One can see the alternating pressure distribution, and the vortexes near the labium.
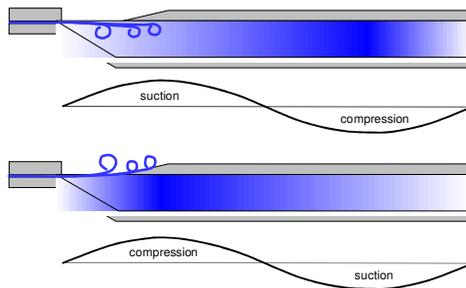
Figure 16: Schematic feedback mechanism for the synchronization of the air reed

Fig. 18 shows the calculated amplitude spectrum of the simulation at the open end of the flute. The overtones are reproduced quite well, the basic frequency (tonic) is correct.
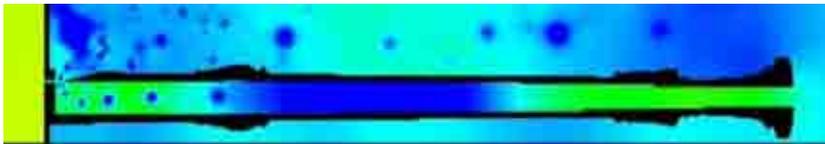
Figure 17: Fluid pressure distribution in an alto recorder
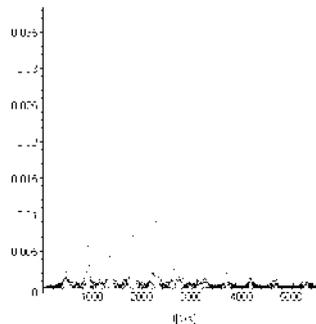
Figure 18: Amplitude spectra at the open end of the recorder

The above mentioned excitation mechanisms of the oscillating air stream around an edge can be directly used as an explanation for all reed or brass instruments. Fig. 19 shows mouthpieces of a clarinet with a single reed and an oboe with a double reed.

Figure 19: Mouthpieces of a clarinet and an oboe

The reed - made of a sort of bamboo (arundo donax) - replaces the air reed. If the fluctuating pressure in the pipe is high, the reed opens, if the pressure is lower than the atmospheric pressure, the reed closes the opening. It chops up the continuous air stream (produced by the instrumentalist) such that the standing wave is fed in resonance. If the player plays piano i.e. softly, then the reed just vibrates a little, a nearly harmonic pressure difference is produced behind the mouthpiece. If the player plays forte i.e. loudly, then - due to the high air speed and pressure differences - the reed completely closes the opening. A sketch of the air pressure behind the mouthpiece is shown in Fig. 20. It is obvious that this generates more overtones than the harmonic excitation, reed instruments, such as clarinets, oboes or bassoons sounds brighter and sharper. This is the reason for the wider sound spectrum of a clarinet compared to a flute.
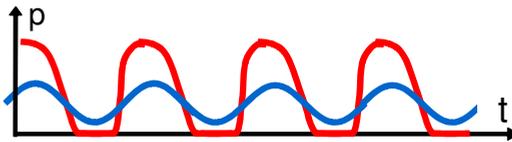
Figure 20: Air pressure after the mouthpiece in piano and forte mode

The frequency of the reed itself is rather high. This can be demonstrated, if the reed is played only with the teeth. These high and strong natural frequencies of the reed are completely damped out by the lips which usually press the reed. Thus the standing wave can take control of the reed.
Brass instruments use the lips of the player as a substitute for a reed. Because lips have a certain mass and show elastic behavior, they can vibrate. The lip vibration is also driven by the alternating pressure of the standing wave in the tube.
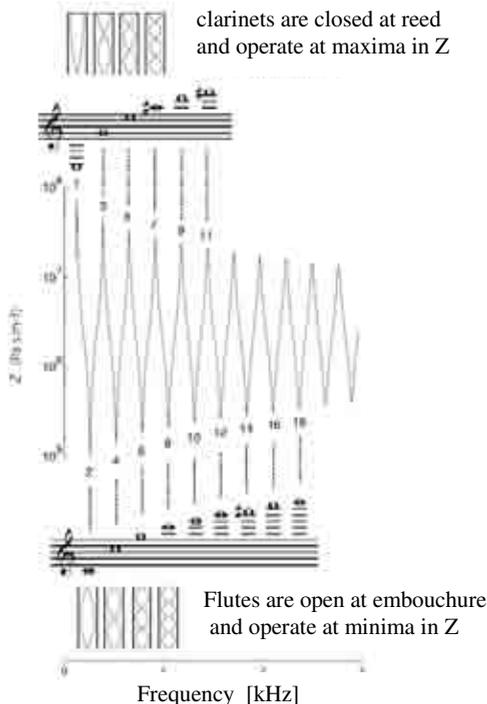
Figure 21: Impedance curves for a clarinet versus a flute, Dickens et al (2007)

The behavior of a flute and a clarinet as an example of a pipe, that is open at both ends and a pipe that is open at one and closed at the other end, can be quantified, both theoretically and experimentally, using the acoustic impedance spectrum. It is defined as the ratio of the acoustic (varying) pressure required at the system input (mouthpiece or embouchure) to produce the acoustic flow in the tube. Its dimension is N/m² s m-3. In an infinite pipe, a harmonically varying pressure causes a wave which never comes back. In a finite pipe, however, the wave reflects at the far end and causes standing waves (resonance), which alters the impedance remarkably. In Fig. 21 the impedance curve of a pipe closed at one end and open at the other and a pipe open at both ends is shown, Dickens et al (2007).

One can see that the clarinet operates at maxima and the flute in minima of the impedance. A reed of a clarinet needs relatively high pressure to move from its initial position; the air reed of a flute operates at small pressure otherwise it would be blown away. Operating at maxima of impedance means that the acoustic swing is pushed when the pressure is high and the speed is very slow. This is the upper point of a swing, i.e. the maximum potential energy. On the other hand operating at minima of impedance means that the pressure is low but the flow is high. The flute pushes the swing at the lowest point, when the speed is high, but the potential energy has a minimum. The ease of playing and the stability of a note depend on the peak and narrowness of the maxima or minima.

The impedance curve in Fig. 21 is measured with a closed-open pipe. If measurements are performed with a real clarinet, then the harmonics deviate from maxima of the impedance curve. This is due to the bell, which gives the instrument an effective length that increases with frequency. Furthermore the amplitudes of the extremes are reduced with increasing frequency due to the bell: The bell radiates especially high frequencies, thus the reflected part of the wave is smaller and the wave is weaker.

Another interesting point is the behavior of the tone holes. As already mentioned, the tone holes open the bore to the outside atmospheric pressure, thus it shortens the effective length of the tube. This is only true for low frequencies: the wave is reflected at (or near) this open tone hole because the hole provides a low impedance with low resistance to the outside air. For high frequencies, however, that does not hold true. The air in and near the tone hole provides some mass. This mass has to be accelerated by the sound wave when it passes through the tone hole. The required acceleration to move the mass increases with the square of the frequency: for a high frequency wave there is little time in half a cycle to get it moving, see Fig. 22. The tone hole acts like a low pass filter: the low frequencies leave through the holes, the high ones through the bell. This effect is used for instance by Gustav Mahler: In his symphonies, special the clarinet group has to lift the instruments sometimes in a horizontal position. The acoustic effect is such that the radiated sound becomes brighter and may be sharper due to the better transferred high frequencies.
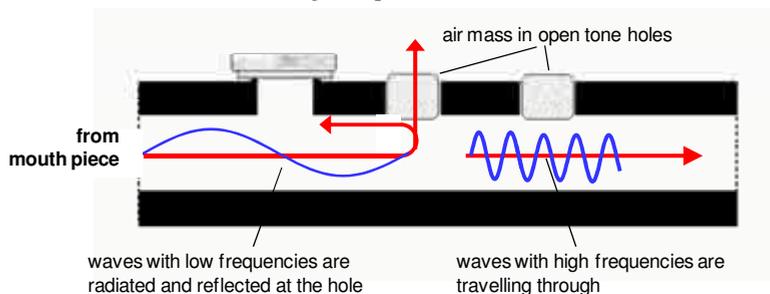
Figure 22: Behavior of tone holes as low pass filters

Due to the inertia of the air mass in the tone holes, the pressure is always a little bit higher than the outside atmospheric pressure. Thus the effective length is always a little bit longer than the tone hole pretends.

5.2 *Structural vibration excitation*

The vibration excitation mechanisms of structures in natural wind are identical to those exciting musical instruments. The already mentioned aeolian harp is an example of vortex induced vibrations of slender structures like chimneys or masts. The string of the wind harp is excited by a wind field which may be assumed to be constant over the small length of the structure (the string). This assumption is also generally used in wind engineering. Since the critical wind speed, which causes resonant lateral vibrations in the structure, is only low but normally shows extremely varying profiles, the assumption of a constant profile is an easy way out but not a realistic one. Fig. 24 shows some profiles measured at our wind measuring mast at Gartow, Germany together with approximations.
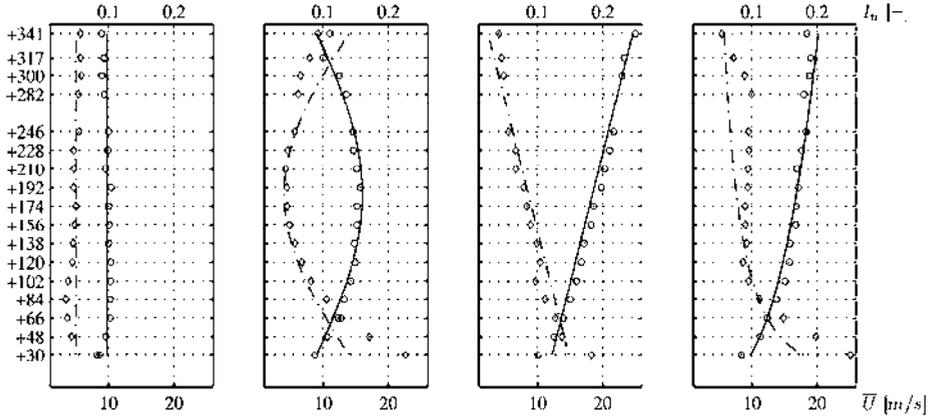
Figure 23: Typical wind profile classes at lower wind speed (o: $\overline{u}$ ◇: I_u)

First the measured wind profiles are classified in predefined classes which are assessed looking over a wide range of measurements, Fig. 25 shows the principle. Every single class can then be described by a vector **μ** of the mean wind speed and the covariance matrix **cov**. In a second step, the profiles will be assigned to typical wind climate situations, thus the duration time can be determined using synoptic weather data. This is important for assessment of the fatigue life time of the structure.
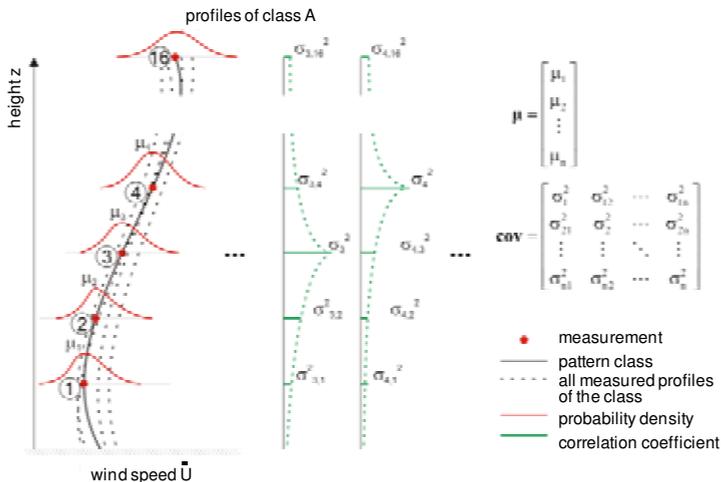
Figure 24: Statistical classification of wind profiles

The determination of structural response due to vortex vibration is a complex problem, because the relation between wind force and speed is quadratic. In addition, the transfer matrix $\mathbf{H}\,(i\omega_n)$ is coupled with the random variable $\bar{U}$ via the excitation frequency and the Strouhal number. Thus the calculation is performed using the Monte Carlo Method together with variance reducing methods like latin-hypercube or importance sampling, see Fig. 26. The lock-in effect can be taken into account by an iteratively adapted excitation frequency.
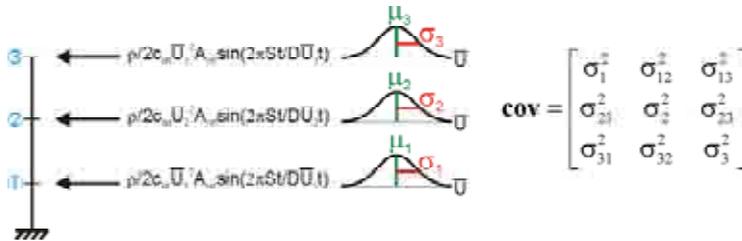
Figure 25: Description of vortex excitation as a probabilistic, correlated harmonic forced vibration

Fig 26 shows as an example the influence of the lock-in process at a 205-m high guyed mast with a circular shaft. The deflections of the mast top are shown. The occasionally occurring vibrations up to approximately the half of the maxima, is caused by resonance excitation at lower heights. When starting at t=350s the excitation frequency at the mast top is in the lock-in range. This causes immediately a strong increase of the lateral vibrations. After t=420s, the excitation frequency leaves the lock-in range, the lateral vibration are reduced straight. The longitudinal vibrations are stochastic as expected. More details are given in Clobes et al. (2009).
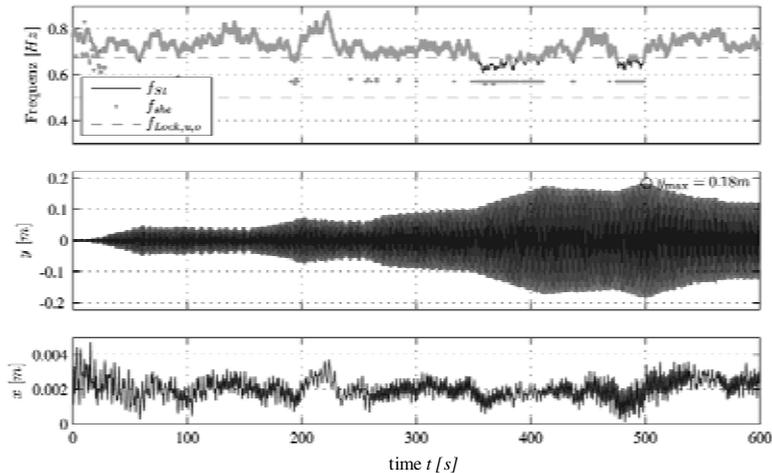
Figure 26: Time history of excitation frequency and corresponded deflection of the mast top

The second above mentioned sound excitation mechanism is a self-excited or motion-induced feedback process of the reed, which is controlled by the pressure variation of the standing wave. This is a process very close to flutter excitation, e.g. of long span bridges. What are we doing in this field?

Flutter vibrations of bridge girders can result in the collapse of the structure within a short time. The Tacoma Narrows Bridge disaster is a well-known example of bridge flutter. Flutter vibrations are generated by so-called motion-induced aerodynamic forces. Together with its structural parameters,

motion-induced wind forces influence the properties of an aeroelastic system. To provide against these phenomena, two standard methods are used to ensure the stability of an aeroelastic bridge system: either the bridge girder is designed with a high torsional stiffness or the girder cross section is aerodynamically optimised.

In recent years, inspired for instance by aerospace engineering, a number of techniques have been investigated to improve the vibration behaviour of extremely slender bridges under wind action with systematically imposed forces. Fig. 27 shows three kinds of actuators that have been proposed for this purpose in the past. Inertial forces can be generated when accelerating a reaction wheel (Miyata et al. 1994; Körlin & Starossek 2007). Rotating gyroscopes that are mounted in a tiltable gimbal can affect the bridge with gyroscopic forces (Murata & Ito 1971). The motion of the actuators can be controlled in different ways. Active and passive controllers are the most important types of controllers. An example of a passive controller is the coupling of the actuator motion with the bridge girder by spring-damper systems. Passive controllers are normally low-maintenance devices and need no energy input. In the case of gyroscopes, only their spin must be kept constant. Passive controllers can be considered as an output feedback that, moreover, has sign constraints for the controller values. With methods of control theory, it can easily be shown that their effectiveness is limited. The characteristics of an aeroelastic system depend on the mean horizontal wind speed. Passive controllers cannot be easily adjusted to these changing conditions. For a wide range of the horizontal mean wind speed, the properties of passive controllers are not optimised. Active controllers, on the other hand, can induce energy into the bridge girder and, if configured appropriately, can take the total state of the aeroelastic system into account. The properties of active controllers can be adjusted to the horizontal mean wind speed without problems. Compared to passive ones, active controllers can thus stabilize the bridge within a wider speed range. This feature, however, causes serious safety problems in permanent operation. Anyway, at least for construction stages of bridges with undesirable aeroelastic characteristics, active controllers are considered to be a useful option. In Peil & Kirch (2008), control limits for slender bridges under wind action are investigated. It is shown that the divergence wind speed of the bridge constitutes an upper limit for the application of the mentioned mechanical actuators.
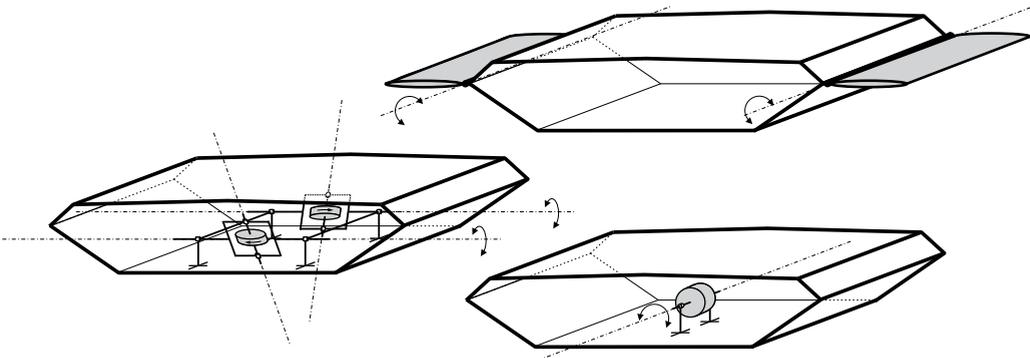
Figure 27: Actuators for stabilising bridges under wind action: aerodynamically effective control shields, twin control moment gyroscope and reaction wheel.

Fig. 27 additionally shows aerodynamically effective control shields as a kind of actuator that was proposed several years ago for extremely slender bridges (Kobayashi & Nagaoka 1992; Ostenfeld & Larsen 1992). In contrast to the other mentioned actuators, the divergence wind speed of the system can be modified as well. The crucial advantage of aerodynamically effective control shields is that additionally imposed forces on the bride deck are generated by the wind flow. Aerodynamically effective, movable control surfaces have been used in aerospace engineering to suppress the influences

of disturbances on aircraft wings for many years. With bridges, however, control shields are extra components that augment the area exposed to the wind. They cannot bear any significant payload and can hence not directly fulfil the intrinsic task of a bridge. In addition to motion-induced aerodynamic forces, new gust-induced forces arise simultaneously, which also need to be suppressed. Therefore, aerodynamically effective control shields are generally less effective for bridges than for aircraft wings. Moreover, control shields need a minimum wind speed to work. They are not suited for damping oscillations in still air. The motion of the control shields can again be controlled actively and passively. Fundamental control limits for bridges equipped with aerodynamically effective control shields are investigated in Kirch & Peil (2009a/b).

A related topic to flutter is galloping as another type of motion-induced vibrations. In particular iced cables often show this type of vibration with low frequencies and large vibrations. Iced cables have a shape which is aerodynamically instable, i.e. when the wind speed reaches a certain value, galloping vibrations occur, because the structure velocity dependent air pressure equals the velocity dependent damping of the structure; the overall damping is zero or becomes negative if the wind speed further increases.

The theoretical treatment is fairly simple. Determining ice shapes dependening on wind and snow or rain characteristics is rather difficult. Ice accretion on conductor bundles can be investigated with experiments or with statistical and numerical models. Experiments are difficult to perform.

In theoretical investigations, both shape and aerodynamic coefficients require simulation of the icing process itself. Known numerical models are restricted to single cables due to the assumptions made in the flow calculation. With the simulation scheme used at our institute, the particle motion based on the stream around the conductor bundles can be determined. The simulation uses a Finite Element Method (FEM) with a Reynolds Average Navier-Stokes (RANS) for an incompressible fluid via a k-ε turbulence model. The stream of air and of precipitation droplets are modelled as one-way coupled two-phase flow. Ice accretion and flow field are calculated iteratively to account for geometrical changes of the ice deposit in the flow calculation. Modelling atmospheric icing includes, in addition, a computation of the mass flux of icing particles as well as a determination of the icing conditions: Icing conditions are defined by the heat balance on the ice surface, Peil & Wagner (2008) and Wagner, Peil & Borri (2009).

Three major types of deposit, namely rime, glaze and wet snow lead to significant loads on structures. For glaze ice and wet snow formation, the heat balance on the ice surface is very important. Computation of the mass flux of icing particles is an important factor in ice accretion. Shape, and to a smaller extent, also density of ice evolution is influenced by the characteristics of the particle trajectories.

Figure 28 shows, on the left, results of simulations with the presented model (−), with the model of Fu (2006) (⋯) and with eperiments (- -).The presented model meets the longitudinal extension of the ice body very well for a larger (left) and a smaller (right) cable diameter. The vertical extension deviates in both cases, which is due to the calculation of the particle impinging points on the surface.
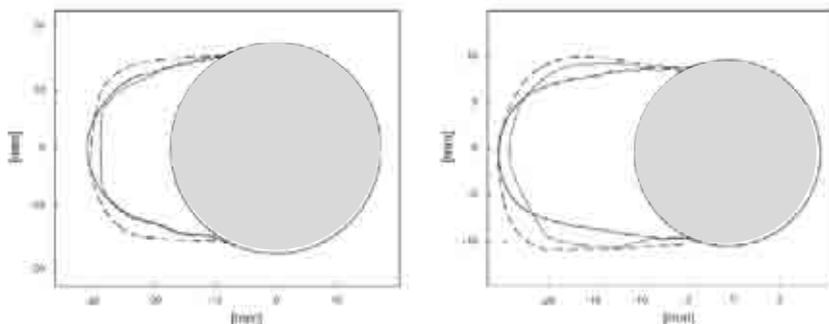
Figure 28: Ice accretion on single cables with different diameter

Fig. 29 shows the simulation of ice accretion on a bundle of two cables. The upstream cable catches a larger fraction of the particle flux than the downstream cable in its wake. In general, the shaded area decreases with decreasing deflection of the particle trajectories. It means that larger droplets will deflect less due to their higher inertia. Once the upstream cable gets a more streamlined shape due to the ice accretion, the particle trajectories are deflected to a smaller extent when passing the first cable. Thus the mass flux on the downstream cable increases.
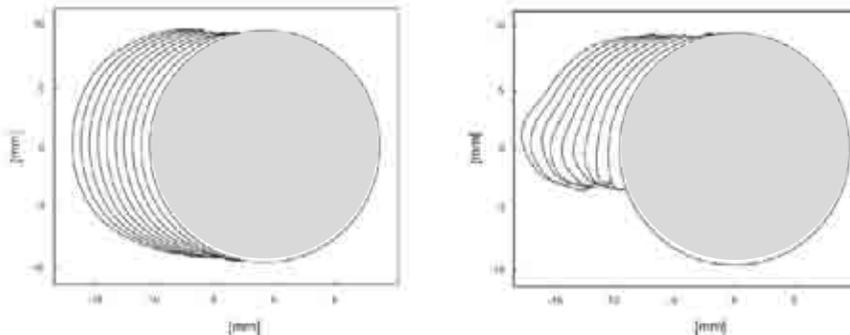
Figure 29: Ice accretion on a cable bundle (left: upstream, right: downstream)

An also motion-induced or self-excited excitation mechanism is the so called rain-wind induced vibration. They are very close to galloping vibrations, except that the shape of the vibrating (iced) cable is not constant over time but varies due to the fluctuating rivulets produced by rain, wind and inertia. In contrast to galloping vibrations, there is not only an onset wind speed, but also a final wind speed beyond the vibration ends. The onset wind speed is not high, about 5m/s could be enough. The final wind speed could be about 15 to 20m/s. The vibration is mainly controlled by damping. The stability plot in Fig. 30 shows that even small damping decrements abandon the vibration, Peil, Narath & Dreyer (2003). A state-of-the- art report is published in Peil & Steiln (2007).
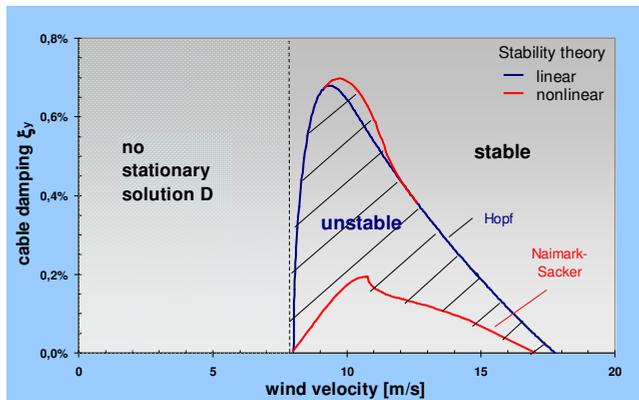
Figure 30: Stability chart of rain-wind induced vibrations of a cable

The investigations are performed under the assumption of a laminar flow. Wind tunnel test show that the response under turbulent flow is smaller. The problem is that the integral length scale of the turbulence is very small compared with the dimension of the specimen. It is nearly impossible to perform wind tunnel experiments in a scale which fits to the usual integral length scale of wind tunnel turbulence.

Therefore we are now investigating the influence of the turbulence of the natural wind by means of full scale measurements. A 1.5-m long specimen is kept by springs and force sensors; the oncoming wind process is measured via Ultrasonic Anemometers. A special raining device ensures correct raining conditions. Fig. 31 gives a rough overview about the device.

Figure 31: Rain-Wind induced vibrations experimental device

Finally some references should be given of our work on gust-induced vibrations. They could hardly be integrated into the musical context because their frequency spectrum is broad, close to white noise. Of course the structure reacts under the influence of turbulent wind at its natural frequencies and modes. The amplitudes are changing probabilistically.
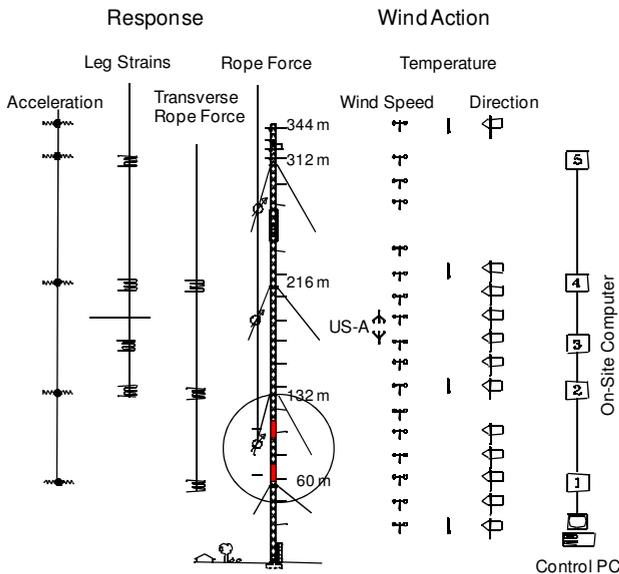
Figure 32: Wind and mast measurement equipment in Gartow

The work can be divided into two parts. One part is focused on the already mentioned measurements of wind characteristics. In 1989 we installed measurement equipment on a 344m mast, which is unique in the world, see Fig. 29. Wind actions and mast responses are measured in parallel by on-site computers located in the mast at different heights. The wind speed is measured in vertical distances of 18m up to the height of 341m. In the lower turbulent range, the wind direction is measured at the same levels. Five years ago the shaft was covered so that the aerodynamic admittance function can be measured. The work is accompanied by theoretical investigations. It is not possible to briefly report on this work in this paper. For further information see for instance Peil & Telljohann (1999), Peil & Behrens (2003), Peil & Clobes (2008).

Now we are starting to extend the equipment remarkably. The cable will be provided with boxes carrying Ultrasonic anemometres, 3D accelerometer and temperature sensors. The boxes can roll on the main cable, the boxes will be pulled up by a thin cable and can be lowered down for maintenance purposes. The main goal of the measurements is to determine the natural 3D-wind field up to a height of about 156m.
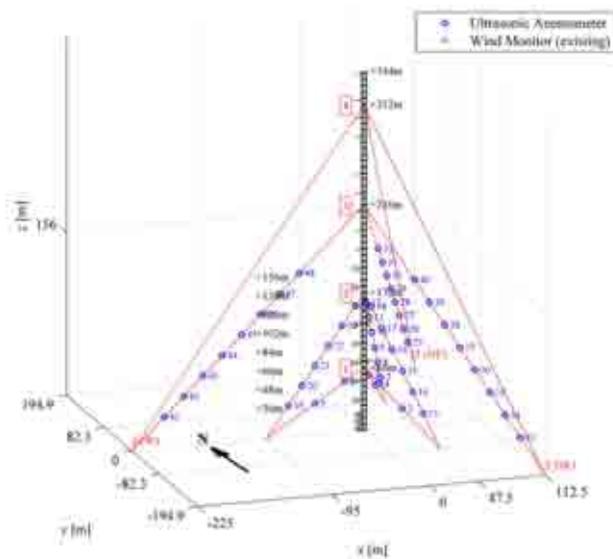
Figure 32: Additional sensor boxes placed on the cables

6. CONCLUSION AND ACKNOWLEDGEMENTS

It is obvious that there are many parallels between music and wind. The structural vibrations produced by the same self-excited or motion-induced mechanisms as in music instruments produce music in inaudible frequencies.

REFERENCES

Clobes,M., A. Willecke, U. Peil (2009) " A refined analysis of guyed masts in turbulent wind". Proc. 5th European-African Conference on Wind Engineering (EACWE 5), Florence 2009.

Dickens,P. R. France, J. Smith, J. Wolfe (2007) „Clarinet Acoustics: Introducing a compendium of impedance and sound spectra. Acoustics Australia, Vol. 35pp 1-17.

Fletcher, N.H., T.D. Rossing (1998) " The Physics of musical instruments" 2nd Edition, Springer Verlag, New York.

Hall, Donald E. (1991) "Musical Acoustics" 2nd Ed, Brooks/Cole Publishing

Kirch, A. and Peil, U. (2009a) "Limits for the control of wind-loaded slender bridges with movable flaps; Part I: Aerodynamic modelling, state-space model and open-loop characteristics of the aeroelastic system" In: EACWE 5 ― Proceedings of the 5th European and African Conference on Wind Engineering EACWE 5, Florence / italy

Kirch, A. and Peil, U. (2009b) "Limits for the control of wind-loaded slender bridges with movable flaps; Part II: Controller design, closed-loop characteristics of the aeroelastic system and gust alleviation" In: EACWE 5 ― Proceedings of the 5th European and African Conference on Wind Engineering EACWE 5, Florence / italy

Kobayashi, H. ; Nagaoka, H. (1992). "Active control of flutter of a suspension bridge" In: Journal of Wind Engineering and Industrial Aerodynamics, 41 (1–3), pp. 143–151

Körlin, R. ; Starossek, U. (2007), "Wind tunnel test of an active mass damper for bridge decks" In: Journal of Wind Engineering and Industrial Aerodynamics, 95(4), pp. 267–277

Miyata, T.; Yamada, H.; Dung, N. N. and Kazama, K. (1994), "On active control and structural response control of the coupled flutter problem for long span bridges" In: First World Conference on Structural Control, Los Angeles, pp. WA4-40 – WA4-49

Murata, M. ; Ito, M. (1971) "Suppression of wind-induced vibration of a suspension bridge by means of a gyroscope" In: Third International Conference on Wind Effects on Buildings and Structures, Tokyo, pp. 1057–1066

Ostenfeld, K. H. ; Larsen, A. (1992). „Bridge engineering and aerodynamics" In: Aerodynamics of Large Bridges — Proceedings of the First International Symposium on Aerodynamics of Large Bridges, Copenhagen / Denmark, pp. 3–22

Peil, U., G. Telljohann (1999) "A Wind Turbulence Model based on long-term measurements", Proc. 10th Int. Conf. Wind Engineering, Copenhagen. Elsevier, 10th Int. Con. Wind Engineering, pp 147-153.

Peil, U., Nahrath, N., Dreyer, O. (2003a) " Rain-wind induced vibrations of cables - Theoretical models" Proc. of the 5th International Symposium on Cable Dynamics, pp. 345-352.

Peil, U., Nahrath, N., Dreyer, O. (2003b) "Modeling of rain-wind induced vibrations". Proc.of the 11th International Conference on Wind Engineering, Lubbock, pp. 389-396,.

Peil, U., Behrens, M (2003) " Aerodynamic admittance models checked by full scale measurements".Proc. of the 11th Intern. Conference on Wind Engineering, Lubbock, pp 1769-1776.

Peil, U., Steiln, O. (2007): „Regen-Wind-induzierte Schwingungen - ein State-of-the-Art Report". Stahlbau 76, pp. 34-46,

Peil, U., Dreyer, O. (2007) "Rain-wind induced vibrations of cables in laminar and turbulent flow". Wind & Structures, Techno - Press, Vol.10, No. 1, pp. 83-97.

Peil, U., Behrens, M (2007) "Aerodynamic Admittance Models for Buffeting Excitation of High and Slender Structures". Journ. of Wind Engineering & Industrial Aerodynamics , pp 73-90 .

Peil, U; Kirch, A. (2008). "Control limits for slender bridges under wind action" In: AWAS'08 – 4th International Conference on Advances in Wind and Structures, Jeju / Korea, Paper WPN274

Peil, U.; Clobes, M. (2008) "Identification and simulation of transient unsteady admittance on guyed masts". 7 th European Conference on Structural Dynamics, Southampton.

Peil, U.,Wagner, T. (2008): Atmospheric Icing of Transmission Line Conductor Bundles. Proc. 2th European COMSOL Conference Göttingen, COMSOL Multiphysics GmbH.

John R. Pierce (1998) "The nature of musical sound". In: The Psychology of Music, 2nd Edition (Cognition and Perception), Academic Press, pp 1–24.

Spitzer, M. (2008) "Musik im Kopf". Schattauer-Verlag, Stuttgart.

Tölke,J., M. Krafczyk (2008) „Towards three-dimensional Teraflop-CFD computations on a desktop PC", Int. Journ. Comput. Fluid Dynamics, Vol. 22, 7, pp 443-456.

Wagner, T., U. Peil, C. Borri (2009): "Numerical investigation of conductor bundle icing". Proc. 5th European- African Conference on Wind Engineering (EACWE 5), Florence 2009.

Wind and Comfort

Ted Stathopoulos

Professor and Associate Dean

Centre for Building Studies, Department of Building, Civil and Environmental Engineering
Concordia University – statho@bcee.concordia.ca – Montreal, Quebec, Canada

Keywords: comfort, design, environment, pedestrian, wind.

ABSTRACT

Wind plays always an important role in dealing with outdoor human comfort in an urban climate. Although various models of different complexity have been proposed to characterize the effect of wind on pedestrians in relation to their specific activities, it has been also recognized that human comfort in general may be affected by a wide range of additional parameters, including air temperature, relative humidity, solar radiation, air quality, clothing level, age, gender etc. Several criteria have been developed in the wind engineering community for evaluating only the wind-induced mechanical forces on the human body and the resulting pedestrian comfort and safety. It is also noteworthy that there are significant differences among the criteria used by various countries and institutions to establish threshold values for tolerable or unacceptable wind conditions even if a single parameter, such as the wind speed is used as criterion. These differences range from the speed averaging period (mean or gust) and its probability of exceedance (frequency of occurrence) to the methodology of evaluation of its magnitude (experimental or computational). The paper attempts to review some of the work carried out in this area and to address some of the most recent efforts to develop wind ordinances, as well as to incorporate additional parameters in order to specify the threshold values or comfort ranges for respective weather parameters. Ideally, for design purposes, an approach towards the establishment of an overall comfort index taking into account wind conditions and other microclimatic factors should be an ultimate objective.

Contact person: T. Stathopoulos, Professor and Associate Dean, 1515 St. Catherine W., Room EV-6.125, 514-848-2424 ext. 3186 and 514-848-7965 (FAX).
E-mail statho@bcee.concordia.ca

1. INTRODUCTION

Comfort in open urban spaces has received a lot of attention in recent years in broad recognition that microclimatic conditions contribute to the quality of life in cities, both from the economic as well as from the social viewpoint. Consequently, in response to significant interest expressed by the community, microclimatic conditions and particularly the effect of wind on the outdoor human comfort has been examined. Perhaps the American Society of Civil Engineers (ASCE) has put out a most pertinent state-of-the-art document (ASCE/SEI 2003), which was developed with input from the European Action C14. The latter, entitled Impact of Wind and Storm on City Life and Built Environment had a working group interested in the effects of wind on pedestrians, their assessment and comparisons, as well as the parameters they influence human comfort and its evaluation. Some of the results of this effort have appeared in the 2002 Workshop in Nantes, e.g. Westbury et al. (2002) and in the International Conference in Urban Wind Engineering and Building Aerodynamics organized by Von Karman Institute for Fluid Dynamics in May 2004.

Furthermore, a 3-year EU-funded project carried out earlier in this decade with surveys at different open spaces complete approximately 10,000 interviews aiming to produce an urban design tool that provides architects, engineers, urban planners and other decision makers with means to assess effectively the construction of new buildings and the development of cities from the economic, psycho-physiological and sociological perspective of human comfort. A unique characteristic of this work consists of involving several aspects of physical environment (microclimate, thermal, visual and audial comfort, urban morphology) as well as social environment. The models and tools developed in the auspices of this project have been included in CRES (2004). The details of this project are available in http://alpha.cres.gr/ruros.

More recently, new criteria for the assessment of wind environment in cities in terms of ventilation performance and thermal comfort have been developed for several Asiatic countries, e.g. Hong Kong. Bu et al (2009) proposed two criteria for the evaluation of local wind environment, namely local air change rate and local kinetic energy.

The paper will describe the aerodynamics of the urban environment and the reasons causing high wind speeds at sidewalks and, consequently, potential discomfort to pedestrians; it will address both experimental and computational evaluations of the wind on people in the urban environment and will note the development of recent wind codes such as that in the Netherlands; finally, it will focus on the state-of-the-art of the development of human outdoor comfort criteria by considering a wide range of parameters, including wind speed, air temperature, relative humidity, solar radiation, air quality, human activity, clothing level, age and the like.

2. AERODYNAMICS OF THE URBAN ENVIRONMENT

Strong winds are usually accelerated at the pedestrian level within the urban environment, say around tall buildings, due to particular aerodynamic configurations generally associated with tall buildings. In the case of a simple rectangular tall building, it is the boundary layer flow that causes descending flows towards the street level due to the pressure differences created by the velocity differences between higher and lower levels. This downflow is significant due the pressure proportionality to the square of the velocity (Bernoulli equation) and its strength increases with the building height. This effect is termed in the literature as downwash. Clearly, downwash is diminished drastically in the absence of boundary layer flow and this explains the lack of adequate representation of wind effects in the building environment for simulations carried out in the past using aeronautical wind tunnels for building aerodynamics applications.

In general, buildings will only induce high wind speeds at lower levels if a significant part of them is exposed to direct wind flows. It is actually the direct exposure to wind rather than building height alone, which causes the problem. This is shown diagrammatically in Figure 1.Another type of pedestrian-level winds is formed when high-speed winds pass through openings between

high-pressure air on the windward wall and low pressure regions on the leeward side of a building. Once more, the fair character of nature, which does not like pressure differences, prevails and strong flow is induced to correct the problem. Pedestrians in arcades of commercial buildings can testify regarding this situation, which is unpleasant to the store owners in these areas as well. Additional flow-induced mechanisms creating disturbances to the urban environment in the vicinity of buildings include but are not limited to the effects of the large standing vortex in front of a building, the vortex flows generated after the flow separates and accelerates along the building front edges and the wake-induced disturbances via the interaction of the flow coming from the building side faces and the re-circulation flow regime created by the shear layer flow above the building. Clearly, wind direction is a significant factor here, in addition to the magnitude of the oncoming wind speed.
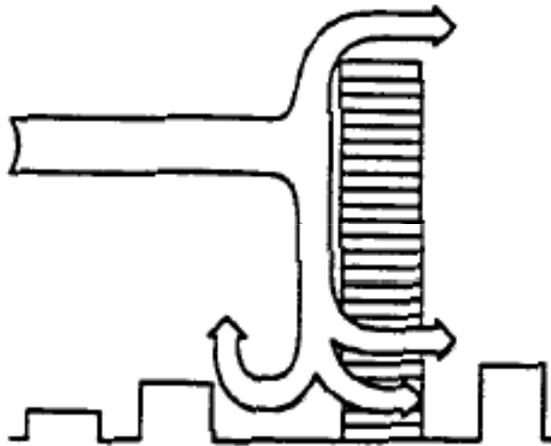
Figure 1: wind flow around buildings significantly taller than their surroundings, after Cochran (2004).

Common building configurations and potential influences on pedestrian-level winds are shown in Figure 2 taken from Cochran (2004). These configurations include the effects of canopies, which may act as deterrents to the strong down-flow prior to impacting on sidewalks or other pedestrian free access areas around the building. However, such measures may create other problems by deflecting the wind from, say, a building entrance to another area around the building corners or across the street. Setbacks on the building surfaces or penthouses are elements generally remediating the pedestrian-level winds and are used rather extensively. Furthermore, a podium not intended for long-term pedestrian activities or vegetation in terms of bushes and coniferous-evergreen trees can also be used as a positive measure to amend harsh wind conditions at pedestrian level. Porous screens are also successful in deflecting winds without relocating the adverse conditions on other places. An entrance alcove, as well as balconies on building facades, generally make sidewalk winds diminish. However, high winds may be transferring on balconies themselves, particularly those near the edges of the building facades.

The previous discussion is really about isolated and mainly rectangular buildings. Curved buildings such as cylindrical shapes generally promote lateral flow, so they behave better as far as effects of pedestrian-level winds are concerned. Channeling effects appearing in the case of two or more buildings are generally critical, particularly if the wind direction is along the street or corridor formed between the buildings. This is a result of the so-called Venturi effect, which can be critical in some cases. However, recent work on the wind flow in passages between buildings (Blocken et al., 2008) has questioned the existence of the classical Venturi effect in such cases.

A building taller than its surroundings can concentrate pedestrian level winds at ground level.

A tall building concentrates wind at its base, particularly at the corners where the downwash is accelerated into horizontal motion.

Undercut corners can aggravate the wind conditions at a building corner. Typically this is not a good location for an entrance.

Downwash can be deflected by a large canopy at the base of a building, producing a pleasant entrance area.

A podium/tower combination concentrates winds at the podium roof (▨) not at the base (☐).

Openings through a building at the base induce high velocities due to pressure differential from the front to the back.

Recessed entry provides low winds at door locations.

Adjacent building placement can cause a compression of the mean streamlines, resulting in horizontally accelerated flows at ground level.

Figure 2: design features to change and/or ameliorate pedestrian wind conditions, after Cochran (2004).

If the wind conditions with one or two simple-shaped buildings in place can become so complex, one can easily imagine what would really happen with buildings of complex shapes interacting with the wind flow passing amongst them, particularly when the effect of ground topography and all adjacent buildings are taken into account. The problem becomes really difficult and for a number of

years could only be solved experimentally via appropriate simulation in a boundary layer wind tunnel. Only recently, more specifically during the last few years with the significant progress in computational technology, attempts were made to address the problem of pedestrian-level winds in the urban environment computationally. More detailed discussion on the state-of-the-art of this approach will be presented in a subsequent section.

Regardless of the approach used to determine the impact of wind flows at the pedestrian level, the previous comments have demonstrated that the direction of the oncoming wind together with its magnitude, i.e. speed, will be of paramount importance. If the wind climate in a city is distinctly directional, i.e. strong winds come always from a particular narrow fetch, it is clear that this set of directions should be really scrutinized because, in all likelihood, critical results will occur when the wind comes from these particular directions. As an example, the basic wind environment of Montreal in terms of wind speeds and probabilities of exceedance from different directions is presented in Figure 3.
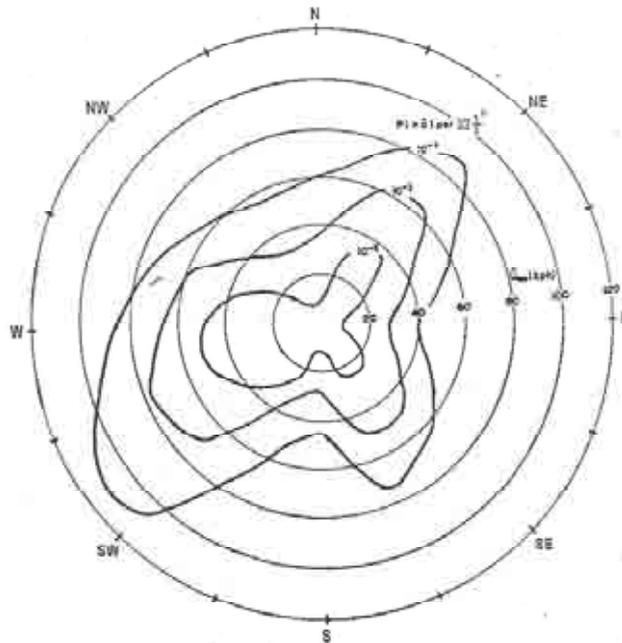
Figure 3: probability distributions of hourly mean wind speed at 300 m over Montreal for daylight hours during the winter (derived from 10 year record of wind data obtained at a height of 10 m at Trudeau Airport).

As clearly shown, westerly and southwesterly winds dominate while north and northeasterly winds may also be high. Note that these are upper level winds and significant changes may occur near the ground areas. In addition, differences exist between summer and winter wind data. Maximum summer winds are dominant from west, while winter winds are certainly higher and they blow primarily from southwest. In the great majority of pedestrian wind studies carried out for tall buildings in Montreal, it has been found that winds for west / southwest and, to a lesser extent from northeast have produced the most critical adverse conditions.

In summary, there are two main flow types causing high pedestrian-level winds in the urban environment: downwash flows and horizontally accelerated flows. The former are diminished by podia, architectural features such as setbacks, balconies and the like; the latter are ameliorated by alcoves, chamfered corners, landscaping (vegetation) or porous screens.

3. WIND COMFORT CRITERIA

Several criteria have been developed in the wind engineering community for evaluating only the wind-induced mechanical forces on the human body and the resulting pedestrian comfort and safety. There are significant differences among the criteria used by various countries and institutions to establish threshold values for tolerable and unacceptable wind conditions even if a single parameter, such as the wind speed is used as criterion. These differences range from the speed averaging period (mean or gust) and its probability of exceedance (frequency of occurrence) to the evaluation of its magnitude (experimental or computational).

Table 1 shows the traditional Beaufort scale used in ship navigation in a modified version applicable to land regions and for heights representative of pedestrians. This table provides an idea of the mechanical effects of wind of different speeds on the human body. Physiological effects are more complex since they depend on additional factors and their interactions. Jordan et al (2008) attempted to evaluate the response of a person to a sudden change in wind speed in terms of wind comfort and wind safety. It was found that the wind speed necessary to cause loss of balance was a function of the incumbent's orientation and weight.

Table 1: Beaufort scale of winds as used on land, after ASCE (2003).

Beaufort Number	Descriptive Term	Speed (km/h)	Specification for Estimating Speed
0	Calm	Less than 2	Smoke rises vertically.
1	Light Air	2 – 5	Direction of wind shown by smoke drift but not by wind vanes.
2	Light Breeze	6 – 11	Wind felt on face; leaves rustle; ordinary vane moved by wind.
3	Gentle Breeze	12 – 19	Leaves and small twigs in constant motion; wind extends light flag.
4	Moderate Breeze	20 – 29	Raises dust and loose paper; small branches are moved.
5	Fresh Breeze	30 – 39	Small trees in leaf begin to sway; crested wavelets form on inland waters.
6	Strong Breeze	40 – 50	Large branches in motion; whistling heard in telegraph wires; umbrellas used with difficulty.
7	Near Gale	51 – 61	Whole trees in motion; inconvenience felt in walking against the wind.
8	Gale	60 – 74	Breaks twigs off trees; generally impedes progress.
9	Strong Gale	75 – 87	Slight structural damage occurs e.g. to roofing shingles, TV antennae, etc.
10	Storm	88 – 102	Seldom experienced inland; trees uprooted; considerable structural damage occurs.
11	Violent Storm	103 – 116	Very rarely experienced; accompanied by widespread damage.
12	Hurricane	Above 116	

A simple rule of thumb has been provided by Wise (1970) and Pendwarden (1973). This is based on mean speeds (V) assuming the following effects:
– V = 5 m/s or 18 km/h   onset of discomfort
– V = 10 m/s or 36 km/h   definitely unpleasant
– V = 20 m/s or 72 km/h   dangerous
   Conditions for pedestrians are considered acceptable if V > 5 m/s less than 20% of the time

(Pendwarden and Wise 1975).

Recognizing the importance of frequency of occurrence along with the magnitude of wind speeds, Figures 4, 5 and 6 provide threshold mean wind speeds for various types of activity as functions of the average annual number of storm occurrences. Naturally the mean wind speed threshold level drops significantly as the yearly average number of occurrences increases.

Utilization of mean wind speeds as comfort criteria for pedestrian-level winds has been questioned by the wind engineering community. In fact, the most prevailing opinion seeks an effective wind speed, which is related to the gustiness of the wind, to be used for that purpose. Such effective speeds can be derived from the following equation expressing their outcome in terms of the mean and a number (ranging from 1 to 3) of standard deviations of the wind speed:

$$V^e = \overline{V} \cdot \left(1 + \kappa \cdot \frac{\overline{v'^2}^{1/2}}{\overline{V}} \right) \tag{1}$$

where:

$\overline{v'^2}^{1/2}$ = rms of longitudinal velocity fluctuations

κ = constant $(\cong 1 \text{ to } 3)$

Figure 4: wind tunnel exposure of people at 10-15 km/h winds.

Figure 5: wind tunnel exposure of people at 20 (left) and 40 (right) km/h winds.

Figure 6: wind tunnel exposure of people at 70 km/h winds.

Wind tunnel experiments and observations of pedestrian performance suggest that $\kappa = 3$ is the most appropriate value. Figure 7 shows acceptance criteria for wind speeds for various annual frequencies of occurrence proposed by Isyumov and Davenport (1975). Note that these criteria are different from previous criteria in that, instead of specifying a wind speed for various activities, frequencies of occurrence are specified for different wind speeds. Murakami et al. (1986) produced the wind comfort criteria described in Table 2.
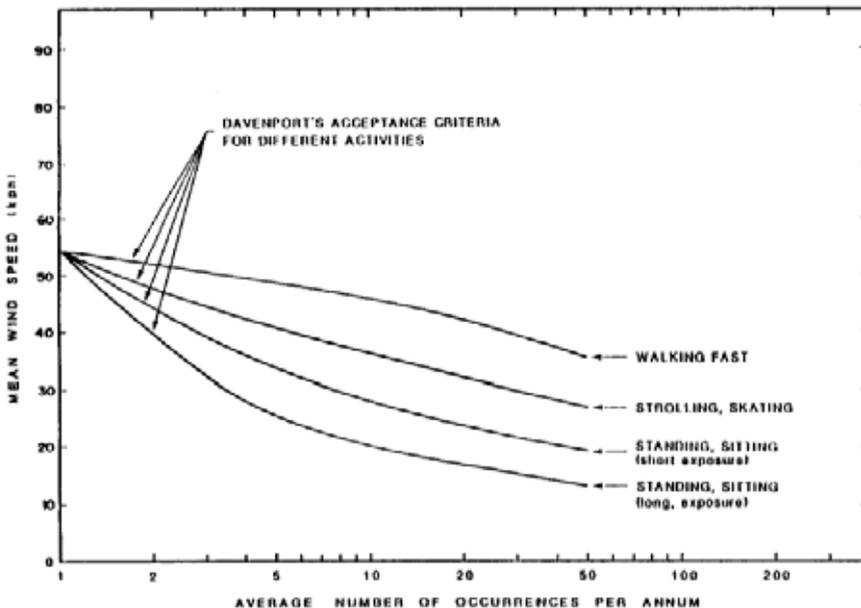
Figure 7: acceptance criteria for wind speeds for various annual frequencies of occurrence, after Isyumov and Davenport (1975).

Table 2: wind environment criteria of Murakami et al. (1986).

Wind Condition	$\hat{U}_{local}$	$P(>\hat{U}_{local})$
Acceptable for walking		
summer:	48 km/h	0.01 (once per month)
winter:	32 km/h	0.01 (once per month)
Hazardous	83 km/h	0.001 (once per year)

Melbourne (1978) has produced separate criteria based on mean and gust speeds. He proposed their application only for daylight hours and on the assumption that the max 2-sec gust speed will be roughly twice as large as the mean speed, he produced the curves shown in Figure 8. These curves identify threshold wind speed criteria for different types of activity similar to those shown in Table 3. Criteria for dangerous wind conditions were also specified.

Such conditions are particularly important for cities with harsh winter conditions where icy sidewalks become source of frequent accidents when combined with high winds. Several cases of this nature have been reported, most involving accidents happened on elderly people. Liability issues are also interesting for such cases and courts have always a hard time dealing with them.

On the basis of experience over a number of projects and wind tunnel studies, it has been concluded that Melbourne's criteria are on the strict side, i.e. if prevailing conditions abide by the prescribed limits, most sets of other criteria available in the literature or included in ordinances of various municipalities will be satisfied. Consequently, these criteria can be used as upper limits for pedestrian-level winds and, in this regard, are indeed valuable.

Table 3: wind environment criteria of Melbourne (1978).

Activity	Probability of Exceedance of $(P(>U))$		
	$\hat{U} = 36\ km/h$	$\hat{U} = 54\ km/h$	$\hat{U} = 72\ km/h$
Long-term and short-term stationary exposure	0.10	0.008	0.0008
Strolling	0.22	0.036	0.006
Walking	0.35	0.07	0.015

Wind ordinances in major cities

There is great variation regarding wind ordinances in various cities / countries around the world. In some cases, specific legislation has passed and new building permits are not provided until the developers/owners demonstrate that the project will not generate dangerous or even uncomfortable and undesirable pedestrian-level wind conditions. In other cases, this is expected to happen as part of assumed good engineering and architectural practice. Koss (2006) carried out a detailed analysis of different wind comfort criteria used at European wind engineering institutions. The study concluded that a code of good practice may be better based on criteria using hourly mean wind speeds. Furthermore, Sanz-Andres and Cuerva (2006) found that the differences in the comfort criteria used in various countries are due, to some extent, to the human perception or acclimatization considered in various countries.

In general, the following points can be made:

− Most major cities (Montreal, Toronto, Sydney, etc) have some guidelines addressing the problem at the approval stage for new construction projects. Montreal's wind comfort criteria, specified in Article 39 of the *Cadre* (1992), refer to **mean** wind speeds rather than **gust** speeds. The critical mean wind speeds, U_{local}, for winter and summer are 14.4 km/h (4 m/s) and 21.6 km/h (6 m/s), respectively, and the maximum acceptable probabilities of exceeding these values are as follows:
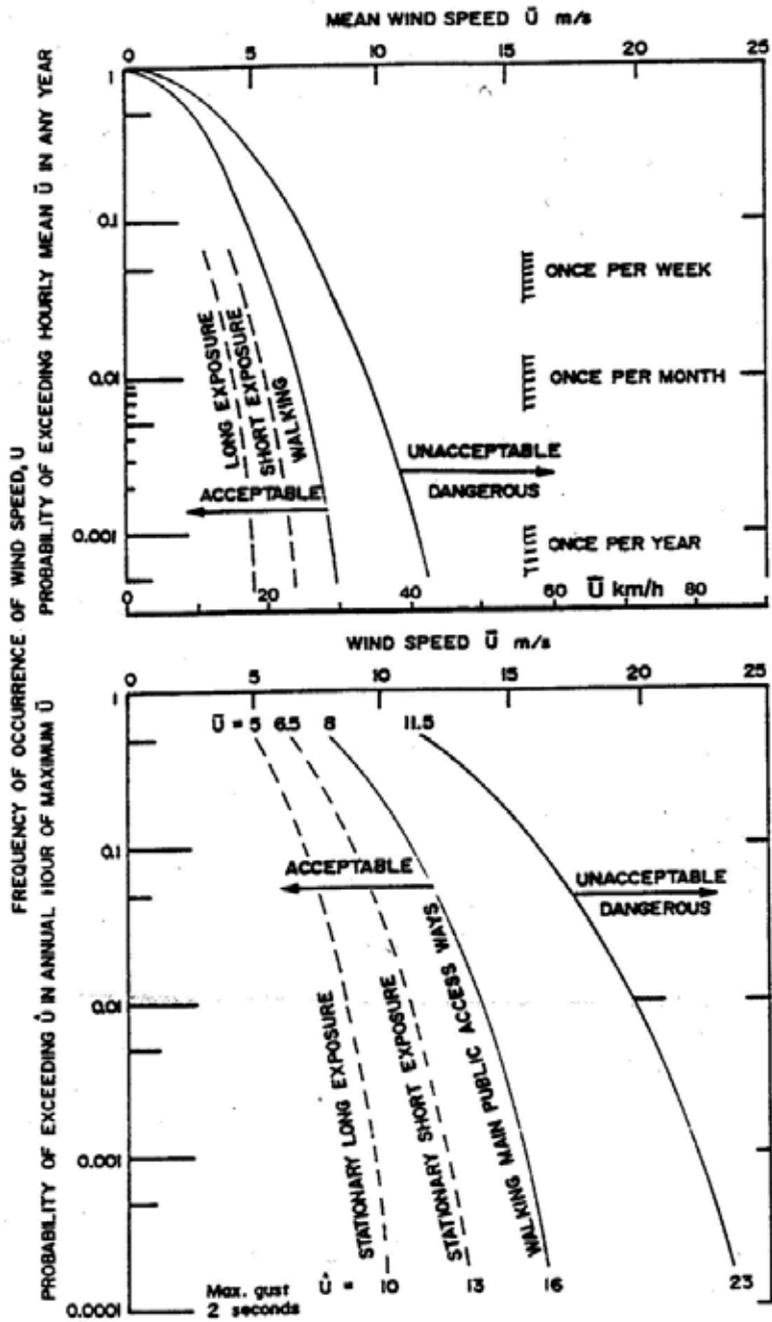
Figure 8: probability distributions of Melbourne's criteria for environmental wind conditions for daylight hours for a turbulence intensity of 30% and û = 2u, after Melbourne (1978).

Location	**Probability of exceedance of U_{local}**
Main Streets	15%
Secondary Streets	25%
Parks	10%

- San Francisco has adopted a very strict wind ordinance; they use V^e = 42 km/h with $P\ (>V^e)$ = 0.01% as safety criterion; this is significantly lower than that proposed in most of the current literature.
- New York has strict air pollution standards, which tend to work against guidelines for the pedestrian wind environment; only 30% of new developments have to go through a review process.
- Boston Planning Department specifies that a wind tunnel study is required to assess wind environmental conditions near new developments for the following cases:
  - i. for any new building taller than 100 ft and at least two times taller than its adjacent buildings
  - ii. for other buildings in special circumstances

As it is always the case with any adoption of code provisions or changes, passing legislation regarding pedestrian wind conditions is always problematic. It is worth mentioning that a new wind ordinance has been approved in the Netherlands only recently after several years of intense efforts by several experts, architects and engineers. Table 4 summarizes the code criteria in terms of hourly averaged wind speed at pedestrian level. As an indicator of wind comfort, the code uses a threshold wind speed of 5 m/s; threshold for danger is 15 m/s. Grades of comfort are introduced related to the probability that a threshold wind speed is exceeded (Willemsen and Wisse, 2007).

Table 4:   criteria for wind comfort and danger in NEN 8100, after Willemsen and Wisse (2007).

Wind comfort				
$P(V_{IS}>5m/s)$ in % hours per year	Grade	Activity area		
		Traversing	Strolling	Sitting
< 2.5	A	good	good	good
2.5–5.0	B	good	good	moderate
5.0–10	C	good	moderate	poor
10–20	D	moderate	poor	poor
> 20	E	poor	poor	poor

Wind danger		
$P(V_{IS}>15\ m/s)$	Limited risk	0.05-0.3 % hours per year
	Dangerous	> 0.3 % hours per year

4. EXPERIMENTAL PROCEDURE: WIND TUNNEL APPROACH

As mentioned previously, the flows around buildings even in simple surrounding environments, let alone in complex urban settings are still extremely difficult to predict by computational methods. However, the testing of scale models in a boundary layer wind tunnel capable of simulating the mean-velocity profile and turbulence of the natural wind has been shown to be a very effective method of prediction by comparison with respective full-scale data. The wind-tunnel model typically includes all buildings in the surrounding landscape; thus, their effect is automatically included. Both existing conditions and those with the new building(s) in place can be readily measured, thus

allowing the impact of the new building(s) to be identified. Furthermore, the effects of changes to the building itself, or to landscaping, can also be studied, particularly where undesirable wind conditions are found.

A typical set up of a wind-tunnel model in a boundary-layer wind tunnel is illustrated in Figure 9. The building itself and the model of its surroundings are mounted on the wind-tunnel turntable, which can be rotated to allow various wind directions to be simulated. Typical model scales for large buildings are in the range of 1:200 to 1:500. Larger scales have been used for smaller buildings. The model of surroundings enables the complex flows created by other buildings near the study building to be automatically included in the tests. However, it is also essential to create a proper simulation of the natural wind approaching the modeled area. The requirements for modeling the natural wind in a wind tunnel are described in the ASCE (1999). In typical wind tunnel tests, the airflow speed above the boundary layer is in the range 10 to 30 m/s.
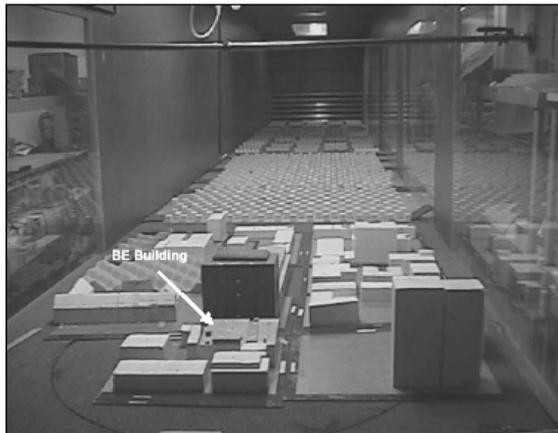
Figure 9: typical wind tunnel set-up for a pedestrian wind assessment study.

The process followed in the experimental approach consists of the following steps:
1. Meteorological records
2. Wind tunnel testing
3. Combination of (1) and (2)
4. Comparison with comfort criteria
5. Remedial measures

The wind tunnel testing considers current conditions and those with the proposed development. Of course, the anticipated wind speeds are based on statistical expectations and actual wind conditions during a particular storm may be different. Future building developments in the surrounding area may also affect the pedestrian wind environment, but this has not been considered in the present study.

5. COMPUTATIONAL PROCEDURE: CFD

In Computational Wind Engineering (CWE) the computer essentially replaces the physical simulation in the boundary layer wind tunnel, at least in principle. CFD methods involve very large amounts of computation even for relatively simple problems and their accuracy is often difficult to assess when applied to a new problem where prior experimental verification has not been done. Castro and Graham (1999) summarized the concerns expressed with respect to these issues. However, there have been cases for which the application of CFD methodologies appears to give somewhat satisfactory responses. These are cases requiring the determination of mean flow conditions and

pressures, i.e. those related primarily with environmental issues. Typical problems of this category include but are not limited to pedestrian level winds, snow dispersion and accumulation, dispersion of pollutants in the near-building and/or urban environment, ventilation and the like. There is increasing evidence that for such problems CFD-based techniques may provide adequate responses – see Stathopoulos (2002).

Pedestrian-level winds can be described quite adequately in terms of mean velocities in the presence and absence of a new building within a specific urban environment. Although it can be argued that pedestrians are mostly affected by gust effects and mean wind speeds may not be sufficient to produce satisfactory results, the fact remains that several major cities require only the satisfaction of certain mean (sustainable) speeds with a specified probability of exceedance. A number of recent computational studies for the evaluation of pedestrian level winds and the comparison of their results with respective experimental data are described in the following sub-section. The process of comparison between computational and experimental results has already been challenged and appears problematic on its own. For instance, is it more meaningful to carry out point-by-point comparisons or does it make more sense to examine pedestrian-level wind speeds affecting a particular zone or area of influence for a specific activity within the urban environment? Furthermore, and after due consideration to the fact that pedestrian level wind speeds measured in the proximity of buildings, i.e. in areas of high turbulence, are not very accurate, it may be conceivable that "errors" in the results might be better described in terms of their impact on design decisions. Clearly, this may be more reasonable, at least in the context of engineering perspective. More details and specific comparison case studies can be found in Stathopoulos (2006).

Mochida and Lun (2008) carried out an excellent review of the CWE advances in the area of wind and thermal environment in Japan. The study suggested that CWE has grown from a tool for analysis to a tool for environmental design.

6. OUTDOOR COMFORT ISSUES

Outdoor human comfort in an urban climate depends on a wide range of weather and human factors. Studies have shown integrated effects of wind speed, air temperature, relative humidity and solar radiation on the human perception, preference and overall comfort in an urban environment. Some analysis of these issues has been presented in the ASCE (2003). Furthermore, the studies by Nicolopoulou et al. (2001; 2002) also address the influence of microclimatic characteristics in outdoor urban spaces and the comfort implications for the people using them. A significant characteristic is the psychological adaptation, which has also been addressed. An equivalent temperature has been defined and related to the outdoor human comfort by considering acclimatization and other bio-meteorological principles (Stathopoulos et al. 2004; Zacharias et al. 2001). However, the implications of this approach are far fetching and the overall assessment problems are still quite intriguing. Some basic ideas are presented in this paper.

Temperature and relative humidity

Both can have a significant impact on a person's comfort, since sensation of comfort in cold conditions is linked to the heat balance of the human body, i.e. the balance of heat generated by metabolic processes and heat lost by conduction, convection, radiation and evaporation. In convective and evaporative losses, the effects of temperature and humidity are closely linked with the wind conditions and cannot be treated in isolation from wind speed. This is why, for example, in the colder regions of Europe and North America, the wind chill equivalent temperature is used to provide a more meaningful description of how cold weather will really feel, rather than simply giving air temperature. The equivalent temperature is obtained by calculating the temperature in standard wind (set at 1.8 m/s = 4 mph) that would give the same rate of heat loss from exposed skin at 33°C as occurs in the actual wind and temperature conditions. Generally, in cold conditions, humidity is low and has

little direct effect on thermal comfort, although there may be indirect effects, such as humidity changing the insulation value of clothing. In hot conditions, the human body needs to increase heat losses to maintain thermal comfort. This is largely achieved by reducing clothing and through sweating and the corresponding heat losses associated with the latent heat of evaporation. Since the efficiency of evaporation is decreased as the relative humidity of the air increases, the relative humidity becomes a much more important parameter in hot climates. Also, since the efficiency of evaporation is increased with wind speed, in cold climates it is often desirable to reduce wind speeds but the opposite is sometimes the case in hot climates. The well-known Humidex is an effective temperature, combining the temperature and humidity into one number to reflect the perceived temperature and to quantify human discomfort due to excessive heat and humidity. In general, almost everyone will feel uncomfortable when the Humidex ranges from 40 to 45, and many types of labor must be restricted when the Humidex is 46 and higher. The incorporation of relative humidity effects into the overall assessment of thermal comfort is discussed in Stathopoulos et al. (2004).

Solar radiation

Any assessment of thermal comfort must account for the effects of sun/shade conditions. The angle of the sun, the amount of radiation absorbed by clouds, dust and particles in the atmosphere, and the sun light absorbed and reflected by buildings need to be taken into account.

Precipitation

In heavy rain conditions, people are less likely to be outside, thus their wind and thermal comfort will usually be less critical compared with other microclimate factors. However, it may be of interest to evaluate how far under a sheltering canopy roof the precipitation will infiltrate and how often this will happen. Dampness of clothes may also be of interest because it will affect thermal comfort.

A working group of the International Society of Biometeorology has attempted to work on a new standardized universal thermal climate index (UTCI), which can also be used in the development of a criterion for human outdoor comfort (Hoppe, 2002). An example of application of such an approach is shown in Figure 10 taken from Stathopoulos et al. (2004). The dependence of the overall comfort is expressed on the basis of a group of survey respondents as a function of the difference of two equivalent temperatures: one based on the weather norm, Te,n and the other based on the actual outdoor conditions, Te,a. Equivalent temperatures take into account the effect of relative humidity and solar radiation as well. It should be noted that (Te,a – Te,n) is the most influential factor on the overall comfort of the respondents.
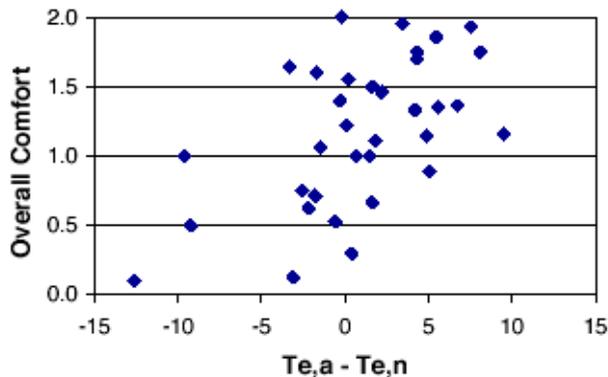
Figure 10: overall comfort example in terms of equivalent temperature difference, after Stathopoulos et al. (2004).

Figure 10 shows that (1) most comfortable conditions occur when the equivalent temperature difference is about 5°C, which may be attributed to the preference of local residents for higher air temperature as well as the temperature difference between an urban environment downtown and the airport; (2) lower comfort occurs with a negative temperature difference, or when the actual equivalent temperature is lower than the norm; and (3) if the temperature difference is beyond a certain limit, say greater than 10°C, less comfortable (overall comfort < 1) outdoor conditions may be perceived, although more field data are necessary to confirm this observation. At present, it is still considered premature to draw a curve for a definite mathematical relationship of overall comfort and equivalent temperature difference.

7. CONCLUDING REMARKS

This paper dealt with the aerodynamics of pedestrian level wind conditions, their experimental and computational assessment in the urban environment, as well as with the criteria used for outside human comfort in different parts of the world. Particular emphasis has been placed on the state-of-the-art and the current capabilities of Computational Wind Engineering to determine at least mean values of wind speeds in the vicinity of buildings in urban areas. An approach towards the establishment of an overall comfort index taking into account, in addition to wind speed, the temperature and relative humidity in the urban area under consideration was presented.

8. ACKNOWLEDGEMENT

REFERENCES

ASCE (1999). *Manual of Practice No.67 on Wind Tunnel Studies of Buildings and Other Structures*, American Society of Civil Engineers.

ASCE (2003). *Outdoor Human Comfort and its Assessment: State of the Art*, Task Committee on Outdoor Human Comfort, American Society of Civil Engineers.

Blocken, B., Monen, P., Stathopoulos, T., Carmeliet, J. (2008). "A Numerical study on the existence of the Venturi-effect in passages between perpendicular buildings", Journal of Engineering Mechanics, ASCE, Vol. 134, No. 12, 1021-1028.

Bu, Z., Kato, S., Ishida, Y., Huang, H. (2009). "New criteria for assessing local wind environment at pedestrian level based on exceedance probability analysis", Building and Environment, 44, 1501-1508.

Cadre (1992). Cadre Règlementaire, Arrondissement Ville-Marie, Module de la gestion du developpement, Ville de Montréal, Avril 1992.

Castro, I.P., Graham, J.M.R. (1999). "Numerical wind engineering: the way ahead?", Proc. Inst. Civ. Engrs. Structs. & Bldgs., Vol. 134.

Cochran, L.S. (2004). "Design Features to Change and/or Ameliorate Pedestrian Wind Conditions", Proceedings of the ASCE Structures Congress, Nashville, Tennessee, May 2004.

CRES (2004). *Designing Open Spaces in the Urban Environment: A Bioclimatic Approach*, ISBN: 960-86907-2-2, Centre for Renewable Energy Sources (C.R.E.S.).

Hoppe P. (2002). "Different aspects of assessing indoor and outdoor thermal comfort", Energy and Buildings, Vol. 34, 661–665.

Isyumov, N., Davenport A.G. (1975). "The ground level wind environment in built-up areas", 4th International Conf. on Wind Effects on Buildings and Structures, London.

Jordan, S.C., Johnson, T., Sterling, M., Baker, C. (2008). "Evaluating and modeling the response of an individual to a sudden change in wind speed", Building and Environment, 43, 1521-1534.

Koss, H. H. (2006). "On differences and similarities of applied wind comfort criteria", Journal of Wind Engineering and Industrial Aerodynamics, 94, 781-797.

Melbourne, W.H. (1978). "Criteria for environmental wind conditions", Journal of Wind Engineering and Industrial

Aerodynamics, Vol. 3, 241-249.

Mochida, A., Lun, I.Y.F. (2008). "Prediction of wind environment and thermal comfort at pedestrian level in urban area", Journal of Wind Engineering and Industrial Aerodynamics, 96, 1498-1527.

Murakami, S., Iwasa, Y., Morikawa, Y. (1986). "Study on acceptable criteria for assessing wind environment on ground level based on residents' diaries", Journal of Wind Engineering and Industrial Aerodynamics, 24, 1–18.

Nicolopoulou, M., Baker, N., Steemers, K. (2001). "Thermal comfort in outdoor urban spaces: understanding the human parameter", Solar Energy, Vol. 70, No.3, 227-235.

Nicolopoulou, M., Lykoudis, S. (2002). "Thermal comfort in open spaces: the human factor", 6ᵗʰPanhellenic Congress of Meteorology, Climatologic and Atmospheric Physics, September 25-28, Ioannina, Greece.

Pendwarden, A.D. (1973). "Acceptable wind speeds in towns", Build. Sci. 8, 259-267.

Pendwarden, A.D., Wise, A.F.E. (1975). "Wind environment around buildings", Building Research Establishment Digest.

Sanz-Andres, A., Cuerva, A. (2006). "Pedestrian wind comfort: Feasibility study of criteria", Journal of Wind Engineering and Industrial Aerodynamics, 94, 799-813.

Stathopoulos, T. (2002). "The numerical wind tunnel for industrial aerodynamics: real or virtual in the new millennium?", Wind and Structures, Vol. 5, Nos. 2-4, 193-208.

Stathopoulos, T., Wu, H., Zacharias, J. (2004). "Outdoor human comfort in an urban climate", Building and Environment, Vol. 39, No. 3, 297-305.

Stathopoulos, T. (2006). "Pedestrian Level Winds and Outdoor Human Comfort", Journal of Wind Engineering and Ind. Aerodynamics, Vol. 94, No. 11, 769-780.

Westbury, P.S., Miles, S. D., Stathopoulos, T. (2002). "CFD application on the evaluation of pedestrian-level winds", Workshop on Impact of Wind and Storm on City Life and Built Environment, Cost Action C14, CSTB, June 3-4, Nantes, France.

Willemsen, E., Wisse, J. A., (2007). "Design for wind comfort in The Netherlads: Procedures, criteria and open research Issues", Journal of Wind Engineering and Ind. Aerodynamics, Vol. 95, 1541-1550.

Wise, A. F. E. (1970). "Wind effects due to groups of buildings", BRS Current Paper CP 23/70, Royal Society Symposium 'Architectural Aerodynamics'.

Zacharias, J., Stathopoulos, T., Wu, H. (2001). "Microclimate and downtown open Space activity", Environment and Behavior, Vol. 33, No. 2, 296-315.

On Wind, Waves, and Surface Drag

C.W. Letchford and B.C. Zachry

Chris.Letchford@utas.edu.au, School of Engineering, University of Tasmania, Hobart, AUSTRALIA,
Brian.C.Zachry@ttu.edu, WISE Research Center, Texas Tech University, Lubbock, USA,

ABSTRACT

This paper reviews studies of the interaction of the wind and the ocean and the consequent landfall of strong winds that bring devastation to coastal regions. Such studies have typically concentrated on wind-wave interaction over deep water which is now reasonably well understood. However wind flow over near-shore shoaling waves and the transition to flow over land with consequent terrain and topography changes remains an area of fruitful research. Some recent studies on this topic are discussed.

1. INTRODUCTION

Almost three-quarters of the earth's surface is covered by water, and a large proportion of the world's population lives in close proximity to a shoreline. Recent migration patterns indicate a further concentration of coastal populations. In the US alone, over 35 million people currently live in hurricane prone coastal regions stretching from Texas to North Carolina. Hurricanes, Typhoons and Cyclones all develop and mature over the ocean, fed by heat exchanges. These major wind storms generate hazards that include strong winds, intense rainfall, and ocean flooding, termed storm surge. Storm surges arise from the combination of forcing from wind, waves and low atmospheric pressures. While wind is structurally destructive in the short term, the greatest casualties and infrastructure damage frequently arise from coastal flooding due to storm surge. Storm surges become particularly damaging if sufficiently large to enable waves to breach coastal defenses and in combination with peak tides. Recent tragedies, such as Hurricane Katrina which saw the inundation of New Orleans and surrounding areas and led to the loss of some 1300 lives and an estimated $150 billion economic loss, illustrate the disasters that await low-lying coastal populations (Pielke et al. 2008). Furthermore, global warming may led to an increased frequency and intensity of these extreme storms.

Clearly the influence of wind on water and *vice versa* has a major influence and impact on human activity and mitigating this impact is a major component of building resilience in communities. This requires, in part: more accurate ocean wave models, hurricane storm surge-, track-, and intensity

---

Contact person: C.W. Letchford, School of Engineering, University of Tasmania, Hobart, Australia, +61 3 6226 2135.
E-mail Chris.Letchford@utas.edu.au

forecasts and, appropriately conservative loading codes (eg., American Society of Civil Engineers, ASCE 7-05) for structures built along the coast.

Of the major hazards associated with landfalling tropical cyclones, storm surge arguably has the greatest potential to cause catastrophic social and economic impacts. Hurricane storm surge is the rise in water level associated with a tropical cyclone, plus tide, wave run-up, and freshwater flooding (Harris 1963). Historically, the majority (approximately 90%) of all hurricane-related fatalities in the US are due to storm surge (American Meteorological Society 1973). Storm surge and wave forecasts are an important component of disaster mitigation strategies since local, state, and national agencies depend on accurate forecasts to prevent loss of life by evacuating vulnerable areas prior to landfall or in providing appropriate storm shelters. Although Hurricane Katrina (2005) is one of the classic examples of the devastation wrought by storm surges, a more recent, less catastrophic event, occurred during Hurricane Ike (2008). Ike made landfall in Galveston, TX with a maximum high water mark of 5.3 m collected by the Federal Emergency Management Agency (FEMA) in Chambers County. Ike's surge devastated structures on Galveston Island and the Bolivar Peninsula – Berg (2009) estimated total property damage at around \$19 billion (2008 USD, fourth costliest hurricane). At least 12 fatalities were directly caused by intense storm surge flooding on Galveston Island and the Bolivar Peninsula. Unique data from this storm will be presented later in this paper. In the following sections previous research in wind-wave interaction will be summarized, recent studies highlighted and priorities for future research efforts established.

2. REVIEW

While storm surge events associated with tropical disturbances are fairly ubiquitous around the world, the near-shore wind forcing mechanisms that, in part, drive the rise in mean water level are not yet well understood. Field measurements of wind and waves in the near-shore environment are a vital asset in the prediction and mitigation of hurricane landfall impacts, but there exist few dense near-shore time series of these important properties (e.g., wind speed and direction, wave height, storm surge, etc). This is primarily due to the episodic and uncertain nature of hurricanes (e.g., Wright et al. 2001) and the profound difficultly in conducting in situ measurements (Csanady 2001). Hence, the majority of previous research studies have been conducted in weak to moderate wind regimes $5 < U_{10} < 25$ m/s and are limited to: (1) field measurements made in deep water in the open ocean (e.g., Smith 1980; Large and Pond 1981; Yelland and Taylor 1996), (2) field measurements in lakes (e.g., Donelan 1982; Atakturk and Katsaros 1999), (3) laboratory measurements (e.g., Banner 1990; Gong et al. 1999), and (4) theoretical studies valid over deep water (e.g., Bye and Jenkins 2006) – all in weak to moderate wind regimes (where U_{10} is the standard 10 m reference height mean wind speed set by the World Meteorological Organization, WMO). The near-shore region is herein defined as the zone extending from the shoreline outward to where the waves begin feel the affects of the sea floor.

The first measurements of air-sea momentum flux across the air-sea interface in deep water in hurricane conditions were obtained shortly after the turn of the 21st century. Our understanding of this exchange has been limited in some regards by the requirement of technologically advanced and rugged instruments needed to make these measurements. Recently, Powell et al. (2003), Black et al. (2007), and Jarosz et al. (2007) made deep water, open-ocean measurements of air-sea momentum flux in strong winds associated with hurricanes. Wind stress or momentum exchange is described in terms of a surface drag coefficient C_D. Donelan et al. (2004) performed laboratory measurements of C_D in simulated hurricane force winds. Results indicate that the 10 m surface drag coefficient increases with wind speed for weak to moderate winds, but reaches a limiting value in strong winds: $C_D \approx 0.0025$ at winds of 33 m/s (Powell et al. 2003; Donelan et al. 2004) and $C_D \approx 0.0018$ at 22–23 m/s (Black et al. 2007). Results from these studies have changed our understanding of drag coefficient

behavior in hurricane force winds in deep water; however, a lack of extreme wind data and wave behaviour in near-shore water remains.

It is well known that wave interaction with the bottom topography (i.e., bathymetry) causes wave conditions in shallow water to be markedly different to those in deep water. This region is characterized by a rapidly changing water surface profile due to wave shoaling and breaking transformation processes (Thornton and Guza 1982; Holman and Sallenger 1985; Dean and Dalrymple 1991; Holland et al. 1995). Wave shoaling is the process whereby waves entering shallow water slow down, become steeper, and increase in height due to interaction with the sea floor. Depth-induced wave breaking occurs when the wave amplitude reaches a critical point and the crest of the wave overturns due to the water velocity exceeding the reduced wave celerity in the shoaling region. Although yet to be determined, the surface drag coefficient in this region is hypothesized to be significantly larger than in deep water due to: (1) decrease in the wave phase speed c_p, defined as the speed at which an individual wave propagates, (2) increase in wave height and steepness in the shoaling region and at the onset of wave breaking, (3) rapidly varying surface wave field, (4) waves may not align with the mean wind near the shore, and (5) broken waves can cause an increase in the local sea surface roughness past the initial breaking region.

Waves that propagate into a region of variable depth will undergo refraction. This leads to irregularities in the surface wave field (increased roughness) along the coast (Munk and Traylor 1947). Therefore, estimation of near-shore surface stress requires knowledge of the sea (wave) state. In a laboratory study, Banner (1990) found that there was up to a 100% increase in wind stress over actively breaking waves compared to waves of similar steepness just prior to breaking ('incipient' breaking waves). Other laboratory experiments have also observed increased surface stress above breaking waves (e.g., Banner and Melville 1976; Kawamura and Toba 1988; Reul et al. 1999). Based on the wave transformation processes listed above, the deep water surface drag coefficient is likely to underestimate near-shore wind stress and thus hurricane storm surge at the coast (particularly over wide shallow shelves such as those in the Gulf of Mexico).

Anctil and Donelan (1996) made some of the first measurements of C_D for waves progressing from deep water to the shoreline. Specifically, they determined drag coefficients over offshore, shoaling, and breaking waves in Lake Ontario, Canada, and found that deep water waves exhibit less drag than both shoaling and breaking waves. For wind speeds of around 14 m/s Anctil and Donelan (1996) estimated shoaling wave drag coefficients to be on the order of $C_D \approx 0.0028$, roughly 40% higher than offshore (deep water) values. Their results support the statements above that the near-shore region is rougher than offshore. Powell (2008) is currently working to compile near-shore (defined by Powell as water depth less than 50 m) dropsonde data to evaluate drag coefficient behavior. Although, his work requires more observations before definitive conclusions can be made, preliminary findings suggest that C_D does not reach a limiting value for wind speeds up to 33 m/s. A limited number of dropsondes (nine) in winds speeds above hurricane force (mean wind speed of 39.6 m/s) indicate that this region is much rougher with $C_D \approx 0.0032$. Additional work is greatly needed to supplement previous and ongoing research efforts.

Near-shore wind stresses cause wind setup, which is a rise in the still water level (the level that the sea surface would assume with high frequency motions such as wind waves averaged out, SWL) at the downwind shore (Harris 1963). In a strong onshore wind regime, it is obvious that wind setup is a significant contributor to the total storm surge. At present, near-shore wind stress in strong winds is not known – the common practice is to adopt deep water estimates of C_D for storm surge modeling and analysis (e.g., Westerink et. al. 2004). In addition to the large differences in maximum surface elevation that arise due to the many deep water parameterizations that exist (Weaver 2004), near-shore drag is currently not taken into account. Most likely this does not allow for reliable estimation of the shoreline setup (IPET 2006b). Due to the aforementioned differences, the wind driven component of storm surge will likely be underestimated using this technique, particularly in

strong onshore winds. This ultimately results in inaccurate forecasts and thus the lack of or inaccurate warnings being issued to communities. Using model hindcasts for Hurricane Katrina, the ADCIRC storm surge model still had an average absolute error of 0.4 m (IPET 2006b), which is likely much lower than the average prediction error.

There is also a need for measurements of near-shore drag to clarify the debate on the ASCE wind load standard. Prior to the work of Vickery and Skerlj (2000) the roughness length in hurricane prone regions was set at $z_0 = 0.003$ m (Exposure D). Using limited data Vickery and Skerlj (2000) argued that near-shore drag is greater than previously believed, and their work resulted in the standard being changed to $z_0 = 0.03$ m (Exposure C). It is anticipated that the upcoming version ASCE 7-10 will most likely defer back to Exposure D in the hurricane prone region (D. A. Smith personal communication). A comprehensive dataset in the near-shore region during hurricane conditions is needed to resolve this debate. The ultimate purpose is to keep coastal structures safe from wind failure, while providing the most economical solution.

3. BACKGROUND

3.1   The Atmospheric Boundary Layer

Although the earth's atmosphere reaches about 150 km, the effects of the earth's surface are typically felt within the lowest 2 km (or less) of the troposphere (surface to roughly 11 km) referred to as the atmospheric or planetary boundary layer (ABL or PBL, Stull 1988). The ABL is usually characterized by turbulence, defined as random or irregular fluctuations (gustiness) superimposed on the mean wind (characterized visually by atmospheric swirls called eddies). The instantaneous wind speed U is comprised of mean - $\overline{U}$ and fluctuating - u′ components of velocity (e.g., U = $\overline{U}$ + u′). Over a flat homogeneous surface, turbulence is caused by friction between the air and the surface over which it is flowing (frictional drag). Mechanical turbulence is also generated via interaction of air flow with objects (e.g., trees, structures) and/or the underlying topography (characterized by elevation, slope, and orientation of terrain features) on the earth's surface. Turbulence generated in this manner is referred to as form (pressure) drag. In other words, form drag is produced by the eddying motions that are set up by air flow passed a body immersed in this flow. Thermal turbulence is caused by localized differential (solar) heating of the earth's surface, resulting in buoyant convective processes. Convective sources include heat transfer from the ground to the air (producing thermals of warm rising air), and radiative cooling from the top of the cloud layer to the ground (generating thermals of cold sinking air, Stull 1988). The largest energy-carrying eddies are on the order of boundary layer depth, roughly 0.1–3 km in diameter (Stull 1988). The smallest eddies feed off the larger ones and are a few millimeters in size. They contain very little energy and are dissipated into heat by viscosity. In general, turbulent eddies are what allow the boundary layer to respond to changes in surface forcings.

It has been documented in the literature that flow characteristics within the atmospheric boundary layer are influenced by thermal stratification and horizontal density gradients (e.g., Deardorff 1968; Stull 1988), termed atmospheric stability. It is generally defined as the atmosphere's resistance to vertical motion. The stability of the atmosphere can be classified as: stable, neutral, unstable, or conditionally unstable. Stability of an atmospheric layer is determined by comparing its change in temperature with height (environmental lapse rate) with either the saturated or dry (9.8°C / 1000 km) adiabatic lapse rates. The saturated lapse rate depends on moisture content, but is typically around 5°C/1000 km. The boundary layer is said to be neutral in absence of buoyancy and significant variations in density. This typically occurs in strong winds, overcast skies, or when there is negligible

temperature advection. More precisely, in a neutral atmospheric boundary layer (NABL), shear production of turbulent kinetic energy is much larger than buoyant production (Stull 1988). In absence of convective processes, a NABL is observed when wind speeds are > 8 m/s (e.g., Vega 2008).

For aerodynamically rough flow (discussed below), the NABL can be divided into two principle regions: surface (inner) and Ekman (outer) layers. The Ekman layer is a hypothetical layer where surface friction and small eddies (local turbulence) cause cross-isobaric winds on a rotating planet (Stull 1988). Lengths in this region are typically characterized by the gradient height z_g or the boundary layer thickness δ. The bottom 10% (tens of meters thick) of the NABL is termed the inner layer (e.g., Simiu and Scanlan 1986; Stull 1988; Holmes 2001). In contrast to the Ekman layer, the surface layer is primarily dependent on surface roughness characteristics and the affect of earth's rotation on this layer is negligible. This region is also termed the constant shear stress layer, as there is fundamentally a constant momentum flux. Lengths in this layer are scaled by the roughness length z_o, which characterizes the size and shape of the roughness elements. It provides a measure of the upwind terrain roughness as experienced by the surface wind. Physically, z_o represents the near-surface eddy size and mixing length, and thus is a measure of the effective roughness of the underlying surface (Atakturk and Katsaros 1999).

The surface layer can be further broken into the interfacial (roughness) and inertial sublayers. The inertial sublayer is the overlap region between the outer and inner layers, and is where the universal surface layer profile is valid. Adjacent to (and within) the surface roughness elements, is a region known as the roughness sublayer. This region is where the universal surface layer profile forms (Garratt 1992). Here, turbulence and wind speed profiles are directly affected by the surface. For aerodynamically smooth flow, this region is termed the viscous sublayer, as molecular transfer is important.

The roughness Reynolds number Re_r, first introduced in the classic pipe flow study by Nikuradse, can be used to characterize the roughness of the surface elements (e.g., Garratt 1992; Kraus and Businger 1994). The roughness Reynolds number is defined as:

$$Re_r = \frac{z_o u_*}{v_a} \tag{1}$$

where ρ_a, v_a is the air density and kinematic viscosity and $u_* = \sqrt{\tau_o / \rho_a}$ is the friction (shear) velocity with τ_o the surface shear stress. Re_r has similar meaning to the classic Reynolds number – it provides a measure of the ratio of inertial to viscous forces, and ultimately characterizes the flow as: smooth, transitional, or rough. For aerodynamically smooth flow, surface shear stress is supported by viscous shear and the flow is not affected by the roughness elements on the surface. However, if the flow regime is considered aerodynamically rough, inertial forces dominate and viscous effects are insignificant (i.e., the flow is independent of Reynolds number). Nikuradse found air flow to be smooth for $Re_r < 0.13$ and rough for $Re_r > 2.5$. These limits were demonstrated in other classical studies (e.g., Sutton 1953), and more recently by Kraus and Businger (1994) and ASCE (1999). Wu (1980) suggested slightly different transitional flow limits $0.17 < Re_r < 2.33$. Over the sea surface the flow is considered aerodynamically rough if $Re_r > 2.0$ (e.g., Fairall et al. 1996; Zilitinkevich et al. 2001).

It has long been observed that wind speed is typically slowest near the earth's surface and increases with height (e.g., Blackadar and Tennekes 1968; Tennekes and Lumley 1972; Tennekes 1973). This is because air movements located within the ABL are complicated through the existence of temperature gradients caused by differential heating of air in contact with the surface, the influence of friction drag, and the topography of the earth's surface. These factors cause a reduction in the magnitude and changes in direction of the mean wind velocity. The reduction in wind speed near the

surface is primarily a function of surface roughness. At the surface frictional drag causes the wind speed to be zero due to the 'no-slip' boundary condition, and pressure gradient forces cause the wind speed to increase with height. The no-slip boundary condition states that the tangential component of the wind velocity as the surface must be zero (since the earth's surface is not moving) and that the normal component must also be zero since the surface does not deform. This is not the case for flow over water, where there can be a velocity jump across the fluid/fluid interface.

The mean velocity profile (change in wind speed with height) is approximately logarithmic in nature, especially in extreme winds associated with tropical cyclones (NABL, ignoring any microscale or mesoscale aspects of weather). The most accurate mathematical representation of the vertical distribution of wind speed within the surface layer in neutral conditions is the logarithmic law (Holmes 2001). The log-law is based on the flat plate boundary layer theory of Prandtl (Schlichting and Gersten 2000):

$$\overline{U}(z) = \frac{u_*}{k}\left[\ln\left(\frac{z-d}{z_o}\right)\right] \tag{2}$$

where k is the von Karman constant (determined experimentally to be $k \approx 0.40 \pm 0.01$) and d is the displacement height (plane). The misconception that z_o is the height of zero wind, is only valid in an algebraic sense (see Eq. 2). Wieringa (1993) stated that this relationship to be valid within a few meters of the earth's surface to 50–100 m in homogeneous terrain, but is dependent on surface roughness and wind speed.

Due to air flow modification by the ground surface, the near-surface lower boundary condition requires an additional parameter to consider - d. The displacement height is a vertical offset of the logarithmic law wind profile due to the boundary condition on wind speed (Jackson 1981). By definition, this height sets up where the wind velocity extrapolates to zero. This height needs to be considered over terrain such as tall crops, forests, and ocean waves, since wind flow is displaced upward, producing an 'effective ground level'. The displacement height is typically determined by the generic formula:

$$d = \alpha h_r \tag{3}$$

where h_r is the roughness height of objects and α is a coefficient determined by the wind profile. Jackson (1981) provided sufficient results from prior studies using bluff body shapes (which had fixed dimensions) that indicted $\alpha = 0.7$ was a good approximation for a large range of roughnesses. Wieringa (1993) provides a summary of z_o and d values for a wide range of surfaces. Bourassa (2006) determined a displacement height that corresponds to 80% of the significant wave height ($d = 0.8H_s$). However, this is dependent on wave characteristics, and for studies over waves the displacement plane has typically been placed at the still water level (SWL) (Tseng et al. 1992). For completeness, if the boundary layer is not considered neutral, Monin-Obukhov (MO) similarity theory predicts that mean gradients in the surface layer are universal functions of the MO length L (Stull 1988).

3.2   The Marine Atmospheric Boundary Layer

The marine atmospheric boundary layer (MABL) is at the heart of understanding air-sea interface. In the marine environment, reduction in wind speed near the surface is primarily a function of the wave characteristics. In the MABL, surface shear stress is controlled by surface roughness, which is influenced by wave steepness, surface current velocity, wave characteristics, the wind profile, and surface current speed and direction (Powell et al. 2003). Under neutral stability and growing seas (wind has just begun to act on the ocean surface to develop waves) the MABL is similar to that over land (i.e., consisting of surface (inner) and Ekman (outer) layers). The datum plane is typically placed

at the SWL. Along with atmospheric stability, the MABL is also dependent on parameters of, or related to, sea state. (e.g., Kitaigorodskii and Volkov 1965; Hsu 1974; Donelan 1982; Taylor and Yelland 2001). Sea state is the condition of the ocean surface relative wave characteristics at a given time and place, such as wave period and wave height. Generally speaking, the mean wind velocity profile in the MABL is logarithmic, but the height at which the log-law becomes valid depends on the wave characteristics.

Sjoblom and Smedman (2003) determined that MO theory is not applicable in regions of the marine surface layer where air flow is influenced by ocean waves, generation of wave-induced circulations, or other wave-induced forcing (e.g., Edson et. al. 1999; Atakturk and Katsaros 1999; Sjoblom and Smedman 2002). Wave influence on the turbulent structure of the MABL was first identified by Volkov (1970). The atmospheric layer where surface waves have a direct influence on the structure of the boundary layer is typically referred to as the wave boundary layer (WBL). The WBL is dependent upon the degree of wave field development. Sjoblom and Smedman (2003) divided the WBL into three layers (under near-neutral conditions) that are dependent on wave state: (1) wave influenced (bottom, level 1), (2) transition (middle, level 2), and (3) undisturbed (top, constant stress, level 3) layers. MO theory is not valid in the wave influenced or transition layers but is assumed valid above these regions where a normal MABL structure exists. For growing seas a logarithmic wind profile exists (similar to that over land), as the profile is essentially undisturbed by the waves (i.e., no WBL). However, during strong swell (long-wavelength surface waves outside the generating area) the wave influenced layer can extend to considerable heights affecting wind measurements. For mature seas a transition layer separates the wave influenced layer (shallower than during swell) from the ordinary surface layer. Typical heights for the layers are: level 1 around 10 m or below, level 2 from level 1 up to about 19 m, and level 3 from level 2 up to near 26 m (Sjoblom and Smedman 2003).

3.3 *Classification of air flow regimes*

Regardless of the underlying surfaces (e.g., waves, buildings, hills) aerodynamic rough flow over an array of such objects can be classified into three categories: isolated roughness flow, wake interference flow, and skimming flow. Morris (1955) was arguably the first person to study various flow classifications (he studied flow in rough conduits). More recently, Oke (1988) examined the various flow types using urban street canyons. Over a single building immersed in boundary layer flow there are three disturbed regions (mean wind direction is normal to the long axis of the building). Upstream of the building, a vortex forms in front of the windward face. This is due to downwash and is dependent on building height. Behind the building is a vortex caused by flow air flow separation from the sharp bluff edges of the building roof and sides. Further downstream of the building is its wake, characterized by increased turbulence and slower horizontal wind speeds than the undisturbed flow (flow prior to interacting with the building).

For an array of buildings (or other objects), flow types are dependent on spacing and height (Stuckley 2003). If the buildings are sufficiently far apart that the wake and vortex at each building are completely developed and dissipated before the following building is reached, the flow is classified as isolated. Essentially the flow acts as if there was only a single object immersed in the flow. As the buildings get closer together, the leading and trailing vortices at each element are disrupted, resulting in complex vortex interaction and turbulent mixing. Wake interference flow is characterized by secondary flow in the canyon space, where the downward flow of the eddy in lee of the building is reinforced by the eddy associated with downwash on the windward face of the following building. When the canyon gets very narrow, only a single vortex exists in the cavities (skimming flow). The bulk of the flow does not enter the canyon and basically moves from rooftop to rooftop, generating quasi-smooth flow.

Flow classification over waves (or hills) is somewhat different (Fig. 1). This is because waves are continuous, in that there is no 'flat' space between them. Isolated roughness only occurs for very shallow waves. For this case, the flow remains attached along the wave profile. As wave steepness increases (H/L), the flow will separate at some location downwind of the wave crest (wake interference flow). As shown in Fig. 1b, a vortex is generated within the separation flow region. The flow reattaches at some point on the following wave. For skimming flow the waves are very close together (i.e., steep waves), and the flow basically skips from crest to crest, bypassing the troughs. In general, the skimming flow regime is relatively smooth compared to other flow regimes, as the wave surface is sheltered.
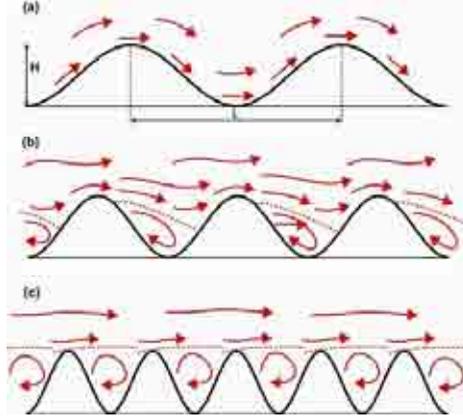
FIG. 1. Schematic diagram of the flow regimes over waves: (a) isolated roughness flow, (b) wake interference flow, (c) and skimming flow.

3.4   Aerodynamic Drag Coefficient

The horizontal component of the wind acting on the sea surface leads to wind stress or, in other words, the vertical transfer of horizontal momentum. The surface momentum flux (wind stress) at the air-sea interface is critical for modeling oceanic and atmospheric circulation. Wind stress over the ocean τ_w is formally defined as the retarding force per unit area exerted by the sea surface on the flow, and is typically described in terms of a 10 m surface drag coefficient (Simiu and Scanlan 1986):

$$\tau_w = \rho_a C_D \overline{U}_{10}^2 = \rho_a u_*^2 \tag{4}$$

Rearranging Eq. 4 the 10 m surface drag coefficient can be defined in terms of u_*, or the aerodynamic roughness length z_o (utilizing the log-law):

$$C_D = \left(\frac{u_*}{\overline{U}_{10}}\right)^2 \quad \text{or} \quad C_D = \left[\frac{k}{\ln\left(\frac{10}{z_o}\right)}\right]^2 \tag{5}$$

The drag coefficient can be thought of as a measure of sea surface roughness in the marine environment (Bye and Jenkins 2006) and is a function of sea state, atmospheric stability, and wind speed (Donelan et al. 2004). Onshore and offshore wind directions have also been shown to affect C_D (e.g., Geernaert and Smith 1997; Vickers and Mahrt 1997; Feddersen and Veron 2005). Deardorff (1967) derived an equation for the total drag coefficient acting on a wave field:

$$C_D \approx \frac{1}{\rho_a U_z^2}\left(\overline{p_\eta \frac{\partial \eta}{\partial x}}\right) + \frac{\mu_a}{\rho_a U_z^2}\left(\overline{\frac{dU}{dz}}\right)_\eta = C_{DF} + C_{DS} = \left(\frac{u_{*z}}{\overline{U}}\right)^2 \qquad (6)$$

where η is the sea surface displacement from the SWL, p_η is atmospheric pressure at the air-sea surface, μ_a is the dynamic viscosity of air, and the overbar represents horizontally averaged quantities over many wavelengths. Deardorff (1967) states that the lowest height z at which u_{*z} (and Eq. 6) can be evaluated is at the highest wave crest. According to Eq. 6, the total drag coefficient is mathematically described as the sum of form drag C_{DF}, and skin friction drag C_{DS}. The latter is related to the vertical wind shear and C_{DF} is dependent on resolving the pressure field relative to the wave slope. For convenience, the total drag coefficient will hereafter be referred to without the word 'total' (and C_{DF} and C_{DS} will continue to be referred to using their full names). Kudryavtsev and Makin (2007) separated form drag into two components $\tau_f = \tau_w + \tau_s$. The first term τ_w describes the transfer of momentum from wind to waves on the upwind portion of the wave. Form (wake) drag produced by air flow separation is described by the second term τ_s (Kudryavtsev and Makin 2001). It has been suggested that in hurricane conditions ($U_{10} > 33$ m/s), wind stress is primarily supported by form drag, thereby affecting the momentum transfer (e.g., Donelan et al. 2004; Kudryavtsev and Makin 2007). In these conditions, waves travel at significantly different velocities than the wind, as the wave field rarely has sufficient time to adjust to the strong wind forcing.

3.5   Estimating the drag coefficient

Determining the drag coefficient is problematical and typically it must be inferred from different experimental techniques. The most common techniques available are; the profile, eddy correlation, inertial dissipation, bulk aerodynamic, turbulence intensity, and gust factor methods. Often laboratory work utilizes the wind profile, eddy-correlation, and turbulence intensity methods while full scale work employs the turbulence intensity method.

3.5.1   Profile method

The earliest estimates of momentum flux over the sea came from applying the profile method to a set of wind data (Csanady 2001). This method utilizes the logarithmic law, which is based on the flat-plate boundary layer theory of Prandtl and von Karman (Schlichting and Gersten 2000). This method is based of the assumption that a nearly logarithmic mean wind velocity profile exists in the constant flux layer (u_* is approximately constant with height throughout the surface layer) under neutral stability, horizontal homogeneity, and stationarity. The profile method can only be employed if the mean wind speed at two or more levels is known. Jones and Toba (2001) suggest using five to seven levels to reduce random variance and permit detection of systematic error or instrument failure. Wieringa (1993) suggests that the number of profile levels necessary to calculate z_0 within a factor of two is dependent on surface roughness – the number of profiles necessary are ≥ 3 over rough terrain ($z_0 \approx 1$ m), ≥ 4 over moderately rough terrain ($z_0 \approx 0.1$ m), and ≥ 5 over smooth terrain ($z_0 \approx 0.001$ m). In order to obtain reliable wind profile measurements, Wieringa (1993) suggests that the following criteria must be met: (1) anemometers must be spaced a sufficient vertical distance apart to avoid interference and far enough away from the mast or boom outside the range of flow distortion of the structure, (2) anemometers must be precisely calibrated and wind speed data should be averaged over at least 10 min, (3) observations should be restricted to near neutral conditions or temperature data should be collected for diabatic profile correction, (4) non-stationary situations should be avoided, and (5) several independent runs of the experiment must be conducted. Wieringa (1993) states an experiment's observation reliability can be considered 'good' if all the above criteria are considered

and 'acceptable' if conditions two and three are assured and there is little doubt that the first condition was neglected.

3.5.2 Eddy-correlation method

The eddy-correlation technique calculates u_* using direct measurements of eddy fluxes in atmospheric surface layer. For this method to be valid, momentum flux must be essentially constant with height from near the surface to the measurement height. In addition, the flow conditions must be statistically stationary and homogeneous. Over the sea surface, these conditions are usually met for a fetch length > 1 km at an observation height ≤ 10 m (Kraus and Businger 1994). This method requires that the covariance be performed between the vertical w′ and horizontal u′ and v′ fluctuating components of velocity. As mentioned above, wind speed is commonly decomposed into mean and fluctuating components – the difference between the instantaneous wind speed U and the mean wind speed $\overline{U}$ is the fluctuating component u′ (i.e., u′ = U − $\overline{U}$). An advantage of this method is that only high-frequency wind data at a single level are needed – sonic, propeller-vane, and UVW anemometers are able to perform these measurements. Several definitions to compute u_* exist in the literature. Using the horizontal Reynolds stress vector to represent surface stress, u_* is defined as (Weber 1999):

$$\tau_{hor} = \rho_a \left[\left(\overline{u'w'} \right)^2 + \left(\overline{u'v'} \right)^2 \right]^{1/2} \tag{7}$$

$$u_* = (\tau_{hor} / \rho_a)^{1/2} = \left[\left(\overline{u'w'} \right)^2 + \left(\overline{u'v'} \right)^2 \right]^{1/4} \tag{8}$$

where $u'w'$ and $u'v'$ are the surface kinematic momentum fluxes in the x and y directions, respectively and the overbar denotes a temporal average over a time interval that is stationary. When the Reynolds stress vector is parallel to the mean wind direction, as in wind tunnel simulations, u_* can be defined in terms of the absolute value of the Reynolds stress vector in the direction of the mean wind typically $u_* = \left| \overline{u'w'} \right|^{1/2}$. Weber (1999) performed least square fits of the logarithmic profile to wind speed data collected on a 70 m instrumented tower and compared the results. According to Weber (1999), this method provides the lowest root mean square (rms) error compared to the other methods available.

3.5.3 Inertial dissipation method

The inertial dissipation technique is an alternative approach of measuring the friction velocity from high-frequency wind velocity measurements. This method was first suggested as a means to measure wind stress in the open ocean by Hicks and Dryer (1972), later applied by Pond et al. (1979), and has most recently been reviewed and evaluated by Edson et al. (1991). The inertial dissipation technique is most commonly formulated in terms of the spectral density of turbulence in which it is assumed that a balance between turbulence production and dissipation exists (discussed below). In short, high-frequency wind measurements are used to determine the energy dissipation rate in the inertial subrange and thus estimate the turbulent flux of momentum. Fairall and Larsen (1986) suggested a different formalization of this method based on the turbulence structure functions (Jones and Toba 2001). Kolmogorov hypothesized that the power spectral density $S_{uu}(\kappa)$ of the alongwind component u beyond the peak of the spectrum in the inertial subrange depends only on the dissipation rate of turbulent kinetic energy (TKE) ε and on the wave number κ. The inertial subrange is an intermediate range of turbulent scales that separates the energy-containing eddies from the viscous eddies in the dissipating range (Kaimal and Finnigan 1994). Using dimensional arguments, this implies that:

$$S_{uu}(\kappa) = K\kappa^{-5/3}\varepsilon^{2/3} \tag{9}$$

where K is the Kolmogorov constant. Lumley and Panofsky (1964) suggested that this constant has a value between 0.5 and 0.6 (Kaimal and Finnigan 1994). Using Taylor's hypothesis of 'frozen' turbulence and that wave number $\kappa = 2\pi f/\overline{U}$ where f is the measurement sampling frequency and $\overline{U}$ is the alongwind component mean wind speed the rate of energy dissipation can then be determined by calculating a mean value of $f^{-5/3}S_{uu}(f)$ over an appropriate frequency range. It follows that the wind stress can be found by using the TKE budget. The difficulty of this method is that the form of these functions are not well known (Fairall and Larsen 1986). However, this methodology of measuring u_* has a distinct advantage over the other methods in that it is relatively insensitive to platform motion, such as the low frequency oscillations on board a ship. Thus, the majority of the major open ocean flux datasets were measured in this way (e.g., Large and Pond 1981; Yelland and Taylor 1996). The weakness of the method is that it is an indirect measure of the momentum flux and that it relies on a number of assumptions and empirical constants. Specifically, this technique requires assumptions with regard to the value of the von Karman and Kolmogorov constants and the form of the dimensionless profile functions. It also assumes a balance between TKE production and dissipation, which has been shown to be approximately true (Frederickson et al. 1997). To get around an imbalance between TKE production and dissipation, an 'effective' Kolmogorov constant can be used when employing this method; however, this is also problematic (Frederickson et. al. 1997). Drennan et al. (1999) found that this method is not valid in the presence of fast moving swells. Nonetheless, Yelland and Taylor (1996) found that this method yielded estimates of the Reynolds flux that were in good agreement with direct measurements.

3.5.4   Turbulence intensity and gust factor methods

An alternative way to calculate the drag coefficient is from the gusts in wind observations using either the turbulence intensity (*TI*) or gust factor (GF) methods. These methods are advantageous to use when only single level anemometer data is available without knowledge of the lateral, longitudinal, and vertical wind components (e.g., wind measurements from a single propeller-vane anemometer at a height of 10 m). The *TI* method requires the use of anemometers that are capable of sampling at a frequency of about 1 Hz or faster. However, the GF method can be applied from maximum gust data collected at typical weather observing stations. The *TI* method is generally preferred over the GF method, due to the latter method having numerous parameters based on anemometer and equipment need compute z_o; however Barthelmie et. al. (1993) found that these methods provide similar results. Both methods have gained popularity over the inertial dissipation method, which suffers from much error.

   Turbulence intensity is a measure of the fluctuating component of the wind. Generally speaking, *TI* characterizes the intensity of gusts in the flow. It is defined as the ratio of the standard deviation σ_u of a given wind speed record to the mean wind speed $\overline{U}$. The *TI* method is based on two assumptions: (1) that a logarithmic wind profile exists and (2) that the ratio of the standard deviation of the wind record to the friction velocity is $\sigma/u_* = 2.5$ (e.g., Beljaars 1987; Barthelmie et al. 1993). Counihan (1974) found this method is valid in smooth terrain for $z_o < 0.1$ m. Under these assumptions, the roughness length can be estimated from the total turbulence intensity at height z_a as follows:

$$z_o = z_a \exp\left[\frac{1}{TI}\right] \tag{10}$$

A second method to determine z_o using the GF method is described by Wieringa (1993, 1996), where the gust factor (GF) is defined as the ratio between the peak and mean wind speeds. In this case it is important to understand the frequency response characteristics of the anemometers.

3.5.5 Bulk aerodynamic method

The bulk aerodynamic method for estimating atmospheric parameters only requires that the mean wind speed be measured to estimate wind stress. Wind speed is typically measured at or translated to 10 m. This trivial requirement makes this technique very attractive in that there is no need for expensive instrumentation to measure atmospheric turbulence. This method parameterizes wind stress in terms of the mean wind speed (bulk gradient) and a bulk transfer coefficient for momentum (C_D). Over the ocean the parameterization of τ_w usually takes the form:

$$\tau_w = \rho_a C_D(z)\left[U(z) - U_c\right]^2 \tag{11}$$

where U_c is the mean ocean surface current. Using this method, the bulk drag coefficient is estimated from linear relationships. Some of the most commonly used linear relationships are shown in Table 1. Based on these relationships, C_D can be estimated from mean wind speed measurements; however they are not valid in extreme conditions (e.g., Powell et. al. 2003), as C_D no longer behaves linearly at wind speeds near hurricane force (tends to plateau or level off and decrease thereafter). During field experiments it is most often the case that direct measurements of turbulent fluxes are made using sonic anemometers and the bulk method is not needed to determine wind stress. However, for modeling and dataset generation purposes it is desirable to use the bulk method. Unfortunately, this technique is not free from sources of error. Errors in the measurements used to determine the drag coefficients can inherently cause errors in the bulk wind stress estimate. Another possible error can result if the atmospheric and oceanic conditions differ from those when the bulk relationship was established. This particular source of error is difficult to avoid. For example, Frederickson et al. (1997) note that the sea breeze circulation, frontal passages, differences in the wave field, and wave field characteristics can result in errors in the bulk wind stress determination.

TABLE 1. Examples of commonly used drag coefficient relationships.

Source	C_D ($\times 10^3$)	Wind Speed Range (m/s)	Sea Type
Smith and Banke (1975)	$0.63 + 0.066 U_{10}$	2.5–21	Open ocean, shoaling
Garratt (1977)	$0.75 + 0.067 U_{10}$	10–52	Various
Smith (1980)	$0.61 + 0.063 U_{10}$	6–22	Open ocean
Wu (1980)	$0.80 + 0.065 U_{10}$	2–22	Various
Large and Pond (1981)	$0.49 + 0.065 U_{10}$	11–25	Open ocean
Geernaert (1987)	$0.58 + 0.085 U_{10}$	5–25	Various
Yelland and Taylor (1996)	$0.60 + 0.070 U_{10}$	6–26	Open ocean
Vickers and Mahrt (1997)	$0.75 + 0.067 U_{10}$	4–16	Shoaling
Drennan et al. (1999)	$0.60 + 0.070 U_{10}$	6–14	Open sea

3.6 Parameterizing sea surface roughness

One of the earliest theories of wind stress over water originates from the work of Charnock (1955). Using a limited dataset collected over a relatively small body of water and dimensional arguments, Charnock suggested that the roughness length that can be used to determine the mean wind profile over the ocean is defined as:

$$z_o = \frac{z_{Ch} u_*^2}{g} = \frac{z_{Ch} C_D \overline{U}_{10}^2}{g} \tag{12}$$

where g is the gravitational constant and z_{Ch} (or α) is an empirical constant known as the Charnock parameter. This equation is assumed valid for a wide range of wind speeds, excluding very low speeds < 3 m/s where the sea surface is considered aerodynamically smooth (e.g., Yelland and Taylor 1996) or in winds above hurricane force (> 33 m/s) where the sea surface experiences wave breaking, sea spray, sea foam, etc. The value of Charnock's constant has been highly debated in the literature and can vary from 0.01 to 0.02. The most commonly used value of 0.0144 was suggested by Garratt (1977). This empirical constant has been observed to increase with increasing wind speed and tends to be site dependent (Yelland and Taylor 1996). The literature has recognized that a constant z_{Ch} should not be assumed as it rarely adequately describes a dataset (Drennan et al. 2005). Numerous experiments have been conducted since Charnock's initial attempt to investigate the dependence of dimensionless sea surface roughness (or drag) on parameters related to sea state. However, no single parameterization has been successfully developed to determine surface roughness for all possible circumstances. Kitaigorodskii and Volkov (1965) provided the first attempt to relate z_{Ch} to sea state, and suggested Charnock's constant is dependent on wave age. Wave age refers to a measure of the time the wind has been acting on a wave group (ratio of wave phase speed to wind speed). Larger values of wave age correspond to older, more developed seas whereas smaller values denote younger, less developed seas. Numerous attempts have been made since (e.g., Geernaert et al. 1986; Toba et al. 1990; Smith 1992; Donelan et al. 1993; Johnson et al. 1998; Oost et al. 2002; Drennan et al. 2003) to relate z_{Ch} to wave age with no definitive conclusions. In a similar fashion, Hsu (1974) and Taylor and Yelland (2001) attempted to parameterize dimensionless sea surface roughness based on the steepness of the dominant waves in the ocean. This dimensionless parameter is often given as H_s/L_p (or H/L in general terms), where H_s is the significant wave height and L_p represents the wavelength at the peak of the wave spectrum. Drennan et al. (2005) assessed these most recent parameterizations provided by Taylor and Yelland (2001) and Drennan et al. (2003). They found that the models yielded different estimates of roughness depending on the sea state. Neither the wave steepness nor the wave age scalings have the ability to predict all datasets or to describe surface roughness in swell dominated conditions.

3.7   Types of wind waves and sea state

A sea surface similar to a sheet of glass or mirror-like appearance is a relatively rare sight. Capillary waves, commonly referred to as ripples, form within a few seconds after the wind starts blowing and dissipate when the wind stops. These waves are nearly always present and are a result of wind-driven surface shear stress and hydrodynamic instability. In short, when the wind blows, small atmospheric eddies very near air-sea interface generate local pressure fluctuations that perturb the water surface, generating ripples. Capillary waves are defined by their wavelength (< 1.7 mm):

$$\lambda = 2\pi \sqrt{\frac{\gamma}{\rho_w g}} \tag{13}$$

where γ is surface tension and ρ_w is the density of the water (Knauss 1996). The apparent roughness of the sea surface can be attributed, in part, to these very small waves often superimposed on wind-driven gravity waves. Ripples continue to grow by direct wind forcing. A shear stress is exerted on the windward side and flow over the wave induces a pressure differential. Nonlinear growth can occur from small waves forming on larger waves. Increasing momentum or energy transfer from the wind to the water surface expands the circular orbits of the water particles in the direction of the wind, resulting in growth of the wave. Wind (gravity) waves are formed once the wavelength exceeds 1.7 mm. Wind waves are also classified by their period. They have periods ranging from approximately

3 to 25 s (Resio et al. 2002). In general, the sea grows from short/high-frequency waves toward longer/low-frequency waves.

The wind and waves are strongly coupled. In moderate to strong winds, waves are irregular (e.g., waves of many different wavelengths, periods, and directions) and rapidly evolving (e.g., chaotic sea), in part, due to interference with other wind-generated waves. Since waves are still growing or being sustained by the wind, a descriptive term was coined for this phenomenon - 'windsea'. Waves in windsea show no consistent wavelength or period. However, 'dominant' waves can be observed with a mean wavelength and celerity. In contrast to swell (described below), windsea and dominant waves often propagate downwind (Csanady 2001).

Free gravity waves, swell for short, are more or less regular waves free of wind forcing. Swell forms as waves in the windsea propagate away from their area of origin and disperse or organize according to direction and wavelength and by nonlinear interaction. In other words, swell is the term for waves that are not growing or being sustained by the wind, but have been generated by the wind some distance away and now propagate freely. Swell is characterized by similar wave heights that move in a uniform directions (which may not align with the wind) and decay much slower than waves in the windsea. As expected, windsea and swell more often occur together rather than separately (Csanady 2001; Garrison 2007).

Wind wave development is governed by water depth, wind speed, fetch, and duration. Wind fetch and duration are defined as the distance over which the wind blows without a significant change in direction and how long the wind blows, respectively. With an unlimited fetch and duration, wind speed determines an upper limit for wave height (and wavelength). Water depth is omitted from the discussion as waves usually form in deep water where there are no restrictions on growth based on depth. The term sea state is a description of the properties of ocean surface waves at a given time and place (e.g., wave height and period), and is classified as fully developed, fetch limited, and duration limited. If the wind blows from a more or less constant direction over a large enough distance and length of time (independent of fetch and duration), waves will be able to develop fully. Waves in the fully-developed sea cannot grow any larger even when the fetch or duration are more than the minimum required for full development and wave height is at a theoretical maximum.

More specifically, the input of energy to the waves from the local wind is in balance with the transfer of energy, and with the dissipation of energy by wave breaking (steady-state). Partially developed seas occur when the fetch or duration (or both) are limited, hence the amount of energy imparted to the waves needed to attain fully-developed does not occur. This results in a limited range of wavelengths and wave periods. Sea state remains partially developed (limited range of wavelengths and wave periods) in hurricane conditions, as the wind speed and direction are highly variable and the fetch is limited (Mitsuyasu and Rikiishi 1978; Csanady 2001; Garrison 2007). The degree of wave field development is often described by the so-called 'wave age' parameter, expressed as c_p/U_{10} or c_p/u_*. Wave age is defined as the developmental stage of the sea relative to the current state of wind forcing (Edson and Coauthors 1999). Wind generated waves will stop growing (W_{grow}) when they reach a wave age of 0.5–0.9 (Dobson 1994; Drennan et al. 1999; Sjoblom and Smedman 2002). Based on the wave age criterion, waves can be classified into three categories (Sjoblom and Smedman 2002):

- Growing seas: $c_p/U_{10} < W_{grow}$
- Mature or saturated waves: $W_{grow} < c_p/U_{10} < 1.2$
- Swell: $c_p/U_{10} > 1.2$.

Growing seas are typically observed in hurricane conditions since $U_{10} \gg c_p$. Numerous investigations have documented enhanced wind stress over developing wave fields compared to seas which are in equilibrium with the wind (e.g., Geernaert et al. 1987; Smith 1992; Donelan et al. 1993). The dependence of wind stress on the wave field can be attributed to the facts that younger waves travel with a slower speed relative to the wind and that younger waves are steeper.

3.8   Air flow over a change in surface roughness

Since it is hypothesized that wave conditions in shallow water cause this region to be rougher than deep water, a discussion of this affect on the boundary layer is warranted. Many books have addressed flow over a change in terrain or surface roughness (e.g., Simiu and Scanlan 1986; Finnigan 1994; Holmes 2001).   This discussion considers an abrupt change (discontinuity) in surface roughness along a line perpendicular to the mean wind direction (taken to be the x-direction). When fully developed boundary layer flow over a horizontally homogeneous surface encounters a discontinuity, the flow is disturbed and must adjust to the new underlying surface. Depending on the transition, the flow either slows down because of increased surface friction (smooth to rough) or speeds up due to a decrease in frictional drag (rough to smooth). Initially, the adjustment is confined to the air layers in contact with the new surface, and is gradually diffused vertically by turbulence. The effect of this change in terrain is a steadily growing internal boundary layer (IBL). It should be noted that pressure gradient forces are also an effect of a transition (they can act outside of the IBL), but are negligible unless there is a significant change in displacement height (e.g., flow from flat open country to tall crop field). Flow within the IBL is characteristic of the new surface, and its depth is denoted by δ_i. At some distance downstream of the transition, the entire boundary layer adjusts to the new roughness.

   The case of air flow over a smooth surface encountering a discontinuity to a rougher surface is shown in Fig. 2. As the flow reaches the change in terrain, it begins to adjust to the new surface. At the discontinuity an outer IBL forms and separates (in theory) the upstream flow conditions from the new surface. Flow in the upper region is essentially unaffected by the change (still characterized by z_{01} and u_{*1}) and the velocity is equal to the velocity upstream of the discontinuity. At some distance downstream of the transition, an inner IBL forms. Below this level, it is very crudely assumed that the flow is in equilibrium with the new surface (determined by z_{02} and u_{*2}). Between the inner and outer limits of the IBL is an transitional regime, where the turbulence generated from the new surface is gradually distributed vertically. It is assumed that the flow in this region has characteristics of both the smooth and rough surfaces.
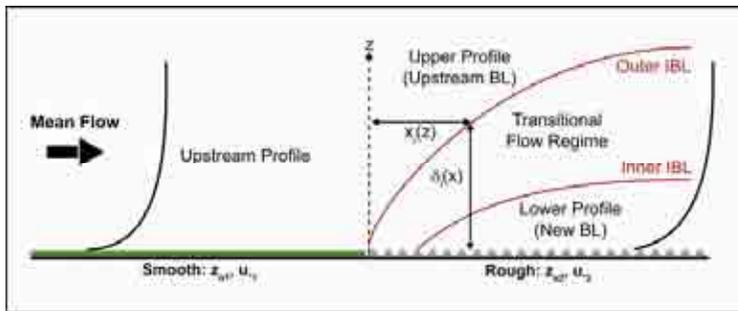
FIG. 2. Schematic diagram of boundary layer transition from a smooth to rough surface.

A formula to model IBL growth is as follows (Simiu and Scanlan 1986):

$$\delta_i(x) = 0.28 z_{0r} \left(\frac{x}{z_{0r}} \right)^{0.8} \tag{14}$$

where z_{0r} is the roughness length of the rougher terrain (e.g., z_{02} in Fig. 2). This model was formulated using data acquired in both smooth to rough and rough to smooth transitions, where δ is the affected boundary layer depth. Holmes (2001) provides a model for identifying the horizontal position of the IBL as a function of its height z. For flow from smooth z_{01} to rough z_{02} terrain, only the latter value has bearing:

$$x_i(z) = z_{02} \left(\frac{z}{0.36 z_{02}} \right)^{4/3} \tag{15}$$

This section has attempted to present an overview of previous research on wind over waves and also in a context of changes in surface roughness's that occur at the shoreline. In the next section recent work involving novel wind tunnel studies and full scale measurements are presented.

4. RECENT STUDIES

4.1 Drag coefficient in extreme winds

Donelan et al. (2004) stated that, "the mechanical coupling of the two fluids is at the heart of modeling the flow of either fluid." Although wind stress over the ocean has been a subject of study (and arguably debate) for over 50 years, present parameterizations still have significant limitations, especially in high wind regimes. Over the last six years air-sea interaction research has focused primarily on measurements of C_D rather than parameterizations. Conducting in situ measurements of the mean wind velocity profile in extreme conditions is exceptionally difficult in the open ocean, but pose an even greater challenge in the near-shore region. Due to this vicissitude, past research efforts have estimated wind stress in only weak to moderate winds ($3 < U_{10} < 25$ m/s). Data from these measurements have been extrapolated to strong wind speeds, where it has been generally accepted that C_D increases linearly with increasing wind speed (e.g. Garratt 1977; Amorocho and De-Vries 1980; Smith 1980; Large and Pond 1981; Yelland and Taylor 1996; Drennan et al. 1999). Extrapolations of this wind tendency are currently being employed in applications such as forecasting the intensity and track of tropical cyclones, determining the wind forcing for storm surge and wave forecasts, input for numerical weather prediction models, and determining extreme wind loads (Powell et al. 2003). Prior to 1997 and the development of the Global Positioning System dropwindsonde (Hock and Franklin 1999), which measures kinematic and thermodynamic properties during its descent, and the novel airborne instruments developed during the Coupled Boundary Layer Air-Sea Transfer Experiment (CBLAST) beginning at the turn of the century (Black et al. 2007), estimates of C_D in extreme wind regimes (for research purposes) were simply not possible.

Recent field and laboratory studies have disproved the general prediction of a monotonic increase in C_D with wind speed, and have, in part, offered a paradigm shift in the way we believe C_D to behave in extreme winds in the open ocean. High-resolution GPS sonde wind profile measurements by Powell et al. (2003) and laboratory wave tank measurements by Donelan et al. (2004) have found that the linear extrapolation method is not valid and that C_D plateaus at wind speeds of ~33 m/s (decreasing thereafter), corresponding to a limiting drag value range of 0.0022–0.0025. A later study by Jarosz et al. (2007) based on current observations recorded during major Hurricane Ivan (2004), offered supporting evidence. They found that the drag coefficient increases initially and reaches a maximum at a wind speed of about 32 m/s before decreasing (for wind speeds up to 48 m/s). Preliminary results from an extension of the Powell et al. (2003) study suggest an azimuthal dependence on C_D relative to the direction of storm motion. Slightly different results were obtained by the CBLAST group (Black et al. 2007) in slightly weaker maximum wind speeds < 30 m/s, where it was found that C_D plateaus at a wind speed close to 23 m/s ($C_D < 0.002$). Although all these are studies have merit, their results are not consistent. Additional research is required to test and confirm these results.

Since the results described above (Powell et al. 2003; Donelan et al. 2004; Black et al. 2007; Jarosz et al. 2007) are significantly different from those previously accepted, explanations of this

phenomenon are critical. Donelan et al. (2004), using a study by Reul (1998) who observed vorticity contours for gentle and steep-sloped waves, suggested that this qualitative change in the surface drag coefficient is a consequence of air flow separation from breaking waves which acts to decouple the MABL from the chaotic (rough) sea surface. Air flow experiences separation from the surface and reattachment near the crest of the following wave, indicative of skimming flow where the flow ultimately bypasses the troughs. Powell et al. (2003) offered an explanation via the role of sea foam and spray that has been observed on the sea surface in wind speeds above hurricane force. He suggested that the thick layer of foam that typically develops in winds in excess of approximately 40 m/s forms a 'slip' surface which impedes the transfer of momentum from the wind to the sea. These explanations were supported by the findings of Kudryavtsev and Makin (2007). Using modeling techniques, Kudryavtsev (2006) investigated the role of sea spray on sea drag at high wind conditions. They showed that the production of spray results in the acceleration of airflow, and the suppression of turbulence and surface drag. At wind speeds of 50–80 m/s, the model predicted the effects of a 'slip' surface, with C_D on the order of 0.0001 (Kudryavtsev 2006). Although both studies offer valuable insight, it is still to be determined if these explanations hold in the near-shore region, where conditions are markedly different.

4.1.1   Observational measurements in hurricanes
Arguably the most important study of the drag coefficient in extreme winds to date is that of Powell et al. (2003), hereafter PVR03. PVR03 used high resolution wind profile measurements from GPS sondes dropped in the vicinity of hurricane eyewalls to observe the behavior of C_D in hurricane winds in deep water. A summary of the important work of PVR03 is highlighted in the following. PVR03's study utilized detailed wind profile measurements acquired by GPS sondes from 1997–1999. During this time span, 331 eyewall (or near-eyewall) wind profiles were sampled in hurricanes located in the Atlantic and Eastern/Central Pacific basins. The GPS sonde samples pressure, temperature, humidity, and position at a frequency of 2 Hz. Sondes are generally dropped at a height of 1.5–3 km above the sea surface and fall at a rate of 10–15 m/s. Failure of these instruments is possible in regions of turbulence or heavy rainfall.

  Derived wind speed and height measurements have an accuracy of 0.5–2.0 m/s and 2 m, respectively (Powell et al. 2003). PVR03 estimated surface layer quantities using composite wind profiles (individual 0.5-s samples from 331 sonde profiles) based on mean boundary layer (MBL) wind speed. MBL wind speed was arbitrarily defined as the mean wind speed below 500 m. The maximum wind speed for each profile was usually contained within this layer. The 331 wind profiles were averaged for all measurements in the lowest 3 km as a function of the MBL wind speed and each profile was organized into one of five MBL groups (in m/s): 30–39 (72 profiles), 40–49 (105 profiles), 50–59 (55 profiles), 60–69 (61 profiles), and 70–79 (38 profiles). A relatively wide range of wind speeds (21–67 m/s) were measured near the surface (8–14 m). PVR03 found a logarithmic increase in wind speed with height in the lower 200 m (Fig. 3). Above 200 m, the mean profile continued to increase, reached a peak near 500 m, and decreased thereafter. The decrease was due to a weakening of the horizontal pressure associated with the warm core of a tropical system. PVR03 attributed the apparent increased variability above 600 m to convective-scale features in the eyewall (identified by Jorgensen (1984). The aforementioned logarithmic profile below 200 m and maximum wind speed at 500 m is consistent with a neutrally stable surface layer. PVR03 used the profile method in the lowest 100–150 m of each MBL group to estimate z_0 and u_* . Then, C_D was estimated using Eq. 5.
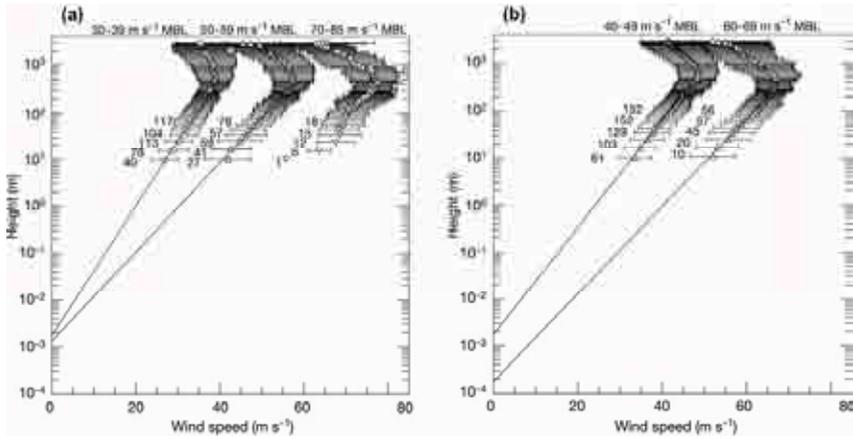
FIG. 3. Mean wind profiles by MBL group: (a) 30–39 m/s (72 profiles), 50–59 m/s (55 profiles) and 70–85 m/s (38 profiles) and (b) 40–49 m/s (105 profiles) and 60–69 m/s (61 profiles) MBL groups. Symbols and horizontal bars represent mean and standard deviation for each vertical bin. Numbers adjacent to each level represent the number of samples within each of the lowest five height bins. From Powell et al. (2003).

Results indicated that surface layer parameter dependence on wind speed is vastly different than previously believed in high wind speeds, as shown in Fig. 4. Observations of C_D are consistent with other investigation in weak to moderate wind speeds. However, above 40 m/s C_D behaved markedly different than what was anticipated. PVR03 observed a leveling off at 40 m/s and a large decrease when U_{10} increased to 51 m/s. Similarly, z_0 and u_* increased up to 40 m/s (this behavior was roughly predicted by previous studies), leveled off around 40 m/s, and decreased as U_{10} increased to 51 m/s (Fig. 4a), u_* not shown). In summary, C_D plateaus near wind speeds of 35 m/s, corresponding to a saturation value near 0.0026 Powell et al. (2003).
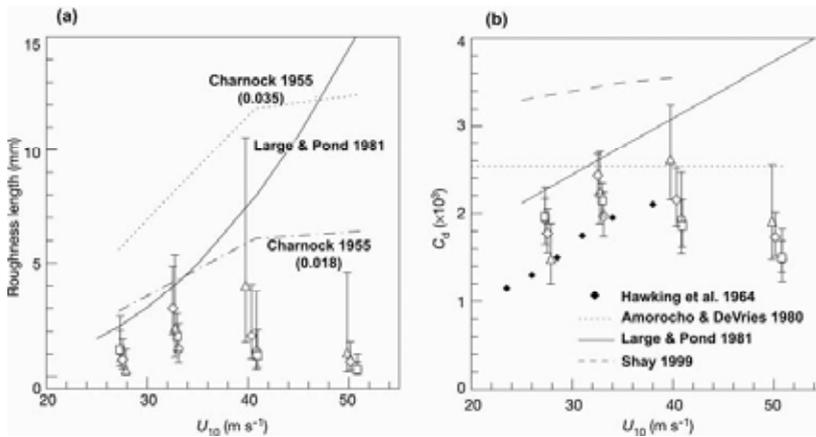
FIG. 4. Momentum exchange quantities as a function of U_{10}. Vertical bars represent the range of estimates based on 95% confidence limits and the symbols represent the different layer depths used in the profile method: ○ 10–100, _ 10–150, △ 20–100, ◇ 20–150 m. (a) z_0 from GPS sonde profiles (symbols) and Large and Pond (1981) relationship (solid line) and Charnock (1955) relationships for comparison (dotted line, á = 0.035; dashed-dot line, á = 0.018) and (b) C_D with relationships and values from tropical cyclone budget studies. Adapted from Powell et al. (2003).

4.1.2 Laboratory measurements in wind speeds near hurricane force

Shortly after the work of PVR03, Donelan et al. (2004) examined the affect of high wind speeds on C_D in a laboratory setting. Donelan et al. (2004), hereafter DHR04, utilized the unique Air-Sea Interaction Facility at the University of Miami. They offered supporting evidence to the observational results found by Powell et al. (2003). The wave tank at the University of Miami is 15 m long, 1 m wide, and 1 m high. The tank was equally divided between air and water with the water side being 0.5 m deep. Wind speed in the tank was set by a programmable fan. Vertical profiles of wind speed and turbulence were not provided. Reynolds stresses were measured directly using an x-film anemometry. Direct measurements of Reynolds stress were made at measured elevations and corrected to surface values using the measured horizontal pressure gradient in the tank. For high wind speeds, DHR04 computed surface stress from a momentum budget using sections of the tank as a control volume (Fig. 5). The momentum budget method was accomplished assuming steady state conditions. The control volume, defined by the shaded area $A_1B_1B_2A_2$ in Fig. 5, extended a unit width into the paper. Under this assumption, wind stress τ_a produced a downwind current near the surface which resulted in an increase in mean surface elevation downwind h_2.
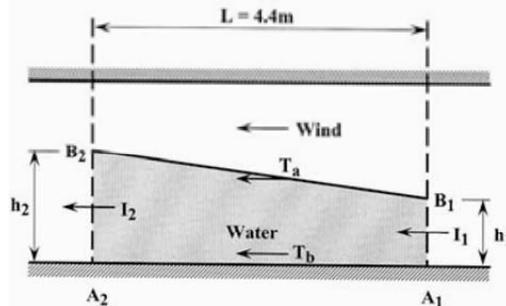
FIG. 5. Schematic outline of the control volume for the momentum budget method. From Donelan et al. (2004).

A return flow in the bottom of the water column in the upwind direction and stress τ_b applied to the bottom of the tank was caused by an induced pressure gradient due to the elevation difference. Momentum fluxes through the tank are respectively denoted as I_1 and I_2 for sections A_1B_1 and A_2B_2. They verified the momentum budget method by comparing results for this method to the other methods utilized, which show good agreement. Verification of this method was important since it allows for the estimate of surface stress in high winds in a way that was insensitive to airborne water droplets (problematic for x-film measurements). Using this method, DHR04 showed that wind stress, τ_w is given by:

$$\tau_w = sh\left(\rho_w g \ + \frac{\Delta P}{L}\right) + \frac{\Delta S_{xx}}{L} - \tau_b \tag{16}$$

where h is the average water depth, ΔP is the air pressure difference, ΔS_{xx} is the radiation stress for deep water, and s is the slope of the water surface. Sidewall stresses were neglected since they tend to cancel out assuming steady state conditions (Donelan et al. 2004).

DHR04 conducted several experiments using the programmable fan in the wave tank. The fan was set to fixed speeds for 300 second runs to obtain a stable estimate of wind stress. DHR04 noted a loss of water droplet spray to the return duct which contributes to wind stress on the surface. They accounted for water loss due to spray by calculating upper limit of 1.5% lost momentum due to spray, which they noted as "generous".

Results from DHR04 compared to those of Large and Pond (1981) and Ocampo-Torres et al. (1994) are shown in Fig. 6. To bring the results to scale, the height of the wind speed measured in the

tank (10 cm) was extrapolated to the standard meteorological height of 10 m using a logarithmic dependence on height. Again, it was not mentioned what the actual wind profile was like above the wave/water surface. The initial decrease in C_D to a minimum at a wind speed of 3 m/s was a result of an aerodynamically smooth surface (Fig. 6). As the waves increased and the surface became aerodynamically rough, C_D increased with increasing wind speed between 3–33 m/s. At 33 m/s, C_D leveled off, corresponding to a limiting value of 0.0025. Results were only slightly lower than the open ocean measurements of Large and Pond (1981) for weak to moderate wind speeds.
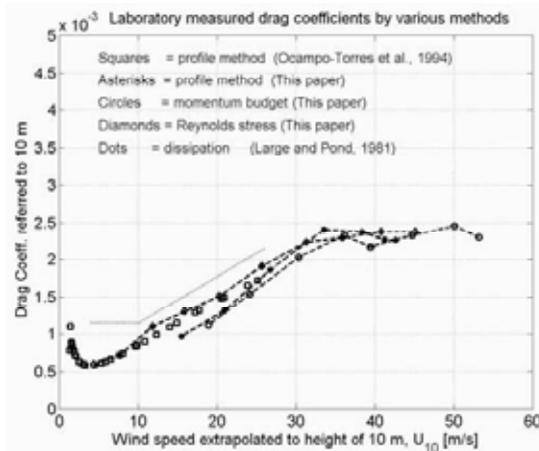
FIG. 6. Laboratory measurements of the neutral stability drag coefficient by profile, Reynolds Stress and momentum budget methods. The drag coefficient refers to the wind speed measured at the standard anemometer height of 10 m. The frequently cited drag coefficient formula derived from field measurements by Large and Pond (1981) is also shown. From Donelan et al. (2004).

4.2   Laboratory measurements over solid waves

Owing to the profound difficulty in conducting field measurements of near-shore wind and waves, laboratory wind tunnel measurements offer valuable insight. There have been numerous laboratory experiments that have studied flow over sinusoid wave trains (e.g., Zilker and Hanratty 1979; Buckles et al. 1984; Kuzan et al. 1989; Belcher and Hunt 1998; Gong et al. 1999). Most authors were interested in studying the spatial variation of the flow field, shear stress, and pressure along the wave surface to develop a better understanding of wind wave generation. A wide variety of wave steepnesses have been studied, ranging from very steep H/L = 0.4 (e.g., Beebe 1972), to steep H/L = 0.2 (e.g., Buckles et al. 1984; Gong et al. 1999), to gentle-sloped H/L = 0.05 (e.g., Zilker and Hanratty 1979). The steepest laboratory waves are important for wind-wave generation (by examining pressure distributions along wave), but mature ocean surface waves tend to exhibit a very gentle slope in the deep ocean H/L $\approx$ 0.02–0.05. Buckles et al. (1984) used laser-Doppler velocimetry to measure the mean and fluctuating velocity for turbulent flow over a solid sinusoid wave train to identify the separated flow region. The wave surface had a wavelength of 50.8 mm and height 10.16 mm for a wave height to wavelength aspect ratio of 0.2. They measured mean pressure and rms pressure fluctuations at 33 locations using surface taps spaced at 1.59 mm intervals over the eighth wave in the wave train at Reynold number Re = 1.2×10^4. They found that flow separated between x/L = 0.1 and x/L = 0.2, where x is the distance along the wave and L is the wavelength. Reattachment occurred between 0.6 $\leq$ x/L $\leq$ 0.7, marked by a positive near-wall velocity. They calculated the stream function for the mean flow and the resulting streamlines and found that separation occurred at x/L = 0.14 and

reattachment at x/L = 0.69, as shown in Fig. 7a. At the separation point the mean direction of flow reversed from a positive to slightly negative value at the nearest wall measurement and the flow is deflected slightly upward then downward. Streamlines were compressed upwards in response to the lifting wave surface downstream of the reattachment point, indicating accelerated flow. Mean velocity profiles (not presented) indicated that accelerated flow was exhibited above the eighth wave crest. The recirculation zone lies between the aforementioned separation and reattachment points. A maximum thickness is reached at x/L = 0.4, approximately 60% of the wave height. Velocity profiles indicated a thin boundary layer (< 0.15 mm) at the point of reattachment, which grows to 0.6 mm by the upstream wave crest, and approximately triples in thickness to the separation point. Roughly past the separation point (x/L = 0.15), the region of maximum turbulence intensity is associated with the free shear layer. They note that this maximum provided a more sensitive means for locating the free shear layer (compared to mean velocity profiles).

Directly over the trough (x/L = 0.5), the turbulence intensity maximum was observed at approximately the wave height. A layering of the flow observed by Buckles et al. (1984) is shown in Fig. 7b. Free shear layers are formed by the separation of a boundary layer at x/L = 0.14 and x/L = 1.14. In general, this study provides a good description of air flow over a train of steep sinusoid waves.

Many wind tunnel studies of flow over wave surfaces have been conducted for aerodynamically smooth flow, with which there is some Reynolds number dependence (e.g., Buckles et al. 1984; Kuzan et al. 1989). Gong et al. (1999) conducted a wind tunnel experiment using aerodynamically rough surfaces. More specifically, they measured turbulent boundary layer flow over rough (and smooth) sinusoid wave surfaces in an attempt to characterize the flow, determine the form drag, and the total horizontal force on the waves.
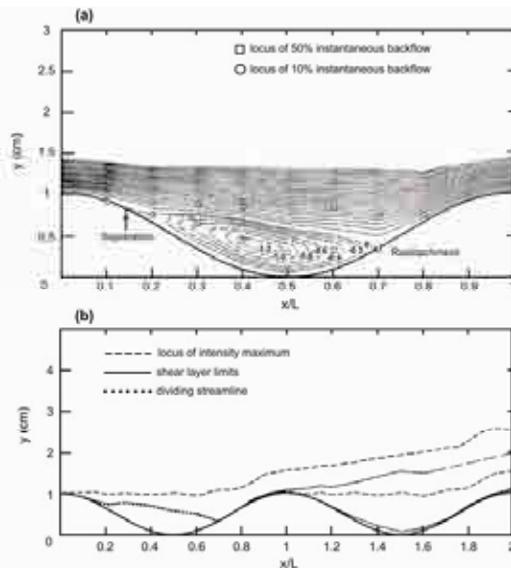
FIG. 7. (a) Streamline map over the crest of the eighth wave (x/L = 0) to the crest of the ninth wave (x/L = 1) in the wave train and (b) shear-layer map indicative of flow at the crest of the eighth wave (x/L = 1). Adapted from Buckles et al. (1984).

Gong et al. (1999) used a large wave train consisting of sixteen sinusoid waves placed along the centerline of a large atmospheric boundary layer wind tunnel. Waves heights were 96.5 mm with a wavelength of λ = 609.6 mm, corresponding to a maximum surface slope of Ak = 0.5 and aspect ratio

of H/λ = 0.158. Roughness lengths over flat pieces of the smooth (foam) and rough (Masonite) surfaces were z_o = 0.03 mm and z_o = 0.4 mm, respectively. They note that the flow reached a periodic, near-equilibrium state after the third or fourth wave. With a maximum surface slope of Ak = 0.5, it was expected that the flow would separate based on a critical slope for separation of A$k \approx 0.3$, determined by Kuzan et al. (1989). Intermittent flow separation was observed in the smooth case but the mean flow remained approximately attached. The flow separated in the wave troughs for the aerodynamically rough simulation. Constant pressure regions, indicative of flow separation, extended from x/L = 0.15 to 0.5. Without the capability to measure reverse flow, Gong et al. (1999) inferred that little or no reverse flow existed in the smooth case. However, the rough simulation possibly had a separated region with relatively stagnant flow in the wake extending to heights of order (0.4a) on the lee slope and in the trough. The flow was sensitive to surface roughness. The greatest speed-up was observed just above the wave crest in the smooth case (still existent but weaker for the rough case) and the order of magnitude larger surface roughness increased the velocity reduction in the outer part of the boundary layer. For the rough case (and the strongly separated flow observed by Buckles et al. (1984) a very strong shear layer was observed close to the wave surface above the crest (followed by a region of constant wind velocity above that and a gradual increase to the free stream wind speed). Measurements of the u-component turbulence fluctuations σ_u showed an increase just above the crest and a significant increase at about the wave height above the trough of the twelfth wave. Using surface pressure measurements, they computed the form drag per unit area on the waves using:

$$\tau_F = \rho C_{DF} U_o^2 = \int p_S^* \frac{dz_S}{dx} dx / \lambda \qquad (17)$$

where τ_F is the stress due to form drag, U_o is the free stream velocity at 600 mm, p_S^* is the surface normal stress, and the integral is over one wavelength. Results indicate that form drag is nearly three times the wavelength-averaged surface shear stress. The form drag for the rough case was less than that found over the smooth case. Results of Gong et al. (1999), presented in Table 2, indicate uncertainties in the data, as there was a 50% difference in the total wind stress using two independent methods (from velocity profiles and pressure measurements and from a momentum budget) for the rough simulation. They concluded that accurate prediction of the drag over topography may be a rather difficult goal to achieve.

TABLE 2. Drag values from Gong et al. (1999). Values are normalized by ρU_o^2 where U_o is the free stream velocity determined at height z = 600 mm. $(u_*^2)_o$ is the upstream stress from the velocity profile, wavelength-averaged values $<(u_*^2)>$, C_{DF} is the normalized form drag calculated from Eq. 17, MTB is the total drag computed from a momentum budget over ten waves and % C_{DF} is the contribution (%) of form drag to the total drag.

Surface Type	$(u_*^2)_o$	$<(u_*^2)>$	C_{DF}	$<(u_*^2)> + C_{DF}$	MTB	% C_{DF}
Relatively Smooth	0.0017	0.0025	0.0085	0.011	0.0092	77
Relatively Rough	0.0038	0.0014	0.0065	0.0079	0.013	82

There is currently a research gap regarding flow over waves in shallow water (h < 50 m). There appears to have been no wind tunnel studies that have modeled the flow over waves in the near-shore region. This may be because wave generation is relatively unimportant due to changes in shape caused by wave transformation. However, understanding flow behavior over near-shore waves is valuable for storm surge forecasts and coastal building design standards. Therefore, gaining an understanding of wind tunnel flow over near-shore shoaling solid waves is a necessary step in gaining this knowledge.

4.3   Recent wind/wave studies at Texas Tech University

Chen (2007) employed a moving belt mechanism to simulate wind waves in the boundary layer wind tunnel at Texas Tech University. This study was aimed at examining the influence of wave speed on the wind flow and was the first such study undertaken. The mechanism was capable of varying belt type and belt speed. To find the wind stress over the simulated waves, the time histories of wind speed at different conditions were sampled. A smooth moving belt was first installed to simulate ocean waves in light or mild wind. The same process was repeated with a rough moving belt with square cleats which was used to simulate wind waves in high wind conditions,ie., a much rougher surface. Surface wind stresses were estimated using the profile method. Four field datasets, HEXOS, RASEX, AGILE, and FETCH were used for comparison. These field data were selected for pure wind sea or dominant wind sea conditions in order to avoid the influence of swells. Using wind tunnel and field data, the relation between surface wind stress, wind speed and wave age as defined by c_p/u_* or c_p/U_{10} was investigated. Different methods of parameterizing the wind stress were studied.

It was concluded from profile measurements and comparisons with full scale that the technique could successfully simulate ocean surface wind waves. The wind profiles changed with wind speed and belt speed. The surface wind stress measured in the wind tunnel increased with increasing wind speed, and decreased with increasing belt speed. These results provide strong support for a wave age dependence of wind stress. Table 3 summarises the wave age relationships obtain from field studies and the moving belt wind tunnel studies.

TABLE 3: Wave age relations for drag coefficient C_D using u_*/c_p .

Source	Relationship	R^2
Rough belt Chen (2007)	$C_D = 1.32 \times 10^{-2} (u_*/c_p)^{0.67}$	0.89
Smooth belt Chen (2007)	$C_D = 1.12 \times 10^{-3} (u_*/c_p)^{0.23}$	0.77
HEXOS	$C_D = 1.45 \times 10^{-2} (u_*/c_p)^{0.71}$	0.85
RASEX	N/A	N/A
FETCH	$C_D = 6.31 \times 10^{-3} (u_*/c_p)^{0.51}$	0.51
AGILE	$C_D = 5.76 \times 10^{-3} (u_*/c_p)^{0.51}$	0.30
Composite field data	$C_D = 6.77 \times 10^{-3} (u_*/c_p)^{0.52}$	0.50
Wenqi Lin (2002)	$C_D = 6.28 \times 10^{-3} (u_*/c_p)^{0.578}$	0.64
Geernaert (1987)	$C_D = 1.48 \times 10^{-2} (u_*/c_p)^{0.738}$	N/A
Vickers & Mahrt (1997)	$C_D = 7.1 \times 10^{-3} (u_*/c_p)^{0.67}$	N/A
Smith (1992)	$C_D = 0.43 (u_*/c_p)^{0.96}$	N/A

Dimensionless roughness z_0/H_s was found to be much better than the Charnock parameter z_{Ch} in explaining the dependence of surface roughness on wave age. The results show a clear wave age dependence of surface roughness. The rough belt in the wind tunnel successfully simulated aerodynamically rough flow over the sea surface which occurs in fetch-limited conditions (i.e., young wave age conditions) either in coastal waters or lakes. The results from the rough belt test are very close to those field study findings in fetch-limited conditions. The smooth belt in the wind tunnel successfully simulated the aerodynamically smooth flow over sea surface which often occurs in open water (i.e., mature wave age conditions). The results from the smooth belt test are a little different to those field study findings in mature wave age conditions because the belt speed was limited.

Recently Zachry (2009) has undertaken wind tunnel studies over stationary waveforms that simulate waves in shoaling regions and also combined wind and wave measurements during the landfall of Hurricane Ike near Galveston in 2008. Only a limited number of laboratory studies have examined form drag on fixed wave models via surface pressure measurements. The majority of these studies utilized steep-sloped sinusoid wave shapes. The shoaling wave model Zachry studied had an asymmetric sinusoid shape. Maximum wave slope for a sinusoid is easily computed as Ak, where A is the wave amplitude and k is the wave number. Here, slopes were computed numerically. Maximum wave slopes on the upstream and downstream portions of the wave were 0.22 and 0.25, respectively. Form drag values are compared to sinusoid waves in Fig. 8. Form drag for the shoaling wave (plotted with respect to its maximum upwind slope) has comparable C_{DF} values to sinusoid waves with slightly smaller maximum slopes. This result is in good agreement with Kuzan et al. (1989), who determined that flow separation occurs for a slope ≥ 0.3. Due to the flow remaining attached, shoaling wave form drag is considerably less than sinusoid waves with slopes of around 0.35–0.40 (above the critical number). The noticeable leveling off of the form drag coefficient for wave slopes exceeding > 0.8, based on the C_{DF} value obtained by Beebe (1972) for a wave slope of 1.27, is due to skimming flow (where the vortex resides between the wave crests and the flow above the wave does not penetrate into the troughs.
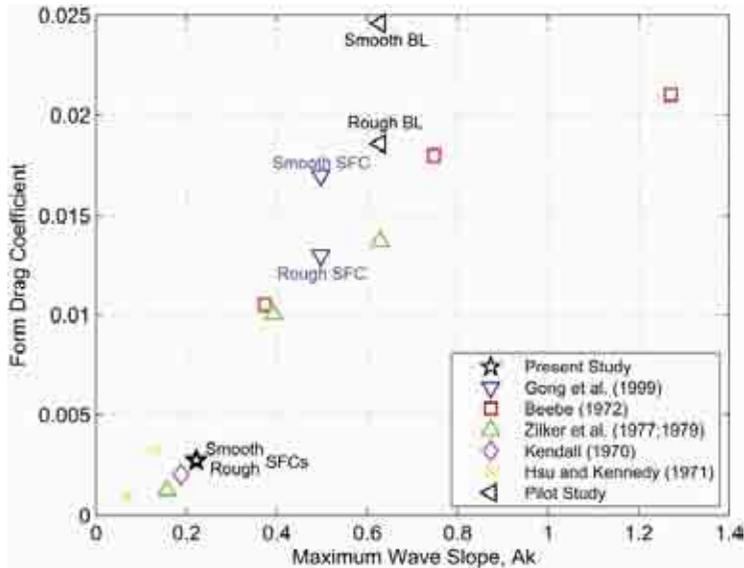
FIG. 8. Comparison of form drag coefficients for the (shoaling wave) and other laboratory studies (sinusoid waves) based on maximum wave slope (upwind wave slope - Zachry 2009), and normalized by the freestream (or maximum) wind speed U$_0$. Figure adapted from Gong et al. (1999).

Zachry compared his full scale measurements captured during Hurricane Ike in the vicinity of Galveston with three well-known deep water studies: (1) Powell et al. (2003), (2) Black et al. (2007), and (3) Donelan et al. (2004). The data were also compared to shallow water drag coefficients reported in Powell (2008). These comparisons are shown in Fig 9. Both the Zachry (2009) and Powell et al. (2003) results indicate that C_D reaches a limiting value and decreases for higher wind speeds. The Hurricane Ike and the deep water limiting values are similar, but the former occurred at wind speeds below hurricane force. Based on the present study, coastal drag coefficient behavior is in

accord with that for deep water, where a limiting value is reached and subsequently decreases for higher wind speeds. Clearly although the overall form appears the same coastal drags are significantly higher for low to moderate wind speeds of < 25 m/s. Shoaling and deep water data decreased rapidly for wind speeds below hurricane force. Crudely extrapolating the Powell et al. (2003) results to slower winds (e.g., 10 m/s) the drag coefficient would be considerably less than those obtained here during Hurricane Ike. Laboratory observations also indicate lower drags for lighter winds and that the trend in C_D with increasing wind speed is much steeper than that found by Zachry (2009). This result is likely a consequence of the complex wave conditions in the Houston ship channel generating a 'rough' (wave) surface even under light winds. Clearly more data in the complex coastal region is required to better understand this phenomenon.
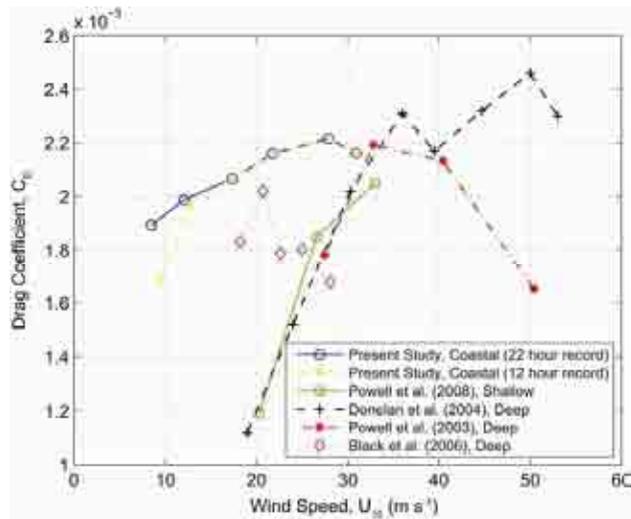
FIG. 9. Comparison of mean 10 m drag coefficient in hurricane conditions for Zachry (2009) Present coastal study, shallow water measurements from Powell (2008), open ocean measurements from Powell et al. (2003) (mean of the four layers) and Black et al. (2007), and in simulated extreme wind in the laboratory from Donelan et al. (2004) (using the momentum budget method).

5. SUMMARY AND APPLICATIONS

This paper summarizes studies of the interaction of the wind and the ocean. Numerous studies have been undertaken, many concentrating on wind-wave interaction over deep water where there is now reasonable understanding of the phenomena. However, wind flow over near-shore shoaling waves and the transition to flow over land with consequent terrain and topography changes remains an area of fruitful research. To conclude this paper, the importance of understanding wind/wave interactions in two specific areas is presented.

5.1 Application of wind stress in storm surge modeling

A minimum of five processes are responsible for hurricane storm surge, one of which is direct wind forcing (Harris 1963). The wind-driven component of hurricane storm surge, wind stress, is exerted when wind blows over water bodies. "Although the wind shear stress is usually very small, its effect,

when integrated over a large body of water, can be catastrophic (Dean and Dalrymple 1991, p. 157)." Wind stresses cause wind setup, which is a rise in the still water level at the downwind shore. In a strong onshore wind regime, it is obvious that wind setup is a significant contributor to the total storm surge. Accurate computation of storm surge requires that the hurricane wind field is correctly modeled, as wind stress is proportional to the square of the wind speed. Slight error in the modeled hurricane wind field can lead to significant error in estimates of wind stress and thus storm surge. The hurricane wind field is typically estimated from the dependence of surface pressure on wind speed and radial distance from the circulation center. In the absence of real time observations, the wind field is estimated using remote sensing techniques or numerical weather prediction. Improving the accuracy of wind models to predict the distribution of wind speeds in a hurricane is an ongoing research effort (e.g., Chen et al. 2006, Zachry 2009).

Storm surge models use the long wave equations to describe the change in water level due to wind forces acting on the water surface (Dean and Dalrymple 1991). Dean and Dalrymple (1991) provide a linearized equation to compute storm surge for onshore flow with a parallel coastline and neglecting lateral shear stresses. More complicated nonlinear equations, eg., Reeve et al. (2004), are typically utilized for storm surge prediction. The most recent and technologically advanced model of coastal ocean hydrodynamics is the advanced circulation hurricane storm surge model (ADCIRC developed by researchers from several universities (IPET 2006a, Luettich et al. 1992). ADCIRC is a multi-dimensional, depth-integrated, barotropic time-dependent long wave, hydrodynamic circulation model that simulates water level and ocean currents over an unstructured gridded domain. The model uses a finite element grid, the Boussinesq approximation, quadratic bottom friction, and vertically integrated continuity and momentum equations for flow on a rotating earth (Luettich et al. 1992). ADCIRC uses the standard quadratic drag law to compute wind stress (Eq. 4), with a surface drag coefficient defined by Garratt (1977) as a linear function of wind speed. This formulation, valid for the wind speed range of $10 < U_{10} < 21$ m/s, is based on regression fits to field measurements primarily in deep water and open ocean conditions, but is generally applied to wind speeds above 21 m/s. Other modeling studies have also adopted deep water drag models (e.g., Tang et al. 1997; Lentz et al. 1999; Reniers et al. 2004).

Weaver (2004) performed an ADCIRC sensitivity simulation of the five storm surge forcings for Hurricane Georges (1998). Of particular interest is the sensitivity of ADCIRC to the various drag coefficient formulations. Weaver (2004) tested the model using the maximum value of the drag laws shown in Table 4. His results (Fig. 10) indicated that the model is quite sensitive to the drag coefficient formulation used as input. It is seen that peak storm surge estimates can vary by as much as ±1.75 m. Thus, it is critical that 'correct' drag laws are applied.

TABLE 4. The drag coefficient formulations used in an ADCIRC sensitivity test performed by Weaver (2004).

Source	$C_D \times 10^3$
Miller (1964)	$1 - 4.0$
Garratt (1977)	$0.75 + 0.067\, U_{10}$
Smith (1980)	$0.61 + 0.063\, U_{10}$
Large and Pond (1981)	$0.49 + 0.065\, U_{10}$
Klapstov (1983)	$0.49 + 0.07\, U_{10} + 2.58/U_{10} - 1.06\, (T_{air} - T_{sfc})/U_{10}^2$
Geernaert (1987)	$0.58 + 0.085\, U_{10}$
Used in a subsequent study	
Amorocho and DeVries (1980)	$0.0015[1+\exp(-((\,U_{10}-12.5)/1.56))]^{-1} + 0.00104$

ADCIRC was recently applied to hindcast storm surges for Hurricane Katrina (2005). The base ADCIRC simulation uses the drag lag defined by Garratt (1977). Sensitivity simulations revealed that application of a drag cutoff of $C_D = 0.0025$ in the base run decreases maximum surge heights by up to 1.2 m (4 ft) compared to the case with no limit. They conducted another sensitivity test comparing the

base simulation without the cutoff applied to the drag law defined by Amorocho and DeVries (1980). This formulation has a built in cutoff of $C_D = 0.00254$. Results indicated that application of Amorocho and DeVries (1980) wind stress formulation slightly reduces the peak surge in water level compared to the base drag law without the cutoff. The official model run was ingested with the base formulation without the cutoff applied. They compared this hindcast to the acquired peak water levels, and found an average error of -0.18 m (-0.6 ft), indicating that ADCIRC slightly underpredicted the storm water level using this drag law. If a drag cutoff were applied, underestimates in peak surges would be even greater.
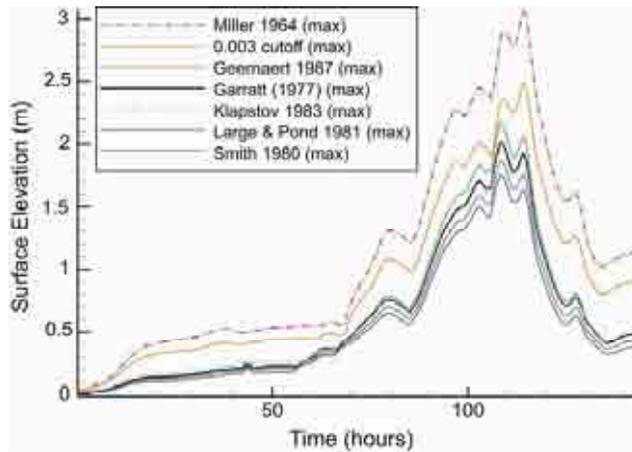
FIG. 10. Peak storm surge generated (ADCIRC) for Hurricane Georges (1998) using the maximum value of the drag coefficient formulations. Adapted from Weaver (2004).

5.2   Hurricane exposure category in ASCE 7-05

The ASCE Wind Load Standard (ASCE 7-05) provides specific design requirements for structures located in hurricane prone regions. For the U.S. this region is defined as areas vulnerable to hurricanes along the Atlantic Ocean and the Gulf of Mexico coasts where the basic wind speeds exceed 40 m/s. Of particular importance is the roughness length (used in determining the logarithmic mean wind profile, Eq. 2), which is prescribed at $z_0 = 0.03$ m (Exposure C, see Table 5) for all hurricane prone regions in the current version (ASCE 7-05). This value was changed from $z_0 = 0.003$ m (Exposure D) in the previous version (ASCE 7-98) based on the work of Vickery and Skerlj (2000). They provided qualitative and quantitative evidence to recommend that Exposure C generates a more appropriate profile along the hurricane coastline. Quantitatively, this recommendation was made without providing a comprehensive set of wind and wave data obtained in the near-shore region in extreme conditions. Their method used to compute C_D is also suspect and does not use direct methods. Neglecting the effects of wave age, Vickery and Skerlj (2000) suggest that z_0 ranges from 0.01 m to 0.025 m for wind speeds of 41–55 m/s. Qualitatively, they argued that hurricane-generated waves act as young waves – a result of fetch-limited conditions. Due to wave interaction with the sea bed causing a reduction in wave celerity, hurricane waves act younger as they approach the coastline. The sea bed also causes the waves to become steeper and change direction due to wave shoaling and refraction. All of the above processes (younger and steeper waves that may become increasingly misaligned with the wind) essentially act to increase the aerodynamic roughness of the sea surface. Contrary to this argument and the overall findings of Vickery and Skerlj (2000), the upcoming

version ASCE 7-10 will most likely defer back to Exposure D in the hurricane prone region (D. A. Smith personal communication). This is due, in part, to a lack of extreme data in the near-shore region.

TABLE 5. Typical roughness lengths z_o and surface drag coefficients C_D for various terrain types. From Holmes (2001).

Terrain Type	ASCE 7-05 Category	z_o (m)	C_D
Very flat terrain	D	0.001–0.005	0.002–0.003
Open terrain	C	0.01–0.05	0.003–0.006
Suburban terrain	B	0.1–0.5	0.0075–0.02

6. ACKNOWLEDGEMENTS

BIBLIOGRAPHY

American Meteorological Society, 1973: Policy statement on hurricanes by the American Meteorological Society. *Bull. Amer. Meteor. Soc.*, **54**, 46–47.

Amorocho, J. and J. J. DeVries, 1980: A new evaluation of the wind stress coefficient over water surfaces. *J. Geophys. Res.*, **85**, 433–442.

Anctil, F. and M. A. Donelan, 1996: Air-water momentum flux observations over shoaling waves. *J. Phys. Oceanogr.*, **26**, 1344–1353.

ASCE, 1999: Wind tunnel studies of buildings and structures: ASCE manuals and reports on engineering practice no 67. Technical report, American Society of Civil Engineers, Reston, Virginia.

ASCE, 1998: Minimum design loads for buildings and other structures, *SEI/ASCE 7-98*, Reston, VA.

—2005: Minimum design loads for buildings and other structures, *SEI/ASCE 7-05*, Reston, VA.

Atakturk, S. S. and B. B. Katsaros, 1999: Wind stress and surface waves observed on Lake Washington. *J. Phys. Oceanogr.*, **29**, 633–650.

Banner, M. L., 1990: The influence of wave breaking on the surface pressure distribution in wind-wave interactions. *J. Fluid Mech.*, **211**, 463–495.

Banner, M. L. and W. K. Melville, 1976: On the separation of air flow over water waves. *J. Fluid Mech.*, **77**, 825–842.

Barthelmie, R., J. Palutikof, and T. Davies, 1993: Estimation of sector roughness lengths and the effect on prediction of the vertical wind speed profile. *Bound.-Layer Meteor.*, **66**, 19–47.

Beebe, P., 1972: *Turbulent flow over a wavy boundary*. Ph.D. thesis, Colorado State University, Fort Collins.

Belcher, S. E. and J. C. R. Hunt, 1998: Turbulent flow over hills and waves. *Annu. Rev. Fluid Mech.*, **30**, 507–538.

Beljaars, A. C. M., 1987: The measurement of gusts at routine wind stations – a review. Technical report, Scientific Report WR87-11, KNMI, de Bilt, Netherlands.

Berg, R., 2009: Tropical cyclone report: Hurricane Ike: 1-14 September 2008. National Hurricane Center.

Black, P. G., E. A. D'Asaro, W. M. Drennan, J. R. French, P. P. Niiler, T. B. Sanford, E. J. Terrill, E. J. Walsh, and J. A. Zhang, 2007: Air-sea exchange in hurricanes: Synthesis of observations from the coupled boundary layer air-sea transfer experiment. *Bull. Amer. Meteor. Soc.*, **88**, 357–384.

Blackadar, A. K. and H. Tennekes, 1968: Asymptotic similarity in neutral, barotropic, atmospheric boundary layers. *J. Atmos. Sci.*, **25**, 1015–1020.

Bourassa, M. A., 2006: Satellite-based observations of surface turbulent stress during severe weather. A*tmosphere -Ocean*, **2**, 35–52.

Buckles, J. J., T. J. Hanratty, and R. J. Adrian, 1984: Turbulent flow over large-amplitude wavy surfaces. *J. Fluid Mech.*, **140**, 27–44.

Bye, J. A. T. and A. D. Jenkins, 2006: Drag coefficient reduction at very high wind speeds. *J. Geophys. Res.*, **111**, C03024.

Charnock, H., 1955: Wind stress on a water surface. *Quart. J. Roy. Meteor. Soc.*, **81**, 639–640.

Chen, D., 2007: *Effects of moving waves on wind profile and wind stress - A wind tunnel study*. Ph.D. Dissertation, Texas Tech University, Lubbock.

Chen, S. S., J. F. Price, W. Zhao, M. A. Donelan, and E. J. Walsh, 2006: The CBLAST Hurricane Program and the next-generation fully coupled atmosphere-wave-ocean models for hurricane research and prediction. *Bull. Amer. Meteor. Soc*, **87**, in press.

Counihan, J., 1974: Flow over concatenated sinusoid hills. Technical Report RD/L/N57/74, Central Elec. Res. Lab., England.

Csanady, G. T., 1985: Air-sea momentum transfer by means of short-crested wavelets. *J. Phys. Oceanogr.*, **15**, 1486–1501.

— 2001: *Air-Sea Interaction: Laws and Mechanisms*. Cambridge University Press, New York, NY, 248 pp.

— 1970: Relative validity of water wave theories. *J. Waterways Harbors Div., ASCE*, **96**, 105–119.

Dean, R. G. and R. A. Dalrymple, 1991: *Water wave mechanics for engineers and scientists*, volume 2. World Scientific Press, Toh Tuck Link, Singapore.

Deardorff, J.W., 1967: Aerodynamic theory of wave growth with constant wave steepness. *J. Oceanographical Soc. Japan*, **41**, 453–480.

— 1968: Dependence of air-sear transfer coefficients on bulk stability. *J. Geophys. Res.*, **73**, 2549–2557.

Dobson, F. W., 1994: Measuring the relationship between wind stress and sea state in the open ocean in the preence of swell. *Atmos.-Ocean*, **32**, 237–256.

Donelan, M. A., 1982: The dependence of the aerodynamic drag coefficient on wave parameters. *First Int. Conf. on Meteorology and Air–Sea Interaction of the Coastal Zone*, Amer. Meteor. Soc., The Hague, Netherlands, 381–387.

—1990: *Air–sea interaction*, volume 9 of *Ocean Engineering Science*.Wiley Interscience, 239-292

Donelan,M. A., F.W. Dobson, S. D. Smith, , and R. J. Anderson, 1993: On the dependence of sea surface roughness on wave development. *J. Phys. Oceanogr.*, **23**, 2143–2149.

Donelan, M. A., B. K. Haus, N. Ruel, W. J. Stianssnie, H. C. Graber, O. B. Brown, and E. S. Saltzman, 2004: On the limiting aerodynamic roughness of the ocean in very strong winds. *Geophys. Res. Lett.*, **31**, L18306.

Drennan, W. M., H. C. Graber, D. Hauser, and C. Quentin, 2003: On the wave age dependence of wind stress over pure wind seas. *J. Geophys. Res.*, **108**, 8062.

Drennan,W.M., K. K. Kahma, and M. A. Donelan, 1999: On momentum flux and velocity spectra over waves. *Bound.-Layer Meteor.*, **92**, 489–515.

Drennan, W. M., P. K. Taylor, and M. J. Yelland, 2005: Parameterizing the sea surface roughness. *J. Phys. Oceanogr.*, **35**, 835–848.

Edson, J. and Coauthors, 1999: Coupled marine boundary layers and air-sea interaction initiative: Combining process studies, simulations, and numerical models. Technical report, Office of Naval Research.

Edson, J. B., C. W. Fairall, P. G. Mestayer, and S. E. Larsen, 1991: A study of the inertial dissipation method for computing air-sea fluxes. *J. Geophys. Res.*, **96**, 10689–10711.

Fairall, C. W., E. F. Bradley, D. P. Rogers, J. B. Edson, and G. S. Young, 1996: Bulk parameterization of air–sea fluxes in TOGA COARE. *J. Geophys. Res.*, **101**, 3747–3767.

Fairall, C. W. and S. E. Larsen, 1986: Inertial-dissipation methods and turbulent fluxes at the air-ocean interface. *Bound.-Layer Meteor.*, **34**, 287–301.

Feddersen, F. and F. Veron, 2005: Wind effects on shoaling wave shape. *J. Phys. Oceanogr.*, **35**, 1223–1228.

Frederickson, P. A., K. L. Davidson, and J. B. Edson, 1997: A study of wind stress determination methods from a ship and an offshore tower. *J. Atmos. Oceanic Technol.*, **14**, 822–834.

Galvin, C. J., 1968: Breaker type classification on three laboratory beaches. *J. Geophys. Res.*, **73**, 3651–3659.

Garratt, J. R., 1977: Review of drag coefficients over oceans and continents. *Mon. Wea. Rev.*, **105**, 915–929.

— 1992: *The Atmospheric Boundary Layer*. Cambridge University Press, New York, 316 pp.

Garrison, T. S., 2007: *Oceanography: An Invitation to Marine Science*. Brooks/Cole Publishing Co., Pacific Grove, CA, USA.

Geernaert, G. L., 1987: On the importance of the drag coefficient in air–sea interactions. *Dyn. Atmos. Oceans*, **11**, 19–38.

Geernaert, G. L., K. B. Katsaros, and K. Richter, 1986: Variation of the drag coefficient and its dependence on sea state. *J. Geophys. Res.*, **91**, 7667–7679.

Geernaert, G. L., S. E. Larson, and F. Hanson, 1987: Measurements of the wind stress, heat flux and turbulence intensity during storm conditions over the North Sea. *J. Geophys. Res.*, **92**, 127–139.

Geernaert, G. L. and J. A. Smith, 1997: On the fetch dependent drag coefficient over coastal and inland seas. Technical Report 227, National Environmental Research Institute, Roskilde, Denmark.

Gill, A. E., 1982: *Atmosphere-ocean dynamics*, Academic Press, San Diego, CA, 662 pp.

Gong,W., P. A. Taylor, and A. Dornbrack, 1999: Turbulent boundary-layer flow over fixed aerodynamically rough two-dimensional sinusoid waves. *J. Fluid Mech.*, **312**, 1–37.

Harris, D. L., 1963: Characteristics of the hurricane storm surge. Technical Report 48, U.S. Department of Commerce, Washington, D.C.

Hasselmann, K. and Coauthors, 1973: Measurements of wind-wave growth and swell decay during the Joint North Sea Wave Project (JONSWAP). *J. Phys. Oceanogr.*, **6**, 200– 228.

Hicks, B. B. and A. J. Dryer, 1972: The spectral density technique for the determination of eddy fluxes. *Quart. J. Roy. Meteorol. Soc.*, **98**, 838–844.

Hock, T. F. and J. L. Franklin, 1999: The NCAR GPS dropwindsonde. *J. of Wind Engng. and Ind. Aerodyn.*, **36**, 381–392.

Holland, K. T., B. Raubenheimer, R. T. Guza, and R. A. Holman, 1995: Runup kinematics on a natural beach. *J. Geophys. Res.*, **100**, 4985–4993.

Holman, R. A. and A. H. Sallenger, 1985: Setup and swash on a natural beach. *J. Geophys.Res.*, **90**, 945–953.

Holmes, J. D., 2001: *Wind Loading of Structures*. Spon Press, London, 194 pp.

Holthuijsen, L. H., 2007: *Waves in Oceanic and Coastal Waters*. Cambridge University Press, 404 pp.

Hsu, H. T. and J. F. Kennedy, 1971: Turbulent flow in wavy pipes. *J. Fluid Mech.*, **47**, 481–501.

Hsu, S. A., 1974: A dynamic roughness equation and its application to wind stress determination at the air-sea interface. *J. Phys. Oceanogr.*, **4**, 116–120.

IPET, 2006a: Performance evaluation of the New Orleans and Southeast Louisiana Hurricane Protection System. Draft final report of the Interagency Performance Evaluation Task Force Vol. I - VIII. Technical report, U.S. Army Corps of Engineers.

— 2006b: Performance evaluation of the New Orleans and Southeast Louisiana Hurricane Protection System. Draft final report of the Interagency Performance Evaluation Task Force. Vol. IV - The storm - Technical appendix. Technical report, U.S. Army Corps of Engineers.

Jackson, P. S., 1981: On the displacement height in the logarithmic velocity profile. *J. Fluid Mech.*, **111**, 15–25.

Janssen, P. A. E. M. 1991. Quasi-linear theory of wind wave generation applied to wave forecasting. J. Phys. Oceanography, 21: 1631– 1642.

Janssen, P. A. E. M. 1992. Experimental evidence of the effect of surface waves on the airflow. J. Phys. Oceanography, 22: 1600–1604.

Janssen, J. A. M. 1997. Does wind stress depend on sea state or not? A statistical error analysis of HEXMAX data. Bound.- Layer Meteor., 83: 479–503.

Jarosz, E., D. A. Mitchell, D. W. Wang, and W. J. Teague, 2007: Bottom-up determination of air-sea momentum exchange under a major tropical cyclone. *Science*, **315**, 1707 – 1709.

Johnson, H. K., J. Højstrup, H. J. Vested, and S. E. Larsen, 1998: Dependence of sea surface roughness on wind waves. *J. Phys. Oceanogr.*, **28**, 1702–1716.

Jones, S. F. and Y. Toba, 2001: *Wind Stress Over the Ocean*. Cambridge University Press, New York, NY, 1 edition, 307

Kaimal, J. C. and J. J. Finnigan, 1994: *Atmospheric Boundary Layer Flows: Their Structureand Measurement*. Oxford University Press, 289 pp.

Kawamura, H. and Y. Toba, 1988: Ordered motion in the turbulent boundary layer over wind waves. *J. Fluid Mech.*, **197**, 105–138.

Kendall, J. M., 1970: The turbulent boundary layer over a wall with progressive surface waves. *J. Fluid Mech.*, **41**, 259–281.

Kitaigorodskii, S. A., 1973: *The physics of air-sea interaction*. Israel Program for Scientific Translations, 237 pp.

Kitaigorodskii, S. A. and Y. A. Volkov, 1965: On the roughness parameter of the sea surface and the calculation of momentum flux in the near-water layer of the atmosphere. *Izv. Atmos. Oceanic Phys.*, **1**, 973–988.

Knauss, J. A., 1996: *Introduction to physical oceanography*. Prentice Hall, Inc., Upper Saddle River, NJ, 2 edition.

Kraus, E. B. and J. A. Businger, 1994: *Atmosphere-Ocean Interaction*. Oxford University Press, New York, 2nd edition, 384 pp.

Kudryavtsev, V. N., 2006: On the effect of sea drops on the atmospheric boundary layer. *J. Geophys. Res.*, **111**, C07020.

Kudryavtsev, V. N. and V. K. Makin, 2001: The impact of air-flow separation on the drag of the sea surface. *Bound.-Layer Meteor.*, **98**, 155–171.

— 2007: Aerodynamic roughness of the sea surface at high winds. *Bound.-Layer Meteor.*, **125**, 289–303.

Kuzan, J. D., T. J. Hanratty, and R. J. Adrian, 1989: Turbulent flows with incipient separation over solid waves. *Exps. Fluids*, **7**, 88–98.

Large, W. G. and S. Pond, 1981: Open ocean momentum flux measurements in moderate to strong winds. *J. Phys. Oceanogr.*, **11**, 324–336.

Lentz, S., R. T. Guza, S. Elgarc, F. Feddersen, and T. H. C. Herbers, 1999: Momentum balances on the North Carolina inner shelf. *J. Geophys. Res.*, **104**, 18205–18226.

Luettich, R. A., J. J. Westerink, and N. W. Scheffner, 1992: ADCIRC: An advanced three dimensional circulation model for shelves, coasts, and estuaries, Report I, Theory and methodology of ADCIRC-2DDI and ADCIRC-3DL. Technical Report DRP-92-6, Department of the Army, US Army Corps of Engineers, Waterways Experiment Station, Vicksburg, MS.

Mitsuyasu, H. and K. Rikiishi, 1978: The growth of duration-limited wind waves. *J. Fluid Mech.*, **85**, 705–730.

Morris, H. M., 1955: Flow in rough conduits. *ASCE Transactions*, **120**, 373–410.

Munk, W. H. and M. A. Traylor, 1947: Refraction of ocean waves: A process linking underwater topography to beach erosion. *J. of Geology*, **55**, 1–26.

Ocampo-Torres, F. J., M. A. Donelan, N. Merzi, and F. Jia, 1994: Laboratory measurements of mass transfer of carbon dioxide and water vapour for smooth and rough flow conditions. *Tellus*, **46**, 16–32.

Oke, T. R., 1988: Street design and urban canopy layer climate. *Energy and buildings*, **11**, 103–113.

Oost, W. A., G. J. Komen, C. M. J. Jacobs, and C. V. Oort, 2002: New evidence for a relation between wind stress and wave age from measurements during ASGAMAGE. *Bound.-Layer Meteor.*, **103**, 409–438.

Pielke, R. A., J. Gratz, C. W. Landsea, D. Collins, M. A. Saunders, and R. Musulin, 2008: Normalized hurricane damage in the United States: 1900–2005. *Natural Hazards Review*, **9**, 29–42.

Pierson, W. J. and L. Moskowitz, 1964: A proposed spectral form for fully-developed wind seas based on the similarity law of S. A. Kitaigorodoskii. *J. Geophys. Res.*, **69**, 5181–5203.

Pond, S., W. G. Large, M. Miyake, and R. W. Burling, 1979: A gill twin propeller-vane anemometer for flux measurements during moderate and strong winds. *Bound.-Layer Meteor.*, **16**, 351–364.

Powell, M. D., 2008: High wind drag coefficient and sea surface roughness in shallow water. Final Report to the Joint Hurricane Testbed (*under review*).

Powell, M. D., P. J. Vickery, and T. A. Reinhold, 2003: Reduced drag coefficient for high wind speeds in tropical cyclones. *Nature*, **422**, 279–283.

Reeve, D., A. Chadwick, and C. Fleming, 2004: *Coastal Engineering: Process, Theory and Design Practice*. E&FN Spon, Routledge, UK, 1 edition, 392 pp.

Reniers, A. J. H. M., E. B. Thornton, T. P. Stanton, and J. A. Roelvink, 2004: Vertical flow structure during Sandy Duck: observations and modeling. *Coastal Engineering*, **51**, 237–260.

Resio, D., S. Bratos, and E. Thompson, 2002: Meteorology and wave climate. *Coasta Engineering Manual, Part II, Hydrodynamics, Chapter II–2, Engineer Manual 1110-2-1100*, L. Vincent and Z. Demirbilek, eds., U.S. Army Corps of Engineers, Washington, DC, Washington, DC.

Reul, N., 1998: *Etude expérimentale de la structure de l'écoulement d'air au-dessus de vagues courtesde´ferlantes*. Ph.D. thesis, Univ. de la Mediterranee, Marseille, France.

Reul, N., H. Branger, and J. P. Giovanangeli, 1999: Air flow separation over unsteady breaking waves. *Physics of Fluids*, **11**, 1959–1961.

Schlichting, H. and K. Gersten, 2000: *Boundary-Layer Theory*. Springer-Verlag Berlin Heidelberg, New York, 8 edition, 801 pp.

Simiu, E. and R. H. Scanlan, 1986: *Wind Effects On Structures*. John Wiley & Sons, New York, NY, 2nd edition, 589 pp.

Sjoblom, A. and A. Smedman, 2002: The turbulent kinetic energy budget in the marine atmospheric surface layer. *J. Geophys. Res.*, **107**, 3142, doi:10.1029/2001JC001016.

— 2003: Vertical structure in the marine atmospheric boundary layer and its implication for the inertial dissipation method. *Bound.-Layer Meteor.*, **109**, 1–25.

Smith, S. D., 1980: Wind stress and heat flux over the ocean in gale force winds. *J. Phys. Oceanogr.*, **10**, 709–726.

— 1992: Sea surface wind stress and drag coefficients: The HEXOS results. *Bound.-Layer Meteor.*, **60**, 109–142.

Smith, S. D. and E. G. Banke, 1975: Variation of the sea surface drag coefficient with wind speed. *Quart. J. Roy. Meteor. Soc.*, **101**, 665–673.

Stanton, T. E., D. Marshall, and R. Houghton, 1932: Growth of waves on water due to the action of the wind. *Proc. Roy. Soc.*, **137A**, 283–293.

Stuckley, A. B., 2003: *Shelter effects on housing in neighborhoods*. Master's thesis, Texas Tech University, Lubbock.

Stull, R. B., 1988: *An Introduction to Boundary Layer Meteorology*, volume 13. Kluwer Academic Publishers, Dordrecht/Boston/London, 680 pp.

Tang, Y. M., P. Holloway, and R. Grimshaw, 1997: A numerical study of the storm surge generated by tropical cyclone Jane. *J. Phys. Oceanogr.*, **27**, 963–976.

Taylor, P. K. and M. J. Yelland, 2001: The dependence of sea surface roughness on the height and steepness of the waves. *J. Phys. Oceanogr.*, **31**, 572–590.

Tennekes, H., 1973: The logarithmic wind profile. *J. Atmos. Sci.*, **30**, 234–238.

Tennekes, H. and J. L. Lumley, 1972: *A first course in turbulence*. The MIT Press, 300 pp.

Thornton, E. B. and R. T. Guza, 1982: Energy saturation and phase speeds measured on a natural beach. *J. Geophys. Res.*, **8**, 9499–9508.

Toba, Y., N. Lida, H. Kawamura, N. Ebuchi, and I. S. F. Jones, 1990: Wave dependence on sea-surface wind stress. *J. Phys. Oceanogr.*, **20**, 705–721.

Tseng, R.-S., Y. H. L. Hsu, and J. Wu, 1992: Methods of measuring wind stress over a water surface — Discussions of displacement height and von Karman constant. *Bound.-Layer Meteor.*, **58**, 51–68.

Vega, R., 2008: *Wind directionality: A reliability-based approach*. Ph.D. thesis, Texas Tech University, Lubbock, Texas.

Vickers, D. and L. Mahrt, 1997: Fetch limited drag coefficients. *Bound.-Layer Meteor.*, **85**, 53–79.

Vickery, P. J. and P. F. Skerlj, 2000: Elimination of exposure d along the hurricane coastline in ASCE 7. *Journal of Structural Engineering*, **126**, 545–549.

Volkov, Y. A., 1970: Turbulent flux of momentum and heat in the atmospheric surface layer over a disturbed sea-surface. *Izv. Acad. Sci, USSR Atmos. Oceanic Phys., (Engl. Transl.)*, **6**, 770–774.

Weaver, R.J., 2004: *Effect of wave forces on storm surge*. Master's thesis, University of Florida, Gainesville, Florida.

Weber, R. O., 1999: Remarks on the definition and estimation of friction velocity. *Bound. Layer Meteor.*, **93**, 197–209.

Westerink, J. J. and Coauthors, 2004: A new generation hurricane storm surge model for Southern Louisiana, in review. *Bull. Amer. Meteor. Soc.*.

Wieringa, J., 1993: Representative roughness parameters for homogeneous terrain. *Bound.-Layer Meteor.*, **63**, 323–363.

— 1996: Does representative wind information exist? *J. Wind Engineering and Industrial Aerodynamics*, **65**, 1–12.

Wright, C., E. Walsh, D. Vandemark, W. Krabill, A. Garcia, S. Houston, M. Powell, P. Black, and F. Marks, 2001: Hurricane directional wave spectrum spatial variation in the open ocean. *J. Phys. Oceanogr.*, **31**, 2472–2488.

Wu, J., 1980: Wind-stress coefficients over sea surface near neutral conditions–A revisit. *J. Phys. Oceanogr.*, **10**, 727–740.

Yelland, M. J., B. I. Moat, P. Taylor, R. W. Pascal, J. Hutchings, and C. V. Cornell, 1998: Wind stress measurements from the open ocean corrected for airflow distortion by the ship. *J. Phys. Oceanogr.*, **28**, 1511–1526.

Yelland, M. J. and P. K. Taylor, 1996: Wind stress measurements from the open ocean. *J. Phys. Oceanogr.*, **26**, 541–558.

Zachry, B.C., 2009: *Wind-Wave Interaction in the Near-shore Environment*, Ph.D. Dissertation, Texas Tech University, Lubbock.

Zilitinkevich, S. S., A. A. Grachev, and C. W. Fairall., 2001: Scaling reasoning and field data on the sea surface roughness lengths for scalars. *Journal of Atmospheric Sciences*, **58**, 320–325.

Zilker, D. P., G. Cook, and T. J. Hanratty, 1977: Influence of the amplitude of a solid wavy wall on a turbulent flow. Part 2. Non-separated flows. *J. Fluid Mech.*, **82**, 29–51.

Zilker, D. P. and T. J. Hanratty, 1979: Influence of the amplitude of a solid wavy wall on a turbulent flow. Part 2. Separated flows. *J. Fluid Mech.*, **90**, 257–271.

BLUFF BODY AERODYNAMICS

Investigation Into Numerical Modeling Of The Drag Crisis For Circular Cylinders

N. Botterill, H. P. Morvan and J. S. Owen

University of Nottingham, Faculty of Engineering, Coates Building, University Park, Nottingham NG7 2RD, United Kingdom

neil.botterill@nottingham.ac.uk , herve.morvan@nottingham.ac.uk, john.owen@nottingham.ac.uk

INTRODUCTION

Circular sections are used in a wide range of engineering applications in which they are subject to flow induced forces, from wind loads on lighting columns, chimneys and electrical and structural cables to tidal and wave loads on offshore risers for example. As well as the classical vortex shedding phenomenon, circular sections are prone to several aero-elastic instabilities as seen in the galloping of bridge cables and the drag instability of tall lighting columns. These instabilities often occur at Reynolds numbers close to the drag crisis and the changes in flow regime associated with this transition may play an important part in driving the observed large amplitude oscillations.

The recent rapid advances in Computational Fluid Dynamics (CFD) have enabled increasingly complex fluid flow phenomena to be simulated. These simulations can now be coupled to models of structural response to predict fluid structure interactions and model various aeroelastic instabilities. The authors are currently applying these techniques to the flow around circular sections with the aim of simulating the instabilities described above. However, as noted, the aero-elastic instabilities of a circular section often occur at Reynolds numbers close to the drag crisis and it is therefore essential to accurately capture this event first. This is the aim of the work reported in the present paper. The authors then plan to study the consequences of the drag crisis on the cylinder's response.

Contact person: J S. Owen, University of Nottingham, Faculty of Engineering, Coates Building, University Park, Nottingham NG7 2RD, United Kingdom.
Email john.owen@nottingham.ac.uk

Given that the complexity of the flow at high Reynolds numbers makes direct numerical simulation technically impossible, a key aspect in the simulation of flow around a bluff body is the appropriate choice of turbulence approach. Traditional Reynolds Averaged Navier-Stokes (RANS) models are unsuitable as unsteadiness forms an important feature of the flow in these problems. Although there are some notionally unsteady RANS (URANS) models available, these are not appropriate because it is still only the mean effects of turbulence, albeit in a transient framework, that are modeled, not the turbulence unsteadiness in the flow. Large Eddy Simulation (LES) offers an appropriate intermediate approach by allowing the direct simulation of the large scale unsteadiness, containing most of the turbulence energy, whilst retaining a closure model to represent the effects of smaller scale turbulence (Sub-Grid Scale model or SGS). However, the choice of this SGS model is critical; the capture of the physics in the near wall region is particularly central to the success of the calculation. In this paper the authors consider the use of two different SGS models in the LES of the flow around a circular cylinder to make this point.

METHODOLOGY

The commercial CFD solver used for all the numerical simulations presented here is ANSYS CFX. The investigations will focus on the use of a LES formulation based on two types of SGS model: (1) the well established Smagorinsky (1963) model, based on an algebraic turbulence viscosity dependent on a constant parameter C_S which tends to be problem specific, needs to be damped at the wall and misrepresents the turbulent eddy viscosity at the wall; (2) the Dynamic model (Germano et al. (1991); Lilly (1992)) for which the parameter C_S is evaluated locally based on the comparison of the sub-grid tensor values computed using two different filters, and which offers enhanced performance in the wall region in particular. A detailed description of each of these turbulence models will be given in the full length paper, however a key feature of the Dynamic approach relevant to the present work is that it does not require any artificial wall damping and is able to capture the transition process (Wagner et al. (2007)). This is important as the prediction of the drag crisis in the cylinder case is dependent on the position of the separation point, and its displacement as a function of the Reynolds number, Re. For each of the turbulence SGS models, simulations were performed for a range of Reynolds numbers within which the drag crisis is expected to occur. For each simulation, time histories of the drag force and lift force experienced by the cylinder were recorded. Mean and RMS values of lift and drag together with estimates of the Strouhal number were used to compare the two SGS models, and evaluate their performance against published experimental data. The domain dimensions in terms of cylinder diameter d are: 18d in the streamwise direction, 8d in the transverse direction, and 2.5d in the spanwise direction. The cylinder axis is positioned 4d away from the inlet.

RESULTS AND DISCUSSION

Figure 1 contains plots of drag coefficient produced by both the LES Smagorinsky and LES Dynamic turbulence models for Reynolds numbers in the range 40,000 to 400,000. It can be seen that the Smagorinsky model does not predict a drop in drag consistent with the drag crisis seen in the published data, Figure 2, whereas the Dynamic model predicts a drop in drag from 1.1 to 0.5 in a Reynolds number range of 60,000 to 100,000. The latter result is encouraging; however the drop predicted by the Dynamic model approach occurs for a lower Reynolds number range and the drag crisis line appears to be shifted to the left. Its slope is also less steep that the curve gradient visible in Figure 2 and the predicted drag coefficient does not drop as low. However, the ESDU data (ESDU 2008) illustrate that the drag crisis is sensitive to inlet turbulence and surface roughness around the cylinder, and there are experimental data that indicate that the drag crisis can occur at a lower Reynolds number due to blockage effects (Richter and Naudascher (1976)).
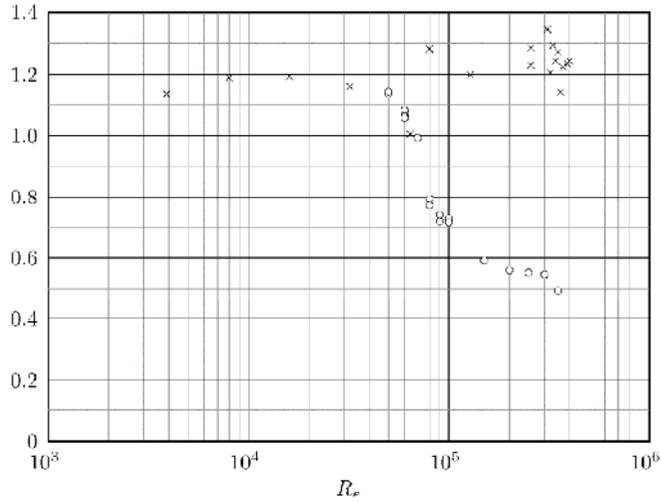
Figure 1: Average drag data (x Smagorinsky; o Dynamic)
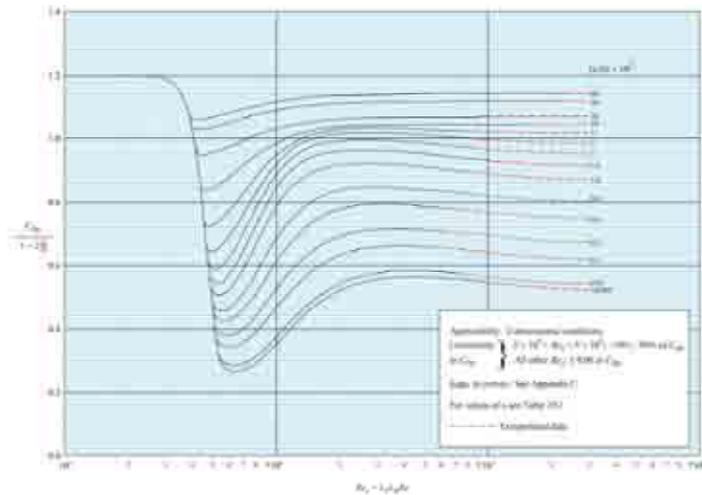
Figure 2: ESDU plot of mean drag through the drag crisis

Corrections for the inlet turbulence are subsequently implemented and shown to benefit the simulations; these will be presented in the full paper. Other experimental literature discusses the effect of varying the spanwise extent of the model (Norberg (2003)). Thus the importance of a correct choice of domain size is highlighted.

The reason for the improved performance of the dynamic model over the Smagorinsky SGS model can be seen by considering the flow fields in the near wake region, Figures 3a and 3b. Zdravkovich (2007) describes the process of the drag crisis in terms of the point of transition to turbulence found in the cylinder wake. The transition to turbulence occurs closer to the rearward face of the cylinder as the Reynolds number increases. At a Reynolds number just below that for the drag crisis two transition points can be observed, one in each shear layer just beyond the point of separation on either side of the cylinder. An increase in Reynolds number causes these points to move causing one or both

separation points to jump from a position at roughly 90˚ to a position 120˚ on the perimeter measured from the upstream stagnation point. This results in a drop in drag caused by the narrowing of the wake behind the cylinder. This happens, to an extent, with the Dynamic model, Figure 3b, but it does not materialise with the Smagorinsky model, Figure 3a, with which the separation point does not appear
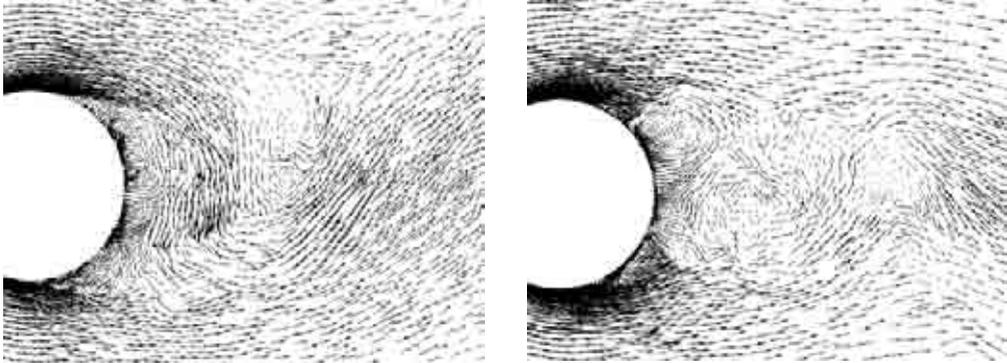
to move as a function of Re.

(a) Smagorinsky   (b) Dynamic

Figure 3: Typical velocity flow field vector plot at the rearward side of the cylinder

REFERENCES

Engineering Sciences Data Unit: ESDU 80025: Mean forces, pressures and flow field velocities for circular cylindrical structures.

Germano M., U. Piomelli, P. Moin, W.H. Cabot (1991). A dynamic subgrid-scale eddy viscosity model, Physics of Fluids A: Fluid Dynamics, 3, 1760–1765.

Lilly D.K. (1992) A proposed modification of the Germano subgrid-scale closure method, Physics of Fluids A: Fluid Dynamics, 4, 633–635.

Norberg C. (2003). Fluctuating lift on a circular cylinder: review and new measurements, Journal of Fluids and Structures 17, 57–96

Richter A., Naudascher E. (1976). Fluctuating forces on a rigid circular cylinder in confined flow, Journal of Fluid Mechanics, 78, 561–576.

Smagorinsky J. (1963). General circulation experiments with the primitive equations, Monthly Weather Review 91(3), 99–164.

Wagner C.A., Hüttl T., Sagaut P. (2007). Large Eddy Simulation for Acoustics, Cambridge University Press

Zdravkovich M. M. (2007). Flow Around Circular Cylinders Vol. 1, Oxford Science Publications

Reynolds number dependence of the velocity shear effects on flow around a circular cylinder

Shuyang Cao[1], Yukio Tamura[2]

[1] cao@arch.t-kougei.ac.jp; 1583 Iiyama, Atsugi, Kanagawa 243-0297, Japan;
Wind Engineering Research Center, Tokyo Polytechnic University

[2] yukio@arch.t-kougei.ac.jp; 1583 Iiyama, Atsugi, Kanagawa 243-0297, Japan;
Wind Engineering Research Center, Tokyo Polytechnic University

ABSTRACT

Vortex shedding behind two-dimensional circular cylinders has been one of the most studied subjects in fluid mechanics in the past several decades because of its practical and theoretical importance. Although quite comprehensive understanding of the vortex dynamics in a cylinder's wake have been achieved, as reflected in the reviews by Williamson (1996) and many other researchers, the simplicity of the geometry and the abundance of interesting flow features continue to make this flow the subject of many current studies. The majority of past studies on unsteady flow past a circular cylinder were conducted under symmetric approaching flow conditions in which vortices are equivalently shed from each side of the body. However, in many practical applications, a cylindrical structural is immersed in a flow with some asymmetries. For example, a bridge deck is located in an atmospheric boundary layer with a velocity shear profile. Since strong local shear flows can be produced by special metrological phenomena, terrain effect and so on, it is important to understand the features of vortex shedding behavior and aerodynamic forces on a circular cylinder in a shear flow. Meanwhile, how the velocity shear, a simple and typical case of a non-uniform approach flow, influences vortex shedding from a circular cylinder and wake dynamics is also a very interesting fundamental problem. With increase in velocity shear, the velocity difference between the high- and low-velocity sides of a cylinder increases. The strength and depth of the boundary layer on the two sides, and then the vorticity generated in the separated shear layers is different on the two sides. This possibly creates differences in vortex shedding behavior or shear layer instability on the two sides of a cylinder. This study was motivated by the need to understand these behaviors both theoretically and practically. In this paper, the extent of velocity shear is expressed by the shear parameter $\beta = G(D/U_c) = (dU/dy)(D/U_c)$, where U_c is the mean velocity at the center plane, D is the diameter of the circular cylinder and G is the velocity gradient.

Several experimental studies have been carried out on the shear effects on flow around a circular cylinder. However, there has been significant disagreement among the results, even on basic issues

---

Contact person: Shuyang CAO; Tel/Fax: 81-46-242-9656
E-mail: cao@arch.t-kougei.ac.jp

associated with vortex shedding behavior. Kiya et al. (1980) investigated vortex shedding from a circular cylinder in moderate Reynolds number shear flows (Re=35-1500) in a water tank. They found that the critical Reynolds number for vortex shedding to take place is higher in shear flow than in uniform flow. They also found that the Strouhal number decreases slightly with shear parameter when the shear parameter is small, and then clearly increases with shear parameter at large shear parameter. Kwon et al. (1992) reported similar results for $0.05 < \beta < 0.25$ at Re =35-1600. Adachi and Kato (1975) investigated the flow around a circular cylinder within a small variation in shear parameter ($0 < \beta < 0.04$) at Re=2.67×10^3-1.07×10^4. They reported that both mean drag and lift force increase with shear parameter, and lift force acts from the high-velocity side to the low-velocity side. Hayashi and Yoshino (1990) investigated the aerodynamic force in one kind of shear flow (β =0.15) at Re=6×10^4 and found that drag decreases in shear flow and lift force acts from the high-velocity side to the low-velocity side. The study of Sumner and Akosile (2003) at Re=4.0×10^4-9.0×10^4 with a low shear parameter range of β =0.02-0.07 showed conclusions with regard to drag and lift forces similar to those of Hayashi and Yoshino (1990), but Strouhal number is shown to be almost unchanged with shear parameter. There have been fewer numerical studies and they have been restricted to two-dimensional calculations. However, their results have also been inconsistent. Tamura et al. (1980) performed a numerical study on shear flow past a circular cylinder at Re=40 and 80 for $0 < \beta < 0.20$. Lei et al. (2000) carried out two-dimensional simulation of flow at Re=80-1000 for $0 < \beta < 0.25$ with an upwind scheme. Both studies indicated that the front stagnation point moved to the high-velocity side in the shear flow. However, they reported different results in regard to the direction of lift force. Lei et al. (2000) found that the lift was toward the low-velocity side, while Tamura et al. (1980) reported that it was in the opposite direction. The disagreements in both experimental and numerical studies also motivated the present study.

Our experimental study (Cao et al., 2007) at Re=3.4×10^4 within a wider shear range ($0 < \beta < 0.27$) showed that the flow and aerodynamic force around a circular cylinder was subject to the combined effects of the movement of stagnation point and velocity shear, which acts in the opposite direction to the aerodynamic force. Thus, many factors, including Reynolds number, body shape and geometry, which may influence the individual contributions of the movement of stagnation point and velocity shear to pressure distribution, influence the effects of velocity shear in the oncoming flow, resulting in different conclusions. We infer that this as a possible reason for the inconsistencies of past studies. However, there are still many unknowns and further detailed study is necessary on this flow configuration.

In this study, we systematically performed three-dimensional Direct Numerical Simulation (DNS) and Large Eddy Simulation (LES) calculations to investigate the effects of velocity shear on vortex shedding from a circular cylinder and wake dynamics. From detailed flow information obtained by numerical simulation, we expect to achieve a comprehensive understanding and arrive at a physical explanation of the mechanism of shear effects. In the numerical simulation, a co-locate mesh was employed in the generalized coordinate system for finite difference approximation of the incompressible Navier-Stokes equations. The simulation was carried out for Re=60, 80, 150, 200, 500 and 1000 to investigate the Reynolds number dependence, which was one possible reason for the inconsistencies in past studies. DNS was performed for Re=60, 80, 150 and 200, while LES was carried out with a dynamic Smagorinsky subgrid model for Re=500 and 1000. A central difference scheme was applied in the simulation in order to avoid unnecessary numerical dissipation accompanying the upwind scheme. More accurate yet stable simulation can be expected from the central difference scheme as shown by Kravchenko and Moin (2000) in their numerical studies of flow over a circular cylinder at Re=3900. However, the Reynolds number has generally been limited to 103 for the central difference scheme till now. Therefore, the Reynolds numbers considered in the present study are up to Re=1000 in order to achieve more precise and stable predictions of shear effects. In this paper, the governing equations in the generalized coordinate system and corresponding numerical procedure are described first, followed by detailed validations. Then, the shear effects on Strouhal number, aerodynamic force, and the corresponding physical mechanism are presented, together with illustrations of the dynamic wake structure.

The numerical model for flow around a circular cylinder is formulated using the generalized curvilinear coordinate system. The governing equations are the continuity and Navier-Stokes equations. The dynamic procedure based on the Smagorinsky model proposed by Germano et al. (1991) is used to determine the unknown model coefficient. The ratio of test filter scale to grid filter scale is the only parameter in the procedure and is chosen to be 2.0, as suggested by Germano et al. (1991). Averaging and test filter operation are performed only in the homogeneous spanwise direction, in conjunction with Lilly's least-squares technique (1992). In order to avoid numerical instability, the negative value of SGS eddy viscosity is truncated to zero. Large Eddy Simulation using the dynamic Smagorinsky model has been widely utilized as a relatively affordable and easy-to-use approach to simulate separated flow and other complicated flow (Kravchenko and Moin 2000).

We utilized the non-staggered-grid method developed by Zang et al. (1994) for solving three-dimensional, time-dependent incompressible Navier-Stokes equations for unsteady calculations in curvilinear coordinates. In the computational space, the Cartesian velocity components and the pressure are defined at the center of a control volume, while the volume fluxes are defined at the mid-point of their corresponding cell surface. Fourth-order central difference and fourth-order interpolation are used for the convection terms while a second-order central differencing scheme is used for the diffusion terms. The continuity equation is discretized at the point where pressure is defined using contravariant velocity components. For time marching, the explicit Adams-Bashforth differencing scheme is applied for the convention term, and the semi-explicit Crank-Nicolson formulation is applied for the diffusion term. The numerical procedure is based on the fractional step method.

Problem formation, numerical discretization and algorithm will be described in the full paper. Numerical validation is carried out by comparing the Reynolds number dependence of Strouhal number and drag coefficient of a circular cylinder on Reynolds number range of Re=50-1000 and the change of three-dimensionality of vortex dynamics from parallel laminar shedding to mode A and then mode B in this Reynolds number regime. Variations of pressure distribution around the cylinder, drag and lift force with shear parameter are studied. The roles of movement of stagnation point and separation points in determining the aerodynamic forces are clarified.

The results and conclusions obtained are summarized below:

(1) The Strouhal number is almost unchanged in the shear parameter range of 0-0.30 at Re=60-1000. Three-dimensionality of mode A wake instability is suppressed to two-dimensional parallel vortex shedding at Re=200. The onset of mode A three-dimensionality is delayed by velocity shear. Karmax vortex shedding was not completely suppressed in the investigated range of Reynolds numbers and shear parameters. However, the vortices on the low-velocity side disappear in the far wake in the strong shear parameter condition. Large acceleration occurs on the low-velocity side, which self-adjusts the asymmetry in the oncoming flow in the near wake of the cylinder.

(2) The stagnation point moves to the high-velocity side in shear flows. The movement of the angle of the stagnation point increases with shear parameter. The Reynolds number has little influence in determining the movement of the stagnation point. The separation point moves downstream on the high-velocity side and upstream on the low-velocity side. The movement of the angle of the separation point increases with shear parameter. Reynolds number greatly influences the magnitude of movements of separation points.

(3) Movement of stagnation point and velocity shear influences the pressure distribution around the cylinder simultaneously, but with opposite contribution. In the range of Re=60-1000 and $0<\beta<0.3$, drag force is almost unchanged with increasing shear parameter. Lift force occurs in the shear flow due to the asymmetry of pressure distribution around the cylinder, and acts from the high-velocity side to the low-velocity side. Movement of the stagnation points contributes more to the lift force than the velocity shear.

through the Global COE Program, 2008-2012.

REFERENCES

Adachi T., Kato E., 1975. Study on the flow about a circular cylinder in shear flow. Transactions of the Japan Society for Aeronautical and Space 256, 45-53.

Cao S., Ozono S., Hirano K., Tamura Y., 2007. Vortex shedding and aerodynamic forces on a circular cylinder in linear shear flow at subcritical Reynolds number. Journal of Fluids and Structures 23, 703-714.

Germano M., Piomelli U., Moin P., Cabot W.H., 1991. A dynamic subgrid-scale viscosity model, Physics of Fluids, A Vol.3 No.7, pp.1760-1765.

Hayashi T., Yoshino F., 1990. On the evaluation of the aerodynamic forces acting on a circular cylinder in a uniform shear flow. Transactions of the Japan Society for Mechanical Engineering 56, No.552, 31-36.

Kiya M., Tamura H., Arie M., 1980. Vortex shedding from a circular cylinder in moderate-Reynolds-number shear flow. Journal of Fluid Mechanics 141, 721-735.

Kwon T.S., Sung H.J., Hyun J. M., 1992. Experimental investigation of uniform shear flow past a circular cylinder. ASME Journal of Fluids Engineering 114, 457-460.

Kravchenko A.G and Moin P., 2000. Numerical studies of flow over a circular cylinder at Re=3900, Physics of fluids 12, No.2, 403-417.

Lei, C., Cheng, L., Kavanagh, K., 2000. A finite difference solution of the shear flow over a circular cylinder, Ocean Engineering 27, 271-290.

Lilly D.K., 1992. A proposed modification of the Germano subgrid-scale closure model, Physics of Fluids, A. Vol.4 No.4, pp.633-635.

Sumner D., Akosile O.O, 2003. On uniform planar shear flow around a circular cylinder at subcritical Reynolds number, Journal of Fluids and Structures 13, 309-338.

Zang Y, Street R.L. and Koseff J.R., 1994. A non-staggered grid, fractional step method for time-dependent incompressible Navier-Stokes equations in curvilinear coordinates, Journal of Computational Physics 114, 18-33.

Tamura H., Kiya M., Arie M., 1980. Numerical study of viscous shear flow past a circular cylinder. Transactions of the Japan Society for Mechanical Engineering 46, No.404, 555-564.

Williamson C.H.K., 1996. Vortex dynamics in the cylinder wake, Annu. Rev. Fluid Mech. 28, 477.

Flying Sphere image © Museo Ideale L. Da Vinci

Unsteady aerodynamic force on square cylinder in the flow with streamwise perturbations

1st Cao Fengchan, 2nd Ge Yaojun

1st State Key Laboratory for Disaster Reduction in Civil Engineering, Tongji University, caofc@tongji.edu.cn, 1239, Siping Road, Shanghai, China, 200092

2nd State Key Laboratory for Disaster Reduction in Civil Engineering, Tongji University, yaojunge@tongji.edu.cn, 1239, Siping Road, Shanghai, China, 200092

Keywords: unsteady aerodynamic force, square cylinder, streamwise perturbation.

INTRODUCTION

The investigation of the aerodynamic force on square cylinder in the flow with streamwise perturbations is of great importance not only as a fundamental problem in fluid mechanics but also for aerodynamic loading estimation in wind engineering. The wind usually has both streamwise and sidewise turbulent components. The relationship between the turbulent wind and the unsteady aerodynamic loadings has been the focal point of research over many decades.

In 1940's, Sears derived a theoretical relationship between the lift or moment on airfoil and the flow with sidewise sinusoidal fluctuation, namely the Sears function, based on the potential flow theory. The Sears function, however, cannot be applied to bluff bodies because the potential flow theory is inapplicable to the flow with separations. In wind engineering applications, the aerodynamic forces on bluff bodies, such as tall buildings, bridge decks and so on, due to turbulent wind often are investigated by wind tunnel test. But it is very difficult to simultaneously archive the similarity of both streamwise and sidewise turbulence in wind tunnel. Only the total forces generated by the mean flow, the streamwise turbulence and the sidewise turbulence can be measured. To clarify the relationship between the unsteady aerodynamic force and the turbulence, Cigada et al. (2002) and Diana et al. (2002) used oscillatory airfoils installed at the jet of a wind tunnel with an open test section to generate wind with single frequency sidewise fluctuation. The relationships between aerodynamic force and fluctuating wind are significantly different from the Sears function, but no interpret is given. Nomura et al. (2003) reported the aerodynamic force on square cylinder in wind with only streamwise fluctuation, where the sinusoidal perturbations were generated by a unique AC servomotor wind tunnel. It is confirmed that Morison equation is applicable to explain the experimental results. But the results are only qualitative due to the circular cross section shape of the wind tunnel and the large blockage rate 38%. Konstantinidis ea al. (2007) used PIV and LDV to examine the vortex shedding in the near wake of a circular cylinder due to periodic streamwise perturbations. Symmetric perturbations imposed on cylinder wakes may result in a modification of

the vortex shedding mode from its natural alternating to a symmetric one where twin vortices are simultaneously shed from both sides of the cylinder.

Besides experimental results, some numerical simulations of cylinders in oscillatory flow with nonzero mean velocity have also been reported, Hessamoddini et al. (1997) used finite difference method to simulate the vortex generation and shedding from a circular cylinder in oscillatory flow plus mean flow, the numerical solution successfully illustrated the eddy shedding and the impact of existing eddies on the flow and the shedding process. Zhou C.Y. (2000) investigated the combination planar oscillatory flow plus an in-line steady stream around a circular cylinder. The main attention is paid to the effects of a small current on in-line fluid forces and vortex patterns in the wake. Morison's equation and an equation with two drag terms are examined. The results show that the presence of a small current in an oscillatory flow can reduce the drag coefficient significantly. Morison's equation gives reasonably good predictions for the in-line forces for an oscillatory flow plus a small current. The authors (Fengchan Cao et al., 2007a, 2007b) investigated the different regularities of aerodynamic forces on bridge decks due to streamwise or sidewise small sinusoidal fluctuations by 2-dimesional lattice Boltzmann method. The lift and moment on the thin flat plate can be well described by the Sears function. The unsteady aerodynamic forces on bridge decks due to streamwise perturbation have completely regularities than that due to sidewise perturbation. The drag on the thin flat plate and bridge decks due to sidewise perturbation has multiple-frequency phenomenon. A nonlinear buffeting forces model is proposed to reproduce the nonlinear aerodynamic force due to the sidewise fluctuating wind.

Altogether, the unsteady aerodynamic forces acting on bodies in oscillating flow with nonzero mean velocity have not been studied extensively. There is still little information about the combined effect of mean flow and perturbations on aerodynamic loading of the structures.

AERODYNAMIC FORCE COMPUTATION

In this paper, a 2-dimesional lattice Boltzmann method is used to study the unsteady aerodynamic force on square cylinder in the flow with streamwise perturbations. Comparing to traditional method based on Navier-Stokes equations, LBM can expediently handle the wake compressible property of streamwise fluctuating flow and has higher temporal accuracy. The quadrate flow region in the present simulation is shown as Figure 1.
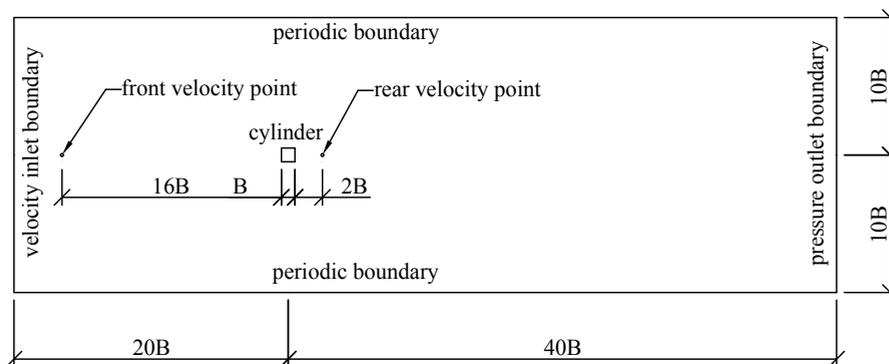
Figure 1: Size of simulated flow region

Contact person: 1st Cao Fengchan, State Key Laboratory for Disaster Reduction in Civil Engineering, 1239, Siping Road, Shanghai, China, 200092, telephone 86-21-65983116-2303 and FAX 86-21-65984882.
E-mail caofc@tongji.edu.cn

The size of the square section is $B = 0.1m$. A mean velocity plus a streamwise sinusoidal fluctuation is used as the boundary condition of the incoming flow.

$$U(t) = U_m + \Delta U \sin(2\pi f_e t + \varphi) \tag{1}$$

where $U_m = 10m/s$ is the mean inflow velocity, $\Delta U = 1m/s$ is the amplitude of velocity oscillation, and $f_e = 2 - 46Hz$ is the frequency of velocity oscillation. The pressure is specified as the atmospheric pressure on the outlet boundary. The periodic boundary condition is used for the other two sides of flow region. The Reynolds number of the flow is $Re = U_m/Bv = 68460$. The reduced velocity $U_r = U_m/f_e B$ is in range of 2.17 to 50.0. The reduced amplitude of velocity oscillation is $A^* = \Delta U/U_m = 0.1$.

RESULTS AND DISCUSSION

(a) When the incoming flow without streamwise fluctuation, the frequency of vortex shedding is $f_n = 13.62Hz$. The Strouhal number $St_n = f_n B/U_m = 0.136$ and drag coefficient $Cx = 1.949$ show well agreement with some previous experimental results.

(b) When the incoming flow with different frequency streamwise fluctuation, the mean and RMS of drag (Cx), lift (Cy) and moment (Cm) are changed with fluctuation frequency dramatically (see Figure 2). The mean of drag reaches the maximum of 2.181 at $f_e = 28Hz$, and reaches the minimum of 1.555 at $f_e = 35Hz$. The mean of lift and moment are always almost zero as expected. When the RMS of drag reaches the maximum of 1.536 at $f_e = 35Hz$, the RMS of lift and moment reaches the minimum of 0.136 and 0.018, respectively. The RMS of lift and moment also has the maximum of 1.166 and 0.159, respectively.
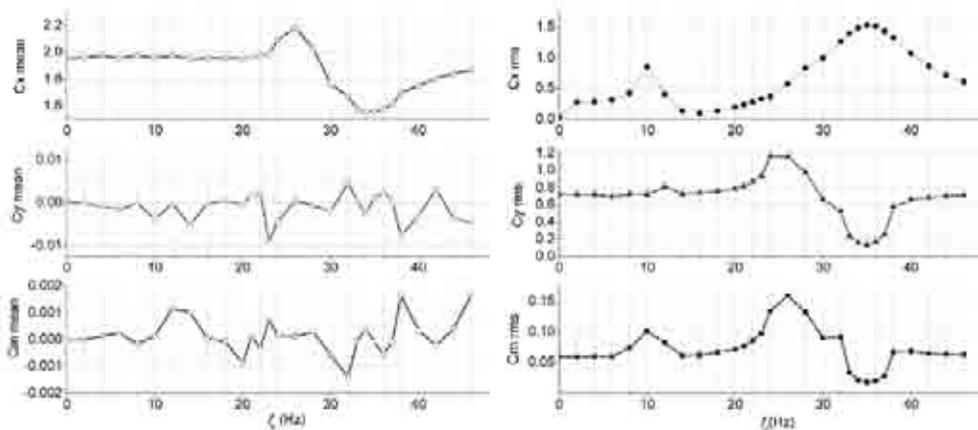
Figure 2: The mean and RMS value of drag (Cx), lift (Cy) and moment (Cm) coefficients at different streamwise fluctuation frequency.

(c) The frequencies of the unsteady aerodynamic forces are the mixing of the nature vortex shedding frequency f_n and streamwise fluctuation frequency f_e. In Figure 3, for example, the frequencies of lift and moment corresponding to the largest 3 amplitude peaks are 9.649Hz ($\approx f_n - f_e$),

13.608Hz ($\approx f_a$) and 17.566Hz ($\approx f_a + f_e$) respectively.
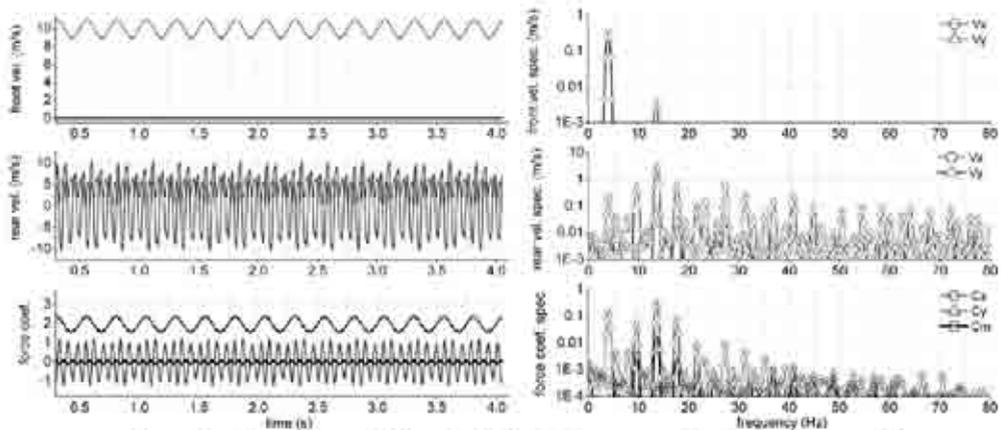
Figure 3: Time history of drag (Cx), lift (Cy), moment (Cm) coefficients and velocity at the reference points when $f_e = 4$Hz.

(d) The vortex shedding mode is dramatically changed from the alternating mode to a symmetric one when the fluctuation frequency changed from 26Hz to 35 Hz.
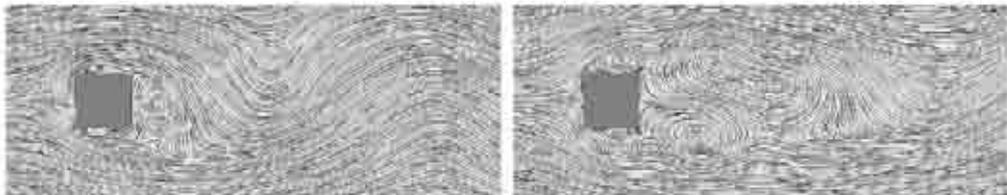
Figure 4: The different flow pattern at $f_e = 26$Hz and $f_e = 35$Hz.

REFERENCES

Cigada A., Diana G., Zappa E. (2002). "On the response of a bridge deck to turbulent wind: a new approach", Journal of Wind Engineering and Industrial Aerodynamics, 90, 1173–1182.

Diana G., Bruni S., Cigada A., Zappa E. (2002). "Complex aerodynamic admittance function role in buffeting response of a bridge deck", Journal of Wind Engineering and Industrial Aerodynamics, 90, 2057–2072.

Nomura T., Suzuki Y., Uemura M., Kobayyashi N. (2003). "Aerodynamic forces on a square cylinder in oscillating flow with mean velocity", Journal of Wind Engineering and Industrial Aerodynamics, 91, 199–208.

Konstantinidisa E.,Balabanib S. (2007) "Symmetric vortex shedding in the near wake of a circular cylinder due to streamwise perturbations", Journal of Fluids and Structures, 23, 1047–1063.

Hessamoddini A., Armfield S.W., Imberge J. (1997). "Finite difference solutions of vortex generation and shedding from a circular cylinder in oscillatory flow plus mean flow", Advanced in Engineering Software, 28, 25-29.

Zhou C.Y., Graham J.M.R. (2000). "A numerical study of cylinders in waves and currents", Journal of Fluids and Structures, 14, 403-428.

Cao F.C., Ge Y.J., Zhu L.D., Xiang H.F. (2007). "Investigation on the different regularities in aerodynamic admittances of bridge decks based on CFD approach", Proceeding of the 12ᵗʰ International conference on wind engineering, Cairns, Australia, 2223-2230.

Cao F.C., Ge Y.J., Zhu L.D., Xiang H.F. (2007). "Nonlinear aerodynamic forces on bridge decks due to transverse sinusoidal fluctuation of wind", Proceeding of the Fifth International Conference on Fluid Mechanics, Shanghai, China, 444-447

Interpretation of aerodynamic pressure measurements by Independent Component Analysis

L.Carassale, A.Vernazzani

Dept. of Civil Environmental and Architectural Engineering, University of Genova
e-mail – luigi.carassale@unige.it

Dept. of Civil Environmental and Architectural Engineering, University of Genova
e-mail – vernazzani@hotmail.it

ABSTRACT

A common activity in experimental bluff body aerodynamics is the measurement of pressure fields acting on models by multi-channel scanners. These measurements are usually idealized as realizations of multi-variate random processes and analyzed by means of statistical approaches usually involving some a-priori assumptions such as stationarity and ergodicity. In this context, one of the most popular techniques is the Principal Component Analysis (PCA), more commonly referred, in bluff body aerodynamics, as Proper Orthogonal Decomposition (POD) (e.g. Solari et al. 2007). According to this technique, a zero-mean N-variate random process $\mathbf{q}$ is represented by the linear combination

$$\mathbf{q}(t) = \sum_{k=1}^{N} \boldsymbol{\phi}_k x_k(t) = \boldsymbol{\Phi} \mathbf{x} \tag{1}$$

involving, for any time instant t, a set of deterministic vectors $\boldsymbol{\phi}_k$ (collected column-wise into the matrix $\boldsymbol{\Phi}$) referred to as the modes of the process; the coefficients of the linear combination, $x_k(t)$ (collected into the vector $\mathbf{x}$), are called principal components (PC). PCA possesses three essential properties: 1 – the modes $\boldsymbol{\phi}_k$ are the eigenvectors of the zero-time-lag covariance matrix of the process $\mathbf{q}$ and are

---

Contact person: L.Carassale, DICAT – University of Genova, Via Montallegro 1 – 16145 Genova, Italy, ph: +39 010 353 2226, FAX: +39 010 353 2534, E-mail: luigi.carassale@unige.it

orthogonal with respect to the Euclidean inner product; 2 – the principal components x_k are uncorrelated with each other; 3 – the sum in Eq. (1) has the fastest possible convergence in the mean square sense among all the possible linear combinations and therefore can be shortened retaining only a small number $n \ll N$ of modes.

In practical applications Eq. (1) is usually interpreted as a tool for the representation of some specific dataset $\mathbf{q}$ obtained from an experiment. In this case, the modes are calculated from the sample covariance matrix of $\mathbf{q}$ and the PC are obtained projecting the data on the modes. The number of modes n to be retained in the representation is variable from case to case and can be selected on the basis of some convergence criteria; however, the application of PCA to several case-studies demonstrated that the number of modes to be considered is usually very small and that the representation of the pressure field can be obtained by the superimposition of very few pressure patterns acting on the body with a complete lack of correlation.

Form a different point of view, the dominant (with higher variance) modes have often been conceived as convenient tools for the qualitative analysis of pressure fields. The modes are indeed interpreted as elementary pressure patterns, whose characteristics reflect the aerodynamic behaviour of the model. Following this approach, it seems natural to ask whether or not the PCA modes have any physical meaning or can separate different physical mechanisms concurring in the generation of the pressure field. These conjectures are encouraged by some interpretations of PCA for which the first mode represents the most recurrent (or typical) deterministic shape hidden in a random phenomenon (Lumley 1970) and by its successful application in several contexts to identify deterministic structures such as dominant eddies (Holmes et al. 1996). In the wind engineering community, it is believed that, even if the PCA modes have some ability in separating some loading contributions (e.g. along-wind and cross-wind forces on symmetrical bodies), their shape do not necessarily resemble any physically consistent pressure distribution.
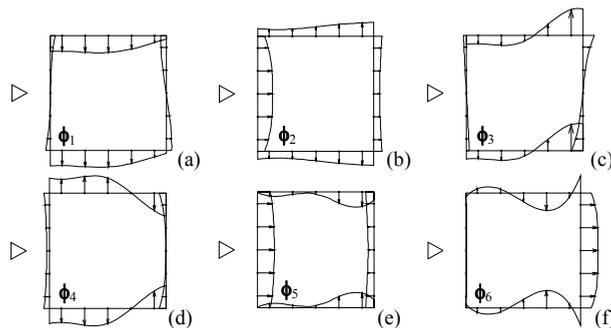
Figure 1: first six PCA modes of pressure field along a high-rise building cross-section.

The above concept is demonstrated by Figure 1, which shows the first six PCA modes of the pressure field measured on a high-rise building model along a cross section at the level of the stagnation point. The wind flow is characteristic of urban terrain and the Reynolds number is 1.4×10^5 (full details on the experimentation and on the PCA analysis of the whole pressure field acting on the model can be found in Kikuchi et al. (1997)). Modes 1 and 3 (Fig. 1a and 1c) are antisymmetric and represent cross-wind and torsional actions, while modes 2, 4, 5 and 6 (Fig. 1b, 1d, 1e and 1d) are symmetric and represent along-wind actions. In spite of this successful separation, some features of the modes seem not to be consistent with the observations. In particular, mode 1 (a) presents pressure distributions deterministically equal (with opposite sign) on the two lateral faces of the model, while, it is well known that the suction generated by vortex shedding tends to be quite more intense than the compression appearing on the opposite face. Besides, mode 4 (d) represents a pressure distribution on the lateral faces that is somehow compatible with the formation of recirculation bubbles after the windward corners and the re-attachment of the boundary layer on the lateral faces just before the

leeward corners; unfortunately, mode 4 represents the synchronous realization of this mechanism on both the lateral faces of the model, while, at the Reynolds number reproduced in the experimentation, the vortex shedding is expected to be alternate.

A strong limitation involved in the use of PCA as a pattern identification tool is related to the orthogonality of its modes that, from a physical point of view, is not justifiable. The elimination of such a condition, however, is not trivial since it is implicitly embedded in PCA formulation (the modes are the eigenvectors of a symmetric matrix) and, even if it were conceptually possible, it would makes the estimation of the modes undetermined.

With the purpose of obtaining a representation formula analogous to Eq. (1), but based on a non-orthogonal set of modes, the concept of Independent Component Analysis (ICA) is briefly described and applied to the case study described above. This technique has a relatively recent formulation and has been largely employed in several contexts for the solution of the so-called Blind Source Separation (BBS) problem. In the wind engineering field, a somehow similar technique called projection pursuit has been applied by Gilliam et al. (2004) for the study of the vortexes emitted by a corner on the roof of a low-rise building; at the author's knowledge, no other application has been presented.

ICA can be formalized as follows. Let us assume that the random fluctuation of the pressure field $\mathbf{q}$ is provided by a generative model of the kind:

$$\mathbf{q}(t) = \mathbf{A}\mathbf{s}(t) \tag{2}$$

where $\mathbf{s}$ is a vector of n statistically independent sources s_j said independent components (IC) and $\mathbf{A}$ is an $N \times n$ full-rank matrix referred to as mixing matrix. The objective of ICA is the estimation of the sources $\mathbf{s}$ and of the mixing matrix $\mathbf{A}$, given the experimental measurements $\mathbf{q}$. It is clear that the ICA model (Eq. (2)) is analogous to the representation formula offered by PCA (Eq. (1)), with the difference that the columns $\mathbf{a}_j$ of the matrix $\mathbf{A}$ are, in general, non-orthogonal and that the ICs s_j are now statistically independent instead of simply uncorrelated like the PCs x_k.

The estimation of $\mathbf{s}$ and $\mathbf{A}$ can be carried out according to different principles including maximum likelihood, mutual information minimization and non-Gaussianity maximization (Hyvärinen et al. 2001). Such estimation can be formulated as an optimization problem and leads to a unique solution (up to a scaling and a permutation of the ICs), provided that the sources are non-Gaussian.

In many practical applications, the experimental data do not have any specific physical reason to follow an ICA model (the pressure field on a body is not necessarily the linear combination of statistically independent sources); however, the application of ICA to these cases is still significant since provides a mixing matrix that makes the components of the vector $\mathbf{s}$ as much statistically independent as possible. In this sense, ICA may be interpreted as a modification of PCA in which the orthogonality condition on the modes is substituted by the maximum-independence condition on the coefficients of the linear combination.

In bluff-body aerodynamics, ICA can be employed, exactly like PCA, to represent pressure fields acting on a body as a linear combination of deterministic pressure patterns determined by the columns of the mixing matrix, modulated by statistically independent (as much as possible) amplitudes corresponding to the ICs.

Figure 2 shows six ICA modes spanning the same space as the six PCA modes shown in Figure 1. In this representation, the cross-wind action is determined by four modes, two for a lateral face and two for the other one. These modes are physically consistent since do not imply, unlike in the case of PCA, a deterministic relationship between the pressure acting on the two lateral faces. Besides, even if no direct observation to support that is available, it seems that they may be related to well known physical mechanisms: modes 1 and 2 may represent the generation of the recirculation bubble and the re-attachment of the boundary layer, while modes 3 and 4 may be consistent with the pressure field generated by passage of the vortex near the leeward corner. Modes 5 and 6 provide along-wind actions and are very similar to the corresponding ones obtained by PCA.

Figure 3a shows a portion of the first two ICs, s_1 and s_2, corresponding to the ICA modes $\mathbf{a}_1$ and $\mathbf{a}_2$ shown in Figure 2a and 2d. The positive peaks of the ICs, representing suction in the regions where

the corresponding modes have large amplitude, are alternate, and any large positive peak of an IC corresponds to a small negative peak of the other IC; this behavior is consistent with Kármán vortex shedding. Figure 3b shows the probability density function (pdf) of the pressure component q_6 measured by a pressure tap located immediately after a windward corner (solid line), compared to the pdf of the first PC x_1 (dashed line) and the pdf of the first IC s_1 (dash-dot line). It is worth noting that, even the first PC represents the maximum possible share of variance associated to the pressure on the lateral faces, its pdf is quite different from the pdf of the local pressure, which is, on the contrary, is well reproduced by the pdf of the first IC.
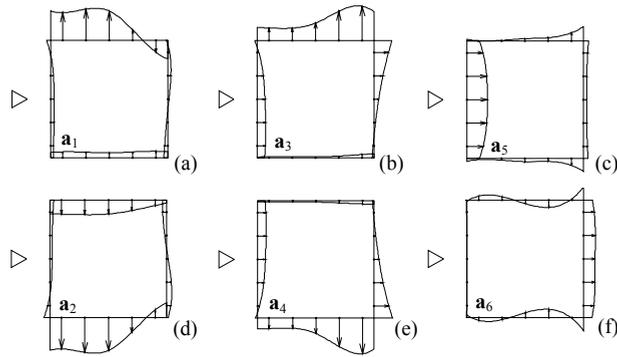
Figure 2: ICA spanning the space defined by the first six PCA modes (Fig. 1).
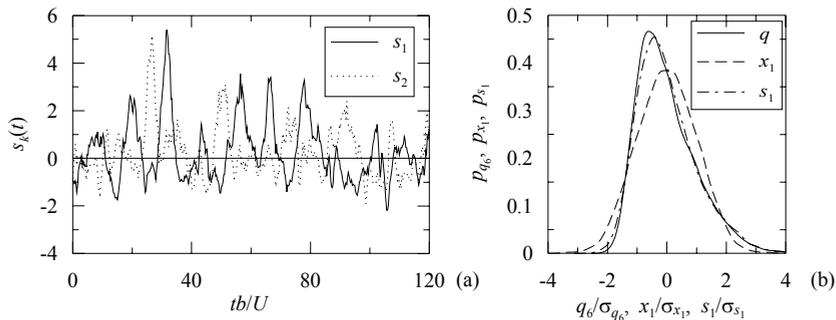
Figure 3: a – First two ICs; b – pdf of local pressure after a windward corner (solid line), pdf first PC (dashed line), pdf first IC (dash-dot line).

REFERENCES

Gilliam X., Dunyak J.P., Smith D.A. Wu, F. (2004). "Using projection pursuit and proper orthogonal decomposition to identify independent flow mechanisms", J. Wind Engng. Ind. Aerodyn, 92, 53-69.

Hyvärinen A., Karhunen J., Oja E. (2001). *Independent component analysis*. John Wiley and Sons, New York.

Holmes P., Lumley J.L., Berkooz G. (1996). *Turbulence: coherent structures, dynamical systems and symmetry*. Cambridge University Press, Great Britain.

Kikuchi H., Tamura Y., Ueda H., Hibi K. (1997). "Dynamic wind pressure acting on a tall building model - Proper orthogonal decomposition". Journal of Wind Engineering and Industrial Aerodynamics, 69-71, 631-646.

Lumley, J.L. (1970). *Stochastic tools in turbulence*. Academic Press, New York.

Solari G., Carassale L., Tubino F. (2007). "Proper Orthogonal Decomposition in Wind Engineering: Part 1: A State-of-the-Art and Some Prospects", Wind and Structures, 10(2), 153-176.

TALL STRUCTURES

Optimum outrigger locations of high-rise steel buildings for wind loading

Gerasimidis S., Efthymiou E. & Baniotopoulos C. C.

Institute of Metal Structures, Department of Civil Engineering, Aristotle University of Thessaloniki, GR-54124, Thessaloniki, Greece

sgerasim@civil.auth.gr, vefth@civil.auth.gr, ccb@civil.auth.gr

Keywords: high-rise buildings, outriggers, design optimization, wind loading.

ABSTRACT

All design projects, regardless of their complexity or their structural approach, are governed by one major principle, that of using the minimum necessary material. In a time of limited resources and financial uncertainty, engineering optimum solutions can eventually affect not only the success but also the accomplishment of several projects. Especially for high-rise buildings, the complexity of the solutions and the difficulty of their implementation, necessitate optimization techniques which are proven crucial for the desired outcome of the design concept.

The race towards new heights has not been without challenges. After the invention of elevators by E.G. Otis and the use of structural steel as the building material, tall structures have continued to climb higher and higher facing strange wind effects and very high wind loading. Usually, any increase in height is combined with unintended increase in flexibility and possible lack of stiffness or damping adds vulnerability for severe wind actions.

Steel and concrete are the two most commonly used materials in the design of high-rise structures. Both have their unique qualities but can be distinguished by their unit price. Determining their optimum performance is a key factor when material price is of concern. By understanding the fundamental physical characteristics of each structural system and then by applying specific optimization techniques, it is possible to monitor the value added through each member's efficiency, relative to drift. This efficiency can be represented as a normalized value.

Undoubtedly, the factor that governs the design of a tall and slender structure most of the times is not the fully stressed state but the drift of the building for wind loading. There are numerous structural lateral systems used in high-rise building design such as: shear frames, shear trusses, frames with shear core (figure 1), framed tubes, trussed tubes, superframes etc. However, the outriggers and belt trusses system is the one providing significant drift control for the building.

Contact person: Gerasimidis Simos, Institute of Metal Structures, Department of Civil Engineering, Aristotle University of Thessaloniki, GR-54124, Greece, +30-6946-336484, FAX: +30-2310-995642. E-mail sgerasim@civil.auth.gr
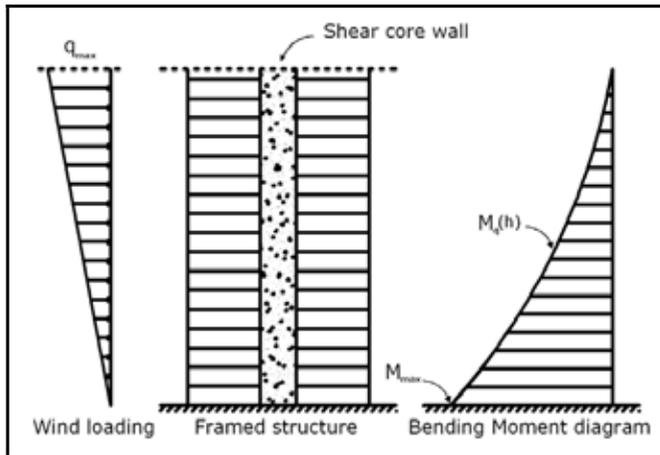
Figure 1: Structure with frames and shear core, under wind loading (left) and the bending moment diagram of the concrete core (right).

The way in which outboard columns resist part of the overturning moment produced by wind on a structure with outriggers, is illustrated in Figure 2. The outrigger trusses which are connected to the core and to the columns outboard of the core, restrain rotation of the core and convert part of the moment in the core into a vertical couple of forces at the columns. Shortening and elongation of the columns and deformation of the outrigger trusses permits some rotation of the core at the outriggers.
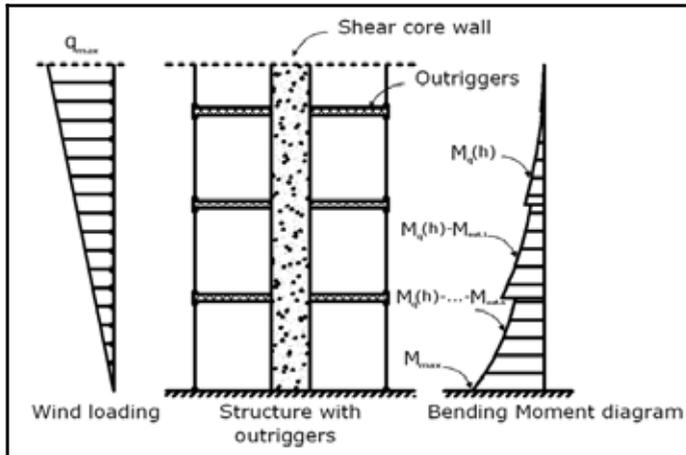
Figure 2: Structure with outriggers, under wind loading (left) and the bending moment diagram of the concrete core (right).

The ability to shed the overturning moment from the core of a building to the outriggers can be improved by tuning the strength of the outriggers to efficiently convert moments into a vertical couple of forces restrained by the columns. The original moment in the core can be viewed as either a vertical couple concentrated at the perimeter of the core, a horizontal couple confined by the depth of the outrigger, or else a combination of both. Depending on the configuration of the core and the

connection of the outrigger to it, one load path may prove favorable to another.

The integration of the outrigger to the concrete core can be further optimized by guaranteeing concentrated core forces into the outriggers. Overall the amount of the steel attributed to the outriggers relative to the steel associated with the columns is preferable in terms of efficiency, namely because adding steel to columns tends to quickly escalate the overall tonnage of the design. Therefore ensuring that the outriggers are operating at full potential not only implies their stiffness is fully engaged but also their core area directly adjacent is also fully engaged.

The optimum location and number of the outriggers still remains a crucial but also pending question. This paper implements a design optimization technique of tall steel structures for lateral loads, mainly wind, into trying to find the optimum locations and number of outriggers for a high-rise building. The structure is analyzed for two different loading conditions. One with the real wind loading calculated according to the appropriate code, for which the structure is designed based on allowable stress criteria. The structure produced by stress based design, although below the stress limit, is very flexible and exhibits horizontal displacements and interstory drifts much above the acceptable limits, due to wind loading. The second analysis is performed with a virtual loading at the point of interest, i.e. the top of the building.

Following the extraction of the results for both analyses, an analytical cycle routine applies the optimization method.

REFERENCES

Charles H. Thornton, Leonard Joseph, Thomas Scarangello, "Optimization of tall structures for wind loading", Journal of Wind Engineering and Industrial Aerodynamics, vol. 36, issues 1-3, October 1990, pages 235-244.

William F. Baker, "Energy-Based Design of Lateral Systems", Structural Engineering International, 2/92, pages 99-102.

Zhang Jie, Zhang Zhong-xian, Zhao Wen-guang, Zhu Hong-ping, Zhou Chun-sheng, "Safety analysis of optimal outriggers location in high-rise building structures", Journal of Zhejiang University Science A, 2007 8(2): 264-269.

A numerical procedure for the dynamic response of tall buildings subject to turbulent wind excitation

G. Barbella[*], F. Perotti[*], V. Simoncini[**]

[*]*Dept. of Structural Engineering, Politecnico di Milano, Italy*
e-mail: barbella@stru.polimi.it, perotti@stru.polimi.it
[**]*Department of Mathematics, University of Bologna, Italy*
e-mail: valeria@dm.unibo.it

Keywords: tall buildings, gust buffeting, iterative methods.

ABSTRACT

One of the most challenging issues in the modern design of tall buildings is related to the evaluation of wind actions, which can be, in some cases, much more demanding in terms of ultimate resistance and serviceability conditions behaviour when compared to seismic actions. The current normative framework (EuroCode 1-4), based on simplified computing methodologies mostly consisting of equivalent static analyses, seems to be inadequate – and thus not applicable – for complex and/or sensitive structures, or when basic regularity requirements are not fulfilled. In these cases, more refined methods are recommended, even though without precise references or guidelines.

On the other hand, the increasing availability and accuracy of Boundary Layer Wind Tunnel (BLWT) tests data allows to obtain a sophisticated description of the aerodynamic behaviour of the structure, which can be exploited, together with a finite element mechanical model, in order to evaluate the dynamic structural response to gust buffeting phenomena. This can be done by considering two different procedures: the first makes use of the whole set of time history recordings, coming from wind tunnel, as forcing terms to be applied to the FE model in a deterministic context; the second consists of a stochastic approach, based on a probabilistic model of the wind turbulence, as well as on a suitable model describing the fluid-structure interaction, characterized by the aerodynamic coefficients computed from the wind tunnel tests.

Contact person: G. Barbella, Department of Structural Engineering, Politecnico di Milano
E-mail barbella@stru.polimi.it

In the present work both the approaches are addressed, by proposing a numerical procedure in the frequency domain which is intended to somehow bridge the gap in terms of design prescriptions. The deterministic and the stochastic problems can be properly handled within the same mathematical framework, giving the opportunity to carry out a complete buffeting analysis of the structure. Moreover, a criterion is proposed to fully exploit the amount of BLWT data, accounting when available, for the statistical properties of experimental time history recordings in order to update the turbulence intensities values provided by the normative. This allows to somehow include in the stochastic model the effects of the building surrounding area on the wind turbulence field. Moreover, the presented procedure accounts for the contribution of higher vibration modes and is suitable for verifying the satisfaction of serviceability requirements related to comfort.

Fluid-structure interaction forces are computed according to the Morison approach, which implies some base hypotheses: body motion does not influence upstream fluid velocity field; interaction forces depend only on the instantaneous fluid-structure relative motion; aerodynamic coefficients are determined through measurements in stationary regime on a fixed body; friction effects are neglected, as well as aerodynamic instability phenomena. Then let v_1, v_2 and v_3 be the wind reference axes, with v_1 parallel to the mean velocity, v_2 orthogonal to the first and lying on the horizontal plane and v_3 in the vertical direction; let W be the wind mean velocity and w_i the turbulence components relative to the v_i axes. The local force per unit length acting on an element with the axis perpendicular to v_1, written in the wind reference $v_1 v_2$ and neglecting inertia contribution, assumes the form

$$\mathbf{p} = \begin{bmatrix} p_{v_1} \\ p_{v_2} \\ p_{\theta_3} \end{bmatrix} = \frac{1}{2}\rho D V_r^2 \begin{bmatrix} C_D \cos\gamma_r - C_L \sin\gamma_r \\ C_D \,\mathrm{sen}\,\gamma_r + C_L \cos\gamma_r \\ D\,C_M \end{bmatrix}, \tag{1}$$

where ρ, D, V_r and γ_r are respectively the air density, the characteristic transversal dimension of the element, the modulus of the fluid-structure relative velocity and the angle of attack fluctuation; while C_D, C_L and C_M are the drag, lift and moment aerodynamic coefficients. Linearization of expression (1) is carried out considering that structure displacements are assumed to be small and, in characteristic design conditions, mean value of wind velocity is much larger than both its fluctuations and structure velocities. As a result, interaction forces are subdivided into the static, dynamic, damping and stiffness contribution, respectively depending on mean wind velocity, turbulence components, structure velocities and structure displacements. Finally, distributed wind loads are applied to the structure by considering two-node "aerodynamic" linear elements, ideally representing the axis of the slender body immersed in the fluid flow. Such an approach, in the case of tall buildings, can be adopted under the hypothesis of in-plane rigid floor diaphragms, so that aerodynamic elements are connected to the centroids of adjacent floors. It has to be noticed that the aerodynamic contributions to viscous damping and stiffness matrices, lead to the loss of symmetry properties.

The three-dimensional description of wind turbulence is formulated according to the current code regulation parameters and to the stochastic model proposed by Solari and Piccardo (2001), based on the hypothesis of stationarity for the turbulence process. The Cross-Spectral Power Density (CSPD) of the wind fluctuations components w_j and w_k', considered in the points $P \equiv \{x, y, z\}$ and $P' \equiv \{x', y', z'\}$, is computed as

$$S_{jk}(P, P', f) = \sqrt{S_j(z, f)\, S_k(z', f)}\; \mathrm{Coh}_{jk}(P, P', f), \tag{2}$$

where S_j and S_k are the auto-spectra of the single components; while the coherence function accounts for both the correlation Γ between different velocity fluctuations, along directions j and k, in the same point, and the spatial correlation Λ between fluctuation components relative to the same direction but considered in different points:

$$\mathrm{Coh}_{jk}(P, P', f) = \mathrm{Sgn}(\Gamma_{jk}) \sqrt{\Gamma_{jk}(z, f)\,\Gamma_{jk}(z', f)} \sqrt{\Lambda_j(P, P', f)\,\Lambda_k(P, P', f)}. \tag{3}$$

Structural response is computed starting from the dynamic equilibrium equation in the frequency

domain, which has the form

$$\left[-(2\pi f)^2 \mathbf{M} + i2\pi f (\mathbf{C}_v + \mathbf{C}_a) + \mathbf{K} + \mathbf{K}_a + i\mathbf{C}_h \right] \tilde{\mathbf{q}}(f) = \mathbf{E}(f)\tilde{\mathbf{q}}(f) = \tilde{\mathbf{p}}(f) = \mathbf{F}\tilde{\mathbf{w}}(f), \tag{4}$$

where $\mathbf{E}(f)$ is the impedance matrix of the system, while $\tilde{\mathbf{q}}(f)$ and $\tilde{\mathbf{p}}(f)$ are the Fourier Transforms (FT) of structural displacements and of the generalized components of external actions. Here damping, stiffness and dynamic contributions of aerodynamic forces are accounted for in the assembling procedure of system matrices and right hand side vectors. Displacements spectral power densities matrix is defined as

$$\mathbf{S}_\mathbf{Q}(f) = \lim_{T\to\infty} \frac{1}{T} E\left[\tilde{\mathbf{q}}(f,T)\tilde{\mathbf{q}}^H(f,T) \right] = \mathbf{E}^{-1}(f)\mathbf{S}_\mathbf{P}(f)\mathbf{E}^{-H}(f) = \mathbf{H}(f)\mathbf{S}_\mathbf{P}(f)\mathbf{H}^H(f), \tag{5}$$

in which $E[\bullet]$ is the expected value operator, $\mathbf{S}_\mathbf{P}(f) = \mathbf{F}\mathbf{S}_\mathbf{W}(f)\mathbf{F}^T$ and $\mathbf{S}_\mathbf{W}(f)$ is the SPD matrix of wind turbulence components, whose single entries take the form of expression (2). In the deterministic case, as already mentioned, global external wind actions are assumed to be directly computed from wind tunnel pressure measurements, hence, impedance matrix keeps being symmetric.

Expression (5) is computed by considering the non-symmetric $N \times N$ complex linear system with multiple right hand sides

$$\mathbf{E}(f)\mathbf{X}_\mathbf{q}(f) = \mathbf{F}, \tag{6}$$

which has to be solved for each value of the frequency parameter. Thus, the use of a direct solver would imply significant costs in terms of computing resources, since impedance matrix is a function of frequency and a new factorization must be performed at each step.

The numerical procedure here adopted is based on iterative schemes which allow for the simultaneous solution of the system for several frequency steps, see (Feriani & al., 2000) and (Simoncini and Perotti, 2002). The standard algebraic formulation of the problem is derived rewriting (4) in terms of acceleration FT, hence, equation (6) becomes:

$$\left[\mathbf{M} + \frac{\mathbf{C}}{i2\pi f} - \frac{\mathbf{K}}{(2\pi f)^2} \right] \mathbf{X}_\mathbf{a}(f) = \mathbf{F}, \tag{7}$$

which can be linearized with respect to the frequency parameter $\lambda = (2\pi f)^{-1}$, providing the shifted system of dimension $2N$

$$\left\{ \mathcal{A}\mathcal{B}^{-1} + \lambda \mathbf{I}_{2N} \right\} \mathbf{z} = \mathbf{d}, \text{ with } \mathcal{A} = \begin{bmatrix} i\mathbf{C} & -\mathbf{M} \\ -\mathbf{M} & 0 \end{bmatrix}, \mathcal{B} = \begin{bmatrix} \mathbf{K} & 0 \\ 0 & \mathbf{M} \end{bmatrix}, \mathbf{z} = \mathcal{B} \begin{bmatrix} -\lambda\tilde{\mathbf{a}} \\ -\tilde{\mathbf{a}} \end{bmatrix}, \mathbf{d} = \begin{bmatrix} \mathbf{F} \\ 0 \end{bmatrix}. \tag{8}$$

Note that system (8) is not symmetric, even though both $\mathcal{A}$ and $\mathcal{B}$ come out to be symmetric, when for example the deterministic case is considered.

The iterative solvers here adopted (Saad, 1996) rely on projection methods onto Krylov subspace, meaning that, given the generic non-Hermitian complex linear system $\mathbf{A}\mathbf{x} = \mathbf{b}$, an approximate solution $\mathbf{x}_m \approx \mathbf{A}^{-1}\mathbf{b}$ is obtained by searching $\mathbf{x}$ in the Krylov subspace generated by the coefficients matrix and a starting vector $\mathbf{v}$, defined as

$$\mathcal{K}_m(\mathbf{A}, \mathbf{v}) = \text{span}\left\{ \mathbf{v}, \mathbf{A}\mathbf{v}, \mathbf{A}^2\mathbf{v}, \ldots, \mathbf{A}^{m-1}\mathbf{v} \right\}. \tag{9}$$

In the implementation, $\mathbf{v}$ is usually set equal to the starting residual vector $\mathbf{r}_0 = \mathbf{A}\mathbf{x}_0 - \mathbf{b}$, where $\mathbf{x}_0$ is an initial guess. The key feature of this strategy is that the generated subspace is invariant under shift, that is $\mathcal{K}_m(\mathbf{A}, \mathbf{v}) = \mathcal{K}_m(\mathbf{A} + \lambda\mathbf{I}, \mathbf{v})$, so that the same search subspace is used for all the considered shifts. Different methods are characterized by the procedure adopted to build a basis for $\mathcal{K}_m$ and to minimize the difference between the approximate and the exact solution. One of the algorithms implemented in this work is the GMRES method, based on the Arnoldi process, which provides an orthonormal basis $\mathbf{V}$ and an upper Hessenberg matrix, containing the orthogonalization coefficients. Note that orthogonalization of the basis vectors has to be performed against all the pre-

vious ones, so that the entire matrix **V** need to be stored. Then, the algorithm updates the approximate solution by minimizing the 2-norm of the associated residual. In order to conveniently handle problem (8), with multiple r.h.s., suitable block versions of the method have to be considered, rather than solving the different systems separately. Thus, the Krylov subspace assumes the form:

$$\mathcal{K}_{m \times s}(\mathbf{G}, \mathbf{r}_0) = \text{span} \left\{ \mathbf{r}_0, \mathbf{G}\mathbf{r}_0, \mathbf{G}^2 \mathbf{r}_0, \dots, \mathbf{G}^{m-1} \mathbf{r}_0 \right\}, \quad \mathbf{r}_0 = \mathbf{F}, \tag{10}$$

with $\mathbf{G} = \mathcal{A}\mathcal{B}^{-1}$, s being the number of r.h.s. and having set the initial guess to zero. Moreover short-term recurrence in the subspace building process can be considered, in particular, a block-QMR method has been implemented, based on the two-sided Lanczos algorithm, which requires the explicit creation of two subspaces: one associated with **G** and the other with its transpose. When the matrix **G** comes out to be **J**-symmetric, as in the deterministic case, the two-sided Lanczos algorithm reduces into the simplified Lanczos – transpose free – variant.

A computing example of the presented methodologies is shown, with reference to a 70 meters high real building, for which a complete wind tunnel test campaign has been carried out. The mechanical finite element model is composed by 3D beam elements, with 2364 dofs. The computing times, in seconds, for the block-GMRES method are 6.675, 8.459 and 10.590, if the number of frequencies is 11, 101 or 201 respectively. Figure 1 depicts some of the results from the stochastic
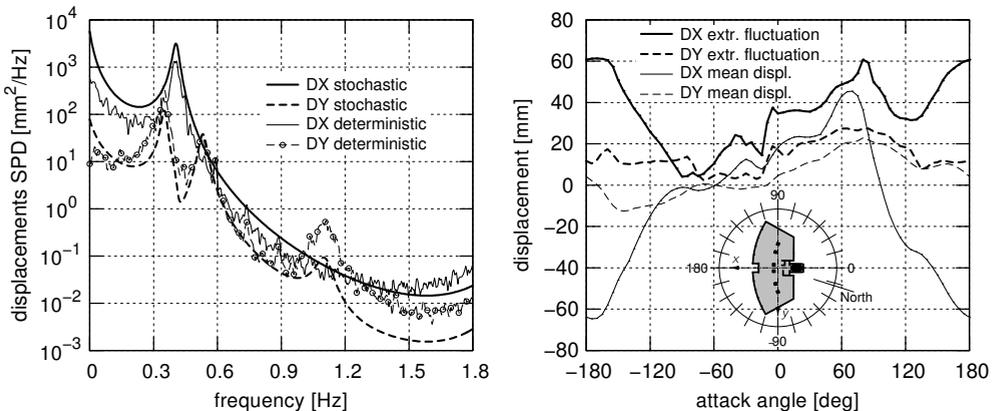
Figure 1: (left) – displacement SPDs for the central node of the highest floor, comparison between stochastic and deterministic analyses, angle of attack is 180°; (right) – extreme values of displacements fluctuations from the stochastic analysis, compared to static values.

and deterministic analyses: on the right, displacements of the last floor, due to the wind static component, are compared with their extreme values for each angle of attack; on the left, the displacement SPD functions from the stochastic analysis (corresponding to an attack angle of 180°) are compared to those obtained from the deterministic case.

REFERENCES

Feriani, A., Perotti, F. and Simoncini, V. (2000), "Iterative system solvers for the frequency analysis of linear mechanical systems", Computer Methods in Applied Mechanics and Engineering, vol. 190, pp. 1719–1739.

Saad, Y. (1996), "Iterative methods for sparse linear systems", PWS Publishing Company.

Simoncini, V. and Perotti, F. (2002), "On the numerical solution of $(\lambda^2 A + \lambda B + C)x = b$ and application to structural dynamics", SIAM Journal on Scientific Computing, vol. 23, no. 6, pp. 1875–1897.

Solari, G. and Piccardo, G. (2001), "Probabilistic 3-D turbulence modelling for gust buffeting of structures", Probabilistic Engineering Mechanics, vol. 16, no. 1, pp. 73–86.

Along wind response of non-classically damped high-rise building

S. Hračov, J. Náprstek, S. Pospíšil, C. Fischer

Institute of Theoretical and Applied Mechanics, v.v.i., Academy of Science of the Czech Republic,
hracov@itam.cas.cz, naprstek@itam.cas.cz, pospisil@itam.cas.cz, fischerc@itam.cas.cz

Keywords: random wind response, non-proportional damping, tall buildings.

ABSTRACT

Dynamic response of high-rise buildings due to wind excitation plays a significant role in the assessment of their functionality. The wind load induces very often undesired vibration regarding occupant discomfort. The wind velocity includes a strong random fluctuating component with respect to time and space. Therefore the dynamic component of the wind speed can be considered as a stationary random process in individual points of a structure.

Description of the static as well as dynamic components has been given by many authors, e.g. Simiu & Scanlan (1996), etc. In particular the problem of structure excitation by fluctuating wind component has been discussed during previous decades, see e.g. Fischer & Pirner (1986), Dyrbye & Hansen (1996) and many others. As a consequence of the random character of the wind load, the structure response dynamic component has a random character as well.

Important role modifying the response character plays a damping and its detailed configuration. Commonly used assumption of proportional damping is satisfactory in many cases providing easier mathematical modeling. In many cases, however, this assumption is far from the reality, as for instance when a structure is equipped with tuned mass dampers (TMD). For example Naprstek & Pospisil (2007) have shown that a TMD is a significant source of the non-proportional damping. This fact being taken into consideration results in an interaction of conventional eigen-forms in the meaning of the structure itself (on the level of a deterministic problem). Moreover the random character of the response generates another source of interaction of eigen-forms.

The contribution of this paper consists in an analysis of the wind response of a high-rise building equipped with TMDs. The paper gives an extension of previous results, see Naprstek & Pospisil (2007), representing a generalization of the problem from line type to two dimensional model of a structure. Only along wind random vibrations due to the effect of wind pressure on windward side are assumed. An application of the theoretical method is demonstrated subsequently on an assessment of a real structure - tall building, see Figure 1.

Analysis of the random response is based on a transformation of the governing system (continuous

---

Contact person: S. Hračov, Institute of Theoretical and Applied Mechanics, v.v.i., Academy of Science of the Czech Republic, Prosecká 76, Prague, Czech Republic, hracov@itam.cas.cz

or discretized) into generalized coordinates written in a normal form (n-number of DOFs respected):

$$\dot{\mathbf{F}}(t) = \mathbf{Q} \cdot \mathbf{F}(t) + \mathbf{P}(t) \;\; ; \quad \mathbf{F}(t), \mathbf{Q} \in \mathbb{R}^{2n \times 2n} \;\; ; \;\; \mathbf{P}(t) \in \mathbb{R}^{2n} \tag{1}$$

$$\mathbf{F}(t) = \begin{bmatrix} \mathbf{f}(t) \\ \dot{\mathbf{f}}(t) \end{bmatrix} \qquad \mathbf{Q} = \begin{bmatrix} \mathbf{0} & \mathbf{I} \\ -\mathbf{\Theta}^2 & -\mathbf{B} \end{bmatrix} \qquad \mathbf{P}(t) = \begin{bmatrix} \mathbf{0} \\ \mathbf{I} \end{bmatrix} \cdot \mathbf{p}(t) = \mathbf{H} \cdot \mathbf{p}(t) \tag{2}$$

$$\mathbf{\Theta}^2 = diag[\Theta_1^2, ..., \Theta_n^2] \qquad \mathbf{B} = \mathbf{U}_0^T \cdot \mathbf{C} \cdot \mathbf{U}_0 \;\; ; \;\; \mathbf{U}_0 = [\mathbf{u}_{01}, ..., \mathbf{u}_{0n}] \tag{3}$$

In Eqs (1-3) we have denoted: $\mathbf{f}(t)$ – time functions representing the movement in generalized coordinates; $\mathbf{p}(t)$ - vector representing wind load adjoined to individual components of the vector $\mathbf{f}(t)$; $\mathbf{\Theta}^2$ - diagonal matrix containing squares of eigen-values of the undamped system; $\mathbf{B}$ - reduced damping matrix $\mathbf{C}$; $\mathbf{u}_{0j}$ - j-th eigen-form of the undamped system;

In the next step the eigen-values ξ_j and eigen-forms $\mathbf{q}_j$ of the system (1) should be done according for instance to Fischer (2000). The solution algorithm is based on the same principle as the subspace iteration in the case of a symmetric real matrix. One iteration cycle consists essentially in complex inverse vector iteration and orthogonalization of the iteration vectors.

Figure 1: Prototype of a tall building and its FEM model with TMDs.

Assuming input and output processes in Eq. (1) in the form with spectral differentials of white noise type processes $d\mathbf{\Phi}(\omega)$:

$$\mathbf{p}(t) = \int_{-\infty}^{\infty} e^{i\omega t} d\mathbf{\Phi}(\omega) \qquad \mathbf{F}(t) = \int_{-\infty}^{\infty} \mathbf{F}^*(\omega, t) d\mathbf{\Phi}(\omega) \tag{4}$$

Expressions (2-4) should be put into Eq. (1). Several modifications and respecting Wiener-Kchinchin relation leads to the following closed form solution:

$$\mathbf{F}^*(\omega,t) = \sum_{k=1}^{2n} \frac{2\mathbf{Z}_k \mathbf{H}}{\mathrm{i}\,\omega - \xi_k}\left(e^{\mathrm{i}\omega t} - e^{\xi_k t}\right) \quad ; \quad \mathbf{Z}_k = \mathbf{q}_k \cdot \mathbf{q}_k^T \tag{5}$$

Matrix $\mathbf{F}^*(\omega,t) \in \mathbb{R}^{2n \times 2n}$ is a matrix of deterministic functions describing transformation of random excitation in generalized coordinates to individual components of the random response in time. Matrices $\mathbf{Z}_k$ are expressed in form of diadic products of complex eigen-forms $\mathbf{q}_k$. Taking into account the stationary part only the second term in parentheses in Eq. (5) can be crossed out. Then the correlation matrix of response can be expressed as follows:

$$\mathbf{K}_F(t) = \int_{-\infty}^{\infty} \mathbf{F}^*(\omega,t) \cdot \mathbf{S}_p(\omega) \cdot \overline{\mathbf{F}^{*T}(\omega,t)} \cdot d\omega = \int_{-\infty}^{\infty} \sum_{k,l=1}^{2n} e^{\mathrm{i}\omega t} \cdot \frac{\mathbf{q}_k \cdot \mathbf{q}_k^T \cdot \mathbf{H} \cdot \mathbf{S}_p(\omega) \cdot \mathbf{H}^T \cdot \mathbf{q}_l^T \cdot \mathbf{q}_l}{\left(\mathrm{i}\,\omega - \xi_k\right)\left(-\mathrm{i}\,\omega - \overline{\xi_l}\right)} \cdot d\omega \tag{6}$$

In order to evaluate the variance matrix time in Eq. (6) should be set zero. Square roots of diagonal elements of variance matrix are decisive to characterize the response due to the random excitation.

The matrix $\mathbf{S}_p$ in Eq. (6) is a matrix of spectral densities of the fluctuating component of the wind pressures being given by:

$$\mathbf{S}_p(\omega) = \int_A \int_A \mathbf{u}_o(P)\overline{\mathbf{u}_o^T(R)} \cdot S_{pu}(P,R,\omega)\, dA_P dA_R \tag{7}$$

Spectral density $S_{pu}(P, R, \omega)$ describes correlation of wind pressures between points P and R of the structure. It is defined considering Davenport's spectral density of wind speed's fluctuation in form:

$$S_{pu}(P,R,\omega) = c_D^2 \rho^2 v_P v_R A_P A_R \cdot 4K \frac{v_{10}^2 \cdot \Omega^2}{\omega(1+\Omega^2)^{4/3}} \cdot e^{-\frac{\omega}{v_{10} 2\pi}\sqrt{(C_x|x_P - x_R|)^2 + (C_z|z_P - z_R|)^2}} \tag{8}$$

where $\Omega = 1200\omega/(2\pi v_{10})$; K- the roughness coefficient; C_x, C_z - decay coefficients in respective directions; c_D - drag coefficient; ρ - air density; v_P - mean value of the wind speed in point P; v_{10} - mean value of the wind speed in ten meters above the ground; A_p - area corresponding to point P.

The proposed theoretical procedure has been used for calculation of the response of the real 100 m high-rise building, see Figure 1. The TMDs are installed at the top of both towers and tuned to the first eigen-value of the basic system. The dampers are modeled as concentrated masses with Kelvin-Voigt damping terms.

Factor of the damping non-proportionality of the system as a whole has been examined as follows: a set of various damping ratio of the TMDs (dashpot absorber) is used, while constant structural damping is kept. For every value of the TMD damping the correlation matrix of the response and root-mean-square (RMS) of the displacements at different levels have been evaluated. The final results are strongly affected by a number of eigen-forms of undamped system being taken into the consideration. This applies especially in case of random vibrations, because the influence of stochastic interaction of the eigen-forms is significant. Nevertheless the interaction of eigen-forms concerning non-proportionality of a deterministic system itself cannot be neglected. The influence of the non-proportionality factor can be observed at Figure 2. This figure represents the response of the building respecting first five eigen-forms. In the same time the figure demonstrates the outcome of the optimization process of TMD parameters.

The article presents an outline of an assessment method of a structure subjected to the random wind load component. The analysis is carried out using generalized coordinates following from the

conventional eigen-forms of an investigated structure. Energy contribution of individual eigen-forms decreases quickly with an increase of their order. It implies a possibility to limit quite easily a number of eigen-forms needed. It also leads to significant reduction of time consumption, when stochastic analysis should be done. The article highlights the necessity of prerequisite of non-proportional damping, when passive or active damping equipment (TMD) is installed into the structure. Also stochastic interactions of eigen-forms are significant although their influence decay exponentially with difference of eigen-form numbers.
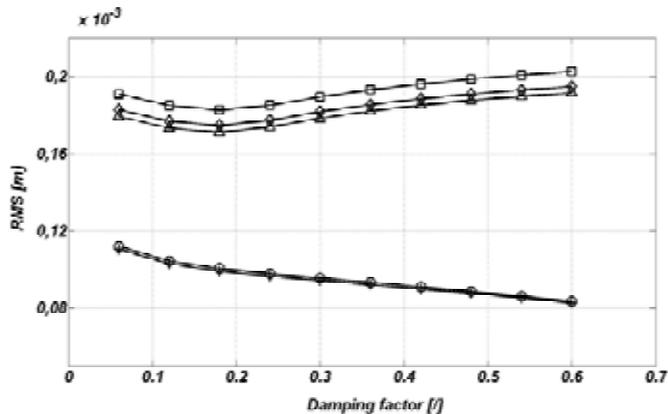
Figure 2: The RMS displacement of the top of the right tower as function of ζ_{TMD} for various number of eigen-modes under consideration

ACKNOWLEDGMENTS

REFERENCES

Davenport A.G. (1967). "The dependence of wind Loads on Meteorological parameters", Proc. International Research Seminar, Wind Effects on Buildings and Structures, Toronto Press, Toronto, Canada, 19-83.
Davenport A.G. (1967). "Gust loading factor", Jour. Struct. Div. ASCE, 93, 11-34.
Náprstek J. (1975)." On non-linear transfer between random variable velocity of fluid motion and frontal pressure on the bypassed cylindrical body", Acta Technica ČSAV, 4, 479-494.
Bolotin V.V. (1979). *Random vibrations of elastic systems* (Russian), Nauka, Moscow.
Koloušek V., Pirner M., Fischer O., Náprstek J. (1983): *Wind Effects on Civil Engineering Structures.* Academia - Elsevier, Praha.
Fischer O., Pirner M. (1987). *Dynamika kotvenych stozaru*, Academia, Praha.
Dyrbye C., Hansen S.O. (1996). *Wind loads on structures*, Wiley and Sons, Chichester.
Fischer P.(2000). "Eigensolution of nonclassically damped structures by complex subspace iteration", Computer Methods in Applied Mechanics and Engineering, Volume 189, Issue 1, 149-166.
Materazzi A.L., Venanzi I. (2005). "Wind response of cable stayed masts". Proc. The Fourth European & African Conference on Wind Engineering . ITAM ASCR, Prague, 10 pgs, CD ROM.
Náprstek J., Pospíšil S. (2006). "Along wind random vibrations of a slender structure - modelling by continuous elements", Proc. Engineering Mechanics 2006, ITAM ASCR, Prague, 8 pgs, CD ROM.
Simiu E., Scanlan R.H. (1996). *Wind Effects on Structures. Fundamentals and Applications to Design*, J. Wiley, New York.
Náprstek J., Pospíšil S. (2007). "Along wind random vibrations of a structure with non-proportional damping", Proc. 12th Int. Conf. Wind Engineering , Monash University, Cairns (Australia)

Wind-induced building interference: increase of wind loads on existing buildings after erection of new high-rises

G.M. van Uffelen

Peutz Ltd.- m.vanuffelen@mook.peutz.nl - PO Box 66, 6585 ZH Mook, The Netherlands

Keywords: wind interference, wind load, high-rises, literature, case studies

ABSTRACT

Because cities grow denser nowadays, new buildings more often have adverse effects upon the wind loading on existing buildings. It contributes to this effect that new buildings tend to get higher and higher at the same time. Figure 1 shows how a new building (left) can change the wind loading upon an existing building: the wind is forced around the building corners, thus generating turbulent eddies.
Wind loading upon buildings is determined according to Building Codes like the Eurocode or by conducting measurements in boundary layer wind tunnels. It mostly concerns the wind loading upon buildings under design, where the effect of existing buildings in the environment is sometimes taken into account as well. The opposite can however sometimes be of paramount importance.
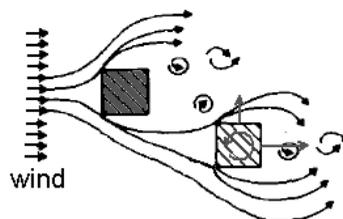
Figure 1: the left building changes the wind loading upon the right one.

The above-described mutual influence is called wind interference, the extent of which depends on the shape and size of the buildings, the distance between them and the roughness of the surrounding terrain. This paper discusses the practical and theoretical knowledge that can be found in scientific literature. Most of this knowledge has been acquired by wind tunnel experiments regarding scale models. Some case studies performed at Peutz Ltd. will be discussed as well and the findings of these experiments will be compared to literature data. It will be shown that more research is desirable on wind interference with respect to local dynamic pressures in particular.

Contact person: G.M. van Uffelen, Peutz Ltd., PO Box 66, 6585 ZH, Mook, The Netherlands,

phone +31 243570744, fax +31 243585150, m.vanuffelen@mook.peutz.nl

SCIENTIFIC LITERATURE ON WIND INTERFERENCE

Little attention is paid to wind interference in Building Codes, as Khanduri (1998) mentions. Bailey (1943) carried out pioneer research on the subject during the Second World War. Thereafter, it kept silent for two decades. When three cooling towers collapsed in the UK in 1965, the interest in wind interference increased substantial. A definition that follows from the resulting research is the interference factor, IF, defined as follows:

IF = wind load upon building in group / wind load upon solitary building   *(1)*

Mean and fluctuating forces and moments acting upon the main bearing structure as well as local pressures acting upon facade elements can be described by the IF. Many researchers used an experimental set-up as shown in figure 2. The position of the new building is varied along the X and Y axis and the existing one is fixed at the origin of the axis system. For each position of the new building the interference factor, IF, is measured.
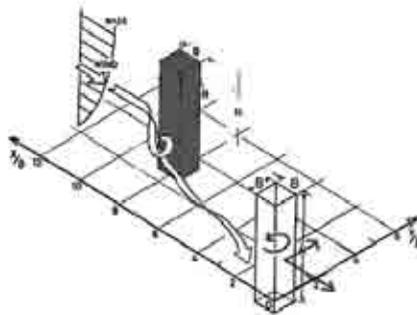
Figure 2: the grey building is the new building in the experimental set-up.

A good example of the effect of wind interference on the main bearing structure is the work of Taniike (1992). The interference factor is plotted for each location of the new building in figure 3. The left plot reveals to what extent the mean force can decrease as a result of shielding by the new building (solid). The fluctuating forces can however be doubled as shown in the right plot.
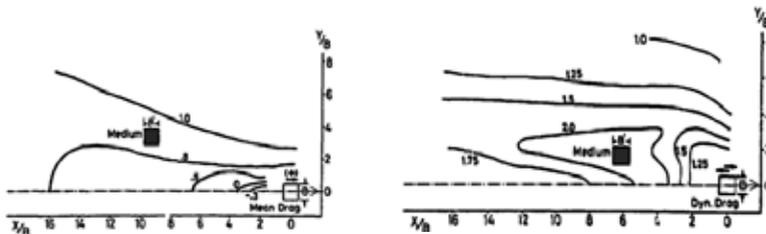
Figure 3: IF for mean and fluctuating forces parallel to wind.

A more recent example is the work of Xie & Gu (2007), who studied the effect of two new upwind buildings. The left graph in figure 4 shows the interference factor for mean moments and the right one shows the fluctuating component. Building C represents the existing one at a fixed position and building A has a fixed, unfavourable, position as well. The position of building B has been varied.
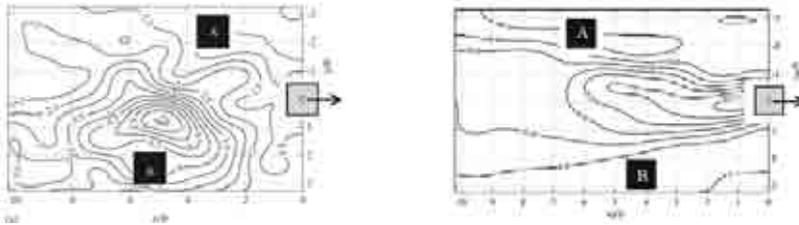
Figure 4: IF for mean and fluctuating moments acting upon building C.

The findings of Taniike (1992) show an increase of the peak forces parallel to the wind by 20 % as a result of the presence of one new building. The results discussed above show an increase of 120 % as a result of the presence of two new buildings. This means a doubling of the design load.

The effect of new buildings upon the local pressures at facade elements of the existing ones is at least as important. Taniike (1992) found a considerable increase of fluctuating pressures, as can be seen in the right plot of figure 5. A striking difference between local pressures and forces and moments is that mean local pressures can be augmented considerably as well.
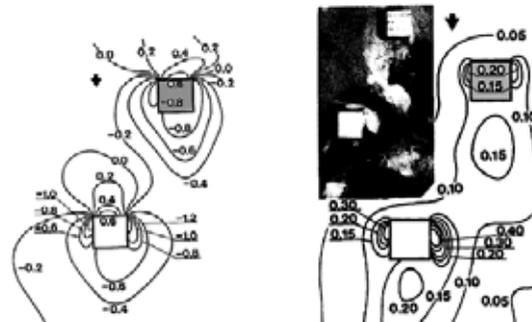
Figure 5: mean and fluctuating pressures (C_p) at combination of two high rise buildings.

CASE STUDIES

Peutz Ltd. have undertaken several wind tunnel studies regarding wind interference, all of which are specific case studies for building plans. A closed boundary layer wind tunnel with a cross section of $3,2 \times 1,8$ m^2 that can generate a mean wind speed in excess of 25 m/s has been used. The measurements as well as the following extreme value analysis and the interpretation of the findings are carried out conforming to the Dutch CUR Recommendation C 103 (2005).

Wind tunnel experiments are carried out in order to determine the effect of a new residential tower upon the roof of the Amsterdam ArenA stadium. The construction engineers of ARCADIS have applied all simultaneously measured time series of fluctuating pressures to a ESA Win finite element model of the steel roof construction. The forces that the roof is imposing upon the large concrete pylons at the corners of the stadium were shown to be limited. However, an increase of local pressures at the envelope of the roof in excess of 30 % has been revealed by this experiment. This made several modifications to the roof cladding and the supporting structure necessary.
   Nevertheless, the value of IF, is somewhat smaller than expected based on data of Taniike (1992). This can be explained by the large amount of turbulence in the approaching wind that is already generated by the dense buildings in the surroundings of the stadium, as shown by Taniike and

others, Besides that, it already yielded high-pressure peaks at the roof in the current situation.

Purpose of a wind tunnel study on the wind loading of the ABN AMRO head office was to determine the effect of new high-rise buildings upon the main bearing structure and the facade cladding. Currently, this effect can be felt in the ABN AMRO head office, whereas this seemed not be the case in the past.

The experiments have revealed that only the torsion moment around the vertical centre line has somewhat been increased. Local pressures at the upper half of the facades increase considerably, the peak suction has risen from 2000 to 3500 Pa. Many other measurement positions benefit from the shielding effect caused by the new buildings.

The influence of the new buildings upon the maximum local pressures matches quite well with the findings of Taniike (1992). The centre-to-centre distance of the buildings approximately amounts to four times the diameter and the maximum increase of local pressures amounts to approximately 70 %. The effect upon the main bearing structure as reported by Xie & Gu (2007) is not at all confirmed by this case study. However, in their experiments the relative height of all buildings was one and a half times higher. Moreover, in this case study there were some more large additional buildings to the west of the new high-rises under development, which possibly had a favourable effect. A clear similarity between either result is that the mean forces and moments tend to decrease whereas the fluctuating parts are augmented.

CONCLUSIONS

The first conclusion that can be drawn from this study is that the impact of wind interference can be considerable, but that the extent might differ greatly among different situations. One can state that in the elaborated case studies and the cited literature findings, the local pressures tend to be augmented by an increase of building density, whereas the peak forces and moments at the main bearing structure tend to benefit from the shielding effect caused by new upwind buildings. Fluctuating components as such often are augmented which is as well deemed significant, because they can yield uncomfortable vibrations or material fatigue.

It is not simple to deduce dedicated design data from the scientific literature, particularly with respect to local pressures acting upon facade cladding systems. Therefore, case studies are deemed necessary for many building plans.

Furthermore, supplementary systematic scientific research is desirable to gather more generalised data. Long lasting on-site measurements regarding wind interference are of paramount importance in order to improve the reliability of the wind tunnel experiments regarding wind interference.

REFERENCES

Khanduri A.C., Stathopoulos T., Bedard C., Wind-induced interference effects on buildings – a review of the state-of-the-art, Engineering Structures. Vol. 20 No. 7 (1998) 617-630

A. Bailey, N.D.G. Vincent, Wind pressures on buildings including effects of adjacent buildings, J. Civil Engineering 20 (8) (1943) 243-275

Taniike -interference mechanism for enhanced wind forces on neighbouring tall buildings, J. Wind Eng. Ind. Aerodyn. 41-44 (1992) 1073-1083

Xie Z.N,, Gu M, Simplified formulas for evaluation of wind-induced interference effects among three tall buildings, J. Wind Eng. Ind. Aerodyn. 95 (2007) 31-52

Sun T.F., Gu Z.F., Interference between wind loading on group of structures, J. Wind Eng. Ind. Aerodyn. 54/55 (1995) 213-225

CUR Recommendation C 103, Windtunnel measurement of wind loads on (high-rise) buildings and construction parts, 2005

Time domain analysis of soil-structure-damper system under wind excitation

1st Ming-Yi Liu[*], 2nd Chi-Min Liu

1st Department of Civil Engineering, Chung Yuan Christian University─myliu@cycu.edu.tw─Taiwan

2nd General Education Center, Chienkuo Technology University─cmliu@cc.ctu.edu.tw─Taiwan

Keywords: wind-induced vibration; tuned mass damper; soil-structure interaction; high-rise building

ABSTRACT

In this research, a mathematical model is proposed for predicting wind-induced response of a building with a tuned mass damper (TMD) when soil-structure interaction (SSI) is considered. It may reasonably reflect soil characteristics. Furthermore, TMDs are effective devices for reducing structural vibration. This study may help researchers to more accurately evaluate wind-induced oscillation of high-rise buildings with SSI as well as select appropriate TMDs in controlling structural response.

Although much work has been done concerning SSI in earthquake engineering, few researchers have studied the effects under wind load. In this research, therefore, a mathematical model is proposed for predicting wind-induced vibration of a high-rise building with a TMD when SSI is taken into account. This model is based on time domain analyses. Numerical examples are also conducted to evaluate the effectiveness of TMD in controlling structural response.

A N-story structure with a TMD considering SSI can be simulated as a shear building model (see Fig. 1). A rigid circular foundation on surface ground is used in this study. The high-rise building is supported by the foundation with swaying and rocking dashpots and corresponding springs. Furthermore, we assume that dynamic mechanisms of building, TMD and foundation in along-wind direction are the same as across-wind direction. M_i, C_i, K_i, I_i and $X_{i_k}(t)$ $(k = x, y)$ are mass, damping, stiffness, mass moment of inertia and time histories of displacement on the i-th floor for the building, respectively. In this research, subscripts k $(= x, y)$ individually denote along-wind and across-wind directions. M_{TMD}, C_{TMD}, K_{TMD} and $X_{TMD_k}(t)$ $(k = x, y)$ represent corresponding parameters of the TMD. M_0 and I_0 are defined as mass and mass moment of inertia for the foundation, separately. C_s and C_r denote damping of swaying and rocking dashpots, while K_s and

---

[*] Contact person: 1st Ming-Yi Liu, Department of Civil Engineering, Chung Yuan Christian University,

No. 200, Chung Pei Road, Jhongli City, Taoyuan County 32023, Taiwan, +886-3-265-4211 and +886-3-265-4299

E-mail myliu@cycu.edu.tw

K_r represent stiffness of corresponding springs. Time histories of displacement and rotation for the foundation are defined as $X_{0_k}(t)$ and $\theta_{0_k}(t)$ $(k = x, y)$, respectively. Z_i is elevation on the i-th floor of the building. The equation of motion can be generated by Lagrange's equation, that is;

$$[m]\{\ddot{x}_k(t)\} + [c]\{\dot{x}_k(t)\} + [k]\{x_k(t)\} = \{f_k(t)\}, \tag{1}$$

where $[m]$, $[c]$ and $[k]$ are mass, damping and stiffness matrices of the (N+3) degrees-of-freedom oscillation system, separately. $\{f_k(t)\}$ and $\{x_k(t)\}$ $(k = x, y)$ are both (N+3) dimensional vectors individually denoting time histories of wind load and displacement for the system. $[m]$, $[k]$ and $[c]$ can be presented, respectively, such that;

$$[m] = \begin{bmatrix} [M]_{N\times N} & \{0\}_{N\times 1} & \{M\}_{N\times 1} & \{MZ\}_{N\times 1} \\ & M_{TMD} & M_{TMD} & M_{TMD}Z_N \\ & & M_0 + \sum_{i=1}^{N} M_i + M_{TMD} & \sum_{i=1}^{N} M_i Z_i + M_{TMD}Z_N \\ \text{symmetry} & & & I_0 + \sum_{i=1}^{N}(I_i + M_i Z_i^2) + M_{TMD}Z_N^2 \end{bmatrix}, \tag{2}$$

$$[k] = \begin{bmatrix} [K]_{N\times N} & \{K_{TMD}\}_{N\times 1} & \{0\}_{N\times 1} & \{0\}_{N\times 1} \\ & K_{TMD} & 0 & 0 \\ & & K_s & 0 \\ \text{symmetry} & & & K_r \end{bmatrix}, \tag{3}$$

$$[c] = \begin{bmatrix} [C]_{N\times N} & \{C_{TMD}\}_{N\times 1} & \{0\}_{N\times 1} & \{0\}_{N\times 1} \\ & C_{TMD} & 0 & 0 \\ & & C_s & 0 \\ \text{symmetry} & & & C_r \end{bmatrix}. \tag{4}$$

Rayleigh proportional damping is considered in this research. Therefore, damping matrix of the N-story structure $[C]_{N\times N}$ can be expressed as the linear combination of mass and stiffness matrices of the building, that is;

$$[C]_{N\times N} = A_0 [M]_{N\times N} + A_1 [K]_{N\times N}, \tag{5}$$

where A_0 and A_1 are both Rayleigh damping coefficients. $\{f_k(t)\}$ $(k = x, y)$ can be expressed as below;

$$\{f_k(t)\} = \left\{ \{F_k(t)\}_{N\times 1}, 0, \sum_{i=1}^{N} F_{i_k}(t), \sum_{i=1}^{N} F_{i_k}(t)Z_i \right\}, \tag{6}$$

where $F_{i_k}(t)$ $(k = x, y)$ represent time histories of wind load on the i-th floor for the building. $\{x_k(t)\}$ $(k = x, y)$ can be written as follows;

$$\{x_k(t)\} = \{X_{1_k}(t), X_{2_k}(t), \cdots, X_{i_k}(t), \cdots, X_{N_k}(t), X_{TMD_k}(t), X_{0_k}(t), \theta_{0_k}(t)\}^T. \tag{7}$$

Optimal parameters of TMD can be evaluated based on dynamic mechanisms of the building in the fundamental mode (Sadek et al., 1997). Furthermore, we can calculate swaying and rocking dashpots and corresponding springs of the foundation from soil parameters (Poisson's ratio ν_s, density ρ_s, shear-wave velocity V_s and shear modulus G_s) and radius of the foundation R_0, respectively (Wolf, 1994). On the basis of the previous research (Shinozuka & Jan, 1972), $F_{i_k}(t)$ $(k = x, y)$ can be individually simulated according to Davenport's along-wind load spectrum (Davenport, 1961) and Ohkuma & Kanaya's across-wind load spectrum (Ohkuma & Kanaya, 1978). Under these conditions, $X_{i_k}(t)$ $(k = x, y)$ can be evaluated through Newmark integration method. Then, we can use statistic approaches to calculating RMS (peak) displacement on the i-th floor of the building X'_{i_k} $(\hat{X}_{i_k})$ $(k = x, y)$. Corresponding acceleration $\ddot{X}'_{i_k}$ $(\hat{\ddot{X}}_{i_k})$ $(k = x, y)$ can be similarly determined. Finally, we employ response ratio R_r (defined as the proportion of controlled to uncontrolled vibration of the building) to assess the effectiveness of TMD.

To illustrate the proposed method in section 2, a 40-story building with a TMD is presented to calculate structural vibration. The foundation is assumed to be on three kinds of ground states including soft, medium and dense soil. Furthermore, the structure with fixed base is also considered. Given these assumptions, the effectiveness of TMD can be analyzed in these conditions.

Breadth, depth and height of the building are 40 m, 40 m and 160 m, respectively. M_i and I_i $(i = 1,2,\ldots,40)$ are 9.80×10^5 kg and 1.31×10^8 kg-m^2, separately. Stiffness decreases linearly with an increase in elevation. K_1 and K_{40} are 2.13×10^9 N/m and 9.98×10^8 N/m, respectively. A_0 and A_1 are 0 and 0.02, separately. Table 1 presents generalized parameters of the building for the first mode. Moreover, parameters of TMDs are shown in Table 2. R_0, M_0 and I_0 for the foundation are 20 m, 1.96×10^6 kg and 1.96×10^8 kg-m^2, respectively. Parameters of soil and foundation are summarized in Table 3 and Table 4, separately. The building is assumed to be in an urban area. Therefore, power-law exponent α and roughness coefficient K_0 are 0.36 and 0.025, respectively.

Table 5(a) and Table 5(b) individually display RMS response and peak oscillation on the 40th floor of the building under wind load when SSI is considered. X'_{40_k}, $\ddot{X}'_{40_k}$, $\hat{X}_{40_k}$ and $\hat{\ddot{X}}_{40_k}$ (k = x, y) with fixed base conform closely to the case in which foundation is on dense soil. In addition, these values decrease as soil stiffness decreases. It shows that SSI may be neglected when soil is extremely stiff. On the other hand, structural vibration is overestimated for small value of soil stiffness when SSI is ignored. Consequently, this model may reasonably reflect soil characteristics. Furthermore, it may be used to more correctly evaluate structural response than the fixed-base model does.

To investigate the effectiveness of TMD to suppress RMS (peak) oscillation in both along-wind and across-wind directions, we discuss variations in vibration ratio R_r over μ for a variety of soil types, as illustrated in Figure 2(a) through Figure 2(d), separately. These four diagrams suggest that R_r with fixed base is close to the case in which foundation is on dense soil. Moreover, an increase in soil stiffness leads to an decrease in R_r. These data reveal that SSI may be neglected and TMD has significant advantages when soil is very stiff. On the contrary, SSI cannot be ignored for small value of soil stiffness. Otherwise, the effectiveness of TMD is underestimated, which may affect structural safety and comfort of building's occupants. TMD therefore more effectively reduces structural response for higher value of soil stiffness. Furthermore, R_r decreases as μ increases. This reduction is due to greater inertia force and higher damping effects caused by incremental mass of TMD. As a result, TMD with greater mass is more useful in controlling structural oscillation under wind load. In addition, it is more useful in suppressing across-wind vibration than along-wind response. These four diagrams also imply that TMD is more advantageous for reducing acceleration than displacement of the building.

This study may help researchers to more accurately predict wind-induced oscillation of buildings with SSI as well as select appropriate TMDs in controlling structural vibration. It may also improve the understanding of wind resistant designs for high-rise buildings.

REFERENCES

Sadek, F., Mohraz, B., Taylor, A.W., Chung, R.M., 1997. A method of estimating the parameters of tuned mass dampers for seismic applications. Earthquake Eng. Struct. Dyn. 26 (6), 617-635.
Wolf, J.P., 1994. Foundation vibration analysis using simple physical models. Prentice-Hall, Englewood Cliffs, New Jersey.
Shinozuka, M., Jan, C.M., 1972. Digital simulation of random processes and its applications. J. Sound and Vib. 25 (1), 111-128.
Davenport, A.G., 1961. The spectrum of horizontal gustiness near the ground in high winds. Q. J. R. Meteorol. Soc. 87, 194-211.
Ohkuma, T., Kanaya, A., 1978. On the correlation between the shape of rectangular cylinders and characteristics of fluctuating lifts on them. In: Proceedings of the Fifth Symposium on Wind Effects on Structures, Tokyo, Japan, pp. 147-154 (in Japanese).

The Solar Updraft Power Plant: Design and Optimization of the Tower for Wind Effects

H.-J.Niemann[1], F.Lupi[2], R.Hoeffer[3], W.Hubert[1], C. Borri[2]

[1] *Niemann & Partner Consultants – Niemann@IGNundP.de – Universitaetsstrasse 142, D-44799 Bochum –* [2] *Università degli Studi di Firenze – francescalupi@alice.it – 501139 Firenze,* [3] *Ruhr-Universitaet Bochum – ruediger.hoeffer@rub.de – D-44780 Bochum*

Keywords: ultra-high towers, wind at high altitudes, mean and fluctuating wind load, structural optimization for wind induced stresses

ABSTRACT

Solar chimney power plants (SCPP) transform thermal energy from solar irradiation into electric power, as discussed in more detail by von Backström et al. (2008). The sun heats the air under a large glass roof, called the collector. The heated air is entrained into a central chimney and then released into great atmospheric heights. This flow of warm air drives turbo-generators at the chimney foot producing electric power. During service, these plants do not need any fuel and are completely free of carbon dioxide emissions. The cost of the electric current fed into the net is nearly exclusively caused by the investment costs in the roof and tower structures, and the turbines. The sun energy drives the process at no expense, maintenance costs are small. The cost per kWh decreases as the dimension of the SCPP increase, mainly due to an increase of efficiency in the thermodynamic process. That is why at present the layout of prospective SCPPs envisages towers up to 1,500 m in height and collectors up to 7 km in diameter. The skepticisms raised whether the technology to build a tower of more than 1000 m in height exists already to-day, has been rectified to some extent at least, since the Burj Dubai Tower is under construction and investors in the Emirates plan even higher towers. Intended service lives of the SCPP are 80 to 120 years, admitting renewals of the turbo-generators and parts of the glass-roof. In addition, concepts have been developed to use the perimeter under the collector roof as a glass house.

The German civil engineer Joerg Schlaich collected service experience from a 50 kW prototype plant which he constructed in 1982 in Manzanares/Spain. His SCPP had a 200 m tower and operated successfully for more than 6 years. Since those days, projects for SCPPs have been developed in arid zones all over the world, but none of them has been brought to realization, up to now.

The wind loading dominates largely the tower costs and thus the economic feasibility of this technology. It is the focus of the present article. The authors discuss in detail the properties of the natural wind flow at high altitudes and present recent research and development regarding the

---

Contact person: 1st Author, Niemann & Partner Consultants, Technologiezentrum Ruhr, Universitaetsstr.142, D-44799 Bochum, Tel. 49 234 9048680, FAX 49 234 9048689   E-mail Niemann@IGNuP.de

stochastic wind pressure fluctuations and the structural response to wind gustiness. They deal with vortex shedding and possible dynamic effects on the tower and finally with the wind loading of the collector roof.
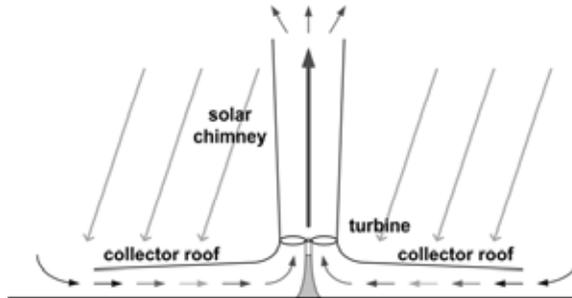
Figure 1: Building components of an SCPP: The central solar chimney and the collector roof

The wind load on the solar chimney (SC) with a height of 1000 m and more cannot be treated as a static gust wind load which is usually an effective and sufficient method. Rather, it must be separated into its mean and fluctuating components. This approach requires in particular reliable information on the structure of wind turbulence which controls the dynamic wind forces. Unfortunately, there is a lack of wind data for heights larger than 300 m above ground applicable to the wind resistant design of structures. However, theoretical models of the turbulent wind beyond 300 m derived from the theories of the Prandtl and the Ekman layers are available and applied as adequate engineering approach following the work of Harris and Deaves (1980).

The tower structure is a hyperbolic or a circular cylindrical shell (or a combination of both) made of reinforced concrete. The aspect ratio is ca. $H/D = 7$, the smallest shell thickness is in the order of 25 to 30 cm. An appropriate number of horizontal ring beams stiffens the shell ensuring largely the circular shape of the cross section. They are vital for improving the distribution of the shell stresses around the circumference and for reducing the local stress maxima.
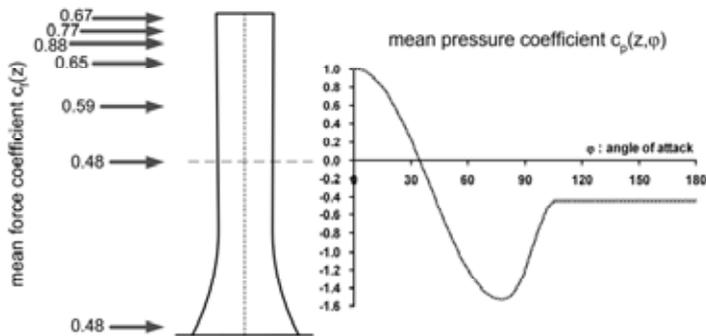
Figure 2: Distribution of wind force coefficients over the tower height

The distribution of the mean wind pressures depends on the very high Reynolds number, which is in the order of $Re \approx 4 \cdot 10^8$ and the wind profile. Full scale measurements at Natural Draught Cooling Towers have approximated such values, Niemann (1993), and provide a basis to derive static and dynamic pressure distributions for the solar tower. As is well known from full scale and wind tunnel tests, surface roughness has in addition an important effect on the mean pressure distribution. This applies not only in the range of critical Reynolds numbers but as well at very high transcritical Re. Surface roughness determines the flow separation and consequently the suction maximum. Similar to Cooling Towers, the effect of magnitude and position of the peak suction on the wind induced

stresses is pronounced also for the SC. The authors discuss this effect and show the optimal solution of surface roughness for the SC.

The rms. Pressure fluctuations and their correlations are the basis to calculate the quasi-static shell stresses induced by turbulence. This approach – called co-variance method – relies on statistical averages obtained from measured time series rather than on the time series themselves. It is preferred here instead of calculating the response in the time domain. The authors show that resonant amplification of the structural response is not relevant and propose to account for resonance-with-turbulence by a dynamic factor. The distribution of the rms. Pressure over the SC surface is derived from full scale data obtained experimentally for TV-towers and cooling towers and referred to turbulence intensity.
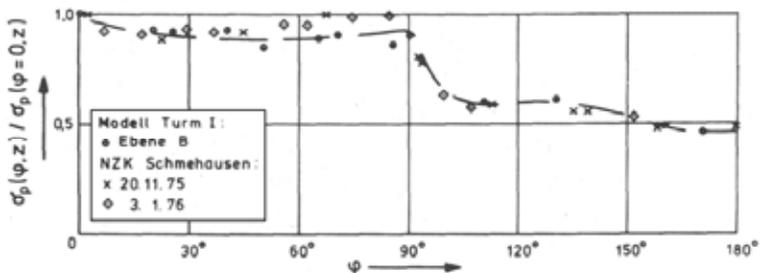
Figure 3: Rms. Pressure distribution at level z

Furthermore, the authors develop a model of the correlation matrixes along each circumference and over the tower height. It is based on previous wind tunnel tests and related to the scales of turbulence. From these data, the gust response factor for any stress or deflection may be calculated. It is then the basis of one or several equivalent static loads which serve as the wind loading input to the detailed design calculations.

Regular vortex excitation will occur at the tower top with large effective correlation length due to a rather smooth flow with small turbulence intensity. Fortunately, both bending nor ovalling oscillation modes will come to a resonant condition as long as the natural frequencies are sufficiently high and the extreme wind speeds at the tower top do not reach the critical wind speed.
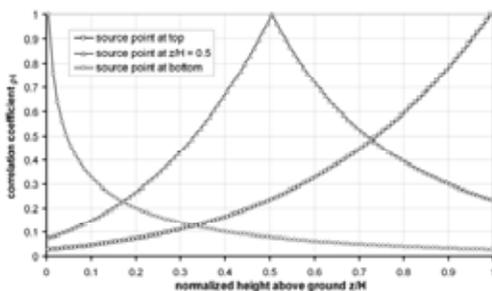
Figure 5: Pressure correlation over the tower height
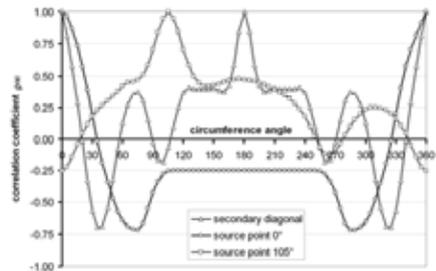
Figure 4: Pressure correlations along the circumference for various reference points

The panels of the glass roof are generally loaded with respect to separated scenarios of the flow regimes upside the panels and beneath. In a regular service the pure flow of heated air below the roof from the collector's outer edge towards the inner diameter attains only low operational flow speeds. An optimized roof shape can avoid relevant accelerations of the internal flow towards the inlets at the chimney's base, s. Pretorius & Kröger (2006). However, possible separations of the flow of heated air

beneath the roof can generate zones of decreased static pressure. In such cases, local suction and gravity load the panels in the same direction. In addition, friction forces, which are generated from the flow beneath the large inner surface of the glass roof, and drag forces on the supports gain importance for the overall stability of the roof. Friction coefficients of 0.0044 up to 0.0052 and mean drag coefficients of 1.0 have been considered by Pretorius and Kröger (2006). A wind flow upside the roof generates both zones of increased pressure and relevant uplift forces at the panels due to stagnation, flow separations, flow parallel to the roof, and vortices shed from the tower which travel downstream over the roof. Fig. 6 shows isolines of mean pressure coefficients and r.m.s. values of pressure coefficients distributed over the roof area in the stagnation zone, at the flanks and in the wake around the base of the tower.

The flow stagnation at the windward side of the tower leads to a positive pressure gradient at the roof in the symmetry line. A necklace vortex system develops around the tower base, a recirculation zone is formed on the leeward side of the tower base, and v. Kármán vortex cells as well as other vortices travel downstream. The isolines of the mean resulting pressures in Fig. 6 quantify the roof pressure at the windward side of the tower and the suction in the wake zone for a typical situation. The r.m.s. values represent the effect of the vortex cells which can travel downstream in mean wind direction over a distance of several multiples of the base diameter of the tower.
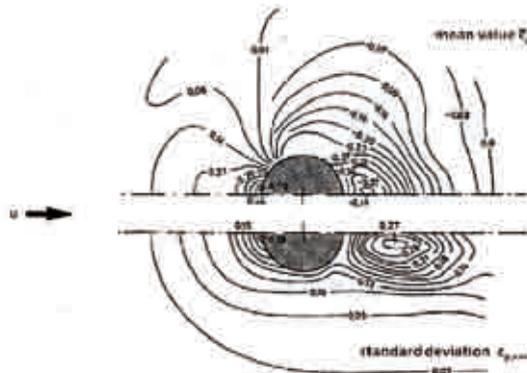
Figure 6: Pressure distribution on ground level for a boundary layer flow around a cylinder, Hölscher (1993)

REFERENCES

Harris, R.I., & D.M. Deaves (1980). The Structure of Strong Winds, Proceedings CIRIA Conf., London.

Hölscher, N. (1993). Ein multivariater Ansatz für die aerodynamische Übertragungsfunktion der Winddrücke in atmosphärischer Grenzschichtströmung, Technical Reports No. 93-3, Institute of Structural Engineering, Ruhr University Bochum.

Niemann, H.-J. (1993). Windwirkungen auf hohe Schalenkühltürme. Bautechnik in Wärmekraftwerken, pp. 248 – 269. Verlag VGB-Kraftwerkstechnik, Essen.

Pröpper, H. (1977). Zur aerodynamischen Belastung großer Kühltürme, Technical Reports No. 77-3, Institute of Structural Engineering, Ruhr University Bochum.

von Backström, Th.W., Harte, R., Höffer, R., Krätzig, W.B., Kröger, D.G., Niemann, H.-J., van Zijl, G.P.A.G. (2008). State and Recent Advances in Research and Design of Solar Chimney Power Plant Technology, VGB PowerTech 88, 64-71.

Pretorius, J.P., Kröger, D.G. (2006). Solar Chimney Power Plant Performance, Transactions of the ASME, Vol. 128, August, pp. 302-311.
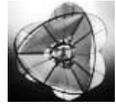
Dynamic response and wind loads of a tall building based on wind tunnel tests

Gisella Tomasini, Lorenzo Rosa, Alberto Zasso

Politecnico di Milano, Dipartimento di Meccanica – gisella.tomasini@polimi.it – via La Masa 1, 20156, Milano, Italy.

Politecnico di Milano, Dipartimento di Meccanica –lorenzo.rosa@polimi.it – via La Masa 1, 20156, Milano, Italy.

Politecnico di Milano, Dipartimento di Meccanica – alberto.zasso@polimi.it – via La Masa 1, 20156, Milano, Italy.

Keywords: wind tunnel testing, tall building, wind load, comfort level, modal numerical simulation

ABSTRACT

This paper presents the research activities carried out on a tall building, designed for office use. The goal of the study is to calculate the maximum displacements and accelerations of the tower caused by the turbulent wind and use these data to check the comfort level and to calculate the wind loads. The displacement and acceleration time histories are obtained using a multi-modal numerical simulation applied using time-space pressure distribution and building modal parameters. The first information are acquired experimentally from a wind tunnel experimentation. The second are obtained numerically from a Finite Element Model of the tower. The study has benn carried out at the Boundary Layer Wind Tunnel of the Politecnico di Milano, Italy.

The dynamic response of the structures can be evaluated fully analytically using codes and formulas, for instance ASCE (2008) or Eurocode1 (2004). However, these codes provide good guidance for calculating the along-wind response but little guidance for the critical across-wind and torsional responses. This could be partially attributed to the fact that the across-wind and torsional responses, unlike the along-wind, are given mainly by the aerodynamic pressure fluctuations in the separated shear layers and the wake flow fields, which have prevented, to date, any acceptable direct analytical relation to the oncoming velocity fluctuations, NatHaz, (2008). Also, these methods have limitations when there are other tall building in the vicinity. Moreover, responses are restricted to the

---

Contact person: Lorenzo Rosa, Politecnico di Milano, via La Masa 1, 20156 Milano, Italy.
tel: +390223998076; fax: +390223998081; E-mail: lorenzo.rosa@polimi.it

first and second modes. For these reasons, a wind tunnel study, associated with a multi-modal numerical simulation, is a valid alternative to calculate the response of a structure.
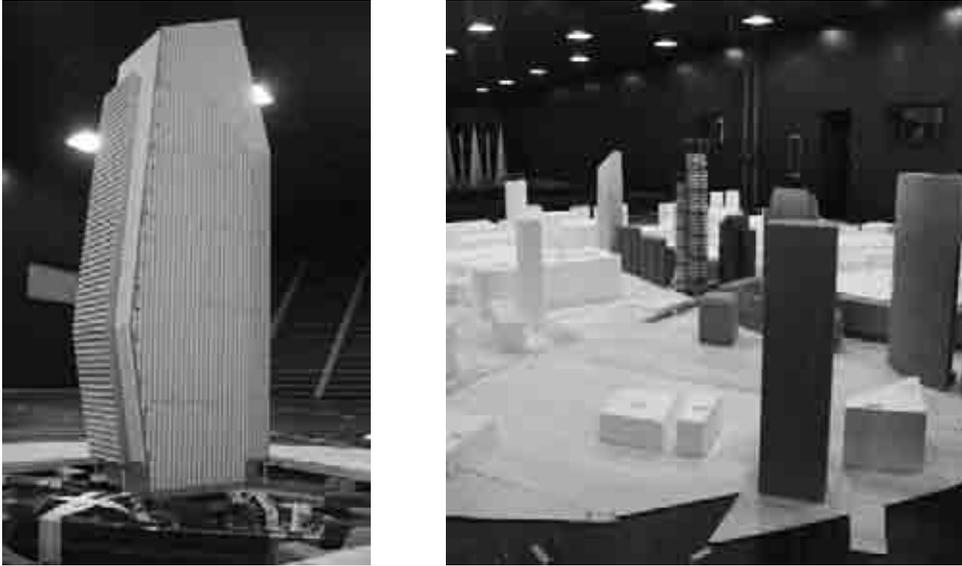
Figure 1: The model of the Tower in the Wind Tunnel, alone and with the surrounding.

The tower, which is 138 meters high in full-scale, is scaled with a ratio of 1:100 and it is instrumented with 208 pressure taps. The sampling frequency is 100Hz and the time history length is 100s (model scale).

In order to simulate the correct turbulence and wind speed vertical profile, passive turbulence generators (spires and roughness elements) and the surrounding buildings in an circumference of 600m (full-scale) around the new tower, are also placed in the wind tunnel, Figure 1.

The numerical analysis is carried out in the time domain, by step by step numerical integration of the motion equations of the tower, known the pressure measurements in correspondence of the pressure taps. The length of the time histories of the pressures (more than 4500s in real scale) was verified being statistically adequate for the structure, in agreement with the scale factors and the design wind speeds.

Equations of motion governing the behavior of the structure under wind loads are:

$$\mathbf{M\ddot{X}} + \mathbf{C\dot{X}} + \mathbf{KX} = \mathbf{F}(t) \tag{1}$$

where $\mathbf{X} = [\mathbf{x}\ \mathbf{y}\ \mathbf{z}]^{T}$ is a $3n \times 1$ vector and n is the number of nodes while $\mathbf{x, y,}$ and $\mathbf{z}$ are vectors of nodal displacements in x, y, and z directions respectively.

The time history of the pressure forces, $\mathbf{F}(t)$, acting at each external surface node is obtained by integrating the wind pressure over the corresponding effective surface area to give the three components of the force. Using simple steps, the previous eq.(1) can be written as:

$$\mathbf{\Phi}^{T}\mathbf{M\Phi}\ \ddot{\mathbf{q}} + \mathbf{\Phi}^{T}\mathbf{C\Phi}\ \dot{\mathbf{q}} + \mathbf{\Phi}^{T}\mathbf{K\Phi}\ \mathbf{q} = \mathbf{\Phi}^{T}\mathbf{F}(t) \tag{2}$$

where, using the first three modal shape in the analysis, $\mathbf{\Phi}$ is (3n x 3) matrix of eigenvectors, $\mathbf{q}$ is (3 x 1) vector of generalized displacements and $\mathbf{\Phi_{i}^{T}}\mathbf{F}(t) = \mathbf{Q_{i}}(t)$ is the generalize force of the ith

mode. By assuming the damping matrix **C** as a proportional damping, the above equations results into three uncoupled equations, solved using Simulink. The response, in terms of time history of displacements and accelerations of the real structure, can so be evaluated using eq.(3):

$$\mathbf{X} = \mathbf{\Phi q}$$

$$\ddot{\mathbf{X}} = \mathbf{\Phi \ddot{q}}$$

(3)

The accelerations $\ddot{\mathbf{X}}$ calculated in some particular point at the top-floor of the building represent the first results of the analysis. In order to compare these accelerations with the maximum comfort values given by the codes, the results are expressed, as suggested in Kwok (2008), in peak-accelerations calculated as 3.5xRMS of the time history. Figure 2 shows an example of this study, in term of peak acceleration of one point at the top floor of the tower in x and y direction. Three different values of damping ratio h were used: h=1%, 2% and 4%.
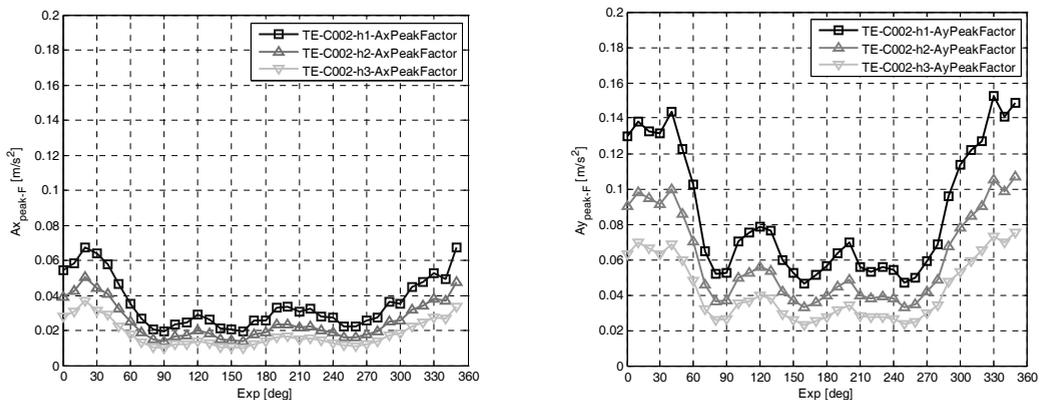
Figure 2: Point at the top-floor: peak-accelerations (3.5xRMS) in x and y direction in function of the exposure angle. Damping h=1%, 2%, 4%.

In the second part of the research, through the modal approach over described, the "load cases" for the considered building are identified in terms of shears, bending moments and torque at base point: these load cases are the most significant combination of the loads for all the considered exposure angles. Moreover, for each "load case", the vertical distribution of the wind loads and the corresponding distributed sectional loads (that is the sum of the external and the inertial load, calculate for each section) to apply to the building to result in the same shears, moments and torques, are calculated.

In order to conduct this study, a lumped parameters model of the tower is made. According to the modal approach over described, the response of the tower to the turbulent wind is calculated in terms of accelerations in correspondence of the nodes of the lumped parameters model. Known the mass and the inertial data of these nodes, it is finally possible to calculate the time-histories of the inertial loads in each node.

As previously described, starting from the same pressure time-histories measured in correspondence of the taps, the time-histories of the external forces are obtained by integrating wind pressure over the corresponding effective surface area.

Obtained the inertial and external loads, the time-histories of the overall wind loads (shears F_x and F_y, bending moment M_{xx} and M_{yy} and torque M_{zz}) at the base of the tower are calculated. As an example, Figure 3 shows the instant values of M_{xx} vs. M_{yy} calculated at base point. From this Figure, the twenty worst loads conditions are identified (numbered points) as "load cases" for the verification of the building.

For each "load case", the vertical distribution of the wind loads and the sectional loads are calculated. As an example, considering the "load case 28", Figure 4 shows the wind load as vertical distribution of the bending moment in *x*-direction in terms of comparison between the total component, the component associated to the external pressure loads and the component associated to the inertial loads.
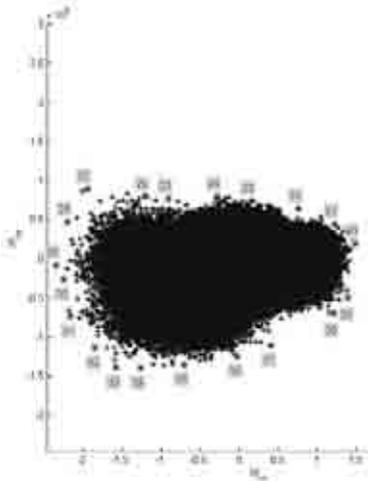
Figure 3: Bending moments M_{xx} as a function of M_{yy} at base point for all wind exposures: worst conditions identified (numbered points).
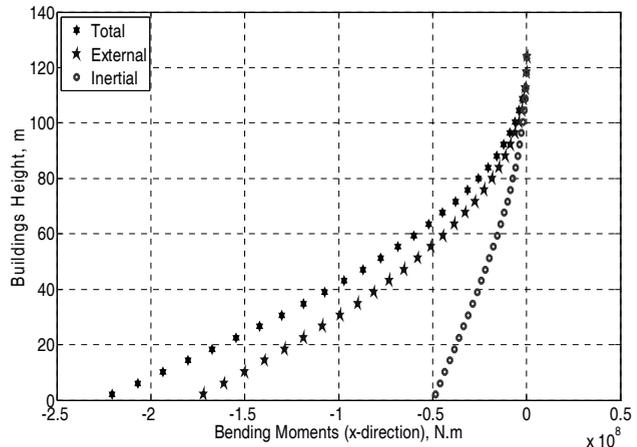
Figure 4: "Load case 28": vertical distribution of total bending moment M_{xx}, moment associated only to the external pressure loads and moment associated only to the inertial loads.

CONCLUSIONS

Developments in civil and mechanical engineering have led to designs that satisfy strength requirements but that are often very flexible. These flexibilities could led unfavorable dynamic responses on the occupants comfort when the structure is subjected to dynamic loads like turbulent winds. The method described in this article shows how it is possible to combine a modal approach analysis, with experimental wind tunnel test in order to simulate the dynamic of a tall building, and suggests a procedure for the identification of significant "load cases" to be used as references for structural evaluations. These "load cases", accounting for the external loads as well as the inertial loads, evidence the very different role played by the inertial loads in determining the load conditions, depending on the wind interaction characteristics, i.e. the exposure angle or vortex shedding effects.

REFERENCES

ASCE, American society of civil engineers (2008). "Minimum design loads for buildings and other structures. SEI/ASCE 7-02", Reston, Virginia.
Eurocode 1, (2004). "Actions on structures - Part 1-4: General actions - Wind actions. prEN 1991-1-4, European Standard.
NatHaz, (2008). Aerodynamic Loads Database, http://aerodata.ce.nd.edu/.
C. S. Kwok, (2008). "Motion simulator study on effects of wind-excited tall building motion on occupants" presented at Wind effects on buildings and urban environment, Tokio, Japan.

Numerical Simulation of the Dynamic Wind Loading on and Response of Tall Buildings

J Revuz*, D M Hargreaves and J S Owen

University of Nottingham, Faculty of Engineering, Coates Building, University Park, Nottingham NG7 2RD, United Kingdom
evxjr2@nottingham.ac.uk, david.hargreaves@nottingham.ac.uk, john.owen@nottingham.ac.uk

INTRODUCTION

In recent years much research has been carried out into the numerical simulation of wind loads on structures and in coupling CFD to dynamic models of structural response. In this paper the authors will present a study on simulating the dynamic response of a tall building to wind excitation. In particular, they will address the issues of:

- Appropriate selection of turbulence model
- Definition of inlet turbulence and simulation of the Atmospheric Boundary layer (ABL)
- Sequential coupling of the CFD solver and structural analysis software
- Analysis of the results to allow statistically meaningful predictions of structural loads and response

Three sub problems are usually distinguished when solving fluid-structure interactions: the fluid, the structure and the mesh. The flow induced forces on the structure are obtained from the solution of the fluid domain, achieved here using the commercial CFD program ANSYS Fluent. The corresponding response of the structure is found from solving the structural domain; here the authors have adopted a modal approach, the response in each vibration mode being treated as a SDOF problem. The corresponding motion of the fluid domain boundaries and displacement of the mesh domain then ensures that the effects of the structural response are accounted for in subsequent solutions of the fluid domain. Here the mesh is partitioned into rigid and deforming regions and the mesh displacement determined by treating the deforming region as elastic. An Arbitrary Lagrangian

---

1

Eulerian (ALE) formulation is used in solving the Navier Stokes Equations so that mesh motion is fully accounted for.

TURBULENCE MODELLING

Turbulence is a key feature of the ABL and so adequate turbulence modelling is an essential part of CWE. Four approaches have been applied to modelling turbulence in wind engineering, RANS, U-RANS, LES and DES (Hanjalic and Kenjeres (2008)). Steady-state Reynolds-Averaged Navier-Stokes (RANS) models have been widely used in wind engineering because of their efficiency and easy implementation. However, standard versions of two equation models lead to poor results in terms of separation and reattachment of the wind flow (Tsuchiya et al, 1997) and they are inappropriate for what is an essentially unsteady problem. One solution to this is the so-called unsteady RANS (URANS), which removes the effects of the smaller scales from the transport equations and expresses their effects in terms of larger scale motions and a modified viscosity (Versteeg and Malalasekera, 2007). However, a more rigorous approach is the Large Eddy Simulations (LES), which applies a spatial filter so that the larger flow structures are fully resolved and only the smaller scale features are modelled. This is a genuinely unsteady approach that should be well suited to wind engineering problems, but is computationally expensive. Detached Eddy Simulation (DES) seeks to combine the efficiency of RANS with the greater accuracy achievable with LES. LES is used in regions where the turbulent length scales are large and RANS models are applied in the near wall regions, where typically the turbulent scales are smaller (Shur et al, 1999). The present work compares the results of a URANS approach (the RNG k-ε model (Yakhot et al., 1992)) with those from DES.

DEFINITION OF THE INLET BOUNDARY LAYER

The wind at the inlet is described by a log-law profile and the reference wind speed is chosen to be equal to 0.5m/s, which corresponds to a Reynolds number of $3x10^5$ based on the width of the tower. The unsteadiness of the wind is modeled by specifying the turbulent kinetic energy and the dissipation rate at the inlet.

FLUID-STRUCTURE COUPLING

Once the equations for the fluid, the structure and the mesh have been set, and the fluid-mesh coupling has been defined (ALE), the fluid-structure coupling routine needs to be defined. There are two main methods that can be used to couple fluid and structure, depending on the application, and the resources available: the sequential method and the monolithic method (Dale et al., 2002, Longatte et al., 2005). The latter method solves fluid, mesh and structure in a single block, which has been described by Piperno et al (1995) as "computationally challenging". For the present work, a sequential method has been chosen (Figure 1) in which the fluid domain is solved first, then the forces acting on the structure are computed and the structural response found. Finally, the mesh is moved according to the forces on the structure. At the next time-step the fluid is solved on the newly computed mesh. This method, known as Conventional Serial Staggered method (CSS), has been extensively developed by Farhat et al. (1995), Farhat and Lesoinne (2000) and Farhat et al (2006). It is popular because of its stability and acceptable performance at low computational cost, and because it allows separate CFD and structural solvers to be used.

TEST CASES

The approach described above has been applied to a three-dimensional cantilever structure with a height of 60 m and plan dimensions of 20 m by 10 m The dimensions of the fluid domain are: height 200 m, 350 m in the wind-direction and 350 m in the cross wind direction. The validation of the fluid-structure coupling is on-going and will be based on a 370m tower in Hong-Kong, for which full scale data are available

RESULTS

Early results show that the RNG k-epsilon model, even applied in an unsteady manner, is not able to capture unsteady phenomena such as vortex shedding. The recirculating vortices induced by the building tend to fade away because the model is not able to maintain turbulence levels in the wake. Results of the DES show a much better capture of the flow past the building: the vortices seem to be maintained in the wake. In addition, a comparison of the flow field for DES and the RNG k-ε model shows that the flow is stretched with the RNG k-ε model, whereas reattachment occurs closer to the cantilever in the DES, Figure 2. This is consistent with an over-prediction of the turbulence kinetic energy with the k-ε model. This results in the overprediction of turbulent viscosity in the wake for the RNG model, may also explain the suppression of unsteady effects. A time history of the Y-velocity oscillations can be seen in Figure 3: it clearly shows that vortex shedding does not occur with the RNG k-ε model. On the other hand, DES is able to predict an oscillating transversal velocity with an amplitude of about 50% of the mean velocity (0.5m/s).
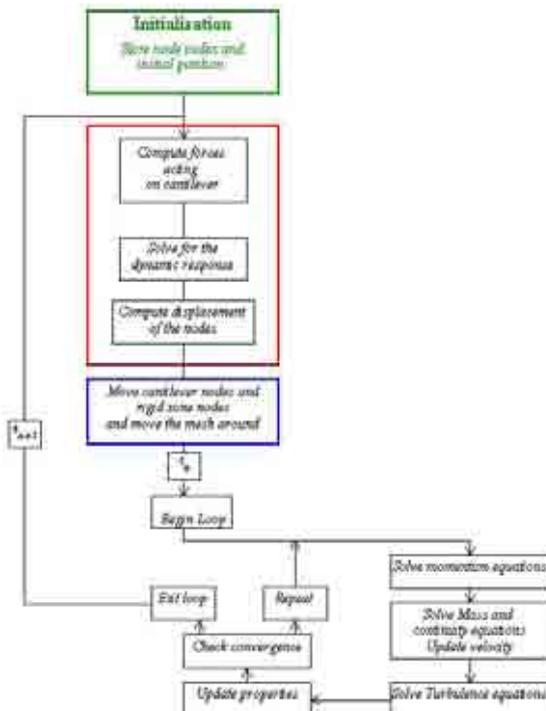
Figure 1: Diagram of the sequential fluid-structure coupling
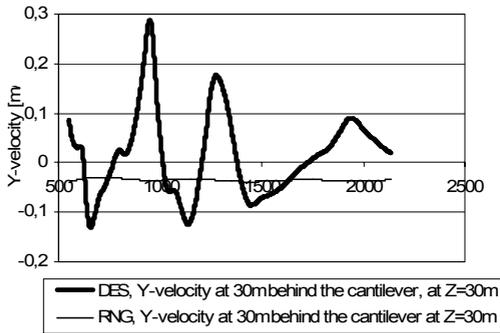
Figure 2: Time history of the Y velocity in the wake, comparison of DES and RNG k-ε model
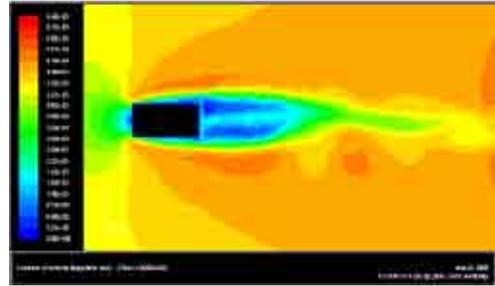
Figure 3: Flow field of the velocity – DES

CONCLUSIONS

Early results of the simulation of the flow around a 60m cantilever using the DES method show better flow field characteristics than the k-ε model. More importantly, the DES method seem to be able to capture and maintain unsteady phenomena such as vortex shedding, which is essential in the perspective of coupling the flow solver with the dynamic response of the building.

REFERENCES

ANSYS Inc. (2007) Fluent, version 6.3, Southpointe, Canonsburg PA, USA.

Dale, J. J., Spalding, D., Hold, A. & Armstrong, M. (2002) Fluid Structure Interaction through simultaneous calculation of velocity and displacement. PVP, Emerging Technologies in Fluids, Structures, and Fluid/Structures Interactions, 446, 129-139.

Farhat, C., Krisstoffer, V. D. Z. & G. & GEUZAINE, P. (2006) Provably second-order time-accurate loosely-coupled solution algorithms for transient nonlinear computational aeroelasticity. Computers methods in applied mechanics and engineering, 195, 1973-2001.

Farhat, C. & Lesoinne, M. (2000) Two efficient staggered algorithms for the serial and parallel solution of three-dimensional nonlinear transient aeroelastic problems. Computer methods in applied mechanics and engineering, 182, 499-515.

FarhatT, C., Lesoinne, M. & Maman, N. (1995) Mixed explicit/implicit time integration of coupled aeroelastic problems: three field formulation, geometric conservation and distributed solution. Int. J. Numer. Meth. Fluids, 21, 807-35.

Hanjalic K. & Kenjeres S. (2008) Some developments in turbulence modelling for wind and environmental engineering. Journal of Wind Engineering and Industrial Aerodynamic,s 96, 1537-1570.

Longatte, E., Bendjeddou, Z., Verreman, V. & Souli, M. (2005) Comparison of strong and partitioned fluid structure code coupling methods. Proceedings of ASME 2005 Pressure Vessels and Piping Division Conference. Denver, Colorado, USA.

Piperno, S., Farhat, C. & Larrouturou, B. (1995) Partitioned procedures for the transient solution of coupled aeroelastic problems. Computer methods in applied mechanics and engineering, 124, 79-711.

Shur, M. Spalart, P. R. , Strelets, M. and Travin, A. (1999) Detached-Eddy Simulation of an Airfoil at High Angle of Attack. In 4th Int. Symposium on Eng. Turb. Modeling and Experiments, Corsica, France, May 1999.

Tsuchiya, M., Murakami, S. Mochida, A., Kondo, K. & Ishida, Y. (1997) Development of a new k-ε model for flow and pressure fields around bluff body. J. Wind Engineering and Industrial Aerodynamics, 67 & 68, 169-182.

Versteeg, H.K. and Malalasekera, W. (2007) An Introduction to Computational fluid dy-namics, The Finite Volume Method. Pearson Education.

Yakhot, V., Orszag, S.A., Thangam, S., Gatski, T.B. and Speziale, C.G. (1992) Development of turbulence models for shear flows by a double expansion technique. Physics of Fluids A, 4, 1510-1520.

Motion effects on the aerodynamic forces for an oscillating tower through wind tunnel tests

G. Diana, S. Giappino, F. Resta, G. Tomasini, A. Zasso

Politecnico di Milano, Dipartimento di Meccanica – giorgio.diana@polimi.it – via La Masa, 1 20156 Milano, ITALY

Politecnico di Milano, Dipartimento di Meccanica – stefano.giappino@polimi.it – via La Masa, 1 20156 Milano, ITALY

Politecnico di Milano, Dipartimento di Meccanica – ferruccio.resta@polimi.it – via La Masa, 1 20156 Milano, ITALY

Politecnico di Milano, Dipartimento di Meccanica – gisella.tomasini@polimi.it – via La Masa, 1 20156 Milano, ITALY

Politecnico di Milano, Dipartimento di Meccanica – alberto.zasso@polimi.it – via La Masa, 1 20156 Milano, ITALY

Keywords: wind tunnel tests, aeroelastic effects, surface pressure measurements, building aerodynamics

ABSTRACT

Wind forces on high-rise buildings are usually defined by wind tunnel tests on scaled models: such tests can provide data on the overall and local loads both in mean and time-varying components and, in some cases, the wind response of the building can be directly measured if aeroelastic simulations are performed (ASCE, 1987).

Nevertheless more often the wind tunnel tests are carried out on rigid models, i.e. static models with geometrically scaled external features. In order to get reliable results also the simulation of the natural wind is important as happens in atmospheric boundary layer wind tunnels: mean vertical wind profile, turbulence intensity, integral length scales and wind spectrum should be reproduced correctly scaled.

In those tests different techniques are used to measure the wind force: overall wind loads are directly measured with base force balances that can give information on both mean and fluctuating loads providing that the structural frequency of the model and balance system is higher than the maximum frequency of interest to avoid distortions due to resonant effects, unless corrections are needed. The surface pressure measurement technique allows for a deeper understanding of the

Contact person: S. Giappino, Politecnico di Milano – Dipartimento di Meccanica, via La Masa, 1 tel. +390223998076 fax. +390223998081
E-mail stefano.giappino@polimi.it

aerodynamic properties of the building because local information on the wind loads are available and, providing that an adequate number of pressure taps is available the overall wind loads can be calculated by integrating the surface pressures over tributary areas. Moreover surface pressures can be used to calculate the generalized forces for the application of the modal approach (Rosa, 2008).

Once the wind loads are known the wind induced response of the structure can be numerically evaluated providing estimations on full scale accelerations and displacements. The calculation of the response can be carried out both in time domain using the time histories of the loads or in frequency domain using power spectral densities of the modal wind loads (ASCE, 1987). Moreover, trough the modal approach, also the inertial loads can be estimated and, as a consequence, also the vertical distributions of shears, bending moments and torque can be evaluated (Rosa, 2008b).

The main limitation of this procedure is that the forces used for the computation are measured on a rigid static model while the prototype will experience motion as a consequence of those loads (Dyrbye, 1999). It is well known that the motion of the body can modify the aerodynamic forces so that the structure is subjected to aeroelastic effects (Vickery, 1993; Gu, 2004; Quan, 2005). These effects are important for slender and flexible structures and wind tunnel aeroelastic simulations are needed to investigate those phenomena. Models used in these tests replicate the dynamic behavior of the prototype structure and they are built with correctly scaled mass and stiffness. In these tests, carried out at different wind speeds, the wind response of the building is directly measured.

A research is going on at the Politecnico di Milano with the aim to investigate the aeroelastic effects on a rectangular section 200m high building. In particular the changes in the aerodynamic forces due to the building motion are studied.

The wind tunnel model is a simplified aeroelastic model with two degrees of freedom that simulate the two orthogonal fundamental sway modes of vibration: it is realized with a rigid body linked to the ground by spring elements, specifically designed to match the scaled building natural frequencies (Figure 1 and 2). The model set-up allows the simultaneous measurement of both the surface pressure and the body motion.

Figure 1: Building wind tunnel model. The elastic suspension system is under the false floor and allows for model oscillations
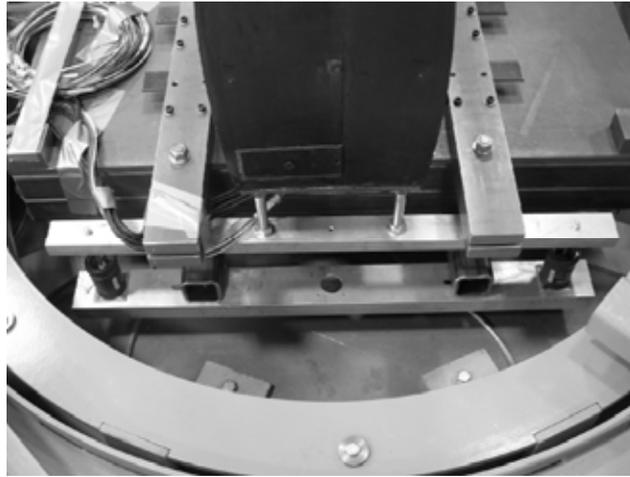
Figure 2: Detail of the suspension device. It is possible to see the elastic elements and the dampers.

The measurements will show the effects of the body motion on the surface pressures, as a function of the oscillation amplitude. As a preliminary result, Figure 3 shows the peak cross-wind acceleration as a function of the incoming flow velocity, measured when the wind is normal to the sides of the rectangular section. The results will be compared with the data achieved on the static rigid model, highlighting the differences with the traditional test methodology. Also the model wind –response is measured by accelerometers and the results will be compared with the numerically predicted ones that used the force time histories measured on the rigid model (Rosa, 2008).

Different test set-up will be investigated to evaluate the effects in particular of the structural damping, the mass-ratio and the incoming wind turbulence intensity. This latter parameter was found to be very important for the possibility of instability phenomena (Zasso, 2007). Also the response to vortex shedding will be investigated.
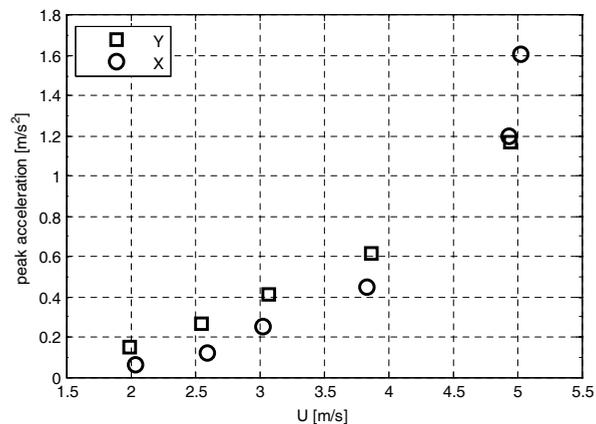
Figure 3: Cross wind peak acceleration in turbulent flow conditions. X: wind perpendicular to the long side of the rectangular section; Y: wind perpendicular to the short side.

REFERENCES

ASCE (1987), "Wind tunnel model studies of buildings and structures", American Society of Civil Engineers, Manuals and Reports on Engineering Practice.

Dyrbye, C. & Hansen, S.O. 1999, Wind loads on structures, J. Wiley, Chichester; New York.

Gu, M. & Quan, Y. 2004, "Across-wind loads of typical tall buildings", Journal of Wind Engineering and Industrial Aerodynamics, vol. 92, no. 13, pp. 1147-1165.

Quan, Y., Gu, M. & Tamura, Y. 2005, "Experimental evaluation of aerodynamic damping of square super high-rise buildings", Wind and Structures, vol. 8, no. 5, pp. 309-324.

Vickery, B.J. & Steckley, A. 1993, "Aerodynamic damping and vortex excitation on an oscillating prism in turbulent shear flow", Journal of Wind Engineering and Industrial Aerodynamics, vol. 49, no. 1-3, pp. 121-140.

Rosa, L., Aly, A.M., Tomasini, G. & Zasso, A. (2008), "Wind induced dynamics of a prismatic slender building with a rectangular section", Proceedings of the BBAA VI International Colloquium on Bluff Bodies Aerodynamics & Applications.

Rosa, L., Tomasini, G. & Zasso, A. (2008b), "Dynamic response and wind loads of a tall building based on wind tunnel tests", submitted to EACWE5.

Zasso, A., Belloli, M., Giappino, S., Muggiasca, S. & Rosa, L. (2007), "Effects of free-stream turbulence and angle of attack on a rectangular prism", Proceedings of the 12TH ICWE, International Conference on Wind Engineering.

On the structural response of steel telecommunication lattice masts for wind loading and combined effects

Efthymiou E., Gerasimidis S. & Baniotopoulos C.C.

Institute of Metal Structures, Department of Civil Engineering, Aristotle University of Thessaloniki GR- 54124, Thessaloniki, Greece

vefth@civil.auth.gr, sgerasim@civil.auth.gr, ccb@civil.auth.gr

Keywords: Steel lattice masts, wind loading, structural codes, combined effects,

ABSTRACT

The present paper investigates the behaviour of steel lattice telecommunication masts subject to wind action and the combined effect of wind and ice. Steel lattice masts belong to the general category of special steel structures used either for telecommunication needs or as systems to transfer energy. As these two industries become strategic and growing in today's economy, their structural safety and stability is considered vital. In some cases, the financial and social consequences caused by a possible collapse of a structure transferring energy, are considered as damaging as those caused by the collapse of traditionally significant infrastructure, such as bridges.

Steel lattice masts are usually flexible and light structures and their common, cost effective practice is using an open lattice, lightweight but adequately stiff system, since a lattice morphology requires only half as much material as a freely standing tubular structure with similar stiffness. Although the majority of these masts include bolted angle profiles, their structural forms vary widely, depending on their geometrical characteristics.

Regarding the typology of steel lattice masts, they can either be square or triangular in plan and they can also be located on the ground or on roofs of buildings, when needed in an urban environment (Fig. 1). As tall and slender structures, their primary loads are environmental loads, while earthquake is occasionally important especially in structures with high concentrated mass. Earthquake commonly leads to high loading values in countries like Greece, where local earthquake codes have become very detailed and severe for all kinds of buildings.

Contact person: Evangelos Efthymiou, Dr. Civil Engineer, Institute of Metal Structures, Department of Civil Engineering, Aristotle University of Thessaloniki, University Campus, GR-54124, Thessaloniki, Greece. Tel: +302310994223, Fax: +302310995642. E-mail vefth@civil.auth.gr

i)   ii)
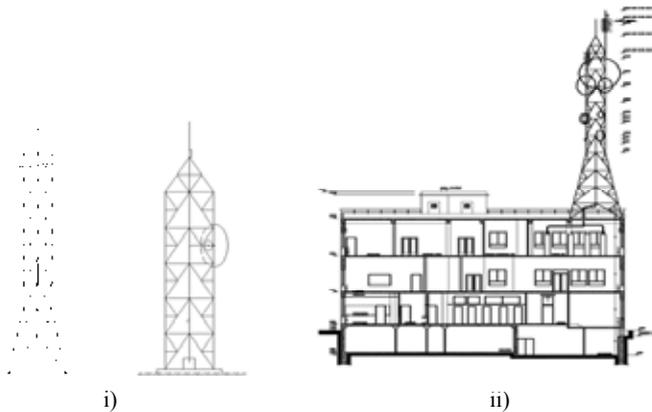
Figure 1: Steel lattice telecommunication masts i) on the ground   ii) on buildings

As far as environmental actions are concerned, the wind and ice loading and their combined effect are often the critical loading case. In a plethora of civil engineering projects, a great number of structures, or parts of them, fail every year due to these actions. The herein presented research activity aims at investigating the behaviour of these special steel structures, under the specific loading conditions caused by wind and icing. For the purpose of the research effort, a total number of 6 steel masts have been analysed, 4 masts located on the ground and 2 masts located on buildings, respectively. A detailed approach was used for the evaluation of wind loading, since its accurate computation is proven very important for lightweight structures, like masts. The results of this detailed calculation, combined with the assessment of icing on the structure, were used to focus on the extraordinary combined action of ice and wind (Fig. 2).

Figure 2: Steel telecommunication lattice masts with ice

The steel lattice masts under investigation cover a big part of the steel telecommunication mast industry of Greece and the study carried out can be applied to all of them. The analysis has been adjusted according to the contemporary relevant codes, i.e. Eurocode 3 and DIN 4131, DIN 1055 and all the basic parameters of the applied methodology are presented and thoroughly described. The study was conducted by means of innovative software and useful conclusions have been

accomplished considering the structural performance of each of the six types of steel telecommunication masts.

In the last part of the paper, comparative deformation diagrams for all the masts have been developed and conclusive remarks concerning the parts of the masts being sensitive to buckling, for each of the six types of the steel masts under investigation, have been extracted.

a)	b)	c)	d)	e)	f)
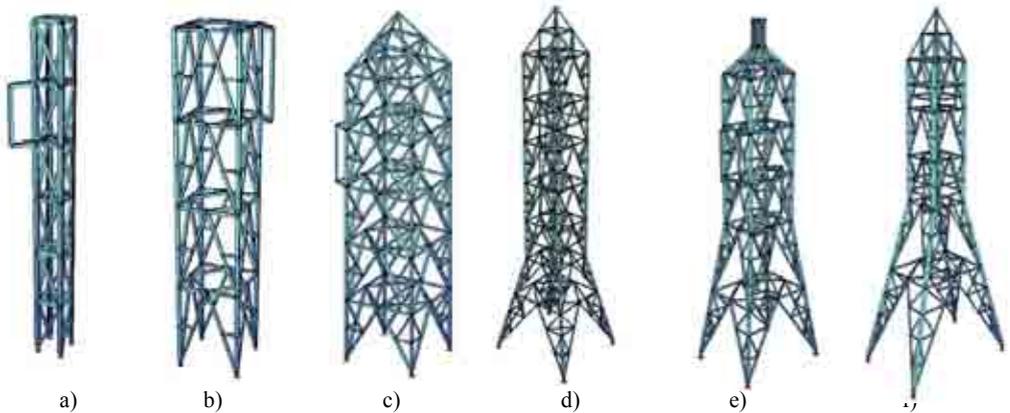
Figure 3: Structural models of steel masts located on the ground (a,b,c,d) and located on buildings (e,f)

REFERENCES

Tsitlakidou A., Lemonia F., Koltsakis E. & Baniotopoulos C.C. (2005). Wind and ice design of ground based steel lattice masts, Proc. of the 5th National Conference on Metal Structures. Xanthi, Greece, Vol. I, pp. 207-214.

Vayas I., Spiliopoulos A., Papageorgiou M. & Chatzinikolis I. (2005). Vulnerability of Telecommunication towers. Proc. of the 5th National Conference on Metal Structure*s*. Xanthi, Greece, Vol. II, pp. 230−237.

DIN Deutsches Institut für Normung. (2002). DIN 1055. *Einwirkungen auf Tragwerke- Teil 4: Windlasten, Teil 5: Schnee- und Eislasten*. DIN Deutsches Institut für Normung.

DIN Deutsches Institut für Normung. (1991). DIN 4131. *Antennentragwerke aus Stahl*, DIN Deutsches Institut für Normung.

Earthquake Planning and Protection Organization-EPPO. (2000). *Greek Antiseismic Code 2000- EAK 2000*, Ministry of Environment, Planning and Public Works, Athens, Greece.

European Committee for Standardisation. (2002). *prEN 1993-7-1, Eurocode 3 :Design of Steel Structures-Part 7.1- Towers and Masts* , CEN, Brussels.

Simiu E., Scanlan R. (1996). *Wind effects on Structures*. John Wiley & Sons, New York.

Dyrbye C., Hansen S.O. (1997). *Wind loads on Structures*. John Wiley & Sons, Chisester.

Stathopoulos T., Baniotopoulos C. C. (2007). *Wind effects on Buildings and design of wind-sensitive structures*. CISM, SpringerWienNewYork, Udine.

Owens G., Knowles P. (1994). *Steel Designer's Manual*. The Steel Construction Institute, 5th Edition, Blackwell Science.

Lin N., Letchford C., Tamura Y., Liang B., Nakamura O. (2005). "Characteristics of wind forces acting on tall buildings", Journal of Wind Engineering and Industrial Aerodynamics, 93, 217-242.

Schmidt H. (2000). "Stability of steel shell structures", Journal of Constructional Steel Research, 55, 159-181.

Baker C. J. (2007). "Wind engineering- Past, present and future", Journal of Wind Engineering and Industrial Aerodynamics. Vol. 95 (9-11), 843-870

A refined analysis of guyed masts in turbulent wind

M. Clobes, A. Willecke, U. Peil

Technische Universität Carolo-Wilhelmina zu Braunschweig

Institute of Steel Structures, Beethovenstraße 51, 38106 Braunschweig, Germany

m.clobes@is.tu-braunschweig.de, a.willecke@is.tu-braunschweig.de, u.peil@is.tu-braunschweig.de

Keywords: unsteady wind loads, wind-induced vibrations, vortex excitation, wind profiles, masts

ABSTRACT

Wind is the only regularly reoccurring load for slender structures, such as guyed masts. In order to reliably evaluate their fatigue safety, modelling of the frequent wind loads under moderate wind velocities is crucial, because these can produce high structural damage.

Particularly in wind events with moderate velocities the wind properties can differ from commonly used wind profiles (Fig. 1). In building codes this is generally not considered.
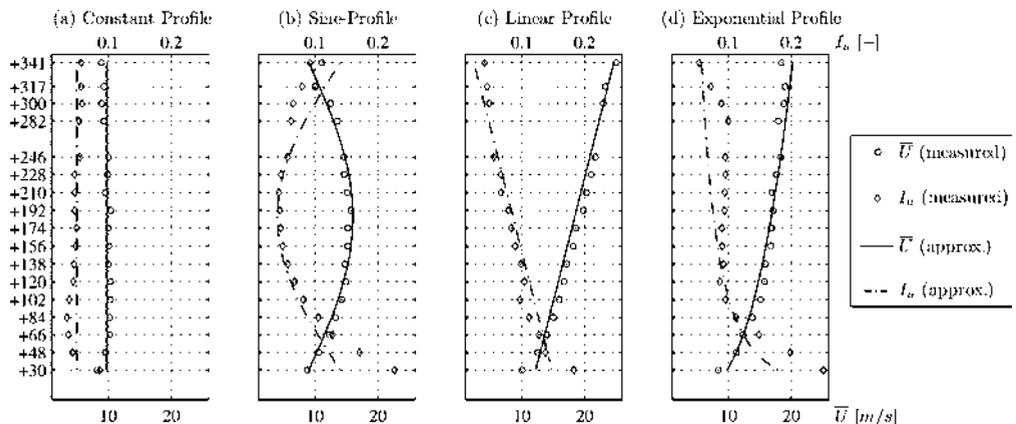
Figure 1: Measured wind profiles at the 344m data acquisition tower Gartow.

In this paper, the wind loads are derived from synthetic, spatially correlated wind fields, whose properties – especially the height-dependent profile of the mean wind velocity – were verified by own

Contact person: A. Willecke, Technische Universität Carolo-Wilhelmina zu Braunschweig
Institute of Steel Structures, Beethovenstraße 51, 38106 Braunschweig, Germany
Phone +49 (0)531 / 391-3375, Fax +49 (0)531 / 391-4592
E-mail a.willecke@is.tu-braunschweig.de

full-scale wind data recorded at the 344m data acquisition tower Gartow. Details on the data acquisition tower are presented in Peil & Nölle (1992) or Peil & Behrens (2007).

Wind forces result from varying wind velocities and directions as well as from body-induced turbulence. In this work, a refined analysis of a multi-guyed mast with a circular cross section subjected to realistic wind profiles is presented – using an unsteady time domain model for the buffeting wind loads and, simultaneously, a simulation of the vortex excitation considering the turbulence-dependent *Strouhal*-frequency and lock-in effects. Hence, the intermittent character of vortex excitation is taken into account.

Common time domain models for buffeting wind loads are based on a quasi-steady transfer of the wind turbulence and do not consider its actual frequency dependence. With respect to high wind velocities, this leads to a realistic loading. However, it significantly overestimates the load under moderate winds, Clobes (2008). Due to this, in this work the buffeting wind load is modelled by an unsteady transfer based on aerodynamic impulse response functions.

Eq. (1) and (2) show the buffeting drag $F_W(t)$ and lift $F_Q(t)$, (Fig. 2), where ρ represents the density of the air, C_W the drag coefficient, D the diameter and L_i the element length. The aerodynamic impulse response functions $I_{F,k}(t)$ are convoluted by the instantaneous wind velocity $W(t)$ and the fluctuating wind direction $\varphi'(t)$. The response functions were determined by a rational function approximation of the complex aerodynamic admittances derived from full-scale measurements of the turbulent wind and the resulting wind forces, Peil & Clobes (2008).

$$F_W(t) = \frac{\rho}{2} \cdot C_W \cdot D \cdot L_i \cdot \int_0^t I_{W,u}(t-\tau) \cdot \left(W(\tau)\right)^2 \cdot \cos\left(\varphi'(\tau)\right) d\tau \tag{1}$$

$$F_Q(t) = \frac{\rho}{2} \cdot C_W \cdot D \cdot L_i \cdot \int_0^t I_{Q,v}(t-\tau) \cdot \left(W(\tau)\right)^2 \cdot \sin\left(\varphi'(\tau)\right) d\tau \tag{2}$$
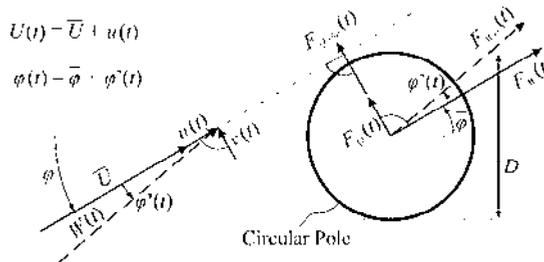
Figure 2: Wind velocities and forces on a circular cross section.

The mechanism of vortex excitation depends on the oscillation behaviour of the structure. In case of a rigid body, the mechanism is purely flow-induced. For a body free to oscillate, this changes to an aeroelastic interaction between the structure and the flow, when the velocity of the incident flow is appropriate. The latter is called lock-in.

The flow-induced lateral forces of vortex excitation $F_{Q,St}(t)$ are modelled by the quasi-steady approach given in Eq. (3) and (4), which represents a pointer in the complex plane rotating with a fluctuating angular velocity, Clobes (2008). Thus, only one frequency is related to each time step t.

$$F_{Q,St}(t) = \frac{\rho}{2} \cdot c_{lat} \cdot D \cdot L_i \cdot \left(W(t)\right)^2 \cdot \sin\left(\theta(t)\right) \tag{3}$$

$$\theta(t) = 2\pi \cdot \frac{St}{D} \cdot \int_0^t W(t)\, dt \tag{4}$$

The instantaneous frequency of the presented vortex forces is equivalent to the *Strouhal*-frequency $f_{St}(t)$. This can be proven using *Hilbert* transforms. Hence, the model considers the dependency of both the amplitude and the vortex frequency on the instantaneous wind velocity $W(t)$. Additionally, the spectral characteristics comply with those observed in wind tunnel tests by Vickery (1972), see Fig. 3. Similar models were published by Höffer & Niemann (1993) and D'Asdia & Noè (1998).
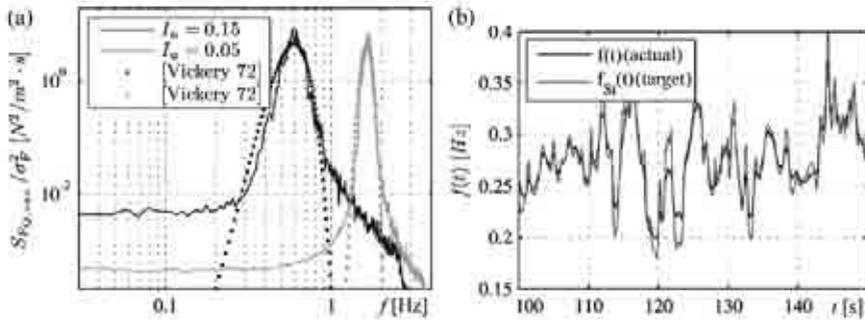
Figure 3: Simulated vortex forces: (a) spectral density, (b) instantaneous frequency.

If the velocity of the incident flow produces a vortex shedding frequency f_{she} close to the oscillation frequency of the structure f_{osc}, the shedding frequency locks on to the structural motion and the *Strouhal*-frequency disappears. This velocity is called critical velocity u_{crit}. In consequence, the lateral oscillation amplitude and the correlation of the vortex forces increase. Herein, this lock-in behaviour is simulated based on the correlation length model designed by Ruscheweyh (1986). For this, the *Strouhal*-Frequency in Eq. (4) is replaced by f_{osc}.
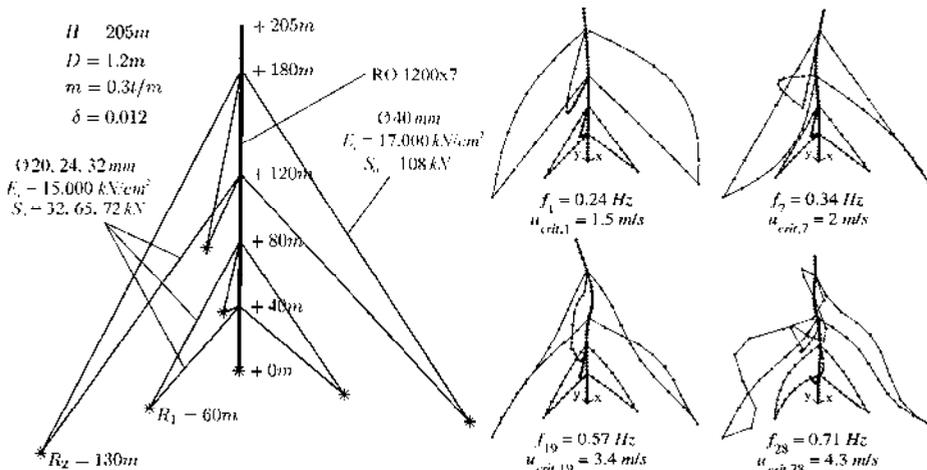
Figure 4: Structural properties and chosen mode shapes with the corresponding u_{crit}.

In order to evaluate the influence of different profile shapes on the stress resultants, a 205 *m* guyed mast (Fig. 4) is analysed in the time domain. This is done by an own finite element software that allows for the dynamic analysis of geometrically nonlinear structures and the consideration of aeroelastic effects. The four mean wind velocity profiles $\bar{U}(z)$ from Fig. 1 and their corresponding, inversely proportional turbulence intensity profiles $I_u(z)$ are applied to the mast. Both are scaled to the 19th mode shape with $u_{crit} = f_{19} \cdot D / St = 3.4 \, m/s$, where the *Strouhal*-number $St = 0.2$ is used.

The results indicate a strong dependency on the applied wind profile, with a maximum lateral tip

deflection $y_{max} = 0.28\,m$ for the constant profile (a) and a difference in the maximum lateral bending moment M_x up to 30 %, (Fig. 5). This is less due to the difference in the absolute wind velocities in different heights, than to the time periods the incident wind velocity remains in the lock-in region.
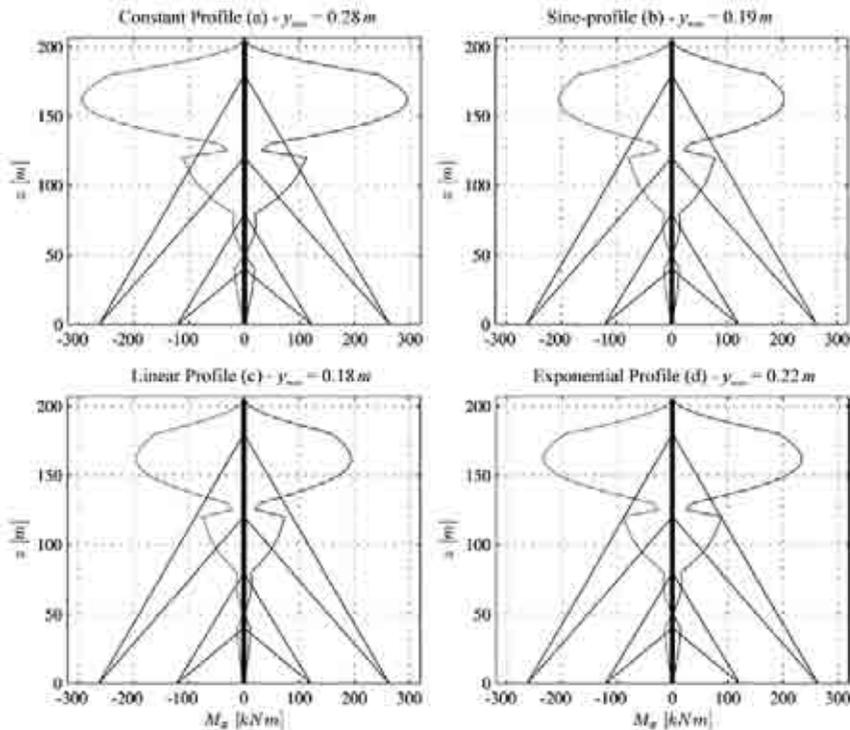
Figure 5: Lateral bending moments for different wind profiles.

So far, no resulting damages could be calculated due to the unknown probability of occurrence of the different profile shapes. This will be addressed in the near future.

REFERENCES

Peil U., Nölle H. (1992). "Guyed masts under wind load", Journal of Wind Engineering and Industrial Aerodynamics, Vol. 41-44, 2129-2140.

Peil U., Behrens M. (2007). "Aerodynamic admittance models for buffeting excitation of high and slender structures", Journal of Wind Engineering and Industrial Aerodynamics, Vol. 95, 73-90.

Clobes M. (2008). *Identifikation und Simulation instationärer Übertragung der Windturbulenz im Zeitbereich.* Dissertation, Technische Universität Braunschweig, Shaker-Publishing.

Peil U., Clobes M. (2008). "Effect of unsteady aerodynamic admittances on life cycle of guyed masts", 1st International Symposium on Life-Cycle Civil Engineering (IALCCE'08), Varenna, Lake Como, Italy, 769-774.

Höffer R., Niemann H.-J. (1993). "Computation of artificial stochastic wind loads and interaction forces on oscillating line-like structures", 2nd European Conf. on Structural Dynamics (EURODYN'93), Trondheim, Norway, 1115-1122.

D'Asdia P., Noè S. (1998). "Vortex induced vibration of reinforced concrete chimneys: in situ experimentation and numerical previsions", Journal of Wind Engineering and Industrial Aerodynamics, Vol. 74-76, 765-776.

Vickery B.J. (1972). "Lift or across-wind response of tapered stacks", Proceeding of ASCE, Journal of the Structural Division, Vol. 98, No. St. 1, 1-20.

Ruscheweyh H. (1986). „Ein verfeinertes, praxisnahes Berechnungsverfahren wirbelerregter Schwingungen von schlanken Baukonstruktionen im natürlichen Wind", Beiträge zur Anwendung der Aeroelastik im Bauwesen, Vol. 20.

WIND CLIMATE
AND ATMOSPHERIC BOUNDARY LAYER

Preliminary elements for an innovative wind map of Italy

L. Pagnini, G. Solari

Dicat, Dept. of Civil, Environmental and Architectural Engineering –pagnini@dicat.unige.it– via Montallegro 1, 16125 Genova, Italy

Dicat, Dept. of Civil, Environmental and Architectural Engineering –solari@dicat.unige.it– via Montallegro 1, 16125 Genova, Italy

Keywords: wind map, current wind speed, extreme wind speed, probability factor

ABSTRACT

Codes and standards on wind action usually assign a reference value of the basic wind speed which represents the characteristic 10 minute mean wind velocity, irrespective of wind direction and time of year, at 10 m above ground level, in open country terrain with low vegetation and isolated obstacles, having a yearly probability of exceedence of 0.02, which is equivalent to a mean return period of 50 years. It is given by design charts and tables according the windiness of the site and the height above the sea level. Wind velocities with different exceedence probabilities are obtained multiplying the basic value for a probability factor. Such coefficient often plays a secondary role, since the analyses are usually carried out for a 50 years return period.

Due to its simplicity, the asymptotic type first is the basic model for the yearly maximum mean wind adopted by most codes and standards on wind action (DM 1996). It is given by:

$$F_M(v) = exp\left\{-exp\left[-A(v-U)\right]\right\} \quad v \geq 0 \tag{1}$$

where A and U are model parameters. The Eurocode for wind action (2004) follows an analogous

Contact person: 1st L. Pagnini, DICAT, Dept. of Civil, Environmental and Architectural Engineering, Via Montallegro 1, tel. +39 (0)10 3532291, FAX: +39(0)10 353 2534.
E-mail: Pagnini@dicat.unige.it

criterion, providing the asymptotic type first distribution to the velocity pressure q, *i.e.* to the mean wind velocity square:

$$F_M(q) = exp\left\{-exp\left[-A'\left(q-U'\right)\right]\right\} \quad (q \geq 0)$$ (2)

being A' and U' are the model parameters.

The evolution of constructions and safety formats often needs the evaluation of structural reliability according different probabilities of exceedence. Fatigue analyses are carried out using current wind velocities, therefore they require the knowledge of the population distribution. Human discomfort to wind induced motion is usually checked with respect to one year return period; the probability factor doesn't apply for this velocity. Design wind loads are usually related to 50 years return period. Structural reliability with respect to aeroelastic instability phenomena is usually checked with respect to even higher periods. In this context, available wind maps turn out to be more and more inadequate.

In order to overcome this shortcoming, the paper aims at formulating a unitary map, suitable for dealing with the whole velocity field, including current and extreme wind velocities. Based on refined statistical analyses of Italian meteorological records, the study expresses the probabilistic distribution F_V of the mean wind with the Weibull function. Since usually data records include several calm periods, it is referred to the so called *hybrid* distribution which assigns a finite probability of observing zero wind speed (Takle & Brown, 1978):

$$F_V(v) = P_0 + \left(1-P_0\right)\left\{1 - exp\left[-\left(\frac{v}{c}\right)^k\right]\right\} \quad v \geq 0$$ (3)

where c and k are, respectively, the scale and the dimensionless shape parameter; P_0 is the probability of zero wind speed occurrence.

The yearly maximum wind speed is described by the process analysis. The distribution function of the maximum value is provided by:

$$F_M(v) = exp\left[-\lambda f_V(v)\right]$$ (4)

where f_V is the density function of the data population and λ is a model parameter, which is estimated by counting the up-crossings of speed thresholds (under the assumption that wind is a stationary process, and that wind speed and wind acceleration are statistically independent).

The definition of the mean return period R of a given wind speed v allows to express the velocity as a function of this quantity:

$$R(v) = [1-F_M(v)]^{-1}$$ (5)

It is demonstrated that Eq. (4) tends to Eq. (2) for $k = 2$ (Cook, 1982), it tends to Eq. (1) for $k = 1$. Moreover, when $k > 1$, the asymptotic analysis, Eq. (1), is more conservative with respect to Eq. (4) when $R > 50$ years, while it becomes not conservative for $R < 50$ years (Lagomarsino *et al.*, 1992). This trend is opposite when $k < 1$. The shape coefficient has therefore a central role in the wind statistics.

At this stage, a data basis of 39 anemometric stations has been collected. It includes refined analyses carried out in recent studies (Freda *et al.*,2008, Solari *et al.*,2006, CMIRL, 2000) and some of the data records analyzed for the definition of the Italian wind zone map (Ballio *et al.*, 1994). The distribution of the stations over Italy is plotted in Figure 1. The observation period is about 50 years for each station.

The anemometric recordings are characterized by high occurrence of calm periods; a closer look to breaks detected on annual mean wind series reveals that such values almost disappear in the later years, when the anemometer is replaced with a more accurate and precise sensor. Nevertheless, it is showed that differences between the later and older measures also concerns the central body of the

distribution, raising a doubt upon the validity of the results obtained from old measures.

The fitting of the population data shows a noteworthy relation between c, k and the 50 years reference wind velocity v_{50}. Figure 2 shows the fitted values; the model proposed is obtained by a linear regression. There is a clear tendency of the shape parameter to decrease with the latitude of the site; k is ranging between 0.9 and 1.15, for southern regions, centre Italy and Liguria; between 1.15 and 1.5 elsewhere. Such values reveal that the asymptotic distribution of the Italian extreme wind might represent a good choice in the northern regions where k is typically unit. As far as the high return periods are concerned, it is quite conservative elsewhere, while the asymptotic type first distribution assigned to the velocity pressure may be very unsafe since, unlike the northern European countries, k is much less than 2.

Based on these outcomes, safe side estimates of the probability factors are derived. For southern regions, centre Italy and Liguria it is given by:

$$c_R = \left\{ 1 - 0.078\ln\left[-600\ln\left(1 - \frac{1}{12R}\right)\right]\right\}^{0.67} \quad 1 \le R < 5$$

$$c_R = \left\{ 1 - 0.078\ln\left[-50\ln\left(1 - \frac{1}{R}\right)\right]\right\}^{0.67} \qquad 5 \le R < 50 \tag{6}$$

$$c_R = \left\{ 1 - 0.078\ln\left[-50\ln\left(1 - \frac{1}{R}\right)\right]\right\}^{0.87} \qquad R \ge 50$$

Elsewhere:

$$c_R = \left\{ 1 - 0.078\ln\left[-600\ln\left(1 - \frac{1}{12R}\right)\right]\right\}^{0.87} \quad 1 \le R < 5$$

$$c_R = \left\{ 1 - 0.078\ln\left[-50\ln\left(1 - \frac{1}{R}\right)\right]\right\}^{0.87} \qquad 5 \le R < 50 \tag{7}$$

$$c_R = \left\{ 1 - 0.078\ln\left[-50\ln\left(1 - \frac{1}{R}\right)\right]\right\}^{1.1} \qquad R \ge 50$$

Figure 3 shows the model provided, together with the values coming from the data recordings and Eq. (5).

The full paper will expound main results and further developments, giving a preliminary proposal for a wind zone map in Italy, suitable for dealing with different wind velocities, ranging from current to extreme values.

REFERENCES

Ballio G., Lagomarsino S., Solari G. (1994). "The new Italian extreme wind map", Giornale del Genio Civile, 7,8,9 , *in italian*.

CMIRL (2000). "The wind map in Liguria" Rel. 12/A, *in Italian*.

Cook N.J.(1982). "Towards a better estimation of extreme winds" , J. Wind Engng. Ind. Aerod., 9.

Decreto 16 gennaio 1996 del Ministero dei Lavori Pubblici, "Norme tecniche relative ai criteri generali per la verifica di sicurezza delle costruzioni e dei carichi e dei sovraccarichi" *in italian*

Eurocode 1 (2004), Actions on structures, European Standard, prEN 1991-1-4.

Freda, A., Solari, G., Torrielli, A., Buonanno, A., Mancini, M., Testa, M. (2008). "Comparison between field measurements and numerical simulations of the wind speed along the HS/HC Rome-Naples railway line", Proc.

BBAA VI, Milano, Italy.

Lagomarsino S., Piccardo G., Solari G. (1992). "Statistical analysis of high return period wind speeds", J. Wind Engng. Ind. Aerod., 41.

Solari G., Repetto M.P., Tubino F., Freda (2006). "Analysis of the extreme wind at the historical quarter of Milano Fair " Report, *in italian*.

Takle E.S., Brown J.M. (1978). Note on the use of Weibull statistics to characterize wind-speed data. *J. Appl. Meteorol.*, 17.

Figure 1. Anemometric stations.
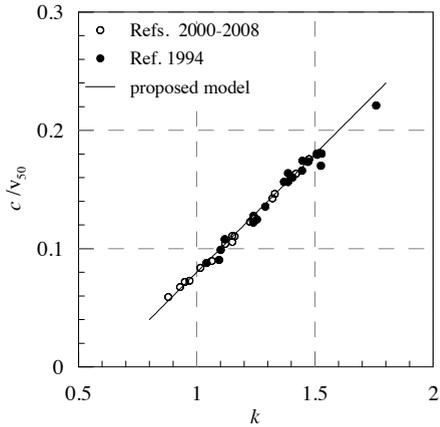
Figure 2. Relation between parameters
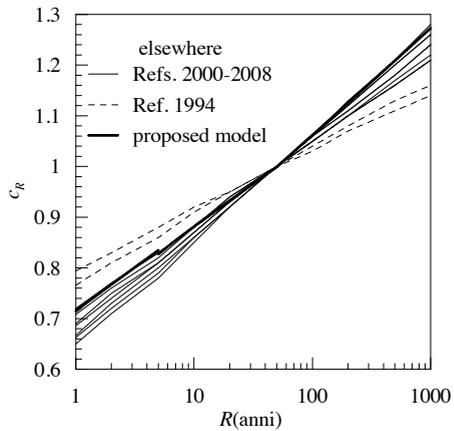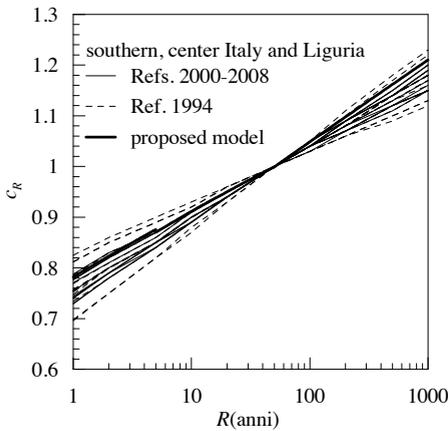
Figure 3. Probability factor

Chasing gust fronts - wind measurements at the airport Munich, Germany

E. Agu, M. Kasperski

Ruhr-University Bochum – Department of Civil and Environmental Engineering Sciences
Ecevit.Agu@rub.de – Michael.Kasperski@rub.de

Keywords: frontal depression, gust front, storm trap, wind field measurement

ABSTRACT

The wind climate of Germany and other parts of Western Europe is governed by three storm types: strong frontal depressions, gust fronts and thunderstorms. All this three storm types cannot be described without given sufficient information. Furthermore, the structure of the corresponding wind fields is unknown. To analyse the wind structure in gust fronts in 2008 a storm trap at the airport Munich has been erected.

INTRODUCTION

The wind climate of Germany and other parts of Western Europe is governed by three storm types: strong frontal depressions, gust fronts and thunderstorms. Gust fronts are strongly connected to strong frontal depressions and are induced by convective processes, e.g. heavy rain [1]. The meteorological observations unfortunately due not provide sufficient information to describe all three storm types with a similar precision. In Germany, per day 24 hourly means of the wind speed and the corresponding wind direction are sampled. Additionally, the maximum gust wind speed is sampled

and the corresponding occurrence time. This information allows the identification of the three different storm types, assuming, that per day only one thunderstorm or one gust front may occur. Strictly speaking, this assumption holds not true even for thunderstorms, since this storm type has an upwind and downwind front, and only the larger one is sampled. For gust fronts, as they may occur in frontal depressions, it is completely unknown, how many independent fronts may occur over the complete duration of the storm. In figure 1, observed gust factors in gust fronts are shown on the example of the meteorological station at Düsseldorf airport for the years from 1956 to 2007. The respective wind speeds are large and therefore have to be considered for the specification of the design wind load [2]. However, for a consistent model, as further parameter, at least the duration of each independent gust front is required.
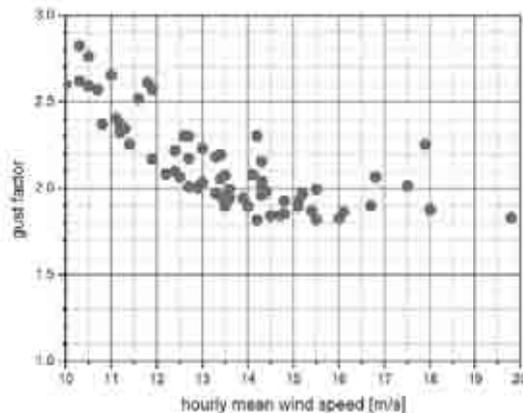
Figure 1: Observed gust factors, Düsseldorf airport 1952 - 2007

Furthermore, the structure of the corresponding wind fields is unknown. While for thunderstorms, several field test station are operated [3, 4], there have been up to now no publications dealing with the wind structure in gust fronts.

In the scope of research project, which is sponsored by the Federal Ministry of Education and Research, a storm trap has been erected at the airport Munich, Germany. The wind field measurements started on 8th of August 2008.

LAYOUT OF THE STORM TRAP

The basic idea of the wind field measurements is to provide 3-D information for the turbulent velocity fields with the restriction that there should be minimum distortion from buildings and trees. Therefore, a position beside the runway has been chosen. At the three corners of an equilateral triangle with side length of 100 m the 3 wind speed components are measured at 10 m height above ground. The Young 3D Sonic Anemometer (model 81000VRE) allow a sampling rate of 32 Hz. Additionally, at the balance point of the triangle, three sensors measure the wind speeds at levels 5m, 10m and 20 m. The atmospheric pressure is measured with a Young sensor 61202V.

The orientation of the triangle corresponds to the dominant wind direction of strong frontal depressions (figure 2), which is for the actual site west (270°). A snap shot of the centre mast is shown in figure 3.
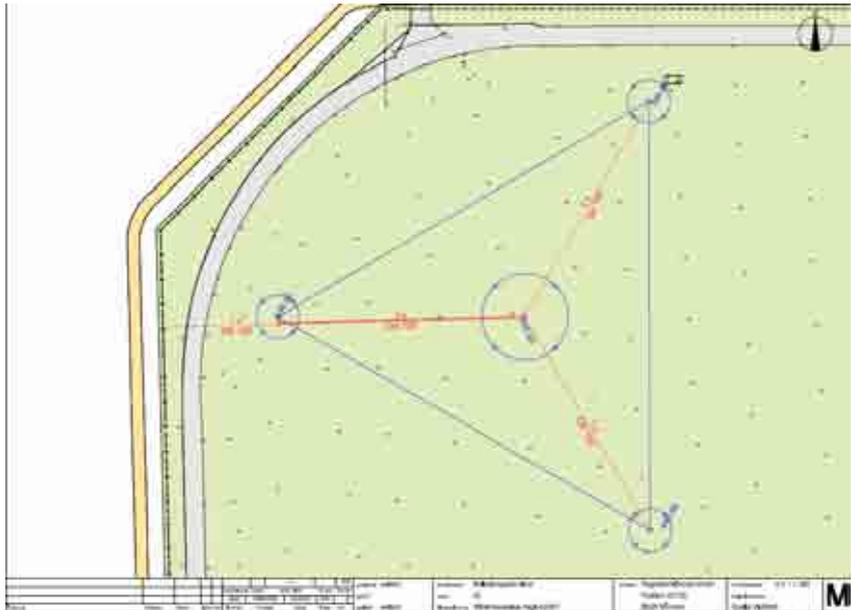
Figure 2: Basic layout of the storm trap at the Airport Munich

Figure 3: Site snap shot of the centre mast of the storm trap at the Airport Munich

The data acquisition system is based on three removable hard drives. In case of power failure, an independent power supply guarantees that there is no loss of data. The data acquisition works permanently, the data are stored for 30 minute intervals. Measuring errors, which are extremely rare, are indicated in the corresponding protocol.

The full paper will present findings for the storms in the upcoming storm season, i.e. winter 2008/2009.

REFERENCES

[1]   M. Kasperski

A new wind zone map for Germany
Journal of Wind Engineering and Industrial Aerodynamics (90) 2002 pp 1271-1287

[2]   M. Kasperski

Specification of the design wind load - a critical review of code concepts
submitted for publication to JWEIA

[3]   D. Orwig, J.L. Schroeder

Near-surface   wind   characteristics   of   extreme   thunderstorm   outflows
Journal of Wind Engineering and Industrial Aerodynamics (95) 2007 pp 565-584

[4]   C.C. Choi

Field measurement and experimental study of wind speed profile during thunderstorms
Journal of Wind Engineering and Industrial Aerodynamics (92) 2004 pp 275-290

Correction of the predicted mean wind speed
based on routine measurements at meteorological stations

J.A.Zuranski
Instytut Techniki Budowlanej, Warsaw, Poland

Keywords: wind speed, terrain roughness, gust factor, wind speed correction

ABSTRACT

One of the most important conditions that should be fulfilled for reliable estimation of the design wind speed is the representative character of a meteorological station and the location of an anemometer. It is evident and commonly accepted that an anemometer should be installed in an open terrain. Unfortunately, many meteorological stations initially situated outside of wooded or built up terrain, have been successively surrounded by new buildings and growing trees.

Correction is then necessary to eliminate the influence of the terrain roughness around meteorological stations on wind speed readings and prediction. However, this correction must take into account the change of the terrain roughness during many years of measurements.

Two approaches are possible: additional measurements at site or use of the existing results of routine measurements at meteorological station. The paper deals with the use of this archive data. Additional measurements are only mentioned here.

There are at least three possible methods of correction using additional measurements at site.

The first is an installation on an anemometer in a fully open terrain and short-term parallel, simultaneous wind measurements at meteorological station and in an open terrain. However, correction factors received from such measurements are representative only for time the measurements were done. Long-term wind speed data should be then reduced to the conditions being in the time of parallel measurements. Next the results of a probabilistic analysis are to be reduced to standard conditions using commonly accepted methods, e.g. according to Eurocode (2005).

The second method would be to measure intensity of turbulence using one anemometer at the meteorological station. Next the roughness length can be calculated using relations between it and the intensity of turbulence.

The third method is to measure wind speeds in several points on a mast situated at the meteorological station and also to define roughness length.

All measurements should be done for chosen wind directions, e.g. for 12 directional sectors.

However, probably most of meteorological stations in a country are in such situation that corrections should be made. It would be then difficult to carry out additional measurements at many stations and for 12 main directional sectors. An attempt of defining correction factors should be then done to use archive results of the routine wind speed measurements from many years. Such an attempt is presented in the paper.

In Poland two kinds of records are collected in archives: ten minute mean wind speeds and

---

Contact person: J.A.Zuranski, Instytut Techniki Budowlanej, Filtrowa 1, 00-611 Warszawa, Poland, tel. +48 22 57 96 267, FAX: +48 22 82 57 730, E-mail: jzuranski@pro.onet.pl

maximal gusts, all recorded for 36 compass directions. Ten minute mean wind speeds are recorded every hour, according to the directive of the WMO. If the difference between instantaneous and mean wind speed is equal or higher than 5 m/s then gust wind speed is also recorded. Figure 1 presents an example of the change during many years of annual maxima of gusts and in the same time measured ten minute mean wind speeds in directional sector 10.
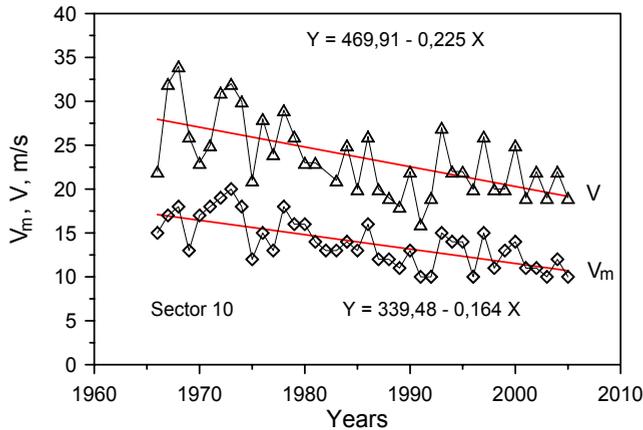
Figure 1. Many year change of the annual maxima of wind speed V (gusts) and V_m (10 min mean) at the meteorological station in Wroclaw, sector 10 (central direction of the sector 10 is 270^0 - western).

Decreasing of the wind speed, mean and instantaneous, seen in Fig.1, may be attributed to the clump of trees, situated westerly to the anemometer, growing during years. Trees are strongly protected and it is very difficult, if possible, to cut them even if there are close to the meteorological station. Similar decrease of wind speed has not been observed at sea side, where an anemometer is exposed to the open sea.

Dividing the equation of regression for gusts (upper expression in Fig. 1) by the equation for mean wind speed we receive maximum yearly gust factor as a function of years (Fig.2).
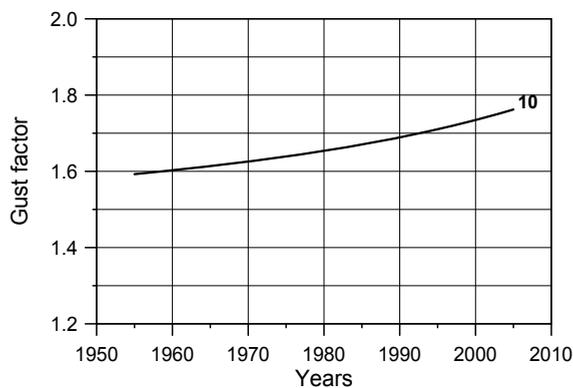
Figure 2. Annual maximum gust factor as a function of years of measurements; meteorological station in Wroclaw, sector 10

Next, taking the gust factor at a level of an anemometer as

$$G = 1 + k_p \cdot I_v(z_a) \tag{1}$$

and turbulence intensity

$$I_v(z_a) = \frac{1}{\ln\left(\dfrac{z_a}{z_0}\right)}, \tag{2}$$

where $z_a = 15$ m is the anemometer height, and assuming $k_p = 3.5$ we can write for 1966

$$1.62 = 1 + 3.5 \cdot \frac{1}{\ln\left(\dfrac{15}{z_0}\right)}. \tag{3}$$

Hence $z_0 = 0.053$ m which is in good agreement with $z_0 = 0.05$ m given in Eurocode (2005) for terrain category II (reference terrain). In sector 10 it is $G = 1.62$ for 1966 then all mean wind speed data should be reduced to this year using regression line given in Fig. 1.

The dependence of annual maxima of 10 min mean wind speed on years received after the correction is presented in Fig. 3. These data, considered as data from standard, reference terrain category can be evaluated using Gumbel probability distribution function.
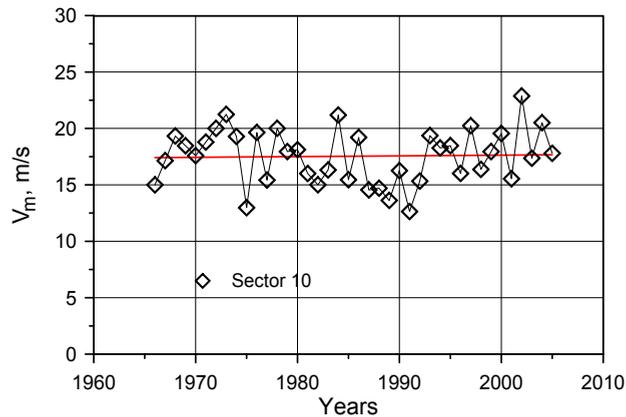
Figure 3. Annual maxima of the 10 min mean wind speed corrected for open terrain

Predicted values of 10 min mean wind speed of 50 year return period are as follows: before correction 22.2 m/s, after correction 24.3 m/s. Parameters of Gumbel probability distribution have been estimated using the last squares method.

In the full paper more examples will be presented. It must be noted that several assumptions have been made in this approach which may decrease the accuracy of the calculations. It must be also noted that some changes in recorded wind speed may be attributed to the change of anemometers, inevitable during many years of measurements. However, new instruments are usually of lower inertia than installed earlier and they rather do not diminish measured values of wind speed.

REFERENCES

EN 1991-1-4:2005 Eurocode 1: Actions on structures - Part 1- 4: General actions – Wind actions

A conditional model for the short-term forecast of severe wind phenomena

A. Freda, L. Carassale, G. Solari

DICAT – Department of Civil, Environmental and Architectural Engineering – University of Genoa – freda@dicat.unige.it – carassale@dicat.unige.it – solari@dicat.unige.it – Via Montallegro 1, 16145 Genoa, Italy

Keywords: wind speed, time series, forecasting.

ABSTRACT

The managing of large infrastructures such as airports, port terminals, railway networks, long-span bridges and wind farms requires the definition of strategies aimed reducing the risks related to the occurrence of strong winds, as well as minimizing the economical impact of wind-related outages. Such strategies usually involve a decision process that is asked, whenever is necessary, to temporarily suspend the infrastructure operation or impose some suitable limitation (e.g. vehicle velocity). These decisions are traditionally made on the basis of the personal experience of the operator, with the knowledge of the current local wind speed (often available to the operator in real time).

The necessity of increasing the reliability of the above decision process, reducing the subjectivity of the judgment and enabling some level of automation, encouraged the development of several mathematical tools aimed at forecasting the wind speed at a particular site within a temporal frame of a few tens of minutes. Railway network companies became particularly sensitive about this problem since, after the introduction of high-speed trains, the risk of overturning due to the wind action became a relevant issue (e.g. Imai et al., 2002, Cheli et al., 2003). Analogously, several port authorities addressed the problem of the wind speed prediction to optimize the terminal operation.

Contact person: Andrea Freda, DICAT – Department of Civil, Environmental and Architectural Engineering, University of Genoa, tel.:+39 (0)10 353 2384, fax: .:+39 (0)10 353 2292.
E-mail: freda@dicat.unige.it

Unfortunately the prediction of the wind speed is very difficult (Sfetsos, 2000) – it originates from a complex interaction between large-scale mechanisms such as earth rotation, solar radiation, temperature and pressure gradients and local-scale phenomena determined by the orographic characteristics of the terrain – and cannot be effectively obtained by typical tools employed in meteorology due to their computational complexity, resulting in time-consuming analyses, and the lack of sufficiently detailed real-time meteorological data.

As an alternative to a physically-consistent modelling of the wind speed, several inferential tools have been developed and used in last decades to simulate and to predict future values of wind time series. Earliest forecasting attempts (Alexiadis et al., 1997) make use of typical time-series analysis tools such as Box-Jenkins ARMA models (Box & Jenkins, 1976). Since ARMA models can be applied when the time series to be forecasted can be assumed as a realization of a stationary and Gaussian process, in most cases the data are first transformed in order to remove non-stationarity or impose a normal distribution. The performance of ARMA is rather variable when applied to wind data, depending on the order and on the time ahead, but is generally similar to the persistent model (i.e. the expected future value is equal to the present value; Fellows & Hill, 1990).

It is worth noting that in many practical applications the wind-speed forecast procedure may be limited (or focused) on the prediction of high-intensity winds, since weak winds are often not responsible of safety issues. This limitation enables the development of specialized models that, being able to predict strong wind conditions, can be implemented into alert and decision-making frameworks.

The present paper proposes a probabilistic model for the short-term forecast (i.e. a few tens of minutes in advance) of the intense values of wind speed time series. The model is based on the knowledge of the conditional probability density functions (cpdf) of the future wind speed, given the present (real-time recorded) value. Such cpdf can be estimated from the recorded data invoking the ergodicity of the time series and assuming some convenient probabilistic model. In the present application, the cpdf is modelled by a truncated Gaussian distribution, which, in spite of its simplicity, produces satisfactory results. This hypothesis should be revised as a short-time Gaussian assumption (i.e. the short-time variation of the wind speed is Gaussian) and does not implies any specific condition on the probability distribution of the time series. Once the cpdf model is known it is possible to evaluate (for any current wind speed) the future wind speed having a specified exceedance probability.

The above procedure has been applied on the wind-speed time series recorded by 11 anemometers installed by RFI (Rete Ferroviaria Italiana, Italian Railway Network) along the high-speed/high-capacity Rome-Naples railway line in Italy. The anemometers, placed at 2 m above rail level, are often in areas with complex orography and high roughness length. This type of installation, that has been chosen to record the wind speed actually encountered by trains, implies that the measurements are rather conditioned by local ground features and result in time series having rather different characteristics, both in intensity and probability distributions. For this reason, the ability of the proposed approach in forecasting time series without requiring any specific assumptions on their probabilistic distribution resulted particularly useful. Analogous applications are currently in progress for the wind-speed forecast in port terminal areas.

The practical applications demonstrate that the method is effective in forecasting the wind data, in particular strong events. Figure 1 shows the comparison between the recorded wind speed (V) and the 30-minutes-ahead forecasted values (V_τ), assuming a non-exceedance probability of the estimates equal to 95%. It can be observed that the forecasted values are generally on the safe side (empty markers) when the effective wind speed is intense, and that the underestimated values (full markers) are quite close to the recorded values.

Figure 2 shows the relative error of the 30-minutes-ahead forecast on the same set of data represented in Figure 1. The errors are not negligible at low wind speed, but such wind intensities are not relevant for the assessment of the wind hazard on lines. As the wind speed increases, the errors become smaller and the underestimations result below 10% of the current wind speed.

The analytical formulation of the method, as well as a more complete experimental validation are presented in the extended version of the paper.
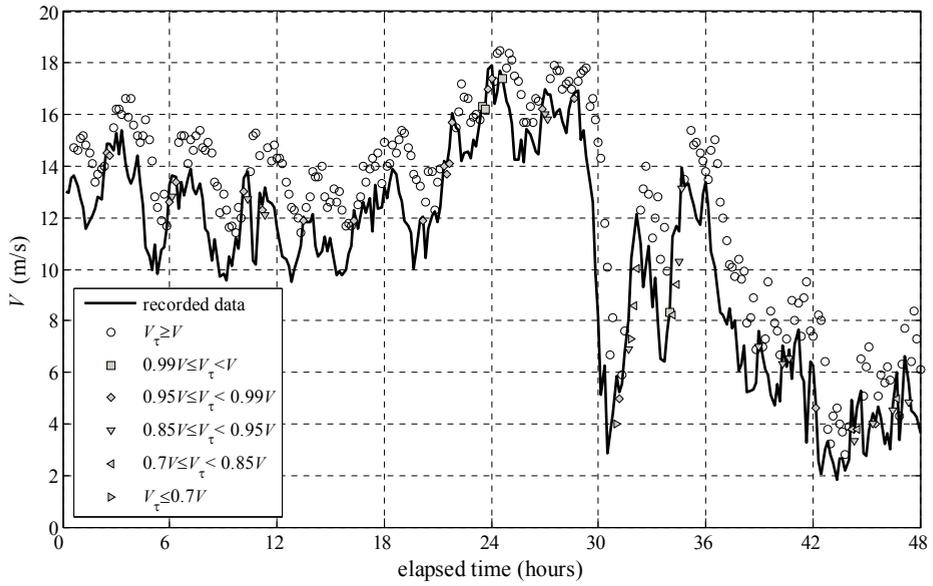
Figure 1. Wind time series (solid line) and 30-minutes-ahead forecast evaluated for non-exceedance probability 95% (symbols).
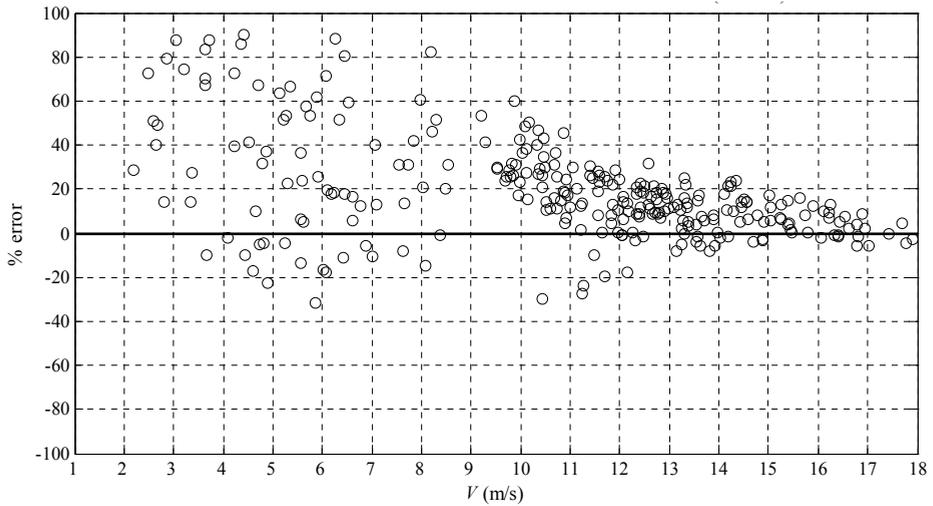
Figure 2. Relative error in the 30-minutes-ahead forecast (non-exceedance probability 95%).

REFERENCES

Sfetsos A. (2000). "A comparison of various forecasting techniques applied to mean hourly wind speed time series", Renewable Energy, 21, 23-35.

Imai T., Fujii T., Tanemoto K., Shimamura T., Maeda T., Ishida H., Hibino Y. (2002). "New train regulation method based on wind direction and velocity of natural wind against strong winds", J. Wind Engng. Ind. Aerod., 90 (12-15), 1601-1610.

Cheli R., Mancini G., Roberti R., Diana G., Cheli F., Corradi R., Tomasini G. (2003). "Cross-wind aerodynamic forces on rail vehicles: wind tunnel experimental tests and numerical dynamic analysis" Proc. WCRR, Edinburgh, UK.

Alexiadis M.C., Dokopoulos P.S., Sahsamanoglou H.S., Manousaridis I.M. (1998). "Short-term forecasting of wind speed and related electrical power", Solar Energy, 63 (1), 61-68.

Box G.E.P., Jenkins G.M. (1976). "Time series analysis: forecasting and control – Revised edition", Holden Day, Oakland, California.

Fellows A., Hill D. (1990). "Wind and load forecasting for integration of wind power into a meso-scale electrical grid", Proc. European Community Wind Energy Conference, Madrid, Spain, 636-640.

A Representation of Wind Velocity by means of Fractional Spectral Moments

G. Cottone, M. Di Paola

Dipartimento di Ingegneria Strutturale, Aerospaziale e Geotecnica (DISAG), Università degli Studi di Palermo, Viale delle Scienze, 90128 Palermo, (Italy)
E-mails:giuliocottone@unipa.it; dipaola@diseg.unipa.it

Keywords: Power Spectral Density, Correlation Function, Spectral Moments, Fractional Spectral Moments, Generalized Taylor Series, Fractional Calculus, Wind Speed Velocity

INTRODUCTION

The Spectral Moments (SM) introduced by Vanmarcke (1972) are the moments of the one-sided Power Spectral Density (PSD) function. Such quantities give information on the excursion failure, the bandwidth parameters and so on. In time domain the SM are covariances of the so-called analytic process in which the imaginary part is its Hilbert transform of the real one, see Di Paola (1985) and Di Paola et al. (1986, 1990). Other applications of the SM may be found in Barbato and Conte (2008), Caddemi et al. (2001), Michaelov et al. (1999), Muscolino (1991), Petrucci et al. (2000), Spanos (1992, 1993, 1994).

Even though the SM may be useful in some applications they are in general divergent quantities when the order of the SM increases. For example, an exponential type correlation function has divergent SM with order greater than two. It follows that the classical SM are not able to reconstruct the PSD.

Recently, the authors introduced new complex quantities that are the fractional spectral moments (FSM). The latter are fractional moments of the one-sided PSD. It has been shown in Cottone and Di Paola (2009, 2009b) that, by these quantities, one can reconstruct both the PSD and the correlation function in the whole domain.

In this paper, the capability of the fractional moments to reconstruct both PSD and correlation function for the Davenport and Kaimal spectra for wind velocity is presented.

FRACTIONAL SPECTRAL MOMENTS

The classical SM are defined as

$$\lambda_X^j = \int_0^\infty \omega^j S_X(\omega)\, d\omega; \qquad\qquad j = 0,1,2,... \qquad\qquad (1)$$

where $S_X(\omega)$ is the one-sided PSD of the stochastic process $X(t)$. It may be shown that λ_X^0 is the variance of $X(t)$. The second spectral moment is the variance of $\dot{X}(t)$ while the first SM is the cross covariance between displacement and velocity of an analytic process whose real part is $X(t)/\sqrt{2}$ while the imaginary part is the Hilbert transform of the real part, Di Paola (1985). Yet, the SM diverge as j increases and then the SM may not reconstruct the PSD.

Now, we introduce new quantities that are the Fractional Moments of the one-sided PSD, that is

$$\lambda_X^\gamma = \int_0^\infty \omega^\gamma S_X(\omega)\, d\omega; \qquad\qquad \gamma \in \mathbb{C} \qquad\qquad (2)$$

Since λ_X^γ is now a function of the complex exponent γ in eq.(2), hereinafter we denote λ_X^γ as $\Lambda_X(\gamma)$. It has been proved, in Cottone and Di Paola (2009), that $\Lambda_X(\gamma)$ restores both the $S_X(\omega)$ and its Fourier transform pair, namely the correlation function denoted as $R_X(\tau)$. It has to be remarked that $S_X(\omega)$ and $R_X(\tau)$ are real functions of ω and τ ($\omega, \tau \in \mathbb{R}$), while $\Lambda_X(\omega)$ is a complex function of the complex variable γ. We now introduce the Riesz fractional integral and derivative as

$$\left(I^\gamma f\right)(t) = \frac{1}{2\nu(\gamma)} \int_{-\infty}^\infty \frac{f(\tau)}{|t-\tau|^{1-\gamma}}\, d\tau; \quad Re\,\gamma > 0, \gamma \neq 1,3,5,...$$
$$\left(\mathcal{D}^\gamma f\right)(t) = \frac{1}{2\nu(\gamma)} \int_{-\infty}^\infty \frac{f(t-\tau)-f(\tau)}{|t-\tau|^{1+\gamma}}\, d\tau; \quad Re\,\gamma > 0, \gamma \neq 1,3,5,... \qquad (3)$$

where $\nu(\gamma) = \Gamma(\gamma)cos(\pi\gamma/2)$, being $\Gamma(\gamma)$ the Euler gamma function and $\gamma = \rho + i\eta$, ($\gamma, \eta \in \mathbb{R}$), and $i = \sqrt{-1}$. We finally recall that the Fourier transform of Riesz integral and derivatives of $f(t)$ may be written as

$$\mathcal{F}\left\{\left(I^\gamma f\right)(t); \omega\right\} = |\omega|^{-\gamma}\, \mathcal{F}\left\{f(t); \omega\right\}; \quad \mathcal{F}\left\{\left(\mathcal{D}^\gamma f\right)(t); \omega\right\} = |\omega|^\gamma\, \mathcal{F}\left\{f(t); \omega\right\} \qquad (4)$$

see Samko et al. (1993) for further properties. It has been shown in Cottone and Di Paola (2009) that the two following relevant relations

$$\left(I^\gamma R_X\right)(0) = \int_0^\infty \omega^{-\gamma} S_X(\omega)\, d\omega = \Lambda_X(-\gamma); \quad \left(\mathcal{D}^\gamma R_X\right)(0) = \int_0^\infty \omega^\gamma S_X(\omega)\, d\omega = \Lambda_X(\gamma) \qquad (5)$$

hold true.

Moreover by using Mellin transform concepts and basic definitions of fractional calculus, it has also been demonstrated that

$$R_X(\tau) = \frac{1}{2\pi i} \int_{\rho-i\infty}^{\rho+i\infty} \nu(\gamma)\left(I^\gamma R_X\right)(0)|\tau|^{-\gamma}\, d\gamma = \frac{1}{2\pi i} \int_{\rho-i\infty}^{\rho+i\infty} \nu(\gamma)\Lambda_X(-\gamma)|\tau|^{-\gamma}\, d\gamma \qquad (6)$$

It has to be stressed that the integral in eq.(6) may be sought as a generalized Taylor expansion in the sense that by knowing the Riesz fractional integral in zero of the correlation function $R_X(\tau)$, then the function may be reconstructed in the whole domain. Moreover, it should be noticed that the usual Taylor series for large value of the variable is always divergent while the generalized Taylor series (6) remains always convergent for $0 < \rho < 1$ since the integral is performed in the imaginary axis. A simple discretization of eq.(6) can be performed as

$$R_X(\tau) \cong \frac{\Delta\eta}{2\pi} \sum_{k=-m}^m \nu(\gamma_k)\Lambda_X(-\gamma_k)|\tau|^{-\gamma_k}; \quad \gamma_k = \rho + ik\Delta\eta \qquad (7)$$

and $m\Delta\eta = \bar{\eta}$ is some cut-off value. Fourier transform of the latter, produces

$$S_X(\omega) = \frac{1}{4\pi i} \int_{\rho-i\infty}^{\rho+i\infty} \Lambda_X(-\gamma)|\omega|^{\gamma-1}\, d\gamma \qquad (8)$$

and in the discrete form

$$S_X(\omega) = \frac{\Delta\eta}{4\pi} \sum_{k=-m}^{m} \Lambda_X(-\gamma_k)|\omega|^{\gamma-1} \tag{9}$$

Eqs.(6) and (8) exactly represent the correlation function and the PSD, respectively, and the approximated forms in eqs.(7) and (9) provide quite accurate results also for pathological PSD shapes like Pierson-Moskowitz spectrum or wind velocity spectra. The latter application will be provided in the next section.

NUMERICAL APPLICATIONS

In this section the approximation proposed is applied to the Davenport and Kaimal power spectra of wind fluctuations that have the form

$$S_V(\omega) = \frac{4\pi k_0 V_{ref}^2}{|\omega|} \frac{q(\omega)^2}{\left(1+q(\omega)^2\right)^{4/3}} \tag{10}$$

$$S_V(\omega) = \frac{200v^* z_0}{4\pi v} \left(\frac{1}{1+50|\omega|z_0/(2\pi v)}\right)^{5/3} \tag{11}$$

respectively, where V_{ref} is the mean wind speed at the reference level, k_0 is a roughness characteristic of the analyzed site and $q(\omega)=1200\omega/(2\pi V_{ref})$ (Eq.(10)); z_0 is the height of the measured mean wind speed, v is the value of the mean wind speed, v^* is a coefficient dependent of the height by the logarithmic relation $v^* = 0.4v/ln(z_0/k)$ and k is a roughness coefficient related to the exposed site.

Figure 1: Comparison between the exact (continuous line) and the approximated (dotted line) Davenport's correlation function (left panel) and PSD (right panel).

In order to approximate the spectra in eqs.(10) and (11), the approximated forms in terms of fractional spectral moments have been used following eqs.(7) and (9). We selected the parameters: $\rho = 0.3$, $\Delta\eta = 0.1$ and m=30 for the Davenport's correlation function and PSD, while in the Kaimal case we selected $\rho = 0.5$, $\Delta\eta = 0.5$ and m=30. The FSM used have been calculated in closed form by means of Mathematica and in Figure 1 and Figure 2 the approximated functions (dotted) are contrasted with the exact expressions, showing the high level of accuracy.

Summing up, the class of FSM calculated from the one-sided PSD and defined in (2) has the important properties: i) it extends in a natural way the classical spectral moments in the same way fractional calculus generalizes the ordinary calculus; ii) is able to represents both the correlation function and the spectral density function, that is, to some extent one might think at FSM as a third

way to characterize processes. iii) The representation proposed, exact in its integral formulation, is extremely useful in its approximated, because by a sum of a finite number of FSM very good approximating functions are given.

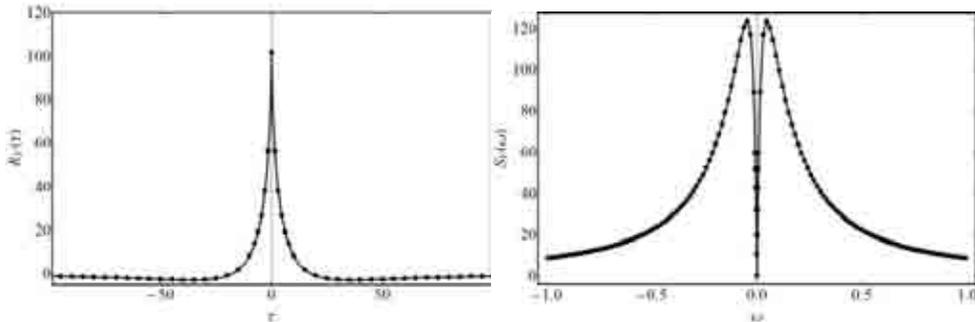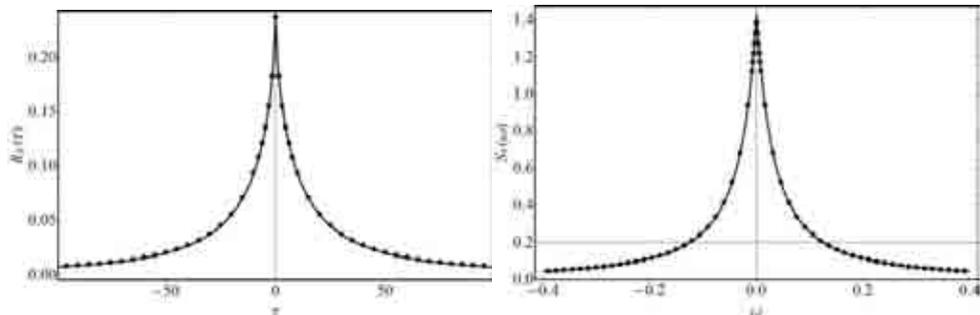
Figure 2: Comparison between the exact (continuous line) and the approximated (dotted line) Kaimal's correlation function (left panel) and PSD (right panel).

REFERENCES

Barbato M., Conte J. (2008). "Spectral characteristics of non-stationary random processes: Theory and applications to linear structural models", Probabilistic Engineering Mechanics, vol. 23, 416–26.

Caddemi S., Colajanni P., Muscolino G. (2001). "On the non stationary spectral moments and their role in structural safety and reliability", Structural Engineering, Mechanics and Computation, 1113–20.

Cottone G., Di Paola M. (2009). "On the use of fractional calculus for the probabilistic characterization of random variables", Probabilistic Engineering Mechanics, 24 (2009) 321-330
doi:10.1016/j.probengmech.2008.08.002.

Cottone G., Di Paola M. (2009b, submitted). "A New Representation of Power Spectral Density and Correlation Function by Means of Fractional Spectral Moments", Probabilistic Engineering Mechanics.

Di Paola M. (1985). "Transient spectral moments of linear systems", SM Archives, vol. 10, 225–43.

Di Paola M., Muscolino G. (1986). "On the convergent parts of high order spectral moments of stationary structural responses", Journal of Sound and Vibration, vol.22, 233–45.

Di Paola M., Petrucci G. (1990). "Spectral moments and pre-envelope covariances of nonseparable processes". Journal of Applied Mechanics, Transactions ASME, vol.57, 218–24.

Michaelov G., Sarkani S., Lutes L. (1999). "Spectral spectral characteristics of nonstationary random processes a critical review", Structural Safety, vol. 21, 223–44.

Michaelov G., Sarkani S., Lutes L. (1999). "Spectral characteristics of nonstationary random processes response of a simple oscillator", Structural Safety, vol. 21, 245–67.

Muscolino G. (1991). "Non-stationary pre-envelope covariances of non-classically damped systems", Journal of Sound and Vibration, 149, 107–23.

Petrucci G., Di Paola M., Zuccarello B. (2000). "On the characterization of dynamic properties of random processes by spectral parameters", Journal of Applied Mechanics, vol. 67, 519–26.

Samko S., Kilbas A.A., Marichev O.I. (1993). *Fractional Integrals and Derivatives. Theory and Applications*. Gordon and Breach Science Publishers, Switzerland.

Spanos P.D., Miller S. (1992). "Linear system spectral moments determination", Probabilistic Mechanics and Structural and Geotechnical Reliability, Proceedings of the Specialty Conference, 192–95.

Spanos P.D., Miller S. (1993). "Hilbert transform generalization of a classical random vibration integral", American Society of Mechanical Engineers, Design Engineering Division, vol. 54, 195–203.

Spanos P.D., Miller S. (1994). "Hilbert transform generalization of a classical random vibration integral", Journal of Applied Mechanics, Transactions ASME, vol. 61, 575–81.

Vanmarcke E. (1972). "Properties of spectral moments with applications to random vibrations", Journal of Engineering Mechanical Division, ASME, vol. 42, 215–20.

**MONITORING OF STRUCTURES
AND VIBRATION CONTROL**

Fuzzy hybrid control of wind response in a tall building using a smart tuned mass damper

H.S.Kim

Division of Architecture, Sunmoon Univ., Asan, 336-708, Korea, hskim72@sunmoon.ac.kr

Keywords: fuzzy hybrid control, smart tuned mass damper, skyhook, groundhook, MR damper

ABSTRACT

To date, building structures become increasingly slender, taller and wind-sensitive with higher strength materials and lighter structural systems. Very often, such slender and tall buildings experience excessive wind-induced vibration, which will cause discomfort to occupants or even shatter windows. Vibration control of tall buildings subjected to wind excitation has been studied extensively, and various types of control devices and algorithms have been developed. The tuned mass damper (TMD) is one of the most widely-used control devices in civil structures for vibration control because it is easy to install no matter for a new or old structure. When properly tuned, it can effectively suppress excessive vibrations of a structure. However, the effectiveness of a conventional TMD may be impaired because of its high sensitivity to frequency mistuning or to variations of the dynamic characteristics of a structure. The mistuning or off-optimum damping of TMD will reduce its vibration control effectiveness significantly. Thus, to improve the effectiveness and robustness of TMD, many types of TMDs, such as active TMD (ATMD), multiple TMD (MTMD), hybrid TMD (HTMD) etc., are being studied. Although ATMD and HMD can demonstrate superior performance than the best possible passive TMD, the active system is more costly, more complex and needs careful maintenance, all of which makes it less reliable than the passive system. Recognizing the performance benefits as well as lack of stability of active systems, the concept of semi-active mass

Contact person: H. S. Kim, Division of Architecture, Sunmoon Univ., Tel.: +82-41-530-2315, fax: +82-41-530-2839
E-mail hskim72@sunmoon.ac.kr

damper system has been introduced. Semi-active control systems, which can vary the stiffness or damping in real time, demonstrate better control effects than the passive systems and consumes less power than the active systems. Additionally, semi-active control devices can behave as passive devices in the event of loss of power, thus they are reliable. Recently, various studies on semi-active control devices, which can provide the reliability of passive systems and the adaptability of active systems, have been conducted for the vibration control of civil structures (Symans & Constantinou, 1999).

In this study, a semi-active smart damper was employed to develop a smart tuned mass damper (STMD). Since damping force of the STMD can be controllable, control performance of STMD is expected to be improved comparing with a conventional passive TMD. A magnetorheological (MR) damper was used as a smart damper as shown in Figure 1 because of its low power requirements and failure-safe advantages. To appropriately change the resisting forces of the smart damper of STMD in real time based on structural responses, a semi-active control algorithm is required. Among conventional semi-active control algorithms, skyhook and groundhook control algorithms are used in this study because they need very simple computation to determine control commands. Usually, skyhook controller can effectively reduce TMD motion and groundhook controller shows good control performance for the reduction of building responses. Hybrid control strategy can be employed to adjust control forces generated by two controllers by using a weighting factor. In this study, fuzzy logic controller was introduced to determine an optimal weighting factor in real time resulting in improvement of control performance of conventional hybrid control strategy.
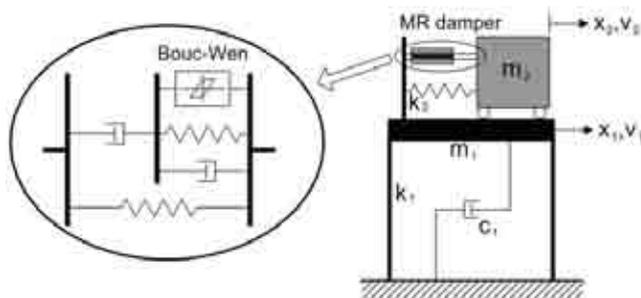
Figure 1: Smart TMD system using MR damper

The wind-induced benchmark building defined by Yang et al. (2004) is used to investigate the control performance of a STMD. The benchmark building is a 76-story concrete office tower in Melbourne, Australia. It is a slender building 306 m tall with a height to width ratio of 7.3; hence, it is wind sensitive. Across wind load data obtained from wind tunnel tests were used in the numerical simulation. The control performances of STMD were evaluated comparing with those of the sample TMD and ATMD proposed in the benchmark problem. Nagarajaiah and Varadarajan (2000) developed a VS-TMD with variable stiffness device, that has the distinct advantage of continuously returning its frequency by real time control and thus, robustness to changes in building stiffness and damping. Varadarajan and Nagarajaiah (2004) applied the VS-TMD to the 76-story benchmark building and evaluate control performances of it. Control results presented by them were compared with those of the STMD proposed in this study. Time history analyses of 900 seconds with a time step of 0.001 sec were performed to investigate the control performances of various TMDs. Four types of mass dampers were used to control the wind-induced vibration of the benchmark building as shown in Figure 2. Among them, the TMD and ATMD are sample controllers presented in the benchmark problem as illustrated in Figures. 2(a) and 2(b). A tuned mass damper presented in Figure 2(c) is a VS-TMD. The STMD proposed in this study is presented in Figure 2(d).

(a) TMD (b) ATMD (c) VS-TMD (f) STMD

Figure 2: Example tuned mass dampers used in this study
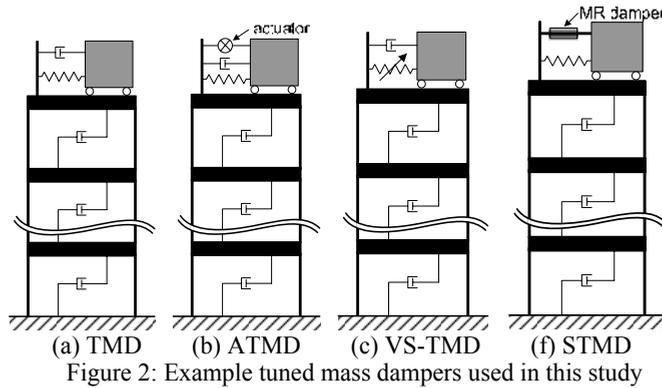
The numerical simulations show that the control performance of STMD is significantly superior to that of the conventional TMD. It is also shown that STMD can reduce the response similar to the ATMD; however, with an order of magnitude less power consumption. In this study, the STMD composed of 50kN damper can appropriately control the benchmark building, thus the smart tuned mass damper proposed in this study can be realized without difficulty under current technology. It is also shown that fuzzy hybrid controller can effectively adjust skyhook and groundhook control algorithms and reduce both responses of TMD and building.

Table 1: Peak responses of the example structure

Floor No.	TMD		ATMD		VS-TMD		STMD	
	Disp. (cm)	Acc. (cm/s^2)	Disp. (cm)	Acc. (cm/s^2)	Disp. (cm)	Acc. (cm/s^2)	Disp. (cm)	Acc. (cm/s^2)
1	0.04	0.21	0.04	0.23	0.04	0.27	0.04	0.21
30	5.60	4.68	5.14	3.37	5.11	3.91	4.92	3.71
50	13.34	9.28	12.22	6.73	12.14	7.54	11.67	7.12
55	15.54	10.74	14.22	8.05	14.13	8.25	13.59	8.17
60	17.80	12.70	16.27	8.93	16.17	8.86	15.54	9.33
65	20.10	14.72	18.36	10.05	18.25	10.37	17.54	10.18
70	22.43	16.77	20.48	10.67	20.35	11.75	19.56	11.42
75	24.84	19.79	22.67	11.56	22.52	14.02	21.65	13.13
76	25.38	20.52	23.15	15.89	23.01	14.68	22.12	14.31
md	42.60	46.18	74.27	72.64	68.01	69.37	87.27	88.58

REFERENCES

Symans M. D., Constantinou M. C. (1999). "Semi-active control systems for seismic protection of structures: a state-of-the-art review," Engineering Structures, Vol. 21, 469-487.

Yang J. N., Agrawal A. K., Samali B., Wu J. C. (2004). "Benchmark problem for response control of wind-excited tall buildings," Journal of Engineering Mechanics, ASCE, Vol. 130, No. 4, 437-446.

Nagarajaiah S., Varadarajan N. (2000). "Novel semiactive variable stiffness tuned mass damper with real time tuning capability," Proc.13th Engineering Mechanics Conf 2000 (CD ROM), Reston, Va.

Varadarajan N., agarajaiah S. (2004). "Wind Response Control of Building with Variable Stiffness Tuned Mass Damper Using Empirical Mode Decomposition/Hilbert Transform," Journal of Engineering Mechanics, ASCE, Vol. 130, No. 4, 437-446.

Application of wind tunnel measurements in the time domain vibration control analysis

1st K.T. Tse, 2nd K.K.C. Wong, 3rd K.L. Wong

Department of Building and Construction, City University of Hong Kong – timtse@cityu.edu.hk – Tat Chee Avenue, Kowloon Tong, Kowloon, Hong Kong.

AECOM – Maunsell AECOM Building Engineering- – kelvin.wong@maunsell.aecom.com – 13/F Grand Central Plaza, Tower 2, 138 Shatin Rural Committee Road, Shatin, Hong Kong.

AECOM – Maunsell AECOM Building Engineering- – Kongloi.Wong@maunsell.aecom.com – 13/F Grand Central Plaza, Tower 2, 138 Shatin Rural Committee Road, Shatin, Hong Kong.

ABSTRACT

Owing to the limited storage capacity and computational power of computers in the 1980s, analyses for aerodynamic model studies, such as high-frequency base balance (HFBB) or synchronous multi-pressure sensing system, have been traditionally conducted in the frequency domain. As computer technology has improved and the necessity to conduct the vibration control analysis in the time domain grows, this paper investigates the feasibility of implementing vibration control analyses in the time domain using measurements of aerodynamic model studies. A series of wind tunnel tests was conducted to determine the wind forces exerted on a benchmarking building and the building peak responses were substantially alleviated by about 25% using smart tuned mass damper (STMD).

INTRODCTION

The wind tunnel HFBB testing technique was developed in the early 1980s (Davenport and Tschanz, 1981) and has become one of the most common techniques for predicting wind-induced forces for tall building design. Predictions of mean and dynamic loads and responses are interpreted analytically

Contact person: 1st K.T. Tse, Department of Building and Construction, Tat Chee Avenue, Kowloon Tong, Kowloon, Hong Kong, TEL: (852) 21942747 and FAX: (852) 27887612. E-mail timtse@cityu.edu.hk

using the modal forces estimated from the overturning and torsional moments experienced by a lightweight and stiff model. The building responses can be obtained in the time domain using random vibration theory or frequency domain using spectral analysis for stationary random loads. Owing to the limited storage capacity and computational power of computer in the 1980s, it is common practice in wind engineering to conduct the analysis in the frequency domain.

With recent advancements in computer technology, the primary objective of this study is to investigate the feasibility of conducting vibration control analysis in the time domain using wind force information obtained from aerodynamic model studies. The second generation wind-excited benchmark building was wind tunnel tested and employed to investigate the accuracy of the analysis method. The results of the vibration analysis in the time domain were evaluated in this paper.

FORMULATION OF EQUATIONS OF MOTION

A general matrix formulation of the equation of motion for a tall structure with rigid floor systems subject to random wind loads can be expressed as,

$$\mathbf{M\ddot{x}} + \mathbf{C\dot{x}} + \mathbf{Kx} = \mathbf{W} \tag{1}$$

where $\mathbf{M}$, $\mathbf{C}$, and $\mathbf{K}$ are the structural mass, damping, and stiffness matrices respectively; $\mathbf{x}$ is the displacement vector in metres or radians; and $\mathbf{W}$ is the wind excitation vector in N or N-m. By means of modal superposition with mode shapes computed at the mass centres, Eq. (1) is transformed as follows for the jth mode,

$$m_j \ddot{\xi}_j(t) + c_j \dot{\xi}_j(t) + k_j \xi_j(t) = w_j(t) \tag{2}$$

For wind engineering, it has been found convenient to express and analyse the effects of wind on a given tall building in the frequency domain, assuming that the wind loads are stationary and normally distributed. The power spectral density (PSD) of the generalised coordinate for the jth mode is determined according to Eq. (3).

$$S_{\xi_j}(\omega) = \frac{1}{k_j^2} \left| H_j(\omega) \right|^2 S_{w_j}(\omega) \tag{3}$$

Traditionally, the effects of the control device were routinely approximated by the modal damping values which were subsequently incorporated in the mechanical admittance function in the HFBB frequency domain analysis, as expressed in Eq. (3). The approximation of modal damping values in the frequency domain analysis, on one hand, does not precisely reveal the performance of the control device and is applicable only to passive-type dampers. On the other hand, it is difficult to characterize the effects of some damping devices as only a modal damping ratio.

TIME DOMAIN ANALYSIS PROCEDURES

For the current study, the time domain dynamic analysis procedures use a state-space technique in which the modal system is initially solved to determine the generalised coordinate time histories (i.e. $\ddot{\xi}_j(t), \dot{\xi}_j(t)$, and $\xi_j(t)$). The state-space form of Eq. (2) is:

$$\dot{\mathbf{Z}} = \mathbf{AZ} + \mathbf{B}w_j(t) \tag{4}$$

By adopting the equivalent static force concept of earthquake engineering, the internal forces associated with the displacement along the x-axis for the jth mode are formulated in Eq. (5).

$$Fx_j(z_i,t) = \omega_j^2 \xi_j(t) m(z_i) \phi_{jx}(z_i) \tag{5}$$

These equivalent static forces, by definition, will cause precisely the jth mode displacements when imposed externally and were employed as the external forcing functions for the subsequent vibration control analysis in the time domain.

NUMERICAL RESULTS

The building model considered in this study is the second generation wind-excited benchmark building (Tse et al., 2007), which undergoes 3D lateral-torsional motions under excitations and represents majority of modern tall buildings. A 1:400 scale rigid model of the benchmark building, as shown in Fig. 1, was constructed from acrylic and wind tunnel tested to measure surface wind pressures acting on the building. The model was installed with 14 layers of pressure-taps over its height, with 32 pressure-taps in each layer. The surface pressures measured from the test were converted into 14 layers of alongwind, crosswind, and torsional wind load distributions, from which the base overturning and torsional moments corresponding to a HFBB test were subsequently synthesised.
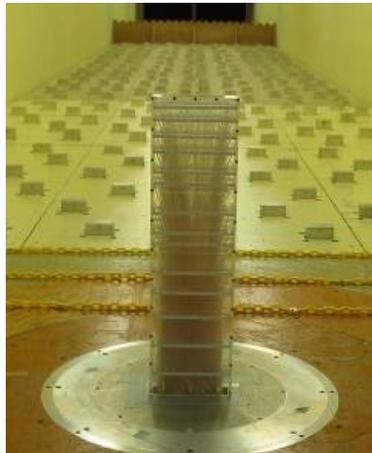
Figure 1: Pressure-tapped benchmark building model inside wind tunnel.

A 20 tonne MR damper (Yang, 2001) was mounted in each orthogonal direction of a bi-directional TMD as a semi-active system to numerically illustrate the vibration control of the benchmark building. The effective mass of the STMD is about 0.4% of the total mass of the building, and its undamped natural frequency in the y-direction and x-direction are set at 0.22 Hz and 0.42 Hz, respectively. The damping ratios of the STMD for both directions are 5% of critical.

Because the benchmark building underwent 3D lateral-torsional motions, the STMD was offset from the geometrical centre of the building at a distance of 32 m in the x-direction and 8 m in y-direction to suppress both translational and torsional motions. It should be noted that it was assumed that the STMD did not induce any additional wind forces on the building although it was installed on the roof. In this study, the linear-quadratic regulator (LQR) was used for the semi-active control. The control force f_c was determined by minimizing a quadratic cost function over a period of time to reduce the tip accelerations, with regards to the maximum available control force generated by the damping device.

The building responses with control were compared with the uncontrolled responses, as shown in Fig. 2. In general, the STMD shows its capability to mitigate the wind-induced orthogonal translation responses as well as the torsion responses.
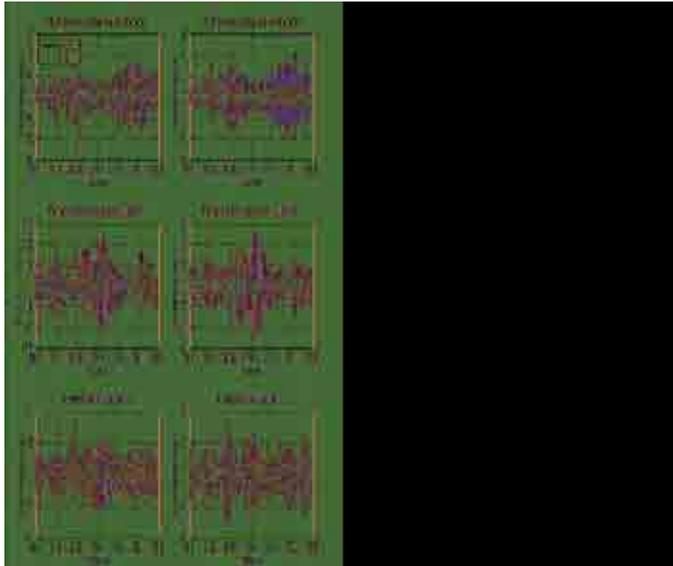
Figure 2: The uncontrolled and controlled tip displacement and acceleration responses of the wind-excited benchmark building.

CONCLUSIONS

The vibration control analysis in time domain using wind force information obtained from aerodynamic model tests, such as the high-frequency base balance, was successfully exercised and demonstrated in this paper. A series of wind tunnel tests were conducted to determine the wind loads experienced by the second generation wind-excited benchmark building, from which the base overturning moments and torsional torque were synthesized. The base moment data were used in the subsequent time domain vibration control analyses to determine the building tip displacement and acceleration responses.

The bi-directional TMD was designed with natural frequencies slightly less than the building's first two natural frequencies and equipped with MR dampers to provide additional controllable damping forces to significantly mitigate both the acceleration and displacement responses in the translation directions and slightly smaller reductions in torsion. The maximum generated control forces were 35kN with a maximum stroke of 42 mm in x-direction and 476 kN with a maximum stroke of 526 mm in y-direction. Correspondingly, the standard deviation and peak responses were reduced by over 50% and about 25%, respectively.

REFERENCES

Davenport A.G. and Tschanz T. (1981). "The response of tall buildings to wind," Proc. 4th U.S. Nat. Conf. of Wind Engineering, July 27-29, Seattle, Washington, U.S.A.

Tse K.T., Kwok K.C.S., Hitchcock P.A., Samali B. and Huang M.F. (2007). "Vibration control of a wind-excited benchmark tall building with complex lateral-torsional modes of vibration," Adv. Struct. Engrg., Vol. 10, pp. 283-304.

Yang G.Q. (2001) "Large-scale magnetorheological fluid damper for vibration mitigation: modelling, testing and control," PhD Thesis, The University of Notre Dame, U.S.

Yang G., Spencer Jr. B.F., Carlson J.D. and Sain M.K. (2002) "Large-scale MR fluid dampers: modelling and dynamic performance considerations", Journal of Engineering Structures, Vol. 24(3), pp. 309-323.

Structural lifetime prediction for wind energy converters based on health monitoring and system identification

1st S. Lachmann, 2nd M. Baitsch, 3rd D. Hartmann, 4th R. Höffer

Faculty for Civil Engineering, Ruhr-University Bochum, stefan.lachmann@rub.de –
matthias.baitsch@rub.de – hartus@inf.bi.rub.de – ruediger.hoeffer@rub.de

Keywords: Wind energy converters, monitoring, wind tunnel experiments, system identification.

Wind energy represents an emerging market offering enormous potential for future development. Today, around 90,000 wind energy converters (WECs) are installed worldwide with a high rate of new plants installed each year. Therefore, the supervision of the correct operation of WECs with respect to a reliable prediction of the lifetime of WECs is of high economical relevance. In the present contribution, an approach for WEC lifetime prediction is proposed. It is based on the combination of continuous monitoring, boundary layer wind tunnel experiments and extensive numerical modeling. In detail, the project aims at two major research objectives: Firstly, the sufficiently precise identification of the location and the extent of existing or evolving deteriorations based on a novel method for system identification. Secondly, the reliable lifetime prediction for damage sensitive parts of the structural system using continuously updated numerical models.

The conceptual core of the project is a continuous adaption of a complete numerical model of the WEC to the current system behavior of an actual facility. This highly realistic numerical model of the WEC, which accurately represents the current state of the real system including damages and deteriorations, is one of the main project objectives. The required model adaption procedure is based on specified data (wind speed, acceleration, strains and temperatures) measured in situ at a selected WEC along with experiments in the wind tunnel at the Ruhr-University of Bochum operated by the authors. The interaction between measurements, experiments and numerical modeling is illustrated in Figure 1.
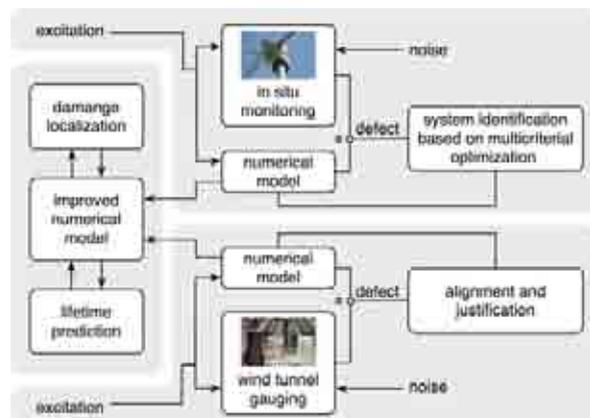
Figure 1: Monitoring, experiments and numerical modeling

It can be seen that damage localization and lifetime prediction are based on the continuously improved numerical model. On the right hand side, the data sources for the model updating procedure of the in situ monitoring and the wind tunnel experiments are shown.

The first steps within the scope of the research project (funded by the German Research Association DFG) are measurements in natural scale at a wind energy plant which is in use for already 10 years. An overview of the planned measurements can be found in Fig. 2. The measurements of the structural response are limited to the steel shaft of the WEC. Six three-dimensional accelerometers are adopted for the identification of the bending and torsion mode. The accelerometers are installed at five different heights at the inner surface of the steel shaft. At the top level, two accelerometers are mounted at a certain distance from each other in order to measure torsion oscillations. One three-dimensional accelerometer is installed at each of the subjacent measurement planes. Furthermore there are two additional planes with three displacement transducers and three temperature measurement points. Based on this data the distribution of stresses in each of these planes can be calculated if a linear material behavior of the steel shaft can be assumed. A three-dimensional Ultrasonic Anemometer USA-1 is placed on a telescopic mast and is used for the continuous monitoring of wind speeds at the location of the WEC. On site, the data is captured by a data-logger, which is connected to the computer used for data collection. This computer sends the measured data via DSL to a server system where a software agent transfers the measurements into a relational database. The data in the database can easily be accessed later on, using a web application equipped with the capability of exporting various data formats.
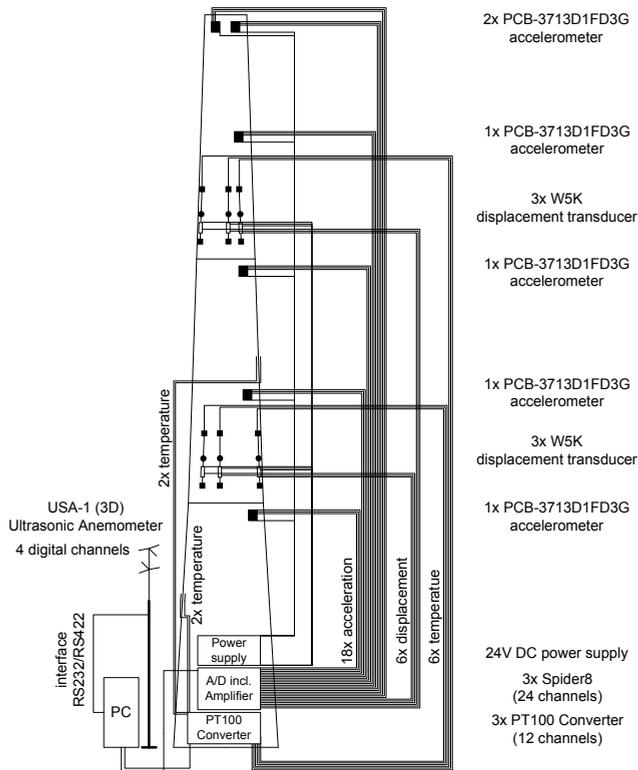
Figure 2: Overview of the planned measurement setup in natural scale

In parallel to the measurements in natural scale, measurements at a vibratory model in the boundary layer wind tunnel are in preparation. A structural replica model of the WEC is produced which allows

the physical simulation of the widely-complete response spectrum of the vibrating WEC. In particular it reflects the geometrical and also the elastic and dynamical characteristics if the structural similarity requirements can be observed. For the replica model, the stiffness and mass distribution of the shaft is simulated by a hollow casting made from a mixture of plastic and metal-powder. By the adjustment of the ratio of mixture of plastic and metal-powder the shaft stiffness of the original structure can be represented in model scale, see eg. Niemann & Rothert (1996). In a turbulent wind field, gust bodies of different sizes and shapes are responsible for the spatio-temporal correlation of wind speeds. The boundary layer turbulence in the wind tunnel emulates such gust bodies. In the boundary layer wind tunnel, comparable downscaled turbulence sizes are generated with the method of Counihan by means of a specific production of gust bodies in the flow, and through thickening the boundary layer. Using special built-in components, a geometric model scale of 1:100 can be realized. The response of the replica - measured in the boundary layer wind channel in a characteristic turbulent flow - can be transferred to the original WEC for the purpose of calibration and in order to increase the accuracy of the measurements.

Adequate experimental and numerical techniques are essential for the accurate identification of the parameters governing the transient dynamic behavior (mass, stiffness, mass moments of inertia, damping etc.).
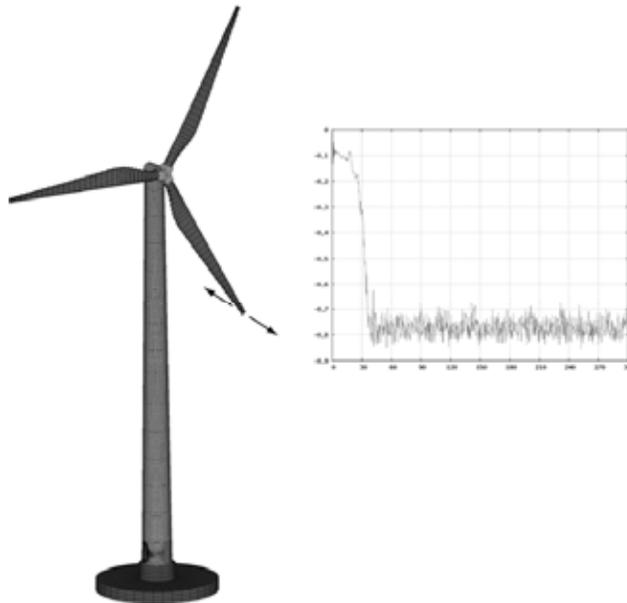
Figure 3: Finite element model and calculated dynamical response of a blade tip

The identification is based on a continuous monitoring of significant system quantities on site. The measured data is utilized to adapt and improve the numerical model repeatedly. The adaptions and improvements are achieved by minimizing the defect between the measured and simulated system response using numerical optimization. To this end, it is important not only to compare deterministic parameters but also to include stochastic properties, like expectation values, variances and probability density functions. The highly nonlinear structural response of the WEC (including gyroscopic effects) require the extensions of existing system identification techniques, see e.g. Müller-Slany (1993).

In a first step of the numerical modeling procedure, a finite element model of the whole wind turbine is been established based upon the commercial FEM software system Ansys. The transient dynamical response of the structure is simulated by a fully nonlinear analysis using an implicit time

integration scheme over a period of five minutes (see Fig. 3). The time histories of turbulent wind velocities, which are required for the calculation of the loads acting on the blades, are generated by the CFD code Ansys-CFX 11.0 based on a Large Eddy Simulation (LES) with Smagorinski turbulence model, see e.g. Guo (2008). In each time step of the structural analysis, loads are updated according to the wind speed and the rotation velocity of the rotor. More details on the structural model and the analysis procedure can be found in Liu (2008).

The realistic prediction of the remaining lifetime of the structure is based on an adapted novel model for operational stability. This includes most importantly the investigation of welded connections according to the notch stress concept (see eg. Galffy et al. (2006)). For parts of the structure which are mostly subjected to proportional loadings, the usual von-Mises equivalent stresses are utilized as effective stress values. For areas with non-proportional loading, a comparison to experiments should be carried out in order to determine which of the available critical-plane concepts is best suited. Consequently, the fatigue- and deterioration process is modeled stochastically, nonlinear and time-variant. Based on a refined representation of the nonlinearities and the time variance, the load history can be used more efficiently for capturing damage evolution compared to current approaches. The classical S-N-concept of Wöhler (based on linear damage accumulation) does not satisfy the requirement. Based on a stochastic model of the wind process, the remaining lifetime of the structure is determined using modern subset simulation techniques. The actual finite element model will be adapted either by modeling damages directly or by using special crack elements (XFEM).

ACKNOWLEDGEMENTS

REFERENCES

Müller-Slany H.H. (1993). "A Hierarchical Scalarization Strategy in Multicriteria Optimization Problems". in: Brosowski/Ester/Helbig/Nehse (Eds.): Multicriteria Decision, Proc. Of the 14th Meeting of the German Working Group "Mehrkriterielle Entscheidung" (Riezlern, Sept. 23-26, 1991), 69-79.
Niemann, H.-J., Rothert, H. (1996). " Beanspruchung von turmartigen Bauwerken bei Erregung durch Windkräfte am Beispiel des neuen Hannoverschen Fernmeldeturms". in: Baustatik und Baupraxis, Weimar, Tagungsheft BB6, 11.
Guo, Y. (2008). "Dynamical analysis of the structural response of a wind turbine – steel shaft and foundation". Master's Thesis, Building Aerodynamics Laboratory, Ruhr-University Bochum.
Liu, X. (2008). "Dynamical analysis of the structural response of a wind turbine – modelling of a rotor". Master's Thesis, Institute for Computational Engineering, Ruhr-University Bochum.
Galffy, M., Baitsch, M. and Hartmann, D. (2006). "Lifetime estimation of vertical bridge tie rods exposed to wind-induced vibrations". in: C. A. Mota Soares, J. A. C. Martins, H. C. Rodrigues, J. A. C. Ambrosio (editors), Proceedings of the III European Conference on Computational Mechanics. Solids, Structures and Coupled Problems in Engineering, Lisbon.

MR dampers with lever mechanism for response reduction in high-rise buildings under multidirectional wind loads

A.M. Aly, A. Zasso, F. Resta

Politecnico di Milano – aly.mousaad@polimi.it – Via G La Masa, 34, Milano, Italy

Politecnico di Milano – alberto.zasso@polimi.it – Via G La Masa, 1, Milano, Italy

Politecnico di Milano – ferruccio.resta@polimi.it – Via G La Masa, 1, Milano, Italy

Keywords: vibration control, MR dampers, tall buildings, wind loads, wind tunnel.

ABSTRACT

This paper presents semi-active control of wind-induced vibrations in tall buildings using MR dampers. The dampers are implemented using both internal and outer bracing systems to reduce the response of the building in the two lateral directions for both structural safety and human comfort concerns. MR dampers with internal bracing system are shown to be effective in one lateral direction where the building is behaving mostly in shear. For cantilever like vibrations, MR dampers with outer bracings are used. A proposed lever mechanism is used with the dampers to improve their performance. The proposed mechanism is shown to be very effective in reducing the capacity and number of dampers required. Semiactive decentralized bang-bang controller is used with the MR dampers.

BACKGROUND

Vibrations in buildings are of increasing importance as the use of high-strength, light-weight materials, longer floor spans, and more flexible framing systems result in structures that are more

---

Contact person: A.M. Aly, Politecnico di Milano, Via G La Masa 34, Milano, Tel: (+39) 0223998023 Fax: (+39) 0223998081 E-mail: aly.mousaad@polimi.it

prone to vibrations. In tall buildings, wind-induced vibrations may cause annoyance to the occupants (especially in the upper floors), impaired function of instruments, or structural damage.

Due to its low power requirements and fail safe property, magnetorheological (MR) dampers have been shown to mesh well with application demands to offer an attractive means of protecting civil infrastructure systems against severe earthquake and wind loading (Dyke et al., 1996; Aly, 2005; Aly and Christenson, 2008a). MR damper is a kind of viscous damper, in which an MR fluid inside the damper alters its viscosity according to the intensity of the applied magnetic field. The viscous force generated in the damper can be controlled by adjusting the current input to the electromagnets.

Successful implementation of dampers in buildings requires that the damper is connected between two points where a significant displacement is expected. Unlike short buildings under earthquake loadings, where dampers may be implemented between adjacent floors, in tall buildings, especially slender ones, the inter-story shear drift is usually not sufficient for a damper to work effectively. In the present study, internal and outer bracings are used with a proposed lever mechanism to provide significant displacements for the MR dampers.

METHODOLOGY

The building tower used in this study (Isozaki tower) is to be constructed in the city of Milan, Italy. The recent version of the tower is a concrete building with a total mass of about 1.4×10^8 kg. First six modes of the building are shown on Figure 1. Modal parameters are given in Table 1. Wind loads obtained from wind tunnel tests conducted at the Wind Tunnel of Politecnico di Milano on a scaled 1:100 rigid model of the tower are used. The response of the tower is shown to be out of the comfort limit required by the building's designer. A damping mechanism is required for both safety and comfort reasons. TMDs and ATMDs were proposed for the tower by Aly et al. (2008b, 2008c). This paper presents a new damping technique using MR dampers with lever mechanism.

| 1st Mode | 2nd Mode | 3rd Mode | 4th Mode | 5th Mode | 6th Mode |
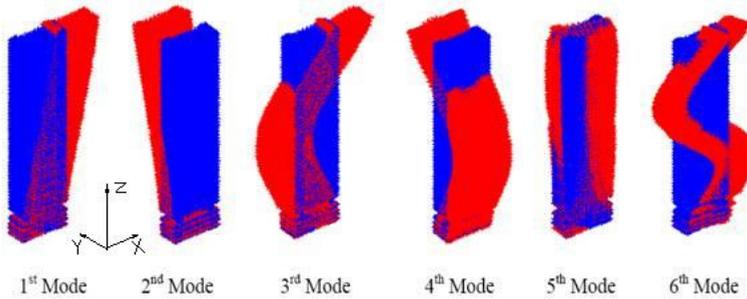
Figure 1: mode shapes of the finite element (FE) model of the tower with the coordinate system

Table 1: modal parameters of the FE model

Mode number	Generalized mass (kg.m^2)	Frequency (Hz)	Modal damping
1	3.55×10^7	0.1223	0.01
2	3.13×10^7	0.1352	0.01
3	3.27×10^7	0.4609	0.01
4	3.27×10^7	0.6473	0.01
5	2.08×10^{10}	1.0789	0.01
6	4.50×10^7	1.0833	0.01
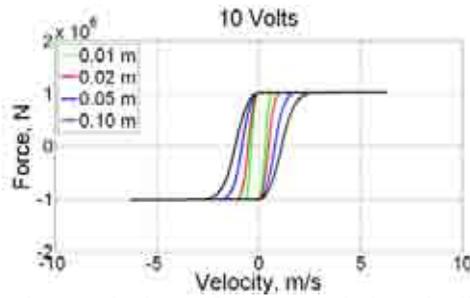
Figure 2: comparison between the damper force versus velocity under different amplitudes, 0.1 Hz sinusoidal displacement excitation at an input voltage of 10 Volts.
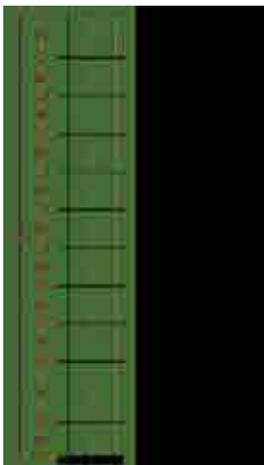
(a) primary structure

(b) damped structure utilizing *internal bracing* (x-direction)
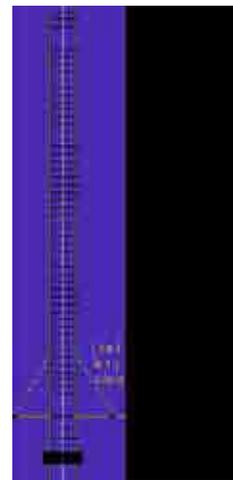
(c) damped structure utilizing *outer bracing* (y-direction)
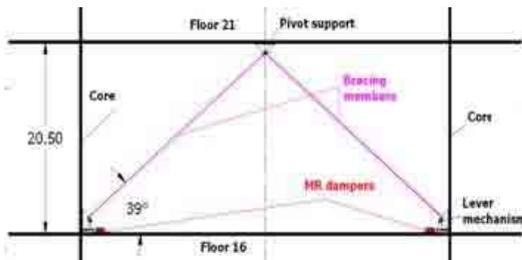
(d) MR damper internal bracing system between floors 16 and 21 (x-direction)
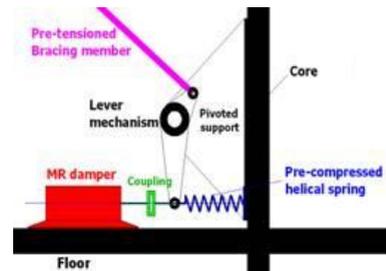
(e) the proposed lever mechanism with the MR damper bracing system

Figure 3: analytical model for primary structure and damped structure

Unlike tuned mass dampers, MR dampers do not require frequency tuning, and while there is an optimum resistance characteristic for each application, the overall damping achieved is usually not very sensitive to the exact resistance characteristic of the device. It is therefore sometimes possible to damp several modes with one device, provided the two points it connects have significant relative movement in each of the several vibrating modes of the structure. MR dampers require low power with no stability concerns. 1000 kN MR dampers model obtained from Khajekaramodin et al. (2007) is used with the lever mechanism. Force versus velocity of the MR damper is illustrated on Figure 2.

Where in the building to put the damper?! It is an important question. Unlike short buildings under strong ground motions, where one may expect significant drift between floors, in tall buildings, the relative shear drift between adjacent floors is usually small for a damper to work effectively. Moreover, slender buildings behave like cantilever, for which even if there is a significant floor drift angles, there is no significant shear drift (Aly, 2009). So, finding a place for the damper where relative displacement across the damper will be achieved is an important target.

The building under consideration behaves in one lateral direction (x-direction) in shear and the other direction (y-direction) as a cantilever. For the x-direction internal bracings are used to transmit the drift between two floors as indicated in Figures 3-(b) and 3-(d). Numerical optimization is conducted to reduce the required number of bracings and to find the most effective placement. The optimization shows that the bracing system between floors 16 and 21is the most effective placement. For response reduction in the y-direction, the floors are rotating and the relative drift across internal bracing is not significant, an outer bracing technique is used as illustrated on Figure 3-(c).

A lever mechanism is used in this study with both internal and outer bracings. The proposed mechanism with the MR damper bracing system is shown on Figure 3-(d). The lever mechanism magnifies the relative drift across the bracing which improves the performance of the damper and its ability to work at low frequencies. The mechanism may provide higher control forces using smaller damping forces which reduce dramatically the number of dampers required. Decentralized bang-bang controller is used to enhance the performance over the passive-on case. Bracing's stiffness is shown to be a key parameter that affects on the performance of the semiactive controller.

CONCLUSIONS

MR dampers with lever mechanism are proposed for reducing wind-induced vibrations in tall buildings in two lateral directions. Optimal placement of the dampers is obtained numerically. Not only the proposed lever mechanism improves the performance of the MR dampers in reducing buildings response, but also it reduces dramatically the required number of dampers. Semiactive controller's effectiveness is shown to be dependent on the stiffness of the bracing system.

REFERENCES

Dyke, S.J., Spencer, B.F., Jr., Sain, M.K., and Carlson, J.D. (1996). "Modeling and Control of Magnetorheological Dampers for Seismic Response Reduction", Smart Material and Structures, Vol. 5, pp. 565–575.

Aly, A.M. (2005). Vibration control in structures due to earthquake effects using MR damper. M.Sc. Thesis, Department of Mechanical Engineering, Alexandria University.

Aly, A.M. (2009). ON THE DYNAMICS OF BUILDINGS UNDER WINDS AND EARTHQUAKES: Response Prediction and Reduction. Ph.D. Dissertation, Department of Mechanical Engineering, Politecnico di Milano, Milan.

Aly, A.M. and Christenson, R.E. (2008a). "Fast hybrid testing of three controlled large-scale MR dampers for a three story nonlinear building", Inaugural International Conference of the Engineering Mechanics Institute (EM08), Department of Civil Engineering, University of Minnesota, Minneapolis, Minnesota.

Aly, A.M., Zasso, A. and Resta, F. (2008b). "Two Directional Active Control of a High-Rise Building Under Wind Loads with Different Attack angles: Comparison between LQR and Fuzzy Logic Controllers", The 7th European Conference on Structural Dynamics, University of Southampton, Highfield, Southampton, UK.

Aly, A.M., Resta, F. and Zasso, A. (2008c). "Active Control in a High-Rise Building under Multidirectional Wind Loads", SEI 2008 Structures Congress - Vancouver, Canada.

Khajekaramodin, A., Haji-kazemi, H., Rowhanimanesh, A. and Akbarzadeh, M.R. (2007), "Semi-active Control of Structures Using Neuro-Inverse Model of MR Dampers", First Joint Congress on Fuzzy and Intelligent Systems, Ferdowsi University of Mashhad, Iran 29-31 Aug 2007.

HUMAN COMFORT, STANDARDS AND CODES

The new Eurocode for wind loads, comparison of application in various countries

1st Chris P.W. Geurts, C.A. van Bentum, and others*

TNO Built Environment and Geosciences, Delft, the Netherlands

Wind loads, Eurocodes

ABSTRACT

The Eurocode system for calculation of building structures will replace the current national codes by 2010, in at least 30 countries. This means that harmonization of European wind loading calculations is almost there. The Eurocode system however allows national normalization bodies to alter values and methods, where allowed by the codes. This paper uses three simple examples, to show the differences which occur in results, when applying the new Eurocode, including National Annexes, in different countries. This paper may be a starting point for a discussion in Europe about the choices made, both in the Eurocode, and in the respective national Annexes.

INTRODUCTION

EN 1991-1-4:2005 specifies the wind loads in the Eurocode system. This code will replace the national wind loading codes in 2010. The Eurocode system allows individual countries to specify nationally determined parameters (NDP's), through National Annexes. In EN 1991-1-4, about 40 clauses are specified, in which such choice is allowed. These choices include the specification of the wind climate statistics, which are geographically dependent, but also include choice of procedures, specification of aerodynamic coefficients etcetera. Besides, EN 1990 specifies through the national Annexes, the safety levels, and consequently partial safety factors. Comparisons between the outcome of different national annexes will be the starting point for the future development of the Eurocode system. We have chosen three simple examples to open this discussion.

DESCRIPTION OF THE CASES

Three buildings have been chosen, for which the wind loads have been calculated. The calculation has been done for various countries. Different location have been chosen on either side near national borders, in order to observe which differences are found across borders. Besides, the loads for these buildings, when located in the respective capitals have been calculated. The cases have been taken

---

Contact person: C.P.W. Geurts, TNO Built Environment and Geosciences, PO Box 49, NL 2600 AA, Delft, The Netherlands, T: +31-152763162, E-mail: chris.geurts@tno.nl

from the work, previously done in the Leonardo da Vinci Pilot Project "development of skills facilitating implementation of Eurocodes', which was done before the final version of EN 1991-1-4 was published. Results from that work have been published elsewhere (Da Vinci, 2005). Every case will be calculated using the recommended values given in the code, assuming a basic wind velocity of 26 m/s.

Case 1: Industrial hall

The first building is a simple industrial hall with a steel structure consisting of six frames with a centre to centre spacing of 5 metres, thus giving a length of 25 metres. The height is 10 metres, and the width is equal to 20 metres. The roofs and facades are without dominant openings. The building is located in a suburban terrain, within an industrial park with similar buildings. About 500 metres upstream, an open exposure is found.

The pressure distributions over the cross section of the hall are calculated, for wind normal to the longer façade. As a final result, the overall horizontal force, calculated at base level, is provided.

Per country and location, the following intermediate results are calculated:
1. The basic wind velocity pressure, q_b, according to chapter 4 of EN 1991-1-4;
2. The peak wind velocity q_p at roof height, $h = 10$ metres, according to clause 4.5 of EN 1991-1-4;
3. The distribution of c_{pe} over the cross section of the frame, determined using clauses 7.2 (tables 7.1 and 7.2).
4. The overall force at the base of the structure, according to clause 5.3 of EN 1991-1-4, taking into account the pressures at windward and leeward side, and friction forces, when applicable.
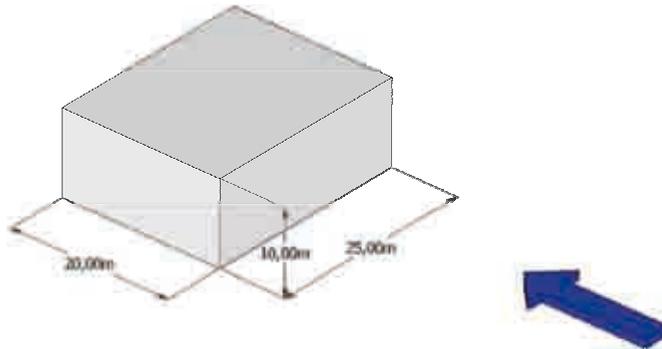
Figure 1: Case 1: Industrial hall.

Case 2: Simple rectangular building with duopitch roof

A second case includes a building with a duopitch roof. The height of the gutter is 2 metres, the total height is 6 metres, with a width of 15 metres. The roof pitch is 28 degrees. The exposure is open, with scattered individual obstacles. The loads will be determined for the wind direction normal to the longer façade, as indicated in figure 2.

Again, per country and location, the following intermediate results are calculated:
1. The basic wind velocity pressure, q_b, which is equal to case 1.
2. The peak wind velocity q_p at roof height, $h = 6$ metres, according to clause 4.5 of EN 1991-1-4;
3. The distribution of c_{pe} over the cross section of the building, determined using clause 7.2 of EN 1991-1-4, tables 7.1 and 7.4.

4. The overall force at the base of the structure, according to clause 5.3, taking into account the pressures at windward and leeward side of both facades and roof, and friction forces, if applicable.
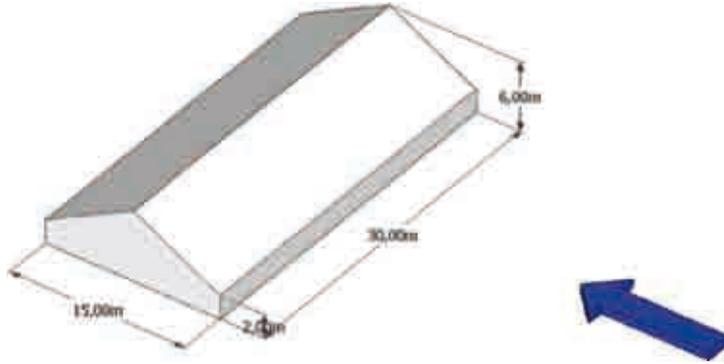
Figure 2: Building with duopitch roof

Case 3: Rectangular tower block

The third example is a simple rectangular block with rectangular plan of 15 x 20 metres, and height 55 metres. The wind loads on the overall structure are determined for wind normal to the longer façade, see figure 3. The building is located in an urban terrain.
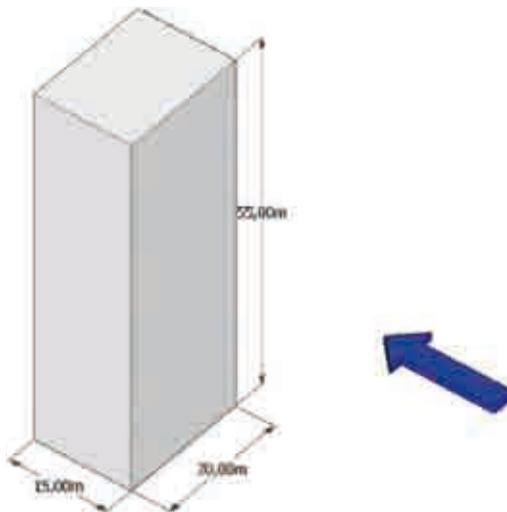
Figure 3: rectangular tower block

Again, per country and location, the following intermediate results are calculated:
1. The basic wind velocity pressure, q_b, according to chapter 4, which is equal to case 1.

2. The peak wind velocity q_p at roof height, $h = 55$ metres, according to clause 4.5.
3. The distribution of c_{pe} over the cross section of the building, determined using clause 7.2 of EN 1991-1-4, table 7.1.
4. The overall force at the base of the structure, according to clause 5.3, taking into account the pressures at windward and leeward side, and friction forces, when applicable

RESULTS

The introduction of the Eurocode-system has been a great improvement of the harmonisation across country borders. For the wind loading, the National Annexes give the individual countries many choices to include their own values. Comparison of three cases indicates that large differences in results may occur between countries. Results are available on the CD with full papers.

DISCUSSION

This paper will be purely technical, and provides an objective comparison of the results obtained when calculating the wind loads on structures. This exercise may be a starting point of further comparative calculations, to create a starting point for the development of the next Eurocode generation.

REFERENCES

CEN (2005). "EN 1991-1-4, Eurocode Wind Actions on Structures", 2005
Da Vinci, L. (2005), Implementation of Eurocodes, handbook 3: Action effects for buildings, Leonardo da Vinci Pilot Project CZ/02/B/F/PP-134007

Dynamics of Tall Buildings under Stochastic Wind Load, applicability of Eurocode EN 1991-1-4 procedures 1 and 2

R.D.J.M. Steenbergen, A.C.W.M. Vrouwenvelder, C.P.W. Geurts

TNO – raphael.steenbergen @tno.nl– PO Box 49, NL 2600 AA Delft, The Netherlands
TU Delft – A.C.W.M. Vrouwenvelder@tudelft.nl – PO Box 5048, 2600 GA Delft, The Netherlands
TNO – chris.geurts @tno.nl– PO Box 49, NL 2600 AA Delft, The Netherlands

Keywords: dynamics, tall buildings, wind loads, Eurocode, comfort.

ABSTRACT

The new generation of tall buildings is higher and more slender than the buildings built before. Additionally, increased use is made of high-strength materials that however do not have a higher stiffness than the conventional materials. Both aspects increase the sensitivity of tall buildings to dynamic behaviour. The design has to ensure adequate reliability but it also has to ensure that people in the building feel comfortable because wind-induced vibrations might cause discomfort. Fulfilling vibration criteria for human comfort turns out to be decisive in structural design of tall buildings. The new Eurocode EN 1991-1-4 provides two different procedures to calculate the structural factor and the comfort level. This paper gives insight in the background theory of wind-induced vibrations. On the basis of this the two procedures are compared. The conclusion is that procedure 1 might be unsafe and it turns out that procedure 2 is preferable.

INTRODUCTION

Modern tall buildings are relatively light and flexible, which makes them sensitive to dynamic loads. In the design of these buildings, two important aspects have to be taken into account; the design has to ensure both the safety of the building and the comfort in the building.

Because of the dynamic behaviour of the building, the maximum load effect, such as moment or stress can be increased with respect to the situation in which the building would react in a quasi-static way. In the building design therefore, a dynamic amplification factor has to be introduced. This means that the wind load is considered to be static, but increased with the dynamic amplification factor.

Vibrating buildings can cause unsafe feelings of the occupants; therefore, with respect to comfort, limit values are prescribed for the vibration intensity of tall buildings. In the current design practice, it is important to pay attention to the dynamic behaviour of tall buildings, because economic losses as a

Contact person: dr. ir. R.D.J.M. Steenbergen, TNO Built Environment and Geosciences, PO Box 49, 2600 AA Delft, The Netherlands. T: +31 15 2763423, F: +31 15 2763018, E-mail raphael.steenbergen@tno.nl

result of malfunctioning of the buildings can be large. Especially the comfort check is increasingly important. Some reasons for this are:

- The application of high-strength materials; these materials have a higher strength, but are not stiffer than the conventional materials. This makes that buildings are more sensitive for wind-induced vibrations.
- The application of less non-structural components such as separation walls. These components are often applied in that way that they stand free with respect to small building motions. Therefore less damping is present in the building.
- The increased perception of comfort by the users of the buildings. The users do not expect vibrations; if this is however the case, it provides unsafe feelings. From an economical point of view, this has to be avoided.

Human beings are not directly sensitive to displacement or velocity; they are sensitive to forces operating on them. Therefore acceleration has become the accepted criterion for evaluation in standards concerning motion perception. Building codes and guidelines give acceleration design criteria to ensure the serviceability of a structure given its destination and use.

This paper discusses the determination of the dynamic amplification factor and the horizontal accelerations of tall buildings subjected to wind load. The theory used is mainly based on the studies of Davenport (1961, 1967) who was the first to develop a procedure to determine the response to along-wind forces that was based on a stochastic approach. The theory is then compared with the current building code EN 1991-1-4 for wind.

STRUCTURAL MODEL

A tall building can be schematised using a *n* degree of freedom system (*ndof*). For this a coupled system of *n* equations of motion is formulated. Applying modal analysis this system is transformed to *n* uncoupled equations of motion in generalised coordinates $\eta(t)$, making use of eigen vectors (vibration modes) $\Phi_i(y,z)$ with natural frequencies n_i. The response *u* of a structure under dynamic load can now be expressed in a time-dependent linear combination of vibration modes:

$$u = u(y,z,t) = \sum_i \eta_i(t) \cdot \Phi_i(y,z)$$

with:

$u = u(z,y,t)$ = response depending on place and time

$\eta_i(t)$ = ith generalised coordinate, depending on time

$\Phi_i(y,z)$ = ith Eigen mode shape

The ith generalised coordinate results from the ith uncoupled equation of motion of the structural system:

$$m_i \ddot{\eta}_i + c_i \dot{\eta}_i + k_i \eta_i = \int_h \int_b \Phi_i(y,z) q(y,z,t) \, dydz = F_i(t)$$

where the ith modal mass is defined by:

$$m_i = \int_h \int_b \Phi_i^2(y,z) \mu(y,z) \, dydz$$

with:

μ = mass per unit area

c_i = ith modal damping constant

k_i = i^{th} modal stiffness constant

n_i = i^{th} natural frequency

These uncoupled (modal) equations are the basis of the dynamic analysis of buildings under wind load. The equations have the character of single degree of freedom (*sdof*) systems, so for the building response the well-known solutions for *sdof* systems under stochastic load can be applied. For buildings, in general the first natural frequency is dominant, however the theory can easily be expanded with the contribution of higher natural frequencies.

WIND LOAD MODEL

Wind is a phenomenon the properties of which such as direction and speed can only be described in statistical terms. The fluctuating part of the wind load causes the dynamic behaviour of the building. The fluctuating part is characterised with a variance spectrum describing how the variance of the stochastic process is distributed over the different frequencies. This spectral description of the wind velocity is valid for one point. The coherence however is important for determining the wind load on large building façades. The coherence function describes the extent of coherence of the fluctuating wind in time and space. The interest is in the total response of a building that does not so much depend on the peak wind load in a single point but rather on the level of coincidence of the peak on a certain surface.

BUILDING RESPONSE UNDER STOCHASTIC WIND LOAD

The variance spectrum $S_{F_iF_i}$ of the ith modal load $F_i(t)$ turns out to be:

$$S_{F_iF_i}(n) = \left(\rho c_h v_{m,h} \sigma_{v_h} A \right)^2 \frac{S_L(n)}{n} X_{\Phi_i}^2(n)$$

with :

$$X_{\Phi i}^2(n) = \frac{1}{A^2} \iiiint \frac{c_k}{c_h} \frac{v_{m,k}}{v_{m,h}} \frac{\sigma_{v,k}}{\sigma_{v,h}} \frac{c_l}{c_h} \frac{v_{m,l}}{v_{m,h}} \frac{\sigma_{v,l}}{\sigma_{v,h}} \Phi_i(y_k, z_l) \Phi_i(y_k, z_l) coh_{v_k v_l} dy_k dy_l dz_k dz_l \qquad (1)$$

where:

ρ = density of the air

c_k = drag coefficient in the point (y_k, z_k)

$v_{m,k}$ = mean wind speed in the point (y_k, z_k)

c_h = drag coefficient at reference height h

$v_{m,h}$ = mean wind speed at reference height h

A = the area of the building

$\sigma_{v,k}$ = the standard deviation of the wind velocity in the point (y_k, z_k)

$\sigma_{v,h}$ = the standard deviation of the wind velocity at reference height h

S_L = the reduced wind spectrum e.g. the Eurocode spectrum

$coh_{v_k v_l}$ = the coherence of the wind speeds in the points (y_k, z_k) and (y_l, z_l)

Expression (1) is called the aerodynamic admittance and this reduction factor takes into account the non-simultaneously occurrence of the wind gusts on large surfaces. Here, often also Φ is taken outside the integral, but Steenbergen (2007) has demonstrated that this leads to a serious

underestimation of the response. For the solution of integral (1) often simplified relationships are used, as done in procedures 1 and 2 of Eurocode EN 1991-1-4.

According to the theory, the background factor B and the resonance response factor R from the Eurocode both depend on the mode shape Φ. In a simplified way they can be written as:

$$B^2 = C(\Phi_i) \int_0^\infty X_{\Phi i}^2 \frac{S_L(n)}{n} dn \text{ and } R^2 = C(\Phi_i) \frac{\pi}{4D_i} X_{\Phi i}^2 (n_i) S_L(n_i)$$

with $C(\Phi_i)$ a factor depending on the mode shape and D_i the modal damping factor.

EUROCODE EN 1991-1-4, PROCEDURES 1 AND 2

The theoretical formulas have been elaborated numerically so that comparisons can be made between the theoretical value and the values provides by procedures 1 and 2 of Eurocode EN 1991-1-4. For the structural factor $c_s c_d$, procedures 1 and 2 provide similar values, although the values of the individual parameters c_s and c_d differ a lot. For the acceleration level, the difference between procedures 1 and 2 are considerable. It appears that for all mode shapes, procedure 2 provides values that are much closer to the theoretical values. In Procedure 1, the mode shape is taken into account in a simplified way; in expression (1) it has been taken outside the integral. For the ultimate limit state, the differences between the methods are small, however, for checking the serviceability limit state, procedure 1 underestimates the accelerations.

Procedure 2 has been developed by Dyrbye and Hansen (1997). The contribution of the mode shape is taken into account correctly via the factors G and K. Because of this, procedure 2 of the Eurocode provides considerably higher values for the acceleration than procedure I, as was also observed by Dyrbye and Hansen (1997). Concluding we can say that procedure 2 of the Eurocode is preferable for the dynamic stochastic analysis of buildings.

CONCLUSIONS

Human comfort of building occupants is the most important design criterion in relation to wind-induced dynamic behaviour of tall buildings. A structural model based on modal analysis is used to describe the dynamic behaviour. Using modal analysis each vibration mode can be studied separately by means of a single degree of freedom model. The fluctuating character of the wind is characterized by two important aspects: the wind velocity spectrum which describes the distribution of the variance of the stochastic wind load over the different frequencies and the aerodynamic admittance function that takes into account the non-simultaneously occurrence of the gusts in space and time. Procedures 1 and 2 from EN 1991-1-4 both present a method to calculate the wind induced building vibrations. It is concluded that procedure 1 might be unsafe and procedure 2 is preferable.

REFERENCES

Davenport, A.G. (1961). "Spectrum of Horizontal Gustiness Near the Ground in High Winds", Journal Royal Meteorological Society, vol. 87.

Davenport, A.G. (1967). "The dependence of wind loads on meteorological parameters". Proceedings of the International Research Seminar on Wind Effects on Buildings and Structures, 19-82, Ottawa.

Dyrbye, C., and Hansen S.O. (1997). "Wind loads on Structures", John Wiley, New York.

Eurocode 1 (2005): Action on structures-Wind actions, EN 1991-1-4, European Committee for Standarization, Brussels.

Geurts, C.P.W. (1997). "Wind-induced Pressure Fluctuations on Building Facades", PhD Thesis, Eindhoven University of Technology, The Netherlands.

Steenbergen, R.D.J.M. (2007). "Super Elements in High-Rise Buildings under Stochastic Wind Load", PhD Thesis, Delft University of Technology, The Netherlands.

The new CNR-DT 207/2008
Guidelines on Actions and Effects of Wind on Structures

G. Solari[1], G. Bartoli[2], V. Gusella[3], G. Piccardo[1],
P. Pistoletti[4], F. Ricciardelli[5], A. Vintani[6]

[1]*DICAT – University of Genoa, Italy, solari@dicat.unige.it*
[2]*DICeA – University of Florence, Italy, gbartoli@dicea.unifi.it*
[3]*DICA – University of Perugia, Italy, guse@strutture.unipg.it*
[4]*SETECO Ingegneria srl, University of Genoa, Italy, ufficiotecnico@setecoge.it*
[5]*DIMET – University of Reggio Calabria, Italy, friccia@unirc.it*
[6]*BCV Progetti, Milan, Italy, vint@bcv.it*

Keywords: wind loads, wind effects, codes of practice

ABSTRACT

The Italian National Research Council (Consiglio Nazionale delle Ricerche, CNR) is a Government-funded institution whose mission is to promote, carry out, disseminate, transfer and improve research activities in the main areas of knowledge growth and of its applications for the scientific, technological, economic and social development of the Italian Country.

In 2006 CNR has started promoting the drafting of documents in areas of Engineering where the recent achievements have made the existing Codes obsolete, or where no Codes exist at all.

In this framework, in 2006 a Panel was established chaired by Prof. G. Solari with the goal of drawing a completely new set of guidelines on actions and effects of wind on structures.

After two years, in January 2008 a draft of the document was presented and public discussion was opened, aimed at receiving any comment or suggestion, before release of its final version.

Finally, in spring 2009, the modified version of the document was issued under the name CNR-DT 207/2008 "Guidelines on Actions and Effects of Wind on Structures" (the Italian version is available for download at following URL: *http://www.cnr.it/sitocnr/IlCNR/Attivita/NormazioneeCertifica-zione/DT207_2008.html*, while the English version is currently under preparation).

Like all similar documents issued by CNR, DT 207/2008 aims at combining two different aspects:

Contact person: Giovanni Solari, DICAT – Dept. of Civil, Environmental and Architectural Engineering, University of Genoa, via Montallegro, 1- 16145 Genova (Italy), phone: +39-010-353.2524, fax: +39-010-353.2534
E-mail solari@dicat.unige.it

on one side, the document contains guidelines for use of Consultants for the evaluation of wind loads and wind effects on structures; on the other side, the document addresses background concepts on the characteristics of wind and on the description of the interaction between the wind field and a wide set of structural types.

This twofold approach has been adopted consistently throughout the document. For each topic, in fact, both general principles and application rules are presented. The latter are aimed at covering the widest possible variety of practical cases, and an attempt has been made to not only provide equations and coefficients to be adopted in practical calculations, but also to provide explanation for their understanding.

The document is divided into four sections.

The first section is an introduction to the document, containing keys for its use (structure of the document, references, symbols).

Section two ("fundamentals") contains background concepts in Wind Engineering, for use of those who are not familiar with them, and who wish to get a basic understanding of the physical underlying concepts. This part (which is innovative in the worldwide scenario) is intended to reduce the gap between theory and practice, so to create at least a common "language" between designers and researchers, giving to the former the necessary background to better understand all the aspects reported in the following sections.

The third section ("recommendations") is the Code body, and contains all the rules and the coefficients to be used for the design of wind exposed structures. In this section an attempt has been made towards a unified definition of the equations and of the coefficients, so to avoid the common difficulty encountered by designers when several (sometimes completely) different expressions are used for the evaluation of different effects. Moreover, it was decided to introduce all the general definitions at the very beginning of the section, without getting into a detailed description of all the coefficient required to apply the procedures. There results a rather short preliminary part, followed by a number of Appendices. The latter have been written such to be independent from each other, thus allowing a simpler maintenance and expansion of the document, when necessary. A total number of fifteen Appendices have been included in the document. Some of these contain information provided by almost all Codes o Practice (pressure and force coefficients, methods for the analysis of vortex-shedding induced response, and so on). Some others, on the other hand, contain information not always available to the designer. Examples are an Appendix devoted to the numerical simulation of wind fields and an Appendix devoted to wind tunnel testing. Generally speaking, many of the Appendices contain some innovative features. Just to mention some, the following topics have been addressed, by merging information derived from both worldwide Codes of Practice and scientific literature:

- two sets of pressure coefficients are provided; detailed pressure coefficients for buildings and detailed net pressure coefficients for canopies are given in Appendix H; in Appendix G global force and pressure coefficients are given for a variety of structures and geometrical shapes; when designing a building, for example, it is possible to choose whether to use global or detailed values; the former are of simpler use, but sometimes tend to overestimate the load, the latter are more accurate and of a less simple use; as an example in Figure 1 simplified pressure coefficient (constant on the whole surface) for a monopitch roof are shown;
- a specific section for irregular buildings has been added (Figure 2);
- in addition to along-wind actions, across-wind and torsional dynamic actions and accelerations has been considered in Appendix M, and simplified procedures have been proposed;
- the problem of ovalling of circular structures has been addressed (Figure 3);
- some simplified approaches for evaluating the flutter susceptibility of bridge decks have been introduced in Appendix P, where the safety criteria are based on bridge dynamic characteristics and a new aerodynamic efficiency coefficient β_F (Figure 4).
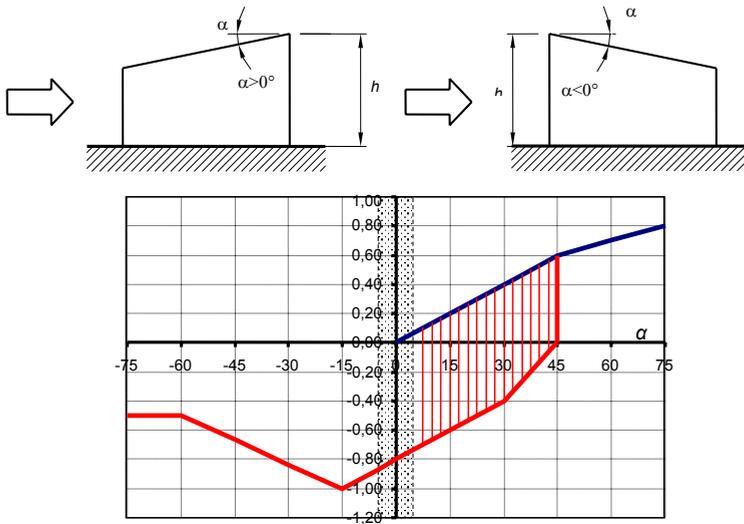
Figure 1: simplified pressure coefficient (constant on the whole surface) for a monopitch roof (Fig. G.7 from CNR-DT 207/2008)
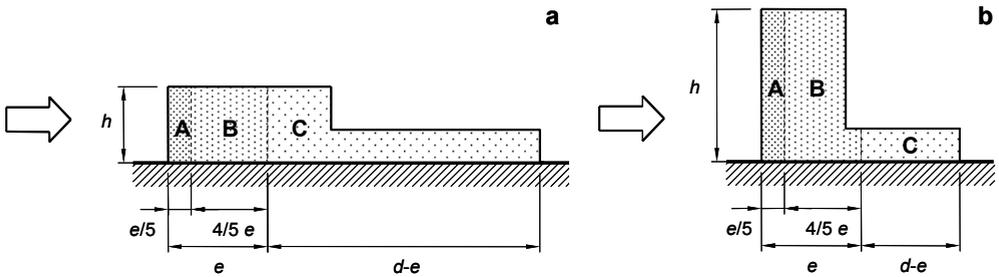
Figure 2: different pressure zones for buildings with non uniform heights (Fig. H.14 from CNR-DT 207/2008)
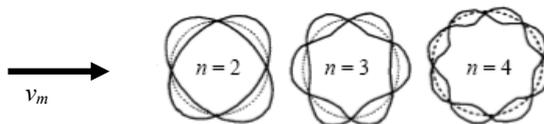
Figure 3: ovalling modes for a circular cylinder (plan view) (Fig. O.18 from CNR-DT 207/2008)
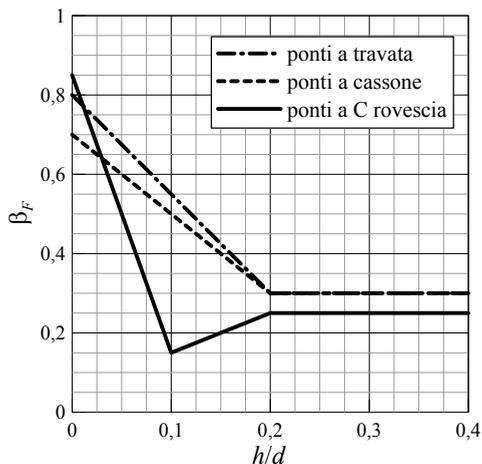
Figure 4: aerodynamic efficiency coefficient β_F as a function of the height/width deck ratio for evaluating the flutter susceptibility of bridge decks (Fig. P.6 from CNR-DT 207/2008)

A attempt has been made to keep the coefficients proposed in agreement with those suggested by Eurocode 1; this was a necessary assumptions as the CNR-DT 207/2008 Instructions could be used in Italy by all the designers as an alternative to other existing recommendations. Being the compatibility of every recommendation issued by all EU Countries with Eurocodes mandatory from next 2011, it was necessary to issue a document in a substantial agreement with sections 1-4 and 2-4 of Eurocode 1, in order not to give a revision necessary in a very few years.

Finally, <u>section four</u> contains 12 worked examples; these should serve as a reference for those who apply the Guidelines for the first time. This section is quite innovative in the Italian scenario, where recommendations usually do not report any examples along the text;

There results a document exceeding 300 pages. This is the result of the necessity of giving a suitable response to the initial request of providing both design guidance to Consultants and an explanatory document on the main phenomena addressed.

REFERENCES

CEN (1994). "Eurocode 1: Basis of design and actions on structures. Part 2-4: Wind actions". ENV 1991-2-4.

CEN (2005). "Eurocode 1: Actions on structures - General actions. Part 1-4: Wind actions". EN 1991-1-4.

ECCS (1987). "Recommendations for calculating the effects of wind on constructions". European Convention for Constructional Steelwork, N. 52.

ASME (19992). "Steel stacks". STS-1-1992, The American Society of Mechanical Engineers.

NRC-CNRC (1995). "National Building Code of Canada".

BSI (1997). "Loading for buildings. Part 2: Code of practice for wind loads". BS 6399.

CICIND (1999). "Model code for steel chimneys".

Committee DB/6 (2002). "Structural design actions. Part 2: Wind actions". Australian / New Zealand Standard, AS/NZS 1170.2.

ISO TC 98/SC (2005). "Wind actions on structures". ISO/CD 4354 (draft version, 20.4.2005).

AIJ (2005). "Recommendations for loads on buildings". Architectural Institute of Japan.

ASCE/SEI (2005). "Minimum design loads for buildings and other structures". Standard N. 7-05, American Society of Civil Engineers, Structural Engineering Institute.

Isyumov, N. (Ed.) (1999). "Wind tunnel studies of buildings and structures". ASCE manuals and reports on engineering practice No. 67, Aerodynamics Committee, American Society of Civil Engineers.

VDI (2000). "Environmental meteorology. Physical modelling of flow and dispersion processes in the atmospheric boundary layer. Application of wind tunnels". Verein Deutscher Ingenieure, VDI 3783.

A probabilistic framework for
Performance-Based Wind Engineering

F. Petrini, M. Ciampoli, G. Augusti

Sapienza Università di Roma, Italy – francesco.petrini@uniroma1.it– Sapienza Università di Roma, – marcello.ciampoli@uniroma1.it– Sapienza Università di Roma – giuliano.augusti@uniroma1.it

Keywords: Performance-Based Wind Engineering, Wind uncertainties, Probabilistic approach, Suspension Bridge.

ABSTRACT

A modern approach to wind engineering must consider performances as key objectives of structural design. Hence optimal design procedures should be developed in the framework of Performance-Based Design or, better, Performance-Based Wind Engineering (PBWE): the relevant structural performance requirements should be satisfied with a sufficiently high probability throughout the whole life-cycle.

Many studies have already been carried out on this topic (see for example Ellingwood et al. 2004). In Italy, Augusti and Ciampoli (2006) suggested the extension of the PEER approach (Porter 2003) into PBWE; Petrini et al. (2008 a, b) applied the risk assessment procedure to the assessment of (a) the fatigue damage of the hangers and (b) the serviceability and ultimate performances of a proposed long span suspension bridge.

At the present state a structured and universal accepted procedure still does not exists to face the wind engineering problems by using a performance-based approach. On the contrary, in other structural disciplines (like seismic engineering and fire engineering), the concepts of the Performance-Based Design (PBD) are currently applied, at least in the design procedures of complex

---

Contact person: Francesco Petrini, Sapienza Università di Roma, via Eudossiana 18, Rome, Italy, phone: +390644585265 FAX: +39064884852.

E-mail francesco.petrini@uniroma1.it

structures. The goal of this paper is to give some further contribution towards the development of a probabilistic procedures for the application of Performance-Based Design concepts to wind engineering.

Namely, a PBWE procedure is proposed that can be summarized in intermediate steps aimed at:

– defining the Aeolian hazard at the site, in terms of wind intensity and/or parameters of the wind velocity field;

– analyzing the structural response;

– defining and evaluating indicators of the structural damage (identified with unacceptable performances);

– defining the decisional variables that are appropriate to quantify the performances required of the structure, in terms of damages;

– evaluating the structural risk by the probabilistic characterization of the decision variables;

– optimizing design, i.e. minimizing risk, by appropriate techniques of decision analysis.

The decision variables that quantify the performances are distinguished between those corresponding to possible consequences on structural and personal safety (low performances), and to effects on service-ability and comfort (high performances).

The Performance-Based approach has to be faced always in probabilistic terms, especially in wind Engineering, in which there are many sources of uncertainties (Fig. 1).
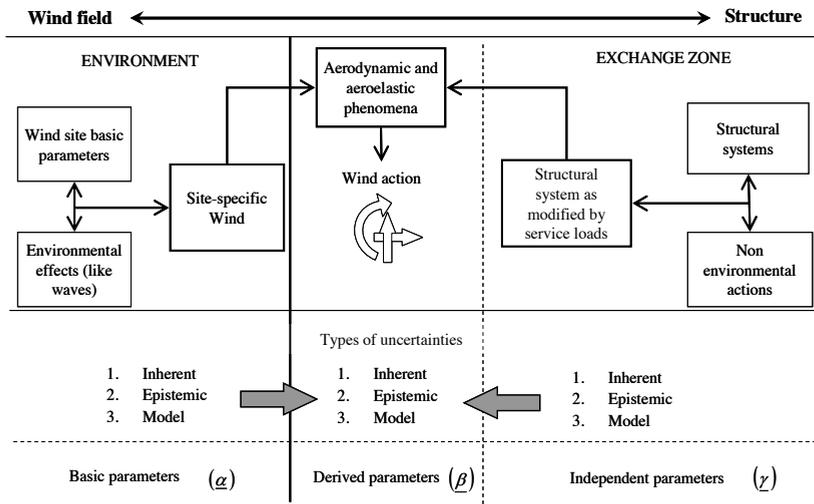
Figure 1: sources of uncertainty in wind engineering.

In Fig. 1 an hypothesis has been done regarding the uncertainties propagation, which is represented by the grey arrows and can be formalized as follows:

$$P(\underline{\alpha}|\underline{\beta}) = P(\underline{\alpha}|\underline{\gamma}) = P(\underline{\alpha}) \tag{1}$$

$$P(\underline{\gamma}|\underline{\beta}) = P(\underline{\gamma}|\underline{\alpha}) = P(\underline{\gamma}) \tag{2}$$

Where the underline indicates a vector and the vectors $\underline{\alpha}$, $\underline{\beta}$ and $\underline{\gamma}$ contain the stochastic parameters describing the various aspects of the wind engineering problems.

In this paper, starting from the approach proposed by the Pacific Earthquake Engineering Research Center (PEER, eq.(3)) for seismic engineering (Augusti & Ciampoli 2008), a probabilistic procedure

for the application of PBD concepts to wind engineering is presented (eq. (4)). This can be considered an ulterior step toward the Performance-Based Wind Engineering (PBWE).

$$\lambda(DV) = \int\int\int P(\,DV|DM)\cdot P(\,DM|EDP)\cdot P(\,EDP|IM)\cdot g(IM)\cdot dDM \cdot dEDP \cdot dIM \qquad (3)$$

$$\lambda(\,DV\,) =$$

$$= \int_{-\infty}^{\infty} P(\,DV|DM\,)\cdot P(\,DM|EDP\,)\cdot P(\,EDP|\underline{IM},\underline{IP},\underline{\gamma}\,)\cdot g(\,\underline{IP}|\underline{IM},\underline{\gamma}\,)\cdot g(\,\underline{IM}\,)\cdot g(\,\underline{\gamma}\,)\cdot \qquad (4)$$

$$\cdot dDM \cdot dEDP \cdot d\underline{IM} \cdot d\underline{IP} \cdot d\underline{\gamma}$$

where:

DV= Decision Variable,

DM= Damage Measure,

EDP= Engineering Demand Parameter,

IM= Intensity Measure,

$\underline{IP}$ = Interaction Parameter(s) = $\begin{bmatrix} _{AD}\underline{IP} \\ _{AE}\underline{IP} \end{bmatrix} = \begin{bmatrix} \text{aerodynamic parameters} \\ \text{aeroelastic parameters} \end{bmatrix}$,

P(X|Y)= conditional probability function of X in respect of Y,

g(X)= joint probability density function of X.

Equations (3) and (4), represent relations between stochastic parameters for the computing of expected value of a decision variable. The decision variable is representative of the generic performance.

A central topic of the work is the use of the reliability analysis tools and of the stochastic system analysis concepts (Schüeller 2006) for the assessment of the wind-exposed structures performances. A partial framework of the PBWE is proposed, and an application on a long span suspension bridge is presented. For the case study structure, the probability of the structural loss of serviceability, caused by wind action, is computed. The analyses have been conducted in time domain and the probability distributions of structural response (Fig. 2) are derived by using of Monte Carlo technique.
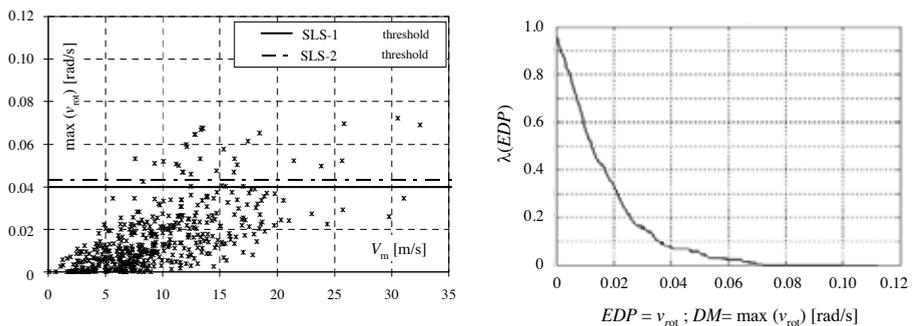
Figure 2. Structural response statistics: population (left), probability curves (right).

REFERENCES

Ellingwood, B.R. & Rosowsky, D. V., Li, Y. & Kim, J. H. (2004), "Fragility Assessment of Light-Frame Wood Construction Subjected to Wind and Earthquake Hazards", J. Structural Engineering, 130 (12), 1921-1930.

Augusti, G. & Ciampoli, M. (2006). "First steps towards Performance-based Wind Engineering". Performance of Wind Exposed Structures: Results of the PERBACCO project (G. Bartoli, F. Ricciardelli, A. Saetta, V. Sepe eds.), Firenze University Press, 13-20.

Porter KA (2003), "An Overview of PEER's Performance-Based Engineering Methodology", Proc of the Ninth International Conference on Applications of Statistics and Probability in Civil Engineering (ICASP9). San Francisco, CA, USA; Millpress Rotterdam; 2003.

Petrini, F., Bontempi, F. & Ciampoli, M. (2008a). "Performance-based wind engineering as a tool for the design of the hangers in a suspension bridge. Proc. Fouth International ASRANet colloquium, Athens, Greece, ISBN: 0-9553550 -2-8 / 978-0-9553550-2-8, paper in CD-ROM.

Petrini, F., Ciampoli, M. & Augusti, G. (2008b). "Performance-based Wind Engineering: risk assessment of a long span suspension bridge". Proc. WG7.5, Toluca, Mexico, August 6-9 (in press).

Augusti, G. & Ciampoli, M. (2008). "Performance-based design in risk assessment and reduction". Probabilistic Engineerig Mechanics 23(4), doi information:10.1016/j.pro bengmech.2008.01.007, 496-508.

Schüeller, GI (2006). "Developments in stochastic structural mechanics", Archive of Applied Mechanics vol. 75 No. 10-12/October 2006.

Effects of building height and spacing on pedestrian-level wind environment

1st C.W. Tsang, 2nd K.C.S. Kwok, 3rd P.A. Hitchcock

1) CLP Power Wind/Wave Tunnel Facility, The Hong Kong University of Science and Technology – ceroytsang@gmail.com – Clear Water Bay, Hong Kong S.A.R., P.R. China

2) School of Engineering, University of Western Sydney – kkwok@ust.hk – Sydney, New South Wales, Australia

3) CLP Power Wind/Wave Tunnel Facility, The Hong Kong University of Science and Technology – wtpete@ust.hk – Clear Water Bay, Hong Kong S.A.R., P.R. China

ABSTRACT

In many densely populated cities, such as Hong Kong, urban renewal is an important kind of sustainable development for the community in terms of good use of land and infrastructure. Under the renewal projects, high-rise buildings are often surrounded by closely packed low-to-middle-rise buildings. It is well known that high-rise buildings affect the surrounding pedestrian-level wind environment. A comprehensive review was conducted by Blocken and Carmeliet (2004) which focused on the unpleasant and dangerous windy conditions caused by buildings that may affect human activities.

In recent years, awareness and concern has increased about the creation of low wind speed areas around buildings which may lead to poor out-door air ventilation. Moreover, many modern building developments are not restricted to a single building but may comprise a group of buildings. There are very few systematic studies focused on the low wind speed areas around a group of buildings (Wise et al. (1971), Stathopoulos and Wu (1995) and Tulapurkara et al. (2005)).

In this research, a series of parametric wind tunnel studies was carried out to investigate building height and spacing effects on the pedestrian-level wind environment around a pair of rectangular buildings. The height of the buildings was changed from 50 m to 150 m; the spacing between buildings was changes from 0 to 31.25 m.

EXPERIMENTAL ARRANGEMENT

The experiments were carried out in the high speed test section (a boundary layer wind tunnel 29.2 m long, with a 3 m wide by 2 m high cross-section) of the CLP Power Wind/Wave Tunnel Facility (WWTF) at The Hong Kong University of Science and Technology. The mean wind speed profile of the approaching turbulent wind flow followed a power law exponent of 0.2, using a series of fences and roughness blocks, to simulate wind flow above a typical suburban terrain. Figure 1 shows the profile of the mean wind speed, U, and turbulence intensity, σ_u/U. The magnitudes of U are normalized by the mean wind speed, U_r, of the approach flow at $z = 150$ m at prototype scale (750 mm at model scale).

The building models were fabricated at a length scale of 1/200 and the experimental arrangement is shown in Figure 2. The building group includes two rectangular buildings with height h, width b and depth d. The spacing between the buildings is denoted by s. The buildings' width and depth are fixed at 50 m and 25 m, in prototype scale, respectively. In these parametric studies, the buildings' height, h, was changed from 1b to 3b at increments of 0.5b. The spacing, s, was changed from 0 to 0.625b at increments of 0.125b. Only one parameter was adjusted at a time.

The distribution of mean wind speeds at pedestrian level U was measured using 175 Irwin Sensors ,Irwin (1981) , that were installed at a height equivalent to 2 m above ground at prototype scale (10 mm in model scale). All of the wind tunnel tests were conducted using a reference mean wind speed U_r of approximately 10 m/s.
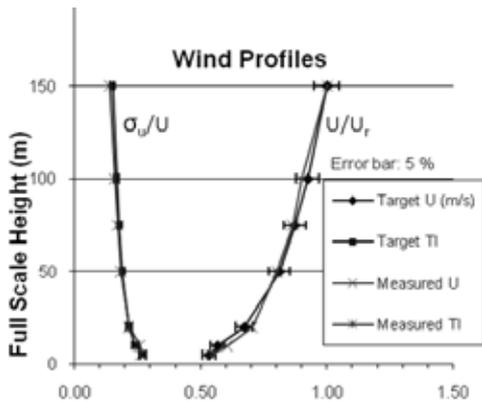
Figure 1: Profiles of mean wind speed and turbulence intensity
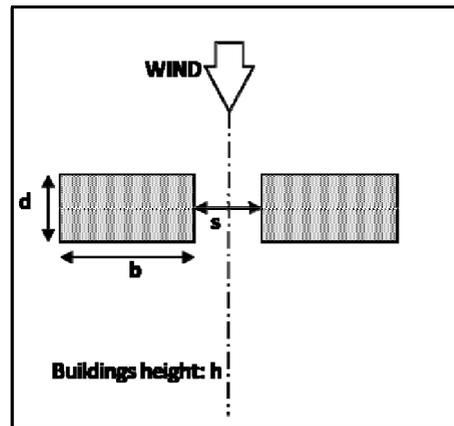
Figure 2: Plan view of the building models

RESULT AND DISCUSSION

Figure 3 shows the general features of pedestrian-level wind environment around the building models, with a configuration of h = 1.5b and s = 0.25b. The normalized pedestrian-level mean wind speed distribution, U/ U_r, is plotted on the left half of the building group. The values of mean wind speed at pedestrian level are normalized by the reference mean wind speed U_r of the approach flow at z = 150 m in prototype scale. The normalized mean wind speeds range from 0.0 to 1.0. An initial test was conducted with no building installed, for which the normalized mean wind speed is around 0.5. A value of U/U_r between 0.3 and 0.8 is considered to be reasonable for normal outdoor wind comfort and air ventilation purposes. Areas with a U/U_r value outside this range, U/U_r ≥ 0.8 and ≤ 0.3, are regarded as high wind speed zones and low wind speed zones respectively.

It can be seen from Figure 3 that there are two high wind speed zones and three low wind speed zones. The two high speed zones occurred at the side and between the buildings. The three low speed zones are located at the near-field upstream, near-field downstream and far-field downstream areas. As the research focused on natural outdoor air ventilation, the effects of building height and spacing on these three low speed zones are of particular interest and they are discussed further in the following sections.

The effects of building height on U/U_r around the buildings are shown in Figure 4. The buildings width, b, depth, d, and spacing, s, were fixed at 50 m, 25 m (0.5b) and 12.5 m (0.25b) respectively. The building height, h, was varied from 50 m (1.0b) to 150 m (3.0b). As the building height increases, the low speed zone at the near-field upstream area does not change significantly. At the near-field downstream area, the extent of the low speed zone decreases as height increases and becomes stable as $h \geq 2.0b$. The far-field downstream low speed zone is located further downstream and shrinks as building height increases, and becomes stable as $h \geq 2.5b$. These results show that as building height increases, the low speed zones in close proximity to the buildings are slightly improved, and the far-field low speed zone is shifted further downstream. The magnitude and extent of the low wind speed zones gradually became insensitive to increases in building height as $h \geq 125$ m (2.5b).
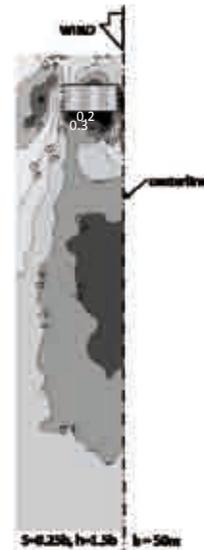
Figure 3: Distribution of normalized pedestrian level mean wind speed: General features
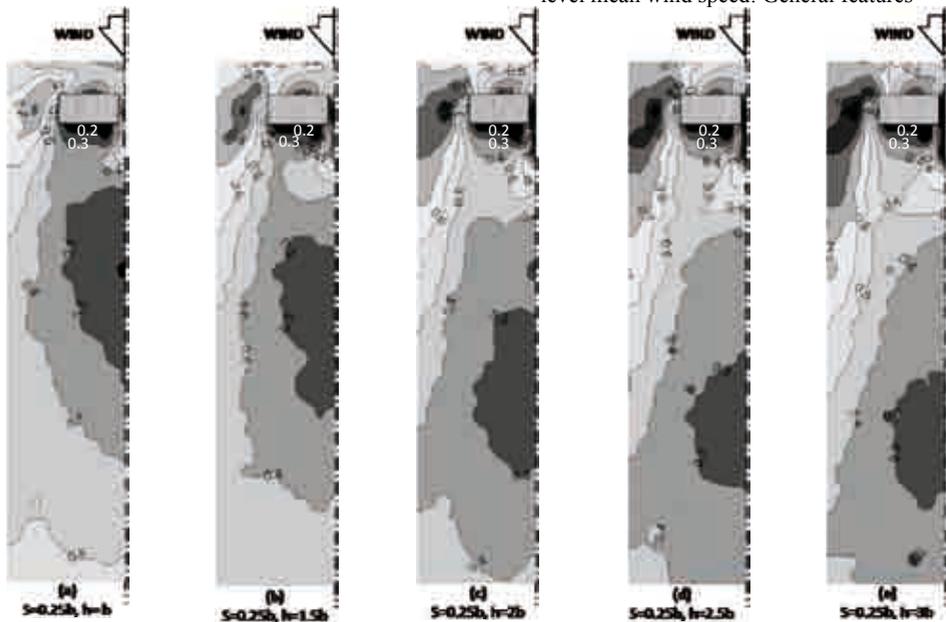
Figure 4: Distribution of the normalized mean wind speed with varying building height and fixed building spacing (b = 50 m)

Figure 5 shows the effects of building spacing on the pedestrian-level wind environment. The building parameters b, d and h were fixed at 50 m, 25 m (0.5b) and 100 m (2.0b), and the building spacing was varied from 0 to 31.25 m (0.625b). For the case of zero spacing, Figure 5 (a), the two buildings are equivalent to a single slab-like building with corresponding wind environment features. There is a low pressure zone at the leeward side of the building that causes horizontal and

vertical recirculation. The horizontal recirculation enhances the near-field wind movements and the vertical recirculation dominates the movements at the far-field area.

In comparison, it was found that there is a slight enhancement at the near-field low speed zone as the spacing is increased; additional horizontal recirculation is created by the flow passing through the gap between the buildings. However, the far-field low speed zone is worsened; this is attributed to the weakening of vertical recirculation by the flow passing through the gap. Furthermore, it was observed that when s $\geq$ 0.5b, the changes in the pedestrian-level wind environment were less significant.
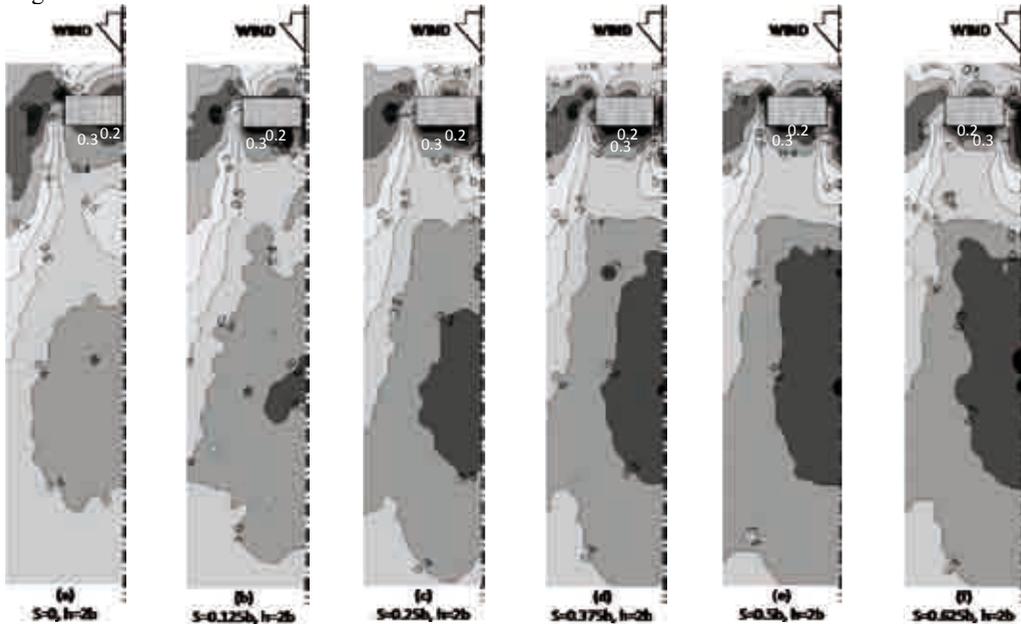
Figure 5: Distribution of the normalized mean wind speed: with varying building spacing and fixed building height (b = 50 m)

ACKNOWLEDGEMENTS

REFERENCES

Blocken B., and Carmeliet J. (2004). "Pedestrian wind environment around buildings: Literature review and practical examples". Journal of Thermal Envelope and Building Science, Vol. 28, No. 2, 107-159

Wise A.F.E, Sexton D.E., Richards D.J.W. (1971). "Effects due to groups of buildings", Philosophical Transactions of Royal Society of London. Series A, Mathematical and Physical Sciences, Vol. 269, 469-485.

Stathopoulos T., Wu H. (1995). "Generic models for pedestrian-level winds in built-up regions", Journal of Wind Engineering and Industrial Aerodynamics, 54-55: 515-525.

Tulapurkara E.G., Gowda B.H.L., and Chaukar J.S. (2005). "Mean velocity field around prismatic bodies in tandem arrangement". Journal of Wind Engineering and Industrial Aerodynamics, 93, 777-796.

Irwin H.P.A.H. (1981). "A simple omnidirectional probe for the measurement of pedestrian level winds", Journal of Wind Engineering and Industrial Aerodynamics, 7(3): 219-239

Assessment of thermal environment sensation for various climatic conditions and fluctuating air flow

<u>F. De Oliveira</u>[1], S. Moreau[1]

1 Centre Scientifique et Technique du Bâtiment – CSTB – 11 rue Henri Picherit,
44300 Nantes,

Keywords: Airflow fluctuation, Thermal comfort, sensory and psychological study.

ABSTRACT

The main objective of HVAC system within buildings and automotive application is to ensure thermal comfort for occupants. Many studies have focused on the static aspect of the airflow influence (considering the mean airflow) on the thermal comfort. Airflow is characterized by its fluctuating component. Fanger et al. (1988) present an empirical model of draught risk which integrates the mean velocity and turbulence. Few studies related to the airflow frequency have been carried out. Xia et al. (2000) established that the preferred average frequency is around 0.4 Hz for air temperature ranging between 26 and 30.5 °C and relative humidity between 35% and 65%. It was also confirmed by Hoffman (1994).

No study considering the airflow fluctuation aspect on global thermal comfort has yet been clearly identified. The aim of the present study is to clarify the impact of airflow fluctuation on various thermal condition sensations and to present a new thermal comfort assessment method.

EXPERIMENTS

Our approach is based on a multi-parametric assessment of felt and objectified thermal comfort. Therefore, we identified physiological, physical and psychological indicators.

Contact person: F. De Oliveira, Centre Scientifique et Technique du Bâtiment, CSTB, 11 rue Henri Picherit, 44000 Nantes, 033 2 40 37 60 09 and 033 2 40 37 20 60, E-mail fabrice.de-oliveira@cstb.fr

In our study, the "Predicted Mean Vote" (PMV) is used as thermal comfort reference index. This index model combines four physical variables (air temperature, air velocity, mean radiant temperature, and relative humidity) and two personal variables (clothing insulation and activity level) into an index that can be used to predict thermal comfort. The PMV is based on ASHRAE 7 thermal sensation scale (-3: cold, -2: cool, -1: slightly cool, 0: neutral, 1: slightly warm, 2: warm, 3: hot).

A fluctuating ventilation system is especially designed to generate calibrated airflow. With this system, seven airflows are generated between 0.08-1.75 Hz and are supplied by a circular outlet (diameter: 0.12 m). This fluctuating ventilation system is composed by an electric fan controlled by a supply in order to control the mean velocity of the airflow. The second part of our fluctuating ventilation system is a rotary disc composed by various porosities (90%, 60 and 40%) in order to chop the airflow. This device allows introducing the air flow fluctuating component by controlling his rotation velocity.

The mean velocity, the turbulence and the frequency were calibrated for each airflow level with a low velocity anemometer, DISA (type 54N50, bandwidth 0-10 Hz, range 0-5 m.s^{-1}). The mean air velocity is close to 0.75±0.2 m.s^{-1} with a turbulence of 31±7%. Minimum and maximum velocities are respectively 0.21±0.09 m.s^{-1} and 1.53±0.15 m.s^{-1}. The Figure 1 presents an example of generated airflow with a frequency of 0.46 Hz.
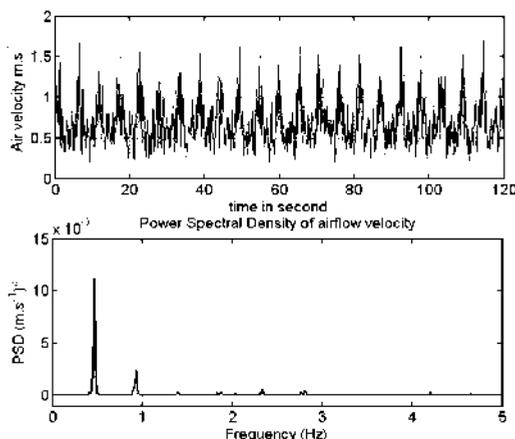
Figure 1: Example of air velocity signal and its power spectral density with a frequency peak of 0.46 Hz.

Our study is carried out in an experimental room. The room air temperature is controlled by an air-conditioning system. In order to avoid the influence of the air-conditioning airflow, the experimental scene is isolated with a protection screen. The surrounding ambient temperatures, relative humidity, mean radiant temperature and airflow temperature are measured simultaneously. Three thermal conditions are tested: 1st condition (air temperature, °C, relative humidity, %), 20.4±0.5 °C , 52.6±8 %, e.g. PMV = -2.7±0.2; 2nd condition, 25.5 ± 0.6 °C, 53.6 ±6.7 %, e.g. PMV = -0.4±0.2; 3rd condition, 28.3 ± 0.6 °C, 49.9 ± 6 %, e.g. PMV = 0.7±0.3;

Twenty-nine subjects (18 men and 11 women) evaluated overall thermal sensation, thermal comfort, thermal states, thermal preference, thermal tolerance and airflow comfort in a climatic chamber during 2007 spring. All questions are in accordance with the ISO 10551 (1995).
Subjects are placed on a chair in front of an infrared camera. The cloth value is around 0.8 Clo (add 0.1 Clo for chair).

The airflow impacts the face on right part (forehead, cheek, nose, Figure 2). The face left part is used as reference in order to evaluate thermal local sensation. Moreover, each subject tests airflows during 3 minute. The direction and the face area are selected in order to minimize the mechanical eye

constraint effect, induced by airflow, on thermal judgment. A head bearing allow obtaining the reproducibility of the face area impacted by the airflow (Figure 2).

An infrared camera (FLIR A20 M, thermal resolution at 0.1°C) is used to record facial skin temperature distribution. A facial thermograph analysis is carried out on infrared thermal sequence in order to measure local temperatures by region of interest (forehead, cheek, nose, periorbital region), De Oliveira et al. (2007) and De Oliveira (2008). The face is a body part corresponding to 7% of the total body area for 20 % of its thermal sensibility. A skin temperature set is built (mean temperature and variance of each region).

Each subject is equipped with the E.motion sensors, Schmitt (2006), in order to assess their cognitive states and the activity of the autonomous nervous system during experiment. E.motion physiological measurements are used to check the cognitive reaction on face thermograph in order to delete temperature measurement artifacts. These temperature artifacts can reach variations of + 0.6°C, Merla and Romani (2007).

In order to estimate the contribution of physical and physiological parameters to overall thermal sensation and comfort, a multivariate analysis is performed. This analysis is based on multiple linear and partial least square regressions and correlation analysis with principal component analysis.

Figure 2: Experimental zone with an air duct on the right side of the subject, an infrared camera in front of the subject and a head position system in order to ensure a good impact area.

RESULTS

The first results show that comfort and thermal sensation are little correlated with the fluctuation airflow component for the tested climatic conditions. Moreover, no preference has been found in our study for a frequency around 0.4 Hz. However, a maximum positive correlation (0.4) with thermal comfort sensation (0 comfortable – 5 very uncomfortable) is found for the frequency 0.8 Hz in the cold environment.

We have observed that airflow temperatures have a more significant contribution to thermal sensation for all thermal conditions (correlation of 0.6) than the fluctuation component.

Nevertheless, let us precise that the few previous studies about impact of fluctuation airflow component on thermal sensation focused on thermal preference, Xia et al. (2000) and not on thermal comfort.

After making multivariate partial least square modeling, we can model thermal sensation from the skin temperature parameters and compare it to PMV index method. The correlation is 0.91 with a statistic significance, $p < 0.0001$ (Figure 3). This result presents a new thermal comfort assessment way from physiological objective measurements. Possible applications of this methodology can lead to the introduction of face infrared measurement as comfort indicator for HVAC regulation (for example in automotive HVAC). We can imagine a simple array of low cost infrared detector on car instrument panel focused on the human face. This device measures the face skin temperature to which

is applied our model of thermal comfort assessment. Finally, this evaluation is then used as set point by the car regulation system.
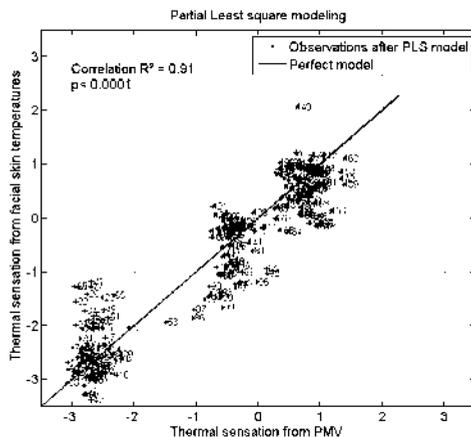
Figure 3: Partial least square regression between skin temperature parameters and PMV.

CONCLUSION

In conclusion, the present study demonstrates that local airflow temperature had an influence on thermal comfort. No significant impacts of airflow frequency on thermal comfort are found. This suggests that local airflow temperature could be considered as the most important factor.

Besides, direct physiological observations can be used for management strategies considering thermal comfort and HVAC system. Sensors for biophysical observations are today sufficiently mature to introduce the human component in our environment (thermal, acoustical and lightning).

REFERENCES

De Oliveira F., Moreau S., Gehin C, Dittmar A (2007). "Infrared Imaging Analysis for Thermal Comfort Assessment", 29th Annual International Conference of the IEEE Engineering in Medicine and Biology Society, France, Lyon, 23-26 august 2007.

De Oliveira F. (2008). "Study of human thermal comfort sensation with objective criteria in climatic environment", INSA Lyon PhD thesis, July 2008.

Fanger P.O., Melikov A.K., Hanzawa H., Ring J. (1988), "Air Turbulence and Sensation of Draught", Energy and Buildings, vol. 12, 21-39.

Fanger P.O. (1970), *Thermal Comfort, Analysis and Applications in Environment Engineering*, McGraw-Hill book company, ISBN 0-07-019915.

Hoffman J-B. (1994), "Le Confort Thermique, où en sommes nous ? ", Promoclim, vol. 25, n° 3, 143-158.

ISO 10551 (1995), "Ergonomics of the thermal environment - Assessment of the influence of the thermal environment using subjective judgment scales", International Organization for Standardization.

Merla A., Romani G.L. (2007), "Thermal Signatures of Emotional Arousal: A Functional Infrared Imaging Study", Proceedings of the 29th Annual International, IEEE EMBS , France, Lyon, 23-26 august 2007.

Schmitt P.M. (2006), "Non–invasive skin sensors for the continuous monitoring in order to assessment of the comfort of the sitting position and to prevent pressure ulcers", INSA Lyon PhD thesis, February 2006.

Xai Y., Rongyi Z., Xu W. (2000). "Human Thermal Sensation to Air Movement Frequency", Air Distribution in Rooms, ROOMVENT 2000, 41-46.

**ON SHORE AND OFF SHORE
WIND POWER GENERATION**

CFD Modeling of the wake interactions of two wind turbines on a Gaussian hill

Alexandros Makridis, John Chick

Institute for Energy Systems, University of Edinburgh - a.makridis@ed.ac.uk - Institute for Energy Systems, University of Edinburgh – john.chick@ed.ac.uk

Keywords: wind turbines, complex terrain, wakes, CFD modeling.

BACKGROUND

One part of the solution to the problem of climate change is the use of wind energy for electricity generation. Onshore wind farms usually consist of a number of horizontal axis wind turbines closely spaced in clusters and they are often sited on complex terrain. The operation of a wind turbine in a wind farm will inevitably affect the others in its vicinity due to velocity deficit and increased level of turbulence in its wake. Wakes of wind turbines sited close to each other are also expected to interact and contribute to a further reduction in wind farm efficiency and increased dynamic loading on the other turbines.

Simple (linear) models have been developed in the past to estimate the wake effects and optimize the siting of a wind farm, but they were mainly developed and validated for flat terrain and often fail in their estimations for complex terrain sites. Computational Fluid Dynamics (CFD) can be a useful tool towards the understanding of wake behavior on complex terrain. The present work involves the use of Fluent 6.3 commercial CFD code to study of the wake interaction of two wind turbines closely spaced next to each other at the top of an ideal Gaussian hill.

METHODOLOGY

The properties of the hill and the wind turbines were chosen to match the test case in the Upwind Project (Prospathopoulos et al. 2008). The idealized complex terrain investigated is a 3D (quasi-2D) Gaussian hill. The hill is chosen to be 700m high with a mean slope value of 0.4 (fig. 1). The wind turbines investigated have the properties of the NREL 5MW machine (Jonkman 2007): 126 m rotor diameter and hub height of 90 m. The rotors are placed at the hilltop with a spacing of 2D (fig. 1). Different turbulence models (k-ε realizable, k-ε RNG and Reynolds Stress Model) are used with the Reynolds Averaged Navier-Stokes equations to model the atmospheric wind flow. The inlet values for velocity and turbulence intensity were chosen as 10 m/s and 13% respectively at the hub height of 90 m. Appropriate roughness height was chosen to match the levels of turbulence and a logarithmic inlet velocity profile was applied by means of user defined functions in order to correspond to fully-developed flow in a neutral Atmospheric Boundary Layer. Fluent's standard wall functions

Contact person: Alexandros Makridis, Institute for Energy Systems – University of Edinburgh, Mayfield road, Kings Buildings, EH9 3JL, Edinburgh, telephone: +447833521488, FAX: +44 (0)131 6506554.
E-mail a.makridis@ed.ac.uk

were chosen for the wall treatment.

The whole domain has a size of [x,y,z]=[24x9.5x10.8]km. A hybrid approach for meshing was successfully applied. The wall adjacent cell height was chosen so that the cell centroids are above the height equal to the roughness length. The mesh around the rotors consists of unstructured tetrahedral elements and the rest of the mesh is structured comprising of hexahedral elements of gradually increasing size from the ground to the top of the domain as well as from the site of the turbines towards the right and left symmetry planes (fig. 1). The need for denser mesh is due to the high pressure and velocity gradients on some parts of the domain (mainly close to the rotors, in the wakes as well as close to the ground).
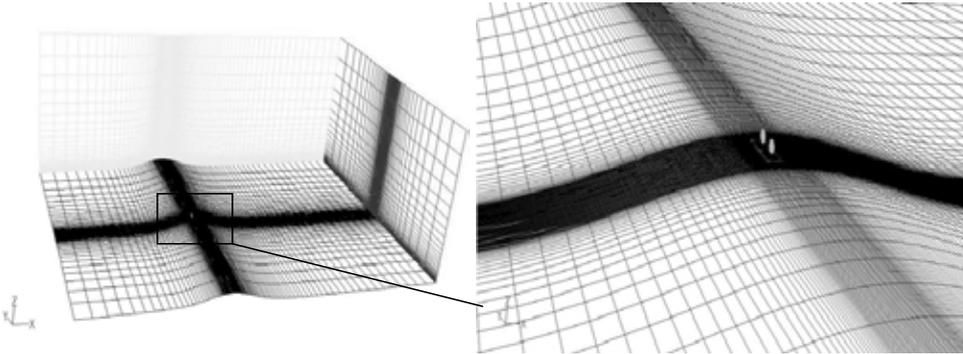
Figure 1: The quasi-2D Gaussian hill with 2 wind turbines on the top.

Fluent's Virtual Blade Model (VBM) was used to model the rotor as an actuator disk. VBM uses the Blade Element Theory and applies a pressure drop across the modeled actuator disk, varying with radius and azimuth. It eliminates the need of creating the actual rotor geometry and the required number of cells and computational time is reduced. The effect of rotor geometry is considered implicitly with the use of airfoil tables (drag and lift coefficient vs. angle of attack) as well as blade twist and chord for each blade section. The rotor rotational speed and collective pitch are also taken into account.

RESULTS

Some results of the simulations are shown in figures 2-4. In the contour plots, horizontal velocity is normalized with the reference velocity of 10 m/s (eq. 1). In the velocity deficit graphs the velocity at the hub in the simulation without a wind turbine is used, according to equation (2). Y-coordinate is normalized with the rotor diameter. The rotor hubs are positioned at $y_{norm} = -1$ and $y_{norm} = 1$ respectively.

$$u_{norm} = \frac{U_x}{10} \tag{1}$$

$$u_{deficit} = \frac{U_{hub-noW/T} - U_x}{U_{hub-noW/T}} \tag{2}$$

$$y_{norm} = \frac{y}{D} \tag{3}$$

According to fig. 2-4, the highest velocity deficit is calculated using the Reynolds Stress Model (RSM). After 12 diameters downwind, the peak velocity deficit seems to move mainly towards the middle but also to the sides showing that the wakes "break" in two parts and join in the middle. This is clearly shown with realizable and RNG k-epsilon models (fig. 2-3). RSM also shows that the wakes "join" after 15 diameters, although the peaks are not as clear as in the rest of the models.

Figure 2: normalized x-velocity contours and velocity deficit – realizable k-ε

Figure 3: normalized x-velocity contours and velocity deficit – RNG k-ε
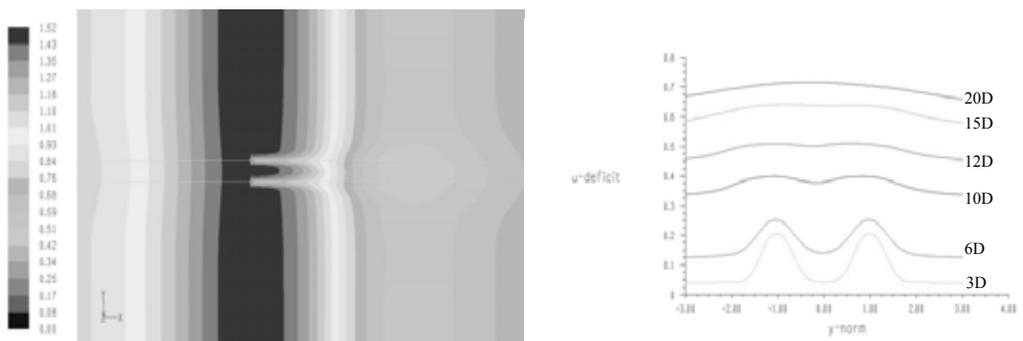
Figure 4: normalized x-velocity contours and velocity deficit – RSM

REFERENCES

Prospathopoulos J.M., Politis E.S., Chaviaropoulos P.K. (2008). "Modelling Wind Turbine Wakes in Complex Terrain", EWEC 2008 proceedings, Brussels.
Jonkman, J.M. (2007). "Dynamics Modelling and Loads Analysis of an Offshore Floating Wind Turbine", National Renewable Energy Laboratory.

Wind tunnel investigation on wake effects of a wind turbine

G. Diana, D. Rocchi, S. Giappino.

Mechanical Department of Politecnico di Milano – giorgio.diana@polimi.it – Via La Masa 1 20158, Milano – Mechanical Department of Politecnico di Milano – daniele.rocchi@polimi.it – Via La Masa 1 20158 Milano – Mechanical Department of Politecnico di Milano – stafano.giappino@polimi.it – Via La Masa 1 20158 Milano

Keywords: Wind Tunnel, CFD, Structural loads, unsteady flow, turbulence.

ABSTRACT

The flow field in the wake of a an horizontal axis wind turbine was studied through wind tunnel tests at the Mechanical Department of the Politecnico di Milano.

Aim of the research is to measure the wind flow in different points in the wake in order to characterize the flow blowing on structures that are positioned downwind a wind turbine and specifically on overhead power lines (OHL). The gathered experimental data consist in anemometric measurements and in the study of the dynamic response of an aeroelastic model of a OHL positioned in the wake of the wind turbine. The wind turbine model represents a 1:50 scaled model of a 3MW full scale wind turbine with a rotor diameter equal to 90 m. The model is equipped with an electric motor able to control the rotor angular velocity to reproduce the correct kinematics in the different wind speed operating conditions. Moreover, a mechanical system allows to change the blade pitch angle in order to have, on the blade profile, the correct velocity composition between the wind velocity and the motion velocity, as it happens in full scale.

Figure 1 reports a picture of the model in the wind tunnel test section and a rendering of the model highlighting the structural scheme inside the nacelle.

Contact person: D. Rocchi, Mechanical Department of the Politecnico di Milano, Via La Masa 1, 20158 Milano, +39 02 2399 8485, FAX +39 02 2399 8492. E-mail daniele.rocchi@polimi.it

Figure 1: 1:50 scaled model of the wind turbine (left) and 3D rendering of the model (right)

Tests were performed both in nominal smooth flow (residual turbulence intensity less than 2 % and block vertical wind speed profile) and in turbulent flow (turbulence intensity at hub height equal to 13 % and atmospheric vertical boundary layer wind speed profile), comparing the flow field measured with and without the wind turbine.

Anemometric measurements were performed in the wake at different downstream position from the wind turbine equal to 1.5D, 2.5 D, 5 D and 8 D, where D is the rotor diameter. Different wind velocity and related wind turbine angular velocity and blade pitch angles have been considered.

Figure 2 reports the trend of the horizontal velocity profiles measured at 4 different distances downstream the wind turbine. The ratio between the measured wind speed and the incoming wind speed upwind the wind turbine U_{ref} is reported versus the dimensionless transversal coordinate y, using the rotor diameter D as reference length. All the results are referred to the same tip speed ratio (TSR) defined as:

$$TSR = \frac{tip\ speed}{wind\ speed}$$
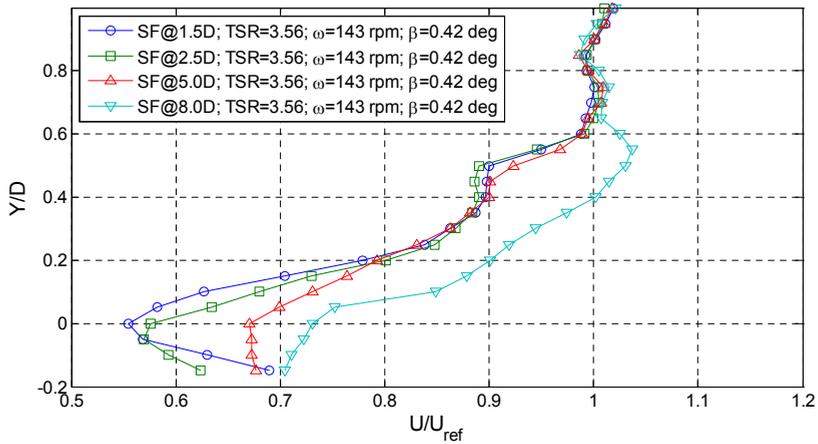
Figure 2: Horizontal velocity profiles at different distances from the wind turbine.

A 1:50 aeroelastic model of a OHL cable, reproducing the dynamic characteristics of an Araucaria full scale cable for a 400 m long span was used to measure the dynamic response of this structure when it is in the wake of a wind turbine. Tests were performed in turbulent flow condition taking into account different relative positions between the OHL model and the wind turbine (1.5 D and 2.5 D) and 3 different height of the line from the ground (distance of the minimum span height from the ground equal to 21.5 m, 31 m and 38.5 m). The motion of the cable was measured in 5 points along the line using infrared cameras.
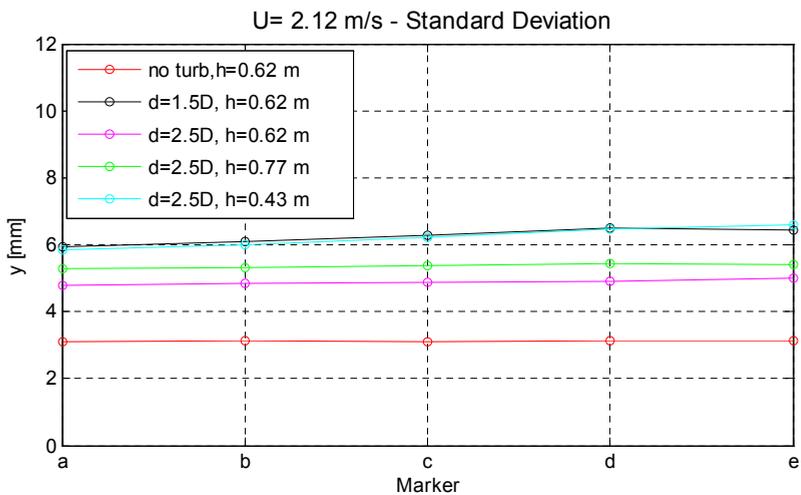
Figure 3: y standard deviation of the 5 monitored points of the aeroelastic cable model.

Figure 3 shows the dependency of the standard deviation of the displacement in the wind direction of the 5 monitored points along the cable model on the distance between the wind turbine and the OHL and on the height from the ground.

REFERENCES

G. M. Joselin Herbert, S. Iniyan, E. Sreevalsan, and S. Rajapandian (2007). A review of wind energy technologies. Renewable and Sustainable Energy Reviews, 11(6):1117–1145, 2007.

Jon G. McGowan and Stephen R. Connors (2000). Windpower: A turn of the century review. Annual Review of Energy and the Environment, 25:147–197

Smith G (2006). Advance wake model for very closely spaced turbines EWEC 2006 Paper. Athens 27 Feb – 2 March

Simiu E., Scanlan R. (1996). *Wind effects on Structures*. John Wiley & Sons, New York

Stefanatos N, Morfiadakis E, Glinou G, (1996) Wake measurements in complex terrain EWEC 1996 Paper pp 773-7

Multi-disciplinary optimization of wind turbines using comprehensive aero-servo-elastic models

C.L. Bottasso, F. Campagnolo, A. Croce, M. Giuliani

Politecnico di Milano, Dipartimento di Ingegneria Aerospaziale, Milano, Italy

carlo.bottasso@polimi.it

Keywords: wind turbine, aero-servo-elasticity, design, optimization.

ABSTRACT

We describe procedures for the multi-disciplinary design optimization of wind turbines using high-fidelity comprehensive models. Design parameters are optimized by maximizing/minimizing user-defined performance indexes, subjected to user-specified constraints. The optimization is performed by means of a variety of global-local techniques. Evaluation of cost function and constraints is performed by running simulations with a parametric high-fidelity aero-servo-elastic model. The proposed procedures are implemented in a computer program currently in use by industry for the optimization of a multi-MW horizontal axis wind turbine.

APPROACH

A parametric model of a wind turbine is developed within the comprehensive aero-servo-elastic non-linear finite-element-based multibody dynamics solver Cp-Lambda (Code for Performance, Loads, Aeroelasticity by Multi-Body Dynamics Analysis, Bottasso et al. (2006), Bottasso & Croce (2009a)). The multibody approach is based on a geometrically exact formulation, scaled index-3 DAE approach, using a non-linearly stable energy preserving/decaying time integration scheme

Contact person: Carlo L. Bottasso, Politecnico di Milano, Dipartimento di Ingegneria Aerospaziale, Via La Masa 34, 20156 Milano, Italy, tel.: +39-02-2399-8315, fax: +39-02-2399-8334.
    E-mail carlo.bottasso@polimi.it

(Bauchau et al. (2001)). Aerodynamic models are based on 2D sectional airfoil characteristics augmented with dynamic inflow, and implement turbulent and gusty wind models according to IEC rules. The wind turbine model includes sensors and actuators, and is coupled with a control logic supervisor and a variety of pitch-torque control laws, including PD, collective and individual blade pitch LQR, and adaptive model-predictive controllers (Bottasso & Croce (2009b)).

The optimization procedures can perform: a) aerodynamic optimization of the rotor (e.g. twist and chord distribution for max Annual Energy Production (AEP), with noise constraints and max chord constraints); b) structural optimization of the blades (e.g. minimum weight configuration for given design load cases (IEC-61400 DLCs), placement of frequencies, stress/strain allowables, etc.); c) combined aerodynamic-structural optimization (e.g. for max AEP over weight). The code allows the user to define a large number of constraints and different combinations of cost function contributors for all design problems. The optimization is performed by means of a variety of global-local state-of-the-art techniques, using the Noesis Optimus (TM) code. Evaluation of cost function and constraints is performed by running simulations (e.g. turbulent response, gust response, eigen-analysis, etc., as necessary) with a parametric high-fidelity aero-servo-elastic model implemented in Cp-Lambda, as shown in Figure 1. The code is also coupled to an aero-acoustics code based on the Ffowcs Williams-Hawkings formulation, which enables the direct inclusion of noise emissions in cost function or constraints.
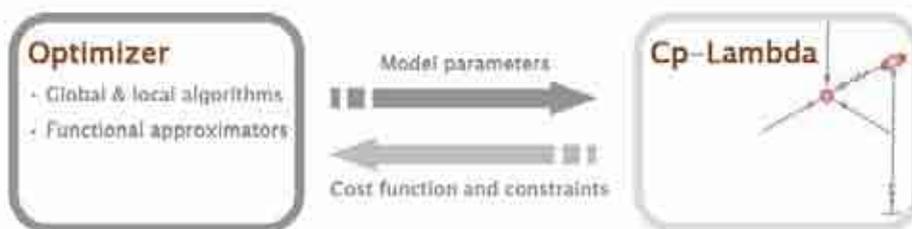
Figure 1: Coupling between optimizer and aero-servo-elastic solver for multi-disciplinary design optimization.

RELEVANCE

The optimization of the configuration of a wind turbine is a complex multi-disciplinary problem, which often relies only on the experience of the designer. Tools which can support such efforts can be useful for improving a tentative configuration, or for studying modifications to existing models.

INNOVATION

The procedures proposed in this paper enable the optimization of the configuration using comprehensive models, which can capture the relevant aero-servo-elastic characteristics of the system to a high level of fidelity. This is in contrast with other published procedures based on cruder reduced models (Selig (1998)).

RESULTS

We describe in detail the application of the procedures to a multi-MW-class wind turbine, and show the possible improvements on a tentative configuration.

CONCLUSIONS

The use of comprehensive multibody models of wind turbines can enable the multi-disciplinary optimization of the configuration of the machine with reasonable computational effort, and can effectively support the design process.

REFERENCES

Bauchau O.A., Bottasso C.L., Nikishkov Y.G. (2001). "Modeling rotorcraft dynamics with finite element multibody procedures", Mathematics and Computer Modeling, 33, 1113-1137.

Bottasso C.L., Croce A., Savini B., Sirchi W., Trainelli L. (2006). "Aero-servo-elastic modeling and control of wind turbines using finite element multibody procedures", Multibody Systems Dynamics, 16, 291-308.

Bottasso C.L., Croce A. (2009a). "Cp-Lambda user manual", Dipartimento di Ingnegneria Aerospaziale, Politecnico di Milano, Milano, Italy.

Bottasso C.L., Croce A. (2009b). "Advanced control laws for variable-speed wind turbines and supporting enabling technologies", Scientific Report DIA-SR 09-01, Dipartimento di Ingegneria Aerospaziale, Politecnico di Milano.

Noesis Optimus, Noesis Solutions NV, Interleuvenlaan 68, B-3001 Leuven, Belgium, www.noesissolutions.com.

Selig M.S. (1998). "PROPID User Manual", UIUC Applied Aerodynamics Group, Department of Aerospace Engineering, University of Illinois at Urbana-Champaign, Urbana, Illinois 61801.

Computing spatial estimates of the over-the-rotor wind distribution for advanced wind turbine active control

C.L. Bottasso, A. Croce, C. Riboldi

Politecnico di Milano, Dipartimento di Ingegneria Aerospaziale, Milano, Italy
carlo.bottasso@polimi.it

Keywords: wind turbine, control, aero-servo-elasticity, Kalman filter.

ABSTRACT

We formulate novel observers of the wind incident on the rotor of a wind turbine. Stochastic filtering processes reconstruct on-line optimal estimates of the tower and blade states, by using readings from accelerometers and strain gages placed along the structural members. From these reconstructed states, another filtering process estimates the wind states which, improving on the commonly used mean hub-height wind estimates or the point measurements available from on-board anemometers, also include information on the wind-over-the-rotor distribution. The proposed procedure is able to approximate vertical and horizontal wind shear, yawed flow and a vertical wind component. The instantaneous estimates of the flexible states of tower and blades and of the spatial wind distribution can be used for enabling sophisticated individual-blade fatigue and load alleviating control laws. The proposed procedures are demonstrated with the help of numerical experiments conducted using a high-fidelity aero-servo-elastic simulator.

APPROACH

In this work we formulate observers of the structural flexible states of a wind turbine and of the wind

---

Contact person: Carlo L. Bottasso, Politecnico di Milano, Dipartimento di Ingegneria Aerospaziale, Via La Masa 34, 20156 Milano, Italy, tel.: +39-02-2399-8315, fax: +39-02-2399-8334.
E-mail carlo.bottasso@polimi.it

blowing on the rotor. The motivation for the proposed observes is to provide estimates of these states to be used by advanced control laws (Bottasso & Croce (2009b)).

For example, knowledge of the tower fore-aft and side-side motions as well as of the blade flapping and lagging can be profitably used for designing sophisticated individual-blade control laws, so as to alleviate fatigue and gust-induced loads. In this work, an assumed modal basis approach is used, and the flexible states reconstructed by the observers are represented by modal amplitudes and velocities of tower and blades. With estimates of these states made available by the proposed observers, one can synthesize model-based control laws which account for the aero-elastic response of such states.

Furthermore, knowledge of the instantaneous wind-over-the-rotor distribution can be exploited so as to explicitly account for this information in the pitch and torque control of a wind turbine. For example, knowledge of the current wind vertical and horizontal shear, as well of the vertical and later wind components can be profitably used for reducing oscillatory loads.

Clearly, this information is of potential crucial efficacy in the design of control laws since it plays a central role in the determination of the aero-elastic response of the machine; however, the same information on the wind spatial distribution cannot be obtained by the on-board anemometer, which can only provide mean hub-height wind values and is also disturbed by interactions with the rotor stream-tube and the nacelle, nor it can be easily obtained by other practical means. Although wind observers have been previously described in the literature (Ma (1997)), these provide only hub-height estimates, i.e. constant-over-the-rotor wind values. While this information is useful and can be profitably used, for example for scheduling the control gains in terms of the wind speed, it does not account for important effects on the aero-elastic response of the wind turbine due to wind non-uniformity. The proposed wind observer tries to remove these limitations, by reconstructing a more complete picture of the instantaneous wind-over-the-rotor distribution.
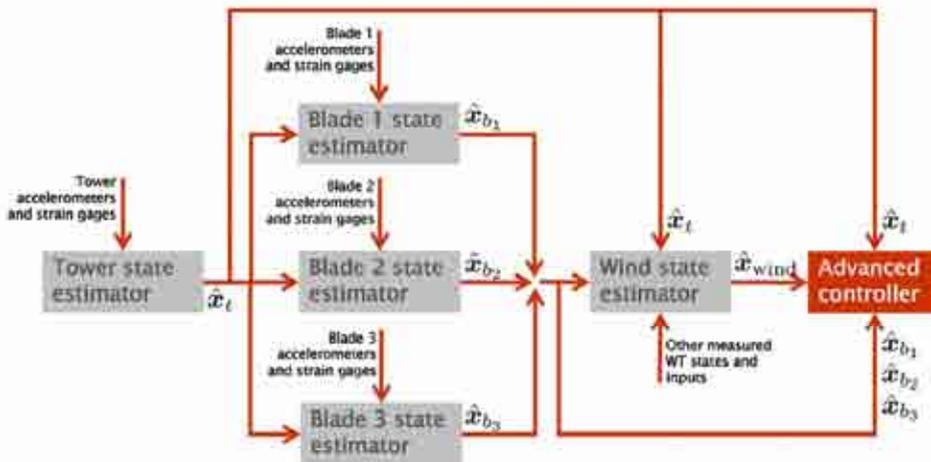
Figure 1: Overall architecture of the estimators of flexible tower and blade states, and of wind states.

In the proposed approach, estimates of all unknown states are obtained by a cascading series of Kalman filters (Bottasso & Croce (2009c)), as shown in Figure 1. A first filter is responsible for the reconstruction of the tower states. A set of governing equations is obtained by expressing the accelerations sensed by accelerometers placed along the tower in terms of an assumed modal basis. At each time instant, the filter first predicts the tower flexible states by integrating forward in time the governing equations, and then corrects the predictions using the readings of a set of strain gages, also

placed along the tower length. This filtering approach accounts for the presence of noise in the measurements of both the accelerometers and the strain gages. For reducing the need for tuning of the filter covariance matrices, an adaptive filtering approach is used, which reconstructs the noise statistics by keeping in memory a buffer of past values. A second set of parallel filters operates in series to the tower filter, with the goal of reconstructing the flexible blade states. For each blade, the accelerations sensed by accelerometers placed along the blade span are expressed in terms of the assumed modes of the blade, and of the accelerations transmitted by the tower; this last piece of information is at this stage known from the first filter. The filters predict the flexible blade states by integrating forward in time the resulting equations of motion, and then correcting the predictions based on readings provided by strain gages.

The filters are formulated so as to be able to operate with an arbitrary number of sensors, under the constraint of observability of the reconstructed states. However, to keep the number of necessary sensors to a minimum, which is important for reasons of simplicity, the filters can operate with one accelerometer and one strain gage for the tower and for each blade, which is a practical configuration already available on many instrumented wind turbines.

A wind state estimator is here formulated by considering that the flexible rotor of a wind turbine is a sophisticated "sensor" which spans the rotor disk and responds to the temporal and spatial variations of the wind blowing on it. By proper interpretation of the turbine response, one can infer the wind blowing on the rotor. In this work, the spatial wind distribution is approximated using a simple model which accounts for mean hub wind, vertical and lateral shear, wind direction and vertical wind component. These unknown wind parameters are promoted to the role of dynamical states and are identified on-line using a third adaptive filter operating in series with the tower and blade ones. To this end, we use a wind turbine reduced model which accounts for the coupled dynamic equilibrium of drive-train, tower fore-aft and side-side motion, and elastic blade motion. At each instant of time, an adaptive extended Kalman filter estimates the wind states by enforcing in a stochastically optimal sense the satisfaction of the reduced model dynamic equilibrium equations. This is obtained by regarding the wind states as the sole unknowns of the model governing equations, whereas all control inputs and states are either available by readings of the on-board sensors or known through the estimates provided by the structural flexible state observers.
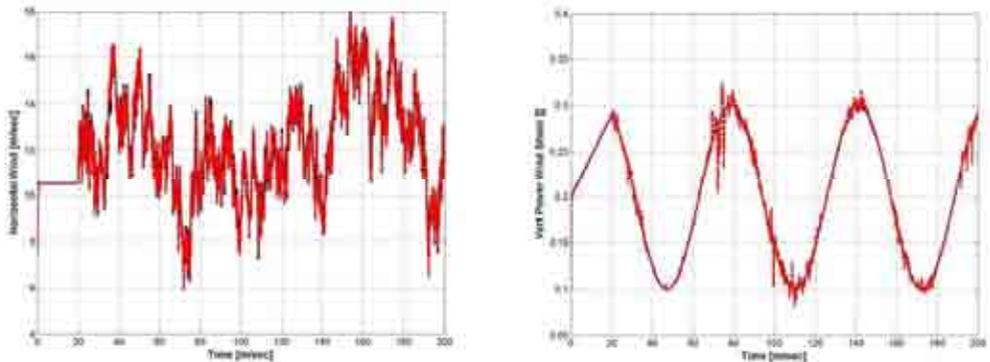
Figure 2: Estimation of generalized wind states. Hub wind (left) and power law exponent (right). Real: solid line; observed: dashed line.

The proposed methodology is demonstrated by using a high fidelity simulation environment, which includes an aero-servo-elastic wind turbine multibody model of the plant (Bottasso & Croce (2009a)), models of the wind, of the sensors, of the actuators and of measurement and process noise.

Extensive simulations in gusty and turbulent wind conditions demonstrate the ability of the proposed observes to identify with good accuracy both the flexible response of the machine and the spatial characteristics of the wind, as shown for example in Figure 2.

REFERENCES

Bottasso C.L., Croce A. (2009a). "Cp-Lambda user manual", Dipartimento di Ingegneria Aerospaziale, Politecnico di Milano, Milano, Italy.

Bottasso C.L., Croce A. (2009b). "Advanced control laws for variable-speed wind turbines and supporting enabling technologies", Scientific Report DIA-SR 09-01, Dipartimento di Ingegneria Aerospaziale, Politecnico di Milano.

Bottasso C.L., Croce A. (2009c). "Cascading Kalman observers of structural flexible and wind states for wind turbine control", Scientific Report DIA-SR 09-02, Dipartimento di Ingegneria Aerospaziale, Politecnico di Milano.

Ma X. (1997). "Adaptive Extremum Control and Wind Turbine Control", Ph.D.thesis, Technical University of Denmark.

WindAccept
Strategies and Design Instruments for Wind-Sites Acceptance

L. Cavallari, P. D'Asdia, F. Girasante, F. Angelucci

L. Cavallari – l.cavallari@unich.it – Università G. d'Annunzio - Viale Pindaro 42, Pescara

P. D'Asdia – p.dasdia@unich.it – Università G. d'Annunzio - Viale Pindaro 42, Pescara

F. Girasante – f.girasante@unich.it – Università G. d'Annunzio - Viale Pindaro 42, Pescara

F. Angelucci – filangel@alice.it – Università G. d'Annunzio - Viale Pindaro 42, Pescara

WINDACCEPT

Background of the work

The Italian background of the actions in the energetic fields is characterized by a cultural program philosophy where attitudes of extreme emphasis on the productive ability of new technologies from renewable sources contrast with positions of total refusal respect everything new. Such situation is registered in particular within the field of the application in wind energy production technologies and in the specific operative situations of installation on-shore/off-shore of large structures for wind production.

One of the main cultural barriers able to stop the process of diffusion of new technologies of wind production on-shore/off-shore is the scarce acceptance of the new wind-energy products by those who are directly implicate in the processes of transforming and use of territory.

Another important cultural barrier is the low integration of the plants with other components of the territory and therefore the absence of plans able to predict programmes which are complementary to the installation of structures for wind production on-shore/off-shore, in order to predict integrative benefit with respect to the variables of energetic dimension.

Contact person: F. Angelucci, Università G. d'Annunzio, Viale Pindaro 42, Pescara, Tel/FAX +39 085 4537252/255.
E-mail filangel@alice.it

With respect to the specific issues of installation of tall structures for wind production it is necessary to act besides the peculiarity of the evaluation and realization events of the plants to use, consequently, to adopt a program integrated vision, able to construct new relationships among the functions, the flows and the dynamical cycle of territory, with its spaces, infrastructural system and with the practices of enhancement and non intensive touristic use of landscape.

With respect to the foreign initiative centred on the so-called environmental tourism the Italian delay is ten year. Some recent experiences had a very important role in order to obtain awareness on energetic-environmental issues, without coping, nevertheless, with the matter of the productivity/profitability of wind plants in the emerging tourism energetic field.

The present Italian situation lacks, therefore, in comparison with the international trend where there is a meeting between hard technologies of building of structures for wind production and soft technologies for the promotions of environmental tourism, as main strategy to promote the technological innovation in the energetic and landscape field.

In this direction the relationship between technological innovation, energetic production from renewable sources and non intensive touristic use of landscape is central in order to study big wind-sites, in order to enhance both the acceptability and the integration of the structures for wind production in the territory, and to start the development of a new awareness and environmental responsibility linked to the practices of enhancement and promotion of local settlements.

The Research Group operating at G. d'Annunzio Chieti-Pescara University (UdA) is studying from many time the themes concerning the acceptance and integration of renewable energetic production technologies in the landscape.

As far as concern the specific aspects of wind-energy sites and large structures for wind production the Uda Group is investigating three thematic:

a.) the development of integrated strategies, models and guidelines to promote and evaluate a landscape use of renewable energy production sites;

b.) the study to recognize the new wind-energy sites as landscape attractions elements;

c.) the investigations on the potentialities of integrated use of last generation tall structures according to a perspective addressed to "Dual" touristic and cultural enhancement, promotion and use of the landscape.

The methodology

The research is referred to the recommendations expressed in two European communitarian papers aimed to promote the theme of technological innovation within the local energetic policies and in the field of the landscape culture programmes: the Strategic Energy Technology Plan (SET-Plan) and the European Landscape Convention.

The SET-Plan, actually, takes back the technological innovation to the centre of policies and strategies of the European Community in consideration to energetic supply and reduction of greenhouse gases, predicting a complete change of energetic infrastructures and an innovation in organization, through the implication of fields connected with energy, but also with environmental technologies, transports, information, cultural tourism and communication.

The European Landscape Convention, on its turn, wish the ripening of an awareness and a collaboration for the elaboration of European local and natural cultures, in order to contribute to the wellness and the satisfaction of different community needs, recognizing that the landscape is in any place an important element of the quality of people life: in the urban areas, in the countryside, in degraded or high quality territories, in the areas considered exceptional and in the common life areas.

The main goals of the research are to enhance the acceptance e the integration of last generation wind-energy sites in the processes of transformation and use of territory, to detect the possibility to reflect on the structures for wind production and their towered structures as alluring landscape elements. Actually, as the European Commission stressed, it is by a point of view a paradox that, in

the beginning of the nuclear development, people could not oppose to the installation of a nuclear reactor but today they can impede the development of structures for renewable energy production. (EU Green Paper Towards a European strategy for the security of energy supply, {COM (2000) 769}). For this reason, the UdA Research Group is working out and develop strategies, tools and scenarios to improve acceptance and the integration of the recent structures for wind production as technological product considered not only for energy production, but as elements with an added productivity/profitability within the so-called non intensive environmental tourism and in the specific emerging energetic tourism sector.

Starting from the European Transfrontier Research Program ENERWOOD, a precedent and ongoing experience within the Interreg IIIA Project, the UdA Group has developed a systemic performance approach to transfer in the landscape the life-cycle characteristics of the new structures for wind production. They will be analyzed – together with their retaining structures or installations on-shore/off-shore – through the reconstruction of the peculiar life cycle stages of a plant, considering the possible inconveniences and the potential positive repercussions on the territory.

This methodological approach has been developed in ENERWOOD program and just transferred on Abruzzo regional territory in the so-called Energy Road (a planning system of renewable energy new production sites).

According to this perspective, the research program will be aimed to cope with the following problems:

1.) the transfer of specific knowledge in a multi-disciplinary approach, outstretched to the enhancement, promotion and use of on-shore/off-shore installation place for their "Dual" touristic-energetic use;

2.) the study of actions aimed to investigate the concepts, the strategic lines, the development models, the evaluating tools and the applied scenarios, to enhance the development of tall towered structures for wind production in alluring elements of landscape and consequently, in new occasion of cultural and touristic use of territory;

3.) the analysis and the study of the peculiar life-cycle stages of structures and wind producer, from the installation to the substitution or the possible remove, considering the possible inconveniences and the potential positive effects on the territory and, predicting lines of intervention and the necessary shrewdness to relieve the impacts and the development of the landscape.

Obtained and in progress results

The obtained and ongoing target of the research can be divided into four themes:

Theme 1. To analyze the characteristics of the new structures for wind production and to evaluate the potentialities as enhancing elements of the territory, on the grounds of the experiences already ripened in the international background.

Theme 2. To detect the strategic guidelines to develop acceptance and integration of the intervention in the transformation scenarios and of touristic-energetic use of territory.

Theme 3. To develop models for the simulation of interaction levels between new plants and the enhancement and non-intensive touristic promotion of territory.

Theme 4. To develop possible applied scenarios on/off-shore to assess the possible "Dual" touristic-energetic use of the installation areas (through simulations on sample places).

Expected results of Uda Research Group as far as concern the study of tall-towered structures for large wind production as alluring element of landscape will be articulated in three levels:

Strategic-conceptual level
Methodological-instrumental level
Operational level

The expected results for strategic-conceptual level are:
- A Dossier on the main Italian and foreign experiences intent on enhancing the acceptance of new generation wind plants in the on-shore/off-shore installation;
- A Summary Paper containing the foundation concepts to stimulate coordinate and integrate initiatives to develop new generation wind-energy sites as appealing elements of the landscape;
- A Guidelines document of policy of installation for new generation structures for wind production in a perspective of enhancement, promotion and touristic-energetic use of territory.

The expected results for Methodological-instrumental level are
- An Analytical–provisional model to detect and value the opportunity to operate and enhance the development of positive impacts on the territory and the integration with the transformation and use for non intensive touristic targets, consequent upon the installation of the large wind plants.

The expected result for Operational level and Scenarios elaboration are:
- A Chart of micro-operational typologies for the compensation of inconvenient effects on the landscape and the development of places for touristic-energetic purposes;
- A system of exemplified applied Scenarios elaborated with simulation on sample places.

REFERENCES

AA.VV. (2003), Offshore Wind Energy in Mediterranean and Other European Seas - Resources, Technology, Applications, ENEA, Roma.

AA.VV. (2000), Energia eolica - Aspetti tecnici, ambientali e socio-economici, ENEA, Roma.

Elliott D., (2003), Energy, Society and Environment, Routledge-Taylor & Francis Group, London.

European Commission, (2000). Towards a European strategy for the security of energy supply, Brussels.

European Commission, (2006), A European Strategy for Sustainable, Competitive and Secure Energy, Brussels.

European Commission, (2008), Towards a "Post-Carbon Society", European Research on Economic Incentives and Social Behaviour, Office for Official Publications of the European Communities, Luxembourg.

Gipe P., Pasqualetti M.J., R. W. Righter, (2002), Wind Power in View: Energy Landscapes in a Crowded World, San Diego Academic Press, San Diego.

Gracceva F., Manna C., Simbolotti G., a cura di, (2008), Tecnologie per l'energia: quali innovazioni e strategie industriali in Europa? Il SET-Plan e le sue proposte, Dossier ENEA, Laboratorio Tecnografico ENEA, Frascati.

Szarka J., (2007), Wind Power in Europe: Negotiating Political and Social Acceptance, Palgrave Macmillan, New York.

Checking Global Warming in Africa with Wind Energy

U. U. Ogwo

NgNOG, rev@solartimeelectric.net

Keywords: Environmental degradation, Power outages, Capital investment

ABSTRACT

There is need to immediately kick-start meaningful investment in the wind energy industry in Africa. The electricity need in Africa is growing concurrently with her ever-increasing population. It is pathetic however that the continental economy managers have been either too naïve or simply careless about the dangerous consequences of not making adequate provision for increasing the electricity supply to Africa commensurately. As a result we are already experiencing an unprecedented era of electrical grid power outages. Initially, those outages were viewed as unavoidable natural consequences of the use of conventional grid electricity. However it is dawning on everyone now that we are in danger of experiencing total grid power collapse if nothing is done to check this dangerous trend.

Today our priority attention seems to be focused on food and survival. But the dream of continental poverty eradication will be a pipe one if everyone's concern is merely that of provision of sufficient food to go round. Poverty eradication cannot be achieved without real economic growth.

CONTACT PERSON: Rev. Ukaegbu Ogwo MD/CE, Solartime Electric Ltd. *Abuja:* #2 Hombori Street, Wuse 11, Abuja, *Aba:* Block 1 Road 1, Federal Housing Estate, Ogbor-Hill, P. O. Box 4674 Aba, Abia State, Nigeria. Tel.: 082-480 165, Mobile: 0803 323 4516,
E-mail: rev@solartimeenergy.com; rev@solartimeelectric.net; Website: www.solartimeelectric.net

Economic self-sufficiency, which should bring an end to the need for aid, is what Africa really needs. No one can achieve this without first putting on ground the necessary infrastructures that will enhance economic growth. Such basic infrastructures as electricity are of invaluable importance in actualizing the entrepreneurial spirit in the African in order to have him on course to achieving economic self dependence.

The ozone layer is a divine protection that limits the heat retention on planet earth and consequently the temperature of the planet. With its depletion due to environmental degradation, the normal temperatures of the earth are now higher than ever before. The result is that critical temperatures that prevent the melting of the Arctic and Antarctic snow are now exceeded. Thus large slabs and chunks of ice are melted in these regions bringing about the swelling of ocean beds with its resultant rise in global sea level. Unprecedented floods are now recorded as a consequence of this. Global climatic changes are now experienced.

There is at the moment a growing environmental degradation in Africa and the flooding and warming of the continent and planet as a consequence. The adverse effect on agriculture which is the mainstay of the economy of the African continent cannot be over-emphasized. The problem of grid power outages in most parts of Africa is the bane of industrial development.

Oil and Gas are the major fuels that power the global industrial drive. As a result of a lack of focus on the implications of the indiscriminate use of these fuels our planet has suffered grave adversity consequently. The bi-products of oil and gas are emissions that deplete the protective ozone layer.

The global search for alternative fuels and energy sources has become imperative if mankind is to save his planet from an impending doom. A lot of research efforts have been initiated in this regard with a view to developing acceptable alternatives to fossil fuels that will not result in dangerous, unacceptable emissions as bi-product. Solar energy, wind energy, geo-thermal, hydro-electric energy and bio-gas are but some examples of the alternative energy sources being proposed.

Quite a few rewarding results have been obtained from the global alternative energy research efforts, each of which comes with its limitations. Wind energy is a cost effective energy option that is steadily marching towards matching grid power in unit energy cost. Its limitation however is that it is only available in areas where the wind resources are available. Fortunately, Africa has quite an abundant distribution of wind energy resources.

With the amount of research efforts being put in the field of alternative energy it is only a matter of time before permanent solutions are found to the global energy problems. The global need to find acceptable alternative energy sources is urgent as industry experts predict prices of up to $500 per barrel within a few years. These research efforts and the rewarding results give oil-dependent economies in Africa like Nigeria notice to find alternative economic earning sources to oil. Nigeria is a special case since there is no other meaningful revenue earner for that economy than oil and gas. Therefore unless such economies are diversified very urgently they stand the risk of collapse.

The call is both immediate and urgent. Something should be done now. With all the writings on the wall it is pathetic to note that the managers of most African economies appear unaware of the impending danger.

There are abundant wind resources all over Africa. These available wind resources could be used to jump-start the African economy and to check the present environmental abuse, provided that the limitation of lack of capital investment funds for the harvesting of wind resources is removed. Diversifying the African economy will save the continent from the dire consequences of over-dependence on exhaustible mineral extraction industries.

An enabling environment needs to be created to aid foreign investors appreciate the viability of investment in wind energy in Africa. Macro-siting data exist in some parts of the continent. However bankable micro-siting data are required by the foreign investors that may want to invest in the wind energy industry in Africa. Sufficient enlightenment needs to be provided for Africa to access available grants in the global energy industry for the development of wind energy in Africa. In this way the available cheap labour force of Africa can be harnessed, crime rates of the developed countries of the world will be reduced as the viable human resources of Africa, which is cheaper than Chinese human resources, is gainfully utilized locally to the benefit of all the world. Thus wind energy can check both the physical environmental degradation of Africa as well as the social degradation. The world is made so that no man is an island. Saving the planet from global warming is a collective responsibility. Unless a unified approach is used, all the wonderful efforts of the developed countries will be reversed by an unchecked abuse by the unassisted countries of Africa.

REFERENCES

Ogwo U. U. (2008). "Optimal management and use of critical resources in campus networks in Africa: The power supply factor." A Presentation at AFREN 2008 Forum Conference on ICTs & Education, at National Centre for Scientific & Technical Research (CNRST) with Mohammedia School of Engineering (EMI) Rabat Morocco

Ogwo U. U. (2007). "The Place of Wind Energy in Checking the Menace of Power Outages in Nigeria." A Presentation at the International Renewable Energy Conference (IREC) at Sheraton Hotel & Towers Abuja Nigeria

Gudopp D. (2007). Lahmeyer International Renewable Energies "Development Bank financed Wind Energy Projects A Case Study." A Presentation at the International Renewable Energy Conference (IREC) at Sheraton Hotel & Towers Abuja Nigeria

Drosch M. (2007). Lahmeyer International Renewable Energies "Wind Farm Implementation." A Presentation at the International Renewable Energy Conference (IREC) at Sheraton Hotel & Towers Abuja Nigeria

Potential output power from the 20 kW Jacobs wind turbine generator across 19 sites in northern Nigeria.

1st G.Y.Pam, 2nd E.J.Bala

Mechanical Engineering Dept, Ahmadu Bello University, Zaria - Nigeria,
gypam2008@yahoo.com; Mechanical Engineering Dept, Ahmadu Bello University, Zaria - Nigeria,
elijidere@yahoo.co.uk

Keywords: Capacity factor, Power output characteristics, Weibull distribution model.

ABSTRACT

Previous estimates of potential output were theoretical maximum extractable power densities from hypothetical wind turbine generators, operating with a constant rotor efficiency of 59.3 % for various locations in Nigeria (Ojosu, 1990; Isiriena, 1991; Iheonu, 2002). The power output from a wind turbine generator at a location depends on wind and generators power output characteristics. This paper applies a method for computing expected output power from a wind turbine generator, given the observed wind speed distribution at a location and the power output characteristics of the wind turbine generator. The output power is evaluated at 50 m hub height for the 20 kW Jacobs wind turbine (model 29-20) generator. The 20 kW Jacobs wind turbine generator has cut-in wind speed V_i = 3.58 m/s, rated wind speed V_r = 11.62 m/s, rated power P_r = 20 kW and cut-out wind speed V_o = 53.63 m/s (www.windturbine.net, July, 2003). The estimates are for the following locations in northern Nigeria: Abuja, Bauchi, Bida, Gusau, Ilorin, Jos, Kaduna, Kano, Katsina, Lokoja, Maiduguri, Makurdi, Minna, Nguru, Potiskum, Sokoto, Yelwa, Yola and Zaria. The results of the output power are expressed as capacity factors.

Contact person: 1st G. Y. Pam, Mechanical Eng Dept, A. B. U., Zaria - Nigeria, telephone: +2348037015397.
E-mail gypam2008@yahoo.com

METHODOLOGY

The mean output power, $\overline{P_o}$, from a wind turbine generator at a location can be estimated from its power output characteristics $P(V)$ and the wind characteristics of the location represented by the probability distribution of wind speeds $p(V)$. This is given by Manwell et al. (2002) as:

$$\overline{P_o} = \int_0^\infty P(V)p(V)dV .$$ (1)

Bala and Pam (2004) described the power output function, $P(V)$ of a wind turbine generator as

$$P(V) = \begin{cases} 0, & V \le V_i \\ A + BV + CV^2 + DV^3, & V_i < V \le V_r \\ P_r, & V_r \le V \le V_o \\ 0, & V > V_o, \end{cases}$$ (2)

assuming a third-degree polynomial for the power output with wind speed V between cut-in and rated wind speeds. The constants A, B, C and D are evaluated based on the following conditions:

$$\begin{aligned} A + BV_i + CV_i^2 + DV_i^3 &= 0 \\ A + BV_r + CV_r^2 + DV_r^3 &= P_r \\ A + BV_m + CV_m^2 + DV_m^3 &= P_r(V_m/V_r)^3 \\ A + BV_x + CV_x^2 + DV_x^3 &= P_r(V_x/V_r)^3 \end{aligned}$$ (3)

where $V_m = (V_i + V_r)/2$ and $V_m = 2(V_i + V_r)/5$.

The two – parameter Weibull wind speed probability distribution, $p(V)$, is expressed by Justus et al. (1978) as:

$$p(V) = \left(\frac{k}{c}\right)\left(\frac{V}{c}\right)^{k-1} e^{-\left(\frac{V}{c}\right)^k},$$ (4)

where c is the scale parameter and k is the shape parameter.

The mean wind speed and standard deviation method for the estimation of Weibull parameters (Pam et al., 2005) was used to estimate the Weibull parameters for the 19 locations. From known mean wind speed $\overline{V}$ and standard deviation σ, k can be computed from (Justus et al., 1978):

$$k = \left(\frac{\sigma}{\overline{V}}\right)^{-1.086} .$$ (5)

Lysen (1983) used the following approximation to find c,

$$\frac{c}{\overline{V}} = \left(0.568 + 0.433/k\right)^{-\frac{1}{k}} .$$ (6)

Weibull parameters c and k at 50 m height were determined for the 19 locations.

From the third-degree variation of power output with wind speed between cut-in and rated wind speeds and the Weibull distribution, defined by the estimated c and k values, equation (1) becomes

$$\overline{P_o} = \int_{V_i}^{V_r} (A + BV + CV^2 + DV^3)\left(\frac{k}{c}\right)\left(\frac{V}{c}\right)^{k-1} e^{-\left(\frac{V}{c}\right)^k} dV + P_r[p(V_r \le V \le V_o)].$$ (7)

Constants A, B, C, D for the 20 kW Jacobs wind turbine, c and k for the 19 locations were substituted into equation (7) and results expressed as capacity factors, CF, given by $CF = \overline{P_o}/P_r$.

RESULTS AND DISCUSSION

The constants for the 20 kW Jacobs wind turbine (model 29-20) generator were found to be $A = -3.713$ kW, $B = 1.402$ kN, $C = -0.1716$ kNm^{-1}s and $D = 0.0195$ kNm^{-2}s^2.

Figures 1 and 2 show annual scale and shape parameters, annual capacity factors from the 20 kW Jacobs wind turbine at a height of 50 m for the 19 locations. The 20 kW Jacobs wind turbine is expected to operate with a maximum capacity factor of 23.47 %. Most of the sites have very low capacity factors. A capacity factor of 23.47 % from a 20 kW Jacobs wind turbine means a mean output power of 4.694 kW or an annual power output of 41,119 kWh. The average American household consumes about 10,000 kWh of electricity annually (Annual Energy Review 2000, 2001). Much less is expected for a Nigerian household. If 3,000 kWh is assumed for a Nigerian household at a rural setting, then the 20 kW Jacob wind turbine can power about 3, 14, 7, 3, 2, 6, 7 and 2 households in Gusau, Jos, Kano, Katsina, Maiduguri, Minna, Sokoto and Zaria respectively. Figures 1 and 2 also show the capacity factor as it relates to annual mean wind speed (or Weibull c) and standard deviation (or Weibull k). It is seen that there is a trend of increasing output with increasing mean wind speed. However, there is variation due to influence of standard deviation of wind speeds about the mean wind speed. There are pairs of locations for which the higher output power occurs at the location with the lower mean wind speed (because of this influence of standard deviation), for example Gusau and Katsina.

CONCLUSION

The 20 kW Jacob wind turbine (model 29-20) generator operating at 50 m height has very low power output for most of the locations. It is expected to operate with a maximum capacity factor of 23.47 % across the 19 locations in northern Nigeria.
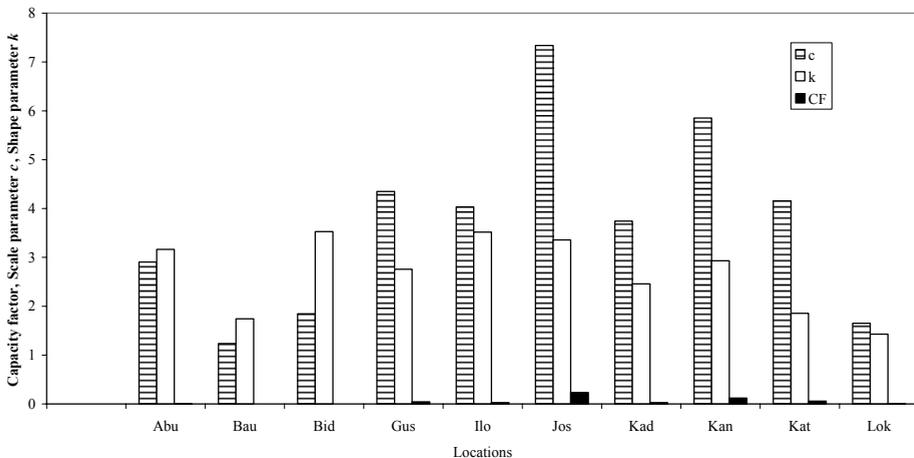
Figure 1: Annual scale and shape parameters, annual capacity factors at a height of 50 m for Abuja, Bauchi, Bida, Gusau, Ilorin, Jos Kaduna, Kano, Katsina and Lokoja.
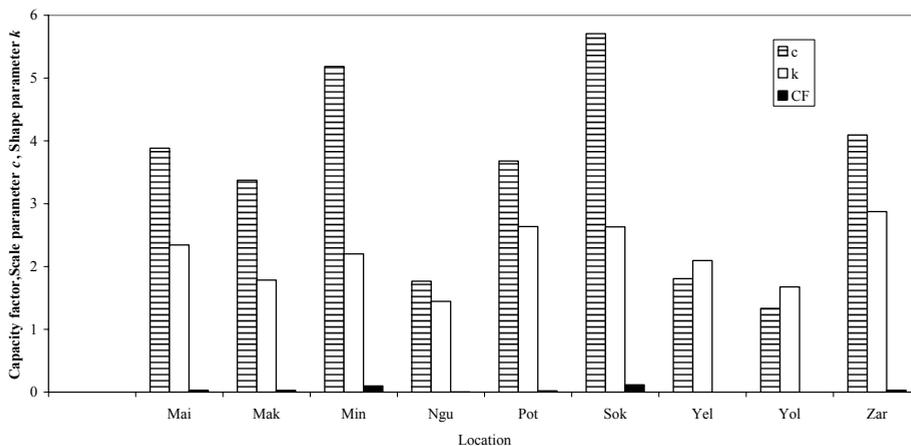
Figure 2. Annual scale and shape parameters, annual capacity factors at a height of 50 m for Maiduguri, Makurdi, Minna, Potiskum, Sokoto, Yelwa, Yola and Zaria.

REFERENCES

Ojosu, J.O. and Salawu, R.I. (1990). "An evaluation of wind energy potential as a power generation source in Nigeria", Solar & Wind technology, 7 (6), 663-673.

Isirisena, U.A., Alfa, B., Bakwa, D.D. and Tsor, J.O. (1991). "Assessment of the wind power potential at Heipang, near Jos," Nigerian Journal of Solar Energy, 10, 44-55.

Iheonu, E.E., Akingbade, F.O.A. and Ocholi, M. (2002). "Wind resource variations over selected sites in the West African sub-region," Nigerian Journal of Renewable Energy, 10 (1&2), 43-47.

www.windturbine.net (July, 2003).

Manwell, J.F., McGowan, J.G. and A.L. Rogers, A.L. (2002). *Wind Energy Explained*. John Wiley & Sons Ltd, West Sussex, England.

Bala, E.J. & Pam, G.Y. (2004). "Mathematical representation of actual power output of four wind turbine generators." Nigerian Journal of Renewable Energy, 12 (1 & 2),128 – 133.

Justus, C.G., Hargraves, W.R., Mikhail, A. and Graber, D. (1978). "Methods for estimating wind speed distributions," Journal of Applied Meteorology, 17, 350-353.

Pam, G.Y., Bala, E.J. & Aku, S.Y. (2005). "Estimating wind speed probability distributions for Kano, Maiduguri, Sokoto and Zaria in northern Nigeria," Nigerian Journal of Renewable Energy, 13 (1 & 2), 60 -67.

Lysen, E.H. (1983). *Introduction to Wind Energy*. SWD Publication SWD 82-1, the Netherlands.

Annual Energy Review 2000 (2001), Washington D.C.: Energy Information Administration, DOE/EIA-0384 (2000).

Reliability Analysis of Offshore Wind Turbines
A BEM Model for Nonlinear Water Waves

1st E. Marino, 2nd C. Borri, 3rd U. Peil

1st *Dept. Civil and Environmental Engineering, University of Florence*
enzo.marino@dicea.unifi.it

2nd *Dept. Civil and Environmental Engineering, University of Florence*
cborri@dicea.unifi.it

3rd *Inst. for Steel Structures, TU Carolo-Wilhelmina, Braunschweig*
u.peil@is.tu-braunschweig.de

Keywords: offshore wind turbines, nonlinear waves.

ABSTRACT

This paper introduces the first part of a wider project in progress aiming at integrating numerical simulations into the general framework of Structural Reliability Analysis of Offshore Wind Turbines. The major needs of offshore systems today are represented by novel design procedures (e.g. structural optimization) which assure the minimization of the costs under the constraint of a fixed Structural Reliability (SR). Namely,

$$Cost\left(\bar{X}\right) \rightarrow \min$$

$$SR\left(\bar{X}\right) > SR^*$$

where $\bar{X}$ is the vector collecting all design variables.

Establishing the lower structural reliability level SR^* most concerns Risk-based decision theories and cost–benefit analysis and lies beyond the goals of this contribution. Nevertheless, the above optimization problem highlights how strongly the cost reduction is linked to a proper estimation of the SR. The better the SR is evaluated, the larger is its expected value, Ditlevsen & Madsen (2007). Indeed, as the SR is never an absolute measure - it considerably depends on many factors such as the accuracy level of the idealized structural model, the number of uncertainties and their statistics, etc. -

---

Contact person: 1st E. Marino, Department of Civil and Environmental Engineering, University of Florence, Via di Santa Marta, 3 – 50139 Firenze. Tel./fax 0039 (0)55 4796306.
E-mail enzo.marino@dicea.unifi.it

here the attention is most paid to restrict as much as possible the sources of uncertainties solely to those parameters which are intrinsically random by providing a tool which does not assume any *a priori* restriction on the water waves model. Figure 1 shows a simplification of this concept.
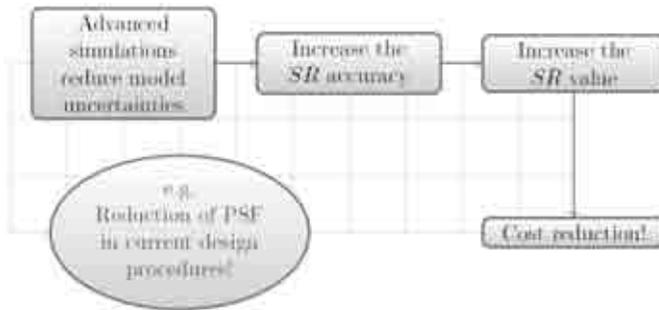
Figure 1: Structural Reliability and cost reduction.

It is also worth pointing out that since SR methods provide the probability of failure of the structure, then an improved reliability analysis naturally leads to the Risk reduction.

In accordance with the Hazard Identification phase of the risk management chain, Plifke et al. (2007), offshore structures are basically exposed to wind, wave and current loads and they may fail because of two different loading conditions: (i) extreme wind coupled with highly nonlinear extreme waves, which lead to the so called ultimate failure condition and (ii) long term fatigue accumulation that gives raise to the growth of cracks. While for long term loads the random process description fits fairly well the nature of the actions, so that the waves can be assumed linear and their superposition is allowed by using standard spectra, for the extreme loads scenario more realistic model are required. At this stage the attention is entirely paid to the water waves model, while further developments of the project will address the combination of the extreme hydrodynamic loads with extreme wind conditions so that, finally, a full simulation can capture the ultimate structural response.

Fully nonlinear 2d water waves

In some design conditions nonlinear effects of ocean waves cannot be neglected, especially when the goal is evaluating the structural safety. To this aim a time-depending BEM code is here presented in order to simulate water waves without introducing any approximation neither on the velocity potential nor on the wave steepness. The fully nonlinear potential flow initial-boundary-value problem is solved by using a MEL approach which consists of a repeated two-steps procedure, Grilli et al. (1989), Grilli & Svedsen (1990), Peil & Corte (2005).

Let Γ_N denote the region of the boundary where Neumann boundary conditions are assigned. Hence the two steps:

1. At a fixed time t, Γ_N and Γ_f are known. The velocity potential $\phi\,(p \in \Gamma_f)$ and the flux on Γ_N are also known. A steady Laplace's equation is solved for the flux $\nabla \phi\,(p \in \Gamma_f) \cdot \bar{n}$ on the free surface and the velocity potential on Γ_N.
2. When all the unknowns have been found, each particle of the boundary of the Eulerian frame, as well as the velocity potential is updated in a Lagrangian manner.

From Euler's equations, valid for an incompressible and inviscid fluid, the additional hypothesis of irrotational flow allows the description of fully nonlinear water waves by means of a potential model

$$\nabla^2 \phi\,(p,t) = 0 \quad \forall p \in \Omega\,(t) \tag{1}$$

The domain $\Omega(t)$ is assumed bounded by four boundaries: $\Gamma_i(t)$, $\Gamma_b(t)$, $\Gamma_o(t)$, $\Gamma_f(t)$ being the inflow wall, the bottom, the outflow wall and the free surface, respectively. The dynamic and kinematic free surface boundary conditions are defined as follows

$$\frac{D\phi(p,t)}{Dt} = -\frac{p_a}{\rho_w} - gy_f + \frac{1}{2}\nabla\phi(p,t)\cdot\nabla\phi(p,t) \quad \forall p\in\Gamma_f(t) \tag{2}$$

$$\frac{D\bar{r}(p,t)}{Dt} = \bar{v}(p,t) = \nabla\phi(p,t) \quad \forall p\in\Gamma_f(t) \tag{3}$$

An inertial coordinate system is fixed with the x–axis along the still water level and the y–axis vertical and upwardly oriented. See Figure 2. At a fixed time, points $p\in\Gamma_f$ are tracked by a Lagrangian position vector $\bar{r}(p) = p - o = x_f\bar{e}_1 + y_f\bar{e}_2$. Where $\bar{e}_1$ and $\bar{e}_2$ denote the unit normal basis.
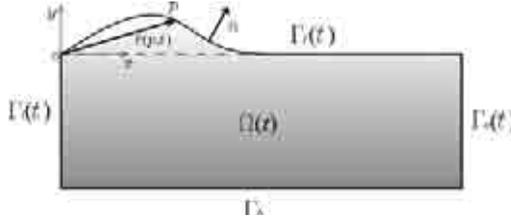
Figure 2: Domain of the potential model.

To solve the above time-depending potential problem, initial conditions must also be assigned. Namely, at the beginning of the simulation the potential along the free surface and its geometry are known. The steady solution at each time-step is achieved by discretizing the following Boundary Value Problem (BVP)

$$c(p_c)\phi(p_c) + \int_\Gamma \phi(p)q^*(p,p_c)\,d\Gamma - \int_\Gamma \phi^*(p,p_c)q(p)\,d\Gamma = 0 \tag{4}$$

where $\phi^*(p,p_c)$ denotes the Green's function, $q = \nabla\phi\cdot\bar{n}$ the flux, $q^* = \nabla\phi^*\cdot\bar{n}$ and c is a scalar which depends on the position of the collocation point p_c. By means of isoparametric quadratic elements, Brebbia & Dominguez (1998), the above equation is discretized into N_e boundary elements

$$c_i\phi_i + \sum_{j=1}^{N_e}\sum_{k=1}^{3} h_{ik}^{(j)}\phi_k^{(j)} - \sum_{j=1}^{N_e}\sum_{k=1}^{3} g_{ik}^{(j)}q_k^{(j)} = 0 \qquad i = 1:N_n \tag{5}$$

where

$$h_{ik}^{(j)} = \int_{-1}^{1} q_i^{*(j)}(s)\,\varphi_k(s)\,\mathcal{J}(s)\mathrm{d}s \tag{6}$$

$$g_{ik}^{(j)} = \int_{-1}^{1} \phi_i^{*(j)}(s)\,\varphi_k(s)\,\mathcal{J}(s)\mathrm{d}s \tag{7}$$

φ_k, with $k = 1,2,3$, denotes the shape functions, N_n is the number of boundary nodes and $\mathcal{J}(s)$ the Jacobian. In matrix form Equation (5) writes

$$c_i\phi_i + \hat{H}_{iq}\phi_q = G_{iq}q_q \tag{8}$$

which, after assembling and accounting for the boundary conditions type, finally turns into a standard linear system.

To integrate the dynamic and kinematic boundary conditions in time, a second-order Taylor series has been implemented. So that both the free profile and the velocity potential are update from the current t time to the subsequent instant $t + \mathrm{d}t$ as follows

$$\bar{r}(p, t+\mathrm{d}t) = \bar{r}(p,t) + \frac{D\bar{r}(p,t)}{Dt}\mathrm{d}t + \frac{1}{2}\frac{D^2\bar{r}(p,t)}{Dt^2}\mathrm{d}t^2 + o\left(\mathrm{d}t^2\right) \tag{9}$$

$$\phi\left(p, t+\mathrm{d}t\right) = \phi\left(p, t\right) + \frac{D\phi\left(p, t\right)}{Dt}\mathrm{d}t + \frac{1}{2}\frac{D^2\phi\left(p, t\right)}{Dt^2}\mathrm{d}t^2 + o\left(\mathrm{d}t^2\right) \tag{10}$$

No special effort is required to compute the first-order coefficients in equations (9) and (10), while the second order Lagrangian derivatives are computed by solving an additional BVP, Nakayama (1990).

Code validation

The code is currently being validated by simulating several kind of waves. Figure 3 shows the simulation of a solitary wave generated by assigning the initial profile (dotted line) and the velocity potential according to Machane & Canot (1997).
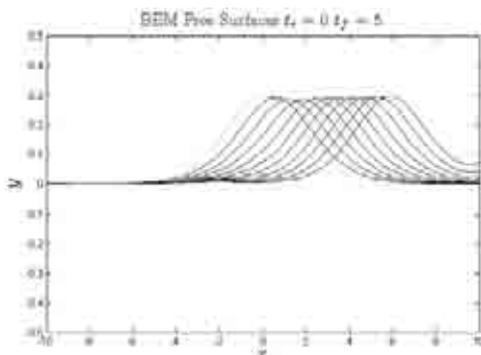
Figure 3. Free surfaces of a solitary wave traveling to the right. Profiles at every 10 time steps.

The free surface has been dicretized into 48 quadratic elements, the time step is $\mathrm{d}t = 0.05s$. The numerical solution in Figure 3 exhibits a good agreement with the analytical solution.

Next steps will be aimed at calculating the hydrodynamic loads associated to highly nonlinear waves.

REFERENCES

Ditlevsen O., Madsen H.O. (2007). *Structural Reliability Methods*. Monograph. First edition published by John Wiley & Sons Ltd, Chichester, 1996, ISBN 0 471 96086 1.

Plifke T., Sperbeck S.T., Urban M., Peil U., Budelmann H. (2007). "A standardized methodology for managing disaster risk - an attempt to remove ambiguity". In Proceedings of the 5th International Probabilistic Workshop, Ghent, Belgium.

Grilli S. T., Skourup J., Svedsen I.A. (1989). "An efficient boundary element method for nonlinear water waves". Engineering Analysis with Boundary Elements, 6(2):97–107.

Grilli S.T., Svendsen I. A. (1990). "Corner problems and global accuracy in the boundary element solution of nonlinear wave flows". Engineering Analysis with Boundary Elements, 7(4):178 – 195.

Peil U., Corte C. (2005). "Numerical simulation of breaking wave load on offshore wind turbines". J. Napstrek & C. Fisher (eds); ITAM AS CR, Prague.

Brebbia C.A., Dominguez J. (1998). *Boundary Elements, An Introductory Course*. WIT Press, Boston, Southamton.

Nakayama T. (1990). "A computational method for simulating transient motions of an incompressible inviscid fluid with a free surface. International Journal for Numerical Methods in Fluids, 10(6):683–695.

Machane R., Canot E. (1997). "High-order schemes in boundary element methods for transient non-linear free surface problems". International Journal for Numerical Methods in Fluids, 24(10):1049–1072.

Renewable Energy Resource in Nigeria:
An Estimation of Wind Power Potentials

M. B. Mu'azu , J. Y. Oricha, J. Boyi

Department of Electrical Engineering, Ahmadu Bello University, Zaria, Nigeria,
muazumb1@yahoo.com, omjosoricha@yahoo.com, pajayomachi@yahoo.com

Keywords: Wind Energy, Wind Power, Wind Speed, Isovents, Surfer-8.

ABSTRACT

The daily average wind speed (v_d, m/s), for 130 sections (1° x 1° of latitude and longitude) that is 2°E – 15°E longitudes and 4°N – 14°N latitudes, enclosing Nigeria, geographically was determined using average wind speed data from meteorological centers in Nigeria and satellite-derived meteorology and solar energy parameters from National Aeronautics and Space Administration (NASA). The data was used to illustrate the isovents across Nigeria at 50meter height, and hence, the average wind power potential across Nigeria was determined.

INTRODUCTION

Wind energy systems convert kinetic energy (associated with the movement of atmospheric air) to more useful forms of power, which have been used over time for irrigation and milling and since the beginning of the 20th century it is being used to generate electric power. Windmills for water pumping have been installed in many countries particularly in the rural areas. Their use has, however, been quite limited or non-existent in Nigeria.

Wind energy is transformed into mechanical power by wind turbines. This can then be used

---

Contact person: M. B. Mu'azu, Department of Electrical Engineering, Ahmadu Bello University, Zaria, Nigeria,
E-mail muazumb1@yahoo.com

directly for grinding and so on or for further conversion to electric power to generate electricity. Wind turbines can be used singly or in clusters called 'wind farms'. Small wind turbines called aero-generators can also be used to charge large batteries.

In Nigeria, the most commonly used renewable energy source is solar energy. There are several rural water supply schemes that are being powered by solar-electric pump systems, especially in the Northern parts of the country. It is pertinent to note that wind power, if properly assessed and harnessed can be applied for irrigational farming, water supply and even rural electrification schemes. Distributed generations, in most cases, are renewable energy resources based, for example using solar radiation, wind power, biomass and so on as primary energy sources. In some cases, a hybrid of diesel generating units and other renewable energy resources based system are be utilized.

This paper analysed the availability of wind speed trends (isovents) across the country, using meteorological data (daily average solar radiation) from meteorological centres in Nigeria and that of surface meteorological and solar power data from the National Aeronautics and Space Administration (NASA), which is a satellite-based meteorological station.

METHODOLOGY

In determining the wind speed spread across the country and eventually the wind energy potentials of the country, the following methodology is adopted:

i)   Data acquisition from the Nigerian Meteorological Agency, Oshodi and National Aeronautics and Space Administration (NASA)
ii) Isovent representation of Nigeria using Surfer-8.
iii) Determination of future wind speed at the turbine sites.
iv) Determination of the availability of particular wind speed levels at given times using the Weibull distribution of wind speed analysis

The specific power of wind speed, $P_{sp,o}$ as a function of wind speed of a particular value, v_0 can be expressed as follows:

$$P_{sp.o}(v_o) = 0.5 \cdot \rho \cdot v_o^3 \text{ ,kW/m}^2 \tag{1}$$

where ρ - air density (1,226 kg/m^3 at S.T.P.), while the specific energy, at a particular wind speed, v_o, in a year as:

$$E_{sp.o}(v_o, t_o) = P_{sp.o}(v_o) \cdot t_o(v_o) \cdot 8.76 \text{ ,kW·hr/m}^2 \tag{2}$$

where $t_o(v_o)$ is the duration, in hours, the wind speed, v_o, occurred in a year.

But the annual specific wind energy, $E_{sp.}^{sum}$, is expressed as a sum of $E_{sp.i}(v_i, t_i)$ for all speed, v_i, ranges (levels) i.e.:

$$E_{sp.}^{sum} = \sum_{i=1}^{n} E_{sp.i}(v_i, t_i) = 0.5 \cdot \rho \cdot \sum_{i=1}^{n} t_i(v_i) \cdot v_i^3 \text{ ,kW·hr/m}^2 \tag{3}$$

where i is the speed range and corresponding time of occurrences.

DATA ACQUISITION AND ISOVENTS' REPRESENTATION

The wind data used in this work are from two sources:

i) The annual mean of the percentage wind frequencies in different directions and for various wind speed ranges from the meteorological department, Oshodi i.e. 3-hourly wind records from 1951 to 1983 (Ojosu (1989))
ii) By considering the geographical location of Nigeria and dividing latitudes 4°N – 15°N and

longitudes 2^oE – 15^oE into 130 sections will give 1° x 1° of latitude by longitude. On the basis of this division, information on average wind speed data for each section were obtained from satellite – derived meteorological and solar energy parameter tables from NASA.

The monthly average wind speed for a given month, averaged for that month (and for year) over the 10-year period (July 1983 - June 1993) where the wind speed is evaluated using the Gipe power law. The wind speed at 50m above the surface of the earth and the surface roughness exponent based on the chosen vegetation type are used in the equation (NASA (2006)):

$$\overline{v}_{nh} = \overline{v}_o \cdot \left(H_{nh} \Big/ H_o \right)^\alpha \qquad (4)$$

where $\overline{v}_o$ is the average wind speed of a particular section and was evaluated as $\overline{v}_o = \dfrac{1}{n} \cdot \sum\limits_{i=1}^{n} v_i \cdot t_i$ at

original height, above earth surface; H_o – original height; H_{nh} – new height (in this case, 50 m above earth surface); $\overline{v}_{nh}$ - average wind speed at new height; and α - surface roughness exponent.

Using the Spreadsheet and drawing functions of the Surfer-8 software, after comparing both data sources, the isovents of Nigeria were gotten and presented as in Figure 1.
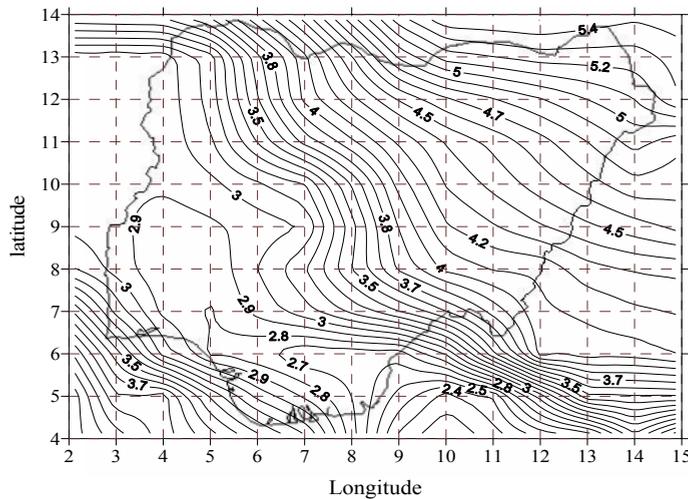
Figure 1: Isovents of Average Daily Wind Speed at 50 m of Height above Earth Surface across Nigeria.

WIND ENERGY CONVERSION SYSTEM (WECS)

The knowledge of future wind speed at the turbine sites is required for the implementation of wind power. This information is very essential for the design of the machines and energy systems, including the economic assessments. The random nature of wind and site - specific characteristics makes obtaining and utilizing such information quite challenging, For useful power conversion, one - parameter Weibull distribution of wind speed analysis is often used to determine the availability of particular wind speed levels at given times (NASA (2006), Twidell & Weir (2006))

There are mainly three types of wind machines (turbines), namely, horizontal axis, vertical axis and concentrators. Most widely used is horizontal axis type, which, basically, converts wind power into mechanical one. From equation (1), the mechanical power extractable from the wind of speed v_o, by wind turbine intercepting a cross – section A (in m^2) of wind front can be expressed through a power coefficient C_p, as

$$P_m = C_p \cdot P_{sp.o}(\overline{v}_o) = 0.5 \cdot A \cdot C_p \cdot \rho \cdot \overline{v}_o^3 \quad ,\text{kW} \tag{5}$$

The value of C_p depend on construction type of wind turbine and A is the area covered by the arrangement of the turbine blades, and is often express as πr^2 or $\pi D^2/4$, where r and D are the length of turbine blade and diameter of the area covered by turbine blades arrangement, respectively (Twidell & Weir (2006)). The equation (5) above can then be written as

$$P_m = \frac{\pi}{8} \cdot D^2 \cdot C_p \cdot \rho \cdot \overline{v}_o^3 \quad ,\text{kW} \tag{6}$$

The average extractable power by clusters of wind turbines (with identical C_p and D) of a given land surface area S, m^2 can be determined from equation (6) by formula:

$$P_{ms} = \frac{S}{20 \cdot H} \cdot \frac{\pi}{8} \cdot D^2 \cdot C_p \cdot \rho \cdot \overline{v}_o^3 \, ,\text{kW} \tag{7}$$

Where H is the height of the wind turbines above the sea level and factor 20H represents the distance, at which the turbines are supposed to be located from each other in order to get maximum power conversion by the wind turbines.

Electricity is an excellent energy vector to transmit the captured mechanical power of a wind turbine. Generation is usually of high efficiency, nearly 95%, and low loss of transmission (Twidell & Weir (2006)). There are basically two types of turbine connections, namely, grid connected and off-grid turbines. These arrangements depend mainly on the turbines' outputs and their closeness to the load centers.

RESULTS AND CONCLUSION

The deviations in results, when comparing wind speed data from earth (ground) stations in Nigeria with those from NASA are very negligible. As shown in Figure 1, the average daily wind speed across the country, at 50meter height above the earth is within the range of 2.7m/s in the central western parts to 5.4 m/s North East. The country's boundary effectively covered eighty-seven (87) sections out of 130 sections of the division. By using the equation 2 and based on (NASA (2006), Twidell & Weir (2006)), the probabilities of these speeds are between 50 – 60%, the annual wind energy, across Nigeria, is estimated to be about $5.205 \cdot 10^9$ kW·hr. But the rates of wind speed for effective power generation is between 3.5 – 25 m/s (cut-in and cut-out speed limits) by most wind turbines (Twidell & Weir (2006)). Therefore, at 50meter height, only 10 – 12% of the above energy can be converted.

The North-Eastern part of Nigeria has higher wind speeds and probabilities of reoccurrence of these wind speed and therefore, has a favourable condition for WECS. Other parts of the country can also utilize wind speed, if higher masts, for turbines (equation 4) are employed in addition to series of ground data on wind speed analysis in these parts and across the country as a whole.

Wind power can be combined, as it is being practice in most part of developed countries, with other renewable energy resources such as biomass, biogas, solar radiation etc. to generate electricity for rural/remote areas as being connected to the regional/central grid. This will be very important to developing countries like Nigeria as it will also reduce over dependency on fossil fuel based electric power generation and firewood as source of heat and cooking, thereby preserving the trees and thus reducing desertification process in most rural areas of the country.

REFERENCES

Ojosu J.O. (1989), "Wind Energy Characteristics and Availability for the Design of Wind Energy Conversion Systems in Nigeria", Nigerian Journal of Solar Energy Vol.8, pp 123-132.
NASA (2006), 'Surface Meteorological and Solar Energy Data Table,.
Twidell J. and Weir T. (2006), Renewable Energy Resources (2.ed.), Taylor & Francis Group, London, 2006.

Application of Wind and Small Hydro Energy Sources for Rural Electric Power Supply in Nigeria

B. Jimoh, Y. Jibril, M. B. Mu'azu

Department of Electrical Engineering, Ahmadu Bello University, Zaria,
pajayomachi@yahoo.com, yjibril523@yahoo.com, muazumb1@yahoo.com

Keywords: Renewable Energy, Power, Wind, Hydro, Hybrid.

ABSTRACT

The paper looks into the possibilities of using available renewable resources in rural areas for electric power generation for remote consumers. Based on meteorological data (the hourly wind speed) collected and analyzed for Dapchi, a north eastern rural settlement of Nigeria, coupled with hydrological data of River Kamadougu Gena, the hourly power produced from a hybrid power system comprising of wind and small hydro power systems is evaluated and considered as a supply source to electrical loads of the settlement.

Contact person: B. Jimoh, Department of Electrical Engineering, Ahmadu Bello University, Zaria, Nigeria,
E-mail pajayomachi@yahoo.com

**EXPERIMENTAL METHODS,
WIND TUNNEL / FULL SCALE MEASUREMENTS**

Wind tunnel tests of aerodynamical interference between two high-rise buildings

1st A.Flaga, 2nd G.Bosak

1st Lublin University of Technology and Cracow University of Technology
– LIWPK@interia.pl – Jana Pawla II 37/3a, 31-864 Cracow, Poland
2nd Cracow University of Technology
– g.bosak@windlab.pl – Jana Pawla II 37/3a, 31-864 Cracow, Poland

Keywords: interference, high-rise buildings, wind tunnel tests.

INTRODUCTION

The paper presents selected results of experiments on a model of a high-rise building carried out in boundary layer wind tunnel of the Wind Engineering Laboratory at the Cracow University of Technology. The examined building is of 150 m height above the ground and characterised of a various cross-section shape on different hieght levels (Fig. 1a). Not far the building, it is planned to be erected another one of a similar height (Fig. 1b.). Influence of aerodynamical interference between the two structures on the response of examined building has been the main aim of aerodynamical analyses.

a)   b)

Figure 1:Computer visualization: a)case of the one building, b)case of two buildings.

Contact person: G.Bosak, Cracow University of Technology, Jana Pawla II 37/3a, 31-864 Cracow, Poland,
phone +48 12 6283570, FAX +48 12 6283566
E-mail g.bosak@windlab.pl

WIND TUNNEL TESTS

Experiments have been performed on a model of the building of a scale of 1:300, which has been manufactured of various plastic materials. In the working section of the wind tunnel a nearest neighbourhood of the building has been modelled (Fig. 2). During the measurements, two models of buildings have been used: an active model equipped with pressure sensors on its outer surface and a passive model without any measurement system. Wind pressure distributions and adequate wind pressure coefficients on the outer walls of the active model have been measured in two different situations. In the first situation, only the active model with its neighbourhood has been placed in the wind tunnel working section. In the second one, the passive model has been placed together with the active one. The influence of aerodynamical interference has been evaluated on the basis of comparison of mean wind pressure distributions on outer surface of the active model in the first and the second measurement situations, respectively. Taking into a count, the mean pressure distributions in the various cross-sections of the building, a set of aerodynamical force coeficients: C_x- drag coefficient, C_y- lift coeficient and C_m- aerodynamical moment coefficient, have been calculated as a function of angle of wind attack.

a)   b)
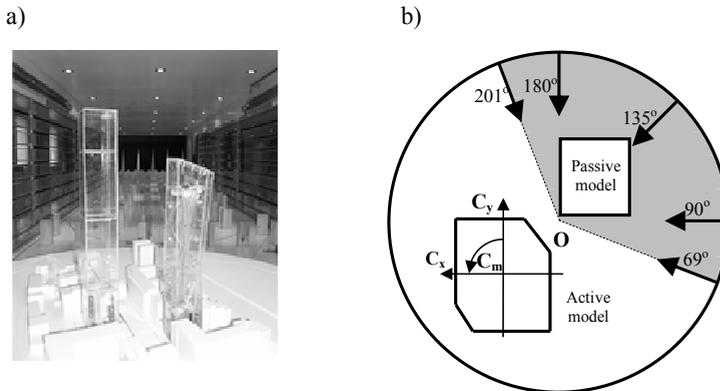
Figure 2: a) Model of the building in the working section of the wind tunnel- case of two high-rise buildings, b) wind attack directions during experiments.

EXEMPLARY RESULTS OF MEASUREMENTS

Exemplary functions of aerodynamical force coefficients C_x, C_y, C_m of the building cross-section on the level 134 m above ground (40th floor) in the two considereted situations (one building and two buildings) are presented in Fig. 3. The angles of wind attack have been changed from 69° to 201° with the step of 3°. The measurements have been completed for 12 cross-sections on different levels above the ground which have corresponded with the particular floors of the building.

a)

b)

c)
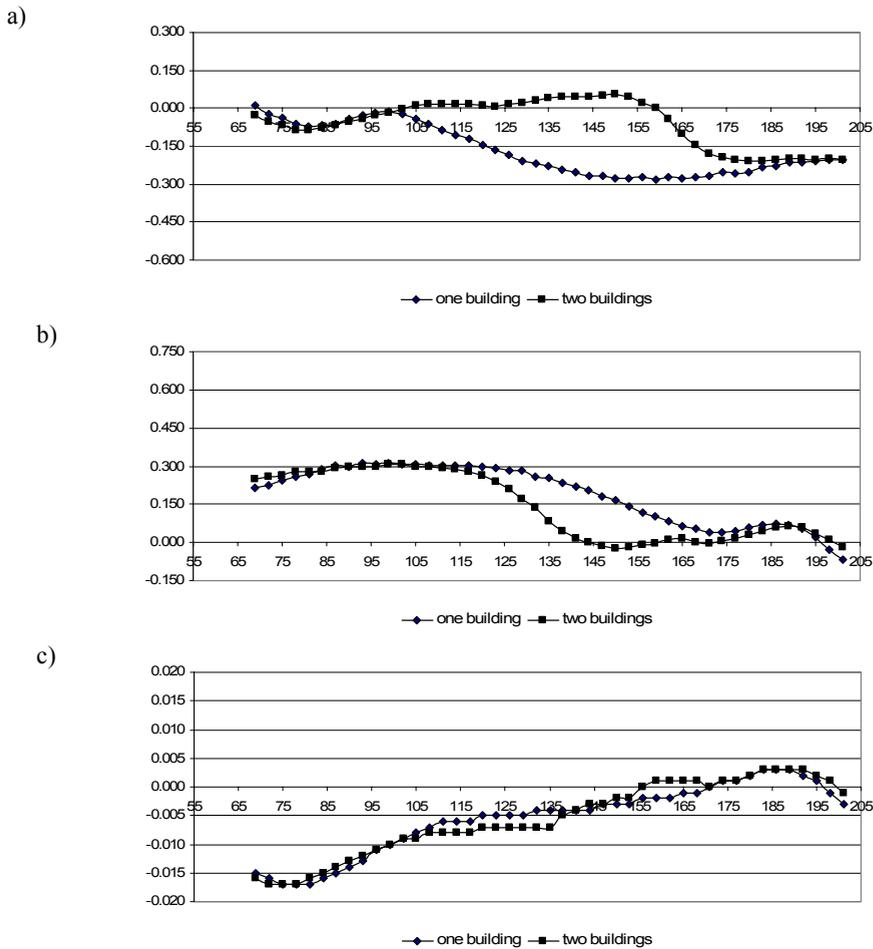
Figure 3: Functions of aerodynamic coefficients – a) drag coefficient C_x, b) lift coefficients C_y, c) moment coefficient C_m for the cross-section of the building on the level 134 m above ground (40th floor) in the two considered situations (one building and two buildings) obtained from wind tunnel tests.

The set of the aerodynamical coefficients functions for various cross-section shapes of the building has made possible the wind action definition on the structure according to the quasi-steady theory. Moreover, responses of the building in condition of aerodynamic influence, as well as, without it have been determined and analyzed (Fig. 4).

a)
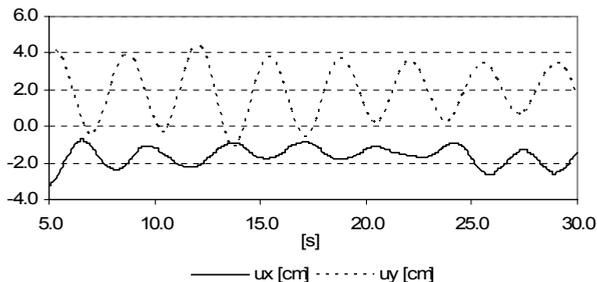
b)
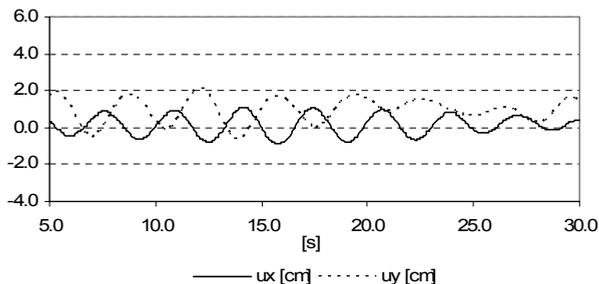
Figure 4: Time history of displacements- u_x, u_y (comp. Fig.2b) -of the middle point of the top floor of the building: a) one building experimental situation- angle of wind attack equal to 135°, b) two buildings experimental situation- angle of wind attack equal to 135°.

CONCLUSIONS

On the base of experimental results of wind tunnel tests following conclusions could be formulated:

1) A comparison of aerodynamic coefficients of the cross-sections of the building in two experimental situations shows that aerodynamic interference has not a significant influence. It has not observed any considerable increase in a level of the wind action on the building.
2) The aerodynamic interference has not changed the character of aerodynamic coefficient functions as well as responses of the building.
3) The tunnel investigations have confirmed correctness of the design project in an aspect of wind action on the building.

Wind pressure and spectrum measurement for three square prismatic buildings arranged in L shape

B.S. Shiau[1,2], L.H. Chiu[2]

[1] *Institute of Physics, Academia Sinica, Taipei, 115 Taiwan, bsshiau@gate.sinica.edu.tw*

[2] *Department of Harbor and River Engineering, National Taiwan Ocean University, Keelung 202, Taiwan, b0085@mail.ntou.edu.tw*

ABSTRACT

It has been frequently suffered typhoon's serious attacks during summer and autumn seasons in Taiwan. Strong winds caused severe damage on high-rise building cladding. Also, surface wind pressure distributions affect the building natural ventilation. For this purpose, it is necessary to study the building surface wind pressure characteristics which can provide more accurate and detail information for the building wall curtain cladding and natural ventilation designs. Previous studies, like Hout et al. (1986), Walker (1995), and Uematsu & Isyumov (1999) had studied on one building. In urban city, two buildings of side by side arrangement are commonly encountered (Shiau & Lai (2005)). In some cases, three buildings arranged in L shape had been existed in urban city. The wind attack angle on the buildings also often changed in time. Therefore the objective of present study is to measure in wind tunnel on the surface wind pressure characteristics and pressure spectrum of three square prismatic buildings arranged in L shape which were attacked under different wind angles in the turbulent boundary layer flow.

The experiments were conducted in the Environmental Wind Tunnel of National Taiwan Ocean University. The test section of the wind tunnel had a cross section of 2 m by 1.4 m with 12.5 m long. The wind tunnel was an open suction type and it contracted to the test section with an area ratio of 4: 1. The turbulence intensity of the empty wind tunnel is less than 05 % at the free stream velocity of 5 m/s. The X-type hot-wire incorporating with the TSI IFA-300 constant temperature anemometer was used to measure the turbulent flow signals. Four spires and roughness elements are arranged on the entrance of test section to simulate a neutral atmospheric boundary layer flow in urban region as the approaching flow. The simulated mean velocity profile was expressed in power law with an exponent of 0.28.

Three prismatic square models are arranged in L shape with gap, D equals to the building width, W. Fig.1 is the schematic diagram of the arrangement of buildings models and coordinate system of measurement. Each prismatic square model is of cross section 10 cm by 10 cm, and 25 cm high. The model is at a geometric scale of 1 to 500. The mean stream velocity at the model height for the present study is 8.5 m/s.

Contact person: B.S. Shiau, Institute of Physics, Academia Sinica, 128 Academia Road, Sec.2, Taipei, 115 Taiwan, Tel:+886-2-27896749, Fax:+886-2-27889829   E-mail bsshiau@gate.sinica.edu.tw

The surface wind pressure was measured by using the HyScan-2000 scanning system of the Scanivalve corporation. The system includes a pressure calibration module SPC-3000, and a control pressure module CPM-3000. Pressure was measured by using the ZOC-23B pressure transducer that has 32 channels. The CSM-2000 unit receives many address information from the IFM2000 module and distributes it to the cable-serviced ZOC-23B modules, then routes the addressed analog signals back to the IFM2000 module. The IFM2000 module is the interface unit for ZOC-23B. The DAQ2000 is the self-contained high speed data acquisition and processing system. The HyScan-2000 system incorporating with the DAQ2000 can sample 16~32 channels of the pressure transducer analog data. In the present study, we sampled 24 channels almost simultaneously at the sampling rate of 2000 Hz and took the sampling time 32.468 seconds for each run.
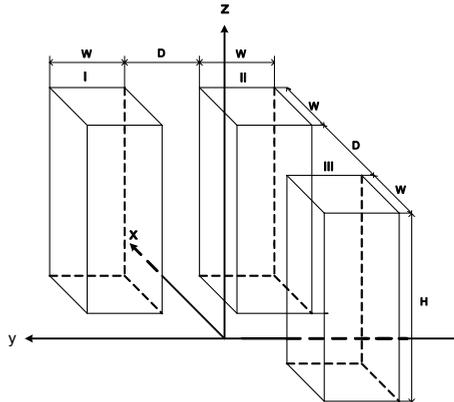

Fig.1 Schematic diagram of building models arrangement and coordinate system

Measurement results were analyzed to obtain the mean wind pressure coefficient, $\overline{C}_p$, and root mean square of wind pressure coefficient, C_{prms} under different wind attack angles. The fluctuating wind pressure spectrum was also investigated. It is indicated as Walker (1195), and Shiau & Lai (2005), that the maximum mean wind pressure occurred close to the location z/H=0.888 for front face of building. So we choose this location for analysis.

The mean wind pressure coefficient as functions of wind attack angle for front faces (at z/H=0.888, y/W=0.38 and -0.38) of three buildings are shown in Fig.2. When the wind flow along the x downstream direction (i.e. attack angle is 0 degree), the mean wind pressure coefficient is the largest for building 1. Due to building 1 is located behind the building 3, the mean wind pressure coefficient alters to negative value for building 2. For building 1, mean wind pressure coefficient decreases as increasing the wind attack angle. Increase of wind attack angle up to 135 degree, the mean wind pressure coefficient reaches the smallest or the largest value of negative pressure. And as wind attack angle increases again, the value of mean wind pressure coefficient increases accordingly.

Fig.3 is the root mean square of wind pressure coefficient, C_{prms} as the function of wind attack angle for front faces (at z/H=0.888, y/W=0.38 and -0.38) of three buildings. It is interesting to reveal that C_{prms} of building 1 alters abruptly at attack angle of 45 degree. Since for this wind attack angle, buildings 2 and 3 is just located before buildings 1. They obstruct the wind flow and make the flow turbulence increase largely behind them. Therefore C_{prms} increases significantly.

The wind spectrum variation at z/H=0.888 for different downstream distances on the inner side of building 1 under wind attack angle 0 degree is shown in Fig.4. The frequency, f is normalized by the width of the building and the approaching mean velocity, W at the building height, U_h. The power density, $S_p(f)$ is scaled with standard deviation of pressure fluctuation, σ_p. The spectra show that peaks

of power density occur at fW/U_h=0.20. It implies that the vortex shedding frequency in this region of building 1 is shown with Strouhal number of $St=fW/U_h$=0.20. Fig.5 is the wind spectrum variation at z/H=0.888 for different downstream distances on the inner side of building 2 under wind attack angle 0 degree. The Strouhal number is St=0.18 which is smaller than that of building1. Since building 2 is located behind the building3, the Strouhal number is reduced.
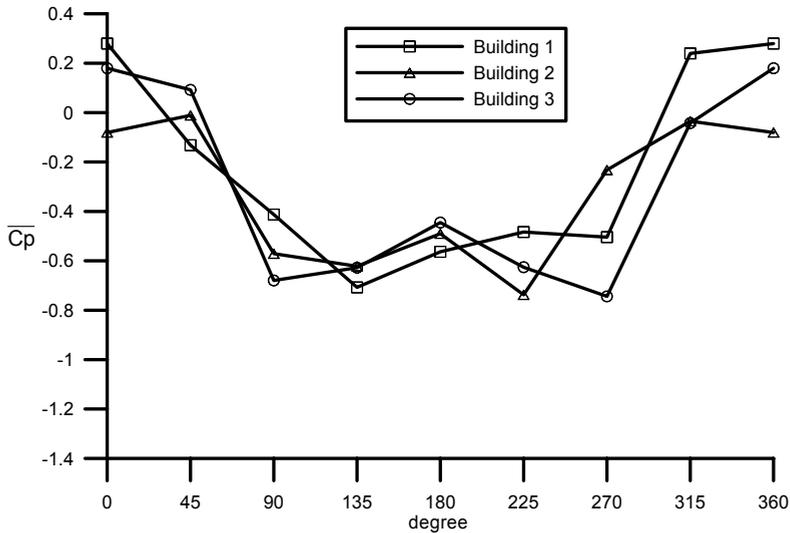
Fig.2 Mean wind pressure coefficient as functions of wind attack angle for front faces of three buildings at location z/H=0.888, and y/W=0.38 and -0.38
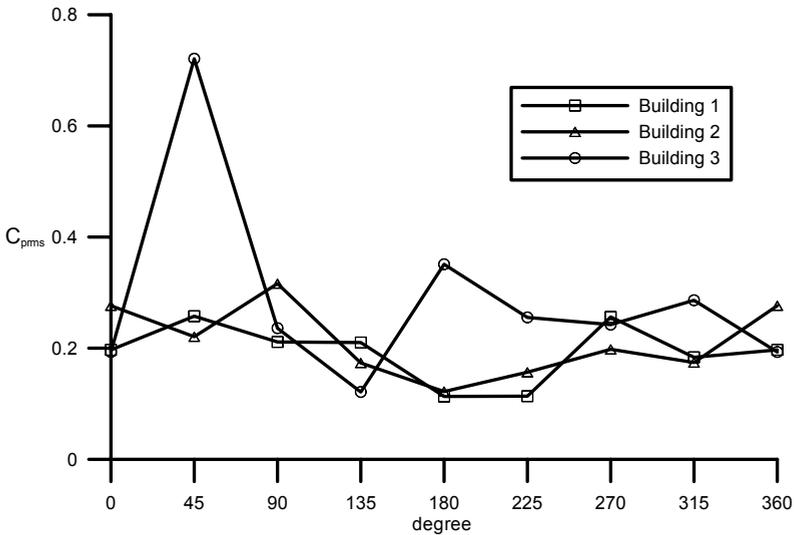
Fig.3 Root mean square of wind pressure coefficient as functions of wind attack angle for front faces of three buildings at location z/H=0.888, and y/W=0.38 and -0.38
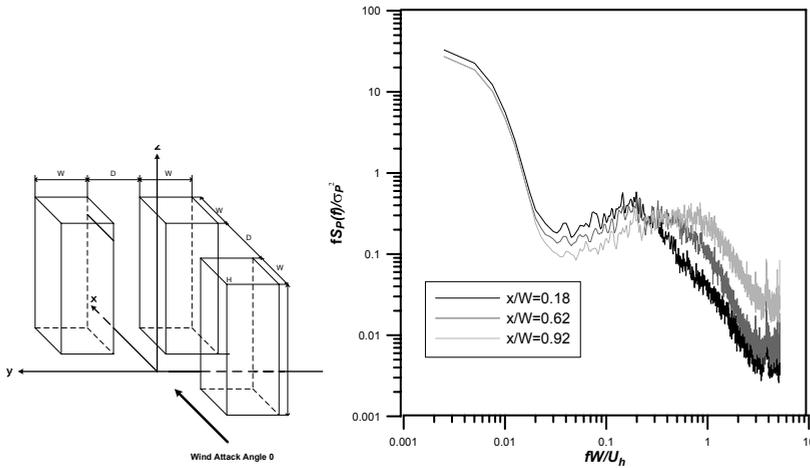
Fig.4 Wind pressure spectrum variations along downstream distance for inner face of building 1 at z/H=0.888
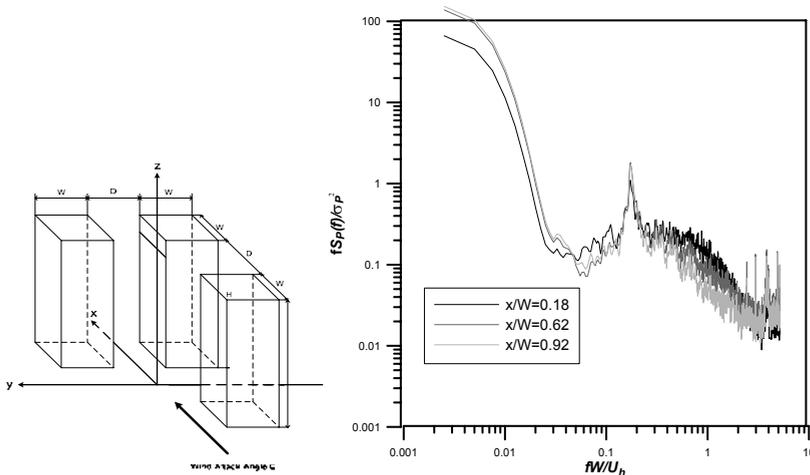
Fig.5 Wind pressure spectrum variations along downstream distance for inner face of building 2 at z/H=0.888

REFERENCES

Huot J.P., Rey C., and Arbey H. (1986). "Experimental analysis of the pressure field induced on square cylinder by a turbulent flow", Journal of Fluid Mechanics, 162, 283-298.

Wacker J. (1995). "Local wind pressure for rectangular buildings in turbulent boundary layers", Wind Climate in Cities, 185-207.

Uematsu Y. , and Isyumov N. (1999). "Wind pressures acting on low-rise buildings", Journal of Wind Engineering and Industrial Aerodynamics, 82, 1-25.

Shiau B.S., and Lai J.H. (2005). "Experimental study on the surface wind pressure and spectrum for two prismatic buildings of side by side arrangement in a turbulent boundary layer flow", Proceedings of the 6th Asia-Pacific Conference on Wind Engineering, 303-317, Seoul, Korea.

Tap Resolution Related to the Accuracy of Pressure Integrated Wind Loads

1st C. Dragoiescu, 2nd J. Garber, 3rd K. Suresh Kumar

1st Senior Engineer, calin.dragoiescu@rwdi.com, Rowan Williams Davies & Irwin, 650 Woodlawn Road West, Guelph, Ontario, Canada

2nd Senior Specialist, jason.garber@rwdi.com, Rowan Williams Davies & Irwin, 650 Woodlawn Road West, Guelph, Ontario, Canada

3rd Managing Director, suresh.kumar@rwdi.com, RWDI Consulting Engineers (India) Pvt. Ltd., Technopark Campus, Kariyavattom P.O., Trivandrum, Kerala State, India

Keywords: HFFB, HFPI, Pressure integration, Wind-induced, Tall building.

ABSTRACT

As a part of an ongoing detailed investigation aimed at quantifying the pros and cons of HFFB (High Frequency Force Balance) and HFPI (High Frequency Pressure Integration) methods, further comparisons are provided for CAARC building with the presence of typical balconies. In addition, this paper presents the results of the investigation concerning the importance of tap resolution in HFPI studies under various circumstances.

INTRODUCTION

Most wind tunnel facilities conduct studies for predicting wind-induced structural loads and responses of tall buildings usually using two main measurement methods, referred to as the High Frequency Force Balance (HFFB) and High Frequency Pressure Integration (HFPI) techniques. With the exception of unusually tall or slender structures, it is generally considered adequate to employ the mentioned methods, which are using rigid models for wind tunnel testing, with the dynamic characteristics of the full-scale structure accounted for in the analysis.

Each method offers advantages as well as limitations. Although both methods are commonly used for wind load predictions on tall buildings, the choice of method for a project is typically made based on engineering judgment and experience, without the benefit of detailed comparisons. There are examples where both methods have been compared for the same project, although the primary purpose was to illustrate how these methods can supplement each other (Flay and Vickery (1997), Lin et al. (2005)). Clearly extensive comparisons quantifying the superiority of one method versus the other are lacking, which is the main objective of the investigation currently underway at RWDI. In a recent article by Simiu et al (2008), the advantage of HFPI over HFFB is discussed.

Detailed descriptions of the HFFB and HFPI methods were presented by Dragoiescu et al. (2006).

Contact person: 3rd K. Suresh Kumar, Managing Director, RWDI Consulting Engineers (India) Pvt. Ltd., T-5, Thejaswini, Technopark Campus, Kariyavattom P.O., Trivandrum, Kerala State, India, Tel: +91-471-4060010 and Mob. +91-9895976686. E-mail: suresh.kumar@rwdi.com

This reference, also, includes comparisons showing similar results between the two methods based on wind tunnel test results conducted using the CAARC model (Melbourne (1980)). The main objective of this paper is to investigate the importance of tap resolution (i.e. the number and location of the pressure taps) used for the HFPI method on the CAARC model with and without balconies. This is done by comparing the results based on different pressure tap scenarios against the base layout that was used in Dragoiescu et al. (2006). This paper also presents comparisons between HFFB and HFPI techniques applied to CAARC model with typical balconies.

EXPERIMENTAL DETAILS

Wind tunnel tests were performed on 1:400 scale model of the CAARC tall building model, for 36 wind directions at 10° intervals, in the presence of three different surrounding scenarios in RWDI's 2.4m x 2.0m boundary-layer wind tunnel. A rural upwind terrain condition power law exponent of 0.17 was simulated for all wind directions by means of floor roughness and upwind spires.

In addition, tests were carried out for further comparison between HFPI and HFFB techniques for CAARC building with typical balconies. The first two photos of Figure 1 show HFPI and HFFB models respectively under urban conditions in RWDI's wind tunnel. Later, the sensitivity of various tap resolution scenarios was investigated for this building with typical balconies. The last photo of Figure 1 is the CAARC model including three interchangeable sections representing different balcony scenarios. Three different balcony scenarios included were typical balconies, continuous balconies and recessed balconies. The three sections were interchanged and tested at different locations such as bottom, middle and top. Each section has two rows of tap; one row at the middle and another row towards the top. The primary purpose of these tests was to assess the requirements imposed on the tap layout by the presence of the balconies; these tests are not meant for determining overall loads.
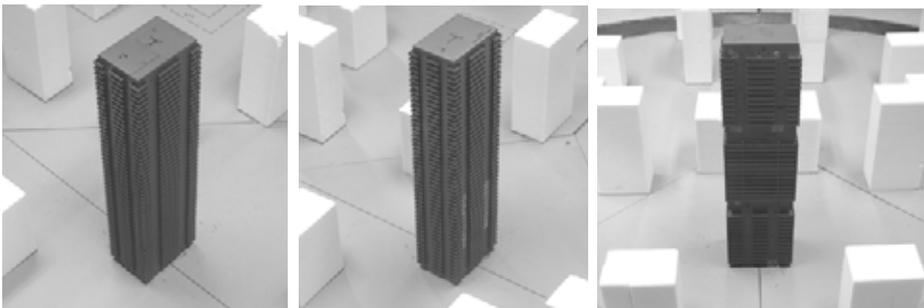
Figure 1: HFPI and HFFB models - CAARC building model with balconies.

Figure 2 presents the naming convention of all rows and columns of the instrumented taps located on the CAARC model. When referring to a row or column the authors mean all 28 or 10 taps in that row or column, respectively. Experimental procedures will be elaborated in the final paper.

RESULTS

The mean and rms of the base moments Mx and My predicted by HFFB and HFPI methods for CAARC building with typical balconies (see first and second photo of Figure 1) as a function of reduced velocity for 90° and 180° are presented in Figure 3. The base moments are the results of a dynamic analysis with linear mode where sway frequencies (n) = 0.2 Hz, damping = 1%. The quality of the comparisons in this figure suggests that the results corresponding to HFPI and HFFB methods are not only matching but also are independent of the design speed and building frequency.
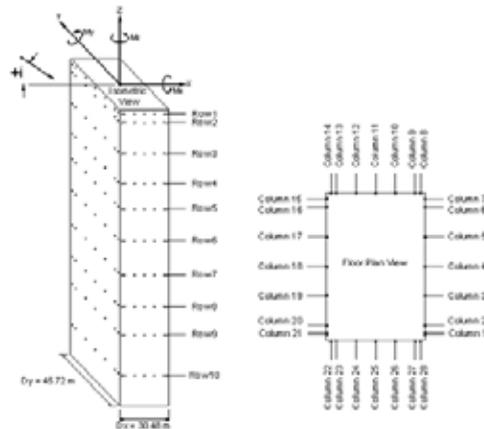
Figure 2: CAARC building model - HFPI pressure tap locations.
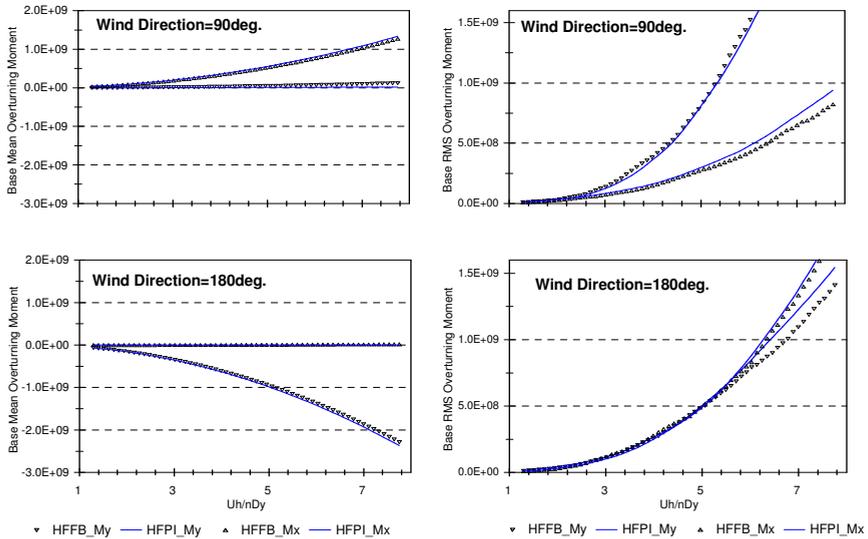
Figure 3: Comparison of base moments predicted by HFFB and HFPI methods
as a function of reduced velocity

Figure 4 shows the effect of tap resolution on wind-induced response of a section of the CAARC building with typical balcony scenario. The results in the format of normalized force coefficients correspond to the mid row of taps when this section is at the top third of the building. Three pressure tap scenarios were analyzed. In scenario S1, all the taps are considered including the taps on balconies; while in S2 and S3, only some taps on balconies are considered. In scenario S2 and S3, the tributary areas of the remaining taps are appropriately adjusted to account for the missing taps. The results are in general not sensitive to the balcony taps. Similar results prevail when this section is tested at middle and bottom locations. Further, similar exercise has been carried out for the CAARC building covered with typical balconies. All the test results will be included in the final paper.

In summary, based on the extensive study carried out at RWDI, it is found that the two test methods can give similar results for simple as well as complicated buildings with balconies situated in
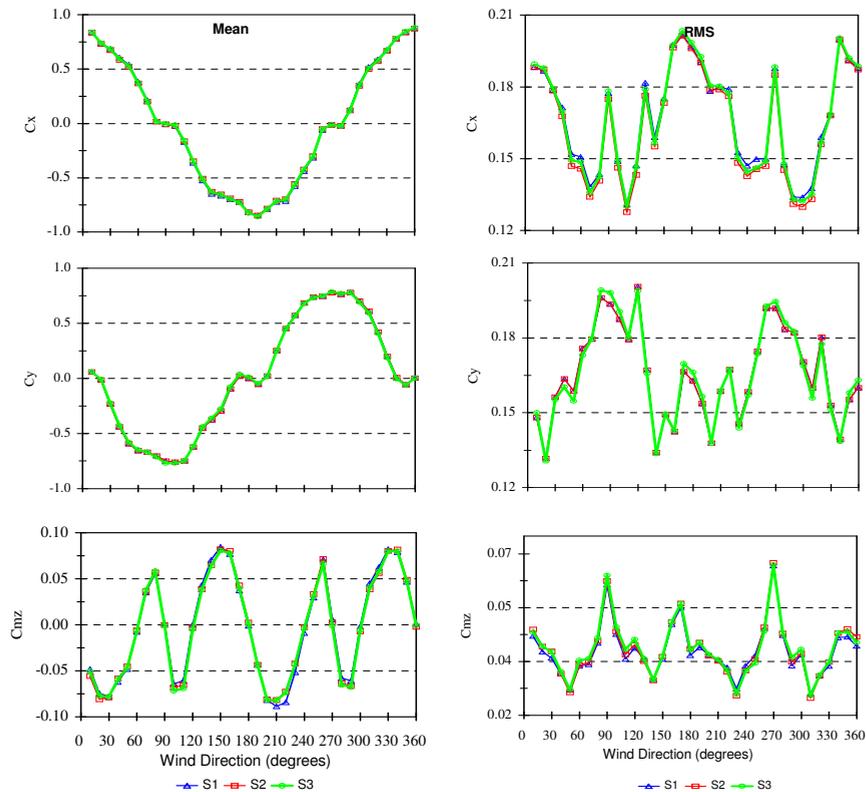
Figure 4: Effect of tap resolution – Typical balcony scenario shown in Figure 1.

complex surroundings. In this circumstance, the HFPI is a preferred method particularly when cladding pressures are already required. In addition, HFPI method has theoretical advantages over HFFB with regards to using true mode shape, using higher order mode shape, obtaining a refined load distribution and obtaining realistic generalized base loads. But in case of slender/complex shaped structures, HFFB method is preferred over HFPI (Dragoiescu et al. (2006)).

   The results from tap resolution study shows that an exhaustive tap layout is not necessary to obtain accurate results. However, care must be taken and a reasonable tap distribution is warranted in case of complex surroundings. In general, horizontal distributions are more important than vertical distributions, especially in case of torsion. Balcony taps appear not so sensitive to the overall results as far as we account for this area with another tap on the façade.

REFERENCES

Flay R.G.J., Vickery B.J. (1997). "A comparison of response predictions for a rough cone from pressure and balance measurements", Journal of Wind Engineering and Industrial Aerodynamics, 69-71, 473-484.

Lin N., Letchford C., Tamura Y., Liang B., Nakamura O. (2005). "Characteristics of wind forces acting on tall buildings", Journal of Wind Engineering and Industrial Aerodynamics, 93, 217-242.

Simiu E., Gabbai R.D., Fritz, W.P. (2008). "Wind-induced tall building response: a time domain approach", Wind and Structures, 11(6), 427-440.

Dragoiescu C., Garber J., Suresh Kumar K. (2006). "A Comparison of Force Balance and Pressure Integration Techniques for Predicting Wind-Induced Responses of Tall Buildings", ASCE Structures Congress 2006 – Extreme Event Loading - Extreme Wind Engineering.

Melbourne W.H. (1980). "Comparison of measurements on the CAARC standard tall building model in simulated model wind flows", Journal of Wind Engineering and Industrial Aerodynamics, 6, 73-88.

The measurements of pressure and wind velocity around square and rectangular cylinders

E.Borowa-Błazik, J.Bęc, T. Lipecki, T. Nowicki, J. Szulej

Lublin University of Technology – e.blazik@pollub.pl – Nadbystrzycka 40, 20-618 Lublin, Poland –
Lublin University of Technology – j.bec@pollub.pl –Nadbystrzycka 40, 20-618 Lublin, Poland –
Lublin University of Technology – t.lipecki@pollub.pl – Nadbystrzycka 40, 20-618 Lublin, Poland –
Lublin University of Technology – t.nowicki@pollub.pl – Nadbystrzycka 40, 20-618 Lublin,
Poland– Lublin University of Technology – j.szulej@pollub.pl – Nadbystrzycka 40, 20-618 Lublin,
Poland

Keywords: *wind tunnel, rectangular cylinder, square cylinder, two-dimensional flow.*

ABSTRACT

The paper deals with the evaluation of the influence of neighbouring higher buildings on pressure distributions on smaller ones and flow velocity fields around them. The analysed problem concerns the wind directed perpendicularly to the buildings. The main aim of the paper is to point out that buildings in urban housing estate cannot be treated as the set of single buildings, but in the design process and especially in the determination of wind action, the interaction between buildings and wind flows should be taken into consideration. The similar problems of the flow around set of buildings were described in many papers, e.g.: Gowda (1995), Louka et al. (1998), Eliassona et al.(2006) and Hanna et al. (2002).

The analyses have been performed on the basis of measurements which have been carried in the wind tunnel of the Wind Engineering Laboratory in Cracow University of Technology. The models have been set at the ground of the wind tunnel and the flow in the middle-plane can be treated as the two-dimensional one. The measurements have been provided for the set of two models: smaller cylinder of the square cross-section with dimensions $h{\times}h{\times}b$ and for the larger one with dimensions $2h{\times}h{\times}b$; where: h = 200 mm and b = 2050 mm. The models' arrangements have been presented in Fig. 1. All measurements have been taken at the velocity above the boundary layer with approximate value of 10 m/s. The measurements have been made for three sets with the following distance between the middles of models: L/h=2.0, L/h =3.0 and L/h =4.0. As the result of the measurements the variations in time of pressure distributions on model walls and time series of velocities in nine cross-sections of the wind tunnel measuring space have been obtained. The measurements of pressures on models have been obtained with use of pressure scanner based on piezoresistive two-directional pressure sensors Motorola MPX 2010. The measurements carried with use of pressure scanner have been made in 30 points distributed over the model surface and with the sample frequency 500 Hz. Additional measurements have been provided with use of hot-

---

Contact person: J. Bęc, Lublin University of Technology, Nadbystrzycka 40, 20-618 Lublin, Poland, phone: +48815384433.
E-mail j.bec@pollub.pl

wire anemometers with the sampling frequency 500 Hz, as well. The measurements have been made with use of two single-wire probes and four X-wire ones. The measurements from both single-wire probes have been used to obtain the mean velocity value, so these devices have been set in the front of the model. In the nearby of the hot-wire anemometers there has been set a small tube connected with the pressure scanner. The results from this measuring point have been used to calculate the pressure coefficient and verification of the hot-wire anemometric velocity measurements. The wires of the probes have been set up to obtain the angle of about π/4 between the wires and the direction of the mean flow. On the basis of measurements there have been calculated time series of velocity components along directions perpendicular to the wires. The resultant velocity have been calculated according to the recommendations which can be found in the papers such as: Evans (1974), Hinze (1975), Shabbir et al. (1996). Such procedure allows removal of the influence of the turbulence in the direction perpendicular to the measurement plane and the influence of wire cooling due to flow along the wire direction.
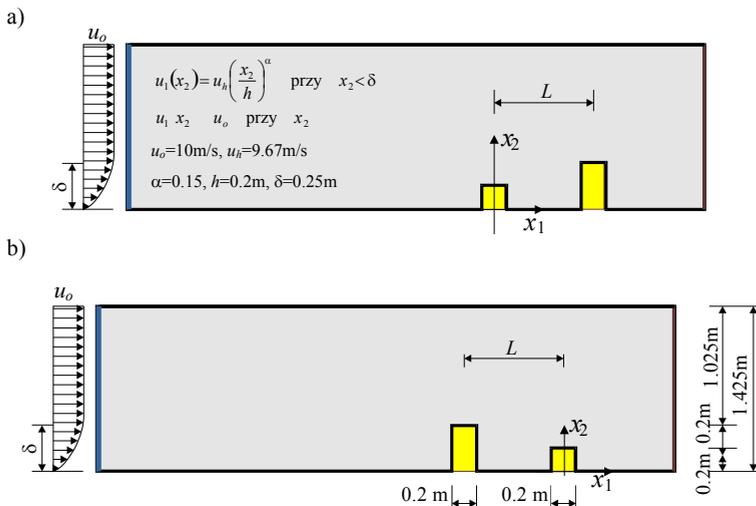
Figure 1: The arrangements of models: a) the set with square cylinder as the upstream model; b) the set with square cylinder as the downstream model.
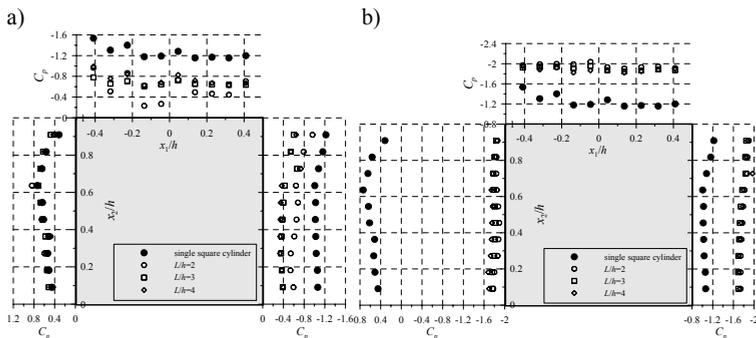
Figure 2: The distribution of the aerodynamic coefficient C_p on the square cylinder at different distance between models for a) the set with square cylinder as the upstream model; b) the set with square cylinder as the downstream model.
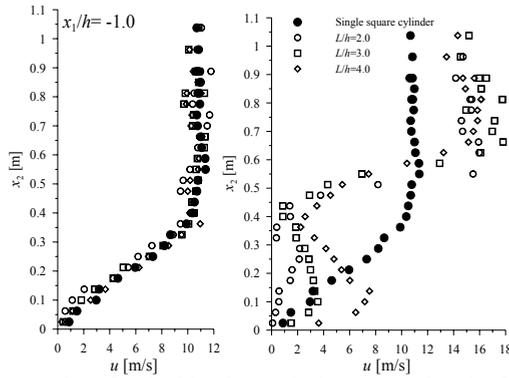
Figure 3: The graphs of velocities in vertical cross-section in front of square cylinder which is: a) the upstream model; b) the downstream model.
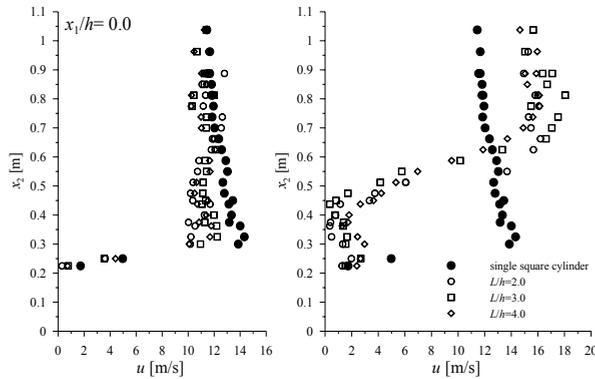
Figure 4: The graphs of velocities in vertical cross-section under square cylinder which is: a) the upstream model; b) the downstream model.
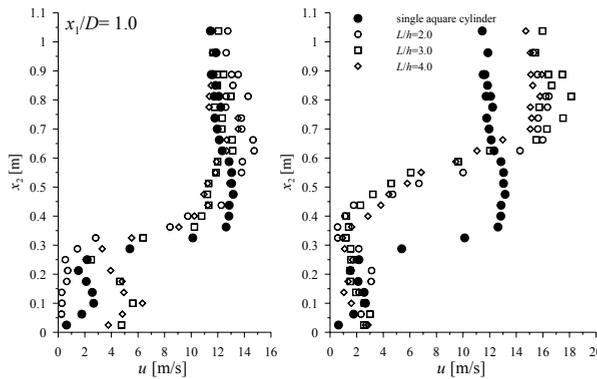
Figure 5: The graphs of velocities in vertical cross-section behind square cylinder (at x_1/h=1.0) which is: a) the upstream model; b) the downstream model.
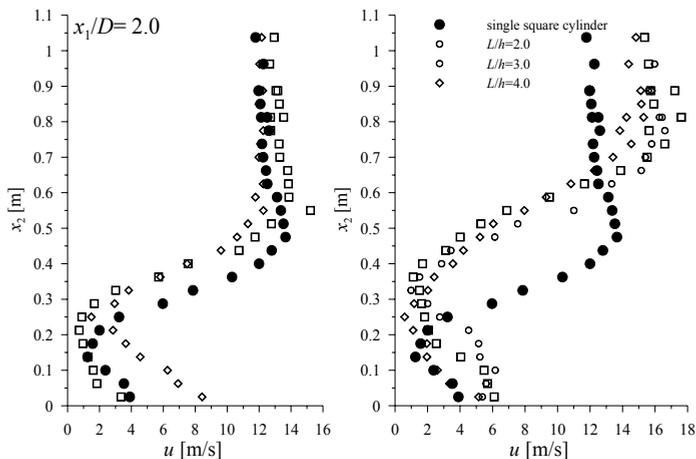
Figure 6: The graphs of velocities in vertical cross-section behind of square cylinder (at x_1/h=2.0) which is: a) the upstream model; b) the downstream model.

The comparisons of the averaged pressure distributions are shown in Figure 2 and the graphs of averaged resultant velocities are shown in Figures 3, 4, 5 and 6. The following conclusion have been drawn out from the research:

– bigger model downstream location causes the decrease of the wind load on the square, but at the opposite wind direction, it means that if the smaller model is located downstream, the wind load for square increases twice in comparison with the load of single square;

– in comparison to the velocity behind the single square, the wind velocity between models is smaller for L/h=2.0, but at bigger distance between centres of models the significant increase of velocities is observed and it is not dependent on the height of the upstream model;

– bigger model upstream location causes the increase of the length of the aerodynamic wake and velocities behind the smaller downstream model.

The determination of wind load on structures in dense buildings complex should be made with consideration of interference effects and the possibility of the double increase of pressure. The analysis of wind comfort should take into account the increase of velocities between buildings which can be caused by the flow directed perpendicularly to buildings.

REFERENCES

Gowda B.H.L. (1995). "Effect of interference on the pressure distribution on the ground plane around a low-rise and a tall body in tandem arrangement", Proc. of 9th ICWE, Vol.1, 228-238.

Louka P., Belcher S.E., Harrison R.G. (1998). "Modified street canyon flow", Journal of Wind Engineering and Industrial Aerodynamics, 74-76, 485-493.

Eliassona I., Offerlea B., Grimmondb C.S.B., Lindqvista S. (2006). "Wind fields and turbulence statistics in an urban street canyon", Atmospheric Environment, 40, 1–16.

S.R. Hanna, S. Tehranian, B. Carissimoa,b, R.W. Macdonaldc, R. Lohner (2002). "Comparisons of model simulations with observations of mean flow and turbulence within simple obstacle arrays", Atmospheric Environment 36 (2002) 5067–5079.

Evans R.L. (1974). "Free stream turbulence effects on the turbulent boundary layer", Report Nr 1282 Procurement Executive, Ministry of Defence.

Hinze J.O. (1975). Turbulence. An introduction to its mechanism and theory, McGraw-Hill, New York.

Field measurement and numerical analysis of wind-driven rain absorption and evaporation on building facades

M. Abuku[(1)], B. Blocken[(2)], S. Roels[(1)]

[(1)] *Laboratory of Building Physics, Department of Civil Engineering, Katholieke Universiteit Leuven, Kasteelpark Arenberg 40, 3001 Leuven, Belgium*
[(2)] *Building Physics and Systems, Eindhoven University of Technology, P.O. Box 513, 5600 MB Eindhoven, the Netherlands*

Keywords: driving rain, building envelope, hygrothermal behaviour, moisture transfer, durability

ABSTRACT

To investigate the validity of the traditional approach to implement wind-driven rain (WDR) in numerical models of heat, air and moisture (HAM) transfer in building components, under real atmospheric conditions, a new set-up was developed at a test building. WDR intensity, other relevant environmental conditions and the resulting moisture response of the wall to these conditions (both hygroscopic loading and WDR) were simultaneously measured. The whole measurement data set was used for validation. Large differences between the measurement and simulation results were found and possible causes discussed. It is concluded that many influencing parameters interact, and that therefore precisely simulating the hygrothermal response of walls to WDR is very difficult.

INTRODUCTION

Wind-driven rain (WDR) is one of the most important moisture sources when analysing the hygrothermal behaviour of building components and thus of great concern in the field of building physics (e.g. Kunzel and Kiessl 1997; Blocken and Carmeliet 2004; Abuku et al. 2009a). In such numerical analysis, the moisture flux at the exterior wall surface g_m (kg/m^{2}s) without runoff is traditionally expressed as

$$g_m = -\beta_e \left(p_e - p_{s,e} \right) - I_{WDR} \tag{1}$$

where β_e is the convective moisture transfer coefficient (s/m), p_e and $p_{s,e}$ are the vapour pressures (Pa) of the outdoor air and at the outside wall surface, respectively, and I_{WDR} is the WDR intensity (kg/m^{2}s). Recent studies (Abuku et al. 2009b) showed that this traditional approach to implement WDR in HAM models (Equation (1)) might be too simplified because of two reasons: (1) the occurrence of splashing and bouncing at raindrop impact and (2) the averaged flux assumption. When splashing or bouncing occur, part of these raindrops does not contribute to the moisture load on the facade. The averaged flux assumption refers to the fact that in Equation (1), the real discrete and

Contact person: M. Abuku, Laboratory of Building Physics, Department of Civil Engineering, Katholieke Universiteit Leuven, Kasteelpark Arenberg 40, 3001 Leuven, Belgium. *E-mail address:* masaru.abuku@bwk.kuleuven.be, Tel: +32 (0)16 321348, Fax: +32 (0)16 321980.

random impingement, uptake and evaporation of raindrops is spatially and temporally averaged. Due to this assumption, numerical analysis with Equation (1) can cause significant overestimations of the moisture content of the wall near the surface (Abuku et al. 2009b).

FIELD MEASUREMENT

To investigate the validity of Equation (1) and the importance of potential errors, a new set-up was developed at the VLIET test building (Figure 1(a)) located at K.U.Leuven, Belgium. The building is equipped with a meteorological mast and rain gauge in the free field (Blocken and Carmeliet 2005). With an ultrasonic anemometer at the mast, the wind speed U_{10} and wind direction φ_{10} at 10 m height are recorded.

    The newly developed set-up at the test section is illustrated in Figure 1(b). It consists of a device to measure the weight change m_{mea} of the specimen, PMMA WDR gauges (Blocken and Carmeliet 2005) on the wall, temperature sensors at the material surface and a collector gauge for the runoff water. The weight change, the surface temperature of the specimen, the amount of the runoff water and the WDR intensity next to the specimen are measured simultaneously. The principle of leverage is used for measuring m_{mea}, achieving a resolution of 5 mg. To prevent horizontal wind disturbance, a roller supports the material at the back side (see Figure 1(b)).
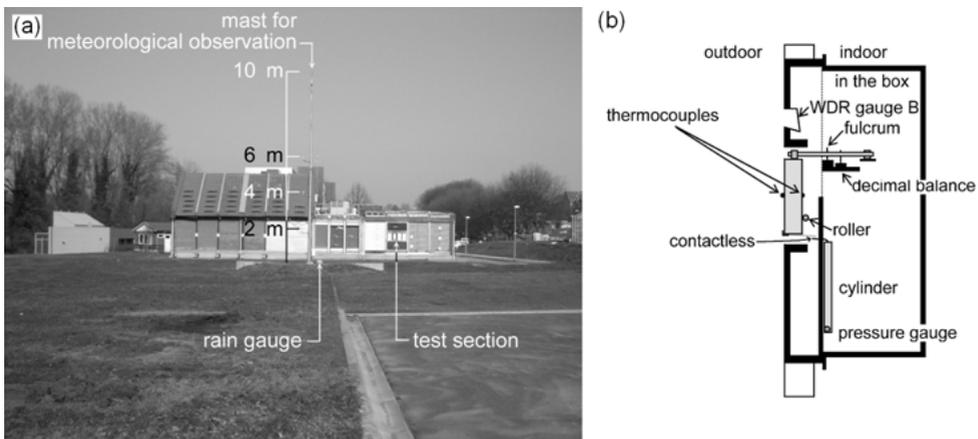
Figure 1: (a) VLIET test building and the surrounding environment (view from south-west) and (b) the schematic diagram of the intersection of the test section and the new set-up.

Figure 2 shows measurement results for two periods in 2007: November 29, 0:00 - December 2, 0:00 (GMT) and December 3, 20:00 - December 12, 15:00. In all measurements, a specimen of calcium silicate (0.25 m × 0.45 m × 0.09 m) was used because of its very high capillary moisture content (803 kg/m^3) and water absorption coefficient (1.22 kg/m^{2}s$^{0.5}$). The specimen was moisture-tight sealed at all sides except the side facing the outdoor environment. Figure 2(a) and (b) show the weight change m_{mea} of the specimen from the initial value, the cumulative amount of WDR ($S_{WDR,mea}$) and the WDR intensity ($I_{WDR,mea}$). m_{mea} increased during WDR and decreased due to evaporation afterwards. Furthermore U_{10} and φ_{10} were measured, as well as the temperatures at the centre of the exterior and interior specimen surfaces and the outdoor air temperature and vapour pressure near the specimen. The adhesion-water evaporation error (Blocken and Carmeliet 2005) of $I_{WDR,mea}$ is estimated at 3 %.
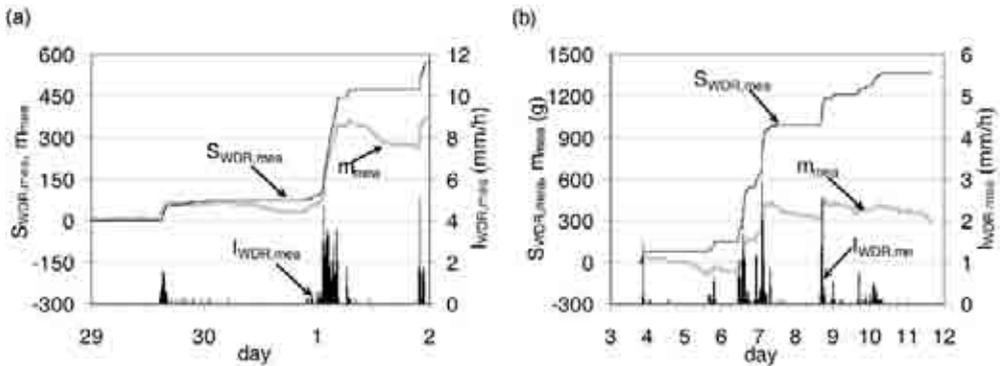
Figure 2: Measurement results of (a) November 29 - December 2, 2007 and (b) December 3 -12, 2007. m_{mea}: weight change of the specimen; $S_{WDR,mea}$: cumulative amount; $I_{WDR,mea}$: intensity of wind-driven rain.

NUMERICAL ANALYSIS AND DISCUSSION

The measurement data of the hygrothermal response of the specimen to the WDR loads are compared to the results of one-dimensional numerical calculations with Equation (1).

For windward facades, which are those exposed to WDR, Janssen et al. (2007) described β_e with the following equation:

$$\beta_e = 7 \times 107^9 \left(3.06U_{10} + 5.44\right) \tag{2}$$

In the current study, three simulations are carried out with different β_e equations based on Equation (2) to check the adequacy of β_e for the given conditions. The first is Equation (2), another is the half (Equation (2) / 2), and the other is double (Equation (2) □2). At the interior surface, a zero vapour flux boundary condition is imposed. For the heat transfer analysis, the measured temperatures at the centre of the exterior and interior surfaces of the specimen are used as boundary conditions. The initial conditions are determined based on the measurement data.

In Figure 3, the results of the simulations with three different β_e equations are compared to the corresponding measurements for each period. This comparison shows that, Equation (2) / 2 seems to be more appropriate for the current cases than the other two β_e equations, when looking at the evaporation rates during drying processes. Nevertheless, important differences between m_{mea} and $m_{sim}(I_{WDR,mea})$ still occur, particularly during rain. Therefore, it seems that β_e is not the only reason that caused the differences. From the above discussion, the differences between m_{mea} and $m_{sim}(I_{WDR,mea})$ presented in the previous section may be attributed to other reasons: the occurrence of splashing and bouncing and the averaged flux assumption. Both errors and their influence on the results will be explained in more detail in the full paper.

CONCLUSIONS

A new measurement set-up was developed to investigate the validity of the traditional approach to implement wind-driven rain (WDR) in numerical models of heat, air and moisture (HAM) transfer in building components, under real atmospheric conditions. WDR loads and the material weight change (hygrothermal response of walls) as well as other environmental conditions were simultaneously measured for two rain events. The measurement results were compared to numerical simulations with the traditional approach. The simulations significantly overestimated the average moisture content in the specimen during rain. Whereas it was shown that the results of the simulations
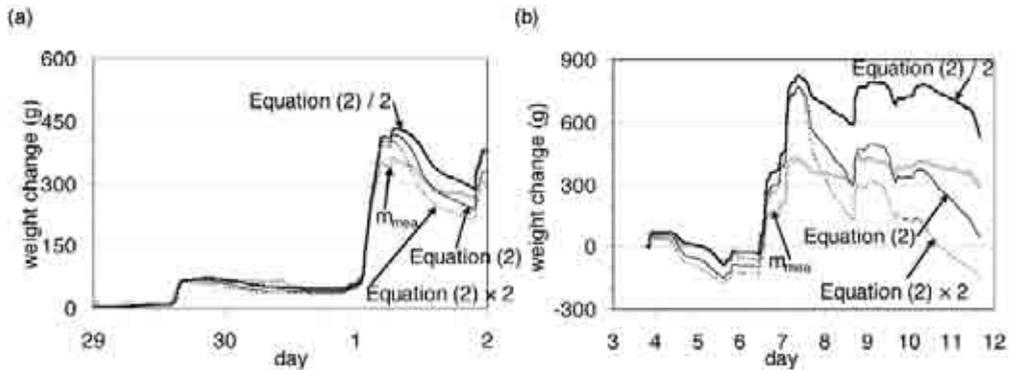
Figure 3: Simulated weight changes $m_{sim}(I_{WDR,mea})$ of the specimen compared to measured ones m_{mea}. (a) 29/11/2007 - 2/12/2007 and (b) 3/12/2007 - 11/12/2007.

depend on the convective moisture transfer coefficient especially during drying periods, large differences between the simulations and measurements also occurred during rain. Therefore, the transfer coefficient is not the only reason of the differences. Hence, the differences may also be attributed to two reasons: the occurrence of splashing and bouncing and the averaged flux assumption. Due to splashing and/or bouncing of raindrops, part of these raindrops do not contribute to the moisture load on the facade. The averaged flux assumption should represent the real discrete and random impingement, uptake and evaporation of raindrops as a spatially and temporally averaged flux. It is concluded that the reliable prediction of the WDR absorption and evaporation on building facades is very difficult.

ACKNOWLEDGEMENTS

REFERENCES

Abuku M., Janssen H., Roels S. (2009a). "Impact of wind-driven rain on historic brick wall buildings in a moderately cold and humid climate: numerical analyses of mould growth risk, indoor climate and energy consumption", Energy Buildings, 41, 101-110.

Abuku M., Janssen H., Poesen J., Roels S. (2009b). "Impact, absorption and evaporation of raindrops on building facades". Building and Environment, 44, 113-124.

Blocken B., Carmeliet J. (2004). "A review of wind-driven rain research in building science", Journal of Wind Engineering and Industrial Aerodynamics, 92(13), 1079-1130.

Blocken B., Carmeliet J. (2005). "High-resolution wind-driven rain measurements on a low-rise building – experimental data for model development and model validation", Journal of Wind Engineering and Industrial Aerodynamics, 93(12), 905-928

Janssen H., Blocken B., Roels S., Carmeliet J. (2007). "Wind-driven rain as a boundary condition for HAM simulations: analysis of simplified modelling approaches", Building and Environment, 42, 1555-1567.

Künzel H.M., Kiessl K. (1997). "Calculation of heat and moisture transfer in exposed building components". International Journal of Heat and Mass Transfer, 40(1), 159-167.

Natural wind simulation in the TUM boundary layer wind tunnel

H. Kozmar

Faculty of Mechanical Engineering and Naval Architecture, University of Zagreb,
Ivana Lučića 5, HR-10000 Zagreb, Croatia, e-mail: hrvoje.kozmar@fsb.hr

Keywords: Atmospheric boundary layer simulation, TUM low-speed boundary layer wind tunnel, Hot-wire anemometry, Counihan method.

ABSTRACT

Precise atmospheric boundary layer (ABL) wind tunnel simulations are essential for a wide variety of atmospheric studies, including wind loading of structures and air pollutant dispersion and deposition, because before wind tunnel tests on structural models can be done, it is necessary to reproduce natural winds in the wind tunnel test section. Once a new boundary layer wind tunnel (BLWT) has been developed, it is a common practice to evaluate its adequacy for ABL simulations. These preliminary studies usually have been carried out using standard methods and procedures, as reported by Cook (1975), Sykes (1977), Holmes (1977), Greenway & Wood (1979), Blessman (1982), Hansen & Sørensen (1985), Augusti et al. (1995), Wittwer & Möller (2000), and Balendra et al. (2002). The scope of this study was to evaluate the characteristics of ABL simulations in the BLWT at the Technische Universität München (TUM). It was intended to provide a basic reference for natural wind simulations in this wind tunnel, as a preparation for follow-up studies.

The Counihan method (1969a, 1969b, 1973) was applied to reproduce the rural, suburban, and urban ABL, as previous applications of this method indicated a very good agreement between the ABL and its wind tunnel models. Experiments were conducted in a 1.80 m high, 2.70 m wide and

Contact person: H. Kozmar, Faculty of Mechanical Engineering and Naval Architecture, University of Zagreb, Ivana Lučića 5, HR-10000 Zagreb, Croatia, Tel: +385/(0)1/6168162, Fax: +385/(0)1/6156940.
E-mail: hrvoje.kozmar@fsb.hr

21 m long test section of the low-speed BLWT at the TUM ('Rudolf-Frimberger-Windkanal'), which is shown in Figure 1. This Göttingen type wind tunnel is operable in a closed circuit and an open circuit mode with a suction configuration. The flow uniformity is achieved by means of a honeycomb, four sets of screens and a section with a contraction ratio of 2.12:1. Preliminary tests reported turbulence intensities at the entrance cross-section less than 0.5%, and measured mean velocities $\bar{u}$ differed less than 1%. The adjustable ceiling enables longitudinal pressure control, i.e. zero pressure gradient can be obtained along the wind tunnel test section by adjusting the ceiling height. Structural models are usually placed at a turntable, whose centre is positioned 11.3 m downwind from the nozzle. Prior to leaving the test section, the air flows through a debris collecting metal grid. The blower is driven by a 210 kW electric motor, which allows a velocity regulation from 1 m/s to 30 m/s. The simulation technique, originally introduced by Counihan (1969a, 1969b, 1973), was based on the use of quarter-elliptic, constant-wedge-angle spires and a castellated barrier wall, followed by a fetch of roughness elements. Instantaneous velocities in the x-, y- and z-direction were sampled at 1.25 kHz and recording 187500 data samples using triple hot-wire probe DANTEC 55P91.

Mean velocities profiles $\bar{u}$ compare well with the power law, as shown in Figure 2. Local velocities, $\bar{u}_z$, were normalized to the reference velocity $\bar{u}_{ref}$ at $z_{ref} = 0.1$ m.
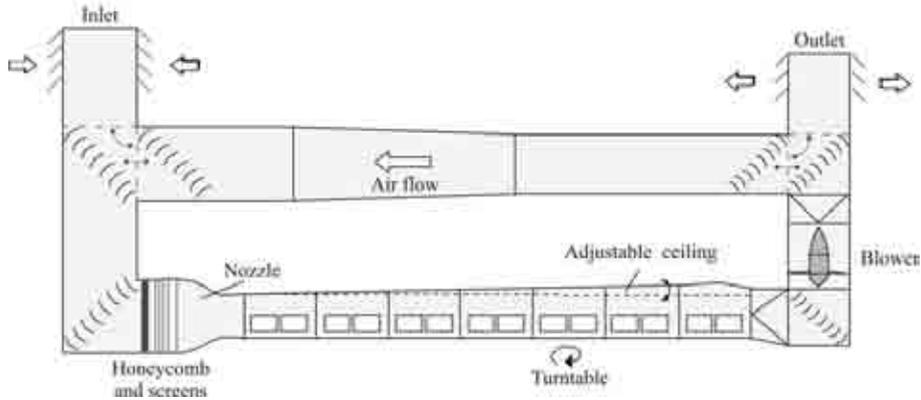
Figure 1: Low-speed boundary layer wind tunnel at the Institute of Aerodynamics, Technische Universität München
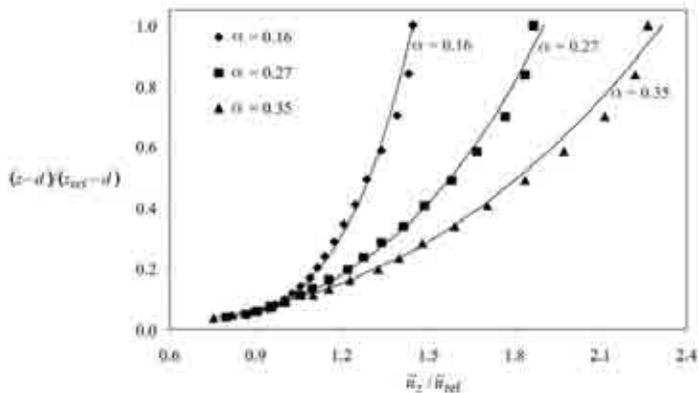
Figure 2: Mean velocity profiles in x-direction compared with the power law (linear presentation)

According to ESDU 72026 (1972), the power law exponents $\alpha = 0.16$, 0.27 and 0.35 can be accepted for the representation of the rural, suburban and urban ABL, respectively. Turbulence intensity profiles I_u normalized to $\bar{u}_\delta$ compare well with the ESDU 85020 (1985) data as shown in Figure 3. The turbulence intensity increases as the upstream surface becomes rougher, due to intensified friction between the surface and the air. The power spectral density of longitudinal velocity fluctuations at $z = 0.2$ m is shown in Figure 4. The simulated spectra show a good agreement with the von Karman spectrum. The presence of a region with a -2/3 declivity in all configurations clearly indicates the Kolmogorov inertial subrange, which is very important for wind load studies. There was a good match of peak frequencies between the measured and design spectra, which indicates the matching of the length scales.
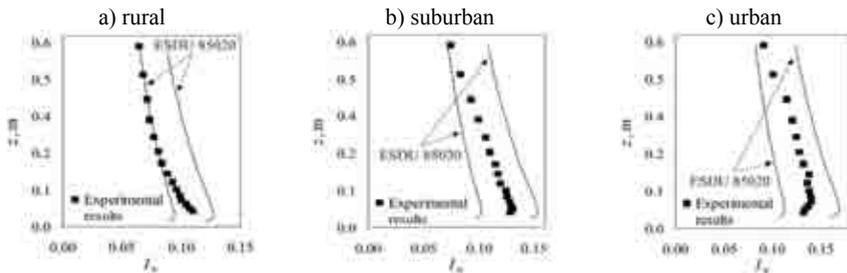
Figure 3: Turbulence intensity profiles I_u compared with ESDU 85020 (1985) data;
a) rural, b) suburban, and c) urban ABL simulation
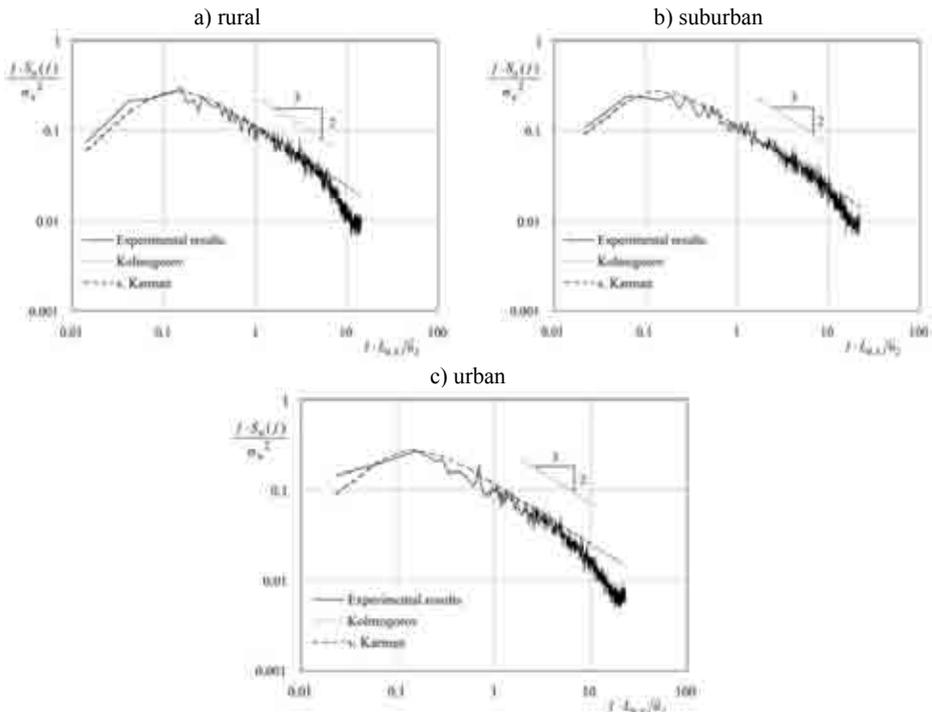
Figure 4: Power spectral density of longitudinal velocity fluctuations at $z = 0.2$ m;
a) rural, b) suburban, and c) urban ABL simulation

The ABL developed over rural, suburban and urban types of terrain was simulated in the TUM BLWT using the Counihan method. Mean velocity profiles proved to be in good agreement with the power law, as well as with the logarithmic law. Turbulence intensity profiles and integral length scales of turbulence also compare well with the ESDU data for the scale factors 1:389, 1:363, and 1:322 in rural, suburban, and urban simulations, respectively. These scale factors were calculated using the Cook's (1978) method. The power spectral density of longitudinal velocity fluctuations compares well with the von Karman spectrum, as well as with the Kolmogorov inertial subrange. The evaluation of obtained results documents the applicability of the TUM boundary layer wind tunnel for ABL simulations. In particular, it indicates this wind tunnel can be employed in a broad spectrum of engineering, environmental and micrometeorology studies, where it is required to accurately reproduce ABL characteristics.

ACKNOWLEDGEMENTS

REFERENCES

Augusti G., Spinelli P., Borri C., Bartoli G., Giachi M., Giordano S. (1995). "The C.R.I.A.C.I.V. atmospheric boundary layer wind tunnel", Proceedings of 9th ICWE, International Conference on Wind Engineering, New Delhi.

Balendra, T., Shah, D.A., Tey, K.L., Kong, S.K. (2002). "Evaluation of flow characteristics in the NUS-HDB Wind Tunnel", Journal of Wind Engineering and Industrial Aerodynamics, 90, 675-688.

Blessmann, J. (1982). "The boundary layer TV-2 wind tunnel of the UFRGS", Journal of Wind Engineering and Industrial Aerodynamics, 10, 231–248.

Cook, N.J. (1975). "A boundary layer wind tunnel for building aerodynamics", Journal of Industrial Aerodynamics, 1, 3-12.

Cook, N.J. (1978). "Determination of the model scale factor in wind tunnel simulations of the adiabatic atmospheric boundary-layer", Journal of Industrial Aerodynamics, 2, 311–321.

Counihan, J. (1969a). "A Method of Simulating a Neutral Atmospheric Boundary Layer in a Wind Tunnel", AGARD Conference Proceedings, Vol. 43.

Counihan, J. (1969b). "An Improved Method of Simulating an Atmospheric Boundary Layer in a Wind Tunnel", Atmospheric Environment, 3, 197-214.

Counihan, J. (1973). "Simulation of an Adiabatic Urban Boundary Layer in a Wind Tunnel", Atmospheric Environment, 7, 673-689.

Counihan, J. (1975). "Adiabatic Atmospheric Boundary Layers: A Review and Analysis of Data from the Period 1880-1972", Atmospheric Environment, 9, 871-905.

ESDU (1972). "Characteristics of wind speed in the lower layers of the atmosphere near the ground: strong winds (neutral atmosphere)", Engineering Sciences Data Unit 72026.

ESDU (1985). "Characteristics of wind speed in the lower layers of the atmosphere near the ground. Part II: single point data for strong winds (neutral atmosphere)", Engineering Sciences Data Unit 85020.

Greenway, M.E., Wood, C.J. (1979). "The Oxford University 4m x 2m industrial aerodynamics wind tunnel", Journal of Industrial Aerodynamics, 4(1), 43-70.

Hansen, S.O., Sørensen, E.G. (1985). "A new boundary layer wind tunnel at the Danish Maritime Institute", Journal of Wind Engineering and Industrial Aerodynamics, 18(2), 213-224.

Holmes, J.D. (1977). "Design and performance of a wind tunnel for modelling the atmospheric boundary layer in strong winds", Summer Conference on Urban Meteorology, Macquire University, Sydney.

Sykes, D.M. (1977). "A new wind tunnel for industrial aerodynamics", Journal of Industrial Aerodynamics, 2(1), 65-78.

Wittwer, A.R., Möller, S.V. (2000). "Characteristics of the low-speed wind tunnel of the UNNE", Journal of Wind Engineering and Industrial Aerodynamics, 84, 307-320.

Modelling flow and pollutant dispersion in urban areas

M.Carpentieri, A.G.Robins

*EnFlo, FEPS, University of Surrey (UK) – m.carpentieri@surrey.ac.uk – a.robins@surrey.ac.uk –
GU2 7XH Guildford, Surrey (UK)*

ABSTRACT

Air pollution in cities is a major environmental concern and, despite significant improvements in fuel and engine technology, present day urban environments are mostly dominated by traffic emissions (Vardoulakis et al 2003). Human exposure to hazardous substances is expected to be higher especially in those areas where population and traffic density are relatively high. Understanding flow and dispersion in urban streets is therefore of paramount importance for air quality management and planning for a number of reasons, mainly related to human health. Furthermore, the particular present international political situation adds concerns, as the deliberate discharge of toxic material in populated areas is a serious threat.

The dispersion of pollutants, its causes and effects on building and population has been the object of a number of works. Many studies available in the literature deal with simplified layouts reproducing the principal features of an urban environment: canyons, intersections, regular and staggered building arrays. Empirical models have been developed along with numerical models and experimental validation in the field and in wind tunnels. Most work has focussed on simple geometries, nevertheless some attempts to study real urban situations have produced some interesting insight into the dispersion process.

This work presents some of the results from wind tunnel experiments in urban areas performed in

Contact person: M. Carpentieri, EnFlo, FEPS, University of Surrey, GU2 7XH Guildford (UK), +44 1483 689675.
E-mail m.carpentieri@surrey.ac.uk

the EnFlo laboratory, University of Surrey. The studies were carried out for two separate projects. The first study is part of a multidisciplinary project, Dispersion of Air Pollution and its Penetration into the Local Environment (DAPPLE, Arnold et al 2004), whose aim is to enhance understanding of pollutant dispersion processes in realistic urban environments. One of the novel aspects of DAPPLE, if compared to other similar studies, is its multidisciplinary approach to the problem: field measurements on meteorology, background pollution levels, traffic flow, personal exposure and inert tracer releases were supported by both wind tunnel and numerical studies. Furthermore, it focussed on a real urban intersection, characterised by buildings of different shape and height, not infinite and uninterrupted canyons of different width and length. The second project, HRModUrb (High Resolution flow and dispersion Models for Urban areas), funded by the EC under the FP7 People programme (Marie Curie Actions) is aimed at studying urban atmospheric flow and pollutant dispersion at the neighbourhood scale. Current state-of-the-art dispersion models have been generally been developed for coarser scales and lower resolutions, and they are not capable of correctly reproducing the spatial and temporal distribution of air pollution within the urban environments where most people live (see e.g. urban street canyons). The neighbourhood scale allows for both a detailed reproduction of the phenomenon and the development of parameterised operational models. The study methodology involves the use of wind tunnel experiments as well as numerical simulations (CFD) in order to enhance understanding of the dispersion phenomena at this particular scale.

A simple physical model (scale 1:200) of an urban area centred on the intersection between Marylebone Road and Gloucester Place in central London was reproduced in the EnFlo wind tunnel. A comprehensive data base of experimental measurements of the flow within the intersection was built, involving both qualitative and quantitative techniques. The concentration of a tracer gas across the area was also measured. LDA (Laser Doppler Anemometry) and FFID ("Fast" Flame Ionisation Detector) devices were then coupled in order to produce simultaneous measurements of velocity and concentration, permitting the estimation of instantaneous and turbulent pollutant fluxes, thus giving an important insight into the understanding of turbulent diffusion.
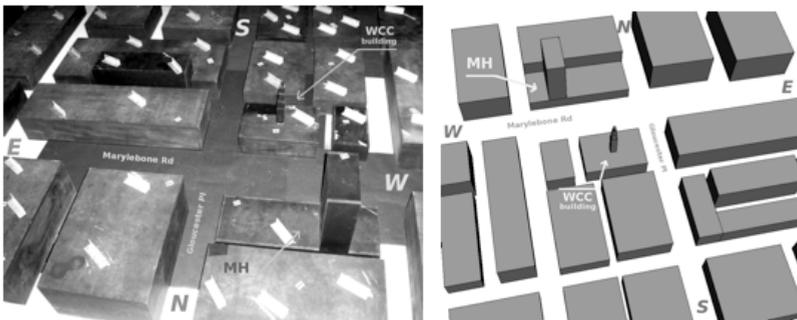
Figure 1: The 1:200 basic block model of the DAPPLE site in the EnFlo wind tunnel (left; WCC, Westminster City Council; MH, Marathon House); and, 3-D rendering of the DAPPLE site model (right).

The velocity field across the model was strongly affected by the geometry of the site and its orientation with respect to the wind direction studied (approximately from SW, while the two streets where directed respectively along N-S and W-E). The flow, especially within the larger of the streets, was found to be very complicated. The measurements also revealed that the intersection itself was characterised by complex 3-dimensional features with vortices and recirculation originating where the flows from the two intersecting roads met. The presence of tall buildings rising significantly higher than the average building height also proved to strongly affect the flow and dispersion processes within the intersection. Streamlines, vorticity, mean and turbulent velocity plots were produced, which allowed for a clear 3-dimensional visualisation of the many different features

characterising the flow. Mass balance calculations revealed the significant effect of the flow close to the ground in the estimation of the pollutant dispersion. On the contrary, mean vertical fluxes between the canopy layer and the flow above were found to be generally small.
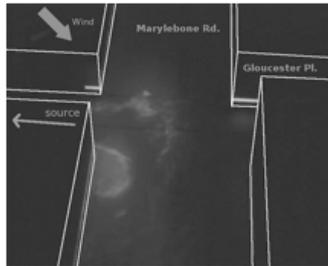
Figure 2: Flow visualization (snapshot); source at Gloucester Place (centre), horizontal light sheet at 20 mm in Marylebone Road showing vortex at the south-east corner of the intersection.
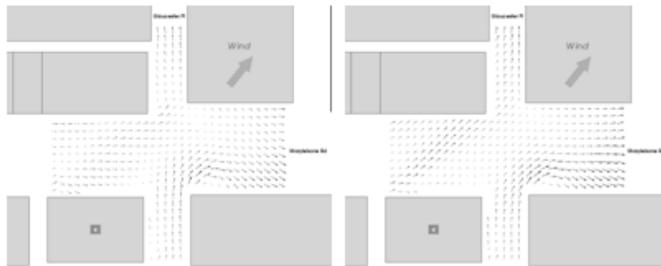
Figure 3: Horizontal velocity field at z = 25 mm (left) and z = 50 mm (right); mean building height = 110 mm.
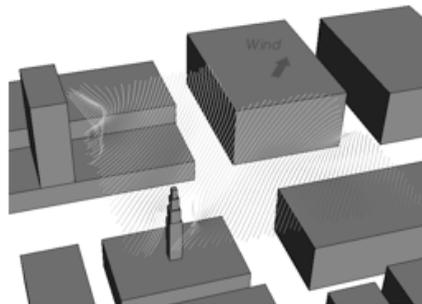
Figure 4: Stream traces for the flow field at the highest horizontal levels(the starting points for the stream traces, forward and backward, are along a diagonal line across the intersection directed from NW to SE at z = 150 mm; where the traces are not visible they are outside of the measurement domain 300 mm < x, y < 300 mm, 25 mm < z < 150 mm).
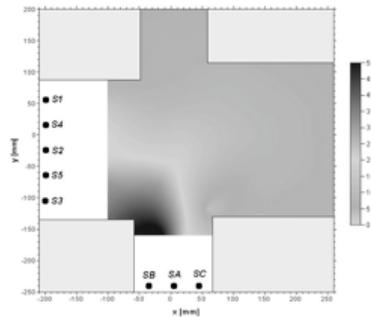
Figure 5: Non-dimensional concentrations at z = 10 mm; all the sources.

The second part of this study presents the preliminary results of the HRModUrb project, which includes both experimental measurements and numerical simulations within several models of urban areas, ranging from simple geometry (e.g. regular building arrays) to complex real urban configurations (e.g. the model of the DAPPLE site in central London). One of the expected outcomes of this project will be the improvement of current parameterisations of turbulent flow and dispersion mechanisms at the neighbourhood scale, aimed at developing new operational models and/or improving the existing ones.

REFERENCES

Vardoulakis S., Fisher B.E.A., Pericleous K., Gonzalez-Flesca N. (2003). "Modelling air quality in street canyons: a review", Atmospheric Environment, 37 (2), 155-182.

Arnold S.J., ApSimon H., Barlow J., Belcher S., Bell M., Boddy J.W., Britter R., Cheng H., Clark R., Colvile R.N., Dimitroulopoulou S., Dobre A., Greally B., Kaur S., Knights A., Lawton T., Makepeace A., Martin D., Neophytou M., Neville S., Nieuwenhuijsen M., Nickless G., Price C., Robins A., Shallcross D., Simmonds P., Smalley R.J., Tate J., Tomlin A.S., Wang H., Walsh P. (2004). "Introduction to the DAPPLE air pollution project", Science of The Total Environment, 332 (1-3), 139-153.

Wind tunnel measurement of flow and dispersion of power plant emission on the coastal region with complex terrain

B.S. Shiau[1,2], B.J. Tsai[2]

[1] *Institute of Physics, Academia Sinica, Taipei, 115 Taiwan, bsshiau@gate.sinica.edu.tw*

[2] *Department of Harbor and River Engineering, National Taiwan Ocean University, Keelung 202, Taiwan, b0085@mail.ntou.edu.tw*

Keywords: complex terrain, dispersion, wind tunnel, power plant emission.

ABSTRACT

Keelung is a harbor city with about four hundred thousands population. It is also the second largest commercial harbor in Taiwan. The harbor city is located in the mountainous region of northeastern coast of Taiwan. The coastal region is of the complex terrain with varying elevations form 1 m in the harbor city center region to near by mountainous region of 200 m. Sen-Au fossil power plant was located not far (4 km) from the city center near the harbor. In the case of accidental release of the pollutant emission from the power plant (two stacks 30 m apart), it will give rise of severe air pollution problems and make great impacts on the harbor city air environment. Therefore, it is necessary to offer air pollutant flow and dispersion information for assessing the air pollution impact on the city near-by.

In the past decades, many numerical and experimental studies on the gas diffusion and dispersion have been studied. Typical numerical study on the gas dispersion in the coastal region, like Jin & Raman (1996), they made numerical study on the air pollutant dispersion from an elevated accidental release in the coastal region. The air pollutant numerical simulation of dispersion mostly focused on the open country and flat terrain. Wind tunnel experimental studies such as: Kato and Hanafusa (1996) conducted wind tunnel simulation of atmospheric turbulent flow over a flat terrain. Literature on wind tunnel experiments for the air pollutant dispersion over the coastal region with complex terrain like Duijm (1996). He proposed an analysis technique to investigate the wind tunnel modeling dispersion of air pollutants over complex terrain in the Hong Kong Territory. He did not probe thoroughly the terrain effect on the dispersion characteristics. MacDonald et al. (1997) did field experiments of dispersion through regular arrays of cubic structures. They tried to identify the effects of arrays of cubic obstacles on plume dispersion. MacDonald et al. (1998) succeeded to perform wind tunnel modeling of dispersion in arrays of obstacles, and they compared the wind tunnel results with the measurements of full-scale field trials.

In order to offer the assessment of pollution dispersion for coastal region with complex terrain, physical modeling of the pollution dispersion was carried out in this study. We mainly investigate the variation of flow and dispersion parameter in such coastal region with complex terrain.

Contact person: B.S. Shiau, Institute of Physics, Academia Sinica, 128 Academia Road, Sec.2, Taipei, 115 Taiwan, Tel:+886-2-27896749, Fax:+886-2-27889829, E-mail: bsshiau@gate.sinica.edu.tw

Experiments were conducted in the environmental wind tunnel. The test section of the wind tunnel had the cross section of 2m by 1.4m and 12.6m long. Four spires were placed at the entrance of the test section and roughness elements succeeded to be arranged 9 m long. This arrangement created a fully developed turbulent boundary layer flow, which was used as the approaching flow. The Reynolds number of the simulated approaching flow is about $\sim 10^5$. This is sufficient for the turbulent flow similarity requirement of the critical number of $\sim 10^4$ (Snyder (1981)).

An X-type hot-wire incorporating with the TSI IFA-300 constant temperature anemometer was applied to measure the turbulent flow signals. Topographical model was constructed at a scale of 1 to 2000. The model was 2 m long and 2 m wide. It was made layer by layer through a number of vertically mounted polystyrene plates of 1 cm thickness around the isopleth of height. The roughness length in the model keeps about 2 mm. As suggested by Snyder (1981), it assures flow to avoid laminar sublayer occurring in the model for flow simulation.

Exact simulation of stack discharge effluent requires rigorous similarities between the prototype and model. It is difficult to meet the rigorous requirements, but consideration of relaxed similarities for the momentum length scale, l_m, between the prototype and model are sufficient for present study of approximated simulation (Snyder (1981)). The heights of power plant two stacks are 75 m with inner diameter of 5.2 m and 4.27 m, respectively. The prototype discharging velocity of two stacks are 20.16 m/s and 19.7 m/s. The densimetric Froude number of two stacks discharge effluent are about 41.4 and 14.5. And momentum length scales for two stacks are 5.25 m and 4.21 m of full scale. For the model experiments, we choose the free stream velocity of 2.56 m/s. And the momentum length scales of two model stacks are 0.0021 m and 0.0017 m.

For flow direction visualization of the wind over complex terrain in coastal region, tufts were used as indicators of flow direction. The tufts are mounted on the model surface at a height of 7 cm, which corresponds to 140 m full scale. Visualization of the flow direction was conducted by employing the charged couple detector (CCD). The top view image of wind over the complex terrain model was grabbed at a sampling rate of 10 frames per second. We took an average of sampled frames of images for each run of flow direction visualization with a period of 30 seconds.

Methane was used as tracer gas, and it mixed with the standard gas. The mixed gas emitted from two stacks as the discharge of sources in the experiments. The rake of sampling tubes was placed at the sampled position. The tube-rake is composed of ten tubes. A cam mechanism is employed for design of the pump to suck the tracer sample to the airbags through the ten tubes simultaneously and efficiently. Each sample was taken for 5 minutes. The sampled tracer gas in airbag was analyzed with FID (Flame Ionization Detector) to count the methane concentration.

A turbulent boundary layer flow is generated as approaching flow, with power law type of mean velocity profile, which the power exponent, n is 0.222. The friction velocity of the simulated boundary layer is about $u_* = 0.23$ m/s. The roughness length of the simulated boundary layer is about $z_0 = 0.236$ cm. This corresponds to the full scale of 3.54 m which lies in the range of 1 to 10 m for urban or complex terrain as indicated by Dyrbye and Hansen (1997). Comparison of the present simulated longitudinal turbulent velocity spectrum of approaching flow with the Von Karman type of spectrum equation was made. A satisfactory agreement is achieved for the turbulent approaching flow structure simulation.

Fig.1 shows the tuft observation for flow direction of easterly wind over the coastal complex terrain at z/h=1.87, where h is the stack height. In the figure the arrows point in the direction of the tufts. The wind flow direction can be observed from the arrows. The other wind direction cases of tuft indicator observational results are obtained. Topographical profiles in some regions of are more irregular, therefore the winds accordingly are flowing irregularly. Reversed flow regions are seen at the tuft indicators observations. In general such regions are the leeside of mountains or hills. We find that the flow turbulence is largely increased when the wind over the mountains. This is shown by the unsteadiness of tufts. The flow turbulence differs from place to place and with the highest turbulence occurs on the leeside of the hills or mountains as expected. The reversed flow is viewed at some regions which are generally the leeside of main hills or mountains.

The mean wind velocity profiles for different downwind stations of sources for easterly wind over the coastal complex terrain are shown in Fig.2. Results indicate that mean wind speed is increased (named as speed-up) at the hill or mountain crest. The longitudinal turbulence intensity profiles at various downwind stations of sources for easterly wind over the coastal complex terrain are shown in Fig.3. The turbulence intensity increases as measured locations shift to leeside of hills or mountains.
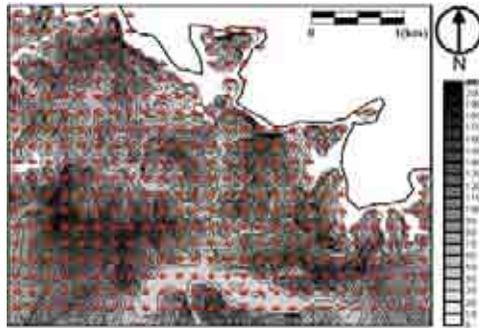
Figure 1: Tuft observation for flow direction of easterly wind over the coastal complex terrain at z/h=1.87
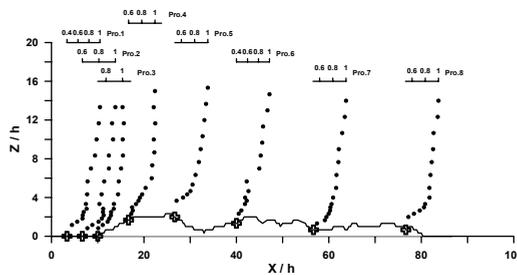
Figure 2: Mean wind velocity profiles for different downwind stations of sources for Easterly wind over the coastal complex terrain
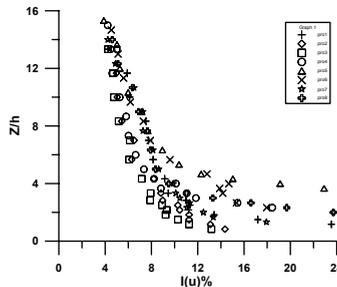
Figure 3: Longitudinal turbulence intensity profiles at various downwind stations of sources for easterly wind over the coastal complex terrain

The tracer concentration C is scaled by the stack height h, emission discharge Q, and ambient cross wind speed U as the dimensionless concentration $K=Ch^2Q/U$. For easterly wind over the coastal complex terrain, the horizontal and vertical dimensionless concentration contours are shown in Fig.4. It is noted that due to hills beside the sources, the double high horizontal concentration contours are occurred in the near-by region of power plant two stacks sources.

Fig.5 shows the variations of vertical dispersion parameters variations downwind of sources for easterly, southeasterly, and northeasterly winds over the coastal complex terrains. It is seen that vertical dispersion parameter increases as the distance downwind of the source increases for wind over different complex terrains. The terrain topography feature for easterly wind direction is the most complexity among three cases. Results also reveal that the complex terrain has a favorable effect on the increase of value for the vertical dispersion parameters. The more complexity of the terrain features becomes, the larger the values for vertical dispersion parameters are.
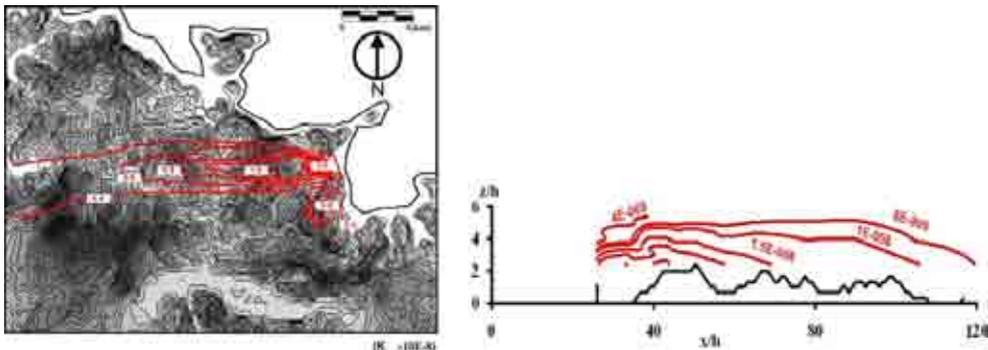
Figure 4: Horizontal (z/h=1.87) and vertical dimensionless concentration contours downwind of sources for easterly wind over the coastal complex terrain
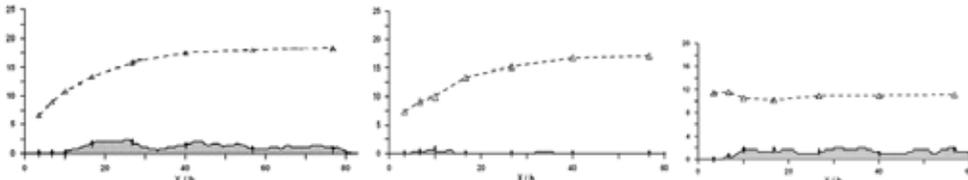
Figure 5: Vertical dispersion parameters variations downwind of sources for easterly, southeasterly, and northeasterly winds over the coastal complex terrains

REFERENCES

Snyder, W.H., (1981), "Guideline for fluid modeling of atmospheric diffusion," EPA Report 600/8-81-009, USA.

Duijm, N.J., (1996), "Dispersion over complex terrain: wind-tunnel modeling and analysis techniques," Atmospheric Environment, 30(16), 2839-2852

Jin, H., and Raman S., (1996), "Dispersion of an elevated release in a coastal region," Journal of Applied Meteorology, 35, 1611-1624

Kato, M., and Hanafusa, T., (1996), "Wind tunnel simulation of atmospheric turbulent flow over a flat terrain," Atmospheric Environment, 30(16), 2853-2858

Dyrbye, C. and Hansen, S.O. (1997), *Wind Loads on Structure*, p.24, John Wiley & Sons Ltd, New York

MacDonald, R.W., Griffiths, R.F., and Cheah, S.C., (1997), "Field experiments of dispersion through regular arrays of cubic structures," Atmospheric Environment, 31(6), 783-795

MacDonald, R.W., Griffiths, R.F., and Hall, D.J., (1998), "A comparison of results from scaled field and wind tunnel modeling of dispersion in arrays of obstacles," Atmospheric Environment, 32(22), 3845-3862

A new approach to wind tunnel similarity criteria for snow load prediction with an exemplary application of football stadium roof

A.Flaga, G.Kimbar, P.Matys

Lublin University of Technology, Cracow University of Technology – liwpk@interia.pl – Al. Jana Pawła II 37/3a 31-864 Krakow, Poland

Cracow University of Technology – g.kimbar@windlab.pl – Al. Jana Pawła II 37/3a 31-864 Krakow, Poland

Cracow University of Technology – p.matys@windlab.pl – Al. Jana Pawła II 37/3a 31-864 Krakow, Poland

Keywords: wind tunnel, snow load prediction, similarity criteria

ABSTRACT

During designing a new atypical roof structure a question arises on the patterns of snow distribution. The snow cover shape is determined in such cases mostly by wind action. The wind action alters the snow cover in two ways: during precipitation (increasing snow fall in wake regions) and during subsequent redistribution (causing snow drifts). Those both phenomena are very difficult to predict for atypical roof shapes, because design rules do not provide appropriate load schemes. In that case wind-tunnel experiments should be carried out.

Wind-tunnel experiments require derivation of similarity criteria involving behaviour of some loose material introduced into working section which is supposed to recreate the behaviour of the real snow in full scale. Criteria used so far took into account only specific phenomena of wind induced snow transportation in steady state such as suspension and saltation. Most of them were made with the assumption of snow transport occurring on an infinite horizontal plane in a homogeneous wind field, for example by Iversen (1979) and Kind (1976). In the case of predicting of a snow load over building roofs, these models may be inappropriate, because of curved roof geometry and occurrences of high positive and negative pressure regions with nonuniform distribution of pressure fluctuations.

A new approach has been made by Kimbar & Flaga (2008), starting with fundamental considerations about multiphase flows theory as described by Crowe et al. (1998). Snow particles (during precipitation or subsequent wind induced redistribution) have been depicted as a homogenous dispersion described by concentration field (k) and mass flux field ($\mathbf{Q}$). These two fields describe both

Contact person: G. Kimbar; Wind Engineering Laboratory of Cracow University of Technology; Al. Jana Pawła II 37/3a, 31-864 Kraków, Poland; +48608046116; fax.: +480126283566; e-mail: g.kimbar@windlab.pl

the direction and the speed of snow particles movement. Mean mass averaged movement speed of dispersion ($\mathbf{v}_d$) has been introduced by defining:

$$\mathbf{Q} = \frac{1}{\|\Omega\|} \sum_i \Omega\, m_{pi}\, \mathbf{v}_{pi} = \mathbf{v}_d\, k = \mathbf{v}_d \frac{1}{\|\Omega\|} \sum_i \Omega\, m_{pi},$$ (1)

where: Ω – some averaging function; m_{pi} – mass of the ith particle; $\mathbf{v}_{pi}$ – velocity of the ith particle. Further dispersion movement modelling has been based on $\mathbf{v}_d$ decomposition into components of different origin, which have lead to involving into the model such quantities as mean dispersion terminal velocity or dispersion movement relaxation time.

Since the snow load on roofs is a primary interest in civil engineering considerations, the snow accumulation rate (Q_{acc}) has been derived. This quantity describes how fast the snow cover is formed (or removed if negative) on the roof during precipitation or redistribution. Simulation of the accumulation rate in wind-tunnel results in proper recreation of natural phenomena with respect to the snow load, because:

$$ds = Q_{acc}\, g\, dt,$$ (2)

where: ds – snow load increase; g – acceleration due to gravity; dt – time increase. The Q_{acc} during precipitation depends on the $\mathbf{Q}$ field and the roof geometry, hence similarity criteria during such an event have been derived by dimensional analysis of appropriate measurable parameters.

Additional considerations are needed for proper redistribution simulation, because in this case the $\mathbf{Q}$ field is shaped by snow cover which is the source of particles. Conditions when particles are lifted (injected) form the snow surface by the wind action have been considered. A completely new dimensionless quantity called "particle bed surface effort" (ψ) has been developed (fig. 1). This variable is a ratio of active force magnitude (wind pressure, weight, returning particle strokes) acting on particles bounded with particle bed to the maximal passive forces (cohesion, friction) which hold particles in place. It means that injections (and hence – redistribution) occurs when active forces prevails over passive forces, that is when $\psi > 1.0$.
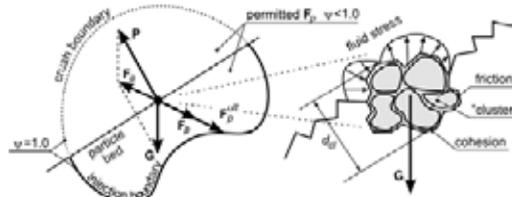
Figure 1: A "cluster" of particles exposed on active ($\mathbf{F}_a$) and passive ($\mathbf{F}_p$) forces not exceeding ultimate passive force ($\mathbf{F}_p^{\text{ult}}$). The $\psi < 1$, hence the cluster is at rest. When $\mathbf{F}_p$ reaches ultimate value ($\mathbf{F}_p^{\text{ult}}$) the $\psi = 1$ and the injection of the particle cluster occurs (alternatively: the particle bed is crushed by active forces).

The dimensional analysis of the parameters shaping active and passive forces leads to final sets of similarity criteria for wind affected snow load formation, respectively: geometrical (3), inflow (4), "ballistic" (5) and particle bed (6) set. So called ballistic set relates to particles movement in air, and particle bed set to injection conditions.

$$\forall \big(a \in (G)\big)\ a = idem,$$ (3)

$$\frac{z_{ref}}{L} = idem; \qquad \alpha = idem; \qquad I_u = idem.$$ (4)

$$\Pi_t = \frac{v_{ref}}{v_t} = idem; \qquad Stk = \frac{v_t\, v_{ref}}{g\, L} = idem. \tag{5}$$

$$\Pi_g = \frac{(\rho_c - \rho_f)d_{cl}g}{v_{ref}^2\, \rho_f} = idem; \quad \Pi_\chi = \frac{\chi\rho_c}{v_{ref}^2\, \rho_f} = idem; \quad \varphi = idem; \tag{6}$$

where: (G) – dimensionless geometrical properties set (mostly ratios of characteristic dimensions and characteristic angles); z_{ref} – reference height; α – velocity profile power law coefficient; I_u – intensity of turbulence; L – reference length; v_{ref} – average reference horizontal flow speed (at z_{ref}); v_t – dispersion terminal speed; g – acceleration due to gravity; ρ_c – snow cover density; ρ_f – fluid (air) density; d_{cl} – "cluster" diameter; χ – kinematical cohesion of the particle bed; φ – particle bed friction angle.

Above mentioned theoretical considerations have been applied to a roof over football Municipal Stadium in Poznań (Poland), which is build for UEFA Euro 2012. The roofing will be a prestressed membrane covering (probably fibreglass reinforced PVC) supported on steel trusses, columns and concrete foundations. Because the membrane is a very lightweight material, the main loads acting on it would be the wind pressure and snow weight. Both loads were anticipated in a boundary layer wind-tunnel of the Wind Engineering Laboratory of the Cracow University of Technology.

The snow needs to be modelled in experiments by some loose material. In this case grinded Styrofoam was used. The structure model (fig. 2) had been manufactured at a reduction scale of 1:200. A special attention had been paid to the recreating of structure details which could affect air flow around the model. The model was put on the revolving table (fig. 3), which allowed simulations with different wind direction. The single experiment result was a measurement of particle cover shape accumulated on the roof model. An own developed photogrammetric method was used, which had been based on laser scanning and digital photo processing.

Overall ten tests was performed: five precipitation simulations and five redistribution simulations. Setups differed in the wind angle direction acting on the model. Because of the model symmetry only directions of one half of the full circle was tested (in 45° step).
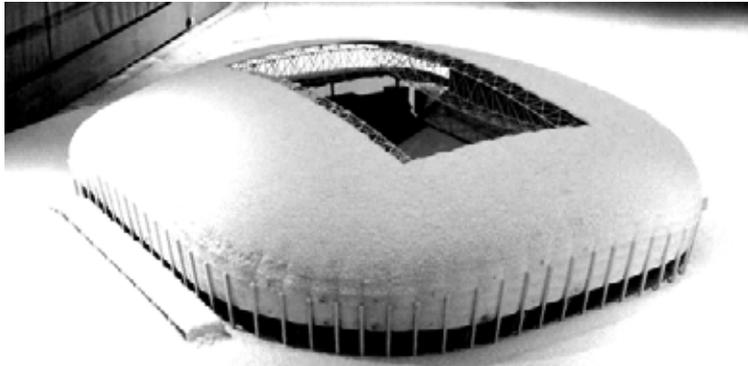
Figure 2: The stadium model covered with grinded Styrofoam ("artificial snow").
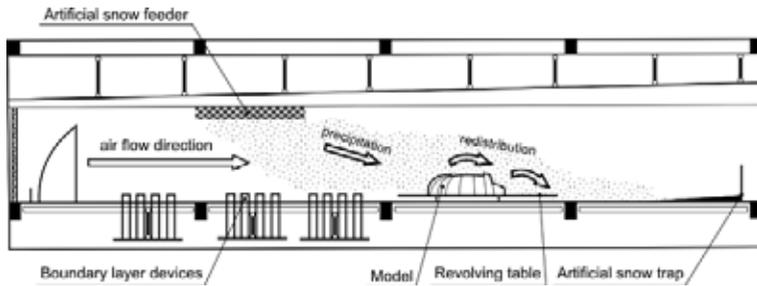
Figure 3: Arrangement of the experiment in the wind tunnel working section.

For every precipitation test (after establishing steady flow conditions) about 60 litres of artificial snow were poured into working section during interval of about 5 minutes. Afterwards, the reference height was measured, and 130 photos were taken by the photogrammetric device.

The first stage of every redistribution simulation was identical as for precipitation simulation. Afterwards, the wind speed was increased what caused the erosion and hence the redistribution of the particle cover. Tests were performed until reaching the state of equilibrium (cessation of erosion), that is for about 15 minutes.

Tests results were relative heights of the particle cover, better known as the shape factor (μ). Raw results mirror real, but single weather incidents. Hence, those data are insufficient for designing process, because the snow cover over a roof forms during long period and many precipitation and redistribution incidents. So called "base scheme" (fig. 4) was obtained by determining the weighted mean from precipitation simulation results for different wind directions. Redistribution patterns were calculated for all eight wind directions, because even single redistribution incident can cause a significant snow drift.
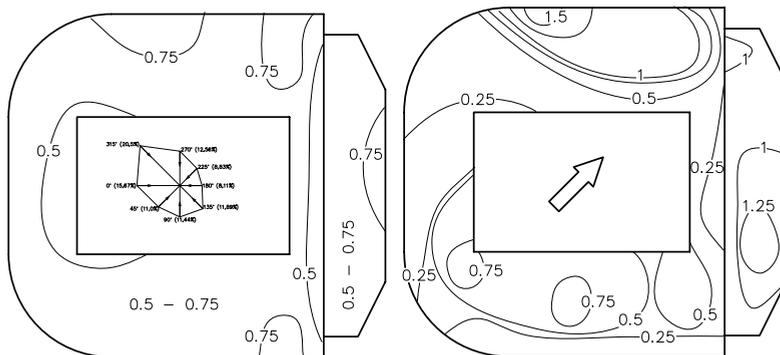
Figure 4: Exemplary results (roof shape factor μ); left: basic load scheme, right: a sample load scheme for wind induced redistribution.

REFERENCES

Crowe, C. T., Sommerfeld M., Tsuji Y. (1998). *Multiphase flows with droplets and particles*. CRC Press, NY.
Iversen, J.D. (1979). "Drifting snow similitude", J. of The Hydraulics Division, June 1979.
Kind, R.J. (1976). "A critical examination of the requirements for model simulation of wind-induced erosion/deposition phenomena such as snow drifting", Atm. Env. 10
Kimbar G., Flaga A. (2008). "A new approach to similarity criteria for predicting a snow load in wind-tunnel experiments", Snow Engineering VI, Whistler, Canada

Fluctuating pressures on cube faces and simulator floor in tornado-like flow

Sabareesh.G.R, Yukio Tamura, Masahiro Matsui, Akihito Yoshida

Ph.D Student, Tokyo Polytechnic University, d0884202@st.t-kougei.ac.jp

Professor, Tokyo Polytechnic University, yukio@arch.t-kougei.ac.jp,

Professor, Tokyo Polytechnic University, matsui@arch.t-kougei.ac.jp

Associate Professor, Tokyo Polytechnic University, yoshida@arch.t-kougei.ac.jp

ABSTRACT

Extreme local weather disturbances like tornadoes, involve very complex interaction between wind and structure, making real time evaluation difficult.
A tornado simulator was developed in the Wind Engineering Research Centre at Tokyo Polytechnic University and wind speeds and pressure distributions on a cubic model in tornado-like flow were measured. The present investigation focuses on the fluctuation of pressure, on the cube faces and the neighborhood floor, under a tornado-like flow. The pressure on the floor was distributed cylindrically and the curve best fitted to Rankine-type showed its core size to be of the same size as one from the wind speed distributions. The pressure was expressed as a wind pressure coefficient based on the central pressure depth. The wind pressure around the cube also showed the effect of swirl flow. A statistical analysis of the pressure coefficients was carried out and the results show the distribution of pressure in the faces of the cube and on the simulator floor. The results are compared with those obtained from a boundary layer flow for the same cube over a range of incidence angles.

INTRODUCTION

Many researchers in the past, Chang (1971), Jischke &Light (1983), and Mishra et al (2008) have contributed to the simulation of tornado-like flow regimes for a cube. These studies have reported that there are large differences between the mean pressures obtained in boundary layer and tornado-like flow fields. This necessitates analysis of the wind loading of structures in such extreme flow situations.

In the present work, an attempt is made to statistically analyze the pressure coefficients for a cubic model placed in the centre of a tornado simulator, Fig.1 (a), and the neighboring floor in the absence of the model. Also the behavior of the same cube when subjected to an approaching boundary layer

---

flow having angles of incidence varying from 0~45deg, Fig.1(b), is compared. The method of defining the pressure coefficients in a tornado-like flow is different from those of earlier related studies.
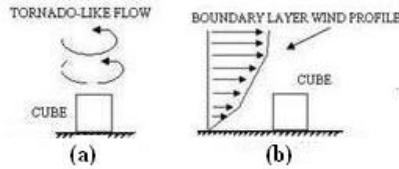
Figure 1: (a) Cube in tornado-like flow (b) Cube in boundary layer flow

DEFINING PRESSURE COEFFICIENT IN TORNADO-LIKE FLOW

The pressure coefficient (Cp$_j$) at any point' j' is defined by equation (1)

$$Cp_j = \frac{P_j - P_\infty}{q_r} \qquad (1)$$

$$q_r = \frac{1}{2}(P_\infty - P_O) \sim \frac{1}{2}\rho V_{RM}^2 \qquad (2)$$
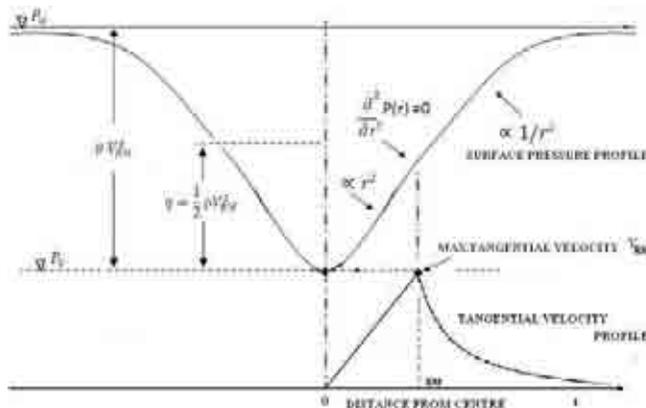
Figure 2: Location of Reference Pressure.

In the tornado-like flow regime, (P$_j$-P$_\infty$) represents the wind pressure acting at the pressure tap location. The reference dynamic pressure q$_r$, is estimated as half the centre pressure depth. Assuming Rankine-Vortex behavior, this value is equal to ½ ρV^2_{RM} at the radius of the maximum tangential velocity (RM) as shown in Fig.2. This mode of defining pressure coefficient is different from those of earlier studies made by Jischke &Light (1983) and Mishra et al (2008).

EXPERIMENTAL SETUP
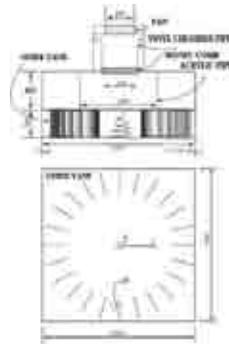
Figure 3: Arrangement for Tornado-Like Flow Simulation

Fig.3.shows the arrangement for tornado-like flow simulation. The convection chamber comprised a cylindrical piece of acrylic material 480mm high. The updraft hole had a diameter of 250mm, and the height of confluence region was 200mm. Air flowed in from the surroundings by generating a vertical updraft in the upper part of the convection region using a variable speed fan. A honey comb structure was used as a flow-straightening device. A cubic model with 100 mm side dimension was positioned in the simulator centre, resulting in a very complex flow field. Pressure taps were distributed uniformly across all five faces of the cube and also on the simulator floor. Contour plots of statistical values, namely the mean, standard deviation, maximum and minimum values, of pressure coefficients, on all faces of the cube and the simulator floor, were obtained.

RESULTS AND DISCUSSION
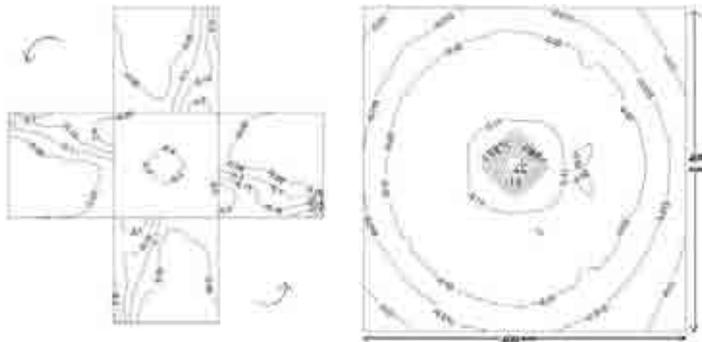
Figure 4: Contour plots showing mean pressure coefficients in tornado-like flow-
30deg vane angle (a) Faces of a cube (b) Floor in the absence of cube

From Fig.4 (a), it is observed that the mean pressure coefficient for all faces of the cube except the roof face registered a value in the range -0.05 to -0.2, whereas the roof face had a value of -0.3. The reason for such a large suction value on the roof face of the cube can be due to the rotational component of wind produced by the tornado-like flow. Also, it is observed that for the anticlockwise tornado-like flow, the leading edges of the cube has smaller values of mean pressure coefficient in the

range of -0.2 to -0.1, whereas for the trailing edge the value falls to the order of -0.05.

When the simulator floor was analyzed without the cube, as shown in Fig. 4 (b), the mean pressure coefficients increased steadily from -1.8 at centre of simulator to -0.01 at the periphery. This justifies the very low pressure at the centre of the tornado-like flow. Also, it is observed that the floor experienced only negative pressures without the cube.

Figure 5: Contour plots showing standard deviation of pressure coefficients in
tornado-like flow (a) Faces of a cube (b) Floor in the absence of cube

It is observed from Fig.5 (a) that the standard deviation values are higher, of the order of 0.03 at the leading edge of the cube facing the anti-clockwise tornadic flow, compared to those at the trailing edge, where the value is of the order of 0.01. Also the distribution of statistical values of pressure coefficients was anti-symmetrical for the opposite faces of the cube as shown in Figs 4(a) & 5(a). Thus the faces of the cube in tornado-like flow, experienced significant pressure fluctuations as observed from the considerable differences in values of the standard deviation of pressure coefficients.

From Fig.5 (b), it is observed that the standard deviation values are of the order of 0.2~0.6 at the centre of the simulator in the absence of the cube. However, at the periphery it is of the order of 0.008~0.009. These values indicate that there are significant fluctuations at the centre of the simulator and no significant fluctuations at the periphery without the cube in a tornado-like flow regime.

For the angle of incident flow, varying in the range of 0 to 45deg, the same cube in a boundary layer flow regime experienced a mean pressure coefficient in the range of -0.5 on the left, right and roof faces and 0.6 on the windward face thus exhibiting a behavior different from the tornado-like flow. The anti-clockwise nature of flow, the existence of a greater contributing tangential velocity component and the anti-symmetry observed in the distribution of pressure values characterizes the flow behavior over a cube in tornado-like flow. Results of other statistical values of pressure coefficients (maximum value, minimum value) in tornado-like flow also indicate differences from a boundary layer flow. The paper discusses in detail the interpretations of these results.

REFERENCES

Chang, C.C. (1971). "Tornado wind effects on buildings and structures with laboratory simulation". In: Proc.of the Third International Conference on Wind Effects on Buildings and Structures, 231–240.

Jischke MC, Light BD. (1983). Laboratory simulation of tornadic wind loads on a rectangular model structure. J. Wind Eng. Ind. Aerodyn.13, 371-382.

Mishra, A.R., James, D.L., Letchford, C.W. (2008). Physical simulation of a single-celled tornado-like vortex, Part B: Wind loading on a cubical model. J. Wind Eng. Ind. Aerodyn.96, 1258-1273.

Influence of swirl ratio and incident flow conditions on generation of tornado-like vortex

Masahiro Matsui and Yukio Tamura

Tokyo Polytechnic University, 1583, Iiyama, Atsugi, Kanagawa, Japan, matsui@arch.t-kougei.ac.jp

Tokyo Polytechnic University, 1583, Iiyama, Atsugi, Kanagawa, Japan, yukio@arch.t-kougei.ac.jp

Keywords: Tornado-like flow, Swirl ratio, Roughness, Flow visualization, Shear flow

1. INTRODUCTION

Damage due to local meteorological disturbances such as tornadoes, downbursts etc., has been reported in Japan in recent years. Those disturbances cause severe winds, but their occurrence is so local that it has not been possible to obtain enough information about them. Therefore, wind resistant design has not allowed for their effects.

Laboratory experiments have been conducted to obtain basic information on tornado-like flow, and some basic characteristics have been investigated.

2. OUTLINE OF TORNADO SIMULATOR

Ward (1972) developed an original tornado simulator for the lower part of an atmospheric boundary layer under mesocyclone wall clouds where kinematic momentum is predominant. A similar type of facility was used in the present studies. The simulator had a top fan that generates an updraft at an updraft hole. Through the updraft hole and the confluence region, surrounding air flows into the convection region. To generate swirl flow in the confluence region, air should circulate around the periphery. In this experiment the circulation was achieved by setting guide vanes.

In tornado-like flow, height of confluence region, radius of updraft hole, inflow angle and speed to confluence region are typical dimensional variables, which were estimated by Church (1979). The Reynolds number in this study is much smaller than that at full scale, but it was evaluated such that it did not greatly affect to the formation of the tornado-like flow. The tornado-like flow depended greatly on the swirl ratio. The value in this study was in the range of full scale values.

Through a visualization experiment, variations of flow shapes were studied under different experimental conditions. Wind velocities were measured for some typical flow shapes. In the velocity measurement experiments, laser-Doppler velocimetry (LDV) was used for some swirl ratios using guide vanes. The tangential component was measured assuming the identical center of flow as the experimental facility. The effect of floor roughness was evaluated in these cases.

Contact person: Masahiro Matsui, Tokyo Polytechnic University, 1583, Iiyama, Atsugi, Kanagawa, Japan,
Tel&Fax+81-46-242-9514, E-mail matsui@arch.t-kougei.ac.jp

3. RESULTS OF VISUALIZATION

Figures 1 (a) to (d) show the variation of flow shapes for various vane angles. At swirl ratio S=0.07 (corresponding to vane angle 10 degrees) no clear swirl flow was observed near the floor. A small core was formed at the top of the confluence region near the updraft hole. From S=0.14 (20 degrees) to S=0.31 (40 degrees), tornado-like flows were formed from the bottom of the confluence region at the floor, and they showed laminar flows. At S=0.45 (50 degrees) swirl flow started to break from the upper part. This spread to all of the swirl flows at S=0.65 (60 degrees). At S=1.0 (70 degrees) the vortex core was turbulent and extended in size.

The relation between swirl ratio and vortex shape is shown in Fig-2, and compared to the results by Church (1979) and Monji (1985). As Church showed results for variation of Reynolds number, the results for the same Reynolds number as this experiment, Re=10^5, are illustrated in Fig-4. Monji's experiments were for a slightly smaller Reynolds number, and are indicated as a reference. Turbulent flow occurred at swirl ratios higher than S=0.3. This result for transition swirl ratio agrees with Church's result, while Monji's result showed a lower transition swirl ratio S=0.2. Multi-cell vortices occurred for S>0.6 in Church's result and for S>0.5 in Monji's result, while in the present study no multi-cell was observed. Only an expanding core was observed in this study.

For a full scale tornado and an atmospheric boundary layer there are no guide vanes that produce circulation. The origin of the circulation was thought to result from a geometrical effect or non-uniformity of flow along a cold front that causes horizontal shear. In this section, the guide vanes were removed from the simulator and horizontal shear flow was applied to the confluence region from outside. Swirl flows were observed for various updraft speeds from 1 to 6 m/s, at a constant horizontal shear flow speed of 1.4 m/s.

Visualized images are shown in Figs-3 (a) to (c). For lower updraft speeds such as 1 to 2m/s, no tornado-like flow was observed, while for 4 to 6 m/s updraft speeds, tornado-like flows were clearly formed.

Results in this section show that it is necessary to form not only tornado-like flow for the circulation supplied to the confluence region but also enough updraft. These results suggest that the forming of the tornado-like flow depends on the helicity at the flow field.

4. VELOCITY MEASUREMENT EXPERIMENT AND ROUGHNESS EFFECT

The tangential component of the tornado-like flow was measured using laser Doppler velocimetry (LDV) for two swirl flows. The circulation was supplied using guide vanes for these cases. Roughness blocks were uniformly arranged on the floor of the confluence region. Three cases of their areal density, 0, 4% and 25%, were tested.

Figure 4 (a) shows the distribution of tangential flow for S=0.14, for roughness areal densities of 0%, 4% and 25%. For areal density 0%, high wind speeds were observed near the center line of the vertical sectional plane. The corresponding visualization image in Fig-1 (b) illustrated a slender core.

For areal densities 4% and 25%, high speed regions appeared away from the center. These results suggest that the turbulence thickened the core size. Wind speeds for areal density 25% showed lower values near the floor area than those for areal density 4%,, and the high speed area moved to a higher position.

Figure 4 (b) shows the distribution of tangential flow for S=0.65, for roughness areal densities 0%, 4% and 25%.

For all cases, the maximum tangential wind speeds appeared at around 20 mm from the center. The distance seemed to be unaffected by roughness. For high swirl ratio, the swirl flow was broken and turbulent even for the smooth floor case. Wind speeds near the floor decreased with increasing roughness density.

Monji conducted visualization experiments and suggested that the vortex core expanded as the swirl ratio increased and the effect of roughness was weak for high swirl ratio. The present results

agree with Monji's results.

A mathematical model of a tornado-like vortex, called Burgers vortex (Burgers, 1948), suggests that the length scale of a vortex core can be estimated as $2\sqrt{\nu/\gamma}$, where ν is kinetic viscosity and γ is a scale parameter. If eddy viscosity can be used instead of ν, the results of the present experiments can be interpreted as follows. Floor roughness produces turbulence that increases eddy viscosity and size of vortex core. When swirl ratio is low and flow is laminar, turbulence significantly affects vortex properties including eddy viscosity. When swirl ratio is high enough, the vortex is broken and turbulent. Swirl flow is not affected by roughness and turbulence.

(a) θ=10 deg., S=0.07   (b) θ=20 deg., S=0.14

(c) θ=60 deg., S=0.65   (d) θ=70 deg., S=1.0
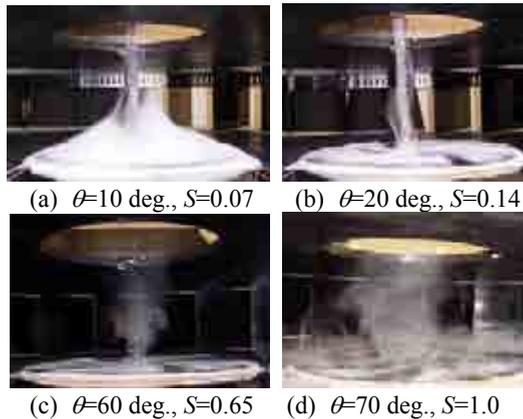
Figure 1: Flow visualization of tornado-like flow for various swirl ratios (without roughness block)

Figure 2: Shape of vortices and swirl ratio
(with results by Church, 1979 and Monji, 1985)

(a) updraft: 3m/s   (b) updraft: 4m/s   (c) updraft: 6m/s
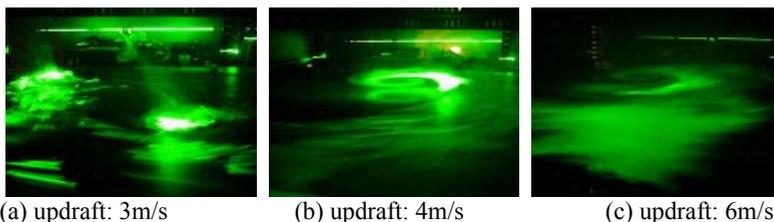
Figure 3: Flow visualization of vortices with horizontal shear flow for various updraft speeds

(a) θ=20 deg., S=0.14   (b) θ=60 deg., S=0.65
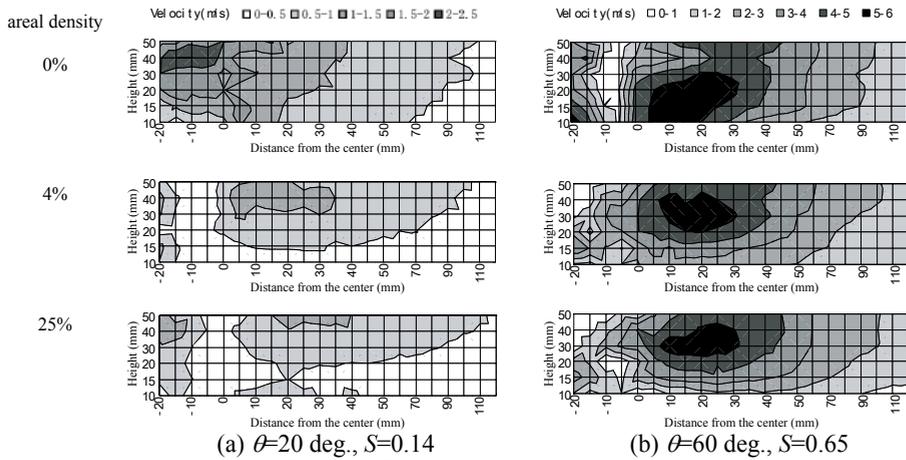
Figure 4: Tangential component of wind speed

CONCLUDING REMARKS

The effects of swirl ratio and applied flow have been investigated using a tornado simulator.

In low swirl ratio conditions, the flows formed laminar tornado-like vortices. With increasing swirl ratio, the laminar swirl flow started to break from the upper part of the vortex. Finally, the tornado-like vortices were turbulent under higher swirl ratio conditions. These situations agreed with previous researches. Horizontal incident shear flows were applied to the confluence region. In these cases, without guide vanes, a tornado-like vortex was observed. It was noted that high updraft was necessary to form stable tornado-like flows.

The tangential velocity of tornado-like flow was measured by LDV. The core size of vortices increased as swirl ratio increased, and the effect of swirl ratio was predominant with small roughness. For high swirl ratios, the roughness did not affect the velocity distributions except for the lower part that was close to the roughness. These results have been qualitatively interpreted as the effect of eddy viscosity.

ACKNOWLEDGMENT

REFERENCES

Ward, N. B. (1972), The exploration of certain features of tornado dynamics using a laboratory model, Journal of the Atmospheric Sciences, Vol. 29, 1194-1204

Church, C. R., T. Snow and E. M. Agee (1979), Characteristics of tornado-like vortices as a function of swirl ratio: Laboratory investigation, Journal of the Atmospheric Science, Vol. 36, 1755-1776

Monji, N. and Yasushi Mitsuta (1985), A laboratory experiment on the multiple structure in tornado-like vortices, Disaster Prevention Research Institute Annals, No.26, B-1, 427-436 (in Japanese)

Monji, N., Yunkuan WANG and Yasushi Mitsuta (1988), A laboratory experiment on the effect of surface roughness on the small scale atmospheric vortices, Disaster Prevention Research Institute Annals, No.31, B-1, 177-182 (in Japanese)

Burgers, J. M. (1948), A mathematical model illustrating the theory of turbulence, Advances in Applied Mechanics, R. von Mises and T. von Karman, Eds., pp. 171-199, Academic Press, New York, NY, USA

A MULTICAMERA DISPLACEMENT MEASUREMENT SYSTEM FOR WIND ENGINEERING TESTING

F. Fossati, R. Sala, A. Basso, M.Galimberti D. Rocchi

Politecnico di Milano – Department of Mechanics

Keywords: Wind tunnel, multi-camera displacement measuring system, photogrammetric measurement

ABSTRACT

The aim of several wind tunnel tests is the evaluation of the static and the dynamic behaviour of properly scaled models due to wind loads. That can be achieved by also measuring the displacements of significant aero-elastic model's points under the wind action.

This research introduces an innovative optical measurement device which overcomes the typical drawbacks of the instruments that are usually used in wind tunnel tests and allows users to obtain results that could not be achieved otherwise. Unlike contact devices it introduces a very weak load effect; moreover it is characterized by a wide measurement volume that can be modified in accordance with the peculiar test needs in term of measurement range and uncertainty. That allows users to overcome the typical laser triangulation transducer drawback of having a very narrow measurement range.

The system is able to measure at a maximum frame rate of 16 Hz the 3D coordinates of any number of model's points. The developed software allows users both to acquire images and to process them on-line in order to compute the points of interest 3D coordinates. Moreover it is provided with some additional features optimizing the analysis that will be showed in the following.

The system is based on the active stereoscopic vision technique [2,3,4,6]: in order to evaluate the 3D position of a point, it is necessary to acquire more than one view of it by using cameras placed in different positions and with different poses. In fact one single camera is unable to get the whole 3D information: usually two of them are used.

Three 1/2'' CCD GigaEthernet greyscale cameras whose resolution is 1392x1040 pixels[2] are the core of the stereoscopic measurement system. Greyscale cameras are preferable to RGB ones when colour information is not required, because their resolution is intrinsically higher and require less memory to store images. The optical systems allow users to vary the focal length in the range 8-48 [mm]; a manual zoom was preferred to a set of interchangeable optical systems in order to easily and quickly modify the measurement volume.

The 3D information is retrieved triangulating the positions of the same physical points in two images (those are called corresponding points). It is obvious that it is necessary to assure the synchronization between cameras in order to perform a valuable 3D reconstructions, because

Contact person: A. Basso, Politecnico di Milano – Department of Mechanics, Via La Masa 1, 20156 Milano (MI), phone: +39 02 23998459 FAX. +39 02 23998492   E-mail: alessandro.basso@polimi.it

triangulating images taken at different times leads to wrong results [3,4].

The main difficulty in order to make the measure fully automated is the capability to automatically recognize the corresponding points, in fact more points are generally acquired at a time. Even if two cameras are sufficient to perform the reconstruction, they hardly allow users to make the corresponding point association automatic. In fact this would be possible only if the marker order was preserved in every grab. As this condition may not be usually assured, the problem was overcome by adding a third camera to the system. Image formation can be modelled as a geometric projective process: it means that if a world point is projected onto a particular point in a camera sensor (i.e. it has a particular position in the image), the same point cannot be projected anywhere in another sensor, but it has to lie on a straight line, called epipolar line (due to the measurement noise the epipolar line actually becomes a stripe). All other sensor points can be filtered out in the correspondence search. Placing three cameras on the vertices of a triangle allows users to implement a very effective epipolar filter which performs the automatic association of corresponding points [4]. At this stage of the research the third camera is used only for this purpose and not in the triangulation process.

The uncertainty of measurement is due to two main significant contributions: the first is introduced by the calibration procedure, the second by the measurement system itself.

In the calibration procedure a first uncertainty source is the discrepancy between the real and the theoretical markers' positions in the calibration grid and it is related to the quality of the manufacturing process. A second source is due to the prismatic slide moving the calibration frame, which is not negligible only in its axial direction.

Uncertainty due to the vision system is essentially due to the discretization introduced by the sensor pixel structure, which causes an angular uncertainty into the direction of the ray used for the triangulation. In order to determine the marker's centre positions sub-pixel algorithms were used: the actual resolution depends on the marker size. The bigger the marker is, the better the resolution becomes: tests showed that a resolution of one tenth of pixel was attained. It is evident that the overall uncertainty strongly depends on the hardware components (i.e. camera sensor dimensions and number of pixels) as well as on the system layout: baseline, camera orientation with respect to the baseline and optical focal length (i.e. the zoom value). Therefore in each test it is fundamental to set a trade-off between measurement volume and uncertainty.

The overall extended uncertainty can be composed by using the rules provided by the GUM [5]. In most experimental layouts the overall measurement uncertainty with a confidence level of 99.7% is smaller than 0.5 mm.

As already stated, the developed software deals with both acquisition and processing stages. It is worth highlighting that it allows users to carry out on-line analysis. The first part of the analysis consists in performing the blob detection in every image: it is possible to set both the threshold value and other useful filters like blob area and circularity. The images are automatically updated, so it is easily possible to find the parameters allowing users to get the best results. Once those have been set, the software performs the 3D reconstruction that is showed in a 3D viewer an user can interact with, modifying pan, rotation and zoom values. Eventually some points belonging to different profiles can be selected: the different profiles are showed on different 2D interactive viewers and some different analysis can be carried out.

In the following some results concerning a long span bridge dynamics due to turbulent wind and the dynamic response of an overhead line positioned in the wake of a wind turbine will be reported. Concerning the former case study, a sectional model of a long span bridge deck was equipped with markers positioned at both transversal model extremities, as illustrated in figure 1. Four markers were placed in the row closest to the acquisition system, in order to perform a more valuable analysis in the measurement volume part where the uncertainty is expected to be the lowest.

Fig.1: Marker (identified with the black dots) positioning on the bridge model

The validation of the new measurement system has been performed comparing its results with those provided by the laser triangulation transducers. The parameter taken into account was the bridge pitch angle. Laser transducer sample rate was 1.25 kHz, while camera frame rate was 17 Hz, however both frequencies were overabundant to estimate forced motions. In fact the model was excited between 0.1 Hz and 1.5 Hz. A sixth order Butterworth low-pass filter with 10 Hz cut off frequency was used to filter high frequency noise in laser outputs.

As an example, in figure 2 a typical aerodynamic instability situation is shown: in particular figures 2a-2b are relevant to a 8 m/s wind speed test and bridge horizontal displacement and pitch time histories are reported. As can be seen vibration amplitudes increase rapidly due to the aerodynamic instability and, as shown in the figures, during the tests the bridge model was manually stopped in order to avoid any damage.
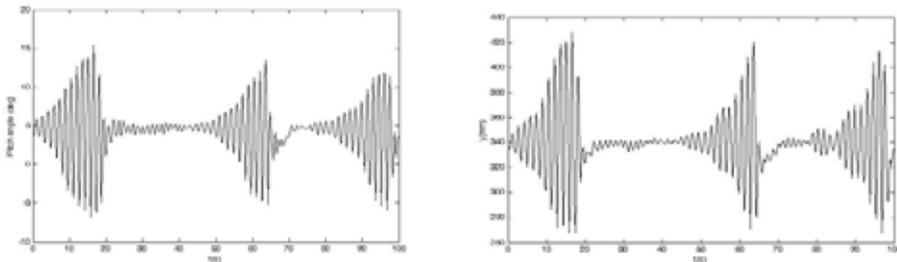
Fig.2: (a) pitch angle – (b) horizontal displacement

Tests on the aeroelastic response of an OHL was performed on a 1:50 scale model of a cable reproducing the dynamic characteristics of an Araucaria 400 m long span cable. Tests were performed in turbulent flow conditions taking into account different relative positions between the OHL model and the wind turbine (1.5 D and 2.5 D) (figure 3) and three different line heights from the ground (distance of the minimum span height from the ground equal to 21.5 m, 31 m and 38.5 m).

The cable dynamic response was studied by means of the spatial displacement of some cable points of interest equipped with markers. The positions of the markers (named "a", "b", "c", "d" and "e") along the cable and the reference frame adopted for the data post processing are reported in figure 3b.

Tests were performed in the following conditions for three wind speed regimes (U = 1.4 m/s, U = 2.12 m/s and U = 2.8 m/s):

➤ without wind turbine (H = 0.62 m)

➤ with the wind turbine at 1.5 D (H = 0.62 m)

➤ with the wind turbine at 2.5 D (H = 0.62 m, 0.77 m and 0.43 m)
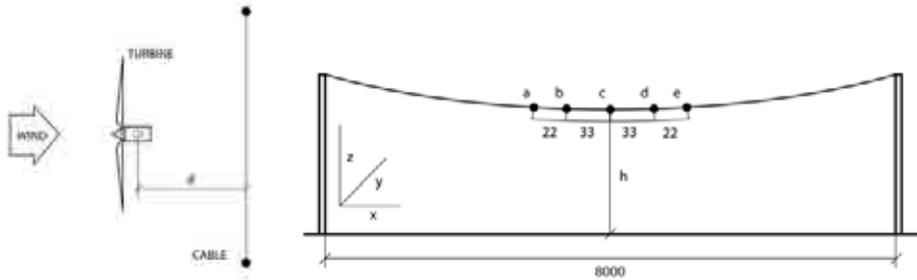
Fig.3: (a) Wind turbine and aeroelastic cable model relative position - (b) Marker
position and reference frame.

In figure 4 the mean y displacements of the five markers are reported for different operating condition at U = 2.12 m/s. It is possible to observe, comparing the case without the wind turbine against the others, that displacements along the wind direction are bigger when the wind turbine is put upwind the cable model. Considering the same height of the OHL from the ground and two different relative distances between the wind turbine and the OHL, bigger displacements are recorded when the cable is closer to the wind turbine. Comparing results at d = 2.5 D, it is possible to observe that the mean lateral displacement is bigger when the OHL is at the lowest height from the ground.
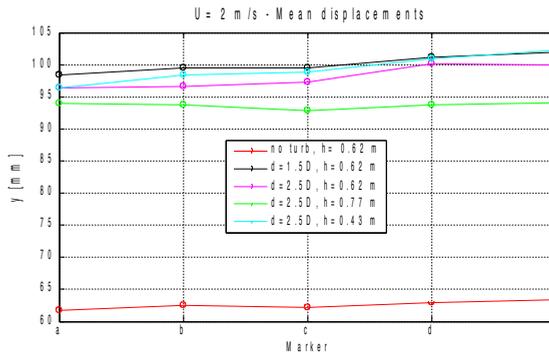
Fig.4 : Mean y displacement of the markers

This work has covered the whole measurement and 3D reconstruction pipeline and presents an innovative and complete framework for displacement analysis in wind tunnel tests. Some significant experimental results have been presented.

REFERENCES

[1] G. Diana , F. Resta , A. Zasso , M. Belloli and D. Rocchi, Forced motion and free motion aeroelastic tests on a new concept dynamometric section model of the Messina suspension bridge, *Journal of Wind Engineering and Industrial Aerodynamics*, *92,* 2004, 441-462.
[2] Zhengyou Zhang, A Flexible New Technique for Camera Calibration, *Technical Report MSR-TR-98-71*, Microsoft Research, 1998
[3] Trucco, Verri, *Introductory techniques for 3D Computer Vision* (Englewood Cliffs, NJ, Prentice-Hall, 1998).
[4] Hartley, Zisserman, *Multiple view geometry in Computer Vision*, Cambridge University Press, 2000.
[5] ISO, Guide to the Expression of Uncertainty in Measurement (GUM), 1995.
[6] Gonzales, Woods, *Digital Image Processing using Matlab* (Englewood Cliffs, NJ, Prentice-Hall, 2004).

Drag coefficients of lattice masts from full-scale wind-tunnel tests

C. T. Georgakis[*], U. Støttrup-Andersen[†], M. Johnsen[*], M. G. Nielsen[†], H. H. Koss[*]

[*] *Department of Civil Engineering, Technical University of Denmark, Building 118, Brovej, 2800 Kgs Lyngby, Denmark, cg@byg.dtu.dk, mariejohnsen5@gmail.com, hko@byg.dtu.dk,*

[†] *Masts and Towers, Rambøll A/S, Teknikerbyen 31, 2830 Virum, Denmark, usa@ramboll.dk, mon@ramboll.dk*

ABSTRACT

The evaluation the wind loading of older lattice masts using the current Eurocodes often reveals that these masts should have little or no available reserve load bearing capacity. Nevertheless, it is rare that masts collapse due to wind, as in most cases collapses can be credited to other causes, e.g. construction faults, bearing failures and poor maintenance. This implies that the current Eurocodes may be overly conservative when estimating the wind loading – with the main cause of this most-likely attributable to the erroneous evaluation of the drag coefficients for lattice masts.

The erroneous evaluation might be traced back to a series of wind-tunnel tests performed in the United Kingdom in the 1970's on scaled models of lattice masts (Whitbread, 1977). As most modern lattice masts are constructed with circular hollow sections, testing at the appropriate Reynolds numbers is important when determining the drag coefficients. The current paper hopes to address the aforementioned problem of testing at scale, by presenting the drag coefficients of several typical lattice mast configurations tested at full-scale.

Four different lattice mast configurations were chosen and built for section model testing. For all of the configurations, the mast is an equilateral triangle in cross-section. The four configurations – 1A, 1B, 1C and 2A, are presented in Fig.1.

Contact person: Christos Georgakis, Associate Professor, Department of Civil Engineering, Technical University of Denmark, Building 118, Brovej 2800 Kgs Lyngby, Denmark, tel. +45 4525 1949, E-mail cg@byg.dtu.dk
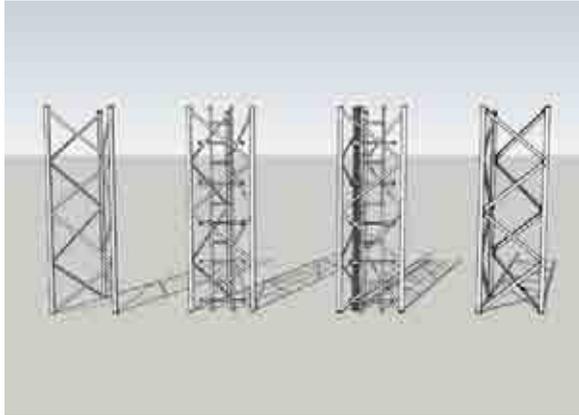
Figure 1: Lattice mast configurations used for full-scale section model testing. From left to right: 1A, 1B, 1C, 2A.

Each section is 3.0m long with a leg-to-leg distance of 1.2m. The diameter of the circular hollow legs is 76mm in all cases and the diameter of the diagonal bars is 33mm for the first three configurations (1A, 1B and 1C, Fig.1). The diagonals in the fourth and final configuration are angles 50mm x 50mm, with a plate thickness of 5mm.

Configuration 1A is a plain lattice mast without an internal ladder or feeders. Configurations 1B and 1C have an internal ladder and an internal latter with attached feeders, respectively. Configuration 2A has no ancillaries, similar to 1A. All of the models were constructed in galvanised steel.

For the tests, the models were placed on rotating turntables horizontally, with the ends attached to 6-DOF dynamic force transducers, which allowed for the measurement of the shear forces parallel to the wind and vertically perpendicular to the wind (Fig.2). The moments about the horizontal axis were also measured.

Figure 2   Turntable and force transducer configuration

The rotating turntables were placed in flow splitter plates that measure 4m x 4m and that were 3m apart (Fig 3).

Two different flow conditions were used to test the mast section, namely smooth and turbulent. Smooth flow was found to have a turbulence intensity of 1.1%, whilst the turbulent flow was found to have an intensity of 9.6%. The turbulence generating grid is shown in Fig.3.

Figure 3: Configuration 1A placed on the rotating turntables between splitter plates
in wind-tunnel with turbulence grid.

The wind-tunnel tests were undertaken at the Velux closed-circuit wind-tunnel in Østbirk, Denmark. The test section of the wind-tunnel is partially open, with the inlet measuring 3.4m x 3.4m and a maximum smooth flow velocity in the current test configuration of 45m/sec.

The results from the smooth-flow tests show that both Eurocode 3 (2007) and ESDU (1993) may be underestimating drag coefficients for several of the mast configurations. Fig.4 shows the Reynolds-dependant drag coefficients for mast configuration 1A at 0 and 60 degrees angle of attach, as obtained from the full-scale tests. The resulting coefficients are compared to those provided by Eurocode 3 and ESDU.
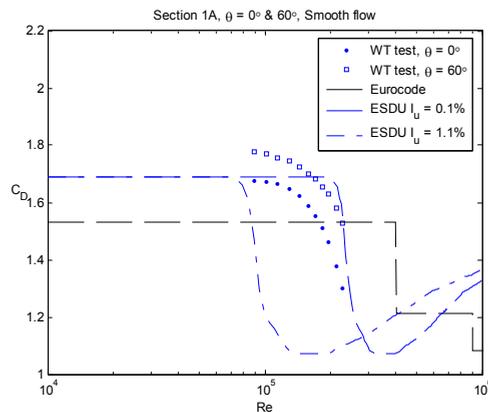
Figure 4: Reynolds-dependant force coefficients in smooth flow for configuration
1A, 0 and 60 degrees angle of attack.

Contrary to the results from the smooth-flow tests, the drag coefficients for the turbulent-flow tests show that both Eurocode 3 and ESDU are generally overestimating drag coefficients for the majority of the mast configurations. Fig.5 provides the comparison of the Reynolds-dependant drag coefficients for mast configuration 1A at 0 and 60 degrees angle of attach, under turbulent flow, whilst Fig.6 provides the velocity-dependant drag coefficients for the same configuration.
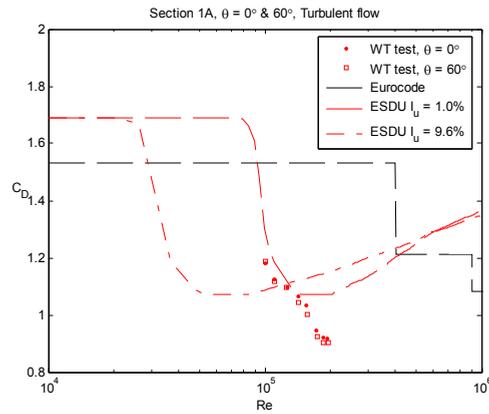
Figure 5: Reynolds-dependant force coefficients in turbulent flow for configuration 1A, 0 and 60 degrees angle of attack.
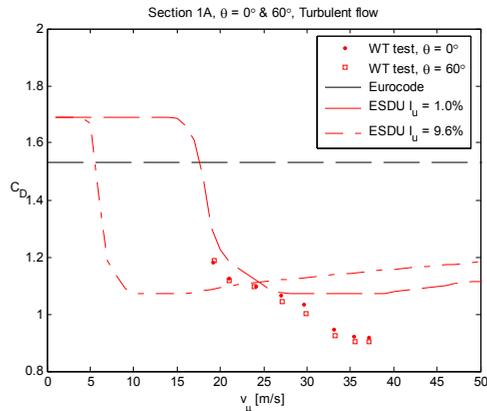
Figure 6: Velocity-dependant force coefficients in turbulent flow for configuration 1A, 0 and 60 degrees angle of attack.

ACKNOLEDGEMENTS

REFERENCES

Whitbread, R. E (1977), "Wind Loading on Lattice Towers", Report on Project Number P352003, National Maritime Institute, UK

Eurocode 3: Design of steel structures - Part 3-1: Towers, masts and chimneys - Towers and masts. DS/EN 1993-3-1 (2007)

ESDU 81028 (1993): Lattice Structures, Part 2: Mean Fluid Forces on Tower-Like Space Frame

Leonardo, the wind and the flying sphere

G. Bartoli[1], A. Borsani[1], C. Borri[1], A. Martelli[2], L. Procino[1], A. Vezzosi[3]

[1]*CRIACIV – Inter-University Research Centre on Building Aerodynamics and Wind Engineering, Italy, gbartoli@dicea.unifi.it, alessandra.borsani@pin.unifi.it, cborri@dicea.unifi.it, lorenzo.procino@pin.unifi.it*

[2]*Studio M, Florence, Italy, studium.firenz@libero.it*

[3]*Museo Ideale Leonardo Da Vinci, Italy, info@museoleonardo.it*

Keywords: Leonardo Da Vinci, flying sphere.

ABSTRACT

The Logo of the 5th European and African Conference on Wind Engineering has been obtained by re-elaborating a drawing by Leonardo Da Vinci, representing a flying sphere carrying a male body in its center.

Amongst several other worldwide known sketches and drawings, this one remained quite unknown since it has been discovered only in 1966, as a part of a Code found in Madrid's Library, but (as usual for the Genius of Vinci) it offers several very interesting aspects.

First of all, among all the "flying machines" conceived by Leonardo, the symbolic content of this one is very impressive: the human being is therefore *assigned* to the center of the giant flying object and is always dominating the machine and its elements. The human being is acting like the magnetic needle of a compass, and his movements cause the object to rotate.

The description, in ancient Italian delivered by Leonardo, is quite impressive, and it can hardly be translated into English:

"Sia fatta una simile ventola, come qui è figurato, e sia composta di zendalo, corde, canne e aste, di diamitro 20 bracci o più. Nel mezzo della quale sia collocata una balla traforata, fatta

Contact person: Lorenzo Procino, CRIACIV – Inter-University Research Centre on Building Aerodynamics and Wind Engineering , Piazza Ciardi 25, 53100 Prato;
E-mail lorenzo.procino@pin.unifi.it

di cierchi verdi, che sieno d'olmo. E sia detta balla con tali cierchi aconcia a uso di bussola di calamita, e nel mezzo d'essa balla stia un omo. E sia tale strumento collocato sopra uno monte, al vento, e tale strumento s'acompanierà col dorso de' venti, e ll'omo sempre starà in piedi"

More or less, in English this paragraph would sound like: "*One builds such a "fan", like the one reported in the figure, made out of clothes, rods, reeds and trusses, with a diameter of 20 arms or more. One places in the centre an open-work light bale, made by green rims, circles of elm-wood. And that bale with such rims will be mounted like a lodestone in a compass, and in the middle of the bale a man will stand. Such a tool will be placed at the top of a hill, toward the wind, and such tool will move riding the ridge of the winds, while the man will always stand*".

a)   b)
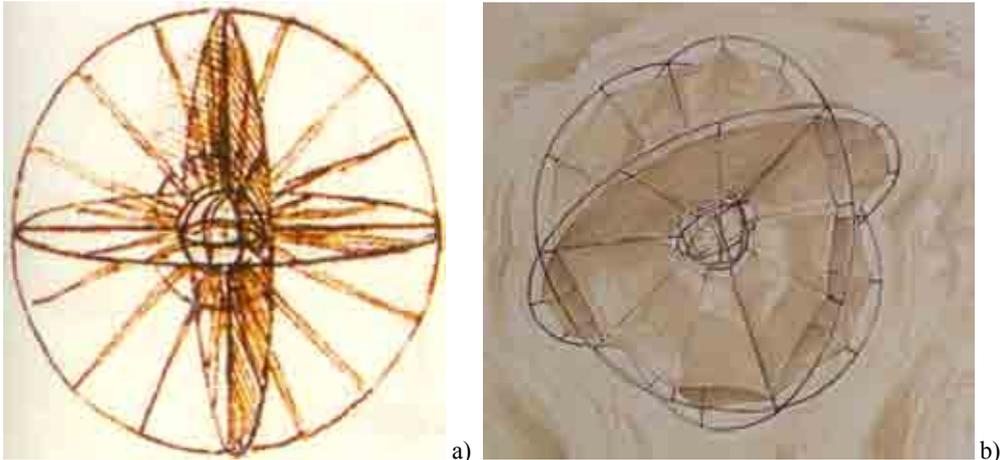
Figure 1: a) the original drawing made by Leonardo; b) reconstruction of the
Leonardo's idea

As it can be immediately realised, Leonardo did not only imagine the "shape" of his invention, but he also took care of the materials to be used. This is only one of many studies in which Leonardo, after having developed a project, kept on searching for forms and materials which were more and more suitable to the innovative functions of the new machine.

This is the reason why he introduced and experimented new materials; he forecasted the use of "plastic" materials, by creating his "*mistioni*" (mixtures) which could have been used to make jewels and tools, and those "unbreakable objects" that "*gittati a terra non si romperanno*" (even if thrown down would never break).

Leonardo mentioned the steel ("*acciaro*"), he studied coals and resins; he elaborated formulas for chemical compounds, by distilling acids and other substances equivalent to nail polish remover.

Moreover, a great effort was devoted by Leonardo to the investigation of modular structures, joints and materials for every light and resistant sail.

Recently, the Museo Ideale "Leonardo Da Vinci" has developed the idea of reproducing, at full scale, Leonardo's dream of the "flying sphere" and make it actually fly: the model will be constituted by carbon-fibre tubes, with teflon of rubber joints, while the sails will be made out of kevlar. At the centre a "cardanic" joint (named after Girolamo Cardano, born in 1501 and son of one of Leonardo's friend, Fazio) will allow the man inside the sphere to freely rotate in the space while maintaining his erected position during the flight.

With a purely artistic/demonstrative function (opening ceremonies of exhibitions and fares), several big spheres will be manufactured, and an artificial ventilation system will allow them to fly, in order to show that, once more, it is possible to realize one of the Leonardo's ideas.

To enable the design of the full-scale sphere, an experimental campaign of wind tunnel tests was commissioned to CRIACIV, and a 1:25 model was manufactured and placed in the wind tunnel, allowing the same degrees of freedom of the real structure.
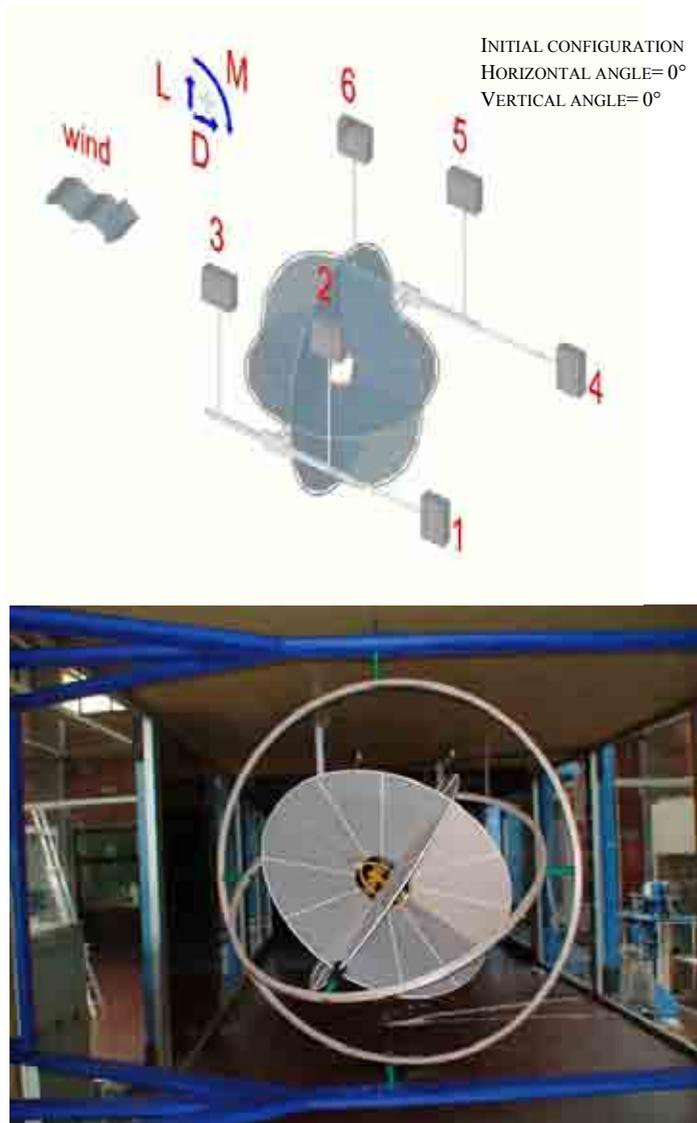
Figure 2: above: experimental setup (6 force measurement points) and sign convention; below: a view of the model in the CRIACIV wind tunnel

Several tests have been performed, in order to assess the (global) force coefficient (and hence the power necessary to make the sphere fly) and to check the "stability" of the reached positions. In fact, one has intuitively expected some wind-incoming directions which will induce a pure rotation the

sphere around one of its symmetry axes.

Some of the obtained results are sketched in Figure 3. Due to confidentiality obligations, force and moment coefficients are reported in a comparative form, i.e. the real values have been normalized with respect to the maximum absolute values.

Results refer to two different configuration: in the first, wind is blowing against the diameter of one of the two main rims, and the angle of incidence has been varying along the vertical axis (horizontal rotations of the sphere); in the second test, measurement have been performed in the same way, starting from the angle 0° referred to as the other main axis (that is 45° apart and above the previous position).

In the full paper, the obtained results will be commented on in details and the feasibility of the whole project will be also addressed.
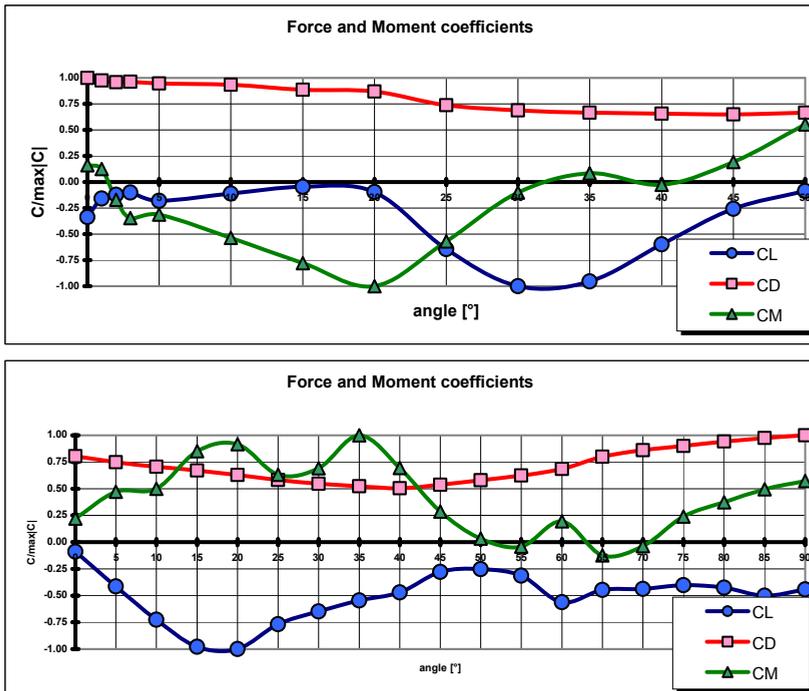
Figure 3: obtained results for two different tested configurations: angle of incidence = 0° (above), angle of incidence = 45° (below); coefficients are plotted as ratios with respect to their maximum absolute values

Field Measurement of Wind Pressure on a Double Skin with a Ventilator

1st H.KAWAI, 2nd H.Nishimura, 3rd M.Suzuki, 4th Y.Oura

1 Kyoto University, kawai@dpri02.mbox.media.kyoto-u.ac.jp
2 General Building Research Corporation of Japan, nishimura@gbrc.or.jp
3 Kajima Technical Research Institute, masayasu@kajima.com
4 Sankyo Tateyama Aluminum ,Inc, y_oura@sthdg.co.jp

Keywords: double skin, peak wind load, field measurement

INTRODUCTION

Recently, double skin glazing façades are becoming popular for modern buildings in Europe, U.S.A., Asia and other countries with new glass supporting systems. The façade can save not only energy for air-conditioning, but also can intake fresh air into a room even under moderate strong wind condition.

Kawai et al (2007) measured wind pressures on double skins by wind tunnel experiments and proposed the design wind loads on the outer skin and the inner skin. Inculeta et al (2007) measured wind pressures on double skins of a 230m high building by using a large scale detailed model set in a boundary layer wind tunnel. Chino et al (1993, 1997) measured wind pressure on a double skin of a full scale building and compared with wind tunnel results.

This paper describes characteristics of wind pressure on a double skin with a ventilator according to field measurements in natural wind for a model with 4 full scale double skin windows. The window in the inner skin can be open or closed and a constant air volume ventilator was installed between the the inner skin and the room.

Contact person: 1st H. Kawai, Kyoto-University, address DPRI., Gokasyo, Uji, Kyoto 350-0313, Japan,
telephone +81-744-38-4165, FAX +81-744-38-4170.
E-mail kawai@dpri02.mbox.media.kyoto-u.ac.jp

OUTLINE OF MEASUREMENT

The model is 5.825m(height) x 5.2m(width) x 2.52m(depth) with air inlets at the top and the bottom, which has two full scale double skin windows (2.052m x 1.4m) on the west side and the east side respectively as is shown in Fig.1. The gap between the outer skin and the inner skin is 0.2m. The inner window has a ventilator at the side, of which width is 0.1m and can ventilate air of $300m^3/h$ for 100Pa. The model was set in an experimental field of Shionomisaki Wind Effect Laboratory of DPRI, Kyoto University.
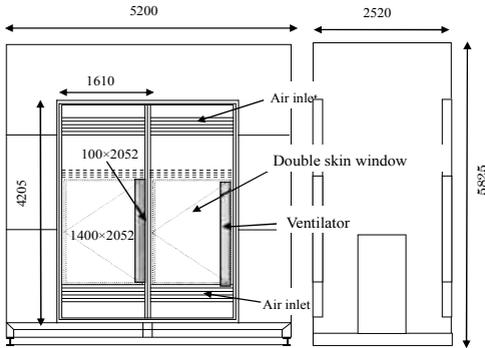
Fig.1 Model with four double skin windows
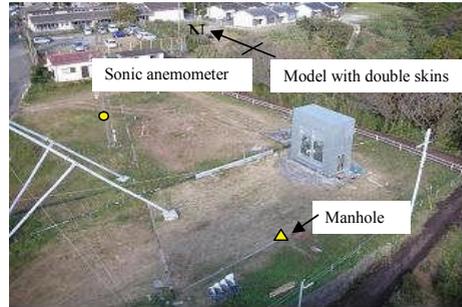
Fig.2 Model set in a field

The reference wind velocity was measured by a three dimensional ultra sonic anemometer at 5m height from the ground where is apart 20m north-west from the model. The reference static pressure was measured in a manhole where locates apart 11m south-west from the model (Fig.2). The 23 pressure holes were set on the outer skin, 22 holes on the cavity side of the inner skin, and 12 holes on the room side of the inner skin for the west side. On the other hands, 13 holes were set on the outer skin, 14 holes on the cavity side of the inner skin, and 6 holes on the room side of the inner skin for the east side. The room pressure was measured also at the north side and the south side (Fig.3). All signals were sampled every 0.01 seconds simultaneously and stored in a hard disk of a computer every 10 minute.
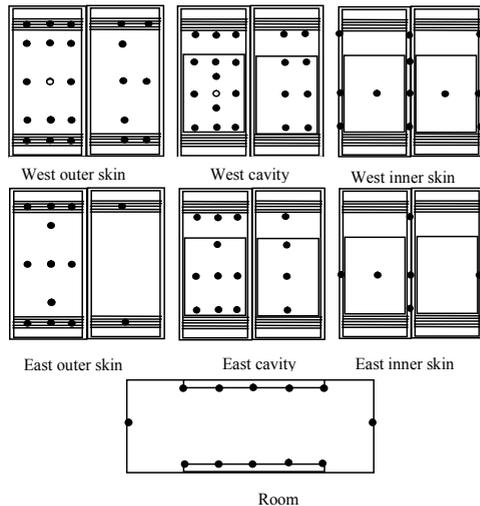
Fig.3 Pressure measurement points

RESULTS OF MEASUREMENT

The measurement was carried out from December 2006 to March 2008. The record analyzed in the paper is obtained from 6th 17:32 to 8th 8:30 January 2007, when 10 minute mean wind speed was larger than 6m/s during the period and the maximum peak gust was 29.6m/s, and wind attacks from west or north west.

Fig.4(a) shows records of wind direction, wind speed and pressure on a center point of the outer skin, the cavity side and the room side of the inner skin for the west side window and the east side window, when maximum peak gust of 29.4m/s was recorded. 10 minute mean wind speed was 11.6m/s and 10 minute mean wind direction is 277 degree (nearly westerly wind). Fig.4(b) shows 10
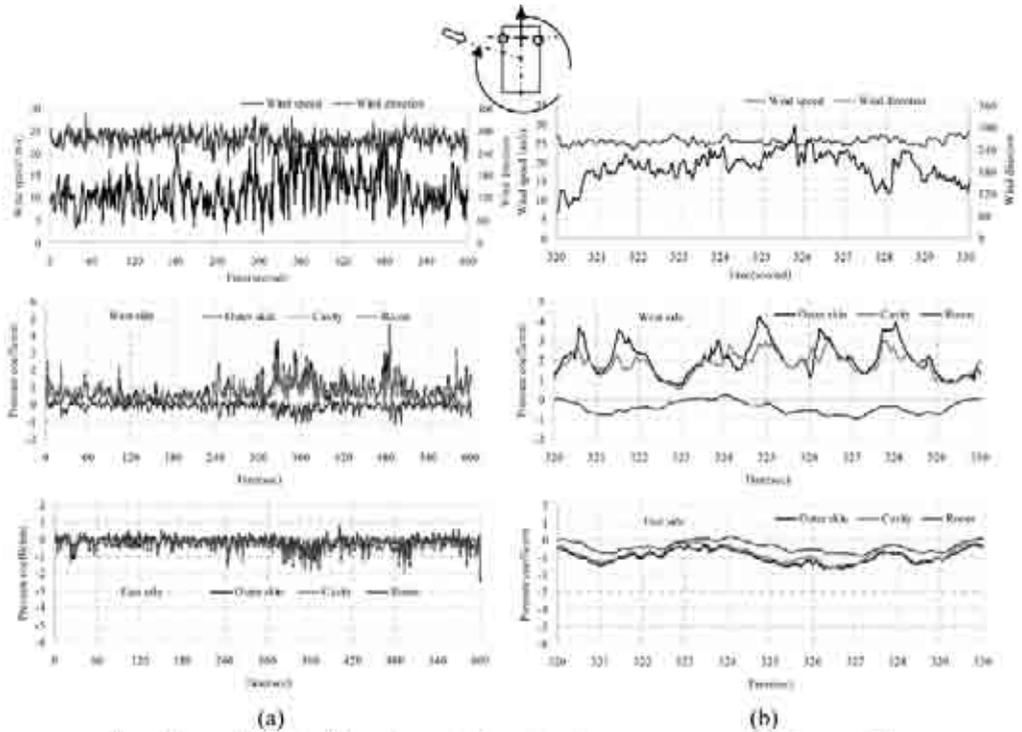
Fig.4 Records of wind direction, wind speed and pressure on west and east windows.
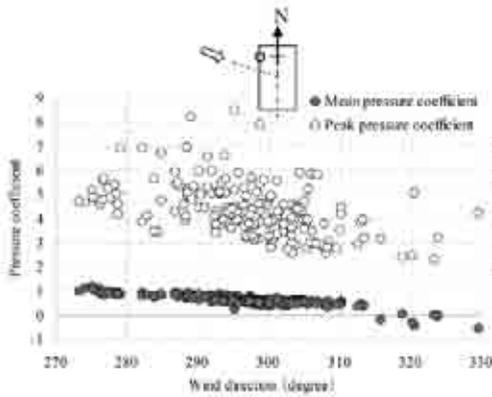
Fig.5 Mean and peak pressure coefficients on the west side outer skin normalized by the 10 minute mean velocity pressure.
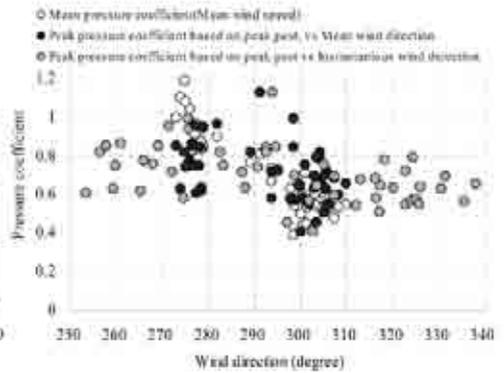
Fig.6 Peak pressure coefficients on the west side outer skin normalized by the peak velocity pressure.

seconds records when the maximum peak gust was observed. In the figure, the pressures are normalized by the mean velocity pressure.

The pressures were fluctuating very violently and non-stationary as shown in Fig.4 and the peak

pressure coefficient for the west side outer skin is more than 4. The pressures on the cavity side of the inner skin fluctuate similarly to that on the outer skin, but the peak pressures are about 80 % of that on the outer skin.

Fig.5 and Fig.6 show the pressure coefficients for the west side of the outer skin when wind attacks normal or from an oblique angle to the west side of the outer skin. The pressure coefficients shown in Fig.5 are normalized by the mean velocity pressure and are plotted against the mean wind direction. The peak pressure coefficients are very large and are scatter. The maximum peak pressure coefficient is larger than 8.

On the other hand, the pressure coefficients shown in Fig.6 are normalized by the peak gust velocity pressure in the 10 minute record and are plotted against the mean wind direction and the wind direction when peak gust occurred. The magnitude of the peak pressure coefficients normalized by the peak velocity pressure are the almost same as the mean pressure coefficients shown in Fig.5.
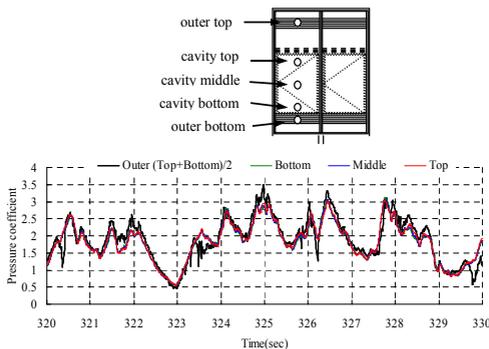
Fig.7 Pressure fluctuations on the cavity side of the inner skin.
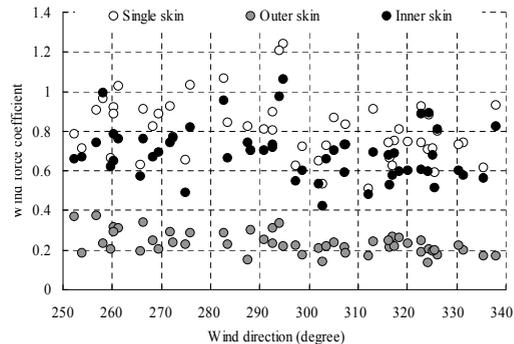
Fig.8 Peak wind force coefficients on the single skin and the outer skin and the inner skin.

Fig.7 shows the pressure fluctuation on the cavity side of the west side inner skin. The pressures on the top, the middle and the bottom measurement points are almost same at any instant. The bold black line shows the average of pressures on the outer skin at a top air inlet and a bottom air inlet. The average of the pressures on the outer skin is almost the same as the pressure on the cavity side at any instant, which means that pressure in a cavity can be estimated from pressure on an outer skin.

Fig.8 shows the comparison between the peak wind force coefficients on the ordinal single skin and the peak wind force coefficients on outer skin and the inner skin of the west side, which are normalized by the peak gust velocity pressure. The peak wind force on the outer skin is 29% of that on the single skin and the peak wind force on the inner skin is 86% of that on the single skin.

REFERENCES

H.Kawai(2007): Wind Force on Double Skin Façade with Building High Grazing, Proceedings of The 12th International Conference on Wind Engineering, 311-318

Inculeta, D. R. Navarro, M.G. Isyumov, N(2007): The effects of an open double facade on structural and cladding wind loads, Proceedings of The 12th International Conference on Wind Engineering, 319-326

Chino, N., Iwasa, Y., Hagiwara, T., Matagi, Y. and Sato, H.(1993), Wind load acting on double composite exteriors - A study on internal pressure of double composite exteriors, Jour. Struc. Constr. Engng, AIJ, No.448, June, 29-36

Chino, N., Iwasa, Y. and Sato, H. (1997): Field measurements of wind load on double composite exteriors, AIJ Jour. Technol. Des. No.4, March, 25-30

Experimental investigation on aerodynamic performance of damaged wings

S.Djellal, A.Ouibrahim

s.djellal@gmail.com   – *EMP, BP 17, Bordj el Bahri, 16111, Alger, Algeria*
ouibraa@yahoo.fr   – *Universite Mouloud Mammeri,15000, Tizi Ouzou, Algeria*

Keywords: aerodynamic, aircraft, damage, drag, fineness.

ABSTRACT

The principal objective of this paper is to predict the aerodynamic response for two and three-dimensional bodies (wings, aircraft and UAV) to the damage. We consider that the damage is only located on the wings, which are from the aerodynamic point of view, the most critical components of the airplane.

The scenarios of damages are expressed in terms of diameters and localizations of the holes of simulated damage in the wing.

In Irwin et al. (1995), the most common type of damage used in simulations is the circular through hole. The study of other shapes reported by Mani & Render (2005) has not shown noticeable differences. The damage size is expressed in terms of a percentage 'diameter d to the local chord length c'. For our tests, five diameters, 0.05c, 0.1c, 0.2c, 0.3c and 0.4c, have been considered.

It is shown that the presence of the damage induces a decrease of the lift and an increase of the drag. This means in other words a loss of the aerodynamic performances. This influence on the aerodynamic coefficients can be attributed to the flow through the hole which in one hand, provokes a perturbation of the pressure distribution between the intrados and the extrados and in the other hand, produces an additional pressure drag. Visualizations consequently performed have indicated as a

Contact person: S.Djellal, Ecole Polytechnique, EMP, BP17, Bordj el Bahri, 16111, Alger, Algeria.
E-mail s.djellal@gmail.com

matter of fact a link of this influence with the type of jet issuing from the damage hole.

Moreover, the various test runs showed that the losses in the aerodynamic performances are functions of the diameter of the damage, the geometry of the wing (taper ratio) and the localization according to the span and the chord.

Besides the aerodynamic performance losses, the effect of the damage is also characterized by a stall angle shift towards higher values and a decrease of the maximum lift coefficient C_L.

Finally, in terms of degradation (or loss), the lift coefficient C_L appears to be more affected than the drag coefficient C_D in most of the damage cases.

With the fineness representation (ratio of C_L over C_D, usually used to evaluate the whole performance of a wing), we can better and fully appreciate the damage extent, result of gathered damages occurring to both C_L and C_D.

For example, Figure 1 gives the rate of fineness loss for different hole diameters. We notice that the fineness, f, is drastically degraded by the damage diameter compared to the degradation of C_L and C_D. For the largest hole (0.4c), the rate of loss reaches 40% to 10% for a varying from 2° to 14°.
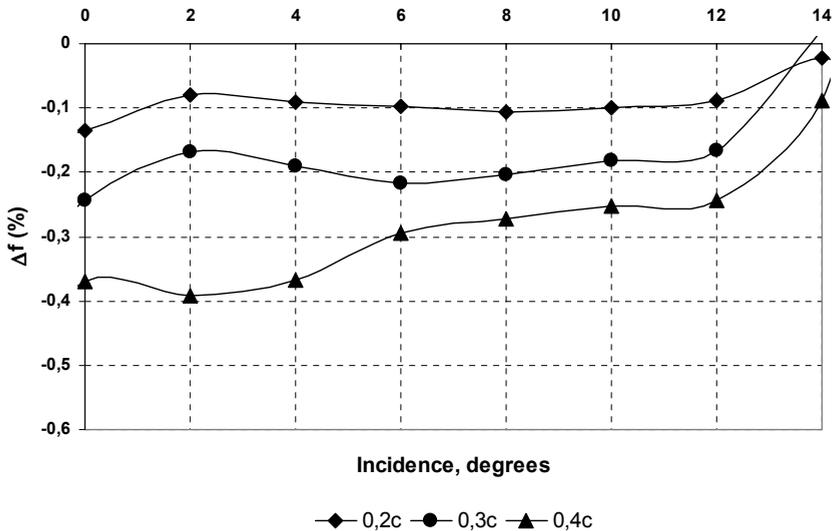
Figure 1: Rate of fineness loss for different hole diameters

REFERENCES

Irwin A. J., Render P. M. (2000) "The Influence of mid-chord battle damage on the aerodynamic characteristics of two-dimensional wings," The Aeronautical Journal, Vol. 104, No. 1033, pp. 153-161.

Mani M., Render P. M. (2005). "Experimental Investigation into the Aerodynamic Effects of Airfoils with Triangular and Star Shaped through Damage," AIAA Paper 2005-4978.

**COMPUTATIONAL FLUID DYNAMICS (CFD)
AND COMPUTATIONAL WIND ENGINEERING (CWE)**

LES study on urban roughness effects on turbulence statistics of atmospheric boundary layer

1st K. Nozawa, 2nd M. Ohashi, 3rd T. Tamura, 4th Y. Okuda

1st *Shimizu Corporation, nozawa@shimz.co.jp*
2nd *National Institute of Land and Infrastructure Management, ohashi-m92j7@nilim.go.jp*
3rd *Tokyo Institute of Technology, tamura@depe.titech.ac.jp*
4th *Building Research Institute, y_okuda@kenken.go.jp*

Keywords: Large-eddy simulation, Actual urban area, Atmospheric boundary layer.

ABSTRACT

The turbulent boundary layer flow over urban-city is studied using large eddy simulation (LES). In order to study urban-type of wind flows, the area around Tokyo Railroad Station at the center of Tokyo is selected as a computed domain which has Marunouchi area in the west and Yaesu area in the east. Currently the Marunouchi area is surrounded with many tall buildings, while the Yaesu area is occupied by low-rise and middle-rise buildings. In this study the wind flow is assumed to a flow from south-southwest. By comparing the mean velocity profiles with experimental data we validate the accuracy of turbulence structures formed in and above the canopy predicted by LES. Spatially averaged Reynolds stress profiles and dispersive shear stress profiles are examined against both Marunouchi and Yaesu areas to investigate the possibility of developing the canopy model on urban area from those statistical data.

Wind tunnel test is carried out at Building Research Institute to verify the accuracy of LES comparing the mean velocity profiles in urban area. Test section of the wind tunnel is 3.0m width and 2.5m height (Fig.1). The model scale is 1/750 and mean wind speed at 1000mm height is 5.5m/sec. The vertical profile of streamwise mean velocity fits to exponential law with its components α=0.33. Mean velocity vertical profiles are measured using I-type hot wire and its sampling time is about 10 minutes in reduced time.

Contact person: 1st K. Nozawa, Research Institute, Shimizu Corporation, 3-4-7 Etchujima, Koto-ku, Tokyo, Japan, +81-3-3820-8327, +81-3-3820-5959. Email nozawa@shimz.co.jp

The computational region has horizontally 2.5km length in streamwise direction and 2km width in transverse direction (Fig. 2). The horizontal mesh size is 4m in the both directions and the height of the lowest mesh is around 1m. The oncoming turbulent inflow is generated using the quasi-periodic method. The computational region of generating inflow is 2km length and 1km width. The boundary layer thickness has developed to almost 800m while the height of the computational region is 3km (Fig.3).

The Navier-Stokes equations for an incompressible fluid combined with subgrid-scale turbulent viscosity are used for the large-eddy simulation. The filtered equations of continuity and Navier-Stokes equations can be described as follows.

$$\frac{\partial \overline{u}_i}{\partial x_i} = 0 \tag{1}$$

$$\frac{\partial \overline{u}_i}{\partial t} + \frac{\partial \overline{u}_i \overline{u}_j}{\partial x_j} = -\frac{\partial \overline{p}}{\partial x_i} + \frac{\partial \tau_{ij}}{\partial x_i} + \text{Re}^{-1} \frac{\partial^2 \overline{u}_i}{\partial x_k \partial x_k} \tag{2}$$

$$\tau_{ij} = -2\nu_{SGS}\overline{S}_{ij} \tag{3}$$

$$\nu_{SGS} = C\Delta^2 |\overline{S}| \tag{4}$$

Where Δ is the filter size, $\overline{S}_{ij}$ is the velocity gradient tensor and $|\overline{S}|$ is $\sqrt{2\overline{S}_{ij}\overline{S}_{ij}}$. The dynamic procedure based on the Smagorinsky model is used to identify the model coefficient C. Fourth-order central difference scheme is used as spatial discretization and second-order time accurate explicit Adams-Bashforth differencing scheme is used for the convective terms and a part of the SGS turbulent diffusion terms. The rest of the diffusion terms are treated semi-implicitly by using Crank-Nicolson formulation. The Reynolds number based on the free stream velocity and the boundary layer thickness is 93,000. The periodic boundary condition is set to the side wall and slip condition is set at ceiling of the computational domain. The outflow boundary condition is convective type boundary condition. The height data for buildings are derived from 2m resolution GIS data (RAMS-e, KOKUSAI KOGYO CO.). The buildings are modeled using immersed boundary method.

The quasi-periodic boundary condition is introduced in streamwise direction to simulate the spatially developing boundary layer in generating turbulent inflow. The quasi-periodic boundary condition was proposed by Lund (1998) and modified by Nozawa and Tamura (2001) to apply to a rough-wall turbulent boundary layer flow. In this method the velocities at the recycle station are rescaled and reintroduced at the inlet and the outflow boundary is set far downstream of the recycle station. The method is originally limited to the generation of turbulent boundary layer over smooth surfaces. We employ the resistance formula of sand-roughened plate by Prandtl (Schlichting, 1979) to introduce the quasi-periodic boundary condition to a flow over rough surface. In this simulation the boundary condition at the ceiling is set as follows.

$$\partial U / \partial z = 0, \quad \partial V / \partial z = 0, \quad W = U_0 \, \partial \delta^* / \partial x \tag{5}$$

Where U_0 is the free stream velocity and δ^* is the displacement thickness of the boundary layer.

Figure 4 compares mean velocity profiles at both Marunouchi and Yaesu areas with experimental data. Both profiles are sufficiently in good agreement with experimental data. It could be said that if the inflow turbulence is properly generated not only the outer-layer mean velocity profiles but also the roughness sublayer mean velocity profiles which are strongly influenced by local roughness elements directly can be predicted with sufficient accuracy by LES. The spatially-averaged Reynolds shear stress profiles and dispersive shear stress profiles are compared for various type of urban roughness in Fig. 5. Dispersive shear stress is defined as follows.

$$\langle u''w'' \rangle = -1/A \int \left(\overline{u} - \langle \overline{u} \rangle \right)\left(\overline{w} - \langle \overline{w} \rangle \right) dA \tag{6}$$

Dispersive shear stress represents the contribution to momentum transfer from correlations between point-to-point variations in the time-averaged flow. Spatially averaged value is obtained by computing over 420m x 560m region in the Marunouchi area and 440m x 400m region in the Yaesu area. Mean height of the buildings in the Marunouchi area is 84m and the height of the tallest building is 197m. While in the Yaesu area mean height is 25m and the height of the tallest building is 75m. Spatially-averaged Reynolds shear stress profile at the inlet has local peak at 75m height. The maximum height of roughness blocks set upstream of the inlet is 75m. The Reynolds shear stress

profile of the Yaesu area almost corresponds to that of the inlet, while the profile of the Marunouchi area has a peak at around 160m height and decreases rapidly above the height of the tallest building in the Marunouchi area. Dispersive shear stress in the Marunouchi area has large value below the height of the tallest building and declines to almost zero just above that height. On the other hand, in the Yaesu area the profile of dispersive shear stress has peak around 60m height and gradually decreases. It declines to zero at almost five times height of the mean height of the buildings. The range of roughness effect does not reach three times height of the mean height of the buildings in the Marunouchi area. The instantaneous spanwise vorticity indicates that strong vortices formed in the wake of the buildings and are limited to three times height of the mean height of the building in the Marunouchi area. Strong vortices extend above the three times height of the mean height of the buildings in the Yaesu area. It shows a certain level of possibility that the turbulent wind over relatively large-scaled urban roughness can be represented by the urban-canopy model based on spatial averaging technique such as LES.

REFERENCES

Lund T. S., Wu X., Squires K. D. (1998). "Generation of turbulent inflow data for spatially-developing boundary layer simulations", J. Comp. Phys., 140, 233-258.

Nozawa K., Tamura T. (2001). "Turbulent boundary layer flow simulations over urban-like roughness using LES", Proc. Turbulent Shear Flow Phenomena vol.2, 443-448.

Schlichting H., (1979). "Boundary-Layer Theory, 7th Edition", McGraw-Hill Book Company.

Figure 1: Photograph of wind tunnel test model.
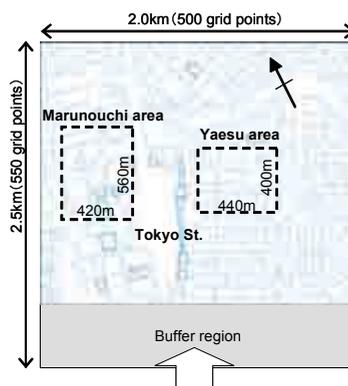
Figure 2: Computational region and spatially averaging area for Marunouchi and Yaesu.
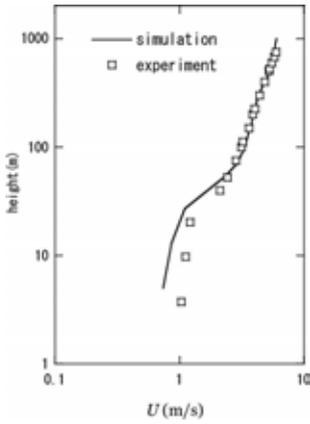
Figure 3: Mean velocity profiles at inlet.
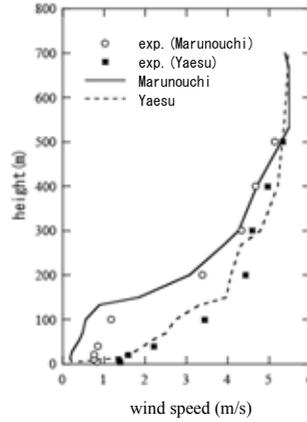
Figure 4: Mean velocity profiles at
Marunouchi area and Yaesu area.
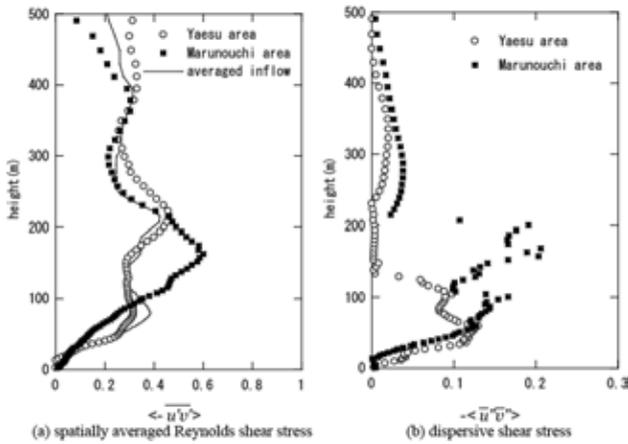
Figure 5: Spatially averaged Reynolds shear stress and dispersive shear stress profiles.
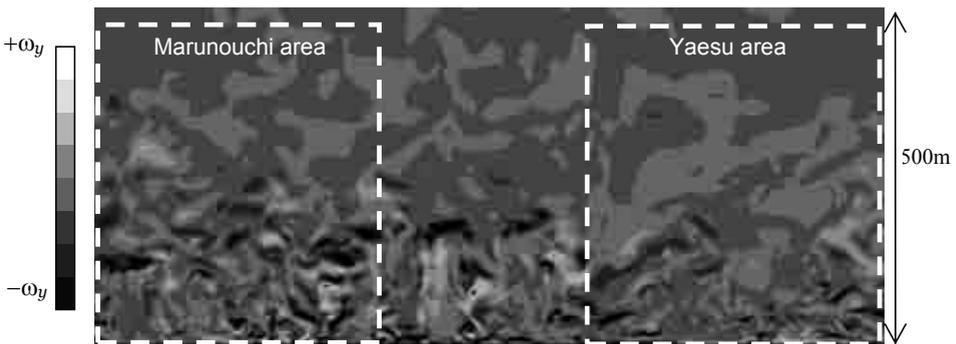
Figure 6: Instantaneous spanwise vorticity contour in mid section of the Marunouchi and Yaesu area.
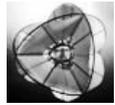
LES of wind turbulence and heat environment around dense tall buildings

Tsuyoshi Nozu[1], Takeshi Kishida[2], Tetsuro Tamura[3],
Yasuo Okuda[4], Hiroko Umakawa[5]

[1] *Shimizu Corporation, nozu@shimz.co.jp*
[2] *Wind Engineering Institute, kishida@wei.co.jp*
[3] *Tokyo Institute of Technology, tamura@depe.titech.ac.jp*
[4] *Building Research Institute, y_okuda@kenken.go.jp*
[5] *Pasco Corporation, haiwra9288@pasco.co.jp*

INTRODUCTION

For the mitigation of heat island effects on coastal cities, it is expected that the sea breeze come into the inland area of a city, where its cold air mingles with the hotter air over and inside the urban canopies. Therefore, it is important not to allow such a sea-breeze penetration to be obstructed by large-scaled buildings and structures on the ground surface. But recently several very tall buildings have been constructed in a concentrated manner near the coast line in Tokyo, so we are concerned about that these tall buildings block a current of sea breeze into a center of a city and amplify a heat-island effect on whole region of an urban city as well as a restricted area around tall buildings. There remain many issues on the existence of such an effect on the whole city. But we think that at least the implementation of an appropriate heat environment on the local area based on the specified re-developing project should be advanced in view of an urban planning.

For the numerical simulation to evaluate a local thermal environment in such a part of an urban region, it is important to reproduce the complex flows among many buildings and their wakes. Especially, for estimating the mitigation of heat-island effect by the meteorological local circulation such as a sea breeze, the numerical model which can predict time sequences of unsteady flow quantities is required because the convection brought about by fluctuation behavior of turbulent flows represents directly and strictly an intense and a range of heat transport. Hence, this study employs the LES (Large Eddy Simulation) technique for wind flow accompanied with heat around dense tall buildings existing in the urban area. Also, determination of the reference absolute values for the simulated wind velocity and temperature is supported by the result of the meso-scale meteorological model. The relation between the heat environment and wind turbulence around these buildings has been clarified. Accordingly we investigate details of a local thermal environment and provide a dominant role of the surface shape of a city from an environmental point of view.

Contact person: Tsuyoshi Nozu, Shimizu Corporation, 3-4-17 Etchujima, Koto-ku, Tokyo 135-8530, Japan
PHONE: +81-3-3820-6914   FAX: +81-3-3820-5955   E-mail nozu@shimz.co.jp

PROPOSAL OF A NEW LES-METEOROLOGY MODEL

Figure 1 illustrates a schematic of the computational model for hybrid method of LES and meso-scale meteorological model (MM5) concerning an urban heat island. For generating turbulent boundary layer under stable stratification based on the sea breeze characteristics, we set up the driver region that consists of two domains (Domain1 and Domain2). Domain1 generates the neutral turbulent boundary layer by using re-scaling technique (Lund et al. 1998) and Domain2 generates thermally stably-stratified turbulent boundary layer developing over the sea surface by using the temperature profile calculated by MM5. Domain3 reproduces the main region in Tokyo area of 1.75 km by 1.0 km and the boundary condition at ground surface is set with the GIS data, which can represent the realistic urban aspect with tall buildings in Tokyo. For setup of thermal boundary condition on the ground and building surface, the radiation temperature measured by air craft is utilized. By filtering the surface temperature field and quantifying approximately it based on the near-ground air measurement temperature, the thermal boundary condition on the bottom is given.

Wind and temperature fields with the urban scale can be simulated by the meso-scale meteorological model, while turbulent flow fields over and inside the urban canopy can be computed by LES that incorporates explicitly the effects of the actual shape for buildings and structures. Generally, LES can estimate the relative value for the wind flow to the reference value but cannot evaluate the absolute value. So, by using the simulated results of MM5, we give a temperature profile at inlet of the stable turbulent boundary layer in Domain2 and estimate a level of the actual wind velocity.

Table 1 shows the domain size, grid points and grid size for the computational domain.
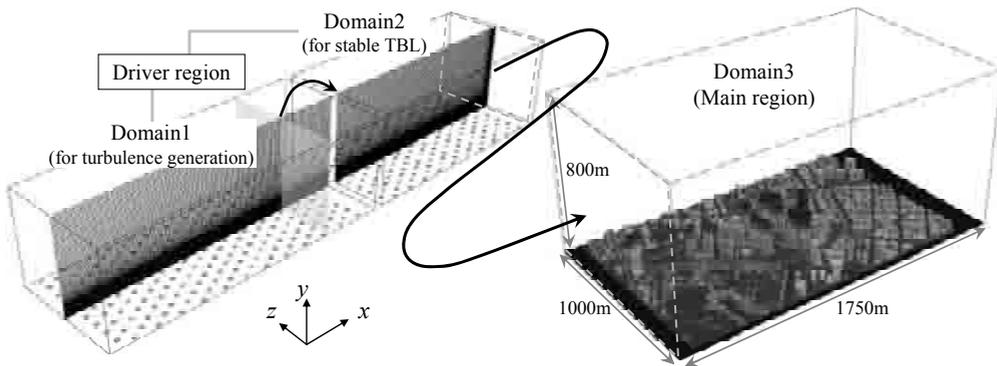
Figure 1: Schematic of the computational model for hybrid method of LES and meso-scale meteorology model concerning urban heat island.

Table 1: Computational domain, grid points and grid size.

	Streamwise(x)			Vertical(y)	Spanwise(z)
	Domain1	Domain2	Domain3		
Computational domains	5.0δ	+ 4.1δ	+ 3.5δ	1.6δ	2.0δ
Grid points	156	+ 151	+ 700	100	400
Grid size (wall unit)	18.9	+ $\frac{18.9}{\sim 2.95}$	+ 2.95	2.95~26.6	2.95

RESULTS

Figure 2 illustrates the LES results for instantaneous streamwise velocity and temperature fields in a vertical section of around dense tall buildings. In this figure, it can be confirmed that dense tall buildings block a current of sea breeze into the urban area and a kind of large cavity region is formed behind these tall buildings. In this cavity region, the heat convection as a result of mixing is active vertically and the high temperature region is recognized even at a high position.

Figure 3 shows time-averaged streamwise velocity field and temperature in vertical section and horizontal section at 60m height. It is recognized that the high temperature region behind a single tall building is small because of a small wake formed behind that, but the high temperature region behind a group of tall buildings is very large because of a merging large wake formed behind such an assembly. The extent of the impact for the heat environment reaches at about 300m downstream behind dense tall buildings and is nearly equal to the height of the buildings. While, at the side of the group of tall buildings, the cooling effect by sea breeze can be seen because of the high wind speed.

Figure 4 shows time histories of the wind velocity and temperature in various local points at 65m height. Above low and medium-rise buildings (outside dense tall buildings), the wind velocities are higher than those inside dense tall buildings, and temperatures are lower than those inside ones. In contrast, inside dense tall buildings, the penetration of a sea breeze between buildings does not advance efficiently in spite of a sufficiently large wind speed fluctuation. Accordingly the temperature magnitudes become higher and their fluctuations are relatively small, as a result of the small heat convection and diffusivity. On the other hand, in the wake behind dense tall buildings, the wind speed level and its fluctuation are very small and the temperature maintains the highest value as a result of heat stagnation.

CONCLUSIONS

In this study, we clarified the detail of the temperature environment within a local area around tall buildings in the urban area and we represented that the hybrid method is a powerful tool for predicting of the wind turbulence and the temperature environment in the urban area.

REFERENCES

Lund T. S. (1998). "Generation of turbulent inflow data for spatially developing boundary layer simulation", Journal of Computational Physics, 140, 233-258.
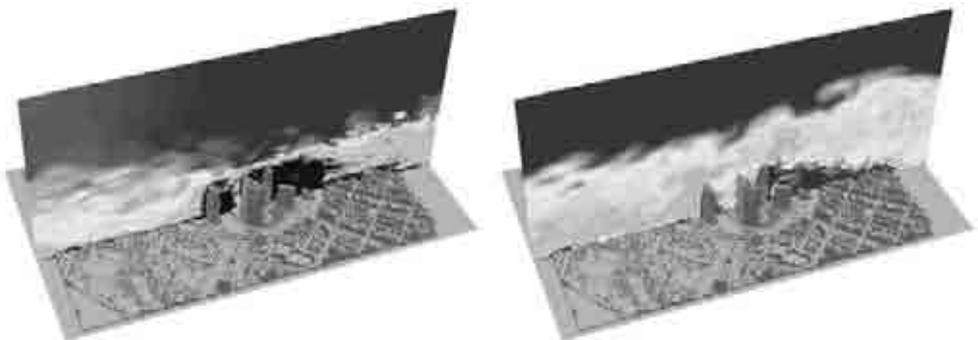
Figure 2: Instantaneous streamwise velocity and temperature field in the roughness layers over the actual city.

(a) Streamwise velocity field

(b) Temperature field
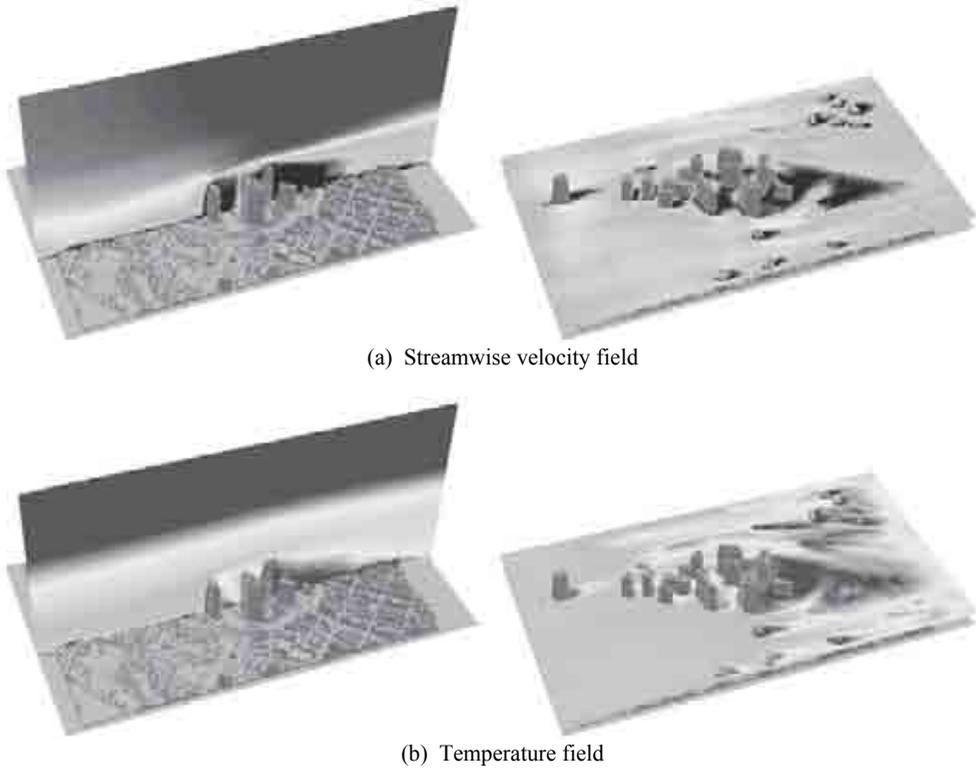
Figure 3: Time-averaged streamwise velocity field and temperature field in vertical section and horizontal section at 60m height.
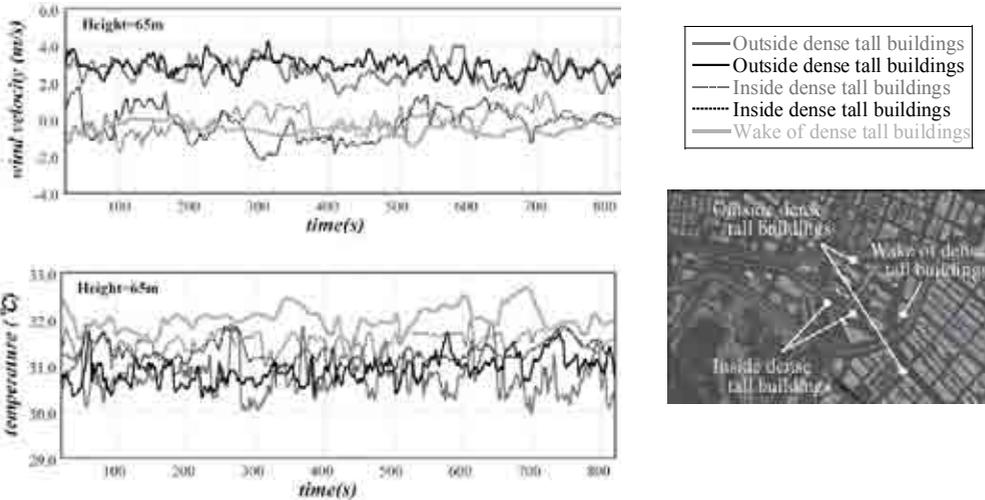
Figure 4: Time histories of the wind velocity and temperature in various local points at 65m height
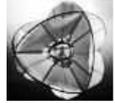
Fluid-structure interaction analysis with the ANSYS software in bridge aeroelasticity

1st G.Szabó, 2nd J.Györgyi

Phd student 1 – mr.gergely.szabo@gmail.com – Szolnok, 5000, Üstökös u. 4., HUNGARY

Associate professor 2 – gyorgyi@ep.mech.me.bme.hu

Keywords: bridge aeroelasticity, 3D flutter analysis, CSD, CFD, fluid-structure interaction.

ABSTRACT

Bridge flutter assessment is usually carried out by means of wind tunnel tests on sectional models. Aerodynamic derivatives can be obtained either through free vibration or forced vibration methods. By using the ADs, equations for flutter stability can be solved and the critical wind speed can be determined as well.

Nowadays, with a strong computational background, CFD simulations appear to be powerful rivals of the wind tunnel tests. Recently, a number of 2D simulations have been made in order to calculate the Ads of an ordinary bridge cross section. In the work of Zhiwen et al. (2008) the Ads of a box bridge girder were calculated with the forced vibration method. Examples for the free vibration method can also be found in the literature. In case of the sectional modeling approach, it is difficult to capture the really complex three-dimensional coupling of the bridge deck motion and the fluid flow around it. For bridge flutter prediction it is hard to find 3D coupled CSD-CFD simulations, but for wing flutter analysis WANG Yi-wei et al. (2008) have good results.

This paper firstly presents a 2D CFD simulation for a box bridge deck to obtain the Ads. Secondly, a three-dimensional coupled CSD-CFD simulation is introduced.

In our 2D study, a bridge cross section has been investigated. A 1:100 sectional model was made to test it in a wind tunnel. The ADs were determined by using the forced vibration method.

Contact person: 1st Gergely Szabó, Phd student, Szolnok, Üstökös u. 4.,HUNGARY, +3630/327-9262, +3612262096
E-mail mr.gergely.szabo@gmail.com

A professional robot-arm ensured the precise sinusoidal motions meanwhile force and moment signals were recorded. To check the results of the wind tunnel tests, a 2D mesh was made around the bridge shape. In Figure 1 the mesh can be seen. On the left side the initial state is shown. At the near region of the wall boundary the mesh has no distortion so to preserve its good quality. The motion of the bridge is handled by the moving of the farther mesh region. The motion frequency of the deck (rotation and heave) and the inflow velocity were varied in order to adjust the required reduced velocities. In Figure 2 the flow field can be seen at two different time steps at Ured=6.42 with rotational motion.
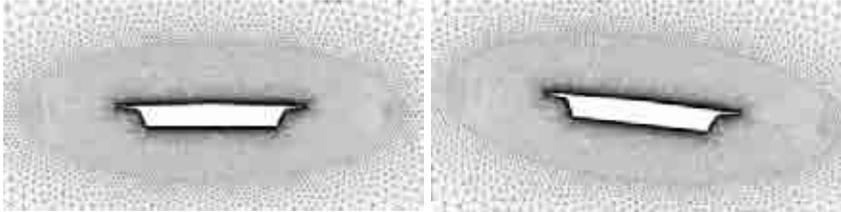
Figure 1: mesh around the bridge deck at two different time steps.
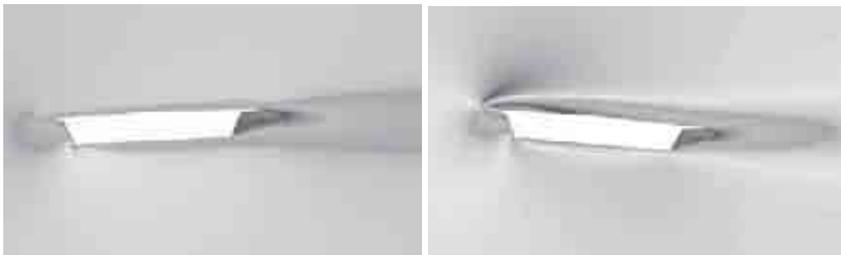
Figure 2: velocity contour plot around the bridge deck at two different time steps.
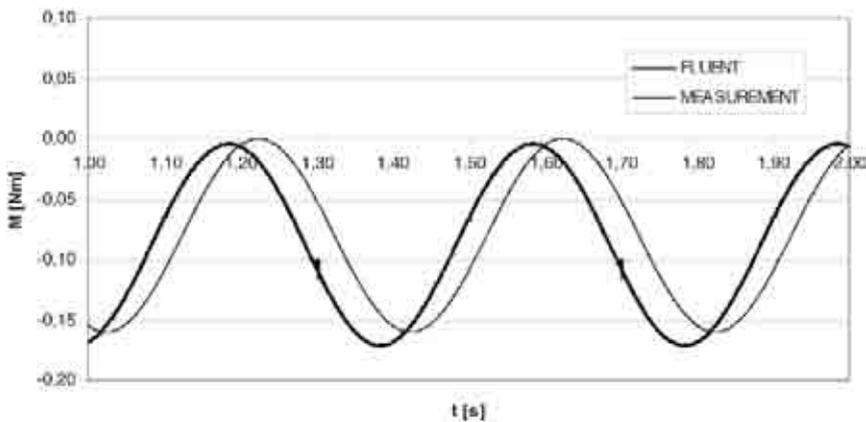
Figure 3: torsion moments as a function of time.

In Figure 3 the measured and the calculated moments against time on the shear center of the bridge deck is shown (Ured=6.42, rotational motion). In the calculations the k-ε turbulence model was used. The time step was set to 0.0002 sec. All the calculated Ads were compared with the measured ones. In some cases (A2*, A3*, H2*, H3*) relatively good agreement was found, but for the H1*, H4* there were certain differences. For the 2D simulations the ANSYS FLUENT 6.3.26 version was applied.

However, the 2D simulations are still to be developed and validated, there is a possibility to exploit the 3D CSD-CFD facilities of the ANSYS software to study bridge flutter. Experiences in wind tunnel testing according to Lajos, T., Balczó, M., Goricsán, I., Kovács, T., Régent, P.,Sebestyén, P. (2006) and 2D CFD runs made by Györgyi, J. & Szabó, G. (2007) were strongly required to start a 3D coupled simulation.

As there are measurements for only sectional models available, a fictive wind tunnel model was considered. This model is a two meters long suspension bridge. The wind tunnel model and the CSD model have to provide the same dynamic behavior though it is not easy to be done. While the wind tunnel model consist of a mechanical part bounded with a light material which gives the shape of the bridge, the CSD model is made up using shell elements, by means of the FEM. The material properties and the thickness value of the shell elements have to be adjusted in case of the CSD model to reach similarity. In the fluid-structure interaction calculation the force-displacement transfer between the structure and the fluid flow only happens on the bridge deck surface and the cable elements have a role on the structural behavior only. In Figure 4 the details of the FEM model can be seen. The FEM mesh consists of regular rectangular 4-node shell elements with six degrees of freedom per each node.
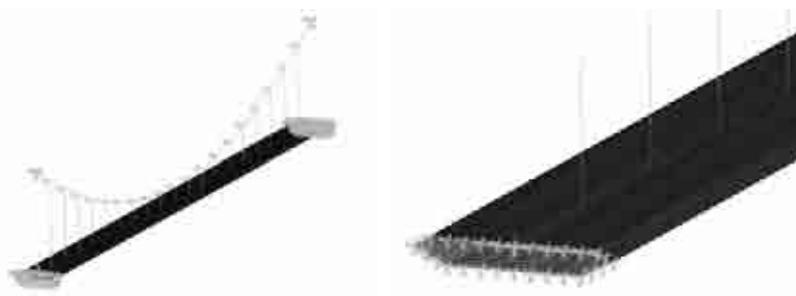
Figure 4: FEM model of the aeroelastic bridge model

For the CFD calculations a relatively coarse mesh was made to reduce the computational efforts. The number of cells was around 200.000. The inflow velocity was varied from 5 to 10m/s. From a non-deformed initial state of the bridge, the developing of the flutter motion would have needed much time. Thus, the bridge deck was loaded with a torsion moment for a certain transient time and then it was released, and the free vibration was investigated afterwards. If the amplitudes do not grow, the system is stable under those conditions. At the velocities of 5.0 and 7.5 m/s flutter does not occur. At the speed of 10.0 m/s the vibration amplitudes grew from the initial value. This state showed a typical flutter phenomenon.

During the simulation, the fluid flow induces forces on the bridge deck, which deforms accordingly. The deformations are fed back to the CFD mesh. The time step was set to 0.0008 sec and the k-ε turbulence model was applied. The end time was 0.48 sec which needed 6 days run time on a four core 2.40GHz computer with 4.0Gb RAM memory. The first torsion frequency of the model is 6.33Hz so within the run time approximately three vibrating phases could be observed.

For the calculation, the ANSYS 11.0 commercial software was used.

In Figure 5 the streamlines around the deformed bridge deck is shown.
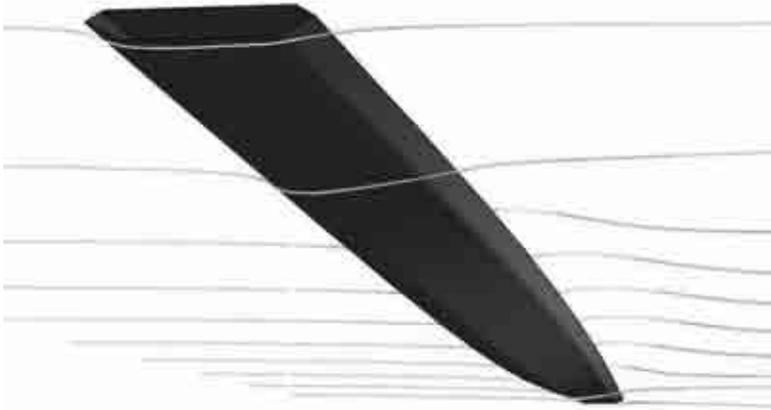
Figure 5: Streamlines around the deformed bridge deck

To conclude, in this paper two different approaches at two different cases have been presented. At first, a wind tunnel sectional test results were compared with that of a 2D CFD simulation. The main results of the CFD simulation were the time dependent forces and moments from which the ADs could be extracted. Acceptable agreement between measurement and simulation shows the niceties of the CFD simulations but great care must be taken in accepting its results. Many simulations must to be done on investigating the effects of the mesh quality, time step size and the chosen turbulence models on the results.

To develop our 2D coupled simulations further, a 3D coupled CSD-CFD simulation was performed. In an attempt to make a validation in the near future, a fictive full aeroelastic wind tunnel model was considered. The FEM model of the bridge was made using shell elements on the border between the fluid and the solid domain. At the inlet, constant velocities were defined, and the free oscillating motion of the bridge deck was studied under airflow. The methodology for finding the critical flutter speed was to apply an inlet velocity increasingly in different runs. When the motion amplitude started growing, the critical velocity was found.

The presented 3D simulation indeed has strong simplifications and can not be regarded as a solution for 3D flutter prediction at this stage of our research. Nevertheless, in the near future, the aeroelastic model should be made so that the methodology can be validated and become a reliable tool in bridge aeroelasticity.

REFERENCES

Zhiwen ZHU, Zhaoxiang WANG, Zhengqing CHEN (2008): Computational fluid dynamic analyses of flutter characteristics for self-anchored suspension bridges, Front. Archit. Civ. Eng. China 2008, 2(3): 267-273.

WANG Yi-wei, LIN Yong.wen (2008): Combination of CFD and CSD packages for fluid-structure interaction, Journal of Hydrodynamics, 2008, 20(6):756-761.

Lajos, T., Balczó, M., Goricsán, I., Kovács, T., Régent, P.,Sebestyén, P. (2006): Prediction of wind load acting on telecommmunication masts #paper A-0206, pp.1-8, IABSE Symposium on Responding to Tomorrow's Challenges in Structural Engineering, Budapest.

Györgyi, J., Szabó, G. (2007): Dynamic calculation of reinforced concrete chimneys for wind effect using the different codes and analysing the soil-structure interaction, #paper 1371, pp.1-12, ECCOMAS Thematic Conference on Computational Methods in Structural Dynamics and Earthquake Engineering, Rethymno, Crete, Greece.

Ansys Help, Release 11.0 Documentation for ANSYS.

Wind-driven rain on building facades: some perspectives

B. Blocken[1], M. Abuku[2], S. Roels[2], J. Carmeliet[3,4]

[1] *Building Physics and Systems, Eindhoven University of Technology, P.O. Box 513, 5600 MB Eindhoven, the Netherlands*
[2] *Laboratory of Building Physics, Department of Civil Engineering, Katholieke Universiteit Leuven, Kasteelpark Arenberg 40, 3001 Leuven, Belgium*
[3] *Chair of Building Physics, Swiss Federal Institute of Technology ETHZ, ETH-Hönggerberg, CH-8093 Zürich, Switzerland*
[4] *Empa, Laboratory for Building Technologies, Swiss Federal Laboratories for Materials Testing and Research, Überlandstrasse 129, CH-8600 Dübendorf, Switzerland*

Keywords: wind-driven rain, building facade, hygrothermal behaviour, moisture transfer, durability

ABSTRACT

In the past 70 years, considerable advances have been made in wind-driven rain (WDR) research in building engineering. Experimental, semi-empirical and numerical simulation methods have been developed and applied to assess the amount of WDR impinging on building facades. Each of these methods has been combined with hygrothermal simulation models to determine the uptake of WDR water by porous building materials, and these models have become standard evaluation tools for building facade performance and durability. In spite of these achievements, considerable challenges remain. Semi-empirical methods are often not accurate enough to capture the complexity of WDR. Numerical simulation based on Computational Fluid Dynamics (CFD) has hardly been explored beyond the case of the isolated building model. Little is known about the contact and surface phenomena that can occur at raindrop impact. More information is also needed on rain penetration mechanisms. At present, research efforts are focusing on at least these four research tracks. The complexity of WDR ensures they will continue to do so for a considerable time in the future.

INTRODUCTION

In the past 70 years, many efforts have been made to increase the understanding of the interaction between wind, rain and buildings. This interaction is important in building design and evaluation. Although WDR is an important parameter in several aspects of building engineering, by far most research efforts have focused on WDR impingement on building facades and the response of building facades to the impinging WDR water. The reason is that WDR is one of the most important moisture sources that determine the hygrothermal performance and durability of building facades. Analysis of the hygrothermal performance is most often performed by numerical simulation with

---

Contact person: B. Blocken, Building Physics and Systems, Eindhoven University of Technology, P.O. box 513, 5600 MB Eindhoven, the Netherlands. *E-mail address:* b.j.e.blocken@tue.nl Tel: +31 (0)40 247 2138, Fax: +31 (0)40 243 8595.

Heat-Air-Moisture (HAM) transfer models. Accurate HAM simulations require adequate knowledge and implementation of WDR as a boundary condition. However, the adequate implementation of WDR in HAM models has been held back by its complexity. It is this complexity that has driven WDR research for the past 70 years.

WDR research in building engineering can be divided into two parts (Fig. 1): (1) assessment of the impinging WDR intensity and (2) assessment of the response of the building facade to the impinging WDR. The impinging WDR intensity is governed by a diversity of parameters: building geometry, environment topography, position on the building facade, wind speed, wind direction, rainfall intensity and raindrop-size distribution. The impinging WDR intensity is the total amount of rain water that comes into contact with the building surface. What happens at and after impact/impingement is the focus of the second part of WDR research. It comprises the study of contact and surface phenomena such as splashing, bouncing, adhesion, runoff, evaporation, absorption and the distribution of the moisture in the facade (rain penetration and wetting-drying). This response is also determined by a diversity of parameters: the WDR intensity and raindrop-size distribution, the raindrop diameter and impact angle, material-surface characteristics such as wall roughness, surface tension, material characteristics such as moisture permeability and moisture retention, construction details, etc. It is not surprising that despite research efforts spanning more than 70 years, WDR is still an active research subject in building engineering, and a lot of work remains to be done. It is however also clear that a very large body of work has been performed in the past, and that this short paper can only attempt to provide some perspectives on some part of this work.
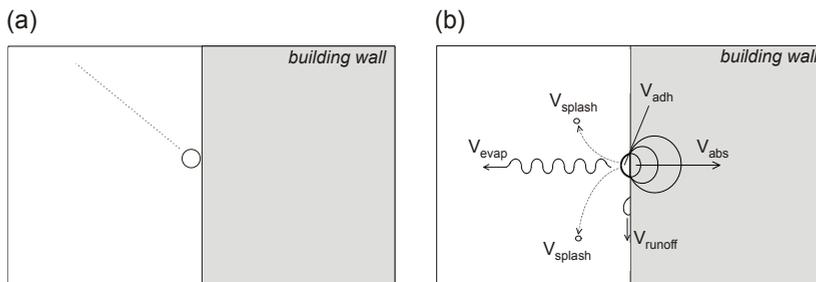
Figure 1: Schematic representation of the two parts in wind-driven rain research: (a) assessment of the impinging wind-driven rain intensity (before rain impact) and (b) assessment of the response of the wall (at and after rain impact).

ASSESSMENT OF IMPINGING WIND-DRIVEN RAIN INTENSITY

A literature review of measurements, semi-empirical models and numerical simulation models for assessing the impinging WDR intensity was provided by Blocken and Carmeliet (2004). This section contains some of the past achievements and future challenges.

WDR measurements have been made since at least 1936 (Beckett 1938). The vast majority of WDR measurements were and are made with wall-mounted gauges that are often assumed to provide a direct indication of local WDR impingement. Probably because of too low demand, WDR gauges have – to the knowledge of the authors – never been industrially manufactured, and almost every research laboratory has designed their own WDR gauge. This was not considered problematic, until van Mook (2002) found very large discrepancies in the readings between different gauges exposed to the same WDR load. Based on his findings, on additional WDR measurements and on laboratory experiments, Blocken and Carmeliet (2006a) identified five possible error sources in WDR measurements, and suggested guidelines for the design of WDR gauges and for WDR measurements. Apart from full-scale measurements, innovative wind tunnel measurements of WDR were made by

Inculet and Surry (1994) and Inculet (2001). Incentives for future measurements are not many, probably because they are time-consuming, expensive, impractical and – as mentioned before – prone to error. However, they are essential to support the development and validation of semi-empirical models and numerical simulation models. Semi-empirical models provide a fast and fairly easy way of assessing the WDR intensity. To the knowledge of the authors, the most extensive semi-empirical models are the model in the European Standard Draft (CEN 2006) and the model by Straube and Burnett (2000). Current studies by the authors are focusing on the intercomparison of these models with the CFD model for WDR. This numerical simulation model was developed by Choi (1991, 1993, 1994) and extended in the time domain by Blocken and Carmeliet (2002). CFD validation studies with full-scale measurements were made by van Mook (2002), Blocken and Carmeliet (2002, 2006b), Tang and Davidson (2004), Abuku et al. (2009a) and Briggen et al. (2009). Hangan (1998) performed validation using the wind tunnel measurements by Inculet and Surry (1994). Choi (1997) investigated the influence of turbulent dispersion on WDR intensities. Choi (2008) also recently used his model for an innovative study of the influence of WDR on building facade surface pressures. In spite of many achievements made, important challenges remain. More information on WDR measurement errors is needed. Due to these errors, the measured intensities are generally an underestimation of the actual impinging WDR intensity. More CFD validation studies are required. Up to now, validation studies have almost exclusively been performed for isolated buildings and for wind direction perpendicular to the facade. Finally, CFD is too complex and time-consuming to be used as a standard and practical tool for WDR assessment. Therefore, the existing semi-empirical models should be improved and extended to increase their predictive capability.

ASSESSMENT OF THE RESPONSE OF THE WALL

A distinction is made between (1) laboratory measurements of single raindrop impact, (2) laboratory tests for rain penetration, (3) on-site observations, (4) on-site measurements and (5) numerical modelling. Detailed laboratory measurements to study the behaviour of water drops at impact on porous materials are important because phenomena such as splashing and bouncing might decrease the amount of WDR that is available for absorption by the facade. Although drop impact has been studied extensively in other research areas, studies of normal and oblique water drop impact on porous building materials are very scarce (Abuku et al. 2009b). Studies of rainwater runoff are also very scarce, and most work has focused on on-site observations or has been part of research in water penetration test facilities. Several highly advanced water penetration testing facilities exist. Some of the most important are (in alphabetical order): the Dynamic Wall Testing Facility of NRC-IRC (e.g., Lacasse 2004), the Insurance Research Lab for Better Homes at the University of Western Ontario (Bartlett et al. 2007), the University of Florida Hurricane Simulator (Masters et al. 2008) and the Wall of Wind at Florida International University (Bitsuamlak et al. 2009). The latter three are used for – among others - hurricane WDR research. On-site measurements of the WDR response of walls under natural exposure were made at many building physics and building science laboratories and research institutes. Some of those measurements were used to validate the implementation of WDR in HAM models. This was for instance done by Künzl and Kiessl (1997), who found that the numerical HAM simulations, based on measured WDR intensities, overestimated the moisture content of the test wall over a period of 80 days by about 30%. Abuku et al. (2009c) performed a similar validation study, and they also found similarly large overestimations. Two reasons were suggested: (1) the occurrence of splashing and bouncing on the test wall; and (2) the simplified way in which WDR is implemented in HAM models, i.e. as a spatially and temporally averaged moisture flux. Also in this second part of WDR research, much work remains to be done. The response of the wall in terms of splashing and bouncing of raindrops needs to be quantified, and models for rainwater runoff need to be developed and validated. These developments need to be implemented in HAM models. Because splashing,

bouncing and runoff will be very pronounced in hurricane conditions, these phenomena and their effect on WDR-induced surface pressures are important future research topics.

REFERENCES

Abuku, M., Blocken, B., Nore, K., Thue, J.V., Carmeliet, J., Roels, S. (2009a). "On the validity of numerical wind-driven rain simulation on a rectangular low-rise building under various oblique winds", Build. Environ. 44(3), 621-632.

Abuku, M., Janssen, H., Poesen, J. Roels, S. (2009b). "Impact, absorption and evaporation of raindrops on building facades", Build. Environ. 44(1), 113-124.

Abuku, M., Blocken, B., Roels, S. (2009c). "Field measurement and numerical analysis of wind-driven rain absorption and evaporation on building facades", this conference.

Bartlett, F.M., Galsworthy, J.K., Henderson, D., Hong, H.P., Iizumi, E., Inculet, D.R., Kopp, G.A., Morrison, M.J., Savory, E., Sabarinathan, J., Sauer, A., Scott, J., St. Pierre L. M., Surry, D. (2007). "The Three Little Pigs Project: a new test facility for full-scale small buildings", 12th International Conference on Wind Engineering, (12ICWE), 2-6 July 2007, Cairns, Australia.

Beckett, H.E. (1938). Building Research Note, No. 755.

Bitsuamlak, G.T., Chowdhury, A.G., Sambare D. (2009). "Application of a full-scale testing facility for assessing wind driven rain intrusion", Build. Environ. Accepted for publication.

Blocken, B., Carmeliet, J. (2002). "Spatial and temporal distribution of driving rain on a low-rise building", Wind Struct., 5(5), 441-462.

Blocken, B., Carmeliet, J. (2004). "A review of wind-driven rain research in building science", J. Wind Eng. Ind. Aerodyn. 92(13), 1079-1130.

Blocken, B., Carmeliet, J. (2006a). "On the accuracy of wind-driven rain measurements on buildings", Build. Environ. 41(12), 1798-1810

Blocken, B., Carmeliet, J. (2006b). "The influence of the wind-blocking effect by a building on its wind-driven rain exposure", J. Wind Eng. Ind. Aerodyn. 94(2), 101-127.

Briggen, P.M., Blocken, B., Schellen, H.L. (2009). "Wind-driven rain on the facade of a monumental tower: Numerical simulation, full-scale validation and sensitivity analysis", Build. Environ. 44(8), 1675-1690.

CEN (2006). Hygrothermal performance of buildings - Calculation and presentation of climatic data - Part 3: Calculation of a driving rain index for vertical surfaces from hourly wind and rain data (ISO/DIS 15927-3:2006). DRAFT prEN ISO 15927-3.

Choi, E.C.C. (1991). "Numerical simulation of wind-driven rain falling onto a 2-D building", in: Proceedings of the Asia Pacific Conference on Computational Mechanics, Hong Kong, 1721-1728.

Choi, E.C.C. (1993). "Simulation of wind-driven-rain around a building". J. Wind Eng. Ind. Aerodyn., 46&47, 721-729.

Choi, E.C.C. (1994)." Determination of wind-driven rain intensity on building faces". J. Wind Eng. Ind. Aerodyn., 51, 55-69.

Choi, E.C.C. (1997). "Numerical modeling of gust effect on wind-driven rain", J. Wind Eng. Ind. Aerodyn., 72, 107-116.

Choi, E.C.C. (2008). "The effect of wind-driven rain on cladding pressure of buildings under wind and rain conditions", BBAA VI International Colloquium on: Bluff Bodies Aerodynamics & Applications, Milan, Italy, July, 20-24, 2008.

Inculet, D., Surry, D. (1994). Simulation of wind-driven rain and wetting patterns on buildings. BLWTL-SS30-1994. Final report.

Inculet, D.R. (2001). The design of cladding against wind-driven rain. Ph.D. thesis, The University of Western Ontario, London, Canada, 297 p.

Künzel, H.M., Kiessl, K. (1997). "Calculation of heat and moisture transfer in exposed building components", International Journal of Heat and Mass Transfer, 40(1), 159-167.

Lacasse, M.A. (2004). "IRC studies on the control of rain penetration in exterior wood-frame walls", Solplan Review, no. 14, January 2004, pp. 14-15.

Masters, F.J., Gurley, K.R., Prevatt, D.O. (2008). "Full-scale simulation of turbulent wind-driven rain effects on fenestration and wall systems", 3rd International Symposium on Wind Effects on Buildings and Urban Environment, March 4-5, 2008, Tokyo, Japan,.

Straube, J.F., Burnett, E.F.P. (2000). "Simplified prediction of driving rain on buildings". Proc. of the International Building Physics Conf., Eindhoven, The Netherlands, 18-21 September 2000, 375-382

Tang, W., Davidson, C.I. (2004), "Erosion of limestone building surfaces caused by wind-driven rain. 2. Numerical modelling", Atmos. Environ., 38(33), 5601-5609.

Van Mook, F.J.R. (2002). Driving rain on building envelopes. Ph.D. thesis. Building Physics Group (FAGO), Eindhoven University of Technology, Eindhoven University Press, Eindhoven, The Netherlands, 198 p.

Computational analysis of natural ventilation in a large semi-enclosed stadium

T. van Hooff[(1,2)], B. Blocken[(1)]

(1) Building Physics and Systems, Eindhoven University of Technology, P.O. box 513, 5600 MB Eindhoven, The Netherlands
(2) Laboratory of Building Physics, Department of Civil Engineering, Katholieke Universiteit Leuven, Kasteelpark Arenberg 40, 3001 Leuven, Belgium

Keywords: Wind flow, semi-enclosed space, natural ventilation, Computational Fluid Dynamics (CFD), validation.

ABSTRACT

The last decades, newly built large sports stadia are also increasingly being used for other events such as concerts, conferences and other activities. An example of such a modern multifunctional stadium is the Amsterdam 'ArenA' in the Netherlands. This stadium is equipped with a roof that can be opened and closed depending on the weather conditions and the type of event. No HVAC systems are present to control the conditions of the relatively large indoor air volume (~10^6 m³). When the roof is closed, the large number of spectators and insufficient natural ventilation can lead to problems concerning the indoor air quality, while overheating can be an additional problem during concerts in summer.

Full-scale measurements were performed to assess the current indoor climate and air exchange rate. In addition CFD simulations were performed to analyse the current air exchange rate and the air exchange rates of four alternative ventilation configurations. CFD was preferred for this study for the detailed simulation of air flow through the relatively small ventilation openings, the discharge coefficients of which are unknown. The CFD simulations showed that the air exchange rate can be increased with up to 43% by creating additional openings in the upper part of the stadium.

DESCRIPTION OF STADIUM AND SURROUNDINGS

The stadium is a so-called 'oval' stadium, with dimensions $235 \times 180 \times 78$ m³ (L×W×H) (Fig. 1a). The stands are made of concrete and consist of two tiers which have their own entries. The roof is dome shaped and can be closed with two large panels with a projected horizontal area of 118 x 40 m². The roof construction is made of steel, covered with semi-transparent polycarbonate sheets and steel sheets as roofing material. There are no HVAC systems present in the stadium, so the indoor air quality and air exchange rate strongly depend on the amount of natural ventilation through openings in the stadium envelope. The largest ventilation opening can be created by opening the roof. During summer however, the roof is closed because of the technical equipment for concerts that is mounted below the roof. The second largest openings are situated in the four corners of the stadium,

---

Contact person: T. van Hooff, Building Physics and Systems, P.O. box 513, 5600 MB Eindhoven, The Netherlands,
Tel: +31 (0)40 247 5877, Fax: +31 (0)40 243 8595.　　　　　　　　E-mail t.a.j.v.hooff@tue.nl

approximately at the same height as the pitch. These four openings each have a surface area of 42.5 m^2 and can be individually opened and closed. Besides these relatively large openings, some additional narrow openings are situated in the upper part of the stadium. Along the entire perimeter an opening is situated between the stand and the roof construction. The total surface area of this opening is about 130 m^2. The fourth and last opening in the stadium is situated between the fixed roof and the movable part of the roof, and is only located along the two longest edges of the stadium. The area of this opening is about 85 m^2.

The stadium is surrounded with medium to high rise commercial buildings and buildings with an entertainment function, such as a cinema and a concert hall. In the proximity of the stadium, office buildings are situated with a height up to 95 m (Fig. 1b).

FULL-SCALE MEASUREMENTS

Full-scale measurements were performed to assess the indoor climate and ventilation of the stadium. To analyse the indoor climate, full-scale measurements were made of the indoor and outdoor air temperature, relative humidity and CO_2 concentration. The measurements were performed at four positions in the stadium, both on the first and on the second tier. Furthermore the irradiance of the sky was measured to investigate the influence of solar irradiation on the indoor air temperature. These measurements showed that the indoor temperature strongly depends on the solar irradiance and can rise throughout the day by up to 6°C, which points to the need for additional ventilation.

To analyse the ventilation, CO_2 measurements were performed during three consecutive evenings at four different locations in the stadium, and converted to air exchange rates using the concentration decay method. The measurements were made after a concert (with closed roof), when CO_2 concentrations had reached a maximum level caused by the attendants. The average air exchange rate during these evenings was about 0.7 h^{-1}.

Finally, 3D wind speed measurements were performed using ultrasonic anemometers for validation of the CFD model of the stadium and its surroundings. The measurements were taken on several different positions inside and around the stadium, including positions in the four openings in the stadium corners. The reference wind speed was measured with an ultrasonic anemometer on a mast of 10 m that was placed on top of a 95 m high office building in the proximity of the stadium.

CFD SIMULATION: COMPUTATIONAL MODEL AND PARAMETERS

The computational domain has a length and width of 2,900 m and a height of 908.5 m. The computational grid consists of 5.5 million prismatic and hexahedral cells (Fig. 1b). The grid is a hybrid grid; it is partially structured and partially unstructured. Special attention was paid to the detailed modelling of the ventilation openings of the stadium, as well as possible extra ventilation openings that will be evaluated. A high grid resolution is applied in the proximity of these openings in view of the expected large flow gradients. A grid sensitivity analysis is conducted with grids of respectively 3.1 million, 5.5 million and 9.1 million cells, indicating the suitability of the 5.5 million cells grid.

At the inlet of the domain a logarithmic wind speed profile is imposed with an aerodynamic roughness length y_0 of 0.5 m and a reference wind speed U_{10} of 5 m/s. The corresponding turbulent kinetic energy and turbulent dissipation rate profiles are those by Richards and Hoxey (1993). The roughness of the bottom of the domain is taken into account by imposing appropriate values for the sand-grain roughness height K_s and the roughness constant C_s (Blocken et al. 2007). The temperature of the inlet air is set to 293 K. Zero static pressure is imposed at the outlet of the domain and the top of the domain is modeled as an adiabatic slip wall (zero normal velocity and zero normal gradients of all variables). To take into account the increasing air temperature inside the stadium as a result of solar irradiation, estimated surface temperatures that vary from 295 K to 323 K are imposed on the surfaces

inside the stadium. Imposing surface temperatures to all surfaces implies that it is not needed to use a radiation model. Note that for detailed thermal analysis, the thermal overheating simulations should be conducted in a transient way, but for the purpose of comparing different ventilation strategies based on the air exchange rates, steady-state simulations are considered sufficient here.

The steady-state wind-flow pattern around and in the stadium is obtained by solving the 3D Reynolds-averaged Navier-Stokes (RANS) equations in combination with the realizable k-ε turbulence model and standard wall functions, using the commercial CFD code Fluent 6.3.26. The realizable k-ε turbulence model by Shih et al. (1995) was chosen as turbulence model for this study because of its good performance in a validation study performed by the authors based on measurements of mixed convection by Nielsen (1974), and the general good performance of this turbulence model in predicting airflow around buildings (Franke et al. 2007). Standard wall functions are used in this study in order to avoid the very large amount of cells needed for low-Reynolds-number modeling.

In the steady-state 3D RANS simulations, pressure-velocity coupling is taken care of by the SIMPLE algorithm, pressure interpolation is standard and second order discretisation schemes are used for both the convection terms and the viscous terms of the governing equations. The Boussinesq model is used for thermal effects.
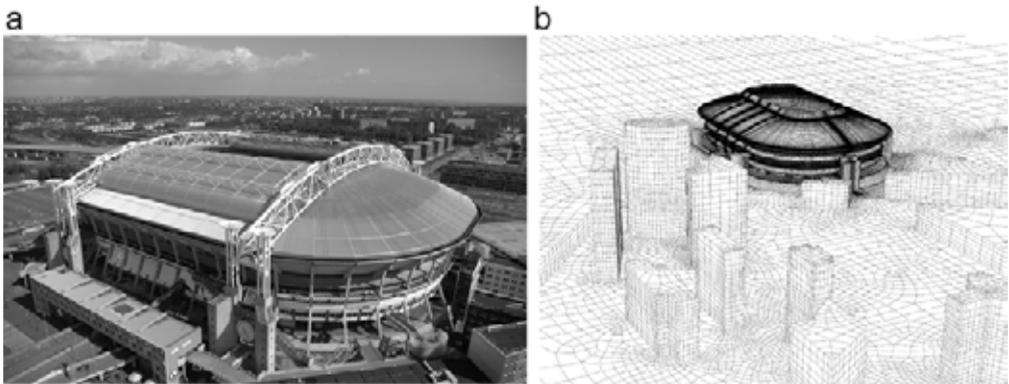
Figure 1: (a) Aerial view of the Amsterdam ArenA; (b) part of the computational grid of the stadium and its surroundings.

CFD SIMULATION: VALIDATION AND RESULTS

The aforementioned wind speed measurements are used for model validation. The measured wind speed at the four locations in the corners of the stadium is compared with the calculated wind speed at these positions in the CFD model. In general, the CFD results deviate less than 30% for the wind speed and less than 15% on average for the wind direction, therefore the validation gives confidence in the use of this CFD model.

Simulations with the validated CFD model are conducted to evaluate the air exchange rate of the current situation and of four additional ventilation configurations. Configuration 1 has eight extra openings on the second tier, which are created by opening large windows that are normally used for logistic purposes. Configuration 2 has an additional opening where the stand meets the roof construction. This opening is created by removing half of the steel sheets that are placed between the concrete stand and the steel roof construction. Configuration 3 has an additional opening at the same place as configuration 2, but now the steel sheets are removed entirely. Configuration 4 has an opened roof.

The air flow around and in the stadium, as well as the temperature distribution, are calculated for

several wind directions, all perpendicular to the long edge of the stadium or at an angle of 45°. For each ventilation configuration the mass flow through the openings that is calculated with CFD is used to determine the air exchange rates. Opening the roof provides the best results; the air exchange rate increases with 158%. Removing the steel sheets half or entirely increases the air exchange rate on average with 17% to 43% respectively. Configuration 1 has on average the same air exchange rate as the current situation.

DISCUSSION

In this study the air flow through existing and optional ventilation openings is modelled with CFD. Further research is needed on several aspects of the study that has been performed. First of all, the CFD simulations in this study were performed steady-state, both concerning the flow and the heat transfer. Performing transient flow and transient thermal simulations will be performed in the future for a more detailed thermal analysis. Furthermore, future research will focus on the balance between buoyancy and wind as driving forces for the natural ventilation. Simulations with different wind speeds will be performed to assess this balance and its effect on ventilation effectiveness.

CONCLUSIONS

Natural ventilation of a large multifunctional football stadium has been measured and assessed with CFD simulations. A particular innovative feature of this study is the combined and simultaneous simulation of the wind flow in the complex urban environment around the stadium and the air flow inside the stadium. The results of both the measurements and the CFD simulations have been presented in this paper.
• Measurements have shown that the air exchange rate of the stadium was insufficient to avoid overheating.
• The air exchange rate of the stadium has been calculated using CO_2 measurements and is about 0.7 h^{-1} on average for the conditions during the measurements.
• Wind speed measurements have been used to validate the CFD model of the stadium and its surroundings and showed a good agreement.
• CFD simulations of different ventilation configurations show that the air exchange rate of the stadium can be increased with 43% by creating additional small openings in the upper part of the stadium. Opening the roof can increase the air exchange with 158%.

REFERENCES

Richards, P.J., Hoxey, R.P., (1993). "Appropriate boundary conditions for computational wind engineering models using the k–ε turbulence model", Journal of Wind Engineering and Industrial Aerodynamics, 46-47, 145–153.
Blocken, B., Stathopoulos, T., Carmeliet, J., (2007). "CFD simulation of the Atmospheric Boundary Layer: wall function problems", Atmospheric Environment 41(2), 238-252.
Shih, T.-H., Liou, W.W., Shabbir, A., Zhu, J., (1995). "A new k-ε eddy-viscosity model for high Reynolds number turbulent flows - model development and validation", Computers & Fluids 24 (3), 227–238.
Nielsen, P.V., (1974). *Flow in air-conditioned rooms*. PhD thesis. Technical Univ. Denmark.
Franke, J., Hellsten, A., Schlünzen, H., Carissimo, B. (Eds.), (2007). *Best practice guideline for the CFD simulation of flows in the urban environment*. COST Office Brussels, ISBN 3-00-018312-4.

Aerodynamic study of the preliminary design of a 425 m cable-stayed bridge deck using CFD

F. Nieto, S. Hernández & J.Á. Jurado

School of Civil Engineering – University of La Coruna, Campus de Elviña, 15071 La Coruna, Spain.
fnieto@udc.es; hernadez@udc.es; jjurado@udc.es

INTRODUCTION

Extensive wind tunnel testing campaigns have been the engineers' method to guarantee the safe and feasible aerodynamic and aeroelastic performance of bridges for decades. Some recent examples of bridges which have surpassed comprehensive wind tunnel test are: the Normandy Bridge, the Akashi Strait Bridge, the Great Belt Bridge, the Stonecutters Bridge or the future Messina Strait Bridge.

However, experimental wind engineering cannot be considered as the only way to assess the aerodynamic behavior of bridges. Computational fluid dynamics (CFD) is finding its way in the wind engineering realm. In fact, this scientific subject has experienced a great development from the 1990 decade and it is nowadays a very dynamic field.

There are two specific design activities where CFD offers certain advantages over conventional wind tunnel tests. They are the conceptual design of long-span bridges and the preliminary design, usually carried out during the period given for the competitive biddings of cable supported bridges.

INITIAL DESIGN

An international competitive bidding was called to build a new highway parallel to a pre-existing one

---

Contact person: F. Nieto, School of Civil Engineering, Campus de Elviña, La Coruna, Spain.
Telephone: 0034 981167000, FAX: 0034 981167170. E-mail fnieto@udc.es

with the aim of improving traffic conditions. The main technical difficulty of the overall project was the construction of a new bridge, parallel to an actual arch bridge, spanning a wide river.

One of the prospective contractors studied a solution consisting in a cable-stayed bridge with a span, between piers, of 425 m and a π deck cross-section made with two longitudinal steel wide flange members and transversal secondary girders standing for a concrete slab (see Fig. 1). The existing bridge would be located at the right according to Fig. 1.
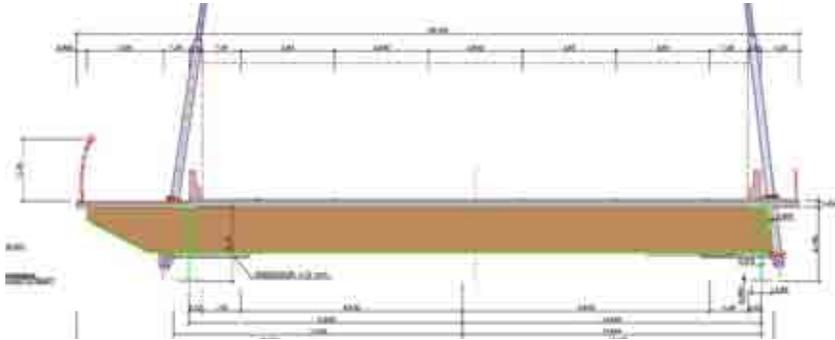
Figure 1: Preliminary design proposal.

However, it is well know that π cross-sections show an unfeasible aerodynamic behavior (Kubo et al. 2001) and also that cable-stayed bridges, as the 420 m central span Vasco da Gama Bridge, are prone to wind instability problems (Mendes and Branco 1998; Branco et al. 2000). Therefore, concerns had risen regarding the efficiency of the aerodynamic solution being considered.

The main goal of this study has been to determinate by means of technical data the aerodynamic feasibility of the proposed cross-section. Additionally, design modifications have been suggested in order to fulfill common aerodynamic design criteria. However, any change in the design should be limited and scientifically justified as it would represent an increment in the construction budget. Due to the short time available before the deadline for the presentation of the tender proposal, experimental wind tunnel tests were not taken into consideration due to the required time to build the models, thus a CFD approach focusing on the evaluation of the qualitative aerodynamic behaviour of the considered deck cross-section was chosen.

In first place the aerodynamic coefficients of the cross-section assuming steady state condition were evaluated. In fact, aerodynamic coefficients play a very significant role because to avoid one degree of freedom instability lift and moment coefficients first derivative must be positive; additionally, greater is the value of those derivatives lower is the flutter critical wind speed of the structure (Larose and Livesey 1997; Diana et al. 2007). Another crucial issue to be addressed in an initial study was the risk of vortex shedding excitation. With the aim of keeping computation times and costs bounded 2D models were chosen as the focus was put on the overall behavior instead of the detailed and precise evaluation of any particular magnitude. In all cases it has been assumed that the flow was coming from the left side according to the below figures.

FLOW MODELLING AND COMPUTATIONAL APPROACH

For both steady and unsteady simulations incompressible turbulent flow around the 2D analyzed sections has been modeled by the classical Navier-Stokes equations, along with the two equations RANS realizable κ-ε model with enhanced wall treatment. Dirichlet conditions have been imposed at inlet and outlet boundaries, moreover no-slip conditions have been imposed at the deck section surface. The turbulent characteristics of the flow have been defined in terms of intensity and length scale.

The Finite Volume solver Fluent by ANSYS has been used to numerically evaluate the flowfield. A quadrilateral mesh using the map scheme near walls and pave scheme in the main part of the flow domain has been employed. The total number of cells in the computational grids that are going to be presented is between 477126 for the initial design proposal and 599465 for one of the analyzed alternatives that will be presented ahead. Both steady and unsteady simulations have been carried out for a Reynolds number of 3.85E+5 considering the deck width of the initial design proposal as reference dimension. For the unsteady simulations the non-dimensional time step chosen for advancement in time has been 0.0178, advancement in time is accomplished by a second-order implicit scheme and PISO algorithm is used for the pressure-velocity coupling. The unsteady simulations have been extended until a periodic behavior was reached for those configurations where vortex induced vibrations were detected.
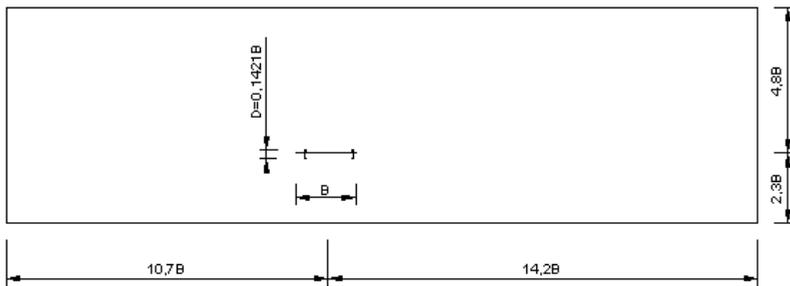
Figure 2: Computational domain.

AERODYNAMIC ANALYSIS OF THE INITIAL DESIGN

In first place the aerodynamic coefficients have been evaluated computationally.
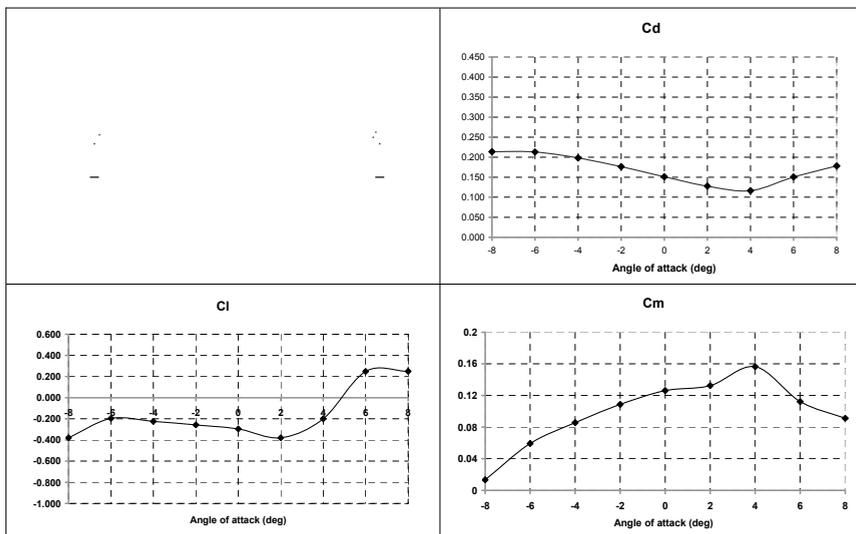
Figure 3: Aerodynamic coefficients for the preliminary design proposal.

The analysis of the force coefficients presented in Fig. 3 makes clear the unfeasibility of the initial aerodynamic design. Regarding the lift coefficient C_l, its negative slope between -6º and 2º shows the risk of one degree of freedom instability. Moreover moment coefficient C_m also presents negative slope from 4º to 8º. Additionally, another key characteristic of the deck cross-section is that the moment coefficient is positive along the interval of studied angles of attack (-8º, 8º). From the analysis of the data it can be concluded that the long left overhang plays a crucial role in the aerodynamic performance of the cross-section.

AERODYNAMIC ANALYSIS OF ALTERNATIVE DESIGNS

A number of cross-sections have been studied with the goal of achieving a better aerodynamic design. Thus, the addition of a wind barrier has been analyzed as well as the total or partial elimination of the deck overhangs. Finally, a configuration considering both fairings and two rows of baffles has been studied. This has been the cross-section which showed the most feasible performance. In Fig. 4 the obtained aerodynamic coefficients are shown.
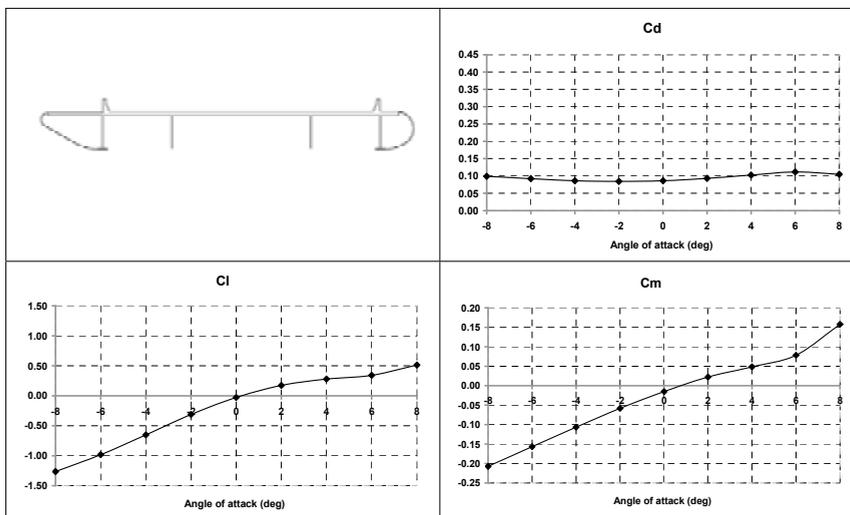
Figure 4: Aerodynamic coefficients for the modified design proposal.

REFERENCES

Branco F.A., Mendes P.M., Guerreiro M.C. (2000). "Special studies for Vasco da Gama Bridge", Journal of Bridge Engineering, 5 (3), 233-239.

Diana G., Belloli M., Rocchi D., Resta F., Zasso A. (2007). "Sensitivity analysis on the effects of different aerodynamic devices on the behavior of a bridge deck", 12th International Conference on Wind Engineering, Cairns, Australia.

Kubo Y., Sadashima K., Yamaguchi E, Kato K., Okamoto Y, Takashi K. (2001). "Improvement of aeroelastic instability of shallow π section", Journal of Wind Engineering and Industrial Aerodynamics, 89 (14-15), 1445-1457.

Larose G.L., Livisey F.M. (1997). "Performance of streamlined bridge decks in relation to the aerodynamics of a flat plate", Journal of Wind Engineering and Industrial Aerodynamics, 69-71, 851-860.

Mendes P.M., Branco F.A. (1998). "Numerical wind studies for the Vasco da Gama Bridge, Portugal", Structural Engineering International, 8 (2), 124-128.

Experimental and numerical study of the pressure distribution on a low rise building (CC)

A. Zasso, D. Rocchi, P. Schito.

Mechanical Department of Politecnico di Milano – alberto.zasso@polimi.it – Via La Masa 1 20158, Milano – Mechanical Department of Politecnico di Milano – daniele.rocchi@polimi.it – Via La Masa 1 20158 Milano – Mechanical Department of Politecnico di Milano – paolo.schito@mail.polimi.it – Via La Masa 1 20158 Milano

Keywords: Wind Tunnel, CFD, Structural loads, unsteady flow, turbulence.

ABSTRACT

The most demanding request, when aerodynamic loads are considered at the design stage of a building, is the definition of the most challenging load conditions with respect to the structure strength. In fact, considering the statistical characteristics of the turbulent wind and the signature turbulence, produced by the fluid and structure interaction, the pressure distribution may lead, at different time instants to different strength conditions on the structure itself. While local peaks of pressure drive the design of local components, the instantaneous pressure distribution on the building facades have to be considered for dimensioning purposes, taking into account the correlation along the structure to identify the effects in terms of global loads.

In the present paper, a comparison of the different techniques actually used to define the loads on a low rise building is presented considering standard prescriptions, wind tunnel tests and CFD (Computational Fluid Dynamics) approaches.

The different approaches were applied to the study of the aerodynamic loads on the Cultural Centre (CC) on Abuja (Niger) whose geometry shows an interesting aerodynamics because of its similarity to a delta wing.

Figure 1 reports a picture of the wind tunnel 1:100 scaled model with its main dimension.

Contact person: D. Rocchi, Mechanical Department of the Politecnico di Milano, Via La Masa 1, 20158 Milano, +39 02 2399 8485, FAX +39 02 2399 8492. E-mail daniele.rocchi@polimi.it
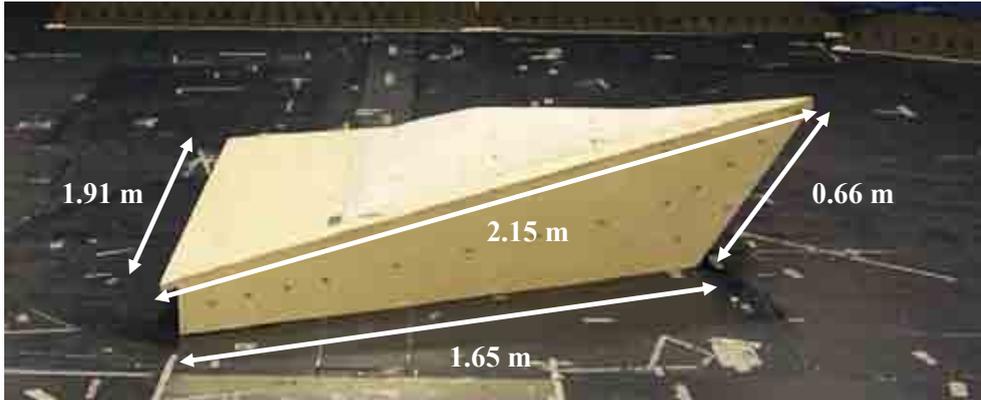
Figure 1: Geometry of the Cultural Centre (CC) building: 1:100 scaled model used for wind tunnel tests. Dimensions in model scale.

The typical geometry of this low rise building, that is simple but different from the very simple geometries covered in the standards, offers a good opportunity to investigate the different tools that are available to the designer to dimension the structure against the aerodynamic loads.

In the paper will be presented the results in terms of mean and peak values of pressure distribution obtained through the application of the Eurocode standard, through wind tunnel tests on a 1:100 scaled model and through CFD simulation using different turbulence modelling.

Standard calculation: The first step is the definition of the fundametal basic wind velocity ($V_{b,0}$) for the location using the maximum measured gust speed, the return period and the terrain category. From this value it is possible to calculate the peak wind velocity using the rules as a function of $V_{b,0}$, terrain category and turbulence intensity. The calculation of pressure coefficients on the building and his parts depends on many factors. The walls use a general approach partitioning the surface in zones, each with a specific coefficient. The wind incidence on the wall has an associated reduction factor. The same approach is used for the roof and the dome.

Wind tunnel tests: A wind tunnel tests campaign has been performed on a 1:100 static model in the atmospheric boundary layer test section of the wind tunnel at the Politecnico di Milano, to measure the pressure distribution on the building facades.

An atmospheric boundary layer vertical profile was reproduced in the wind tunnel according to the characteristic of the Abuja area where the stadium will be built, corresponding to an Eurocode Terrain Category II-III with a roughness length of $z_0 = 15\,m$.

The model was equipped with 128 pressure taps distributed on the building facades to capture the most important pressure values in the critical zones for different incoming wind directions.

Aeroelastic effects are negligible, during the wind tunnel tests, because of the large model stiffness. Wind tunnel tests allow a more realistic pressure distribution on the

An example of the pressure distribution and of the pressure taps position (black dots) on the model is reported in Figure 2 where the mean value and the minimum peak value are reported for each pressure taps though contour plots of the dimensionless pressure coefficient defined as:

$$C_p = \frac{p(t) - \overline{p}_s}{\overline{q}_H}$$

(1)

where p is the pressure measured by the transducer, $\overline{p}_s$ is mean static reference pressure and $\overline{q}_H$ is the mean dynamic pressure at the reference height of 0.5 m in model scale.

It is possible to appreciate the large negative values measured close to the upper vertex of the building and the large pressure fluctuations leading to large suction in this region where most of the

time dependent effects are due to the large flow separations. Wind tunnel results allow to highlight positive pressure where standard rules fail to predict the phenomenon.

Computational Fluid Dynamics approach: Flow separations from bluff bodies are a very challenging problem for CFD approaches [Tsuchiya 1997] but are a very common features in building aerodynamics. Moreover the definition of the design values of pressure distribution from CFD approaches requires the evaluation of the time dependent component of the wind and of the pressure field through unsteady simulations.

In this paper the results of both steady and unsteady simulations using RANS turbulence models will be analyzed and compared to the wind tunnel experimental data and with numerical results obtained using a LES approach.

Simulations were performed considering the wind tunnel test conditions, by imposing at the computational domain boundary the turbulent wind characteristics measured in the wind tunnel.
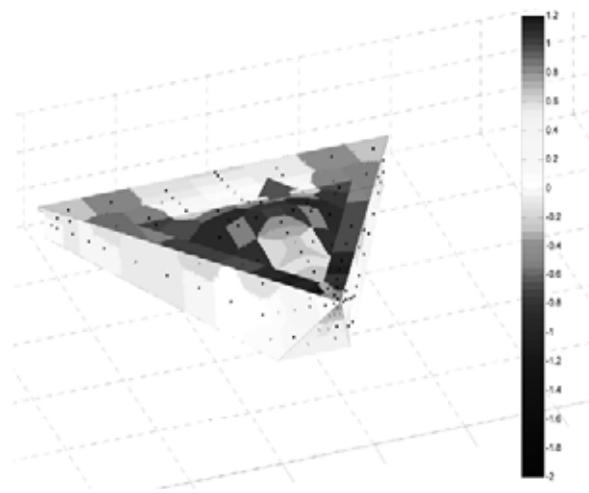
Figure 2: contour plot of the mean pressure coefficient for an incoming wind direction of 0 deg.

The comparison between numerical and experimental results will be proposed in terms of mean and peak values (when available) of the pressure coefficient at the same location where the pressure taps were positioned. An explanation of the fluid dynamic phenomena leading to the measured pressure distribution will be proposed exploiting the CFD solution of the flow field. Some considerations on the correlation between the frequency content of the incoming turbulent wind, and the frequency content of the pressure field on the building facades will be proposed also to analyze the effects driven by the signature turbulence. In Figure 3 is possible to see the pressure coefficient on the taps close to the roofs edge: RANS simulations cannot predict the correct flow and pressure distribution where large separation and large pressure gradients occur. A preliminary comparison between the time histories of the pressure coefficient measured during the wind tunnel tests and simulated by a LES approach is reported in Figure 4.

Standard approach gives a pressure distribution that cannot predict local effects for particular geometries, and defines the peak value as a function of the wind site turbulence, not considering self made signature turbulence, while in wind tunnel and CFD it is possible to see big turbulent structures that influence the peak values. With RANS simulations it is possible to have a good evaluation of mean values, while for the fluctuating part LES simulation offers a good calculation, but is far more demanding. CFD reproduces the local effects that standard approach is not able to calculate; for a correct flow calculation the choosing of the correct set of equations is very important.
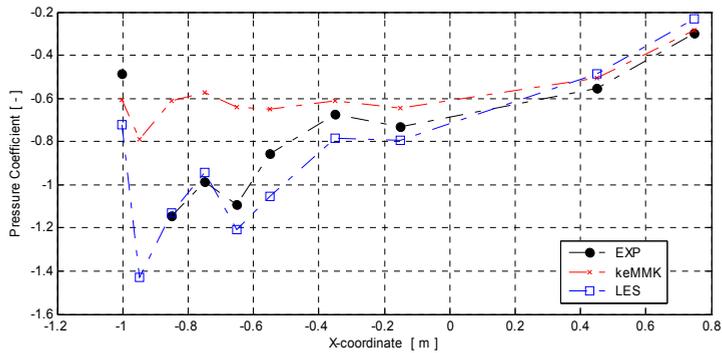
Figure 3: Wind tunnel vs CFD results comparison: pressure coefficient mean values for different simulations compared with experimental results.
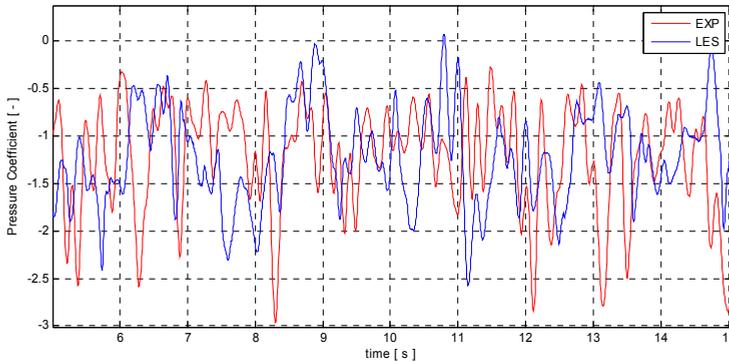
Figure 4: Wind tunnel vs CFD results comparison: time histories of the instantaneous values of the pressure coefficient.

REFERENCES

M. Tsuchiya, S. Murakami, A. Mochida, K. Kondo and Y. Ishida (1997). Development of a new k-e model for flow and pressure fields around bluff body Journal of Wind Engineering and Industrial Aerodynamics, 67/68,.169-182

A. Mochida Y. Tominaga, S. Murakami, R. Yoshie, T. Ishihara and R. Ooka (2002). Comparison of various k-e models and DSM applied to flow around a high-rise building – report on AIJ cooperative project for CFD prediction of wind environment Journal of Wind and Structures, 5,.227-244

Y. Tominaga, A. Mochida, S. Murakami and S. Sawaki (2008). Comparison of various revised k–ε models and LES applied to flow around a high-rise building model with 1:1:2 shape placed within the surface boundary layer, Journal of Wind Engineering and Industrial Aerodynamics, 96,.389-411

E. Simiu, R. Scanlan (1996). Wind effects on Structures. John Wiley & Sons, New York

A. Smirnov, S. Shi, I. Celik (2001), Random flow generation technique for Large Eddy Simulations and Particle-Dynamics Modeling, Journal of Fluids Engineering 123, pp 359-372

Validation metrics of Reynolds stresses and turbulent kinetic energy for the MUST wind tunnel case of COST action 732

J. Franke

Department of Fluid- and Thermodynamics – joerg.franke@uni-siegen.de – University of Siegen, Germany

Keywords: Validation metrics, hit rate, Reynolds stresses, CFD, RANS.

ABSTRACT

To meet the needs for a stringent quality assurance of CFD codes and simulations that are increasingly used in the prediction and analysis of flows in the urban environment, the European COST action 732 "Quality Assurance and Improvement of Micro-Scale Meteorological Models" is working on a model evaluation protocol. The first version of the proposed protocol was published in 2007 (Britter & Schatzmann, 2007a) together with a background and justification document (Britter & Schatzmann, 2007b) and best practise guidelines (Franke et al., 2007). The protocol and especially its validation part, which describes the proposed way to compare simulation results and measurements, was tested by more than 13 groups with up to 40 simulation results by applying it to the MUST (Mocked Urban Setting Test) case. The validation was till now only performed against the wind tunnel results of Bezpalcova (2007), but field experiments exist too (Yee & Biltoft, 2004).

Both experiments consist of velocity and concentration measurements. Olesen et al. (2008) presented a qualitative analysis of the many simulation results in comparison to these measurements while Franke et al. (2008) showed the validation metrics resulting from the comparison. As in both publications results for the single Reynolds stresses were not given, this work provides the metrics for these quantities, based on the simulation results of Franke (2009).

The wind tunnel experiment of the MUST case used 119 wooden models of the shipping con-

_____

Contact person: Dr.-Ing. J. Franke, Institut für Fluid- und Thermodynamik, Paul-Bonatz-Strasse 9-11, D-57076 Siegen, Germany, Tel.: +49(0)271 740 4683, FAX: +49(0)271 740 2666. E-mail: joerg.franke@uni-siegen.de

tainers with height H=2.54m, used in the field experiments, at a scale of 1:75. Together with the so called VIP building the 120 obstacles were arranged on the turntable of the wind tunnel as shown in Figure 1. Two wind directions were examined, referred to as 0° and –45° case in the following.
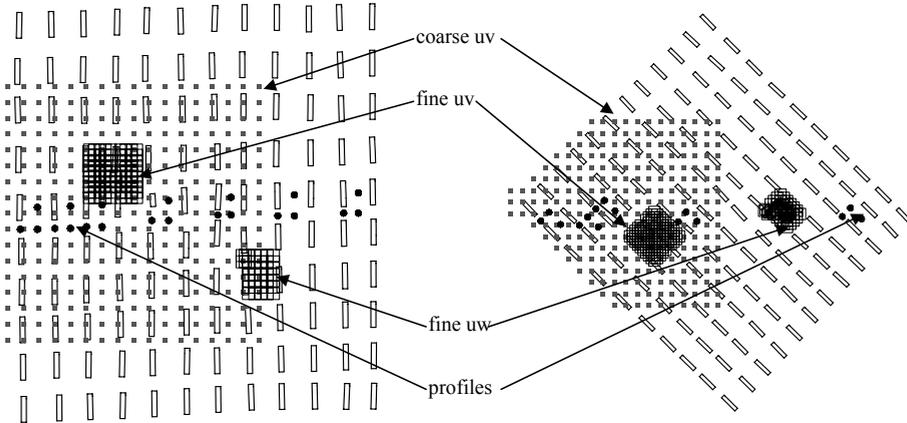
Figure 1: Obstacle arrangement and velocity measurement zones for the MUST wind tunnel case. Left: approach flow direction 0°. Right: approach flow direction –45°. Wind always from left.

The simulations were performed with FLUENT V6.2 using the statistically steady RANS approach with the standard k-ε turbulence model. The inflow boundary conditions for velocity, turbulent kinetic energy (TKE) and turbulent dissipation rate ε were generated with the aid of the measured roughness z_0=0.0165m under the assumption of local equilibrium. All numerical approximations were of second order and the iterative as well as the grid convergence were estimated to be sufficient (Franke, 2009).

The individual Reynolds stresses were calculated from the Boussinesq hypothesis,

$$\overline{u_i'u_j'} = \frac{2}{3}k\delta_{ij} - v_t\left(\frac{\partial \overline{u}_i}{\partial x_j} + \frac{\partial \overline{u}_j}{\partial x_i}\right),$$ (1)

with the turbulent viscosity v_t=0.09k^2/ε, and interpolated on the measurement positions shown in Figure 1. There the computed Reynolds stresses were compared with the corresponding measurements with the aid of the hit rate as validation metric. The hit rate q is defined as

$$q = \frac{1}{N}\sum_{n=1}^{N}i_n\,, \quad i_n = \begin{cases} 1 & \text{if } \left|(O_n - P_n)/O_n\right| \leq \varDelta_r \text{ or } \left|O_n - P_n\right| \leq \varDelta_a \\ 0 & \text{otherwise} \end{cases},$$ (2)

where N is the number of measurement positions, O_n the non dimensional observed value and P_n the non dimensional predicted value (VDI, 2005), where the stresses are made non dimensional with the approach flow velocity U_{ref} at z=7.29m. A hit is therefore obtained if either the relative difference is smaller than the allowed relative difference $\varDelta_r$, or if the absolute difference is smaller than the allowed absolute difference $\varDelta_a$. Following VDI (2005) $\varDelta_r$=0.25 is used by COST 732, but the measurement uncertainties are used for the absolute allowed differences of the individual stresses, see Table 1.

The results of the hit rates at the individual measurement zones (cf. Figure 1) are listed in Table 1 for the two approach flow cases. Due to the 2D velocity measurements not all Reynolds stresses are available at each measurement zone. This also leads to the situation that the turbulent kinetic

energy can not be calculated from the measurements as only two normal Reynolds stress compo-
nents are available at each measurement position. Therefore the experimental k was calculated in
the following way,

$$k_{2D} = \frac{1}{2}\left(\overline{u'^2} + 2\overline{v'^2}\right) \quad \text{or} \quad k_{2D} = \frac{1}{2}\left(\overline{u'^2} + 2\overline{w'^2}\right),$$ (3)

depending on the measurement zone. This allows for an easy comparison with the readily available
k from simulation results, which is defined as

$$k_{3D} = \frac{1}{2}\left(\overline{u'^2} + \overline{v'^2} + \overline{w'^2}\right)$$ (4)

To analyse the influence of this approximation the numerical k was computed in the same way as in
the experiment from only two normal stress components. The results of the hit rate for this can be
found under heading k_{2D} in Table 1, while k_{3D} shows the hit rates when comparing the three compo-
nent numerical k (4) with the two component experimental k (3). The differences between the corre-
sponding hit rates are in general small, but the correct two component comparison between simula-
tion and experiment gives slightly higher hit rates on the average. The obtained hit rates are how-
ever relatively small especially for the 0° case. The reason for this is that the equilibrium inflow
profile for k is much smaller than the measured one (Franke, 2009). This difference is mainly
maintained through the array for the 0° case, while for the –45° case the turbulence production by
the buildings is much larger, leading to higher hit rates.

Table 1: hit rates of non dimensional Reynolds stresses, turbulent kinetic energy and RMS velocities.

Zone	$\overline{u'^2}$	$\overline{v'^2}$	$\overline{w'^2}$	$\overline{u'v'}$	$\overline{u'w'}$	k_{3D}	k_{2D}	u_{rms}	v_{rms}	w_{rms}
Δ_a	0.005	0.004	0.003	0.002	0.002	0.005	0.005	0.006	0.005	0.005
0° - coarse uv										
z=1.275m	0.18	0.09	—	0.36	—	0.09	0.08	0.36	0.46	—
z=2.550m	0.12	0.40	—	0.43	—	0.25	0.25	0.35	0.74	—
z=5.100m	0.09	0.55	—	0.45	—	0.42	0.42	0.40	0.84	—
0° - fine uv										
z=0.900m	0.19	0.13	—	0.39	—	0.15	0.13	0.40	0.40	—
z=1.725m	0.17	0.34	—	0.53	—	0.22	0.12	0.39	0.59	—
z=2.550m	0.06	0.47	—	0.45	—	0.25	0.26	0.25	0.59	—
0° - fine uw										
z=2.550m	0.15	—	0.51	—	0.49	0.46	0.44	0.41	—	0.87
0° - profiles										
z variable	0.05	—	0.53	—	0.36	0.44	0.47	0.28	—	0.79
45° - coarse uv										
z=1.275m	0.35	0.37	—	0.26	—	0.36	0.39	0.70	0.72	—
z=2.550m	0.34	0.46	—	0.38	—	0.44	0.44	0.77	0.84	—
z=5.100m	0.12	0.69	—	0.63	—	0.46	0.45	0.62	0.98	—
45° - fine uv										
z=0.900m	0.34	0.38	—	0.37	—	0.34	0.35	0.79	0.74	—
z=1.275m	0.40	0.44	—	0.31	—	0.45	0.49	0.78	0.90	—
z=1.575m	0.40	0.52	—	0.38	—	0.49	0.53	0.82	0.84	—
z=2.550m	0.41	0.70	—	0.40	—	0.67	0.70	0.86	0.89	—
45° - fine uw										
z=2.550m	0.51	—	0.32	—	0.43	0.59	0.62	0.84	—	0.68
45° - profiles										
z variable	0.27	—	0.49	—	0.50	0.89	0.88	0.74	—	0.84

The positive influence of the turbulence produced by the building array is of course also visible in the hit rates for the normal Reynolds stresses. First of all the hit rates of the –45° case are higher than the ones of the 0° case. And in both cases the hit rates decrease with increasing z in the coarse and fine uv measurement zones due to the fact that the flow above the obstacle array is stronger influenced by the inflow k, which in the simulations is approximately half of the experimental value. In the –45° case this influence is reduced by the larger turbulence production caused by the oblique buildings.

Another result is that the hit rates are substantially higher when they are based on the root mean square (RMS) velocity fluctuations and not on their variances, which define the normal Reynolds stresses. These hit rates are shown in the last three columns of Table 1. The explanation of this behaviour by simple mathematics is not presented here due to space limitations. It will be provided in the extended abstract. The important result from these differences is that good results for the RMS values, which are normally provided by experiments, do not automatically lead to good results for the metrics of the turbulent kinetic energy which is calculated from the normal Reynolds stresses.

Finally the metrics of the Reynolds shear stresses are also presented in Table 1. First of all they do not vary as much as the hit rates of the normal stresses as a function of measurement zone and measurement plane within a zone. While for the coarse uv zone of the 0° and –45° case there is an increase of hit rate with height, contrary to the behaviour of the normal stresses' metrics, the metrics of the fine uv zones do not show any clear tendency with height. The magnitude of the hit rates is on average larger than the one of the normal stresses, especially in the 0° case. Taking into account that only a two equation turbulence model with the Boussinesq hypothesis was used to model the Reynolds stresses the result for the Reynolds shear stresses is acceptable.

In this work information on the validation of the Reynolds stress components for the MUST wind tunnel case was provided to complete the description of this validation case for the COST action 732. The availability of velocity measurements with corresponding uncertainties at more than 1700 measurement positions for the 0° and –45° case together with concentration measurements with corresponding uncertainties at more than 250 measurement positions for the –45° case makes this case a *must* for validation of CFD codes for urban dispersion simulations.

REFERENCES

Bezpalcova, K. (2007). *Physical Modelling of Flow and Dispersion in an Urban Canopy*. PhD thesis, Faculty of Mathematics and Physics, Charles University, Prague.

Britter, R., Schatzmann, M., Eds. (2007a). *Model Evaluation Guidance and Protocol Document*. COST Office, Brussels.

Britter, R., Schatzmann, M., Eds. (2007b). *Background and Justification Document to Support the Model Evaluation Guidance and Protocol Document*. COST Office, Brussels.

Franke, J., Hellsten, A., Schlünzen, H., Carissimo, B., Eds. (2007). *Best Practise Guideline for the CFD Simulation of Flows in the Urban Environment*. COST Office, Brussels.

Franke, J., Bartzis, J., Barmpas, F., Berkowicz, R., Brzozowski, K., Buccolieri, R., Carissimo, B., Costa, A., Di Sabatino, S., Efthimiou, G., Goricsan, I., Hellsten, A., Ketzel, M., Leitl, B., Nuterman, R., Olesen, H., Polreich, E., Santiago, J., Tavares, R. (2008). "The MUST Model Evaluation Exercise: Statistical Analysis of Modelling Results", Proceedings of the 12th International Conference on Harmonization within Atmospheric Dispersion Modelling for Regulatory Purposes, 6-10 October, Cavtat, Croatia, 414-418.

Franke, J. (2009). "Validation of a CFD model for the prediction of flow and dispersion in the urban environment", Proceedings of the 4th International Building Physics Conference, 15-18 June, Istanbul, Turkey.

Olesen, H. R., Baklanov, A., Bartzis, J., Barmpas, F., Berkowicz, R., Brzozowski, K., Buccolieri, R., Carissimo, B., Costa, A., Di Sabatino, S., Efthimiou, G., Franke, J., Goricsan, I., Hellsten, A., Ketzel, M., Leitl, B., Nuterman, R., Polreich, E., Tavares, R. (2008). "The MUST Model Evaluation Exercise: Patterns in Model Performance", Proceedings of the 12th International Conference on Harmonization within Atmospheric Dispersion Modelling for Regulatory Purposes, 6-10 October, Cavtat, Croatia, 403-408.

VDI (2005). *Environmental meteorology – Prognostic microscale windfield models – Evaluation for flow around buildings and obstacles*. VDI guideline 3783, Part 9. Beuth Verlag, Berlin.

Yee, E., Biltoft, C. A. (2004). "Concentration Fluctuation Measurements in a Plume Dispersing Through a Regular Array of Obstacles", Boundary-Layer Meteorology, 111, 363-415.

CFD modeling of wind induced mean and fluctuating external pressure coefficients on the Texas Technical University building

1st T.K.Guha, 2nd R.N.Sharma, 3rd P.J.Richards

1st Ph.D. Candidate - tguh001@aucklanduni.ac.nz - Department of Mechanical Engineering

2nd Senior Lecturer - r.sharma@auckland.ac.nz - Department of Mechanical Engineering

3rd Associate Professor - pj.richards@auckland.ac.nz - Department of Mechanical Engineering

The University of Auckland, Private Bag 92019, Auckland, New Zealand

Keywords: Mean pressure; Fluctuating pressure; Shear Stress Transport (SST) model; Full scale data; TTU building.

ABSTRACT

This paper considers the possibility of predicting both external mean and fluctuating wind pressures on buildings by using a finite volume based CFD method in conjunction with an advanced k- ω based two equation turbulence model called Shear Stress Transport (SST) model developed by Menter (1994). The building studied in this case is the low rise Texas Technical University (TTU) building located at Lubbock, Texas, USA. Results from the computer model are compared with the results obtained for the same building configuration using standard k-ε model, RNG k-ε model and full scale data. The Kato-Launder (KL) modification was incorporated in all turbulence models for the production limiter. The SST model gives improved performance in terms of predicting the windward edge roof top separation and reattachment compared to other models. The fluctuating rms pressure coefficients were calculated using the equations proposed by Paterson & Holmes (1989), Selvam (1992) and Richards & Wanigaratne (1993). While all the three equations under predict the windward wall fluctuating pressure coefficients, the equation proposed by Richards & Wanigaratne provides conservative results in the leeward and roof top reattachment zone in comparison to full scale data.

The United States National Science Foundation sponsored Colorado State University/Texas Technical University Cooperative Program on Wind Engineering provided valuable insights into wind effects on TTU experimental building, a typical example of a low rise structure. The study

───────────────

Contact person: 1st T.K.Guha, Department of Mechanical Engineering, The University of Auckland, Private Bag 92019, Auckland, New Zealand, Tel.: +649 3737599, fax: +649 3737479, Email: tguh001@aucklanduni.ac.nz

involved field tests on the high plains of Lubbock, Texas and 1:100 scale model studies in the Meteorological Wind Tunnel (MWT) at Colorado State University (Yeatts & Mehta, 1993). Since then a number of wind tunnel simulations and numerical studies have been conducted on the flow around the TTU building using different turbulence models; Reynolds time Averaged Navier Stokes (RANS) models as well as Large Eddy Simulations (LES) by researchers with TTU field data as benchmark. This paper specifies the computational work done using commercial computational fluid dynamics package CFX to simulate the flow field around TTU building using standard k-ε model, RNG k-ε model and a k-ω based two equation turbulence model called the SST model. The main reason for using SST turbulence model lies in the limitation of standard two equation turbulence models to accurately predict the onset and extent of flow separation (separation bubble) at the roofs of the buildings.

In the present work, 0° angle of attack corresponding to wind flowing perpendicular to the shorter wall of TTU containing the door has been investigated. The results from numerical computation are compared with the full scale data considering the average of all measured data within ± 1 degree of the intended angle of attack. While all the turbulence models are found to predict the windward wall mean pressure coefficients fairly accurately, the SST model is found to most accurately predict the leading edge roof separation bubble and reattachment and hence mean roof pressure coefficients. The k-ε model and its variants are found to over-predict the windward edge roof mean pressure coefficient due to overestimation of turbulent kinetic energy (and hence eddy viscosity) in the windward wall stagnation region thereby causing increased mixing of turbulent structures. The leeward wall mean pressure coefficients are found to be sensitive to mesh variations with all the models under predicting mean pressure coefficients.

The initial problem involved successful modeling of atmospheric boundary layer in CFX based on specifying appropriate inlet and wall boundary conditions as per the recommendations of Richards & Hoxey (1993). The TTU building was modeled as a rectangular block placed inside the bigger rectangular domain of dimensions 23 H (i.e. building height) stream wise, 23 H transverse and 12 H high. The domain was meshed using three different unstructured mesh formats consisting of tetrahedral cell as shown in Table 1 to study the sensitivity of the solution to different mesh configurations. The TTU building skeleton was removed out of the domain to reduce computational overhead since our interest is limited to the flow around the building.

Mesh Setup	Mesh Type	Number of Elements	Number of Nodes
1	Unstructured	64932	22123
2	Unstructured	681506	218228
3	Unstructured	1312566	361925

Table 1: Mesh configurations investigated

A steady state solution for flow field around the building was obtained for different mesh setups and turbulence models namely SST model, k-ε model and RNG k-ε model for 0° angle of attack for a ridge height velocity of 30 m/s. Convergence was considered to be achieved when the maximum residual for each transported quantity was less than 10^{-4}. A high resolution scheme (Ansys CFX, 2007) was used to discretize the advection terms. Kato- Launder modification was incorporated for the production limiter term for all the turbulence models investigated. The computed mean external pressures ($\overline{C_{pe}}$) are represented in terms of mean pressure ($\overline{p}$) referenced to the ridge height dynamic pressure (q) as:

$$\overline{C_{pe}} = \frac{\overline{p}}{q} = \frac{\overline{p}}{\frac{1}{2}\rho u_h^2} \tag{1}$$

where u_h is the mean ridge height velocity of flow. Figures 1 (a), (b) and (c) show the centre-line mean windward, roof and leeward pressure coefficients respectively for mesh setup 1 for different turbulence models in comparison with full scale data. While all the models predict the windward wall pressure coefficients fairly accurately, SST model gives the best prediction as far as the windward edge roof centre-line mean pressures are concerned. The leeward wall pressure coefficients are significantly under-predicted by all models irrespective of the mesh density.
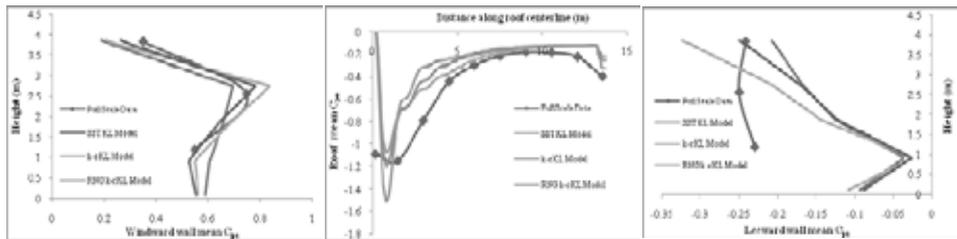
Figure 1: (a) Windward wall (b) Roof and (c) Leeward wall centre-line mean pressure coefficient for mesh setup 1

A systematic mesh sensitivity study was carried out using the method outlined in the editorial policy of Journals of Fluids Engineering, in particular to investigate the sensitivity of roof centre-line pressure coefficients to different mesh configurations. Richardson extrapolation technique used to work out the extrapolated solution using available data show a global average order of accuracy of 3.2 with oscillatory convergence occurring at 38% of the 391 points on the roof top centre-line. The maximum fine Grid Convergence Index (GCI) is 16% corresponding to a discretization uncertainty of $\overline{C_{pe}} = 0.09$. The average relative and extrapolated errors are 1.5% and 2% respectively. The leeward wall mean pressure coefficients also show some mesh sensitivity, all models however under predict the leeward wall pressure coefficients; the average deviation ($\overline{\delta C_{pe}}$) being 0.10. The deviations are more prominent in the lower part of the leeward wall.

The fluctuating (rms) pressure coefficients ($\widetilde{C}_{pe}$) cannot be calculated directly from CFD solutions since there are no straight forward equations to solve for rms pressure coefficients in k-ε and k-ω based models or their variants. However, since both the models (and their variants) solve for the transport equation of turbulence kinetic energy (k), the rms pressure coefficients are computed using the following equations suggested by Paterson & Holmes, Selvam and Richards & Wanigaratne respectively:

$$\widetilde{C}_{pe} = 2\left(\frac{k}{3} + 0.816\left|\overline{C_{pe}}\right|u_0\sqrt{k_0}\right)\Big/u_h^2 \tag{2}$$

$$\widetilde{C}_{pe} = 2\left|\overline{C_{pe}}\right|\left(1.414 u_h\sqrt{k_h} + k_h\right)\Big/u_h^2 \tag{3}$$

$$\widetilde{C}_{pe} = 2\left[Ek_0^2\left(u_0^2\sigma_{u0}^2 + Ek_0^2\right)\left\{(1-F) + \frac{F\,\overline{C_{pe}}\,u_h^2}{u_0^2 + 2k_0}\right\}^2\right]^{0.5} \tag{4}$$

In these equations, $\overline{C_{pe}}$ and k are the local mean pressure coefficient and turbulent kinetic energy, u_0 and k_0 are the velocity and turbulent kinetic energy in the approach flow at the height of interest; u_h and k_h are the velocity and turbulent kinetic energy in the approach flow at the building height; $\sigma_u^2{}_0 \approx k_0$; E is a constant taken as 0.5 and F is a correlation factor taken as 0.64. Equation (4) assumes the azimuthal gradient of mean pressure coefficient ($\partial\overline{C_{pe}}/\partial\theta$) to be zero along the centre-line plane perpendicular to the shorter edge of the building. Figures 2 (a), (b) and (c) give the centre-line fluctuating pressure coefficient ($\widetilde{C}_{pe}$) for the building windward, roof and leeward side respectively for mesh setup 1 calculated using the proposed equations.
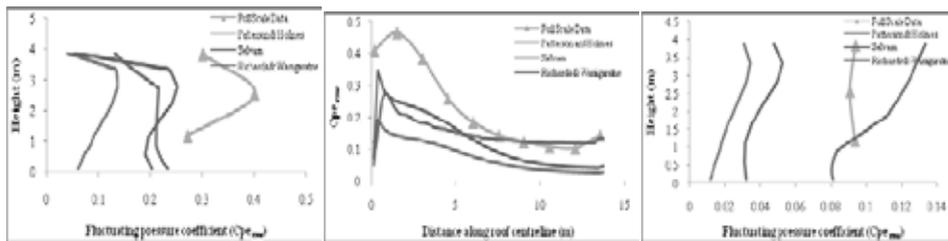
Figure 2: (a) Windward wall (b) Roof and (c) Leeward wall centre-line fluctuating pressure coefficient for mesh setup 1

The results show that while all the proposed equations under predict the windward wall fluctuating pressure coefficients, the equation proposed by Richards & Wanigaratne provides conservative results in the leeward and roof top reattachment zone in comparison to full scale data.

From the overall analysis of results it is concluded that SST model gives more accurate flow predictions of the rooftop separation bubble and hence mean pressure coefficients on the windward wall and roof of TTU building using significantly low computational overheads compared to more popular k-ε based models. Leeward mean pressure coefficients are however under-predicted by all the models for all mesh configurations and needs further investigation. The model proposed by Richards & Wanigaratne provides the best estimate of fluctuating roof pressures in the flow attachment and leeward zone with all models significantly under-predicting the windward and windward edge roof top centre-line fluctuating pressures.

REFERENCES

Menter F. R. (1994). "Two-Equation Eddy-Viscosity Turbulence Models for Engineering Applications", *AIAA Journal*, Vol. 32(8), 1598 – 1605.

Paterson D. A., Holmes J. D. (1989). "Computation of Wind Flow Around the Texas Tech Building", Proceedings, Workshop on Industrial Fluid Dynamics, Heat Transfer and Wind Engineering, CSIRO-DBCE, Highett, Victoria, Australia, 33-34.

Selvam R. P. (1992). "Computation of Pressures on Texas Tech Building", *Journal of Wind Engineering and Industrial Aerodynamics*, 41-44, 1619-1627.

Richards, P. J., Wanigaratne B. S. (1993). "A comparison of computer and wind-tunnel models of turbulence around the Silsoe Structures Building", *Journal of Wind Engineering and Industrial Aerodynamics*, 46&47, 439-447.

Yeatts B. B., Mehta K. C. (1993). "Field experiments for building aerodynamics", *Journal of Wind Engineering and Industrial Aerodynamics*, 50, 213-224.

Richards P. J., Hoxey R. P. (1993). "Appropriate boundary conditions for computational wind engineering models using the k-ε turbulence model", *Journal of Wind Engineering and Industrial Aerodynamics*, 46&47, 145-153.

Ansys CFX help manual (2007), *Ansys CFX-11.0*, ANSYS Inc.

The evolution of the application of CFD on pedestrian wind comfort in engineering practice, a validation study

L. Aanen, G.M. van Uffelen

Peutz BV – l.aanen@mook.peutz.nl– Peutz BV– m.vanuffelen@mook.peutz.nl

Keywords: *CFD wind tunnel pedestrian wind-comfort.*

ABSTRACT

Starting in 2002, Peutz BV in the Netherlands is developing an application using CFD for the prediction of pedestrian wind comfort. The first models used the standard k-ε model and a hybrid differencing scheme and showed moderate agreement with measurement results from wind tunnel test on physical models of the same building projects. Nowadays better agreement is found using the RNG k-ε model, a second order differencing scheme (MINMOD), improved boundary conditions and an increasing number of grid cells. However, a numerical 'virtual wind tunnel' cannot yet replace a real one. But, the location of 'hot spots' can be predicted, which can be advantageous for certain projects and can be of help to the set up of measurements. For projects with a rather simple geometry CFD can even by used as an alternative for wind tunnel measurements.

INTRODUCTION

Peutz is a consultancy, active in the fields of acoustics, industrial noise, building physics, fire safety, environmental technology and wind tunnel research. Peutz has branches in the Netherlands, Belgium, Germany, France and the United Kingdom and is involved in the design of office and residential buildings, railway stations, airports etc.

In Mook in the Netherlands, besides a certified acoustical laboratory and a laboratory for building physics, an atmospheric boundary layer wind tunnel is present. In the wind tunnel studies are performed with respect to:
− pedestrian wind comfort;
− dispersion of air pollution;
− mean pressures on ventilation openings for ventilation of parking garages and natural ventilation for CFD;
− forces and moments on building constructions.

This paper deals with the comparison between numerical simulation and experimental work. Numerical CFD models concerning wind around buildings and pedestrian wind comfort are tested and the results are compared with measurements on physical scale models in the wind tunnel.

Contact person: L. Aanen, Peutz BV, PO Box 66, 6585 ZH, Mook, The Netherlands,
phone +31 (0) 24 357 07 07, fax +31 (0) 024 358 51 50, E-mail l.aanen@mook.peutz.nl

The possibilities of CFD for application in the field of wind around buildings and pedestrian comfort are studied. The code Phoenics 2006 of Cham Ltd. is employed with a Cartesian mesh.

Recently, Hu and Wang [2005] showed that using CFD, an adequate prediction of street-level winds can be obtained. However, there remain some drawbacks, especially concerning the so-called Venturi-effect between tall buildings, as Blocken et. al. [2007] show. Comparison of wind tunnel measurements on pedestrian comfort with CFD predictions was investigated by a.o. Lam and To [2006], Richards et. al. [2002], Li et. al.[2004]. Lam and To [2006] show that with the RNG k-ε model a accuracy of +/- 10% can be achieved.

CFD MODELS

In the first stage of developing our CFD-application for predicting pedestrian wind comfort a model of a large part of our wind tunnel was constructed so as to be able to validate the computed atmospheric boundary layer and the resulting wind flow distribution around buildings. This first model comprises the entire (former) wind tunnel of 15 m x 3 m x 0.9 m including the development of the boundary layer by the method of Counihan, consisting of a turbulence generator array as well as roughness elements over a length of 10 m. These object have been modelled in Phoenics as a bottom plate with a surface roughness of 3 cm applying the so-called 'roughness wall functions' for fully rough surfaces. Furthermore inlets have been placed at the ends of the 'virtual wind tunnel' with a turbulence intensity of 100 % and a uniform velocity equal to the average tunnel velocity of 8 m/s respectively. The first model uses the standard k-ε model and the hybrid differencing scheme. The total amount of grid cells was approximately 250,000. All models discussed in this article concern steady flow simulations.

The CFD model is capable of predicting the wind around a given geometry for 12 wind directions one after another. The CFD model of the wind tunnel has exactly the same size as the former wind tunnel at Mook so as to facilitate mutual comparison of the results, without need to worry about the effect of scaling and as a result Reynolds number effects.

Since in the approach described above a large part of the computer capacity is used to compute the flow approaching the geometry of interest, a second model was build. This model contains only the measurement section (with has a diameter of 2.3 m) with velocity and turbulence profiles forced at inlets around this section.

The second model has a wind profile with again an average wind velocity of 8 m/s but the velocity has been distributed over the height according to a power law with a coefficient of 0.35. Furthermore the RNG k-ε model and a second order differencing scheme (MINMOD) for the three velocity components have been applied in this model. The total amount of grid cells is approximately 250,000. Later versions of this latter model used more grid cells (approximately 600,000).

In the most recent versions of the model a number of improvements were applied. The flow around the geometry of interest is still computed for 12 different wind directions, but the inlet profiles for the velocity is now prescribed using the log-law and the models are no longer scaled down to wind tunnel scale. The roughness for each wind direction can be prescribed separately. This is important if the location is situated at the shore or other location with large differences in roughness for the different wind directions. The inlet profiles for the turbulence intensity k and the dissipation ε match with the velocity profile using the equations of the k-ε theory for a stable boundary layer. The equations for the velocity magnitude U, turbulence k and dissipation ε are:

$$U(z) = U_{ref} \frac{\ln\left(\dfrac{z-d}{z_0}\right)}{\ln\left(\dfrac{z_{ref}-d}{z_0}\right)} \text{ or } U(z) = \frac{u*}{\kappa}\ln\left(\frac{z-d}{z_0}\right),$$

(1)

$$k = \frac{u^{*2}}{\sqrt{C_\mu}},$$ (2)

and

$$\varepsilon = \frac{u^{*3}}{\kappa(z-d)}.$$ (3)

In these equations U_{ref} is the velocity at a reference height z_{ref}, d the displacement height, z_0 the roughness height, κ the Von Karman constant, u* the friction velocity and C_μ a model constant of the k-ε model.

A constant pressure boundary condition is used for the outlets. With increasing computer power the amount of cells used, is increased to about 1,000,000 or more.

The results of computations for the 12 wind directions are combined with a local wind statistics to be able to judge the wind climate. In the Netherlands an official standard, the NEN 8100 (2006), is present, which prescribes that the wind climate has to be judged after the probability of exceeding a critical wind speed of 5 m/s.

RESULTS

The first model with the developing atmospheric boundary layer is very well capable of reproducing the wind tunnel flow. This means that at the measurement section the turbulence intensity at a height of 10 m (full scale) adopts the above mentioned value of 35% and that the resulting velocity profile shows to approximate the power law mentioned in the above.

The demand of CPU capacity to create the right velocity profile was relatively large (approximately 250,000 grid cells). This left too little grid cells available for the measurement section itself (approximately 150,000 grid cells). However, for rather simple rectangular building geometry's promising results were produced, even with standard k-ε model and hybrid differencing scheme. For more complex simulations no reliable results were obtained due to the lack of cells in the region of interest, in combination with the first order differencing scheme and the use of the simple turbulence model.

In the second model, with only the measurement section modeled, more grid cells are available in the region of interest. This means that in a typical street between two buildings 7 to 10 grid cells are available in the region of interest. In combination with the use of the RNG k-ε turbulence model, a second order differencing scheme (MINMOD) for the three velocity components and increasing computer power, more complex geometry's could be simulated.

In the present model a good agreement can be found in the predicted probabilities of exceeding the critical wind speed of 5 m/s, comparing the results of wind tunnel measurements and the results of a CFD computation. Even for a rather complex geometry like a group of high rise buildings a reasonable estimate of the wind climate can be made. A comparison between a wind tunnel measurement and a CFD computation is given in the figure below. The results of the wind tunnel measurements are indicated by the dots, with the probability of exceeding the critical wind speed printed next to it. The scale of the CFD results is limited to 20%. Above 20% the wind climate is qualified as "poor". In this case the maximum percentages in the CFD results are slightly underestimated (38% in the CFD, 44% in the measurements). In the CFD however the area in which a poor wind climate is expected is much easier to determine. For a complicated geometry like this in engineering practice a wind tunnel measurement is preferred. With the present computer power available the CFD model becomes too large and the computations too time consuming to be competitive with the wind tunnel. Especially if the local effects of e.g. screens and canopies have to be determined, more grid cells are needed. Phoenics offers the possibility of local grid refinement. This feature might be used in the future to determine the effects of local measures.

Figure 1. A comparison between a wind tunnel measurement and a CFD computation of the expected wind climate around a group of buildings.

CONCLUSIONS AND FUTURE WORK

From comparing the results of the numerical wind tunnel model with measurements in the real one it can be deduced that the numerical approach is promising.

A numerical 'virtual wind tunnel' cannot yet replace a real one.

For projects with a rather simple geometry CFD can even by used as an alternative for wind tunnel measurements for prediction of pedestrian wind comfort.

In order to get a reasonable performance a very fine grid with typically 7 to 10 grid cells or more per street between buildings should be applied.

Furthermore, the RNG k-ε model should be used in combination with second order numerical differencing schemes (MINMOD) for the velocities and a high number of grid cells (approx. 1,000,000) should be applied.

Further work will involve validation on cases with a more complex geometry. By means of local grid refinement the applicability of CFD on testing the effect of local measures like screens and canopies will be evaluated.

REFERENCES

Blocken, B., Carmeliet, J., Stathopoulos, T. (2007), CFD evaluation of wind speed conditions in passages between parallel buildings - effect of wall-function roughness modifications for the atmospheric boundary layer flow, Journal of Wind Engineering and Industrial Aerodynamics, Vol. 95, No. , pp 941-962.

Hu, C-H., Wang, F. (2005), Using a CFD approach for the study of street level winds in a built-up area, Building and Environment, Vol. 40, No. , pp 617-631.

Richards, P.J., Mallison, G.D., McMillan, D., Li, Y.F. (2002), Pedestrian level wind speeds in downtown Auckland, Wind and Structures, Vol. 5, No. 2-4, pp 151-164.

Li, L., Hu, F., Cheng, X.L., Han, H.Y. (2004), The application of computational fluid dynamics to pedestrian level wind safety problem induced by high-rise buildings, Chinese Physics, Vol. 13, No. 7, pp 1070-1075.

Lam, K.M., To, A.P. (2006), Reliability of numerical computation of pedestrian-level wind environment around a row of tall buildings, Wind and Structures, Vol. 9, No. 6, pp 473-492.

NEN 8100 (2006), Wind comfort and wind danger in the built environment. Nederlands Normalisatie-instituut.

RANS CFD modelling of particle dispersion behind a rectangular building in the atmospheric boundary layer

C.Gorlé[1,2], J. van Beeck[1], P. Rambaud[1]

1 Von Karman Institute for Fluid Dynamics – gorle@vki.ac.be – Waterloosesteenweg 72 1640 Sint-Genesius-Rode Belgium
2 University of Antwerp, Department of Physics, EMAT – Groenenborgerlaan 171 2610 Wilrijk Belgium

Keywords: Computational Fluid Dynamics, Atmospheric Boundary Layer, turbulence, dispersion.

ABSTRACT

Because of the increasing interest in urban air quality modelling, the application of Computational Fluid Dynamics (CFD) to study atmospheric dispersion processes in the lower part of the Atmospheric Boundary Layer (ABL) has become an important research subject. When considering the modelling of small particle dispersion in the lower part of the Atmospheric Boundary Layer (ABL) using Reynolds Averaged Navier Stokes simulations combined with a discrete phase particle tracking algorithm, the particle paths depend on the velocity and on the turbulence kinetic energy, from which the fluctuating velocity components are derived to predict turbulent dispersion. It is therefore important to correctly reproduce the atmospheric boundary layer flow, both for the velocity and the turbulence kinetic energy.

When performing CFD simulations it is not straightforward to correctly simulate a fully developed ABL with velocity and turbulence profiles that are preserved inside the computational domain. For RANS simulations with the standard k–ε model, Richards & Hoxey (1993) proposed a set of boundary conditions which result in horizontally homogeneous profiles. The drawback of this method is that it assumes a constant profile of turbulence kinetic energy, which is not always consistent with field or wind tunnel measurements. In Franke et al. (2007) it is suggested to use measured (height dependent) values for the turbulence quantities when available. This however can

Contact person: C. Gorlé, von Karman Institute for Fluid Dynamics, Waterloosesteenweg 72 1640 Sint-Genesius-Rode, Belgium, Tel.:+3223599678 ,FAX:+3223599600. E-mail gorle@vki.ac.be

result in a non-homogenous boundary layer which is developping inside the computational domain. Therefore, in Gorlé et al. (2009), a method was developed which enables the modelling of a horizontally homogeneous turbulence kinetic energy profile that is varying with height. The methodology consists of specifying the following inlet boundary conditions for the velocity, the turbulence kinetic energy and the turbulence dissipation:

$$U = \frac{u_*}{\kappa} \ln\left(\frac{z + z_0}{z_0}\right) \quad ; \quad k = \sqrt{A\ln(z + z_0) + B} \quad ; \quad \varepsilon = \frac{\sqrt{C_\mu} u_*}{\kappa(z + z_0)} \sqrt{A\ln(z + z_0) + B} \qquad (1\text{-}3)$$

where z_0 is the roughness height, u_* the boundary layer friction velocity, κ the von Karman constant, C_μ a constant for the turbulence model and A and B are constants that can be chosen to fit the turbulence profiles to e.g. test data. In order to obtain a horizontally homogeneous velocity profile, the inlet profile for U should be in equilibrium with the wall functions. It has been shown by Blocken et al. (2007) that in Fluent this can be obtained by setting the wall roughness constant equal to:

$$C_s = \frac{9.793 z_0}{k_s} \qquad (4)$$

where k_s is the roughness height, which is equal to or smaller than the height of the centre of the first cell, z_1. In addition to specifying these inlet conditions and wall roughness parameters, the constants C_μ and σ_ε should be adjusted to ensure that the inlet profiles are an approximate solution to the system of equations that is solved. The values for the constants can be determined using (Gorlé et al., 2009):

$$C_\mu = \frac{u_*^4}{A\ln(z_1 + z_0) + B} \qquad ; \qquad \sigma_\varepsilon = \frac{\kappa^2\left(-A/2 + k(z)^2\right)}{u_*^2(C_2 - C_1)k(z)} \qquad (5\text{-}6)$$

It is obvious that the influence of changing these turbulence model constants on the solution for the flow around buildings should be verified. Therefore the methodology has been applied to model the flow around a rectangular building configuration (CEDVAL A1-1). In addition, particle dispersion in the wake of this rectangular building was considered. The atmospheric boundary layer was modelled using equations 1-3 with $u_* = 0.374$, $z_0 = 0.00075$, $A = 0.025$ and $B = 0.41$. C_μ as calculated from equation 6 is equal to 0.07 as opposed to the standard value of 0.09. σ_ε is equal to 1.35 in the wall adjacent cell and increases to 1.57 at $z = 0.4$m as opposed to the standard constant value of 1.3. Figure 1 shows the building configuration and the location of the planes where measurement data is available. The computational domain extends 1m upstream and 4m downstream of the building and is 1.3m wide.

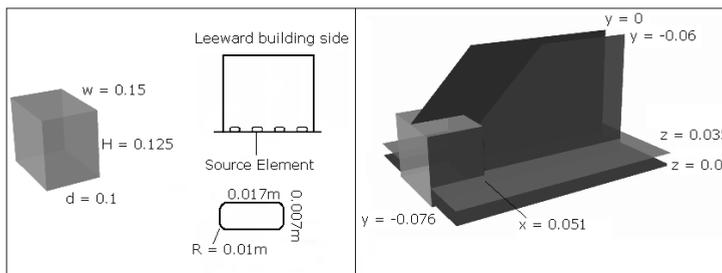Figure 1: Building configuration and location of measurement planes

Four different simulations were performed using identical inlet and wall boundary conditions, but varying the turbulence constants C_μ and σ_ε as indicated in Table 1. The reason for testing different settings of the turbulence model constants is the fact that the equations for C_μ and σ_ε are derived for

equilibrium between turbulence production and dissipation, which is not necessarily valid in the wake or within the influence area of the building. In addition to the modification of the turbulence model constants, the influence of applying the Kato-Launder modification to the production term of the turbulence kinetic energy was also investigated, since this correction is known to improve the prediction of the turbulence kinetic energy in front of blunt bodies (Lakehal et al., 1997).

Table 1: Settings of turbulence model constants considered in simulations

k-ε standard	Standard constants in entire computational domain
k-ε modified	Modified constants in entire computational domain
k-ε hybrid 1	Modified constants, but standard constants in the wake (region extending 2 building heights downstream)
k-ε hybrid 2	Modified constants, but standard constants within the influence area of the building (half sphere, r =0.22m, centre 0.02m downstream of building)

When comparing the velocity field, the main influence of varying the turbulence model constants or the production term is found in the predicted wake length. Table 2 compares the length in terms of the building height H for the different settings.

Applying the Kato-Launder correction results in an increased wake length, which is the result of the decreased turbulence production in front of the building. Although this improves the overall prediction of the turbulence kinetic energy field, the local prediction in the wake is not in better agreement with the test data. Applying the modified constants in the entire computational domain slightly increases the turbulence kinetic energy in the wake, resulting in a marginally better agreement with the test data for this quantity. On the building sides, however, a small decrease in the turbulence kinetic energy results in a slightly larger separation bubble, which induces an increased wake length. This effect is eliminated when applying the standard constants in the wake, which also induces a further increase in the turbulence kinetic energy in the wake. The best agreement in the wake length is found when applying the standard constants around the building. The separation bubble on the building sides becomes very small, which results in a significant decrease of the wake length. In this case, however, there is a large overprediction of the turbulence kinetic energy, both in the stagnation region and in the wake.

The dispersion results will depend both on the mean velocity and the turbulence kinetic energy. Since there is not one simulation which provides the best agreement with the test data for both quantities, a trade-off between a good prediction of the wake length and a good prediction of the turbulence field is required. In order to investigate which is the more important, all the flow results highlighted in Table 2 were used for calculating the concentration field by tracking 80 000 particles (d=1μm).

Table 2: Predicted wake length (wake length test data = 1.7H). Highlighted cases were selected for dispersion modelling using discrete phase model.

	Standard production term	Kato-Launder production term
k-ε standard	2.6H	2.8H
k-ε modified	2.9H	3.1H
k-ε hybrid 1	2.5H	2.7H
k-ε hybrid 2	2.0H	**1.9H**

The concentration is expressed non-dimensionally as $K = \left(C_m/C_s\right)\left(U_{ref} H^2/Q_s\right)$, where C_m is the local measured concentration, C_s is the concentration at the source, U_{ref} is the reference velocity and Q_s is the source strength. In Table 3 a comparison between the performance of the different simulation settings is presented in terms of a hit rate. The hit rate at a measurement point is equal to 1

when $\left(K_{CFD} - K_{Test}\right)/K_{Test}$ is smaller than 0.2 or when $\left(K_{CFD} - K_{Test}\right)$ is smaller than 0.83 (corresponding to $C_m/C_s = 0.0001$), otherwise the hit rate is 0. Table 3 presents the averages over the different measurement planes and the average over all points. The prediction right behind the source is poor, with all simulations overpredicting the maximum concentration by 60 to 80%. The prediction on the symmetry plane and the plane y = -0.06 is reasonable and the modified model with the standard constants in the wake and the kato-launder modification for the production term gives the best result. On the plane y = -0.076, to the side of the building, the standard and the hybrid 1 settings overpredict the upstream pollutant dispersion. The model without the kato-launder modification performs better, since the separation bubble is slightly smaller thereby limiting the upstream movement of the pollutant. When applying the hybrid 2 settings, the further decrease of the separation bubble size results in an underprediction of the upstream pollutant dispersion. On the plane z = 0.01, the hybrid 2 settings provide the best results, which is probably related to the correct prediction of the wake length. On the higher plane, however, the influence of the turbulence kinetic energy seems to become more important and the hybrid 2 settings, which overpredict the turbulence kinetic energy, also overpredict the dispersion of the pollutant to higher locations. Here, the hybrid 1 settings show a better performance. Overall, the performance of the hybrid 1 model without the Kato-Launder modification is slightly better than the performance of the other models, but it is not possible to identify one model which provides the best result at all measurement locations.

The results indicate that both the prediction of the mean velocity and the turbulence kinetic energy are crucial in obtaining an accurate result for pollutant concentrations. Further work will focus on comparing the results obtained using the discrete phase model to results obtained using a passive scalar model and on performing LES simulations, from which additional information could be extracted to optimise the settings of the RANS simulations.

Table 3: Average hit rate for non-dimensional concentration K

	x=0.051	y=0	y=-0.06	y=-0.076	z=0.01	z=0.035	all
k-ε standard	**0.12**	0.72	0.53	0.10	0.36	0.53	0.49
k-ε hybrid 1	0.05	0.71	0.60	**0.16**	0.35	**0.57**	**0.51**
k-ε hybrid 1 with kl	0.07	**0.74**	**0.63**	0.13	0.31	0.51	0.49
k-ε hybrid 2	**0.12**	0.65	0.47	0.09	**0.51**	0.47	0.49
k-ε hybrid 2 with kl	0.07	0.65	0.50	0.08	0.49	0.49	0.49

REFERENCES

Richards P., Hoxey R. (1993). "Appropriate boundary conditions for computational wind engineering models using the k–e turbulence model", Journal of Wind Engineering and Industrial Aerodynamics, 46-47, 145–153.

Franke J., Hellsten A., Schlunzen H., Carissimo B. (Eds.) (2007). "Best Practice Guideline for the CFD Simulation of Flows in the Urban Environment", COST Action 732.

Gorlé C., van Beeck J., Rambaud P., Van Tendeloo G. (2009) "CFD modelling of small particle dispersion: The influence of the turbulence kinetic energy in the atmospheric boundary layer", Atmospheric Environment 43, 673-681.

Blocken B., Stathopoulos T., Carmeliet J. (2007). "CFD simulation of the atmospheric boundary layer: wall function problems", Atmospheric Environment 41, 238–252.

Lakehal D., Rodi W. (1997). "Calculation of the flow past a surface-mounted cube with two-layer turbulence models", Journal of Wind Engineering and Industrial Aerodynamics, 67&68, 65-78.

LONG-SPAN BRIDGES

Limits for the control of wind-loaded slender bridges with movable flaps
Part I: Aerodynamic modelling, state-space model and open-loop characteristics of the aeroelastic system

A. Kirch[1], U. Peil[1], C. Borri[2]

[1]*Technische Universität Carolo-Wilhelmina zu Braunschweig*

Institute of Steel Structures, Beethovenstraße 51, 38106 Braunschweig, Germany
a.kirch@is.tu-braunschweig.de, u.peil@is.tu-braunschweig.de
[2]*Università degli Studi di Firenze*
Dipartimento di Ingegneria Civile, Via di S. Marta 3, 50139 Firenze, Italy
cborri@dicea.unifi.it

Keywords: bridges, flutter, divergence, active aerodynamic control

ABSTRACT

In recent years several ideas have been investigated to improve the vibrational behaviour of bridges especially under wind action using controlled actuators. These devices should reduce the system deflection due to wind action and avoid the occurrence of aeroelastic instabilities. In this paper, damping and stabilisation of a bridge-like system with aerodynamically effective flaps are investigated. The flaps are attached to both sides of the bridge girder (Fig. 1) and actively controlled. They efficiently change the flow around the girder and generate additional external, aerodynamic forces. Not only the flutter but also the divergence wind speed of the aeroelastic system can thus be modified.

Aerodynamically effective, movable control surfaces have been used in aerospace engineering to suppress the influences of disturbances on aircraft wings for many years (e.g. Edwards 1977). Their application to bridge decks was investigated by Kobayashi & Nagaoka (1992) and Ostenfeld & Larsen (1992) for the first time. A list of journal papers and dissertations on bridges that are actively controlled with aerodynamically effective control shields is given in the full paper. In aerospace engineering, the primary task of a wing is to produce a lift. Flaps, as integrated parts of the aerofoil, modify its surface in order to evoke positive effects without increasing the disturbing impact of gusts.

Contact person: A. Kirch, Technische Universität Carolo-Wilhelmina zu Braunschweig
Institute of Steel Structures, Beethovenstraße 51, 38106 Braunschweig, Germany
Phone +49 (0)531 / 391-3378, Fax +49 (0)531 / 391-4592
E-mail a.kirch@is.tu-braunschweig.de

With bridges, however, control shields are extra components that augment the area exposed to the wind. They cannot bear any significant payload and can hence not directly fulfil the intrinsic task of a bridge. In addition to motion-induced aerodynamic forces, new gust-induced forces arise simultaneously, which also need to be suppressed. Therefore, the use of aerodynamically effective control shields is generally less efficient for bridges than for aircraft wings. Moreover, control shields need a minimum wind speed to work. They are not suited for damping oscillations in still air. Aircraft wings do not possess this disadvantage either.
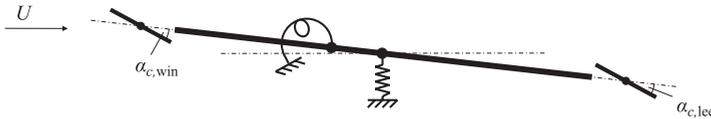

Figure 1: Two-dimensional aeroelastic system extended with aerodynamically balanced flaps.

Two kinds of aerodynamic forces acting on the total aerodynamically effective cross section are considered. Together with its structural parameters, motion-induced wind forces influence the properties of an aeroelastic system. Gust-induced forces, which are also called buffeting forces, act as disturbances on the bridge-flap system. In order to investigate an aerodynamically controlled bridge with methods of control theory, a realistic and mathematically consistent description of the forces caused by the wind flow around the girder is of particular importance. Motion-induced and gust-induced forces can be represented in the frequency domain as unilateral Laplace transforms with transfer equations of linear, time-invariant transfer elements.

Aerodynamic derivatives constitute a main part of the transfer function of motion-induced aerodynamic forces. For the system displayed above, the theoretical derivatives based on potential theory are used as proposed by Küssner & Göllnitz (1964). In the mentioned reference the results are derived for a wing-aileron-tab combination, which is typical of aerospace engineering. The geometry and the derivatives of the airfoil can be linearly transformed into the corresponding properties of the system shown in Fig. 1. Bridges which aerodynamically effective flaps are applied to are assumed to have streamlined cross sections. Therefore the derivatives of the bridge-flap system are similar to the ones of the flat plate combination based on potential theory. The transfer functions of gust-induced forces are also derived on the basis of potential theory according to Sears (1940).

The transfer functions of the aerodynamic forces are approximated with rational functions. In this paper, rational functions according to the Minimum-State Method (Karpel 1981) are used. Together with a linear description of the structure, rational functions allow the aeroelastic system to be represented with a linear, time-invariant state-space model.

The dynamic characteristics of the aeroelastic system can be evaluated with an eigenvalue analysis of its system matrix. System stability is of major interest in this context. Due to the effect of motion-induced aerodynamic forces, aeroelastic instabilities can occur in the form of flutter and divergence. Since the system matrix contains the mean horizontal wind speed U, a parameter-dependent, linear eigenvalue problem must be solved. Neutral-stable states occur at the zero crossing of the eigenvalue real-part curves (Fig. 2). The parameters of the numerical example are given in the paper.

The mathematical description of the flap-extended plant depends on the type of the chosen control input. One possibility is to act on the extended plant through forces in the form of torques around the flap hinges. In this paper, the flaps are modelled without a mass and it is assumed that there is no passive coupling between the flaps and the bridge girder. Under these assumptions, a force input usually leads to very non-robust controllers and various numerical problems. Hence, a displacement input in the form of the flap angles $\alpha_{c,\text{win}}$ and $\alpha_{c,\text{lee}}$ (Fig. 1) is chosen. After appropriately separating
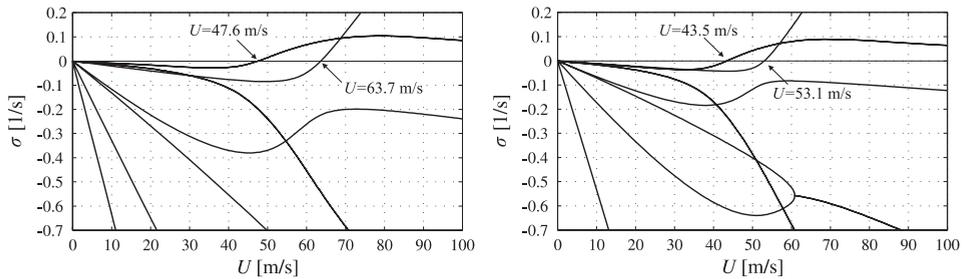
Figure 2: Real part σ of the system eigenvalues against the mean horizontal wind speed U. For a flap-free system on the left, for a system extended with unmoved flaps on the right.

the aerodynamical forces, a state-space model of the flap-extended aeroelastic plant can be derived.

When extending the plant with unmoved flaps, its eigenvalue curves are altered (Fig. 2). Since a larger area is exposed to the wind, the flutter and the divergence wind speed decrease. To systematically influence the extended aeroelastic system, the displacement inputs of the extended plant must depend on its outputs or states. Hence, the control loop must be closed.

As a consequence of the rational function approximation, the vector of control inputs contains not only the displacement inputs but also their first and second derivatives. These subvectors are not independent of one another and necessitate an actuator model, which is at least mathematically motivated (ZAERO 2004). For this purpose, a state-space model can be used that consists of three parallel PT_3 elements. If the static gain of this actuator is set to one and the transient response is tuned to be sufficiently fast and non-oscillating, the displacement input can be transferred to itself and its derivatives with a sufficient precision. The model of the flap-extended plant can be combined with the actuator model to a single state-space model.

With linear relations, the displacement inputs can be kinematically coupled to one another. For the numerical example, three different cases are considered. Separately driven flaps, flaps rotated in opposite directions ($\alpha_c = -\alpha_{c,\text{lee}} = \alpha_{c,\text{win}}$) and flaps rotated in the same direction ($\alpha_c = \alpha_{c,\text{lee}} = \alpha_{c,\text{win}}$).

Controller design, the closed-loop characteristics of the aeroelastic system and the efficiency of flaps for gust alleviation will be discussed in the second part of the paper.

REFERENCES

Edwards, J. W. (1977). "Unsteady aerodynamic modeling and active aeroelastic control" NASA. (NASA-CR-148019). – Contractor Report

Karpel, M. (1981). "Design for active and passive flutter suppression and gust alleviation" NASA. (NASA-CR-3482). – Contractor Report

Kobayashi, H. ; Nagaoka, H. (1992). "Active control of flutter of a suspension bridge" In: Journal of Wind Engineering and Industrial Aerodynamics, 41 (1–3), pp. 143–151

Küssner, H. G. ; Göllnitz, H. (1964). „Tabellen der aerodynamischen Derivativa des schwingenden Streckenprofils mit Knicken und Stufen" Deutsche Luft- und Raumfahrt. (DLR FB 64-05). – Forschungsbericht (in German)

Ostenfeld, K. H. ; Larsen, A. (1992). „Bridge engineering and aerodynamics" In: Aerodynamics of Large Bridges — Proceedings of the First International Symposium on Aerodynamics of Large Bridges, Copenhagen / Denmark, pp. 3–22

Sears, W. R. (1940). "Operational methods in the theory of airfoils in non-uniform motion" In: Journal of the Franklin Institute, 230 (1), pp. 95–111

ZAERO (2004). "Engineers toolkit for aeroelastic solutions" Version 7.2. ZONA Technology, Inc., – Theoretical Manual

Limits for the control of wind-loaded slender bridges with movable flaps
Part II: Controller design, closed-loop characteristics of the aeroelastic system and gust alleviation

A. Kirch[1], U. Peil[1], C. Borri[2]

[1]*Technische Universität Carolo-Wilhelmina zu Braunschweig*
Institute of Steel Structures, Beethovenstraße 51, 38106 Braunschweig, Germany
a.kirch@is.tu-braunschweig.de, u.peil@is.tu-braunschweig.de
[2]*Università degli Studi di Firenze*
Dipartimento di Ingegneria Civile, Via di S. Marta 3, 50139 Firenze, Italy
cborri@dicea.unifi.it

Keywords: bridges, flutter, divergence, active aerodynamic control

ABSTRACT

Based on the flap-extended aeroelastic system with displacement inputs, which is derived in the first part of the paper, this part addresses controller design and the behaviour of the controlled aeroelastic system.

For bridges, controller design aims at disturbance rejection. Acting disturbances should excite the system states or the measured plant output as little as possible. This requires a specific stability level. Due to the occurring instabilities, a certain level of stability is particularly important for aeroelastic systems. When closing the control loop with a linear, proportional controller, stability can again be examined regarding its eigenvalues. In order to ensure that the design objective is achieved, the controller is designed as a function of the plant parameter U, the mean horizontal wind speed. The controller gains are calculated for closely spaced discrete nodes of the wind speed and cubically interpolated afterwards. If ― in addition to guaranteeing a specific stability level ― there are no further conditions for the controller matrix, the design generally leads to an active controller. It allows for energy input into the plant and, when combined with the chosen state feedback, it is the most favourable controller type concerning stabilisation. Output feedback can only give worse results.

Contact person: A. Kirch, Technische Universität Carolo-Wilhelmina zu Braunschweig
Institute of Steel Structures, Beethovenstraße 51, 38106 Braunschweig, Germany
Phone +49 (0)531 / 391-3378, Fax +49 (0)531 / 391-4592
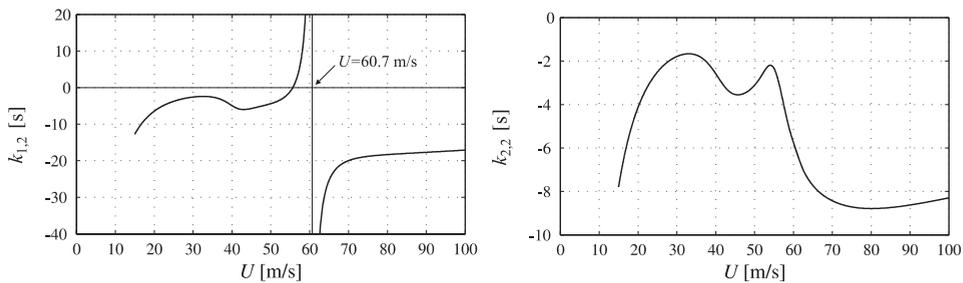E-mail a.kirch@is.tu-braunschweig.de

Figure 1: Typical controller gains; for kinematically coupled flaps that are moved in the same direction on the left, for separately driven flaps on the right.

Therefore and due to their dissipative nature, passive controllers also behave less favourably. Negative aspects of active stabilisation, like safety in permanent operation, are not considered here.

The chosen linear-quadratic control or optimal control reduces the controller design to the minimisation of a quadratic cost functional. A specific level of stability can be achieved for optimal controllers by modifying the system matrix of the aeroelastic plant.

Only the part of a plant that is both controllable and observable can be controlled in a closed loop. Two methods are chosen to examine these properties. The Hautus criteria and, for systems with a single input and a single output, locating pole-zero cancellations in the transfer functions of the aeroelastic system. When using the Minimum-State Method (Karpel 1981) for approximating the derivatives of motion-induced aerodynamic forces, the extended aeroelastic plant is generally controllable by the chosen input, with one exception in the case of kinematically coupled flaps. If the output signals are selected appropriately, the extended system is observable for all wind speeds. For each case of kinematically coupled flaps, the controller gains show one pole-like singularity at a certain wind speed (Fig. 1). These singularities can be traced back to non-controllable, non-stable eigenvalues. When moving in the modal shape of the non-controllable eigenvalue, the effect of the generated motion-induced aerodynamic forces is neutralised by the excited structural forces. The non-controllable eigenvalues cannot be stabilised by the controllers. Fig. 1 shows that there are no singularities of the controller gain and thus no non-controllable, non-stable eigenvalues, if the flaps are driven separately.

Fig. 2 displays the eigenvalues of the closed loops. As expected, the controllers move the low-damped or instable parts of the curves, except for the non-stable, non-controllable eigenvalues, below the selected level of the frequency real part. Active controllers are able to stabilise the plant in all wind speed ranges if a linear theory is applied. For both cases of kinematically coupled flaps neutral stability appears in the form of an aeroelastic divergence. For flaps that are rotated in the same direction, the numerical example shows a divergence wind speed that compares to the divergence wind speed of the flap-free aeroelastic system. For flaps that are rotated in opposite directions, divergence occurs at a relatively low speed that is identical to the divergence wind speed of the flap-extended open-loop system. Based on this result, coupled flaps that are moved in opposite direction perform distinctly worse than the ones that are moved in the same direction. For separately driven flaps there is no instability. When using a linear theory, the aeroelastic plant can be stabilised for all wind speeds by independently moved flaps. All results are derived based on small rotations of the plates. The size of the acting disturbances determines whether the limits that have been found so far can be reached at all.

The disturbing gust-induced forces can be described by a state-space model in an elegant way. Together with the model of the aeroelastic system, the gust model can be combined to a single state-space model. The input of the gust model, the fluctuating gust speeds, are generated from a given spectrum. Fig. 3 displays the standard deviation of the bridge deck rotation of the controlled systems. Additionally the rotation of the flap-free system is shown. Especially near the point at which the systems that are controlled with kinematically coupled flaps become instable, the rotation angles
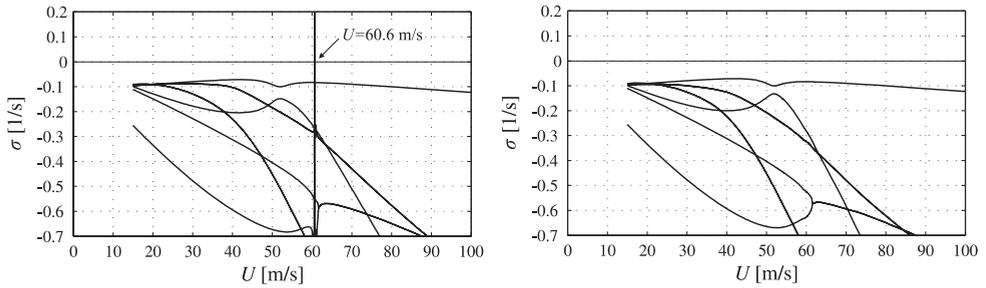
Figure 2: Eigenvalues of the aeroelastic system; controlled with kinematically coupled flaps that are moved in the same direction on the left, controlled with separately driven flaps on the right.
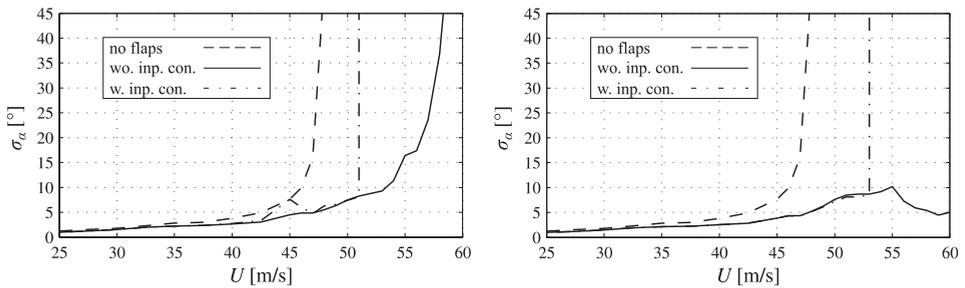

Figure 3: System response to a gust disturbance; for kinematically coupled flaps that are moved in the same direction on the left, for separately driven flaps on the right. (abbr.: w. / wo. inp. con.: with / without input constraints)

noticeably increase. In these ranges, the rotations of the girder cross section and particularly the rotations of the flaps have large numerical values that are not realistic. In addition they violate the assumption of small rotations, especially for the model of aerodynamic forces. Fig. 3 additionally shows simulation results for the same controller gains as before where the flap rotations are limited to $\alpha_{c,\text{lee}}$, $\alpha_{c,\text{win}} \leq 20°$. For all cases, stabilisation with flaps fails in the range of a mean horizontal wind speed that is $10 \div 15\ \%$ higher than the comparable one of the flap-free system. A real application of the favourable state feedback requires state estimators. They worsen the results of Fig. 3. Within the range of application of the flap-free system, the deflections under the effect of gust disturbances are in some ranges practically not alleviated by flaps.

Further investigations of stabilisation and disturbance rejection of aeroelastic bridge systems with actively controlled flaps should be performed with a more realistic modelling of the flow around the girder for large displacements. This could be done with the help of CFD algorithms that are for instance applied by Ostenfeld & Larsen (1997).

REFERENCES

Karpel, M. (1981). "Design for active and passive flutter suppression and gust alleviation" NASA. (NASA-CR-3482). – Contractor Report

Lunze, J. (2004). "Regelungstechnik 1: Systemtheoretische Grundlagen, Analyse und Entwurf einschleifiger Regelungen" 4th Edition, Springer, Berlin (in German)

Lunze, J. (2005). "Regelungstechnik 2: Mehrgrößensysteme, Digitale Regelung" 3rd Edition, Springer, Berlin (in German)

Ostenfeld, K. H. ; Larsen, A. (1997). "Elements of active flutter control of bridges" IABSE Conference on New Technologies in Structural Engineering, Lisbon, pp. 683–694

Aerodynamic stabilization for box-girder suspension bridges with super-long span

Y.J. Ge, H.F. Xiang

State Key Laboratory for Disaster Reduction in Civil Engineering, Tongji University – yaojunge@tongji.edu.cn – 1239 Siping Road, Shanghai 200092, China

College of Civil Engineering, Tongji University – hfxiang@tongji.edu.cn – 1239 Siping Road, Shanghai 200092, China

Keywords: aerodynamic stabilization, suspension bridge, box girder, central stabilizer, central slot.

INTRODUCTION

The construction of long-span suspension bridges around the world has experienced a considerable development for more than a century. Among ten longest-span suspension bridges in the world (Internet address A, 2007), the top four suspension bridges, including Akashi Kaikyo Bridge in Japan, Xihoumen Bridge in China, Great Belt Bridge in Denmark and Runyang Bridge in China, as well as Tsing Ma Bridge in Hong Kong China have been suffered in wind-induced problems in aerodynamic flutter or vortex shedding, and some control measures have been adopted to improve aerodynamic performance, for example, central stabilizer for Runyang Bridge, central slot for Xihoumen Bridge and Tsing Ma Bridge, both slot and stabilizer for Akashi Kaikyo, and guide vane for Great Belt (Ge 2008).

CENTRAL STABILIZER MOUNTED ON SINGLE BOX GIRDER

Runyang Bridge completed in 2005 is the second longest suspension bridge in China and the fourth longest in the world. The main section of the bridge was designed as a box-girder suspension bridge with span arrangement of 510m + 1490m + 510m as shown in Figures 1 and 2.

Contact person: Y.J. Ge, Department of Bridge Engineering at Tongji University, Tel.: +86-21-65983451 and FAX: +86-21-65984882. E-mail yaojunge@tongji.edu.cn
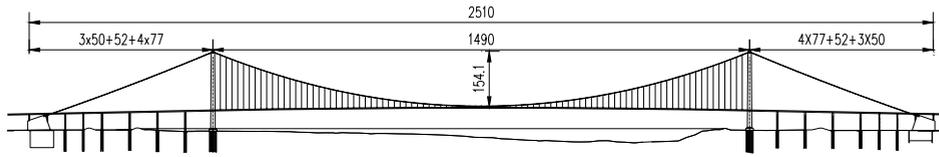
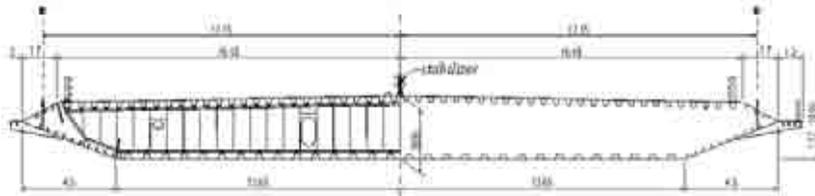Figure 1: Elevation of Runyang Bridge (Unit: m)

Figure 2: Deck cross-section of Runyang Bridge (Unit: m)

In order to study the aerodynamic stability, a wind tunnel experiment with a 1:70 sectional model was carried out in the TJ-1 Boundary Layer Wind Tunnel. It was found in the first phase of the testing that the original structure could not meet the requirement of flutter speed of 54m/s. With a stabilizer on the central deck as shown in Figure 2, further sectional model testing was conducted, and the confirmation wind tunnel tests with the full aeroelastic model were also performed in TJ-3 wind tunnel. The critical flutter speeds obtained from the sectional model (SM) and full model (FM) wind tunnel tests show good agreement with each other, and the central stabilizer of 0.88 m height as shown in Figure 3 can raise the critical flutter speed over the required value (Chen et al. 2002).

Figure 3: Central stabilizer mounted on the deck of Runyang Bridge

CENTRAL SLOT IN TWIN BOX GIRDER

Xihoumen Bridge becomes the longest suspension bridge in China and the second longest in the world just behind Akashi Kaikyo Bridge after completion in 2009. This bridge is part of the Zhoushan Island-Mainland Connection Project, and is finally designed as a two-span continuous suspension bridge with a main span of 1650m, as shown in Figure 4.
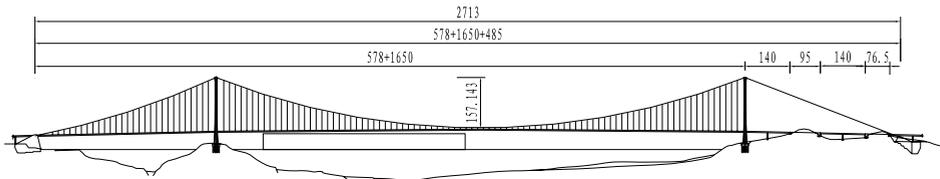
Figure 4: Elevation of Xihoumen Bridge (Unit: m)

Based on the experience gained from the 1490 m Runyang Bridge with flutter speed of 51 m/s and the 1624 m Great Belt Bridge with 65 m/s flutter speed, the span length of 1650 m may cause problems of aerodynamic instability for suspension bridges, even with the stricter stability requirement of 78.4 m/s in Xihoumen Bridge. Four alternative configurations of box girders were proposed and were investigated through sectional model wind tunnel tests. Apart from the traditional single box, the other three deck sections, including the single box with a central stabilizer of 2.2m (Figure 5a) and the twin box decks with a central slot of 6 m (Figure 5b) or 10.6 m (Figure 5c), can satisfy the flutter stability requirement, and the 6 m slotted twin-box girder was adopted, which was further modified to the final configuration as shown in Figure 5d (Ge et al. 2003).

(a) Single box

(b) Twin box with a 6m slot

(c) Twin box with a 10.6m slot

(d) Final scheme
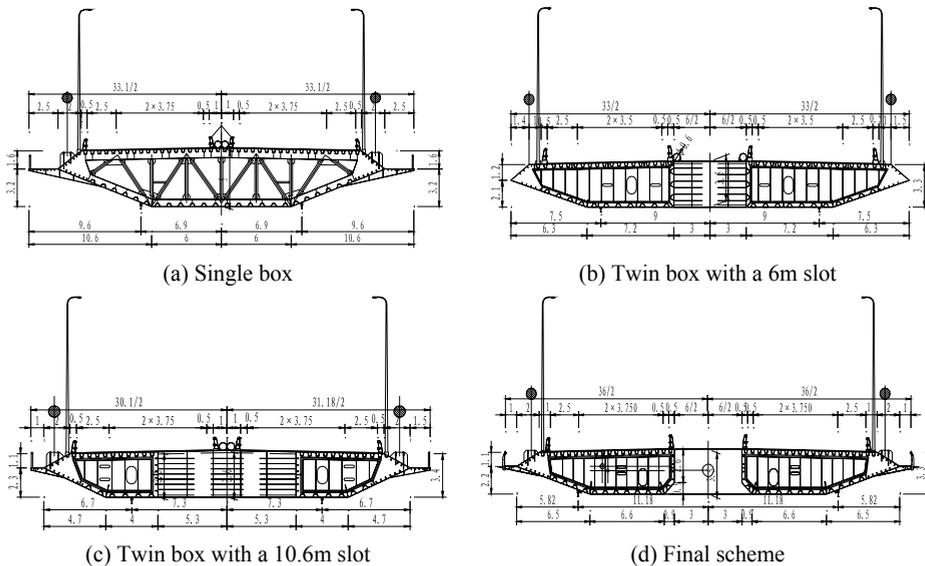
Figure 5: Proposed box girder sections for Xihoumen Bridge (Unit: m)

AERODYNAMIC METHODS FOR SUPER-LONG SPAN

The dominant concerns of super long-span bridges to designers are basically technological feasibility and aerodynamic considerations. With the emphasis on aerodynamic stabilization for longer span length, a typical three-span suspension bridge with a 5,000m central span and two 1,600m side spans is considered as the limitation of span length as shown in Figure 6. Two kinds of generic deck sections, namely widely slotted deck (WS) without any stabilizers (Figure 7a) and a narrowly slotted deck with vertical and horizontal stabilizers (NS) (Figure 7b), were investigated (Xiang & Ge 2003, Ge & Xiang 2006).

Figure 6: Elevation of the 5,000m long suspension bridge (Unit: m)

(a) WS Cross section   (b) NS Cross section
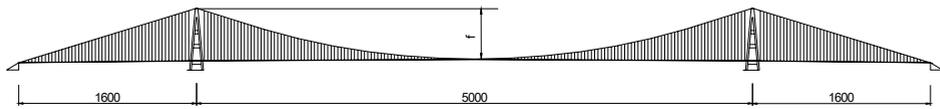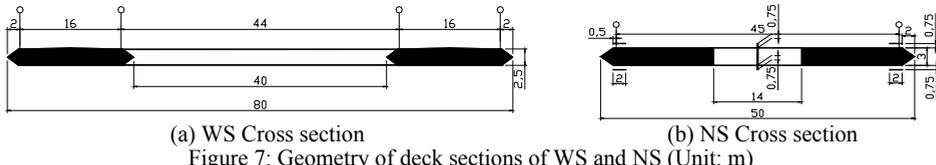Figure 7: Geometry of deck sections of WS and NS (Unit: m)

With the dynamic characteristics and the numerically identified flutter derivatives, the critical wind speeds of the suspension bridges were calculated by multi-mode flutter analysis assuming a structural damping ratio of 0.5%. The minimum critical wind speeds for the WS and NS sections are 82.9 m/s and 74.7 m/s, respectively (Ge & Xiang 2006, Ge & Xiang 2007).

CONCLUSIONS

With the experience gained from the recently built suspension bridges, such as Akashi Kaikyo, Xihoumen, Great Belt, Runyang and Hong Kong Tsing Ma, the intrinsic limit of span length due to aerodynamic stability is about 1,500m for a traditional suspension bridge with either a streamlined box deck or a ventilative truss girder. Beyond or even approaching this limit, designers should be prepared to improve aerodynamic stability of a bridge by modifying cable system or adopting some countermeasures for girder, including vertical and/or horizontal stabilizer and slotted deck as well as passive and active control devices. Based on a preliminary study, either a widely slotted deck or a narrowly slotted deck with vertical and horizontal stabilizers could provide a 5,000m span-length suspension bridge with high enough critical wind speed, which can meet aerodynamic requirement in most typhoon-prone areas in the world.

REFERENCES

Internet address. (2007). http://en.wikipedia.org.wiki//List_of_longest_suspension_bridge_spans
Ge, Y.J. (2008). "Aerodynamic challenges in long-span bridges", Keynote paper in the Proceedings of Centenary Conference of Institution of Structural Engineering, Hong Kong, China, January 24-26.
Chen, A.R., Guo, Z.S., Zhou, Z.Y., Ma, R.J and Wang, D.L. (2002). Study of Aerodynamic Performance of Runyang Bridge, Technical Report WT200218, State Key Laboratory for Disaster Reduction in Civil Engineering at Tongji University (in Chinese)
Ge, Y.J., Yang, Y.X., Cao, F.C. and Zhao, L. (2003). Study of Aerodynamic Performance and Vibration Control of Xihoumen Bridge, Technical Report WT200320, State Key Laboratory for Disaster Reduction in Civil Engineering at Tongji University (in Chinese)
Xiang, H.F. and Ge, Y.J. (2003). "On aerodynamic limit to suspension bridges", Keynote paper in the Proceedings the 11th International Conference on Wind Engineering, Texas, USA, June 2-5
Ge, Y.J. and Xiang, H.F. (2006). "Outstanding Chinese steel bridges under construction", Keynote paper in the Proceedings of the 6th International Symposium on Steel Bridges, Prague, Czech Republic, June 1-3
Ge, Y.J. and Xiang, H.F. (2007). "Great demand and various challenges - Chinese Major Bridges for Improving Traffic Infrastructure Nationwide", Keynote paper in the Proceedings of the IABSE Symposium 2007 on Improving Infrastructure Bringing People Closer Worldwide, Weimar, Germany, September 19-21.

Reliability of multiple tuned mass dampers
for bridge flutter control

F. Ubertini, A.L. Materazzi

Department of Civil and Environmental Engineering, University of Perugia
filippo.ubertini@strutture.unipg.it – materazzi@unipg.it

Keywords: suspension bridge, flutter, structural control, multiple tuned mass damper, reliability.

ABSTRACT

Due to their low inherent damping and high flexibility, long-span suspension bridges are particularly prone to wind loads which may produce large amplitude oscillations or even a catastrophic instability (Simiu & Scanlan 1996). Increasing the safety against aeroelastic instability is therefore a priority of bridge engineering. To this end, a great attention was recently devoted in the literature to conceiving control strategies against bridge flutter. On this respect, many studies were focused on the use of single and multiple tuned mass dampers (Lin, *et al.* 1999, Lin, *et al.* 2000, Chen & Kareem 2003 Kwon & Park 2004, Ubertini 2008). Single tuned mass dampers (STMDs) are especially prone to mistuning effects (see for instance Lin, *et al.* 2000). This circumstance, in the case of the classic coupled flutter instability of a bridge deck, makes the STMD solution practically unfeasible. Indeed, in such a case, the calculation of the optimal tuning of the device, close to the critic frequency of the system, is affected by aerodynamic and structural uncertainties (Ubertini 2008) and mistuning is basically unpreventable. Multiple tuned mass dampers (MTMDs), with equal amount of mass with respect to the STMDs, are known to enhance the control robustness in presence of mistuning effects (Kwon & Park 2004). These devices are composed by several small tuned mass dampers (TMDs) whose natural frequencies are equally spaced around a mean value which corresponds to the frequency that has to be controlled. The concept of irregular multiple tuned mass dampers (IMTMDs)

Contact person: F. Ubertini, University of Perugia, Via G. Duranti 93, 0039 075 5853954 and 0039 075 5853897.
E-mail filippo.ubertini@strutture.unipg.it

for deck flutter control was also proposed by Kwon & Park (2004). These devices are obtained by irregularly distributing either the natural frequencies or the damping ratios of the small TMDs. Such an approach allows to obtain enhanced control effectiveness with respect to the regular MTMD case (Kwon & Park 2004). However, despite the rich technical literature devoted to the topic, some aspects about the use of regular and irregular MTMDs still deserve further investigations. Indeed, these control devices significantly enhance the complexity of the system and the optimization of the control parameters may become a very difficult task, especially when IMTMDs are concerned. Moreover, the reliability of these devices against aerodynamic-structural uncertainties and their robustness against the variations of the mechanical parameters still deserve further investigations.
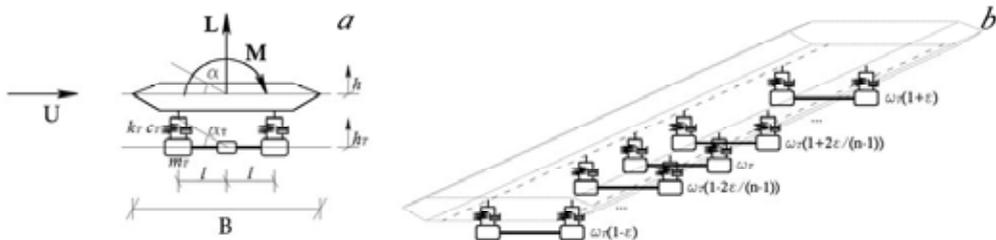

Figure 1: two-DOFs aeroelastic deck model equipped with two DOFs STMD device (a); sketch of the MTMD system.

In the full length paper, the optimal probabilistic design of regular and irregular MTMDs is addressed with reference to a practical case study. To this end, a probabilistic measure of the critic velocity of the system is introduced and adopted in the optimization problem. The aeroelastic stability analysis is performed in the time domain, via a direct eigenvalue problem, by representing the aeroelastic loads through indicial functions. The results show that a special class of IMTMDs, obtained though an irregular mass distribution, allows to improve the symmetry of the control effectiveness with respect to frequency tuning. This entails a significant increment of control robustness against mistuning effects. In the following, some details on the aeroelastic stability analysis of a deck-MTMD system and on the optimal deterministic design of IMTMDs are presented with reference to a preliminary case study.

Let us consider the aeroelastic stability of a classic two degrees-of-freedom (DOFs) deck model, subjected to an incoming wind flow with mean velocity U (see Fig. 1). The aeroelastic lift force L, the pitching moment M, the vertical DOF h (heaving) and the rotation α are defined as shown in Fig. 1(a). A classic STMD device (Lin, et al. 2000), with vertical DOF h_T and rotation α_T, is also attached to the deck (see Fig. 1a). The STMD has total mass m_T, total inertial mass I_T, total vertical stiffness k_T, and total damping coefficient c_T. The mass ratio of the STMD is equal to $\psi = m_T/m$, m being the translational mass of the deck. The STMD is designed in such a way to have the same vertical and rotational natural frequencies, equal to ω_T.

In most of the cases it is beneficial to substitute the STMD by a multiple tuned mass damper (MTMD) with the same total amount of mass. The MTMD is composed by n small TMDs, n usually being an odd number (see Fig. 1b). The MTMD is said to be "regular" if the assembled TMDs have same masses (equal to m_T/n), same damping ratios and their natural frequencies are regularly spaced. In the successive developments, the following expression of the natural frequency ω_{Ti} of the i-th TMD composing the MTMD is adopted:

$$\omega_{Ti} = \omega_T \left(1 + \varepsilon - \frac{2\varepsilon \cdot (i-1)}{(n-1)}\right), \quad i = 1,2,\ldots,n \tag{1}$$

The detuning parameter $\varepsilon = 0 \div 1$ is utilized in Eq. (1) to define the frequency bandwidth of the MTMD.

It is worth noting that, according to Eq. (1), the TMDs are ordered from the one having the largest natural frequency $\omega_T(1+\varepsilon)$ to that having the lowest one $\omega_T(1-\varepsilon)$. From Eq. (1) it can be recognized that the STMD device can be interpreted as the MTMD with $\varepsilon=0$.

The IMTMD can be obtained in many ways by destroying the regularity of the MTMD as, for instance, by considering irregular frequency spacing between the TMDs, different damping coefficients and so on. An irregular mass distribution of the TMDs, with the same total amount of mass of the regular MTMD, is here obtained as:

$$\psi_j = \frac{\psi}{n} \cdot \delta + \psi \cdot (1-\delta) \cdot \frac{(j-1)}{\sum\limits_{k=1}^{n-1} k}, \quad j=1,2,\ldots,n \qquad 0 \le \delta \le 1 \tag{2}$$

where ψ_j indicates the mass ratio of the j-th TMD. From Eq. (2) it is clear that δ indicates the quote of the total mass which is equally distributed among the TMDs, while $(1-\delta)$ indicates the quote of the total mass which is linearly distributed among them. Obviously, the regular MTMD can be interpreted as the considered IMTMD with $\delta=1$.

Representing the self-excited aerodynamic loads in the time domain reveals to be particularly convenient in the presented case. To this regard, the most effective and up-to-date method to express aeroelastic forces for bridge deck sections in the time domain, is probably represented by the load model using indicial functions (Costa & Borri 2006). This model was formulated directly in the time domain for the thin airfoil. Its extension to bluff cross-sections is due to Scanlan, *et al.* (1974) and it is based on the exponential approximation of Wagner's function. Practically, indicial functions are often approximated via truncated series of exponential filters and the unknown parameters are identified from measured aeroelastic derivatives via optimization procedures (Costa & Borri 2006).

The aeroelastic stability analysis of the deck-MTMD system is reduced to a straightforward eigenvalue problem by rewriting the equations of motion in the form of a first order autonomous system. This approach results rather easy in the case of the thin airfoil in which the equations of motion of the uncontrolled system can be reduced in a 6-dimensional state space form, by adding two additional variables based on Wagner's function. For a general bluff deck section, an additional state variable for each exponential filter adopted in the approximation of indicial functions must be introduced. After some mathematic manipulations, the equations of motion of the deck-MTMD system can be reduced in state space form as:

$$\dot{x} = A(U)x \tag{3}$$

where A is a real matrix depending on the wind velocity U and the state vector x contains structural degrees of freedom (generalized displacements and velocities) and additional aerodynamic variables. The dimension of matrix A in Equation (3) results to be equal to $\underline{n} \times \underline{n}$, where $\underline{n}=4(n+1)+k$, k being the number of exponential filters adopted in the approximation of indicial functions.

After rewriting the equations of motion in first order form (3), the aeroelastic stability analysis of the deck-MTMD system can simply be performed by calculating the eigenvalues of matrix A. The flutter instability is encountered when a pair of complex conjugate eigenvalues have zero real parts (Hopf bifurcation point). The minimal velocity U_{crit} at which this condition is satisfied is the critic velocity of the system, while the imaginary part ω_{crit} of the critic eigenvalue represents the circular frequency of the motion at criticality. In order to evaluate the control effectiveness of the MTMDs, the parameter η is introduced as:

$$\eta = \frac{U_{crit}^{MTMD} - U_{crit}}{U_{crit}} \tag{4}$$

where U_{crit}^{MTMD} denotes the critic velocity of the deck-MTMD system.

In the preliminary example here considered, the IMTMD with $\varepsilon=0.15$ and $\delta=0.50$ proves to be a good compromise between control effectiveness and robustness. Indeed, this case is characterized by a rather "flat" optimum with a performance index η which is larger or equal to the one of the STMD

for a wide range of frequency tunings ω_T. By contemporary optimizing both ω_T and the damping ratios ξ_T of the vertical modes of the IMTMD (equal for all the composing TMDs), for the case ε=0.15 and δ=0.50, a sort of global optimal solution is found. To this end, a full domain search of the point of maximum control effectiveness is performed. Figs. 2(a) and 2(b) show the variation of the objective function η with frequency tuning ω_T and damping ratio ξ_T. In such figures ζ^{opt} denotes the optimum Den Hartog's damping ratio. The results outline that the objective function has five distinct relative maxima which are related to the presence of the five TMDs. These relative maxima are placed above a wide region of large control effectiveness (see Fig. 2b) and are almost aligned along the same value of the damping ratio. These results outline the large control robustness of the IMTMD against mistuning effects.
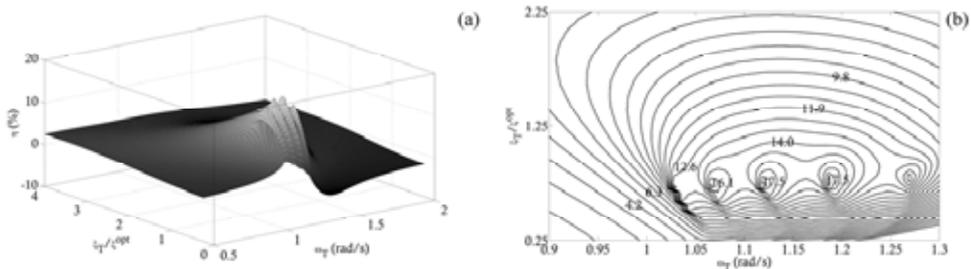

Figure 2: Control effectiveness of IMTDs (ε=0.15 and δ=0.50) as a function of the damping ratio and of the frequency tuning: tridimensional view of the objective function η (a); contour plot of the objective function η in the region of the optimal solution (values in percentage) (b).

The above outlined procedure allows to design optimal MTMDs for bridge flutter control. Now, having found the best compromise between control robustness and effectiveness, the design of the control devices is incorporated into a probabilistic framework that accounts for the large uncertainties usually arising in technical conditions. Most of all, it is of interest to analyze the effectiveness of MTMDs when the aeroelastic properties of the system are different from those assumed in the design stage. Moreover, the robustness of the devices against the variation of the relevant mechanical parameters is also investigated. These topics generally deal with the overall reliability of the MTMDs and are addressed in detail in the full-length paper with reference to the practical case study of the New Carquinez Bridge, located in San Francisco, California.

REFERENCES

Simiu E., Scanlan R. (1996). *Wind effects on Structures*. John Wiley & Sons, New York.
Lin Y.Y., Cheng C.M. (1999). "Multiple tuned mass dampers for controlling coupled buffeting and flutter of long-span bridges", Wind and Structures, 2 (4).
Lin Y.Y., Cheng C.M., Lee C.H. (2000). "A tuned mass damper for suppressing the coupled flexural and torsional buffeting response of long-span bridges", Engineering Structures, 22, 1195-1204.
Chen X., Kareem A. (2003). "Efficacy of tuned mass dampers for bridge flutter control", ASCE Journal of Structural Engineering, 129 (10), 1291-1300.
Kwon S.D., Park K.S. (2004). "Suppression of bridge flutter using tuned mass dampers based on robust performance design", Journal of Wind Engineering and Industrial Aerodynamics, 92 (11), 919-934.
Ubertini, F. (2008), *Wind effects on bridges: response, stability and control.* PhD Dissertation, University of Pavia, Italy.
Ubertini F. (2008). "Flutter prediction in suspension bridges: sources of uncertainty and open issues", Proceedings of the Fourth European Conference on Structural Control (ECSC4), September 8-12, S. Petersburg, Russia.
Costa C., Borri C. (2006). "Application of indicial functions in bridge deck aeroelasticity", Journal of Wind Engineering and Industrial Aerodynamics, 94, 859-881.
Scanlan R.H., Béliveau J.G., Budlong, K. (1974), "Indicial aerodynamics functions for bridge decks", ASCE Journal of Engineering Mechanics, 100, 657–72.

Innovative configurations for long-span suspension bridges

G. Bartoli[*], P. D'Asdia[†], S. Febo[†], C. Mannini[*], S. Noè[‡], L. Procino[*]

[*]*CRIACIV/Department of Civil and Environmental Engineering, University of Florence, Italy*
gbartoli@dicea.unifi.it, claudio.mannini@dicea.unifi.it, lorenzo.procino@pin.unifi.it

[†]*CRIACIV/PRICOS, University "G. D'Annunzio" of Chieti-Pescara, Italy*
pidasdia@tin.it, sofia.febo@gmail.com

[‡]*CRIACIV/Department of Civil Engineering, University of Trieste, Italy*
noe@units.it

Keywords: Suspension bridges, Aeroelasticity, Flutter, Twin-box girder deck, Wind-tunnel tests.

ABSTRACT

This paper reports the results of a piece of research about long-span road suspension bridges with steel deck, composed by longitudinal beams supporting the roadway, and transversal beams connected to the hangers. Classical multiple-box girder decks, whose roadway is placed mainly internally with respect to the main suspension cables, are characterized by low drag coefficient and high aeroelastic stability. Therefore they represent a good solution for long-span suspension bridges. The most outstanding example is the design studied for the crossing of Messina Strait, Italy (Brancaleoni & Diana, 1993; Diana et al., 1995; D'Asdia & Sepe, 1998). For this type of bridge configurations by increasing the span length the contribution to the stiffness of the suspension cables becomes dominant with respect to that of the deck, so that the ratio of the frequency of the first torsional mode to the frequency of the first vertical bending mode approaches unity (for example 1.3 if the mass distribution is constant over the deck width, as shown in Bartoli et al., 2006b). As a consequence, if the cross-section geometry does not allow single-degree-of-freedom torsional flutter, one would observe the onset of two-degree-of-freedom classical flutter at a more or less high wind speed depending on the dynamic and aerodynamic properties of the structure (e.g. Simiu & Scanlan, 1996; Dyrbye & Hansen, 1997). In this case, to increase the frequency separation by means of

Contact person: G. Bartoli, CRIACIV/Department of Civil and Environmental Engineering, University of Florence, Via S. Marta 3 – 50139 – Florence, Italy. Tel.: +39.055.4796218, FAX: +39.055.4796230
E-mail gbartoli@dicea.unifi.it

particular structural solutions, such as crossed hangers (Bartoli et al., 2006b; Febo, 2007), can be effective up to large span lengths but it requires an ever improved aerodynamic performance of the deck and therefore a higher cost of the structure.

The ongoing research presented herein, limiting so far to road bridges only, proposes an innovative approach to the design of long-span suspension bridges by studying decks with frequency ratios of first torsional to vertical bending modes susceptible to couple lower than unity (Febo, 2007; Bartoli et al., 2007; D'Asdia & Febo, 2007). As a matter of fact, it is known that a two-degree-of-freedom linear oscillator with frequency ratio lower than one cannot undergo classical flutter instability (Dyrbye & Hansen, 1997; Bartoli et al., 2008). The main purpose of this paper is to investigate the potentiality of such a design to allow significant savings in the costs of construction, which is an aspect of primary importance for this type of structures.

In a first phase, starting from Messina Strait Bridge design and keeping unchanged the main span length (3300 m), the approaching span lengths (960 m on the Sicilian coast and 810 m on the Calabrian coast), the main suspension cable sag (300 m) and the height of the towers (about 380 m), twin-box girder decks with spacing between the main cables of 26 m (Figure 1), 39 m (Figure 2) and 52 m (Figure 3) have been taken into account (Bartoli et al., 2008). In the first case the transversal width is the same as in the reference bridge, whereas in the second and third cases it is increased in order to reduce the torsional rotations due to particular unfavorable traffic load configurations (for instance for the same diameter of the suspension cables the second deck presents torsional rotations equal to one half of those of the first deck). It is also worth noting that the bending moment and the shear stress in the transversal beams is practically the same in the three cases and therefore their weight (and cost) increases only linearly with the spacing between the suspension cables, so that the difference in the total weight of the three decks is negligible. Obviously the new deck configurations have implied a modified design of the towers and suspension cables as well, according to the performance requirements of the 1992-original design of Messina Strait Bridge.

In addition, given the key role played by the aerodynamic and aeroelastic load in the design of this type of decks, a wind-tunnel test campaign has been performed in the CRIACIV laboratory in order to study the sensitivity of the structural response to the wind action. Static and aeroelastic tests have been performed on section models scaled of about 1:100 (Bartoli et al., 2008). Both the experimental investigation and the numerical aeroelastic simulations on a complete finite-element model of the bridge based on the aerodynamic coefficients measured in the wind tunnel confirmed that for the aforementioned bridge structures the lower modes of vibration cannot couple and therefore cannot give rise to classical flutter instability.
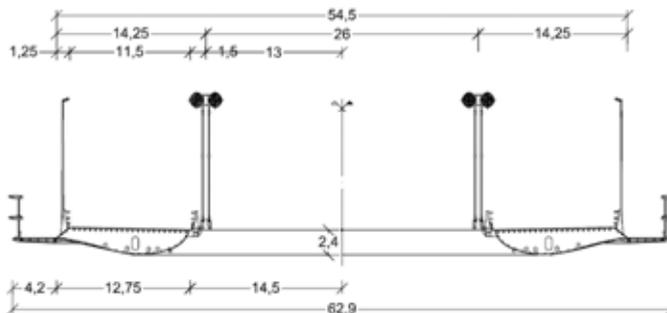

Figure 1: Cross-section of the deck with main suspension cables spaced apart of 26 m.
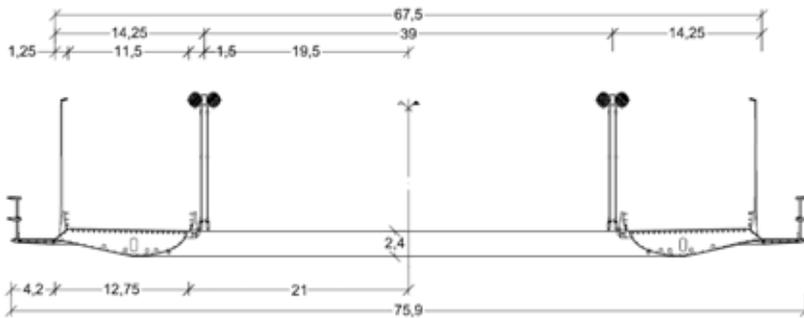
Figure 2: Cross-section of the deck with main suspension cables spaced apart of 39 m.
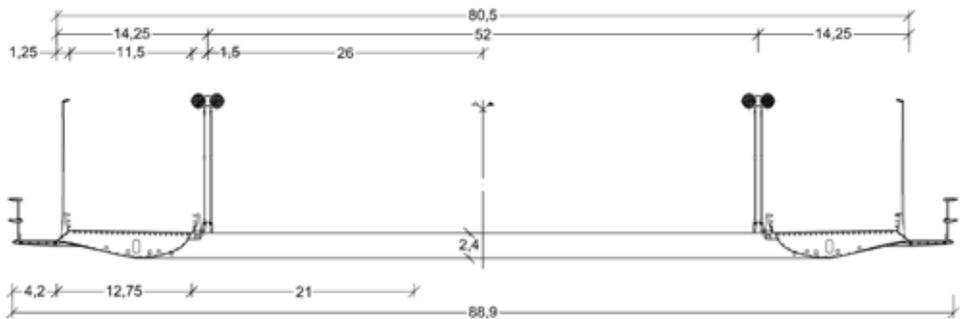

Figure 3: Cross-section of the deck with main suspension cables spaced apart of 52 m.

However, the use of boxes similar to those of the design of the deck of Messina Strait Bridge, at least for spans up to 3300 m, leads to the design of structures which are slightly heavier and therefore more expensive than those obtainable in a "traditional" way. In order to understand whether this type of deck with inverted frequencies can be economically advantageous for span lengths of the order of Messina Strait Bridge or lower, it is necessary to verify if the relaxation of the aerodynamic constraints on the longitudinal beams can allow a cost reduction by means of the use of solutions much simpler from the constructional point of view. As a matter of fact in the structures with frequency ratios lower than unity the aerodynamic optimization of the deck is supposed to be much less enhanced, since only a reduction of the static (in particular the drag and moment coefficients) and dynamic wind loads due to buffeting and vortex shedding is required and not a substantial increment of the flutter critical wind speed.

In order to estimate the possible cost reduction with respect to aerodynamically more sophisticated solutions (such as the one of Messina Strait Bridge), for two different main span lengths several simple typologies have been considered, some of which definitely unusual for suspension bridge decks. Considering also a possible reduction of the spacing between the hangers (in a range between 20 and 30 m) and therefore between the transversal beams, the possibility to employ longitudinal rectangular or trapezoidal boxes or even open-section beams has been investigated. In this case the minimal required aerodynamic performance can be guaranteed through more or less simple non-structural aerodynamic appendices and in particular fairings (e.g. De Miranda & Bartoli, 2001).

The opportunity to use truss girders as transversal beams has been taken into account as well, these elements requiring high stiffness in spite of relatively low level of stresses they are supposed to face. Moreover, for the roadway of bridges with span significantly lower than 3000 m, beside the usual orthotropic slab, the solution represented by a composite cross section with a high-performance concrete slab has also been investigated. For all these configurations both the static local behavior and above all the global static and dynamic response of the bridge have been studied.

During this research campaign an analytical-experimental approach has been followed. Assuming reasonable values of the aerodynamic coefficients for the different deck solutions, pre-designs of the bridge have been obtained with a suspension scheme able to guarantee the inversion of the first couples of modal frequencies (i.e. the torsional frequencies are lower than the corresponding vertical bending frequencies). Then the designs have been refined in order to limit the torsional rotations due to traffic loads: as a matter of fact, with respect to the reference solution for the new conceived decks the torsional rotations tend to be higher for the reduced torsional stiffness (Figure 1) or for the increased torsional moment (Figure 3). Afterwards static tests have been performed in the wind tunnel in order to determine the actual aerodynamic coefficients for the different deck configurations and rigorously verify the conceived bridge structures. The results obtained for a certain number of case studies are summarized in the paper and seem to lead to the conclusion that the proposed solution is feasible and can imply significant saving of material and reduction of costs of construction with respect to the traditional solutions so far employed.

ACKNOWLEDGEMENT

REFERENCES

Bartoli G., D'Asdia P., Febo S., Mannini C., Pastò S., Procino L. (2006). "Analisi di sensibilità aeroelastica nella progettazione di ponti sospesi di grande luce. Parte II: aspetti progettuali", In P. D'Asdia, V. Sepe and S. Febo (Eds.), Proc. 9th Italian National Conference on Wind Engineering IN-VENTO, Pescara, Italy.
Bartoli G., D'Asdia P., Febo S., Mannini C., Pastò S., Procino L. (2007). "Innovative solutions for the design of long-span bridges: investigation on the aeroelastic behavior of multiple-box girder deck sections", Proc. 12th International Conference on Wind Engineering, Cairns, Australia.
Bartoli G., D'Asdia P., Febo S., Mannini C., Pastò S., Procino L. (2008). "Innovative solutions for long-span suspension bridges", In M. Belloli, F. Cheli, G. Diana, S. Muggiasca, D. Rocchi and A. Zasso (Eds.), Proc. 6th International Colloquium on Bluff Bodies Aerodynamics and Applications, Milan, Italy.
Brancaleoni F., Diana G. (1993). "The aerodynamic design of the Messina Strait Bridge", J. Wind Eng. Ind. Aerodyn., 48, 395-409.
D'Asdia P., Febo S. (2007). "Proposta di ponte sospeso con frequenze torsionali più basse delle flessionali", Proc. 21st CTA, Catania, Italy.
D'Asdia P., Sepe V. (1998). "Aeroelastic instability of long span suspended bridges: a multi-mode approach", J. Wind Eng. Ind. Aerodyn., 74-76, 849-857.
De Miranda M., Bartoli G. (2001). "Aerodynamic optimization of decks of cable-stayed bridges", Proc. IABSE Symposium, Seoul, South Korea.
Diana G., Falco M., Bruni S., Cigada A., Larose G.L., Damsgaard A., Collina A. (1995). "Comparisons between wind tunnel tests on a full aeroelastic model of the proposed bridge over Stretto di Messina and numerical results", J. Wind Eng. Ind. Aerodyn., 54-55, 101-113.
Dyrbye C., Hansen S. (1997). *Wind loads on Structures*. John Wiley & Sons, New York.
Febo S. (2007). *Impalcati e schemi strutturali per ponti di grandissima luce*. Ph.D. thesis, University of Chieti-Pescara, Italy.
Simiu E., Scanlan R. H. (1996). *Wind effects on Structures: Fundamentals and Application to Design*. Third edition, John Wiley & Sons, New York.

HIGHWAY / RAILWAY / PEDESTRIAN BRIDGES

Mitigation of the Wind Buffeting on a Suspended Bridge by Smart Devices

M. Domaneschi, L. Martinelli

Department of Structural Engineering, Politecnico di Milano – domaneschi@stru.polimi.it, luca.martinelli@polimi.it – P.zza L. da Vinci, 32, 20133 Milano, Italy

Keywords: simulations, smart control, wind buffeting, spatial correlation, suspended bridge.

ABSTRACT

A suspended bridge model, developed at the numerical level in the Ansys finite element code, is used to simulate the structural response under wind excitation. Advanced structural control solutions are modeled also, with due attention to their feasibility and reliability.

Two strategies have been implemented herein for the bridge protection. The control devices are defined as smart systems combining together different features and they are organized in different geometric schemes. The control strategies have been compared to each other and with the uncontrolled configuration. Their efficacy is shown and the factors contributing to their positive performance are highlighted.

The world today is faced with a growing need of control of the great, and still increasing, number of large structures as suspended bridges. The modern design of complex structures must be in line with the definition and evaluation of performance, while safety must be assessed under different conditions. Structural control solutions can give an important contribution so as to satisfy the high standards of performance, feasibility and safety.

Dynamic loading from interaction with the wind is regarded as the most aggressive external

---

Contact person: Marco Domaneschi, Department of Structural Engineering, Politecnico di Milano – domaneschi@stru.polimi.it – P.zza L. da Vinci, 32, 20133 Milano, Italy, FAX +39.02.2399.4220

excitation for long-span flexible structures in terms of displacements and internal actions. The numerical simulations here presented consider wind loading on the towers, the cables and the deck of a suspended bridge. The wind load, here simulated as a spatially correlated process, acts in the horizontal direction, transversal to the deck. The structural response is compared with a previous investigation, Domaneschi (2006), which adopted a coarser bridge model and a completely correlated wind loading condition.

In this work the attention is focused on a passive control solution, this enhances both the reliability and robustness of the control, reduces the on-line computational efforts and simplifies or eliminates the need of data transmission. When compared to active solutions, in fact, the passive one does not require power supply, control feedback connections and computing power to produce the control forces; in addition, a diffuse sensor network for the structure monitoring is not required. This implies, Casciati et al. (2004), Domaneschi (2005), a huge simplification in all the control implementation with an important contribution toward the application and feasibility of the system.

The wind loading descends from generated 3D turbulent wind field non-homogeneous in space to consider the atmospheric boundary layer, Martinelli et al. (2001), Martinelli et al.(2005).

The suspended bridge is the Shimotsui- Seto Bridge in Japan, spanning from the side of Mt. Washu to the Hitsuishijima Island. Figure 1 shows the main dimensions of the bridge.
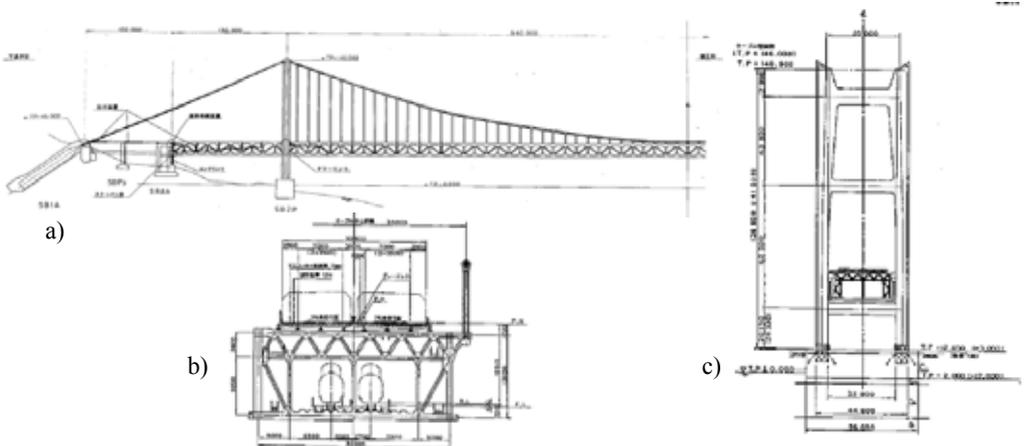

Figure 1: Bridge geometry (Courtesy of Dr. M. Nishitani HBSE-JP): (a) longitudinal profile, (b) deck section, (c) tower.

In comparison to a previous work (Domaneschi, 2007) this study introduces new refinements in the numerical model of the structure and the wind loading. They consist in a detailed deck discretization by frame elements and the spatially correlated wind loading as the dynamic excitation; applied on the deck, towers and cables.

The geometry of the bridge and the boundary conditions suggest to perform the transient analyses in large displacements establishing the equilibrium on the deformed shape. It means that the relation between displacements and strains in the structure is not linear and the solution is determined by numerical iterations with a tangent stiffness method, the Newton Raphson one.

During the analyses, damping is modelled by means of a Rayleigh damping matrix enforcing a 1% damping ratio for the 1ˢᵗ and 4ᵗʰ mode.

The attention is focused on the reliability and robustness of the control solutions, on the reduction of computational efforts and on the simplification of data transmission connections.

Passive control strategies have been implemented herein for the protection of the suspended bridge and compared with the uncontrolled bridge. They are robust in the sense that they require less operative conditions for their functioning and the failure of a device does not influence the efficacy of the remaining ones, because none depends from any other.

Two geometric distributions of the control devices are considered in this study. Both apply the control devices to the bridge between the deck and the peripheral supports. In the first distribution the control devices are placed at the extremities of the deck to manage the longitudinal movements and between the deck and the towers to manage the longitudinal and transversal movements. The second configuration is similar to the first one but with additional devices in transversal direction applied between the deck and the bents. In both the configurations the deck is supported at the extremities in the vertical direction.

Results pertaining to the uncontrolled configuration and the control arrangements herein considered are reported in Table I. It details the statistical parameters of the responses. It is worth noting a reduction in terms of internal actions and displacements. The mean values are substantially unchanged or slightly reduced; the standard deviation parameter is, however, generally smaller. This last is an important aspect in view of fatigue problems inherent to the structural members.

Table I: numerical results

Control schemes	Uncontrolled	TDa	TDb
Deck displacement at mid span [m]			
Max	1.10	1.19	1.02
Mean	0.50	0.63	0.63
Min	-0.13	0.04	0.03
Sdv	0.20	0.17	0.15
Tower base shear (leeward, in the horizontal plane, transversal to the bridge axis) [KN]			
Max	6191	5910	5884
Mean	3880	3889	3891
Min	1501	1629	1659
Sdv	688	551	600
Tower base bending moment (leeward, in the vertical plane, transversal to the bridge axis) [KNm]			
Max	-6347	-8509	-8629
Mean	-32159	-31645	-31669
Min	-59950	-55616	-55354
Sdv	8237	6543	7122

This paper deals with the control systems of a cable suspended bridge. In each of the solutions offered herein, robustness and simplicity are given priority. Accordingly, passive systems are investigated.

The control strategies have been compared with each other and with the uncontrolled structural configuration. Their efficacy in the reduction of the internal actions is reached. It is also worth underling the positive contribution of the structural devices in terms of damping in spite of the small relative displacements of the nodes where they are connected.

New efforts are introduced in the numerical simulations with respect to a previous investigation on the same structure: the wind action is processed as spatial correlated and the drag forces are applied on all the structural element with the support of wind tunnel tests. The bridge deck is simulated reproducing the steel frame in detail. The modal analyses performed confirm the model identification.

Future developments will consider the aspects on the aerodynamic forces, for the lift component in particular, which herein have not been implemented.

Finally, the authors would like to express their gratitude to Dr. M. Nishitani (Honshu-Shikoku Bridge

REFERENCES

Domaneschi M. Passive Control Mitigation of the Wind Buffeting Effects on a Suspended Bridge. Proceedings of The Eleventh International Conference on Civil, Structural and Environmental Engineering Computing, Paper 13, St. Julians, Malta 18-21 September 2007. ISBN 978-1-905088-16-4.

Casciati F., Domaneschi M. Confinement of Vibration Applied to a Benchmark Problem. Proc. of Second European Workshop on Structural Health Monitoring, 811-818, Monaco D, July 7-9, 2004.

Domaneschi M. Structural Control of Cable-stayed and Suspended Bridges. Ph.D. Thesis, University of Pavia, Italy, 2005.

Martinelli L., Perotti F. Numerical analysis of the non-linear dynamic behaviour of suspended cables under turbulent wind excitation. International Journal of Structural Stability and Dynamics, vol. 1, pp. 207-233, 2001.

Martinelli L., Pomar A. Analysis of cableway non-linear oscillations induced by wind forces. In Proc. of the 6th Asian-Pacific Conference on Wind Engineering (APCWE-VI), C.K Choi, Y.D. Kim H.G. Kwak (Editors), Seoul (Korea), September, 12-14, 2005 (CD-ROM) Techno-Press, Daejeon, Korea.

Solari G., Piccardo G. Probabilistic 3-D turbulence modelling for gust buffeting of structures. Prob. Eng. Mechanics, 16, 73-86, 2001.

Hao H., Oliveira C. S., Penzien J. Multiple-Station Ground Motion Processing and Simulation Based on SMART-1 Array Data, Nucl. Eng. and Des., 111, 293-310, 1989.

CEN – European Committee for Standardization, Eurocode 1, EN 1991-1-4, 2005.

ESDU Report n°81027, LATTICE STRUCTURES. PART 1: Mean Fluid Forces on Single and Multiple Plane Frames Engineering Sciences Data Unit, London.

ESDU Report n°71012, Fluid forces on non-streamlined bodies Background notes and description of the flow phenomena, Engineering Sciences Data Unit, London.

WIND TUNNEL TEST OF NABOKU-BISAN-SETO BRIDGES WITH STIFFENING TRUSS, Shin Narui (in Japanese).

CNR-DT 207/2008, Instructions for the wind effects and actions evaluations on buildings (in Italian).

Response of bluff and streamlined bridge girder in the wind as function of natural frequency tuning

R. Král, S. Pospíšil, J. Náprstek

Institute of Theoretical and Applied Mechanics, v.v.i., Academy of Sciences of the Czech Republic, kral@itam.cas.cz, naprstek@itam.cas.cz, pospisil@itam.cas.cz – Prosecká 76, 19700 Prague, Czech Republic

Keywords: flutter derivatives, aero-elastic response, streamlined bridge deck, bluff body.

ABSTRACT

The analysis of the aero-elastic stability of engineering structures creates an important part of industrial aerodynamics for many years. It is still of great interest also nowadays due to the development in theory and experimental techniques. During previous decades motivated by the famous Tacoma Narrows bridge collapse many questions regarding the physical phenomenon have been answered in sufficient manner. Sophisticated methods for the aero-elastic instability prediction have been evolved and successfully applied to real structures. The majority of them are based on the so called aero-elastic derivatives representing the coefficients of self-excited forces induced by the wind-structure interaction. In terms of the trend of these coefficients one can declare the aero-elastic characteristics and usability of the considered cross-section shape. On the other hand, it is known that the aero-elastic derivatives (AD's) are quantities that depend on the experimental conditions. Paper by Noda et al. (2003) demonstrated the effects of oscillating amplitude on them. He found that for different cases of the torsional amplitude there exist different courses of the aerodynamic derivatives. In order to eliminate possible discrepancies in the aero-elastic instability prediction, it is recommended to perform the measurement and thus highlight the role of the oscillating amplitudes.

In this paper, the experiment elucidating the influence of the natural frequencies tuning and other properties on the stability of the test girders is performed. The phase shift, flutter frequency and the range of the critical velocity with respect to the frequency ratio have been determined. The aero-elastic instability analysis of two cross-sections (rectangular and bridge-like) including also AD's has been performed using a wind tunnel experiment. The special attention is paid to the response of the girders at the critical state. The first examined deck has a rectangular shape with the height-to-width ratio of $1:5$. The geometrical similarity of a bridge-like girder is maintained while the aspect ratio is respected. Table 1 gives basic information about characteristics and tuning (rotation to heave) of both models. Both decks have been equipped with pressure sensors allowing to observe the wind forces in direct way. Both sections have been tested on the unique testing stand. This stand is originally

---

Contact person: R. Král, Institute of Theoretical and Applied Mechanics, v.v.i. Academy of Sciences of the Czech Republic, Prosecká 76, 19700 Prague, Czech Republic. kral@itam.cas.cz

designed respecting an easy and quick tuning of model eigen-frequencies and with regards to the excessive deflection amplitude in both heave and torsion, see Náprstek et al. (2007). The influence of the initial amplitudes on the stability of the body can be observed and measured.

cross-section	h [m]	B [m]	m [kg]	I [kgm^4]	f_p/f_h [Hz]	Sc$_p$	Sc$_h$	δ_p	δ_h
⬭	0.05	0.25	3.50	0.0204	⟨0.93 − 1.20⟩	5.9	30.3	0.017	0.008
⬗	0.05	0.30	3.74	0.0202	⟨0.93 − 1.20⟩	3.9	36.4	0.016	0.009

Table 1: Aerodynamic characteristics of the tested sections: h-height, B-width, I-mass moment of inertia, f_h-heave eigen-frequency, f_p-pitch eigen-frequency, Sc-Scruton number, δ-logarithmic decrement.

Being the essential parameters necessary to the flutter analysis, the aerodynamic derivatives were evaluated. Respective coefficients characterizing the self-excited forces have been determined from a decay free oscillation induced by a certain initial deflection. The data acquisition has been carried out by two approaches. The first one consisted of the measurement of the oscillations in the vertical and torsional mode separately. Thus the so-called direct derivatives could be obtained. In similar way measuring the coupled heave and torsional free decay oscillation the remaining indirect derivatives have been evaluated. For all aerodynamic derivatives holds that the initial torsional and heave amplitudes were kept constant.
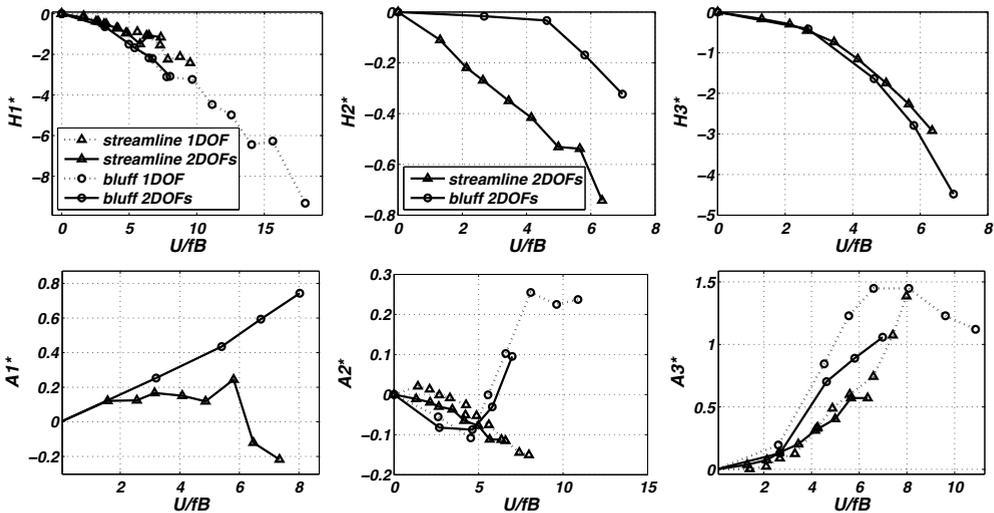

Figure 1: Aerodynamic derivatives of the tested sections obtained by modified method; pictures including four graphs represent the cases, where both single and coupled system measurements have been performed; rectangular body: ○, bridge-like deck: △.

The unified least-square flutter parameter identification method (ULS) proposed by Gu et al. (2000), Chen et al. (2002) with the partial modification has been applied. The initial values of parameters α, β used in the iteration procedure of the AD's optimization are originally based on the modified Ibrahim time domain algorithm (MITD), see Sarkar P. et. al. (1994). In this paper, the initial parameters determination is done by the procedure coming out of the main principle of the ULS method. Instead of finding the solution for two degrees of freedom oscillations requesting to identify four parameters

simultaneously, the procedure is adapted to one degree of freedom only. Thus, this procedure operating with two parameters can be employed for each degree of freedom separately and moreover its convergence to the exact solution does not require as the accurate initial parameter estimations as in the original form. Using a free decay time history signal under no wind conditions, taken from the torsional tuning for example, the first set of the initial parameter values α, β relating to the rotary degree of freedom is specified. The same method is performed for the second degree of freedom resulting in the determination of the remaining part of the parameters. Obtained solutions serve as an estimation of all four parameters existing in the original method. Figure 1 shows the aero-elastic derivatives $A_1^*, A_2^*, A_3^*, H_1^*, H_2^*, H_3^*$ for both rectangular and bridge-like cross-sections.

In the most papers, the flutter stability assessment has been based upon the assumption that the torsional to heave natural frequency ratio is greater than one. This empirical condition follows from the long-term engineering experience concerning fundamental dynamic characteristics of suspended long-span bridges. The fundamental part of the experiments performed here has been concentrated on the bridge deck (both versions) response at variable natural frequency ratio. The left part of Figure 2 demonstrates the influence of the frequency ratio on the phase shift of the torsional and heave motion component for the rectangular deck. In the course of the wind tunnel measurement the frequency ratio had been changed subsequently in the interval $\langle 0.9 - 1.2 \rangle$. At the ratio $\frac{f_p}{f_h} \approx 1.2$ the deck rotation center is situated near the windward side and the response resembles somewhat like the "dolphin" motion. With the decreasing eigen-frequency ratio the phase shift is changing rapidly as the results of a relocation of the rotation center to the leeward part of the girder.
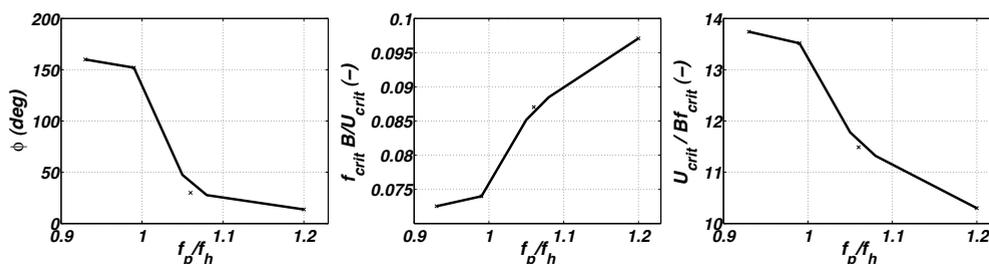

Figure 2: Influence of the eigen-frequency ratio on the the response of the rectangular deck: phase lag between the pitch and heave movements-left, flutter frequency-middle, critical velocity-right.

The influence of the eigen-frequency ratio on the flutter frequency is shown in the middle part of the Figure 2. The left and middle pictures emphasize that the eigen-frequency ratio $\frac{f_p}{f_h} \approx 1$ represents an important point separating two different regimes of the deck response. The right picture in Figure 2 confirms a hypothesis that the flutter velocity within the chosen frequency ratio interval is approximately inversely proportional to the eigen-frequency ratio. It is possible to assume that at ratio $\frac{f_p}{f_h} \approx 1.2$ the aero-elastic system reaches a certain minimal barrier to start flutter while at the higher ratios the critical velocity may change the tendency. Classical flutter experiments carried out on the bridge-like deck proved that stability domain are wider compared to rectangular deck. From the experiment we assume that frequency ratio less than 1.1 leads to the stability lost due to the static divergence.

Another important consideration should be given to the deck response depending on the wind velocity. The wind velocity has been growing continually up to the critical velocity of the examined coupled problem. After reaching the flutter and steady-state oscillation, the wind speed is slowly decreased. By means of this procedure the definition of the lower velocity boundary of the critical state could be given. It means that the oscillating deck is still able to gain the energy from the

wind and consequently remain in the coupled motion at one frequency. It follows from the Figure 3, representing the rectangular deck response, that the flutter instability has occurred in the proximity of a certain wind speed. The left and right hand sides of the picture show the amplitudes in the vertical and torsional directions, respectively. The reduced velocity represented along the horizontal axis in both pictures is derived from the natural frequency of the given motion component. In spite of the fact that the instability of the flutter type occurred at this velocity, the fluttering sustained its amplitudes lowering flow velocity. It is thus appropriate to consider this velocity range as a critical velocity domain, where the flutter instability can occur under certain circumstances. It has been verified by many experimental observations, that the deck looses the stability at even a small angle change from the original position. Practically, such initial deflection can be caused by a random imperfection e.g. gust or other impulse.
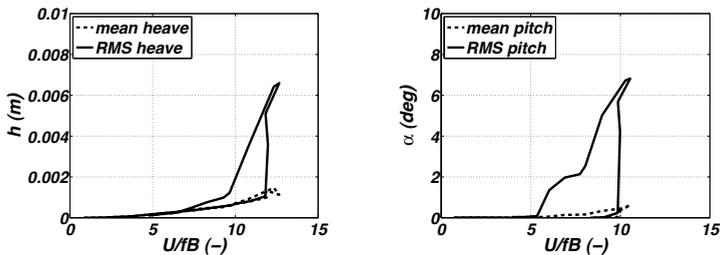

Figure 3: Heave (left) and pitch (right) amplitude rectangular deck characteristics as the functions of the wind velocity. The dashed line and solid line denotes the mean and root mean square value, respectively.

The aim of this paper is to present the aero-elastic properties and characteristics of two fundamental shape of bridge deck cross-sections. The assessment has been carried out with respect to the various values of eigen-frequency ratios. Flutter derivatives of the decks have been studied and additional instability properties have been demonstrated. It has been shown that the instability onset can start in particular cases at lower wind speeds than those determined by the classical approaches when influence of initial conditions and non-linear effects are neglected. Especially in the case of the bluff deck, the high sensitivity to the external disturbance has been observed.

ACKNOWLEDGMENT

REFERENCES

Noda M., Utsunomiya H., Nagao F., Kanda M., Shirashi N. (2003). "Effects of oscillation amplitude on aerodynamic derivatives", Journal of Wind Engineering and Industrial Aerodynamics, 91, 101-111.

Náprstek, J., Pospíšil S., Hračov. S. (2007). "Analytical and experimental modeling of non-linear aeroelastic effects on prismatic bodies", Journal of Wind Engineering and Industrial Aerodynamics, 2007, 95, 1315 –1328.

Gu M.,Zhang R., Xiang M. (2000). "Identification of flutter derivatives of bridge decks", Journal of Wind Engineering and Industrial Aerodynamics, 2000, 151–162.

Chen A., He X., Xiang H. (2002). "Identification of 18 flutter derivatives of bridge decks", Journal of Wind Engineering and Industrial Aerodynamics 90, 2002, 2007–2022.

Sarkar P., Jones N. P., Scanlan R. H. (1994). "Identification of aeroelastic parameters of flexible bridges", Journal of Engineering Mechanics 120, 1994, 1718–1741
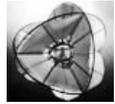
POD-based representation of the Equivalent Static Force for long span bridges

Alessandra Fiore, Pietro Monaco

Politecnico di Bari, a.fiore@poliba.it p.monaco@poliba.it, Department of Civil and Environmental Engineering, Via Orabona 4, 70125 Bari, Italy

Keywords: Long-span bridge; alongwind effects; Proper Orthogonal Decomposition; Gust Effect Factor technique; Equivalent Static Force

ABSTRACT

The codes in force and in particular Eurocode 1 (UNI EN 1991-1-4 2005) do not furnish any indication in order to calculate the Equivalent Static Force (ESF) of wind in the case of long-span bridges, such as suspension and cable-stayed bridges. The ESF of wind should represent the force able to reproduce all the maximum load effects of the deck. In this way engineering calculation may be carried out by applying on the structure only one static load. The first methods aimed at determining an ESF able to simultaneously reproduce the maximum effects due to the wind action have been pioneered in recent years with regard to large-span roofs and vertical structures. More precisely Katsumura et al. (2005) proposed a universal Equivalent Static Wind Load (ESWL), expressed by a combination of eigenmodes, simultaneously reproducing maximum load effects on large-span cantilevered roofs. Repetto & Solari (2004), with reference to vertical structures, developed the Global Loading (GL) technique defining a unique loading condition able to furnish, for each motion direction, all maximum load effects. The GL technique expresses the ESF through a polynomial expansion and is proposed in two different versions: one is based on the application of the Gust Factor technique and is denoted by GL/1; the other is used within the framework of the Load

---

Contact person: Alessandra Fiore, Politecnico di Bari, Department of Civil and Environmental Engineering, Via Orabona 4, 70125 Bari, Italy, Telephone +39 0805963525, FAX +39 0805963719, E-mail a.fiore@poliba.it

Combination technique and is denoted by GL/2. This paper develops and discusses a method by which it is possible to evaluate the alongwind ESF in the case of long-span bridges. Attention is focused on the GL technique. Differently from vertical structures, the GL technique does not furnish correct results in the case of bridges; this is due to the orthogonality properties between power functions and the influence lines of wind-induced effects acting on the deck such as displacements, bending moments or shears. Thus, in order to define a load distribution suitable for long-span bridges and able to estimate simultaneously the maximum alongwind effects of the deck, a modified GL/1 technique is proposed. It consists in expressing the ESF through a linear combination of loading modes, which are obtained by the Proper Orthogonal Decomposition (POD) of the wind velocity field. In particular a comparison is carried out between spectral and covariance eigenfunctions, with the aim of identifying the most efficient method to simulate the ESF.

Let us consider a bridge deck immersed in a turbulent wind field. Let x, y, z be a Cartesian reference system with the x and the z axes belonging to a horizontal plane, z being parallel to the bridge deck axis; the y axis is vertical. For the sake of simplicity, the representation of the wind field is here simplified introducing the following hypotheses: the mean wind velocity is orthogonal to the bridge deck axis; the longitudinal turbulence component is uncorrelated with the lateral and vertical components; the contribution of the vertical turbulence component is neglected; wind actions are applied only to the bridge deck. The mean wind velocity is expressed by the logarithmic law; the mean wind velocity $\overline{u}(h)$ at the height h of the deck is assumed constant. The longitudinal turbulence component is expressed as the product of the standard deviation σ_u and the reduced turbulence $u'(z,t)$, characterized by unit variance. The cross power spectral density function (cpsdf) of the reduced turbulence $S_u(z,z',\omega)$ is expressed in the form proposed by Carassale & Solari (2002). The spectral eigenfunctions $\theta_k(z,\omega)$ are furnished by:

$$\theta_k(z,\omega) = \overline{A}_k(\alpha)\sin\left[\frac{(k\pi - 2\varepsilon_k(\alpha))}{L_T}z + \varepsilon_k(\alpha)\right]; \qquad (k=1,2...); \tag{1}$$

with:

$$\alpha = \frac{C_{uz}L_T}{2\pi\overline{u}(h)}|\omega|; \quad \varepsilon_k(\alpha) = \arctan\left[\frac{\mu_k(\alpha)}{\alpha}\right]; \quad 2\cot(\mu_k) = \frac{\mu_k}{\alpha} - \frac{\alpha}{\mu_k}; \quad \overline{A}_k(\alpha) = \sqrt{\frac{2(k\pi - 2\varepsilon_k)}{\sin(2\varepsilon_k) + k\pi - 2\varepsilon_k}} \tag{2}$$

where L_T and C_{uz} are respectively the overall length of the deck and the exponential decay factor of turbulence. The covariance function can be approximated by the formula (Carassale et al. 1999):

$$C_v(z,z') = e^{-\beta\sqrt{\delta|z-z'|/L_T}}; \qquad \delta = \frac{L_T C_{uz}}{L_u(h)}; \qquad \beta \cong 0.38[L_u(h)/\overline{u}(h)]^{-0.52}; \tag{3}$$

$L_u(h)$ being the integral length scale of turbulence. The covariance eigenfunctions ϕ_k are given by:

$$\phi_1 = \frac{1}{\sqrt{2}}; \qquad \phi_{k,1}(z) = \sin[2(k-1)\pi z/L_T]; \qquad \phi_{k,2}(z) = \cos[2(k-1)\pi z/L_T]; \quad (k=2,3,...). \tag{4}$$

The wind-induced effects acting on the deck are derived by applying the Gust Effect Factor (GEF) technique. The following expressions are introduced:

$$\overline{e}_{x,\max}(r) = \overline{e}_x(r)G_{x,\max}^e(r); \qquad G_{x,\max}^e(r) = 1 + g_x^e(r)\frac{\sqrt{[\sigma_{Qx}^e(r)]^2 + [\sigma_{Dx}^e(r)]^2}}{|\overline{e}_x(r)|}; \tag{5}$$

with:

$$[\sigma_{Qx}^e(r)]^2 = 2\int_0^{\omega_{x1}}\int_0^{L_T}\int_0^{L_T} S_{Fx}(z,z',\omega)\eta_x^e(r,z)\eta_x^e(r,z')dzdz'd\omega; \quad S_{Fx}(z,z',\omega) = (\rho\overline{u}\sigma_u Bc_D)^2 S_u(z,z',\omega) \tag{6}$$

$$\left[\sigma_{Dx}^{e}(r)\right]^{2} \cong \sum_{k=1}^{N_{t}} \left[\sigma_{Dx,k}^{e}(r)\right]^{2} = \sum_{k=1}^{N_{t}} \frac{\left[m_{xk}^{e}(r)\right]^{2}}{\left[m_{xk}\right]^{2}} \frac{\pi \omega_{xk}}{2\left(\widetilde{\xi}_{xk} + \widetilde{\xi}_{xk}^{o}\right)} \int_{0}^{L_{T}} \int_{0}^{L_{T}} S_{Fx}(z,z',\omega_{xk}) \varphi_{xk}(z)\varphi_{xk}(z')\mathrm{d}z\mathrm{d}z'; \tag{7}$$

where $G_{x,\max}^{e}(r)$ is the GEF; $\bar{e}_{x}$ is the mean value of the effect e_{x}; $\eta_{x}^{e}(r,z)$ is the influence function of e_{x}; $g_{x}^{e}(r)$ is the peak factor of the fluctuation $e_{x}^{'}$; $\sigma_{Qx}^{e}(r)$ and $\sigma_{Dx}^{e}(r)$ are respectively the root mean square values of the quasi-static and resonant parts of $e_{x}^{'}$; $S_{Fx}(z,z',\omega)$ is the cpsdf of the buffeting alongwind force $F_{x}^{'}(z,t)$; φ_{xk} is the k-th structural mode; $\omega_{xk}, m_{xk}, \widetilde{\xi}_{xk}, \widetilde{\xi}_{xk}^{o}$ and m_{xk}^{e} are respectively the alongwind natural circular frequency, the modal mass, the damping ratio, the aerodynamic damping coefficient and the effect influence mass of the k-th structural mode; N_{t} is the number of significant structural modes; ρ is the air density; c_{D} is the aerodynamic drag coefficient; B is the deck width (Repetto & Solari 2004, Fiore & Monaco 2007).

The ESF that produces the effect $\bar{e}_{x,\max}(r)$ in section r is given by:

$$F_{x,eq}^{e}(r) = G_{x,\max}^{e}(r)\overline{F}_{x}. \tag{8}$$

The ESF so defined depends on the effect e and the section r considered. Generally in the case of long-span bridges the application of the ESF associated to a specified maximum effect does not furnish the correct maximum values of other wind-induced effects acting on the deck. This aspect makes the GEF technique unsuitable for engineering applications.

Therefore a modified GL/1 technique is proposed which defines a unique ESF able to simultaneously reproduce the maximum alongwind effects of the bridge deck. It consists in expressing the alongwind ESF through a combination of spectral eigenfunctions $\theta_{k}(z, \omega_{x1})$:

$$F_{x,eq}(z) = \overline{F}_{x} \sum_{k=1}^{N} c_{xk}\theta_{k}(z,\omega_{x1}) \tag{9}$$

where c_{xk} ($k=1,2,....N$) are N coefficients used to impose that Eq. (9) gives rise to the correct values of the N specified load effects and ω_{x1} is the first natural circular frequency of the deck in the x direction. Applying the Influence Function technique and considering together Eqs. (8) and (9), a system of N equations in N unknowns c_{xk} is obtained:

$$\overline{F}_{x} \sum_{k=1}^{N} c_{xk} \int_{0}^{L_{T}} \theta_{k}(z,\omega_{x1})\eta_{x}^{e}(r,z)\mathrm{d}z = G_{x,\max}^{e}(r)\overline{F}_{x} \int_{0}^{L_{T}} \eta_{x}^{e}(r,z)\mathrm{d}z. \tag{10}$$

The procedure can be used also expressing the ESF through a combination of covariance eigenfunctions $\phi_{k}(z)$.

The numerical applications deal with the case of a self-anchored cable-stayed bridge with two spans, a curtain suspension, stays disposed fanwise and an A-shaped pylon (Fig.1). The following data are assumed: L_{T}=358.02 m; l_{1}=147.42 m; Δz=21.06 m; B=23.46 m; h=40.4 m; h_{P}=74.2 m; ρ=1.25 kg/m³, C_{uz}=10, c_{D}=0.1. The mean wind velocity $\bar{u}(h)$ is equal to 49.41 m/s. The structural modes are derived by applying the numerical method proposed by Monaco & Fiore (2005); the alongwind fundamental circular frequency is ω_{x1}=2.66 rad/s. The values of the other parameters can be found in Fiore & Monaco (2007). The proposed method is utilized in order to research a load distribution whose application on the bridge deck produces bending moment (e=b) and shear (e=s) diagrams as close as possible to the diagrams of the maximum values of these effects.

Using the spectral eigenfunctions, N=14 conditions are sufficient in order to obtain a good approximation. Fig. 2 shows the shape of the ESF $F_{x,eq}(z)$ obtained by considering the following effects: $\bar{b}_{x,\max}(21.06)$, $\bar{b}_{x,\max}(126.36)$, $\bar{b}_{x,\max}(147.42_{\mathrm{Left}})$, $\bar{b}_{x,\max}(147.42_{\mathrm{Right}})$, $\bar{b}_{x,\max}(189.54)$, $\bar{b}_{x,\max}(252.72)$, $\bar{b}_{x,\max}(273.78)$, $\bar{s}_{x,\max}(0)$, $\bar{s}_{x,\max}(63.18)$, $\bar{s}_{x,\max}(147.42_{\mathrm{Left}})$, $\bar{s}_{x,\max}(147.42_{\mathrm{Right}})$, $\bar{s}_{x,\max}(252.72)$, $\bar{s}_{x,\max}(315.9)$, $\bar{s}_{x,\max}(336.96)$. In Figs. 3a and 3b the diagrams of bending moments and shears generated by the ESF $F_{x,eq}(z)$ so defined are compared respectively with the diagrams of their maximum values.

The method has been applied also using covariance eigenfunctions, showing that spectral eigenfunctions are more effective if compared to covariance eigenfunctions.
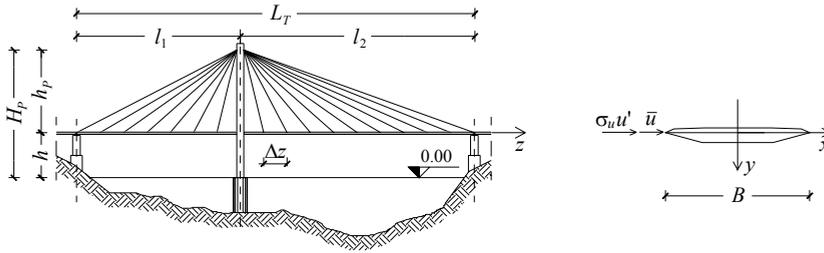
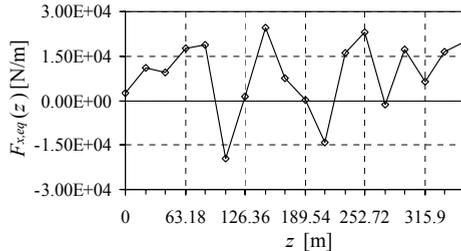Figure1: Cable-stayed bridge under examination.

Figure 2: ESF $F_{x,eq}(z)$ obtained by using spectral eigenfunctions and imposing 14 conditions.
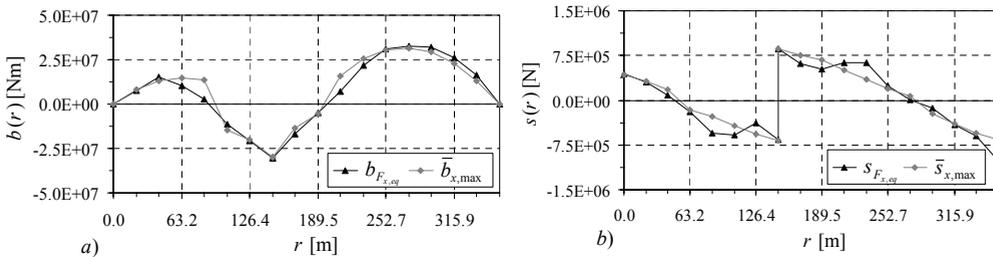
Figure 3: Diagrams of $\bar{e}_{x,\max}(r)$ and of the load effects $e_{Fx,eq}$ generated by the ESF $F_{x,eq}(z)$ obtained using spectral eigenfunctions and imposing 14 conditions: a) $e=b$; b) $e=s$.

REFERENCES

Katsumura A., Tamura Y., Nakamura O. (2005). "Universal wind load distribution simultaneously reproducing maximum load effects in all subject members on large-span cantilevered roof", Proceedings of the Fourth European & African Conference on Wind Engineering, Prague, July.

Repetto M.P. and Solari G. (2004). "Equivalent static wind actions on vertical structures", Journal of Wind Engineering and Industrial Aerodynamics, **92**, 335-357.

Carassale L., Solari G. (2002). "Wind modes for structural dynamics: a continuous approach", Probabilistic Engineering Mechanics, **17**, 157-166.

Carassale L., Piccardo G. and Solari G. (1999). "Double modal transformation in continuous modeling", Proceedings of the 10th International Conference on Wind Engineering, Copenaghen, 1479-1484.

Fiore A., Monaco P. (2007). "Alongwind load effects for cable-stayed bridges", Proceedings of the Seventh International Symposium on CABLE DYNAMICS, Vienna, Austria, 37-44.

Monaco P. and Fiore A. (2005). "A method to evaluate the frequencies of free transversal vibrations in self-anchored cable-stayed bridges", Computers and Concrete, **2** (2), 125-146.

Model investigations of the cable-stayed bridge over Vistula River in Cracow

1st A.Flaga, 2nd G.Bosak

1st Lublin University of Technology and Cracow University of Technology

– LIWPK@interia.pl – Jana Pawla II 37/3a, 31-864 Cracow, Poland

2nd Cracow University of Technology

– g.bosak@windlab.pl – Jana Pawla II 37/3a, 31-864 Cracow, Poland

Keywords: interference, cable-stayed bridge, wind tunnel tests.

INTRODUCTION

The paper presents selected results of experiments on the sectional model of the span (model scale 1:67) with respect to determination of aerodynamic coefficients as functions of angle of wind attack. Measurements of aerodynamic forces (F_x- aerodynamic drag; F_y- aerodynamic lift; M- aerodynamic moment) have been obtained by means of the three component aerodynamic balance based on electric resistance wire strain gauges. The span of the bridge consists of two decks placed parallel to each other. Influence of aerodynamic interference between the windward and leeward decks of the bridge span has been the main aim of aerodynamic analyses.

OBJECT OF INVESTIGATIONS

The object of investigations is a new cable-stayed bridge over Vistula River in Cracow. The bridge crossing Vistula River is placed along national road S-7. The whole length of the bridge is equal to 390 m (the main span: 200 m, two side spans-each of the length 95 m).

Figure 1: cross-section of the deck.

Contact person: G.Bosak, Cracow University of Technology, Jana Pawla II 37/3a, 31-864 Cracow, Poland,
phone +48 12 6283570, FAX +48 12 6283566
E-mail g.bosak@windlab.pl

The span of the bridge consists of two decks placed parallel to each other (Fig. 1). Each deck, of the width 18.99 m, is hanged to two reinforced concrete pylons with use of 64 steel cables. Height of the two symmetrical pylons is equal to 42.5 m.

WIND TUNNEL TESTS

The experiments have been performed in boundary layer wind tunnel of the Wind Engineering Laboratory at the Cracow University of Technology. A sectional model of the each deck has been made of aluminium profiles and various plastic materials. The geometrical scale of the model is equal to 1:67. Tests have been carried out for mean wind velocity of 20 m/s, turbulence intensity of 12% and different angles of wind attack from -10° to +10° with step of 1°. Measurements of aerodynamic forces (F_x- aerodynamic drag; F_y- aerodynamic lift; M- aerodynamic moment) have been obtained by means of the three component aerodynamic balance based on electric resistance wire strain gauges. On the base of the mean values of the measured forces, aerodynamic coefficients (C_x- aerodynamic drag coefficient; C_y- aerodynamic lift coefficient; C_m- aerodynamic momentum coefficient) have been calculated as functions of wind attack angle (Fig.2) according to formulae (1).
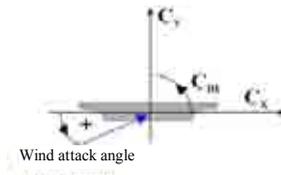

Figure 2: Coordinate system of aerodynamic coefficients.

$$C_x = \frac{\overline{F}_x}{q_{ref} \cdot D}, \; C_y = \frac{\overline{F}_y}{q_{ref} \cdot D}, \; C_m = \frac{\overline{M}}{q_{ref} \cdot D^2} \tag{1}$$

where: q_{ref}- reference pressure, D- characteristic transverse dimension: width of the deck.

Measurements situations, during the tests of the windward and the leeward decks, realized in the wind tunnel working section are presented in Fig.3.

a)   b)

Figure 3: Sectional model of the deck in the wind tunnel working section:
a) during tests of the windward deck, b) during tests of the leeward deck;

EXEMPLARY RESULTS OF MEASUREMENTS

Comparison of the aerodynamic coefficients – drag coefficient C_x, lift coefficients C_y, moment coefficient C_m for the windward and the leeward deck of the bridge are presented in Fig.4.
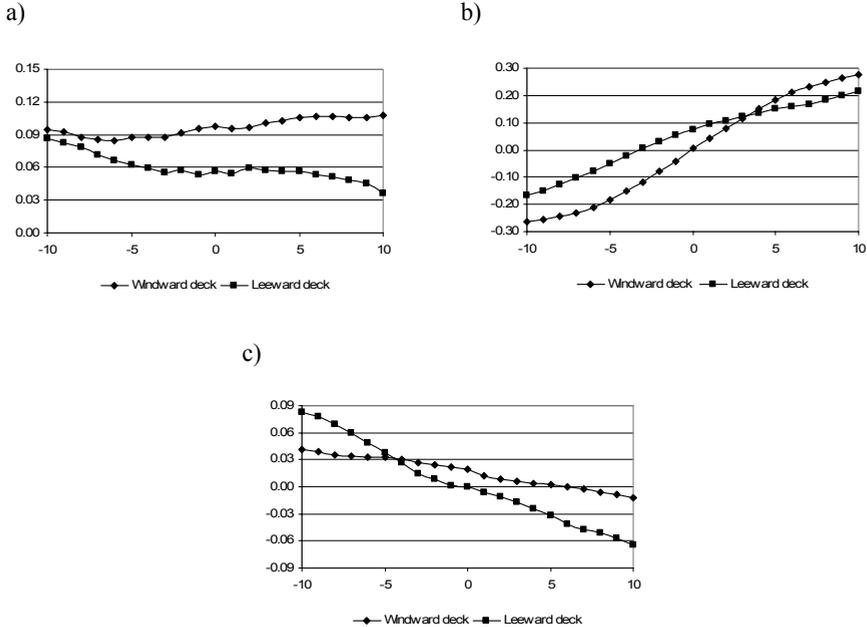
a)

b)

c)

Figure 4: Functions of aerodynamic coefficients – a) drag coefficient C_x, b) lift coefficients C_y, c) momentum coefficient C_m for the windward and leeward decks of the Cracow cable-stayed bridge obtained from wind tunnel tests.

Basing upon wind tunnel tests wind action on the bridge has been simulated according to the quasi-steady theory and own computer programme. Next, the responses of the bridge have been determined and analyzed (Fig. 5 and Fig.6).
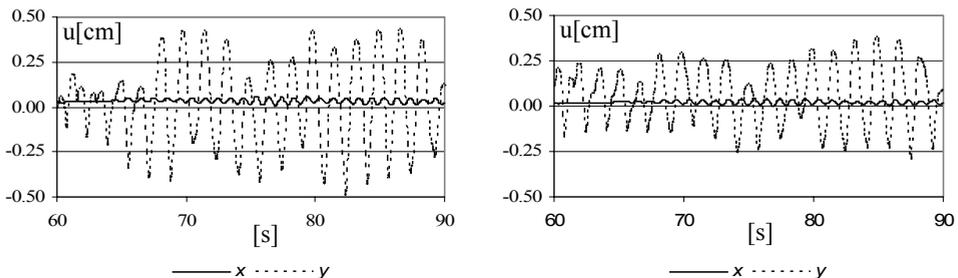
Figure 5: a) Displacements- u_x (horizontal), u_y (vertical)-of the middle point of the windward deck, b) displacements- u_x (horizontal), u_y (vertical)-of the middle point of the leeward deck.

CONCLUSIONS

On the base of experimental results of wind tunnel tests following conclusions could be formulated:

1) A comparison of aerodynamic coefficients of the windward and the leeward decks of the bridge shows that aerodynamic interference has a significant influence especially on a drag coefficient.

2) The aerodynamic interference has not changed the character of aerodynamic coefficient functions, as well as the responses of the bridge.

3) On the base of the coefficients functions, according to den Hartog conditions, galloping of the windward and the leeward decks of the bridge is not supposed to occur.

Mechanisms of the vertical vortex induced vibration of the Storebælt bridge

J.M. Terrés-Nícoli, G.A. Kopp

University of Granada, Spain – jterres@ugr.es – CEAMA, Avda. del Mediterraneo s/n, Granada, Spain

University of Western Ontario, Canada – gakopp@uwo.ca – Boundary Layer Wind Tunnel Laboratory, The University of Western Ontario, London, Ontario, Canada

Keywords: vortex induced vibration, long span bridges, Storebaelt Bridge.

ABSTRACT

Vortex induced vibrations of circular cylinders have been studied for nearly a century and a half. Nevertheless there are still fundamental questions for which there are not clear answers. For instance, new insights into cylinders oscillating with considerably higher amplitudes than previously reported have been published recently (Zasso, Belloli, Giappino, & Mugiasca, 2008). Different shedding modes are related to the different stages of the oscillating cylinder: i.e., 2S (S, single), 2P, S+P (P, pair) modes (Govardhan & Williamson, 2000). Considerable research has focused also on the flow around rectangular prisms that involves different mechanisms, which depend on the chord to depth ratio, including trailing edge vortex shedding (TEVS), leading edge vortex shedding (LEVS), impinging leading edge vortices (ILEV) and interactions among them (vortex interaction, VI). It has been observed that this vortex formation and structure is sensitive to perturbations in the mean flow, which, acting at a particular frequency, can trigger the instability at the same frequency (Parker & Welsh, 1983). Vortices originating due to this excitation can be referred to as motion induced vortices (MIV). The existence of MIV together with the gradual development of a different flow structure due to the body motion, such as what is observed for circular cylinders, enhance the different nature and magnitude of the pressure field and resulting forces in comparison to the stationary case.

In the search for reduced drag response and increased torsional stiffness, modern bridge decks tend to shapes that cross the boundary between classical bluff bodies and airfoils. There is a need for fundamental physical investigations of the mechanisms which trigger VIV for these shapes, with their complex aerodynamics. The present work focuses on the Storebælt bridge which exhibited unacceptable maximum amplitude oscillations around the time of its inauguration. The Storebælt is a notable example of hexagonal shape common in modern suspension bridges with a single deck. Furthermore, the availability of extensive numerical and experimental data at full and model scale makes it a remarkable case study.

Contact person: J.M. Terrés-Nícoli, Universidad de Granada, CEAMA, Avda. del Mediterraneo s/n, 18006, Granada, T: +34958241000 x 31155, F: +34958132479. E-mail jterres@ugr.es
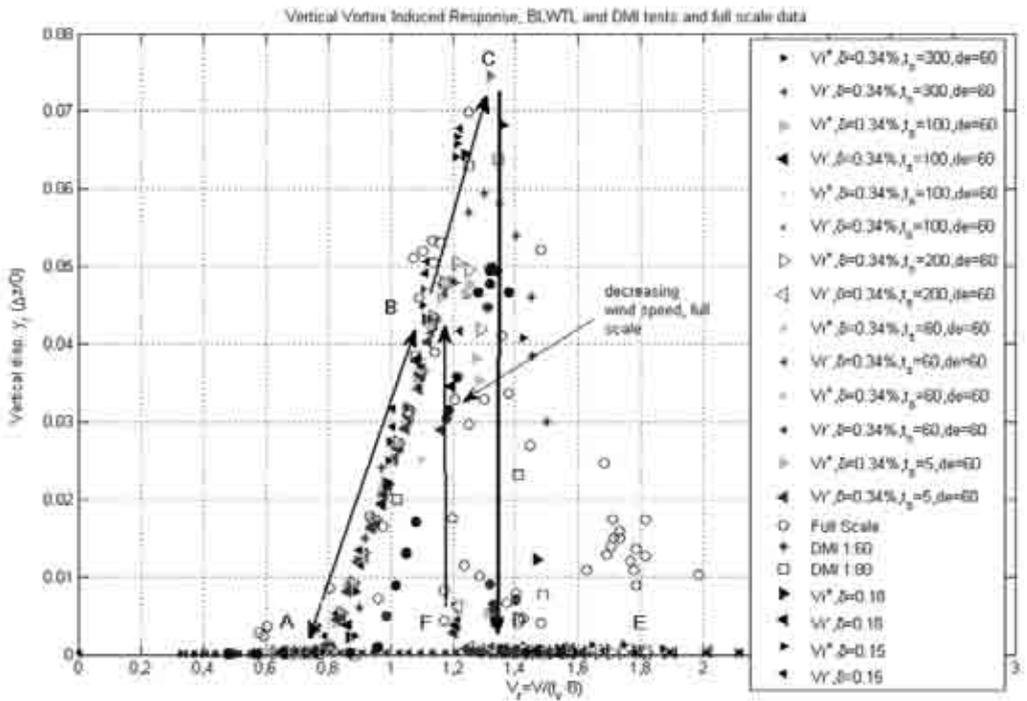
Figure 1: Observed vertical vortex induced response observed for different damping ratios and wind speed history compared with previous wind tunnel and full scale data.

METHODOLOGY

Simultaneous measurements of force and response of the bridge undergoing vertical VIV were carried out to investigate the motion induced mechanisms involved. A 1:70, carbon fiber, section model was designed to house up to 11 high frequency pressure scanners. The forcing was studied in detail, looking at the simultaneous pressure field throughout the different phases of the response for increasing and decreasing wind speeds. The pressure field was analyzed in detail by means of the phase averaging technique. The pressure tap distribution is presented in Figure 2 below.
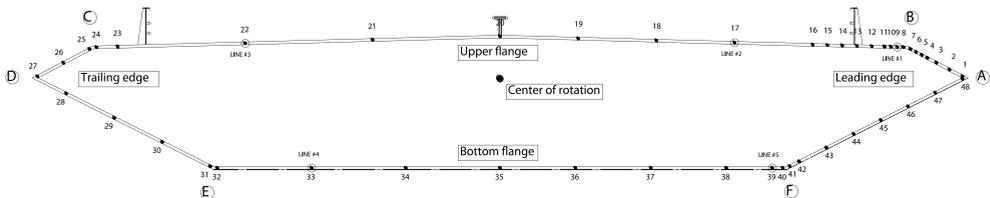

Figure 2: Pressure measurement distribution of a typical ring. Three rings of taps distributed along the span were used. Another set of taps is distributed in five lines along the span (line #1-5). Wind is from right to left.

RESULTS

Figure 1 presents the observed response (rms values of normalized amplitude, y_r) for different damping values and wind speed history. The present results are in good agreement with previous experiments at different laboratories (DMI and SINTEF, 1993). The vertical vortex induced response exhibits clear hysteresis as was the case for the torsional VIV: different response was observed when the maximum amplitude oscillation wind speed (Vcr+), point "C", is approached from lower wind speeds compared to when the wind speed is decreased from V->Vcr+. The former correspond to the path marked as ABCDE in Figure 1, compared to EDFBA for the latter, in the figure. Different response was observed for different rates of increasing wind speed. In general, higher values of maximum amplitude oscillations are observed for slower rates in increasing or decreasing wind speeds. This was also clearly observed in the torsional VIV (Terrés-Nicoli, Kopp, & King, 2003).

Vortex shedding at the trailing edge (TEV) seems to be the only source of significant pressure fluctuations of the motionless deck. The motion induced by these trailing edges vortices may be responsible for the control of the impinging shear layer instability (ISL) at the leading edge. The onset of the oscillation is therefore attributed to TEV as was again the case of the torsional VIV (Terrés-Nicoli, Kopp, & King, 2003). Significant pressure fluctuations are observed at the leading edge when the motion takes place. The build-up of larger amplitude vibrations appears to be caused by leading edge vortices generated by motion induced instability at the natural frequency. A mechanism that has been referred to as vortex interaction (Mills, Sheridan, & Hourigan, 2002) of these vortices and those forming at the trailing edge could be responsible for the enhancement of maximum amplitude oscillations, however this requires further investigation. An increasing phase is observed in the force, with respect to the response, reaching values of /2 consistent with a typical resonant response, as can be seen in Figure 3.
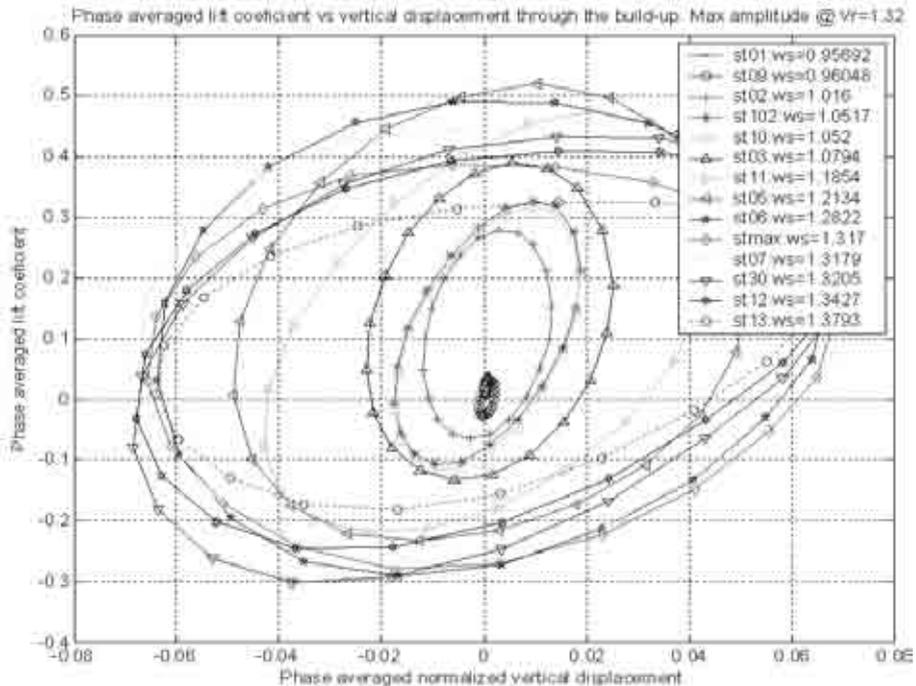

Figure 3: Phase plan diagrams for the simultaneously measured lift force and response for the different phases of the response.

The pressure fluctuation on the bottom flange of the leading edge up to the end of the separation bubble are all in phase with the response and, therefore, do not contribute to the energy transfer or the increase in the response. This can be observed in Figure 4 (left) and will be consistent with the body motion controlling the instability of ISL. Downstream of it a phase shift is observed in the pressure along the bottom flange Figure 4 (right). The resulting phase, with respect to the rotation when the ILEV approaches the trailing edge, is 90 , which results in optimum contribution to the increase of the magnitude of oscillations. This would explain the effectiveness of the guide vanes located around point E on the retro-fit of the actual bridge. The vanes on the leading edge corner F would distort the structure of the separation bubble and on the trailing edge corner would act complicating the interaction with the body surface as they leave the bottom flange and the consequent out of phase force. The full paper will examine these mechanisms in detail.
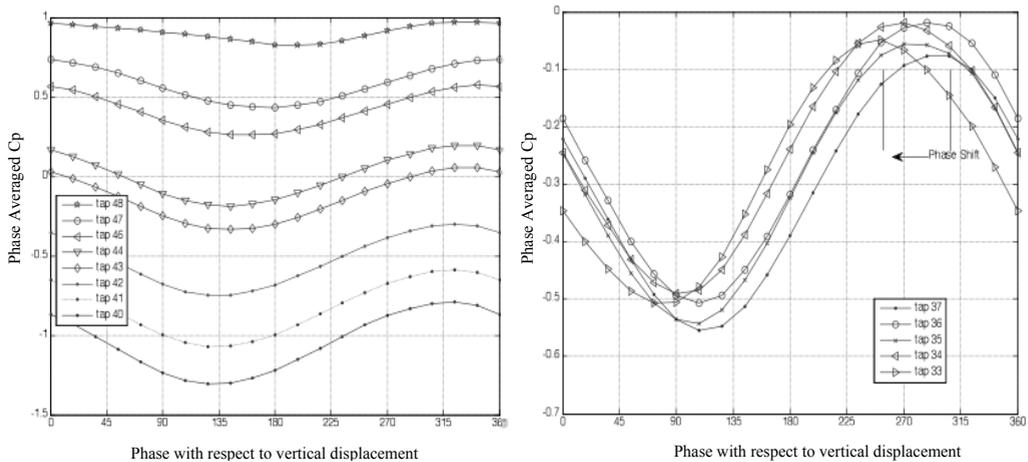

Figure 4: Left, pressure coefficients at maximum amplitude oscillation on the lower flange of the leading edge with approximately constant phase equal to 0. Right, pressure coefficients at maximum amplitude oscillations along the bottom flange, progressive phase shift up to 90º near the trailing edge corner.

REFERENCES

DMI and SINTEF. (1993). *Wind Tunnel Tests, Storebaelt, East Bridge. Detailed Design Suspension Bridge Section Model Tests.*

Govardhan, R., & Williamson, C. (2000). Modes of vortex formation ad frequency response of a freely oscillating cylinder. *Journal of Fluid Mechanics , 420*, 85-130.

Mills, R., Sheridan, J., & Hourigan, K. (2002). Response of base suction and vortex shedding from rectangular prisms to transverse forcing. *Journal of Fluid Mechanics , 461*, 25-49.

Parker, R., & Welsh, M. (1983). Effecs of sound on flow separation from blunt plates. *International Journal of Heat Fluid Flow , 4*, 113-128.

Terrés-Nicoli, J., Kopp, G., & King, J. (2003). Mechanisms of the Torsional Vortex Induced Vibration of The Storebaelt Bridge. *11th International Wind Engineering Conference.* Lubbock, TE, USA: ICWE.

Zasso, A., Belloli, M., Giappino, S., & Mugiasca, S. (2008). Pressure field analysis on oscillating circular cylinder. *Journal of Fluids and Structures , 24*, 628-650.

Wind tunnel study on the Pescara footbridge

A Zasso, M. Belloli, S. Muggiasca

Dipartimento di Meccanica, Politecnico di Milano – alberto.zasso@polimi.it – Via La Masa 1, 20156 Milano, Italy – Dipartimento di Meccanica, Politecnico di Milano – marco.belloli@polimi.it – Via La Masa 1, 20156 Milano, Italy – Dipartimento di Meccanica, Politecnico di Milano – sara.muggiasca@polimi.it – Via La Masa 1, 20156 Milano, Italy

Keywords: footbridge, wind tunnel, wake effects, flutter derivatives.

ABSTRACT

This paper deals with the aerodynamic project of the new Pescara footbridge. This is a flexible and slender structure less critical than a normal bridge in terms of structural issues, it is lighter and with small loads. The dynamic behavior must be accurately analyzed, considering the excitation exerted by the pedestrians and by the wind. This second aspect needs a deep analysis to determine the dynamic stability and the excitation due to the turbulent wind. Experimental analysis to determine the static and dynamic wind actions are needed because of the very particular design of the bridge itself. In fact, it is a stayed bridge with two different curved decks, one for the bicycles and one for the pedestrians, see Figure 1.

Figure 1: Render of Pescara Footbridge

The two decks are not symmetrical respect to the bridge axis, they have similar shape but they are characterized by different dimensions, in particular the bicycle deck have larger chord than the pedestrian one (*B=3.1 m* for pedestrian section and *B=4.1 m* for the bicycle section). The relative position of the two girders changes along the bridge, with the maximum distance at mid-span. Scaled models of the two girders have been realized and an appropriate experimental set-up has been

Contact person: S. Muggiasca, Dipartimento di Meccanica, Politecnico di Milano – sara.muggiasca@polimi.it – Via La Masa 1, 20156 Milano, Italy, +390223998072, +390223998081   .

E-mail sara.muggiasca@polimi.it

adopted to measure the static aerodynamic coefficient and the flutter derivatives, keeping into account the non symmetry of the bridges and also the wake effects. Each deck has been distinctly studied considering the two possible exposures: wind blowing from the sea and wind blowing from the country (Figure 2).

EXPERIMENTAL SET-UP AND FORCED MOTION TESTS

The core of the measurement system is a dynamometric frame that fits both the deck models, moreover each one can be installed on the frame on opposite direction, in order to measure the forces exerted by the sea wind and by the land wind. Thanks to the large dimension of the test section, it was also possible to place the two models in the wind tunnel simultaneously, evaluating the wake effects when the decks are at the maximum distance (Figure 3 (b)). An appropriate constrain system let us install the upwind deck at the right height.
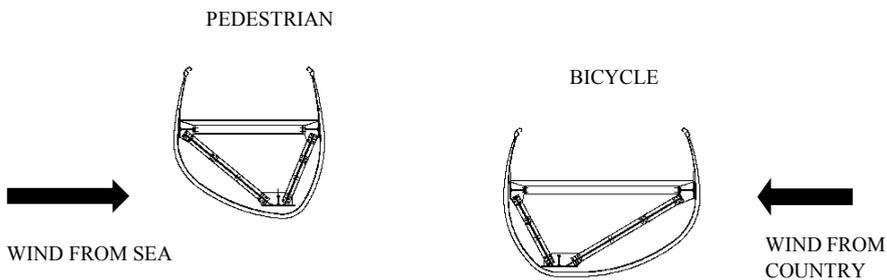

Figure 2: Pedestrian and bicycle deck sections: geometry of the models and wind direction
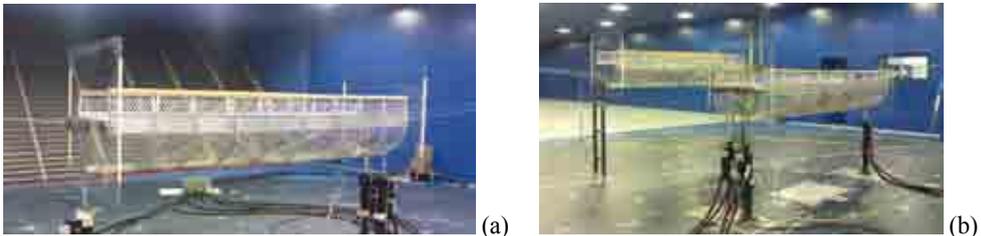

Figure 3: Sectional model in the wind tunnel: (a) test on a single deck (b) Wake effect tests.

The measurement set-up was finally completed by three accelerometers to define the dynamic model behavior and a pitot tube to measure the dynamic pressure acting on the deck. Three computer-controlled hydraulic actuators (figure 3 (a)) let us impose to the model the desired motion, i.e. torsional or flexural in a wide range of frequencies. The procedure used to perform these tests is well described in Cigada et al. (2001) applied to the Messina bridge sectional model. Forced motion tests have been performed to measure the static wind coefficients and the flutter derivatives.
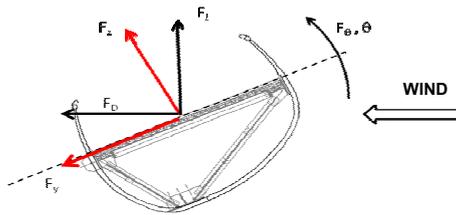
Figure 4: Forces directions respect to the model

Forced motion results

Static aerodynamic forces acting on the model have been measured as a function of the angle of attack. Figure 5 shows respectively drag, lift and moment coefficients for the pedestrian deck and wind coming from the land side, the same quantities are reported also when the model is in the wake of the other girder.
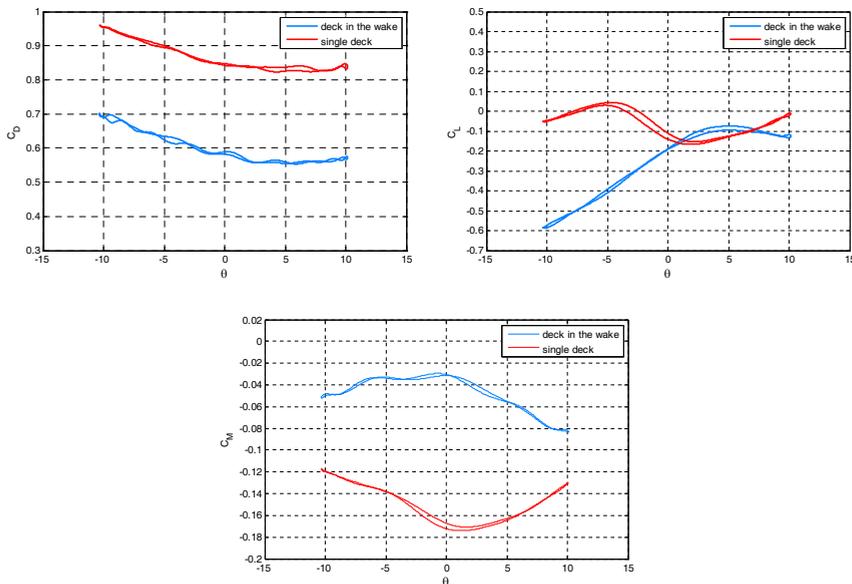

Figure 5: C_D, C_L, C_M measured on pedestrian deck, wind blowing from the land side, with and without wake effects.

As observable, there are some critical results: the lift coefficient first derivative presents negative values for angle of attack around 0 deg. Negative values of could mean a possible dynamic instability for the model and it was observed for both the wind directions (from the sea and from the country). The occurrence of an instability should be confirmed by the evaluation of the flutter derivatives and the trend of the aerodynamic force field with the reduced velocity. So that, to completely investigate the aerodynamic behavior of the deck it is necessary to measure the flutter derivatives on a wide range of reduced velocities. Figure 6 shows as an example the flutter derivatives *h1** e *a1** as a function of

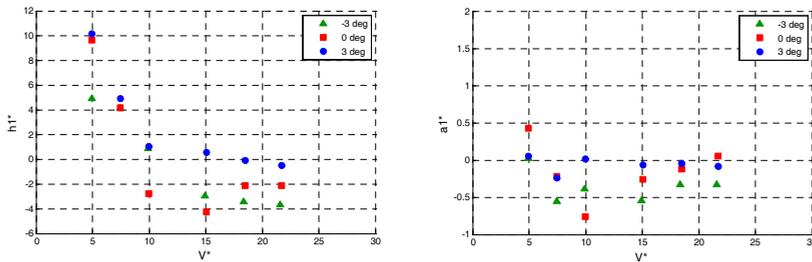V* for different mean angle of attack. (pedestrian deck, wind blowing from the sea).

Figure 6: Flutter derivatives as a function of V* measured on pedestrian deck, wind blowing from the sea, for different mean angle of attack : (a) h1* (b) a1*.

The flutter derivatives confirm the critical behavior of the pedestrian deck, assuming negative values at high reduced velocities.

Free motion results

To confirm the results obtained with forced motion tests, aerodynamic coefficient and flutter derivatives, free motion tests have been carried out. To simulate the correct kinematic due to the bridge curvature and to the constrain system an appropriate set-up was designed based on the modal deflected shape.
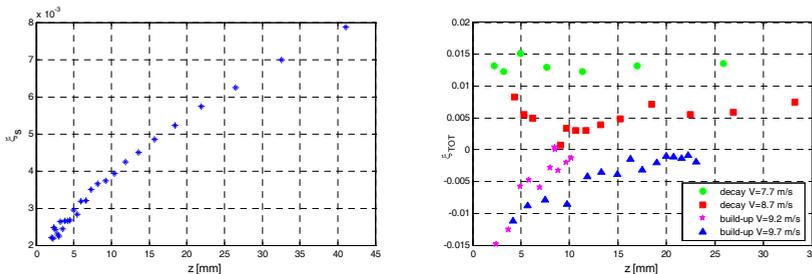

Figure 6: (a) structural non dimensional damping as a function of the oscillation amplitude (b) total damping (structural and aerodynamic) measured during wind free motion tests as a function of the oscillation amplitude.

Decay and build-up tests performed on suspended model confirm the results obtained from forced motion tests, in particular it is possible to note that for wind velocity higher than 9 m/s the bridge became instable. All the experimental results have been used to develop a simple 1 d.o.f. model to verify the critical wind velocity for the deck. Finally it was possible to conclude that real bridge needs an additional damping system.

REFERENCES

Zasso A. (1996). "Flutter derivatives: Advantages of a new representation convention", Journal of Wind Engineering and Industrial Aerodynamics, 60, 135-47

Cigada A., Falco M., Zasso A. (2001), "Development of new systems to measure the aerodynamic forces on section models in wind tunnel testing", Journal of Wind Engineering and Industrial Aerodynamics 89 (7-8), 725-746

FLOW - STRUCTURE INTERACTION
AND AEROELASTICITY

Stable and unstable limit cycles and nonlinear quasiperiodic response of aeroelastic structure

J. Náprstek, S. Pospíšil

*Institute of Theoretical and Applied Mechanics, v.v.i., Academy of Sciences of the Czech Republic,
naprstek@itam.cas.cz, pospisil@itam.cas.cz – Prosecká 76, 19700 Prague, Czech Republic*

Keywords: aeroelastic system, limit cycles, instability, post-critical behaviour

ABSTRACT

The vibration and the stability of a prismatic body in an air flow is often a result of the aero-elastic interaction of the response and the forces varying in time which have the non-conservative and gyro-scopic nature. Several types of aero-elastic oscillation are known using technical language in the wind engineering: flutter, galloping or self-excited motion induced by separating vortices at the body or in the wake of it. Each of them can be observed separately depending on the geometry and mechanical properties of the structure and the flow conditions. Very often however, the distinction may not be so clear. A bluff body structure can display both flutter and galloping characteristics, whereas each of them may be also affected by the wind turbulence. For example, during the life of the Tacoma Narrows bridge the experience with the vertical and torsional vibration had been associated with the galloping or torsional flutter respectively, see e.g. Billah & Scanlan (1991). General view at the conditions of dynamic stability and physical interpretation is given in Náprstek (2007), where several types of aero-elastic stability loss known from engineering practise and experimental data are identified in the frequency × frequency × velocity domain.

During the past decades, many explanations of the aero-elastic phenomenons and many mathematical models have been suggested. However all of them are suffering from uncertainty regarding the role of individual parameters being fundamental for the instability origin in a particular technical branch. Moreover, the analysis has revealed relatively considerable diversity of conclusions following from experimental studies. This is probably due to historical treatment of these problems in a number of branches as well as due to the existence of various instability domains and of a number of bifurcation points types. In the course of time, however, the research has succeeded in understanding that the majority of the models have either obvious or hidden linear character being based on various types of convolution formulations. Although some of these approaches are able to predict lower limits of aero-elastic stability, they do not provide any possibility to investigate the post-critical behavior, which is of strongly non-linear character. In any case, the detailed knowledge of the post-critical state

---

Contact person: S. Pospíšil, Institute of Theoretical and Applied Mechanics, v.v.i. Academy of Sciences of the Czech Republic, Prosecká 76, 19700 Prague, Czech Republic. pospisil@itam.cas.cz

is very important being decisive from the viewpoint of a possible secondary re-stabilization due to non-linear effects.

There are many papers dealing with just the one degree-of-freedom aero-elastic system starting with the paper by Parkinson & Smith (1963). This paper deals with the quasi-steady analysis of transverse galloping of a long square prism in a normal steady wind. The aerodynamic force coefficient is modeled as the polynomial of the seventh degree and the respective equation is solved by Krylov and Bogolyubov method. More recently, other paper appeared. In Oudheusden (2000) for example, galloping oscillation with a single rotational degree-of-freedom is investigated with the unsteady aerodynamics forces taken as a combination of aerodynamic stiffness and damping terms. In the paper by Leech (1979) the aerodynamic yaw moment is written in a form of Taylor-Fourier expansion and then a mathematical model similar to the Van der Pol equation is created. The stable and instable limit cycles are discussed. The paper of Matsumoto (1997) describes the torsional flutter mechanism of 2D rectangular cylinders and 2D H-shaped cylinders based upon unsteady pressure measurements under forced torsional vibration. For cylinders with fixed side ratio in the high reduced velocity range, the torsional flutter mechanism is in principle identical with that of coupled flutter. However, in the low reduced velocity range the torsional flutter is induced by vortices along side-surface of the cylinder and thus differs from mechanism of coupled flutter. In the paper by Vio et al. (2007), the square cross-section beam in a normal steady flow is analysed with regards to the global stability conditions. Several methods are used in this paper in order to predict bifurcation points. Comparison with numerical integration is given. Luongo et al. (2008) evaluated the branches of periodic solutions and their stability as functions of wind velocity. The existence of quasi-periodic solutions is proved.

Generally speaking, however, some types of non-linear effects can act like stabilizing factors. They are able at least for a limited period of time, to restitute one of lower types of stability after the structure has lost its exponential or asymptotic stability, see Tondl (1999). In Lumbantobing & Haaker (2004) the model of the parametric excitation of the aero-elastic oscillators is considered in a form of Mathieu nonlinear equation. The possibility of re-stabilization of the trivial solution after up-crossing the critical state is shown.

The subject considered in this paper is the non-linear dynamics of a mechanical oscillator with one degree of freedom in a wind field arising from reduction of the model described in Náprstek et al. (2008). It has been shown that such system has several types of bifurcation manifolds. The conditions of existence and relevant portraits of the principal limit cycles have been carried out. In this paper, the new approach is introduced. The gyroscopic forces are written in a form of the polynomial of the fourth order in order to assume the possibility of occurring also a nonstable limit cycles, which are not possible to be identified by means of experiments or numerical integration.

The relevant equation can be written in a form:

$$\ddot{u} + g(u) = \mu f(u, \dot{u}) \tag{1}$$

The right hand side of the equation, the aerodynamic forcing function $f(u, \dot{u})$ is depending on the geometry and the wind speed. Generalizing the common harmonic assumption for the response, we assume the solution in a form $u(t) = -a\cos\varphi(t) + b$. In this formula, the generalized phase $\varphi(t)$ is used. It can be naturally explained as a function given by a relation $\mathrm{d}\varphi(t)/\mathrm{d}t = \Phi(\varphi)$. The generalized frequency $\Phi(\varphi)$ is the periodic function with the period 2π. The coefficient a is the amplitude of the function and the coefficient b determines the eccentricity of the response with respect to the origin. Using the chain differentiation rule, we may rewrite Eq. (1) in the following form:

$$\Phi \cdot \frac{\mathrm{d}}{\mathrm{d}\varphi}(\Phi u') + g(u) = \mu f(u, \Phi u') \tag{2}$$

Eq. (2) represents a transform of Eq. (1) into the coordinate $\varphi(t)$. The both sides of the Eq. (2) should be multiplied by u' and integrated across the interval $\widetilde{\varphi} \in \langle 0, \varphi \rangle$. Hence the fundamental expression, which enables to deduce the governing equations for limit cycles is obtained:

$$\frac{1}{2}(\Phi a \sin \varphi)^2 + h(a \cos \varphi + b) - h(a + b) = \mu a \int_0^{\varphi} f\left(a \cos \widetilde{\varphi} + b, -a\Phi \sin \widetilde{\varphi}\right) \sin \widetilde{\varphi} \, \mathrm{d}\widetilde{\varphi} \quad (3)$$

The function $h(u)$ represents the indefinite integral of $g(u)$ i.e. $h(u) = \int g(u) \, \mathrm{d}u$. Evaluating Eq. (3) for $\widetilde{\varphi} \in \langle 0, 2\pi \rangle$ and $\widetilde{\varphi} \in \langle 0, \pi \rangle$, two important conditions can be deduced:

$$\begin{array}{rcl}
\int_0^{2\pi} f\left(a_k, b_k, \varphi, \Phi_k\right) \sin \varphi \, \mathrm{d}\varphi & = & 0 \quad \text{(i)} \\
h(a_k + b_k) - h(-a_k + b_k) - \mu a_k \int_0^{\pi} f\left(a_k, b_k, \varphi, \Phi_{k-1}\right) \sin \varphi \, \mathrm{d}\varphi & = & 0 \quad \text{(ii)}
\end{array} \quad (4)$$

Eqs. (4) allow to calculate values of a and b and approximation of $\Phi(\varphi)$ and hence the solution of non-linear equation in an iterative loop. This approximation is converging rapidly to the exact solution (calculated for example numerically). For the $k - \text{th}$ approximation and $\mu > 0$ can be written:

$$\Phi_k(\varphi) = \left[\frac{2h(a_k + b_k) - 2h(a_k \cos \varphi + b_k) - 2\mu a_k \int_0^{\varphi} f\left(a_k, b_k, \widetilde{\varphi}, \Phi_{k-1}\right) \sin \widetilde{\varphi} \, \mathrm{d}\widetilde{\varphi}}{a_k^2 \sin^2 \varphi}\right]^{1/2} \quad (5)$$

Finally, the divergence of the flow and, consequently, the phase volume evolution are determined by the exponent

$$\lambda = \int_0^T \frac{\mathrm{d}f(u, \dot{u})}{\mathrm{d}\dot{u}} \, \mathrm{d}t \quad (6)$$

When λ has negative value, the limit cycle is stable, whereas for λ positive, the limit cycle is instable. If trajectory is stable according to Lyapunov, then arbitrary initial perturbation doesn't prove any grow, on average, along the trajectory.

Let us demonstrate this approach on the equation describing the motion of the system with one degree-of-freedom oscillating in the flow (torsionally or laterally), possibly reaching even the destructive amplitudes. In particular the following model will be discussed:

$$\ddot{u} + \alpha u + \beta u^3 = \mu(\eta - \nu u^2 + \vartheta u^4)\dot{u} \quad (7)$$

where $\alpha, \beta, \nu, \eta = 1, \mu = 2$ and parameter ϑ is varying in the interval $\vartheta \in \langle -0.2, 0.2 \rangle$. It should be noticed that the right hand side of Eq.(7) includes the fourth degree of the response in order to encompass possibly both stable and unstable limit cycles as it has been observed experimentally in a wind channel. Their existence is predetermined by a particular ratio of parameters η, ν, ϑ. The theoretical solution of the above equation shows the considerable sensitivity of the system self-excited vibration with respect to particular values of parameters. After the loss of trivial solution stability the response in one degree of freedom tends to stabilize itself in the form of a stable limit cycle, see Figure 1. The solid curve in the left picture represents an attractor for all configurations of initial conditions, when parameter $\vartheta < 0$, see the right picture. For $\vartheta > 0$ stable ($\lambda < 0$) and unstable ($\lambda > 0$) limit cycles exist until the point ($\vartheta = \vartheta_{max}, \lambda = 0$) is reached. This point provides a twofold limit cycle and represents a strong energy barrier. When this energy barrier is overcame by means of further wind

energy supply, for example, the limit cycles don't exist any more and the final stability loss occurs. The system response starts to grow beyond all limits. This process can be initiated from the viewpoint of our analysis when a is increasing and inducing a transition of λ through the zero value, see Fig. 1, right picture. The twofold limit cycle making an important separatrix manifold cannot be directly determined neither by means of experiments nor the numerical integration.
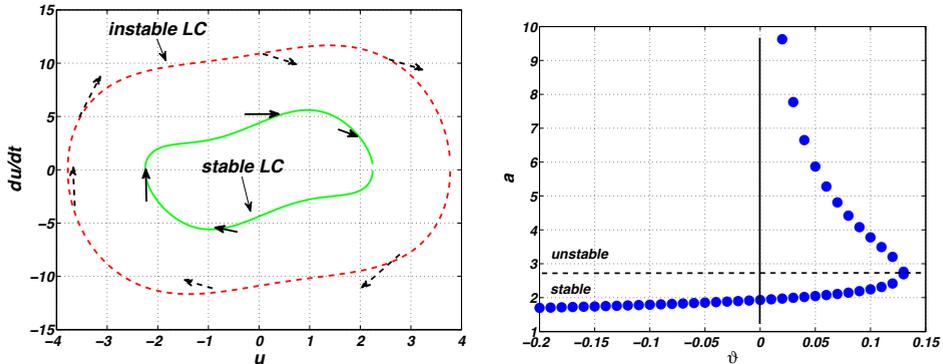

Figure 1: Attractive and repulsive limit cycles stemming from the solution of the basic Eq. (1) - left; The stability diagram for the parameter ϑ - right.

ACKNOWLEDGEMENT

REFERENCES

Billah Y.K, Scanlan R.H. (1991). "Resonance, Tacoma Narrows bridge failure, and undergraduate physics textbooks", American Journal of Physics, 59 (2).

Náprstek J. (2007). "Domains and types of aeroelastic instability of slender beam", In: Procedings of the ASME2007 International Design Engineering technical Conferences, Computers and Information in Engineering Conference. September 4-7, 2007, Las Vegas, Nevada , USA.

Parkinson G.V., Smith J.D. (1963). "The square prism as an aeroelastic non-linear oscillator", Quart. Journal of Mechanics and Applied Mathematics, Vol. XVII, pp. 225–239.

Oudheusden B.W. (2000). "Aerodynamic stiffness and damping effects in the rotational galloping of a rectangular cross-section", Journal of Fluids and Structures, 14, 1119–1144.

Leech C.M. (1979). "Limit cycle stability of aerodynamically induced yaw oscillations", International Journal Mechanical Science, 517–525.

Matsumoto M., Daito Y., Yoshizumi F., Ichikawa Y., Yabutani T. (1997). "Torsional flutter of bluff bodies", Journal of Wind Engineering and Industrial Aerodynamics, 69-71, 871–882.

Vio G.A. Dimitriadis G., Cooper J.E. (2007). "Bifurcation analysis and limit cycle oscillation amplitude prediction methods applied to te aeroelastic galloping problem", Journal of Fluids and Structures, 23, 983-1011.

Luongo A., Zulli D.., Piccardo G. (2008). "Analytical and numerical approaches to nonlinear galloping of internally resonant suspended cables", Journal of Sound and Vibration, 315, 373–393.

Tondl, A. (1999). "Non-linearly coupled systems" In: C.Kratochvíl et al. (eds.): Proceeding of the Conference Engineering Mechanics '99, Svratka (CZ) , 87–96.

Lumbantobing, Haaker T.I. (2004). "On the parametric excitation of some nonlinear aeroelastic oscillators", Journal of Fluids and Structures 19, 221–237.

Náprstek, J., Pospíšil, S., Fischer, C. (2008). "Post-critical limit cycles and nonstationary response types of aeroelastic system", In: Zolotarev, Horáček (eds.): Proceedings 9th International Conference on Flow-Induced Vibrations, Prague, 30 June-3 July 2008, 41–47.

Aeroelastic Analysis of Miradoiros Bridge in La Coruña (Spain)

J. A. Jurado, S. Hernández, A. Baldomir, F. Nieto,
School of Civil Engineering of the University of La Coruña. jjurado@udc.es

LOCATION AND ESTRUCTURAL FEATURES OF THE BRIDGE

Miradoiros Bridge has been projected as a solution for the traffic congestion problem generated as the existing bridge over the Ría of La Coruña is not able to cope with the current number of vehicles. The figure 1 shows its location. The proposed alternative is a new cable stayed bridge upstream the existing bridge.

Figure 1: Location of future Miradoiros Bridge.

The projected bridge has a main span of 658 m and two secondary spans of 270 m each. The chosen deck cross-section is a 34 m wide and 3 m depth symmetric aerodynamic box. Special care has been taken in the aesthetics of the bridge. One of the key issues of this proposal is the envision of the bridge receiving pedestrians as it will communicate two populated urban areas and the bridge surroundings will attract a number of visitors due to the wonderful existing landscape. Its balcony zones have been dedicated around the towers at deck level to allow the recreational use of the structure. In fact, Miradoiros means balcony with beautiful views in Galician language. The figure 2 shows the geometry of the bridge and the cross section of the deck.
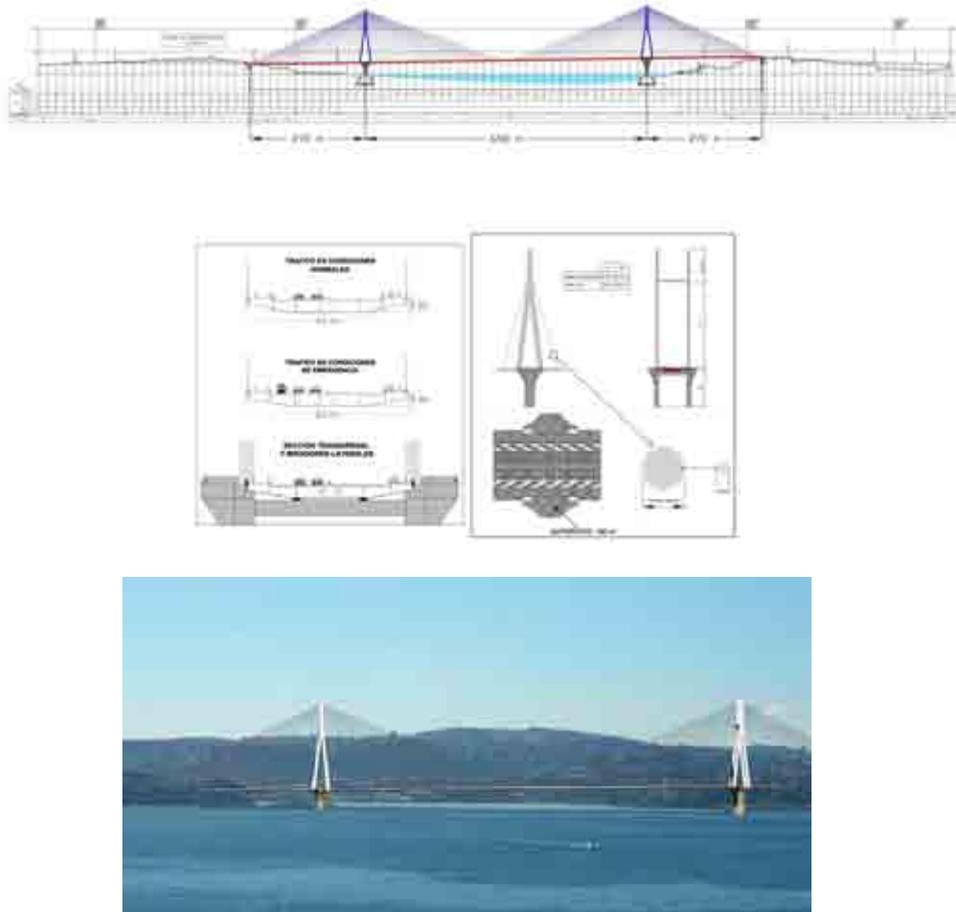

Figure 2: Main dimensions of Miradoiros Bridge and virtual view.

FLUTTER DERIVATIVES DETERMINATION

To avoid experimental tests of completed bridge models in large wind tunnels that are complicated and expensive, it is necessary to use an hybrid method which is computational based but needs experimental parameters. Sectional models of the deck are initially tested in an aerodynamic wind tunnel of small dimensions to obtain the flutter derivatives. These functions are then used in the computational analysis of the aeroelastic behaviour of the full bridge. According to Simiu and Scanlan (1996) formulation, the aeroelastic forces are linelized as functions of the displacements and velocities of the system for vertical w, lateral v and torsional rotation φ_x degrees of freedom. The expressions can be written as

$$\mathbf{f}_a = \begin{Bmatrix} D_a \\ L_a \\ M_a \end{Bmatrix} = \frac{1}{2}\rho U^2 KB \cdot \begin{pmatrix} P_1^* & -P_5^* & -BP_2^* \\ -H_5^* & H_1^* & BH_2^* \\ -BA_5^* & BA_1^* & B^2 A_2^* \end{pmatrix} \begin{Bmatrix} \dot{v} \\ \dot{w} \\ \dot{\varphi}_x \end{Bmatrix} + \frac{1}{2}\rho U^2 K^2 \cdot \begin{pmatrix} P_4^* & -P_6^* & -BP_3^* \\ -H_6^* & H_4^* & BH_3^* \\ -BA_6^* & BA_4^* & B^2 A_3^* \end{pmatrix} \begin{Bmatrix} v \\ w \\ \varphi_x \end{Bmatrix} \quad (1)$$

$$\mathbf{f}_a = \mathbf{C}_a \dot{\mathbf{u}} + \mathbf{K}_a \mathbf{u}$$

where B is the deck width, ρ is the air density, U is the mean wind speed, $K = B\omega/U$ is the reduced frequency with ω the frequency of the response, and $P_i^*(K)$, $H_i^*(K)$, $A_i^*(K)$ $i = 1...6$ are the flutter derivatives which are functions of K. $\mathbf{K}_a$ and $\mathbf{C}_a$ are called aeroelastic matrices.

Sectional tests of bridge desk are carried out in an aerodynamic wind tunnel to obtain the flutter derivatives. Free vibration approach with the sectional model of the deck supported by several vertical and horizontal springs was used (figure 3). By carrying out test for different speed flow the complete set of eighteen coefficients A_i^*, P_i^*, H_i^* ($i = 1,…6$) was identified. The Ibrahim time domain method has been use to extract the vibration parameters of the sectional model and from then the flutter derivatives are defined. The frequency similarity is not necessary to evaluate flutter derivatives because they are functions of the reduced velocity $U^* = 2\pi U / \omega B$. Changing the wind speed in the tunnel and the stiffness constants of the springs, a wide range of reduced velocities can be simulated. A more detailed description of sectional tests can be found in Nieto, Jurado and Hernández (2005).
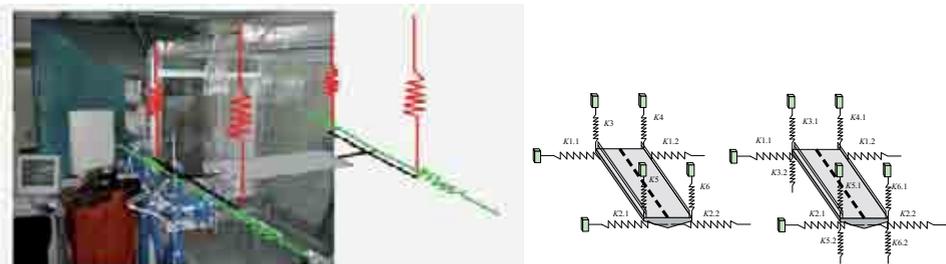

Figure 3: Spring support system of a sectional model deck in wind tunnel.

FLUTTER ANALYSIS

In the present work, a coherent matrix formulation has been used for the computational phase of hybrid flutter analysis. Jurado and Hernandez (2004) explain that this formulation stems from the dynamic balance equation

$$\mathbf{M}\ddot{\mathbf{u}} + (\mathbf{C} - \mathbf{C}_a)\dot{\mathbf{u}} + (\mathbf{K} - \mathbf{K}_a)\mathbf{u} = \mathbf{0} \quad (2)$$

ensambling the matrices and vector for the full structural model. Through modal analysis it is possible

to approximate the deck displacements by means of a linear combination of the most significant mode shapes. Assembling them in columns into the modal matrix $\mathbf{\Phi}$, the displacement vector can be expressed as $\mathbf{u} = \mathbf{\Phi q}$. Each element of the vector $\mathbf{q}$ represents the participation of each mode shape in the displacement vector $\mathbf{u}$. Premultiplying (2) by $\mathbf{\Phi}^T$ it becomes

$$\mathbf{I\ddot{q}} + \mathbf{C}_R\mathbf{\dot{q}} + \mathbf{K}_R\mathbf{q} = \mathbf{0} \tag{3}$$

where $\mathbf{C}_R = \mathbf{\Phi}^T (\mathbf{C} - \mathbf{C}_a)\, \mathbf{\Phi}$, $\mathbf{K}_R = \mathbf{\Phi}^T (\mathbf{K} - \mathbf{K}_a)\, \hat{\mathbf{\Phi}}$ and $\mathbf{\Phi}^T\mathbf{M\Phi} = \mathbf{I}$ Using mass normalized modes. Knowing that the solution of this equation has the form $\mathbf{q}(t) = \mathbf{w}e^{\mu t}$, becomes

$$\left(\mu^2\mathbf{Iw} + \mu\mathbf{C}_R\mathbf{w} + \mathbf{K}_R\mathbf{w}\right)e^{\mu t} = \mathbf{0} \tag{4}$$

which can be transformed into an eigenvalue problem by adding the identity $-\mu\mathbf{Iw} + \mu\mathbf{Iw} = \mathbf{0}$:

$$\left[\mu\begin{pmatrix}\mathbf{I} & \mathbf{0} \\ \mathbf{0} & \mathbf{I}\end{pmatrix}\begin{pmatrix}\mu\mathbf{w} \\ \mathbf{w}\end{pmatrix} + \begin{pmatrix}\mathbf{C}_R & \mathbf{K}_R \\ -\mathbf{I} & \mathbf{0}\end{pmatrix}\begin{pmatrix}\mu\mathbf{w} \\ \mathbf{w}\end{pmatrix}\right]e^{\mu t} = \mathbf{0} \tag{5}$$

or in short

$$\left(\mathbf{A} - \mu\mathbf{I}\right)\mathbf{w}_\mu e^{\mu t} = \mathbf{0} \tag{6}$$

The imaginary part β of the eigenvalues μ counts on the frequency ω, while the real part α of the eigenvalues is associated with the damping ratio ξ. The condition of flutter corresponds to the lowest wind speed U_f which gives one eigenvalue with vanished real part. However, the problem (6) is non-linear because the matrix $\mathbf{A}$ assembles the aeroelastic matrices $\mathbf{K}_a$ and $\mathbf{C}_a$. These matrices contain the flutter derivatives, which are functions of the reduced frequency $K = B\omega/U$, and the frequency for each eigenvalue ω remains unknown until the problem has been solved. For example, figure 4 shows graphs with the evolution of the eigenvalues for increasing wind velocities. It is observed that the critical flutter velocity is 77 m/s in this case.
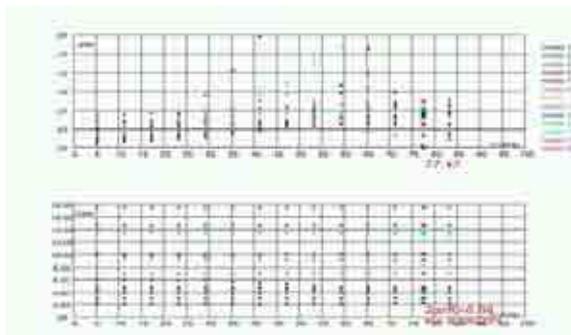

Figure 4: Evolution of eigenvalues with respect to wind velocity U until flutter condition with a null damping.

REFERENCES

Simiu E., Scanlan R. (1996). *Wind effects on Structures*. John Wiley & Sons, New York.

Jurado J. Á., León A., Hernández S. (2005) Wind Tunnel Control Software for Identification of Flutter Derivatives on Bridge Sectional Tests. EACWE 4. 4º European and African Congress in Wind Eng. Prague, Check Republic.

Jurado, J. Á., Hernandez S. (2004) Sensitivity analysis of bridge flutter with respect to mechanical parameters of the deck. Structural and Multidisciplinary Optimization Vol. 27, Nº 4. June, 2004.

Time domain representations of unsteady aeroelastic wind forces by rational function approximations

1st Ch. Neuhaus, 2nd O. Mikkelsen, 3rd J. Bogunović Jakobsen, 4th R. Höffer, 5th W. Zahlten

1Bergische Universität Wuppertal - neuhaus@uni-wuppertal.de - 2University of Stavanger - ove.mikkelsen@uis.no - 3University of Stavanger - jasna.b.jakobsen@uis.no - 4Ruhr-Universität Bochum - ruediger.hoeffer@rub.de - 5Bergische Universität Wuppertal - zahlten@uni-wuppertal.de

Keywords: bridge aeroelasticity, rational function approximation, indicial function

ABSTRACT

Of main concerns in the design of long-span bridges is the question of the ability of the structure to withstand wind loads. Cable-supported bridges in a wind field do continuously interact with the wind and are prone to vibrations. Unsteady loading acts by pressure fluctuations on the surfaces of the bridge. Modelling of wind loads for response calculations are done by separating and superposing a mean stationary load and a fluctuating part of the load. A load model for the non-stationary part has to incorporate both loads due to turbulence in the undisturbed wind field and aeroelastic loads. Aeroelastic loads originate from motions of the structure in the wind. In bridge engineering aeroelastic loads are traditionally described through aerodynamic frequency-dependent coefficients (flutter derivatives) according to the equation of Scanlan (1996). Scanlan and Sabzewari (1969) did tests and measurements with scaled section models in a wind-tunnel determining flutter derivatives both for steady state and transient oscillatory motions of bridge section models under initially laminar flow conditions. They argued that low Reynolds number flow fell short in duplicating true full scale conditions but pointed out that valuable design-guiding information could nonetheless be gained from their results. Established methods for determining flutter derivatives from measurements in wind tunnel exist. Commonly a 2 DOF system with coordinates corresponding to heave- and pitch-motions of the bridge section is implemented. Turbulence can be generated in model flow but

unwanted effects due to problems of scaling arise. When loads are transferred to the full span and full width of the bridge correlation effects must be accounted for.

Present work is on rational function approximations for aeroelastic self excited section model loads. It is amongst others motivated by the need of implementing aeroelastic loads for finite element analyses of long-span bridges. In this context the present work also serves as a supplement regarding applications of future experimental results.

With regard to a proposed bridge design, descriptions of self excited wind loads are needed to determine the critical flutter velocity. As far as the bridge spans increase and constructions become more slender nonlinear structural effects and interaction with buffeting loads come into interest of bridge aerodynamics. A rational function approximation of the wind loads, self excited and buffeting loads, offers a comprehensive formulation for this purpose. The critical wind speed in laminar flow can be found in a stability analysis of a state-space representation of the complete aeroelastic system given by the structure and the flow around it. A superposition of self excited loads with buffeting loads was presented by Chen, Matsumoto & Kareem (2000). Time domain functions of the aeroelastic forces, needed for a structural nonlinear analysis, can be derived by inverse Laplace transformation. The aeroelastic loads in the Laplace domain are given by

$$
\begin{bmatrix} L \cdot B \\ M \\ D \cdot B \end{bmatrix} = \begin{bmatrix} L_z + L_\alpha + L_x \\ M_z + M_\alpha + M_x \\ D_z + D_\alpha + D_x \end{bmatrix} = q_0 B^2 \cdot \begin{bmatrix} Q_{11} & Q_{12} & Q_{13} \\ Q_{21} & Q_{22} & Q_{23} \\ Q_{31} & Q_{32} & Q_{33} \end{bmatrix} \cdot \begin{bmatrix} r_z/B \\ \alpha_y \\ r_x/B \end{bmatrix} = q_0 B^2 \cdot Q(p^*) \cdot r(p^*) \tag{1}
$$

In Eq. 1 q_0 defines the dynamic pressure. L, M and D are lift, torsional moment and drag per unit length respectively, with corresponding degrees of freedom r_z (vertical), α_y and r_x (lateral). B indicates the bridge deck width and Q can be interpreted as a nondimensional aeroelastic transfer function matrix whose components are functions of the nondimensional Laplace variable p^*.

This work is based on the methods of Roger (1977) and Karpel (1981). Roger suggested a consistent rational function approximation for all force components of an aeroelastic system. Roger's method of approximation was modified by Karpel to the minimum-state method where the number of augmented state degrees of freedom is reduced. The nondimensional matrix Q is approximated in the Laplace domain as follows:

$$
Q(p^*) = A_0 + A_1 p^* + A_2 p^{*2} + D[p^* I - R]^{-1} E p^* \tag{2}
$$

A_i, D, E and R are coefficient matrices and I the appropriate identity matrix. This approximation can be divided into a polynomial part representing the aeroelastic stiffness, damping and mass and a rational part representing the instationary influence of the wake. The diagonal matrix R contains the denominator coefficients representing the poles of the rational part of the approximation. The components Q_{mn} of the complex nondimensional influence matrix in the frequency domain (Eq. 3) are expressed by experimentally determined Scanlan derivatives

$$
Q(K) = \begin{bmatrix} Q_{11} & Q_{12} & Q_{13} \\ Q_{21} & Q_{22} & Q_{23} \\ Q_{31} & Q_{32} & Q_{33} \end{bmatrix} = \begin{bmatrix} K^2\left(iH_1^* + H_4^*\right) & K^2\left(iH_2^* + H_3^*\right) & K^2\left(iH_5^* + H_6^*\right) \\ K^2\left(iA_1^* + A_4^*\right) & K^2\left(iA_2^* + A_3^*\right) & K^2\left(iA_5^* + A_6^*\right) \\ K^2\left(iP_1^* + P_4^*\right) & K^2\left(iP_2^* + P_3^*\right) & K^2\left(iP_5^* + P_6^*\right) \end{bmatrix} \tag{3}
$$

The approximations are done by a least square minimisation algorithm where the Laplace domain approach (Eq. 2) is reduced to the frequency domain with the relation $p^* = \beta + iK$ for $\beta = 0$. K is the reduced frequency defined by the ratio $B\omega/u$.

The present work implements and applies the extended minimum-state method from Tiffany and Adams (1988) with the use of the software package MATLAB®. The optimisation process is divided into a linear least square problem for the calculation of the coefficients in A_i, D and E and a nonlinear least square problem for the calculation of the denominator coefficients in R.

The impulse response functions follow from Eq. 2 by inverse Laplace transformation. The step response functions, in this context called indicial functions, are given by the integral of the impulse

response functions. The indicial function Φ_{mn} corresponding to each of Q_{mn} is then given by

$$\Phi_{mn}(t^*) = A_{0,mn}\varepsilon(t^*) + A_{1,mn}\delta(t^*) + A_{2,mn}\dot{\delta}(t^*) + \sum_{l=1}^{N} D_{ml}E_{lm}e^{-\gamma_l t^*} \tag{4}$$

where ε, δ, and γ_l are the unit step function, the Dirac delta function and the approximated poles respectively. Φ_{11} e.g. represents the indicial function that links the lift force to the vertical velocity of the structure. A convolution of the velocity component with the respective indicial function results in the self excited forces.

The extended minimum-state method has been implemented for 2 and 3 DOF aeroelastic systems and an arbitrary number of poles. A verification of the algorithm for the analytical solution of a flat plate in potential flow, derived by Theodorsen (1934), is done. The step response function Φ_{12} of the minimum-state approximation for simplified circulatory force components of Theodorsens equation fits to the Jones (1939) approximation of the Wagner (1925) function.

Aeroelastic force components of the influence matrix Q of experimentally determined 2 and 3 DOF flutter derivatives for different sections according to references below have been approximated using the extended minimum-state method. Rational functions have been established from flutter derivatives of a 2 DOF Gibraltar bridge deck section model tested by Bergmann (2004) in a water channel. Also 3 DOF flutter derivatives obtained by Chowdhury & Sarkar (2003/2004) and Chen, He & Xiang (2004) for streamlined bridge deck sections and an airfoil have been utilised. Approximations of rational functions with different number of poles are compared. Boundary conditions and constraints for the coefficients and the pole locations are discussed, impulse and step response functions are calculated as well.

Figure 1a depicts examples of step response functions Φ_{11} representing approximations according to different number of lag terms for a streamlined bridge deck section model (B1) taken from Chowdhury & Sarkar (2004).
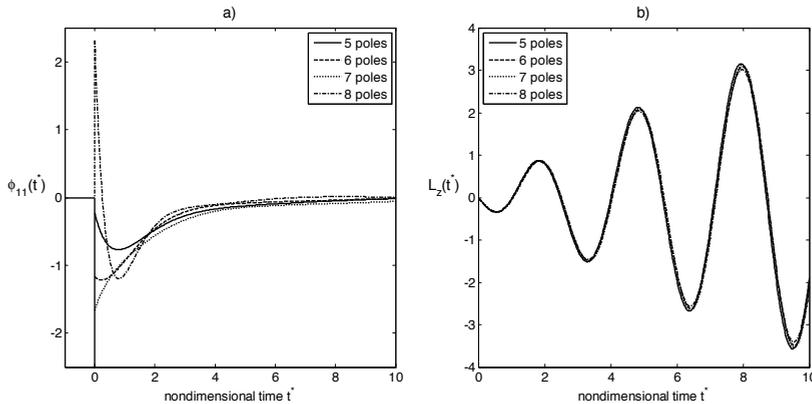

Figure 1: (a) Step response functions Φ_{11} (amplitude cutoff at zero t*) (b) Reference forces L_z

Table 1 shows the identified approximation parameters $A_{1,11}$ of the force component Q_{11} dedicated to the indicial functions in Figure 1a, which can be interpreted as aeroelastic damping, for approximations with different numbers of poles N.

N	5	6	7	8
$A_{1,11}$	-3,8065	-3,4265	-3,3831	-4,1127

Table 1: Approximation parameters – aeroelastic damping coefficients

The solution of the convolution of these indicial functions with a nonstationary reference movement, arbitrary movement function starting from idle state with a smooth evolution at the beginning, is shown in Figure 1b. The frequency range of the data for the approximations is limited by measurement techniques. High reduced frequencies, linked to low reduced velocities, are experimentally hard to realise due to high inertia forces or very low wind speeds in the experiments. The lack of this information produces uncertainties of the characteristics of the indicial functions for small values of the nondimensional time $t*$. Although the indicial functions (Figure 1a) show variability the respective force components L_z (Figure 1b) are in good agreement.

Forces due to horizontal displacements or velocities are weak compared to forces due to pitch or heave. Two different weighting methods, considering the division into a linear and a nonlinear least square approximation step according to Tiffany & Adams (1988), are implemented and compared to each other and to non weighted approximation results.

As described above, this paper examines different methods for determination of time domain functions for the wind structure interaction in terms of rational functions. In particular, an extended minimum-state approximation has been studied. The main advantage of the minimum-state approximation is the reduction of so called additional lag states while using the same poles for all force components. The complete system of the mechanical structure and the flow around it can be transformed into a state-space representation. A stability analysis of the state-space matrix representation of the system as an eigenvalue solution yields to critical wind velocities and thereby identifies the corresponding aeroelastic phenomena. This has been e.g. presented by Peil & Kirch (2008) for several 2 DOF systems. The influence of the third degree of freedom on the aeroelastic stability is discussed in this study.

REFERENCES

Simiu, E, Scanlan R., (1996). *''Wind effects on structures''*, 3rd edition, New York, Wiley-Interscience.
Scanlan R. H., Sabzewari A. (1969). ''Experimental aerodynamic coefficients in the analytical study of suspension bridge flutter'', Journal of Mechanical Engineering and Science,
vol 11, no. 3 1969.
Chen X., Matsumoto M., Kareem A. (2000). ''Time domain flutter and buffeting response analysis of bridges'', Journal of Engineering Mechanics, Vol.126, No. 1, January 2000.
Roger K., (1977). ''Airplane math modelling methods for active control design'', Structural aspects of active controls, Agard Conference Proceedings 1977, p.4.1-4.11.
Karpel M., (1981). ''Design for active and passive flutter suppression and gust alleviation'', NASA Contractor report 3482.
Tiffany S., Adams W., (1988). ''Nonlinear programming extensions to rational function approximation methods for unsteady aerodynamic forces''. NASA Technical paper 2776.
Theodorsen T., (1934). ''General theory of aerodynamic instability and the mechanism of flutter'', NACA Report No.496.
Jones R., (1939). ''The unsteady lift of a wing of finite aspect ratio'', NACA Report No. 681.
Wagner H., (1925) ''Über die Enstehung des dynamischen Auftriebes von Tragflügeln'', Zeitschrift für angewandte Mathematik und Mechanik, VDI Verlag G.M.B.H., Berlin 1925.
Bergmann D., (2004). ''Experimentelle Ermittlung der instationären aerodynamischen Eigenschaften von Brückenprofilen im Wasserkanal'', Institut für Aerodynamik und Gasdynamik, Universität Stuttgart, Doctoral dissertation.
Chen A., He X., Xiang H., (2004)''Identification of 18 flutter derivatives of bridge decks'', Journal of Wind Engineering and Industrial Aerodynamics, Vol 90, 2002.
Chowdhury A. G., Sarkar P. P., (2003). ''A new technique for identification of eighteen flutter derivatives using a three-degree-of-freedom section model'', Engineering Structures, Vol 25, 2003.
Chowdhury A. G., Sarkar P. P., (2004). ''Identification of eighteen flutter derivatives of an airfoil and a bridge deck'', Wind and Structures, Vol. 7, No. 3, 2004.
Peil A., Kirch A., (2008). ''Approximation of unsteady aerodynamic derivatives by rational functions'', Conference proceeding, 7th European Conference on Structural Dynamics, Southampton 2008.

Galloping of an inclined square cylinder

1st K.M. Shum, 2nd K.C.S. Kwok, 3rd P.A. Hitchcock

1) *CLP Power Wind/Wave Tunnel Facility, The Hong Kong University of Science and Technology –*
wtisaac@ust.hk – Clear Water Bay, Hong Kong, China
2) *School of Engineering, The University of Western Sydney – k.kwok@uws.edu.au – Sydney,*
New South Wales, Australia
3) *CLP Power Wind/Wave Tunnel Facility, The Hong Kong University of Science and Technology –*
wtpete@ust.hk – Clear Water Bay, Hong Kong, China

Keywords: galloping, wake excitation, inclination, wind incidence, structural damping.

ABSTRACT

Slender structures with inherently low damping can be prone to serious vibration excited by galloping. Galloping is a form of single-degree-freedom aerodynamic instability which affects structural cross-sections such as square, rectangular, crucifix and other sections with fixed separation points. Extensive wind tunnel studies on galloping of cantilevered structures, such as Kwok & Melbourne (1980) and Kawai (1995), have been carried out to understand the excitation mechanism of galloping. Kwok & Melbourne (1980) found that a slender square cylinder with an aspect ratio of 18:1 vibrated excessively under the combined effect of galloping and wake excitation when the reduced velocity was between 15 and 20. The effect of wake excitation diminished when the reduced velocity was above 20. Kawai (1995) showed that galloping of a building model with an aspect ratio of 10:1 could not be observed when the angle of wind incidence was larger than 10°. Ziller & Ruscheweyh (1997) presented two different methods of determining the onset velocity of galloping using the aerodynamic coefficients measured from wind tunnel tests. A review of the existing literatures indicated that there was no relevant research carried out to investigate the wind effects on inclined cantilever structures. Studies on the wind effects on inclined structures have mostly focused on stay-cables. However, structures are now designed with more complex and innovative architectural features. For instance, some bridge pylons are designed with an inclination mainly for aesthetic purposes. It is obvious that wind flow around an inclined structure can be significantly different from that around a vertical structure.

This paper presents the results from a program of wind tunnel studies on the galloping of an inclined square cylinder. A single-degree-freedom model simulating the vibration of a slender structure in its crosswind direction was designed and fabricated. A series of wind tunnel tests were conducted to study the galloping of the structure in terms of angle of wind incidence, inclination angle and structural damping ratio. The flow condition being considered in this study was a uniform smooth flow and the reduced wind velocity was 16. Different flow conditions and reduced wind velocities will be studied further in another series of wind tunnel tests.

Contact person: 1st K.M. Shum, CLP Power Wind/Wave Tunnel Facility, The Hong Kong University of Science & Technology, Kowloon, Hong Kong, China, TEL: 852-2358 0170 and FAX: 852-2243 0040.
E-mail wtisaac@ust.hk

EXPERIMENTAL SETUP

A series of wind tunnel tests were carried out in the upstream test section of the high speed section of the CLP Wind/Wave Tunnel Facility at the Hong Kong University of Science and Technology. The cross-section of the test section is 3 m wide and 1.6 m high. A slender square tower model was designed and fabricated with dimensions of 30 mm × 30 mm × 540 mm (W×B×H), resulting in a height to breadth ratio of 18:1. The natural frequency and the pivot point of the model were adjusted by the length of a 2 mm steel plate that was installed at the base of the tower model. The density and the natural frequency of the model were found to be about 223 kg/m^3 and 9.0 Hz. The model was effectively pivoted at its base and had a straight line deflection mode. The crosswind displacement (y) of the model was measured by four strain gauges. Two strain gauges were installed on each side of the 2 mm thick steel plate forming a Wheatstone bridge circuit. The output signals from these strain gauges were amplified and low-pass filtered at a frequency of 100 Hz by a solid-state signal conditioner prior to data acquisition. The signals were sampled at a frequency of 1000 Hz for a duration of 180 s. The orientation of the inclined square tower model with respect to the mean wind direction was represented by an inclination angle α in the vertical plane and a yaw angle β in the horizontal plane, as shown in Figure 1. In this study, the tower model is defined as backward (forward) inclined when the inclination angle is positive (negative).
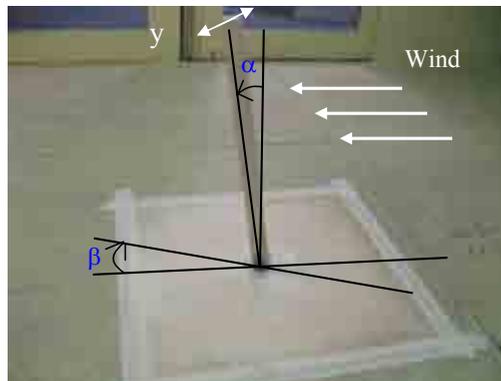

Figure 1: Orientation of square tower model

Mean wind speeds and turbulence intensities were measured at the cross-section where the model was positioned. Measurements were taken at seven designated height levels ranging from 75 mm to 540 mm above the ground along three different vertical lines. The positions of the three vertical lines were selected at the centre of model, 100 mm to the left of the model, and 100 mm to the right of the model. The maximum turbulence intensity was found to be less than 1% and the standard deviation of the mean wind speeds was found to be less than 1% of the average value of the mean wind speeds. Hence, the uniformity of the wind was satisfactory for the test.

RESULTS AND DISCUSSION

Effect of Inclination Angle

For aesthetic reasons, it is inevitable that structures or their slender parts may be designed to have certain inclination which can affect the wind flow around it. The effect of inclination angle on the transverse wind response of a slender structure was thus investigated by a series of wind tunnel tests. The measured normalized transverse responses of the square tower at different angles of incidence of the mean wind with various inclination angles are shown in Figure 2. The normalized transverse

response of the structure is defined as the ratio of the standard deviation of transverse displacement response of the tower model to the width of the square tower model. The inherent damping ratio of the model was essentially the same at different angle of inclinations and was found to be about 0.33% of critical damping. Evidently, the maximum normalized transverse response of the tower model increases when the inclination angle of the model is increased from -30° to $+10^o$. When the model is inclined at an inclination angle of $+30^o$, the maximum normalized transverse response is smaller than that at an inclination angle of 0°. For wind incidence angle within $\pm7.5^o$, considerable normalized transverse response can always be observed for the case where the model is backward inclined to wind, up to the tested maximum angle of $+30^o$. However, when the model is forward inclined to the wind, not only does the normalized transverse response of the tower decrease with the decreasing inclination angle, but so too does the range of wind incidence angles that can excite the tower to vibrate significantly. For the case where the model is inclined to the wind at -30°, a notable normalized transverse response of the tower model can only be observed at a wind incidence angle of 0°. The effect of inclination is considered to be an influencing factor affecting the transverse response of square-sectioned tower structures.
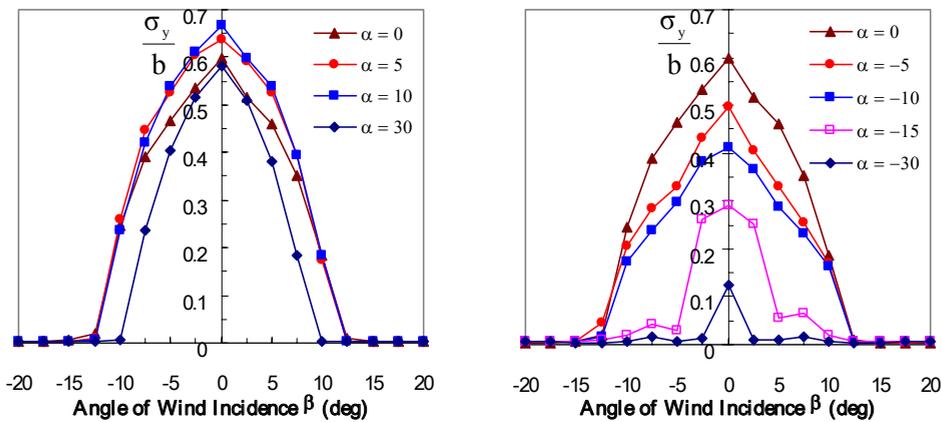

Figure 2: Normalized transverse response of square tower model as a function of angle of incidence of mean wind for various angles of inclination angle

Effect of Structural Damping

Galloping usually occurs when the negative aerodynamic damping due to structural motion is larger than the structural damping. The effect of structural damping is thus an important factor affecting the onset velocity of galloping. The effect of structural damping on the transverse response of the tower model was investigated in this study. The normalized transverse responses of the square tower at different angles of incidence and various levels of structural damping are shown in Figure 3. It can be seen that the transverse response of the tower model decreases as the structural damping is increased, as expected. A larger damping value is required for the structure with a larger inclination angle to prevent the occurrence of galloping at zero angle of incidence. Large galloping response of tower model with different inclination angles can be observed at zero angle of incidence when the structural damping is below a certain value. This normally suggests that the structure starts to gallop when the structural damping is below a certain value. However, it was pointed out by Kwok and Melbourne (1980) that the effect of wake excitation can be significant for a square vertical tower at a reduced velocity of 16. Hence, large transverse response of tower model may be observed even if the structural damping was larger than the negative aerodynamic damping. The transverse response of the tower model when forward inclined at -10° decreased significantly due to a slight increase in

damping from 0.31% to 0.44%. When the tower model is backward inclined at $+10^o$, considerable galloping response continued to be observed for structural damping values ranging from 0.34% to 0.85%. This suggests that the effect of galloping (and may be even the wake excitation) may be less dominant for the case where the model was forward inclined. However, to accurately account for the effect of wake excitation, a further wind tunnel study will be carried out to determine the transverse force coefficient of an inclined cantilever structure.
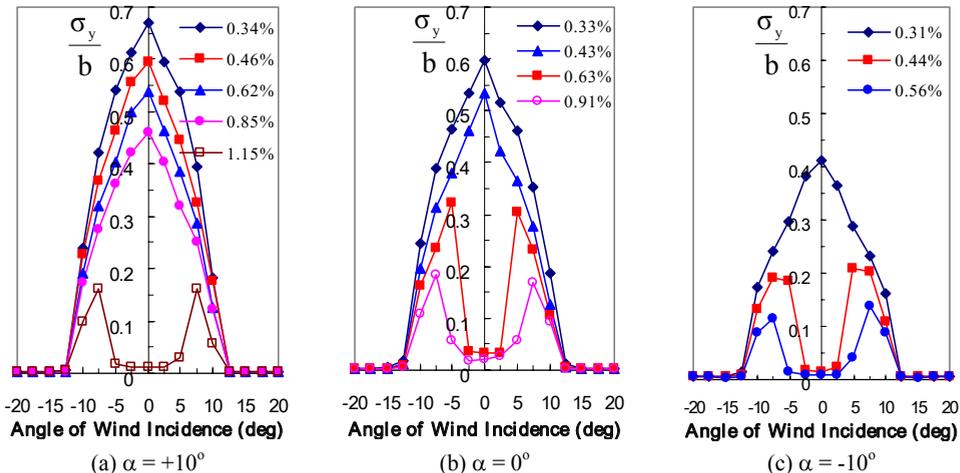

Figure 3: Normalized transverse response of the square tower model as a function of angle of incidence of mean wind for various levels of structural damping

SUMMARY

A wind tunnel investigation on the transverse response of a slender square tower model in a uniform smooth wind has been carried out. The test results indicate that the maximum normalized transverse response of tower model that is backward inclined to the approaching wind is much larger than that for a forward inclined model with the same magnitude of inclination. For wind incidence angles within $\pm 7.5^o$, considerable galloping response can always be observed for the case where the model is backward inclined. When the model was forward inclined, not only does the galloping response of the tower decrease with the decreasing inclination angle but so too does the range of wind incidence angle that can excite the tower to gallop. It was also found that the transverse response of the tower model decreased as the structural damping value was increased. A larger damping value is generally required for the structure with larger inclination angle to prevent galloping at zero angle of incidence. This suggests that the effect of galloping may be less dominant for the case where the model was forward inclined.

REFERENCES

Kwok K.C.S. and Melbourne W.H. (1980). "Freestream turbulence effects on galloping", Journal of Engineering Mechanics, ASCE, vol. 106(2), 273-288.

Kawai H. (1995). "Effects of angle of attack on vortex induced vibration and galloping of tall buildings in smooth and turbulent boundary layer flows", Journal of Wind Engineering and Industrial Aerodynamics, 54-55, 125-132.

Ziller C. and Ruscheweyh H. (1997). "A new approach for determining the onset velocity of galloping instability taking into account the nonlinearity of the aerodynamic damping characteristic", Journal of Wind Engineering and Industrial Aerodynamics, 69-71, 303-314.

Aerodynamic Loads on Flexible Bodies
for Sailing Simulation

M. Giuliani, P. Caccavale, C. de Nicola, V. Landolfi

*Redam – info@redam.it –Parco Cappuccini, 9C(83100 Avellino - IT) – University of Naples –
paolo.caccavale@gmail.com – Piazzale Tecchio, 80 (80100 Napoli - IT) – University of Naples –
denicola@unina.it – Piazzale Tecchio, 80 (80100 Napoli - IT)– University of Naples –
vittland@unina.it – Piazzale Tecchio, 80 (80100 Napoli - IT)*

ABSTRACT

Aeroelasticity phenomena play an important keyrole for aircraft engineering, but also civil applications such as buildings and antennas and other require fluid-structure interaction analysis. Sailing represent a very interesting field since wind effects has a major impact on performance and generally on design activities. Sail system and its constraints are bounded to other deformable structures like mast, boom, rigging etc. that determine sail shape themselves; so a reliable method for predicting fluidynamics loads, structural behaviour and their coupling effects represents an useful aid for designers.

Some well known numerical techniques for fluid-structure interaction are nowadays available but time e costs of simulation usually limit the industrial application also due to the high level skill required and results are not repeatable and satisfactory at all. Anyway also experimental testing can not solve this problem typically for scale and environment problems.

It can be easily recognized that FEM solvers rule the structure simulation with good and certificated results in many cases; CFD solvers, based on Finite Volumes, usually need some post processing and critical analysis for off design condition that unfortunately rule the design processes. The main database and modelling differences also determine complex data exchange interfaces that become critical or prohibitive for unsteady computations. Finally even if accurate and expansive CFD simulation data are available, coupling procedure affects resolution reducing the meaning of the gained accuracy.

In order to resolve the problems of this major issue, here a numerical strategy is presented: it has been chosen MSC.Nastran modelling approach to freeze interfaces and structural environment; PaMS, a BEM solver for unsteady non viscous flows, has been developed and coupled on the same

---

Contact person: 1st M. Giuliani, Redam, Parco Cappuccini, 9C (83100 Avellino – Italy), tel. +39 0825 792502, fax +39 0825 792504. E-mail info@redam.it

FE structural topology. In this way pressure loads are directly computed on structural nodes at each time step; node position changes accordingly to deformation under aerodynamic loads and so it happens for BEM panels updating. FE modelling requires just a few of rules to achieve an acceptable body description; the limited computing time and the simple data processing largely cover the approximation due ideal flow model here adopted. The developed tool is very effective in preliminary design but can also provide important data for structural sizing.

Considering a wing with aileron, the method here shown has been applied to simulate the initial moment of a turning, where aerodynamics and geometry changes interact with basic deformation shape; the results are in good agreement with classical theories (Fig.1). After a model set up to analyze mast and rigging configuration a sail simulation has been afforded considering all bodies involved deformation under wind loads.
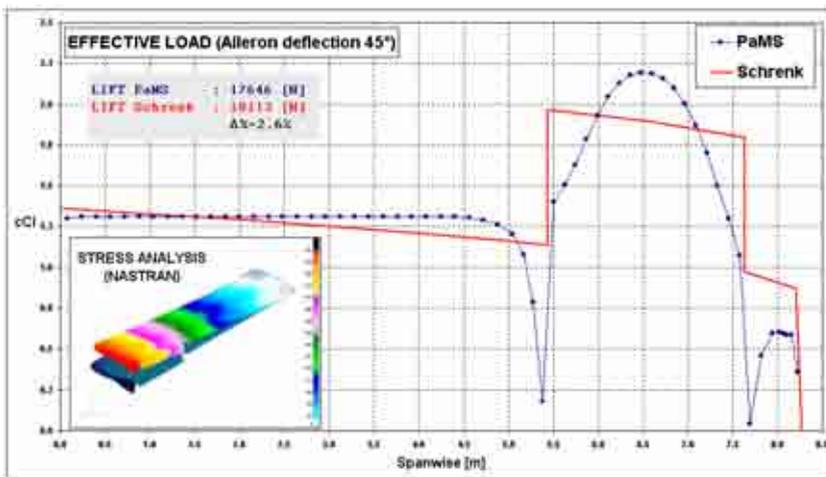

Figure 1: Nastran-PaMS coupling - results compared to a classical preliminary design method (Schrenk)

REFERENCES

Samareh J.A., Bhatia K.G. (2000). "A unified approach to modeling multidisciplinary interactions", AIAA-2000-4704.

Friedl N. (2002). "Membrane structures in unsteady potential flow", WCCM V 2002.

Whiting B., Neill D.J. (1997). "Interfacing external, high order aerodynamics into MSC/Nastran for aeroelastic analyses", MSC/Nastran.

Caccavale P., de Nicola C. (2007). "A new panel method for unsteady flows", XVIII AIMETA Congress.

Iuliano E. et al., Caccavale P., de Nicola C. (2008). "Evolutionary-based aero-structural optimization of a joined wing UAV using advanced potential methods", 8th. World Congress on Computational Mechanics (WCCM8), 5th. European Congress on Computational Methods in Applied Sciences and Engineering (ECCOMAS 2008).

Caccavale P. (2007). "A new potential method for fluidynamics analysis", University of Naples – PhD thesis.

The MacNeal-Schwendler Corporation (2005). MSC/NASTRAN User Guide 2005.

Investigation on the flutter mechanism of thin plate sections

Yong-Xin YANG, Yao-Jun GE, Wei ZHANG

State Key Laboratory for Disaster Reduction in Civil Engineering, Tongji University, Shanghai, China

INTRODUCTION

With the rapid increase of bridge span length, bridge structures are becoming more flexible and more vulnerable to wind-induced vibrations. Among all these vibrations flutter is the most important one for long-span bridges, since it will lead to structural collapse. In order to improve the aerodynamic stability, streamlined box girders are widely adopted in the design of long-span bridges, as the flutter performance and flutter characteristics of this type of girder section are similar to the thin plate section. Therefore, the research of the flutter-driving mechanism and flutter modality of the classical coupled flutter for thin plate sections are of great importance with reference to the flutter instability of long-span bridges. In this paper, the flutter mechanism of the classical coupled flutter of thin plate sections are investigated by the two-dimensional three-degree-of-freedom flutter analysis method (2d-3DOF method) which was proposed by the authors (Yang 2002, Yang 2007), with emphases on the aerodynamic damping, flutter modality and the relationships between flutter performance, flutter modality and structural frequency ratio. The particle image velocimetry (PIV) measurement of wake flow field is also presented to illustrate the relationship between vortices movement and structure vibration.

WIND TUNNEL TEST AND THEORETICAL CALCULATION

A thin plate section model which has an aspect ratio of 22.5 was used in the current research. The other parameters of this sectional model are: mass per unit length, m=11.25 kg/m; mass moment of inertia per unit length, I_m=0.2828 kg-m^2/m; heaving circular frequency, ω_h=12.11 rad/s; torsional circular frequency, ω_α=19.0 rad/s. The sectional model test was conducted in the TJ-1 Boundary Layer Wind Tunnel of Tongji University. The tested structural flutter onset speed is 16.5m/s.The tested structural flutter onset speed is 16.5m/s. With the aerodynamic derivatives of ideal thin plate section, the flutter critical speed of this sectional model was calculated by the 2d-3DOF method. The calculated flutter critical speed is 16.0m/s and with good agreement with the tested result. The evolution trends of systematic damping ratios and circular frequencies with wind speed are also calculated and shown in figure 1 and figure 2. As figure 1 shown, the systematic torsional damping decreases with the increase of wind speed when wind speed goes above 12m/s, and finally turns negative, indicating the flutter onset point is reached.

Contact person: Yong-Xin YANG, State Key Lab for Disaster Reduction in Civil Engineering, Shanghai, 200092, China, Tel.: 86-21-65983116-23-5 and FAX: 86-21-65984882. E-mail yang_y_x@tongji.edu.cn
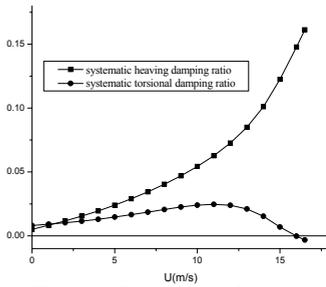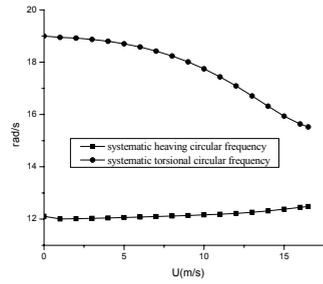
Figure 1: Damping ratios

Figure 2: Oscillation frequencies

AERODYNAMIC DAMPING

For a two-dimensional section model with three degrees of freedom including heaving, swaying and torsion, systematic oscillation frequencies and damping ratios of three degrees of freedom can be derived and represented by the combination of flutter derivatives and phase lags between motions having the same oscillation frequency with 2d-3DOF method. For example, through double iterations of wind speed and oscillation frequency, the systematic torsional damping ratio can be written by the following formulas (Yang 2002).

$$
\begin{aligned}
\xi_\alpha = & \frac{\xi_{\alpha s}\omega_{\alpha s}}{\omega_\alpha} - \frac{1}{2}\frac{\rho B^4}{I}A_2^* \\
& -\frac{1}{2}\frac{\rho B^4}{I}\frac{\rho B^2}{m_h}\Omega_{h\alpha}\left[A_1^* H_3^* \cos\theta_{\alpha h} - A_4^* H_3^* \sin\theta_{\alpha h} + A_1^* H_2^* \cos(\theta_{\alpha h}+\frac{3}{2}\pi) - A_4^* H_2^* \sin(\theta_{\alpha h}+\frac{3}{2}\pi)\right] \\
& -\frac{1}{2}\frac{\rho B^4}{I}\frac{\rho B^2}{m_p}\Omega_{p\alpha}\left[A_5^* P_3^* \cos\theta_{\alpha p} - A_6^* P_3^* \sin\theta_{\alpha p} + A_5^* P_2^* \cos(\theta_{\alpha p}+\frac{3}{2}\pi) - A_6^* P_2^* \sin(\theta_{\alpha p}+\frac{3}{2}\pi)\right]
\end{aligned}
$$

(1)

where ω_α is iterative circular frequencies of torsional degrees of freedom; Ω_{ij} is dimensionless equivalent frequency between two motions and is defined as

$$
\Omega_{ij} = \frac{\omega_i^2}{\sqrt{\left(\omega_j^2 - \omega_i^2\right)^2 + 4\left(\xi_i\omega_i\omega_j\right)^2}} \quad (i, j = \alpha, h, p)
$$

(2)

and θ_{ij} is phase lag between two motions and is expressed as

$$
\theta_{ij} = arctg\frac{2\xi_j\omega_j\omega_i}{\omega_j^2 - \omega_i^2} \quad (i, j = \alpha, h, p)
$$

(3)

In the case of heaving-torsional coupled flutter, the most important aerodynamic damping is in torsional motion. As for two-degree-of-freedom vibration, aerodynamic damping ratio in torsion can be represented by the summation of five parts reduced from nine parts as shown in Equation 1. Figure 3 describes the evolution trends of these five parts for the investigated thin plate section.

Part A with the reference of A_2^* is always positive and makes the greatest contribution to aerodynamic stability among five parts, while Part D with the reference of $A_1^* H_3^*$ keeps negative all the way and causes the worst influence on aerodynamic stability. The influence of Part E is also negative but with much smaller effect, and the values of both Parts B and C are very small. It should be noted that the aerodynamic damping which generated directly from torsional motion itself is always the main force to keep structure aerodynamically stable, and it is the aerodynamic damping comes from the coupling effect of heaving and torsional motion, especially Part D negative damping, that drives the whole oscillation system into flutter onset condition.
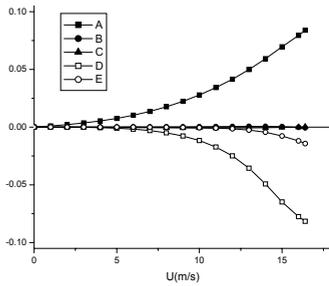
$$A \iff -1/2 \cdot \rho B^4 / I \cdot A_2^*$$

$$B \iff -\rho^2 B^6 / 2m_h I \cdot \Omega_{h\alpha} \cdot A_1^* H_2^* \cos(\theta_{\alpha h} + \frac{3}{2}\pi)$$

$$C \iff \rho^2 B^6 / 2m_h I \cdot \Omega_{h\alpha} \cdot A_4^* H_2^* \sin(\theta_{\alpha h} + \frac{3}{2}\pi)$$

$$D \iff -\rho^2 B^6 / 2m_h I \cdot \Omega_{h\alpha} \cdot A_1^* H_3^* \cos\theta_{\alpha h}$$

$$E \iff \rho^2 B^6 / 2m_h I \cdot \Omega_{h\alpha} \cdot A_4^* H_3^* \sin\theta_{\alpha h}$$

Figure 3: Aerodynamic damping of the systematic torsional motion

DEGREE PARTICIPATION

Another important result of the application of 2d-3DOF method is the coupling effect of degrees of freedom in flutter oscillation. The participation level of motion in each degree of freedom at the flutter onset can be described by three flutter modality vectors (Yang 2002). The flutter modality vector of the original thin plate section is plotted in figure 4.
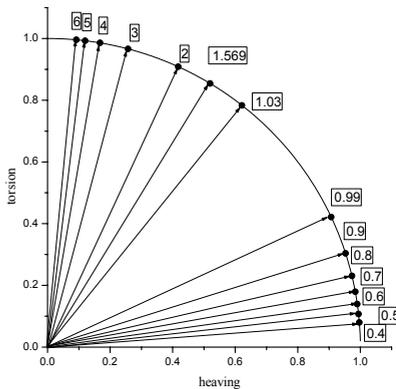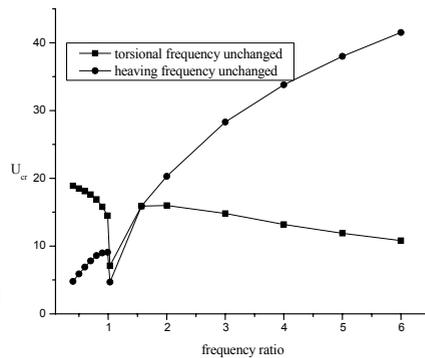

Figure 4: Flutter modality vectors

Figure 5: Flutter critical velocities

In order to investigate the relationship between flutter modality and structural frequency parameter especially the structural frequency ratio between torsional and heaving motions ($f_{torsion}/f_{heaving}$), flutter modality vectors of thin plate sections with various frequency ratios are calculated and displayed in figure 4. In figure 4 the numbers in rectangular are the values of different frequency ratios and the number 1.569 is the value for the original model. The position of the flutter modality vector for the original thin plate section indicates the participation level of heaving motion is considerably high, which implies strong coupling effect between torsional and heaving motions. With the increase of structural frequency ratio, the modality vector moves closer to the axis of torsion DOF gradually, showing that the participation level of heaving motion decreases and the coupling effect gets weaker. And with the decrease of structural frequency ratio, the flutter modality vector moves away from the axis of torsion DOF and gets very close to the mid-line between the two axes, indicating stronger coupling effect in flutter oscillation. When the structural frequency ratio gets below 1.0, the heaving

motion becomes dominant in the DOF coupling effect, and with the further decrease of frequency ratio the modality vector goes closer to the axis of heaving DOF, implying the torsional participation level and the DOF coupling level become lower and lower.

There are two ways in changing structural frequency ratio: one is keeping structural torsional frequency constant and only adjusting the value of structural heaving frequency, the other is keeping heaving frequency constant and adjusting torsional frequency. No matter which way is, the flutter modality is the same if structural frequency ratio is identical. But flutter critical velocities are different due to different ways of changing structural frequency ratio even if the structural frequency ratio is the same. For various conditions, the structural flutter critical velocities were calculated and shown in figure 5. The results indicate that although the relationship between flutter modality and structural frequency ratio is simple and unique, the relationship between flutter modality and structural flutter performance is rather complicated, since the absolute values of structural frequencies also influence the structural flutter performance.

WAKE FLOW FIELD MEASUREMENT

In order to clarify the relationship between the behavior of vortices and the wind-induced vibration of thin plate section, the wake flow field of the investigated thin plate section was measured by PIV technique under different wind speed conditions. The sectional model test was conducted in the TJ-4
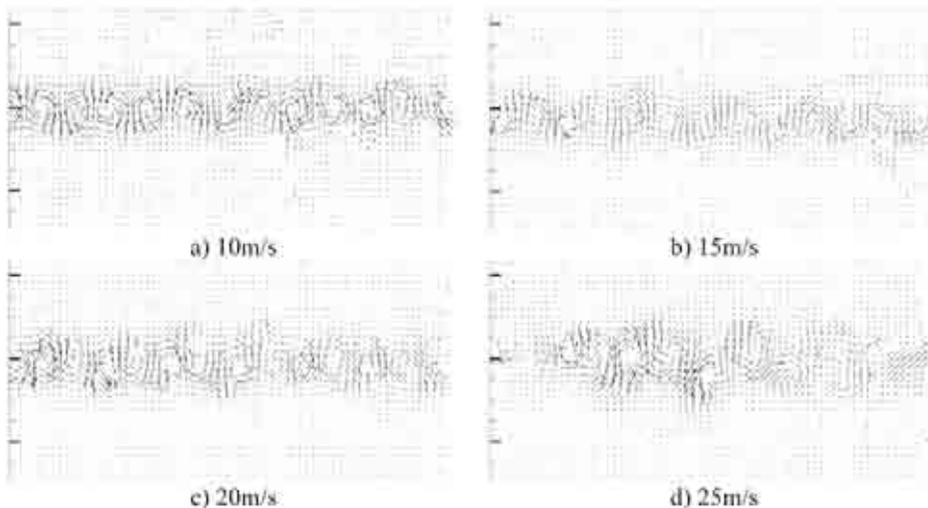

a) 10m/s   b) 15m/s

c) 20m/s   d) 25m/s

Figure 6: Wake flow field of thin plate section

REFERENCES

Yang, Y.X. (2002). Two-Dimensional Flutter Mechanism and its Applications for Long-Span Bridges (in Chinese), Ph.D Thesis Supervised by H.F. Xiang, and Y.J. Ge, Tongji University, China

Yang, Y.X., Ge, Y.J., Xiang, H.F. (2007). "Investigation on flutter mechanism of long-span bridges with 2d-3DOF method", Journal of Wind and Structures, Vol.10, No.5, 421-435

Effects of non-linear propagation of random turbulence fields on bridge flutter instability

L. Caracoglia

Northeastern University, Boston, MA 02115, USA – lucac@coe.neu.edu

Keywords: Long-span Bridges, Aeroelastic Instability, Turbulence, Uncertainty Propagation.

INTRODUCTION

Current research activities at Northeastern University (NEU) are concentrated on the analysis of the effects of uncertainty on the dynamic, wind-induced response of long-span bridges. Uncertainty is being used in this context as a general term indicating both the lack of knowledge in the structural system or resulting from unavoidable experimental and measurement errors, for example in wind tunnel. Such errors can be indirectly related to reference design quantities of the loading (e.g., turbulence spectra, aerodynamic forces, etc.). This problem is of relevance since wind-induced bridge response, derived from ambient vibration records during extreme winds, has, on occasion, revealed discrepancies in comparison with response simulations (Xu & Zhu, 2005). In particular, a framework for the analysis of uncertainty and its effects on the dynamic response of bridges under wind hazards is currently under development (Caracoglia, 2008a).

The influence of turbulence on bridge flutter has been a problem of interest to the research community over the years. Since the "classical" solution to the flutter problem neglects the presence of oncoming turbulence (e.g., Jones & Scanlan, 2001), researchers have developed methods to possibly overcome limitations of this assumption.

Two main methods have been proposed, based on either flutter derivatives in the frequency domain (Scanlan, 1997) or stochastic calculus in the time domain (Bucher & Lin, 1988). While the application of the first method suggests that the presence of turbulence delays the instability onset, turbulence may be detrimental if the second approach is employed. The second observation has also been suggested by other investigators, who confirmed potential negative effects of turbulence on aeroelastic instability, either dominated by a torsional mode (Bartoli et al., 1997) or influenced by modal coupling (Sepe & Vasta, 2005).

Recently, an alternative formulation for simulating the effects of turbulence on flutter was explored by the writer (Caracoglia, 2008b) in the context of the uncertainty estimation framework described above. The key aspect of this method is related to the fact that, while turbulence effects have preferably been described in terms of a perturbation to the reference flutter solution, both aeroelastic and buffeting loading terms, although linearized, were retained in the system of dynamic equations. The reference dynamic equilibrium scenario was modified by simulating an uncertain spatial distribution of wind turbulence. An equivalent modal force correlation term was employed as a random variable simulating turbulence effects.

Contact person: L. Caracoglia, Northeastern University, Boston, MA 02115, USA, 1-617-373-5186, 1-617-373-4419(F).
E-mail lucac@coe.neu.edu

The solution was developed in terms of second-moment stochastic stability (Grigoriu, 2002). It was shown that, if the perturbed system of dynamic modal equations was represented as a linear combination of an augmented state vector, no effects of turbulence on flutter were numerically observed in the simulations (flutter with coupling dominated by two modes only). However, there was also a limitation in the proposed algorithm since specific assumptions were made on the characteristics of the random state vector, possibly incompatible with a real turbulence field, but leading to a linear dynamic equation system. This fact allowed the straightforward solution of the stability as a function of second moments.

In this study this original hypothesis is replaced by a non-linear turbulence propagation scheme, proposed to overcome the original restriction. Dynamic instability of a two-mode equivalent system with aeroelastic coupling is introduced and discussed.

ANALYTICAL BACKGROUND

The dynamic response of a long-span bridge due to wind excitation was derived from the multi-mode formulation in the frequency domain (Jones & Scanlan, 2001), in which wind-induced forces can be represented as a superposition of aeroelastic and aerodynamic (turbulence-induced) components. The equations were transformed into equivalent time-domain terms to allow for the subsequent derivation of a Markov-type stochastic differential equation system.

Aeroelastic forces (self-excited drag, lift and moment per unit length) were based on flutter-derivative formulation. The components of the loading depend on $p(x,t)$ lateral, $h(x,t)$ vertical and $\alpha(x,t)$ angular bridge deck displacement and velocities, with x being the longitudinal coordinate along the deck axis and t the time variable. Aeroelastic forces were subsequently converted to time domain via indicial-function formulation as a function of the dimensionless time domain variable $s=tU/B$, with B being the reference deck width and U the mean wind velocity at the deck level.

The dynamic displacement components of the bridge deck were represented through modal superposition as,

$$p(x,t) = \sum \xi_g(t) B p_g(x), \quad h(x,t) = \sum \xi_g(t) B h_g(x), \quad \alpha(x,t) = \sum \xi_g(t) \alpha_g(x). \tag{1}$$

In Eqs. (1) $h_g(x)$, $p_g(x)$ and $\alpha_g(x)$ denote dimensionless eigen-mode components associated with the generic g-th mode, and $\xi_g(t)$ the corresponding generalized coordinate.

Turbulence-induced forces were similarly based on a linearized multi-mode approach (Jones & Scanlan, 2001) and represented in terms of quasi-steady theory. The dependence on the vertical (w) and lateral (u) turbulence components was obtained by linear expansion about the equilibrium position under static wind (initial angle of attack α_0). Static coefficients of the deck cross section per unit length, constant along the x axis, were denoted as: C_L and C_D for drag and lift, $\hat{C}_L = dC_L/d\alpha$, $\hat{C}_D = dC_D/d\alpha$ and $\hat{C}_M = dC_M/d\alpha$ (all evaluated at α_0). Buffeting loading was subsequently recast into generalized modal forces as a function of $\hat{u}(s) = u(s)/U$ and $\hat{w}(s) = w(s)/U$.

The span-wise loss of correlation, depending on the selected mode, was simulated through an equivalent "modal correlation length", derived in a least squares sense. As an example, the term $L_{\psi hj}$ associated with mode j and the vertical lift component depends on $\hat{w}(s)$, and was defined from

$$\left[(\hat{C}_L + C_D) L_{\psi_{hj}} \right]^2 = l^{-2} \iint (\hat{C}_L + C_D)^2 h_j(\upsilon) h_j(\sigma) \exp(-\tilde{c}_{wj} |\upsilon - \sigma|/l) d\upsilon d\sigma. \tag{2}$$

In Eq. (2) l denotes the total bridge length and $\tilde{c}_{wj} \approx 7\omega_j l / (2\pi U)$ with ω_j j-th circular natural frequency. An equivalent correlation length can be derived for the k-th mode and the torsional modal shape $\alpha_k(x)$, $L_{\psi ak}$. Chord-wise admittance was neglected at this stage.

Influence of turbulence on flutter was simulated by considering as independent random variables, the non-zero span-wise modal correlation lengths of aerodynamic forces, $L_{\psi hj}$ and $L_{\psi ak}$.

Coupled flutter analyses were restricted to the contribution of two modes only, namely a purely flexural and a purely torsional one. These are respectively denoted as j with $h_j(x) \neq 0$ and k with $\alpha_k(x) \neq 0$ exclusively, by neglecting the contribution of other modal components.

Equations of motion were recast into a first-order Itô-type stochastic differential system as a function of dimensionless time s. State augmentation was employed; the state vector $\mathbf{Z}(s) = [\mathbf{Z}_{AE}(s), \mathbf{Z}_{TB}(s)]^T$ was decomposed into the vector of modal and aeroelastic states, $\mathbf{Z}_{AE}(s)$ (Caracoglia, 2008b), and $\mathbf{Z}_{TB}(s) = [\hat{u}(s), \hat{w}(s), L_{\psi h j}, L_{\psi \alpha k}]^T$ the vector regrouping the turbulence terms and $L_{\psi h j}$ and $L_{\psi \alpha k}$, where $[\bullet]^T$ is the transpose operator.

The input turbulence excitation was transformed into two independent uni-variate filtered processes dependent on a scalar Wiener process $W(s)$. As an example, $\hat{u}(s)$ was simulated, in Itô-form, as an autoregressive filter $d\hat{u} = -G_{1u}\hat{u}ds + G_{2u}dW(s)$, with G_{1u} and G_{2u} suitable parameters. A similar expression was derived for $\hat{w}(s)$ with parameters G_{1w} and G_{2w}. An n-dimensional non-linear stochastic differential system with appropriate initial conditions was derived as (Grigoriu, 2002)

$$dZ(s) = \mathbf{a}_{NL}(\mathbf{Z}_{AE}(s), \mathbf{Z}_{TB}(s))ds + \sqrt{2\pi}\mathbf{q}dW(s), \tag{3}$$

with $\mathbf{q}$ being a vector of zeros and constants (G_{2w}, G_{2u}), and $\mathbf{a}_{NL}$ a non-linear vector-function of $\mathbf{Z}_{AE}(s)$ and $\mathbf{Z}_{TB}(s)$. The latter quantity can be rewritten as

$$\mathbf{a}_{NL} = \left\{ \begin{matrix} \mathbf{A}_{AE}^{(r \times r)} \mathbf{Z}_{AE}(s) + \mathbf{a}_{TB,NL}(\mathbf{Z}_{TB}(s)) \\ \mathbf{T}_L \mathbf{Z}_{TB}(s) \end{matrix} \right\}, \quad \mathbf{T}_L^{(n-r) \times (n-r)} = \begin{bmatrix} \mathbf{T}_{uw} & \mathbf{0}^{(2 \times 2)} \\ \mathbf{0}^{(2 \times 2)} & \mathbf{0}^{(2 \times 2)} \end{bmatrix}, \quad \mathbf{T}_{uw}^{(2 \times 2)} = \begin{bmatrix} -G_{1u} & 0 \\ 0 & -G_{1w} \end{bmatrix}. \tag{4a, 4b, 4c}$$

In Eqs. (4a) to (4c) the dependence on the s variable was omitted for brevity; the superscript indices in parentheses denote the dimension of linear matrices and vectors. It must be observed that the square matrix $\mathbf{A}_{AE}$ is linear, depends on $\mathbf{Z}_{AE}(s)$, has dimensions $r \times r$ with $r = (n-4)$ equal to the number of structural and aeroelastic states, and includes the two dynamic modal equilibrium equations and indicial-function-based first-order state equations, responsible for coupling. Details on the $\mathbf{A}_{AE}$ matrix can be found in Caracoglia (2008b).

As evident from Eq. (4b) and (4c), the linear matrix $\mathbf{T}_L$ is associated with the dimensionless wind turbulence components and the parameters G_{1u}, G_{2u}, G_{1w} and G_{2w}. Non-linearity is concentrated in the sub-component $\mathbf{a}_{TB,NL}$ of the vector-function $\mathbf{a}_{NL}$ in Eq. (4a), which has dimensions r and exclusively depends on $\mathbf{Z}_{TB}(s)$ through multiplicative terms of random processes and variables.

Equation (3) is non-linear, the solution to the stochastic stability problem in closed-form is not usually possible, especially for a state-space system of medium dimensions (Note that $n > 20$ is a typical value for the system such as in Eq. 3; Caracoglia, 2008b). Moreover, if a stability analysis Eq. (3) in terms of statistical moments (Bucher & Lin, 1988) is selected as a suitable indicator of the behavior, the solution usually requires a "hierarchical scheme", which calls for a numerical solution algorithm based on closure (truncation) techniques.

ANTICIPATED RESULTS

The first- and second-moment stochastic stability of Eq. (3) was analyzed in this section by application of the Itô's derivation rule (Grigoriu, 2002) to Eq. (3). The first-order deterministic system was rewritten in terms of expectations $E[\bullet]$ and $E'[\bullet] = d[\bullet]/ds$, as a set of two coupled equations associated with the upper and lower partitions of Eq. (3),

$$E'[\mathbf{Z}_{AE}(s)] = \mathbf{A}_{AE}E[\mathbf{Z}_{AE}(s)] + E[\mathbf{a}_{TB,NL}(\mathbf{Z}_{TB}(s))], \quad E'[\mathbf{Z}_{TB}(s)] = T_L E[\mathbf{Z}_{TB}(s)]. \tag{5a, 5b}$$

Equation (5) must be solved with initial conditions imposed on the state-vector expectation. In Eq. (5a) the hierarchical scheme is evident since the nonlinear term, $E[\mathbf{a}_{TB,NL}(\mathbf{Z}_{TB}(s))]$, depends on the s-dependent auto- and cross-covariance of the turbulence-field states, $\mathbf{Z}_{TB}$. Inspection of Eq. (5b)

reveals that $E[\mathbf{Z}_{TB}(s)]$ is asymptotically stable, while further manipulation of Eq. (5a) leads to

$$E'[\mathbf{Z}_{AE}(s)] = \mathbf{A}_{AE}E[\mathbf{Z}_{AE}(s)] + \mathbf{N}_{\mathbf{a},TB}\boldsymbol{\tau}(s), \tag{6}$$

with $\mathbf{N}_{\mathbf{a},TB}$ being a linear matrix and $\boldsymbol{\tau}(s)$ a strictly positive vector reordering the non-zero elements of $E[\mathbf{Z}_{TB}(s)\mathbf{Z}_{TB}(s)^T]$. The elements of $\boldsymbol{\tau}(s)$ are cross-covariances $E[\hat{u}(s)L_{\psi hj}]$, $E[\hat{w}(s)L_{\psi hj}]$, $E[\hat{u}(s)L_{\psi \alpha k}]$, and $E[\hat{w}(s)L_{\psi \alpha k}]$. It can be shown that and $L_{\psi hj}$ and $L_{\psi \alpha k}$, are independent of time.

As expected, if the turbulence field is stationary, $\boldsymbol{\tau}(s)$ is also constant and independent of time. The stability of Eq. (6) is therefore exclusively controlled by matrix $\mathbf{A}_{AE}$, i.e., flutter instability is unaffected by turbulence. It must be observed that asymptotic stability is excluded by Eq. (6). Furthermore, the same observation is valid even in the presence of non-stationary turbulence field, for example typical of a hurricane-type wind, provided that $|\boldsymbol{\tau}(s)|$ is a bounded functional.

In a similar way, the second-moment stability deterministic equations were derived. In this case equations were rewritten in scalar form to allow for a further implementation of the numerical algorithm. If the auto- and cross-covariance operators of $\mathbf{Z}(s)$, along with higher-order moment, are rewritten in scalar form as $E[Z_{j1}(s)]$ and $E[Z_{j1}(s)Z_{j1}(s)]$, the second-moment stability can be associated with the solution of the following non-linear deterministic equation,

$$E'[Z_{m1}(s)Z_{m2}(s)] = E[(\mathbf{a}_{NL})_{m1}Z_{m2}(s)] + E[(\mathbf{a}_{NL})_{m2}Z_{m1}(s)] + 2\pi\mathbf{q}\mathbf{q}^T, \tag{7}$$

with $m1$ and $m2$ being two indices, either referring to the components of $\mathbf{Z}_{AE}(s)$, $\mathbf{Z}_{TB}(s)$ or a combination thereof.

A numerical method was employed to investigate the instability of Eq. (7) depending on the initial conditions imposed on the statistical moments of $\mathbf{Z}(s)$. Simulated bridge models, employed as examples, will be analyzed and discussed in the final presentation of this study.

ACKNOWLEDGEMENTS

REFERENCES

Bartoli, G., Borri, C., Gusella, V. (1997). "On the influence of wind turbulence on bridge deck flutter", in: *Aspects in modern computational structural analysis* Meskouris Vittek, eds. Balkema, Rotterdam, NL, 3-17.

Bucher, C. G., Lin, Y. K. (1988). "Effect of spanwise correlation of turbulence field on the motion stability of long-span bridges", Journal of Fluids and Structures, 2 (5), 437-451.

Caracoglia, L. (2008a). "Influence of uncertainty in selected aerodynamic and structural parameters on the buffeting response of long-span bridges", Journal of Wind Engineering and Industrial Aerodynamics, 96 (3), 327-344.

Caracoglia, L. (2008b). "Some implications of the effects of turbulence on bridge flutter", Fourth International Conference on 'Advances in Wind and Structures (AWAS'08)', Jeju, South Korea. C.-K. Choi, J.D. Holmes, Y.-D. Kim, H.G. Kwak, eds. Techno-Press, Korea, ISBN 978-89-89693-23-9-98530, 1667-1675

Grigoriu, M. (2002). *Stochastic calculus. Applications in Science and Engineering*. Birkhäuser, Boston, MA, USA.

Jones, N. P., Scanlan, R. H. (2001). "Theory and full-bridge modeling of wind response of cable-supported bridges", Journal of Bridge Engineering, ASCE, 6 (6), 365-375.

Scanlan, R. H. (1997). "Amplitude and turbulence effects on bridge flutter derivatives", Journal of Structural Engineering, ASCE, 123 (2), 232-236.

Sepe, V., Vasta, M. (2005). "Turbulence effects on the aeroelastic stability of long-span bridges", Proceedings of the Mini-Symposium on "Large bridge aerodynamics and aeroelastic phenomena", Sixth European Conference on Structural Dynamics (EuroDyn 2005), Paris, France, vol. 1, 421-426.

Xu, Y. L., Zhu, L. D. (2005). "Buffeting response of long-span cable-supported bridges under skew winds. Part 2: case study", Journal of Sound and Vibration, 281 (3-5), 675-697.

Flutter analysis of an extradosed bridge in Hungary

M. Hunyadi

*Budapest University of Technology and Economics, Department of Structural Engineering –
hunyadi@vbt.bme.hu – H-1111 Budapest, Bertalan L. u. 2., Hungary*

Keywords: flutter, extradosed bridge.

ABSTRACT

A new bridge will be constructed on the motorway M43 in the south of Hungary. The bridge will cross the river Tisza at Szeged. An extradosed superstructure was designed with spans of 95+180+95 m, the total length of the structure is 372,60 m. The 30 m wide, three cellular deck is a composite one: prestressed concrete upper and lower slabs with steel webs of trapezoidal cross section. The depth of the deck is 4,08 m. The transversal rigidity of the deck is assured by steel trusses at every 5,00 m. The prestressed deck is supported by a system of 64 stay cables anchored in the two 22 m high pylons.

Since today no such structural form with these dimensions has been used in Hungary several special studies were investigated, among others aerodynamic instability analysis. Even though a preliminary study proved that the structure holds against aerodynamic instability problems with adequate safety level, detailed test series were investigated in the constructional design phase. The analysis concerned only the aerodynamic stability of the deck, the stability analysis of the cables and other structural members was made by the designer of the bridge.

The primary goal of the analysis was to determine the safety of the structure against flutter in temporary construction phases, when due to the cantilever construction method used the deck is in its

---

Contact person: M. Hunyadi, Budapest University of Technology and Economics, Department of Structural Engineering, H-1111 Budapest, Bertalan L. u. 2., Hungary., telephone +36-1-4631724, FAX +36-1-4631784.
E-mail hunyadi@vbt.bme.hu

most vulnerable position.

A wind tunnel investigation was done at the Department of Fluid Mechanics (2008) for the first time in Hungary. The aim was to determine both aerostatic and aeroelastic coefficients for the deck. A sectional model was used instead of a whole structural test, not only because the latter would have been too expensive and would have demanded too much time, but even because of the relatively small size of the available wind tunnel's diameter. The experimental study was made in the Theodore von Karman Wind Tunnel Laboratory in such a way that it could result the aerostatic coefficients and even the aeroelastic ones according to Scanlan (1996). The model of the deck was made of aluminium plates with a scale of 1:100 and was supported and forced by a mechanical robot arm.
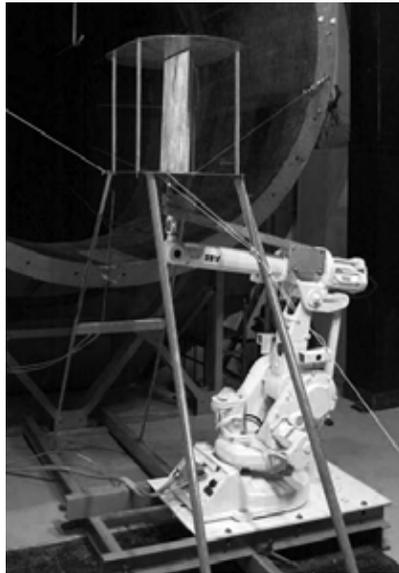
Figure 1: Wind tunnel arrangement. The vertically positioned model is forced by a robot arm.

The determination of the static coefficients was done at different angles of attack (from -10° to +10°). The resulting drag, lift forces and torsional moment were measured by six dynamometers incorporated in the robot arm.
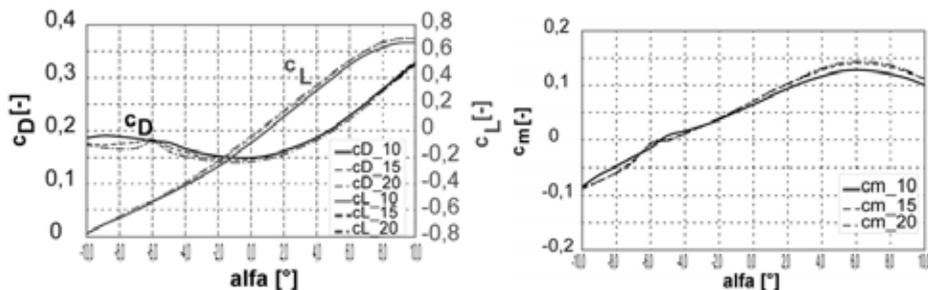

Figure 1: Drag, lift and moment coefficient in function of angle of attack at different wind speeds.

The diagrams of the static aerodynamic coefficients show that their first derivatives are positive in the range of an angle attack of -6° to +6°. It means that the deck doesn't have problematic or pathologic behavior, thus its behavior form will be as it can be assumed for box girder sections, and shows a stable behavior in terms of single degree of freedom flutter instability.

In the sense of the deck, vertical and torsional forced motion tests were required for the determination of the corresponding flutter derivatives. The robot arm was able to make movement with a frequency up to 2,5 Hz, the used highest wind speed was 20 m/s. To prevent the distortions of the measures due to gravity the model was placed vertically. The used wind velocities resulted thus in reduced velocities in the range of 5,5 to 75. Although results in the range of reduced wind speed above 20 were out of interest, they were retained to judge the character of the derivates resulted. The data provided by the dynamometers were modified by the forces due to forced motion with no wind. Although no precise data were at disposition in lower reduced velocity range the results obtained by the detailed analysis didn't require the investigation of new test series. Flutter derivatives were determined at angles of attack of -6°, 0° and + 6°.
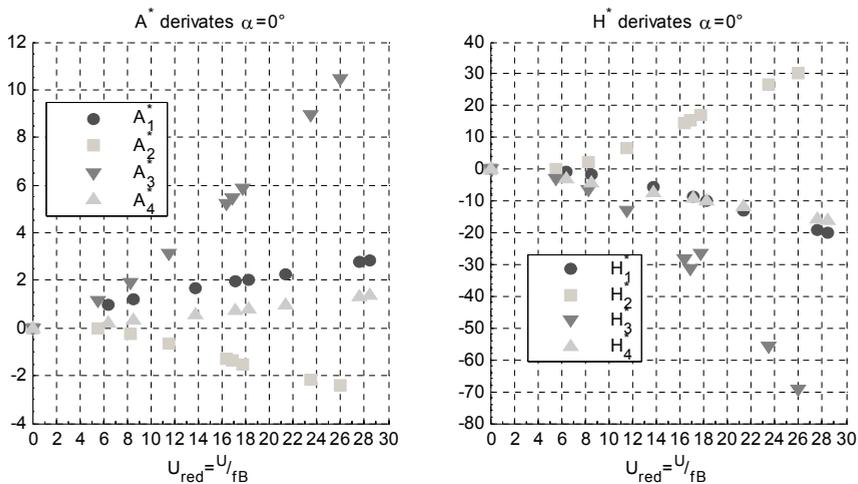

Figure 2: Flutter derivates at 0° angle of attack plotted versus reduced velocity.

The data provided by the wind tunnel tests were verified through relations between the measured data themselves, and with results of previous measures. The stability analysis was composed of two main steps. First the critical wind speed has had to be determined, at which flutter instability occurs. In the second step we had to determine the highest possible value of wind speed in the analyzed direction. The ratio of these two values represented the safety of the deck against flutter.

The methodology to determine the critical wind speed according to the flutter instability was designed on bases of the theory described by dr. Imre Kovács. The complex analysis resulted in an oscillatory motion of the two degree of freedom system with a complex frequency at a given wind speed. When the imaginary part of the calculated frequency annulated the supposed structural damping ratio, the critical value of wind speed was reached with the resulted motional state. Supposing many combinations of bending and torsional eigenfrequencies a lot of critical wind speeds resulted. The lowest of them gave the global critical wind speed which has had to be higher than the highest wind speed than can occur at the bridge's site.

Dynamic analysis of the bridge at temporary stages resulted in eigenfrequencies of 0,55 Hz, 0,78 Hz and 2,33 Hz for bending modes, and 2,47 Hz and 2,80 Hz for torsional modes. Only the first eight modes were examined. Although all six combinations of these frequencies were analyzed, only two of them could have been critical: where both bending and torsional frequencies were close to

each other. The critical wind speeds were calculated for all angles of attack which flutter derivatives were determined for. For angles of attack of 0° (horizontal attack) and -6° (an angle of attack from under the horizontal) the determined critical wind speeds were all above ~50 m/s denoting a stability of the structure against flutter with a 35,5 m/s determined maximal occurring wind speed for that region. For +6° angle of attack (wind from above the horizontal) critical conditions held at every examined wind speeds, the sum of structural and aerodynamic damping was negative for all wind speeds. The same phenomenon occurred for every bending-torsional frequency pairs at this angle of attack. This has raised the questionability of the flutter derivates for that angle of attack. Reanalyzing the model for different fictive parameters showed that the resulted solutions tended to the ones given by the other two angles of attack at high wind speeds. This showed us that unfortunately errors burden the wind tunnel test or the processing of data particularly in the range of lower reduced velocities. Due to dead lines of the work there was no possibility to elaborate new wind tunnel tests.

Our observations showed that small uncertainties in the values of flutter coefficients could result in huge distortions of critical value of wind speed. Based on the observations we can conclude that the wind tunnel investigation has to provide more precise flutter coefficients values, especially in the domain of lower reduced wind velocities, which could be achieved by maneuvering the model at higher frequencies.

CONCLUSIONS

The work presents the wind tunnel investigation and analysis to determine the flutter behavior of a new extradosed bridge to be built in Hungary. Wind tunnel investigation gave static aerodynamic coefficients and flutter derivates of the model with a scale of 1:100. The analysis was realized on a sectional model, only a two degree of freedom model of the mid-span section of the bridge was calculated in a temporary constructional cantilevered phase. The obtained critical wind speed according to flutter were in the range of 50-60 m/s. The flutter coefficients determined for an angle of attack from above the horizontal were burden with errors particularly in the range of lower reduced velocities, thus the critical velocity was undoubtedly unreliable. The critical velocity was determined by other reasoning for that angle of attack. Finally we could declare the stability of the structure against aeroelastic instability.

REFERENCES

BME Áramlástan Tanszék (2008). "Az M43 Tisza-híd szélcsatorna vizsgálata", report, *in Hungarian*.
Simiu E., Scanlan R.H. (1996). "Wind Effects on Structures: Fundamentals and Applications to Design", John Wiley & Sons, New York.

Identification of 18 Flutter Derivatives by Forced Vibration Tests – A New Experimental Rig

1st Ch. Neuhaus, 2nd S. Roesler, 3rd R. Höffer, 4th M. Hortmanns, 5th W. Zahlten

1Bergische Universität Wuppertal - neuhaus@uni-wuppertal.de - 2Bergische Universität Wuppertal - roesler@uni-wuppertal.de - 3Ruhr-Universität Bochum - ruediger.hoeffer@rub.de – 4Eusani Hortmanns Zahlten Ingenieurgesellschaft mbH - m.hortmanns@ezi-tragwerke.de - 5Bergische Universität Wuppertal - zahlten@uni-wuppertal.de

ABSTRACT

The aeroelastic stability of slender and line-like structures, e.g. wide-span bridges, is described through the critical wind speed at which aeroelastic phenomena like flutter, galloping or torsional divergence can occur. The critical wind speed, determined for a specific structure and its cross section geometry, has to be higher than wind speeds occurring at the structure's location. Therefore a description of the aeroelastic properties of the respective cross section is needed. For a flat plate an analytical solution for the aeroelastic forces during an harmonic oscillation in a potential flow exists. The description of the frequency dependent forces was derived by Theodorsen (1934). But these equations cannot be directly transferred to realistic bridge deck sections. Scanlan & Sabzewari (1969) derived a force model based on Theodorsen's equation. This model contains dimensionless frequency dependent force coefficients, so called Scanlan derivatives, which can be determined by wind tunnel experiments. The force model used in this paper is based on the work of Scanlan and co-workers (Eq. 1):

$$
\begin{aligned}
L_{se} &= q_0 B \left[KH_1^* \frac{\dot{z}}{U} + KH_2^* \frac{B\dot{\alpha}}{U} + K^2 H_3^* \alpha + K^2 H_4^* \frac{z}{B} + KH_5^* \frac{\dot{x}}{U} + K^2 H_6^* \frac{x}{B} \right] \\
M_{se} &= q_0 B^2 \left[KA_1^* \frac{\dot{z}}{U} + KA_2^* \frac{B\dot{\alpha}}{U} + K^2 A_3^* \alpha + K^2 A_4^* \frac{z}{B} + KA_5^* \frac{\dot{x}}{U} + K^2 A_6^* \frac{x}{B} \right] \\
D_{se} &= q_0 B \left[KP_1^* \frac{\dot{z}}{U} + KP_2^* \frac{B\dot{\alpha}}{U} + K^2 P_3^* \alpha + K^2 P_4^* \frac{z}{B} + KP_5^* \frac{\dot{x}}{U} + K^2 P_6^* \frac{x}{B} \right]
\end{aligned}
\tag{1}
$$

Contact person: Ch. Neuhaus, Bergische Universität Wuppertal, Pauluskirchstr. 7, 42285 Wuppertal, Germany, Phone: +49 (0)202 4394102, Fax: +49 (0)202 4394268, E-mail: neuhaus@uni-wuppertal.de

The aeroelastic force components in a two dimensional flow based on strip theory are the lift force L_{se}, the pitching moment M_{se} and the drag force D_{se}, the indices "se" stand for self excited. The forces are normalised by the dynamic pressure q_0 and the overall bridge deck width B. U is the undisturbed mean wind speed and K is the reduced frequency. The forces are dependent on the motions and the velocities of the section in its degrees of freedom. The respective coordinate system, the degrees of freedom and the positive force directions are depicted in Figure 1.
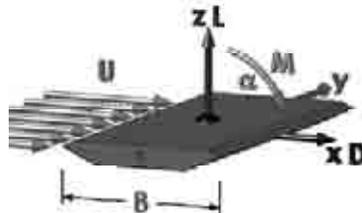
Figure 1: Coordinate system and force directions

Two main strategies are used for the experimental identification of the Scanlan derivatives: the free vibration and the forced vibration method. In free vibration tests a model of a bridge deck section is supported elastically by springs. Höffer, Lachmann & Pospicil (2008) presented an experimental setup for free vibration tests with a guide construction. Borri & Höffer (2000) used a model which was only supported by springs. Using this method the degrees of freedom can be released or restricted independently, or can be combined. The eigenfrequencies and the damping of the model can be varied. The derivatives are determined by mathematical algorithms. A discussion of respective algorithms is presented e.g. by Jakobsen & Tanaka (2003). In forced vibration tests the model is harmonically moved by a motor and an adequate mechanism in the wind tunnel. Such an approach is presented by Hortmanns (1997) with a horizontally mounted bridge deck model, and by Höffer (1997), where the model is placed vertically in the wind tunnel. These mechanisms allow harmonic movements in two degrees of freedom. A forced random excitation in two degrees of freedom is presented by Bergmann (2004). A discussion of these methods and the algorithms for the determination of the Scanlan derivatives is presented in the full paper.

A new experimental rig for forced vibration tests in 3 degrees of freedom is presently undergoing a test procedure at Ruhr-Universität Bochum (Figure 2). As a benchmark for this new setup a complete set of 18 derivatives (Eq. 1) for a NACA 0020 airfoil is determined from experiments with the new test rig.

Figure 2: New experimental rig in the wind tunnel at Ruhr-Universität Bochum

An electric motor under the wind tunnel activates a mechanism on both sides of the wind tunnel synchronously via a continuous shaft. A con rod rotates an aluminium disk on each side of the wind tunnel. This disk is eccentrically connected to a traverse. The traverse can now be guided by two rods or fixed directly onto the disk. The two rods are mounted on an aluminium ring in order to adjust the angle of translation of the model. A measurement device for forces is tightened on the traverse. The possible main degrees of freedom are shown in Figure 3 (a-c). With this mechanism the translation can be realised under an arbitrary angle α, so the angle of attack of the oncoming wind is variable in a body fixed coordinate system (Figure 3d) and while rotating the model in its bearing in a wind fixed coordinate system. The movement in a body fixed coordinate system simulates the correct movement of the full scale structure under an angle of attack of the oncoming wind. This is one of the main innovations of the new test rig. The model is directly fixed on the force balance to reduce the ratio of inertia forces to wind forces. Consequently the inertia forces of the most moving parts are not included in the measured data. The force balances measure two vertical and one horizontal force component on each side of the wind tunnel by adapted strain gages. The pitching moment and the lift force are calculated from vertical force components. It is also possible to measure transient motions in all degrees of freedom in order to identify indicial functions as presented by Neuhaus & Zahlten (2008).
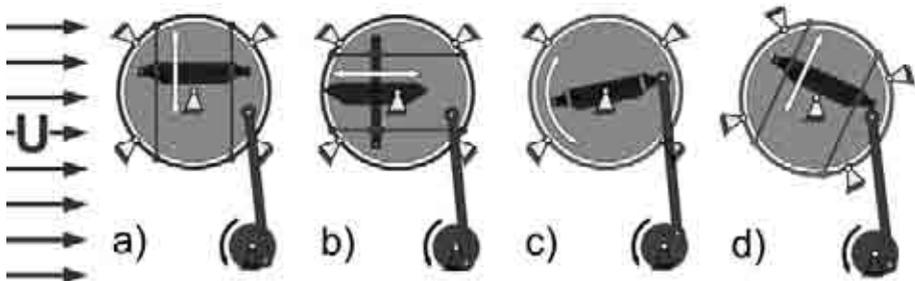

Figure 3: Degrees of freedom for forced vibration experiments

Oscillation frequencies up to 7 Hz can be realised. The maximum amplitude amounts ± 7.5 cm or ± 15 °. A combination of oscillation frequency f, model mass M and amplitude A is limited by the maximum force acceptance of the force balances. This limitation is needed for ensuring sufficient sensitivity of the force balance for very small wind forces. The overall resulting inertia forces have to be limited by Equation 2. Two electrooptical laser sensors measure the translations of the model on both sides of the wind tunnel. The rotation angles for respective experiments are calculated from translation measurements.

$$(M + 2kg) \cdot A \cdot (2 \cdot \pi \cdot f)^2 \leq 500N \tag{2}$$

To identify the aeroelastic forces in the presence of large inertia forces one test must consist of a pair of measurements, with and without wind. To overcome any interferences in the measured signals they are first analysed by Fast-Fourier-Transform to get an estimate of amplitude, phase and frequency. In a second step a nonlinear least square fit to a pure sinusoidal oscillation is performed, this provides the amplitudes of the force and the motion signals. Further the phase difference between the force and the motion is determined for all three force signals. The derivatives can be derived from this data by expressing each pair of amplitude and phase as a complex number and then calculating the difference between the two measurements. A complete presentation of the algorithm, c.f. Roesler (2008), will be given in the full paper.

The models pass through the whole wind tunnel and have a length of 1780 mm. The airfoil model has an overall width of 465 mm and a weight of 2.8 kg inclusive an aluminium axis. It is built from polystyrene foam, the axis is placed in the center of gravity in a distance of 200 mm from the airfoil's nose. The first eigenfrequency of the simply supported model mounted in the experimental rig is

21.1 Hz. Experiments are made with an amplitude of 1.0 cm for horizontal and vertical displacements and 2.3° for rotation. The lowest reduced velocity u_{red} was chosen to 1.0. Examples of derivatives are shown in Figure 4. For comparison the analytical solution of the flat plate of Theodorsen (1934) is included in the figure as a straight bold line. For the investigated airfoil geometry Chowdhury & Sarkar (2003) determined a complete set of 18 derivatives by free vibration experiments. The data, marked with "+", shown in Figure 4 are taken from this reference.
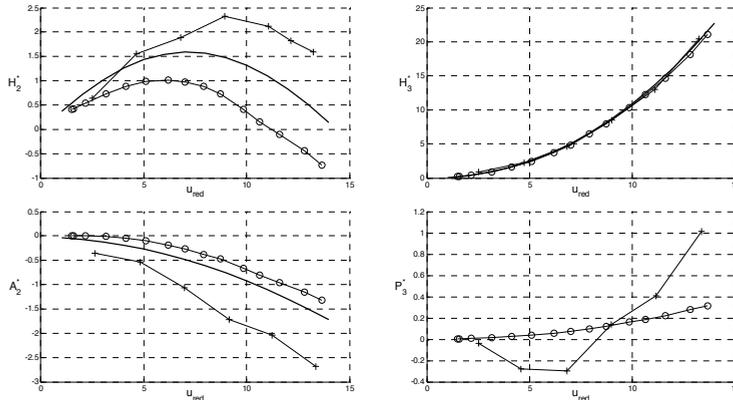
Figure 4: Examples of aeroelastic derivatives for a NACA 0020 airfoil ("-" Theodorsen's analytical solution, "+" free vibration measurement of Chowdhury and Sarkar (2003), "o" forced vibration measurement results)

A good agreement to the references can be observed. Experiments for a streamlined and a bluff bridge deck section are undertaken at present, results will be presented in the full paper. The importance of the horizontal degree of freedom for the aeroelastic stability of large bridges will be examined in further studies.

REFERENCES

Theodorsen T., (1934). ''General Theory of Aerodynamic Instability and the Mechanism of Flutter'', NACA Report No.496.

Scanlan R. H., Sabzewari A. (1969). ''Experimental Aerodynamic Coefficients in the Analytical Study of Suspension Bridge Flutter'', Journal of Mechanical Engineering and Science, vol 11, no. 3 1969.

Höffer, R., Lachmann, S., Pospíšil, S., (2008), "Transition of Fow Induced Bridge Girder Oscillations from Resonance to Critical and Post-Critical Behaviour" Proceedings Flow Induced Vibrations, No. 286,Prague 2008

Borri, C., Höffer, R., (2000), "Aeroelastic Wind Forces on Flexible Bridge Girders", MECCANICA vol. 35, 1-15, 2000

Jakobsen, J.B., Tanaka, H., (2003), "Modelling Uncertainties in Prediction of Aeroelastic Bridge Behaviour", J. Wind Eng. Ind. Aerodyn. 91, 1485 – 1498, 2003

Hortmanns, M., (1997), "Zur Identifikation und Berücksichtigung nichtlinearer aeroelastischer Effekte", Ph.D. thesis, Shaker Verlag, Aachen, 1997

Höffer, R., (1997), "Stationäre und instationäre Modelle zur Zeitbereichssimulation von Windkräften an linienförmigen Bauwerken", Ph.D. thesis, Ruhr-Universität-Bochum, 1997

Bergmann, D., (2004), ''Experimentelle Ermittlung der instationären aerodynamischen Eigenschaften von Brückenprofilen im Wasserkanal'', Ph.D. thesis, Institut für Aerodynamik und Gasdynamik, Universität Stuttgart, 2004

Neuhaus, Ch., Zahlten, W., (2008), „On the Identification of Indicial Aerodynamic Functions by a Recursive Filter Approximation", Proceedings EURODYN 2008, E 111, Southampton 2008

Roesler, S., (2008), Entwicklung eines Berechnungswerkzeugs zum Nachweis der aeroelastischen Stabilität weitgespannter Brücken, diploma thesis, online publication, Bergische Universität Wuppertal, 2008

Chowdhury A. G., Sarkar P. P., (2003). ''A New Technique for Identification of Eighteen Flutter Derivatives Using a Three-Degree-of-Freedom Section Model'', Engineering Structures, Vol 25, 2003.

Wake visualization and pressure field analysis on an oscillating cylinder

S. Malavasi[1], R. Corretto[1], M. Belloli[2], S. Giappino[2], S. Muggiasca[2]

[1]Dip. DIIAR, Politecnico di Milano – stefano.malavasi@polimi.it –roberto.corretto@mail.polimi.it
Piazza Leonardo da Vinci, 32 – 20133 Milano – [2]Dip. Meccanica, Politecnico di Milano –
marco.belloli@polimi.it - stefano.giappino@polimi.it – sara.muggiasca@polimi – Via La Masa 1 –
20156 Milano

Keywords: VIV, flow visualization, circular cylinder, pressure measurements

ABSTRACT

Vortex induced vibrations are a key feature to consider in designing slender structures with circular section, because of fatigue damage that they could produce. This typology of structures has several engineering applications as overhead transmission line, stays of cable-stayed bridges or hangers of suspension bridges: over the last decades many experimental activities have been performed to study the aerodynamic behavior of bluff bodies, with particular reference to circular section.

An extensive experimental campaign has been performed at Politecnico di Milano wind tunnel to study the vortex induced vibration of a rigid cylinder in the subcritical Reynolds range ($Re \cong 5 \cdot 10^4$) with the aim of investigating its response in terms of motion parameters and also in terms of instantaneous pressure distribution on the cylinder surface (Zasso et al. (2008), Zasso et al. (2006)). The simultaneous measurement of these quantities has permitted to correlate the dynamic behavior and the fluid-dynamic states that the cylinder encounters when the vortex shedding occurs.

Further experimental tests have been performed completing the set up with an image acquisition device to have at the same time information about the cylinder displacements, the aerodynamic forces, the pressure field and the wake structures.

The subject of the present study is a rigid cylinder (diameter *D=0.2*; length *L=2 m*) oscillating in cross flow in the lock-in region. The experimental set-up is shown in Figure 1. The very large test section (14x4m) allows for negligible blockage effects with smooth flow conditions ($I_T \cong 2\%$) and wind speed in the range *3.2 < U < 5.3 m/s*. No blockage effects together with 2 and plates placed on the extremities of the model permit to realize 2D flow conditions. The rigid cylinder has been suspended by means of tensioned cables allowing separation between horizontal, torsional and vertical modes, so that it was possible to study the vortex induced oscillations of the cylinder vibrating in cross wind direction at a frequency *f_s=3.2 Hz*.

High frequency pressure scanners have been installed inside the model to map the instantaneous pressure field on 64 pressure taps, while the oscillation was acquired by two accelerometers.

Contact person: S. Muggiasca, Politecnico di Milano, Via La Masa 1, +390223998072, FAX: +390223998081.
E-mail sara.muggiasca@polimi.it

Figure 1: The instrumented rigid cylinder oscillating in cross flow direction in Politecnico di Milano Wind Tunnel

The pressure taps have been placed along two separated sections (Ring A and Ring B) and aerodynamic forces acting on the sections have been defined integrating pressure data.

Tests have been carried out at low level of structural damping ($4 \cdot 10^{-4} < \xi_s < 13 \cdot 10^{-4}$), resulting in a low Scruton number range $Sc < 1$. It's worth remember that, being the tests performed in air, the mass ratio parameter m^* shows very high values ($m^* = 145$) resulting in negligible flow added mass effects.

The cylinder behavior has been studied evaluating its steady state response in the lock in region: steady state conditions have been acquired at constant wind speed and each of these points was reached from the previous one changing by small steps the wind velocity. Figure 2, reproduced from Williamson & Roshko (1988), is given a plot of the state of the art knowledge related to the different states observed in the vortex street wake structure, showing superimposed the steady oscillations response curve obtained from these tests.
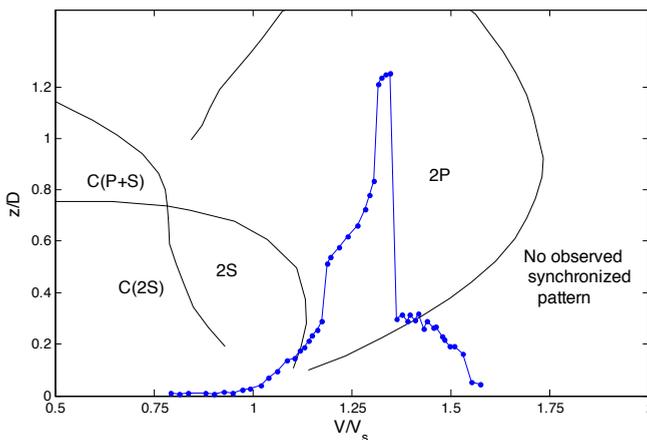
Figure 2: Williamson & Roshko (1988) map of wake modes with superimposed steady state oscillating response

The characterization of the vortex shedding was provided using a time resolved PIV technique (SPIV, Stripe Particle Image Velocimetry) which differs by conventional PIV applications for both the acquisition system and the velocity detections methodology. 2D velocity fields were obtained measuring the bi-dimensional trajectories of seeding particles in a defined time interval. This is possible by filming the seeding flow on the measurement plane and by using a delayed exposure time. The length of each trajectory is due to the corresponding instantaneous local flow velocity and to the

shutter time of the video-camera. A blob analysis algorithm identifies each particle trajectory signed on each single image and measures its geometric characteristics. These data allow to calculate the length, the orientation and the location of each trajectory. The direction ambiguity was resolved by considering the velocity information (module, orientation and location) available at two consecutive instant of time.

The image acquisition rig was composed by two optical fibre line-converters with a 150W light source, a seeding apparatus and a progressive scan camera drove by a personal computer.

A soap bubble generator allowed as to extend the range of investigable phenomenon by the original SPIV system, developed for water channel application (Malavasi et al. 2004; Malavasi and Negri 2008).

In order to address both the flow velocity and the position of the oscillating cylinder, we use a reference marker on the cylinder to provide, within the same frame, the measurement of the flow velocity and the position of the obstacle (Mirauda et al.2007). This method allows high resolution of the obstacle displacement as prove the comparison between the measurement via image analysis and accelerometer.

The vortex shedding reconstruction was provided by a phase-averaged reconstruction of the flow velocity maps, using the cylinder motion as reference signal.

Figure 3 shows an example of comparison between flow maps and pressure distribution on the cylinder in different positions of the oscillating period for $V/V_s=1.3$.
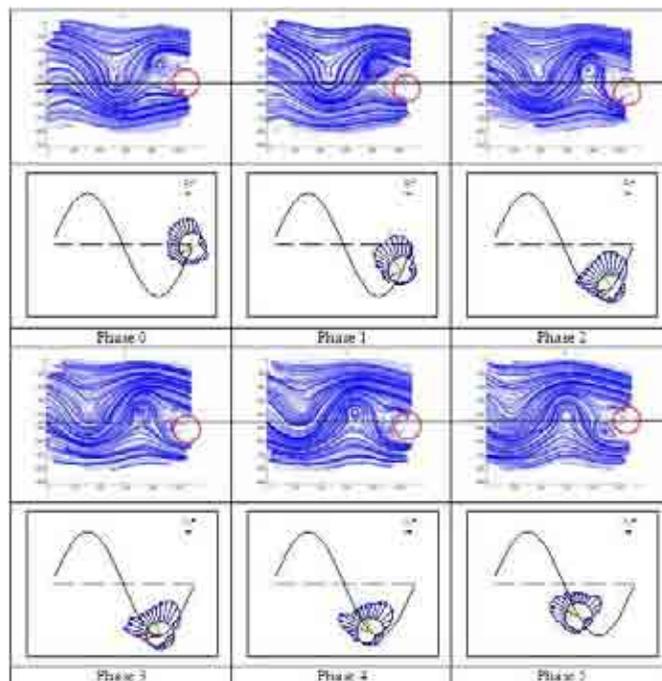

Figure 3: Comparison between flow maps and pressure distribution for different cylinder position at $V/V_s=1.3$

REFERENCES

Malavasi S., Franzetti S., Blois G. (2004) "PIV Investigation of Flow Around Submerged River Bridge", River Flow,

Napoli (Italy) June 23-25.

Malavasi S. and Negri M. (2008), "Analysis of non-stationary flow around a rectangular cylinder", Sixth International Colloquium on: Bluff Body Aerodynamics & Applications. Milano 20-24 July.

Mirauda D., Malavasi S., Greco M., Volpe Plantamura A. (2007), "Effects of free surface flow on a tethered sphere" 9th Intl. Symp. Fluid Control, Measurement and Visualization, Flucome 2007, Paper 151, Tallahassee, FL.

Williamson C. H. K., Roshko A. (1988) "Vortex formation in the wake of an oscillating cylinder", J. Fluids Struct. 2, 355-381.

Zasso A., Belloli M., Giappino S., Muggiasca S. (2008). "Pressure field analysis on oscillating circular cylinder", Journal of Fluids and Structures 24 628–650

Zasso A., Belloli M., Giappino S., Muggiasca S. (2006). "On the Pressure and Force Field on a Circular Cylinder Oscillating in the Lock-In Region at Sub-Critical Reynolds Number" Proc. of PVP2006-ICPVT-11, ASME Pressure Vessels and Piping Division Conference, Vancouver, Canada (BC), July 23-27, 2006.

ROOFING SYSTEMS AND CLADDING

3D numerical simulations and full scale measurements of snow depositions on curved roofs

T. K. Thiis, J. Potac , J. F. Ramberg

Norwegian University of Life Sciences, Department of Mathematical Sciences and Technology,
thomas.thiis@umb.no

Keywords: snow, deposition, CFD, curved roof.

ABSTRACT

Two phase CFD simulations with transient changing snow surface have been used to simulate the snow deposition on a large curved roof. The results from the simulations have been compared with full scale measurement and it is revealed how important the accuracy of the wind flow simulation is for a successful outcome in the prediction of snow depositions. As small changes in the wind flow field will alter the deposition and erosion rates and regions, the results also underlines the importance of considering the transient development of the snow drift when determining snow loads in different climates.

METHODS

Field measurements

The investigated building has a roof formed as a quarter of a cylinder with a radius of 60.7 meters. The curved roof is met by a flat roof on each side, where the slope of the arch reaches 45 °, making the arch span about 85 meters. The building's overall dimensions are 123 meters long, 106 meters wide and 25 meters tall. A total of twenty smoke hatches are placed 11 meters from the top of the curved roof, ten on each side. These hatches are 0.3 meters tall, 2 meters long and 1 meter wide. The building is located in Oslo in an area where the characteristic ground snow load with a 50 year return period is 3.5 kN/m². As the building site can be expected to have a normal exposure to the wind, the exposure coefficient, according to Eurocode EN 1991-1-3 9 (July 2003), has the value 1.0.

The snow depositions on the roof were measured twice, in February 2007 and in January 2008. The snow depth was measured in several sections perpendicular to the top of the roof and samples of the density was taken from different places in the snowdrift.

Contact person: T. K. Thiis, Norwegian University of Life Science, Department of Mathematical Sciences and Technology, P.O. Box 5003 IMT, 1432 Ås, phone +4764965444, fax +4764965401.
E-mail thomas.thiis@umb.no

According to a local meteorological weather station placed two hundred meters north of the building, the governing wind direction during snow fall is between 60 ° and 80 ° with governing wind speeds during snowfall between 4 and 6 m/s. A wind rose from this weather station is presented in figure 1, as well as a three dimensional CAD model of the building. Note that the building model to the right is not oriented correctly according to the wind rose.
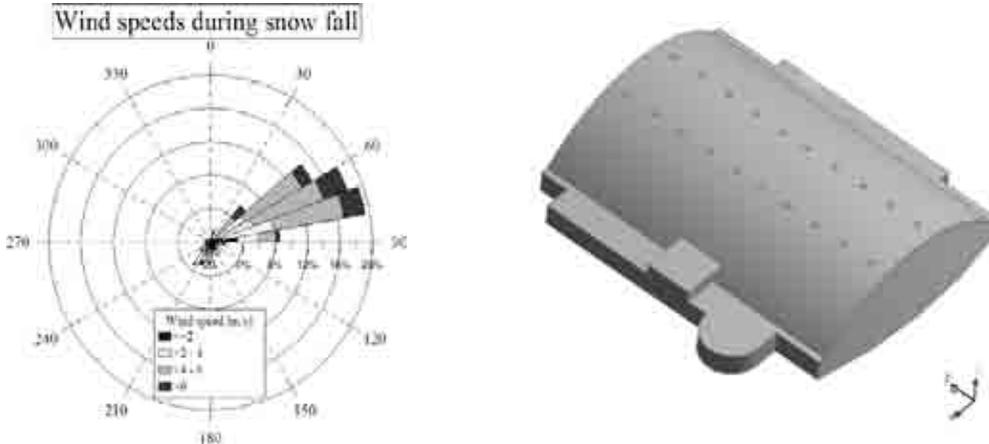

Figure 1: Wind direction and velocity during cold precipitation at the building site (left); 3D digital model of the building (right).

When the wind direction is 80 °, the wind approaches perpendicular to the long side of the building. The contribution of snow drifting from the upwind areas of the building can be ignored due to the height of the investigated building and the surrounding topography. Further, the climate at the site is relatively mild and with low wind speeds. Therefore, the driving force forming the drifts on the leeward side is believed to be the wind during snow fall and the effect of snow particles being relocated between snowfalls is believed to be of minor importance.

Numerical simulations

To simulate the wind field and snow accumulation, the general purpose finite volume CFD code ANSYS CFX 11 was applied. The simulations were three dimensional with a transient developing snow surface. The model of the building was placed in a domain measuring 150 x 500 meters. The CFD code solves the incompressible, time averaged Navier-Stokes equations, using the k-ε RNG turbulence model to close the equations. This turbulence model includes terms for dissipation rate development that improves the accuracy compared to the standard k-ε turbulence model. It is widely used in simulations of wind around buildings and it is capable of producing realistic results, Kim et al (2000). The two phase fluid flow is solved with the Euler-Euler approach. Both the air and the snow phase possess its own flow field and the fluids interact via the drag force.

The roof in consideration is probably not affected by redistributed snow. The wind conditions and the fetch at the site do not imply that snow is moved from the ground to the roof. The simulation boundary conditions are therefore assumed to be similar to precipitating snow during low wind velocity. The wind velocity is set to 5 m/s at 10 meters above the surface. The vertical wind velocity distribution is assumed as logarithmic function.

To simulate a transient development of the snow surface the mesh is deformed after each time step by applying the erosion flux and the deposition flux given by Naaim et al (1981). Finally, the change in snow surface level is calculated and applied as a mesh deformation.

In the present analysis the snow particles are simulated with a density of 50 kg/m³. However, the density of the snowpack is set to 150 kg/m³. The density of the snow particles is described as "loose fresh dry snow" by Kind (1981).

RESULTS

Field measurements

Measurements were carried out in February 2007 and in January 2008, hereby referred to as F07 and J08. For both measurements the snow had accumulated into a one side snowdrift at the leeward side parallel to the top of the building. At F07 the maximum snow depth was 0.73 cm measured 29 meters from the ridge of the roof, equivalent to a roof slope of 29 ° and at J08 the maximum depth was 0.35 cm measured 22 meters from the top, equal to a roof slope of 21 °. A plot comparing the measured snow depths at the same section at F07 and J08 is shown in Figure 2. The x axis represents the distance from the ridge projected to horizontal plane.
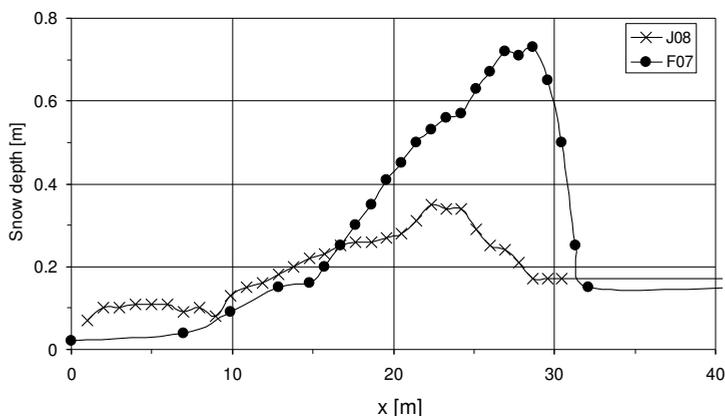
Figure 2: Snow depth on the roof of Vallhall arena measured at 27.02.07 (F07) and at 07.01.08 (J08).

At F07 the maximum snow load on the roof was 1.5 kN/m², and with a mean ground snow load of only 0.33 kN/m² the appearing shape coefficient was as high as 4.5 at the peak. For comparison, the design load in EN 1991-1-3 should be considered as two sided with a triangular shape coefficient with a peak value equal to two on the leeward side and one on the windward side (a recommended limited upper value for the shape coefficient).

The snow on the roof at J08 was a result of a single snow fall lasting about three days with around 23 mm of water equivalent precipitation. Prior to this snow fall there was no snow neither on the roof nor the ground. The snow measured at F07 was on the other hand a result of about a month of accumulation with partial melting in between. The last snow fall before the time of measurements was lasting about a week with about 18 mm of water equivalent precipitation.

Numerical simulation

Figure 3 shows a contour map based on the measurements from F07, and 3D simulation snow surface and wind stream lines. The location of source data for Figure 2 is labeled as F07.

The numerical simulations reproduce the overall snow distribution reasonably well. Also the transient change in shape of the snow drift is well simulated. Further work will include scaling of the transient simulations according to measurements. To do this work additional measurements are required.
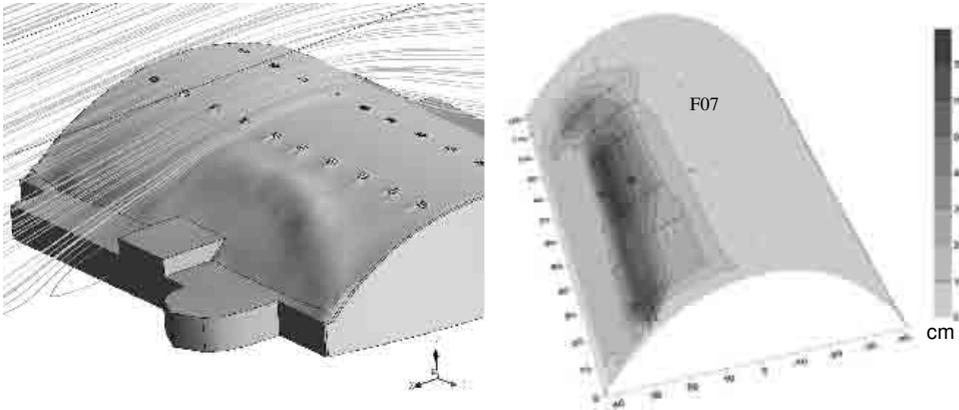

Figure 3: Snow depth measured at 27.02.07 (right). 3D simulation snow surface and wind stream lines (left).

REFERENCES

EN 1991-1-3. (July 2003). Eurocode 1, Action on structures - Part 1-3: General actions – Snow Loads.
Kim H. G., Patel V. C. (2000). "Test of turbulence models for wind flow over terrain with separation and recirculation", Boundary layer meteorology, 64 (1), 5-21.
Kind R. J. (1981). *Snow drifting, Handbook of snow*. Pergamon Press, Canada, ISBN 0-08-025375-X, 338-359.
Naaim M., Naaim-Bouvet F., Martinez H. (1998). "Numerical simulation of drifting snow: erosion and deposition models", Annals of Glaciology 26, 191-196.

Wind pressure loading cycles for evaluating the wind resistance of mechanically attached waterproofing systems on flat roofs

Y. Uematsu[1], S. Nakamura[2], M. Sera[3]

[1]*Tohoku University, yu@venus.str.archi.tohoku.ac.jp*

[2]*Sumitomo Bakelite Co. Ltd., nakamura-shuuji@sumibe.co.jp*

[3]*Sumitomo Bakelite Co. Ltd., sera-masaya@sumibe.co.jp*

Keywords: waterproofing system, flat roof, fatigue, loading cycle, wind tunnel experiment.

ABSTRACT

Recently, mechanically attached single-ply roofing has become popular for flat-roofed buildings in Japan. In such roofing systems, the roof membrane is either welded or glued to gridded circular disks that are mechanically fastened to the roof deck by screws. The distance between the disks ranges from 0.45 m to 0.6 m, depending on the location. High suctions are induced by conical vortices in the corner and edge zones of flat roofs in oblique winds, causing strong stresses on the attached parts. Fluctuating pressures may induce fatigue damage to the attached parts. When designing such roofing systems, it is important to evaluate the dynamic effects of wind loading appropriately. Furthermore, flat roofs generally have parapets, which significantly affect the dynamic wind pressures. Many researchers, e.g. Kopp et al. (2005), studied the effect of parapets on the peak pressure coefficients on flat roofs. However, the effect on the fatigue-related characteristics of wind pressures has not been investigated so far, to the authors' best knowledge.

The present paper describes the characteristics of fluctuating wind pressures on flat roofs with parapets, based on a series of wind tunnel experiments. A discussion is made of the wind pressure loading cycles for evaluating the wind resistance of the mechanically-attached roofing systems. A wind pressure loading cycle model, named 'TS-WiLMARS' (Tohoku University and Sumitomo Bakelite –Wind Load Model for Mechanically Attached Roofing Systems), is proposed.

───────────────────
  Contact person: Y. Uematsu, Department of Architecture and Building Science, Tohoku University, Sendai 980-8579, Japan, TEL & FAX: +81-22-795-7875, e-mail: yu@venus.str.archi.tohoku.ac.jp

(1) Wind tunnel experiment

The subject of the study is a flat-roofed residential house with parapets built in suburban areas. Figure 1(a) and Table 1 show the model buildings. The geometric scale of the wind-tunnel models is assumed 1:100. The parapet is represented by attaching thin plates on the walls. Figure 1(b) shows the location of pressure taps. The wind tunnel flow is a turbulent boundary layer with a power low exponent of $\alpha \approx 0.24$ and a roughness length of $z_0 \approx 1.5$ mm. The design wind speed U_H at eave height H is determined from the AIJ Recommendations for Loads on Buildings (2004), assuming that the basic wind speed U_0 is 38 m/s and the terrain category is III. The velocity scale of the wind tunnel flow is approximately 1:2.7, which results in a time scale of approximately 1:73.

The wind pressures at the pressure taps are sampled at a rate of 400 Hz on each channel for a period of about 330 sec, from which 18 sets of time-history of pressures are obtained; each data set corresponds to 10 min in full scale. The statistics of wind pressures are computed by applying an ensemble average to the results of these 18 runs. The pressure coefficient C_p is defined in terms of the velocity pressure q_H at eave height. The wind direction θ is varied from 0° to 45° for square models (Models 1 – 3 and 5) and from 0° to 90° for rectangular models (Models 4 and 6) with an increment of 15°. The instrumented area is divided into three zones, R1 to R3, as shown in Figure 1(b).

| (a) Geometry of model buildings and notation | (b) Pressure-tap location and definition of roof zones and wind direction |

Figure 1: Model buildings.

Table 1: Building dimensions in full scale

Model	B (m)	D (m)	H (m)	h_p (cm)	t_p (cm)
1	10	10	5	0, 10, 30, 60, 120	3
2	10	10	10	0, 10, 30, 60, 120	3
3	10	10	15	0, 10, 30, 60, 120	3
4	20	10	10	0, 10, 30, 60, 120	3
5	10	10	10	10, 30, 120	15
6	20	10	10	10, 30, 120	15

(2) Results and discussion

1) Minimum peak pressure coefficients

Figure 2 shows the effect of h_p on the minimum peak pressure coefficients C_{P_peak} irrespective of wind direction in Zones R1 and R2. The value of C_{P_peak} decreases in magnitude monotonically with an increase in h_p. This feature is contradictory to the results of some previous papers, e.g. Lythe and Surry (1983) and Kopp et al. (2005), which showed that low parapets on low buildings increased the magnitude of C_{P_peak} in the corner region. However, Lythe and Surry (1983) also showed that higher parapets on low buildings and any parapets on high buildings decreased the magnitude of C_{P_peak}. Kind (1988) indicated that the worst suctions in the corner region decreased monotonically with increasing h_p in the same manner as in our experiment. The worst peak suction occurs very close to

the roof corner in oblique winds. Therefore, a very high density of pressure taps is required to capture the real worst peak suction. Furthermore, the value seems sensitive to many factors, such as building shape and details, turbulence of flow and wind direction. The density of pressure taps in our models is not high enough to capture the real worst peak suction. However, the values of C_{p_peak} are consistent with those reported in the previous studies.
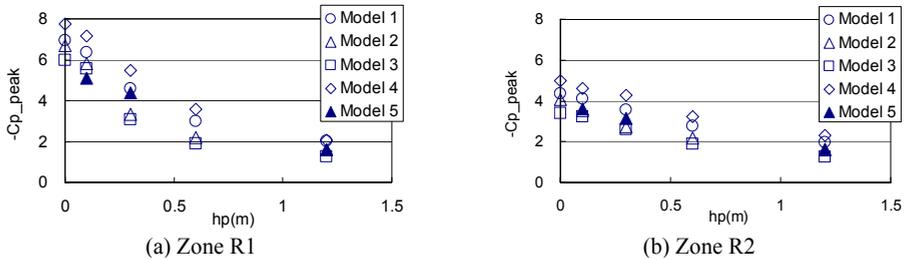
(a) Zone R1   (b) Zone R2
Figure 2: Effect of parapet height h_p and thickness t_p on C_{p_peak} in Zones R1 and R2.

2) Wind pressure loading cycles

First, the pressure tap subjected to the worst peak suction, or C_{p_peak} in each zone is detected. Then, the pressure loading cycles in a full-scale period of 10 min are counted by using the rainflow count method. In the analysis, a low-pass filter is applied to the time history of pressures. The cut-off frequency f_c of the low pass filter is determined based on the root coherence of pressure fluctuations in each zone as well as on the tributary area A_c of each fixation, approximately 0.25 m² (see Furuichi et al., 2007). The rainflow count method can identify cycles as closed hysteresis loops and provide a mean and a range for each cycle, resulting in a three-dimensional cycle histogram that shows load cycle distribution over both cycle range A and cycle mean level M.

Figure 3 shows sample results on the cycle histograms for a corner tap when $\theta = 30°$. In the figure, the number N of cycles for given ranges of A and M in each cell of the matrix is normalized by the total number of cycles (N_{total}) and represented by F_r. The value of A is normalized by $|C_{p\_peak}|$, while that of M by C_{p_peak}; they are represented by A_r and M_r, respectively. The results for all cases are computed. From these results, it is found that the cycle histogram is not affected by B/D and t_p, significantly. Furthermore, the effect of H is also small. On the other hand, the parapet height h_p and wind direction θ affect the cycle histogram significantly.

3) Models of pressure loading cycles for laboratory testing

Considering the above-mentioned features of pressure cycle histograms, the mean load cycle histogram is computed; that is, the mean value of $F_r(A_r, M_r)$ for each matrix cell is computed by averaging the values of $F_r(A_r, M_r)$ for two kinds of B/D ratios, three kinds of H values and two kinds of t_p values. Then, a new load cycle matrix is formulated by selecting the maximum value among all wind directions for each matrix cell. The results for $h_p = 0$ m and 0.1 m are similar to each other, and those for $h_p = 0.6$ m and 1.2 m are also similar to each other. Thus, the parapet height h_p is categorized into three groups; i.e. $h_p \leq 0.1$m, $h_p \approx 0.3$m and $h_p \geq 0.6$m. Finally, the mean load cycle histogram for each category of h_p is computed.

For development of a laboratory procedure for testing full-scale roofing assemblies, the data of the load cycle matrix is recognized into several pressure zones with respective number of cycles. Figure 4 shows models of pressure loading cycles for Zone R1. In the figure, the ordinate represents the pressure normalized by the minimum peak suction (= $q_H C_{p\_peak}$). Each model consists of six steps. The numbers in the figure, such as 1,070, represent the number of cycles. Similar models are obtained for the other zones. However, it may be more convenient if a model can be applied to all three zones. Considering the practical values of pressures applied to each zone and the accumulated fatigue damage estimated from the Miner's rule, we found that the pressure loading cycles for Zone

R1 could be applied to all zones, as shown in Figure 4. In the case of $h_p \leq 0.1$m (Figure 4(a)), for example, if the specimen has passed the first step, the roofing system can be used for Zone R3. Similarly, if the specimen has passed the second step, it can be used for Zone R2. Finally, if the specimen has passed all steps, it can be used for Zone R1.
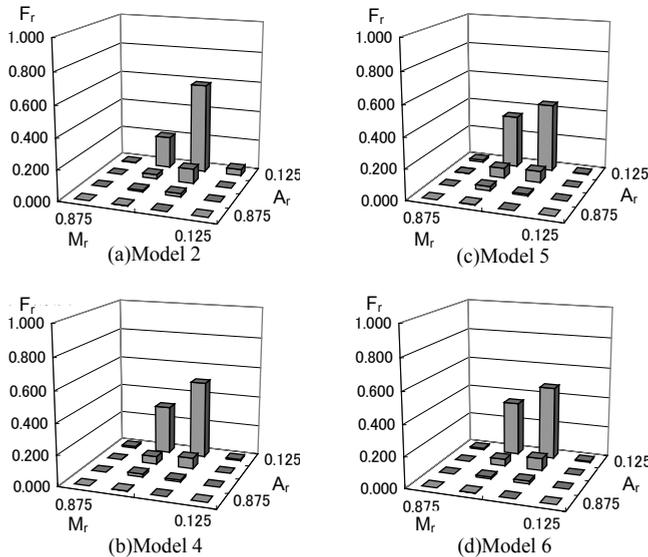
Figure 3: Three-dimensional cycle histogram that shows load cycle distribution over both cycle ranges A and cycle mean levels M ($h_p = 0.1$ m , $\theta = 30^o$, Zone 1)
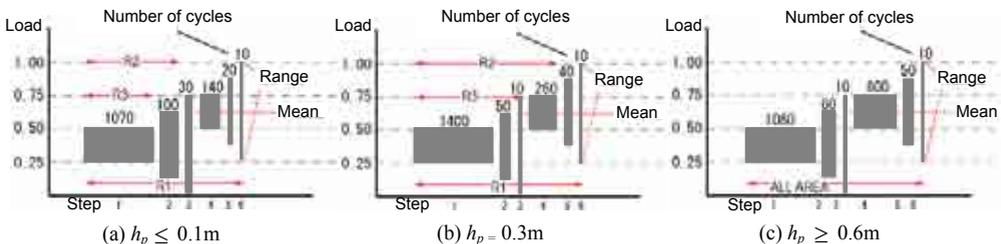
Figure 4: Pressure loading cycles for laboratory testing for a period of 10 mim

REFERENCES

Architectural Institute of Japan (2004). *Recommendations for Loads on Buildings*.

Furuichi K., Uematsu, Y., Nakamura, S. Sera, M. (2005). "Evaluation of dynamic wind loads for mechanically-attached waterproofing systems", Proc. 19th National Symposium on Wind Engineering, Tokyo, Japan, 471-476. (in Japanese)

Kind, R.J. (1988). "Worst suctions near edges of flat rooftops with parapets", Journal of Wind Engineering and Industrial Aerodynamics, 31, 251-264.

Kopp G. A. , Surry, D., Mans C. (2005). "Wind effects of parapets on low buildings: Part 1. Basic aerodynamics and local loads", Journal of Wind Engineering and Industrial Aerodynamics, 93, 817-841.

Lythe, G., Surry, D. (1983). "Wind loading of flat roofs with and without parapets", Journal of Wind Engineering and Industrial Aerodynamics, 11, 75-94.

Design wind loads for cladding elements

N. Aylanc, M. Kasperski

Ruhr-University Bochum – Department of Civil and Environmental Engineering Sciences
Naim.Aylanc@rub.de – Michael.Kasperski@rub.de

Keywords: cladding element, wind tunnel experiment, design wind load, local loads, structural responses

ABSTRACT

The aim of this study is a refined analysis of the wind load on trapezoidal sheeting. To allow more economic design, structural responses for continuous beam systems are calculated based on simultaneously measured surface pressures. Additionally, a comprehensive comparison to the Eurocode specifications is presented.

INTRODUCTION

The Eurocode for wind actions specifies two values for surface pressures, a first value referring to an area of 1 m² or smaller and a second value referring to an area of 10 m² or larger. For intermediate values, a logarithmic interpolation is recommended. Especially for trapezoidal sheeting the question arises, if a refined analysis of the wind load enables a more economic design. These cladding elements usually are designed as continuous beam with two or three fields. Then, part of the loading will lead to favourable load effects.

Contact person: M. Kasperski, Ruhr-University Bochum – Department of Civil and Environmental Engineering Sciences, Building IA 4/32, Tel: +49 234 32 24148, FAX: +49 234 32 14317
E-mail Michael.Kasperski@rub.de

WIND TUNNEL EXPERIMENTS

The wind tunnel experiments have been performed in the wind tunnel of the Department of Civil and Environmental Engineering Sciences at the Ruhr-University Bochum. In figure 1, the mean wind speed profile and the profile of the turbulence of the along-wind fluctuations are compared to the target values as specified in ESDU [1] using a length of 1:400. While the mean wind speed profile of the wind tunnel experiments is in good agreement with the targets specified in ESDU, the turbulence intensity is a bit too high for heights above 20 m.
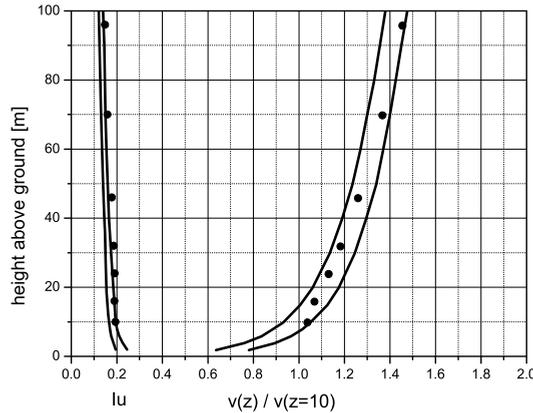
Figure 1: Comparison of the boundary layer flow in the wind tunnel experiment to the ESDU-model for flat, open country

The wind tunnel model represents a simple block-shaped building and is shown in figure 2. Altogether, the simultaneous surface pressures are monitored for four cross sections, which are edge, mid-span, the quarter and the eight positions. Along each cross section, 23 surface pressures are measured. The flow direction is varied with a step width of 10°.
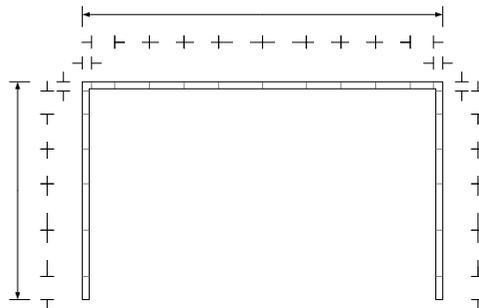
Figure 2: Wind tunnel model and position of the measured cross sections

For each cross section and for each flow direction a set of independent runs is obtained, corresponding to 100 runs of 10 minute duration in full scale.

STRUCTURAL ANALYSIS

Beside the local surface pressures, the study concentrates on the structural responses of the trapezoidal sheeting elements. Structural responses are obtained by convolving the instantaneous pressure distribution with the respective influence line. The influence lines of some selected responses are shown in figure 3 and 4 on the example of a continuous beam with three equal fields.
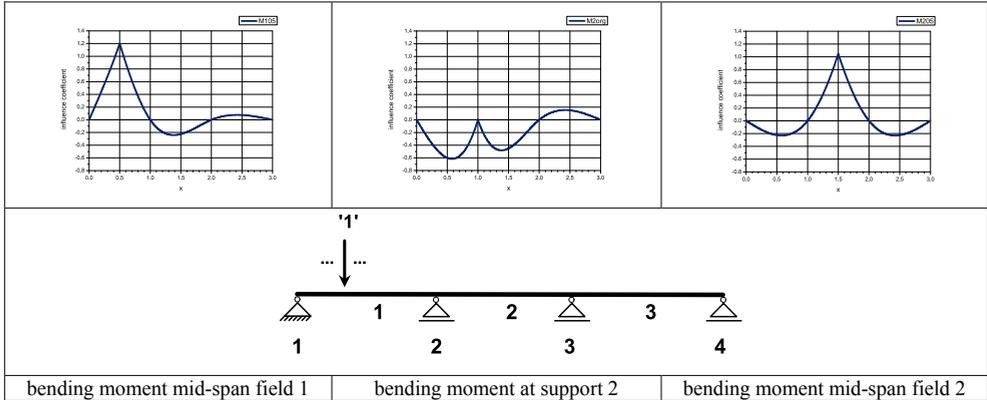
Figure 3: Influence lines for selected bending moments
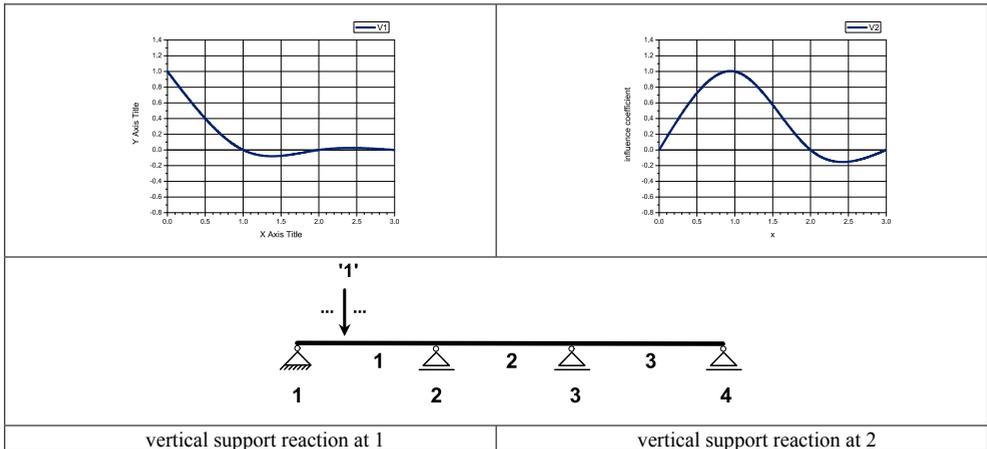
Figure 4: Influence lines for selected support reactions

All influence lines have in common that there is a change of sign along the axis of the continuous beam. For highly correlated local pressures this may lead to considerable favourable effects.

STATISTICAL ANALYSIS

The time series of the simultaneous surface pressures are weighted in each time step with the influence lines of the structural responses, thus leading to a new set of time series for the structural responses. In the scope of the further statistical analysis, for each variable (local pressure or structural

response) the maximum and the minimum value in each single run are sampled. For each set of 100 sampled extremes, the parameters of a type I extreme value distribution are estimated based on a least square fit in the corresponding probability paper. The type I distribution is given as follows:

$$F(x) = \exp\left[-\exp\left(-\left[\gamma + \frac{\pi}{\sqrt{6}} \cdot \frac{x - m}{\sigma} \right] \right) \right] \tag{1}$$

m - mean value of x
σ - rms value of x
γ - Euler constant = 0.5772

As design value, the 80% fractile value with reference to one hour is used. The respective values for the local pressures are compared to the specified values in the Eurocode.

EXTREME STRUCTURAL RESPONSES

In figure 5, the traces of the non-exceedance probability are shown on the example of the bending moments in mid-span position of field 1 and field 2. These structural responses are obtained for the centre bay of the building for a flow normal to the front wall.
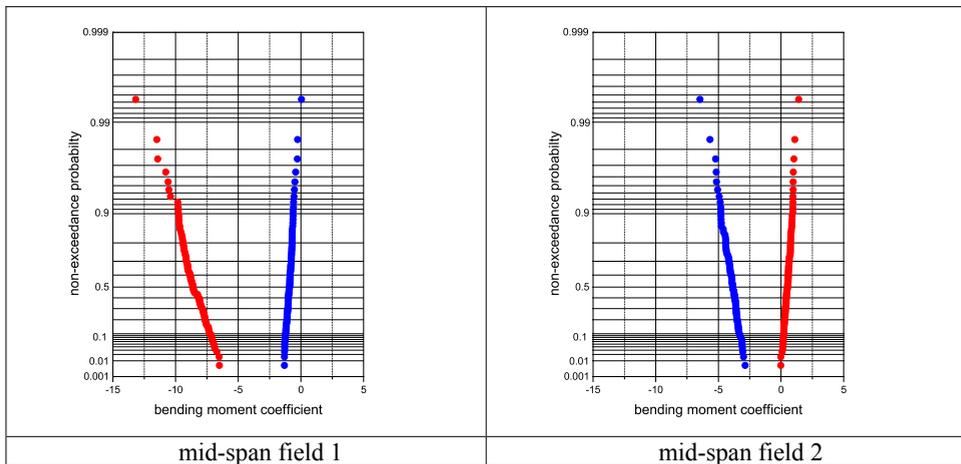
Figure 5: Example of extreme values of structural responses

In the final paper, a comprehensive comparison to the Eurocode specifications will be presented for all investigated cross sections and flow directions.

REFERENCES

ESDU - Engineering Science Data Unit (1993). "Wind speed profiles over terrain with roughness changes", ITEM 84011 with amendments A to D.

Numerical simulations of flowfield and pressure distribution around various roofs

Y.Gao   H.R.Mi

College of Ceivil Engineering, Harbin Engineering University

gaoye66@126.com   *Harbin, Heilongjiang, China*

Keywords: flowfield; pressure coefficient; turbulent kinetic energy

ABSTRACT

Greenhouses are often used for planting in the north of China. As building roofs, the greenhouse are various in their heights and roof shapes. In the north of China, the dominant wind in spring is north wind. In order to understand the flowfield and pressure distribution around the roofs, a lot of similar work has been performed by many scholars. Martinnuzzi and Tropea (1993) and Hussein and Martinuzzi (1996) have done experiments on wall mounted cubic obstacle placed in a fully developed turbulent channel flow at a high Reynolds number 40000. The mean velocity components and various Reynolds stresses around the obstacles are available from their work.

As many researchers improved the performance of the k-ε model to bluff bodies through the modifications of the standard k-ε model, Y. Gao and W.K. Chow (2005,2006,2005)had pointed out that there might be problems in using wall function in simulating approach air turbulent flow towards a cube with staggered grids. By limiting the velocity component in the flow direction with standard k-ε model and wall function, the value and position of the maximum turbulent kinetic energy k_{max} and the mean pressure coefficient C_p agreed better with the experimental results. In this paper, flowfield and pressure distribution around different greenhouse roofs are investigated.

Six two-dimensional roof shapes of lower greenhouses with different geometry will be investigated in this paper and are presented in Figure1. The six roof shapes have the same height (H) , and the widths of roofs in (a) to (e) are all 2H. While the one in (f) is 20H. The computational zone has a length of 23H and a height of 10H (g). The horizontal distance between the inlet and the roof shape is 6H. Non-slip condition is imposed at the wall. At the inlet, there exists a uniform air flow with velocity (U_0, 0). Pressure outlet is applied at the downward boundary. The Reynolds number Re (Re=U_0H/ν) calculated by the inlet velocity and roof shape height is 4×10^5. Additionally, six higher roofs were studied. The six roofs in Figure 2 are the same shapes as in Figure 1, but 2H height walls under them. Therefore, 2H height are add to every model and the computational zone. No change is made on other conditions.

The flow is considered two dimensional and incompressible. The governing equations includes Reynolds averaged continuity equation, momentum equations and standard k-ε equations. Standard

---

Contact person: Y.Gao, College of Ceivil Engineering, Harbin Engineering University, Harbin, Heilongjiang, China, (086)045182519210. E-mail gaoye66@126.com

wall function is employed to compute the near wall quantities. Second-order upwind scheme is utilized to discretize the convective term while central difference scheme is used for diffusive term.
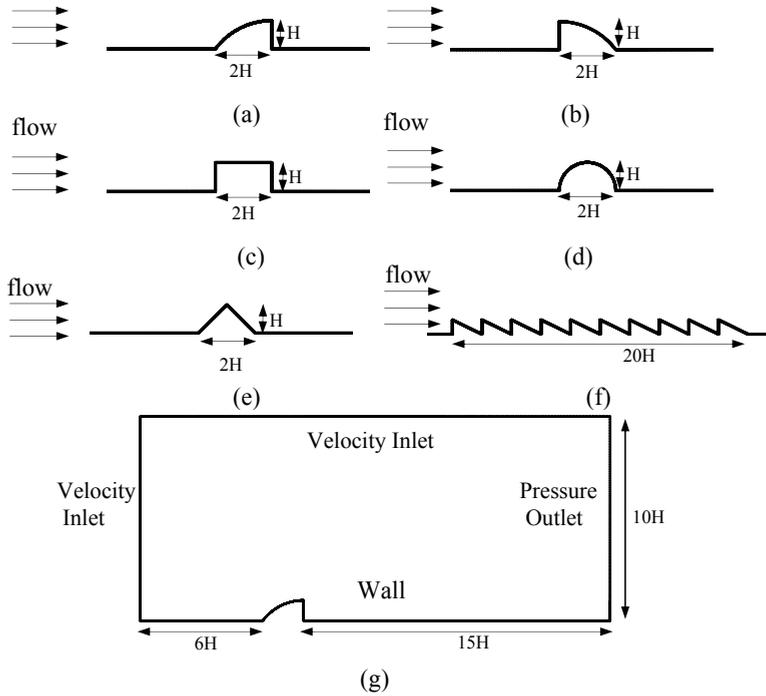
Figure 1: shapes of lower roofs and the computational zone
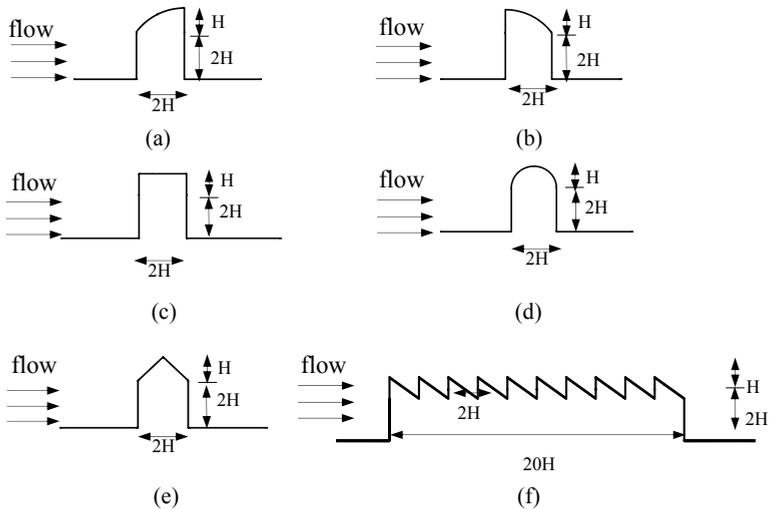
Figure 2: shapes of higher roofs and the computational zone
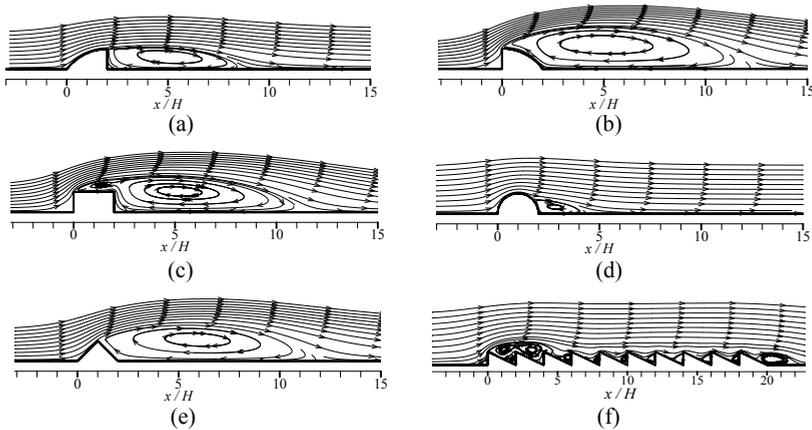
Figure 3: Streamlines distribution around the roofs of lower greenhouses

Figure 3 presents the streamline distribution around the different roof shapes of lower greenhouses. It can be seen that the length of the recirculation zone is different for different roof shape. The recirculation zone in Figure 3 (b) has the largest length while semi-circular roof shape has the smallest one. The reason is that the semi-circular roof shape has the most streamlined contour. In Figure 3(f), periodically varied flow field is observed between adjacent roofs.
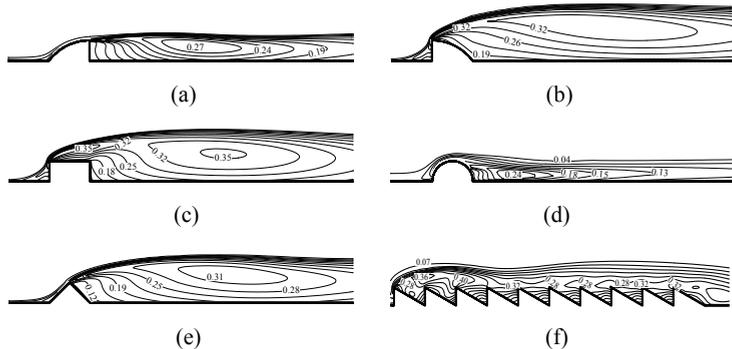
Figure4: Distribution of $\sqrt{k}/U_0$ around the roofs lower greenhouses

The non-dimensional turbulence kinetic energy distribution around the roofs of lower greenhouses is shown in Figure 4. From the figures, the roof shape with sharp tip toward the upwind direction has larger turbulence kinetic energy behind the roof. Under the same computational conditions, there is the largest turbulence kinetic energy around the rectangular roof, which indicates the most intensive variation of velocity around this kind roof. While, turbulence kinetic energy around the semi-circular roof is the smallest.

Figure 5 presents the variation of pressure coefficient C_p along the roofs of lower greenhouses. "S" is the whole curve length of the roof shape. "s" is the position on the roof. Static pressure at the backward of the first and forth roof shapes is larger than that of others. At the beginning of the roof shape, C_p has its maximum value for the second kind roof shape. For the periodically placed roofs (Figure 5(b)), C_p varies periodically between the forth and tenth roof with maximum value at the tip.

The streamline distribution, non-dimensional turbulence kinetic energy and distribution

variation of pressure coefficient C_p around the different roof shapes of higher greenhouses were also studied in the paper. The results of higher roofs were similar with those of the lower ones. Furthermore, there are lager changes of those variables around higher roofs. Therefore, more reinforcement should be add on the higher roofs.
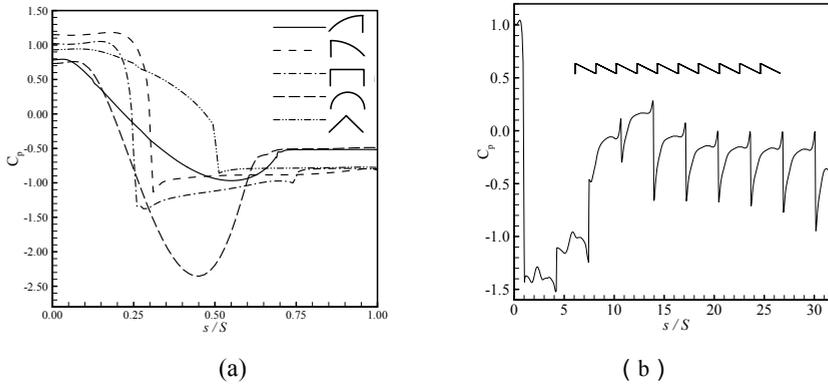
Figure 5: Variation of pressure coefficient C_p with curve length ofperiodically placed roofs of lower greenhouses

Some useful conclusions can be obtained as follows:
(1) The rectangular roof is the most frangible and the semi-circular roof is the most infrangible either for the higher greenhouse or lower greenhouse. So the semi-circular roof should be used for plastic greenhouse.
(2) The structure of higher roof should stronger than lower one for the larger variation of turbulence kinetic energy around the higher roof.
(3) The fluctuation of pressure coefficient around higher roofs is stronger than lower roofs. The fluctuation of pressure will destory the plastic cloth which greenhouse is covered with. Therefore, harder plastic cloth or glass should be used for higher greenhouse.

REFERENCES

R. Martinuzzi, C. Tropea (1993). "The flow around surface-mounted prismatic obstacles placed in a fully developed channel flow", Trans. ASME J. Fluid Eng, 115 (1), 85–91.

H.J. Hussein, R.J. Martinuzzi (1996). "Energy balance for turbulent flow around a surface mounted cube placed in a channel", Phys. Fluids, 8 (3), 764–780.

M. Tsuchiya, S. Murakami b, A. Mochida, K. Kondo, Y. Ishida (1997). "Development of a new k-ε model for flow and pressure fields around bluff body" , Journal of Wind Engineering and Industrial Aerodynamics 67&68, 169-182.

W. K. Chow, Y. Gao (2005). "On using the wall function and the staggered grid arrangement at upwind sharp convex corners in simulating approach air flow", International Journal of Computational Fluid Dynamics, 19(5) , 381 - 398

Y. Gao, W. K. Chow (2006). "Wall function at the upwind sharp corners in simulating incident air flow on a cube", Journal of Wind Engineering and Industrial Aerodynamics, 108, 629-632.

Y. Gao, W. K. Chow (2005). "Numerical studies on air flow around a cube", Journal of Wind Engineering and Industrial Aerodynamics, 93, 115–135.

Experimental study on wind load in roof and overhang of a gable building

1st A.D.John, 2nd A.Gairola, 3rd M.Mukherjee

1 Department of Civil Engineering, Indian Institute of Technology, Roorkee, India
2 Assoc. Prof. in Civil Engg., Centre of Excellence, Disaster Mitigation & Mgmt., Indian Institute of Technology, Roorkee, India
3 Department of Architecture and Planning, Indian Institute of Technology, Roorkee, India.

ABSTRACT

The present paper discusses on effect of boundary-wall on wind load in the roof and overhang of gable building. Pressures on roof and overhang are measured at varying distances of boundary-wall away from the building. Data were obtained in simulated conditions for open country and suburban terrain, at a scale of 1:25, in a Boundary Layer Wind Tunnel at Indian Institute of Technology Roorkee. Plan dimensions of gabled roof building model are 300mmx150mm and wall height 130mm with roof slope10^o. An overhang eaves length of 60mm and boundary-wall of height 66mm have been chosen for the experiment. Significant changes have been observed in magnitude of pressure coefficients on the roof and overhang with varying distances of boundary-wall from the building. In addition, the wind loads on roof and overhang have been compared with different codal values.

A gable roof building model representing a building of plan dimensions 7.5m × 3.75m × 3.25m (wall height, H) was fabricated as shown in Figure 1. Roof overhang extended upto 1.5m from building wall. These buildings are regarded as simplified model of typical low rise building in India for warehouses and residential houses. Experiment for the stand-alone condition was performed for different angles of wind incidence ranging from 0° to 90° at an interval of 15°. In the case of interference, the experiment was performed for 0°, 30°, 60° and 90° angles of wind incidence by shifting the boundary wall position at 1H, 1.5H, 2H, 3H, 4H, 5H, 6H and 7H from the wall of building. Detailed study of interference of boundary wall has been carried out where D/H=0 implies no boundary wall for the subsequent discussion. The different zones for roof & overhang and lay out of pressure taps are shown in Figure 2. Particular attention has been paid to position of pressure taps near the edge and corner of the eaves where airflow may become separated to form a region of high velocity gradient with high local turbulence and vortices.

Establishing Flow Conditions: For the present study, mean wind velocity and longitudinal turbulence intensity profiles for terrain category 2 (open country and sub-urban terrain) with scattered obstructions having heights up to 1.5 m pertaining to IS: 875 (Part 3) – 1987 with a power law index, α of 0.14 have been simulated in the wind tunnel. The values of mean velocity and longitudinal turbulence intensity at the eave height (H) of the model have been found to be 9.2 m/s and 18.26%

Contact person: A.D.John, Research Scholar, Contact number +91 9756656117, E-mail alok_john85@yahoo.com

respectively. The longitudinal length scale of turbulence L_{ux}, was determined by calculating the area under the autocorrelation curve of the fluctuating velocity component and is about 0.45 m at the eaves height.

Data Acquisition: Pressure taps (10mm long, 1mm internal diameter) of stainless steel tube were fixed through the holes drilled in to the Perspex sheet. One end of the tap was flushed with the roof and wall surface. Tubing for measuring surface pressure consisted of 300mm vinyl tube with a 20mm long restrictor placed at 200mm from the pressure point. Pressure measurements were carried out by using a Scanivalve ZOC23B, a 32-port pressure scanner, having approximately flat response up to 200 Hz. The sampling rate was kept at 500 samples per second per channel and the duration of each run was 16 seconds.
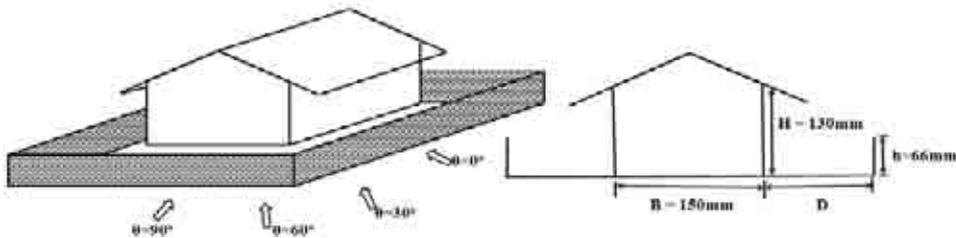
Figure 1. Building model with interfering boundary-wall
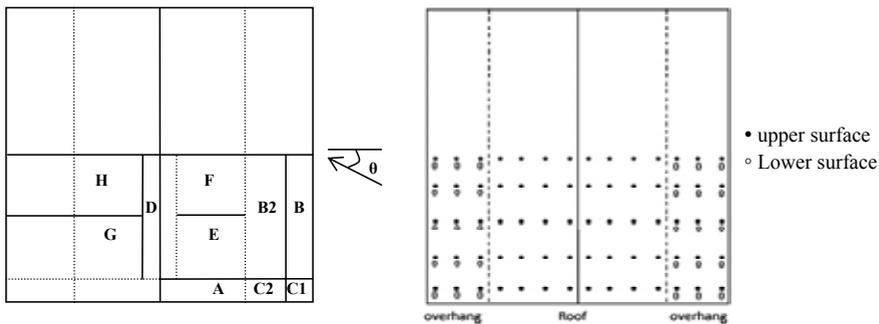
Figure 2. Different zones on roof and overhang of building and location of pressure taps

Pressure Measurement: Wind pressures measured on the building models are expressed in the form of a non-dimensional pressure coefficients defined as follow:

$$C_p = \frac{p_i - p_0}{1/2\rho U^2}$$

where, p_0 = static (ambient, atmospheric) reference pressure, p_i = instantaneous surface pressure, ρ = air density, U = mean velocity measured at eaves height of the model.

Since pressure at any point on roof of the building is fluctuating with time, the pressure coefficient can also be treated as time varying quantity. Following statistical quantities of pressure coefficient were obtained from sampled time history, C_p.

Mean value = $C_{pmean} = \frac{1}{N}\sum_{i=1}^{N} C_{p(i)}$, where N is the total number of samples

C_{pmin} = minimum of C_p, C_{pmax} = maximum of C_p

Standard deviation of C_p, $C_{psd} = \sqrt{\dfrac{1}{N-1}\sum_{i=1}^{N}[C_{p(i)} - C_{pmean}]^2}$, variance = $\sigma_x = (C_{psd})^2$

Design pressure coefficient = C_{pmean} + (C_{psd} × peak factor), where peak factor is the ratio of maximum and mean value of C_p. The average value of peak factor is estimated as 3.0. In figures 3 and 4, maximum values of design pressure coefficients (0°, 30°, 60° and 90° angles of wind incidences) have been considered.

For overhang, net peak pressures have been estimated by taking difference between the value of peak pressure coefficient of upper and lower surface of the overhang.

Effect of boundary-wall on roof of building: Wind pressure coefficients recorded on roof of building models in presence of boundary-wall distance at varying distances are shown in Figure 3. With increment of distance of boundary-wall from the building there is a significant decrease in the magnitude of negative pressure coefficients on the roof upto D/H=3 and Further increment in the distance of boundary-wall tapers off pressure variations.

Net peak pressure coefficient ($C_{pq-upward}$ and $C_{pq-downward}$) on overhang in presence of boundary-wall: The Figure 4 shows that values of $C_{pq-upward}$ decreases as wall distances (D) decrease upto 2H and value of $C_{pq-downward}$ increases towards positive side upto boundary-wall distance of 3H from the building.
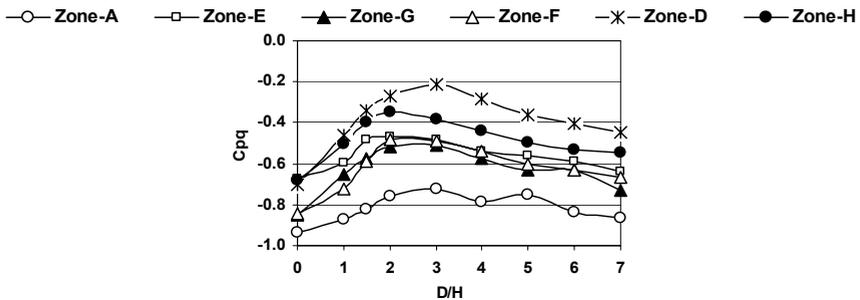
Figure 3. Variation of C_{pq} on roof surface in presence of boundary-wall
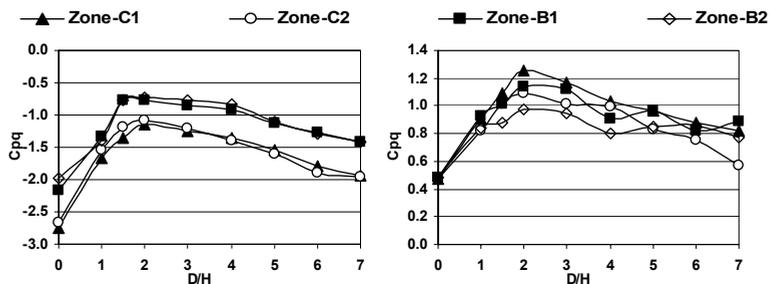
Figure 4. Variation of Net C_{pq} of overhang in presence of boundary-wall
a) - C_{pq} b) + C_{pq}

Table 1 Comparison of experimental C_{pq} of overhang with ASCE 7-05

| Zone | Experimental C_{pq} | | ASCE-7-05 |
	Without boundary-wall $C_{pq\text{-upward}}$	With boundary-wall at D/H=2 $C_{pq\text{-downward}}$	
B1	-2.17	1.14	-2.2
B2	-1.99	0.98	
C1	-2.74	1.26	-3.7
C2	-2.66	1.09	

Comparison of C_{pq} with the ASCE 7-05: Comparison of design pressure coefficients of overhang with values recommended by ASCE 7-05 has been tabulated in Table 1. A comparison of these results with ASCE 7-05 shows values of C_{pq} for stand-alone condition on conservative sides for all zones of overhang. However, experimental design values of C_{pq} change from negative to positive when boundary-wall position is at a distance of two times the height of building wall. These positive values are considerably higher and these values have not been mentioned by ASCE 7-05 and other Standards/ Codes.

The work reported in this paper are based on an experimental study carried out to determine variation of wind pressure coefficients appropriate for the design of roof with extended overhang of length 1.5m for gable roof building in presence of boundary-wall at varying distances. Commonly used roof angle of 10° were considered; and corner, edge and centre load on roof and overhangs have been evaluated. It has been found that,

1. Experimental values of design pressure coefficients for different zones of the roof have been compared with various Codes. Even for the most straightforward case, a scatter exists amongst the codal values. Experimental values for all cases are less as compared to codal values i.e. codal values are on conservative side.
2. In presence of boundary-wall, suction on roof of different zones decreases when boundary-wall distance is between two to four times the height of building wall. Further increase in the distance of boundary-wall from the building tapers off the effect of pressure variation.
3. Net peak upward pressure of overhang shows maximum positive value in presence of boundary-wall, located at a distance of 2H and 3H, however for stand-alone condition overhang is subjected to maximum negative (upward) pressure.
4. A comparison of the results with the ASCE 7-05 recommended provisions shows that the pressure coefficient values of overhang are on conservative side for the stand-alone condition; however, it needs to be revised if those buildings are surrounded by boundary-wall.

REFERENCES

Leutheusser H.J. (1965). "The effect of eaves on the roof pressure-coefficients of block type and cylindrical structures". UT Mech., E TP 6503, Deptt. of Mechanical Engg., University of Toronto, Toronto, Canada.

Dreher K.J., Cermak J.E. (1973). "Wind load on the house roof". Report CER 72-73, KJD-JEC22, Colorado University, College of Engg., Ft. Collins, Colorado.

Best R.J., Holmes J.D. (1978). "Model study of wind pressures on an isolated single storey house", Wind Engg. Report 3178, Deptt. of Civil and System Engg., James Cook University of North Queensland, Australia.

Stathopoulos T. (1981). "Wind load on eaves of low buildings", Journal of the Structural Division, ASCE, 107, ST10, Proc. paper 16543: 1921-1934.

Stathopoulos T., Luchian H. (1994). "Wind-induced forces on eaves of low building", Journal of wind Engineering and Industrial Aerodynamic, vol 52, 249-261.

ASCE 7-05 (2005), Minimum Design Loads for Buildings and Other Structures, Structural Engineering Institute of the American Society of Civil Engineers, Reston, VA.

John A.D., Gairola A., Krishna P. (2008). "Wind load on overhangs in a low gable building in presence of free standing wall", Journal of wind and Engineering, vol. 5, (1), 39-46.

Behavior of mechanically anchored waterproofing membrane exposed during typhoon
- Part 1 Characteristics of wind and wind pressure -

1st Nobuo Katou, 2nd Hiroyuki Miyauchi, 3rd Shuuji Nakamura, 4th Kyoji Tanaka

1st Tokyu Construction – katou.nobuo@tokyu-cnst.co.jp – 3062-1 Tana, Sagamihara, Kanagawa, 229-1124, JAPAN

2nd Chungnam National University – miyauchi@cnu.ac.kr – 220 Gung-Dong, Yuseong-Gu, Daejeon, 305-764, KOREA

3rd Tsutsunaka Sheet Waterproofing System Co., Ltd. – nakamura-shuuji@sumibe.co.jp – 2-5-8 Higashishinagawa, Shinagawa-ku, Tokyo, 140-0002, JAPAN

4th Tokyo Institute of Technology – tanaka@serc.titech.ac.jp – 4259 Nagatsuta-cho, Yokohama, Kanagawa, 226-8503, JAPAN

ABSTRACT

Mechanically anchored waterproofing membrane systems are directly fixed to the roof substrate with a series of fasteners. When comparing the performance of these systems to that of an adhered waterproofing membrane system, mechanically anchored waterproofing membrane systems do not depend on the condition of substrate to ensure adequate attachment to the roof and given the means of attachment, are also reasonably easy to replace. However, the wind resistance of mechanically anchored waterproofing membrane systems depends on the reliability of the fasteners and there is some apprehension by designers about the safety of these systems in respect to wind resistance and in particular when such systems are subjected to winds loads as are evident during a typhoon. For example, for typhoons No.18 and 22 that recently occurred in Japan, the maximum instantaneous wind speeds exceeded 50-m/s (180 kph) and as such, these apprehensions may indeed be well founded. In this paper, the response of a mechanically anchored waterproofing membrane system installed atop a test building located on the island of Miyako was measured when subjected to strong winds from a typhoon that occurred in 2007. The experimental method and the behavior of wind conditions during the typhoon are provided and the results in respect to loads acting on, and strains induced in the membrane are given.

The test building, shown in Figure 1, was the Japan Weathering Test Center located on the island of Miyakojima, which is part of the Ryukyu Island chain situated in the East China Sea, and at approximately the same latitude north as Taipei. The roof of the building serving as field test site has dimensions of 6m by 6m, is at an elevation of 3m above ground level and does not have parapets. The

---

Contact person: 2nd Hiroyuki Miyauchi, Chungnam National University — 220 Gung-Dong, Yuseong-Gu, Daejeon, 305-764, KOREA, Tel:+82-42-821-7732, Fax: +82-42-823-9467

E-mail: miyauchi@cnu.ac.kr

polyvinylchloride waterproofing membrane (1.5mm thick), reinforced with polyester fiber, was constructed atop the roof of the test building and was attached by fasteners spaced every 600 mm as shown in Figure 2. During the typhoon event, the wind direction, wind speed, and wind pressure on the roof were measured as was the degree of billowing of the waterproofing membrane and the strain of waterproofing membrane at specific fastener points. Wind direction and wind speed was measured using a sonic anemometer located at roof height. The external and internal wind pressures on the membrane were measured by connecting to a "Y" type pressure tube and pressure sensor. The strain on the waterproofing membrane was measured using strain gauges affixed to the back of the membrane.

Figure 1: test building
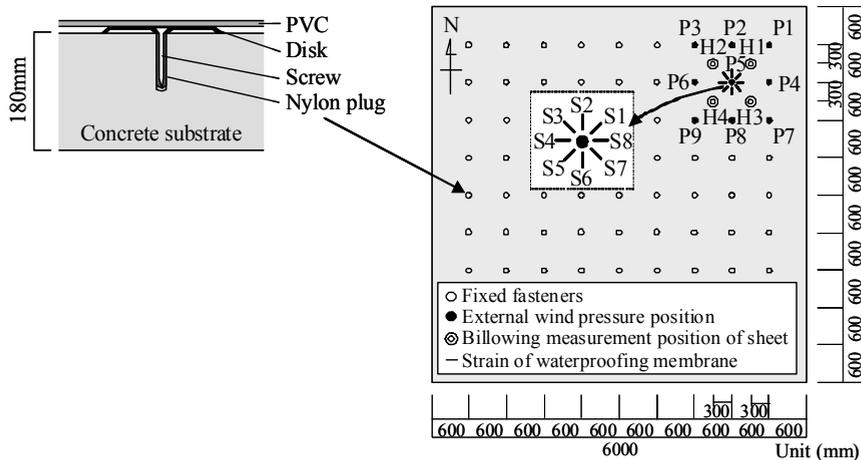
Figure 2: waterproofing membrane system and outline of the measurement

Results from the measurements taken during the typhoon, as given in Figure 3, indicated that the maximum wind speed was 16.8 m/s, and maximum instantaneous wind speed was 28.1 m/s. Figure 4 shows the mean wind pressure coefficient and peak wind pressure on the roof for ten minutes at the maximum recorded wind speed of 16.8 m/s. As might be expected, the negative pressure on the windward side was large, generating, for example at point P7, a value for peak wind pressure coefficient of -8.4 (peak value: -1454Pa). As is evident in Figure 5, the wind pressure coefficient averaged over 10 minutes at this same point showed pressure-spiking phenomenon. Given these results, it is useful to note that the values for external pressure coefficient measured in this study were considerably greater than those given in the "Recommendations for Loads on Buildings" and "Building Standard Law" as provided in Japan. This suggests that changes should be proposed to these recommendations to take into account the heightened loads on roof membranes that occur during typhoons.
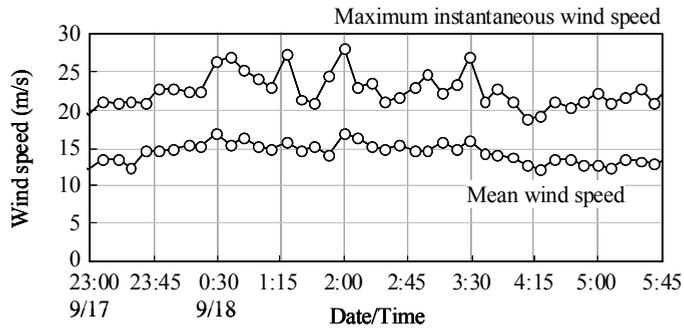
Figure 3: the mean wind speed and the maximum instantaneous wind speed
for ten minutes in Typhoon No.12 in Japan
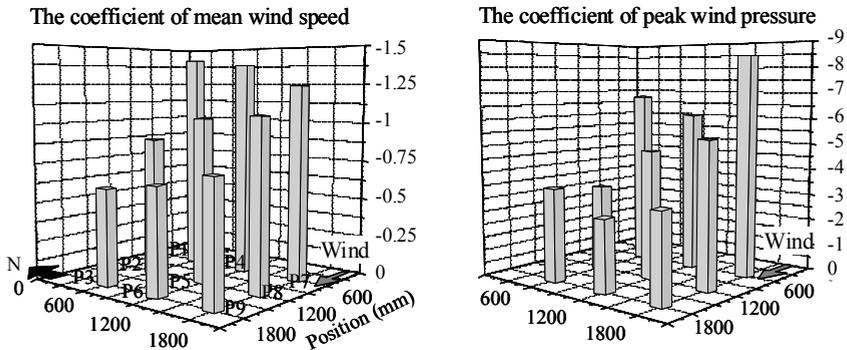
Figure 4: the coefficient of mean wind pressure and peak wind pressure on the roof
(Maximum wind speed for 10 minutes)
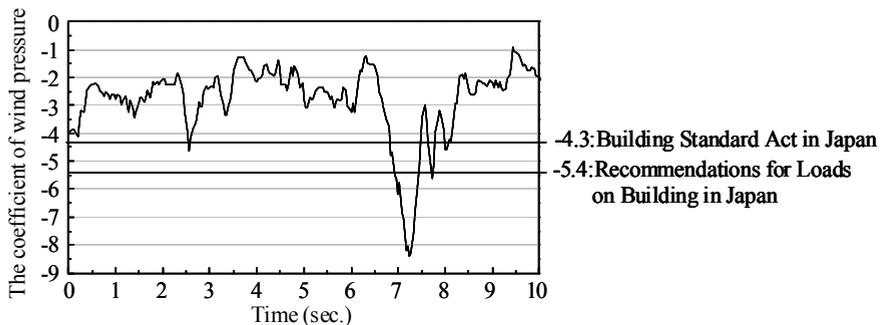
Figure 5: the coefficient of wind pressure for 10 minutes at P7 point

REFERENCES

Baskaran, B. A., Ko. S.K.P. (2005). A Guide for the Wind Design of Mechanically Attached Flexible Membrane Roofs, Construction Innovation, Volume 10, Number 4, *NRC-IRC*

Baskaran, B. A. (2006). "Which is the weakest link? Wind performance of mechanically attached systems," *Proceedings of the RCI 21st International Convention* (Phoenix, Arizona, 3/23/2006), 29-39

Baskaran, B. A. (2005). "Newsbrief - SIGDERS project, Phase IV," *Construction Innovation,* 10, (4), December, pp.5

Lei. W and Baskaran, B.A. (2001). "SIGDERS Wind Uplift Resistance Data on Mechanically Attached Single Ply Roofing Systems – Effect of vapour/Air Barrier", *Research Report IRC-RR-823 National Research Council*, Canada

Baskaran, B.A., Chen, Y. and Vilaipornsawai, U. (1999) A New Dynamic Wind Load Cycle to Evaluate Flexible Membrane Roofs", *ASTM Journal of Testing and Evaluation*, 27 (4), 249-265

Hirokazu ICHIKAWA, Michal BARTKO, Nobuo KATOU, Hiroyuki MIYAUCHI, Takanori SASAKI and Kyoji TANAKA (2005) Behavior of mechanically anchored waterproofing membrane exposed to high wind speed of wind tunnel, *Journal of Structural and Construction Engineering*, No.593, 17-24

Kyoji Tanaka (2005) Investigation into the actual condition and the wind tunnel result of mechanically anchored waterproofing membrane system, *The 3rd Symposium on waterproofing membrane system in Japan*

Recommendations for loads on building. (2004). *Architectural Institute of Japan* (AIJ)

Behavior of mechanically anchored waterproofing membrane exposed during typhoon
- Part 2: Relationship between wind force and membrane -

1ˢᵗ Hiroyuki Miyauchi, 2ⁿᵈ Nobuo Katou, 3ʳᵈ Kyoji Tanaka

1ˢᵗ Chungnam National University – miyauchi@cnu.ac.kr – 220 Gung-Dong, Yuseong-Gu, Daejeon, 305-764, KOREA

2ⁿᵈ Tokyu Construction – katou.nobuo@tokyu-cnst.co.jp – 3062-1 Tana, Sagamihara, Kanagawa, 229-1124, JAPAN

3ʳᵈ Tokyo Institute of Technology – tanaka@serc.titech.ac.jp – 4259 Nagatsuta-cho, Yokohama, Kanagawa, 226-8503, JAPAN

Keywords: Mechanically anchored waterproofing system, Wind, Field test, Sheet, Fastener, Strain

ABSTRACT

In 2004, the passage of typhoons No.18 and 22 over Japan damaged several mechanically anchored waterproofing membrane systems. The authors undertook a survey of damage to these systems, reviewed the wind resistance design of such membrane systems, and published results of this survey as part of the technical papers offered by the Architectural Institute of Japan. Although wind tunnel testing has also been carried out by different researchers to gain an understanding of the behavior of mechanically anchored waterproofing membrane systems, the data obtained from such tests is limited because these were only carried out under constant wind load conditions.

A study was subsequently conducted in 2007 to measure the response of a mechanically anchored waterproofing membrane system located atop a test building on the island of Miyakojima when subjected to strong winds from a typhoon. The island of Miyakojima, is part of the Ryukyu Island chain situated in the East China Sea, and at approximately the same latitude north as Taipei. From the field test data collected during the typhoon event, a relationship was found between wind pressure and the behavior of the waterproofing membrane system. The billowing of the membrane was observed visually, as shown in Figure 1, and the billowing height measured as was the wind speed and direction, loads and strains induced in the membrane and in selected fasteners. For example as given in Figure 2, at one location on the roof (H3), at the maximum recorded wind speed of 16.8m/s, the mean billowing height was 38mm as compared to the maximum value of 57mm. It was also evident from visual observation that the billowing height of the waterproofing membrane on the windward side was higher than that of leeward side. Based on the results derived from the field study, a relationship was determined between the maximum wind pressure, membrane billowing height and membrane strain, as shown in Figure 3. The strain in the membrane is large on the windward side and

Contact person: 1ˢᵗ Hiroyuki Miyauchi, Chungnam National University — 220 Gung-Dong, Yuseong-Gu, Daejeon, 305-764, KOREA, Tel:+82-42-821-7732, Fax: +82-42-823-9467
E-mail: miyauchi@cnu.ac.kr

the membrane strain was greatest along a 45-degree diagonal to the direction of the minimum fastener span. This indicated that a horizontal force is induced in the fastener from the billowing effect. Correlation between wind pressure and billowing height of waterproofing membrane, as given in Figure 4 was evident, and indicates that increases in the membrane billowing height are brought about by an corresponding increases in negative pressure on the roof. The relationship between the billowing height and strain on the waterproofing membrane is given in Figure 5. As is apparent, the greater the billowing height the greater the stain on the membrane. The results from this study also appear to coincide with those derived from wind tunnel test on comparable mechanically fastened waterproofing membranes subjected to similar wind loads. It therefore is very useful to use both these relations as a basis to design for the wind resistance of mechanically anchored waterproofing membrane systems since both of these parameters can be determined from testing different waterproofing membranes.
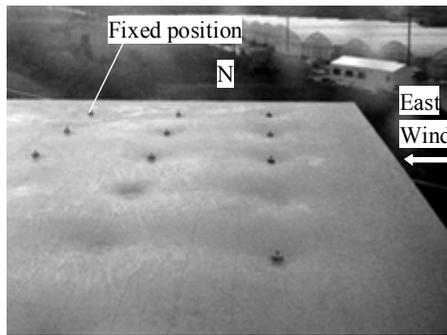
Figure 1: billowing condition of waterproofing membrane on roof during Typhoon No.12 in Japan
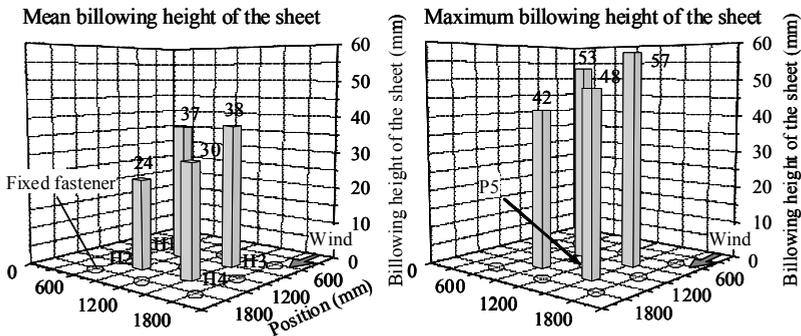
Figure 2: the result of billowing height of waterproofing membrane
(Maximum wind speed :16.8m/s)
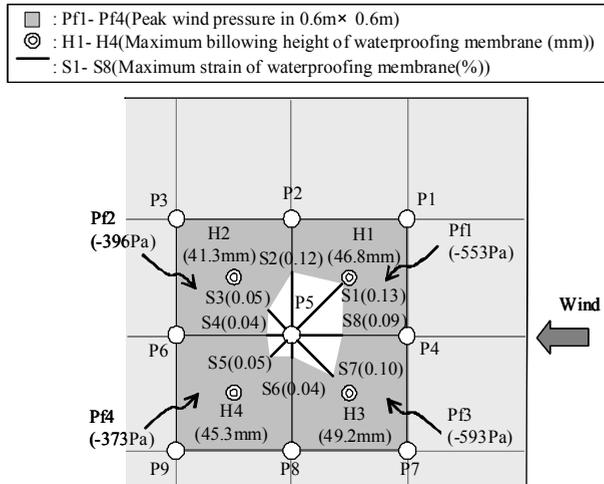
Figure 3: relationship between peak wind pressure,
maximum billowing height-strain of waterproofing membrane
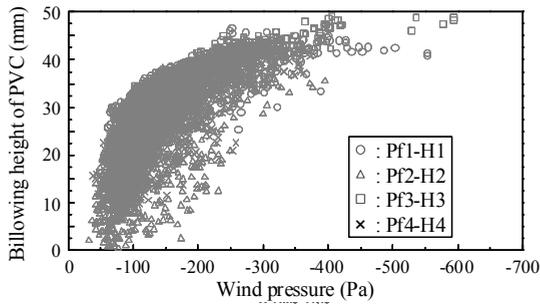
Figure 4: relationship between wind pressure and the billowing height of PVC
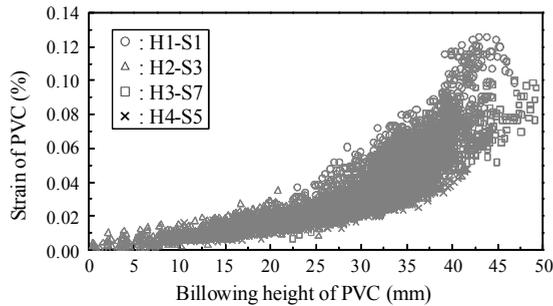
Figure 5: relationship between billowing height of PVC and strain of PVC

REFERENCES

Baskaran, B. A., Ko. S.K.P. (2005). A Guide for the Wind Design of Mechanically Attached Flexible Membrane Roofs, Construction Innovation, Volume 10, Number 4, *NRC-IRC*

Baskaran, B. A. (2006). "Which is the weakest link? Wind performance of mechanically attached systems," *Proceedings of the RCI 21st International Convention* (Phoenix, Arizona, 3/23/2006), 29-39

Baskaran, B. A. (2005). "Newsbrief - SIGDERS project, Phase IV," *Construction Innovation,* 10, (4), December, pp. 5

Lei. W and Baskaran, B.A. (2001). "SIGDERS Wind Uplift Resistance Data on Mechanically Attached Single Ply Roofing Systems – Effect of vapour/Air Barrier", *Research Report IRC-RR-823 National Research Council*, Canada

Baskaran, B.A., Chen, Y. and Vilaipornsawai, U. (1999). A New Dynamic Wind Load Cycle to Evaluate Flexible Membrane Roofs", *ASTM Journal of Testing and Evaluation*, 27 (4), pp.249-265

Hirokazu ICHIKAWA, Michal BARTKO, Nobuo KATOU, Hiroyuki MIYAUCHI, Takanori SASAKI and Kyoji TANAKA (2005). Behavior of mechanically anchored waterproofing membrane exposed to high wind speed of wind tunnel, *Journal of Structural and Construction Engineering*, No.593, 17-24

Kyoji Tanaka (2005). Investigation into the actual condition and the wind tunnel result of mechanically anchored waterproofing membrane system, *The 3rd Symposium on waterproofing membrane system in Japan*

Simulation of turbulent wind action on a new membrane roof over Municipal Stadium in Poznań, Poland, for UEFA EURO 2012

A.Flaga, J.Bęc, T.Lipecki

Lublin University of Technology – a.flaga@pollub.pl – Nadbystrzycka 40, 20-618 Lublin, Poland –
Lublin University of Technology – j.bec@pollub.pl – Nadbystrzycka 40, 20-618 Lublin, Poland –
Lublin University of Technology – t.lipecki@pollub.pl – Nadbystrzycka 40, 20-618 Lublin, Poland

Keywords: stadium roof, wind action, filtered quasi-steady model, wind tunnel tests.

ABSTRACT

Two approaches to the new model of wind action on a stadium roof are presented in this paper. These are: space filtered quasi-steady model and time filtered quasi-steady model. Both approaches eliminate small disturbances in wind action and represent a large gusts travelling over the roof.

The wind field is generated using one of the simulation methods (WAWS, AR, ARMA) using own software. The distribution of the simulation points is regular in the square grid in horizontal plane view. Wind tunnel tests have been carried out to obtain aerodynamic coefficients in selected points on the roof.

STADIUM ROOF

The new roof has been designed over the old stadium in Poznań, Poland, where some football competitions will take place during UEFA EURO 2012.

The roof is a membrane structure. The span of the roof is 203.5 m and 185.70 m in perpendicular directions.

Contact person: J.Bęc, Lublin University of Technology, Nadbystrzycka 40, 20-618 Lublin, Poland,
phone +48 81 5384436, FAX +48 81 5384435
E-mail j.bec@pollub.pl

The main bearing structure consists of large, spatial steel cable-bar trusses, steel frames, reinforced concrete columns and foundations. Two longer main trusses of the span 172.5 m and 159.6 m are supported on four reinforced columns. The other two main trusses are supported on the two main trusses. Its dimensions are: span – 135m, width – 9 m, maximum height – 15.3 m.

The isometric view of the stadium is presented in Fig. 1.
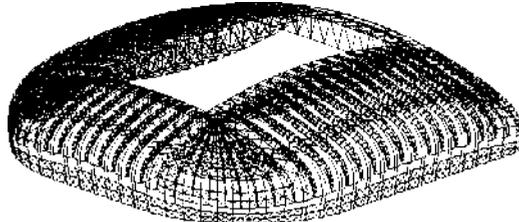
Figure 1: Isometric view of the stadium roof.

EXEMPLARY WIND TUNNEL TESTS RESULTS

Wind tunnel tests of the stadium roof have been performed in the Wind Engineering Laboratory of the Cracow University of Technology. Extremely unfavourable pressure distributions on the roof have been determined in the tests. The following aerodynamic coefficients have been measured: mean, maximum and minimum wind pressure coefficients. Distributions of these values have been obtained on the basis of measurements conducted in 105 points in 21 roof cross-sections in each half of the whole roof. Tests have been carried out for the whole range of wind attack angle, with the step of 10°.

Exemplary results of measurements are presented in Fig. 2.
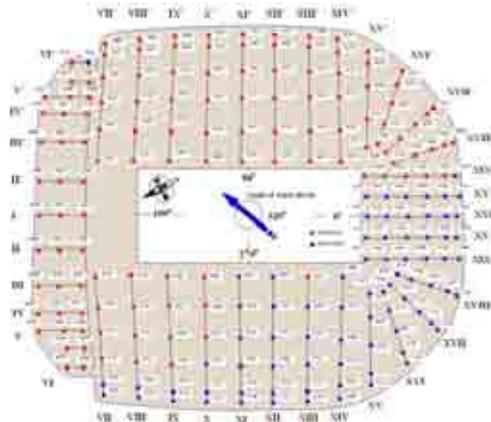
Figure 2: Exemplary mean wind pressure coefficient $\bar{C}_p$ distribution for the wind attack angle 320°.

WIND ACTION MODEL

Two approaches have been used to create our new model of wind action on the roof. The main idea of the model is to determine time dependent wind action on the roof based on wind velocity field in front of the structure and averaged in time or in space. All small-scale wind fluctuation disturbances are eliminated when these models are used (Flaga (1994), Flaga (1995), Flaga (2008)).

The mean value of wind action in point i of the structure is calculated according to the formula:

$$\bar{p}_i = \frac{1}{2} \rho \bar{u}_{ref}^2 \bar{c}_{p_i} , \tag{1}$$

where: ρ – air density, $\bar{u}_{ref}$ – reference averaged wind speed in point in the front of the structure, $\bar{c}_{p_i}$ – aerodynamic coefficient in point i referred to $\bar{u}_{ref}$. The last parameter has been obtained during wind tunnel tests.

The proposed methods may be described as follows:

1. Space filtered quasi-steady model

The pressure variation in a selected point i on the roof is connected with the wind speed spatially averaged in point ref,i in front of the structure as follows:

$$p_i^{\Delta S}(t) \cong \frac{1}{2} \rho \left(u_{ref,i}^{\Delta S}(t) \right)^2 \bar{c}_{p_i} , \quad u_{ref,i}^{\Delta S}(t) = \frac{1}{N} \sum_{k=1}^{N} u_{ref,k}^{\Delta S}(t) \tag{2}$$

where: $u_{ref,i}^{\Delta S}(t)$ is a spatially averaged wind speed and $k = 1...N$, N is a number of points or subdomains $d\Delta S_k$ in area ΔS_i where wind is simulated. The areas of averaging may overlap as it can be seen in Fig. 3.
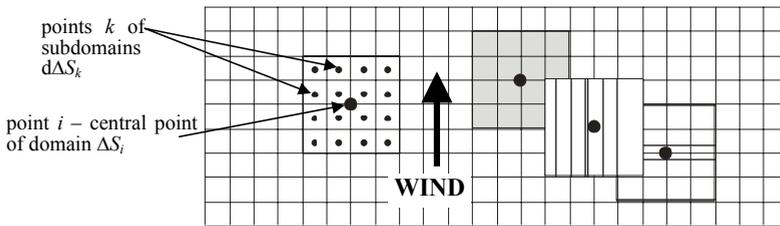
Figure 3: Plane view of domains ΔS_i in front of the structure corresponding to the roof surface point i.

2. Time filtered quasi-steady model

The pressure variation in a selected point i on the roof is connected with the time averaged wind speed in reference point ref,i in front of the structure according to the formula:

$$p_i^{\Delta T}(t) \cong \frac{1}{2} \rho \left(u_{ref,i}^{\Delta T}(t) \right)^2 \bar{c}_{p_i} , \quad u_{ref,i}^{\Delta T}(t) = \frac{1}{\Delta T} \int_{t-\Delta t}^{t} u_{ref,i}^{\Delta T}(t) dt \tag{3}$$

where: $u_{ref,i}^{\Delta T}$ is a reference time averaged wind speed and ΔT is the time domain of averaging.

SPACE OR TIME DOMAIN DIMENSIONS

The main problem in both methods is the domain (space or time) in which the process should be averaged. It is proposed to take into consideration the following rules:

1. Space filtered quasi steady model

It is assumed that the dimension of large scale vortices are represented by correlation length scales L, i.e. the distance in which the substitute equivalent stochastic process is fully correlated. So, correlation length scales of wind fluctuation in horizontal directions L_x and L_y are the parameters used to determine the area of averaging. These scales are given in ESDU (1985) or in Duchene-Marullaz (1975).

2. Time filtered quasi-steady model

Time averaged filter is used to eliminate all the frequencies that do not have any particular influence on dynamic wind action on the roof. The cut-off frequencies in two horizontal directions are calculated according to the following relationships:

$$f_x^* = \frac{\overline{v}_{ref,i}}{C_x L_x^*}, \quad f_y^* = \frac{\overline{v}_{ref,i}}{C_y L_y^*}, \tag{4}$$

where: C_x and C_y are directional coefficients used in calculation of coherence functions defined e.g. by Borri et al. (1995), L_x^* and L_y^* – are frequency scales (depending on wind direction) where substitute equivalent stochastic process is fully stochastically dependent.

The wind speed time series have been simulated with use of WAWS, AR and ARMA methods. The exemplary simulation is presented in Fig. 4. On the basis of the wind speed simulations and our new models, series of wind local pressures on the roof have been generated.

time [s]
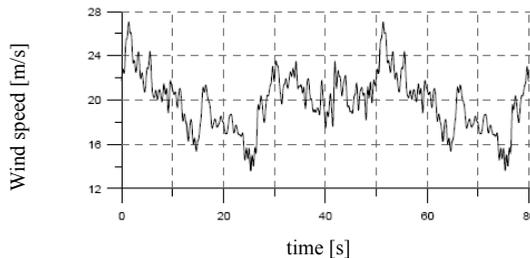
Figure 4: Exemplary wind speed (*x* component) simulated with WAWS method.

CONCLUSIONS

On the basis of the performed simulations some differences in the results coming from the approaches have been observed. Space or time averaging allows elimination of small scale disturbances in dynamic wind action on the roof which are producing local effects on the roof. With use of the presented methods only large scale vortices are taken into account which are important when the whole structure is analysed.

The complete results as well as full comparison of the two methods will be in details considered and presented in the full paper.

REFERENCES

Flaga A (1994): *Quasi-steady Models of Wind Load on Slender Structures*. Sonderforschungsbereich 151 – Tragwerksdynamik, Wissenschaftliche Mitteilungen Berichte Nr. 25, Ruhr Universität Bochum.

Flaga A (1995): "Treatment of Buffeting in Wind Engineering – Theoretical and Experimental Aspects", Windingenieurwesen, Baudynamik und Umwelttechnik: Aktuelle Entwicklungen in Forschung und Praxis, Festschrift zum 60. Geburtstag von Prof. Dr.-Ing. Hans-Jürgen Niemann, Herausgeber: Gornandt V., Kasperski M., SFB 151 – Berichte Nr. 27, Ruhr Universität Bochum, 1995, pp. 109-123.

Flaga A (2008): *Wind Engineering: Basics and Applications*. Wydawnictwo Arkady, Warszawa 2008. (in Polish)

ESDU 85020 (1985): *Characteristics of atmospheric turbulence near the ground. Part II: single point data for strong winds (neutral atmosphere)*. ESDU Ltd, London.

Duchene-Marullaz P. (1975): *Full-scale measurements of atmospheric turbulence in a suburban area*. WEBS, Heathrow, London.

Borri C., Crocchini F., Facchini L., Spinelli P. (1995): "Numerical simulation of stationary and nonstationary stochastic processes: a comparative analysis for turbulent wind fields", Ninth International Conference on Wind Engineering, "Retrospect and Prospect", Vol. 1, New Delhi January 9-13, 1995, pp. 47-55.

Wind tunnel tests on the roof of the new Turin stadium

G. Diana, D. Rocchi, E. Sabbioni, S. Giappino, A. Collina

Department of Mechanical Engineering, Politecnico di Milano – giorgio.diana@polimi.it – Via La Masa 1 20158, Milano – Department of Mechanical Engineering, Politecnico di Milano – daniele.rocchi@polimi.it – Via La Masa 1 20158 Milano – Department of Mechanical Engineering, Politecnico di Milano – edoardo.sabbioni@polimi.it – Via La Masa 1 20158 Milano – Department of Mechanical Engineering, Politecnico di Milano Milano – stefano.giappino@polimi.it – Via La Masa 1 20158 Milano – Department of Mechanical Engineering, Politecnico di Milano – andrea.collina@polimi.it – Via La Masa 1 20158 Milano

ABSTRACT

An analysis of the aerodynamic loads on the roof of the new Turin stadium is presented in this paper, relying on an experimental test campaign performed on a 1:100 static model in the atmospheric boundary layer test section of the wind tunnel of the Politecnico di Milano.

The stadium represents the future football field of Juventus F.C. soccer team that will replace the old Delle Alpi Stadium and will be built on the same site of the older one.

The new plant will be smaller than the previous one and it will contain up to 40000 people on a two levels grandstand. All the grandstands are covered by a cantilevered roof and curvilinear lateral shields, running all around the external perimeter of the roof, join the upper surface of the roof to the outer walls of the stadium.

During wind tunnel tests, the overall aerodynamic forces acting the roof have been directly measured using two six-components dynamometric balances. Moreover, pressure taps placed on the roof have allowed to indirectly calculate the overall wind loads by integrating the pressure distribution on the roof. Pressure measurements also allowed to assess the contribution of each section of the roof to the overall aerodynamic loads.

The results obtained by the two measurement systems will be compared for different roof configurations (with and without skylights), in presence or in absence of the lateral shields and for

---

Contact person: D. Rocchi, Mechanical Department of the Politecnico di Milano, Via La Masa 1, 20158 Milano, +39 02 2399 8485, FAX +39 02 2399 8492. E-mail daniele.rocchi@polimi.it

different exposure angles.

Finally the roof sections presenting the higher pressure peaks, both in terms of mean and extreme values, will be highlighted.

METHODOLOGY

The 1:100 static model of the new Turin stadium is shown in Figure 1. The scale factor has been chosen to allow a reliable reproduction of the geometrical details and of the interaction between the model and the wind boundary layer. The tested model includes also the neighboring buildings within a distance of 500m (full scale) from the football field.

The roof, covering all the grandstands of the stadium, is 40m high (full scale) with respect to the football field and the stadium is partially dipped into the surrounding structures hosting the commercial activities connected to the stadium. The flow characteristics of the wind blowing on the roof are therefore affected by local effects due to the interaction with the surrounding structures that has to be properly reproduced during the wind tunnel tests.

The structural scheme of the roof is shown in Figure 2 and it is made of a supporting structure, hinged to the strands along the external perimeter and hanged through cables to two supporting towers placed outside the stadium behind the ends (Figure 1). Four vertical cables connect the corners of the roof inner edge to the ground. The model of the roof has been designed in order to have its first natural frequency much higher than the range of interest for the study (0-10Hz). Thus, during wind tunnel tests, aeroelastic effects, related to the motion of the model of the roof, can be neglected.

Curvilinear lateral shields (Figure 1), running all around the external perimeter of the roof, join the upper surface of the roof to the outer walls of the stadium. The lateral shields are connected to the outer walls of the stadium and, even if they contribute in the definition of the aerodynamic loads acting on the roof, they do not transmit any aerodynamic force to the roof supporting structure.

During wind tunnel test, the boundary layer of the suburban area where the stadium will be built has been simulated by means of passive turbulence generators (floor roughness elements and triangular spires at the test section entrance).

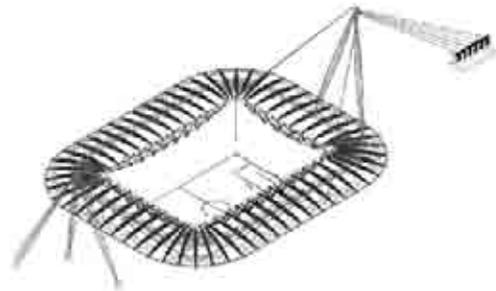Figure 1: 1:100 model of the new Turin stadium.   Figure 2: Roof structural scheme.

In order to measure the overall wind loads and the pressure distribution on the stadium, the model has been instrumented with 548 pressure taps distributed on the roof (Figure 4) and on the lateral shields, with two six-components dynamometric balances and with four dynamometers measuring the cables strength. Thus, the overall aerodynamic forces have been directly measured by the dynamometric balances and indirectly calculated by integrating the pressure distribution on the stadium roof and lateral shields. Pressure measurements have also allowed to separate the contribution of the roof from the lateral shields one, and to evaluate the contribution related to each section of the roof to the overall wind loads.

The aerodynamic force/moment coefficients (C_F/C_M) have been calculated according to the quasi-static theory (Simiu (1996)):

$$C_{Fi} = \frac{F_i}{\overline{q}A}; \qquad C_{Mi} = \frac{M_i}{\overline{q}AC}; \qquad (i = x, y, z) \qquad (1)$$

where F_i/M_i are the force/moment components along the i-th direction measured either by the dynamometric balances or obtained by integrating the pressure distribution on the roof, A is a reference area and $\overline{q}$ the wind gust dynamic pressure calculated according the Eurocode 1 (2005) definition:

$$\overline{q} = \frac{1}{2}\rho U^2 \left(1 + 7I_u\right) \qquad (2)$$

being U is the mean wind speed at the reference height (the height of the roof), I_u is the turbulence intensity and ρ is the air density.

The reference area A of eq. (1) has been assumed equal to the roof surface for the calculation of the overall aerodynamic coefficients, or equal to the surface of only one section for the computation of the contribution associated to each of the eight parts of the roof shown in Figure 3.

Overall aerodynamic coefficients have been referred to a reference system placed in the centre of the football field at the ground level and orientated as indicated in Figure 3. The aerodynamic coefficients associated to each roof section have instead been referred to a reference system placed in the middle of the considered section at the roof height.

Different roof configurations have been considered during wind tunnel tests:
1) with and without the skylights on the upper surface (Figure 4);
2) with and without the lateral shields (Figure 1).

For all the tested configurations, different incoming wind directions have been simulated. In particular, an exposure angle of 0° corresponds to the wind blowing north to south.

The cross-comparison of force and pressure measurements have allowed to investigate the contribution of each roof section and of the lateral shields on the overall wind loads in order to identify the worst loads conditions to be considered during the roof design and also for comparison with the standard prescriptions.
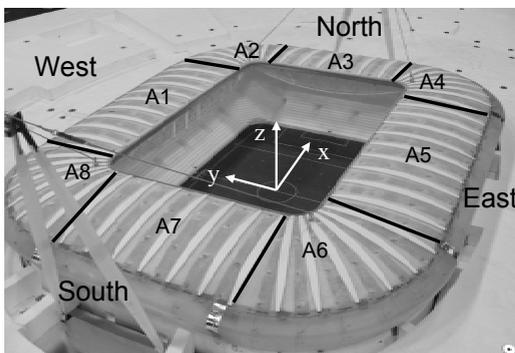
Figure 3: Reference system and roof sections.
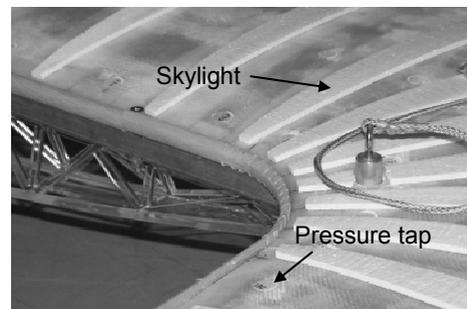
Figure 4: Model roof: skylights and pressure taps.

RESULTS

The total forces computed by integrating the measured pressure distribution over the whole roof surface have been compared to the measurements provided by the dynamometric balances in order to investigate the effects induced by the lack of the shear force components contribution in the pressure measurement system and by the perturbation due to the presence of the skylights on the upper surface

of the roof. As an example of the obtained results, Figure 5 shows the comparison between the overall mean lift force coefficient (C_{Fz}) vs. the exposure angle measured by the dynamometric balances (grey circles) and computed by integrating the pressure distribution on the roof in absence (black triangles) and in presence of skylights (black squares). As it can be seen, skylights, placed on the upper surface of the roof along the roof chord (Figure 4), alter the flow on the upper part of the roof because of their thickness. This produces an underestimation of the overall lift force coefficient obtained by integrating the pressure distribution on the roof.

As previously said, pressure measurements have also been processed in order to highlight the roof sections where the higher peaks of pressure occur not only in terms of mean values but also in terms of extreme values due to turbulence buffeting effects. Thus, mean and peak values of the aerodynamic forces on each section and for each wind exposure angle have been evaluated in order to describe how the overall wind loads are distributed on the different parts of the roof and to identify the more demanding load conditions for the global structure. As an example, the standard deviation of the lift force coefficient vs. the exposure angle on each section of the roof (see Figure 3) is reported in Figure 6. A symmetric behavior with respect to the exposure angle can be observed for the different sections. In particular, for each section, the maximum standard deviation occurs when it is perpendicular to the wind direction and downwind.
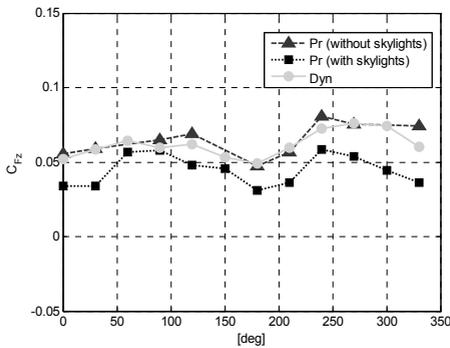
Figure 5: Mean lift force coefficient: force vs. pressure measurements.
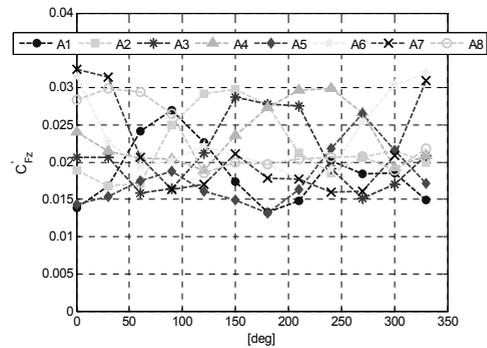
Figure 6: Mean lift force coefficient of each section of the roof.

REFERENCES

Simiu E., Scanlan R. (1996). *Wind effects on Structures*. John Wiley & Sons, New York.

Melbourne W.H. (1995). "The response of large roofs to wind action", Journal of Wind Engineering and Industrial Aerodynamics, 54/55,.325-335.

Majowiecki M. (1998). "Snow and wind experimental analysis in the design of long-span sub-horizontal structures", Journal of Wind Engineering and Industrial Aerodynamics, 74-76, 795-807.

Kawai H., Yoshie R., Wei R., Shimura M. (1999). "Wind-induced response of a large cantilevered roof", Journal of Wind Engineering and Industrial Aerodynamics, 83, 263-275.

Majowiecky M., Vickery B.J. (1992). "Wind Induced Response of a Cable Supported Stadium Roof", Journal of Wind Engineering and Industrial Aerodynamics, 41-44, 1447-1458.

Borri C., Majowiecki M., Spinelli P. (1992). "Wind Response of a Large Tensile Structure: The New Roof of the Olimpic Stadium in Rome", Journal of Wind Engineering and Industrial Aerodynamics, 41-44, 1435-1446.

Biagini P., Borri C., Majowiecki M., Orlando M., Procino L. (2006). "BLWT tests and design loads on the roof of the new Olympic stadium in Piraeus", Journal of Wind Engineering and Industrial Aerodynamics, 94, 293–307.

Belloli M., Rocchi D., Zasso A. (2003). "Wind-structure interaction of a large flexible roof: comparison of wind tunnel-numerical results and full scale measurement", Proc. of ICWE, Lubbock, Texas, USA.

EN 1991-1-4 (2005). "Eurocode 1 – Actions on structures – Part -4: General actions: wind actions".

Aerodynamic behaviour of hyperbolic paraboloid shaped roofs: wind tunnel tests

Fabio Rizzo[1], Piero D'Asdia[2], Massimiliano Lazzari[3]

[1]University "G. D'Annunzio" Chieti-Pescara, Viale Pindaro, 42, Pescara, Italy
e-mail: fabiorizzo79@libero.it
[2]University "G. D'Annunzio" Chieti-Pescara, Viale Pindaro, 42, Pescara, Italy
e-mail: pidasdia@tin.it
[3]University of Padova, Via Marzolo, 9 - 35131 Padova, Italy
e-mail: lazzari@caronte.dic.unipd.it

Keywords: Aerodynamic, hyperbolic paraboloid, wind tunnel

ABSTRACT

The purpose of this research is to evaluate aerodynamic loads on large span hyperbolic paraboloid shaped roofs. This geometrical shape is specific to the design of tension roofs with a cable structure. In this case, however, the roof structure is a rigid body which enables us to evaluate the pressure coefficients for this particular geometrical shape. In the future, attention will also be paid to analysing the pressure coefficients variation that occurs with structural deformation. The parabolic shape selected is often used to build tension structures. These kinds of structures are light and characterized by innovative construction materials and technical elements such as air conditioning, lighting, etc. The design of tension roofs is always striving towards technological and structural innovation in order to build ever lighter structures to cover equally ever larger spans. Tension structures are in line with the new contemporary architectural concept of space, allowing for the construction of large open spaces where the flexibility and the modifiability of the structures in question are the most important prerequisites. They also meet the demand for structures that only need basic planned maintenance and can also withstand seismic pressure too. In Italy, this constructive typology has so far been largely neglected and to a certain extent even ignored by building regulations. In fact no mandatory standards have been set for the design and construction of these structures, except for temporary constructions.

Contact person: Fabio Rizzo University "G. D'Annunzio" Chieti-Pescara, Viale Pindaro, 42, Pescara, Italy
e-mail: fabiorizzo79@libero.it tel. 3200384186

There is also a lack of information about wind action on hyperbolic paraboloid shapes. While there are precise indications for shells, slopes and domes, there are currently no wind regulations for this shape in Italy. No prescriptions are provided in the new CNR-2008 for the calculation of wind action, either. This research followed three consecutive steps: the first one was aimed at developing an optimized procedure of preliminary design for the cable structure; the second one focussed on the study of the wind action on these structures. The third phase of this research is illustrated in "*Aerodynamic behaviour of roofs with hyperbolic paraboloid shapes: P.O.D. and C.F.D. analysis*". The procedure of preliminary design consists in evaluating prefixed cable spans and sags, the minimum values of pretensions and areas of the two series of cables (load bearing and stabilizing) so as to maintain the cable stress within the limit value under the two opposite load configurations: maximum snow load and maximum wind depression. By using the procedure for a set of values of spans and sags, a statistical sample of different roof shapes has been produced (Figure 1 a, b). Having in mind the design of sport arenas, swimming-pools and meeting rooms, we have taken into account another geometrical parameter (in the following Hb) measuring the distance between the roof and the ground floor. This parameter has been added to the span/sag ratio in the experimental tests in the wind tunnel. In fact, the model is built in two different heights. In the second phase of the research, experimental tests were performed in the CRIACIV wind tunnel, in Prato, in order to assess the wind action on tension roofs with a hyperbolic paraboloid shape.
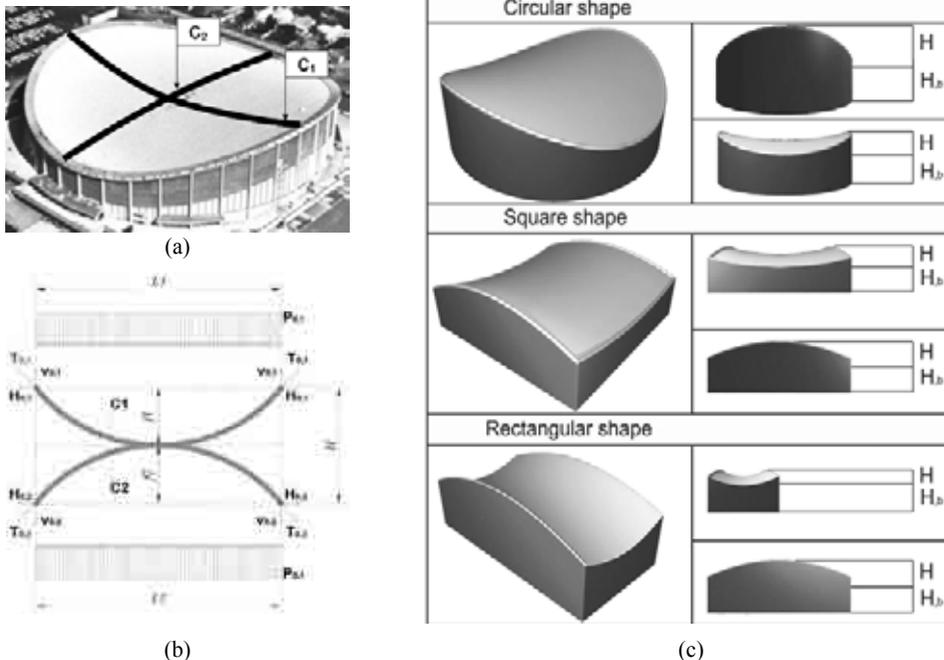
Figure1: Roof Structure: Load bearing cable (C1) and Stabilizing cable (C2) (a), Roof structure: 2D - structural system (b); model shape tested (c).

From the statistical sample of different geometrical shapes under study (about one thousand different configurations), certain configurations were selected to be tested in the wind tunnel in order to highlight their aerodynamic behaviour and calculate the pressure coefficients. Three different building shapes were chosen: square, circular and rectangular shape, i.e. (Figure 1.c) the most common shapes for sport arenas. All wind tunnel wood models were constructed with two different roof heights (sum of the load bearing cable sag and the stabilizing cable sag) obtained by changing the

height of the ground level with an additional base. The ratio between the two sags of the two sets of cables is 2. The stabilizing cable sag is twice the one of the bearing cable sag. This ratio provides optimized stress on the cables under extreme loads.

   Some pictures of wind tunnel models are presented below (Figure 2). All models have about 150÷230 pressure take-offs that are distributed across the roofs and over the four lateral surfaces. The dimensions of twelve of the models are equal to 80 cm (L1, L2) whereas the dimensions of only one are equal to half this size (40 cm) in order to assess the influence of the model scale factor on vortex-shedding. The wind tunnel test frequency of measure is equal to 252 Hz and the time step is equal to 30 seconds; for each model the measures have been obtained for 16 angles of wind incidence.

(a)

(b)

(b)

(c)

(d)

(e)

(f)

(g)
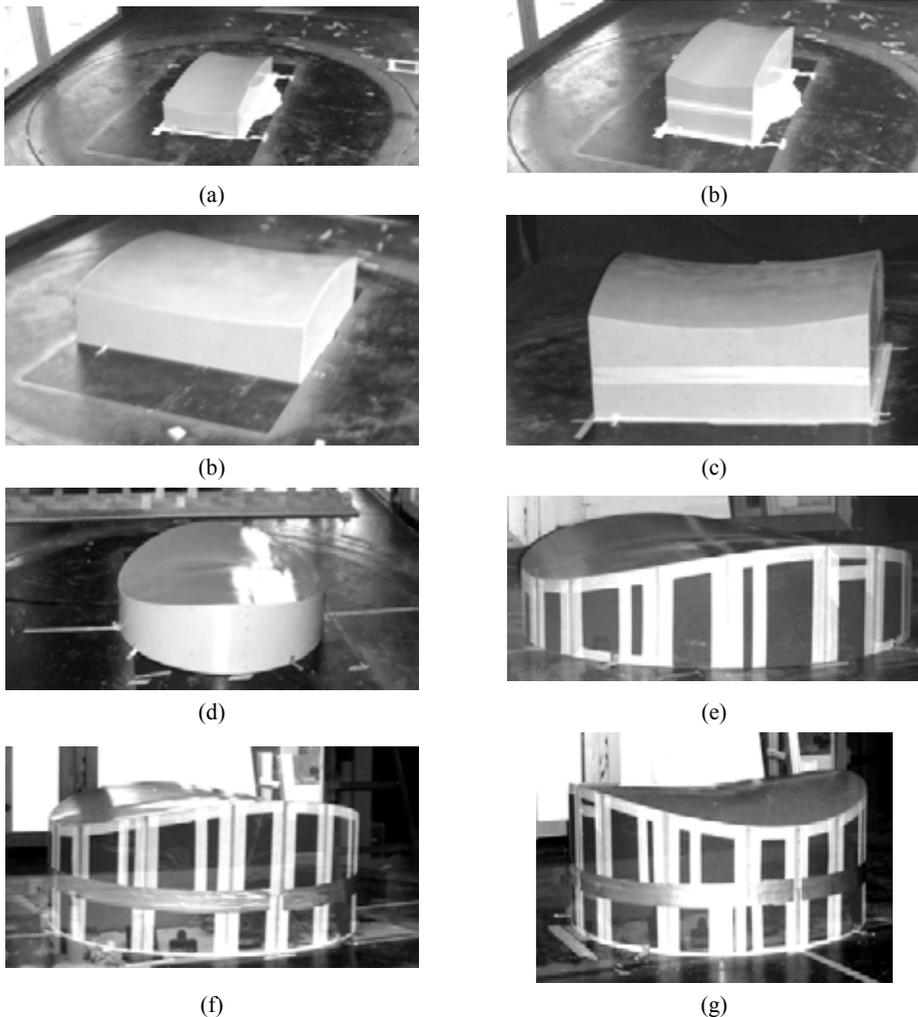
Figure 2: Wind tunnel tests: some of the different geometrical configurations tested. Rectangular (a, b) and square (c, d) models with two different geometrical configurations; Circular models (d, e, f, g) with two different geometrical configurations and two different types of roughness.

   The boundary layers are developed with a city-configuration in the wind tunnel. Some pictures of

the tests are shown below. The roughness of the lateral surface in the circular model was altered in order to raise the Reynolds number and avoid the range between the subcritical and the critical zone of the drag coefficient curve.

(a)

(b)
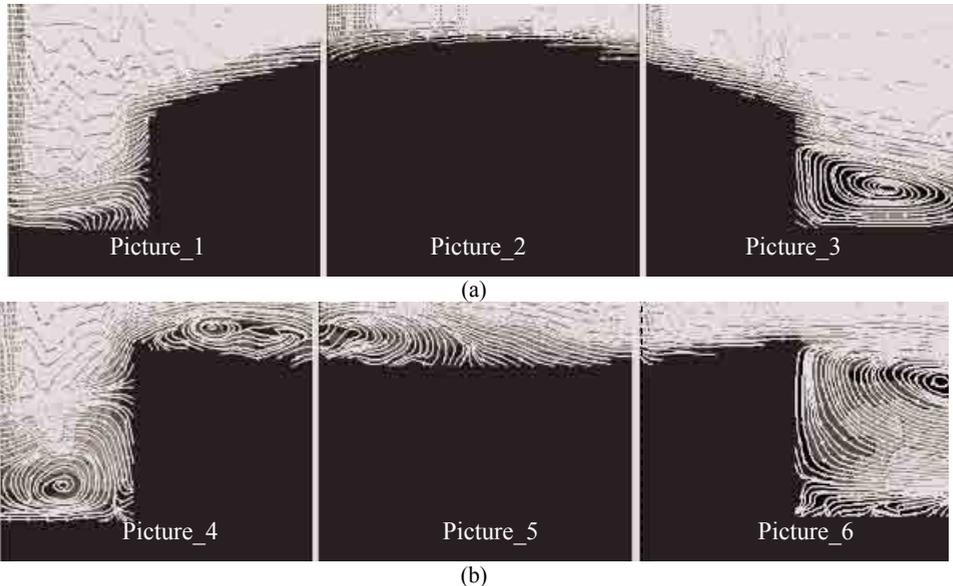
Figure 3: Wind tunnel tests: P.I.V. analysis. 0° (a) and 90° (b)Streamlines – three pictures for each wind direction angle

However, two tests with a low Reynolds number were also carried out in order to evaluate the influence of this variable. In addition to aerodynamic tests and in order to obtain pressure coefficients, P.I.V. (Particle image velocimetry) tests were also executed. Pictures of vortex shading (Figure 3, a, b) are used to compare with the C.F.D. data. For each test a map of pressure coefficients has been plotted (mean, min and max values) and has been compared to the different aerodynamic behaviour between different plan shape, roof curvature and height. Functions in order to simplify the roof design are obtained with experimental data. So, it is possible to evaluate the wind action for a preliminary design with simple functions that describe the three dimensional behaviour of the structure. The third phase of this research is illustrated in "*Aerodynamic behaviour hyperbolic paraboloid shaped roofs: P.O.D. and C.F.D. analysis*".

ACKNOWLEDGEMENTS

REFERENCES

F.Rizzo, P. D'Asdia, M. Lazzari, F. Fattor, "Aerodynamic and non linear analysis of cables nets-Part I: design aspects" Proceeding of 11° INVENTO 2008, Cefalù, Italy, 2008. (in Italian).
F.Rizzo, P. D'Asdia, L. Procino, F. Fattor, "Aerodynamic and non linear analysis of cables nets-Part II: wind tunnel tests" Proceeding of 11° INVENTO 2008, Cefalù, Italy, 2008. (in Italian)

Aerodynamic behaviour of hyperbolic paraboloid shaped roofs: POD and CFD analysis

Fabio Rizzo[1], Piero D'Asdia[1], Massimiliano Lazzari[3], Giuseppe Olivato[4]

[1]*University "G. D'Annunzio" Chieti-Pescara, viale Pindaro, 42, Pescara, Italy*
e-mail: fabiorizzo79@libero.it
[2]*University "G. D'Annunzio" Chieti-Pescara, viale Pindaro, 42, Pescara, Italy*
e-mail: pidasdia@tin.it
[3]*University of Padova, Via Marzolo, 9 - 35131 Padova, Italy*
e-mail: lazzari@dic.unipd.it
[4]*IUAV, Dorsoduro 2206 – 30123 Venice, Italy*
e-mail: olivato@iuav.it

ABSTRACT

Referring to the previous paper "*Aerodynamic behaviour hyperbolic paraboloid shaped roofs: wind tunnel tests"* the aim of this research has been to investigate the aerodynamic behaviour of structures tested in a wind tunnel, with Computational Fluid Dynamic (CFD) analysis and with the Proper Orthogonal Decomposition (POD.) technique. The purpose of CFD analysis is to describe vortex shading and to compare data in order to identify characteristics for each different geometrical shape considered. Analysis with the POD. technique aims instead to describe the action on hyperbolic paraboloid surfaces of randomly fluctuating wind pressure fields.

CFD analyses were evaluated to simulate a life size configuration. Therefore a logarithmic speed profile was chosen, derived from the profile of the wind tunnel speed but also in line with Italian building regulations (z_0, reference height is equal to 0.05 metres and speed value of 27m/s for height equal to 10 meters). Model sizes are in metres and have a span of 80m (structures with square plan), or 80m and 40m (structures with rectangular plain). The diameter of structures with a circular plain is equal to 80m. The fluid-space size around the structures is square and equal to a span of 400 m and a height of 80m.

The method chosen to discretize the spatial domain is the Finite volume method (FVM). So, continuous fluid has been discretized into variable size cells. The mesh is regular and size cells

Contact person: Fabio Rizzo University "G. D'Annunzio" Chieti-Pescara, Viale Pindaro, 42, Pescara, Italy
e-mail: fabiorizzo79@libero.it tel. 3200384186

change from a spacing value of 0.8 (near to model) to one of 8 in the extreme zones of the model.

Turbulent flow produces fluid interaction at a large range of length scales. This problem means that calculations are needed to attempt to take this into account with the modification of the Navier-Stokes equations. Failure in this procedure may result in an unsteady simulation. When attempting to solve the turbulence model, a trade-off between accuracy and speed of computation is present. So, a balance between solution accuracy and the computational power is required. In accordance with what has previously been stated, the Turbulence models chosen are Reynolds-averaged Navier-Stokes equations (RANS formulation). Two broad approaches of RANS models were used, the first being the k-ω model, based on the Boussinesq hypothesis, and which solves transport equations for the determination of the turbulent kinetic energy and dissipation; the second is the Reynolds stress model (RSM), which solves transport equations for the Reynolds stresses and is much more costly in terms of CPU effort.

(a)   (b)

(c)   (d)

(e)   (f)

(g)   (h)
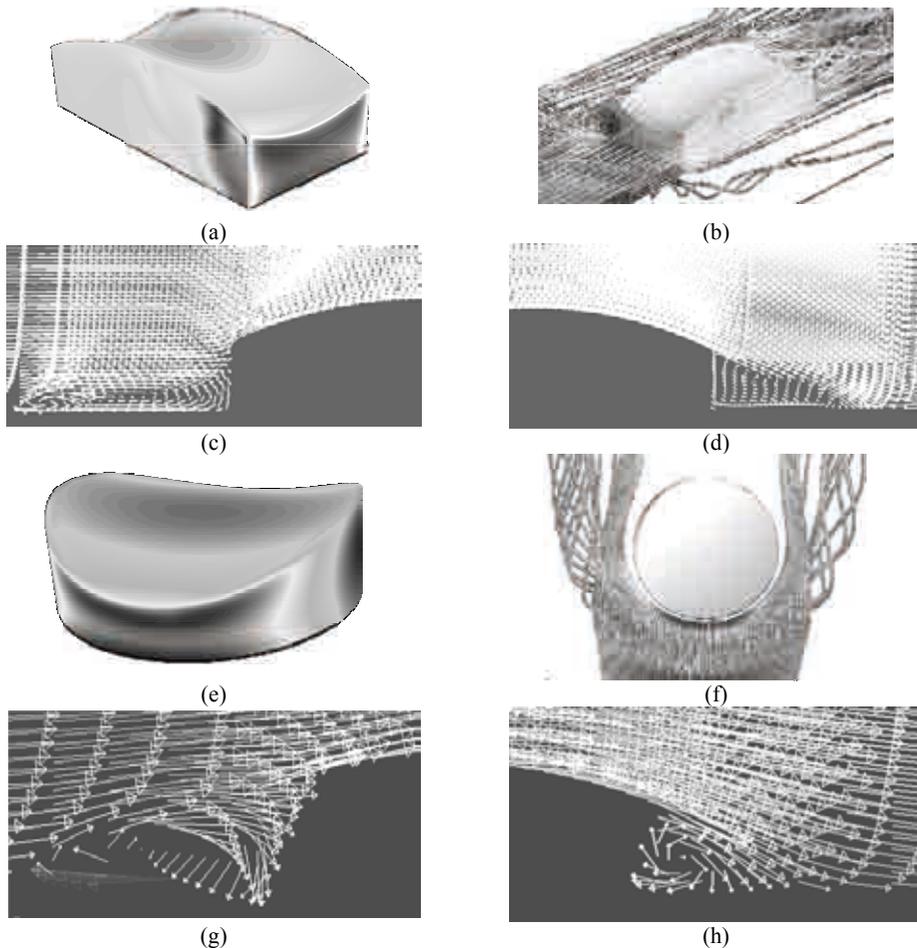
Figure 1: Examples of CFD analyses data: pressure coefficients variation of structures with rectangular (a) an circular (e) plain, streamlines of structures with rectangular (b) an circular (f) and vortex shading in the middle section of building with wind direction angle equal to 0°, rectangular (c,d) and circular (g, h).

Interesting effects are shown, as for instance the different behaviour between structures with square and rectangular plans and structures with a circular plan. An analysis of the data from a structures with a rectangular and circular plan, with a wind direction angle equal to 0°, is presented as an example in Figure 1. The analysis with the POD technique describes the action of randomly fluctuating wind pressure fields. POD is a powerful and elegant method of data analysis aimed at obtaining low-dimensional approximated description of high dimensional process. This research presents an application of the POD technique in the evaluation of properties and in the prediction of the responses to wind forces acting on hyperbolic paraboloid shaped roofs.

The POD technique is a vector space transform, a change of coordinate system, often used to reduce multidimensional data sets into lower dimensions for quasi-steady analyses. Depending on the field of application, it is also named the discrete Karhunen-Loève transform (KLT), the Hotelling transform or, as the original theory, principal component analysis (PCA). PCA involves the calculation of the eigenvalue decomposition of a data covariance matrix or singular value decomposition of a data matrix, ordinarily after mean centering the data for each attribute, Figure 2, 3.

An interesting feature of the POD analysis is the possibility to set up a resonance alert criteria for the double curve roofs. It will be shown by power spectral analysis that every proper mode includes all the frequencies stored in the original wind field. So some high correlations between the proper modes and the free vibrations suggest the resonance sensitivity of the structure. It is also possible to relate the most energetic modes to aerodynamic phenomena such as incident wind turbulence and vortex shedding.

(a)

(b)

(c)

(d)
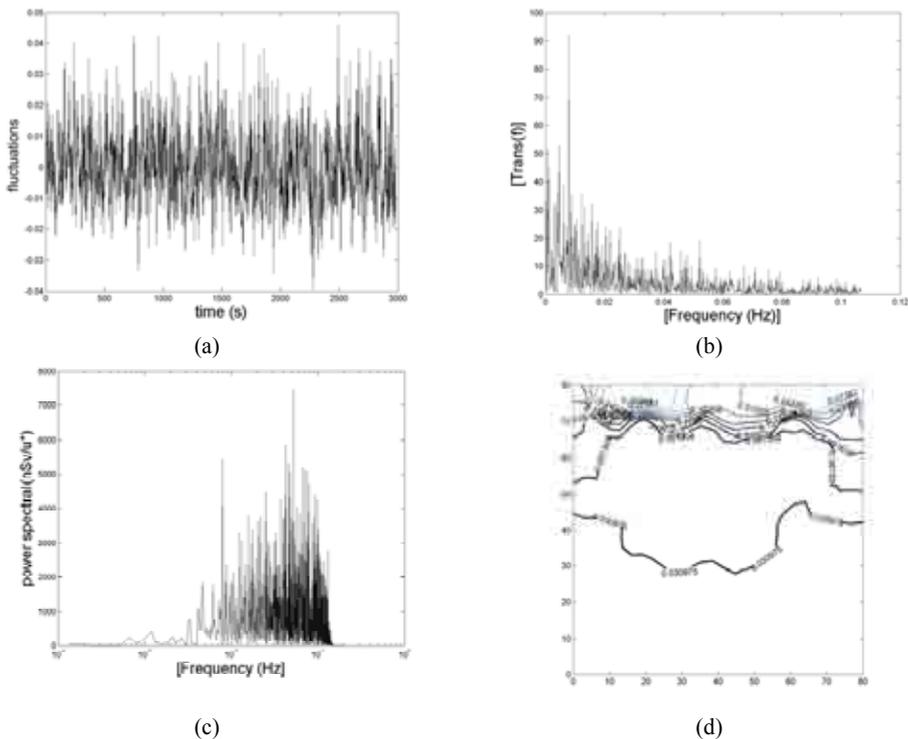
Figure 2: Referring to mode 1, wind direction angle equal to 0° and square plan structure (test p.2) – wind pressure fields calculated with POD. technique: fluctuations of pressure fields with (a), Fourier transform of the frequency (b), Power spectral densities (c), 1st mode shape (d).
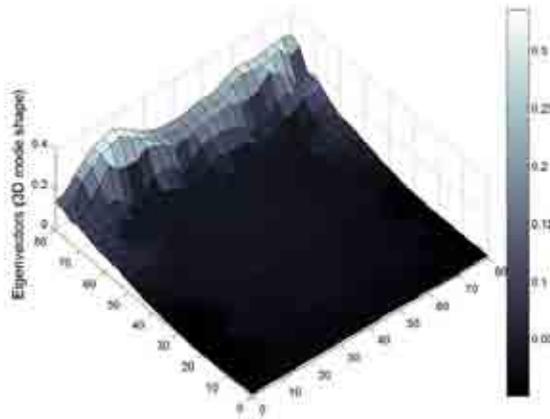
Figure 3: Referring to mode 1, wind direction angle equal to 0° and square plain structure (test p.2) – wind pressure fields processing with POD. technique: Eigen vectors three dimensional variation.

CFD and POD analysis complete the research by highlighting the complex three-dimensional behaviour of structures with hyperbolic paraboloid roofs. In particular, vortex shading is asymmetrical referring to the building's axis of symmetry, which is related to the different roof curvatures. So, it is impossible to simplify structural analyses with a simple model. The lack of regulations, moreover, makes it difficult to design with these shapes. It is important to remember that this research considers roofs as a rigid body and pressure coefficients have been evaluated for this specific configuration even if tension structures are deforming structures. However, frequently, shape variation under load application, as for example wind action or the weight of snow, does not significantly modify the distribution of roof pressure coefficients. Our future perspective is to study the dynamic and vibration behaviour of tension structures under wind action with new experimental designs. New shapes, for instance elliptical plans, will also be tested in a wind tunnel.

ACKNOWLEDGEMENTS

REFERENCES

Jeong S. H., Bienkiewicz B. (1997). Application of autoregressive modeling in proper orthogonal decomposition of building wind pressure. Journal of Wind Engineering and Industrial Aerodynamics, n.69-71, pp. 685-695.

Katsumura A., Tamura Y., Nakamura O. (2007). Universal wind load distribution simultaneously reproducing largest load effects in all subject members on large-span cantilevered roof. Journal of Wind Engineering and Industrial Aerodynamics, n.95, pp. 1145-1165.

Kho S., Baker C., Hoxey R. (2002). POD/ARMA reconstruction of the surface pressure field around a low rise structure. Journal of Wind Engineering and Industrial Aerodynamics, n.90, pp. 1831-1842.

Ruan D., He H., Castanon D. A., Mehta K. C. (2006). Normalized proper orthogonal decomposition (NPOD) for building pressure data compression. Journal of Wind Engineering and Industrial Aerodynamics, n.94, pp. 447-461.

Sengupta T. K., Dey S. (2004). Proper Orthogonal Decomposition of Direct Numerical Simulation Data of By-Pass Transition. Computer and Structures, n. 82, pp. 2693-2703.

Tamura Y., Suganuma S., Kikuchi H., Hibi K. (1999). Proper Orthogonal Decomposition of Random Wind Pressure Field. Journal of Fluids and Structures, n.13, pp. 1069-1095.

Bruno L. (2000). Aerodynamic behavior of large span bridge. Dottorato di Ricerca in Ingegneria delle Strutture e in Meccanica dei fluidi, Politecnico di Torino.

STATIC AND DYNAMIC WIND LOADS
AND COMBINED EFFECTS

Wind loads on stand-off photovoltaic systems

C.P.W. Geurts, R.D.J.M. Steenbergen

chris.geurts@tno.nl – PO Box 49, NL 2600 AA, Delft, the Netherlands

raphael.steenbergen@tno.nl – PO Box 49, NL 2600 AA, Delft, the Netherlands

Keywords: Wind loads, Solar energy, pitched roofs

ABSTRACT

Solar energy systems are becoming increasingly popular. A large potential for these systems is found on buildings, in particular on roofs. For existing buildings with pitched roofs, stand-off systems, which can be applied as retrofit solutions, are frequently applied. Wind loads for such systems are not found from current codes and standards. A full scale and wind tunnel experiment was carried out in the EU 6th Framework project EUR ACTIVE ROOFer. The full scale experiment is presented here. Results are now available which can be used to draft guidance on the installation of these stand-off systems.

INTRODUCTION

There is a considerable growth in solar energy products mounted on buildings. Roofs, both existing and new, have a great potential in supporting these products. For pitched roofs on existing buildings, mainly stand-off systems are applied, to support photovoltaic (PV) panels.

Stand-off systems are mounted above the existing roof covering, such as roofing tiles. The wind loads will be generated by the pressure difference between the top surface of the module and the underside of the module. This pressure difference is influenced by the shape and dimensions of both panel and roof, by the distance between roof and panels, and by the presence of gaps between the panels installed. Some general guidance on wind loads on stand-off PV systems is given in recent guidelines, such as NVN 7250 and BRE Digest 489. These data are based on very limited measurements from the 1970's and an interpretation of data given in current building codes and is likely to be appropriate for a limited range of roof forms. These data are also assumed to be conservative, being uneconomic in some cases.

In order to provide more reliable wind loading data, both a full scale and a wind tunnel test have been set up to investigate these pressure differences. This contribution describes the full scale test conducted including the results obtained.

Contact person: C.P.W. Geurts, TNO Built environment and Geosciences, PO Box 49, Delft, The Netherlands.
T: +31 152763162, F: +311527623016 E-mail chris.geurts@tno.nl

FULL SCALE EXPERIMENT

A full-scale experiment ran between October 2007 and August 2008. For this experiment two 'dummy' PV modules were mounted on a house with a hipped roof in The Netherlands. The fetch to the west (the prevailing wind direction) is generally flat and open with few obstacles upwind. The wind pressures were measured on the top and bottom surfaces of this dummy PV panel along with the wind speed and direction. Figure 1 gives a view of the house.

Figure 1: View of the experiment; view from the west.

The experiment described here consists of measurements of the wind pressures on two wooden panels, representing size and dimensions of solar panels. The length of these panels is 1.60 m; the width is 0.80 m and the thickness of the wood in the panels is 18 mm. This is more than the size of glass panels, used for PV. For the wind loading, this is of minor importance. Panel 1 was fixed to the slope of the roof at the Western side (figure 2). A distance is kept between the tiles and the panel using steel hooks. Panel 2 was attached to the Southern slope of the roof as shown in Fig. 3.

During the measurements, wind induced pressures have been determined, simultaneously at the top and the bottom of the wooden panels. Differential pressure transducers, of the type Honeywell 163PC01D36, have been applied to measure the difference between the pressure on the location of the pressure tap and a reference pressure, obtained at a reference pressure location at ground level. A total of 12 pressure taps have been used, each connected to a transducer. The pressure is transposed from the pressure tap in the panels to the transducers through plastic tubing, with internal diameter of 10 mm. A calibration system is installed to measure a zero signal after every run.

The measurement locations are situated in the middle of the width of the panel (Figs. 2 and 3), three positions on the top surface of the panel, and three at the bottom surface. Simultaneous measurements of pressures at the top and the bottom of the panels are made, together with measurements of the wind speed and wind direction on a meteorological mast.

The wind speed and wind direction are measured on a mast (see Fig. 1). The wind speed and wind direction are measured with a cup anemometer and a directional vane at 10 metres height above the field level. Additional to the pressure measurement at ground level, a static pressure probe has been mounted on the meteorological tower. The data are gathered in runs of 10 minutes length. Both the wind data, and the wind induced pressures are determined with a sampling rate of 10 Hz.

Figure 2 (left) Panel 1, located on southern roof pitch; Figure 3 (right) Panel 2, located on western roof pitch. The gray boxes under the gutter contain the pressure transducers. Pressure taps are present at the vertical centre line, at ¼, ½ and ¾ of the height of the panel, both on top and on the bottom.

The measurements started in September 2007 and lasted until August 2008. Average values of both wind and pressures of every 10 minute runs are saved. When the mean wind speed of this 10 minute-period exceeds a preset threshold, the rough data are saved for further analysis. This threshold has been set to 7 m/s, low enough to gather a sufficient number of data. All data are grouped in wind direction intervals. Due to malfunctioning of the wind vane, the data measured on site have not been used. Instead, during the analysis, the directional data of a nearby meteorological station have been used. This station provides average wind directions with 6 hours intervals. These directions are given in 10-degree intervals.

RESULTS

The data have been analysed stepwise. After removing suspicious data records, all time series with an average wind speed over 7 m/s have been classified by wind direction, with 10 degree increments. For all wind directions with more than 32 data series, extreme value analyses have been done for the individual taps, and for combinations of taps. These combinations are: differential pressures per location; the overall pressure on top, or on the bottom; and the overall pressure difference per panel. To distinguish in wind loading data with different loaded areas, a moving average window of different lengths was applied. For the loading of a full panel, a moving average of 1 second has been applied. In figure 4, the differential pressure coefficients, which are found after analysis of the data where a moving average window of 1 seconds is applied, are given.

Values for the differential pressures for these panels are not available for all wind directions. Panel 1 misses more wind directions, because of some instrumental errors in part of the data.

The minimum values are only slightly varying with wind direction, with a maximum uplift value (negative value for Cp) of about 0,55. The force directed towards the roof is less relevant for design, and seems to scatter more. The maximum value is about 0,40. A wind direction of 330 degrees corresponds to wind normal to the Northern façade. All these Cp values have been related to the wind at 10 metres height, and have been obtained by using Cook-Mayne analysis procedures. Resulting pressure differences for other averaging times have also been analysed and will be discussed in a full paper.
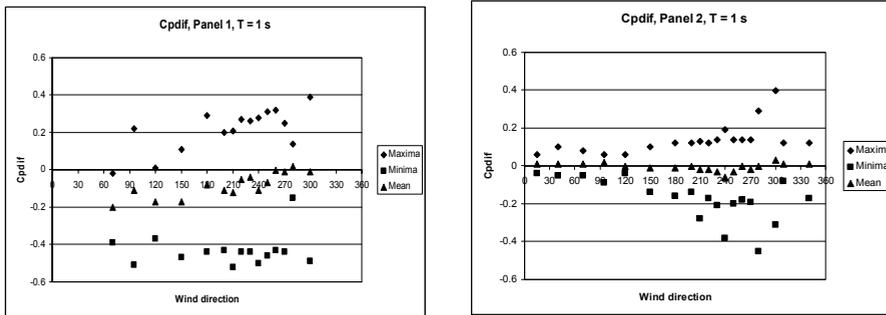
Figure 4: Differential pressures over both panels; negative values represent uplift loads; positive values represent forces directed to the roof.

DISCUSSION

The data measured may be applied in the design of roof fixings of stand off systems for individual solar panels. However, this type of structures is frequently used to mount multiple solar energy panels. The wind loads on these arrays may be different from the loads on individual elements.

Secondly, the effect of distance between roof and solar energy panel has not been investigated in full scale. Wind tunnel tests, performed on a model of the same house (Blackmore et al, 2008), indicate that within the range of 25 to 300 mm, there is no relevant effect of this distance to the loads.

ACKNOWLEDGEMENT

REFERENCES

NEN, 2007, NVN 7250, Solar energy systems - Integration in roofs and facades - Building aspects
Blackmore, 2004, BRE Digest 489, Wind loads on roof-based photovoltaic systems
Blackmore et al, 2008, Paper presented at the WES Conference

Stochastic wind response of SDoF structures with non linear viscous dampers

Claudio Floris

Dept. of Structural Engineering, Politecnico di Milano, Milano, Italy, floris@stru.polimi.it

Keywords: wind excitation, non linear viscous devices, stochastic dynamics, stochastic averaging.

ABSTRACT

Introduction

Nowadays, the use of damping devices for reducing or suppressing the vibrations caused by wind has become very frequent (e.g. see Xu et al., 1992, Kareem, 1997). To quote a notable case, the Millenium bridge in London (UK), exhibited unacceptable flexural and torsional vibrations, which have been reduced by adding viscous dampers at the supports.

In engineering practice it is common to account for these devices by increasing the damping ratio in the linear equations of motion. However, many devices for suppressing vibrations have a pronounced non linear behavior. Among these, there are the friction devices and the devices that profit from the movement of a semifluid material, which goes from a cell to another. Attention is here focused on the latter.

The force-displacement and stress-strain relationships for a solid material in the uniaxial state of stress and for a Newtonian fluid are, respectively

$$F = k \cdot d \quad \text{or} \quad \sigma_{11} = E\varepsilon_{11}, \qquad F(t) = \eta_d \cdot \dot{d} \quad \text{or} \quad \sigma_{11} = \eta\dot{\varepsilon}_{11} \tag{1, 2}.$$

Some materials that are used in the damping devices are neither a perfect solid or a perfect fluid so that the suitable force-displacement relationship is

$$F(t) = C_d \cdot \left|\dot{d}\right|^{\alpha} \text{sgn}(\dot{d}) \tag{3},$$

where sgn denotes the sign function [sgn(a) = −1, 0, +1 when a is negative, zero, or positive]. The exponent α falls in the interval $(0, 1)$. When $\alpha = 0$ we have the pure (Coulombian) friction.

The exact determination of the dynamics of an oscillator with a damping device governed by Eq. (3) subjected to a stochastic force is not possible. Two approximate methods will be presented in next section that take the non-linearity into account.

Contact person: Dept. of Structural Engineering, Politecnico di Milano, Piazza Leonardo da Vinci 32, 20133 Milano; phone 390223994382; fax 390223994220.
E-mail floris@stru.polimi.it

Formulation

With reference to wind excitation, the motion of a SDoF oscillator with a non linear viscous device is governed by the following equation

$$\ddot{X}(t) + 2\zeta_0\omega_0\dot{X}(t) + \xi_d \left|\dot{X}(t)\right|^\alpha \text{sgn}(\dot{X}) + \omega_0^2 X(t) = \gamma\overline{U}^2 + bU(t) \tag{4}$$

where $\overline{U}$ is mean wind speed blowing in x direction, $U(t)$ is wind turbulence in the same direction. The other symbols mean: $\xi_d = C_d/M$, $\gamma = 1/2\,\rho AC_p/M$, $b = 2\gamma\overline{U}$, being M the structural mass, ρ the air density, and C_p the aerodynamic coefficient. Moreover, ω_0 is the structural pulsation, and ζ_0 the ratio of critical damping. For simplicity's sake, the square of $U(t)$ is neglected.

For general consent $U(t)$ is assumed to be a zero mean stationary colored Gaussian random process. Notwithstanding the Gaussianity of the input, exact methods for finding the response of (4) in a statistical sense do not exist. The simplest approximate method is the stochastic equivalent linearization (EL), which replaces the non linear system (4) by an equivalent linear one so that the response is easily found. This method was used by Di Paola and Navarra (2005) for earthquake excitation, and by Rüdinger (2006) for white noise excitation. The EL method gives a Gaussian response to a Gaussian exitation, while the true response of a non linear system is not Gaussian. Thus, it is important to ascertain the validity of the EL method.

To do that, and to seize the response non-Gaussianity, Monte Carlo Simulation (MC) and approximate analytical method are available. The last are the moment equation approach of Itô's stochastic calculus (ME), the stochastic averaging (STA), and the path integral solution (PIS). Now, a brief presentation of the first two methods will be given, while for the last method see Barone et al. (2007). Both ME and STA methods require that the excitation is a Gaussian broad band process, which might be approximated by a white noise.

However, for applying ME, a narrow band process may be approximated by the output of a linear filter excited by a Gaussian white noise. The colored process $U(t)$ is represented by the output $\hat{U}$ (or by $\dot{\hat{U}}$) of a second order linear filter such as (Benfratello et al. 1996, Floris et al. 2001)

$$\ddot{\hat{U}}(t) + 2\zeta_f\omega_f\dot{\hat{U}}(t) + \omega_f^2\hat{U}(t) = \sqrt{\pi w_f}\,W(t) \tag{5}$$

where $W(t)$ is a zero mean stationary Gaussian white noise with unit PSD. The filter parameters ζ_f, ω_f, w_f must be selected in such a way that the PSD of $\hat{U}(t)$ as given by Eq. (5) matches the actual turbulence PSD.

Then, the augmented system of Eqs. (4, 5) is recast in incremental form by introducing the four state variables $z_1 = X$, $z_2 = \dot{X}$, $z_3 = \hat{U}$, $z_4 = \dot{\hat{U}}$, and in this way four Itô's stochastic differential equations are obtained (for the principles of Itô's stochastic calculus the reader may refer to Di Paola, 1993, and to Soong and Grigoriu, 1993). By applying Itô's differential rule to the non-anticipating function $\phi = z_1^p z_2^q z_3^r z_4^s$, the differential equations ruling the evolution of the response moments are written down. In symbolic form they read as:

$$\dot{m}_{pqrs} = p\,m_{p-1,q+1rs} + q\left\{-\beta_0 m_{pqrs} - \xi_d E\left[\left|z_2\right|^\alpha z_1^p z_2^{q-1} z_3^r z_4^s \text{sgn}(z_2)\right] - \omega_0^2 m_{p+1,q-1rs} + \gamma\overline{U}^2\cdot\right.$$

$$\left. m_{p,q-1rs} + b\,m_{p,q-1r+1,s}\right\} + r\,m_{p,q,r-1,s+1} + s\left(-\beta_f m_{pqrs} - \omega_f^2 m_{pqr+1,s-1}\right) + \frac{\pi}{2}w_f m_{pqrs-2} \tag{6}$$

where $\beta_0 = 2\zeta_0\omega_0$, $\beta_f = 2\zeta_f\omega_f$. Eq. (6) contains the expectation $E\left[\left|z_2\right|^\alpha z_1^p z_2^{q-1} z_3^r z_4^s \operatorname{sgn}(z_2)\right]$, whose evaluation requires the knowledge of the joint PDF of the response. As was done by Fatica and Floris (2002) for the case of the oscillator with pure friction, this can be expressed by a modified truncated Gram-Charlier series, that is

$$p(u_1 u_2 u_3 u_4) =$$

$$= \sum_{i=0}^{i+j+k+l=N} \sum_{j=0} \sum_{k=0} \sum_{l=0} \frac{E\left[H_i(u_1)H_j(u_2)H_k(u_3)H_l(u_4)\right]}{i!\,j!\,k!\,l!} \frac{\mathrm{d}^i p_0(u_1)}{\mathrm{d}u_1^i} \frac{\mathrm{d}^j p_0(u_2)}{\mathrm{d}u_2^j} \frac{\mathrm{d}^k p_0(u_3)}{\mathrm{d}u_3^k} \frac{\mathrm{d}^l p_0(u_4)}{\mathrm{d}u_4^l} \quad (7)$$

where $H_i(x)$ is the Hermite polynomial of order i in the variable x, the numerator of the fraction can be named Hermite moment, $u_i = z_i/\sigma_{z_i}$, and p_0 is the standard Gaussian univariate PDF. $N = 4$, that is a closure at the fourth order, should be enough for the present problem. Since EL and STA perform well, this method of solution is not pursued further here.

The classic (first order) stochastic averaging method is considered here (e.g. see the Chap. 6 of the textbook by Soong and Grigoriu). The stochastic averaging was applied to wind response probably for the first time by Lin and Holmes (1978) in their pioneer work. More recently, it has been applied to a wind problem by Krenk and Nielsen (1999).

In order to apply the stochastic averaging method to the present problem, Eq. (4) is recast as

$$\ddot{X}(t) + \omega_0^2 X(t) = -\zeta_0\left[2\omega_0\dot{X}(t) + \bar{\xi}_d\left|\dot{X}(t)\right|^\alpha \operatorname{sgn}(\dot{X}) + \bar{\gamma}\overline{U}^2\right] + bU(t) = -\zeta_0\,h(\dot{X}) + F(t) \quad (8),$$

where $\bar{\xi}_d = \xi_d/\zeta_0$, $\bar{\gamma} = \gamma/\zeta_0$, $F(t) = bU(t)$. With the variable transformation $X(t) = A(t)\cos\varphi(t)$, $\dot{X}(t) = -A(t)\omega_0\sin\varphi(t)$, in which $\varphi(t) = \omega_0 t + \Psi(t)$, the averaged equations of the method are

$$\dot{A}(t) = \frac{\zeta_0^2}{\omega_0}\,h_s(A) + \frac{\zeta_0^2\,\pi S_{FF}(\omega_0)}{2\omega_0^2 A} + \frac{\zeta_0\sqrt{\pi S_{FF}(\omega_0)}}{\omega_0} W_1(t) \quad \dot{\Psi}(t) = \frac{\zeta_0^2}{\omega_0 A}\,h_c(A) + \frac{\zeta_0\sqrt{\pi S_{FF}(\omega_0)}}{\omega_0} W_2(t)$$

$$(9, 10)$$

In Eqs. (9, 10) W_1 and W_2 are uncorrelated unit strength Gaussian white noises, the PSD of $F(t)$ is calculated in the structural frequency ω_0, being $S_{FF}(\omega) = b^2 S_{UU}(\omega)$. The function $h_s(A)$ is

$$h_s(A) = \frac{1}{2\pi}\int_0^{2\pi} h\left(A\cos\varphi, -A\omega_0\sin\varphi\right)\cos\varphi\,\mathrm{d}\varphi =$$

$$= \frac{1}{2\pi}\int_0^{2\pi}\left[-2\omega_0^2 A\sin^2\varphi - \bar{\xi}_d\omega_0^\alpha|A|^\alpha\sin^{\alpha+1}\varphi\,\operatorname{sgn}(A\sin\varphi) + \bar{\gamma}\overline{U}^2\sin\varphi\right]\mathrm{d}\varphi$$

$$(11).$$

It must be stressed that: (1) the second addendum in the integral (11) must be numerically evaluated as $\alpha + 1$ is not an integer number; (2) clearly, the integral of the third addendum vanishes. As regards the point (2), this fact is a feature of the first order stochastic averaging method, which is not capable of accounting for an excitation with non zero mean. However, in the present case the non-linearity is confined to the damping so that the effect of $\bar{\gamma}\overline{U}^2$ can be considered apart.

The FPK equations associated with Eqs. (9, 10) respectively are easily solvable giving that the PDF of Ψ is uniform between 0 and 2π, and

$$p_A(a) = q\, a \exp\left[\frac{2\omega_0}{\pi S_{FF}(\omega_0)} \int_0^a h_s(u)\, \mathrm{d}u \right] \qquad p_{X\dot{X}}(x,\dot{x}) = \frac{1}{2\pi a}\, p_A(a) \qquad (12, 13).$$

where q is a normalization constant, and $a = \left(x^2 + \dot{x}^2/\omega_0^2\right)^{1/2}$. Eqs. (12, 13) allow the computation of the second order statistics of the response. Since $\gamma \overline{U}^2$ is dropped in Eq. (8), these statistics refer to the oscillations around the mean value. Once the second order statistics are known, it is necessary to determine the largest value statistics, which can be obtained only approximately.

Analyses

Suitable computer programs are written for the three methods that are compared, MC, EL, and STA, being the results of MC the reference for evaluating the performance of the other methods. The standard deviations σ_X, $\sigma_{\dot{X}}$ and the largest values average $E\left[\max X | T\right]$ with $T = 40\ s$ are computed for two couples of values of the parameters α and ξ_d by varying $\overline{U}$. Changing the value of $\overline{U}$, the PSD of the turbulence $S_{UU}(\omega)$ is changed accordingly. The latter quantity is expressed by the modified Kaimal's spectrum (Simiu and Scanlan 1996).

The EL method performs very well as regards the standard deviations, while even using Vanmarcke's largest value distribution $E[\max X | T]$ is overestimated. On the contrary, STA method has a good performance for $E[\max X | T]$.

REFERENCES

Barone G., Navarra G., Pirrotta A. (2007). "Stochastic dynamics of linear structures with non linear damper devices (PIS method)". *Computational Stochastic Mechanics*, Deodatis G. and Spanos P.D. editors, Millpress, Rotterdam, 57-64.

Benfratello S., Falsone G., Muscolino G. (1996). "Influence of the quadratic term in the along-wind stochastic response of SDOF structures". *Engng. Struct.*, 18, 685-695.

Di Paola M. (1993). "Stochastic differential calculus". In *Dynamic Motion Chaotic and Stochastic Behaviour*, Casciati F. editor, Springer-Verlag, Wien, 29-92.

Di Paola M., Navarra G. (2005). "Aspetti di dinamica dei ponti", in *Nuovi Orientamenti per la Progettazione di Ponti e Viadotti*, Arici M. and Siviero E. editors, Flaccovio, Palermo, 231-241 (in Italian).

Fatica G., Floris C. (2002). "Random vibration of Coulomb oscillators subjected to support motion with a non-Gaussian moment closure method". *Mech. Struct. & Mach.*, **30**(3), 381-410.

Floris C., Pastorino M., Sandrelli M. (2001). "Stochastic along-wind response of point-like structures". *J. Wind Engng. Ind. Aerod.*, **89**(2), 165-185.

Kareem A. (1997). "Modelling of base-isolated buildings with passive dampers under winds". *J. Wind Engng. Ind. Aerod.*, **72**, 323-333.

Krenk S., Nielsen S.R.K. (1999). "Energy balanced double oscillator model for vortex-induced vibrations". *ASCE J. Engng. Mech.*, **125**(3), 263-271.

Lin Y.K., Holmes P.J. (1978). "Stochastic analysis of wind-loaded structures". *ASCE J. Engng. Mech. Div.*, **104**(2), 421-440.

Rüdinger F. (2006). "Optimal vibration absorber with nonlinear viscous power law damping and white noise excitation" *ASCE J. Engng. Mech.*, **132**(1), 46-53.

Simiu E., Scanlan R.H. (1996). *Wind Effects on Structures*. 3rd edition, John Wiley, New York (NY).

Soong T.T., Grigoriu M. (1993). *Random Vibration of Mechanical and Structural Systems*. Prentice Hall, Englewood Cliffs (NJ).

Xu Y.L., Samali B., Kwok, K.C.S. (1992). "Control of along-wind response of structures by mass and liquid dampers". *ASCE J. Engng. Mech.*, **118**(1), 20-39.

Wind action according to the Brazilian Code: a case study

1st A.M.Wahrhaftig, 2nd R.M.L.R.F. Brasil

Department of Construction and Structure, Polytechnic School of Federal University of Bahia – alexandre.wahrhaftigl@ufba.br – Rua Aristides Novís, nº 02, 5º andar – Federação, Salvador – BA, Brazil, CEP 40210-630.

Department of Structural and Geotechnical Engineering, Polytechnic School of University of São Paulo – reyolando.brasil@poli.usp.br – Av. Prof. Almeida Prado tv. 2, n. 83, Cidade Universitária - São Paulo – SP, CEP 05508-900.

ABSTRACT

Wind was not a problem for low-rise heavy structures of the past, but has come to be as the constructions have become more and more slender, using less material. The danger of the wind causing accidents is particularly significant for power lines structures, radio, TV and microwaves towers, radar antennas and other such structures, according to Blessmann (2001). Wind effects upon slender poles and towers are reported by Simui; Scalan (1996), Sachs (1972), Kolousek et al (1984) and Navara (1969).

Accidents with power lines tower, one of them involving the fall of more than 10 consecutive towers in the state of São Paulo, Brazil, were reported by Blessmann (2001). Further, Blessmann (2001) reports a study on the effect of hurricanes in Miami at 1950 that completely destroyed 11 metal radio towers due to buckling of individual members. Occurrences of accidents with mobile phone antennas supporting poles in Brazil are reported by Brasil e Silva (2006). In this paper, we call poles long bar structures with circular or polygonal section. In the other hand, towers are metal frames, stayed or not.

It is particularly important to investigate the effects of the wind on slender structures. A

Contact person: 1rd A.M.Wahrhaftig, Department of Construction and Structure Of Polytechnic School of Federal University of Bahia, Rua Aristides Novís, nº 02, 5º andar - Federação, CEP 40.210-630, (5511) 3283-9725. E-mail alexandre.Wahrhaftig@ufba.br

particularly interesting case are de mobile phone antennas supporting poles.

In Brazil, a profound reform of the legal apparatus of telecommunications allowed for a new structure for that industry. Previously government owned Telebrás System was sold to private enterprise 29 of July of 1998 in 12 consecutive auctions carried out at the Rio de Janeiro Stock Exchange, the largest such an operation in the world to the time.

Brasil and Silva (2006) report that during the implementation of the mobile phone system in Brazil, more than 10.000 support structures were designed, manufactured and installed. 2000 of those were reinforced concrete poles. In the early 1990 years, there were not enough experienced companies and personnel to supply the existing demand. Other products makers had to adapt their production lines to the telecommunications market. In the other hand, structural engineers specialized in other applications had to adapt their mathematical models to the analysis of such structures. Some of those models, according to Brasil and Silva (2006), consider the wind effects as static loads, neglecting the dynamic aspects.

Nevertheless, for structures whose first natural frequency is under 1 Hz, the dynamic effects of Wind are important and to consider them static or deterministic in nature is too rough an approximation. About the importance of considering dynamic effects of wind, Durbey, C. & Hansen, O S. (1996) wrote that flexible structures could vibrate in different modes when excited by the Wind. Further they wrote that for slender structures, the dynamic effect of wind might cause resonance.

The Brazilian code dealing with the analysis of structures excited by the wind is NBR 6123/88 – Loads due to wind upon constructions. The Code provides models to consider the effects of wind to design structures. All of them consider the real dynamic load as an equivalent static one (Blessmann, 1989). The choice among them is related to the frequency of the first vibration mode.

In the first model, called static model, the influence of the fluctuating part of the Wind is taken into account by a Gust Factor in the calculation of the characteristic Wind velocity. It is considered that no resonance occurs.

The model that deals specifically with the dynamic responses along the average Wind, called the discrete model, is described in Chapter 9 of NBR 6123/88 – Loads due to Wind upon constructions. It considers that the fluctuations of the wind occur in the band of the lower frequencies of the structure. The procedure starts with the computation of the natural frequencies that are used in order to obtain the corresponding dynamic amplification factors. Thus, the frequency computation process is fundamental to the procedure.

To evaluate the procedures of NBR 6123/88 – Loads due to wind upon constructions., we apply them to a mobile phone antenna support pole (Fig.1). The dynamic computation carried up to the 5th vibration mode. We considered the geometric stiffness in the procedure, that is, the influence of the axial loads were taken into account.

Mass discretization and modal shapes were obtained via Finite Element models. Connections were simulated as short bar elements, 0.2 m long, of variable section and thickness equal to the sum of the thicknesses of the sections bellow and above the connection.

Frequencies were computed from the corresponding eigenvalue problem were the stiffness matrix included the geometric stiffness part, a nonlinear effect. This geometric stiffness matrix follows formulations to be found in, for example, Bathe (1996), Clough (1993), Cook (1974) and Cook at al (2002). The procedure is also recommended by Rutemberg (1982) and Wilson (1987) to linearize second order effects.
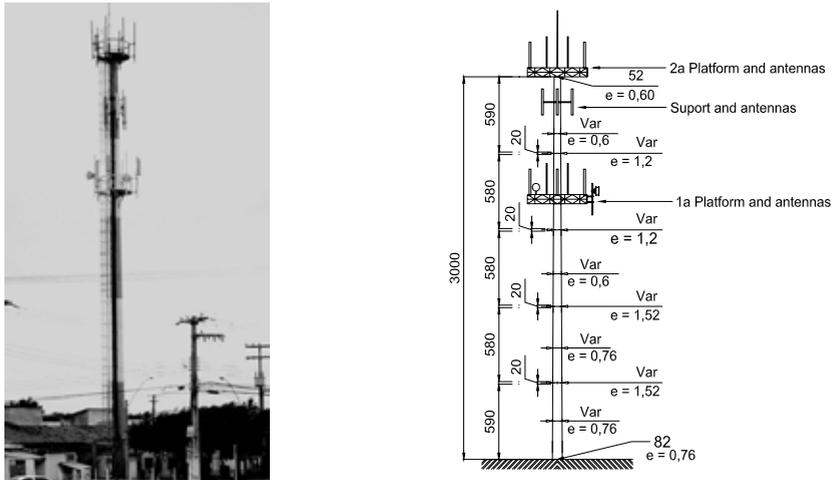
Figure 1: the mobile phone antennas support pole (centimetres).

The structure was modelled by 40 variable section bar elements. Vibration modes and frequencies are displayed in Fig.2.

	1st mode	2nd mode	3rd mode	4th mode	5th mode
Frequencies	0.532 Hz	2.884 Hz	8.654 Hz	16.985 Hz	26.174 Hz

Figure 2: natural modes and frequencies via FEM.

Structural data was collected in the field. Diameters were measured using a measure tape and thickness using an ultrasonic apparatus. Local survey indicated the presence of antennas and other accessories fixed to the structure, which are additional masses and forces.

Field determination of the frequencies of the structure under environmental excitation was carried out using a Brüel & Kjaer piezoresistive accelerometer, with DC response, 1021 mV/g sensibility, integrated cable, capable of measuring accelerations in the band ± 2 g. This device was fixed to the top of the pole. Data acquisition was carried out for 40 hours, using system ADS2000,

AqDados (Lynx Computer), connected to a notebook for signal recording. The fundamental frequency of the structure was obtained from the time series via FFT, using the program AqDAnalysis 7.02. The resultant value was 0.53 Hz. Applying the Brazilian Code to compute the resulting maximum bending moment (Fig.3), the response of the so-called discrete model NL is 55.69 % larger the the response of the static model. We observed little influence of higher modes than the fundamental one. These are responsible for 66% of total dynamic response of the structure.
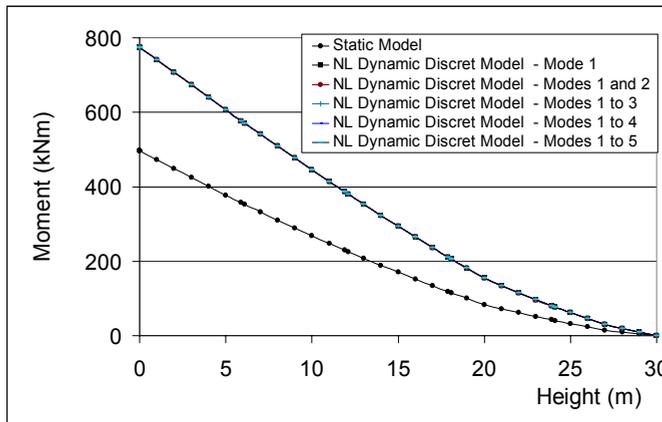
Figure 3: wind action**.**

REFERENCES

Blessmann J. (2001). "Acidentes causados pelo vento". (Accidents Caused by Wind), 4 ed, Ed by Federal University of Rio Grande do Sul. Porto Alegre.(in Portuguese).

Simiu E., Scanlan R. (1996). "Wind effects on Structures". John Wiley & Sons, New York.

Sachs P. (1972)."Wind Forces in Engineering", Pergamon Press. New York.

Koulousek V., Fischer O., Naprstek J. (1984)."Wind Effects on Civil Engineering Structures", Elsevier. New York.

Navara A. (1969). "Dinâmica de Estruturas", (Dynamic of Structures), LNEC – Laboratório Nacional de Engenharia Civil (National Laboratory of Civil Engineering). Lisboa. (in Portuguese).

Brasil R.M.L.R.F. Silva M.A (2006). "RC large displacements: Optimization applied to experimental results". Journal of Computers & Stuctures 84 (2006) 1164-1171, Ed Elsevier.

Dyrbye C.;Hansen S.O. (1996). "Wind Loads on Structures". England, John Wiley & Sons.

Associação Brasileira de Normas Técnicas (ABNT) - Forças devidas ao vento em edificações (1988), Rio de Janeiro. (in Portuguese).

Blessmann J. (1989). "Ação do Vento em Edifícios". 2 ed., rev. Ed. Universidade/UFRGS. Porto Alegre.

Galindez E. E. (1979). "Structural Dynamic Response on Wind Average Velocity". Thesis of Mater – Federal University of Rio Grande do Sul. Porto Alegre. (in Portuguese).

Bathe K. J. (1996). "Finite element procedures"; Englewood Cliffs, N.J. Prentice Hall.

Clough, R.W.; Penzien, J.(1993). "Dynamic of Structures". Taiwan: McGraw Hill International Editions, 2nd Edition.

Cook R. D. (1974). "Concepts and Applications of Finite Element Analysis". John Wiley and Sons, Inc., NJ, USA.

Cook R. D., Plesha D. S. M., Witt R. J. (2002). "Concepts and Applications of Finite Element Analysis". John Wiley and Sons, Inc., NJ, USA.

Venâncio F. Fernando. (1975) (Aeronautic Technology Institute). "Análise Matricial de Estruturas (Estática e Dinâmica), Almeida Neves – Editores. Rio de Janeiro.(in Portuguese).

Rutemberg A. (1982). "Simplified P-Delta Analyses for Asymmetric Structures". *Journal of the Structural Division*, ASCE, Vol.108, N0 ST9. New York.

Wilson E.L., Habibullah, A. (1987). "Static and Dynamics Analysis of Multi-Story Buildings, Including P-Delta Effects". *Earthquake spectra*, v. 3, Nº 2, 1987.

AqDados 7.02 (2003): Signal Acquisition Program: Handbook, ver. 7, Lynx Computers, São Paulo.

AqDAnalysis 7 (2004): Signal Analysis Program: Handbook, rev 6, Lynx Computers, São Paulo.

The effect of background leakage on wind induced internal pressure fluctuations in low rise buildings with dominant openings

1st T.K.Guha, 2nd R.N.Sharma, 3rd P.J.Richards

1st Ph.D. Candidate - tguh001@aucklanduni.ac.nz - Department of Mechanical Engineering

2nd Senior Lecturer - r.sharma@auckland.ac.nz - Department of Mechanical Engineering

3rd Associate Professor - pj.richards@auckland.ac.nz - Department of Mechanical Engineering

The University of Auckland, Private Bag 92019, Auckland, New Zealand

Keywords: background leakage; internal pressure; low rise building; dominant opening.

ABSTRACT

The objective of this paper is to numerically investigate the effect of background leakage on wind induced internal pressure fluctuations in a low-rise building with a windward dominant opening. The leakages were lumped on the leeward side for simplicity and the governing differential equation of internal pressure response was further simplified by ignoring the effect of inertia and pipe-friction losses through leakages. The loss coefficients of individual leakages were replaced by a representative average loss coefficient and a time and area averaged leeward wall pressure coefficient was used in the forcing term of the governing analytic equation. The simplifications adopted partly due to limitations posed in procuring reliable data and partly due to reasoning are considered to be adequate compared to the uncertainties associated with the distribution of leakage paths, lack of knowledge regarding the loss coefficient and effective air slug length of individual leakage path. The presence of background leakage generates an additional linear damping term in the governing analytic equation of internal pressure response. The results show that background leakages damp out the turbulence induced internal pressure fluctuations caused by the presence of windward dominant opening as reported by Vickery & Bloxham (1992) and shifts the system behavior from that with a single dominant opening to a two opening system with openings located on opposite (windward and leeward) faces. A linear variant based on the force balance on air-slugs through windward dominant opening and lumped leeward opening is proposed which closely approximates the non-linear model.
Past research by Vickery & Bloxham (1992), Holmes (1979), Liu & Saathoff (1982) and Sharma

---

Contact person: 1st T.K.Guha, Department of Mechanical Engineering, The University of Auckland, Private Bag 92019, Auckland, New Zealand, Tel.: +649 3737599, fax: +649 3737479, Email: tguh001@aucklanduni.ac.nz

& Richards (1997) among others has indicated that internal pressure in a building is nominally induced by the wind through the external pressure field via three mechanisms: transmission through leakages in buildings, transmission through dominant openings like doors and windows and through flexibility of building envelope, with the most significant effects occurring in the presence of dominant openings. Since the flow field developed past a bluff body such as a building is highly anisotropic, geometry and location of the dominant openings with respect to the prevailing wind directions, internal volume and compartmentalization of the building, turbulence in the upstream flow affect the internal pressure response significantly. Complicating this further and the subject of discussion in this paper is the presence of background leakages on the building surfaces caused by normal construction tolerances and small openings for ventilation purpose, the effect of which is to mitigate the wind induced internal pressure fluctuations transmitted through the dominant opening.

While theoretical advancement coupled with experimental observations (both wind tunnel and full scale) have greatly led to the understanding of internal pressure response in presence of a dominant opening (both transient and steady state effects) as well as the effect of building "skin" flexibility, a closed form solution to the effect of background leakage as noted by Vickery (1994) is yet to be developed. Wind tunnel investigations of the effect of background leakage on internal pressure response had been carried out in the past by Woods & Blackmore (1995) and Oh et al. (2007) using models with uniformly distributed well defined leakage openings. The study by Oh et al. (2007) also presented results of numerical simulations carried out using external pressure coefficients measured at individual leakage openings in wind tunnel. In reality, however, the building leakages are not well defined (in terms of geometry) and measurement of external pressure coefficient at individual leakage openings is impossible. This problem challenging a designer in real life can be overcome by making reasonable simplifications and numerical solutions of the simplified governing equation can nevertheless provide us with valuable insights into the effect of background leakage into the internal pressure dynamics of buildings with a windward dominant opening. Simplifications made to the overall problem were (1) lumping of leakages on the leeward side (with suction pressure) (2) ignoring the effect of inertia and pipe-friction type losses for leakages and (3) using a representative average loss coefficient for leakage openings as well as using a time and area-averaged leeward wall pressure coefficient in the forcing term of the governing analytic equation.

Figure 1 presents a schematic of a typical low rise building with a windward dominant opening and leakage openings lumped on the leeward side. Deduction of the model assumes $C_{peW} > C_{pei} > \overline{C}_{peL}$.
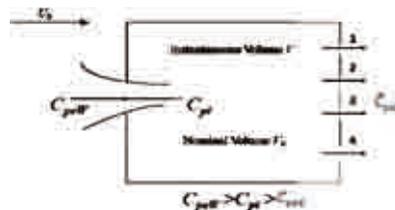
Figure 1: Schematic of the proposed non-linear model

Using the unsteady discharge equation of flow through a sharp edged windward dominant opening, ignoring the effects of inertia and pipe friction losses in the discharge equation through leakages lumped on the leeward side and employing mass balance of air flow inside the building using continuity equation with isentropic density formulation, the internal pressure response can be shown to be governed by the following equation:

$$\frac{\rho l_e V_0}{\gamma A_w P_a}\frac{dC_{pi}}{dt}+\frac{A_w\rho U_h l_e}{2A_w\cdot q\sqrt{C_L}|C_{pi}-\overline{C_{peL}}|}\frac{dC_{pi}}{dt}+\frac{C_L\rho V_0}{2(\gamma A_w P_a)}\left|\frac{dC_{pi}}{dt}\right|\frac{dC_{pi}}{dt}\cdot\frac{A_w\gamma U_h P_a}{qV_0}\sqrt{\frac{C_{pe}-C_{pi}}{C_L}}\left|\frac{dC_{pi}}{dt}\right|\frac{A_w\gamma U_h P_a}{qV_0}\sqrt{\frac{C_{pi}-C_{peL}}{C_L'}}\cdot C_a=C_{pe}$$

(1)

Where ρ is the density of fluid inside the building cavity, l_e is the effective length of the oscillatory air slug at the opening, A_W is the area of the windward dominant opening, A_L is the combined area of the leakages on the leeward side and V_0 is the internal volume of the building , $\gamma = 1.4$ is the ratio of specific heat capacities for isentropic process, P_a is the ambient pressure of air, c is the discharge coefficient of the opening, C_L is the loss coefficient of the windward opening, C'_L is the representative loss coefficient of the lumped leakage openings, $\overline{C}_{peL}$ is the area and time averaged leeward wall external pressure coefficient, $q = 0.5\rho U_h^2$ is the reference dynamic pressure; U_h being the ridge height velocity, $C_{pi} = p_i/q$ and $C_{peW} = p_e/q$; p_i and p_e being internal and windward external pressure coefficients at the opening respectively.

Numerical simulations were carried by solving the governing equation using a second-order Runga-Kutta method for a range of porosities (A_L / A_W) varying from 0 to 50%. Figure 2 (a) and (b) shows the response of building internal pressure following a step change in windward area averaged external pressure coefficient at the opening ($C_{peW} = 0.7$) and forcing due to turbulent atmospheric external pressure time history synthetically generated from Kaimal spectrum using appropriate aerodynamic admittance respectively.
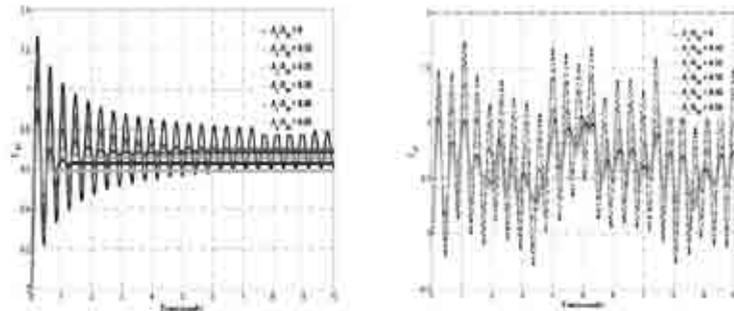
Figure 2: Time history response of internal pressure under (a) step change in windward external pressure and (b) turbulent windward external fluctuating pressure

Figure 3 (a) represents a plot of the maximum gain of internal pressure fluctuations over a sinusoidally varying external pressure fluctuation for a range of porosity ratios. The sinusoidal forcing function is given by $0.6 + 0.2\sin (2\pi f – \pi/2)$ with f varying from 0 to 10 Hz. The internal volume (V_0) and area of windward dominant opening (A_W) of the building representative of the TTU full scale test setup was taken 497 m^3 and 1.94 m^2 respectively. The discharge coefficient(c) and the opening loss coefficient (C_L) for the windward opening were taken as 0.6 and 1.2 respectively as per Sharma and Richards [4]. A representative loss coefficient of C'_L = 2.68 was taken for the lumped leeward leakage opening. An area and time averaged leeward wall external pressure coefficient of -0.2 was used to simulate the model for up to 1 second at a design ridge height wind speed (U_h) of 30 m/s. Figure 3 (b) shows the plot of the ratio of internal pressure fluctuations with background leakage to that of the internal pressure fluctuations without background leakage as function of porosity ratio for a range of non-dimensional opening area-building internal volume ($A_W^{3/2}/V_0$).
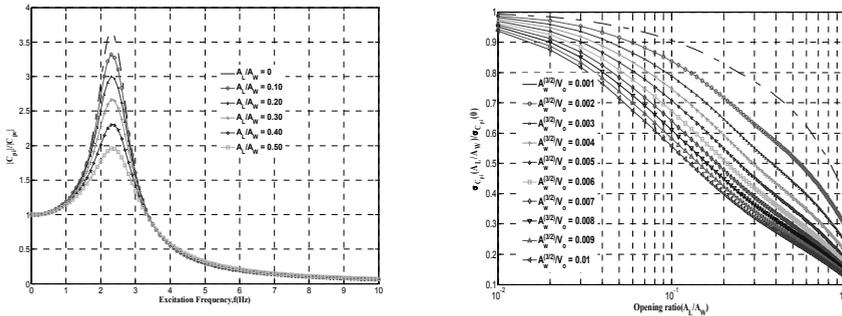
Figure 3: (a) Gain of internal pressure fluctuations over windward external pressure for a range of porosity ratios (b) Influence of background leakage and non-dimensional area-volume ratio on fluctuating internal pressure

The effect of additive damping caused by background leakages is evident from figures 2 (a), (b) and 3 (a). There is a reduction in the amplitude of internal pressure fluctuation by around 40% with increase in porosity ratio from 0 to 50%. A very interesting observation made from figure 3 (b) is that for an opening ratio of 10%, the internal pressure fluctuations were within 90% of that for no leakage configuration for $A_W^{3/2}/V_0 = 0.001$, 0.002 and 0.003 respectively. This is in agreement with the observations of Vickery and Bloxham (1992) and a conservative estimate is to neglect the mitigation effect of leakage as background vibration for design purpose. However, for values of $A_W^{3/2}/V_0$ greater than 0.003, the internal pressure fluctuations decrease rapidly with a 20% decrease in internal pressure fluctuations for $A_W^{3/2}/V_0 = 0.01$. The system, thus gradually proceeds to behave like a two opening system situated on opposite faces and some reduction in internal pressure gust factor may be permitted provided the internal building volume and envelope flexibility provides sufficient damping to prevent occurrence of significant Helmholtz resonance.

REFERENCES

Vickery B. J., Bloxham C. (1992). "Internal pressure dynamics with a dominant opening", Journal of Wind Engineering and Industrial Aerodynamics, 41 (1), 193-204.

Holmes J. D. (1979). "Mean and fluctuating internal pressures induced by wind", Proceedings of the 5th International Conference on Wind Engineering, Colorado State University, 435-450.

Liu H., Saathoff P. J. (1982). "Internal pressure and building safety", Journal of the Structural Division, 108 (10), 2223-2234.

Sharma R. N., Richards P.J. (1997). "Computational modeling of the transient response of building internal pressure to a sudden opening", Journal of Wind Engineering and Industrial Aerodynamics, 72, 149-161.

Vickery B. J. (1994). "Internal pressures and interactions with the building envelope", Journal of Wind Engineering and Industrial Aerodynamics, 53 (1-2), 125-144.

Woods A. R., Blackmore P. A. (1995). "The effect of dominant openings and porosity on internal pressures", Journal of Wind Engineering and Industrial Aerodynamics, 57, 167-177.

Oh Hee Jeong, Kopp Gregory A., Inculet Dianna R. (2007). "The UWO contribution to the NIST aerodynamic database for wind loads on low buildings: Part 3. Internal pressures", Journal of Wind Engineering and Industrial Aerodynamics, 95, 755-779.

Aerodynamic analysis of a photovoltaic solar tracker

S. Hernández, J. Méndez, J.A. Jurado and F. Nieto

School of Civil Engineering University of Coruña, Campus de Elviña, 15071 A Coruña –
hernandez@udc.es – jmendez@udc.es – jjurado@udc.es– fnieto@udc.es

Keywords: Solar tracker, wind profiles, wind loads, aerodynamic analysis.

ABSTRACT

Electrical energy obtained by photovoltaic panels is increasingly used in many countries. To improve the efficiency of the system usually photovoltaic panels are mounted on mobile structures that rotate with respect to vertical and horizontal axes for tracking the sun trajectory in the sky. Figure 1 shows a solar trackers located in a photovoltaic farm in Spain.

It can be seen that the surface exposed to wing pressure is very large and for the product to be competitive the structure must be designed to resist wind loads but with the strictly necessary amount of material.

The authors have carried out a study for a prototype of this kind of photovoltaic solar tracker trying to identify its performance under the required set of loads for the Spanish code of practice. The methodology consisted in the following steps:

    a) Identification of wind speed at the site
    b) Evaluation of wind loads
    c) Generation of structural model
    d) Identification of ultimate limit state
    e) Calculation of critical wind speed.

Contact person: S. Hernández. School of Civil Engineering University of Coruña, Campus de Elviña, 15071
A Coruña Tf.: 34 981167000; Fax: 34 981167170, E-mail hernandez@udc.es

Figure 1.: Picture of solar tracker

a) *Identification of wind speed*: According with monthly data of maximum wind speed from two weather station close to the farm location an extreme analysis of maximum expected wind speed was worked out (1-2). In this phase of the study the existing data of wind velocities were adjusted to the most appropriate extreme value distribution. Several distributions as Weibull, Frechet or Gumbel were considered. For one weather station the Weibull distribution was more appropriate while the Frechet curve was more precise in the other one. Figure 2. shows the fitting curves resulting for each weather station.

The Weibull expression is written as

$$H_z(z) = e^{-\left[\frac{a-z}{b}\right]^c}$$

Where z is a value of wind speed, a, b, c are three parameters and $H_z(z)$ the cumulative distribution function of wind speed.

By taking logarithms twice in the expression, a linear regression can be carried out to fit the values of actual wind speed recorded and therefore identifying values of parameters a, b, c.

In figure 2a. vertical data represent values of $\ln(-\ln(H_z(z)))$ and horizontal data values of $\ln(a-z)$

Similarly Frechet curve is expressed as

$$H_z(z) = e^{-\left[\frac{b}{z-a}\right]^c}$$

Proceeding as before a linear regression can be done. In figure 2b. vertical data represent again values of $\ln(-\ln(H_z(z)))$ and horizontal data values of $\ln(z-a)$
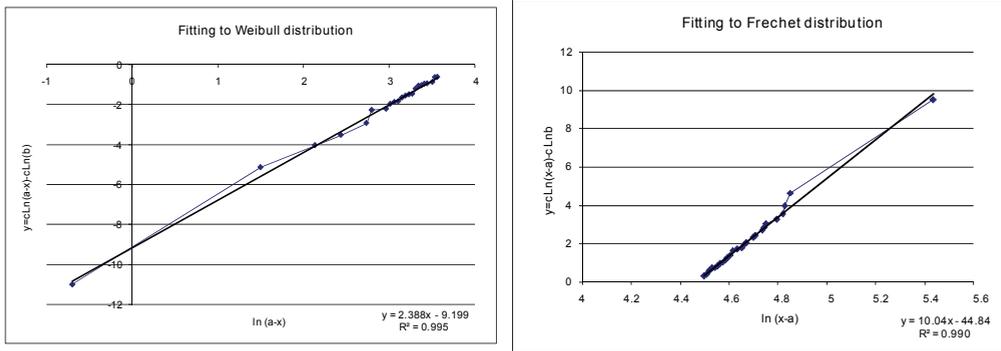
Figure 2.: Fitting of monthly maximum wind speed

b) *Evaluation of wind speed*: Having obtained the maximum wind speed during the expected service life of the photovoltaic solar tracker, wind pressures on the panel for different geometries of the panel resulting for variations of the inclination angle with respect to the horizontal axis were obtained by applying the procedure indicated in the Spanish code of practice (3) to such value of wind speed.

Figure 3.: Solar tracker at different inclination angles

c) *Generation of structural model:* A finite element model was created to find out the stress level at each component of the structure. First the finite element mesh was analyzed for 8 different configurations of the solar tracker and six load combinations. Figure 3 shows the structure at two different inclination angles

Having obtained the internal forces for each loading combination the complete set of requirement indicated in the Spanish code of practice for steel structures (4) was checked out at each element of the structure.

d) *Identification of ultimate limit state*: Three different ultimate limit state (ULS) were defined:

1) Maximum slope at panel boundary: A maximum slope of a degree was fixed for performance considerations.
2) Maximum stress of material: The yield stress of material was considered as upper limit for the Von Mises stress at any point of the structure.
3) Tracker turn over: Wind pressures leading to negative values of vertical reactions at any support points were assumed unacceptable.

e) *Calculation of critical wind speed:* Having in account the previously phases of the study and the numerical results provided by the set of 48 structural analysis, the maximum acceptable wind speed for each criteria and inclination angle of solar tracker was identified. Some of them were lower than expected, therefore a strategy had to be implemented to improve the solar tracker performance. A research study concluded that by addying prestessing cables to the main truss supporting the panels, an consequently stiffening the structure some advantage was achieved. With data obtained from the structural analyses the class of graphical representation presented at Figure 4. was elaborated showing the comparison between the wind speed leading to the initiation of ULS for each indication angle and the mandatory wind speed considered in the design of solar tracker.
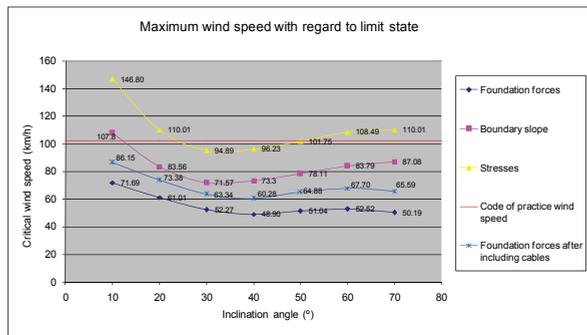
Figure 4: Graph of maximum allowable wind speed

REFERENCES

1. Haldar A. and Mahadevan S. (2000). *Probability, Reliability and Statistical Methods in Engineering Design,* John Wiley & Sons, New York.
2. Simiu E., Scanlan R. (1996). *Wind Effects on Structures*. John Wiley & Sons, New York.
3. *AE-88*. *Acciones en la edificación* (in Spanish)
4. *Norma MV-103*. *Acero en la edificación* (in spanish)

The Flight of Wind Borne Debris: An Experimental, Analytical, and Numerical Investigation. Part I (Analytical Model)

P. Martinez-Vazquez[1], C. J. Baker[2], M. Sterling[3], A. Quinn[4]

[1]*Research Fellow, University of Birmingham, UK; p.vazquez@bham.ac.uk –* [2]*Professor, School of Civil Engineering, University of Birmingham, UK, c.j.baker@bham.ac.uk –* [3] *Senior Lecturer, School of Civil Engineering, University of Birmingham, UK, m.sterling@bham.ac.uk –* [4] *Robert's Research Fellow, School of Civil Engineering-RCUK, University of Birmingham, UK, a.d.quinn@bham.ac.uk*

Keywords: Wind-borne Debris, Debris Flight, Wind

ABSTRACT

The destructive effects that storms or hurricanes have had over the infrastructure of urban areas, illustrates the necessity of investigating the behaviour of wind borne projectiles. Tachikawa (1983, 1988), Willis , et.al. (2002), Holmes (2004), Holmes, et.al. (2006), Baker (2007), and Richards, et. al. (2005), have all examined this phenomenon. For example, Tachikawa established the relationship between the magnitude of drag and lift force coefficients with auto-rotational response of flat plates in a wind tunnel; Willis examined compact and rod-like objects and found a method to assess the velocity that results in their flight, and established a damage function using the kinetic energy of the moving object; Holmes (2004), and Holmes, et.al. (2006), proposed a mathematical model to determine the trajectory of compact and sheet-type debris, assessing the risk of damage and incorporating Magnus effects; Baker (2007) solved the equations of movement for compact and sheet-type debris and carried out a parametric study to identify the variables that control the phenomenon, which had also been reported by Tachikawa; whilst Richards, et.al. (2005) put together a three-dimensional model which was compared to wind tunnel tests over sheet-like debris. The present paper builds on these contributions and intends to provide a mathematical solution for the prediction of the trajectory of sheet-type debris by taking into account frictional forces and evaluating the magnified forces which arise from the rotational response of the projectile. This approach will be compared in the near future to computational CFD simulations as well as to the pressure field registered over the surface of a flying sheet-type specimen implemented with wireless electronic devices, to be tested in a wind tunnel. The purpose of this paper in therefore only to present the theoretical model. The results of the comparison will be disseminated in the future.

The following sections review the different aspects of the problem and provide mathematical expressions that allow the computation of the trajectory of sheet-type debris under the action of uniform wind in three dimensions,

I. FORCES

Sections 1, 2 below are largely based on the review of the work developed by Richards, et.al. (2005) and are important for the development of the current model.

Contact Person: Pedro Martinez-Vazquez, School of Civil Engineering, The University of Birmingham, UK, B15 2TT; Tel. +44(0) 780 597 0235; Fax +44(0) 121 414 3688

1. Coordinate Transformation

1.1 Force Vectors

The wind vectors within a Cartesian coordinate system can be defined in a general *(G)* and principal *(P)* reference systems. Figure 1 shows a sequence of rotations that enable transformation between the two systems of reference, i.e. $G \rightarrow P$.
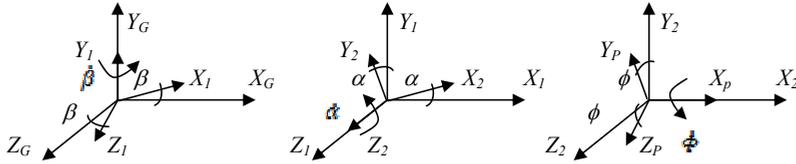

Figure 1

The following matrix expresses the above transformations mathematically:

$$\begin{Bmatrix} X_p \\ Y_p \\ Z_p \end{Bmatrix} = \begin{bmatrix} \cos\beta\cos\alpha & \sin\alpha & -\sin\alpha\cos\alpha \\ -\cos\beta\sin\alpha\cos\beta + \sin\beta\cos\phi & \cos\alpha\cos\phi & \sin\beta\sin\alpha\cos\phi + \cos\beta\sin\phi \\ \cos\beta\sin\alpha\sin\phi + \sin\beta\cos\phi & -\cos\alpha\sin\phi & -\sin\beta\sin\alpha\sin\phi + \cos\beta\cos\phi \end{bmatrix} \begin{Bmatrix} X_g \\ Y_g \\ Z_g \end{Bmatrix}$$

1.2 Rotations

The identities given in equations *(1-3)* lead to the computation of the angular velocities of equation *(4)*, here *p, q, r*, are angular velocities in principal axis.

$$\dot\beta = \frac{q - \alpha\sin\varphi}{} = \frac{p - \varphi}{} = \frac{r - \alpha\cos\varphi}{} \tag{1}$$

$$\dot\alpha = \frac{q - r\cos\alpha\cos\varphi}{} = \frac{r + p\cos\alpha\sin\varphi}{} \tag{2}$$

$$\dot\varphi = p - \dot\beta\sin\alpha \tag{3}$$

$$\{\dot\alpha, \dot\beta, \dot\phi\} = \left\{ q\sin\varphi + r\cos\varphi c \frac{q\cos\varphi - r\sin\varphi}{\cos\alpha}, p - (q\cos\varphi - r\sin\varphi)\tan\alpha \right\} \tag{4}$$

2. Centre of Pressures

The following expressions define the location of the centre of pressure are consistent with tilt angle γ within the range 0-360 degrees. Here ℓy *(vertical)*, ℓz *(horizontal)* are the main dimensions of the board in principal coordinates.

$$\tan(\xi) = \frac{\tan\gamma}{\ell_Z / \ell_Y} \quad 0°<=\gamma<=90° \; \xi=\xi; \; 90°<\gamma<=270° \; \xi=\xi+\pi \text{ rad}; \quad 270°<\gamma<=360° \; \xi=\xi+2\pi \text{ rad}; \tag{5}$$

$$b = \ell_m|\cos\gamma| + \ell_{mv}|\sin\gamma| \quad ; \; c = \frac{\ell_Z x \ell_y}{\ell_Z|\cos\gamma| + \ell_Y|\sin\gamma|} \tag{6}$$

$$\{y_{CP}, z_{CP}\} = \left\{ \frac{c}{4} \frac{(\pi/2 - |\varepsilon|)}{\pi/2} \sin\xi, \frac{c}{4} \frac{(\pi/2 - |\varepsilon|)}{\pi/2} \cos\xi \right\} \quad ; \; \text{If } \varepsilon>180; \; \varepsilon-360 \tag{7}$$

Holmes, et.al. (2006), suggests a semi-linear variation of c/ℓ which ranges from 0-0.3 for any angle of attack, in a two dimensional model. The equations *(5-7)* above are consistent with those limits.

In addition to the contributions made by Richards et.al. (2005), the following ideas have been

considered for the tri-dimensional model.

3. Friction Forces

It is suggested that friction forces be computed using equation *(8)*, which follows from the definition of boundary layer given by Prandtl (1963) and Schlichting (2000).

$$P_\tau = \iint_A \tau(dzdy) = 2V\sqrt{\rho V \mu \ell_Y}\,\ell_Z \tag{8}$$

Here V is the undisturbed wind velocity, ρ is the air density, μ represents absolute viscosity.

4. Pressure Coefficients
4.1 Normal Force Coefficient

Holmes suggests a bilinear function for the computation of the normal force C_N, which depends on the angle of incident wind (ε). This function agrees with measurements made by Tachikawa (1983), Flachsbart (1932), and also compare to the values suggested by Richards et.al. (2005).

$$C_N = 1.2\ (\varepsilon)/30 \qquad 0 <= \varepsilon <= 30 \tag{9}$$

$$C_N = 1.2 \qquad 30 < \varepsilon \tag{10}$$

4.2 Magnus Effect

Tachikawa (1983) suggested bilinear functions in order to determine magnified drag and lift coefficients as a function of the frequency of rotation. Figure 2 and equation *(11)* presents the variation of C_{Kr}/C_{K0} with ω/ω_0, but modified by the present authors for the interval $0<\omega/\omega_0<0$, in order to reflect the static case, i.e. $C_{Kr}/C_{K0} \rightarrow C_S/C_{K0}$, $\delta \rightarrow 0$, when $\omega/\omega_0 \rightarrow 0$.

$$C_K = C_{Kro}\left(\frac{C_{Kr}}{C_{Kro}}\right) + \delta\left(C_{Ks} - \overline{C}_{Ks}\right) \tag{11}$$
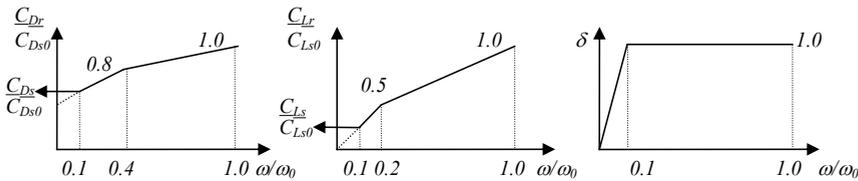
Figure 2

II. TRAJECTORY
5. Excitation

The forces and moments acting over the board will be computed in local coordinates, as follows:

$$F_x = \frac{1}{2}\rho V_x^2 \ell_y \ell_z C_x \tag{12}$$

$$F_y = \frac{1}{2}\rho V_y^2 \ell_x \ell_z C_y + 2V_y\sqrt{\rho V_y \mu \ell_y}\,\ell_z \tag{13}$$

$$F_z = \frac{1}{2}\rho V_z^2 \ell_x \ell_y C_z + 2V_z\sqrt{\rho V_z \mu \ell_z}\,\ell_y \tag{14}$$

$$M_x = F_y e_z + F_z e_y \tag{15}$$

$$M_y = F_x e_z \tag{16}$$

$$M_z = F_x e_y \qquad\qquad (17)$$

The variables in these expressions are self-explicit. Note that the second term on equations *(13, 14)*, which includes the viscosity term μ, corresponds to friction forces computed according to section 3.

6. Differential Equations

The application of a transformation matrix to the pressure field and to the partial response of the object allows the formulation of the corresponding equations of movement within a local system of coordinates, explicitly eliminating their dependency on the relative incidence of the wind.

6.1 General Formulation

$$F_k = m_k \dot{u}_k \qquad\qquad (18)$$
$$M_k = I_{kk} \dot{\omega}_k \qquad\qquad (19)$$

If *m* (mass), *I* (mass moment of inertia) are constants, *F, M,* are excitation, and *u, ω,* represent response, equations *(18, 19)* can be generalised using the variables *g, E, R*, as follows:

$$E_k = g_k \dot{R}_k \qquad\qquad (20)$$

Assuming that the excitation *E* can be represented as a linear function for any interval of time *i-j*, then the linear excitation with slope *s*, can be expressed as in *(21)*, with its solution given in *(22)*:

$$E_k(t) = s_{E_k} t + E_{k,i} \qquad\qquad (21)$$

$$R_k = \frac{1}{g_k} \int E_k dt = \frac{1}{g_k} \left(\frac{1}{2} s t^2 + E_{k,i} t + R_k(0) g_k \right) \qquad\qquad (22)$$

The tri-dimensional model presented in this paper, is current being processed.

REFERENCES

Tachikawa M. (1983), Trajectories of flat plates in uniform flow with application to wind-generated missiles, J. Wind Eng. Ind. Aerodyn., 14, 443-453

Tachikawa M. (1988), A method for estimating the distribution range of trajectories of wind-borne missiles, J. Wind Eng. Ind. Aerodyn., 29, 175-184.

Willis J.A.B., Lee B.E., Wyatt T.A. (2002), A model of wind-borne debris damage, J. Wind Eng. Ind. Aerodyn., 90, 555-565

Holmes J.D. (2004), Trajectories of spheres in strong winds with application to wind-borne debris, J. Wind Eng. Ind. Aerodyn., 92, 9-22.

Holmes J.D., Letchford C.W., Lin N. (2006), Investigations of plate-type windborne debris – Part II: Computed trajectories, J. Wind Eng. Ind. Aerodyn., 94, 21-39.

Baker C. J. (2007), The debris flight equations, J. Wind Eng. Ind. Aerodyn., 95, 329-353.

Richards P.J., Williams N., Laing B. (2005), 3D aerodynamics and motion of plate type wind-borne debris, 6th Asia-Pacific Conf. on Wind Eng., Seoul, Korea, 12-14 Sept., 762-777.

Prandtl L. (1963), Essentials of fluid dynamics, Blackie & Son Limited, pp. 98-108.

Schlichting H., Gersten K. (2000), Boundary layer theory, Springer-Verlag, pp. 29-49.

Flachsbart (1932), Messungen an eben und gewolbten Platten, Ergebnisse der AVA. I V.

A framework for generalized gust-front factor

1st D. Kwon, 2nd A. Kareem

[1]*Postdoctoral research associate, NatHaz Modeling Laboratory, University of Notre Dame,*
dkwon@nd.edu

[2] *Robert M. Moran Professor, NatHaz Modeling Laboratory, University of Notre Dame,*
kareem@nd.edu

ABSTRACT

This paper presents a generalized gust-front factor that realistically models gust-front winds and their attendant load effects on structures. This is akin to the gust loading factor format used in codes and standards world-wide for the treatment of conventional boundary layer winds. The generalized gust-front factor encapsulates dynamic features of gust-front induced wind effects on structures for estimating design loads associated with gust-fronts originating from a thunderstorm/downburst.

INTRODUCTION

To account for the gustiness of the turbulent boundary layer wind in structural loading, most international codes and standards have adopted the concept of a gust loading factor which was first introduced by Davenport (1967) and has been extensively improvised by a host of researchers (e.g., Solari 1993) and more recently recast into a new format by Zhou & Kareem (2001). In comparison with boundary layer winds that have generally been regarded as stationary, gust-front winds associated with gust-fronts originating from a thunderstorm/downburst exhibit distinct nonstationarity, i.e., rapid changes in wind speed during a short time interval which may be

Contact person: 1st D. Kwon, NatHaz Modeling Laboratory, University of Notre Dame, Notre Dame, IN 46556, USA, TEL: 574-631-5380, FAX: 574-631-9236, dkwon@nd.edu

accompanied by changes in direction. The significance of these transient wind events, as they relate to subsequent load effects, can be readily surmised based on the analysis of thunderstorm databases both in the U.S. and around the world, which suggest that these winds actually represent the design wind speed for many locations.

In order to realistically capture characteristics of gust-front winds and their attendant load effects, Kwon & Kareem (2006) proposed a new analysis framework, gust-front factor, which expresses a generalized description of the genesis of the overall wind load effects on structures under both gust-front and boundary layer winds. It is designed to be used in conjunction with the existing codes and standards, especially ASCE 7 standard. In the case of conventional boundary layer winds it simply reduces to the gust loading factor.

In this study, a generalized gust-front factor is introduced, which is intended not only to analytically model gust-front winds independent of any reference design standard, e.g., ASCE 7, but also to highlight more general features like conventional gust loading factor concept (Davenport 1967). The generalized gust-front factor encapsulates dynamic features of gust-front induced wind effects on structures, which is designed to estimate design loads under gust-front winds.

GUST-FRONT FACTOR

With the exemplary success of the gust loading factor (Davenport 1967) in capturing the dynamic wind effects introduced by buffeting action of wind and its popularity in design standards and codes worldwide, the "Gust-Front Factor" (G_{G-F}) (Kwon & Kareem 2006) was proposed for use in conjunction with the existing design codes and standards to formulate a framework along the lines of the gust loading/effect formulation existing in ASCE 7 standard that encapsulates critical features of downburst winds to capture their load effects. The design wind loading in a gust-front (F_{Design}) is then expressed by

$$F_{Design} = F_{ASCE\,7} \cdot K_{z,G-F} \cdot G_{G-F}$$
$$G_{G-F} = I_1 \cdot I_2 \cdot I_3 \cdot I_4$$

(1)

where, $F_{ASCE\,7}$ represents the recommendation of ASCE 7 equivalent static wind load (ESWL), the G_{G-F} is the gust-front factor that relates F_{Design} in a gust-front to the $F_{ASCE\,7}$ in conventional boundary layer winds and $K_{z,G-F}$ accounts for the velocity/pressure profile in a gust-front as opposed to boundary layer winds in ASCE 7. In this format, the G_{G-F} takes into account the following features: variation in the vertical profile of wind speed - kinematic effects factor (mean load effects), I_1; dynamic effects introduced by the sudden rise in wind speed - pulse dynamics factor (rise-time effects), I_2; nonstationarity of turbulence in gust-front winds - structural dynamics factor (nonstationary turbulence effects), I_3; transient aerodynamics - potential load modification factor (transient aerodynamics effects), I_4. Accordingly, the G_{G-F} embodies an intuitive picture of the underlying mechanisms that represent the fundamental building blocks of both the kinematic (I_1) and dynamic (I_2, I_3, I_4) load effects associated with gust-front winds on structures as compared to those of conventional boundary layer winds. Details can be found in Kwon & Kareem (2006).

GENERALIZED GUST-FRONT FACTOR

The gust-front factor is successfully expressed as the product of four underlying factors to reveal specific physical aspects, however, it is strongly linked with ASCE 7 format as shown in Eq. (1) (Kwon & Kareem 2009). For the general prospect, the generalized gust-front factor is here introduced being independent of a reference standard.

Assuming that $x_{B-L}(z,t)$ is the structural displacement in boundary layer winds, the expected maximum response, $\max[x_{B-L}(z,t)]$, can be expressed in terms of the gust loading factor format used

in Davenport (1967):

$$\max[x_{B-L}(z,t)] = \max[\overline{x}_{B-L}(z) + \tilde{x}_{B-L}(z,t)] = \overline{x}_{B-L}(z)\left[1 + \frac{g_{B-L} \cdot \sigma_{B-L}(z)}{\overline{x}_{B-L}(z)}\right] = \overline{x}_{B-L}(z) \cdot G_{GLF} \tag{2}$$

where, subscript *B-L* represents boundary layer; superscripts – and ~ represent mean and fluctuating components of displacement, respectively; g_{B-L} = peak factor; $\sigma_{B-L}(z)$ = RMS displacement by fluctuating wind components; G_{GLF} = gust loading factor. As such, the gust loading factor accounts for the dynamics of wind fluctuations and any load amplification introduced by the dynamics of structure, and this factor is utilized to estimate design loads of structure, i.e., ESWL.

In the case of gust-front winds, structural displacement by gust-front winds [$x_{G-F}(z,t)$] may be described in terms of nonstationary wind model being recast that includes storm-translation effect (Kwon & Kareem 2006):

$$x_{G-F}(z,t) = \overline{x}_{G-F}(z,t) + \tilde{x}_{G-F}(z,t) + x_{s-m} \tag{3}$$

where, subscript *G-F* represents gust-front; superscripts – and ~ represent time-varying mean and nonstationary fluctuating components of displacement, respectively; x_{s-m} = displacement introduced by the storm-translation speed. Accordingly, the corresponding maximum response can be approximately expressed as (Kwon & Kareem 2006):

$$\max\left[x_{G-F}(z,t)\right] \approx \max\left[\overline{x}_{G-F}(z,t)\right] + \max\left[\tilde{x}_{G-F}(z,t)\right] + x_{s-m}$$
$$\approx \max\left[\overline{x}_{G-F}(z,t)\right]\left[1 + \frac{g_{G-F} \cdot \max\left[\sigma_{G-F}(t)\right]}{\max\left[\overline{x}_{G-F}(z,t)\right]} + \frac{x_{s-m}}{\max\left[\overline{x}_{G-F}(z,t)\right]}\right] \tag{4}$$

where, g_{G-F} and $\sigma_{G-F}(t)$ represent mean peak factor and time-dependent RMS displacement by nonstationary fluctuating components of gust-front winds.

In this study, analytical/empirical models of downburst winds that characterize their spatio-temporal features are employed. It is generally assumed that gust-front wind field at any time and height may be factorized in terms of the product of a vertical profile [$V_{G-F}(z)$] and a time function [$V_{G-F}(t)$], i.e., $V_{G-F}(z,t) = V_{G-F}(z) \cdot V_{G-F}(t)$ (e.g., Kwon and Kareem 2006). Accordingly, the maximum displacement of time-varying mean component can be divided into static and dynamic parts:

$$\max\left[\overline{x}_{G-F}(z,t)\right] = \overline{x}_{G-F}(z) \cdot \max\left[\overline{x}_{G-F}(t)\right] \tag{5}$$

Here, the generalized gust-front factor, denoting $G_{G,G-F}$, is defined as:

$$G_{G,G-F} = \frac{\max\left[x_{G-F}(z,t)\right]}{\overline{x}_{G-F}(z)} = \max\left[\overline{x}_{G-F}(t)\right]\left[1 + \frac{g_{G-F} \cdot \max\left[\sigma_{G-F}(t)\right]}{\max\left[\overline{x}_{G-F}(z,t)\right]} + \frac{x_{s-m}}{\max\left[\overline{x}_{G-F}(z,t)\right]}\right] \tag{6}$$

In this way, $G_{G,G-F}$ can best capture the dynamic effects of gust-front winds akin to the concept of conventional gust loading factor. Note that strictly speaking, x_{s-m} may be categorized as static component, but since its contribution becomes relatively small due to a large value in the denominator, i.e., the maximum displacement of time-varying mean component (Kwon & Kareem 2006), this term may be treated as negligible in the consideration of overall static effect. For reference, the relationship between gust-front factor with its underlying factors and generalized gust-front factor can be described as (Kwon & Kareem 2006):

$$G_{G,G-F} = I_2 \cdot \left(I_3 \cdot G_{GLF}\right) \tag{7}$$

Finally, the design loads associated with the generalized gust-front factor are expressed as:

$$F_{G-F}(z) = G_{G,G-F} \cdot \overline{F}(z) = \frac{1}{2}\rho \cdot A \cdot C_{D,G-F} \cdot V_{G-F}^2(z) \cdot G_{G,G-F} \tag{8}$$

where, ρ = air density; A = tributary area; $C_{D,G-F}$ = drag coefficient by gust-front winds.

EXAMPLE AND DISCUSSION

An example building is used to evaluate the $G_{G,G-F}$, its associated ESWL and ASCE 7-based ESWL under boundary-layer winds: building width and depth = 40 m; building height = 200 m; natural frequency = 0.2 Hz; building bulk density = 180 kg/m^3; air density = 1.225 kg/m^3; damping ratio = 0.01; Vicroy model for vertical profile [$V_{G-F}(z)$] (Vicroy 1991); V_{max} = 57 m/s and z_{max} = 60 m; half-sine pulse for time function [$V_{G-F}(t)$] (Kwon & Kareem 2006); pulse duration t_d = 200 sec; exposure C condition with 3-sec wind speed of 40 m/s; storm-translation speed = 0. $C_{D,G-F}$ is assumed to be the same as conventional C_D value, 1.3.

This results in $G_{G,G-F}$ = 1.49 and G_{GLF} = 1.82, which show that dynamic effects by gust-front winds are relatively lower significance than those by conventional boundary-layer winds: nonetheless, one should not overlook the possible load enhancement due to transient aerodynamics ($C_{D,G-F}$), which may result in enhancing local pressures or overall force coefficient in the neighborhood of 5~20 % based on preliminary observations thus far in comparison to conventional C_D (e.g., Butler & Kareem 2007; Matsumoto et al. 2007). In addition, the kinematic effects due to the wind profile [$V_{G-F}(z)$] result in locally enhanced loads around z_{max}, therefore, this underscores the role of enhancement in the kinematic effects to the overall design load even though the dynamic effects are not significant for this particular example (Figure 1). This enhancement effect may be significantly influenced by the choice of gust front velocity profile used.
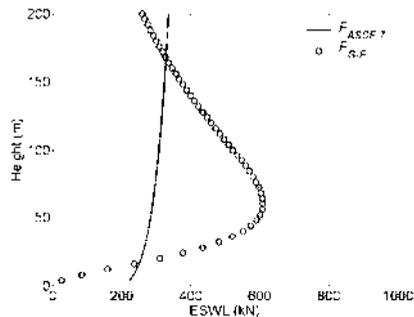
Figure 1: $F_{ASCE\ 7}$ and F_{G-F} in an example building

REFERENCES

Davenport, A. G. (1967). "Gust loading factors" J. Struct. Div., ASCE, 93(3), 11-34.
Solari, G. (1993). "Gust buffeting. II : Dynamic along-wind response", J. Struct. Eng., ASCE, 119(2), 383-397.
Zhou, Y., Kareem, A. (2001). "Gust loading factor: New model", J. Struct. Eng., ASCE, 127(2), 168-175.
Kwon, D., Kareem, A. (2006). "Gust-front factor", NatHaz Modeling Laboratory Report, University of Notre Dame.
Kwon, D., Kareem, A. (2009). "Gust-Front Factor: A New Framework for Wind Load Effects on Structures", J. Struct. Eng., ASCE, in press.
Am. Soc. of Civil Eng. *Minimum design loads for buildings and other structures*, ASCE 7-98, 7-02, 7-05, VA.
Vicroy, D. D. (1991). "A simple, analytical, axisymmetric microburst model for downdraft estimation", NASA Tech. Memo, 104053.
Butler, K., Kareem, A. (2007). "Physical and numerical modeling of downburst generated gust fronts", Proc. 12th ICWE, Cairns, Australia, 791-798.
Matsumoto, M., et al. (2007). "Drag forces on 2-D cylinders due to sudden increase of wind velocity", Proc. 12th ICWE, Cairns, Australia, 1727-1734.

Neural simulation of wind induced nongaussian loads based on BLWT results

Luca Facchini

University of Florence – luca.facchini@unifi.it – via S. Marta 3 – 50139 Firenze - Italy

ABSTRACT

Boundary layer wind tunnel experiments are intended to give insight into complex phenomena which can hardly be tackled analytically. The distribution of wind induced pressure upon the surface of a given structure is a typical example: in most cases, owing to the geometric complexity of structural surfaces, it is impossible to determine even a satisfactory approximation of the actual load.

When structural safety against wind loads is of concern, it is desirable to obtain as many samples of the pressure distribution as possible, and often even more: risk assessment needs to investigate the tails of the distributions of loads and structural response, and therefore a great amount of data are usually needed. This amount can well exceed the number of samples usually collected in a boundary layer wind tunnel experiment.

The need to accurately reproduce and simulate the wind induced loads arises in such situations, see f.i. Ditlevsen *et al*. (1996), and this motivates the great amount of specialized literature devoted to the subject.

The history of numerical simulation of wind induced loads dates back to late 60's – early 70's with such pioneering works as CAWS, WAWS and autorgressive models. While the first two meth-

---

Contact person: Luca Facchini, Dept. of Civil & Environmental Engineering, via S. Marta 3 – 50139 Firenze – Italy. Tel. +39 055 4796597   E-mail luca.facchini@unifi.it .

ods can be considered as the first examples of parametric processes, the last one is the application of digital filters – identified by means of Yule-Walker equations, see f.i. Iwatani (1982) – to the case of wind velocity.

The mentioned methods generated samples of gaussian cross-correlated vector processes. The simulation of nongaussian processes is more recent and can be based on several approaches, the main ones being:

− the transfer method, or translation method, is perhaps the easiest and most reliable procedure to tackle the simulation of nongaussian processes. It is based on the generation of the so-called underlying gaussian process, which is subsequently transformed by means of a proper nonlinear function. Thus, the nongaussian process $x(t)$ is simulated by means of the relation

$$x(t) = f[u(t)] \tag{1}$$

where $f(\circ)$ is a nonlinear function, which can be memoryless – see f.i. Grigoriu (2000) – or can even possess some memory. This method dates back to the works of Galton (1879) and Mc Alister (1879). Between the end of the XX and the beginning of XXI century important contributions due to Gioffré *et al.* (2000), Grigoriu (2000), and Puig *et al.* (2002a) have been published. The problem of the determination of the nonlinear function $f(\circ)$ is of central importance and might admit more than one solution. Besides, the final simulation of the nongaussian process is influenced by the gaussian process being completely characterized by its mean and covariance structure: it can therefore be difficult to impose given constraints on the process higher moments.

− The second procedure consists in a correction on the source process phase and a subsequent application of a Fourier transform. The paper by Seong & Peterka (1997) is certainly worth mentioning. By means of this procedure it is possible to simulate a nongaussian process with given probability distribution and spectral density function, but the effects on the higher order statistics remain to be investigated.

− The third procedure lies in the definition of a linear autoregressive digital filter which admits a nongaussian input with given characteristics. The approach is employed in Gaver & Lewis (1980) but its implementation is difficult, especially in the case of strongly asymmetric probability distributions with time histories which exhibit series of frequent peaks. The control of higher order statistics is still difficult.

Neural simulation of nongaussian processes is inspired by a general property of stochastic processes, which also gave birth to linear autoregressive filters for gaussian processes.

If n consecutive observations of a particular realization of a stochastic process $x_{t-n} \cdots x_{t-1}$ are available, then the expected value of the observation at time t is given by the expression:

$$h(\boldsymbol{y}_t) = E[x_t | \boldsymbol{y}_t] = \int_{-\infty}^{\infty} x_t \, p_{x_t|\boldsymbol{y}_t}(x_t | \boldsymbol{y}_t) \, dx_t \tag{2}$$

where $\boldsymbol{y}_t = [x_{t-1} \quad \cdots \quad x_{t-n}]^t$ is the vector which groups the preceding observations, see f.i. Kailath (1981). With this background, a general expression for an autoregressive digital filter is therefore

$$x_t = h(\boldsymbol{y}_t) + \epsilon_t \tag{3}$$

If x_t is a gaussian process, then $h(\boldsymbol{y}_t)$ is a linear function, $\epsilon_t = x_t - h(\boldsymbol{y}_t)$ is gaussian and tends to a white noise for increasing dimension of vector $\boldsymbol{y}_t$, n : this is the underlying concept of a digital autoregressive filter.

When gaussianity of process x_t is lost, $h(\boldsymbol{y}_t)$ is no longer a linear function of its argument, and can be evaluated by means of equation (2); in this case, the numerical evaluation of the involved integral can be numerically difficult. In the case of reproducing a wind tunnel experiment there is the additional difficulty that the actual joint probability density $p_{x_t|\boldsymbol{y}_t}(x_t | \boldsymbol{y}_t)$ is unknown.

Neural networks can then be extremely helpful for the correct definition of function $h(\boldsymbol{y}_t)$, as their use may override the problems connected to the numerical integration of expression (2). The nonlinear function $h(\boldsymbol{y}_t)$ may in fact be approximated by the output of a properly trained neural network:

$$h(\boldsymbol{y}_t) = N(\boldsymbol{y}_t) \tag{4}$$

where the network $N(\boldsymbol{y}_t)$ can take several forms: feed-forward back-propagation, radial basis, generalized regression, and so on; see f.i. Broomhead & Lowe (1988), Gotovac & Kozulic (1999), Haykin (1996), Nelles (2001), Poggio & Girosi (1990)

A crucial factor is the training method of the network. In fact, it can be trained in several ways.

The first way is also the most obvious: the network is trained directly on the results of the wind tunnel experiment, in order to obtain

$$N(\boldsymbol{y}_t) \simeq x_t \tag{5}$$

This approach can directly employ the most common training algorithms nowadays available, such as the simplex algorithm, the steepest gradient and related ones, the Newton, quasi-Newton and related ones (such as the Levenberg-Marquardt), but it can also exhibit some severe drawbacks: for instance, results may be inaccurate when the number of collected samples is not high enough.

In this case, the evaluation of some particular statistical moments can lead to more accurate results. The function $h(\boldsymbol{y}_t)$ is in fact characterized by some important relations (Kailath (1981)), which are substantially due to the fact that $h(\boldsymbol{y}_t)$ is the best possible estimate (in a least square sense) for x_t given n consecutive observations $\boldsymbol{y}_t = [x_{t-1} \cdots x_{t-n}]^t$. This can be summarized by the relation

$$E[(x_t - h(\boldsymbol{y}_t))^2] = min \tag{6}$$

which can well be taken as a training criterion. A consequence of equation (6) is also that

$$E[(x_t - h(\boldsymbol{y}_t)) g(\boldsymbol{y}_t)] = 0 \quad \forall g(\boldsymbol{y}_t) \tag{7}$$

A neural network can be often expressed by an expression like

$$N(\boldsymbol{y}_t) = \sum_{k=1}^{N_\phi} w_k \phi_k(\boldsymbol{y}_t, \boldsymbol{\theta}) \tag{8}$$

where the characterizing coefficients can be subdivided in a vector $\boldsymbol{w}$ collecting linear coefficients and a vector $\boldsymbol{\theta}$ collecting the nonlinear ones (Nelles (2001)). The reason for such classification lies in the determination of the coefficients: in fact, the vector $\boldsymbol{w}$ can be determined by the solution of the linear system

$$E[\phi_k(\boldsymbol{y}_t, \boldsymbol{\theta}) \phi_l(\boldsymbol{y}_t, \boldsymbol{\theta})] w_l = E[x_t \phi_k(\boldsymbol{y}_t, \boldsymbol{\theta})] \tag{9}$$

while the vector of the nonlinear coefficients $\boldsymbol{\theta}$ has to be determined by means of nonlinear minimization algorithms starting directly from equation (6).

The expected value operator can be evaluated in two different ways. The first one is to evaluate the empirical means involved in equation (9): this leads to the direct approach described by equation (5), together with its drawbacks.

The other one is to approximate the joint probability density $p_{x,y}(x, \boldsymbol{y})$ by means of a proper choice of functions and then evaluate $p_{x|y}(x|\boldsymbol{y})$ by integration. In this case, a number of different choices is available.

An extremely used way to approximate the joint pdf $p_{x,y}(x, \boldsymbol{y})$ is to express it as a combination of gaussian bells:

$$p_{x,y}(x, \boldsymbol{y}) = \sum_{k=1}^{N_\phi} w_k \phi_k(x, \boldsymbol{y}) \tag{10}$$

where $\phi_k(x, \boldsymbol{y}) = \exp\left(-[z - c^{(k)}]^t (\alpha \boldsymbol{R})^{-1} [z - c^{(k)}]\right)$; $z = [x \quad \boldsymbol{y}]^t$; $\boldsymbol{R} = E[z z^t]$ and eventually $c^{(k)} = [c_x^{(k)} \quad \boldsymbol{c}_v^{(k)}]^t$ and α are parameters to be determined for each function ϕ_k.

This form of the approximation of the joint pdf is extremely useful to compute the conditional probability $p_{x|y}(x|\boldsymbol{y})$ and the expected value $h(\boldsymbol{y}) = E[x|\boldsymbol{y}]$. In fact, it gives the expression of

the conditional expected value in the form:

$$E[x|\boldsymbol{y}] = \frac{\sum_{k=1}^{N_\phi} c_x^{(k)} w_k \phi_k(\boldsymbol{y})}{\sum_{k=1}^{N_\phi} w_k \phi_k(\boldsymbol{y})}$$

(11)

which clearly represents the expression of a normalized radial basis network.
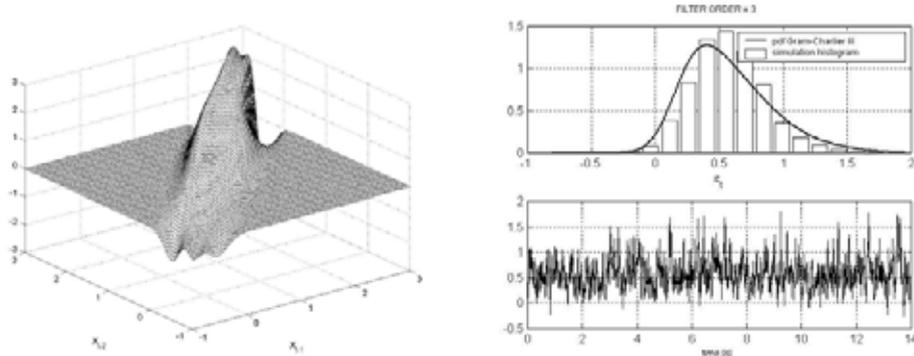
Figure 1: on the left, the function $h(\boldsymbol{y})$ obtained for an order 3 autoregressive filter; on the right, above the target distribution with the histogram of a realization and below a window of the realization itself.

REFERENCES

Broomhead D.S., Lowe D. (1988). "Multi-variable Functional Interpolation and Adaptive Networks", Complex Syst., Vol. 2, pp. 269-303.

Ditlevsen O., Mohr G., Hoffmeyer P. (1996). "Integration of non-Gaussian fields", Probabilistic Engineering Mechanics, Vol. 11, pp. 15-23.

Galton F. (1879). "The geometric mean, in vital and social statistics", Proc. Roy. Soc. London, Vol. 29, pp. 365-367.

Gaver D.P., Lewis P.A.W. (1980). "First-order autoregressive Gamma sequences and point processes", Adv. Appl. Prob., Vol. 12, pp. 727-745.

Gioffré M., Gusella V., Grigoriu M. (2000). "Simulation of non-Gaussian field applied to wind pressure fluctuations", Probabilistic Engineering Mechanics, Vol. 15, pp. 339-3.

Gotovac B., Kozulic, V. (1999). "On a selection of basis functions in numerical analyses of engineering problems", International Journal for Engineering Modelling, Vol. 12, pp. 17-24.

Grigoriu M. (2000). "Non-Gaussian models for stochastic mechanics", Probabilistic Engineering Mechanics, Vol. 15, pp. 15-23.

Haykin S. (1996). *Adaptive Filter Theory*, Prentice Hall, Upper Saddle River.

Iwatani Y. (1982). "Simulation of multi-dimensional wind fluctuation having any arbitrary power spectra and cross-spectra", Journal of Wind Engineering, vol. 11.

Kailath T. (1981), *Lectures on Wiener and Kalman Filtering*, Springer Verlag, Wien – New York.

McAlister D. (1879). "The law of the geometric mean", Proc. Roy. Soc. London, Vol. 29, pp. 367-376.

Nelles O., (2001), *Nonlinear System Identification*, Springer Verlag, Berlin Heidelberg.

Poggio T., Girosi F. (1990). "Networks for approximation and learning", Proc. IEEE, Vol. 78, pp. 1481-1497.

Puig B., Poirion F., Soize C. (2002). "Non-Gaussian simulation using Hermite polynomial expansion: convergence and algorithms", Probabilistic Engineering Mechanics, Vol. 17, pp. 253-264.

Seong S.H., Peterka J.A. (1997). "Computer simulation of non Gaussian multiple wind pressure time series", J. Wind Eng. Ind. Aerodyn., Vol. 72, pp. 95-105.

BARC
(BENCHMARK ON THE AERODYNAMICS OF A RECTANGULAR 5:1 CYLINDER)

BARC:
a Benchmark on the Aerodynamics of a Rectangular 5:1 Cylinder

G. Bartoli[1], L. Bruno[2], G. Buresti[3], F. Ricciardelli[4], M.V. Salvetti[3], A. Zasso[5]

[1] *CRIACIV-DICeA, University of Florence, Italy, gbartoli@dicea.unifi.it*

[2] *DISTR, Politecnico di Torino, Italy, luca.bruno@polito.it*

[3] *DIA, University of Pisa, Italy, g.buresti@ing.unipi.it, mv.salvetti@ing.unipi.it*

[4] *DIMET, University of Reggio Calabria, Italy, friccia@unirc.it,*

[5] *DIMEC-CIRIVE*, *Politecnico di Milano, Italy*, *alberto.zasso@polimi.it*

Keywords: Benchmark problems, Bluff body aerodynamics, Rectangular cylinders, Wind tunnel tests, CFD.

ABSTRACT

Recently a Benchmark problem has been started, in the field of bluff body aerodynamics (Bartoli et al 2008a). The aim of the Benchmark is to provide a contribution to the analysis of the turbulent, separated flow around a fixed rectangular cylinder with chord-to-depth ratio equal to 5. In spite of the simple geometry, it is believed that the problem is of interest not only for the purpose of fundamental research, but also to provide useful information on the aerodynamics of a wide range of bluff bodies of interest in Civil Engineering (e.g. long span bridges decks, high-rise buildings, and so on) and for other Engineering applications. Given the possible interest of Research Institutions and Industries operating in different fields of Engineering, using both computational and experimental tools, the benchmark addresses both the numerical and the experimental approach.

The aims of the Benchmark are the following:
(1) to deeply investigate one specific problem in the aerodynamics of bluff bodies, with contributions coming from as many researchers as possible worldwide;
(2) to assess the consistency of wind tunnel measurements carried out in different facilities;
(3) to assess the consistency of computational results obtained through different flow models and numerical approaches;
(4) to compare experimental and computational results;

Contact person: L. Bruno, Dipartimento di Ingegneria Strutturale e Geotecnica, Politecnico di Torino, Viale Mattioli 39, 10126 Torino, Italy, Phone +39 (0)11.090.4870, Fax +39 (0)11.090.4999, e-mail: luca.bruno@polito.it

(5) to assess the possibility of developing integrated procedures relying on both experimental and computational outcomes;

(6) to develop Best Practices for experiments and computations.

In addition, the results provided by the participants are meant to create a database to be made available to the Scientific and Technical communities for future reference.

The Benchmark problem is promoted by the Organising Committee, with the support of the Italian National Association for Wind Engineering (ANIV), under the umbrella of the International Association for Wind Engineering (IAWE) and in cooperation with the European Research Community On Flow, Turbulence And Combustion (ERCOFTAC). The activities will be carried out under supervision of the International Advisory Board.

The Benchmark addresses the high Reynolds number, external, unsteady flow around and past a stationary, sharp-edged rectangular cylinder, and the associated aerodynamic actions. The breadth (B) to depth (D) ratio is set equal to 5.

Participants are invited to submit their original contributions following specified formats. These can include both results already available to the participants and results specifically obtained for the purpose of participation in the Benchmark. In addition, participants are invited to share with the Scientific and Technical communities the literature and the published results available to them.

The following common requirements are set for both wind tunnel tests and numerical simulations:

(1) the depth-based Reynolds number has to be in the range of 2×10^4 to 6×10^4;

(2) the oncoming flow has to be set parallel to the base of the rectangle;

(3) the maximum intensity of the longitudinal component of turbulence is set to 0.01;

(4) the minimum spanwise length of the cylinder for wind tunnel tests and 3D numerical simulations is set to $L/D=3$.

(5) the maximum radius of curvature of the edges of the cylinder is set to $R/D = 0.05$

(6) the minimum sampling frequency is set to $f_s D/U = 8$, f_s being the shedding frequency.

In addition, the following requirements are specified for wind tunnel tests:

(7) the maximum wind tunnel blockage is set to 5%;

(8) all the points of measurement have to be outside the boundary layers developed at the tunnel floor, roof and side walls. Uniformity of the flow at the locations where measurements are taken must be checked in the bare tunnel and appropriately documented.

In Figures 1 and 2 sketches of the experimental and computational setups are shown.
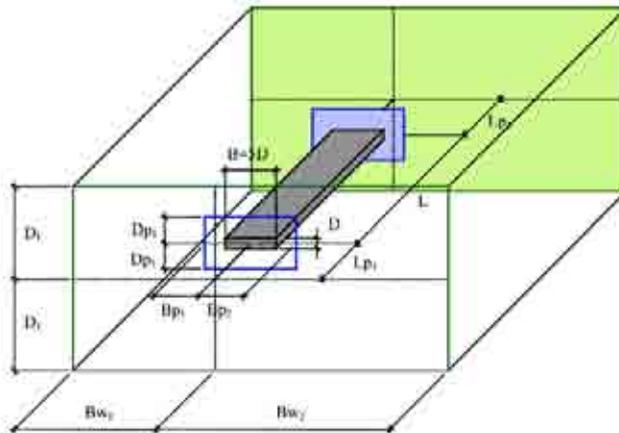
Figure 1: sketch of the experimental set-up
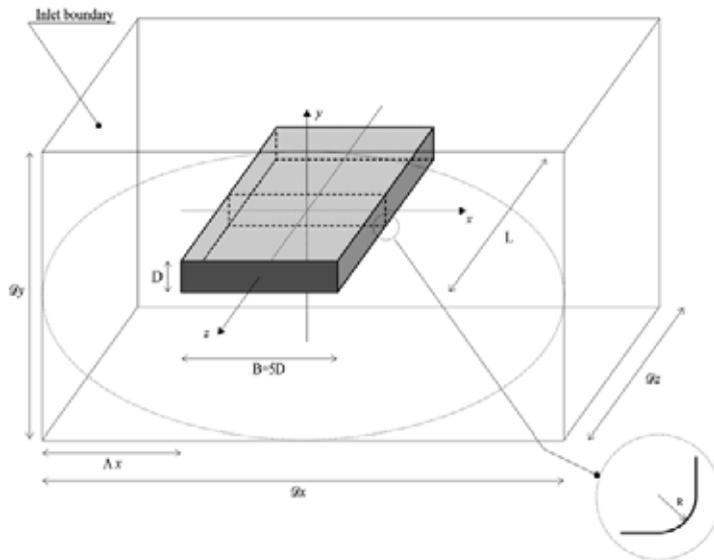
Figure 2: sketch of the computational domain

For participation in the Benchmark, information concerning the setup and a minimum set of output data must be provided by the participants, through upload on the Benchmark web page http://www.aniv-iawe.org/barc. These data will be available to all participants for download. This is to allow researchers to compare the results obtained by other researchers. All the problem quantities must be scaled with respect to the following reference dimensions:
- section depth D;
- fluid density ρ;
- undisturbed flow field velocity U_∞;

Both set-up information and output data are classified as "required", i.e. data that participants are requested to provide, and "encouraged", i.e. additional data that participants are encouraged to provide (Bartoli et al 2008b, 2008c). Finally, any further data can be provided by the participant, as "additional". As an example, Figure 3 shows required points of pressure measurement, and Figure 4 the additional points suggested.
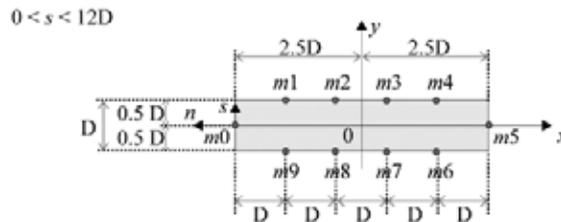
Figure 3: required points of measurement

Figure 4: additional points of measurement

Reference information can be shared among participants, upgrading the non-exhaustive bibliographic database provided to the participants (Bartoli et al 2008d)

In addition to the main set-up, sensitivity studies are strongly encouraged. The follow additional values of the parameters are suggested for both wind tunnel tests and numerical simulations:
- Angles of incidence of $1°$, $3°$, $6°$;
- Reynolds number of 1×10^3, 1×10^4, 1×10^5, 1×10^6;
- Turbulence intensities of 0.02, 0.05, 0.10.

REFERENCES

Bartoli G., Bruno L., Buresti G., Ricciarelli F., Salvetti M.V., Zasso A. (2008) BARC Overview Document, http://www.aniv-iawe.org/barc.
Bartoli G., Bruno L., Buresti G., Ricciarelli F., Salvetti M.V., Zasso A. (2008) Requests for Computational Simulations, http://www.aniv-iawe.org/barc.
Bartoli G., Bruno L., Buresti G., Ricciarelli F., Salvetti M.V., Zasso A. (2008) Requests for Wind Tunnel Tests, http://www.aniv-iawe.org/barc.
Bartoli G., Bruno L., Buresti G., Ricciarelli F., Salvetti M.V., Zasso A. (2008) Reference, http://www.aniv-iawe.org/barc.

Three-dimensional numerical simulation of flow around a 1:5 rectangular cylinder

C. Mannini[*], K. Weinman[†], A. Šoda[+], G. Schewe[‡]

[*]CRIACIV/Department of Civil and Environmental Engineering, University of Florence, Italy
claudio.mannini@dicea.unifi.it

[†]Institute of Aerodynamics and Flow Technology, German Aerospace Center, Göttingen, Germany
Keith.Weinman@dlr.de

[+] Faculty of Mechanical and Naval Engineering, University of Zagreb, Croatia
ante.soda@fsb.hr

[‡] Institute of Aeroelasticity, German Aerospace Center, Göttingen, Germany
Guenter.Schewe@dlr.de

Keywords: Computational Fluid Dynamics, Bluff bodies, Rectangular cylinder, Detached-Eddy Simulation, Turbulence modelling.

ABSTRACT

This paper deals with the numerical simulation of the unsteady flow field around a rectangular cylinder with a chord-to-thickness ratio $B/H = 5.0$ at zero flow incidence, low Mach number ($M = 0.10$) and high Reynolds number ($Re_B = 132,000$). The flow around this simple geometry shows several interesting and challenging features such as massive separation, unsteady shear-layer reattachment, formation of three-dimensional flow structures, shedding of large eddies. In addition, this geometry is considered to be a benchmark test case for studies dealing with bridge aerodynamics and aeroelasticity and for this reason it is also investigated from the experimental point of view by one of the authors in the high-pressure wind tunnel of the German Aerospace Center in Göttingen (Schewe, 2006).

The three-dimensional Detached-Eddy Simulation technique associated with the one-equation turbulence model of Spalart and Allmaras (SA-DES) is employed (Spalart et al., 1997; Shur et al., 1999). This is a hybrid method which combines the Unsteady Reynolds-Averaged Navier-Stokes (URANS) approach near the walls and the Large-Eddy Simulation (LES) approach away from the walls. It is particularly useful in case of flows with regions of massive separation, where the URANS

Contact person: C. Mannini, CRIACIV/Department of Civil and Environmental Engineering, University of Florence, Via S. Marta 3 – 50139 – Florence, Italy. Tel.: +39.055.4796326, FAX: +39.055.4796598
E-mail claudio.mannini@dicea.unifi.it

approach shows limited accuracy, and thin turbulent boundary layers, where wall-resolved LES becomes unaffordable due to the necessary grid refinement.

Numerical simulations have been performed using the finite-volume unstructured solver DLR-Tau code (Schwamborn et al., 1999), developed by the German Aerospace Center (DLR). The code solves the compressible governing equations using vertex-centered metrics with second-order spatial and temporal accuracy. Fluxes are approximated using second-order central differencing scheme. For time marching the dual-time-stepping and explicit Runge-Kutta methods are employed.

In this work hybrid meshes are employed, characterized by a structured-like node arrangement around the profile (body-aligned quadrilateral cells) and unstructured triangular cells in the remaining part of the domain. Figure 1 shows the 3-D grid (1,703,585 nodes and 2,957,440 cells) obtained by extruding a 2-D grid for one-chord length in the spanwise y-direction, using 65 nodes to discretize the resulting edges. The first structured layer height in the mesh is chosen in order to have wall unit values in the normal direction $z^+ \approx 1$. Isotropic cells are obtained in the "focus region" which represents the optimal conformation for the LES mode of DES (Spalart, 2001). The nondimensional time-step size is $\Delta s = 0.0034$, where $s = tU_\infty/B$ is the number of traveled chord lengths in a time unit ($U_\infty = 34.0$ m/s is the undisturbed flow speed), in order to discretize the expected period of vortex shedding with more than 500 time steps. This temporal discretization is slightly finer than the one suggested by Spalart (2001) on the basis of cell size and maximum flow velocity in the focus region.

Farfield (zero gradients) boundary condition is assumed at one-hundred chord lengths away from the center of the prism, while viscous wall and periodic boundary conditions are imposed respectively at the body contour and at the lateral planes of the computational domain. Free-stream value initial condition characterizes all the computations.

The chosen value for the DES constant is $C_{DES} = 0.45$, as suggested for the DLR-Tau code by Weinman et al. (2006), which implies that the LES modus of DES is active on 86 % of the computational domain.

In a previous paper (Mannini et al., 2008) it was shown that with the 3-D SA-DES approach significant improvement of the results can be obtained with respect to 2-D and 3-D URANS simulations, even if combined with advanced turbulence models. Figure 2 shows the lift and drag coefficients computed with the SA-DES technique, while comparison with experiments of a few important integral quantities is reported in Table 1. The Strouhal number is underestimated roughly by 7 % but the agreement is definitely satisfactory. Figure 3 depicts the contour plots of four time- and spanwise-averaged computed second-order statistical moments of the flow velocity. The symmetry of the results suggests the reasonable statistical convergence of the computation.
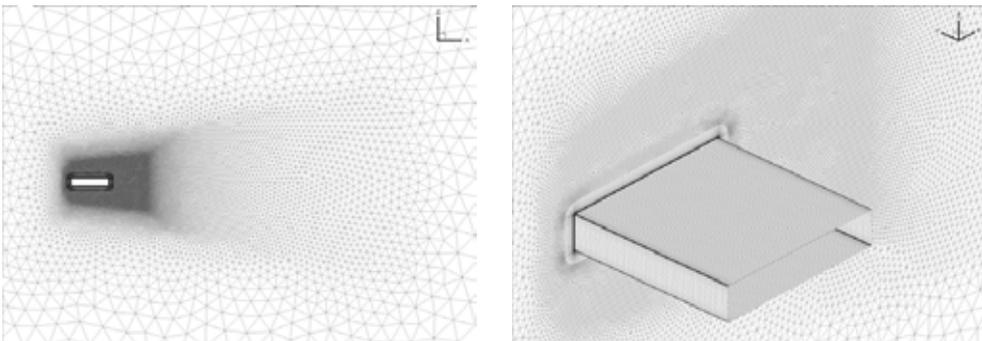
Figure 1: three-dimensional mesh used in the computations.
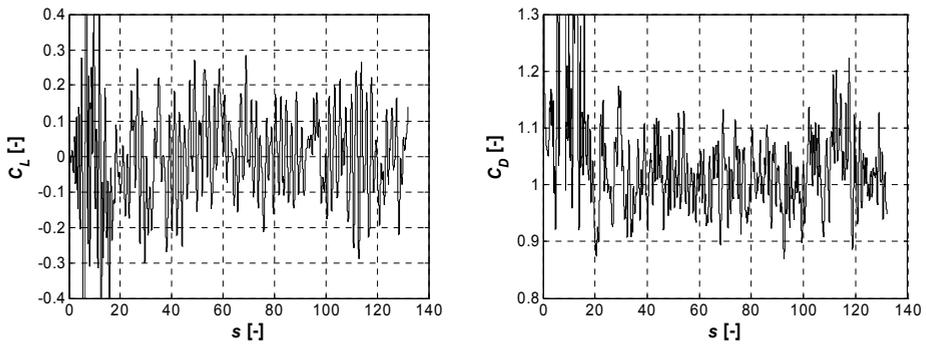
Figure 2: computed lift and drag coefficients (C_L and C_D are normalized respectively referring to the cylinder chord length B and height H).

	St	C_D	C_L^{RMS}	C_D^{RMS}
3-D SA-DES	0.103	1.016	0.111	0.055
Exp. (Schewe, 2006)	0.111	1.029	~ 0.1	

Table 1: comparison between numerical and experimental results. St is the Strouhal number based on the cylinder height H, C_D and C_D^{RMS} are respectively the mean and RMS values of the drag coefficient, C_L^{RMS} is the RMS value of the lift coefficient.
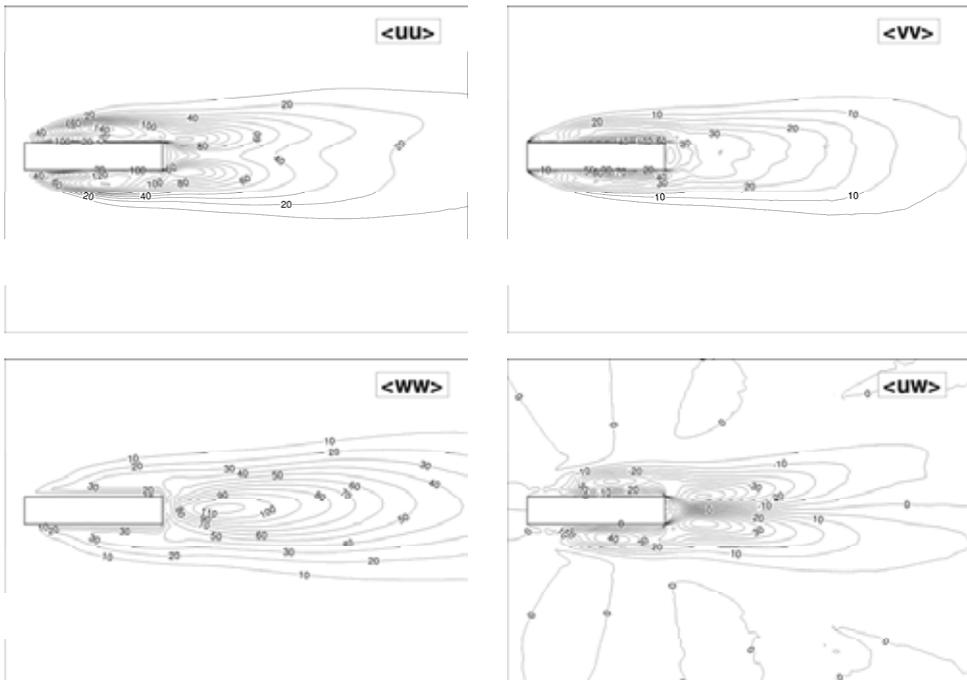
Figure 3: time- and spanwise-averaged second-order statistical moments of the flow velocity.
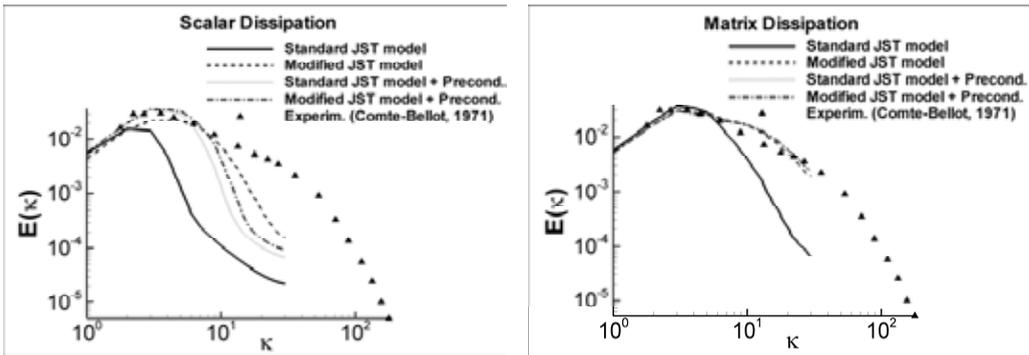
Figure 4: comparison against experiments of the spectrum of isotropic turbulence computed with several numerical approaches.

In order to improve the results and in particular to resolve smaller scales of turbulence in the cylinder wake, computations are underway employing matrix instead of scalar artificial dissipation to stabilize the convective central difference operators, along with a modified version of the Jameson-Schmidt-Turkel (JST) central differencing algorithm based on Ducros sensor (Ducros et al., 2000). Figure 4 clearly shows that with both scalar and matrix dissipation, standard JST model and no preconditioning the simulation of the basic test case of decaying isotropic turbulence is quite poor. Using scalar dissipation and low Mach-number preconditioning (Choi & Merkle, 1993) or modified JST model a significant improvement can be obtained but the simulation fails to reproduce the experimental spectrum at high wavenumber κ. Conversely the result is satisfactory with matrix dissipation and modified JST model both with and without preconditioning.

Finally another computation has been performed employing a 3-D mesh identical to the one depicted in Figure 1 but with double extension of the computational domain in the spanwise direction (3,380,961 nodes and 5,914,880 cells). Preliminary results show a significant reduction of the RMS value of fluctuating lift and drag coefficients with respect to the basic grid.

REFERENCES

Choi Y.-H., Merkle C.L. (1993). "The application of preconditioning in viscous flows", Journal of Computational Physics, 105 (2), 207-223.

Ducros F., Laporte F., Soulères T., Guinot V., Moinat P. and Caruelle B. (2000). "High-order fluxes for conservative skew-symmetric-like schemes in structured meshes: application to compressible flows", Journal of Computational Physics, 161 (1), 114-139.

Mannini C., Soda A., Schewe G., Weinman K. (2008). "Detached-Eddy Simulation of flow around a 1:5 rectangular cylinder", In M. Belloli, F. Cheli, G. Diana, S. Muggiasca, D. Rocchi & A. Zasso Eds., Proceedings of the 6th International Colloquium on Bluff Body Aerodynamics and Applications, Milan, Italy.

Schewe G. (2006). "Influence of the Reynolds-number on flow-induced vibrations of generic bridge sections". In J. Radić Ed., Proceedings of the International Conference on Bridges, SECON HDGK, pp. 351-358, Dubrovnik, Croatia.

Schwamborn D., Gerhold T., Kessler K. (1999). "DLR-TAU code – an overview". In Proceedings of the 1st ONERA/DLR Aerospace Symposium, Paris, France.

Shur M.L., Spalart P.R., Strelets M.Kh., Travin A. (1999). "Detached-eddy simulation of an airfoil at high angle of attack". In Engineering Turbulence Modelling and Experiments 4, W. Rodi and D. Laurence Eds., pp. 669-678.

Spalart P.R. (2001). Young-person's guide to Detached-Eddy Simulation grids. NASA CR-2001-211032.

Spalart P.R., Jou W.-H., Strelets M.Kh., Allmaras S.R. (1997). "Comments on the feasibility of LES for wings, and on a hybrid RANS/LES approach". In Advances in DNS/LES, C. Liu and Z. Liu Eds., Greyden Press, Columbus, OH.

Weinman K.A., van der Ven H., Mockett C.R., Knopp T.A., Kok J.C., Perrin R.T.E., Thiele F.H. (2006). "A study of grid convergence issues for the simulation of the massively separated flow around a stalled airfoil using DES and related methods". In Proceedings of the European Conference on Computational Fluid Dynamics, Egmond aan Zee, The Netherlands.

Analysis of the separated flow around a 5:1 rectangular cylinder through computational simulation

1st L.Bruno, 2nd N. Coste, 3rd D. Fransos

*Dipartimento di Ingegneria Strutturale e Geotecnica, Politecnico di Torino - luca.bruno@polito.it -
Viale Mattioli 39, 10126 Torino, Italy*

*OptiFlow Company - coste@optiflow.fr -
Bât. Azurburo, 27, boulevard Charles Moretti, 13014 Marseille, France*

*OptiFlow Company - fransos@optiflow.fr -
Bât. Azurburo, 27, boulevard Charles Moretti, 13014 Marseille, France*

ABSTRACT

The aerodynamic behaviour of rectangular cylinders has attracted the attention of the scientific community since the experimental reference works of Okajima (1982) and Norberg (1993). On one hand, both the two dimensional (2D) and three dimensional (3D) features of the low-Reynolds number flow around rectangular cylinders has been clarified in several studies, e.g. in Nakamura et al. (1996), Hourigan et al. (2001), Tan et al. (2004). On the other hand, the high-Reynolds number flow (i.e. Re $\geq$ 1.e + 4) has been studied by means of both experimental and computational approaches, with emphasis on its dependence on the chord-to-depth ratio, e.g. in Yu & Kareem (1996,1998), Shimada & Ishihara (2002). Recently, a Benchmark on the Aerodynamics of a 5:1 Rectangular Cylinder (ʙᴀʀᴄ) has been proposed in order to provide a contribution to the analysis of the high-Reynolds number, turbulent, separated flow around a fixed rectangular cylinder with chord-to-depth ratio equal to 5 (Bartoli et al. 2008). This ratio is far enough from those at which discontinuities in the aerodynamic regime arise, i.e. the 2.8 and 6 ratios (Shimada & Ishihara 2002), in order to avoid the introduction of further difficulties in the study. For this benchmark, the depth-based Reynolds number Re = UD/ has to be in the range of 2.e+4 to 6.e+4, the oncoming flow has to be set parallel to the base of the rectangle (such angle of attack is termed = 0) and the maximum intensity of the longitudinal component of turbulence has to be I_u = 0.01. The selected cylinder is considered as a representative benchmark of a bridge deck or high-rise building elongated section.

In the perspective of the benchmark, an exploratory study has been performed by the present authors (Bruno et al. 2008) adopting Re = 4.e+4 in order to focus on two main aspects.

First, the evaluation of the 3D features of the flow around nominally 2D bluff cylinders remains

Contact person: 1st L. Bruno, Dipartimento di Ingegneria Strutturale e Geotecnica, Politecnico di Torino, Viale Mattioli 39, 10126 Torino, Italy, Phone +39 (0)11.090.4870, Fax +39 (0)11.090.4999, e-mail: luca.bruno@polito.it

an inescapable task also for rectangular sections. Studies through both experimental (Matsumoto et al. 2003) and computational (Tamura et al. 1990) approaches have contributed to this topic in the case of rectangular cylinders. Apart from the span-wise correlation coefficient (Vickery 1996) and the coherence spectral function (Matsumoto et al. 2003), which are generally employed for long cylinders, the Proper Orthogonal Decomposition (POD) methodology is more and more being adopted for the analysis and synthesis of random wind pressure fields, especially on high-rise buildings (e.g. Best & Holmes 1983, Holmes 1990, Tamura et al. 1999). The POD has been applied by the authors to the benchmark cylinder in order to quantify the 3D flow features: the POD analysis shows that, even though the 3D flow features are not negligible, the main phenomena which drive the aerodynamic forces remain 2D.

Second, according to the authors, some difficulties remain in describing the expected complex flow phenomena around the cylinder and in relating such phenomena to the fluctuating aerodynamic forces acting on the cylinder itself. The computational approach post-processing facilities has been employed by the present authors to look for significant relationships between flow structures, pressure field and aerodynamic forces: homogeneous regions along the side surfaces have been proposed and the so-called "mean pressure recovery" region has been identified as the one that gives the most significant contribution to the lift force.

The present study aims to give a deeper insight in the computational results previously obtained, with special emphasis to the relationships between the sectional fluctuating pressure field along the side surface and the velocity-vorticity fields in its neighborhood, resulting from the boundary layer separation and the vortex-shedding.

In this study, the 3D, turbulent, unsteady flow around the cylinder is modelled in the frame of the Large Eddy Simulation (LES) approach to turbulence using the classical time-dependent filtered Navier-Stokes equations. The sub-grid stress tensor is expressed according to Boussinesq's assumption and the equation system is closed by a transport equation for the kinetic energy k_t of the unresolved stresses (Yoshizawa 1986). The k_t equation is damped approaching the solid wall.

The computational domain and the boundary conditions are shown in Figure 1. The spanwise length of the domain is equal to $L/B = 1$. Dirichlet conditions on the velocity field and on the sub-grid kinetic energy are imposed at the inlet boundaries. Neumann conditions on the normal component of the stress tensor $\mathbf{\Gamma}$, as well as the same Dirichlet conditions on k_t, are imposed at the outlet boundaries. Periodic conditions are imposed on both the side surfaces and on the upper-lower surfaces, as depicted in Figure 1. No-slip conditions are imposed at the section surface. The initial conditions are obtained from a previous LES simulation, where the standard Smagorinsky sub-grid model (Smagorinsky 1963) was employed.
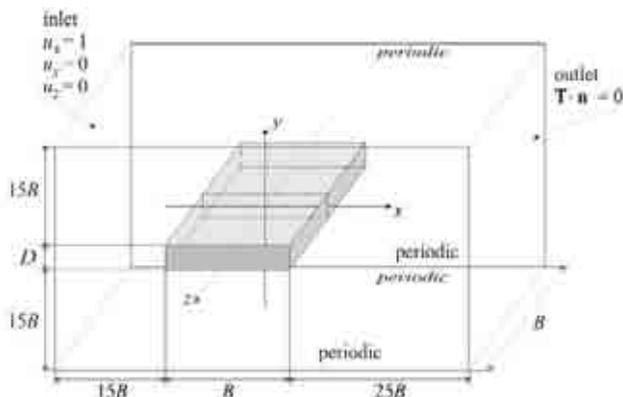
Figure 1: Analytical domain and boundary conditions

A hexahedral grid is adopted to discretise the spatial computational domain. A body-fitted, structured boundary layer grid is generated near the wall and a paved quadrangular grid is used to fill the remaining part of the domain in the *x,y* plane; the 3D grid is then obtained through an extrusion in the *z* direction. The computational grid in space consists of about 1.65e+6 cells. The resulting non-dimensional mean wall distance value y^+ is close to the unit. The non-dimensional time-step needed for an accurate advancement in time is Δt = 5.e-3 *tU/D*. The simulation is extended over *T* = 800 *tU/D* non dimensional time units in order to overcome the transient solution and to allow the statistical analysis of the periodic flow.

The OpenFoam® Finite Volume open source code is used in the following to numerically evaluate the flow-field. The cell-center values of the variables are interpolated at face locations using the second-order Central Difference Scheme for the diffusive terms and the Limited Linear scheme for the convection terms (Jasak et al. 1999). Advancement in time is accomplished by the two-step Backward Differentiation Formulae method. The pressure-velocity coupling is achieved by means of the pressure-implicit PISO algorithm, using a predictor-corrector approach for the time discretisation of the momentum equation, whilst enforcing the continuity equation. Computations are carried out on 8 Intel Quadcore X5355 2.66GHz CPUs and require about 2.5GB of memory and 15 days of CPU time for the whole simulation.

A conceptual partition of the side-surface has been proposed in Bruno et al. (2008) on the basis of the mean flow topology, of the pressure statistics and its spectral content. Four regions has been pointed out: the separation bubble length (*sb*), the vortex shedding length (*vs*), the mean pressure recovery length (*pr*) and the mean reattached flow length (*rf*). In particular, the pressure coefficient evolution in time at the mid point of each length and the normalised Power Spectral Densities (PSDs) of the pressure are related to the regions in Figure 2.
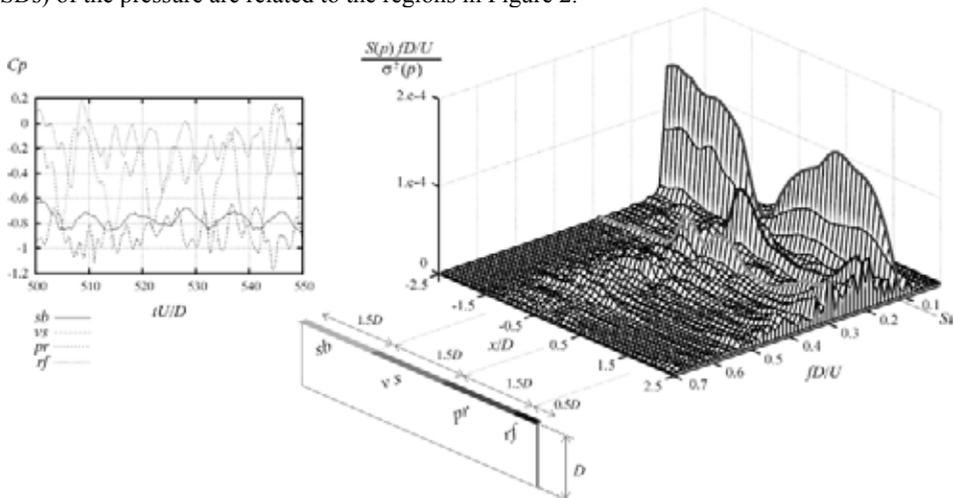
Figure 2: Pressure coefficient time histories and PSD along the upper side surface

The pressure fluctuations in the *sb* and *pr* lengths are mainly characterised by one frequency component, which corresponds to the prevailing frequency in the lift coefficient (Strouhal number *St*). On the contrary, the points in the *vs* and *rf* lengths show a broad band spectrum, where the most significant frequencies are higher than *St*. According to the authors, these differences can be related to the main vortex formation process, mainly driven by the high-frequency shedding from the separation point of small-scale vorticity structures, as suggested by the isosurfaces of the second invariant tensor of the velocity gradient plotted in Figure 3. The mean vortex sheds from the apex of the separation bubble once a given number of such vorticity structures coalesce.
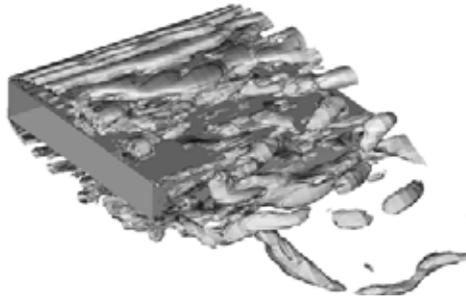
Figure 3: Second Invariant Tensor isosurfaces

The final paper will verify this assumption by means of a quantitative description of the relationships between the vortical structures, the main vortex shedding and the spectral content of the sectional pressure field.

REFERENCES

Okajima A. (1982). "Strouhal numbers of rectangular cylinders. Journal of Fluid Mechanics", 123, 379–398.

Norberg C. (1993). "Flow around rectangular cylinders: pressure forces and wake frequencies", Journal of Wind Engineering and Industrial Aerodynamics, 49, 187–196.

Nakamura Y., Ohya Y., Ozono S., Nakamaya R. (1996). "Experimental and numerical analysis of vortex shedding from elongated rectangular cylinders at low Reynolds numbers 200-1000", Journal of Wind Engineering and Industrial Aerodynamics, 65, 301–308.

Hourigan K., Thompson M. C., Tan B. T. (2001). "Self-sustained oscillations in flows around long blunt plates", Journal Fluid and Structures, 15, 387–398.

Tan B. T., Thompson M.C., Hourigan F.(2004). "Flow past rectangular cylinders: receptivity to transverse forcing", Journal of Fluid Mechanics, 515, 33–62.

Yu D., Kareem A. (1996). "Two-dimensional simulation of flow around rectangular prism", Journal of Wind Engineering and Industrial Aerodynamics, 62, 131–161.

Yu D., Kareem A. (1998). "Parametric study of flow around rectangular prisms using LES", Journal of Wind Engineering and Industrial Aerodynamics, 77-78, 653–662.

Shimada K., Ishihara T. (2002). "Application of a modified k-ε model to the prediction of aerodynamic characteristics of rectangular cross-section cylinders", Journal of Fluid and Structures, 16, 465–485.

Bartoli G., Bruno L., Buresti G., Ricciarelli F., Salvetti M.V., Zasso A. (2008) "BARC Overview Document", http://www.aniv-iawe.org/barc .

Bruno L., Fransos D., Coste N., Bosco A. (2008). "3D flow around a rectangular cylinder: a computational study", Proc. Sixth International Colloquium on Bluff Body Aerodynamics & Applications, Milan.

Matsumoto M., Shirato H., Aaraki K., Haramura T., Hashimoto T. (2003). "Spanwise coherence characreristic of surface pressure field on 2D bluf bodies", Journal of Wind Engineering and Industrial Aerodynamics, 91, 155–163.

Tamura T., Otha I., Kuwahara K. (1990) "On the reliability of two-dimensional simulation for unsteady flows around a cylinder-type structure", Journal of Wind Engineering and Industrial Aerodynamics, 35, 275–298.

Vickery B.J. (1966) "Fluctuating lift and drag on a long cylinder of square cross-section in a smooth and in a turbulent stream", Journal of Fluid Mechanics, 25, 481–494.

Best R.J., Holmes J.D. (1983) "Use of eigenvalues in the covariance integration method for determination of wind load effects", Journal of Wind Engineering and Industrial Aerodynamics, 13, 359–370.

Holmes J.D. (1990) "Analysis and synthesis of pressure fluctuations on bluff bodies using eigenvectors", Journal of Wind Engineering and Industrial Aerodynamics, 33, 219–230.

Tamura Y., Suganuma S., Kikuchi H., Hibi K. (1999). "Proper Orthogonal Decomposition of random wind pressure field", Journal of Fluids and Structures, 13, 1069–1095.

Yoshizawa A. (1986). "Statistical theory for compressible shear flows with the application of subgrid modelling", Physics of Fluids A, 29, 2152–2163.

Smagorinsky J.(1963) "General circulation experiments with the primitive equations. I. The basic experiment", Month. Weather Rev., 91, 99–164.

Jasak H., Weller H. G., Gosman A. D. (1999). "High resolution NVD differencing scheme for arbitrarily unstructured meshes", International Journal for Numerical Methods in Fluids, 31, 431–449.

Reynolds-Number-Effects in flow around a rectangular section with aspect ratio 1:5

Günter Schewe

DLR – Institut für Aeroelastik, 37073 Göttingen, Germany, guenter.schewe@dlr.de

Keywords: Reynolds number, bluff body, sharp-edged section, rectangular section 1:5, BARC, separation bubble

ABSTRACT

The paper reports on experiments carried out over a wide range of Reynolds numbers $(2 \cdot 10^4 < Re < 2 \cdot 10^6)$ in the high pressure windtunnel in Göttingen. The model was a rectangular cylinder with aspect ratio 1:5. It is a sharp-edged generic section, which was selected as benchmark problem for bluff bodies in general (www.aniv-iawe.org/barc/BARC). The high Reynolds numbers were reached by increasing the pressure in the flow medium up to 70 bar. The steady and unsteady forces were measured with a piezoelectric balance whose major characteristic is its stiffness, which makes the instrument particularly useful for investigating unsteady phenomena. Thus apart from the steady values including the base pressure coefficient also power spectra and probability density functions were measured yielding for example Strouhal Nos statistical moments etc.

As an example the figure 1 shows the lift coefficient upon the Reynolds number for different angles of incidence α. For α = 4° a significant Re No effect is obvious in the curve, which is double bent and the values are ranging from 0.3 to 0.6. In addition the trend to lower or to higher Re Nos indicates a further decrease and increase of the lift coefficient, respectively. Also for α = 6° and α = 2° there is a significant increase of the lift in the range $Re < 10^5$, at which the rise is shifted to lower- for α = 6° and to higher Re in case of 2°.

Contact person: G. Schewe, DLR – Institut für Aeroelastik, 37073 Göttingen, Bunsenstrasse 10, Germany ,
Tel.: +49551 709 2423, E-mail guenter.schewe@dlr.de
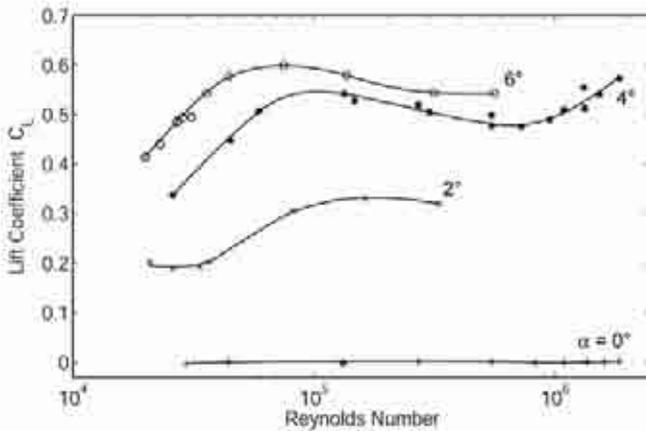
Figure 1: Lift coefficient upon the Reynolds number for different angles of incidence α
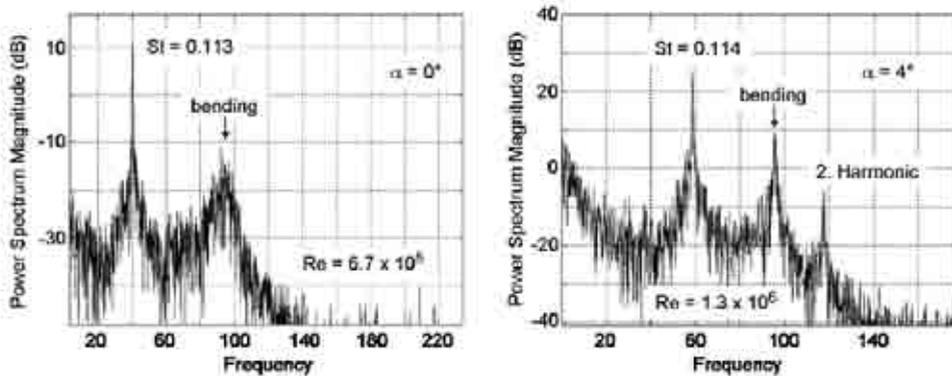
Figure 2: Power spectra of lift for rectangular section for two angles of incidence α

Figure 2 displays two representative power spectra of the lift fluctuations for two angles of incidence. In both cases there are rather narrow peaks due to the vortex shedding which have nearly the same Strouhal No St = 0.11. The bending frequency of the model is visible at $f \approx 94$ Hz, its power spectral density is more than 20 db below the Strouhal peak. Further, for the asymmetric case ($\alpha = 4°$, pressure in the windtunnel p = 70 bar, flow speed u_∞ = 5.7 m/s) the low frequency part is more pronounced and the occurrence of a significant second harmonic is obvious. It should be remarked here, that no parasitic resonances of the balance are present. For $\alpha = 0°$ the flow parameter were as follows: p = 50 bar, u_∞ = 3.9 m/s. The Reynolds numbers are in the figures.
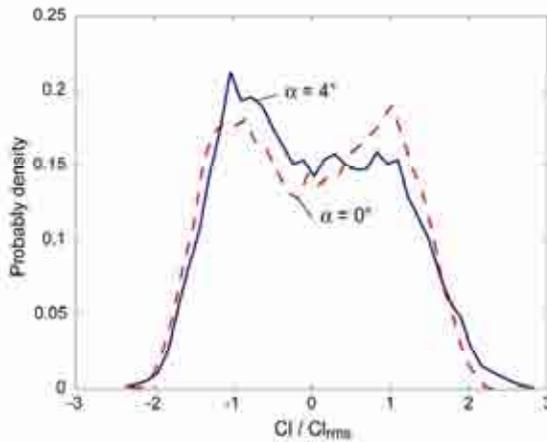
Figure 3: Probability density functions of lift fluctuations for two angles of incidence

Figure 3 shows the probability density functions for two angles of incidence α and the same flow conditions in figure 2. For $\alpha = 4°$ (solid line), the asymmetric case, a significant skewness of the PSD is obvious, which is reflected in a positive third moment with a value of 0.2.

Finally the Re No dependent shape of separation bubbles is probably responsible for the described effects, these are stronger in asymmetric flow ($\alpha \neq 0°$) than in the symmetric case ($\alpha = 0°$), where the effects on the upper and the lower side can compensate each other.

The present investigation confirms the conclusion drawn in Schewe (2001) that also bluff bodies having sharp-edged sections may suffer pronounced Reynolds-number effects.

REFERENCES

Schewe, G. "Reynolds Number Effects in Flow around more or less bluff bodies", J.Wind Eng. Ind. Aerodyn. 89 (2001) 1267-1289

CABLE DYNAMICS

Corotational cable elements to model suspended cables under wind loading

1st M. Di Pilato, 2nd F. Martelli, 3rd L. Martinelli

Department of Structural Engineering, Politecnico di Milano – dipilato@stru.polimi.it –
Piazza Leonardo da Vinci, 32 20133 Milan –

Structural Engineering – martelli.frn@gmail.com

Department of Structural Engineering, Politecnico di Milano – martinel@stru.polimi.it –
Piazza Leonardo da Vinci, 32 20133 Milan

Keywords: finite element models, wind turbulence loading, fluid structure interaction.

ABSTRACT

Cables are very efficient structural members widely used in many mechanical, civil, electrical and ocean engineering applications. Due to their slenderness and flexibility, they have a dynamic behaviour strongly affected by various nonlinear phenomena.

In this work a numerical procedure is enhanced to study the nonlinear interaction between flexible structures and a fluid flow. The numerical procedure is based upon the Newmark method, modified according to Hilber, Hughes and Taylor, and on finite elements capable of computing the cable mechanical response as well as the interaction forces induced by a steady or random wind flow.

A three-node cable isoparametric finite element (FE) in the small strain and large displacement regime was formerly used in Martinelli & Perotti (2001-2004); however, whenever rotations are large, C_0 models based on nodal displacements are inappropriate for capturing the system response since they cannot fully describe the system orientation. Moreover, when these models are augmented with local degrees of freedom to describe the cable twist, the nodal equilibrium conditions are not fully satisfied.

Recent studies on cable dynamics show that flexural stiffness plays an important role, especially in low-tension cables. It can be also noted that neglecting flexural stiffness can lead to singularities as numerical algorithms may become unstable when the tension approaches zero anywhere along the

---

Contact person: 3rd L. Martinelli, Department of Structural Engineering, Politecnico di Milano, Piazza Leonardo da Vinci, 32 20133 Milan, 00390223994247 and FAX 00390223994220. E-mail martinel@stru.polimi.it

cable. Moreover unacceptable errors in the prediction of high order frequencies can also arise (see Koh & Rong (2004)).

These problems were initially faced in Di Pilato et al. (2007), where the cable was described using two different superimposed FEs: a corotational 3D beam element used to compute the nodal restoring forces considering large displacements and rotations, and a second corotational 'aerodynamic' element (three-node isoparametric FE) for evaluating the aerodynamic nonlinear forces within the Quasi-Stationary theory in the varied dynamic configuration. The main idea of the corotational formulation is to decompose the motion of the element into rigid body and pure deformational parts through the use of a local (corotational) reference system (Figure 1a). The geometric non-linearity due to large displacements and rotations is incorporated in the transformation matrices relating local to global (Figure 1b) coordinates.

a)   b)
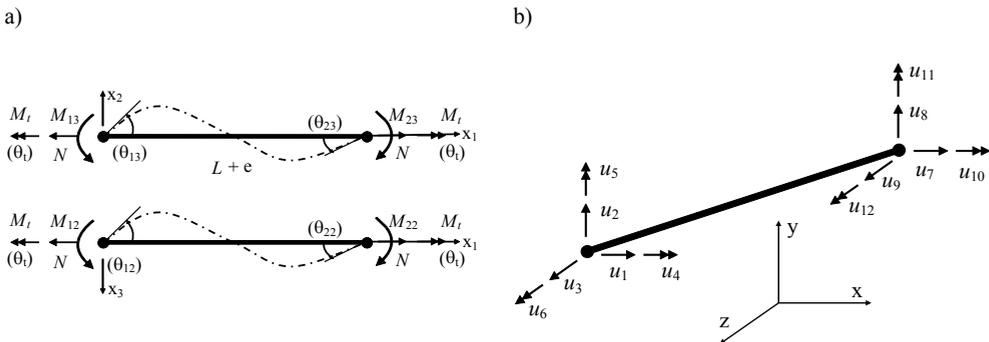
Figure 1. (a) Member basic displacements and forces (principal system); (b) Global reference system displacements.

The transformation procedure proposed by Di Pilato et al. (2007), performed defining a conventional rigid body motion (mainly based on the Oran (1973) approach), suffers from the drawback of being valid only when nodal rotations and their increments are small, hence leading to very small time steps and high computational cost when applied to cable dynamics.

This modelling procedure, in the following named small-small approach (S-S), has been enhanced by overcoming the expound limitations. First in Di Pilato et al. (2008) the limitation about the smallness of the nodal rotations was removed employing the Euler angles framework for describing the nodal configuration. Based on the Euler's decomposition theorem, the rotation matrix that describes the orientation of any frame in the space can be decomposed as a product of three elemental rotations described by the Euler angles, that were chosen according to the convention (1,3,2) (Diebel (2006)). Such an approach, named in the following large-small (L-S), has the advantage to retain the meaning the rotation variables in the small-small approach in case of small Euler angles and thus to simplify interfacing cable elements with other structural elements not formulated on the base of Euler angle.

Proceeding in the enhancements, the further hypothesis of small incremental rotations has been removed in this paper, leading to the approach named as large-large (L-L). The removed limitation regards the procedure for updating the orientation of the element. In the framework of the L-L approach, the joints orientation, which controls that of the element, is updated through a parametrization of the rotations by means of quaternions which, as known, form a convenient 4-parameters representation of rotations and allow for large increments.

Moreover a modified element stiffness matrix has been built to correctly represent the rigid-body invariance even for large rotations. As shown by Nour-Omid & Rankin (1991) the co-rotational formulation exhibits difficulties in terms of invariance, that is the internal force field derived from the strain energy is not in equilibrium. To force the equilibrium, the element stiffness matrix should be obtained as the consistent linearization of the internal forces which involves also the derivative of the transformation equations from global to local coordinate system. As a matter of facts, a numerical approximation of the stiffness matrix has been implemented in this work, obtained as the derivative of

the vector of restoring forces.

The aim of the paper is the comparison between the proposed incremental rotations approaches S-S, L-S and finally L-L, evidencing the relative advantages and disadvantages, also respect to the classical cable formulation. Furthermore the feasibility and the accuracy among all procedures are deeply investigated with reference to the amplitude of the global and incremental rotations, and the size of the finite element discretization.

The corotational (CR) formulation here described has been implemented in the Fortran code "NONDA" (Martinelli et al. (1996)). To validate the numerical model and the integration scheme, nonlinear dynamic analyses have been performed on a suspended cable with horizontal supports, already investigated by Luongo & Piccardo (1998) by means of the perturbation method and by Martinelli & Perotti (2001-2004) with the finite element technique.

Due to its mechanical characteristics, the cable is initially close to the first cross-over point (Irvine (1981)), with an internal resonance condition of 2:1 type. This means that the first in-plane normal mode has a natural frequency which is twice of the one of the first out-of-plane mode. The aerodynamic properties of the cable are those of the U-shaped section in Yu et al. (1993), schematically depicted in Figure 2. as well as the lift, drag and moment coefficients versus angle of attack.
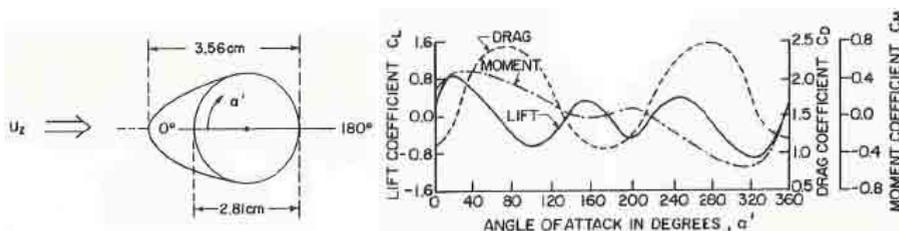
Figure 2. U-shape aerodynamic cable section and aerodynamic coefficients vs angle of attack (Yu *et al.*, 1993)

Numerical simulations on the cable modelled using CR beam elements superimposed to aerodynamic elements (CR cable element), have been carried out on two cases named respectively: twist-constrained and twist-allowed. In the first case, cross-section rotation is constrained (case: TC in Figure 3.b) at both cable ends and the aerodynamic coefficients are evaluated as per freezing the cross-sections in the static equilibrium configuration for no-wind condition. In the second case considered the sections rotation is allowed (case: TA in Figure 3.c) and the aerodynamic coefficients are computed in the effective cable spatial configuration.

a)   b) case: TC   c) case: TA
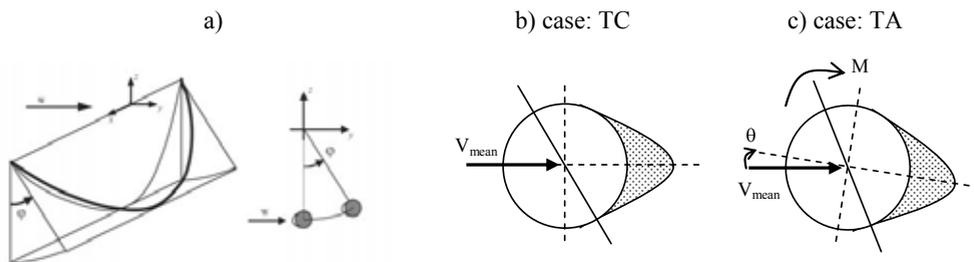
Figure 3. a) Geometric configuration of the cable; b) U-shape aerodynamic cable section for twist-constrained case, TC; c) U-shape aerodynamic cable section for twist-allowed case, TA

The dynamic response of the cable under either steady or multi-correlated 3D turbulent wind flow is reported in order to investigate the effects of aerodynamic coupling between flexural and torsional behavior. Time histories analyses of the cable model under steady wind velocity are presented. Results also compare two extreme modelling scenarios: the corotational and the traditional cable

modelling approach, the second is able to reproduce the twist-constrained condition only. It is worth to note that twist restrained conditions can significantly affects the cable response especially at increasing wind velocity.

Response of cable model under turbulent wind field is also presented. Turbulence is modelled by generating artificial time histories, according to a 3D turbulent model based on the definition of direct spectral densities and coherency functions. Looking at the results it can be said that, for the analyzed cable, displacement amplitudes are almost comparable for both cases twist allow and twist constrained. Nevertheless the slightly larger difference for the TA case suggests that the effects of torsion and static rotation cannot be generally neglected.

The capability and the accuracy of the procedures, to predict and simulate the complexity of the dynamic response of flexible structures under fluid forces, are further discussed in terms of computational cost.

REFERENCES

Martinelli L., Perotti F. (2001). Numerical Analysis of the non-linear dynamic behaviour of suspended cables under turbulent wind excitation, *Int. J. of Struct. Stab. and Dyn.*, Vol. 1(2), pp. 207-233.

Martinelli L., Perotti F. (2004). Numerical analysis of the dynamic behavior of cables under turbulent wind, *2nd Int. Conf. Struct. Eng. Mech. & Comput. (SEMC 2004)*, Cape Town, South Africa.

Koh C.G., Rong Y. (2004). Dynamic analysis of large displacement cable motion with experimental verification, *Journal of Sound and Vibration*, Vol. 272, pp. 187-206.

Di Pilato M., Martelli F., Martinelli L. (2007). Corotational Cable Element for the Study of Fluid-Structure Interaction, *7th Int. Symposium on Cable Dynamics*, Vienna, Austria, (CD-ROM).

Oran C. (1973). Tangent stiffness in space frames, *J. Struct. Div. ASCE*, Vol. 99(ST6), pp. 987-1001.

Di Pilato M., Martelli F., Martinelli L. (2008). Corotational Cable Elements to Simulate the Behaviour of Suspended Cables under Wind Loading, *InVENTO*, Palermo, Italy.

Diebel J. (2006). Representing Attitude: Euler Angles, Unit quaternions, and Rotation Vectors.

Nour-Omid B., Rankin C.C. (1991). Finite rotation analysis and consistent linearization using projectors, *Computer Methods in Applied Mechanics and Engineering*, Vol. 93, pp. 353-384.

Martinelli L., Mulas M.G. and Perotti F. (1996). The seismic response of concentrically braced moment-resisting steel frames, *Earth. Eng, & Struct. Dyn.*, Vol. 25, pp. 1275-1299.

Luongo A., Piccardo G. (1998). Non-linear galloping of sagged cables in 1:2 internal resonance, *J. of Sound and Vibration*, Vol. 214(5), pp. 915-940.

Irvine M. (1981). *Cable structures*, The M.I.T. Press, Cambridge, MA, U.S.A.

Yu P., Desai Y.M., Shah A.H., Popplewell N. (1993). Three-degree-of-freedom model for galloping, part II: solutions, *Journal of Engineering Mechanics*, Vol. 119, pp. 2426-2448.

Numerical investigation of conductor bundle icing

T. Wagner[1], U. Peil[2], C. Borri[3]

[1] *Technische Universität Carolo-Wilhelmina zu Braunschweig, International Graduate School for Risk Management of Natural Hazards, Beethovenstraße 51, 38106 Braunschweig, Germany, t.wagner@tu-bs.de*
[2]*Technische Universität Carolo-Wilhelmina zu Braunschweig, Institute of Steel Structures, Beethovenstraße 51, 38106 Braunschweig, Germany, u.peil@is.tu-braunschweig.de*
[3]*Università degli Studi di Firenze, Dipartimento di Ingegneria Civile, Via di S. Marta 3, 50139 Firenze, Italy, cborri@dicea.unifi.it*

Keywords: transmission line icing, CFD, particle tracing

ABSTRACT

Atmospheric icing occurs when freezing raindrops, supercooled cloud droplets or snow flakes hit a surface. This phenomenon can cause significant damage to electric power transmission networks, especially in combination with wind. Therefore shape and density of ice forming on cables are of major interest in investigating the risk of failure. Large amplitude oscillations at low frequencies or also twisting due to asymmetrical icing of cables can cause fatigue damages. In extreme events atmospheric icing can cause severe damage on towers and power lines (Bendel 1981, Jones 1998). A large number of small-scale failures can cause enormous damage just as well as a single major winter storm event (Llinca 1996, Muhlerin 1998). Examples of such events took place in northern America in 1998 and to a much smaller extent in Germany in 2005, where the devastating power of winter storms left many people without electricity for weeks and caused significant monetary damage (Makkonen 2000, Bundesnetzagentur 2006, Lämpke 2006).

   The following three reasons make it seem useful to develop a simulation scheme allowing for particle motion based on the stream occurring around conductor bundles: Firstly, meteorological observations from the 1950s give a first hint that tandem arrangements of cylinders have an effect on the icing process (Diem 1955, Waibel 1956). Secondly, the vulnerability of modern societies to blackouts is growing with the increasing demand of energy and increasing use of capacity. Since public authorities in Germany tend to restrict the construction of new transmission lines, bundled conductors are used increasingly to cope with the rising energy demand (Kießling 2001). Thirdly,

---
Contact person: T. Wagner, Technische Universität Carolo-Wilhelmina zu Braunschweig,
   International Graduate School for Risk Management of Natural Hazards,
   Beethovenstraße 51, 38106 Braunschweig, Germany, Phone +49 (0)531 / 391-3369, Fax +49 (0)531 / 391-4592.
   E-mail t.wagner@tu-bs.de

available numerical models are restricted to single cables due to the assumptions made in the air flow calculation, for example Lozowski et al. (1983), Makkonen (1984, 1989, 1998), Jones (1998) and Fu et al. (2004, 2006). A good overview of cable icing models and the mechanism of ice accretion is given by Poots (1996) and Makkonen (2000, 2005).

Modelling atmospheric icing includes a computation of the mass flux of icing particles as well as a determination of the icing conditions:

Icing conditions are defined by the heat balance on the ice surface. Messinger (1953) proposed a basic scheme to investigate heat balances on ice surfaces. The icing condition influences the accretion mass and furthermore the evolving ice density. Three major types of deposit, namely rime, glaze and wet snow lead to significant loads on structures. For glaze ice and wet snow formation the heat balance on the ice surface is very important. It is termed as wet growth, because a liquid layer forms on the ice surface. In contrast to that, rime ice develops in dry growing conditions. The heat transfer within the system can be neglected, because the latent heat of the droplets released during freezing is dissipated without changing the state of the ice and the surface conditions, hence no liquid layer arises.

Computation of the mass flux of icing particles is an important factor in the ice accretion. Shape and to a smaller extent also density of ice evolution is influenced by the characteristics of the particle trajectories. The present work focuses on the mass flux of icing droplets and the formation of the ice front. In a first step, this model is limited to a dry ice growing regime, in other words, only rime ice evolution is considered. With further development the model is to include also wet ice conditions.

To calculate air flow around the conductors the finite element software COMSOL Multiphysics and a Reynolds Average Navier-Stokes (RANS) solver are used (Comsol 2007). The fluid dynamic calculation is based on the incompressible and isothermal Navier-Stokes equation. It assumes a constant density and a constant temperature throughout the fluid domain. A k-ε turbulence model is chosen to solve the closure problem of the RANS equations. Figure 1 shows the model dimensions, which are chosen to provide enough clearance between the external boundaries and the iced cable. So that even for the largest possible blockage in the flow, the influence of the boundaries on cable and ice body is irrelevant.
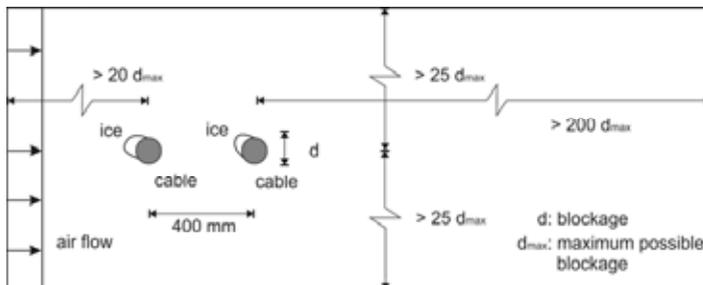
Figure 1: Sketch of the model layout

The mixed stream of air and precipitation particles is described by a one-way coupled two-phase flow. A Lagrangian approach is used to describe the droplet motion in the fluid, meaning that individual particle trajectories are modelled. This approach is used even though it does not provide information about the particle density in the flow field. It is presumed, that there will be a low particle concentration in the flow. Based on this assumption any effect of the particles on the fluid flow is neglected. Therefore, decoupling of the fluid dynamic calculation and the droplet motion description by the Lagrangian method is justified. Newton's second law is the governing equation describing the particle motion. The solver rewrites this second order ordinary differential equation (ODE) into a pair of coupled first order ODE. In each direction it has one equation for velocity and one for location. This system is then solved by a pair of four and five order Runge-Kutta algorithms.

Obviously the droplet diameters in natural precipitation are not uniform. They can be described via droplet spectra stating the fractions of the individual droplet diameters (Langmuir & Blodgett 1946). To calculate the motion for every single diameter fraction of particles would be computationally expensive. Fortunately, for the simulation of transmission line icing it is sufficient to deduce the behaviour of the whole spectrum from the motion of a droplet of medium volume diameter (MDV) (Fu 2004).

The droplet trajectory calculation provides information about the impinging particles, which determine the mass flux on the surface. Once the mass flux is given, the computation of the ice evolution can start. The mass flux can be visualised as a stream tube starting from the undisturbed flow to the surface, limited by the computed droplet trajectories. Within each tube the particles stream from the undisturbed flow towards the surface. The local collection efficiency is the ratio of droplet mass flux in the undisturbed incoming flow to mass flux of droplets impinging on the surface. The developing ice density is determined by empirical equations derived by Bain & Gayet (1982). Mass flux and ice density are used to determine the growth of the ice front. In the full paper experimental and numerical results are given for comparison to verify the icing model.

The presented model shows the influence of tandem arrangements of cables on icing. As to be expected, one can see in Figure 2 that the upstream cable is catching a larger fraction of the particle flux than the downstream cable in its wake. In general, the shaded area decreases with decreasing deflection of the particle trajectories. It means that larger droplets will deflect less due to higher inertia, presuming a flow pattern with the same Reynolds number. Once the upstream cable gets a more streamlined shape due to the ice accretion, the particle trajectories are deflected to a smaller extent when passing the first cable. Thus the mass flux on the downstream cable increases.
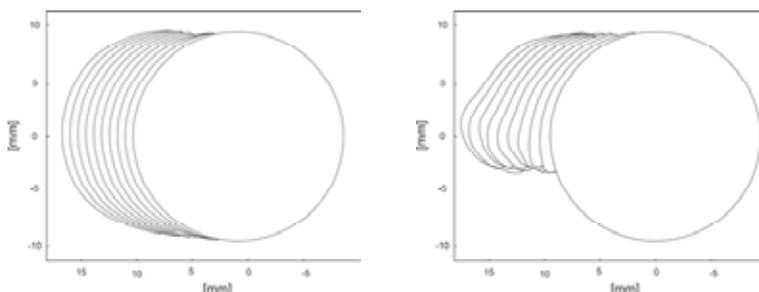
Figure 2: Ice accretion on an upstream (left) and downstream (right) cable with a cable spacing of 400mm. Icing conditions: wind velocity u=10 m/s, characteristic precipitation diameter MDV=75μm, air temperature T=−10°C, cable diameter d=349mm

So far, the model does not account for wet ice growing conditions. Therefore a thermodynamic model will be implemented. Then, further studies should be performed to prove the model validity for a broader range of meteorological conditions beyond the given examples of model verification. Also the relative movement of the individual conductors of the bundle is not considered. The shielding effect on the downstream cable can periodically vanish, when the cables are not in line due to cable oscillation. Different ice loading on the cables leads to deviating sag and thus changes the shielding affect.

REFERENCES

Bain, M. & Gayet, J. F., 1982. Contribution to the modeling of the ice accretion process: Ice density variation with the impact surface angle, *Annals of Glaciology 4*: 19-23

Bendel, W. B. & Paton, D. 1981. A review on the effect of ice storms on the power industry, *Journal of Applied Meteorology 20*: 1445-1449

Bundesnetzagentur für Elektrizität, Gas, Untersuchungsbericht Telekommunikation Post und Eisenbahnen, 2006. *Über die Versorgungsstörung im Netzgebiet des RWE im Münsterland vom 25.11.2005*

Comsol, 2007. *Heat Transfer and Chemical Engineering Model User Guide for Comsol Multiphysics 3.4,* COMSOL AB

Diem, M., 1956. Ice loads on high voltage conductors in the mountains, *Archiv für Meteorologie, Geophysik und Bioklimatologi B7*: 87-95

Fu, P., 2004. Modelling and simulation of the ice accretion process on fixed or rotating cylindrical objects by boundary element method, *Ph.D.,* Thesis University of Quebec

Jones, K. F. 1998. An evaluation of the severity of the January 1998 ice storm in northern New England, *Technical report for FEMA Region 1*

Jones, K. F. 1998. A simple model for freezing rain ice loads, *Atmospheric Research 46*: 87-97

Kießling, F. & Nefziger, P. & Kaintzyk, U., 2001. *Freileitungen: Planung, Berechnung, Ausführung*, Springer

Langmuir, I. & Blodgett, K.B., 1946. A Mathematical Investigation of Water Droplet Trajectories. *AAF Technical Report 5418*

Lämpke, D., 2006. Schadensanalyse an im Münsterland umgebrochenen Strommasten, Bundesanstalt für Materialforschung und Materialprüfung

Llinca, A. & Llinca, F. & Ignat, I., 1996. Numerical study of iced conductors aerodynamics, *7th International Workshop on Atmospheric Icing of Structures*

Lozowski, E. P. & Stallabrass, J. R. & Hearty, P. F., 1983. The icing of an unheated non-rotating cylinder Part 1: A simulation model, *Journal of Climate and Applied Meteorology 22*: 2053-2074

Makkonen, L., 1984. Modelling of ice accretion on wires, *Journal of Climate and Applied Meteorology 23*: 929-939

Makkonen, L., 1989. Estimation of wet snow accretion on strucutres, *Cold Regions Science and Technology 17*: 83-89

Makkonen, L., 1998. Modeling power line icing in freezing precipitation, *AtmosphericResearch 46*:131-142

Makkonen, L., 2000. Models for the growth of rime, glaze, icicles and wet snow on structures, *Phil. Trans. R. Soc. London 358*: 2913-2939

Makkonen, L. & Lozowski, E., 2005. Fifty years of progress in modelling the accumulation of atmospheric ice on power network equipment, *11th International Workshop on Atmospheric Icing of Structures*

Messinger, B. L., 1953. Equilibrium temperature of an unheated icing surface as a function, *Journal of the Aeronautical Sciences 20*: 29-41

Muhlerin, N. D., 1998. Atmospheric icing and communication tower failure in the united states, *Cold Regions Science and Technology 27*:91-104

Poots, G., 1996. *Ice and snow accretion on structures*, Research Studies Press LTD.

Waibel, K., 1956. Die meteorologischen Bedingungen für Nebelfrostablagerungen an Hochspannungsleitungen im Gebirge, *Archiv für Meteorologie, Geophysik und Bioklimatologie B3*: 74-83

Wind tunnel testing of an inclined aeroelastic cable model-Pressure and motion characteristics, Part I

N. Nikitas, J.H.G. Macdonald, T.L. Andersen, J.B. Jakobsen, M.G. Savage, B.R. McAuliffe

Department of Civil Engineering, University of Bristol, UK – N.Nikitas@bristol.ac.uk – Department of Civil Engineering, University of Bristol, UK – John.Macdonald@bristol.ac.uk – Department of Mechanical and Structural Engineering and Material Science, University of Stavanger, Norway – terje.l.andersen@uis.no – Department of Mechanical and Structural Engineering and Material Science, University of Stavanger, Norway – jasna.b.jakobsen@uis.no – Aerodynamics Laboratory, National Research Council Canada, Ottawa, Canada – Michael.Savage@nrc-cnrc.gc.ca – Aerodynamics Laboratory, National Research Council Canada, Ottawa, Canada – Brian.McAuliffe@nrc-cnrc.gc.ca

Keywords: Cable aerodynamics, inclined circular cylinder, critical Reynolds number.

ABSTRACT

Wind-induced vibrations of inclined cables has attracted much attention since 1980's due to large incidents observed in existing cable-stayed bridges, of concern for their structural integrity. Predicting and preventing such large scale motions necessitates a formulation of the driving parameters of such phenomena. It is well established that rain and ice accretion have a major impact as driving conditions but there are cases of dry unstable cable vibrations that unveiled the influence of additional factors not being fully understood yet. Recent treatises ascribe possible driving mechanisms to high reduced wind speed vortex shedding, three-dimensionality of the flow with coherent wind structures propagating in an axial mode and the Reynolds number effect designating the unstable region of flow transitions in shear and boundary layer, from laminar to turbulent, with all these being possibly linked to each other.

   Previous wind tunnel tests, conducted on a 6m aeroelastic model of a full-scale inclined cable model at the National Research Council Canada (NRC), produced data of significant vibrations including a record of seemingly divergent character, see Cheng et al. (2003). Various attempts have been made to explain these and other significant vibrations observed, including through use of pressure tap data from separate wind tunnel tests on a static inclined cable model, see Jakobsen et al. (2003),(2005) and Macdonald & Larose (2008a, b). The current paper deals with a new series of tests,

---

Contact person: N.Nikitas, University of Bristol, Queens Building, University Walk, BS8 1TR, Bristol, UK,
Tel: +44 117 331 7396, Fax: +44 117 928 7783, E-mail N.Nikitas@bristol.ac.uk

using the same large-scale aeroelastic model as previously, but additionally instrumented with pressure taps. Thus unsteady pressure measurements from the actual moving model are employed to incorporate the motion induced forces in the pressure readings (i.e. allow for motion correlated forcing estimates), validate their effect in comparison with previous outcomes and possibly recover the real flow structures that interact with the cable setting it to motion. These tests have been carried out under a collaborative project between NRC, Canada, the University of Stavanger, Norway and the University of Bristol, UK.
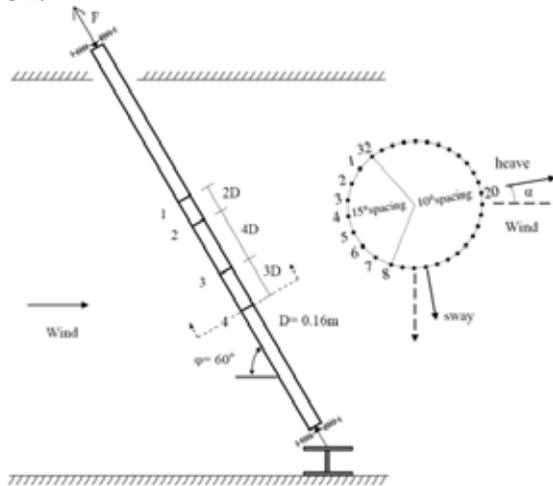
Figure 1: Illustration of the pressure tap arrangement. Cross-sectional arrangement refers to the case of zero rotation of the spring supports i.e. principal axes along and transverse to the flow.

The cable model design adopted typical properties of a full-scale bridge cable, including the mass per unit length (approximately 60kg/m), diameter (D=160mm), surface finish (smooth HDPE duct) and natural frequency (approximately 1.4Hz). It was tested in the 3m x 6m open circuit wind tunnel at NRC, giving an aspect ratio approaching 40, which according to the rationale of Larose et al. (2003) is sufficient for preserving contamination of pressure data by end effects as low as possible. The wind speed range for most tests was 10-40m/s, corresponding to Reynolds numbers of 1.1×10^5 to 4.2×10^5, spanning the critical Reynolds number range.

The cable was mounted on spring supports at either end, allowing motion in "sway" and "heave" directions normal to the cable axis. Damping ratio was of the order of 0.1% i.e. similar to typical values for a full-scale cable without dampers. Since the orientation relative to gravity is assumed not to be important for the aerodynamic behaviour of a dry cable, the three-dimensional geometry of an inclined cable in a skew wind can be transformed into a cable-wind angle, equal to the cable inclination angle in the wind tunnel (φ), and the orientation of the principal vibration axes relative to the cable-wind plane (α). For identical natural frequencies in the two vibration planes, the orientation of the principal axes is arbitrary. However, real cables have slight detuning of the natural frequencies in the vertical and horizontal directions due to the cable sag. This was modelled with slightly different spring stiffnesses of the model in the two directions. With the detuning, the orientation of the principle axes becomes significant. To cover a range of possible geometric arrangements, the cable was tested at three different inclination angles (approximately 60°, 77° and 90°), with the support spring axes in two different orientations for each inclination angle, and with different detuning between the natural frequencies in the two planes.

For each inclination angle, a set of tests was also taken with the model fixed in position, to record the forces on the stationary cylinder. Tests for the inclinations of 60° and 90° were conducted with the

hole around the top end of the cable both open and sealed so as to assess the influence of end conditions. Judging from the attained pressure profiles, small differences of the two cases illustrate that end effects are not important, at least in the region that pressure measurements were recorded.

The instrumentation included 162 pressure taps, in four rings of 32 taps each -see Figure 1- and two longitudinal rows. The displacements and accelerations of each end of the model were measured in the two planes. Since the turbulence of the oncoming wind can be significant for the flow transitions in the critical Reynolds number range, the entry wind velocity was measured with a dynamic three component cobra probe.

Large responses, of primarily across wind character, were observed only for the inclination of $\varphi=60°$ for both the cases of spring rotations examined (namely $\alpha= 0°$ and $54.7°$). Large vibrations were restricted to a certain range of wind speeds, thus being distinguished from classical galloping vibrations, which occur for all wind speeds exceeding a certain threshold. The maximum amplitudes observed were of the order of 1.5D but this was limited from the physical setup, so it is likely that the aerodynamic limit state, if one exists, would be larger. In any case responses were elliptical with the major axis at an angle to the spring directions, indicating coupling action induced by aeroelastic forces.

The regions of large response were positioned close to the end of the drag crisis and were always accompanied by a considerable mean lift force as previously indicated by Larose et al. (2003). This implies that the sudden appearance of the lift force has to be involved in any possible driving mechanism to be suggested. The pressure measurements show asymmetric pressure cross sectional profiles indicating one-sided laminar bubbles. This behaviour as described e.g. by Zdravkovich (1997) comes to rise only in the critical Reynolds number regime.
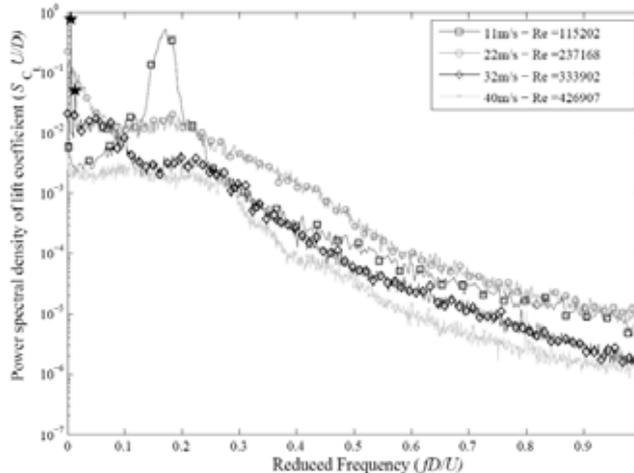
Figure 2: Spectra of the lift coefficient average from the four pressure rings. Star-marked points, 32m/s case, show the resonant peaks that correspond to the structural frequency of 1.4Hz and to twice this value. Model setup, $\varphi=60°$ and $\alpha= 0°$.

Spectra of the fluctuating lift coefficient for different wind speeds (thus different Reynolds numbers) are given in Figure 2. The structural response was small except in the case of 32m/sec. For the subcritical range, represented by the wind speed of 11m/sec, clear vortex shedding can be indentified at a Strouhal number of 0.17 corresponding to 12Hz. As pointed by Jakobsen et al. (2003) the inclination broadens the observed forcing in relation to the normal wind case. Increasing Reynolds number, leads to vortices being less coherent, thus reducing the power of the spectra in that region. On the other hand some very low frequency components emerge, which could be described as high reduced wind speed vortex shedding. For the record exhibiting response ($U= 32$m/sec) it seems

that this low frequency forcing locks in to the structural frequency and large motion builds up, while conventional vortex shedding is indistinguishable. In the supercritical regime (U= 40m/sec) this phenomenon is suppressed and only low level broadband excitation near the conventional vortex shedding peak remains.

The lift force above was calculated as the average from all four rings. For further elucidating the relationship between rings, lift and drag correlation functions have been estimated. Figure 3 gives an illustration of such functions showing the systematic force delays along the cable span. Such delays imply some flow structures propagating in the axial direction. When transformed to a propagation velocity, these delays compare very well with the axial component of the free-stream wind velocity.
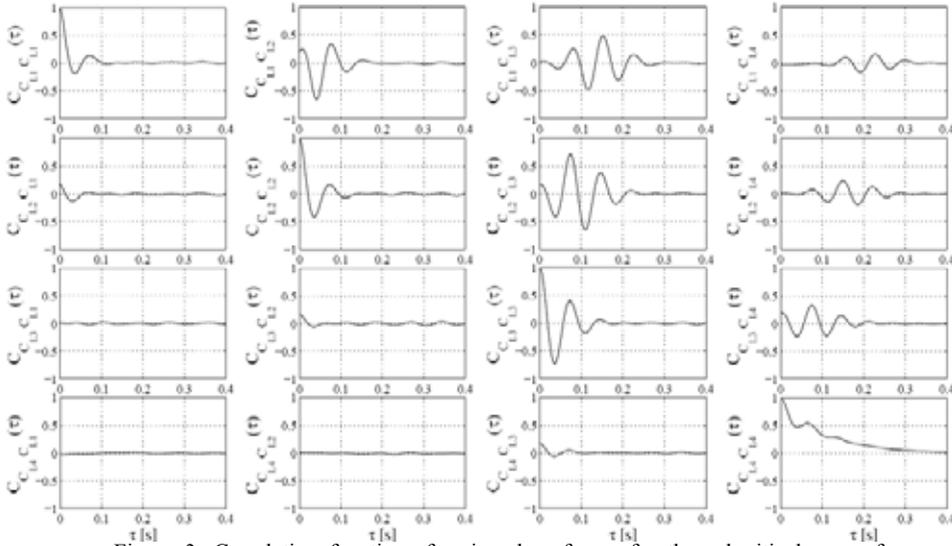
Figure 3: Correlation functions for ring drag forces for the subcritical case of U=12m/sec. Propagation is evidently one-sided. Model setup, φ=60° and α= 0°.

To verify the existence of coherent structures in the acquired pressure data and map changes in the mechanisms that drive the cable, Principal Component Analysis was performed. Further probability density distributions for the pressure fluctuations were evaluated for all taps and their qualitative differences were examined.

REFERENCES

Cheng S., Larose G.L., Savage M.G., Tanaka H. (2003). "Aerodynamic behaviour of an inclined circular cylinder", Wind Structures, (6), 197-208.

Jakobsen J.B., Larose G.L., Savage M.G. (2003). "Instantaneous wind forces on inclined circular cylinders in critical Reynolds number range", 11th Int. Conf. on Wind Engineering, Lubbock, Texas, 2165-2173.

Jakobsen J.B., Andersen, T. L., Larose G.L. (2005). "Interpretation of wind forces monitored on inclined stationary cylinder in critical Reynolds number range in relation to observed aeroelastic model response", 6th International Symposium on Cable Dynamics, Charleston, 287-294.

Macdonald J.H.G., Larose G.L. (2008a). "Two-degree-of-freedom inclined cable galloping - Part 1: General formulation and solution for perfectly tuned system", J. Wind Eng. Ind. Aerodynamics, (96), 291–307.

Macdonald J.H.G., Larose G.L. (2008b). "Two-degree-of-freedom inclined cable galloping - Part 2: Analysis and prevention for arbitrary frequency ratio", J. Wind Eng. Ind. Aerodynamics, (96), 308–326.

Larose G.L., Savage M.G., Jakobsen J.B. (2003). "Wind tunnel experiments on an inclined and yawed circular cylinder", 11th Int. Conf. on Wind Engineering, Lubbock, Texas, 279-286.

Zdravkovich M.M. (1997). *Flow around circular cylinders Vol 1*: *Fundamentals*. Oxford University Press, Oxford.

Wind tunnel testing of an inclined aeroelastic cable model- Pressure and motion characteristics, Part II

J.B. Jakobsen, T.L. Andersen, J.H.G. Macdonald, N. Nikitas,
M.G. Savage, B.R. McAuliffe

Department of Civil Engineering, Department of Mechanical and Structural Engineering and Material Science, University of Stavanger, Norway – jasna.b.jakobsen@uis.no – Department of Mechanical and Structural Engineering and Material Science, University of Stavanger, Norway — terje.l.andersen@uis.no – University of Bristol, UK – John.Macdonald@bristol.ac.uk – Department of Civil Engineering, University of Bristol, UK – N.Nikitas@bristol.ac.uk – Aerodynamics Laboratory, National Research Council Canada, Ottawa, Canada – Michael.Savage@nrc-cnrc.gc.ca – Aerodynamics Laboratory, National Research Council Canada, Ottawa, Canada – Brian.McAuliffe@nrc-cnrc.gc.ca

Keywords: Circular cylinder, Surface pressures, Critical Reynolds number range, High reduced wind speed cable vibrations

ABSTRACT

This paper deals with dry cable vibrations in critical Reynolds number range and the associated wind forcing mechanism. Recently, the issue has been studied in the third phase of the experimental campaign at the National Research Council Canada (NRC), in research cooperation with the University of Bristol and the University of Stavanger. The investigation focused on the simultaneous surface pressure and cable dynamic response measurements, in the attempt to bridge the gap between separate data on i) cable aeroelastic response and ii) surface pressures on a fixed cable model, available from two previous test campaigns, see e.g. Cheng et al. (2003) and Larose et al. (2003).

More details about the background for the experimental campaign, model arrangement and test programme are given in the companion paper by Nikitas et al. (2008). The key data for the tests are summarized in Table 1. The aspect ratio given is for the case of cable inclined at nominal 60°, which

Table 1. Test parameters

Diameter D [mm]	Aspect ratio L/D [-]	Rough-ness ε/D	Wind-cable angle φ [˚]	Wind speed U [m/s]	Turb.intens. I_u [%]	Eigen-freq. f [Hz]	Damp. ratio ξ [-]	Modal mass [kg]
161.7	38	6.5 x 10⁻⁶	59.3, 76.7, 90.9	9.0 –40.0	~0.5	~ 1.4	~0.1%	403.5

Contact person: J. B. Jakobsen, University of Stavanger, N-4036 Stavanger, Norway, Phone: +47 51831666, Fax: +47 51831750, E-mail: jasna.b.jakobsen@uis.no

is the main cable orientation studied. Relative surface roughness is estimated for the high-density polyethylene tube covering the steel pipe, excluding handling marks and occasional accumulations of insects. Damping ratio given is for small amplitudes, app. 5% of the cable diameter.

As described by Nikitas et al. (2008), both tests with freely responding and fixed cable section have been performed. This paper treats general characteristics of surface pressure field and the associated forces recorded, throughout the critical Reynolds number range. These characteristics are then discussed in relation to observed vibrations, in the attempt to identify certain conditions representative for the events of vigorous cable response. As reported by Nikitas et al. (2008), in various test configurations the cable vibrations took place primarily in the across-flow direction, at high-reduced wind velocities, e.g. $U/(fD) \sim 130$ in one of the cases. Among the three inclinations tested, cable at nominal inclination of 60º appeared to be most susceptible to vibrations. In Figure 1 mean pressure distributions on four rings along the model are displayed for four different wind speeds, corresponding to four different Reynolds numbers.
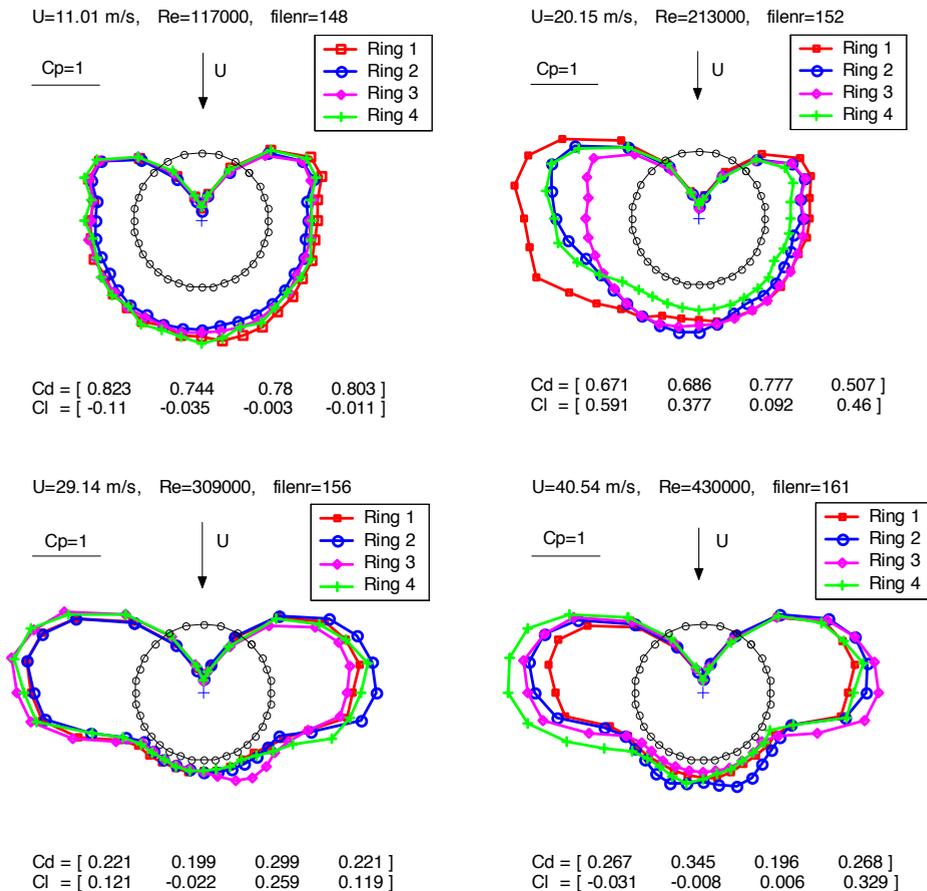
Figure 1: Mean pressure coefficients around cylinder at different Reynolds numbers, fixed cylinder inclined at 59.3º to the approaching flow

   The data were recorded with the fixed model and the hole in the ceiling of wind tunnel working section closed off. The hole, through which the model protruded to its upper support, was open during the dynamic tests. Surface pressures on the fixed model were also surveyed with the top hole open, and mean pressures are not found to depart significantly from those for the data with the hole closed. Since the latter spans a wider range of wind speeds, it is chosen for the illustration in Figure 1. Ring 3 is located halfway between the floor and the ceiling of a 6m high and 3 m wide wind tunnel working section. Ring 2 and 1 are, respectively, four and six diameters above and upstream along the cable, while Ring 4 is three diameters below/downstream of Ring 3. In the figure, magnitude of the pressure coefficient of Cp=1 is given the same length as the cable radius. The "drag" and lift coefficients quoted are for the forces *normal* to the cable axis, in the along- and across-wind direction respectively. The upper left part of Figure 1 displays a uniform pressure distribution along the cylinder span, in the upper subcritical flow regime. In this regime, lift fluctuations are dominated by a more or less regular vortex-shedding process. To a modest extent, drag force fluctuates with twice the frequency of the vortex shedding, but its dominant variations are at very low frequencies as governed by base pressure fluctuations. These variations, also found in case of the cylinder perpendicular to the flow, reflect the three-dimensional character of the flow, visualized also as random modulations of the lift force.

   The upper right hand part of the figure gives pressure distribution at the threshold of the so-called TrBL1 regime according to Zdravkovich (1997), in which a laminar bubble forms at one side of the cylinder, as turbulence progresses from the shear layer to the boundary layer. A quite large variation in pressure distribution along the cable is evident in Figure 1. While Ring 3 appears to be only in the starting stage of transition from laminar to turbulent flow in boundary layer regime, the so-called TrBL0 regime, pressures on the remaining rings are on the way to their asymmetric distributions associated with the establishment of the single laminar bubble. As opposed to a uniform mean pressures distribution on the leeward side of the cylinder found on the cylinder perpendicular to the flow, quite a large variation of base pressures as well as pressure distributions around the cylinder base line is evident in Fig. 1. This indicates a pronounced three-dimensional character of these transitions.

   For a slightly higher wind speed, time-histories of the lift coefficient, defined with reference to the free stream wind speed, were recorded as given in Figure 2. Positive lift coefficient points to the left in Fig.1. Interestingly the lift coefficient on Ring 2 changes from mainly positive to mainly negative with the slight increase in wind speed. In this state, the low frequency components are present and quite coherent, together with a rather disrupted vortex shedding process. Occasional change of the local mean lift coefficient by even approx. 0.7 on Ring 2, at around 51 s, or by approx. ± 0.4 on Rings 1 and 3, can be thought of as flow oscillations between the no bubble and one bubble regime. The low frequency part of the signal encompasses the model translational eigen-frequencies of around 1.4 Hz, i.e. a period bellow 0.7s. In Jakobsen et al. (2003) and (2005), it has
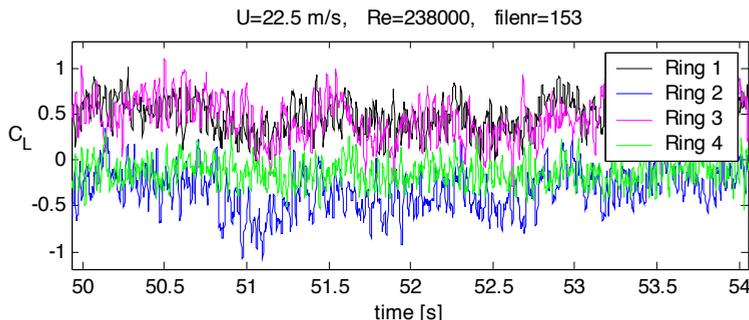
Figure 35: Time histories of lift coefficient at Re=238000,
fixed cylinder inclined at 59.3° to the approaching flow

been argued that such a wind forcing might give rise to cable vibrations. Cheng et al. (2003) monitored the across-flow cable vibrations with the amplitude of 0.4D in such a Reynolds number range, in the first phase of the wind tunnel investigation. In the most recent wind tunnel tests, Nikitas et al. (2008), the across-flow vibrations with the amplitude of about 0.1D were identified in the same wind speed range, in the repeated test configuration. The vigorous changes in the lift coefficients are also associated with the rapid change in the drag coefficient. Andersen et al. (2008) pointed out that a number of large cable response episodes, in the first phase of the wind tunnel study (Cheng et al. (2003)), were associated with the largest derivative of the normal force coefficient with respect to Reynolds number.

The largest cluster of significant cable response, in the most recent wind tunnel tests, have been observed at higher wind speeds than the Reynolds number region discussed. In most cases, large vibrations appear to take place around the minimum drag coefficient. Inspection of force coefficient time series and their power spectral densities indeed suggests that the vibrations may occur as the flow transits in its final stage from the single to the two-bubble regime, with increase in wind speed. Flow visualisations with smoke also confirmed that the wake was very narrow, i.e. that the vibrations took place in the vicinity of the TrBL2 regime In Fig. 1, the lower left plot depicts pressure distribution on the cylinder just prior to formation of the uniform TrBL2 flow regime. Region of the flow around Ring 3 is the last one to develop the stable second bubble. The TrBL2 flow regime designates the formation of two laminar bubbles, one on each side of the cylinder, and the associated narrowing of the near wake. Once the TrBL2 regime has been established, a vortex shedding process with a Strouhal number of about 0.24 is found to take place in the narrowed wake. At $Re=4.3\times10^5$, in the lower right hand side of Fig.1, the flow is most likely in the TrBL3 regime, in which the separation bubbles are disrupted and fragmented. The process is linked to a varying base pressure along the cylinder span. A variable distribution of the pressures in the rear of the cylinder also points on the highly three-dimensional shape of the near wake and the separation lines.

In the full-length paper, the link between the specific vibration events and the general characteristics of the flow around the inclined circular cylinder described above will further be expended on, complementing the work presented by Nikitas et al. (2008).

REFERENCES

Andersen, T.L. and Jakobsen, J.B.,(2008), "Static Response Coefficients form Dynamic Cable Response", Sixth Int. Coll. on Bluff Body Aerodynamics and Applications, Milano, Programs and Summaries, 249-252.

Cheng S., Larose G.L., Savage M.G. and Tanaka H. (2003). "Aerodynamic behaviour of an inclined circular cylinder", Wind and Structures, (6), 197-208.

Jakobsen J.B., Larose G.L. and Savage M.G. (2003). "Instantaneous wind forces on inclined circular cylinders in critical Reynolds number range", 11th Int. Conf. on Wind Engineering, Lubbock, Texas, 2165-2173.

Jakobsen J.B., Andersen, T. L. and Larose G.L. (2005). "Interpretation of wind forces monitored on inclined stationary cylinder in critical Reynolds number range in relation to observed aeroelastic model response", 6th International Symposium on Cable Dynamics, Charleston, 287-294.

Larose G.L., Savage M.G. and Jakobsen J.B. (2003). "Wind tunnel experiments on an inclined and yawed circular cylinder", 11th Int. Conf. on Wind Engineering, Lubbock, Texas, 279-286.

Macdonald J.H.G. and Larose G.L. (2008). "Two-degree-of-freedom inclined cable galloping - Part 1: General formulation and solution for perfectly tuned system", J. Wind Eng. Ind. Aerodynamics, (96), 291–307.

Nkitas, N., Macdonald, J.H.G., Andersen, T.L., Jakobsen, J.B., Savage, M.G., McAuliffe, B.R., (2008), "Wind tunnel testing of an inclined aeroelastic cable model-Pressure and motion characteristics, Part I", Abstract for 5th European and African Conference on Wind Engingeering, to be held in Florence 2009

Zdravkovich M.M. (1997). "Flow around circular cylinders", Vol 1, Fundamentals, Oxford University Press, Oxford, UK.

A comparison between dry cylinder galloping and rain-wind induced excitation

O. Flamand, O. Boujard

CSTB – 11 rue H. Picherit 44000 Nantes France olivier.flamand@cstb.fr, LRPC– 23 Avenue de l'amiral Chauvin 49136 Les Ponts de Cé France olivier.boujard@developpement-durable.gouv.fr

Keywords: cable, galloping, vibration

ABSTRACT

Over the last decades, aerodynamics of inclined cables has become a crucial issue with the development of long-span cable-stayed bridges. In recent years, several phenomena at the origin of vibrations of stay-cables have been identified by full-scale observations and wind-tunnel tests. Among those, research has particularly focused on the rain-wind-induced vibration phenomenon which leads to large amplitudes with relatively moderate wind and rain. Nevertheless, wind induced vibrations of inclined cables without rain have also been reported at full scale and as results of wind-tunnel tests, for instance by Larose (2003) who introduced the idea of dry inclined cable galloping. They explained that a circular cylinder in the critical Re range shows a fast drop in the drag coefficient with increasing Re, due to reattachment of the turbulent boundary layer and formation of laminar separation bubbles, on each side of the cylinder.

This paper presents a comparison between various wind tunnel measurements realized on dry circular cables at full scale with various surface roughnesses, opening the way to an explanation of convergence between rain-wind induced excitation and dry cable galloping.

FULL-SCALE EVIDENCE OF DRY INCLINED CABLE GALLOPING

A medium size 400m span cable-stayed bridge, facing the Atlantic ocean in Brest (France) was monitored for more than 3 years. Boujard (2007) used these data for his PhD showing that few excitation processes can give rise to cable vibrations on the same bridge, among which numerous vibrations occurred without rain or icing and for a wind speed range clearly different from vortex shedding excitation. Wind direction and speed during these occurrences corresponds to the parameters reported by Larose (2003) for the dry cable galloping.

Some of the characteristics of the observed vibrations, such as wind critical directions, spectral content of displacements and instability in a limited range of wind speeds, are similar to those of the rain-wind-induced vibrations, but the phenomenon also occurs without rain. Following the assumption of a possible link between RWIV and dry cable galloping wind tunnel tests were performed with the aim to better understand the phenomenon of inclined cables vibrations.

Contact person : Olivier Flamand, CSTB – 11 rue Henri Picherit – 44000 Nantes – France
phone : (33) 2 40 37 20 46   fax : (33) 2 40 37 20 60   E-mail : olivier.flamand@cstb.fr

PRESSURE MEASUREMENTS ON A STEADY INCLINED CYLINDER AT FULL SCALE IN WIND TUNNEL

A first experimental campaign of pressure measurements at the surface of a steady 25° inclined circular cylinder was performed in 2006 in the CSTB 2.1m (H) x 4m (W) atmospheric wind-tunnel.

A 0.2 m diameter and 4.7 m long PVC cylinder was used. Simultaneous measurements of time varying surface pressures were made by use of 64 pressure tapes arranged in 2 cross-sectional rings located in the middle of the model.

For yaw angle $10<|\beta|<30°$, the critical Reynolds number range was characterized by 2 steep variations of the lift coefficient CL with Reynolds number Re, correlated with a decrease of the drag coefficient CD (with $CL = FL/(0.5\rho DU²)$, $CD = FD/(0.5\rho DU²)$, and: FL and FD the lift and drag forces, ρ the air density, D the cable diameter, U the wind velocity). Figure 2 shows that these variations of CL are caused by a sudden increase of the negative pressures on the lower part of the cylinder, followed by the formation of a second negative pressure lobe on the upper part for Re > 3.10^5.

R_e = 2.33 10^5   R_e = 2.80 10^5   R_e = 3.47 10^5
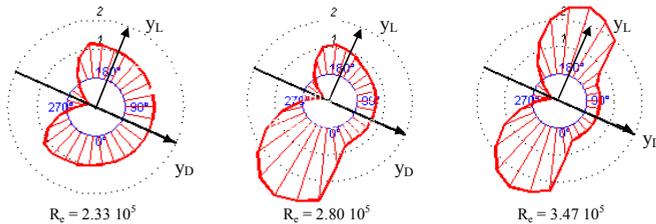
Figure 2: Evolution of the mean pressure distribution around the cylinder with Reynolds number for yaw angle $\beta = -17.5°$ (upper ring)

These characteristics of the pressure distribution are quite similar to those observed at the surface of a cylinder normal to wind direction in the critical regime, when the transition to turbulent flow occurs in the separated shear layer and induces a re-attachment on one side of the cylinder (TrBL1 regime). Nevertheless in the present case the first negative pressure lobe always appears on the same side of the cylinder and leads to higher values of CL compared to previous results. This result may be attributed to the influence of the inclination angle, which is responsible for an asymmetry of the section "as seen" by the wind.

PRESSURE MEASUREMENTS ON A STEADY CYLINDER NORMAL TO ONCOMING FLOW AT FULL SCALE IN WIND TUNNEL

A new cylindrical model was designed and tested perpendicular to wind tunnel flow in January 2009 in order to study the effect of surface roughness only and with a higher number of sensors.

New model was build from a PVC tube diameter 200mm thickness 8.5mm the roughness of which was made homogeneous by sanding with sand paper number 400 in the cylinder axis direction. This surface was denoted smooth, its roughness Ra=30μm measured by optical roughness sensor.

The same 2.1mx4m wind tunnel was used, the new model was placed vertical and therefore its length was 2.1m. It was equipped with 4 series of 30 pressure tapes arranged in 4 cross sectional rings placed 0.6m, 1.0m, 1.2m and 1.5m from wind tunnel ground, the tapes on one pressure ring were separated by 12°. Pressure rings were denoted 1, 2, 3 and 4, from ground to ceiling.

Figure 3 shows that drag crisis was attained at wind speed Re=2.17E5 and spectra of the near wake velocity measured by hot wire anemometers also showed vortex shedding suddenly vanished. The lift force jump from null to a value similar to drag force when passing from the subcritical to the super critical state.
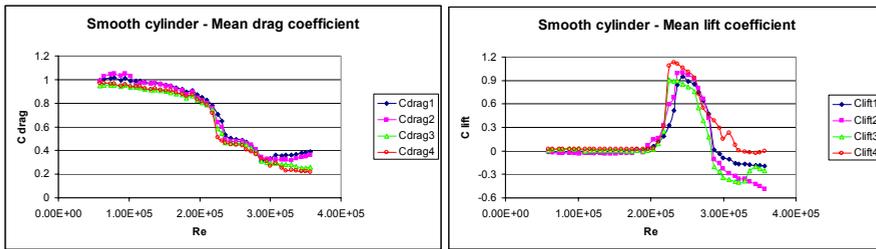
Figure 3: Mean drag and lift coefficients calculated by integration from the four pressure rings, denoted 1 to 4 from ground to ceiling, for a smooth surface cylinder.

The first model surface processing achieved was a homogeneous increase of surface roughness with sand paper n°60, leading to Ra=50μm.

Measurements in wind tunnel showed once again that a lift force exists with varied directions at various locations. Two pressure tapes rings out of four measured the same non symmetrical pressure distribution, the crisis regime appearing at a lower wind speed than for the smooth cylinder, Re=1.8E5. Pressure fields show the jump to TrBL1 regime occurred either on one side of the model or the other side, at various wind speeds, depending on the pressure tape ring considered.
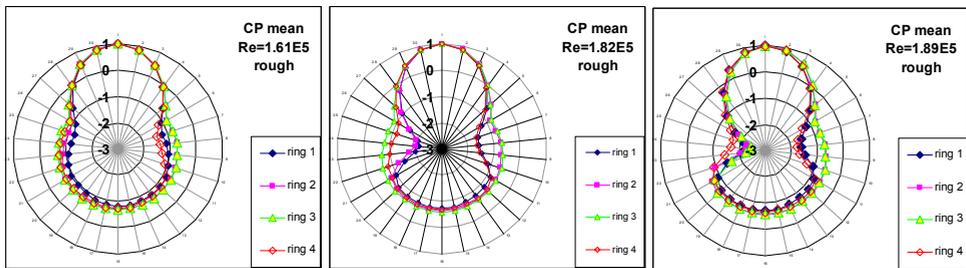
Figure 4: Mean pressure coefficients evolution with Re from the four pressure rings, denoted 1 to 4 from ground to ceiling, rough surface model.
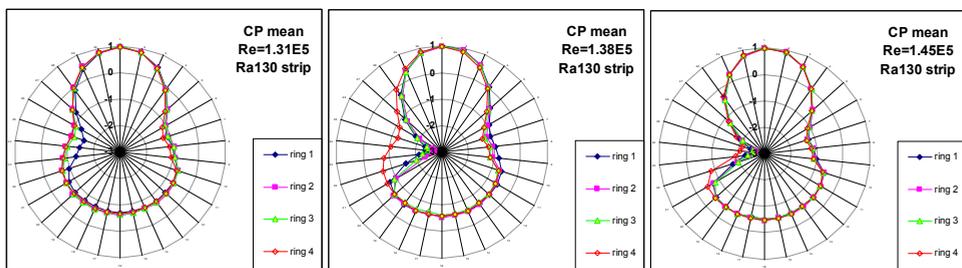
Figure 5: Mean pressure coefficients evolution with Re from the four pressure rings, denoted 1 to 4 from ground to ceiling, Ra130 stripped surface model.

In order to check the influence of surface roughness on the TrBL1 regime emergence, the model was made more rough by use of 2mm wide x 0.13mm thick stripes glued following cylinder axis. These stripes were placed every 12°, at midway between two pressure tapes, continuous along the 2.1m of the model. This configuration was denoted "Ra130" by reference to the roughness thickness, 130μm. The TrBl1 regime appeared at Re=1.38E5.

The same test was performed for a roughness twice thicker, obtained by gluing a second stripe upon the first one. This configuration was called "Ra260", the critical regime was attained for Re=1 E5. Increasing roughness apparently reduced the sharpness of the non symmetrical state generated by TrBL1 regime: the detached area was less pronounced, what lead to less negative pressures and an integrated lift force smaller than for smaller roughness.

EFFECTIVNESS OF AN HELICAL STRAND AROUND THE CABLE

The cable model with a "smooth" surface, circular cylindrical shape 200mm diameter, perpendicular to wind flow, was equipped with an helical strand similar to the one designed to avoid rain-wind induced vibrations on bridge stays, Flamand (1995). Two wires of diameter 2.2mm were wrapped around the cable model with a helix step of 600mm on each wire. This means the distance between two protrusions due to the wires along the model axis was 300mm.

The pressure pattern around the model showed that the TrBL1 regime never happened. When passing the critical state the four pressure measurement rings detected a passage from subcritical to TrBL2 regime without having a single bubble formed on one side only of the cylinder.

This result is liable to explain why the helical strand is efficient against RWIV. If this shape suppress TrBL1 regime, there is no more lift force due to pressure asymmetry around the circular cylinder. This assumption still needs to be checked on model inclined to wind.

CONCLUSION

The instable and not symmetrical pressure pattern observed at full scale in wind tunnel on an inclined dry smooth surface cylinder was also observed on a smooth and on a rough cylinder normal to wind flow. The transition from subcritical to TrBL1 regime was seen to be responsible for a strong fluctuating lift force, the jump from one state to the other appearing for minor change in Reynolds number. If the direction of the lift force was randomly distributed for wind normal to the model, on an inclined cylinder the detached bubble was fixed on one side only. The cable surface roughness proved to be a very important parameter of TrBL1 triggering, a large roughness being suitable in mitigating the phenomenon. A helical wire wrapped around a smooth cable also reduced the amplitude of the TrBL1 regime and consequently the lift force generated on the cable. This could explain the efficiency of helical wires for mitigation of the rain-wind induced excitation of bridges inclined stays. These results also show the possibility of a strong ling between RWIV and dry galloping of cables.

REFERENCES

Boujard, O. (2007). "Etude du phénomène de galop des câbles inclinés secs appliquée aux haubans de ponts, application au pont de l'Iroise " PhD thesis, University of Nantes, in french.

Boujard, O., Grillaud, G. (2007). "Inclined stay-cable vibrations: confrontation of full-scale measurements and quasi-steady analysis of wind-tunnel tests", Proceedings of 12th International Conference on Wind Engineering, Cairns, Australia

Cosentino, N., Flamand, O. & Ceccoli, C. (2003). "Rain-wind induced vibration of inclined stay cables. Part I: Experimental investigation and physical explanation". Wind and Structures 6, 471-484.

Larose, G.L., Savage, M.G., Jakobsen, J.B. (2003). "Wind tunnel experiments on an inclined and yawed circular cylinder in the critical Reynolds number range". Proceedings of 11th International Conference on Wind Engineering, Lubbock, Texas, USA, 1705–1712.

WIND EFFECTS ON SHIELDS AND VEHICLES

Experimental study of statistical and spectral characteristics of wake flow around the rear view side mirror of a passenger car

Jeong-Hyun Kim*, Yong Oun Han* and Byoung-Duk Lim*

*School of Mechanical Engineering, Yeungnam University, Gyeongsan, Gyeongbuk, 712-749, Korea
davidkim@ynu.ac.kr, yohan@yu.ac.kr, bdlim@yu.ac.kr

ABSTRACT

In order to study the turbulent structure around the rear view side mirror of a passenger car, statistical and spectral measurements were carried out in a blow down wind tunnel. The Reynolds number of the flow based on the height of the mirror (d) was 2×10^5. Velocity profiles and energy spectra were obtained by using a single normal hot wire probe at 0.7d, 1,4d and 2.8d downstream of the rear view mirror, respectively. The values of higher order moment such as skewness and flatness factors measured behind the tip region of the mirror were significantly deviated from ideal Gaussian behavior due to the vortex shedding. Spectral analysis showed that most of the energy was concentrated in the lower frequencies and the magnitude of energy distribution was reduced with downstream. The dominant frequency of vortices shed from the mirror housing was measured in the range of 24 to 42 Hz.

Rear view side mirror is a conventional device to obtain the rear sight of the driver. At high speed, it has the problems related to intrinsic noise induced by pressure fluctuation near the separation line on the mirror housing and rotational vibration of the mirror surface due to the vortex shed from the mirror housing.

O Dolek et al (2004) published that noise radiated from the mirror was induced by an intrusion of the mounting support and abrupt curvature of the mirror housing. These noise generated from the mirror housing was easily detected when the car has a negative yaw angle (T. Lounsberry, 2007). S. Watkins (2004) analyzed aerodynamic parameter inducing mirror surface vibration through the flow measurement vicinity of the A-Pillar. Also, in order to reduce the magnitude of pressure fluctuation on the mirror surface, the increase of the shroud length of the mirror housing was suggested by S. Watkins (2007). Han and Kim (2007, 2008) characterized the mirror wake with mean vertical velocities and vortex body frame interaction. However, there is little work to measure vortex shedding frequency and turbulent structure of wake flow around the mirror.

The objective of this paper was to experimentally study statistical and spectral characteristics of turbulent flow on the downstream wake of the rear view mirror.

To establish the real flow condition, one of the side walls of the blow down wind tunnel was replaced by the side skin of the real scale car including the rear view mirror which positioned at the

Contact person: Jeong-Hyun Kim, Graduate Assistant, School of Mechanical Engineering, Yeungnam University, Gyeongsan, Gyeongbuk, 712-749, Korea, +82 53 810 3255 and +82 53 810 4627. E-mail davidkim@ynu.ac.kr

center of wind tunnel test section. Also, in order to prevent the blockage effect, slit-wall was attempted in the other side wall of the test section with calibration to get kinematic similarity.

To obtain the wake properties of the mirror, hot wire anemometry (KANOMAX 7000 series) was utilized with single normal hot wire sensor. Wake properties were measured at the three downstreams (0.7d, 1.4d and 2.8d) to the main flow direction on the middle plane of the mirror wake as shown in figure 1. The figure 1(a) shows profiles of axial velocities which indicate the flow accelerations in the vicinity of the mirror housing, upper and lower sides, respectively at 0.7d position. Hot wire probe does not get the negative streamwise velocity, and therefore flow velocities of the inner near wake are not correct. However flow acceleration in the vicinity of the mirror housing and velocity profiles in other planes are still meaningful. In the final paper, presence of recirculation zone measured by LDV system will explains well characteristics of the near wake. Profiles of the rms fluctuation velocity plotted in the figure 1 (b) show that maximum velocity fluctuations occur in the vicinity of the upper and bottom tip region of the mirror. Also, the values of skewness and flatness factors as shown in the figure 1 (c)(d) are significantly deviant from ideal Gaussian random distribution (S=0, F=3) due to the vortex shedding from the mirror housing.
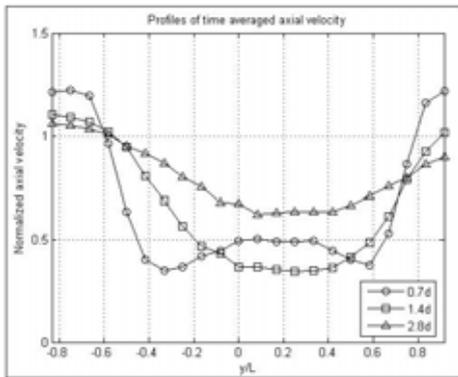
(a) Profiles of the axial velocity   (b) Profiles of rms fluctuation velocity
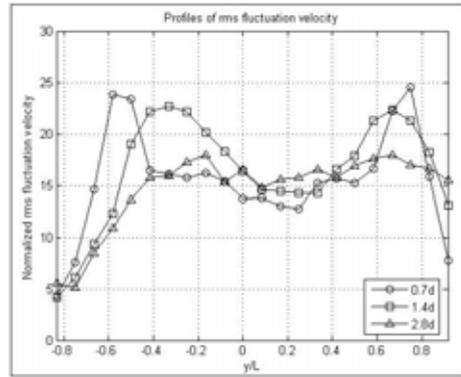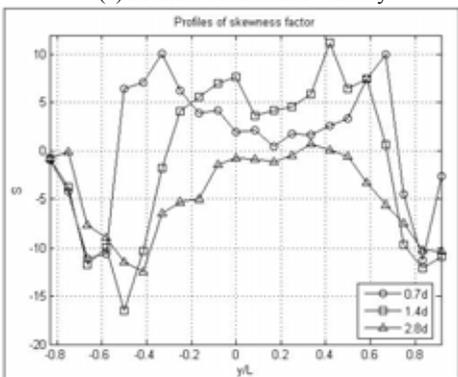
(c) Profiles of skewness factor   (d) Profiles of flatness factor
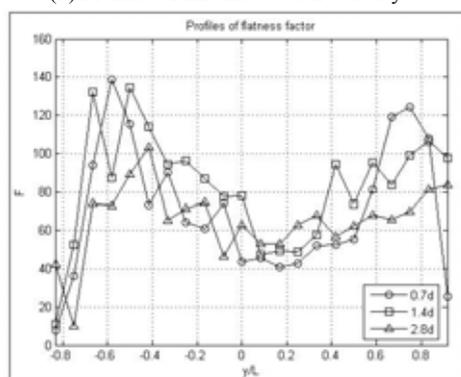
Figure 1: Variation of wake flow properties with the three downstream positions.

To analyze the energy characteristics of fluctuating velocity in the mirror wake, dynamic signal analyzer (35670A, HP) was utilized. Their results measured at three vertical sections are shown in figure 2 (a) (b). The spectra plots indicate that fluctuating velocity are broad band type and most energy is located in low frequencies. There is a decrease in the power spectrum as the downstream is

increased.

To measure the dominant frequency shed from the mirror housing, single normal hot wire probe was utilized at the significant fluctuation location. Until 0.3d to 1.0d downstream behind the upper tip of the mirror housing, dominant shedding frequency was measured in the range of 24 to 42 Hz. It seems likely that dominant energy of mirror surface vibration due to the vortex shedding was in that range. The corresponding Strouhal number was 0.11 to 0.2.
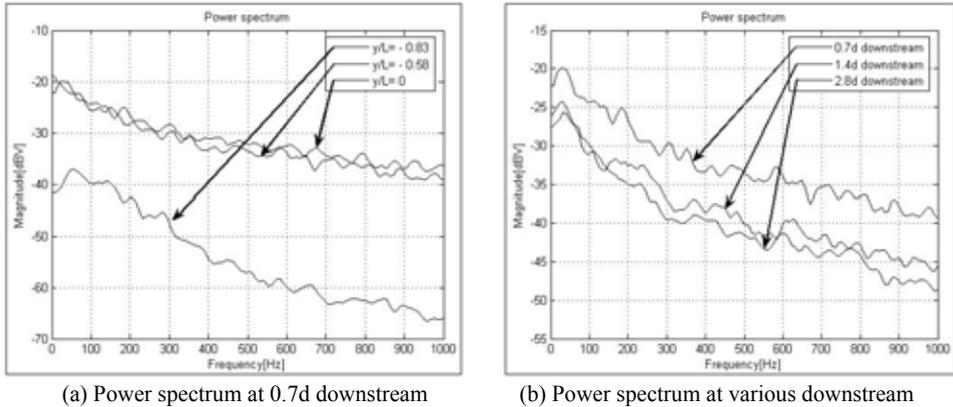
(a) Power spectrum at 0.7d downstream   (b) Power spectrum at various downstream
Figure 2: Power spectrum for both 0.7d downstream and various downstream

Hot wire measurements were conducted at three vertical sections with the Reynolds number of 2×10^5. Statistical and spectral properties measured at three downstreams showed that significant vortex shedding phenomenon as the aerodynamic parameter to induce mirror surface vibration was induced from the mirror housing. At this range of Reynolds number, dominant shedding frequency was 24 to 42 Hz. Detail observations including the contour plots of the statistical and spectral properties and the correlation test to measure the vortex size will be discussed in the final paper.

REFERENCES

O. Dolek, G. Ozkan and I. B. Ozdemir (2004). "Structures of flow around a full scale side mirror of a car with relevance to aerodynamic noise", Journal of Automobile Engineering, Volume 218 Number 10, 1085-1097.

T. Lounsberry, M. Gleason and M. Puskarz (2007), "Laminar Flow Whistle on a Vehicle Side Mirror", SAE Paper 2007-01-1549, V 116-6, Detroit, Michigan, USA.

S. Watkins (2004), "On The Causes of Image Blurring in External Rear View Mirrors", SAE Papers 2004-01-1309, SP-1874, Detroit, Michigan, USA.

R. Jaitlee, F. Alam and S. Watkins (2007), "Pressure Fluctuations on Automotive Rear View Mirrors", SAE Paper 2007-01-0899, SP-2066, Detroit, Michigan, USA.

Y. O. Han (2007). "Research for the Low Noise Rear View Side Mirror of a Passenger Car", Report of Aerodynamic & Turbulence Research Laboratory.

Y. O. Han, J. H. Kim, I. H. Hwang, J. B. Seo, B. H. Lim and U. H. Jung (2007). "Wake Flow Characteristics around the Side Mirror of a Passenger Car", KSME Conference, BEXCO Building, Busan, Korea.

Jeong-Hyun Kim, Yong Oun Han, Min Hwa Lee, In Ho Hwang and Ui Hun Jung (2008), "Surface Flow and Wake Structure of a Rear View Mirror of the Passenger Car", BBAA VI, Milan, Italy.

The struggle against the wind on the motorway

A.Krecak Tomic, P.Sesar

Civil Engineering Institute of Croatia – ana.krecak@igh.hr – J. Rakuse 1, 10000 Zagreb, Croatia -

Civil Engineering Institute of Croatia - J. Rakuse 1, 10000 Zagreb, Croatia

Keywords: wind speed measurements, traffic safety, traffic interruptions due to wind blowing, evaluation of the measured data

ABSTRACT

This paper intention is to present the problem of traffic safety on A1 motorway in Croatia, which is exposed to gusty north wind "bora". Due to safety requirements, motorway section on the slopes of the Velebit Mountain, passing near the Adriatic coast is frequently closed for traffic. This requires adequate protection using specially designed structures. The aim of building wind protection structures is to reduce closing of traffic and maintain a safe traffic flow in case of strong wind.

So called test sections with three types of wind protecting structures were built next to the motorway. Testing is done in order to evaluate their efficiency, mostly by measuring wind speed reduction on the motorway. Results of measurements are also intended to be used for establishing safety criteria on the motorway in case of strong wind. The aim of the project is to define solutions for achieving approximately uniform wind speed distribution along the motorway. Maintaining absolute protection along the motorway was never observed. It is not possible due to many reasons, among others it is not profitable and structurally not achievable. Acceptable level of protection means decrease of number of hours when motorway is closed for traffic and reduction of penalty due to the

---

Contact person: M.Sc.Ana Krecak Tomic, Address: Civil Engineering Institute of Croatia, J. Rakuse 1, 10000 Zagreb, Croatia; Phone: 00385 1 6125 880; Fax: 00385 1 6125 826.

E-mail *ana.krecak@igh.hr*

same reason.

This paper will present results of dynamic measurements. A term dynamic measurement denotes measurements of the wind speed with vehicle equipped with measurement set driving along the motorway. It enables better understanding of real wind influence on the vehicle in motion. Measurements are done by means of measurement set which includes ultrasonic wind speed and direction sensor which is fixed on the car roof, odometer and laptop which notes measured data. This unique measurement procedure will be described.
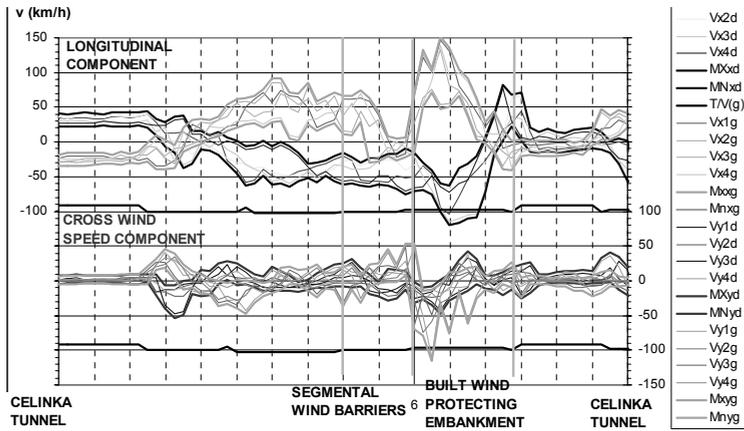
Figure 1: Measured three-second wind speed obtained during four measurement series

Figure 1 shows partial view on the measured data on the motorway A1 where some wind protection structures were already built as the first phase of this project. Motorway is highly curved and surrounding relief directs wind in such a way that wind speed peaks occur which is not desired.

Measured three-second cross wind speed behind the segmental barriers is under 40 km/h, which is not causing slip or vehicle instability. Behind the embankment, the situation is significantly different – there is not only strong longitudinal, but also strong cross wind speed (over 100 km/h). This is a serious problem for vehicle stability, especially because strong cross wind blows on the short part of the motorway lane (about 50 meters long). Few accidents were caused by non-uniform traffic conditions on that short part of the motorway. It must be pointed out that accidents happened while the motorway was closed for motorcycles.

It is obvious that the first phase of built wind protection structures does not fulfill the principle of achieving approximately uniform driving conditions along the motorway. Therefore the project goes on and new types of wind protection structures are proposed. Some solutions will be shown.

REFERENCES

Holmes, J.D. (2007). *Wind loading of Structures*. Taylor &Francis Group, London and New York.

Wang, D. et al. (2006). "Wind speed criteria of traffic safety on a long trans-oceanic bridge". Proc. IABSE Symposium "Responding to tomorrow's challenges", Budapest.

Bajic, A. (2003). Expected airflow regimen on the Sveti Rok (South) – Maslenica motorway route. *Gradjevinar* 55 (2003) 3, 149 – 158 (in Croatian).

Experimental investigation on the force induced by a high speed vehicle passing by a traffic sign

A. Sanz-Andres, C. Gragera, J. Meseguer, F. Zayas

1: Professor, Universidad Politécnica de Madrid (IDR /UPM) E.T.S.I. Aeronauticos, 28040 Madrid, Spain – angel.sanz.andres@upm.es – 2: Assistant Professor, Universidad de Extremadura Escuela de Ingenierías Industriales, 06071Badajoz, Spain– cgragera@unex.es– 3: Professor, Universidad Politecnica de Madrid (IDR /UPM) E.T.S.I. Aeronauticos, 28040 Madrid, Spain –j.meseguer@upm.es– 4: Professor, Universidad de Extremadura Escuela de Ingenierías Industriales, 06071Badajoz, Spain–fzayas@unex.es

Keywords: *Non-steady loads; Train; Traffic sign.*

ABSTRACT

The aim of this paper is to present a new experimental facility developed and tuned with the purpose of carrying out tests to measure the forces produced by a moving vehicle on a fixed object, like a traffic sign or a human body placed close to the track or road where the vehicle is moving along.
 The force on an object placed close to the vehicle path have received a wide attention in the literature (Gerhardt & Krüger (1998), Cali & Covert (2000), Quinn, Baker & Wright (2001), Johns & Dexter (1998) Sanz-Andres & Santiago-Prowald (2002), Sanz-Andres et al (2003)) both under experimental and theoretical points of view. Sanz-Andres et al (2003) showed that the initial variation of the force can be explained by using a simple potential model, based on assumptions which were shown to be valid to this application. It should be pointed out that it is not the aim of this facility to study the effect of the slipstream or the wake generated by the vehicle, only to study the initial phase, when the potential flow can be assumed, to explore the range of validity of potential flow theoretical models.
 The idea is to avoid as much as possible the realisation of experiments on tracks or roads, and replace them with tests on a lab, which show some obvious advantages: comfort, convenience, repeatability, accessibility, affordability, just to mention a few. The facility devised (Figs. 1 and 2) is based on a rotating arm (like the first aerodynamic test facilities, before wind tunnels were developed). At the tip of the arm the vehicle mock-up is firmly supported. The rotation of the arm creates the linear motion of the vehicle along a circular path. The object carrying the force generated by the passing vehicle is supported by two load cells carefully mounted in a rigid structure, to obtain a first resonant frequency high enough to allow good measurements. One load cell measures the longitudinal force component and the other one the transversal force component. The rotating arm is 1.8 m in length, and allows to obtain linear speed in the range 0 to 7 m/s. The typical size of the object tested is some 4 cm wide and 20 cm high, and the vehicle size is some 0.2 m x 0.2 m cross section and

Contact person: 1st Author, Professor, Universidad Politécnica de Madrid (IDR /UPM), E.T.S.I.Aeronauticos, 28040 Madrid, Spain, telephone +34913366353 FAX +34913366363.   E-mail angel.sanz.andres@upm.es

0.5 m length.

The force acting on the sign is very small, asking for very sensitive load cells. So that special care is needed in the operation of the facility.

A relatively large number of tests has been already performed in order to develop the facility, to tune it, and check for repeatability. The results are reasonably promising. The aim of this paper is to show some of the results obtained, concerning the passing of several types of objects by vehicles of different types.

An example of these tests is shown in Figs. 3 and 4. In this case, a box-like vehicle (a parallelepiped with square 0.2 m x 0.2 m cross section, and 0.46 m length) passes by a rectangular flat plate (0.025m width, 0.2m high). The plate is placed parallel to the vehicle motion. In Fig. 3 the net force variation with time, at three different speeds, is shown, while in Fig. 4 the same results are plotted but in dimensionless form: the force coefficient variation with dimensionless time $T = tU/d$ where U is the vehicle speed, d is the distance from the plate centre to the vehicle symmetry plane. The force coefficient C_f is the force made dimensionless with the dynamic pressure relative to the vehicle, and the plate area.

It can be shown in Fig. 4 that the passes at different speeds collapse to just one line when plotted in dimensionless variables, but only in the initial phase, when potential flow related to the nose effect can be assumed, from $T = -4$ to $T = 0.3$. Then the potential flow continues with the effect of the end of the vehicle (first negative peak) and the elasticity of the load cells, until the start of the wake effect (irregular force variation which appears after the second positive peak). Note that in these cases the most important effect is the pass of the nose and the vehicle's end, and the effect of the wake is smaller.

The same behaviour is shown in different configurations, as it will be presented in the final version of the paper.

REFERENCES

Gerhardt, H.J. , Krüger, O. (1998). "Wind and train driven air movements in train stations", J. Wind Eng. Ind. Aerodyn. 74–76, 589–597.

Cali, P.M. , Covert, E.E. (2000) . "Experimental measurements of loads on an overhead highway sign structure by vehicle-induced gusts", J. Wind Eng. Ind. Aerodyn. 84 , 87–100.

Quinn, A.D. , Baker, C.J., Wright, N.G. (2001). "Wind and vehicle induced forces on flat plates. Part 2: vehicle induced force", J. Wind Eng. Ind. Aerodyn. 89, 831–847.

Johns, K.W. , Dexter, R.J. (1998) ."The development of fatigue design load ranges for cantilevered sign and signal support structures", J. Wind Eng. Ind. Aerodyn. 77&78, 315–326.

Sanz-Andres, A. , Santiago-Prowald, J. (2002) ."Train-induced pressure on pedestrians", J. Wind Eng. Ind. Aerodyn. 90, 1007–1015.

Sanz-Andres, A. , Santiago-Prowald, J. , Baker, C.J. , Quinn, A.D. (2003) . "Vehicle induced loads on traffic sign panels", J. Wind Eng. Ind. Aerodyn. 91, 925–942.
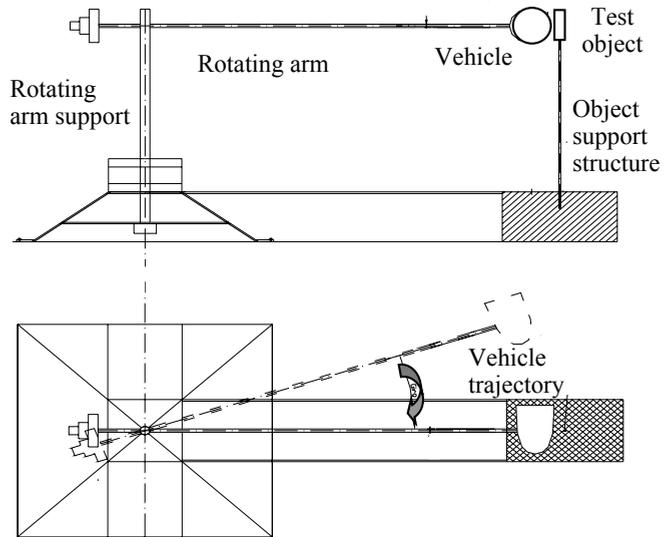
Figure 1: Sketch of the experimental set-up.
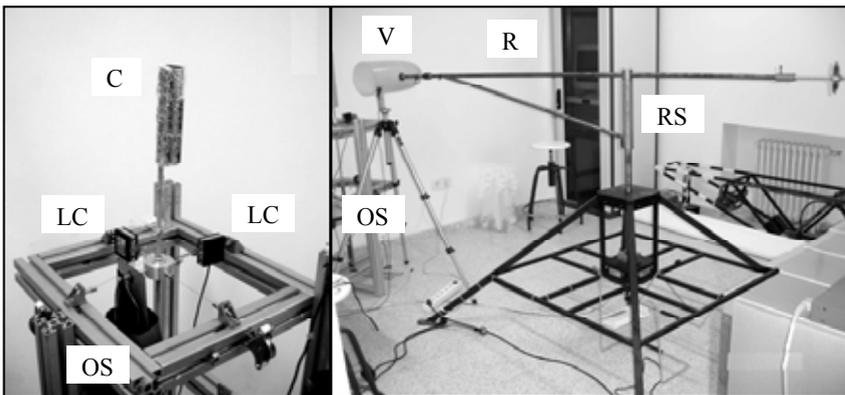
Figure 2: Sketch of the experimental set-up. V: vehicle. R: rotating arm. RS: rotating arm support. C: cylinder. LC: Load cell. OS: Object support structure.

Ensayo 080801_CB_P2
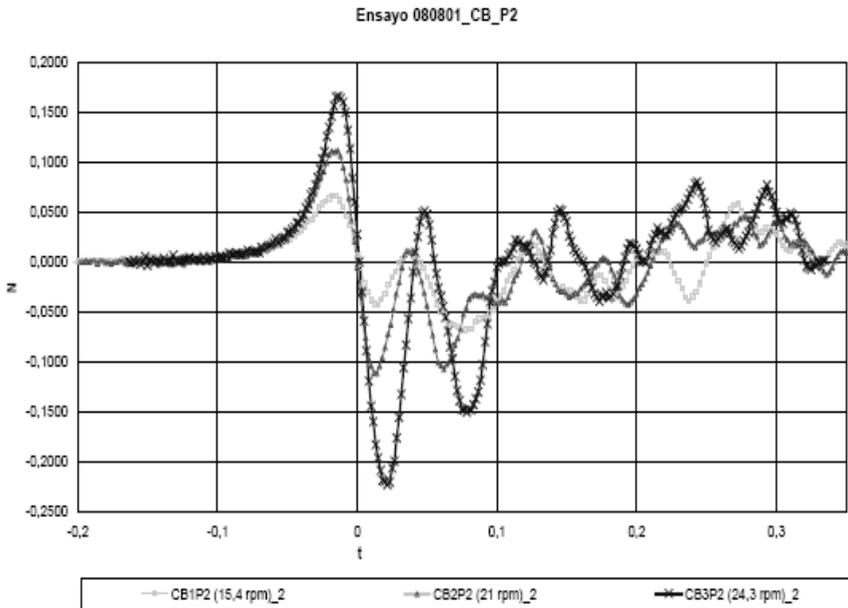
Figure 3: Variation of the transversal force acting on the plate N [N] with the time [s]. The legend indicates the angular rotation speed of the centrifuge arm. The plate is placed parallel to the motion direction.

Ensayo 080801_CB_P2
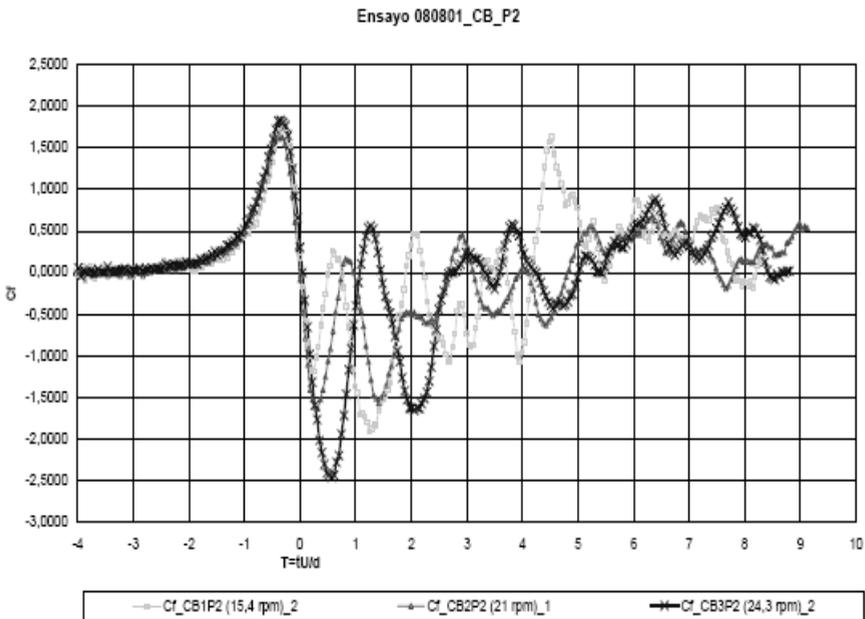
Figure 4: Variation of the transversal force coefficient C_f with the dimensionless time $T = tU/d$. The legend indicates the angular rotation speed of the centrifuge arm. The plate is placed parallel to the motion direction.

A probabilistic assessment of infrastructural measures against overturning risk of railway vehicles under stochastic crosswind

C. Wetzel, C. Proppe

wetzel@itm.uka.de / proppe@itm.uka.de – Institut für Technische Mechanik, Universität Karlsruhe (TH), 76128 Karlsruhe

Keywords: crosswind, gust model, overturning probability, vehicle dynamics, wind-fences.

INTRODUCTION

Aerodynamic loads have a great impact on the dynamics of ground vehicles, and especially the crosswind stability of railway vehicles is very important as this is a major safety issue. Fortunately, overturning of vehicles occurs not very often but unfortunately if it happens there is a high risk of fatalities and of badly injured persons. Consequently, crosswind stability has become a crucial topic of modern high-speed and light-weight railway design that cannot be solved easily because counter-measures are very expensive. Typical counter-measures are for example putting wind-fences along the track, ballasting the vehicles, reducing the driving velocity and altering the aerodynamic shape of the car. Wind-fences are very expensive and are disliked by drivers and passengers as they obstruct the view on the landscape. Ballasting modern light-weight designs is also very unwanted and reducing the velocity is not possible because of tight schedules. A new, less wind sensitive, design is mostly infeasible as it is fixed very early during the product development process and wind tunnel experiments are very expensive.

Therefore sufficient crosswind stability is an important approval criterion for railway vehicles. In many countries the approval process foresees safety predictions based on worst case scenarios, where uncertainties are taken into account by means of safety factors and comparison with reference vehicles. In recent years probabilistic methods have been introduced, which are coming from the

---

design of offshore wind turbines, Bierbooms & Cheng (2002). Following these investigations a stochastic wind excitation, based on a probabilistic gust scenario, is proposed and the crosswind stability is quantified by failure probabilities which are computed using reliability methods. The failure probability is presented in the so-called probabilistic characteristic wind curve (PCWC), which has been introduced by Carrarini (2004).

To determine the influence of the mentioned, different counter-measures, a sensitivity analysis with respect to the stochastic variables has been undertaken and the most important effects are shown. This implies the change of the failure probability under variation of the heights of wind-fences along the track.
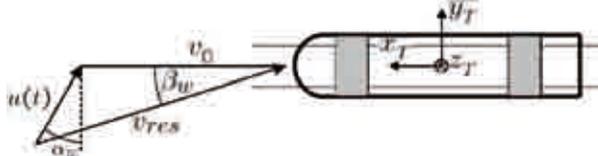
Figure 1: Sketch of the wind excitation vector acting on a multi-body railway vehicle system

AERODYNAMIC CONSIDERATIONS

The railway vehicles are operating in the atmospheric boundary layer, where the turbulent wind velocity is often modeled as a Gaussian process, described by the von Kármán power spectral density (PSD). For a point moving with constant velocity v_0 through the turbulent, spatial wind field this PSD has to be modified according to Cooper (1984). In this paper, the wind forces and wind moments are modeled as concentrated loads, which can be expressed by the equations

$$F_{y,z} = \frac{1}{2}\rho A_c C_{y_T, z_T}(\beta_w) v_{res}^2, \quad M_{x,y,z} = \frac{1}{2}\rho A_c l_c C_{mx_T, my_T, mz_T}(\beta_w) v_{res}^2, \tag{1}$$

where C_{y_T, z_T} and C_{mx_T, my_T, mz_T} are the aerodynamic coefficients of the vehicle, A_c is a characteristic area, l_c is a characteristic length and ρ is the density of air. The aerodynamic coefficients are nonlinear functions of the angle of attack β_w and in this work are assumed to be stochastic variables with a coefficient of variation of $\delta = 0.1$. The resultant velocity is calculated by the quadratic functional

$$v_{res}^2 = v_0^2 + u^2(t) + 2u(t)v_0 \sin\alpha_w, \tag{2}$$

which means, that the wind loads are not Gaussian anymore but follow a non central chi-square-distribution. Because of the spatial dimension of the vehicles, every point on the surface sees a different wind velocity and therefore at that point a different pressure is acting. This pressure distribution is taken into account by an averaging of the wind loads over the side area of the vehicle. This approach leads directly to the aerodynamic admittance function $\chi^2(f)$, which is suitable in considering the transient behavior of the wind excitation, Baker (2003), see figure 2.

Overturning of a vehicle comes always along with high gust wind speeds and so it is possible to reduce the turbulent wind process to an artificial gust model. The gust scenario is modeled according to the recently introduced constrained-simulation approach, Bierbooms & Cheng (2002),

$$u(t) = \left(u_0 + u'(t)\right) + u_B(t - t_B)\left(A - u'(t_B)\right) - \frac{\dot{u}_B(t - t_B)\dot{u}'(t_B)}{\ddot{u}_B(t_B)}, \tag{3}$$

where

$$u_B(\Delta t) = \exp\left[-\frac{1}{2Tu_0}\sqrt{\left(C_{u'x}v_0\Delta t\sin\alpha_w + u_0\Delta t\right)^2 + \left(C_{u'y}v_0\Delta t\cos\alpha_w\right)^2}\right] \tag{4}$$

is the gust characteristic with duration T, amplitude A and coherence parameters $C_{u'x}, C_{u'y}$.

A sketch of the gust characteristic and a simulated gust scenario are displayed in figure 3. The gust amplitude and the gust duration are considered as stochastic variables with a half-Gaussian and a conditional lognormal distribution, respectively, following the results of Delaunay & Locatelly (1990).
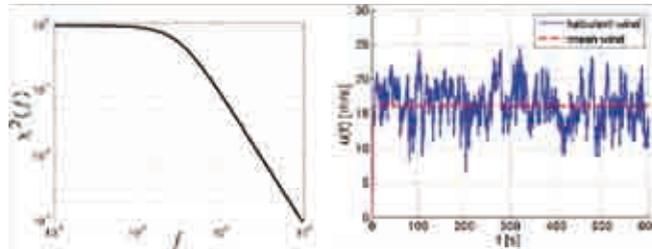
Figure 2: Admittance function of the railway vehicle (left) and turbulent crosswind velocity process (right)
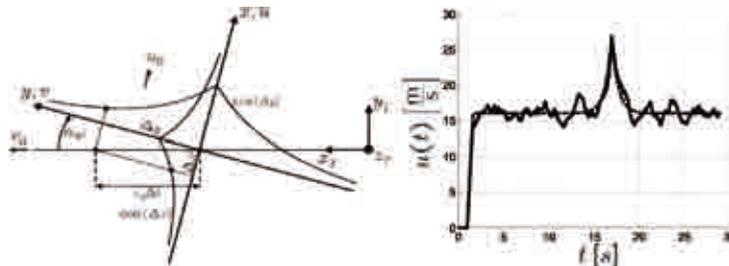
Figure 3: Sketch of exponential gust (left) and gust scenario with superposed turbulence (right)

PROBABILISTIC ANALYSIS

After the transformation of the physical, stochastic variables $C_{()_T}$, A and T to standard normally distributed variables $\underline{z}$ the overturning probability for a gust event

$$P_G(u_0, v_0, \alpha_w) = \int_{\Omega_f} f(\underline{z}) d\underline{z} \tag{5}$$

can be computed as a function of u_0, v_0 and α_w, where Ω_f describes the set of all combinations of $\underline{z}$, which lead to failure of the vehicle and $f(\underline{z})$ is the probability density function. The evaluation of the failure probability P_G can be done by means of semi-analytical reliability procedures (FORM) or by efficient Monte Carlo Simulations, Pradlwarter et al. (2007).

RESULTS

Using the introduced gust scenario, the failure probability of the railway vehicle model has been computed, neglecting in a first approach the superposed turbulent fluctuations.
From figure 4 it becomes clear that a wind blowing right perpendicular to the track is a worst case scenario and that reducing the driving velocity is a good measure to increase the crosswind stability. The different influence of the stochastic variables is displayed in figure 5 on the left, where it can be seen, that the roll moment coefficient C_{mx_T}, the amplitude A and the duration T are most important. Following this result it would be most appropriate to alter the roll moment coefficient to decrease the failure probability. Along the track this can be done by setting up wind-fences. Based on the investigation of Barcala &Mesequer (2007), the failure probability for different heights of

wind-fences has been determined (figure 5 right), where η is the dimensionless height of the wind-fence, scaled with the height of the vehicle. From the displayed results it can be stated that wind fences are a powerful tool to increase the safety. As the overturning risk is commonly expressed in mean wind velocity which can be tolerated by the vehicle, a fence with a normalized height of $\eta = 0.6$ increases the mean wind from 13 to 18 [m/s] ($\Delta u_0 = 5$ [m/s]) at the same magnitude of probability of failure. Hence the proposed method in this paper is able to quantify the influence of infrastructural measures on the overturning risk of railway vehicles on the basis of computed failure probabilities.
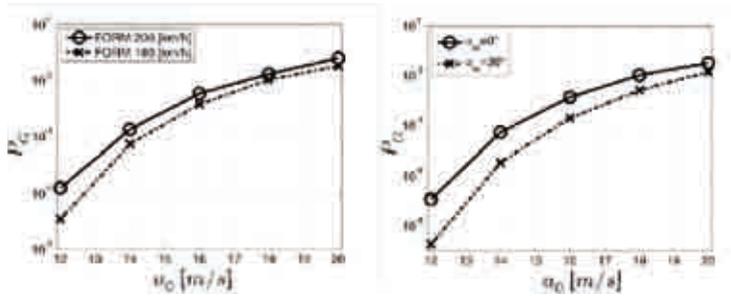
Figure 4: Computed PCWCs of the railway vehicle
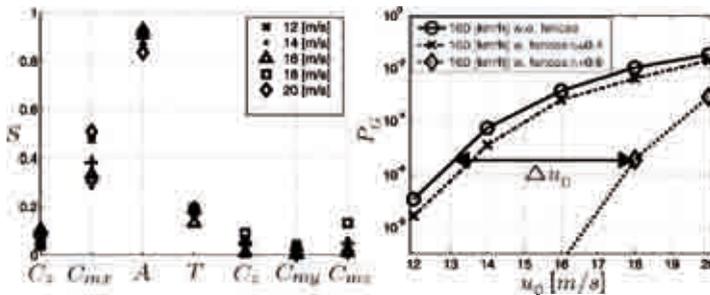
Figure 5: Sensitivity coefficients S (left) and PCWC for different heights of wind-fences (right)

REFERENCES

Bierbooms, W., Cheng, P.W. (2002). "Stochastic gust model for design calculations of wind turbines", Journal of Wind Engineering and Industrial Aerodynamics, 90, 1237-1251.

Carrarini, A. (2004). "A probabilistic approach to the effects of cross-winds on rolling stock", Proc. European Congress on Computational Methods in Applied Sciences and Engineering, Jyväskylä, Finland.

Cooper, R.K. (1984). "Atmospheric Turbulence with Respect to Moving Ground Vehicles", Journal of Wind Engineering and Industrial Aerodynamics, 17, 215-238.

Baker, C.J. (2003). "Some complex applications of the wind loading chain", Journal of Wind Engineering and Industrial Aerodynamics, 91, 1791-1811.

Delaunay, D., Locatelly, J.P. (1990). "A gust model for the design of large horizontal axis wind turbines: completion and validation", Proc. European Community Wind Energy Conference, Madrid, Spain, 176-180.

Pradlwarter, H.J., Schuëller, G.I., Koutsourelakis, P.S., Charmpis, D.C. (2007). "Application of line sampling simulation method to reliability benchmark problems", Structural Safety, 29, 208-221.

Barcala, M.A., Meseguer, J. (2007). "An experimental study of the influence of parapets on the aerodynamic loads under cross wind on a two-dimensional model of a railway vehicle on a bridge", Journal of Rail and Rapid Transit, 221, 487-494.

The effect of unsteady crosswind forces on train dynamic behaviour

C.J. Baker

School of Civil Engineering, University of Birmingham – c.j.baker@bham.ac.uk

INTRODUCTION

Whilst not common, a number of incidents of train overturning in high winds have been reported from around the world. A great deal of work has been carried out in recent years to determine the risk of such accidents occurring and to develop suitable alleviation methods – in the UK for the Advanced Passenger train in the late 1970's, and more recently to investigate the crosswind stability of the Class 390 Pendolino train. A number of pan-European projects have also studied the problem - TRANSAERO, RAPIDE, DEUFRAKO and AOA, and considerable progress has recently been made in the development of European standards and TSI documentation in this field. Work is also underway out in Japan and Korea. Train overturning is not however the only problem caused by high crosswinds. For example the train body can be deflected sideways on its suspension system that can, in extreme circumstances, result in the infringement of the kinematic envelope, or can cause the pantograph (the electrical current collection system) to deflect such that it loses contact with the overhead transmission wire - the so-called pantograph dewirement problem.

To make proper assessments of these effects, it has come to be realised that the static overturning calculations used in earlier investigations are not wholly adequate, and that some account has to be taken of the train dynamic systems, and some simulation of the unsteady nature of wind gusts is also required. Currently a number of alternative recommendations are made concerning how such calculations are carried out – from the use of relatively simple linearised models, through the use of a typical, average, gust profile (the so called "Chinese" hat profile") in multi-body simulations, to the use of simulated wind fields on full dynamic models of vehicles.

It is the purpose of this paper to address some of the fundamental issues associated with work of this sort. It describes in some detail how the fluctuating crosswind force and moment time histories on trains can be specified and calculated. The outline of the calculation procedure is as follows.

- The specification of the wind field seen by a train moving along a track, through the development if a relatively simple computational method.
- The specification of the aerodynamic admittances and weighting function on which the calculation method is based, through an analysis of wind tunnel experimental results.
- The transformation of the admittances and weighting functions that were obtained from static wind tunnel experiments into a form suitable for the application to moving vehicles in the full scale situation.

- The calculation of the aerodynamic forces through the convolution of the velocity time histories with the weighting functions, and the application of these forces to the practical issues outlined above.

    Each of these steps are briefly considered in what follows. In the full paper the application of this method to a number of simplified gust shapes will also be considered that enables certain aspects of the problem to be better understood.

THE SPECIFICATION OF THE WIND FIELD SEEN BY A MOVING TRAIN

We make the basic assumption that the train is travelling along a section of track, with the mean wind direction normal to the track. The mean wind velocity relative to the vehicle $\overline{V}$ and the angle of the wind relative to the train (Ψ) are then given by

$$\overline{V} = (v^2 + \overline{u}^2)^{0.5} \qquad \tan \Psi = \frac{\overline{u}}{v} \tag{1}$$

To examine the effect of unsteady cross winds on train forces and moments we need to generate an unsteady cross wind field as experienced by the train. Ding et al (2008) carried out such a procedure by numerically simulating wind time histories at a large number of points, separated by short distances, along a track, using complex methodologies to ensure that the time series at each point have the correct spectral characteristics, and correlations between the time series at adjacent points have statistics that are consistent with those measured at full scale. This approach proved to be robust and easy to use, although very computationally intensive, with the result that either only short sections of track could be simulated, or that the simulation points had to be widely separated. In this paper however we take a different approach, and simulate one wind time series only, corresponding to the wind velocity at the location of the train at any one instance. This is done by a simple decomposition of the wind spectrum relative to the moving train into a series of sinusoidal velocity variations of random phase, and the combination of these time series into the unsteady velocity time series relative to the train. The spectrum that is used is that of Cooper (1985) which is given by

$$\frac{nS_u}{\sigma_u^2} = \left[\frac{4(nL'/\overline{V})}{(1 + 70.8(nL'/\overline{V})^2)^{5/6}} \right] \left[\left(\frac{\overline{u}}{\overline{V}} \right)^2 + \left(1 - \left(\frac{\overline{u}}{\overline{V}} \right)^2 \right) \frac{0.5 + 94.4(nL'/\overline{V})^2}{1 + 70.8(nL'/\overline{V})^2} \right] \tag{2}$$

σ_u^2 is the variance of the unsteady wind velocity. This is essentially a modification of the well known von Karman spectrum in the plane of reference of a moving vehicle. The values of the spectral density at discrete frequencies n_j are then used to calculate the unsteady wind velocity time series at the position of the train, through the use of the algorithm

$$u_j = \sum \left[2S_u(n_j)\Delta n_j \right]^{0.5} \sin(2\pi n_j t + 2\pi r_j) \tag{3}$$

where r_j is a random number between 0 and 1. A typical time series trace is given in figure 1.

THE SPECIFICATION OF AERODYNAMIC ADMITTANCES AND WEIGHTING FUNCTIONS

Now from the standard definition for force coefficient, one may assume that the fluctuating force, consisting of a mean value $\overline{F}$ and a fluctuating value F', is related to the mean wind velocity $\overline{V}$ relative to the train and a fluctuating value V' by the equation

$$\overline{F} + F' = 0.5\rho A C_F (\overline{V} + V')^2 \tag{4}$$

where ρ is the density of air, A is a reference area and C_F is a force coefficient. This is the quasi-steady

expression and assumes that force fluctuations follow velocity fluctuations. Although it is a good approximation in many circumstances, in reality the quasi-steady assumption does not hold completely, and the force fluctuations do not completely follow the velocity fluctuations as the small scale turbulence in the oncoming wind is not fully correlated over the entire exposed area of a vehicle of a train. To allow for this we introduce the concept of the aerodynamic weighting function (h_F) and equation (7) becomes

$$F' = \rho A C_F \overline{V} \int_0^\infty h_F(\tau) V'(t-\tau) d\tau \tag{5}$$

The weighting function thus allows the time history of a fluctuating force to be obtained from the time history of a fluctuating velocity i.e. it is a time domain operator. It effectively weighs the contribution of fluctuating velocities over the preceding time period to the fluctuating forces. Essentially it is calculated from its frequency domain equivalent, the aerodynamic admittance, X^2. This parameter is effectively a normalised ratio of the force spectrum to the wind spectrum and is more easily measured in experiments. It is found that to a good approximation the admittance can be described by

$$X^2 = \frac{1}{\left(1 + (\overline{n}/\overline{n}')^2\right)^2} \tag{6}$$

where $\overline{n}$ is a normalised frequency and $\overline{n}'$ is a parameter found from experiments. Through a Fourier Transform this results in the following expression for weighting function

$$\overline{h}_F = (2\pi\overline{n}')^2 \overline{\tau} e^{-2\pi\overline{n}'\overline{\tau}} \tag{7}$$

where $\overline{\tau}$ is a normalised time. Typical weighting functions are shown in figure 2.

TRANSFORMATION TO THE MOVING VEHICLE CASE

The normalisation used in the formulation of the above expressions involved the wind tunnel velocity $\overline{u}$. In applying these to the moving vehicle case it is necessary first to assume that the relevant normalisation velocity is the wind velocity relative to the vehicle $\overline{V}$, but also that equation (5) above is replaced by

$$F' = \rho A C_F \overline{u} \left(1 + \frac{1}{2C_F} \frac{dC_F}{d\Psi} \cot\Psi\right) \int_0^\infty h_F(\tau) u'(t-\tau) d\tau \tag{8}$$

This reflects the fact that whilst streamwise velocity fluctuations in the wind tunnel with a stationary do not change the yaw angle of the flow, for a moving vehicle such fluctuations also result in yaw angle variations.

AERODYNAMIC FORCE TIME HISTORIES AND APPLICATION TO PANTOGRAPH DEFLECTIONS

Using equations (7) and (8), the simulated wind time histories and a knowledge of the mean force coefficients, then typical force time histories can be calculated. An example for side force on a typical multiple unit train is shown in figure 3 below, together the results that would have been obtained from a quasi-steady analysis. In addition, if both lift and side forces are simulated, then care must be taken to ensure that they have the correct degree of correlation, as experimental results suggest that the higher frequency ranges of these parameters are not well correlated. This will be explored further in the full paper. The simulated force time histories can then be used in a train dynamic model to calculate train displacements, and thus the relative displacement of the pantograph to the overhead

electric wire. A typical displacement time history is shown in figure 4. The periodic component is because the contact wire position is fixed on the mounting gantries. The random component is due to the combined effects of track roughness and unsteady cross winds. Some of the displacements shown in the figure exceed allowable limits.
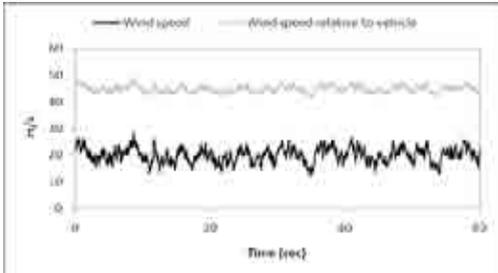
Figure 1 A typical simulated wind velocity time history at the train position
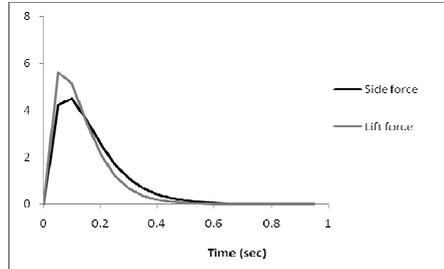
Figure 2 Typical aerodynamic weighting function forms for a high speed train
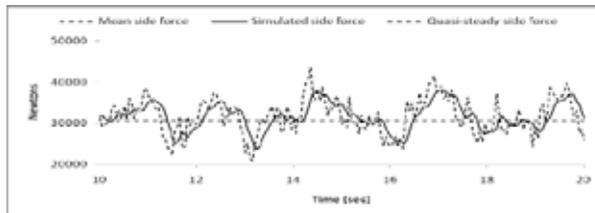
Figure 3 Simulated side force time histories
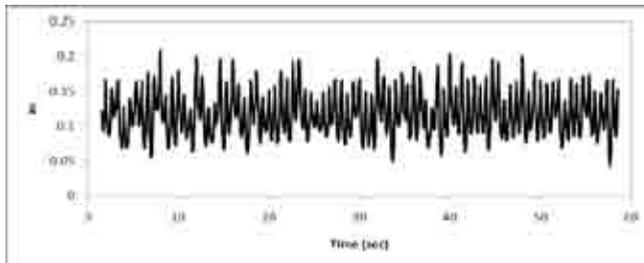
Figure 4 Calculated value of relative displacement of pantograph and overhead contact wire

REFERENCES

Cooper R K (1985) "Atmospheric turbulence with respect to moving ground vehicles", Journal of Wind Engineering and Industrial Aerodynamics 17 215–238.

Ding, Y, Sterling, M and Baker, C J (2008) "Train stability in cross winds, a new approach?" Proceedings of the Institute of Mechanical Engineers Part F: Journal of Rail and Rapid Transport. 222.1.85-97

Numerical and experimental
evaluation of the wind-field behind living shelterbelts

1st A.D.Ferreira, 2nd P.D.Sanchez

Department of Mechanical Engineering – University of Coimbra – almerindo.ferreira@dem.uc.pt –
DEM-Polo II, 3030-788 COIMBRA, Portugal

Keywords: living shelterbelt, aerodynamic barrier, numerical simulation, porous fence

ABSTRACT

Living shelterbelts are often used to create protected areas, being the extension of that zone a function mainly of the porosity and vertical dimension of the barrier.

Living shelterbelts, commonly composed of different kinds of vegetation, are used to control the wind conditions in restricted areas. Some of the cases where shelters are used include farming areas to protect cultures or animals, energy saving, and also to minimize the wind erosion of soil. The same principle is widely used to diminish and control the aeolian erosion of stocking piles, for example in power plants where coal is placed in exposed piles (e.g. Borges & Viegas, 1988, Lee & Lim, 2001, Huang et al, 2005)

The present situation deals with a complex sportive are, where a rowing channel is being planned for high-level competitions.

Analysis of the local revealed unequal windy conditions, across the competition channel, which is unacceptable in terms of sport competitions, specially for high levels.

This work aims the presentation of both numerical and experimental results from the study on the use of a barrier vegetable, two kilometers long, to improve the flow field in an high-competition rowing channel. The work is based on the computational fluid dynamics (CFD) and, for validation of

Contact person: 1st A. D. Ferreira, Department of Mechanical Engineering – University of Coimbra – Polo II, 3030-788 COIMBRA, Portugal, +351 239 790 732, FAX +351 239 790 770.
    E-mail almerindo.ferreira@dem.uc.pt

the numerical results, wind-tunnel tests were performed on a 1:200 scale model. The computational model assumes steady state conditions, and an extra source-term, function of the porosity, is included in the momentum equations to model the pressure loss across the shelter.

Different configurations, using one or more parallel fences, where computationally analyzed, and validated against experimental results, where the erosion technique and discrete measurements, using a seven-hole probe, were used. Figure 1 exemplifies one of the physical configurations studied.

Figure 2 shows some results from the computational modeling, and it depicts the isolines of the wind speed downstream of the shelter-fence, for several configurations.
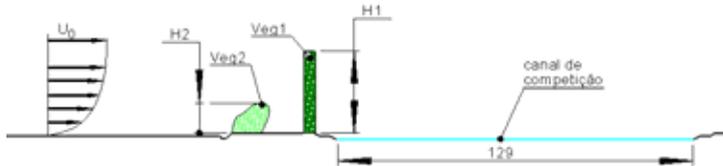
Figure 1: Characterization of one of the shelterbelt configurations studied.

REFERENCES

Borges, A. R., and Viegas, D. X., 1988, Shelter effect on a row of coal piles to prevent wind erosion, Journal of Wind Engineering and Industrial Aerodynamics, 29, 145-154.

Huang, Lee, C.-H., C.-I and Tsai, C.-J., 2005, Reduction of particle re-entrainment using porous fence in front of dust samples, Journal of Environmental Engineering, 131, 1644-1648.

Lee, S.-J. and Lim, H.-C., 2001, A numerical study on flow around a triangular prism located behind a porous fence, Fluid Dynamics Research, 28, 209-221.
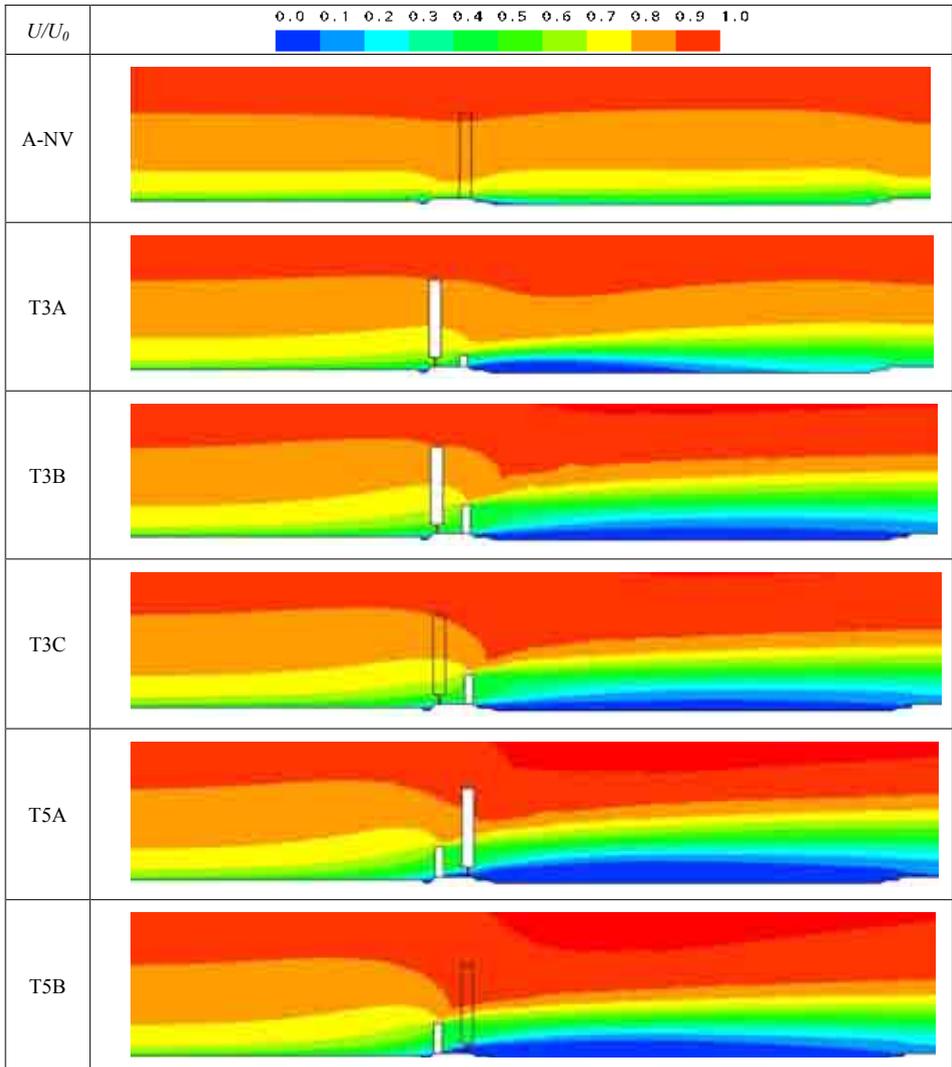
Figure 2: Predicted isolines of the wind velocity for several configurations of the shelterbelt.

AUTHOR INDEX